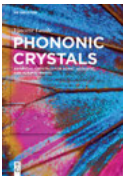# UNCONVENTIONAL LIQUID CRYSTALS AND THEIR APPLICATIONS

Edited by Wei Lee and Sandeep Kumar

Wei Lee, Sandeep Kumar (Eds.)
Unconventional Liquid Crystals and Their Applications

Also of interest

Phononic Crystals.
Artificial Crystals for Sonic, Acoustic, and Elastic Waves
Laude, 2020
ISBN 978-3-11-063728-1, e-ISBN 978-3-11-064118-9

Intermetallics.
Synthesis, Structure, Function
Pöttgen, Johrendt, 2019
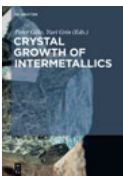ISBN 978-3-11-063580-5, e-ISBN 978-3-11-063672-7

Electrons in Solids.
Mesoscopics, Photonics, Quantum Computing, Correlations, Topology
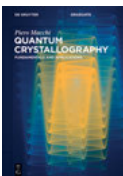Bluhm, Brückel, Morgenstern; von Plessen, Stampfer, 2019
ISBN 978-3-11-043831-4, e-ISBN 978-3-11-042929-9

Crystal Growth of Intermetallics
Gille, Grin, (Eds.) 2019
ISBN 978-3-11-049584-3, e-ISBN 978-3-11-049678-9

Quantum Crystallography.
Fundamentals and Applications
Macchi, 2021
ISBN 978-3-11-060710-9, e-ISBN 978-3-11-060712-3

Unconventional Liquid Crystals and Their Applications

Edited by
Wei Lee and Sandeep Kumar

DE GRUYTER

Editors
Prof. Dr. Wei Lee
National Yang Ming Chiao Tung University
College of Photonics
301 Gaofa 3rd Road
Tainan 711010
Taiwan
wlee@nctu.edu.tw

Prof. Sandeep Kumar
1. Raman Research Institute
C.V. Raman Avenue
Bangalore 560080
India
skumar@rri.res.in

2. Department of Chemistry
Nitte Meenakshi Institute of Technology (NMIT)
Yelahanka
Bangalore 560064
India

Preface

Liquid crystals have been known for more than a hundred years. In the twenty-first century, we are all more or less acquainted with liquid crystals, as the number of liquid-crystal displays (LCDs) is greater than the number of human inhabitants on the planet. There is hardly anyone on the earth who does not use LCD-based devices such as electronic watches, calculators, phones, laptop computers, flat-panel televisions, and the like. Apparently, the ubiquitous liquid-crystal devices have become part of our everyday life. Liquid crystals represent a fascinating and delicate state of matter that combines both order and mobility from the molecular level to the macroscopic scale. Due to the growing interest in the field during the past six decades, liquid-crystal science and technology has received much attention in the communities of chemistry, physics, biology, engineering, and nanoscience.

Liquid-crystalline materials which deviate from conventional design principles and molecular systems, especially those employed beyond display applications, can be classified as unconventional liquid crystals. This book aims to provide an overview of the fast sprouting subfield of unconventional mesophases. It focuses on the recent developments of most charming, emerging, and rapidly evolving areas in the field of liquid crystals beyond conventional materials and device applications. A complete description of all principal aspects within one volume is virtually impossible. As such, we hope that the book can render a representative impression of noticeable evolution and research achievements in the field even if there are missing pieces.

We have collected 15 chapters covering different respects of unconventional mesogens or mesogenic mixtures. A general introduction is given in Chapter 1 entitled "Introduction: From Conventional to Unconventional Liquid Crystals" to bridge the two grand categories of liquid-crystalline materials and their applications. This is followed by a chapter on chemical aspects of unconventional liquid crystals (Chapter 2). Chapter 3 offers a comprehensive, self-contained treatment of short-pitch ferroelectric liquid crystals and their application in modern displays and photonics, whereas Chapter 4 accounts for selected liquid-crystalline materials for efficient solar energy harvesting. Liquid crystal-based, label-free biosensing is presented in Chapter 5, and thermotropic liquid crystals from biomolecules are described in Chapter 6. Various physical properties are successively covered in Chapters 7–9, including electrically induced anchoring transitions in liquid crystals doped with ionic surfactants, time-resolved dynamics of dye-doped liquid crystals and the origin of their optical nonlinearity, and light-reconfigurable chiral liquid-crystal superstructure for dynamic diffraction manipulations. Chapters 10 and 11 look into the photoalignment of liquid-crystalline polymers attained from the free surface and photoresponsive liquid-crystalline block copolymers with hierarchical structures, respectively. Molecular modeling of liquid-crystal elastomers and liquid-crystal polymer films with high reflectivity are the subject matter of Chapters 12 and

13, respectively. Finally, nanomaterial-related topics are included in the last two chapters: while Chapter 14 reveals a lyotropic liquid-crystalline system and its sensing applications derived from ultrathin films of nanomaterials, Chapter 15 presents mesogenic science of quantum-dot-dispersed liquid crystals and their smart applications.

The chapters are written by experts on their topics of specialty, often supported by young researchers. It would have not been possible to bring this volume without their deep interest and dedication to taking on the full range of the topics which are assembled in this book. Most of the chapters may be read independently, without necessarily going through the preceding chapters. This impressive book, devoted to the fast-developing field of liquid-crystal science and technology, comprises the whole spam from basic science to applications of unconventional liquid crystals. The book addresses broad audiences from chemists, physicists, materials scientists, and engineers to biologists. It would be beneficial to readers ranging from students and non-specialized beginners to experienced researchers.

We would like to express our gratitude to Kristin Berber-Nerlinger at De Gruyter (Walter De Gruyter GmbH) for inviting us to compile this book. We are indebted to Dr. Vivien Schubert, Content Editor, and the production staff represented by Anne Hirschelmann, Production Editor, for their constant support and cooperation. We could have not achieved the publication of this book without their competence and excellent assistance. We thank all the distinguished contributors for their dedicated efforts in writing various chapters of this book. We are indebted to our family members and friends for their affectionate support and encouragement.

Wei Lee
Sandeep Kumar

Contents

List of contributing authors

Dr. Po-Chang Wu
College of Photonics
National Yang Ming Chiao Tung University
301 Gaofa 3rd Road, Guiren District
Tainan 711010
Taiwan
jackywu@nctu.edu.tw

Prof. Wei Lee
Institute of Imaging and Biomedical
Photonics
College of Photonics
National Yang Ming Chiao Tung University
301 Gaofa 3rd Road, Guiren District
Tainan 711010
Taiwan
wlee@nctu.edu.tw

Prof. Sandeep Kumar[1,2]
1. Raman Research Institute
C.V. Raman Avenue
Sadashivanagar, Bangalore 560080
India
skumar@rri.res.in
2. Department of Chemistry
Nitte Meenakshi Institute of Technology
(NMIT)
Yelahanka
Bangalore 560080
India

Dr. A. R. Yuvaraj
Raman Research Institute
C.V. Raman Avenue
Sadashivanagar, Bangalore 560080
India
yuvaraj.chem123@gmail.com

Asst. Prof. Abhishek Kumar Srivastava
Department of Electronic and Computer
Engineering
Hong Kong University of Science
and Technology
Clear Water Bay
Kowloon 999077

Hong Kong
eeabhishek@ust.hk
abhishek_srivastava_lu@yahoo.co.in

Dr. Valerii V. Vashchenko
Department of Electronic and Computer
Engineering
Hong Kong University of Science
and Technology
Clear Water Bay
Kowloon 999077
Hong Kong
eevvv@ust.hk

Dr. Neelam Yadav
Centre of Materials Sciences
University of Allahabad
Prayagraj, Uttar Pradesh 211002
India
neelamyadav533@gmail.com

Prof. Ravindra Dhar
Centre of Materials Sciences
University of Allahabad
Prayagraj, Uttar Pradesh 211002
India
dr.ravindra.dhar@gmail.com

Prof. Mon-Juan Lee
Department of Bioscience Technology
Chang Jung Christian University
1 Changda Road, Guiren District
Tainan 711301
Taiwan
mjlee@mail.cjcu.edu.tw
d908205@gmail.com

Dr. Chao Ma
Department of Chemistry
Tsinghua University
D206 Biomedicine Building
Beijing 100084
China
chaoma_chem@tsinghua.edu.cn
c.ma@foxmail.com

Prof. Dong Chen
Institute of Process Equipment
College of Energy Engineering
Zhejiang University
No. 38 Yuquan Campus
Hangzhou, Zhejiang 310027
China
chen_dong@zju.edu.cn
0016008@zju.edu.cn

Prof. Kai Liu
Department of Chemistry
Tsinghua University
D207 Biomedicine Building
Beijing 100084
China
kailiu@tsinghua.edu.cn

Dr. Mikhail N. Krakhalev
Kirensky Institute of Physics
Federal Research Center – Krasnoyarsk
Scientific Center
Siberian Branch of the Russian Academy of
Sciences
50/38 Akademgorodok
Krasnoyarsk 660036
Russia
kmn@iph.krasn.ru

Dr. Vitaly S. Sutormin
Kirensky Institute of Physics
Federal Research Center – Krasnoyarsk
Scientific Center
Siberian Branch of the Russian Academy of
Sciences
50/38 Akademgorodok
Krasnoyarsk 660036
Russia
sutormin@iph.krasn.ru

Dr. Oxana O. Prishchepa
Kirensky Institute of Physics
Federal Research Center – Krasnoyarsk
Scientific Center
Siberian Branch of the Russian Academy of
Sciences
50/38 Akademgorodok
Russia
p_oksana@iph.krasn.ru

Dr. Anna P. Gardymova
Institute of Engineering Physics and Radio
Electronics
Siberian Federal University
79 Svobodny
Krasnoyarsk 660041
Russia
gard@iph.krasn.ru

Dr. Alexander V. Shabanov
Kirensky Institute of Physics
Federal Research Center – Krasnoyarsk
Scientific Center
Siberian Branch of the Russian Academy of
Sciences
50/38 Akademgorodok
Krasnoyarsk 660036
Russia
shabanov.av@iph.krasn.ru

Dr. Victor Ya. Zyryanov
Kirensky Institute of Physics
Federal Research Center – Krasnoyarsk
Scientific Center
Siberian Branch of the Russian Academy of
Sciences
50/38 Akademgorodok
Krasnoyarsk 660036
Russia
zyr@iph.krasn.ru

Prof. Kenji Katayama
Department of Applied Chemistry
Chuo University
1-13-27 Kasuga Bunkyo
Tokyo 112-8551
Japan
kkata@kc.chuo-u.ac.jp
kkata.33g@g.chuo-u.ac.jp

Asst. Prof. Woon Yong Sohn
Department of Chemistry
Chungbuk National University
Chungdae-ro 1, Seowon-Gu
Cheongju, Chungbuk 28644
Republic of Korea
nunyong@chungbuk.ac.kr

Assoc. Researcher Wenbin Huang
School of Optoelectronic Science and
Engineering
Soochow University
1 Shizi Street
Suzhou, Jiangsu 215000
China
wbhuang@suda.edu.cn
wbhuang1987@hotmail.com

Prof. Zhi-gang Zheng
Department of Physics
East China University of Science
and Technology
130 Meilong Road
Shanghai 200237
China
zgzheng@ecust.edu.cn

Prof. Dong Shen
Department of Physics
East China University of Science
and Technology
130 Meilong Road
Shanghai 200237
China
shen@ecust.edu.cn

Prof. Yan-qing Lu
College of Engineering and Applied Sciences
Nanjing University
163 Xianlin Avenue
Nanjing, Jiangsu 210093
China
yqlu@nju.edu.cn

Res. Prof. Quan Li
Liquid Crystal Institute and Chemical Physics
Interdisciplinary Program
Kent State University
800 E. Summit Street
Kent, OH 44242
USA
qli1@kent.edu
quanli3273@gmail.com

Prof. Takahiro Seki
Department of Molecular and Macromolecular
Chemistry
Graduate School of Engineering
Nagoya University
1 Furo-cho, Chikusa-ku
Nagoya 464-8603
Japan
tseki@chembio.nagoya-u.ac.jp
taka_seki2002@yahoo.co.jp

Prof. Nobuhiro Kawatsuki
Department of Applied Chemistry
Graduate School of Engineering
University of Hyogo
2167 Shosha
Himeji, Hyogo 671-2280
Japan
kawatuki@eng.u-hyogo.ac.jp

Dr. Shuai Huang
School of Chemistry and Chemical
Engineering
Southeast University
Nanjing, Jiangsu 211189
China
huangshuai1991@seu.edu.cn

Prof. Haifeng Yu
Department of Materials Science
and Engineering
College of Engineering
Peking University
5 Yiheyuan Road
Beijing 100871
China
yuhaifeng@pku.edu.cn

Asst. Prof. Gregor Skačej
Faculty of Mathematics and Physics
University of Ljubljana
19 Jadranska
Ljubljana SI-1000
Slovenia
gregor.skacej@fmf.uni-lj.si

Emer. Prof. Claudio Zannoni
Department of Industrial Chemistry "Toso
Montanari"
University of Bologna
viale Risorgimento 4
Bologna 40136
Italy
Claudio.Zannoni@unibo.it
claudio.zannoni@gmail.com

Assoc. Prof. Dan Luo
Department of Electrical & Electronic
Engineering
Southern University of Science
and Technology
1088 Xueyuan Boulevard, Nanshan District
Shenzhen, Guangdong 518055
China
luod@sustc.edu.cn

Assoc. Prof. Yue Shi
School of Physical Science and Technology
Ningbo University
818 Fenghua Road, Jiangbei District
Ningbo, Zhejiang 315211
China
shiyue@nbu.edu.cn

Assoc. Prof. V. Manjuladevi
Department of Physics
Birla Institute of Technology and Science–
Pilani
FD3 Vidya Vihar Campus
Pilani, Rajasthan 333031
India
manjula@pilani.bits-pilani.ac.in

Assoc. Prof. Raj Kumar Gupta
Department of Physics
Birla Institute of Technology and Science–Pilani
FD3 Vidya Vihar Campus
Pilani, Rajasthan 333031
India
raj@pilani.bits-pilani.ac.in

Prof. Rajiv Manohar
Department of Physics
University of Lucknow
1 University Road
Lucknow, Uttar Pradesh 226007
India
rajiv.manohar@gmail.com

Po-Chang Wu, Sandeep Kumar, Wei Lee

1 Introduction: from conventional to unconventional liquid crystals

Abstract: Liquid crystals have received tremendous attention from both the academic and technological points of view by virtue of their unique molecular structures characterized by the mesogenic cores and fluidity but long-range orientational order and stimuli-responsive material properties. To date, a variety of liquid crystal materials have been systematically synthesized and extensively employed in a wide spectrum of daily products. Further potential applications have been suggested as well, based on their superior particularities and remarkable advances made in the twenty-first century. Among the thermotropic liquid crystals, rod-like and disk-like molecules are generally considered as conventional liquid crystals, whereas liquid crystals with other molecular shapes, showing unusual material properties distinct from those of conventional ones, are unconventional liquid crystals. In addition, liquid crystal-based mixtures and composites, comprising certain types of substances (e.g. dyes, monomers, and nanomaterials) as additives, can also be regarded as unconventional liquid crystals in that concern of modified and improved properties have led to a surge of research activities to discover and develop new material systems in attempt to tailor the host liquid crystals to extend their applications beyond displays. According to the contents of the book entitled *Unconventional Liquid Crystals and Their Applications*, this chapter is aimed at providing the reader with a background on the basis of what has been established about conventional rod-like liquid crystals and unconventional liquid crystals in terms of their structures, material properties, and potential applications. We start from an overview on the evolution of liquid crystal research, followed by introducing fundamental concepts, including types, structures, material properties, and well-known applications of various rod-like liquid crystal mesophases. Furthermore, an introduction to recent developments of specific hybrid liquid crystal systems with unusual or modified material characteristics, adoptable for revolutionary liquid crystal technologies, is presented to draw the reader's attention from conventional to unconventional liquid crystals from an application perspective.

1.1 Overview

Matter in nature can commonly be classified into three states – solid, liquid and gas, according to the strength of intermolecular force and the mobility of the molecules. When substances have anisotropic properties, mesophases known as liquid crystals (LCs) can be obtained in between solid and liquid states. The material

properties of LCs are intriguing because they combine features of both the solid and liquid states. That is, molecules in an LC phase are capable of flowing like liquids and can be self-assembled to form long-range orientational order and in some cases together with one- or two-dimensional translational order like solids. Moreover, LC molecules are susceptible to external stimuli so that their physical properties such as dielectric and optical anisotropy can be tuned by the electric field, magnetic field, temperature, acoustic waves or ultrasound pulses (Lee and Chen, 2001), and the like. This enables a variety of readily unique electro-optical responses of LCs and, thus, successful applications to ubiquitous flat-panel displays in this day.

The discovery of LCs could trace back to the year 1888 when an Austrian botanist by the name of Friedrich Reinitzer observed an intriguing phenomenon of double melting points during his study of the organic material cholesterol benzoate. After receiving samples sent from Reinitzer, the German physics professor Otto Lehmann then performed careful analysis on this unusual state at various temperatures by his state-of-art polarizing optical microscope equipped with a sample stage with precise control of temperature and eventually coined the term "liquid crystal" in 1904 as known today (Sluckin et al., 2004). Existing LCs can broadly be divided into lyotropic and thermotropic LCs, depending on the nature of their formation. Lyotropic LCs are typically obtained by dissolving amphiphiles with certain solvents. Molecules of such two-component systems are composed of a hydrophilic (polar) head group in connection with a hydrophobic tail. Varying the solvent concentration as well as the temperature results in the observation of various lyotropic mesophases, such as micellar, cubic (micellar cubic I and bicontinuous cubic V), hexagonal columnar (H) and lamellar (L_α) phases (Lagerwall and Scalia, 2012). Certain chromonic dyes (e.g. Sunset Yellow FCF), drugs (e.g. disodium cromoglycate) and short strands of nucleic acids form assemblages that give rise to LC phases in a dissimilar manner from amphiphilic molecules. When these flat molecules, usually containing two end polar groups, are mixed with a polar solvent, typically water, stacks of molecules construct sufficiently long assemblies, resulting in (lyotropic) chromonic LC phases, including the nematic (N) and columnar (M) phases, depending on the temperature and concentration (Tam-Chang and Huang, 2008). In contrast, thermotropic LCs possessing anisotropic molecular shape in their pure forms are stably obtained in given temperature ranges upon heating (cooling) from the solid (liquid) phase. The shape anisotropy of a molecule with a rigid core plays a crucial role in the design of a thermotropic LC and, in turn, its mesophases as well as material properties. In view of all existing thermotropic LCs with well-defined chemical/molecular structures, rod-like (or calamitic) and disk-like (or discotic) molecules are the two simple and common forms of LCs so that they are normally defined as conventional LCs. Other chemically synthesized LCs with unusual molecular shapes different from those of conventional LCs, such as bowl-like or bowlic (Wang et al., 2017b), bent (or banana)-shaped (Antal Jákli et al., 2018), hockey-shaped (Sarkar et al., 2011), λ-shaped (Ooi and Yeap, 2018), Y-shaped (Kashima et al., 2014), star-shaped (Vinayakumara et al., 2018) mesogenic compounds

and the like (Li et al., 2018c; Osman et al., 2016; Radhika et al., 2013), are generalized as unconventional LCs, which are reviewed from the chemical aspect in Chapter 2 of this book.

To date, mesophases of conventional LCs – such as nematic, smectic, and cholesteric (or chiral nematic) phases in rod-like LCs as well as columnar and nematic phases in disk-like LCs – have been enormously explored as reported in many scientific and technological investigations. Among them, rod-like LCs with unique structural and material features are the most widely synthesized and used molecules for developing LC technologies. The best known is the application of nematic LCs in displays that have been commercialized in a wide spectrum of our daily seen information products, ranging from large-size TVs over medium-size laptops, monitors, and automotive panels to small-size mobile phones and watches (Chen et al., 2018a; Ko et al., 2018). This great achievement makes rod-like LCs fascinating in a variety of research fields, including chemistry, physics, materials science, and engineering (Geelhaar et al., 2013). In addition to displays, applications of rod-like LCs in other electro-optical and photonic devices (Coles and Morris, 2010; Si et al., 2014) and even in biological sensing/detections (Hussain et al., 2016; Lee and Lee, 2020; Popov et al., 2017) have been evaluated. With rapid growth of contemporary LC science and technology, unconventional LCs whose material properties are distinct from those of conventional counterparts are desirable in order to rectify or promote the performance of LC-based systems and to extend LCs to other applicable domains. Aside from those chemically synthesized LCs with unconventional molecular structures, incorporating conventional LCs with other nanomaterials or molecular additives have been proven promising for developing unconventional LC systems with unique combination of properties derived from the fascinating material features of the additives and their mutual interaction with LC molecules (Lee et al., 2004; Liu and Lee, 2010a). It was first reported in 1968 that dissolving a proper amount of a dichroic dye into an LC gives birth of a hybrid material with additional (selective) absorption properties and the guest–host electro-optical effect (Heilmeier and Zanoni, 1968). Since then, dye-doped LCs have widely been exploited for upgrading the LC applications into polarizer-free displays, light shutters, gratings, and smart windows (Sims, 2016; Yang, 2008), and extending LCs to the fields of lasers (H. Coles and Morris, 2010) and biosensors (Chiang et al., 2018; Wu et al., 2018a). Polymers are another popular additives to LCs, forming composite materials with excellent mechanical properties that can couple with optical characteristics of LCs. In this regard, polymer–LC composites with mismatched refractive index between polymer and LCs exhibit superior light-scattering properties that have held a great deal of promise for developing polarizer-free and flexible electro-optical and photonic devices (Ahmad et al., 2017a, 2017c; Bronnikov et al., 2013). There are abundant reports declaring that the formation of polymers with desired morphologies in LCs can modify the electro-optical characteristics, support complicated LC configurations (Yang, 2013), control the LC pretilt angle (Hsu et al., 2016b; Liu et al., 2017a), and stabilize LC textures and phases

(Chen and Wu, 2014; Rumi et al., 2018; Varanytsia and Chien, 2016). Specifically, the polymers enclosed in LC cells can memorize various helical superstructures, forming polymeric templates after the removal of LCs. By refilling certain LCs into the designated polymer templates, many unusual features beyond the optical limit of conventional chiral LCs have progressively been demonstrated, such as wide-temperature blue phases (Castles et al., 2012) as well as multi-color and hyper reflection (Chen et al., 2014b; Li et al., 2017c; Lin et al., 2017a). Thanks to the rapid growth of nanoscience and nanotechnologies, numerous scientists have reached out their research foci to the development of unconventional LC colloids by dispersing nanomaterials into LCs. The most attractive virtue of nanomaterial–LC dispersions or colloidal solutions is that doping ferroelectric, metallic, and semiconducting nanoparticles or carbon-based allotropes can modify fundamental physical properties (e.g. dielectric anisotropy, birefringence, elastic constants, and viscosity) of the conventional LCs and repress the annoying ionic effect, giving rise to the improvement in electro-optical performance of traditional and emerging LC displays (LCDs) and devices (Mertelj and Lisjak, 2017; Sharma et al., 2017; Yadav and Singh, 2016). The ability of controlling LC alignment by some specific nanomaterials as additives, including polyhedral oligomeric silsesquioxane (POSS®), silica, metal, and semiconducting nanoparticles, has been suggested for alignment-layer-free LC devices (B. Liu et al., 2017b; Wang et al., 2016b) and for the application of LCs in biosensing (Wei and Jang, 2017; Zhao et al., 2015). Moreover, the dispersion of nanomaterials in an LC matrix can create novel composites and elements with additional functionalities by involving the inherent features of both the nanomaterial and the LC host, such as the combination of the quantum confinement effect in quantum dots doped into LCs and the surface plasmonic resonance of metal and graphene nanomaterials for realizing tunable LC lasers and other photonic devices (Chen et al., 2018b; De Sio et al., 2016; Guo et al., 2017a).

Owing to the uniqueness and advantages such as tailorable functionality, unconventional LCs are receiving more and more attention for the revolutionary development of the LC science and technology. Some discussions of such attractive unconventional systems are included in this book, primarily in Chapter 2. Herein, we build up the following sections in an attempt to help readers comprehend the evolution and research focus from conventional to unconventional LCs. First, we consider rod-like compounds as the representative of conventional LCs, highlight key structures, alignment and physical characteristics of some well-documented mesophases, and signify the industrial development of rod-like LCs from an application point of view in Section 1.2. For unconventional LC systems, we emphasize those materials with LC/non-LC hybrid structures, reviewing their ability of modifying structural and material properties of pristine LCs and technological innovations in Section 1.3. A brief conclusion of this chapter and a short introduction to various types of unconventional LCs covered in this book are summarized in Section 1.4.

1.2 Conventional liquid crystals

1.2.1 Types and structures of rod-like liquid crystal mesophases

Rod-like LCs are the most common class of thermotropic LCs whose molecules are elongated with a long axis. The chemical structure of such a rod-like molecule is composed of two constituents: a rigid mesogenic core for determining the orientational ordering and a flexible chain or two chains for providing the fluidity. Varying the structure of the rigid core leads to the change in mutual interaction with substituent peripheral chains and, thus, the formation of diverse mesophases. The single compound 4-cyano-4′-pentylbiphenyl (better known as 5CB) showing the nematic phase in the temperature range between 24 °C and 35 °C is the first cyano-based rod-like LCs, made of two directly linked phenyl rings as the rigid core, a flexible alkyl moiety (C_5H_{11}), and a cyano (CN) polar group. The molecular size of 5CB is in the nanometer scale with 2 nm in length and 0.5 nm in width, as illustrated in Figure 1.1. Rod-like LC mesophases with distinct molecular structures and orientational orderings can briefly be divided into nematics (N) and smectics (Sm). In regard to the chirality, each of them can be further subdivided into achiral and chiral counterparts. Till now, a variety of mesophases with well-established structures have been discovered. Although there is no single compound that can show all the existing mesophases, a hypothetical phase (transition) sequence of rod-like LCs could be generally written as: Isotropic (Iso) – N – SmA – SmC – SmB – SmI – SmF – Crystal B – J – G – E – K – H – Solid for achiral LCs and Iso – blue phase (BP) – cholesteric (N*) – twist gain boundary (TGBA) – SmA* – SmC* – SmI* – SmF* for chiral LCs. Note that if the structure of the molecules that form a mesogenic phase is chiral (namely, lacking inversion symmetry), then the chiral (X*) phase exists in place of its achiral (X) analog.
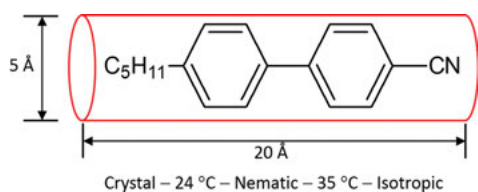
Figure 1.1: Graphical representation of the chemical structure and phase transition sequence of the typical rod-like liquid crystal 4-cyano-4′-pentylbiphenyl (5CB).

For an achiral LC phase, molecules are preferably arranged along a specific direction. The average molecular axis, also known as the director (or in most cases, the optic
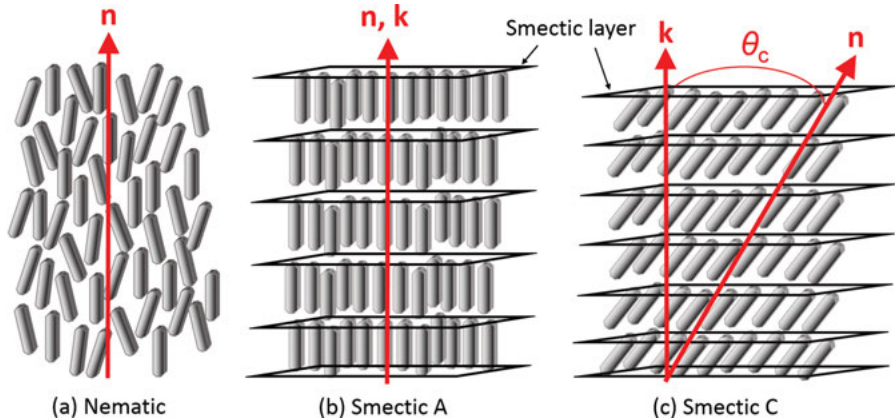
Figure 1.2: Schematics of the molecular orientations of the (a) nematic, (b) smectic A, and (c) smectic C phases. $\hat{\mathbf{n}}$ and $\hat{\mathbf{k}}$ denote vectors of the liquid crystal director and the layer normal for smectics, respectively.

axis) of LCs, can be represented by a unit vector $\hat{\mathbf{n}}$ while the orientational order parameter S is given by

$$S \equiv \langle \mathrm{P}_2(\cos\theta) \rangle = \left\langle \frac{1}{2}\left(3\cos^2\theta - 1\right) \right\rangle = \frac{3}{2}\langle\cos^2\theta\rangle - \frac{1}{2}. \tag{1.1}$$

$S = 1$ indicates perfect order in the crystal phase while $S = 0$ corresponds to completely random order in the isotropic liquid phase. LC is a partially ordered system. A typical value of S is in the range of 0.4 to 0.7 in the nematic phase and 0.7 to 0.8 in the smectic phase. Figure 1.2 displays the molecular structures of three typical achiral LC phases. The nematic phase is the simplest and the most useful one amid all LC mesophases although its order is lower than those of the other two phases. As illustrated in Figure 1.2(a), molecules in the nematic phase are on average parallel to $\hat{\mathbf{n}}$ due to the presence of orientational order but they are of lack of long-range translational order. Because LC molecules exhibit head–tail symmetry, $\hat{\mathbf{n}}$ is equivalent to $-\hat{\mathbf{n}}$ and the configuration with uniformly aligned molecules makes nematic phase optically uniaxial with anisotropic material properties. For smectic phases, molecules are confined between smectic layers; thus, their structures exhibit long-range orientational order and a certain level of positional order. The smectic-A (SmA) phase is the least ordered and orthogonal smectic whose director $\hat{\mathbf{n}}$ is parallel to the layer normal $\hat{\mathbf{k}}$ as shown in Figure 1.2(b). The molecular ordering in each smectic layer shows two-dimensional orientation order and the molecules are able to translate and rotate freely around their long axis. The ordering of smectic-C (SmC) phase is closely related to that of the SmA, and it constitutes a class of tilted smectics with the director $\hat{\mathbf{n}}$ being tilted from the layer normal $\hat{\mathbf{k}}$ by an angle θ_c as illustrated in Figure 1.2(c). The value θ_c gets increased with decreasing temperature in the second-order

(or continuous) phase transition but it changes directly from zero to a given value and is independent of the temperature in the first-order (or discontinuous) transition. Other smectic phases, such as hexatic smectics of smectic B_{hex}, smectic I, and smectic F and crystal-like smectics of smectic B_{cryst}, smectic E, smectic J, smectic G, smectic K, and smectic H have been classified based on their molecular packing (Bahr, 2001).

Chiral LCs are best known for the self-assembly of helical superstructure owing to the presence of chirality or handedness that drives molecules to rotate periodically along a unidirectional axis known as the helical axis. In general, LCs with chiral molecules can be created by either physically doping chiral additives into achiral LCs or by chemically synthesizing mesogens with intrinsic chirality (Lagerwall, 2016). As mentioned in the preceding paragraph, chiral LCs with diverse versions of chiral molecules are indicated by labeling an asterisk symbol "*" to the shorthand of the corresponding achiral phases, such as N* for chiral nematic and SmC* for chiral smectic C. Among existing chiral LCs, the cholesteric LC phase, also known as the chiral nematic phase, has widely been investigated in the literature on account of its ubiquity, simplicity, and applicability. As illustrated in Figure 1.3(a), a cholesteric LC has molecular ordering comparable to that of the nematic phase and its helical structure can be represented as a stack of a series of nematic-like layers containing molecules with orientational order in the plane; the director $\hat{\mathbf{n}}$ in each layer twists in space continuously along the helical axis by a constant angle with respect to its neighboring plane. The profile of a cholesteric LC helix is evaluated by the helical pitch or the period of the helix (p), defined as the length of the helical periodicity by 2π radians, and the twist sense (either the left or right handedness). To date, most of cholesteric LCs for investigations are obtained from a physical way by incorporating a chiral dopant or dopants into an achiral nematic LC host. If the cholesteric LC mixture satisfying the miscibility conditions is considered a dilute blend containing a low dopant content (say, <5 wt%), the value of p can be precisely determined by the helical twisting power (HTP) of the chiral substance and its concentration (c) in the LC host, following the equation $p = (HTP \times c)^{-1}$ (De Gennes and Prost, 1993). Specifically, when the helical pitch of a highly twisted nematic LC is on the order of a few hundred nanometers, a class of thermodynamic LC phases known as blue phases (BPs) could sequentially be observed in a narrow temperature range between the isotropic and the cholesteric LC phases. Up to now, three types of blue phases, namely, BPI, BPII, and BPIII have been discovered and their cubic configurations confirmed experimentally and theoretically. For BPIII, it is amorphous with nearly the same symmetry as the isotropic phase (Rokhsar and Sethna, 1986). In BPI and BPII, the LC molecules rotate simultaneously along a central axis in two dimensions, constructing the double twist cylinder to minimize the free energy. The packing of these double twist cylinders builds up three-dimensional lattice structures with body-centered cubic and simple cubic symmetries in BPI and BPII, respectively. Theses cubic symmetries in blue phases are thermodynamically stable owing to the presence of disclinations (i.e., line defects) inside defect sites among double twist cylinders (Castles et al., 2010).
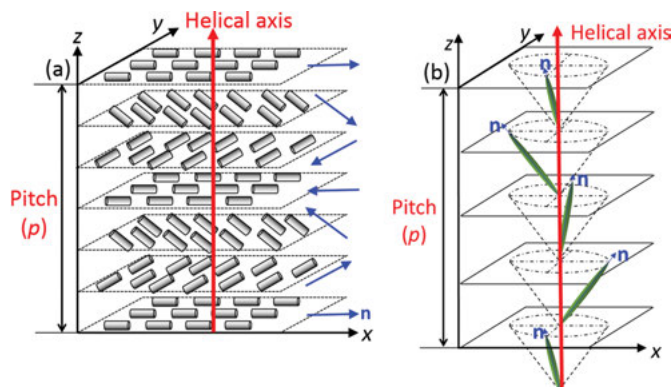
Figure 1.3: Schematic illustrations for the molecular orientation of (a) chiral nematic (N*) and (b) chiral smectic C (SmC*).

On the other hand, the SmC* phase, the chiral analog of the SmC phase, is a special class of chiral LC phases showing a local spontaneous polarization ($\mathbf{P}_s$) arising from ferroelectricity; thus, it is also called ferroelectric liquid crystal. As illustrated in Figure 1.3(b), SmC* molecules, arranged in layers, tilt by an angle θ_c with respect to the layer normal (i.e., the helical axis). The chirality of the molecules in the SmC* phase causes the director to progressively rotate together with the vector $\mathbf{P}_s$ – whose direction is determined by the chemical structure of the molecules, moving slowly from one to another layer around the cone, preserving a constant azimuthal angle within each layer. This creates a helical structure with its helical axis perpendicular to the layer plane. In this configuration, the $\mathbf{P}_s$ vector is coupled to $\hat{\mathbf{n}}$, pointing it along $\pm\hat{\mathbf{k}} \times \hat{\mathbf{n}}$, where $\hat{\mathbf{k}}$ denotes the vector of the layer normal. From the macroscopic view, the spontaneous polarization will average to zero when the director rotates a periodicity of the helix around the layer normal. Nevertheless, the ferroelectricity can be preserved by injecting SmC* molecules into a very thin sandwich cell to effectively suppress the helix. Such a cell geometry enables the so-called surface-stabilized ferroelectric LC proposed by Clark and Lagerwall in 1980 (Clark and Lagerwall, 1980). In the above-mentioned achiral and chiral rod-like LC mosephases, the director $\hat{\mathbf{n}}$ of the nematic phase can readily be controlled by external stimuli in that they reveal fluidity with reasonably high mobility and low viscosity. For this reason, the nematic phases, including both achiral and chiral versions, are of technological importance, having been applied to most of known LC techniques. Introducing the alignment and physical properties of conventional LCs, the succeeding sections (i.e., Sections 1.2.2 and 1.2.3) will thus be focused on nematic phases unless explicitly specified.

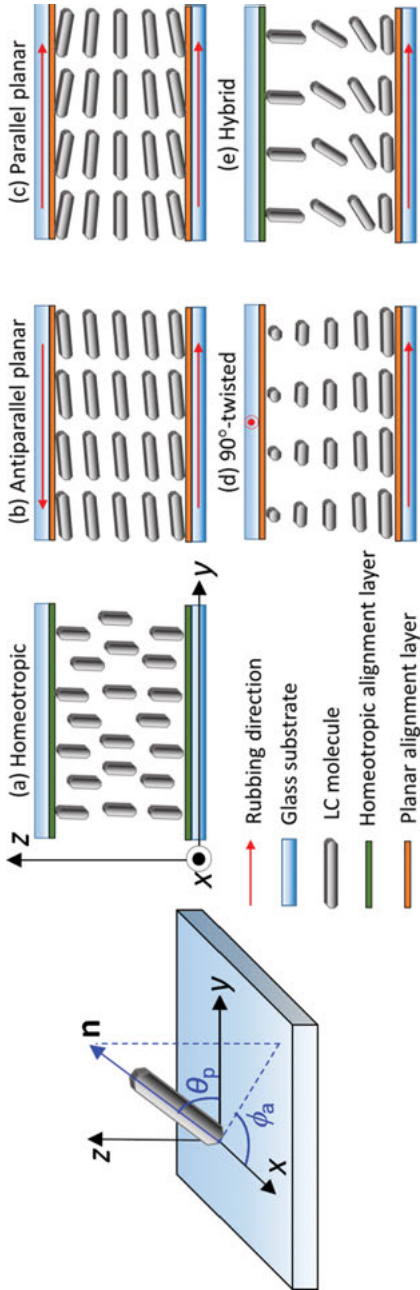**Figure 1.4:** Molecular orientation of (a) homeotropic, (b) antiparallel planar, (c) parallel planar, (d) 90°-twisted, and (e) hybrid alignment in a sandwich-type LC cell, covered with proper alignment layer and surface rubbing on each substrate.

1.2.2 Liquid crystal alignment and physical properties

LC alignment refers to the bulk orientation of LC molecules, often induced by the confining surfaces, and it constitutes one of the prerequisites in considering fundamental research and practical applications of LCs. For example, defect-free LC alignment with uniform director is essential to make use of anisotropic material features effectively in electro-optical applications of most LC devices. The changes in the LC director orientation on different surfaces (such as disrupted alignment caused by immobilized biomolecules at the LC–substrate interface) are the main working principle of LC-based biosensing techniques. In most cases, an LC material under investigations is sandwiched between a pair of glass substrates making up a cell, separated by a distance of several micrometers to tens of micrometers typically to ensure the thickness of the LC layer. The cell gap is often readily determined by spacers having a known size; it can be more accurately specified by optical (interference) method before filling the cell with LC. For electro-optical purposes, the transparent conducting material of indium–tin oxide (ITO), with excellent electrical conductivity and optical transparency, is deposited on both substrates (or on either one with interdigitated electrode patterns) to allow the application of electric field to an LC cell in the direction perpendicular (or parallel) to the substrate plane. Conventionally, the LC alignment in such a sandwich-type cell geometry can be controlled by covering with a certain aligning agent to form an alignment film on the substrate (Cognard, 1982). When LC molecules are in contact with the alignment layer, an anchoring force will be induced at the interface and the director in the vicinity of the surface will tend to be oriented along a preferred direction, known as the easy axis with given polar (θ_p) and azimuthal (ϕ_a) angles. The surface anchoring provided by alignment layers can thus be classified in terms of θ_p, also known as the pretilt angle measured from the substrate plane, into homeotropic (or vertical) anchoring ($\theta_p = 90°$) with $\hat{\mathbf{n}}$ normal to the substrate plane, planar anchoring ($0° < \theta_p < 10°$) with $\hat{\mathbf{n}}$ parallel to the substrate, and tilted anchoring ($10° < \theta_p < 90°$) with $\hat{\mathbf{n}}$ tilted by an angle from the substrate plane. Accordingly, the LC alignment in a sandwich-type cell can be formed with the director either fixed or deformed toward a certain direction by the penetration of the surface anchoring into the bulk via intermolecular interactions (i.e., the continuum effect) and hence the minimization in free energy through the balance between the anchoring forces at the surface and the LC elasticity. Homeotropic (Figure 1.4(a)) and planar (Figure 1.4(b)–1.4(d)) configurations with fixed director perpendicular and parallel to the plane, respectively, are two general LC alignments which can be achieved by coating with an organic thin film on both substrates via spin-coating, dip-coating, imprinting or spraying. Technologically, polymeric polyimides with excellent thermal, chemical and physical stabilities and high resistivity are used as aligning agents in mass production of modern-day LCDs, to prevent the degradation of electro-optical performances from the alignment layer. Specific for planar alignment, an additional surface treatment on the alignment layer is required to well define the azimuthal

direction in the plane for $\hat{\mathbf{n}}$ so as to obtain homogeneous planar anchoring without molecular disclinations or line defects. The conventional way to fulfill this goal relies on mechanically rubbing the planar alignment film with velvet cloth, resulting in the formation of micro- or nano-grooves on the surface and reorienting side-chain polymers uniformly to create anisotropic characteristics. LC molecules on a rubbed polyimide film thus prefer to align themselves in the plane, often along the rubbing direction, to minimize the free energy. As a result, various planar configurations can be obtained by controlling the rubbing directions of the top and bottom substrates, such as antiparallel planar alignment with 180° rubbing (Figure 1.4(b)), parallel planar alignment (i.e., splay alignment) with 0° rubbing (Figure 1.4(c)) and twisted alignment with 90° rubbing (Figure 1.4(d)). In a special case where one of the substrates has planar anchoring and the other substrate has homeotropic anchoring, the LC alignment is referred to as hybrid alignment with the magnitude of θ_p varying in the LC bulk from ~0° on one substrate to ~90° on the other (Figure 1.4(e)). Although the rubbing method – with attributes of convenience, simplicity and low cost – has widely been used in research laboratories and even commercially applied in some present-day LCDs, crucial disadvantages incurred by the contact operation, including the generation of unwanted dust particles, defects and uneven surfaces, and the notorious accumulation of static charge on the alignment layers in particular, can be problematic, leading to the reduction in reliability in mass production and degradation in electro-optical performance for applications. In order to overcome these drawbacks and further to flexibly regulate the director profile, several non-contact alternatives, such as oblique evaporation (Janning, 1972), ion-beam irradiation (Chaudhari et al., 2001), and photoalignment (Chigrinov, 2013; Gibbons et al., 1991; Yaroshchuk and Reznikov, 2012), have successively been suggested and exploited. Among them, the photoalignment is the most successful non-contact alignment method which has been adopted in the medium-to-large-sized active-matrix LCD industries, replacing the seemingly old-fashioned surface rubbing technique during the past decade. In this predominant method, photoresponsive polymers with angular or polarization dependence of light absorption are employed as the aligning substance formed by photopolymerization from their precursors or prepolymeric counterparts by illumination with polarized ultraviolet (UV) light to induce molecular anisotropy. The director of LC molecules on the photoalignment layer can be aligned along or perpendicular to the polarization direction of the UV light, depending on the nature of the photoresponsive material.

The control in pretilt angle (θ_p) of an LC cell is a key aspect for electro-optical applications. It is known that a non-zero pretilt angle is essential to prevent the generation of defects from reverse tilt of LC molecules under the application of an external voltage. Optimizing the pretilt angle can improve the electro-optical performance and create various types of LC alignment in an LC device. Examples are the homeotropic alignment with $\theta_p > 80°$ for multidomain vertical (MVA) mode LCs, antiparallel planar alignment with $\theta_p < 10°$, and hybrid LC alignment for the electrically controlled birefringence (ECB) mode LCs, bend alignment with $47° < \theta_p < 65°$ for optically

compensated bend (OCB) mode LCs, parallel planar with $\theta_p \sim 0°$ for in-plane switching (IPS) mode LCs, and twisted alignment with $\theta_p < 5°$ and $5° < \theta_p < 10°$ for 90° twisted-nematic (TN) and super-twisted nematic (STN) mode LCs, respectively (Hasegawa, 2005). For traditional rubbed polyimide films, the pretilt angle is primarily determined by the type of the aligning material used. The rubbing parameters in the processes, such as the rubbing depth and the number of rubbings, may affect the pretilt angle but the tunable range is limited, typically around 1°–10°. Thus far, various approaches to the control of pretilt angle in a wide range between 0° and 90° have been developed by modification of the alignment layer surfaces. These include (1) inhomogeneous, chemically patterned surfaces by covering a substrate with a surfactant, say, DMOAP-coated substrate with thin metallic islands (Ong et al., 1985), (2) nanostructured surfaces by mixing planar and homeotropic polyimides in a solution with mixture concentration (Ahn et al., 2009; Yeung et al., 2006), baking temperature (Kang et al., 2009), and rubbing depth (Wu et al., 2008) as variables, (3) Ion-beam-modified surfaces by regulating irradiation time for the homeotropic polyimide (Seo et al., 2007), incident angle for carbon-rich SiC layer (Kim et al., 2007a), power ratio for amorphous fluorinated carbon thin film (Ahn et al., 2007), and (4) UV exposure on rubbed homeotropic polyimide (Ata Alla et al., 2013), and mixed polyimide (Ho et al., 2007).
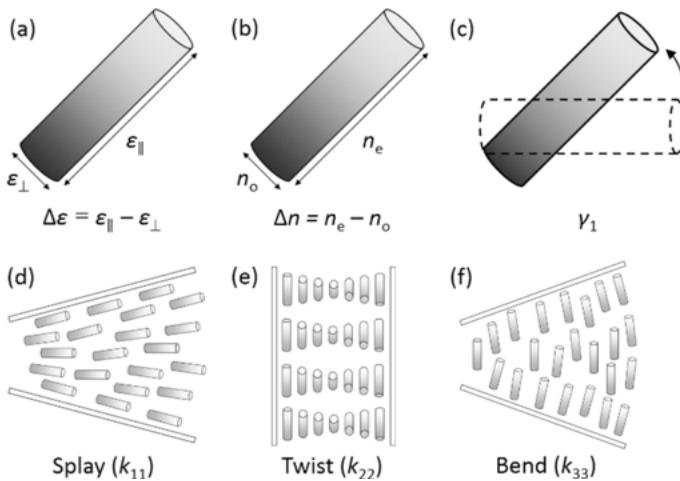

Figure 1.5: Definitions of key physical properties or parameters of LCs: (a) dielectric anisotropy ($\Delta\varepsilon$), (b) birefringence (Δn), (c) rotational viscosity (γ_1), and (d) splay (k_{11}), (e) twist (k_{22}), and (f) bend (k_{33}) elastic constants.

Physical properties of uniaxial rod-like LCs, such as the refractive index (n), dielectric permittivity (ε), conductivity (σ), magnetic susceptibility (χ_m), and shear (flow) viscosity (η), are anisotropic. Anisotropy substantially diminishes as the temperature approaches the nematic–isotropic transition temperature and vanishes in the

isotropic state. Depending on the geometrical conditions characterized by the relative orientation of the director with respect to the shear force and velocity gradient, there are three (shear) viscosities of a nematic LC, sometimes called the Miesowicz coefficients: η_1 measured when the director is perpendicular to the flow and parallel to the velocity gradient, η_2 measured when the director is parallel to the flow, and η_3 obtained when the director is perpendicular to both the flow and the velocity gradient. Typically, the dynamic viscosity η_1 is of the order of 100 mPa·s whereas η_3 (> η_2) and η_2 are of the order of 10 mPa·s. They all decrease with increasing temperature as expected for fluids. Note that the LC specification sheets give kinematic viscosity in $mm^2 \cdot s^{-1}$ instead of the dynamic viscosity in poise (1 poise = 100 mPa·s). Because the kinematic flow viscosity is equal to the dynamic viscosity divided by the mass density (approximately 1,000 kg·m^{-3}), the numerical parts are identical for the expressions in mPa·s and in $mm^2 \cdot s^{-1}$. Each of the other properties has two different values in the direction parallel and perpendicular to the director. This originates from the fact that LC molecules have anisotropic shape and charge distribution, tending to align themselves with their long axes parallel to one another to yield orientational order. Moreover, LC molecules are susceptible to external stimuli, making anisotropic properties tunable by the electric field, magnetic field, temperature, and so forth. The dielectric anisotropy ($\Delta\varepsilon$) of a uniaxial LC is the difference between the parallel ($\varepsilon_{\parallel}$) and perpendicular ($\varepsilon_{\perp}$) components of dielectric permittivity of the director, expressed as $\Delta\varepsilon = \varepsilon_{\parallel} - \varepsilon_{\perp}$ (Figure 1.5(a)). The profile of $\Delta\varepsilon$ can generally be characterized by the dipole moment μ and its orientation angle θ with respect to the principal molecular axis or the director, and is proportional to the order parameter S, which, as a simplified analytical expression derived from the Maier–Saupe theory, can be given by

$$S = \left(1 - \frac{T}{T_c}\right)^{\beta}, \tag{1.2}$$

where T is the absolute temperature, T_c denotes the clearing temperature corresponding to the nematic–isotropic transition in Kelvin, and β is a unitless material parameter around 0.25. The value of $\varepsilon_{\parallel}$ ($\varepsilon_{\perp}$) is also a function of the temperature which decreases (generally increases) with rising temperature, reaching a constant value at the temperature beyond the clearing temperature. The dielectric permittivity is a key parameter determining the extent of response of LC molecules to an electric field which depends on the charge distribution and intermolecular interactions. In the case of an LC with polar molecules, an orientational polarization occurs owing to the reorientation of the permanent dipole moments, which tends to be parallel to the electric field. Furthermore, the reorientation of LC molecules under the application of an electric field relies mainly on the sign of $\Delta\varepsilon$. For LCs with $\Delta\varepsilon > 0$ and $\Delta\varepsilon < 0$, molecules will have greater polarizability along their long and short axis, respectively. Consequently, in order to achieve the lowest energy state, the orientation

of the molecular long axis tends to become parallel to the direction of electric field for an LC with $\Delta\varepsilon > 0$ and perpendicular to it for an LC with $\Delta\varepsilon < 0$. Similarly, the optical anisotropy, also known as birefringence, of a uniaxial LC with the optic axis parallel to the director $\hat{\mathbf{n}}$, is defined as $\Delta n = n_{\parallel} - n_{\perp} = n_e - n_o$ (Figure 1.5(b)). Here, the ordinary refractive index $n_o = n_{\perp}$ and the extraordinary refractive index $n_e = n_{\parallel}$ are the measured indices of refraction for the light wave where the polarizing vector vibrates perpendicular and parallel to the optic axis, respectively. As a general rule of thumb, the value of Δn is positive ($\Delta n > 0$) for rod-like LCs and negative ($\Delta n < 0$) for disk-like LCs. At a fixed wavelength, the temperature-dependent birefringence follows Haller's semi-empirical equation

$$\Delta n(T) = \Delta n_0 S(T) = \Delta n_0 \left(1 - \frac{T}{T_c}\right)^{\beta}, \tag{1.3}$$

where Δn_0 (of the order of 0.1) is the extrapolated birefringence at $T = 0$ (Haller, 1975). The birefringence dispersion dependent on the chemical structure can be explained based on the single-band birefringence equation

$$\Delta n(T, \lambda) = G(T) \left(\frac{\lambda^2 \Lambda^2}{\lambda^2 - \Lambda^2}\right), \tag{1.4}$$

where the variable λ denotes the wavelength, Λ is the mean resonance wavelength in the UV range (~200–350 nm), and the proportionality $G(T)$ is of the order of μm^{-2} (Wu, 1986). The birefringence ($\Delta n = n_e - n_o$) in the visible spectrum can also be expressed using the extended Cauchy dispersion equations

$$n_{e,o}(\lambda) = n_{e,o}^{\infty} + \frac{A_{e,o}}{\lambda^2} + \frac{B_{e,o}}{\lambda^4} + ..., \tag{1.5}$$

on the basis of the mechanistic concept of an elastic solid derived by Augustin Louis Cauchy. In eq. (1.5) n^{∞} is the refractive index extrapolated to infinite wavelength and A and B are the Cauchy coefficients. Employing the fit to three known index values at three different wavelengths allows to obtain the respective refractive indices n_o and n_e and consequently the optical anisotropy Δn as a function of the wavelength. The birefringent behavior of an LC can further be represented in terms of an index ellipsoid to interpret the induced optical polarization for a light wave from an arbitrary direction of propagation into it. The birefringence of the LC thus becomes $\Delta n = n_{eff} - n_o$, where the effective refractive index n_{eff} has two extrema, n_e and n_o. For a polarized light ray with a given wavelength (λ) passing through an LC thin film with a designed thickness (d), the resulted phase retardation (δ) can be expressed as

$$\delta = \frac{2\pi d \Delta n}{\lambda} = \frac{2\pi}{\lambda} d(n_{eff} - n_o). \tag{1.6}$$

Stemming from the intermolecular interaction in motion, the viscosity is regarded as an internal resistance to flow of a fluid medium. For nematic LCs, there are two types of viscosities – the shear viscosity and the rotational viscosity, characterizing the flow and rotational motions of molecules in confined geometry under an external force, respectively. Analogous to conventional liquids, the shear viscosity (η) dominates the flow behavior under shearing so that it is defined as the ratio of the shearing stress to the velocity gradient. Owing to the nature of anisotropy, the magnitude of shear viscosity of a nematic LC depends primarily on the mutual orientation of the flow and director fields, as described in the beginning of the preceding paragraph. When the bulk flow is hindered and the director reoriented by external stimuli, the rotational viscosity (γ_1) is introduced to describe the ratio of a viscous torque acting on the director to the corresponding angular velocity of the director rotation. On the other hand, both the elasticity and viscosity are unique features of LCs determining respectively the orientational deforming and flowing behaviors of molecular director under the influence of an external force. In general, an LC with viscoelastic properties can be considered as a continuum fluid and its molecular orientation in equilibrium is thought to be uniform with unidirectional director $\hat{\mathbf{n}}$ throughout the bulk medium. On the basis of the static continuum theory (Frank, 1958; Oseen, 1933), when the director $\hat{\mathbf{n}}$ varies smoothly in space with a greater characteristic length than the molecular dimension, three fundamental deformation states, designated splay, twist, and bend, with distinct spatial variations in the unit vector $\hat{\mathbf{n}}$ have been formulated in terms of the spatial derivatives of a vector field. The spatial distribution of $\hat{\mathbf{n}}$ satisfies the condition of $\nabla \bullet \hat{\mathbf{n}} \neq 0$ in the splay state (Figure 1.5(d)), $\hat{\mathbf{n}} \bullet (\nabla \times \hat{\mathbf{n}}) \neq 0$ in the twist state (Figure 1.5(e)) and $\hat{\mathbf{n}} \times (\nabla \times \hat{\mathbf{n}}) \neq 0$ in the bend state (Figure 1.5(f)). The characteristic length of each deformation is thus described as the distance to the diverged point for a splay-type, the pitch of the molecular twist for a twist-type, and the curvature for a bend-type. When an LC is subjected to a stimulus (e.g. electric or magnetic field or thermal fluctuation) or constrained at cell walls, various types of molecular deformation can possibly be induced but any of them is describable by one or combination of the aforementioned deformation states. The elastic free energy density f_{elastic} (in $J \cdot m^{-3}$) of a nematic LC can thus be written as the sum of the splay, twist and bend terms in the following form:

$$f_{\text{elastic}} = \frac{k_{11}}{2} (\nabla \cdot \hat{\mathbf{n}})^2 + \frac{k_{22}}{2} (\hat{\mathbf{n}} \cdot (\nabla \times \hat{\mathbf{n}}))^2 + \frac{k_{33}}{2} (\hat{\mathbf{n}} \times (\nabla \times \hat{\mathbf{n}}))^2, \qquad (1.7)$$

where k_{11}, k_{22}, and k_{33} as the intrinsic material properties of an LC are the Frank elastic constants for quantifying the elastic energy of the splay, twist and bend deformations (Figure 1.5(d)–(f)), respectively. The magnitudes of the three elastic parameters are of the order of 1–10 pN, and they are proportional to the order parameter squared ($k_{ii} \propto S^2$) based on the Maier–Saupe theory. In general calamitic LCs, 30 pN > $k_{33} > k_{11}$ ($\sim 2k_{22}$) > k_{22} > 3 pN. However, bent-core molecules such as the LC dimer 1″,7″-bis

(4-cyanobiphenyl-4′-yl) heptane (CB7CB) exhibit much smaller k_{33}. For CB7CB, $k_{11} > 2k_{22}$ and $k_{22} > 1$ pN $> k_{33}$ (Babakhanova et al., 2017).

According to the response of the physical properties to external electric field, LCs can be regarded as phase retarders and optical rotators for modulating the polarization properties of incident light by electro-optical responses of the electrically controlled birefringence (or ECB) and polarization rotation (namely, wave-guiding) effects, as depicted in Figures 1.6(a) and (b), respectively. Figure 1.6 illustrates the operation principles of a conventional vertically aligned (VA) cell with negative LCs ($\Delta\varepsilon < 0$) as an example of a phase retarder and a 90°-twisted-nematic (TN) cell with positive LCs ($\Delta\varepsilon > 0$) as an example of an optical rotator. For the setup of the optical path, each cell is placed between a pair of linear polarizers with the front polarizer employed to convert the state of incident light from unpolarized state to linear polarization and the back one (i.e., the rear polarizer), also known as the analyzer, used to determine the light transmission. The configuration of a VA cell shows fixed director perpendicular to the substrate in the undisturbed or field-off state while that of a TN cell reveals deformed director twisting continuously from one substrate to the other over an angle of 90°. In practice, the pretilt angle of a VA cell is set to be ~89° rather than 90° in order to prevent defect generation from reverse tilt of molecular reorientation under voltage applied. Similarly, the rubbing angle between the top and bottom substrates of a TN cell is not perfectly 90° but ~88° to avoid the formation of reverse twist which can also be solved by adding a minute amount of a chiral agent to impose the twisting handedness. In the case of a VA cell in the field-off state, the incident polarized light, normally entering into the LC layer, encounters the same refractive index (i.e., n_o), meaning that no phase difference is experienced. Subsequently, the light is absorbed by the analyzer and the cell appears dark. Upon the application of voltage beyond a threshold value, the nematic directors are tilted toward the substrate plane by the dielectric effect and the effective birefringence (n_{eff}) is varied as a function of the voltage strength (Figure 1.6(a)). This leads to the change in transmission after the analyzer because of the vector sum of the extraordinary and the ordinary components of light and thus the change in its polarization state. The efficiency for optical transmission based on ECB LCs can be described by the irradiance equation (Yu et al., 2017c):

$$I = I_0\sin^2[2\Psi(V)]\sin^2\left[\frac{\delta(V)}{2}\right] = I_0\sin^2\{2[\Psi_0 + \Delta\Psi(V)]\}\sin^2\left[\frac{\pi d}{\lambda}\Delta n(V)\right]. \qquad (1.8)$$

Here, I_0 is a constant, Ψ_0 is the azimuthal angle between the transmission axis of the polarizer and the optic axis projected onto the substrate plane at zero voltage, λ is the wavelength of the incident light in vacuum. $\Delta\Psi(V)$ and $\Delta n(V) = n_{eff}(V) - n_o$ are the deviation angle of the director in the plane of substrates and the birefringence of the LC, respectively. Initially, Ψ_0 is optimally set at 45° and the optical transmission is maximum when the optical path length difference $\Delta n(V)d$ equals to $(m + 1/2)$ λ, where m is an integral. In contrast, the adiabatic following (or wave-guiding)

instead of the birefringence effect is utilized for light modulation in a TN cell. Principally, when a linearly polarized light beam is incident, its polarization direction will be guided, following the LC twist to rotate 90° without changing the polarization state. The output light is thus solely transmitted and obstructed under the conditions of crossed polarizers (said to be normally white; NW) and parallel polarizers (normally black; NB), respectively. The condition of the optical path length difference $d\Delta n$ of a TN cell has to be much greater than $\lambda/4$ for efficient wave-guiding along the twist (i.e., satisfaction of the Mauguin limit $\varphi \leq 2\pi d\Delta n/\lambda$; for the twist angle $\varphi = \pi/2$, $\lambda/4 << d\Delta n$) so that the production of elliptically polarized light can be avoided for better utilization of the light energy. Moreover, the output light transmission ($T\%$) of a 90°-TN cell for linearly polarized light is dependent on the wavelength (λ) of light, the birefringence of the LC, and the cell gap (d), which can be calculated with the Gooch–Terry expression in the case of the NB configuration as:

$$T\%_{\mathrm{NB}} = \frac{1}{2}\frac{\sin^2\left(\frac{\pi}{2}\sqrt{1+u^2}\right)}{1+u^2}, \tag{1.9}$$

and in the NW mode as (Kelly and O'Neill, 2001):

$$T\%_{\mathrm{NW}} = \frac{1}{2} - \frac{1}{2}\frac{\sin^2\left(\frac{\pi}{2}\sqrt{1+u^2}\right)}{1+u^2}, \tag{1.10}$$

where u is dimensionless, defined as $2d\Delta n/\lambda$. Note that $T\%_{\mathrm{NB}}$ in eq. (1.9) becomes only the second term of eq. (1.10) for the NB condition. As a consequence, I_{TN} of NW (NB) TN can be maxima (minima) in a series of conditions, following the rule of $(d\Delta n/\lambda)^2 = (m^2 - 1/4) = 3/4, 15/4, 35/4, \ldots$ or

$$u = \sqrt{4m^2 - 1} = \sqrt{3}, \sqrt{15}, \sqrt{35}, \ldots, \tag{1.11}$$

where $m \geq 1$ is an integral (Gooch and Tarry, 1974). Upon the application of a vertical electric field to a TN cell, the LC molecules will be gradually reoriented from the initial twist state to the voltage-sustained homeotropic state with increasing voltage strength as shown in Figure 1.6(b). This kind of electro-optical switching enables the monotonous change in light transmission before reaching Gooch–Terry's first extremum from brightness to darkness for the NW mode and from darkness to brightness for the NB mode.

When an external voltage is applied across the thickness of an LC cell, a threshold voltage is essential to overcome the elastic force so as to induce molecular reorientation from the uniform to deformed states via the well-known Fréedericksz (or Frederiks) transition. Moreover, two characteristic times, τ_{on} and τ_{off}, are defined to evaluate the response characteristics of molecular reorientation and relaxation, respectively, upon the application of an electric field and the removal of it. These two parameters together with the efficacy of optical transmission are important parameters for
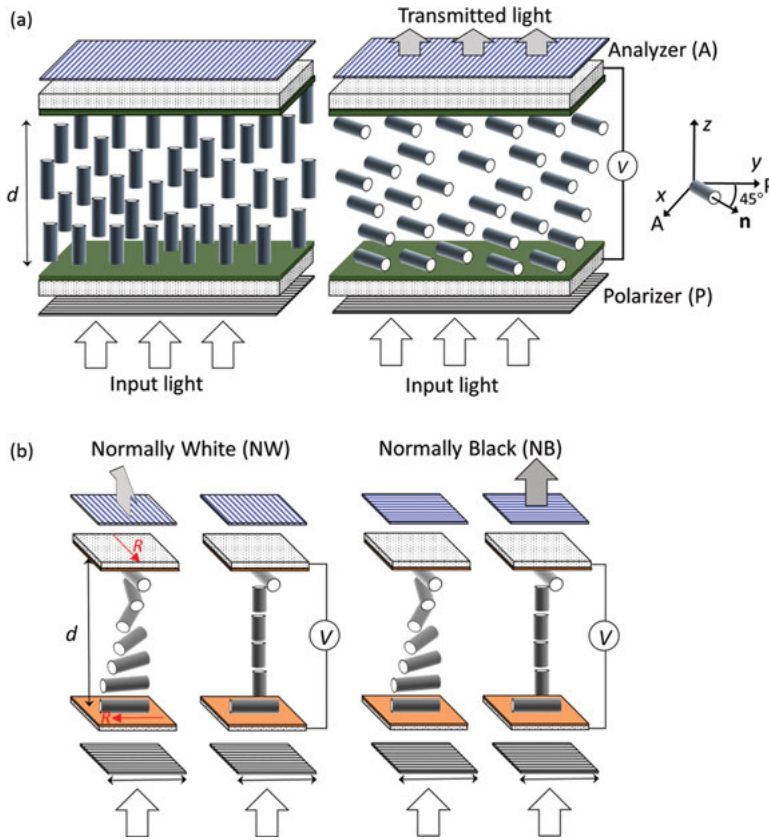
Figure 1.6: Operation principles of LCs as phase retarders and optical rotators driven by external voltages in (a) a vertically aligned cell and (b) a 90°-twisted-nematic cell.

evaluating LC cells for electro-optical applications. In general, the optical transmission is related to the optical anisotropy (as manifested in eq. (1.8)). Consider the condition of strong surface anchoring. The threshold voltage V_{th} and the voltage-on and voltage-off response times are affected by dielectric anisotropy ($\Delta\varepsilon$), elastic constants (k) and rotational viscosity (γ_1), which can be expressed in general forms by the following equations:

$$V_{th} = \pi\sqrt{\frac{k}{\varepsilon_0 \Delta\varepsilon}}, \tag{1.12}$$

$$\tau_{\mathrm{on}} = \frac{\gamma_1 d^2}{k\pi^2 \left[\left(\frac{V}{V_{\mathrm{th}}} \right)^2 - 1 \right]},$$ (1.13)

and

$$\tau_{\mathrm{off}} = \frac{\gamma_1 d^2}{\pi^2 k},$$ (1.14)

respectively. Equations (1.12)–(1.14) are critical formulas for the design of LC electro-optical devices (Kelly and O'Neill, 2001), where k equals to k_{11} for planar-aligned LCs, k_{22} for IPS LCs, k_{33} for VA LCs, or $k_{11} + (k_{33} - 2k_{22}/4)$ for 90°-twisted LC. Note that the two response times are proportional to d^2 for surface-treated cells to impose a hard boundary condition (i.e., strong surface anchoring such that the energy W needed to move the director $\hat{\mathbf{n}}$ from its easy axis is on the order of 10^{-4} J·m^{-2}). The quadratic form describing the response properties becomes invalid for LC cells with weak anchoring ($W \sim 10^{-7}$ J·m^{-2}) where the exponent drops (<2). Because the rotational viscosity γ_1, typically greater than the flow viscosity, is temperature-dependent, expressed as

$$\gamma_1 \propto S \cdot \exp\left(\frac{E_a}{k_B T} \right) = \left(1 - \frac{T}{T_c} \right)^{\beta} \cdot \exp\left(\frac{E_a}{k_B T} \right),$$ (1.15)

the viscoelastic coefficient γ_1/k (in ms·µm^{-2}), which is an intrinsic material parameter governing the response times, takes the form

$$\frac{\gamma_1}{k} = \frac{c \cdot \exp(E_a/k_B T)}{(1 - T/T_c)^{\beta},}$$ (1.16)

where c is a proportionality constant of *c.a.* 10^6 ms·µm^{-2}, E_a is the activation energy for diffusion of molecular motion, and k_B is the Boltzmann constant ($k_B = 1.38 \times 10^{-23}$ J·K^{-1}), resulting in lowered viscoelasticity at a higher temperature.

1.2.3 Conventional liquid crystal technologies

Conventional LCs with superior material properties have intensively been exploited for developing various electro-optical devices, including displays, optical switches, spatial light modulators, tunable lenses, beam-steering devices, and so on. Especially LCDs are the best known electro-optical applications offering advantages of compact size, light weight, no radiation, low cost, low power consumption and portability for replacing traditional cathode-ray tubes as modern visual elements. LCDs with tremendously commercial opportunities behind have thus received considerable attention and numerous technologies developed, facilitating the promotion in the practicality as well as applicability. Nowadays, LCD modes occupy the dominance in

the display market, showing widespread utilizations in most of our daily used consumer electronics and information products, ranging from large-size TVs and billboard over medium-size laptops, monitors, and automotive panels to small-size smartphones and watches (Chen et al., 2018a; Ko et al., 2018). Apart from display applications based virtually on achiral nematics, chiral LCs as a class of soft photonic crystals – such as cholesteric LCs and blue phases – with Bragg reflection bandgaps have gained increasing momentum for developing photonic devices, such as optical switches (Bao et al., 2009; Huang et al., 2003), optical diodes (Hwang et al., 2005), optical modulators (Gevorgyan, 2011), and lasers (Coles and Morris, 2010), not to mention the commercialized cholesteric-LC products such as the reflection cholesteric LCDs and the Boogie Board™ eWriter by Kent Displays, Inc. With rapid growth in concepts of energy saving and carbon footprint reduction, chiral LCs having at least two optically stable and electrically switchable states are finding increasing interests as green products, such as electronic books, e-papers, tags, and wearable as well as flexible devices (Fernández et al., 2015). Herein, we will focus on those of commercialized and emerging LC modes for display and chiral LCs for photonics applications, introducing their features, challenges, and recent developments.

1.2.3.1 Evolution of liquid-crystal cell modes for display applications

Twisted-nematic (TN), multidomain vertical (MVA), in-plane switching (IPS) and fringe-field switching (FFS) displays are commercial representatives using achiral nematic LCs. Accordingly, many LC technologies for promoting the LCD performance (e.g. contrast ratio, viewing angle, and response time) have been realized on the basis of these LC modes in order to meet the growing demand, from the rapid development of modern science and technology, to widen application domains and to prevent replacement by other emerging self-emissive displays, such as organic LEDs and mini- as well as micro-LEDs (Kim et al., 2014a). Particularly, fast response has long been the prerequisite of an LCD for realizing blur-free and sharp moving pictures and enriching image quality with great details. It further becomes the urgent need for applying LCDs to next-generation displays whose images are demanded for ultra-high definition and high refreshing rate. Typically, the total time for data addressing, LC response, and light emission is determined by the frame rate (e.g. 16.7 ms at 60 Hz). Increasing the number of data lines for high-resolution displays requires faster LC response due to the increase in data addressing time. Moreover, the LC response time must become one half for three-dimensional displays to show individually left and right images to human eyes without crosstalk. For field sequential color (FSC) LCDs where a triple frame rate is required to flash red, green, blue backlights sequentially, the time for LC has to be even reduced to one-third. However, the response times of commercial LCDs are still insufficient for these applications although it has been advanced from tens of millisecond to ~5 ms. The fact that LCs have insufficient response

times results from the slow molecular relaxation from a voltage-on state to the off state (i.e., τ_{off}). To date, approaches to improving the response rate have been considered from the following three standpoints: First, reducing the cell gap d (Gauza et al., 2007) and synthesizing new materials with low viscosity (Chen et al., 2013b; Mazur et al., 2017; Peng et al., 2013) are direct ways according to eq. (1.14). Since light intensity of an LCD is tuned by the change in phase retardation, thin cell gap must be compensated with high-birefringence LCs to maintain the peak brightness. Moreover, for the development of novel nematic LC material with a small viscoelastic coefficient γ_1/k via chemical synthesis, there are always tradeoffs between LC properties of viscosity, dielectric anisotropy and birefringence, and the mesophase temperature range, and the chemical and optical stability are sometimes questionable in practice. Second, from the point of view of cell configuration, several modified VA, IPS, and FFS modes with special designs on electrode structures and LC alignment have been pursued. These include optically compensated bend mode (Ishinabe et al., 2010), VA mode with in-plane switching (Pankaj Kumar et al., 2016b) or with triode electrodes (Yoon et al., 2018), FFS with alternating tilted pixel electrodes or with vertical wall insertions (Kim and Lee, 2015), and IPS with triode electrodes (Ma et al., 2018), to name a few. However, these modified versions require more complicated driving circuits which, in turn, lead to increased cost and reduced production yield. Third, since the efficiency on improving response time of nematic-LC-based LCDs is limited by the difficulty in optimizing material properties, some other emerging LC materials of ferroelectric LCs, blue phases, and short-pitch cholesteric LCs, with intrinsic features of wide-viewing angle and sub-microsecond response time, have progressively been proposed in considering the promotion of LCDs to next-generation displays. Unlike nematic-based LCs where the operation principles are dominated by the dielectric effect, the reorientation of LC molecules in response to external voltages for fast response is attributable to the spontaneous polarization effect in ferroelectric LCs, the Kerr effect in blue phases, and the flexoelectric effect in short-pitch cholesteric LCs. Although these emerging LC technologies in practice are still challengeable, numerous studies and approaches aiming to overcome their drawbacks have been demonstrated and potential applications of them suggested.

The attraction of ferroelectric LCs for electro-optical applications began from 1981, when Clark and Lagerwall demonstrated the surface-stabilized ferroelectric LC with alluring features of fast response, wide viewing angle and bistability (Clark and Lagerwall, 1980). Figure 1.7(a) illustrates the cell configuration and operation principle of the surface-stabilized ferroelectric LC. Ferroelectric LC material is filled in a planar-aligned cell with extremely thin cell gap typically smaller than 2 μm in order to unwind the helix and constrain the director to lie in the surface plane. In an ideal case, the smectic layers are themselves perpendicular to the surface, resulting in the so-called bookshelf geometry. Such a layer geometry leads to the coexistence of two stable, homogeneously aligned domains with opposite spontaneous polarization vectors $\mathbf{P_s}$ perpendicular to the surfaces in the cell. Projections of the LC director on the plane of the cell in these
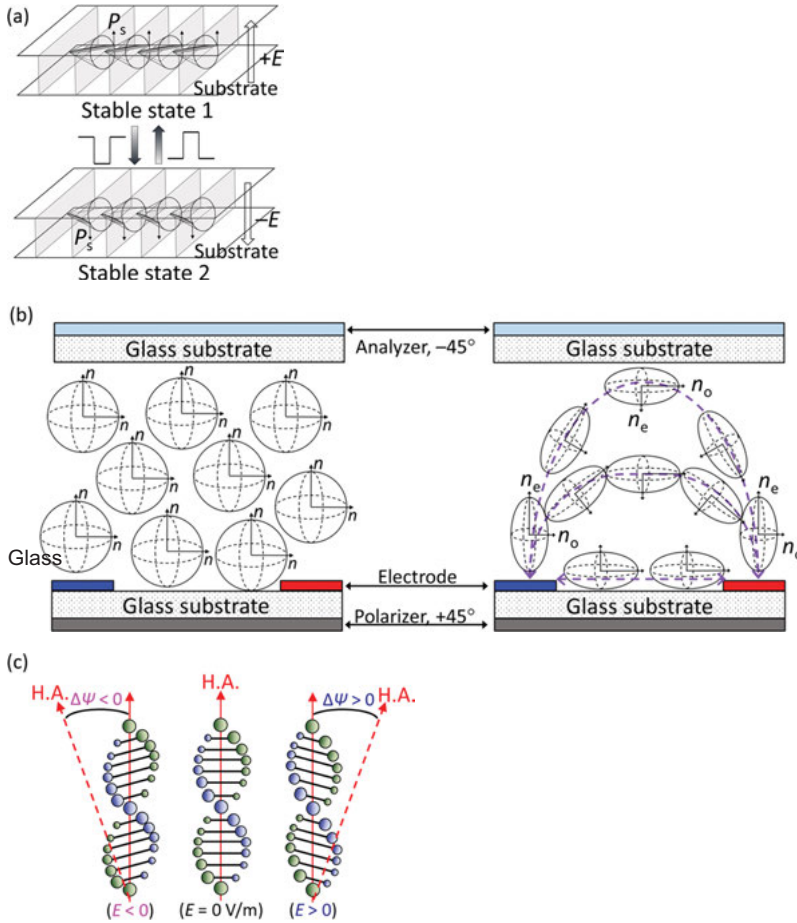
Figure 1.7: Schematic illustration of structures and operation principles of (a) a surface-stabilized ferroelectric LC, (b) a blue phase driven by in-plane electric fields, and (c) a cholesteric LC in the uniform lying helix structure driven by the flexoelectric effect.

two domains are at an approximately $2\theta_c$ angle (i.e., the cone angle). According to the ferroelectric torque ($\mathbf{\Gamma} = \mathbf{P_s} \times \mathbf{E}$), the molecules can be switched between the two states by applying positive and negative direct-current (DC) electric pulses across the cell, respectively. The response (i.e., switching) time of ferroelectric LC molecules under voltage applied is inversely proportional to the applied electric field; that is,

$$\tau_s \sim \frac{\gamma_1}{P_s E}, \tag{1.17}$$

rather than the square of the field as that in the nematic case; thus, the electro-optical response of the ferroelectric LC (in the microsecond scale) is faster than that of nematics (in the millisecond order). In addition, the molecular axes of the two

states are always parallel to the surface plane (in-plane switching), rendering the advantages of wide viewing angle and high contrast ratio. In a practical situation, however, the surface-stabilized ferroelectric LC has several inherent drawbacks, especially the non-uniform alignment on account of defected layer structures and lack of grayscale capability from the bistable switching, making difficulty of realizing ferroelectric LC displays by modern techniques. In general, there are two types of defects, vertical and horizontal chevron layer defects, respectively observed in surface-stabilized ferroelectric LC cells with SmA–SmC⋆ and N⋆–SmC⋆ phase transitions. When cooling the material from SmA to SmC⋆ phase, the tilted angle starts increasing with decreasing temperature and the layer structures shrink in the meantime. As a result, two possible chevron layers, C1 and C2 with chevron apex opposite to each other, could be formed simultaneously, leading to the formation of hairpin and lightning defects of zigzag lines in the surface-stabilized ferroelectric LC cell. To date, some approaches, such as rubbing (Furue et al., 1998), photoalignment (Kurihara et al., 2001), and SiOx deposition (Reznikov et al., 2010), to the formation of either uniform C1 or C2 structure have been attempted based on essential criteria for the stability of C1 and C2 (Koden et al., 1992). In regard to the material with N⋆–SmC⋆ phase transition, the molecules in a cell with identical alignment conditions do not align themselves ideally along the rubbing direction, but tilt by a small angle with respect to it so that the smectic layers in the horizontal plane of the cell incline by an angle θ_c with respect to the LC directors during this phase transition. Because the molecules with spontaneous polarizations directing upward and downward to the substrate have equal possibility to be generated, two types of domains whose layer planes inclining in opposite directions coexist in the cell, resulting in the formation of horizontal chevron defect (Dierking, 2000). There are mainly two feasible approaches to eliminating horizontal defects and obtaining monodomain alignment for this kind of ferroelectric LC material in a surface-stabilized ferroelectric LC cell geometry: (1) Electric field treatment: The effect of electric field on the molecular configuration and layer structure in the ferroelectric LC cell with N⋆–SmC⋆ phase sequence was first investigated by Patel and Goodby (Patel and Goodby, 1986). In their study, the electric field is applied at the temperature which is about 3 °C lower than the N⋆–SmC⋆ phase transition temperature. They concluded that while the rubbing direction determines the molecular orientation the electric field is responsible for controlling the layer tilt direction. On this basis, Asao et al. proposed to apply a DC voltage during the N⋆-to-SmC⋆ phase transition and monodomain molecular alignment with uniform tilted bookshelf layer structure was thus obtained by virtue of the induction of ferroelectric LC molecules with identical polarity (Asao et al., 1999). This method has been modified using non-DC or alternating-current (AC) voltage in attempt to prevent the degradation of electro-optical performance from the generation of electrical double layers inside the cell due to the application of long lasting DC voltage (Hotta et al., 2004; Wu and Wu, 2007). It is worth mentioning that the electro-optical response of surface-stabilized ferroelectric LC with N⋆–SmC⋆ is not bistable but shows half-V-shaped

switching when the molecular configuration exhibits monodomain alignment. (2) Hybrid alignment: The hybrid alignment method has two different meanings. One is asymmetric surface anchoring strength between the top and bottom substrates by combining weak rubbing for one substrate and strong rubbing for the other, or combining rubbing for strong anchoring and photoalignment for weak anchoring. In this manner, because the smectic layer grows from the rubbed polyimide surface to the photoalignment surface, the cell can show monodomain alignment when the asymmetric ratio of anchoring strength is large enough (Murakami et al., 2003). The other hybrid alignment considered the use of the alignment films with opposite surface polarities coated on the top and bottom substrates, respectively. The mechanism is that the assembly of these two substrates in a sandwich-type cell produces an inner electric field serving as the same effect as that of the external DC electric field. Accordingly, Chen et al. demonstrated monodomain ferroelectric LC alignment in a polyvinyl alcohol (PVA)–polyimide cell and explained the aligning mechanism via theoretical calculation (Chen and Lin, 2009). Chiang et al. followed this aligning mechanism and found that the half-V shape switching can be obtained by further treatment of AC electric field even when the cell was filled with the material with SmA–SmC⋆ phase sequence (Chiang et al., 2009). Nevertheless, the surface-stabilized ferroelectric LC has faced some technical challenges – especially for production of large-size devices, such as thinner (<2 μm) cell gap, low mechanical stability, and high sensitivity of alignment uniformity to cell gap; thus, one can only see commercial product of surface-stabilized ferroelectric LC in microdisplays. In addition to the surface-stabilized ferroelectric LC, some other ferroelectric LC modes, including the deformed-helix ferroelectric LC (Chiang et al., 2007; Jo et al., 2003) and electrically suppressed ferroelectric LCs (Shi et al., 2018, 2017; Srivastava et al., 2015), have been exploited for both display and photonic applications. The interested reader is referred to Chapter 3 for detailed information.

Using blue phases instead of achiral nematic LCs have been considered as a feasible way for the enhancement of display performance since Samsung Electronics in 2008 demonstrated for the first time the blue phase LCD prototype in the world, offering 15 inch in size and more natural moving images with an unprecedented image-driving speed of 240 Hz (Lee et al., 2011). In contrast to commercial LCDs, blue phases render wider viewing angle and could lend faster response without any additional driving scheme (e.g. overdrive or undershoot). Moreover, the molecular orientation of blue phases is self-assembled and optically isotropic in macroscopic viewpoint so that it can be obtained uniformly and show excellent dark state under crossed polarizers without any necessitated substrate treatment for surface alignment. These benefits simplify the fabrication process required, thereby allowing considerable saving on production costs. Typically, a blue phase cell is driven by transverse electric field using IPS electrodes. Figure 1.7(b) depicts the general scheme for the operating principle of a blue phase in such a cell geometry. The IPS cell is placed between crossed polarizers and electrode stripes are set 45° with respect to the transmission axis of

either of the crossed polarizers. In the absence of an electric field, dark appearance can readily be achieved because the molecular configuration of blue phases is of cubic symmetry and thus optically isotropic. When an in-plane electric field is applied, the molecular deformation in the double-twisted cylinders induces birefringence in such a way that the isotropic refractive-index sphere is changed to an elongated or a flattened ellipsoid (i.e., the isotropic-to-anisotropic transition, characterized by the Kerr effect) with the optic axis along the electric field direction. The magnitude of such a field-induced birefringence (Δn_{ind}) and the response time (τ_{BP}) of a blue phase LC cell can be expressed as (Ge et al., 2009; Rao et al., 2009)

$$\Delta n_{\mathrm{ind}} = \lambda K E^2, \tag{1.18}$$

and

$$\tau_{\mathrm{BP}} = \frac{\gamma_1}{k}\left(\frac{P}{2\pi}\right)^2, \tag{1.19}$$

respectively. In accordance with eq. (1.18), the field-induced birefringence in a blue phase is proportional to the wavelength λ, the square of the amplitude of the electric field E, and the Kerr constant K (in $\mathrm{nm \cdot V^{-2}}$) predominated by Δn, $\Delta\varepsilon$ and k_{33}/k_{11} of the blue phase material. The resulting transmittance of a blue phase LC cell associated with the induced phase retardation can be described by eq. (1.8). The most severe problem impeding commercial applications of blue phases is the extremely narrow temperature range (typically 1–2 °C) which can hardly be solved using conventional LCs alone. As such, currently available techniques to widen the temperature range of blue phases are mostly developed by unconventional LCs such as those composites comprising polymers, nanoparticles or bent-core molecules (Nordendorf et al., 2014). Other bottlenecks of blue phases that need to be urgently overcome for commercialization of displays as well as other electro-optical devices are the high operating voltage and low optical efficacy because the IPS electrode configuration is essential for electro-optical switching of blue phases. Since technologies for manufacturing IPS electrodes are mature in display industries, enlarging the Kerr constant by employing a blue phase mixture with high Δn and $\Delta\varepsilon$ would be a straightforward way for lowering the operation voltage (V_{op}) required for attaining maximum transmittance. Examples demonstrated in the literature are $V_{\mathrm{op}} > 100$ V with $K \sim 0.4$–4 $\mathrm{nm \cdot V^{-2}}$ (electrode width $w = 10$ μm and cell gap $d = 10$ μm) and $V_{\mathrm{op}} \sim 48$ V with $K \sim 13.7$ $\mathrm{nm \cdot V^{-2}}$ at $\lambda = 633$ nm and $T = 20$ °C (for $w = 10$ μm, electrode interval $l = 10$ μm and $d = 7.5$ μm) (Rao et al., 2011). Accordingly, some nematic host compounds with appropriate Δn and $\Delta\varepsilon$ have been developed and their long-term stability tested by LC material suppliers (e.g. Merck and Japan New Chisso) (Chen et al., 2013c; Wittek et al., 2012). Although high Δn and large $\Delta\varepsilon$ are desirable for promoted K, the magnitude of $\Delta\varepsilon$ suggested should not exceed 100 so that the response time can still be smaller than 1 ms and the slow charging issue can be surmounted by the driving scheme using the bootstrapping method (Tu

et al., 2012). However, after more than two decades of extensive efforts at material optimization, V_{op} of IPS-blue phase is still too high for pixel driving by a single thin-film transistor (TFT). Although some novel pixel circuits have been invented to supply high enough voltages, the use of more TFTs gives rise to considerable increase in power consumption, which is in conflict with the global concept of energy conservation. For this reason, attention has been paid to optimizing IPS parameters and designing new electrode structures to gain improvement in both driving voltage and optical efficacy. For an IPS-blue phase, electrode dimensions – such as the electrode width and interval and the cell gap – have been optimized to reduce V_{op} without losing transmittance (Sun et al., 2014c). A modified IPS structure, in which the substrate is etched between electrodes with a depth to elevate electrodes above it, has shown ~30% improvement in V_{op} and is further used for designs of viewing angle controller, transflective displays, and LC lenses (Sun et al., 2014a). Besides, some other unique IPS structures with distinct electrode shapes have been proposed to provide stronger and deeper penetrating electric field, which could possibly lower V_{op} to 15 V, thereby making IPS-blue phase suitable for a single TFT circuit. These include protruding electrodes on one or both substrates (Fan et al., 2015; Zhao et al., 2014), slit-shaped electrodes (Li et al., 2013a), wedge protrusion (Sun et al., 2014b), sidewall electrodes (Algorri et al., 2015), concave electrodes (Mao et al., 2016), high dielectric protrusion (Liu et al., 2016a), diamond-shaped protruding electrodes (Chen et al., 2017c), double-side concave-curved electrodes (Xing et al., 2018), single-penetration electrodes (Guo et al., 2017b), dielectric protrusion (Tian et al., 2019), opposite polar electrodes (Li et al., 2018b), and three-dimension-corrugated electrode (Chan and Choi, 2019). It should be noted here that most of the relevant studies were carried out by simulation, presumably due to complicated fabrication processes, implying that commercial applications of them are challengeable in the current stage.

The idea of flexoelectro-optical effect, rendering IPS-like optical responses to external voltages and sub-millisecond response time (~100 μs), was first proposed by Patel and Meyer using short-pitch cholesteric LCs stabilized in a so-called uniform lying helix structure whose helical axis is oriented in the substrate plane along a preferred direction (Patel and Meyer, 1987). Figure 1.7(c) illustrates the configuration of a short-pitch cholesteric LC in the uniform lying helix state and the working principle for the molecular switching by the voltage-induced flexoelectric and dielectric effects. Generally speaking, the cholesteric in the uniform lying helix state can be regarded as a uniaxial birefringent medium analogous to achiral nematic LCs with the helical axis being the optic axis in that the helical pitch length is comparable to or even shorter than wavelengths of visible light. Upon the application of an external electric field perpendicular to the helical axis (i.e., normal to the substrate plane), the coupling between the flexoelectric polarization and the electric field induces splay and bend deformations of the local director field, resulting in an in-plane deflection of the optic axis by a given angle which is a function of the

applied voltage. Moreover, because the flexoelectric switching is polar, the deflections of optic axis in response to the positive and negative electric fields are in opposite directions. The equation for such a voltage-induced deviation angle ($\Delta\Psi$) and the response time (τ_{flexo}) for the flexoelectric switching can respectively be written as (Patel and Lee, 1989; Patel and Meyer, 1987)

$$\tan \Delta\Psi = \frac{(e_{\mathrm{s}} + e_{\mathrm{b}})P}{2\pi(k_{11} + k_{33})} Vd, \tag{1.20}$$

and

$$\tau_{\mathrm{flexo}} = \frac{\gamma_{\mathrm{f}}P}{2\pi^2(k_{11} + k_{33})}. \tag{1.21}$$

Here, γ_{f} is the effective viscosity associated with the helix distortion for the flexoelectric switching and e_{s} and e_{b} are the splay and bend flexoelectric coefficients, respectively. Equation (1.20) is established under the condition in which the dielectric effect is insignificant or negligible. In a practical situation, dielectric anisotropy in most of conventional rod-like LCs is typically non-zero so that, at the voltage beyond a critical value, the helical configuration of a cholesteric LC is gradually unwound with increasing voltage and finally sustained in the homeotropic state at high voltage. This leads to the change in effective birefringence from $(n_{\mathrm{e}} + n_{\mathrm{o}})/2$ in the field-off uniform lying helix state to n_{o} in the voltage-sustained homeotropic state, which is beneficial for phase modulation using the uniform lying helix structure. Consequently, the magnitude and linearity of the flexoelectro-optical response of the uniform lying helix using conventional LCs are very limited for the flexoelectric behavior is observable only in a very narrow voltage regime where the helical profile is preserved and not dominated by the dielectric effect. To effectively modulate the light intensity between the minimal and maximal values, $\Delta\Psi$ should ideally be 45° (22.5°) in the case of $\Psi_0 = 0°$ (22.5°) under unipolar (bipolar) voltage applied according to eq. (1.8). An LC material with large flexoelectric coefficients and low elastic constants as well as long helical pitch length is thus desirable for attaining high optical performance at low voltages, as given by eq. (1.20). However, the magnitude of the flexoelectric angular deflection of the optic axis of the uniform lying helix using conventional rod-like LCs is quite restricted (typically smaller than 10°) because of inherently low flexoelectric coefficients (Komitov et al., 1999; Patel and Lee, 1989). For this reason, a number of unconventional LCs, especially those with bent-core molecular shape and bimesogenic properties, have progressively been developed (Coles et al., 2006; Morris et al., 2007; Varanytsia and Chien, 2017). The other hurdle impeding practical uses of the uniform lying helix is the difficulty in obtaining a desirably stable and defect-free alignment; hence, various technologies concerning the generation of uniform lying helix alignment have been successively proposed based on the electric-field treatment, surface pretreatment and the combination of them. The earliest electric-field method enabling the generation of uniform lying helix configuration

in a planar-aligned cholesteric LC cell is to apply an AC electric field across the cell thickness during the isotropic-to-cholesteric LC phase transition (Patel and Meyer, 1987). The optic axis of the resulting uniform lying helix accomplished by this method is deviated by a given angle with respect to the buffing (or rubbing) direction, determined by the amount of twist in the transition region whose distance away from the substrate surface is on the order of the dielectric coherent length (Lee et al., 1990). Salter et al. further explained two possible director field configurations of the interface between a bulk uniform lying helix and a planar aligning surface by means of a finite difference numerical simulation based on the Frank elastic distortion. The first one reveals a half-pitch periodicity together with singular disclination lines close to the surface whereas the second situation is a smooth transition from the bulk helix to the planar substrate periodically over a full cholesteric pitch (Salter et al., 2009b). They also found that the uniform lying helix alignment in either parallel (0° rubbing) or anti-parallel (180° rubbing) planar cell is usually non-uniform, suggesting it to be caused by the formation of uniform lying helices in opposite directions to the rubbing direction on each substrate and, in turn, the two-domain structure. As such, on the basis of this method, the improvement in uniformity of uniform lying helix alignment has been proposed by using planar-aligned cell with 90°-twisted rubbing (Salter et al., 2009a), by forming interdigitated planar/homeotropic anchoring conditions with the periodicity matched to one-half of the helical pitch of the cholesteric LC medium on one substrate (Hegde and Komitov, 2010), by using cholesteric alignment layer with the same pitch as that of the injected material to create periodic boundary conditions (Komitov et al., 1999), or by optimizing the pretilt angle as well as the anchoring energy (Park et al., 2016). On the other hand, approaches aiming to induce uniform lying helix alignment by voltage treatment at ambient temperature have been reported, but additional treatments and/or limitations were required. For example, Inoue et al. indicated that the shearing rate is critical to the transition of cholesteric LC texture from the focal conic to the uniform lying helix state and its effect on the alignment uniformity is inversely proportional to the cell thickness (Inoue and Moritake, 2015). Specifically for positive cholesteric LC ($\Delta\varepsilon > 0$) with significant ionic effect, Wang et al. proposed to achieve a stable and switchable uniform lying helix state via the electrohydrodynamic instability by applying a low-frequency (30 Hz) AC voltage (Wang et al., 2011). Nian et al. then specified by means of dielectric spectroscopy that the optimized frequency regime for the formation of electrohydrodynamics-induced uniform lying helix is in between f_L and f_R, where f_L is the lower frequency at which the real-part ε' and imaginary-par ε'' curves intersect each other and f_R refers to the one corresponding to the maximum value of tan δ or tan ($\varepsilon'/\varepsilon''$) (Nian et al., 2016). Recently, Yu et al. disclosed a new electric-field technique without the need of a temperature controller for phase transition or the requirement of ion-rich LC materials or mechanical shearing for textural transition. This method entails sustaining the cholesteric LC in the homeotropic state by the voltage V_H and then precisely decreasing the voltage to zero to induce uniform lying helix alignment in a 90°-twisted cell through the nematic-to-cholesteric LC textural transition (Yu et al., 2017c). In regard to various surface pretreatment methods,

the concept is to spontaneously form the uniform lying helix structure with free energy lower than that of the Grandjean planar state by modifying the surface morphology of alignment layers. Accordingly, Qutram and Elston proposed to coat weak homeotropic alignment films on scratched substrates with depths ranging from 10 nm to 30 nm to allow defect-free uniform lying helix formation by cooling the sample slowly from the isotropic phase through the blue phase (Outram and Elston, 2013c). Other technologies to create specific grooved alignments on substrates have been suggested by means of two-photon excitation laser lithography (Carbone et al., 2009), mold-templating (Outram et al., 2013), and laser writing (Carbone et al., 2011). However, the manufacturing processes of uniform lying helix by surface treatment would become too complicated to be promoted for mass production.

1.2.3.2 Chiral liquid crystal photonics and bistability

As outlined in Section 1.2.2, chiral LC phases such as cholesteric LCs and blue phases reveal periodical orientation of director yielding molecular helix in one and three dimensions can be regarded as soft one-dimensional and three-dimensional photonic crystals (PCs), respectively. The most attractive fingerprint of chiral LCs is the photonic bandgap or, in other words, the Bragg bandgap in the predominant Grandjean planar state, corresponding to the reflection of circularly polarized light with the same handedness as that of the helix; thus, the maximum reflectance of a photonic bandgap is 50% for unpolarized light. This makes chiral LCs potential for photonic applications, such as reflective displays, reflectors, and lasers. According to Bragg's law, the central wavelength (λ_c) of a cholesteric LC, given by the equation

$$\lambda_c = \langle n \rangle p \cos \theta_i = \left(\frac{n_e + n_o}{2} \right) p \cos \theta_i, \tag{1.22}$$

is determined by the average refractive index $\langle n \rangle$ – namely, the arithmetic mean of the ordinary (n_o) and extraordinary (n_e) refractive indices, the helical pitch (p) of the chiral material, and the light incident angle (θ_i). Consider the special case of normal incidence so that $\cos \theta_i = 0$. The pitch falls typically between 250 nm and 500 nm for the Bragg reflection to occur in the visible spectrum, giving an iridescent appearance. The shorter and longer wavelengths at the reflection band edges are

$$\lambda_S = n_o p \tag{1.23}$$

and

$$\lambda_L = n_e p, \tag{1.24}$$

respectively, and the bandwidth is calculated by

$$\Delta\lambda = \lambda_L - \lambda_S = (n_e - n_o)p = \Delta n \cdot p. \tag{1.25}$$

If a cholesteric LC is created by doping a chiral agent, either right-handed (R) or left-handed (S), into a nematic host, the magnitude of p is predominated by the dopant concentration (c) and the helical twisting power (HTP) of the chiral dopant (HTP > 0 for R-dopant; HTP < 0 for S-dopant), following the relation $p = 1/(c \times \text{HTP})$. While for blue phases, the reflection wavelength λ_{BP} is defined by some other factors, such as the Miller indices (h, k, and l) of a crystal plane and the blue phase lattice constant (a), corresponding to one pitch in BPI and half a pitch in BPII as the following (Chen and Wu, 2014; Chilaya, 2001)

$$\lambda_{BP} = \frac{(n_e + n_o)a}{\sqrt{k^2 + h^2 + l^2}}\cos\theta_i. \tag{1.26}$$

This makes the photonic bandgap profile tunable, which is fascinating for realization of a photonic device with highly flexible tunability of optical properties. For this purpose, there have been a good number of approaches demonstrating tunable λ_c of conventional chiral LCs by either the thermal or electrical bandgap tuning.

Using the temperature (T) as a stimulus, approaches toward thermally tunable λ_c of the photonic bandgap and thus the reflective color have been proposed on the basis of the temperature-dependent material properties, phase transition, and dopant solubility. In general, the central wavelength of photonic bandgap of a thermotropic cholesteric LC will slightly shift with the temperature near the cholesteric LC−isotropic phase transition. On the other hand, if the cholesteric LC material used is polymorphic and has the SmA* phase at a lower temperature, the value of λ_c can effectively be regulated in a wide wavelength range by the temperature especially near the cholesteric LC−SmA* phase transition (Huang et al., 2006; Natarajan et al., 2008; Tzeng et al., 2010). This temperature-varying behavior of λ_c has nicely been fitted by Keating's theory (Tzeng et al., 2010), and has experimentally been explained in terms of the temperature dependence of the twist elastic constant and the pitch of the CLC with SmA*−CLC transition (Zhang and Yang, 2002). By mixing the CLC with two kinds of chiral dopants, red-shift of λ_c with increasing temperature has been obtained and suggested to be caused by the temperature-dependent HTP of the binary chiral mixture (Cheng et al., 2011).

In considering the ease of operation and compatibility with modern optoelectronic technologies, tuning λ_c by external voltage would be more appropriate than by temperature for practical applications. In the case where the electric field is supplied vertically to the cell, a CLC with negative dielectric anisotropy tends to avoid voltage-induced helical distortion. Upon the application of such a DC voltage to a negative CLC ($\Delta\varepsilon < 0$), Lin et al. demonstrated blue-shifted λ_c by ~10 nm at $V_{dc} = 200$ V, explained by the voltage-induced electrohydrodynamic instability (Lin et al., 2006a). Later, Natarajan et al. obtained a wider tunable λ_c range of ~50 nm by a DC voltage $V_{dc} = 322$ V, and the

tuning mechanism is interpreted as the defect annealing of the helical structure together with the contraction of the pitch by high DC voltages (Natarajan et al., 2008). The same research group also found bandwidth broadening of the photonic bandgap by ~150 nm with unchanged λ_c by applying AC voltages at frequencies lower than 1 kHz (instead of DC voltages) across the cell gap of a negative (dielectric anisotropy) CLC (S811 + ZLI-4788). In 2010, Bailey et al. proposed to electromechanically tune the λ_c of a negative CLC cell by contracting the pitch through the bending of the ITO substrates caused by the induction of Maxwell's stresses under the voltage application. With increasing DC voltage or field strength, their experimental results showed the blue-shift of λ_c from 720 nm to 660 nm by $V_{dc} = 165$ V and from 1,550 nm to 1,290 nm by $V_{dc} = 140$ V (Bailey et al., 2010). They concluded that the tunable λ_{CLC} range by the voltage-induced cell-gap bending depends on various factors, including the pitch of the CLC, the DC voltage, the cell configuration, the thickness of the ITO glass, and the surface anchoring energy. This approach can also be obtained by AC voltage but the effect for λ_c is somewhat weaker than that by DC voltage (Bailey et al., 2012). Differently, Choi et al. suggested to tune λ_c of a negative CLC by AC voltage via the assistance of voltage-induced in-plane molecular switching of ferroelectric LCs. They obtained blue-shift of λ_c by ~20 nm with increasing AC voltage from 0 V_{rms} to ~135 V_{rms} at 1 kHz in the case of ferroelectric LCs as a thin film coated on the alignment layer (Choi et al., 2007) or by ~50 nm with increasing AC voltage to ~134 V_{rms} at 5 kHz in the case of ferroelectric LCs as a dopant, incorporated in the cholesteric LC (S. S. Choi et al., 2009). The tunable λ_c ranges based on the above-mentioned electric-field methods are factually quite limited (<100 nm) and the operating voltages relatively high (>100 V).

To solve the aforementioned shortcomings, Hsiao et al. proposed to electro-thermally tune λ_c by means of voltage-induced dielectric heating. In their case, a dual-frequency cholesteric LC cell was made with strong temperature-dependent λ_c by doping a thermosensitive chiral dopant together with a regular chiral dopant R5011 into a dual-frequency nematic host. By applying AC voltages of 45 V_{rms} at frequencies above the crossover frequency, the dielectric anisotropy in the dual-frequency cholesteric LC becomes negative and the value of λ_c can sufficiently be controlled between ~470 nm and ~650 nm by modulating the frequency to induce temperature variation via dielectric heating (Hsiao et al., 2018). Recently, Wu et al. discovered a voltage-induced temperature heating phenomenon in a standard sandwich-type cell comprising a conventional negative LC (i.e., LC possessing negative dielectric anisotropy). The observed heating behaviors were confirmed as a result of electro-thermal heating, called the pseudo-dielectric heating effect, induced by the pseudo-dielectric relaxation from the cell geometry because of the use of ITO electrodes with non-zero resistance. This novel electro-thermal feature was further utilized for tuning λ_c. In this case, a material with cholesteric LC–SmA* phase transition was made by doping 45 wt% of S811 into a negative nematic LC (ZLI-6608) to induce intrinsically thermo-sensitive spectral properties, as shown in Figure 1.8(a). When AC voltages are applied to the cell with ITO resistivity of 310 Ω, the performance in terms of both the tunable λ_c range and operating voltage
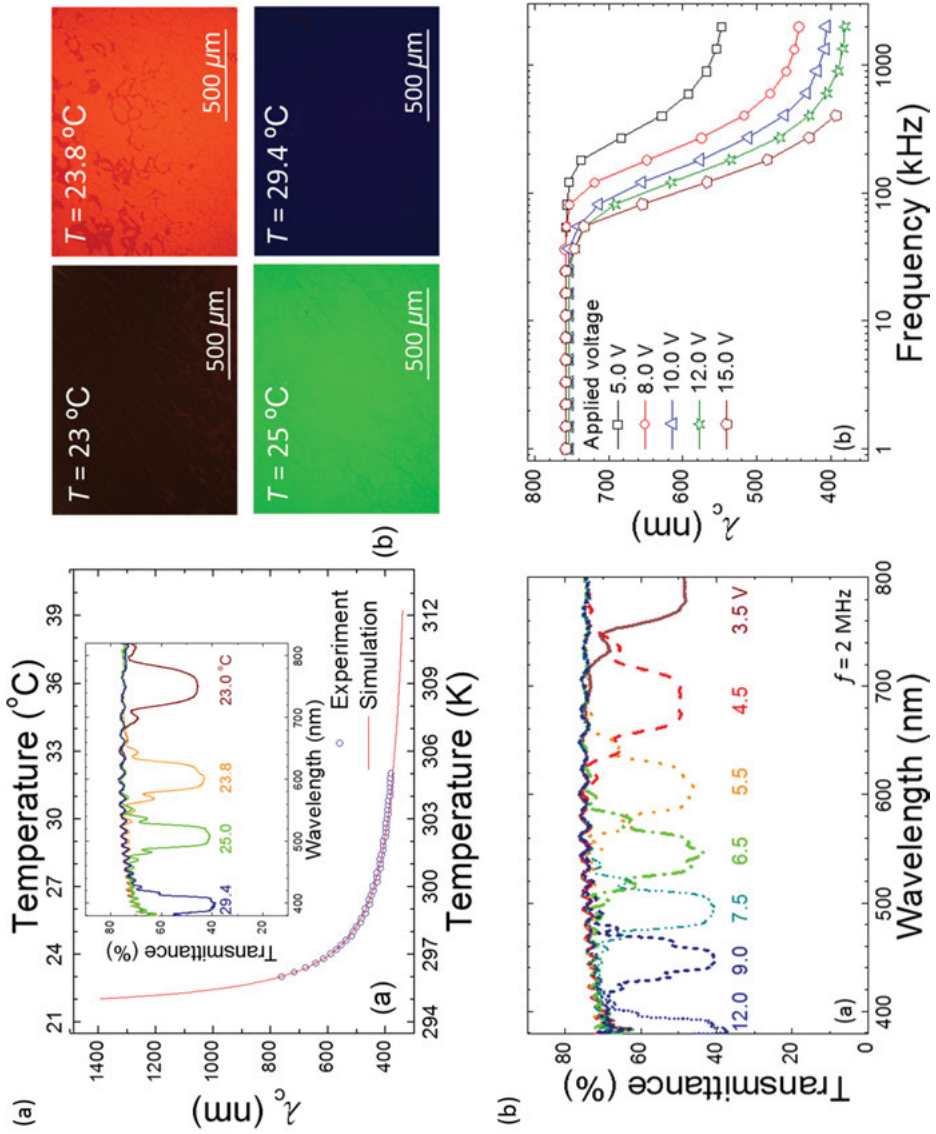
Figure 1.8: λ_{CLC} tuning in a planar-aligned CLC (composed of the $-\Delta\varepsilon$ LC ZLI-6608 doped with 45-wt% S811) cell by (a) thermal variation and (b) AC electric field application. Figure adopted from Wu et al. (2018b).

required is much superior to any of existing electric tuning techniques. For example, λ_c can be electrically modulated within the entire visible regime, ranging from ~380 nm to ~800 nm by varying the amplitude of the applied voltage in the range between 3.5 V_{rms} and 12 V_{rms} at a fixed frequency of 2 MHz or by varying the frequency in the range between 1 kHz and 2 MHz at 12 V_{rms} (see Figure 1.8(b)) (Wu et al., 2018b).

On the other hand, bandgap tuning in pristine blue phases – namely, blue phase cells without further stabilization by polymers or some other additives – are quite rare, presumably due to the structural instability as well as the relatively narrow temperature range. Referring to eq. (1.26), Yan et al. controlled the angle of incidence of light and investigated the angular dependence of λ_{BP} (Yan et al., 2013). They concluded that λ_{BP} can be blue-shifted and red-shifted with increasing angle of incidence when the blue phase experiences the first- and second-order reflection, respectively. While temperature tuning is expected, electrically tunable λ_{BP} have also been suggested. Chen et al. demonstrated a study of electrically induced bandgap shifting and broadening of a polymer-stabilized BP. Prior to polymer stabilization, they found that the photonic bandgap of BPI can be red-shifted by ~22 nm at $T = 31.5$ °C under voltage applied at $V \sim 44.4$ V_{rms} and frequency of 1 kHz. If the cell in BPI is subjected to DC voltage, the uniform BP texture will be distorted and then transfer into the cholesteric LC phase owing to the induction of electrohydrodynamic instability (Chen et al., 2015). The underlying mechanism of the voltage-induced bandgap shifting in blue phase is explained by the lattice elongation along the field axis.

Aside from the bandgap tuning, there have been a good number of studies concerning the development of bi- or tri-stable LC devices based on chiral-doped LCs. Conventionally, the molecular orientation is monostable in a nematic LC cell with symmetric surface conditions on two substrates. When doping chiral additives into nematic LCs, two topologically equivalent states can possibly be obtained by optimizing the cell gap-to-pitch ratio (d/p) and surface conditions. Switching between the two states is mainly attained by designated voltage pulses to induce a certain degree of hydrodynamic flow. The 2π bistable twisted nematic (2π-BTN) was the first demonstration of bistable chiral nematic, showing 0 (0°) and 2π (360°) twists as stable states in the conditions of $d/p \sim 0.5$ and simple planar alignment with pretilt angle of ~55° achieved by SiO$_x$ evaporation (Berreman and Heffner, 1980). Electrical switching between the two states was achieved by voltage-sustaining the cell in the homeotropic state first and then turning off the voltage suddenly to form stable 2π-twist or decreasing the voltage gradually to form the stable 0°-twist state. By setting d/p to ~0.25, various π-BTNs with 0- and π-twists as stable states – such as surface-controlled bistable nematic (SCBN) (Barron et al., 2005; Joubert et al., 2003), comb-on-plane BTN (COP-BTN) (Xie et al., 2002), and bistable chiral splay nematic (BCSN) (Kim et al., 2012; Lee et al., 2009; Lee et al., 2010b; Yao et al., 2009) – have been proposed with stabilities superior to that of 2π-BTN. When the d/p ratio is neither 0.25 nor 0.5, Hsu et al. demonstrated a new type of bistable LC mode, called the bistable chiral-tilted homeotropic nematic (BHN),
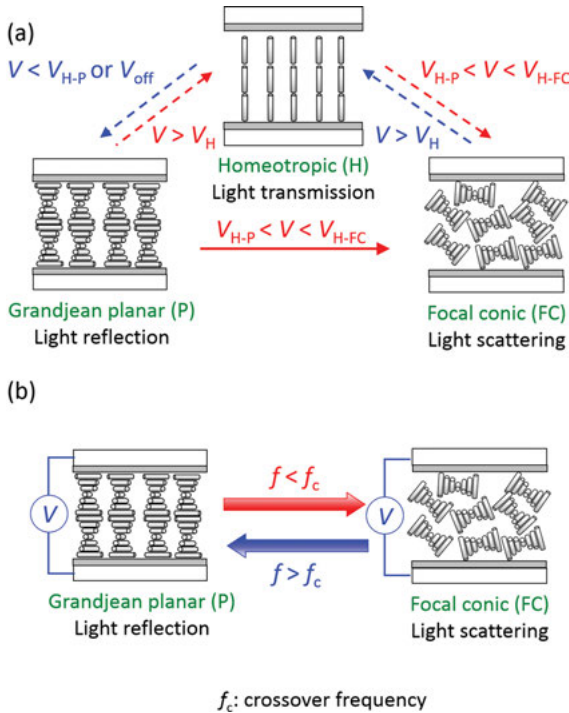
Figure 1.9: Driving scheme for electrically textural switching of (a) a conventional cholesteric LC with positive dielectric anisotropy and (b) a dual-frequency cholesteric LC.

possessing two optically stable states – 0°-tilted-homeotropic (tH) and 2π-tilted-twist (tT) states – by injecting chiral-doped dual-frequency LC into a cell with tilted homeotropic surface alignment and $d/p \sim 1$ (Hsu et al., 2004).

Unlike the aforesaid bistable chiral nematics where the switching between stable states results in the change in phase retardation of incident polarized light, a cholesteric LC with $d/p \gg 1$ in a planar-aligned cell is well known to exhibit Grandjean planar (P) and focal conic (FC) textures as two optically stable states and they have extensively been regarded as light-reflecting (bright) and light-scattering (translucent or "dark") states for the development of bistable cholesteric LCs in energy-efficient light shutters, reflective displays, and transparent displays. Figure 1.9(a) illustrates the general scheme for electrically controlled bistable switching of a positive cholesteric LC. Here, five voltage conditions are established and their magnitudes follow the relation of $V_H > V_{H-FC} > V_{FC-H} > V_{P-FC} > V_{H-P}$. V_H is the voltage required for unwinding the molecular helix and sustaining the cholesteric LC in the homeotropic (H) state. The magnitudes of V_{H-P} and V_{H-FC} are typically ~0.42 V_H and 0.9 V_H, respectively, whereas V_{P-FC} (V_{FC-H}) is the threshold voltage for inducing the P–FC (FC–H) textural transition (Jones, 2012). According to the dielectric coupling between LC molecules and the electric field, the cholesteric

LC texture in the initial P state can directly be switched to the FC state by the voltage in between $V_{\text{H-P}}$ and $V_{\text{FC-F}}$ ($V_{\text{H-P}} < V < V_{\text{FC-H}}$). In contrast, switching from FC to P needs to first sustain the cell in the H state and then alters the voltage immediately from V_{H} to the one lower than $V_{\text{H-P}}$ or switches the voltage off directly. Note that the FC state can alternatively be obtained from the H state by decreasing the voltage gradually from V_{H} to the one between $V_{\text{H-P}}$ and $V_{\text{H-FC}}$ ($V_{\text{H-P}} < V < V_{\text{H-FC}}$). It is clear from Figure 1.9(a) that reverse switching from FC to P can only be achieved indirectly through a transit of the H state and it is time-consuming because of the slow relaxation from H to P state (precisely, from H through a conical helical process to the transient planar and eventually to the P state). For this reason, Hsiao et al. proposed to attain direct two-way bistable switching using dual-frequency nematic LC as the host material to fabricate a dual-frequency cholesteric LC cell. They demonstrated that forward and backward switching between stable P and FC states with millisecond response time can be electrically obtained by a fixed voltage magnitude at the frequency conditions of $f < f_{\text{c}}$ and $f > f_{\text{c}}$, respectively (Figure 1.9(b)) (Hsiao et al., 2011). Here, f_{c} is the crossover frequency at which the magnitude of dielectric anisotropy is zero ($\Delta\varepsilon = 0$ at $f = f_{\text{c}}$). Accordingly they further established a passive-matrix driving scheme for reflective displays (Lin and Lee, 2011) and suggested methods for reducing operating voltage by employing hybrid-aligned cell mode (Hsiao et al., 2015) or electro-thermal characteristic of dual-frequency LCs (Hsiao and Lee, 2013). Such a frequency-modulated bistable switching has also been suggested using negative cholesteric LCs. In this case, the P-to-FC switching is realized by a low-frequency voltage via the electro-hydrodynamic effect whereas a high-frequency voltage is applied to achieve the reverse switching from FC to P by the dielectric effect (Moheghi et al., 2016). On the other hand, based on vertical-aligned long-pitch cholesteric LCs, Kim et al. and Cheng et al. independently demonstrated driving schemes for bistable switching between H and FC states of positive cholesteric LCs and for that between two fingerprint states with distinct domain sizes of negative cholesteric LCs in vertically aligned cells by regulating the types of electrical signal (AC or DC) (Cheng et al., 2016; Kim et al., 2017b). In addition to the stable P and FC textures, some other methods for generating fingerprint or uniform lying helix texture as the third stable state have been suggested, allowing the development of tristable cholesteric LCs. For example, considering a positive cholesteric LC injected in a simple cell geometry comprising planar alignment layers. Wang et al. employed an ion-rich cholesteric LC and proposed to apply low-frequency (several tens of Hz) voltage to switch the cholesteric LC from either the P or FC to the uniform lying helix state via electrohydrodynamic instability (Wang et al., 2011). Using the homeotropic state as the transit state, Yu et al. suggested the switching between any two of the P, FC, and uniform lying helix states by adjusting the voltage strength (Yu et al., 2017c). While the switching between the Grandjean planar and uniform lying helix (ULH) states based on these two schemes is indirect, Li et al. designed a tri-electrode configuration to achieve P-to-ULH switching by in-plane field and ULH-

to-P switching by vertical field using cholesteric LC with negative dielectric anisotropy (Li et al., 2018a). In contrast to cholesteric LC, approaches to the bistable switching in blue phase have also been reported. Wang et al., and Tiribocchi et al. independently reported on the electrical switching of two stable blue-phase lattices by particular pulse voltages (Tiribocchi et al., 2011; Wang et al., 2010). The difference between these two approaches is the sign of dielectric anisotropy of the used LC host which is negative in Wang's study. Another manifestation of bistability was unraveled between the blue phase and the cholesteric LC states in a polymer-stabilized system (Zheng et al., 2012).

1.3 Unconventional liquid crystals

1.3.1 Introduction

Unconventional LCs can broadly be defined to cover those novel LC materials whose structural and inherent properties are unique in comparison with those of conventional LCs. One common type of unconventional LCs is referred to LC compounds with molecular architectures wherein the anisometric shape deviates from the conventional rod- or disk-like forms. Bent-core (also called banana-shaped) LCs would be the most attractive and the most widely investigated unconventional mesogenic compounds during the last two decades owing to the particularity in molecular orientation with polar order and supramolecular chirality in their mesophases despite the achiral nature of the mesogens (Takezoe, 2014). The molecular structure of bent-core LCs in the general form is composed of one central bent unit, two rod-like aromatic wings, and two flexible tails. Since Niori et al. in 1996 demonstrated the first mesophase with antiferroelectricity in non-chiral bent-core molecules (Niori et al., 1996), a rich variety of mesophases have progressively been predicted and even experimentally demonstrated, including ferroelectric and antiferroelectric banana phases (named from B1 to B8 according to the sequence of their discovery) and biaxial twist–bend nematic phases (N_{tb}) specifically available in bent-core LCs and typical nematic, chiral nematic as well as smectic phases analogous to those created by rod-like LCs (Jákli, 2013; Takezoe and Takanishi, 2006). Notably, interesting and unusual features, having no counterpart in conventional LCs, have been discovered in certain bent-core LC mesophases, such as phase transitions, electroconvection (Lubensky and Radzihovsky, 2002), dielectric relaxations (Marino et al., 2012; Srivastava et al., 2017), flexoelectricity, Kerr effect (Harden et al., 2006; Shamid et al., 2013), viscoelasticity (Dorjgotov et al., 2008; Kaur, 2016; Sathyanarayana et al., 2010), and textural switching (Xiang et al., 2014). Specific bent-core LCs have been designed and potential applications suggested, especially bent-core LCs with ferroelectric switching in smectic or banana phases or flexoelectric switching and Kerr effect in chiral nematic phases for fast-response optical devices and displays (Chiang et al., 2014; Khan et al., 2017a; Panarin et al., 2017; Sreenilayam et al.,

2016; Wang et al., 2018a; Xiang et al., 2017). In considering the scope of this book and the role of this chapter, further discussion on recent development of unconventional LC compounds is omitted in this introductory chapter. Interested readers can follow Chapter 2 and several review articles to learn more information in detail about the design as well as remarkable and unique properties of LCs with unconventional molecular shapes reported in the literature (Gleeson et al., 2014; Jákli et al., 2018; Kato et al., 2018). To date, none of any practical application has yet been demonstrated using bent-core LCs. One of the possible reasons is that bent-core LCs are not as commercially available as rod-like counterparts and they might be owned by certain research groups. Other shortcomings impeding the applicability of bent-core LCs would be the difficulty in making defect-free alignment and the relatively high operating temperature ranges.

In recent years, researchers have moved their attention to physical doping of rod-like LCs with bent-core mesogens and have found extraordinary characteristics, such as the stabilization of blue phases (Taushanoff et al., 2010; Zheng et al., 2010) and modifications in physical properties (Lee et al., 2012, 2013; Salamon et al., 2010), in designated binary bent-core/rod-like LC mixtures. Mixing rod-like LCs with unconventional bent-core LCs has been adopted to suppress the image flickering effect in the fringe-field switching (FFS) LC mode (Kim et al., 2014b), accelerate the response speed in the hybrid-aligned in-plane-switching (IPS) LC mode (Zhou et al., 2017), and enhance the flexoelectro-optical switching of the cholesteric LCs (Tan et al., 2017; Varanytsia and Chien, 2016) because of the promotion in the flexoelectric effect. Moreover, Outram and Elston have clarified theoretically the impact of flexoelectric polarization on the dielectric spectra of a negative ($\Delta\varepsilon < 0$) bent-core/rod-like CLC mixture and, respectively, suggested the approach to the formation of ULH alignment by in-plane electric fields (Outram and Elston, 2013b) and the frequency-modulated textural switching between the Grandjean planar and uniform lying helix states by vertical electric fields via the voltage-induced electrohydrodynamic and dielectric effects (Outram and Elston, 2013a). With regard to the bandgap tuning in cholesteric LCs, Xiang et al. adopted a mixture consisting of two bent-core LC dimers (CB7CB and CB6OCB), a standard rod-like LC (5CB) and a left-handed chiral agent (S811) to form the cholesteric LC with $k_{33} < k_{22}$ and manifested electrically tunable selective reflection of light from UV to visible and infrared in the so-called oblique helicoid structure under relatively low electric field (<2 V/μm) applied (Xiang et al., 2015). In conjunction with the literature review in Section 1.2.3, both the tuning range and driving voltage in Xiang's study outperform existing electrical approaches toward bandgap tuning in the well-known Grandjean planar state of conventional cholesteric LCs. Later, the magnetic analog of the selective reflection effect has been demonstrated (Li et al., 2016). By doping rod-like cholesteric LCs with N_{tb} bent-core trimer, Wang et al. have found an exceptional feature exhibiting thermally tunable and reversible reflective colors in a wide range between UV and near infrared wavelengths (Wang et al., 2016c).

Without changing the low-molar-mass molecular shape, unconventional LCs have alternatively been discovered from macromolecular materials possessing certain LC

phases via chemical linking with mesogen groups or via self-assembly in a given solvent. These functional materials can combine properties of non-mesogenic materials with LC anisotropy, furnishing alluring characteristics that are not inherent to the individual components. For example, Chapter 6 of this book addresses the formation of thermotropic liquids and liquid crystals that exhibit mechanical properties much different from the individual components of surfactants and biomacromolecules (Liu et al., 2014). Besides, liquid crystal polymers are macromolecules which can exhibit various types of LC phases when mesogen groups are chemically linked on polymer backbones (i.e., the main-chain LC polymers) or covalently incorporated as side-chains on a polymer main-chain (i.e., the side-chain LC polymers) by flexible spacers (Shibaev, 2009). LC polymers are of particular because they can effectively unite anisotropic nature and stimuli-responsive orientation of LCs and mechanical properties of polymers, allowing a wide range of applications, such as nematic and cholesteric LC polymers for tunable optical elements, azobenzene-containing photochromic LC polymers for photoalignment, actuators, sensors and nonlinear optical devices, and LC elastomers for responsive or smart materials (Pang et al., 2019; Seki, 2014; Shibaev and Bobrovsky, 2017; Ula et al., 2018; Yu, 2014; Yu and Ikeda, 2011). To grasp more specific subjects pertaining to LC polymers and their unconventional applications, one can refer to this book for an introductory and self-contained account of photoalignment of azobenzene-containing LC polymers from the free surface in Chapter 10, an overview on self-assembly and photomanipulation of azobenzene-containing liquid-crystalline block copolymers in Chapter 11, and a topical review on molecular modeling of LC elastomers in Chapter 12. Moreover, certain types of nanomaterials (e.g. metallic and semiconducting materials, carbon nanotubes, and graphene) with one- and two-dimensional anisomeric shapes in aqueous and organic solutions beyond critical concentrations can exhibit LC mesophases (e.g. nematic, biaxial nematic, lamellar, columnar, and cellulose nanocrystals) by means of either chemical or physical functionalization to self-organize the molecular orientation from disordered isotropic phase to partially ordered LC mesophases. These newly developed functional materials with stimuli-responsive material properties intrinsic to LC mesophases have emerged as potential candidates for developing tunable organic electronics, optical element, display, drug delivery, and biomedical applications (Ermakov and Myshkin, 2018; Narayan et al., 2016; Singhvi et al., 2018a. 2018b; Zakri, 2007). One example for sensing applications in which a lyotropic LC is formed in a stable Langmuir monolayer by ultrathin films of nanomaterials, such as single-walled carbon nanotubes, gold nanoparticles and quantum dots, will be introduced in Chapter 14.

In the present LC community, conventional calamitic or rod-shaped LCs are still the mainstream materials and technologies based on them are extending from the major development in optical, photonic and electro-optical devices to several other unconventional applications. Especially, recent achievements of short-pitch ferroelectric LC for modern displays and photonics, disk-like LCs for efficient solar energy harvesting, and thermotropic rod-like LCs for biosensing are summarized in Chapters 3, 4, and 5 of

this book, respectively. However, it can be recognized, in accordance with the content of Section 1.2.3, that technological innovations arising from conventional LCs are facing challenges due to inherent limitations on their material properties. As such, there have been many studies aiming to demonstrate unconventional LC mixtures/composites/colloids by doping at least one of molecular additives as the guest into conventional LC hosts. The attraction of such non-synthesized blend systems stems from the combination of anisotropic properties of LCs with inherent features of dopants and the guest–host molecular interactions, opening opportunities for modifying the physical, optical, and structural properties of LCs, giving novel functionalities, and obtaining unusual phenomena. One type of unconventional LC systems involving dispersions of ionic surfactants in LCs will be discussed for the purpose of electrically induced anchoring transition in Chapter 7. Owing to the uniqueness, dyes, polymers, and nanomaterials are currently the three primary groups of additives to conventional LCs for the design of unconventional LC systems which have stimulated fundamentally scientific interest and further offered numerous potentials for innovative applications of existing LC technologies and beyond. In this section, we will focus on those dye-doped LC mixtures, polymer–LC composites and nanomaterial–LC colloids having intriguing characteristics that are capable of impacting technological innovations of as-reported conventional LC technologies in Section 1.2.3 for displays, photonic devices, and unconventional applications. Other subjects of intensive studies based on the three unconventional LC systems are comprised in Chapters 8, 9, 13, and 15 of this book.

1.3.2 Dye-doped liquid crystals

Dye molecules typically elongated in shape are attractive for their absorption anisotropy that permits them to absorb certain wavelengths of light with a varying degree of efficacy depending on the geometrical or angular relation between the molecular axis of dyes, or, more precisely, the axis of absorption, and the polarization direction of the light. This optical feature known as the dichroism is characterized by the dichroic ratio $D = A_{\parallel} / A_{\perp}$, where $A_{\parallel}$ and $A_{\perp}$ are absorption coefficients for linearly polarized light in which the polarization states are parallel and perpendicular to the long axis of dye molecules, respectively. For a positive dye, the major component of the transition dipole moment is located toward the long molecular axis so that the absorption strength along this direction is stronger than along an orthogonal one (i.e., $A_{\parallel} > A_{\perp}$). When proper amounts of dyes are homogeneously dissolved into LC, many elongated dye molecules as the guest will be preferably aligned with their long axis parallel to the director of the LC host, yielding a unique absorption characteristic that is tunable by the reorientation of dye molecules through the response of LC molecules to external stimuli. In addition to the dichroism, certain types of dyes exhibit an alluring characteristic known as the photochromism, enabling reversible switching of the chemical species between two structurally distinct isomers with different

absorption spectra and physical properties upon the illumination of specific wavelengths of light to trigger the photochemical isomerization. While conventional LC technologies typically rely on using electric fields as the stimuli, doping photochromic dyes into LCs offers the possibility of implementing linear and nonlinear optical manipulation of a device by light irradiation. Accordingly, by virtue of the guest–host effect and inherent properties of dyes as well as LCs used, various dye-doped LC systems have been explored and a diverse range of unconventional applications been suggested, especially dichroic-dye-doped LCs for absorption-based devices and technologies, fluorescent-dye-doped LCs for mirrorless lasers, and photochromic-dye-doped LCs for light-driven optical and photonic devices.

1.3.2.1 Dichroic-dye-doped liquid crystals for developing light-absorption-based devices

Figure 1.10 shows a simple example of tuning the absorption strength by the electric field in a dye (dispersed orange 3)-doped nematic LC (E7) cell with planar alignment. Here, a polarizer with the transmission axis parallel to the rubbing direction is inserted between the cell and the unpolarized light source. In the undisturbed or field-off state, both dye and LC molecules are oriented in the rubbing direction so that light at wavelengths in the absorption band of the dye is absorbed with absorption coefficient of $A_{\parallel}$ and the cell exhibits a colored background. The absorptivity of the cell under voltage applied gets decreased with increasing voltage, reaching a minimum with absorption coefficient of $A_{\perp}$ until the dye and LC molecules are electrically sustained in the homeotropic state perpendicular to the light polarization direction; thus, the cell becomes highly transparent. Since the operation principle shown in Figure 1.10 was demonstrated in 1968 with the aim toward the improvement in display performance (Heilmeier and Zanoni, 1968), guest–host dye-doped LC devices with stimuli-responsive light absorption characteristics have widely been suggested as light shutters and optical switches for developing transmissive/reflective displays, privacy/smart windows and laser protection systems and so on (Sims, 2016; Yang, 2008). The linear polarizer used in the scheme as illustrated in Figure 1.10 can further be negated by inserting a quarter waveplate (i.e., the Cole–Kashnow type) or by using a cholesteric LC instead of a nematic LC as the host material (i.e., the White–Taylor type) (Yang, 2008), highlighting a simple fabrication process and high brightness as compared with conventional LC counterparts which require crossed polarizers. The optical contrast of a dye-doped LC for these applications is predominated by the cell thickness, the dye concentration and the dichroic ratio as well as the order parameter of the dye. As such, it can be recognized in relevant studies that a commercial black dichroic dye S428 (Mitsui, Japan), known as a mixture comprising red azo, yellow azo, and blue anthraquinone dyes, with excellent order parameter in LCs, high dichroic ratio ($A_{\parallel}$ of 30.45 and $A_{\perp}$ of 2.78), and a wide absorption band covering the whole visible light, is
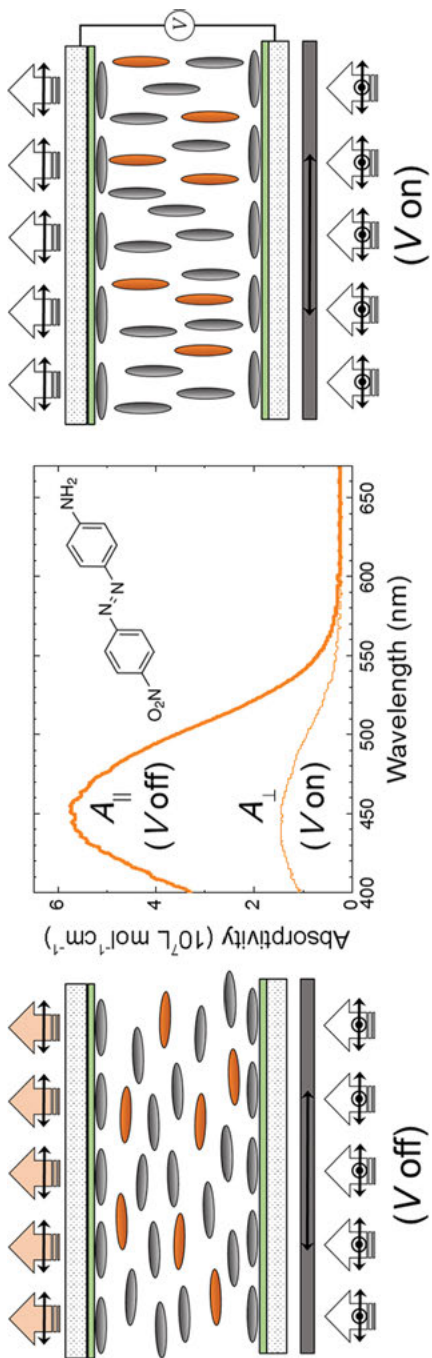
Figure 1.10: Schematic illustration of electrically tunable absorption strength of a dye (disperse orange 3)-doped nematic LC (E7) cell with planar alignment. Note that E7 is a eutectic mixture (composed of 51-wt% 5CB), having positive dielectric anisotropy.

often adopted to yield a high contrast (Kim and Yoon, 2016). While the value of dichroic ratio of a dye is limited, doping dichroic dyes into a polymer–LC composite with mismatch in refractive index between LC and polymer has been proven beneficial for achieving high contrast and enabling polarizer-free electro-optical devices due to the excellent dark state derived from the combined effect of light scattering and absorption (Oh et al., 2016; Yu et al., 2017b; 2017a). Other methods attempting to generate light scattering in a dye-doped LC cell have been proposed, including doping ions into a vertically aligned negative LC to electrically induce dynamic scattering via the electrohydrodynamic effect (Huh et al., 2018), injecting a cholesteric LC into a hybrid-aligned cell to attain initial focal conic state (Kim et al., 2018), thermal controlling the phase transition between the SmA* (homeotropic) and the cholesteric LC (focal conic) in a vertically aligned polymorphic LC cell (Oh et al., 2018c), and doping SmC* LC into a nematic LC with negative dielectric anisotropy to achieve random orientation of nematic LC molecules in a vertically aligned cell (Jo et al., 2018).

Specifically, there have been numbers of studies concerned with the dispersion of achiral or chiral azobenzene dyes into black dye/LC systems in attempt to achieve controllable light transmittance via light-driven textural switching. Wang et al. revealed a photoresponsive tristable optical switch by incorporating S428-doped E7 with 2 wt% of a commercial left-handed chiral azobenzene ChAD-3C-S (Beam Co.) to form a cholesteric LC in a 11-μm-thick cell with vertical alignment (Wang et al., 2014a). The initial value of the helical twisting power of the azo-chiral ChAD-3C-S in E7 is -42.6 μm^{-1} in the dark but it becomes -30.7 μm^{-1} in the stationary state under green light illumination; the magnitude of helical twisting power further decreases with increasing UV light intensity on account of the *trans*-to-*cis* isomerization of the azo dye (Chen et al., 2014a). The three stable states proposed are homeotropic, focal conic and fingerprint states and the switching between arbitrarily two states can be attained by controlling the irradiance and radiant energy per unit area of blue light of 408 nm in wavelength (for the *trans*-to-*cis* transition) and those of the 532-nm green light (for the *cis*-to-*trans* isomerization) to optimize the value of d/p, as depicted in Figure 1.11(a). For instance, the fingerprint state can be generated from the focal conic (homeotropic) state by exposure to appropriate UV (green) light (in terms of the intensity and exposure time) such that d/p lies in the range between 1 and 4. Another light-driven tristable LC element was developed by Huang et al. and Hsiao et al. based on a mixture comprising the LC host E7 doped with the chiral azobenzene ChAD-3C-S in a cell configuration similar to that of a bistable chiral-tilted homeotropic nematic (i.e., with high pretilt angle of 74° or 78° and $d/p \sim 1$) (Hsiao et al., 2017; Huang et al., 2016b). The driving scheme shown in Figure 1.11(b) indicates that the stable tilted-homeotropic (transparent) and tilted-twist (translucent) textures are obtained after illumination with strong 365-nm UV light and 524-nm green light to unwind and rewind the helix, respectively. The third stable state, which is the fingerprint texture (opaque), can be generated from the tilted-homeotropic texture by a weak 524-nm green light source or from the tilted-twist texture by weak 365-nm UV light.
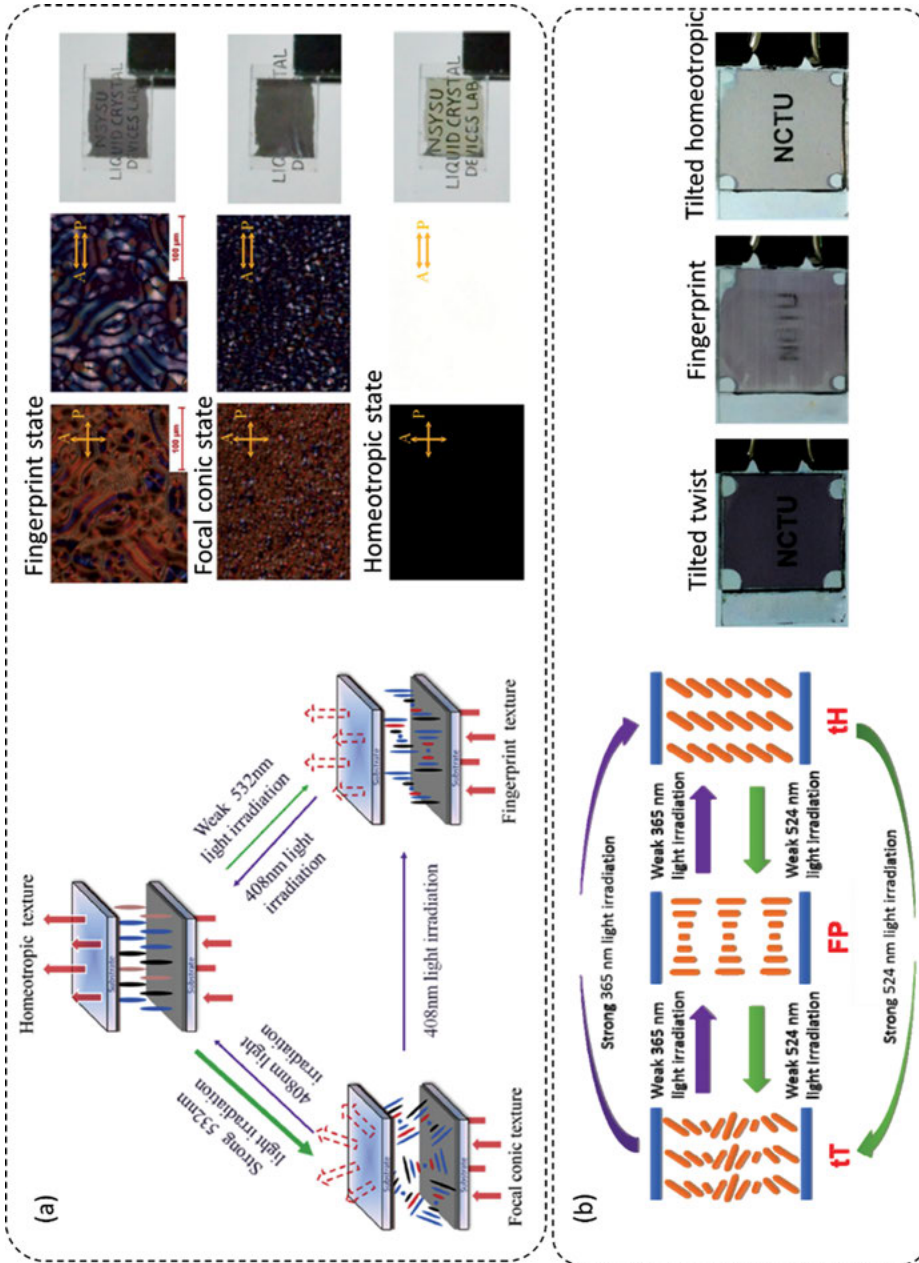
Figure 1.11: Schematics of photo-switching mechanisms and configurations of (a) three optically stable states and their corresponding optical images of a tristable cholesteric LC and (b) a tristable chiral-tilted homeotropic nematic in tilted-twist (tT), fingerprint (FP), and tilted-homeotropic (tH) states and the corresponding optical images. (a) Reproduced from Wang et al. (2014a) with permission. Copyright 2014 Elsevier. (b) Adopted from Hsiao et al. (2017).
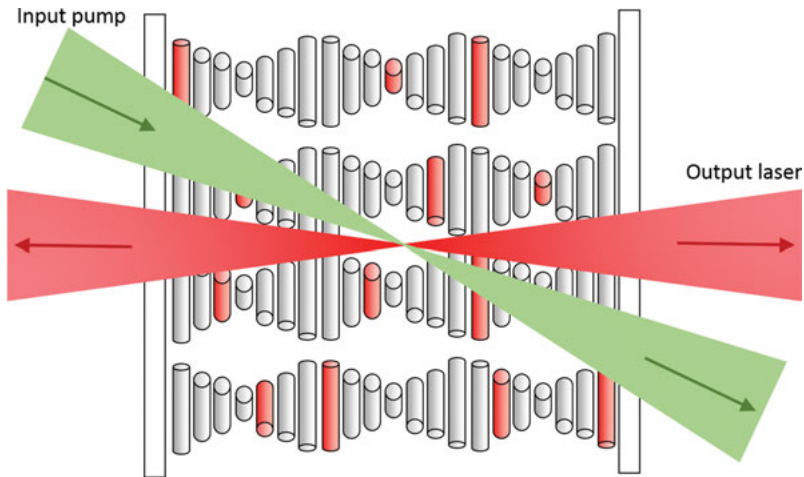
Figure 1.12: Schematic of lasing emission based on a dye-doped cholesteric LC cell with a pump beam incident at an angle to the cholesteric helix. Adapted from Ford et al. (2006).

Aside from the majority for the innovation of LC-based optical devices, the unique merit of integrating the LC orientation with dye dichroism has recently been applied to quantitative biosensing. Instead of a dye-doped system, Wu et al. considered the use of a dye-LC, having two azo groups as chromophores on its chemical structure, as a sensing platform for protein detection and quantification. The working principle originates from the change in dye-LC orientation from the homeotropic alignment to a disrupted state caused by immobilized biomolecules at the solid substrate-LC interface, leading to the increase (decrease) in absorbance (transmittance). They claimed that the concentration of the standard protein bovine serum albumin (BSA) in the range between 1 µg/ml and 7.5 µg/ml can be quantitated in terms of the relative loss in transmittance according to the linear correlation between the absorbance and the degree of disrupted alignment determined by the protein concentration on the aligning layer (Wu et al., 2018a). Later, it is reported by Chiang et al. that the detection sensitivity of a doped LC system comprising the black dye S428 for detecting the protein BSA can be enhanced when a linearly polarized light with polarization state parallel to the rubbing direction is used for measuring the transmission spectra. They also demonstrated the applicability of dye-doped LC biosensing technique for immunodetection of the cancer biomarker CA125 (Chiang et al., 2018). A comprehensive account underlying the mechanism, the principle of operation, and the sensitivity of LC-based biosensing can be found in Chapter 5 of this book.

1.3.2.2 Fluorescent-dye-doped liquid crystals for fabricating tunable liquid crystal lasers

Another particular application based on dye-doped LC systems involves the fabrication of tunable lasers by doping fluorescent dyes into a certain type of LCs. In this regard, fluorescent dyes – with high quantum yield, high photoluminescence, short fluorescence lifetime, and well-separated absorption and emission spectra – serve as optical gain media for population inversion. Common types of fluorescent dyes also known as laser dyes that have been suggested for realizing visible light lasing include coumarins, xanthenes and pyrromethenes (Shankarling and Jarag, 2010). A nano- or pico-second pulsed laser with an appropriate wavelength for the absorption band of the dye is typically adopted as the pumping light source to prevent degradation of lasing performance from distortion of LC molecular structure by heat generation and from dye bleaching. The first type of LC lasers known as the band-edge laser was experimentally demonstrated by Kopp et al. in 1998 using a planar-aligned cholesteric LC doped with the laser dye PM597 – a class of pyrromethene dyes with strong fluorescence between 570 nm and 600 nm (Kopp et al., 1998). They reported that the photonic bandgap of the cholesteric LC in the Grandjean planar texture can support a resonant cavity, giving rise to laser modes at the band-edge wavelengths, where the group velocity of incident light is approximately zero and the density of photon states is high with long dwell time. Therefore, when the pump light having pulse energy beyond a threshold value (i.e., the lasing threshold) is incident at a given angle to a dye-doped CLC cell, coherent laser light at the wavelength corresponding to either edge of the photonic bandgap can be generated via stimulated emission in one dimension along the helical axis in both forward and backward directions, as illustrated in Figure 1.12. Later on the band-edge LC laser has become the most common and widely investigated type of LC lasers in that the lasing characteristics can be readily observed in a simple cell geometry by doping laser dyes into an LC with a photonic bandgap, such as the cholesteric LC (Kopp et al., 1998) in general and the chiral SmC phase (Ozaki et al., 2002), blue phases (Cao et al., 2002; Yokoyama et al., 2006), and microfluidic generated cholesteric LC microdroplets in polymer matrix (Humar and Muševič, 2010) in particular. Another attractive feature of a band-edge LC laser is the fine tuning of lasing wavelength within the fluorescence emission spectrum of laser dyes by manipulating the photonic bandgap properties via the control of the helical pitch. This has electrically, thermally, mechanically, or spatially been achieved with a variety of degrees of tuning range in the case of using conventional chiral LCs as the host material (Coles and Morris, 2010; Ford et al., 2006; Takezoe, 2012; Woltman, 2007). An example of an electrically tunable band-edge LC laser device is made by doping the laser dye of either DCM or LD688 into an unconventional bent-core/rod-like CLC mixture. Electrical tuning in lasing wavelength within the whole fluorescence emission spectrum of the laser dye DCM or LD688 of this device is implemented by manipulating the helical pitch of the cholesteric LC in the oblique heliconical state (Xiang et al., 2016).
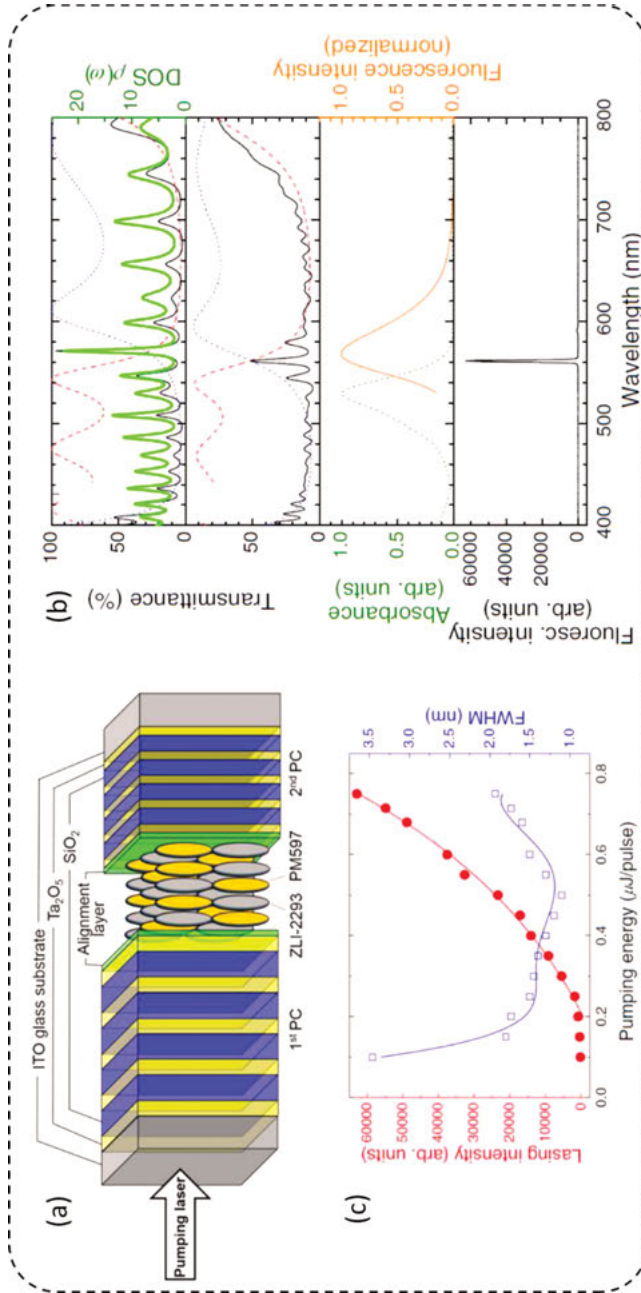
Figure 1.13: (a) Configuration of a one-dimensional asymmetric PC/dye-doped nematic LC as a lasing device. (b) Spectral properties of the combined photonic bandgap device. (c) Pumping energy dependence of the lasing intensity and linewidth of the photonic device. Figure adopted from Wang et al. (2014b).

Other methods entailing unconventional LCs have progressively been proposed in attempt to widen the tunable lasing wavelength range, such as electrical tuning in polymer-stabilized blue phase (Wang et al., 2017c) and cholesteric LC (Lu et al., 2019), spatial tuning in achiral LC-refilled gradient-pitched cholesteric LC polymer template (Lin et al., 2017a), and phototuning in photosensitive azo-chiral-doped cholesteric LC cells (Mykytiuk et al., 2014) and cholesteric LC microshells (Chen et al., 2014e). When a defect layer is introduced into a photonic LC structure to interrupt the structural periodicity, an additional resonant mode known as the defect mode with higher density of photon states than that of the band-edge mode could be generated inside the photonic bandgap. Such a hybrid structure allowing lasing at the defect-mode wavelength with lowered threshold (i.e., the defect-mode laser) has been implemented by introducing a phase jump in between two polymerized cholesteric LC layers (Schmidtke et al., 2003), or by sandwiching a thin layer of isotropic material or anisotropic LC between two polymerized cholesteric LCs (Jeong et al., 2007; Song et al., 2006). Defect-mode lasing has alternatively been revealed in an unconventional manner where a fluorescent-dye-doped LC is sandwiched between two identical one-dimensional multilayered photonic crystals consisting of periodically stacked polymerized cholesteric LC and PVA films (Ha et al., 2008) or alternate dielectric layers of high and low refractive indices (Ozaki et al., 2003). In this sense, Wang et al. have shown ultralow-threshold single-mode lasing using an unconventional configuration consisting of a dye (PM597)-doped nematic LC (ZLI-2293) as a central defect layer sandwiched between two asymmetric photonic structures. As illustrated in Figure 1.13(a), the two different multilayered photonic structures are PC 1 with the configuration of [glass-$(H_1L_1)^4H_1$] and PC 2 with the configuration of [$H_2(L_2H_2)^4$-glass]. For effective lasing emission with low threshold, H_1 (H_2) as the high- and L_1 (L_2) as the low-refractive-index dielectric layers are chosen to have thickness of one quarter of 660 nm (480 nm) so that the overlap of both photonic bandgaps of the two photonic crystals (i.e., dielectric mirrors) is obtained at around 570 nm corresponding to the excitation maximum of the laser dye (PM597). It is shown in Figure 1.13(b) and 1.13(c) that an intense defect-mode signal at the intersection of the two photonic band edges is generated due to the high density of photon states at band edges and single-mode lasing takes place with a threshold at around 0.2 μJ/pulse pumping (Wang et al., 2014b). Following the idea of asymmetric photonic crystal/dye-doped LC configuration, Huang et al. further proposed to realize white light lasing by enclosing a dye-doped cholesteric LC between two distinct dielectric mirrors with configurations of [$(HL)^4H^2(LH)^3$] and [$(HL)^3H^2(LH)^4$] (Figure 1.14(a)). In this case, the two asymmetric photonic crystals are designated to generate a defect mode at around 446 nm for blue light lasing and the cholesteric LC is chosen with a given photonic bandgap possessing short- and long-wavelength band edges at around 550 nm and 630 nm for green and red light lasing, respectively. When the pumping light energy exceeds 7.4 μJ/pulse and the dye composition (C540A, PM580 and LD688) doped in the cholesteric LC is optimized for fluorescence between 450 nm and 700 nm, simultaneous lasing emissions at 507 nm,
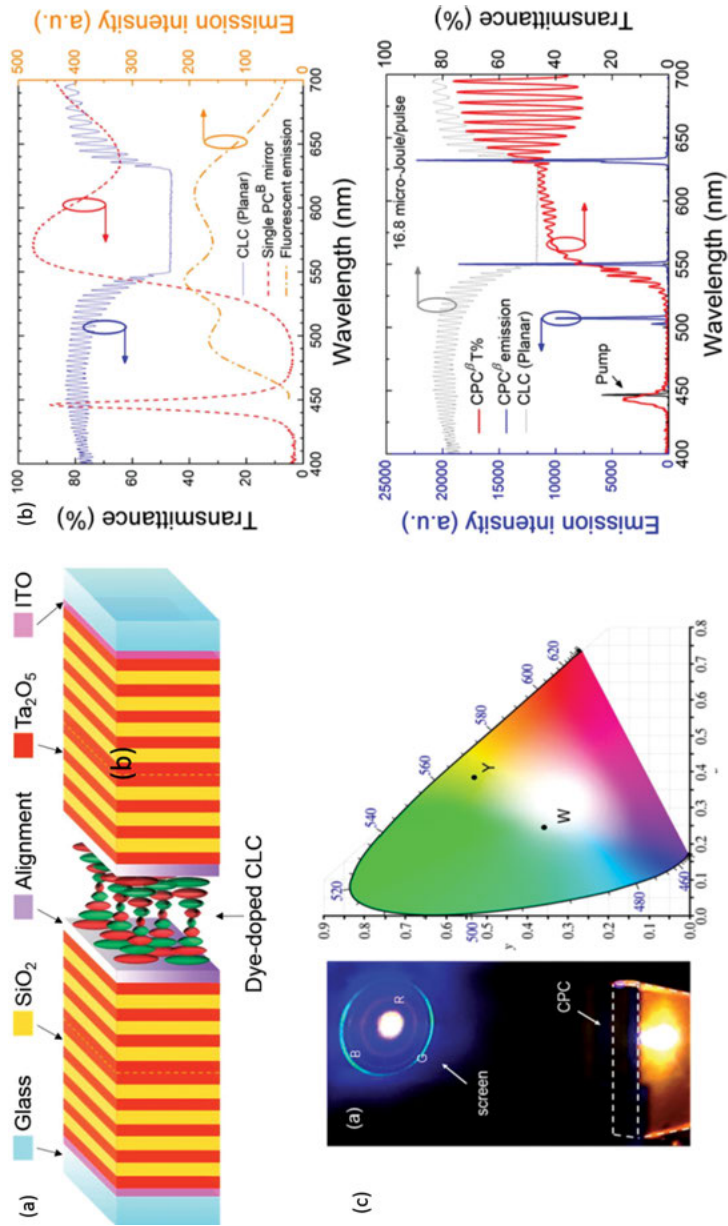
Figure 1.14: (a) Schematic of a photonic bandgap hybrid containing a dye-doped CLC layer sandwiched between two imperfect but identical dielectric mirrors for white-light lasing. (b) Fluorescent emission spectrum of the laser dyes (C540A, PM580 and LD688) and transmission spectra of a single dielectric mirror and the CLC alone in the Grandjean planar state (top) and the emission signals from the CLC laser (bottom). (c) Photograph of the CLC laser device and its discrete emissions on a screen and the true color space coordinates of the laser on the CIE 1931 chromaticity diagram. Figure adopted from Huang et al. (2016a).

550 nm, and 632 nm can be generated (Figure 1.14(b)). The resultant white color emission shown in Figure 1.14(c) is attributable to the color mixing of the three lasing colors with the scattered intensity of the pumping light as the blue background (Huang et al., 2016a).

In addition to the band-edge and defect-mode LC lasers, there are several other types of LC lasers, differing in the LC material exploited, the cell configuration, and the lasing mechanism as well as performance. These include sandwiching nematic LC between two broadband-cholesteric LC/PVA multilayers for cavity-mode lasing (Choi et al., 2010), employing blue phase with disordered platelet textures (Chen et al., 2012), TN LCs in thick or wedged cells (Chen et al., 2017a; Lin et al., 2017b; Lin et al., 2018), nematic LC in a quartz cuvette (Bian et al., 2016), sphere LC phase in an untreated cell (Zhu et al., 2015) and cholesteric LC microspheres in glycerol (Li et al., 2016) to produce multiscattering or interference in confined geometry for random lasing, using the fingerprint cholesteric LC texture as the host material to form diffraction grating for electrically switchable single-/multi-/random-mode lasing (Huang et al., 2017). Undoubtedly, dyedoped, LC-based lasers with potential benefits of small size, simple fabrication, low power consumption, low cost and especially the wide tunability in lasing wavelength are one of the topics of immense interest in research fields of physics and, in particular, optics and photonics. Introductory and comprehensive journal papers and monographic articles on various configurations for LC laser devices, operating principles, performances and their potential applications, ranging from biology and medicine to displays and miniature lab-on-a-chip devices, can be found in some review papers and book chapters (Coles and Morris, 2010; Ford et al., 2006; Muševič, 2016; Palffy-Muhoray et al., 2006; Takezoe, 2012; Woltman, 2007). The improvement in lasing performance (e.g. lasing threshold, tunability, and stability) and the fabrication of novel laser devices based on polymer–LC composites and nanomaterial-doped LCs will be described later in Sections 1.3.3 and 1.3.4.

1.3.2.3 Photochromic-dye-doped liquid crystals for implementing photoresponsive optical and photonic devices

Guest–host LC systems comprising photochromic dyes as additives have received particular interests for the development of all-optical devices because the molecular orientation and thereby the optical properties of the LC host can become responsive to light irradiation by the photosensitive nature of photochromic dyes and the guest–host intermolecular interaction. Azobenzenes containing the central $-N = N-$ linkage group are the most common and widely employed photochromic compounds thanks to their easy synthesis together with their efficient and fully reversible photoisomerization. Normally, azobenzene molecules can photochemically be switched between the thermally stable *trans* isomer and the metastable *cis* isomer. The rod-shaped *trans* isomer with ~9 Å in length reveals strong $\pi–\pi^\star$ absorption in the UV wavelength range

whereas the bent-shaped *cis* isomer with ~5.5 Å in length exhibits weak $n-\pi^\star$ absorption in the visible spectrum (Wang et al., 2018b). Accordingly, the *trans* isomer can transform to the *cis* counterpart through photoisomerization upon UV irradiation. Reversible transformation from the *cis* to *trans* form can be attained over time or by visible light exposure or thermal relaxation as shown in Figure 1.15(a). When an azobenzene dye is dispersed in a conventional rod-like LC, the *cis* isomer is structurally incompatible with the surrounding LC molecules. The photoisomerization of azobenzene molecules from the *trans* to *cis* state is, therefore, responsible for disturbing the LC ordering, which could further lead to LC phase transition from one to another or to the isotropic phase in an isothermal manner (Figure 1.15(b)) (Bisoyi and Li, 2016a; Ikeda, 2003). On the basis of this light-induced effect, various azo-dye-doped LC devices with photoresponsive properties upon UV and visible light illuminations have been suggested, such as reversibly photo-tunable bandgap wavelengths through the deformation of cubic lattices in blue phases (Liu et al., 2010), phase transition from SmA to CLC (Guan et al., 2012), photo-switchable lasing characteristics through BPI–BPIII phase transition in a band-edge blue phase laser (Lin et al., 2014) and through nematic–isotropic phase transition in a random LC laser (Lee et al., 2010a), and photo-controllable visible light transmittance through light-induced isothermal SmA–nematic phase transition in a vertically aligned cholesteric LC cell (Oh et al., 2018a) or through light-induced isothermal nematic–isotropic phases in vertically aligned achiral LC cells (Goda et al., 2018; Oh et al., 2018b) and in an alignment-layer-free and polymer-stabilized LC cell (Oh et al., 2017). Notably, the *trans–cis* isomerization and further reorientation of azobenzene molecules in the *trans* isomer can be induced by exposure to linearly polarized light at a wavelength lying in the absorption region. As illustrated in Figure 1.15(c), when the polarization state of incident polarized light is set parallel to the long axis (i. e., the transition moments) of the *trans* isomer of azobenzene molecules, which absorbs energy effectively, the molecules will be activated to an excited state, followed by the *trans–cis* isomerization. In the meantime, molecules with transition moments perpendicular to the light polarization are virtually inactive and no isomerization happens. After repetitive *trans–cis–trans* isomerization cycles, azobenzene molecules in the *trans* form are eventually realigned with their long axis perpendicular to the light polarization direction, meaning that they become unresponsive to the incident light and no more isomerization occurs (Yu and Ikeda, 2004). The polarized light-induced effect together with strong interaction between dye and LC molecules could induce the isothermal nematic–isotropic phase transition or reorient LC molecules from being parallel to perpendicular to the polarization direction (Figure 1.15(d)) (Oscurato et al., 2018), allowing azo-dye-doped LCs to be employed as diffraction gratings for applications in various nonlinear optical devices, such as holographic displays, optical storages, and optical limiters (De Sio et al., 2010; Li et al., 2017b; Lucchetti and Tasseva, 2012; Zhou et al., 2016). Other mechanisms featuring the LC reorientation by polarized light have also been explored in specific dye-doped LC cells and explained in terms of light-induced photothermal,

intermolecular torque, anchoring transition and photorefractive-like effects (Khoo, 2009). The subsequent changes in birefringence and refractive index entailed by the above-mentioned optically induced effects have made azo-dye-doped LCs highly potential candidates for investigating a vast variety of nonlinear optical phenomena with low-power laser systems due to the significant increase in nonlinear optical coefficient (n_2). It has been reported that the value of $n_2 \sim 10^{-4}$ cm^2/W in pure nematic LC can be considerably promoted to $n_2 \sim 10^{-3}$–10^{-1} cm^2/W in dye-doped LCs by the intermolecular torque and photorefractive-like effects for giant optical nonlinearities, to $n_2 \sim 10$–10^3 cm^2/W in methyl-red-doped LC by the photorefractive-like effect for supra optical nonlinearities, and to n_2 of even greater than 1,000 cm^2/W in methyl-red-dye-doped LC by the surface effect for colossal optical nonlinearities (Khoo, 2011). Further discussion on the photochemical phase transition and giant optical nonlinearity in dye-doped LC systems and a study of time-resolved dynamics based on the transient grating technique will be introduced in Chapter 8 of this book.

Another active subject of research, utilizing the photochromism of azobenzene molecules, is concerned with the development of light-driven chiral LCs with phototunable helical pitch by doping an achiral LC with azobenzene-based chiral molecular switches. Such unconventional LC mixtures with photoresponsive properties are attractive for their abilities to allow implementation of a wide-range bandgap tuning and helicity manipulation which are quite unique from as-reported conventional chiral LCs described in Section 1.2.3. Figure 1.16(a) illustrates the operation principle of light-directed bandgap tuning of a photoresponsive cholesteric LC, loaded with a chiral azobenzene switch whose helical twisting power (HTP) can be photochemically varied and reversibly switched between two photostationary states (PSS$_{\lambda 1}$ and PSS$_{\lambda 2}$) by exposure to light at two different wavelengths of λ_1 (UV light in general) and λ_2 (visible light in general). The HTP in PSS$_{\lambda 1}$ is typically smaller than that in PSS$_{\lambda 2}$ so that the pitch (being inversely proportional to HTP) of the photoresponsive cholesteric LC is lengthened under the irradiation of light at λ_1, leading to redshift in reflection colors and vice versa by visible light at λ_2 according to eq. (1.22). It is thus desirable to obtain a chiral molecular switch with high HTP and large HTP variation so as to widen the tunable bandgap range at a lowered dopant concentration. Reported by Ma et al., Figure 1.16(b) shows an example of a photoresponsive cholesteric LC that enables reversible color tuning in the whole visible spectrum upon alternating visible ($\lambda_1 = 520$ nm) and UV light ($\lambda_2 = 365$ nm) irradiations by mixing the commercial nematic LC E7 with a nanoscale, axially chiral azobenzene (HTP = 60 μm^{-1} at PSS$_{\lambda 2}$ and HTP = 27 μm^{-1} at PSS$_{\lambda 1}$) (Ma et al., 2010). Alternatively, numerous novel chiral molecular switches based on azobenzene derivatives have been synthesized and the resulting photoresponsive chiral LCs demonstrated, showing light-enabled reflection color tunability in full or over visible light regime for designated photonics applications. Representatives of these azo-containing molecules in the last decade include axially chiral azobenzene (Morris et al., 2013; Wang et al., 2012b), cyclic chiral azobenzene (Lu et al., 2016; Mathews et al., 2010), ortho-tetrafluoro-functionalized axially chiral azobenzene
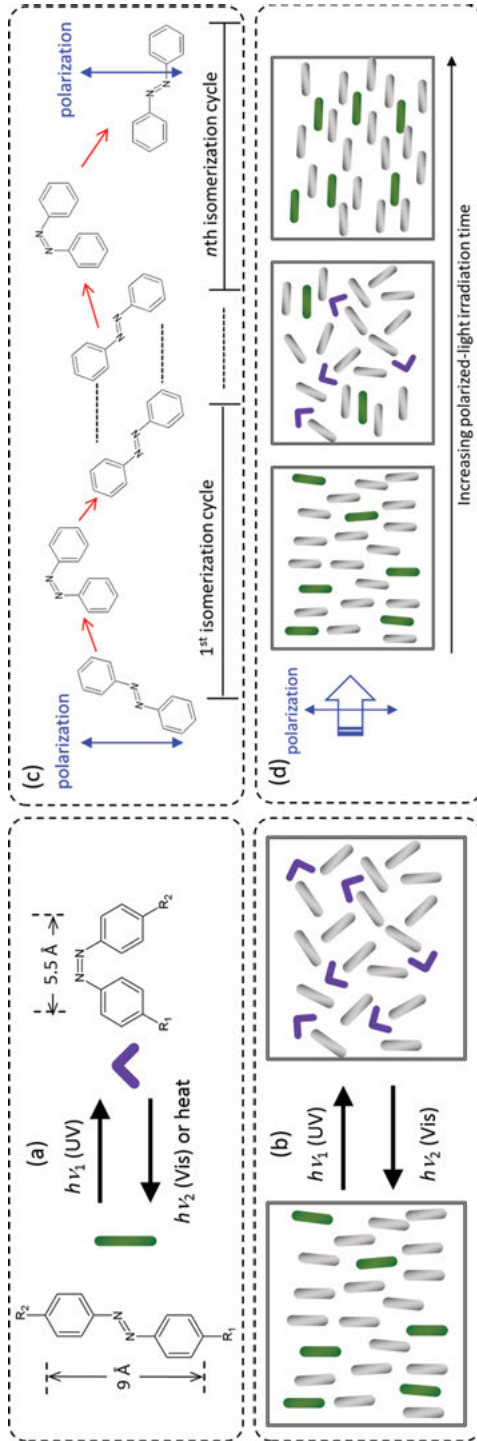
Figure 1.15: Schematic illustrations of photo-induced (a) structural transformation of azobenzene molecules and (b) order–disorder transition in a dye-doped LC cell and of polarized light-induced molecular reorientation of (c) azobenzene and (d) LC molecules from being parallel to perpendicular to the polarization direction. Figure adapted from Oscurato et al. (2018).
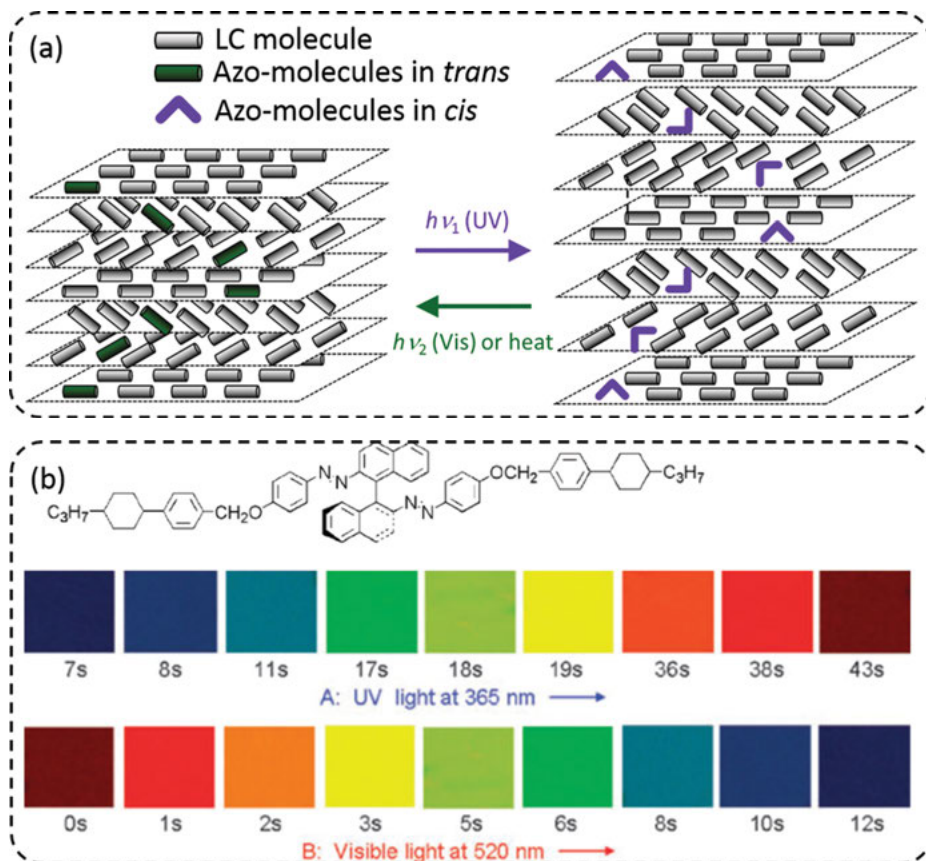
Figure 1.16: (a) Schematic illustration of dynamical tuning in helical pitch of a photoresponsive cholesteric LC and thereby reflective color by light irradiation. (b) An example of light-driven color tuning by mixing the commercial nematic LC E7 with a nanoscale, axially chiral azobenzene (HTP = 60 μm^{-1} at PSS$_{\lambda 2=520\ nm}$ and HTP = 27 μm^{-1} at PSS$_{\lambda 1=365\ nm}$). (b) Reproduced from Ma et al. (2010) with permission. Copyright 2010 Royal Society of Chemistry.

(Qin et al., 2018a, 2019; Wang et al., 2019; Zhao et al., 2018), close/open-type axially chiral azobenzene (Nishikawa et al., 2017), and planar chiral azobenzene (Kim and Tamaoki, 2014) for photoresponsive cholesteric LCs. And axially chiral azobenzene (Lin et al., 2013b) and hydrogen-bonded chiral azobenzene (Jin et al., 2014) were also employed in blue phases. Noticeably, while most of chiral azobenzenes were found to have two light-driven photostantionary (i.e., bistable) states, Qin et al. recently developed a unique design of a tristable chiral molecular switch containing a binaphthyl-derived chiral structure linked with two kinds of azobenzene moieties of parent azobenzene (Azo) and o-fluoroazobenzene (F-Azo). This photoactive material exhibits three photoswitchable and optically stable molecular configurations subject to impinging light at appropriate wavelengths, which are configuration I (*trans, trans,*
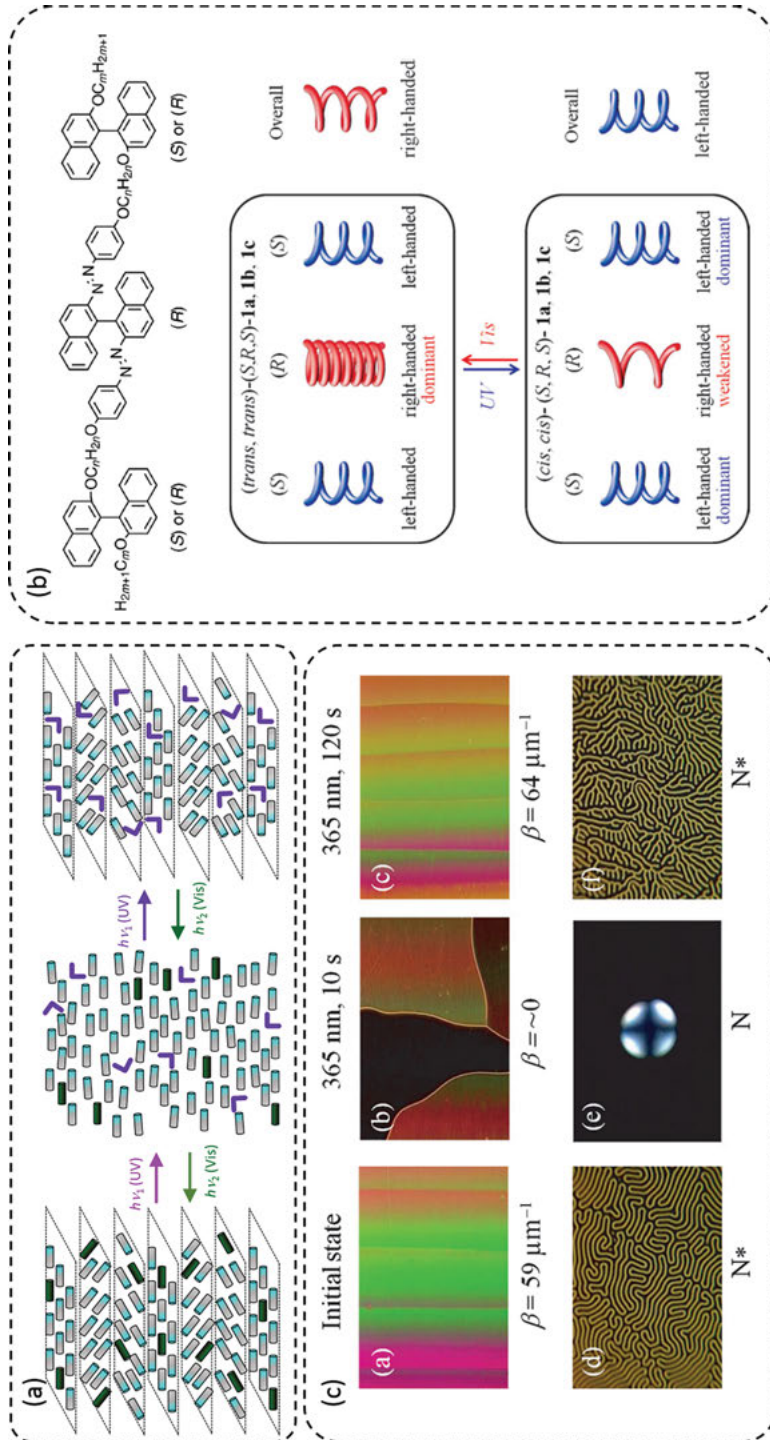
Figure 1.17: Schematic illustration of (a) the operation principle, (b) mechanism and (c) results of photo-induced helical inversion of a photoresponsive CLC doped with azoarenes containing multiple chiral binaphthyls (S-R-S) with opposite chirality. Reproduced from (Li et al., 2013b) with permission. Copyright 2013 John Wiley and Sons.

trans, trans) with HTP (mol%) = 160 μm^{-1} by irradiation at λ_1 = 470 nm, configuration II with HTP (mol%) = 112 μm^{-1} (*cis, trans, trans, cis*) by irradiation at λ_2 = 530 nm light, and configuration III (*cis, cis, cis, cis*) with HTP (mol%) = 36 μm^{-1} by irradiation at λ_3 = 365 nm. Accordingly, they claimed that the light-driven cholesteric LC, comprising the photoactive and tristable chiral additive, is applicable for a reflective display featuring precise control of red, green, blue colors and a black background due to the existence of two continuous and adjacent phototunable color regions of visible spectrum upon illumination of 470-nm and 530-nm visible light and near-infrared region by exposure to 530-nm and 365-nm light (Qin et al., 2018b).

Apart from the bandgap tuning, development of a photoresponsive cholesteric LC with unconventional characteristic of light-directed handedness inversion of the chirality has received much attention owing to the advantages of excellent spatial/temporal precision and remote/digital controllability. It is illustrated in Figure 1.17(a) for a general description that when a photoresponsive cholesteric LC is irradiated with light at an appropriate wavelength, the helix of one handedness is expected to become gradually unwound, successively vanish at a compensated state with an infinite pitch length, and eventually rewind through self-assembly to exhibit another helix of opposite handedness. To carry out the idea of helical inversion (Figure 1.17(a)), extensive efforts have been made toward advancing powerful chiral azobenzene compounds whose signs of helical twisting power are opposite in the two photostantionay states. Using the work done by Li et al. as an example, a series of azoarenes whose molecular structures contain multiple chiral binaphthyls (S-R-S) with opposite chirality were designed as shown in Figure 1.17(b), where R and S stand for right- and left-handedness of chirality, respectively. The helical twisting power (mol%) of one compound (S-R-S with m = 18 and n = 11 in Figure 1.17(b)) doped in 5CB was found to change from +54 μm^{-1} (right-handedness) in PSS_{Vis} to −65 μm^{-1} in PSS_{UV} (left-handedness) upon UV irradiation and helical inversion occurred on account of the chiral conflict and the equilibrium shift between chiral moieties as delineated in Figure 1.17(c) (Li et al., 2013b). Afterward, Fu et al. followed the same principle and developed hydrogen-bonded chiral azoarenes with binaphthyl units of opposite chiral structures (R-S-R) doped in either SLC1717 or 5CB for dynamic handedness inversion under light illumination (Fu et al., 2015). Without complicated molecular design, another strategy of achieving helical inversion is to co-dope oppositely handed photosensitive chiral switch and photoinsensitive chiral molecules into an achiral LC (Gvozdovskyy et al., 2012; Lee et al., 2015c; Ryabchun et al., 2015). However, it can be recognized, based on relevant studies, that light-enabled helical inversion by this method is typically obtained in the infrared region, presumably due to the limitation in HTP variation as well as poor miscibility between two dopants. In addition to chiral azobenzene compounds, many other photochromic molecular switches, including overcrowded alkene, diarylethene, fulgide, spirooxazine, and naphthopyran, have successively been exploited in the development of photoresponsive cholesteric

LCs and blue phases with desired bandgap tuning efficacy and/or helical inversion ability (Bisoyi and Li, 2014; 2016b; Kim and Tamaoki, 2019; McConney et al., 2019; Wang and Li, 2012). In view of particular photonic applications based on photoresponsive cholesteric LCs, endeavors have been made to fabricate optically tunable diffraction gratings by photocontrollable helical rotation and handedness inversion primarily in fingerprint states, which will be reviewed in Chapter 9.

1.3.3 Polymer–liquid crystal composites

Polymer–LC composites are known as a kind of phase-separated or two-phase systems consisting of low-molecular-weight LCs and polymers that are separated from each other in a confined geometry. There are many routes to obtaining polymer–LC composite systems, typically prepared from a fluid system composed of both the polymer or polymer precursor and the LC. As opposed to emulsion or emulsification methods, phase-separation processes are another branch of well-adopted pathways. The three broad classifications of the phase-separation processes include the polymerization-induced phase separation (PIPS), thermally induced phase separation (TIPS), and solvent-induced phase separation (SIPS). Among the developed phase-separation methods, the photopolymerization-induced phase separation has been thought to be the most useful approach to producing a polymer–LC composite because it is convenient, reliable, rapid, inexpensive and solvent-free and it allows precise control in the composite morphology by many parameters, including the types of materials used, the mixture composition, the polymerization rate, and the curing intensity as well as the temperature (Mucha, 2003). In this method, proper amounts of photo-curable prepolymers or monomers are mixed with LC to form a precursor, followed by the exposure to UV light, usually at 365 nm, to initiate the free radical polymerization of unsaturated monomers and to accomplish phase separation through the reduction in miscibility between polymer and LC over time. According to the intriguing properties of the blend combining LC anisotropy with mechanical strength, stability, and flexibility of polymer and surface interactions between the two dielectric media, various polymer–LC composites have been proven advanced in developing new and ameliorated LC technologies, which can broadly be divided, in terms of the polymer morphologies, into polymer-dispersed LCs (PDLCs) and polymer-stabilized LCs (PSLCs).

A polymer-dispersed LC in general reveals a Swiss cheese-like configuration in which the LCs in the form of droplets are encapsulated in a rigid polymer matrix. This configuration can be acquired by mixing more than 20 wt% of thiol-ene-based prepolymers (e.g. NOA65) into an LC host to form a homogeneously fluidic precursor which is then illuminated with a significantly high intensity of UV radiation; thus, phase separation in the whole sample area takes place in a spatially isotropic
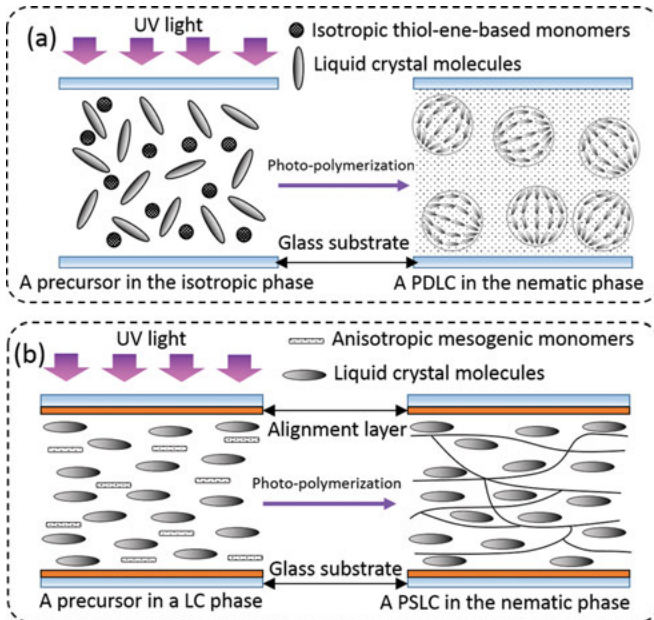
Figure 1.18: Schematic illustrations of fabrication processes and morphologies of (a) a polymer-dispersed liquid crystal (PDLC) with randomly distributed LC droplets in a cell without alignment and (b) a polymer-stabilized liquid crystal (PSLC) with polymer network in a cell with planar alignment.

way, as illustrated in Figure 1.18(a). By optimizing fabrication parameters, such as the (curing) temperature, mixture composition, UV exposure conditions – UV irradiance (in $mW \cdot cm^{-2}$) and exposure time (in min) – and, in some cases, (curing) voltage, various polymer-dispersed LC configurations, differing in the droplet size and the distribution of LC droplets have been proposed for advanced applications. Best-known systems are polymer-dispersed LCs with micro-sized LC droplets for the design of polarizer-free and flexible LC devices based on the light-scattering feature from the refractive-index mismatch between the polymer and LC. Other types of polymer-dispersed LCs, differing in the droplet size and the film morphologies, have also been fabricated for novel photonic applications, such as holographic polymer-dispersed LCs with periodic distribution of nano-sized droplets for 3D displays and lasers and stratified polymer-separated composite films (PSCOF) with a well-separated LC/polymer bilayer framework for single-substrate displays and LC lenses. In contrast, polymer-stabilized LCs are classified as those polymer–LC composites having polymer networks of fibrils as "templates" that can play the role of memorizing and stabilizing LC molecules in desired orientations or chiral structure. In a polymer-stabilized LC, acrylate or methyl-acrylate monomers having mesogenic structures with rigid cores similar to that of nematic LC molecules are typically used and the overall monomer

concentration (<10 wt%) is much lower than that of polymer-dispersed LCs (>20 wt%). Therefore, prior to photopolymerization, the monomer/LC mixture is in a liquid crystalline phase and the guest–host effect analogous to that of dye-doped LC systems leads to the molecular orientation of mesogenic monomer along the LC director field. In the chain or addition polymerization, a dilute amount of photo-initiator (e.g. Irg 184 and BME at 1–5 wt% to the monomer) is normally added to initiate the chain reaction of polymerization through the generation of free radicals to react with the double bonds of the monomer. While performing photopolymerization by UV exposure in an LC phase, the LC orientation is preserved and polymer fibers separated from the concocted mixture start cross-linking to each other along LC directors and mimic their exact orientation, resulting in the formation of polymer networks typically in three dimensions throughout the bulk of a cell (Figure 1.18(b)) or, in some cases, in two dimensions near both substrate surfaces. Owing to the uniqueness, polymer-stabilized LCs have widely been applied for stabilizing LC configurations/phases, enhancing electro-optical responses, and implementing unusual optical properties and tunabilities. A brief overview on the technological achievements will be given in the succeeding passages focusing on the above-mentioned two primary types of polymer–LC composites, namely, polymer-dispersed LCs and polymer-stabilized LCs.

1.3.3.1 Polymer-dispersed liquid crystals (PDLCs)

Polymer-dispersed LCs consisting of randomly distributed LC droplets with a diameter on the order of micrometer scale in a continuous polymer matrix represent a fundamental class of polymer–LC composites for the development of light-scattering-based LC devices. As illustrated in Figure 1.19(a), the curved or spherical polymer boundary serves as an aligning surface, providing tangential anchoring on the LC droplet surface. The droplets thus exhibit the bipolar configuration as LC molecules inside the droplets are supported to become oriented along the droplet walls. Some other configurations, such as toroidal, radial, and directors, can be possibly formed depending on the elastic constants of LC, anchoring condition on the droplet surface, and the droplet shape and size (Deshmukh and Malik, 2014). In the meantime, because the droplets are isolated from one another, their directors have no preferred orientation, namely, they are randomly distributed in a polymer-dispersed LC film. When the refractive index of the polymer (n_p) is selected to differ appreciably from the effective refractive index n_{eff} of the LC ($n_p \neq n_{eff} = (n_e + 2n_o)/3$ in average), light passing through the polymer-dispersed LC in the field-off state is highly scattered due to the index mismatch, making opaque (milky) appearance of the composite film. Note that forming LC droplets with sizes comparable to visible light wavelengths can further promote the light-scattering strength. Upon the application of a suitable vertical electric field across the thickness of the polymer-dispersed LC with $\Delta\varepsilon > 0$ to reorient the LC director along the field (i.e., perpendicular to the plane of the film), the composite film can act as

an anisotropic material, highly transparent for normally incident light in the situation where the refractive index of the polymer is very close to the ordinary refractive index of the LC ($n_p \approx n_o$) (Figure 1.19(a)). While polymer-dispersed LC with this type of electro-optical operation is referred to as the normal mode, there exists a reverse counterpart called the reverse mode with the opposite operation (i.e., transparent in the field-off state and opaque in the field-on state) (Cupelli et al. 2009, 2011; De Filpo et al., 2017). Consequently, polymer-dispersed LCs with the trait of electrically tunable light scattering first developed in 1986 have long been a means alternative to conventional LCs and absorption-type (dye-doped) LCs for developing displays, light shutters and privacy as well as smart windows (Ahmad et al., 2018; Doane et al., 1986; Kim et al., 2015; Su et al., 2015). It is worth to mention that polymer-dispersed LCs for these applications can be fabricated and adopted without employing polarizers and alignment layers, granting advantages of high transmittance, low cost, high production yield, and great compatibility with plastic substrates and roll-to-roll processes for making large-size flexible devices. Other applications of light-scattering-based polymer-dispersed LCs beyond electro-optical devices have been suggested for random lasing (Lin and Hsiao, 2014; Sznitko et al., 2015; Ye et al., 2017), sensing (Ailincai et al., 2018; Lai et al., 2014; Song et al., 2017), and spatially tunable photonic devices (Wu et al., 2014).

If the droplet size is on the order of nanometer scale smaller than visible light wavelengths, the light-scattering effect would be suppressed and the nano-sized polymer-dispersed LCs can behave as electrically tunable phase modulators with polarization-independent optical properties and fast response (Chang et al., 2017; Choi et al., 2015; Manda et al., 2017). One of the intriguing types of nano-sized polymer-dispersed LCs that has extensively been explored in the literature is called holographic polymer-dispersed LCs (HPDLCs) owing to the ability for light diffraction, originating from the presence of periodic distribution of LC droplets in space. A holographic polymer-dispersed LC, structured with alternating polymer-rich and LC-rich patterns/layers, can be fabricated by illumination of interference pattern derived from two coherent laser beams onto a mixture of LCs and photocurable monomers. The resulting holographic polymer-dispersed LC can operate in the transmission and reflection modes by producing interference fringes with a periodicity in a direction parallel and perpendicular to the substrates, respectively. In the field-off state, the incident light is diffracted in a single-order (±1) beam with a given efficiency for the transmission-mode holographic polymer-dispersed LC (Figure 1.19(b)) and on the same side for the reflection-mode holographic polymer-dispersed LC (Figure 1.19(c)). The application of electric field normal to the substrate results in reorientation of LC directors in the droplets along the field so that the spatial periodicity of refractive index diminishes and the incident light transmits under the condition of $n_p \sim n_o$. Consequently, the conjunction of polymer-dispersed LCs and holography has extended the applicability of polymer-dispersed LCs to a number of photonic devices, such as focus-switchable lenses, optical filters, wavelength division multiplexers, 3D displays, electro-optical filters, distributed feedback lasers, free-space optical switches, image storages and
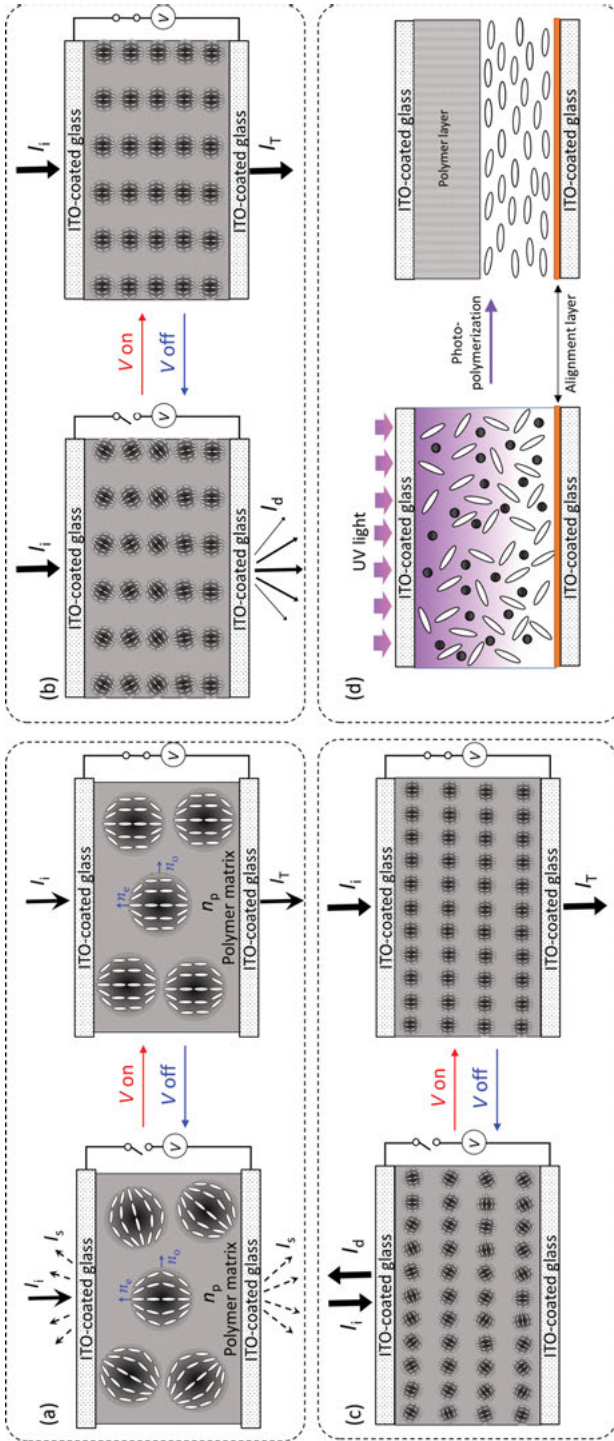
Figure 1.19: Schematic illustrations of the operation principles of (a) conventional polymer-dispersed LC with random distribution of micro-sized LC droplets for light-scattering-based device and (b) transmission and (c) reflection types of holographic polymer-dispersed LCs with periodical distribution of nano-sized LC droplets for light-diffraction-based device, and (d) fabrication of a PSCOF with a bilayer polymer/LC structure. I_i, I_s, I_d, and I_T are incident, scattered, diffracted, and transmitted light intensities, respectively.

electrically addressable security holograms, to name a few (Chen et al., 2017b; Liu et al., 2016b; Ma et al., 2018; Ogiwara et al., 2013; Wang et al., 2015b).

In a special case where the LC host used is capable of absorbing UV light and thereby producing intensity gradient of UV radiation normal to the substrate plane, anisotropic phase separation occurs and a bilayer configuration rendering a polymer-separated composite film (PSCOF) is created with the LC layer in contact with the substrate farther away from the incoming UV light and the polymer layer formed between the LC layer and the other substrate (Figure 1.19(d)). The stratified polymer/LC configuration was initiated in order to achieve thin LC layer comparable to optical wavelengths and fast response (see eq. (1.14)) for display applications (Vorflusev and Kumar, 1999; Wang and Kumar, 2005). However, its feasibility has been challenged on account of the selective adsorption of positive charge by the single alignment layer of nylon 6 (Wu et al., 2010). By modifying the fabrication processes, the idea of polymer-separated composite films has further been extended to generating vertical LC orientation without alignment layer and fabricating single-substrate and flexible displays, wide-viewing-angle cholesteric LC displays, and LC lenses (Avci et al., 2017; Fan et al., 2005; Ho and Lee, 2011; Lin et al., 2006b; Lin and Lin, 2011; Liu et al., 2016b).

The primary shortcoming of polymer-dispersed LC devices is the relatively high operating voltage (>20 V) due to strong surface anchoring at the polymer boundaries and the low dielectric permittivity of the polymer (with $\varepsilon \sim 3$). In this regard, reducing the cell gap, lowering the polymer content, and enlarging the droplet size are direct ways to lower the voltages, but these approaches would incur the decrease in light-scattering intensity of polymer-dispersed LCs. As such, researchers have considered the improvement of electro-optical characteristics of polymer-dispersed LCs by optimizing the polymer materials (Gao et al., 2013; Meng et al., 2010; Zhang et al., 2012; Zhang et al., 2013), adopting tri-electrode configuration (Liang et al., 2018d) and doping with dyes (Ahmad et al., 2017a; 2017b; Kumar and Raina, 2016) or nanoparticles (Hsu et al., 2016a; Jayoti et al., 2017; Katariya Jain and Deshmukh, 2019; Ni et al., 2017; Shim et al., 2016b; Zobov et al., 2016). Recently, a coexistence system (PD&S LC) of polymer-dispersed and polymer-stabilized LCs with polymer networks inside the LC droplets that could lend strong light scattering at a low voltage has been demonstrated by using a mixture of a cholesteric LC, isotropic acrylate monomers (e.g. HPMA, LMA, PEGDA600, and Bis-EMA15), a liquid crystalline vinyl-ether monomer (e.g. C4V) and a photo-initiator (e.g. Irg651) exposed to UV in a two-step curing process (Li et al., 2019; Liang et al., 2018a). After introducing the mixture into a cell, the first step of UV exposure is to preliminarily form polymer-dispersed LC-like, porous polymer morphology with cholesteric LCs and liquid crystalline vinyl-ether monomers inside the droplets through the gradual consumption of the isotropic acrylate monomers over time. The UV exposure time in this step needs to be precisely controlled to avoid the complete consumption of the liquid crystalline acrylate monomer C4V. Afterward, a sufficiently high (curing) voltage is applied across the cell thickness to sustain LC molecules in the homeotropic state and, in the meantime, the second step of UV

exposure is performed to fully consume the liquid crystalline acrylate monomers, leading to the formation of homeotropically oriented polymer fibers within the LC droplets. Eventually, the PD&S LC cell without voltage applied exhibits randomly oriented cholesteric LC helices, which can be used as the light-scattering state. It is claimed that the threshold/saturated voltages can be reduced from 43.3 V/ 88.7 V to 21.2 V/35.5 V when the homeotropically oriented polymer fibers are formed inside the LC droplets (Li et al., 2019). Based on the aforementioned procedures of fabricating PD&S LC systems, various flexible smart films allowing the control of transmittance by electric field and/or temperature variations have been proposed by using an LC with negative dielectric anisotropy (Wang et al., 2015a), LC with the N*–SmA phase transition (Guo et al., 2017a; Liang et al., 2018a) or a dual-frequency LC (Liang et al., 2018b) as the host material and by doping the mixture with W–VO_2 nanorods (NRs) (Liang et al., 2018c) or surface-functionalized indium-oxide nanocrystals (Liang et al., 2017).

1.3.3.2 Polymer-stabilized liquid crystals (PSLCs)

It has been well proven that the polymer network formed can maintain LC orientation in the state where the prepolymer is polymerized due to the imposed anchoring at polymer network interfaces from the interaction between LC molecules and polymer fibrils. The parameters determining the morphologies of polymer networks include the chemical structure of the monomer, the monomer concentration, the configuration of LC mesophases, the curing UV intensity, and the curing temperature for photopolymerization. Accordingly, numerous polymer-stabilization technologies with a variety of aligning and stabilizing effects on LC molecules because of the presence of polymer networks have been exploited with the aim toward the revolutionary development of conventional LC-based technologies and devices as reported in Section 1.2.2. For example, in contrast to conventional methods where complicated surface treatments are required for the control of LC pretilt angle, several polymer-stabilization technologies involving the formation of two-dimensional polymer network near both substrate surfaces have been proposed to effectively tune the pretilt angle of LC molecules in a simple geometry. The most common one is to dope a reactive mesogenic monomer of less than 5 wt% into LC and to apply a significantly high voltage to sustain LC molecules in homeotropic orientation during the photopolymerization process, allowing controllable pretilt angle in given ranges of ~45° (between 45° and 90°), ~58° (between 2° and 60°), and ~90° (between 0° and 90°) by varying the UV exposure time (Chen and Chu, 2008), curing field strength (Sergan et al., 2010), and overall concentration of monomers (Liu and Chen, 2013), respectively. This polymer-stabilization technology for pretilt angle control has been applied to implementing initial twist alignment for the optically compensated bend (OCB) cell mode without the warmup time (Chen et al., 2008), transflective displays without a dual-gap configuration (Chen and Chu, 2008),

and protrusion-free multidomain vertical (MVA) configuration with promoted electro-optical performance (Kim et al., 2007b; Kwon et al., 2016; Lim et al., 2011). Without voltage applied during the photopolymerization, another polymer-stabilization method for controlling pretilt angle is to adopt isotropic prepolymers instead of reactive mesogen monomers. It was independently claimed by Kang et al., based on the mixture of a negative LC (MLC-7026-000) doped with NOA65 in planar-aligned cells (Kang et al., 2015b), and by Hsu et al., based on the mixture of a positive LC (E7) doped with NOA65 in vertical-aligned cells (Hsu et al., 2016b), that the NOA65 prepolymers tend to diffuse to the substrate surfaces during performing photopolymerization by UV light irradiation and the pretilt angle can be varied from 0° to 90° by increasing the NOA65 concentration. For the innovation of display performance, it has been suggested that the polymer network can basically reduce the field-off response time of commercial LCD modes (e.g. MVA, IPS, and FFS) due to strong interaction between LC molecules and polymer fibrils, thereby shortening the relaxation time of LC molecules from the field-on to field-off state. Other achievements highlighting improved display performance on the basis of the polymer-stabilization method has been demonstrated, such as suppressing the low-frequency-voltage-induced image flicker effect in the fringe-field switching (FFS) mode (Jiang et al., 2018), reducing gamma distortion in oblique viewing directions in MVA mode (Kim et al., 2017a), and promoting the contrast ratio in in-plane switching (IPS) modes (Zhou et al., 2015). On the other hand, blue phase, uniform lying helix in short-pitch cholesteric LC, ferroelectric LC, and optically compensated bend (OCB) LC modes with unique features of fast response and wide viewing angle are emerging LC modes for the development of next-generation displays. However, they are still far from practical uses in consequence of inherent drawbacks, especially the difficulty in obtaining stable LC configurations and mesophases, which can hardly be overcome by conventional LC technologies, as reported in Section 1.2.2.2. By means of polymer stabilization, it was manifested that polymer-stabilized blue phases have a much widened blue-phase temperature range, dramatically changing from about 1–5 °C for pristine blue phases to more than 60 °C covering the room temperature for polymer-stabilized counterparts (Kikuchi et al., 2002). This pioneering work has led to most of blue phase-related studies being carried out in the twenty-first century based on the polymer-stabilization method. Although some additional shortcomings (of electro-optical hysteresis, questionable long-term stability and residual birefringence) in association with the addition of polymer emerged, they have been properly overcome after extensive efforts (Castles et al., 2012; Chen and Wu, 2014; Yan et al., 2011). By sustaining LC at desired orientation or inserting a photomask during photopolymerization, polymer-stabilization technologies with three-dimensional polymer network morphologies have been utilized to achieve initial bend or twist alignment in optically compensated bend LCs (Asakawa et al., 2006; Chen et al., 2006; Huang et al., 2007; Kizu et al., 2009; Wu et al., 2009), stable uniform lying helix alignment in short-pitch cholesteric LCs (Broughton et al., 2006; Tartan et al., 2016; Andrii Varanytsia and Chien, 2017), gray-scale operation in surface-stabilized ferroelectric LCs

(Furue et al., 2013; Furue et al., 2002; Furue et al., 2001), and spatially gradient refractive index in LC lenses (Lin et al., 2017c; Ren et al., 2013).

As emphasized repeatedly in this chapter, chiral LCs including cholesteric LCs and blue phases are promising for development of a vast variety of tunable and switchable photonic devices owing to the unique optical properties of the photonic bandgap that can reflect specific wavelengths of circularly polarized light with the same handedness as that of the helical structure. In general, the optical profiles for light reflection of a chiral LC are characterized by the central wavelength and the bandwidth of the photonic bandgap. It is reported in Section 1.2.2.2 that many conventional LC technologies have been proposed for electrical tuning in the central wavelength of the bandgap but the tunable ranges are quite limited and the operating voltages are high. One can also be recognized based on the content of Section 1.3.2.3 that wide tunability in bandgap characteristics via light irradiation have been demonstrated by doping photochromic dyes into chiral LCs to obtain unconventional dye/LC systems. However, the wavelength range of light reflection from a single-pitch chiral LC bandgap is quite narrow due to the fact that the photonic bandwidth, typically smaller than 150 nm in the visible light spectrum, is limited to the finite birefringence (<0.3) of the LC host used. As such, several polymer-stabilization technologies have been proposed, enabling the robust cholesteric LCs with a pitch gradient or non-uniform pitch distribution in the Grandjean planar state after photopolymerization. In order to broaden the photonic bandwidth, on the basis of polymer stabilization in the Grandjean planar CLC texture, there have been a good number of polymer-stabilization technologies permitting both the central wavelength and bandwidth of the photonic bandgap of chiral LC with positive or negative dielectric anisotropy to be effectively manipulated under DC voltage applied after the formation of three-dimensional polymer networks. The bandgap broadening as well as tuning mechanism by DC voltage for cases of polymer-stabilized polymer-stabilized cholesteric liquid crystals with negative dielectric anisotropy can be explained by the induction of non-uniform helical pitch from the deformation of polymer networks across the cell gap, which has been confirmed by means of textural observation using in-plane switching cells (Nemati et al., 2015) and dielectric spectroscopy (Tondiglia et al., 2014). Consider that there are considerable amounts of positive and negative ions dispersing in the bulk of a cholesteric LC cell. After polymerization in the Grandjean planar state, three-dimensional polymer network with uniform structural chirality mincing the helicity of the cholesteric LC is formed and ions with one polarity are expected to be trapped on surfaces of polymer networks. Upon the application of a significantly high DC electric field, the motion of positive (negative) ions to top (bottom) side of the cell results in the distortion in polymer-network morphologies under the electrostatic force with a shorter (longer) helical pitch near the top (bottom) side of the cell by the contraction (expansion) of polymer fibrils. This deformation could further lead to spatial pitch length gradient in the cholesteric LC in the direction normal to the substrate plane by the strong aligning force of polymers on LC molecules. Accordingly, DC-voltage-

induced bandwidth broadening from linear deformation of polymer network and blue (red) shift in central wavelength of the photonic bandgap from shortened (lengthened) average pitch length have progressively been demonstrated depending on the monomer and photoinitiator materials used and cell configuration and voltage as well as UV exposure conditions (Khandelwal et al., 2016; Lee et al., 2017; Lee et al., 2015b; Lee et al., 2014c; Lee et al., 2018; McConney et al., 2013; Nemati et al., 2018; Tondiglia et al., 2018). The mechanism of DC-voltage-induced polymer network deformation has also been administered to realize electrical tuning in bandgap of blue phases (Chen et al., 2015; Wang et al., 2017c). Besides dynamic tuning, several polymer-stabilization approaches have been proposed to create a broad bandwidth by forming non-uniform helical pitches after photopolymerization (Duan et al., 2017; Kim et al., 2017c). Notably, it is found in cases of polymer-stabilized chiral LCs that when LC components are removed from the composite, the residual polymers can behave as a template responsible for memorizing various helical superstructures. After certain types of LCs are refilled, many unusual features – such as stabilizing blue phases in a wide temperature range (Castles et al., 2012; Gandhi et al., 2016; Xiang and Lavrentovich, 2013) and implementing photonic bandgap properties beyond the optical limit (Chen et al., 2014b; Li et al., 2017c; Lin et al., 2017a) – have been clarified. The interested reader can refer to Chapter 13 for further information on this subject.

1.3.4 Nanomaterial-doped liquid crystals

Nanomaterials with physical sizes smaller than 100 nm in zero, one, and two dimensions have drawn considerable attention owing to their size-dependent thermal, chemical, mechanical, optical, electric, and magnetic properties that quite differ from those of bulk media as well as individual atoms or molecules. These nanosized and nanostructured materials have revolutionized many research fields and have widely been exploited for a diversity of applications, including data storage, optoelectronics, drug delivery, photocatalysis, biosensing, biomedical imaging, medications, environmental protection, and energy harvesting (Khan et al., 2019). The combination of LCs with nanomaterials possessing inherent characteristics or merits is expected to create an entirely new and potentially functional material with unusual and intriguing functionalities distinct from the individual components on account of various synergistic effects. The idea of doping particles into LCs was initiated in 1970, when Brochard and de Gennes proposed the so-called ferronematic structure (i.e., a colloid of nematic LCs doped with elongated and micro-sized magnetic particles) and theoretically predicted to lead to an enhancement in sensitivity of LC reorientation to external magnetic fields (Brochard and De Gennes, 1970). Although the concept of ferronematics has further been confirmed and corrected experimentally (Chen and Amer, 1983), relevant studies in the early stage focused mainly on theoretical estimations, presumably due to the crucial problem of the notorious colloidal instability

from particle aggregation that dominated difficulties in the reliability and reproducibility of experimental results. This circumstance slowed down the research of LC–nanomaterial colloids until the 2000s. In 2002, Yoshikawa et al. adopted a dispersion of a nematic LC possessing positive dielectric anisotropy doped with negative nematic LC-decorated palladium (Pd) nanoparticles and demonstrated unusual frequency-modulated electro-optical responses in electrically controlled birefringence (ECB)-mode LCs (Yoshikawa et al., 2002). Referring to the concept of ferronematics, it was reported by Reznikov et al. in 2003 that doping ferroelectric nanoparticles ($Sn_2P_2S_6$) into a positive nematic LC (ZLI-4801) can result in a considerable increase in dielectric anisotropy and, in turn, a decrease in operating voltage (Reznikov et al., 2003) in accordance with eq. (1.12). Apart from the use of zero-dimensional nanoparticles, the milestone work, exploiting the dispersion of one-dimensional carbon nanotubes in the nematic LC 5CB or E7 and showing rectified physical and electro-optical properties of the colloid in the TN mode, was conducted by Lee et al. in 2004 (Lee et al., 2004). Since these pioneering studies were carried out, various types of nanomaterials – such as ferroelectric, magnetic, metallic, and semiconducting (metal oxides) materials as well as carbon allotropes, differing in sizes, shapes, and intrinsic physical and chemical properties, have been employed as nanoadditives doped in nematic, cholesteric, blue phase, or smectic LCs. During the past two decades, accomplishments along this line have been noted, including (1) modifying physical properties, (2) repressing the ionic effect for the performance improvement of LCDs and related devices, (3) controlling LC alignment, and (4) inducing new functionalities for the development of novel LC technologies by incorporation of nanomaterials into LCs.

1.3.4.1 Modification in liquid crystal physical properties

LC with improved material properties is in urgent need for promoting the performance of LCDs and other LC-based devices so as to meet the increasing demand from the rapid growth of modern technology and to compete with emerging competitors (e.g. OLED and mini- or micro-LED for displays). For instance, a nematic LC with unique physical characteristics of high dielectric and optical anisotropy and optimized viscoelasticity is desirable to upgrade the image quality, lower the operating voltage, and accelerate the response of an electro-optical LC device for the development of next-generation displays. Except for complicated design in molecular structure via chemical synthesis, the scenario has alternatively been implemented by incorporating trace amounts of nanoadditives into existing and emerging LC materials. To date, many kinds of nanomaterials have evidently shown their ability of enhancing fundamental characteristics and improving electro-optical responses of LCs, as keynoted in some review articles (Mertelj and Lisjak, 2017; Mirzaei et al., 2012; Sharma et al., 2017; Yadav and Singh, 2016; Yadav et al., 2018). Especially a comprehensive review on recent development of quantum dot-doped LC technologies can be found in Chapter 15
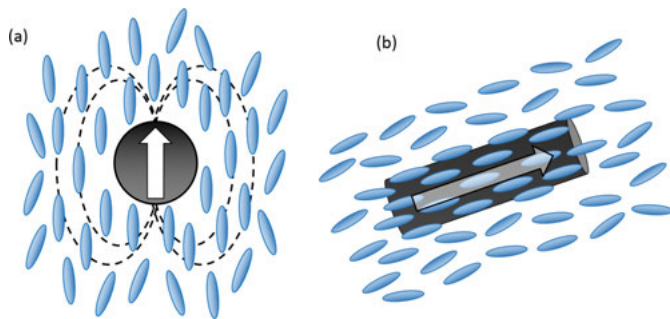
Figure 1.20: Enhanced short-range molecular ordering in (a) ferroelectric-nanoparticle and (b) carbon-nanotube-doped LCs. Adapted from Lopatina and Selinger (2009) and Basu and Iannacchione (2010).

of this book. Herein, we intend to focus on some representatives of LC–nanomaterial dispersions and provide a brief overview on both the general mechanism and recent achievements.

Using ferroelectric nanoparticles possessing spontaneous polarization as an example for the case of zero-dimensional nanomaterials, the ferroelectric nanoparticles immersed in the bulk of an LC cell can produce an electric field around them to polarize the surrounding LC molecules and induce an additional dipole moment (Lopatina and Selinger, 2009). Supported by the well-established theories and experimental results (Hakobyan et al., 2014; Lopatina and Selinger, 2011), the significant coupling between LC molecules and the dipole moment of nanoparticles together with the enhancement of the angular part of intermolecular van der Waals interaction enables the promotion in the LC ordering (Figure 1.20(a)) and thus the order parameter S as well as those physical properties in direct correlation to S, such as the birefringence ($\Delta n \propto S$), dielectric anisotropy ($\Delta \varepsilon \propto S$), and elastic constants ($k \propto S^2$). Accordingly, through doping with a minute amount of ferroelectric nanoparticles, for example, $BaTiO_3$, $Sn_2P_2S_6$ and $LiNbO_3$, improvements in electro-optical properties, especially lowering the operating voltage and shortening the response time, have successfully been demonstrated in nematic LCs (Al-Zangana et al., 2017; Dubey et al., 2017; Mishra et al., 2016; Nayek and Li, 2015; Podoliak et al., 2014), blue phases (Wang et al., 2012a; Xu et al., 2015), smectic LCs (Pradeep Kumar et al., 2016c; Shoarinejad et al., 2018; Shukla et al., 2016a; Shukla et al., 2014b), polymer-dispersed LCs (John et al., 2018; Shim et al., 2016a, 2016b), and bent-core LCs (Khan et al., 2017b; Kumar et al., 2018a).

Similarly, the magnetic nanoparticles can induce magnetic moment of particles in the magnetic field, causing the magnetic orientational effect onto the underlying LC matrix through the strong magnetic coupling between the particles and the LC molecules. Consequently, attention based on the magnetic nanoparticle-doped LCs has been paid primarily to the improvement of magneto-optical responses (Y. Lin et al., 2017d; Mouhli et al., 2017; Prodanov et al., 2016; Zhang et al., 2018).

In regard to one-dimensional nanomaterials, carbon nanotubes with rod-like molecular shape are a well-known representative used as a dopant for modifying the physical and electrical properties of LC in the percolated system (Rahman and Lee, 2009). When a dilute amount of carbon nanotubes are well dispersed in aligned nematic LC, the nanotubes will be oriented with their long axes along the LC director by the surface anchoring with a binding energy of about -2 eV in π–π stacking (Baik et al., 2005; Park et al., 2007). This anchoring force could induce a local short-range orientational order of LC molecules around the nanotubes and thus the local director along the tube axis, giving rise to the enhancement in the orientational order as depicted in Figure 1.20(b) (Basu and Iannacchione, 2009, 2010). On the basis of the interaction between a carbon nanotube and LC molecules, more remarkable features about the modification in physical characteristics of LCs, such as increased dielectric anisotropy and elastic constant as well as decreased viscosity, have continually been explored in nanotube-doped ECB (García-García et al., 2015; Li et al., 2017a; Middha et al., 2016; Vimal et al., 2015), TN (Kumar et al., 2016a), blue-phase (Kemiklioglu and Chien, 2016), SmC* (Cetinkaya et al., 2018; Shukla et al., 2018) and bent-core (Turlapati et al., 2017) LC modes, encouraging the development of LC electro-optical devices with lower threshold voltage and shorter response time.

Alternatively, the increase in LC ordering in nematic LC suspensions have been realized by incorporating with graphene oxide known as a class of two-dimensional carbon allotropes. In this hybrid system, the anchoring force, derived from π–π electron stacking between the graphene-honeycomb structure and LC molecules' benzene rings, stabilizes the LCs with the director along the graphene surface; thus, supporting the improvement in physical properties and the electro-optical responses by the increased dielectric anisotropy and/or splay elastic constant as well as the surface anchoring energy (Al-Zangana et al., 2016; Al-Zangana et al., 2016; Basu, 2017; Su et al., 2015, 2016a). The trapping of mobile ions by graphene in an LC cell can further reduce the viscosity and pretilt angle, resulting in faster electro-optical response (Su et al., 2015; Basu et al., 2016b). In addition to the above-mentioned nanomaterials, other inorganic nanoparticles as the dopants, such as metallic nanoparticles, quantum dots and oxides, can also play a significant role in the enhancement of the physical, optical, and electro-optical characteristics of LCs; selected property alterations reported in the past five years are summarized in Table 1.1.

1.3.4.2 Suppression of the ionic effect

The existence of a certain amount of impurity ions in a standard sandwich-type LC cell is unavoidable in that the ions are naturally released from the LC material and may be injected from the alignment layers with finite electrical conductivity (Naemura and Sawada, 2003). In general, ions in equilibrium (i.e., no voltage applied)

Table 1.1: Examples of nanomaterial-doped LCs with modified physical and electro-optical properties.

Nanomaterial/size (nm)	LC/phase	Modified parameters	Reference
Hexanethiolate-covered Au NPs/1.6	ZLI-3497/N	$\Delta\varepsilon\uparrow$, $k_{11}\downarrow$, $\gamma_1\uparrow$, $V_{th}\uparrow$, $\tau\downarrow$, $I_{PL}\downarrow$	(Roy et al., 2019)
CTAB-capped Au NRs/$L \sim 42$; $W \sim 14$	8CB/N	$T_{NI}\uparrow$, $T_{AN}\downarrow$, $\Delta\varepsilon\downarrow$, $k_{11}\downarrow$, $\gamma_1\downarrow$, $V_{th}\downarrow$, $\tau\downarrow$	(Dos Santos et al., 2019)
CTAB-capped Au NRs/$L \sim 38$; $W \sim 10$			
Au NPs/3.5	6CHBT/N	$\Delta\varepsilon\uparrow$, $k_{11}\downarrow$, $\gamma_1\downarrow$, $V_{th}\downarrow$, $W_A\downarrow$	(Elkhalgi et al., 2018)
PVP-capped Au NPs/5	E7/N	$\Delta\varepsilon\uparrow$, $k_{11}\downarrow$, $\gamma_1\downarrow$, $V_{th}\downarrow$, $\tau\downarrow$	(Hsu et al., 2017)
chiral ligand-capped Au NPs/5.5	FLC/SmC*	$\Delta\varepsilon\uparrow$, $\gamma_1\downarrow$, $P_s\uparrow$, $\theta_c\downarrow$, $\tau\downarrow$,	(Shukla et al., 2016b)
CTAB-capped Au NRs/$L \sim 53$; $W \sim 17$	6OCB/N	$\Delta\varepsilon\downarrow$, $k_{11}\downarrow$, $k_{33}\downarrow$, $\sigma\uparrow$, $V_{th}\downarrow$	(Madhuri et al., 2016)
Au NPs/5	8CB/N	$\Delta\varepsilon\downarrow$, $k_{11}\downarrow$, $\sigma\uparrow$, $V_{th}\downarrow$	(Mishra et al., 2015)
Ag NPs/6–7			
Hexane thiol-capped Ag NPs/5	5PCH/N	$T_{NI}\downarrow$, $\Delta\varepsilon\uparrow$, $\Delta n\uparrow$, $k_{11}\uparrow$, $k_{33}\uparrow$, $\sigma\downarrow$, $V_{th}\downarrow$	(S.J. et al., 2019)
Ag NPs/50	6CHBT/N	$T_{NI}\downarrow$, $\Delta\varepsilon\downarrow$, $k_{11}\downarrow$, $V_{th}\downarrow$	(Pandey et al., 2019)
Ag NPs/2–4	6CHBT/N	$\Delta\varepsilon\uparrow$, $\Delta n\uparrow$, $k_{11}\downarrow$, $V_{th}\downarrow$	(Vimal et al., 2019)
Hexane thiol-capped Ag NPs/2–4	W343/SmC*	$P_s\downarrow$, $\theta_c\downarrow$, $\tau\downarrow$,	(Vimal et al., 2017)
Ag NPs/10	5CB/N	$\Delta\varepsilon\downarrow$, $k_{11}\uparrow$, $\gamma_1\downarrow$, $V_{th}\uparrow$, $\tau\downarrow$	(Vardanyan et al., 2017)
Co-ZnO (Core)-ZnO (Shell) QDs/?	KCFLC 7S/SmC*	$\gamma_1\downarrow$, $P_s\uparrow$, $\theta_c\uparrow$, $\tau\downarrow$, $I_{PL}\uparrow$	(Doke et al., 2019)
InP (Core)-ZnS (Shell) QDs/3–4	1823A/N	$\Delta\varepsilon\uparrow$, $k_{11}\uparrow$, $k_{33}\uparrow$, $\sigma\uparrow$, $V_{th}\downarrow$, $\tau\downarrow$	(Roy et al., 2018)
InP (Core)-ZnS (Shell) QDs/~ 6	Hockey-stick LC/N	$\Delta\varepsilon\uparrow$, $\Delta n\uparrow$, $k_{11}\uparrow$, $k_{33}\uparrow$, $\sigma\uparrow$, $V_{th}\downarrow$	(Kumar et al., 2018b)
Cd$_{1-x}$Zn$_x$S (Core)-ZnS (Shell) QDs/8.5	NLC2020/N	$\Delta\varepsilon\downarrow$, $\Delta n\uparrow$, $k_{11}\downarrow$, $\gamma_1\downarrow$, $\gamma_1\downarrow$, $\tau\downarrow$	(Rastogi et al., 2018)
ZnO NPs/< 50 nm	W206E/SmC*	$P_s\uparrow$, $\tau\downarrow$, $I_{PL}\uparrow$	(Jayoti et al., 2018)
Cd$_{1-x}$Zn$_x$S (Core)-ZnS (Shell) QDs/8.7	Felix 17,100/SmC*	$\varepsilon\uparrow$, $\gamma_1\uparrow$, $P_s\uparrow$, $\theta_c\uparrow$, $\tau\uparrow$, CR$\uparrow$, $\sigma\uparrow$	(Pandey et al., 2016)
ZnS:Mn QDs/2.25–2.6	Felix 17,000/SmC*	$P_s\uparrow$, $\theta_c\uparrow$, $\tau\downarrow$, $I_{PL}\downarrow$	(Singh et al., 2016)
Mn$_3$O$_4$ NCs/550	E7/N	$\Delta\varepsilon\uparrow$, $k_{22}\uparrow$, $k_{33}\downarrow$, $V_{th}\downarrow$, CR$\uparrow$	(Ma et al., 2019)
TiO$_2$ NPs/20	HTG135200/N	$\Delta\varepsilon\downarrow$, $k_{11}\downarrow$, $V_{th}\downarrow$, $\tau\downarrow$, $\alpha\downarrow$	(Huang et al., 2019)
Modified-hydrophobic silica NPs/7	E7 + CB15/BP	$\Delta T_{BP}\uparrow$, $\lambda_{BP}\downarrow$, $\Delta V\downarrow$, $\tau\downarrow$	(Hsu et al., 2018)
MnTiO$_3$/< 50	6CHBT/N	$T_{NI}\uparrow$, $\Delta\varepsilon\uparrow$, $k_{11}\downarrow$, $V_{th}\downarrow$,	(Elkhalgi et al., 2018)

Abbreviations: NPs: nanoparticles; NRs: nanorods; NCs: nanocages; $\Delta\varepsilon$: dielectric anisotropy; k_{11}: splay elastic constant; k_{33}: bend elastic constant; γ_1: rotational viscosity; α: pre-tilted angle; V_{th}: threshold voltage; τ: response time; I_{PL}: photoluminescence intensity; T_{NI}: Nematic–isotropic transition temperature; T_{AN}: SmA–nematic transition temperature; Δn: birefringence; P_s: Spontaneous polarization in SmC*; θ_c: molecular tilted angle in SmC*; CR: contrast ratio; ΔT_{BP}: temperature range of blue phase; λ_{BP}: central wavelength of blue phase bandgap.
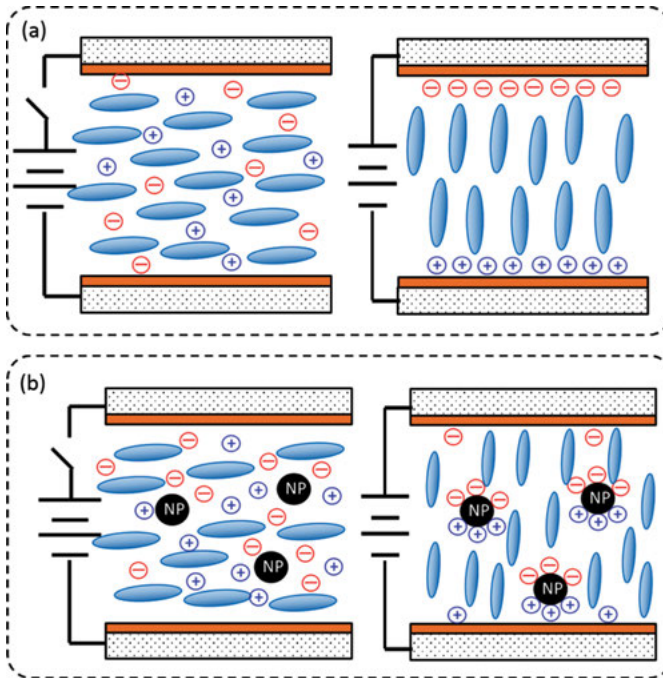
Figure 1.21: Schematic illustration of transport behaviors of (a) a pristine LC and
(b) a nanoparticle-doped LC cell.

are distributed uniformly within the bulk of the cell. Upon the application of a uni-
polar or DC voltage, the field-induced space charge separation dominates the migra-
tion of ions in such a way that positive (negative) ions drift toward the negative
(positive) electrode (Figure 1.21(a)). The accumulation of ion charges near the electro-
des forms electrical double layers and produces internal and counteracting electric
field to compete with the applied electric field, resulting in the decrease in effective
voltage across the LC layer by the so-called field screening effect (Chen and Lee,
2006; Sawada et al., 2000). It has been confirmed that the severe ionic effect has a
negative impact on the performance of LC devices, such as the increased threshold
and driving voltages, gray-level shift, lowered voltage holding ratio (VHR), prolonged
response time and, in turn, image sticking, image flicker as well as non-uniform im-
ages in LCDs (Mizusaki et al., 2011; Xu et al., 2014). The direct way to tackle this prob-
lem is to use LC and aligning materials with high resistivity and low ion density.
However, it has been indicated that the amount of ions can further be increased by
some of external situations and factors. For example, the application of sufficiently
high voltage across the LC cell thickness may lead to the injection of ions from elec-
trodes into the LC bulk (Murakami and Naito, 1997). The LC material in contact with
the surrounding sources (e.g. air, moisture, and solid surfaces) or under UV light

exposure often gets contaminated over time, leading to the increase in ion density (Garbovskiy, 2018b; Hung et al., 2012; Liu and Lee, 2010b; Wu et al., 2016). Doping nanomaterials into an LC cell has long been proven as an efficacious, physical means for suppressing the ionic effect. The mechanism behind has generally been explained by the dispersed nanoadditives that trap ions on their surfaces and restrain their transport (Figure 1.21(b)). To date, many nanomaterials have been found to play the role in repressing the ionic effect and furthermore improving the electrical properties (e.g. threshold voltage, response time, and VHR), including zero-dimensional ferroelectric (e.g. $BaTiO_3$ (Basu and Garvey, 2014; Hsiao et al., 2016) and $Sn_2P_2S_6$ (Garbovskiy and Glushchenko, 2015)), metallic (e.g. Au (Infusino et al., 2014; Podgornov et al., 2018; R. Shukla et al., 2014a) and Ni (Lee et al., 2014a)), semiconductor (e.g. CdS (Malik et al., 2012), CdSe (Shcherbinin and Konshina, 2017), graphene quantum dots (Cho et al., 2014) and ZnS (Konshina et al., 2014)), oxides (e.g. MgO (Chandran et al., 2014), SiO_2 (Liao et al., 2012), TiO_2 (Wu et al., 2016; Yadav et al., 2015), Y_2O_3 (Jung et al., 2012), CeO_2 (Mun et al., 2017), CO_3O_4 (Chung et al., 2013), NiO (Lee et al., 2015a) and ZrO_2 (Park et al., 2012)), carbon-based nanoparticles (e.g. diamond (Tomylko et al., 2011), fullerenes (Shukla et al., 2014c) and carbon dots (Shukla et al., 2015)), one-dimensional carbon nanotubes (Jian et al., 2011; Lee et al., 2014b; Lee et al., 2008; Lin et al., 2013a), and two-dimensional graphene (Su et al., 2015; Wu et al., 2015). Recently, Garbovskiy published a series of papers, theoretically interpreting the impact of nanomaterials as dopants on the ionic behaviors in LC cells. Aside from the decreased ionic density through the adsorption/desorption processes in LCs by doping with pure nanomaterials, Garbovskiy has established a model based on the modified Langmuir isotherm and pointed out that the effect of nanomaterials on the ion concentration is governed by the purity of both LCs and nanomaterials, and the ratio of the adsorption rate to the desorption rate as well (Garbovskiy, 2016b, 2016a, 2018a). On this basis, further clarified are the roles of the combined effect of the alignment layer and nanomaterials (Garbovskiy, 2017a), the temperature (Garbovskiy, 2017d, 2017c) and the cell parameters (Garbovskiy, 2017b) on the efficacy of ion trapping and releasing in LC–nanomaterial suspensions.

1.3.4.3 Control of liquid crystal alignment

Controllable and uniform LC alignment along a preferable direction plays a crucial role in the development of LC technologies and applications. As reviewed in Section 1.2.2, a large number of techniques for the control of LC alignment have been purported on the basis of an organic or inorganic thin film as the alignment layer deposited or coated on a substrate surface, followed by a specific treatment. Differently, with regard to the hybrid LC–nanomaterial systems, certain zero-dimensional nanoparticles with distinct surface morphologies have been suggested as effective aligning agents to induce homeotropic (vertical) or homogeneous (planar) molecular orientation of LCs in a sandwich-

type cell without additional surface treatment. The general mechanism is that the nanoparticles suspended within the bulk of the LC matrix tend to move toward the inner surfaces of substrates, thus producing surface anchoring of the nearby LC molecules around the substrate surface. Following this framework, it has been demonstrated by Zhao et al. that vertical and planar LC alignment can be prompted by doping 0.01 wt% of spherical and bowl-like nickel nanoparticles into the nematic LC 5CB, respectively. They also experimentally confirmed the immobilization of nanoparticles on substrate surfaces by SEM images of a polymer-templated cell (Zhao et al., 2011). Liu et al. synthesized flower-like and frame copper sulfide (CuS) nanoparticles with average diameters of 3 μm and 4 μm, respectively. They found that doping 0.05-wt% flower-like CuS nanoparticles with compact nanosheets into 5CB can impose vertical LC alignment whereas frame CuS (at 0.05 wt%) with sparse nanosheets doped in 5CB leads to random orientation of LC molecules and, hence, to the schlieren texture (exhibiting schlieren brushes) under crossed polarizers. Furthermore, they investigated the electro-optical properties of CuS-doped 5CB in planar-aligned cells and reported the effectively decreased threshold voltage, increased contrast ratio, and accelerated response as the dopant concentration of either flower-like or frame CuS is 0.05 wt% (Liu et al., 2017b). Wang et al. attempted to induce the LC alignment by doping Cu_2O nanocrystals into nematic, cholesteric, or smectic LCs. In this case, Cu_2O cubes, octahedra, and rhombic dodecahedra of identical sizes with an average diameter of 600 nm were employed as the nanodopants. Results based on the observed optical textures indicated planar LC alignment in 0.1-wt% Cu_2O cubes/5CB because of weak interaction between 5CB molecules and Cu_2O cubes. For comparisons, the coordination between the cyano group and surface Cu atoms with dangling bonds resulted in the strong interaction between LC and Cu_2O nanocrystals and thus the vertical LC alignment in 0.1-wt% Cu_2O octahedral/5CB and 0.06-wt% Cu_2O rhombic dodecahedra/5CB (Figure 1.22(a)). The results were further applied to the manipulation of LC alignment in LC–polymer composites via the photomechanical effect (Wang et al., 2016b). From an application point of view, the nanoparticle-induced vertical alignment by polyhedral oligomeric silsesquioxanes (POSS) nanoparticles has been further adopted for controlling the pretilt angle of LC molecules in planar-aligned cells by varying the concentration of POSS mixed in LC (Jeng et al., 2009) or in polyimide (as alignment layers) (Hwang et al., 2010) and for developing various electro-optical and photonic LC devices with improved electro-optical performance, such as alignment-layer-free vertical-alignment (VA) LC (Hwang et al., 2008; Jeng et al., 2007; Kang et al., 2015a), hybrid-aligned-nematic (HAN) LC (Kuo et al., 2007), dye-doped guest–host LC (Teng et al., 2008), single-cell-gap transflective LC (Chen et al., 2009b), multi-wavelength cholesteric LC laser (Chen et al., 2016), and electrically tunable polarization-dependent LC phase grating (Chen et al., 2009a; Fuh et al., 2011).

Recently, the technique of nickel (Ni)-nanoparticle-induced vertical alignment has been applied for the development of label-free LC biosensors. As reported by Zhao et al., a sandwich cell of nickel aptamer/thrombin was fabricated to obtain vertical
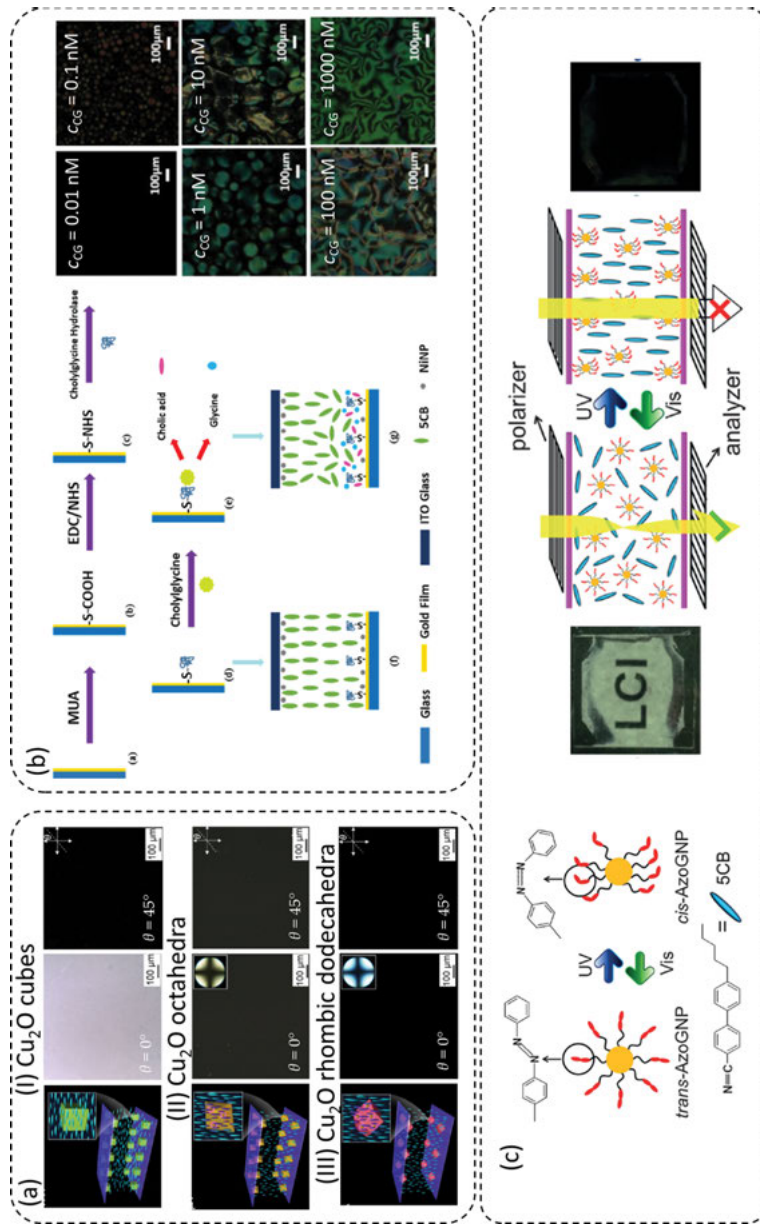
Figure 1.22: (a) Nanoparticle-induced vertical alignment in 5CB doped with (I) Cu₂O cubes, (II) Cu₂O octahedra, and (III) Cu₂O rhombic dodecahedra, (b) operation principle of bio-detection of cholylglycine based on a nickel-nanoparticle-assisted LC cell, and (c) light-driven order (homeotropic)–disorder (planar) switching based on an azo-thiol-grafted-gold-nanoparticle-doped 5CB cell. (a) Reproduced from Wang et al. (2016b) with permission. Copyright 2016 Springer Nature. (b) Reproduced from Wei and Jang (2017) with permission. Copyright 2017 Elsevier. (c) Reproduced from Xue et al. (2015) with permission. Copyright 2015 John Wiley and Sons.

alignment. The detection signal originating from the disruption of LC alignment and thus the bright optical texture under crossed polarizers were then produced by the anticipation that thrombin molecules linked the monodispersed thrombin-aptamer-modified Au nanoparticles (~13 nm in diameter) to form the aggregates. The limit of detection of this technique is 0.06 nM and the concentration of thrombin in the range of 10 nM to 100 nM shows linear correlation to the area ratio of the bright LC regions to the whole image (Zhao et al., 2015). Similarly, Wei et al. demonstrated a Ni-nanoparticle-assisted LC cell system that can be used to visualize the enzymatic activities between cholylglycine hydrolase (CGH) and cholylglycine (CG). Referring to the mechanism of disruption of Ni-nanoparticle-induced homeotropic LC alignment by introducing CG to the binding-immobilized CGH surface, the detection limit of CG was determined in the 10-pM level and a working range of 0.1 nM to 1 μM defined quantitatively (Figure 1.22(b)) (Wei and Jang, 2017). The flexibility and solubility of Ni–LC dispersions can further be promoted by functionalizing the nanoparticles with alkyl or mesogens (Qi and Hegmann, 2009; Qi et al., 2008). When the surface of gold (Au) nanoparticles was grafted with photoresponsive azo thiol, Xue et al. manifested the direct and reversible switching between planar and vertical LC alignment in Au-nanoparticle-doped nematic LC (5CB) upon irradiation with light (i.e., planar-to-vertical switching by UV light and vertical-to-planar switching by visible light) via the *tans–cis* photoisomerization of the azo groups (Figure 1.21(c)) (Xue et al., 2015). This concept has alternatively been realized by grafting liquid crystal polymer with side-chain azobenzene mesogens onto the gold nanoparticles (Kuang et al., 2018).

1.3.4.4 Addition of new functionalities

In addition to modifying the electro-optical response and alignment of LC materials mentioned above, the dispersion of nanomaterials in LCs has drawn a great deal of academic and technological interest because of the capability of providing additional functionalities by taking advantage of both constituents – the nanomaterials and LCs. For instance, ferroelectric nanoparticles dispersed in LC share their ferroelectricity to the mesogenic molecules, leading to the observed sensitivity of electro-optical response to the sign of the electric field in the nematic phase (Reznikov et al., 2003). The electromechanical memory effect in the isotropic phase of LC nanocomposites has also been demonstrated by the response of the dipole moments of ferroelectric nanoparticles as well as the reorientation of carbon nanotubes and graphene to the external electric fields (Basu, 2014). For the photonic functionalities, semiconductor quantum dots reveal optical and electronic features of the strong quantum confinement effect, tunable fluorescence emission, long-term stability, and low lasing threshold as well as low relative intensity noise such that they have been considered as promising gain media for the development of LC lasers. Bobrovsky

et al. proposed a polymer-stabilized cholesteric LCs doped with CdSe/ZnS core/shell quantum dots to realize optically and electrically controllable, circularly polarized emission (Bobrovsky et al., 2012). On this basis, Kumar and Raina suggested that the voltage for manipulating the circularly polarized fluorescence intensity can be reduced by impregnating 0.06-wt% CdSe quantum dots in a polymer-stabilized cholesteric LC gel (Kumar and Raina, 2016). Chen and coworkers designed various tunable quantum-dot–cholesteric-LC composites offering superior optical stability, higher damage threshold, and smaller divergence of lasing emission than those of a traditional dye-doped cholesteric LC. They showed that the profile of lasing emission (e.g. energy threshold, emission wavelength, and linewidth) can be tuned by thermal variation and electric-field application in CdSe/ZnS core/shell quantum dot-doped cholesteric LC (Chen et al., 2013a) and all-inorganic perovskite quantum dot-doped cholesteric LC (Chen et al., 2018b) as well as by light irradiation in chiral-azobenzene-dye-doped quantum-dot–cholesteric LC (Chen et al., 2014d). Apart from the design of polymer-templated quantum-dot–cholesteric LC for lessening the lasing threshold (Chen et al., 2014c), they found that the line width (~0.2 nm) and energy threshold (0.15 µJ/pulse) of the lasing emission from all-inorganic perovskite quantum dot-doped cholesteric LC laser can be comparable to or even better than those of traditional dye-doped cholesteric LCs (Chen et al., 2018b). For the amplified spontaneous emission, Cao et al. adopted a quantum dot-doped polymer-dispersed LC to lower the threshold (from 25 mJ·cm^{-2} to 6 mJ·cm^{-2}) (Cao et al., 2016) and proposed to tune the emission peak thermally between 662 nm at 50 °C and 669 nm at 90 °C based on a graphene quantum dot-doped cholesteric LC (Cao et al., 2017). On the other hand, metal nanomaterials and carbon allotropes with high photothermal conversion efficiency have been regarded as potential photothermal agents, enabling the local increase in temperature through the absorption and conversion of specific wavelengths of light into heat. Based on the photothermal effect, a number of LC nanocomposites impregnated with metal nanoparticles, metal nanorods, or graphene have been proposed for tuning the molecular orientation and physical and optical properties of LCs by light irradiation during the past years. Pezzi et al. experimentally observed the photothermal effect in 6-wt% cetyltrimethylammonium chloride (CTAC)-capped Au-NP/nematic-LC dispersions by a CW pump laser emitting at λ = 532 nm and theoretically established a model to characterize the photoinduced temperature variation (Pezzi et al., 2015). Gutierrez-Cuevas et al. achieved near-infrared (NIR at λ = 808 nm)-induced phase transition between the nematic and isotropic phases by doping 0.5-wt% hydrophobic mesogen-grafted plasmonic Au nanorods into the eutectic nematic LC E7 (Gutierrez-Cuevas et al., 2015). The photothermal induction of phase transition has also been implemented in cubic matrix of blue phases loaded with anisotropic and plasmonic hybrid nanorods. Upon NIR irradiation, it was reported by Wang et al. that the phase of nanocompoiste can sequentially be varied from BPI (with a body-centered cubic lattice) over BPII (with a simple cubic lattice) to the isotropic phase and the lattice constant as well as

reflection color tuned with increasing NIR exposure time (Wang et al., 2015c). Combining the thermo-sensitivity of the helical superstructure with the photothermal effect, Wang et al. accomplished NIR-directed helical inversion and NIR-driven bandgap shifting by dispersing mesogen-grafted Au nanorods into the cholesteric LC (Wang et al., 2016a) while De Sio et al. proposed to tune the reflectance of the bandgap of a gold nanorod-doped cholesteric LC without bandgap shift by exposing CW NIR pump laser emitting at $\lambda = 660$ nm (De Sio et al., 2016). Recently, Wang et al. adopted a mesogen-functionalized graphene as the photothermal agent doped in a polymer-dispersed cholesteric LC whose phase sequence exhibited SmA phase at lowered temperature. According to the NIR-driven phase transition between the SmA and cholesteric LC, this design revealed controllable optical efficacy by photothermal switching between the homeotropic SmA phase (transparent state) and the focal conic cholesteric LC phase (opaque state), which was suggested for the application to adaptive windows (Wang et al., 2017a).

1.4 Concluding remarks

We have considered pristine thermotropic LCs with rod-like molecular shapes as the representative of conventional LCs and attempted to build up a background on their fundamental characteristics in terms of types of LC phases, LC alignment, and physical properties in Section 1.2. Conventional thermotropic rod-like mesogens, also known as calamitics, are the largest group of LC materials because they are easy to synthesize, optically and chemically stable, commercially available and ubiquitously employed in our everyday life products. Especially, the great success of calamitic nematic LCs for display applications has driven enormous growths of commercialization of conventional LC compounds and device technologies based on their primary applications to optical and optoelectronic devices and electronic products. However, technological innovations using conventional LCs alone are limited and even challengeable due to inherent drawbacks originating from the nature of mesogenic materials. For display applications, it is described in Section 1.2.3.1 that three kinds of conventional LC phases (i.e., blue phases, short-pitch cholesteric LCs, and ferroelectric LCs) with inherently fast response and wide viewing angle over those of commercial nematics have progressively emerged to promote image quality for next-generation display applications. However, critical problems – such as narrow temperature range and high operating voltage for blue phases, low stability, and low flexoelectric coefficient for rod-like short-pitch cholesteric LC and lack of grayscale capability and low mechanical strength for ferroelectric LC – make them still far from practical applications. For electrically tunable and switchable photonic devices using chiral LCs, it is indicated in Section 1.2.3.2 that the range of tunability in bandgap wavelength of cholesteric LCs and blue phases are quite narrow even when high voltages are applied.

In contrast, unconventional LCs in general are novel LC compounds with molecular shapes other than conventional rod-like and disk-like forms. If one considers the particularities of material properties, unconventional LCs can further involve those functional substances and mixtures/composites/colloids, rendering a unique combination of characteristics that can hardly be obtained from conventional LCs alone. Among these, it has extensively been documented in the literature that doping certain types of additives, such as dyes, polymers, and nanomaterials, into conventional LCs constitute a class of unconventional LC systems that are promising for solving drawbacks and further promoting performance of as-reported conventional LC devices in Section 1.3. Moreover, the integration of inherent features of the additive and anisotropy in LC could give rise to new functionality, allowing one to extend LC utilizations to new frontiers. It is summarized in Section 1.3.2 that dye-doped LCs with additional dichroism and/or photochromism can be exploited to develop tunable lasers and polarizer-free, absorption-based LCDs, and to carry out unusual manipulation in bandgap properties and textural switching via light irradiation. In regard to polymer–LC composites discussed in Section 1.3.3, light-scattering-based polymer-dispersed LCs with micro-sized LC droplets have found potential as light shutters and optical switches for implementing polarizer-free flexible devices, whereas light-diffraction-based holographic polymer-dispersed LCs with periodical distribution of nano-sized LC droplets between polymer-rich zones have been suggested as gratings and for laser applications. On the other hand, polymer-stabilized LCs with designated network morphologies have widely been applied for stabilizing complicated LC configurations (i.e., pi-cell, ULH, and MVA), widening blue phase temperature range, implementing monostable ferroelectric LC, and electrical tuning in bandgap wavelength and bandwidth in a wide range. Notably, various LC-refilled polymer templates have been fabricated with the aim at demonstration of unusual bandgap properties beyond optical limits. The dispersion of nanomaterials in LCs has primarily been considered as a simple and non-synthesis approach to modifying physical and ionic properties of LCs, leading to effectively improved electro-optical performance at optimal dopant concentrations.

In the current LC community, fundamental characteristics of conventional LCs have been well established and technologies and applications based on them are getting mature. An increasing number of researchers are thus paying attention to unconventional LC systems in order to explore and create new knowledge in the wilderness, observe unusual phenomena, develop new and improved LC technologies, and extend research territories to other multidisciplinary fields. Owing to the uniqueness in the new era entering the 2020s, a book entitled *Unconventional Liquid Crystals and Their Applications* was proposed in the end of the 2010s. In addition to this leading chapter, there are other 14 chapters comprised in this book that cover recent developments of most fascinating, emerging and rapidly evolving unconventional LC functional materials, systems, and applications. After giving the reader a background on the evolution of research focus from conventional to unconventional LCs in Chapter 1 based on an application point of view, recent developments of LC compounds with unconventional molecular shapes are

introduced in Chapter 2 from the chemical aspect. For those "unconventional" applications based on conventional LCs, the developments of short-pitch rod-like ferroelectric LCs for modern photonics and disk-like LCs for solar energy harvesting are revealed in Chapters 3 and 4, respectively. Chapter 5 provides a review on recent technologies of using various LC phases as the sensing platforms together with conventional optical or electro-optical measurements as a means for quantitative bioassays. Going into unconventional systems based on conventional LCs doped with molecular additives, a solvent-free method that allows observation of thermotropic liquid and LC phases from biomacromolecules (e.g. nucleic acids, proteins, and virus particles) is demonstrated and the potential for electrical and electrochemical applications is suggested in Chapter 6. One type of unconventional LC systems concerning the dispersion of ionic surfactants in LCs is discussed for the purpose of electrically induced anchoring transition in Chapter 7. In regard to phtotresponsive dye-doped LCs and functional materials, Chapter 8 intends to clarify the origin of giant optical nonlinearity via photoinduced phase transition and to introduce the transient grating technique for time-resolved dynamics of dye-doped LC systems while recent development of optically tunable diffraction grating based on dye-doped LCs is reviewed in Chapter 9. Two other chapters related to LC polymers with photoresponsive optical features as well are an account of the photoalignment of azobenzene-containing LC polymers from the free surface as delineated in Chapter 10 and an overview on the self-assembly and photomanipulation of azobenzene-containing liquid-crystalline block copolymers as given in Chapter 11. From the point of view of fundamental theory, authors of Chapter 12 concentrate on a kind of unconventional LC polymers known as LC elastomers and discuss theories for modeling molecular behaviors. Chapter 13 reports on an unconventional technology adopting the idea of LC-refilled polymer templates for implementing high reflectivity. Another subject of functional materials in which a lyotropic LC is formed in a stable Langmuir monolayer by ultrathin films of nanomaterials, such as single-walled carbon nanotubes, gold nanoparticles, and quantum dots, is introduced for sensing applications in Chapter 14. Chapter 15 demonstrates the use of quantum dot-dispersed LCs for smart applications.

References

Ahmad, F., Jae Jeon, Y., Jamil, M. (2018). Graphene-based polymer dispersed liquid crystals display- an overview. Molecular Crystals and Liquid Crystals, 669(1), 46–60.

Ahmad, F., Jamil, M., Jeon, Y.J. (2017a). Advancement trends in dye-doped polymer dispersed liquid crystals – a survey review. Molecular Crystals and Liquid Crystals, 648(1), 88–113.

Ahmad, F., Jamil, M., Jeon, Y.J. (2017b). New developments in the dye-doped polymer dispersed liquid crystals gratings: a review. International Journal of Polymer Analysis and Characterization, 22(8), 659–668.

Ahmad, F., Jamil, M., Jeon, Y.J. (2017c). Reverse mode polymer stabilized cholesteric texture (psct) light shutter display–a short review. Journal of Molecular Liquids, 233, 187–196.

Ahn, D., Jeong, Y.-C., Lee, S., Lee, J., Heo, Y., Park, J.-K. (2009). Control of liquid crystal pretilt angles by using organic/inorganic hybrid interpenetrating networks. Optics Express, 17(19), 16603–16612.

Ahn, H.J., Kim, J.B., Kim, K.C., Hwang, B.H., Kim, J.T., Baik, H.K., Park, J.S., Kang, D. (2007). Liquid crystal pretilt angle control using adjustable wetting properties of alignment layers. Applied Physics Letters, 90(25), 253505.

Ailincai, D., Pamfil, D., Marin, L. (2018). Multiple bio-responsive polymer dispersed liquid crystal composites for sensing applications. Journal of Molecular Liquids, 272, 572–582.

Algorri, J., Urruchi, V., Sánchez-Pena, J. (2015). Reflective sidewall electrodes for low voltage and high transmittance blue-phase liquid crystal displays. Liquid Crystals, 42(7), 941–946.

Al-Zangana, S., Iliut, M., Boran, G., Turner, M., Vijayaraghavan, A., Dierking, I. (2016). Dielectric spectroscopy of isotropic liquids and liquid crystal phases with dispersed graphene oxide. Scientific Reports, 6(1), 1–10.

Al-Zangana, S., Iliut, M., Turner, M., Vijayaraghavan, A., Dierking, I. (2016). Properties of a thermotropic nematic liquid crystal doped with graphene oxide. Advanced Optical Materials, 4(10), 1541–1548.

Al-Zangana, S., Turner, M., Dierking, I. (2017). A comparison between size dependent paraelectric and ferroelectric batio3 nanoparticle doped nematic and ferroelectric liquid crystals. Journal of Applied Physics, 121(8), 085105.

Asakawa, Y., Yokota, K., Nanaumi, M., Takatuka, N., Takahashi, T., Saito, S. (2006). Stabilization of bend alignment using optical polymerization of uv curable liquid crystalline monomers. Japanese Journal of Applied Physics, 45(7R), 5878.

Asao, Y., Togano, T., Terada, M., Moriyama, T., Nakamura, S., Iba, J. (1999). Novel ferroelectric liquid crystal mode for active matrix liquid crystal display using cholesteric–chiral smectic c phase transition material. Japanese Journal of Applied Physics, 38(10R), 5977.

Ata Alla, R., Hegde, G., Komitov, L. (2013). Light-control of liquid crystal alignment from vertical to planar. Applied Physics Letters, 102(23), 233505.

Avci, N., Lee, Y.-H., Hwang, S.-J. (2017). Switchable polarisation-independent blue phase liquid crystal fresnel lens based on phase-separated composite films. Liquid Crystals, 44(7), 1078–1085.

Babakhanova, G., Parsouzi, Z., Paladugu, S., Wang, H., Nastishin, Y.A., Shiyanovskii, S.V., Sprunt, S., Lavrentovich, O.D. (2017). Elastic and viscous properties of the nematic dimer cb7cb. Physical Review E, 96(6), 062704.

Bahr, C. (2001). Smectic liquid crystals: ferroelectric properties and electroclinic effect. In Chirality in Liquid Crystals, Springer, 223–250.

Baik, I.-S., Jeon, S.Y., Lee, S.H., Park, K.A., Jeong, S.H., An, K.H., Lee, Y.H. (2005). Electrical-field effect on carbon nanotubes in a twisted nematic liquid crystal cell. Applied Physics Letters, 87(26), 263110.

Bailey, C., Tondiglia, V., Natarajan, L., Bricker, R., Cui, Y., Yang, D.K., Bunning, T. (2012). Surface limitations to the electro-mechanical tuning range of negative dielectric anisotropy cholesteric liquid crystals. Journal of Applied Physics, 111(6), 063111.

Bailey, C., Tondiglia, V., Natarajan, L., Duning, M., Bricker, R., Sutherland, R., White, T., Durstock, M., Bunning, T. (2010). Electromechanical tuning of cholesteric liquid crystals. Journal of Applied Physics, 107(1), 013105.

Bao, R., Liu, C.-M., Yang, D.-K. (2009). Smart bistable polymer stabilized cholesteric texture light shutter. Applied Physics Express, 2(11), 112401.

Barron, C., Angele, J., Bajic, L., Dozov, I., Leblanc, F., Perny, S., Brill, J., Specht, J. (2005). Development of binem® displays on flexible plastic substrates. Journal of the Society for Information Display, 13(3), 193–198.

Basu, R. (2014). Soft memory in a ferroelectric nanoparticle-doped liquid crystal. Physical Review E, 89(2), 022508.

Basu, R. (2017). Enhancement of polar anchoring strength in a graphene-nematic suspension and its effect on nematic electro-optic switching. Physical Review E, 96(1), 012707.

Basu, R., Garvey, A. (2014). Effects of ferroelectric nanoparticles on ion transport in a liquid crystal. Applied Physics Letters, 105(15), 151905.

Basu, R., Garvey, A., Kinnamon, D. (2015a). Effects of graphene on electro-optic response and ion-transport in a nematic liquid crystal. Journal of Applied Physics, 117(7), 074301.

Basu, R., Iannacchione, G.S. (2009). Nematic anchoring on carbon nanotubes. Applied Physics Letters, 95(17), 173113.

Basu, R., Iannacchione, G.S. (2010). Orientational coupling enhancement in a carbon nanotube dispersed liquid crystal. Physical Review E, 81(5), 051705.

Basu, R., Kinnamon, D., Garvey, A. (2015b). Nano-electromechanical rotation of graphene and giant enhancement in dielectric anisotropy in a liquid crystal. Applied Physics Letters, 106(20), 201909.

Basu, R., Kinnamon, D., Garvey, A. (2016a). Graphene and liquid crystal mediated interactions. Liquid Crystals, 43(13–15), 2375–2390.

Basu, R., Kinnamon, D., Skaggs, N., Womack, J. (2016b). Faster in-plane switching and reduced rotational viscosity characteristics in a graphene-nematic suspension. Journal of Applied Physics, 119(18), 185107.

Berreman, D., Heffner, W. (1980). New bistable cholesteric liquid-crystal display. Applied Physics Letters, 37(1), 109–111.

Bian, H., Yao, F., Gao, Y., Pei, Y., Zhang, J., Sun, X. (2016). Random lasing in unbounded dye-doped nematic liquid crystals. Liquid Crystals, 43(5), 581–586.

Bisoyi, H.K., Li, Q. (2014). Light-directing chiral liquid crystal nanostructures: from 1d to 3d. Accounts of Chemical Research, 47(10), 3184–3195.

Bisoyi, H.K., Li, Q. (2016a). Light-driven liquid crystalline materials: from photo-induced phase transitions and property modulations to applications. Chemical Reviews, 116(24), 15089–15166.

Bisoyi, H.K., Li, Q. (2016b). Light-directed dynamic chirality inversion in functional self-organized helical superstructures. Angewandte Chemie International Edition, 55(9), 2994–3010.

Bobrovsky, A., Mochalov, K., Oleinikov, V., Sukhanova, A., Prudnikau, A., Artemyev, M., Shibaev, V., Nabiev, I. (2012). Optically and electrically controlled circularly polarized emission from cholesteric liquid crystal materials doped with semiconductor quantum dots. Advanced Materials, 24(46), 6216–6222.

Brochard, F., De Gennes, P. (1970). Theory of magnetic suspensions in liquid crystals. Journal de Physique, 31(7), 691–708.

Bronnikov, S., Kostromin, S., Zuev, V. (2013). Polymer-dispersed liquid crystals: progress in preparation, investigation, and application. Journal of Macromolecular Science, Part B, 52(12), 1718–1735.

Broughton, B., Clarke, M., Morris, S., Blatch, A., Coles, H. (2006). Effect of polymer concentration on stabilized large-tilt-angle flexoelectro-optic switching. Journal of Applied Physics, 99(2), 023511.

Cao, M., Yang, S., Zhang, Y., Song, X., Che, Y., Zhang, H., Yu, Y., Ding, G., Zhang, G., Yao, J. (2017). Tunable amplified spontaneous emission in graphene quantum dots doped cholesteric liquid crystals. Nanotechnology, 28(24), 245202.

Cao, M., Zhang, Y., Song, X., Che, Y., Zhang, H., Yan, C., Dai, H., Liu, G., Zhang, G., Yao, J. (2016). Enhanced amplified spontaneous emission in a quantum dot-doped polymer-dispersed liquid crystal. Nanotechnology, 27(26), 26LT01.

Cao, W., Munoz, A., Palffy-Muhoray, P., Taheri, B. (2002). Lasing in a three-dimensional photonic crystal of the liquid crystal blue phase ii. Nature Materials, 1(2), 111–113.

Carbone, G., Corbett, D., Elston, S.J., Raynes, P., Jesacher, A., Simmonds, R., Booth, M. (2011). Uniform lying helix alignment on periodic surface relief structure generated via laser scanning lithography. Molecular Crystals and Liquid Crystals, 544(1), 37/[1025]–1049/[1037].

Carbone, G., Salter, P., Elston, S.J., Raynes, P., De Sio, L., Ferjani, S., Strangi, G., Umeton, C., Bartolino, R. (2009). Short pitch cholesteric electro-optical device based on periodic polymer structures. Applied Physics Letters, 95(1), 011102.

Castles, F., Day, F., Morris, S., Ko, D., Gardiner, D., Qasim, M., Nosheen, S., Hands, P., Choi, S., Friend, R. (2012). Blue-phase templated fabrication of three-dimensional nanostructures for photonic applications. Nature Materials, 11(7), 599–603.

Castles, F., Morris, S.M., Terentjev, E.M., Coles, H.J. (2010). Thermodynamically stable blue phases. Physical Review Letters, 104(15), 157801.

Cetinkaya, M., Yildiz, S., Ozbek, H. (2018). The effect of-cooh functionalized carbon nanotube doping on electro-optical, thermo-optical and elastic properties of a highly polar smectic liquid crystal. Journal of Molecular Liquids, 272, 801–814.

Chan, B.-H., Choi, W.-K. (2019). Three-dimensional corrugated electrode structure for low-voltage high-transmittance blue-phase liquid crystal displays. Liquid Crystals, 46(5), 806–815.

Chandran, A., Prakash, J., Naik, K.K., Srivastava, A.K., Dąbrowski, R., Czerwiński, M., Biradar, A. (2014). Preparation and characterization of mgo nanoparticles/ferroelectric liquid crystal composites for faster display devices with improved contrast. Journal of Materials Chemistry C, 2(10), 1844–1853.

Chang, C.-M., Lin, Y.-H., Reshetnyak, V., Park, C.H., Manda, R., Lee, S.H. (2017). Origins of Kerr phase and orientational phase in polymer-dispersed liquid crystals. Optics Express, 25(17), 19807–19821.

Chaudhari, P., Lacey, J., Doyle, J., Galligan, E., Lien, S.-C.A., Callegari, A., Hougham, G., Lang, N.D., Andry, P.S., John, R., Yang, K.-H., Lu, M., Cai, C., Speidell, J., Purushothaman, S., Ritsko, J., Samant, M., Stöhr, J., Nakagawa, Y., Katoh, Y., Saitoh, Y., Sakai, K., Satoh, H., Odahara, S., Nakano, H., Nakagaki, J., Shiota, Y. (2001). Atomic-beam alignment of inorganic materials for liquid-crystal displays. Nature, 411(6833), 56–59.

Chen, C.-W., Huang, H.-P., Jau, H.-C., Wang, C.-Y., Wu, C.-W., Lin, T.-H. (2017a). Polarization-asymmetric bidirectional random laser emission from a twisted nematic liquid crystal. Journal of Applied Physics, 121(3), 033102.

Chen, C.-W., Jau, H.-C., Wang, C.-T., Lee, C.-H., Khoo, I.C., Lin, T.-H. (2012). Random lasing in blue phase liquid crystals. Optics Express, 20(21), 23978–23984.

Chen, C.-W., Li, -C.-C., Jau, H.-C., Lee, C.-H., Wang, C.-T., Lin, T.-H. (2014a). Bistable light-driven π phase switching using a twisted nematic liquid crystal film. Optics Express, 22(10), 12133–12138.

Chen, C.-W., Li, -C.-C., Jau, H.-C., Yu, L.-C., Hong, C.-L., Guo, D.-Y., Wang, C.-T., Lin, T.-H. (2015). Electric field-driven shifting and expansion of photonic band gaps in 3d liquid photonic crystals. Acs Photonics, 2(11), 1524–1531.

Chen, G., Ni, M., Peng, H., Huang, F., Liao, Y., Wang, M., Zhu, J., Roy, V., Xie, X. (2017b). Photoinitiation and inhibition under monochromatic green light for storage of colored 3d images in holographic polymer-dispersed liquid crystals. ACS Applied Materials & Interfaces, 9(2), 1810–1819.

Chen, G., Wang, L., Wang, Q., Sun, J., Song, P., Chen, X., Liu, X., Guan, S., Zhang, X., Wang, L. (2014b). Photoinduced hyper-reflective laminated liquid crystal film with simultaneous multicolor reflection. ACS Applied Materials & Interfaces, 6(3), 1380–1384.

Chen, H., Lan, Y.-F., Tsai, C.-Y., Wu, S.-T. (2017c). Low-voltage blue-phase liquid crystal display with diamond-shape electrodes. Liquid Crystals, 44(7), 1124–1130.

Chen, H.-M.P., Lin, C.-W. (2009). Free alignment defect, low driving voltage of half-v ferroelectric liquid crystal device. Applied Physics Letters, 95(8), 083501.

Chen, H.-W., Lee, J.-H., Lin, B.-Y., Chen, S., Wu, S.-T. (2018a). Liquid crystal display and organic light-emitting diode display: present status and future perspectives. Light: Science & Applications, 7(3), 17168–17168.

Chen, H.-Y., Lee, W. (2006). Suppression of field screening in nematic liquid crystals by carbon nanotubes. Applied Physics Letters, 88(22), 222105.

Chen, L., Li, Y., Fan, J., Bisoyi, H.K., Weitz, D.A., Li, Q. (2014e). Photoresponsive monodisperse cholesteric liquid crystalline microshells for tunable omnidirectional lasing enabled by a visible light-driven chiral molecular switch. Advanced Optical Materials, 2(9), 845–848.

Chen, L.-J., Dai, J.-H., Lin, J.-D., Mo, T.-S., Lin, H.-P., Yeh, H.-C., Chuang, Y.-C., Jiang, S.-A., Lee, C.-R. (2018b). Wavelength-tunable and highly stable perovskite-quantum-dot-doped lasers with liquid crystal lasing cavities. ACS Applied Materials & Interfaces, 10(39), 33307–33315.

Chen, L.-J., Lee, C.-R., Chu, C.-L. (2014c). Surface passivation assisted lasing emission in the quantum dots doped cholesteric liquid crystal resonating cavity with polymer template. RSC Advances, 4(95), 52804–52807.

Chen, L.J., Lin, J.D., Huang, S.Y., Mo, T.S., Lee, C.R. (2013a). Thermally and electrically tunable lasing emission and amplified spontaneous emission in a composite of inorganic quantum dot nanocrystals and organic cholesteric liquid crystals. Advanced Optical Materials, 1(9), 637–643.

Chen, L.-J., Lin, J.-D., Lee, C.-R. (2014d). An optically stable and tunable quantum dot nanocrystal-embedded cholesteric liquid crystal composite laser. Journal of Materials Chemistry C, 2(22), 4388–4394.

Chen, S.-C., Lin, J.-D., Lee, C.-R., Hwang, S.-J. (2016). Multi-wavelength laser tuning based on cholesteric liquid crystals with nanoparticles. Journal of Physics D: Applied Physics, 49(16), 165102.

Chen, S.-H., Amer, N.M. (1983). Observation of macroscopic collective behavior and new texture in magnetically doped liquid crystals. Physical Review Letters, 51(25), 2298–2301.

Chen, T.-J., Cheng, Y.-H., Wu, S.-M. (2008). Twisted liquid crystal pi cell stabilized by polymer-sustained alignment. Applied Physics Letters, 93(22), 221103.

Chen, T.-J., Chu, K.-L. (2008). Pretilt angle control for single-cell-gap transflective liquid crystal cells. Applied Physics Letters, 92(9), 091102.

Chen, T.-J., Kuo, Y.-P., Wu, -J.-J., Sun, C.-H. (2006). Effect of curing voltage on formation of polymer-aligned liquid-crystal pi cells. Japanese Journal of Applied Physics, 45(4R), 2702.

Chen, W.-Z., Tsai, Y.-T., Lin, T.-H. (2009a). Photoalignment effect in a liquid-crystal film doped with nanoparticles and azo-dye. Applied Physics Letters, 94(20), 201114.

Chen, W.-Z., Tsai, Y.-T., Lin, T.-H. (2009b). Single-cell-gap transflective liquid-crystal display based on photo-and nanoparticle-induced alignment effects. Optics Letters, 34(17), 2545–2547.

Chen, Y., Peng, F., Wu, S.-T. (2013b). Submillisecond-response vertical-aligned liquid crystal for color sequential projection displays. Journal of Display Technology, 9(2), 78–81.

Chen, Y., Wu, S.T. (2014). Recent advances on polymer-stabilized blue phase liquid crystal materials and devices. Journal of Applied Polymer Science, 131(13).

Chen, Y., Xu, D., Wu, S.-T., Yamamoto, S.-I., Haseba, Y. (2013c). A low voltage and submillisecond-response polymer-stabilized blue phase liquid crystal. Applied Physics Letters, 102(14), 141116.

Cheng, K.-T., Lee, P.-Y., Qasim, M.M., Liu, C.-K., Cheng, W.-F., Wilkinson, T.D. (2016). Electrically switchable and permanently stable light scattering modes by dynamic fingerprint chiral textures. ACS Applied Materials & Interfaces, 8(16), 10483–10493.

Cheng, Z., Li, K., Guo, R., Wang, F., Wu, X., Zhang, L., Xiao, J., Cao, H., Yang, Z., Yang, H. (2011). Bandwidth-controllable reflective polarisers based on the temperature-dependent chiral conflict in binary chiral mixtures. Liquid Crystals, 38(2), 233–239.

Chiang, C.-H., Tzeng, S.-Y.T., Sie, F.-C., Huang, R.-H., Wu, P.-C., Wu, -J.-J., Lin, T.-Y., Liu, A.-S., Hsu, L.-H., Liau, W.-L. (2007). Reduction in driving voltage of vertically aligned ferroelectric liquid crystal display by diminishing anchoring force of alignment layer. Japanese Journal of Applied Physics, 46(9R), 5917.

Chiang, C.-H., Wu, P.-C., Wu, -J.-J. (2009). Effect of alignment layers on the response time in a half v-shaped ferroelectric liquid crystal cell. Japanese Journal of Applied Physics, 48(2R), 020215.

Chiang, I.-H., Long, C.-J., Lin, H.-C., Chuang, W.-T., Lee, -J.-J., Lin, H.-C. (2014). Broad ranges and fast responses of single-component blue-phase liquid crystals containing banana-shaped 1, 3, 4-oxadiazole cores. ACS Applied Materials & Interfaces, 6(1), 228–235.

Chiang, Y.-L., Lee, M.-J., Lee, W. (2018). Enhancing detection sensitivity in quantitative protein detection based on dye-doped liquid crystals. Dyes and Pigments, 157, 117–122.

Chigrinov, V.G. (2013). Photoaligning and photopatterning – a new challenge in liquid crystal photonics. Crystals, 3(1), 149–162.

Chilaya, G. (2001). Cholesteric liquid crystals: optics, electro-optics, and photo-optics. In Chirality in Liquid Crystals, Springer, 159–185.

Cho, M.-J., Park, H.-G., Jeong, H.-C., Lee, J.-W., Jung, Y.H., Kim, D.-H., Kim, J.-H., Lee, J.-W., Seo, D.-S. (2014). Superior fast switching of liquid crystal devices using graphene quantum dots. Liquid Crystals, 41(6), 761–767.

Choi, H., Kim, J., Nishimura, S., Toyooka, T., Araoka, F., Ishikawa, K., Wu, J.W., Takezoe, H. (2010). Broadband cavity-mode lasing from dye-doped nematic liquid crystals sandwiched by broadband cholesteric liquid crystal Bragg reflectors. Advanced Materials, 22(24), 2680–2684.

Choi, S.S., Morris, S.M., Coles, H.J., Huck, W.T. (2007). Wavelength tuning the photonic band gap in chiral nematic liquid crystals using electrically commanded surfaces. Applied Physics Letters, 91(23), 231110.

Choi, S.S., Morris, S.M., Huck, W.T., Coles, H.J. (2009). Electrically tuneable liquid crystal photonic bandgaps. Advanced Materials, 21(38-39), 3915–3918.

Choi, W.-K., Hou, S.-L., Chen, J.-Y., Su, G.-D.J., Li, Y.-M. (2015). Fast-response & polarization-independent optical shutter using nano-pdlc inside a fabry-perot cavity. Molecular Crystals and Liquid Crystals, 612(1), 232–237.

Chung, H.-K., Park, H.-G., Ha, Y.-S., Han, J.-M., Lee, J.-W., Seo, D.-S. (2013). Superior electro-optic properties of liquid crystal system using cobalt oxide nanoparticle dispersion. Liquid Crystals, 40(5), 632–638.

Clark, N.A., Lagerwall, S.T. (1980). Submicrosecond bistable electro-optic switching in liquid crystals. Applied Physics Letters, 36(11), 899–901.

Cognard, J. (1982). Alignment of nematic liquid crystals and their mixtures. Molecular Crystals and Liquid Crystals, A5(Suppl. Ser. II), 1–77.

Coles, H., Morris, S. (2010). Liquid-crystal lasers. Nature Photonics, 4(10), 676.

Coles, H.J., Clarke, M.J., Morris, S.M., Broughton, B.J., Blatch, A.E. (2006). Strong flexoelectric behavior in bimesogenic liquid crystals. Journal of Applied Physics, 99(3), 034104.

Cupelli, D., Nicoletta, F.P., De Filpo, G., Formoso, P., Chidichimo, G. (2011). Reverse mode operation polymer dispersed liquid crystal with a positive dielectric anisotropy liquid crystal. Journal of Polymer Science. Part B, Polymer Physics, 49(4), 257–262.

Cupelli, D., Nicoletta, F.P., Manfredi, S., Vivacqua, M., Formoso, P., De Filpo, G., Chidichimo, G. (2009). Self-adjusting smart windows based on polymer-dispersed liquid crystals. Solar Energy Materials and Solar Cells, 93(11), 2008–2012.

De Filpo, G., Formoso, P., Manfredi, S., Mashin, A.I., Nicoletta, F.P. (2017). Preparation and characterisation of bifunctional reverse-mode polymer-dispersed liquid crystals. Liquid Crystals, 44(10), 1607–1616.

De Gennes, P.-G., Prost, J. (1993). The Physics of Liquid Crystals, Vol. 83, Oxford university press.

De Sio, L., Placido, T., Comparelli, R., Curri, M.L., Tabiryan, N., Bunning, T.J. (2016). Plasmonic photoheating of gold nanorods in thermo-responsive chiral liquid crystals. Journal of Optics, 18(12), 125005.

De Sio, L., Serak, S., Tabiryan, N., Ferjani, S., Veltri, A., Umeton, C. (2010). Composite holographic gratings containing light-responsive liquid crystals for visible bichromatic switching. Advanced Materials, 22(21), 2316–2319.

Deshmukh, R.R., Malik, M.K. (2014). A method for estimating interfacial tension of liquid crystal embedded in polymer matrix forming pdlc. Journal of Applied Polymer Science, 131(23).

Dierking, I. (2000). Domain growth in a ferroelectric liquid crystal with horizontal chevron layer geometry. Journal of Physics: Condensed Matter, 12(12), 2657–2665.

Doane, J., Vaz, N., Wu, B.G., Žumer, S. (1986). Field controlled light scattering from nematic microdroplets. Applied Physics Letters, 48(4), 269–271.

Doke, S., Martinez-Teran, E., El-Gendy, A.A., Ganguly, P., Mahamuni, S. (2019). Sustained multiferroicity in liquid crystal induced by core/shell quantum dots. Journal of Molecular Liquids, 288, 110836.

Dorjgotov, E., Fodor-Csorba, K., Gleeson, J.T., Sprunt, S., Jákli, A. (2008). Viscosities of a bent-core nematic liquid crystal. Liquid Crystals, 35(2), 149–155.

Dos Santos, R., De Melo, P., Nunes, A., Meneghetti, M., Lyra, M., De Oliveira, I. (2019). Electro-optical switching in twisted nematic samples doped with gold nanorods. Journal of Molecular Liquids, 295, 111704.

Duan, M.-Y., Cao, H., Wu, Y., Li, E.-L., Wang, H.-H., Wang, D., Yang, Z., He, W.-L., Yang, H. (2017). Broadband reflection in polymer stabilized cholesteric liquid crystal films with stepwise photo-polymerization. Physical Chemistry Chemical Physics, 19(3), 2353–2358.

Dubey, R., Mishra, A., Singh, K., Alapati, P., Dhar, R. (2017). Electric behaviour of a schiff's base liquid crystal compound doped with a low concentration of batio3 nanoparticles. Journal of Molecular Liquids, 225, 496–501.

Elkhalgi, H.H., Khandka, S., Singh, U., Pandey, K., Dabrowski, R., Dhar, R. (2018). Dielectric and electro-optical properties of a nematic liquid crystalline material with gold nanoparticles. Liquid Crystals, 45(12), 1795–1801.

Ermakov, S.F., Myshkin, N.K. (2018). Structure and properties of liquid-crystal nanomaterials. In Liquid-Crystal Nanomaterials: Tribology and Applications, Cham, Springer International Publishing, 1–20.

Fan, H., Cui, J., Wang, Q.-H. (2015). High transmittance blue-phase liquid crystal display with improved protrusion electrodes. Liquid Crystals, 42(4), 481–485.

Fan, Y.-H., Ren, H., Wu, S.-T. (2005). Electrically switchable fresnel lens using a polymer-separated composite film. Optics Express, 13(11), 4141–4147.

Fernández, M.R., Casanova, E.Z., Alonso, I.G. (2015). Review of display technologies focusing on power consumption. Sustainability, 7(8), 10854–10875.

Ford, A.D., Morris, S.M., Coles, H.J. (2006). Photonics and lasing in liquid crystals. Materials Today, 9(7–8), 36–42.

Frank, F.C. (1958). I. Liquid crystals. On the theory of liquid crystals. Discussions of the Faraday Society, 25, 19–28.

Fu, D., Li, J., Wei, J., Guo, J. (2015). Effects of terminal chain length in hydrogen-bonded chiral switches on phototunable behavior of chiral nematic liquid crystals: helicity inversion and phase transition. Soft Matter, 11(15), 3034–3045.

Fuh, A.Y.-G., Huang, C.-Y., Liu, C.-K., Chen, Y.-D., Cheng, K.-T. (2011). Dual liquid crystal alignment configuration based on nanoparticle-doped polymer films. Optics Express, 19(12), 11825–11831.

Furue, H., Amano, M., Shime, T., Horiguchi, T., Oka, S., Komura, S., Kobayashi, S. (2013). Influence of fabrication conditions on monostability of polymer-stabilized ferroelectric liquid crystals. Japanese Journal of Applied Physics, 52(9S1), 09KE03.

Furue, H., Iimura, Y., Miyamoto, Y., Endoh, H., Fukuro, H., Kobayashi, S. (1998). Fabrication of a zigzag defect-free surface-stabilized ferroelectric liquid crystal display using polyimide orientation film. Japanese Journal of Applied Physics, 37(6R), 3417.

Furue, H., Takahashi, T., Kobayashi, S., Yokoyama, H. (2002). Models of molecular alignment structure in polymer-stabilized ferroelectric liquid crystals. Japanese Journal of Applied Physics, 41(11S), 7230.

Furue, H., Yokoyama, H., Kobayashi, S. (2001). Newly developed polymer-stabilized ferroelectric liquid crystals: microsized bistable domains and monostable v-shaped switching. Japanese Journal of Applied Physics, 40(9S), 5790.

Gandhi, S.S., Kim, M.S., Hwang, J.Y., Chien, L.C. (2016). Electro-optical memory of a nanoengineered amorphous blue-phase-iii polymer scaffold. Advanced Materials, 28(40), 8998–9005.

Gao, Y., Song, P., Zhang, T., Yao, W., Ding, H., Xiao, J., Zhu, S., Cao, H., Yang, H. (2013). Effects of a triethylamine catalyst on curing time and electro-optical properties of pdlc films. RSC Advances, 3(45), 23533–23538.

Garbovskiy, Y. (2016a). Electrical properties of liquid crystal nano-colloids analysed from perspectives of the ionic purity of nano-dopants. Liquid Crystals, 43(5), 648–653.

Garbovskiy, Y. (2016b). Switching between purification and contamination regimes governed by the ionic purity of nanoparticles dispersed in liquid crystals. Applied Physics Letters, 108(12), 121104.

Garbovskiy, Y. (2017a). Ion capturing/ion releasing films and nanoparticles in liquid crystal devices. Applied Physics Letters, 110(4), 041103.

Garbovskiy, Y. (2017b). Ions and size effects in nanoparticle/liquid crystal colloids sandwiched between two substrates. The case of two types of fully ionized species. Chemical Physics Letters, 679, 77–85.

Garbovskiy, Y. (2017c). Ions in liquid crystals doped with nanoparticles: conventional and counterintuitive temperature effects. Liquid Crystals, 44(9), 1402–1408.

Garbovskiy, Y. (2017d). Nanoparticle enabled thermal control of ions in liquid crystals. Liquid Crystals, 44(6), 948–955.

Garbovskiy, Y. (2018a). Nanomaterials in liquid crystals as ion-generating and ion-capturing objects. Crystals, 8(7), 264.

Garbovskiy, Y. (2018b). Time-dependent electrical properties of liquid crystal cells: unravelling the origin of ion generation. Liquid Crystals, 45(10), 1540–1548.

Garbovskiy, Y., Glushchenko, I. (2015). Ion trapping by means of ferroelectric nanoparticles, and the quantification of this process in liquid crystals. Applied Physics Letters, 107(4), 041106.

García-García, A., Vergaz, R., Algorri, J., Geday, M., Otón, J. (2015). The peculiar electrical response of liquid crystal-carbon nanotube systems as seen by impedance spectroscopy. Journal of Physics D: Applied Physics, 48(37), 375302.

Gauza, S., Zhu, X., Piecek, W., Dabrowski, R., Wu, S.-T. (2007). Fast switching liquid crystals for color-sequential lcds. Journal of Display Technology, 3(3), 250–252.

Ge, Z., Gauza, S., Jiao, M., Xianyu, H., Wu, S.-T. (2009). Electro-optics of polymer-stabilized blue phase liquid crystal displays. Applied Physics Letters, 94(10), 101104.

Geelhaar, T., Griesar, K., Reckmann, B. (2013). 125 years of liquid crystals – a scientific revolution in the home. Angewandte Chemie International Edition, 52(34), 8798–8809.

Gevorgyan, A. (2011). Tunable reflectance of a two-defect-layer cholesteric liquid crystal. Physical Review E, 83(1), 011702.

Gibbons, W.M., Shannon, P.J., Sun, S.-T., Swetlin, B.J. (1991). Surface-mediated alignment of nematic liquid crystals with polarized laser light. Nature, 351(6321), 49–50.

Gleeson, H.F., Kaur, S., Görtz, V., Belaissaoui, A., Cowling, S., Goodby, J.W. (2014). The nematic phases of bent-core liquid crystals. ChemPhysChem, 15(7), 1251–1260.

Goda, K., Omori, M., Takatoh, K. (2018). Optical switching in guest–host liquid crystal devices driven by photo-and thermal isomerisation of azobenzene. Liquid Crystals, 45(4), 485–490.

Gooch, C., Tarry, H. (1974). Optical characteristics of twisted nematic liquid-crystal films. Electronics Letters, 10(1), 2–4.

Guan, J., Zhang, M., Gao, W., Yang, H., Wang, G. (2012). Reversible reflection color-control in smectic liquid crystal switched by photo-isomerization of azobenzene. ChemPhysChem, 13(6), 1425–1428.

Guo, S.-M., Liang, X., Zhang, C.-H., Chen, M., Shen, C., Zhang, L.-Y., Yuan, X., He, B.-F., Yang, H. (2017a). Preparation of a thermally light-transmittance-controllable film from a coexistent system of polymer-dispersed and polymer-stabilized liquid crystals. ACS Applied Materials & Interfaces, 9(3), 2942–2947.

Guo, Y., Fu, M., Ren, Y., Wang, Y., Mu, Q., Ma, H., Zhu, J., Sun, Y. (2017b). Low-voltage blue-phase liquid crystal display with single-penetration electrodes. Liquid Crystals, 44(14–15), 2321–2326.

Gutierrez-Cuevas, K.G., Wang, L., Xue, C., Singh, G., Kumar, S., Urbas, A., Li, Q. (2015). Near infrared light-driven liquid crystal phase transition enabled by hydrophobic mesogen grafted plasmonic gold nanorods. Chemical Communications, 51(48), 9845–9848.

Gvozdovskyy, I., Yaroshchuk, O., Serbina, M., Yamaguchi, R. (2012). Photoinduced helical inversion in cholesteric liquid crystal cells with homeotropic anchoring. Optics express, 20(4), 3499–3508.

Ha, N.Y., Jeong, S.M., Nishimura, S., Suzaki, G., Ishikawa, K., Takezoe, H. (2008). Simultaneous red, green, and blue lasing emissions in a single-pitched cholesteric liquid-crystal system. Advanced Materials, 20(13), 2503–2507.

Hakobyan, M., Alaverdyan, R., Hakobyan, R., Chilingaryan, Y.S. (2014). Enhanced physical properties of nematics doped with ferroelectric nanoparticles. Armenian Journal of Physics, 7(1), 11–18.

Haller, I. (1975). Thermodynamic and static properties of liquid crystals. Progress in Solid State Chemistry, 10, 103–118.

Harden, J., Mbanga, B., Éber, N., Fodor-Csorba, K., Sprunt, S., Gleeson, J.T., Jakli, A. (2006). Giant flexoelectricity of bent-core nematic liquid crystals. Physical Review Letters, 97(15), 157802.

Hasegawa, M. (2005a). Applications of nematic liquid crystals. In: Alignment technologies and applications of liquid crystal devices, Ch. 4, pp. 99–138, Taylor & Francis, ISBN 0-748-40902-5, London and New York.

Hegde, G., Komitov, L. (2010). Periodic anchoring condition for alignment of a short pitch cholesteric liquid crystal in uniform lying helix texture. Applied Physics Letters, 96(11), 113503.

Heilmeier, G.H., Zanoni, L. (1968). Guest-host interactions in nematic liquid crystals. A new electro-optic effect. Applied Physics Letters, 13(3), 91–92.

Ho, C.-Y., Lee, J.-Y. (2011). The electro-optical characteristics and applicability evaluation of a photo-induced vertical alignment negative-type liquid crystal/photo-curable acrylic

pre-polymer mixture system mixed with chiral smectic a phase liquid crystal. Liquid Crystals, 38(1), 65–86.

Ho, J.Y., Chigrinov, V., Kwok, H. (2007). Variable liquid crystal pretilt angles generated by photoalignment of a mixed polyimide alignment layer. Applied Physics Letters, 90(24), 243506.

Hotta, A., Hasegawa, R., Takatoh, K. (2004). Effect of non-dc voltage applied during n*–smc* phase transition on alignment of half-v-shaped switching ferroelectric liquid crystal. Japanese Journal of Applied Physics, 43(9R), 6243.

Hsiao, Y.-C., Huang, K.-C., Lee, W. (2017). Photo-switchable chiral liquid crystal with optical tristability enabled by a photoresponsive azo-chiral dopant. Optics Express, 25(3), 2687–2693.

Hsiao, Y.-C., Huang, S.-M., Yeh, E.-R., Lee, W. (2016). Temperature-dependent electrical and dielectric properties of nematic liquid crystals doped with ferroelectric particles. Displays, 44, 61–65.

Hsiao, Y.-C., Lee, W. (2013). Lower operation voltage in dual-frequency cholesteric liquid crystals based on the thermodielectric effect. Optics Express, 21(20), 23927–23933.

Hsiao, Y.-C., Tang, C.-Y., Lee, W. (2011). Fast-switching bistable cholesteric intensity modulator. Optics Express, 19(10), 9744–9749.

Hsiao, Y.-C., Timofeev, I.V., Zyryanov, V.Y., Lee, W. (2015). Hybrid anchoring for a color-reflective dual-frequency cholesteric liquid crystal device switched by low voltages. Optical Materials Express, 5(11), 2715–2720.

Hsiao, Y.C., Yang, Z.H., Shen, D., Lee, W. (2018). Red, green, and blue reflections enabled in an electrically tunable helical superstructure. Advanced Optical Materials, 6(5), 1701128.

Hsu, -C.-C., Chen, Y.-X., Li, H.-W., Hsu, J.-S. (2016a). Low switching voltage zno quantum dots doped polymer-dispersed liquid crystal film. Optics Express, 24(7), 7063–7068.

Hsu, C.-J., Chen, B.-L., Huang, C.-Y. (2016b). Controlling liquid crystal pretilt angle with photocurable prepolymer and vertically aligned substrate. Optics Express, 24(2), 1463–1471.

Hsu, C.-J., Huang, M.-K., Tsai, P.-C., Hsieh, C.-T., Kuo, K.-L., You, C.-F., Lo, K.-Y., Huang, C.-Y. (2018). The effects of silica nanoparticles on blue-phase liquid crystals. Liquid Crystals, 45(2), 303–309.

Hsu, C.-J., Lin, L.-J., Huang, M.-K., Huang, C.-Y. (2017). Electro-optical effect of gold nanoparticle dispersed in nematic liquid crystals. Crystals, 7(10), 287.

Hsu, J.-S., Liang, B.-J., Chen, S.-H. (2004). Bistable chiral tilted-homeotropic nematic liquid crystal cells. Applied Physics Letters, 85(23), 5511–5513.

Huang, C.-Y., Fu, K.-Y., Lo, K.-Y., Tsai, M.-S. (2003). Bistable transflective cholesteric light shutters. Optics Express, 11(6), 560–565.

Huang, C.Y., Fung, R.X., Lin, Y.G., Hsieh, C.T. (2007). Fast switching of polymer-stabilized liquid crystal pi cells. Applied Physics Letters, 90(17), 171918.

Huang, C.Y., Selvaraj, P., Senguttuvan, G., Hsu, C.J. (2019). Electro-optical and dielectric properties of tio2 nanoparticles in nematic liquid crystals with high dielectric anisotropy. Journal of Molecular Liquids, 286, 110902.

Huang, J.-C., Hsiao, Y.-C., Lin, Y.-T., Lee, C.-R., Lee, W. (2016a). Electrically switchable organo–inorganic hybrid for a white-light laser source. Scientific Reports, 6, 28363.

Huang, K.-C., Hsiao, Y.-C., Timofeev, I.V., Zyryanov, V.Y., Lee, W. (2016b). Photo-manipulated photonic bandgap devices based on optically tristable chiral-tilted homeotropic nematic liquid crystal. Optics Express, 24(22), 25019–25025.

Huang, W., Yuan, C.-L., Shen, D., Zheng, Z.-G. (2017). Dynamically manipulated lasing enabled by a reconfigured fingerprint texture of a cholesteric self-organized superstructure. Journal of Materials Chemistry C, 5(28), 6923–6928.

Huang, Y., Zhou, Y., Doyle, C., Wu, S.-T. (2006). Tuning the photonic band gap in cholesteric liquid crystals by temperature-dependent dopant solubility. Optics Express, 14(3), 1236–1242.

Huh, J.-W., Kim, J.-H., Oh, S.-W., Ji, S.-M., Yoon, T.-H. (2018). Ion-doped liquid-crystal cell with low opaque-state specular transmittance based on electro-hydrodynamic effect. Dyes and Pigments, 150, 16–20.

Humar, M., Muševič, I. (2010). 3d microlasers from self-assembled cholesteric liquid-crystal microdroplets. Optics Express, 18(26), 26995–27003.

Hung, H.-Y., Lu, C.-W., Lee, C.-Y., Hsu, C.-S., Hsieh, Y.-Z. (2012). Analysis of metal ion impurities in liquid crystals using high resolution inductively coupled plasma mass spectrometry. Analytical Methods, 4(11), 3631–3637.

Hussain, Z., Qazi, F., Ahmed, M.I., Usman, A., Riaz, A., Abbasi, A.D. (2016). Liquid crystals based sensing platform-technological aspects. Biosensors & Bioelectronics, 85, 110–127.

Hwang, J., Song, M.H., Park, B., Nishimura, S., Toyooka, T., Wu, J., Takanishi, Y., Ishikawa, K., Takezoe, H. (2005). Electro-tunable optical diode based on photonic bandgap liquid-crystal heterojunctions. Nature Materials, 4(5), 383–387.

Hwang, S.-J., Jeng, S.-C., Hsieh, I.-M. (2010). Nanoparticle-doped polyimide for controlling the pretilt angle of liquid crystals devices. Optics Express, 18(16), 16507–16512.

Hwang, S.-J., Jeng, S.-C., Yang, C.-Y., Kuo, C.-W., Liao, -C.-C. (2008). Characteristics of nanoparticle-doped homeotropic liquid crystal devices. Journal of Physics D: Applied Physics, 42(2), 025102.

Ikeda, T. (2003). Photomodulation of liquid crystal orientations for photonic applications. Journal of Materials Chemistry, 13(9), 2037–2057.

Infusino, M., De Luca, A., Ciuchi, F., Ionescu, A., Scaramuzza, N., Strangi, G. (2014). Optical and electrical characterization of a gold nanoparticle dispersion in a chiral liquid crystal matrix. Journal of Materials Science, 49(4), 1805–1811.

Inoue, Y., Moritake, H. (2015). Formation of a defect-free uniform lying helix in a thick cholesteric liquid crystal cell. Applied Physics Express, 8(7), 071701.

Ishinabe, T., Wako, K., Uchida, T. (2010). A fast-switching ocb-mode lcd for high-quality display applications. Journal of the Society for Information Display, 18(11), 968–975.

Jákli, A. (2013). Liquid crystals of the twenty-first century–nematic phase of bent-core molecules. Liquid Crystals Reviews, 1(1), 65–82.

Jákli, A., Lavrentovich, O.D., Selinger, J.V. (2018). Physics of liquid crystals of bent-shaped molecules. Reviews of Modern Physics, 90(4), 045004.

Janning, J.L. (1972). Thin film surface orientation for liquid crystals. Applied Physics Letters, 21(4), 173–174.

Jayoti, D., Malik, P., Prasad, S.K. (2018). Effect of zno nanoparticles on the morphology, dielectric, electro-optic and photo luminescence properties of a confined ferroelectric liquid crystal material. Journal of Molecular Liquids, 250, 381–387.

Jayoti, D., Malik, P., Singh, A. (2017). Analysis of morphological behaviour and electro-optical properties of silica nanoparticles doped polymer dispersed liquid crystal composites. Journal of Molecular Liquids, 225, 456–461.

Jeng, S.-C., Hwang, S.-J., Yang, C.-Y. (2009). Tunable pretilt angles based on nanoparticles-doped planar liquid-crystal cells. Optics Letters, 34(4), 455–457.

Jeng, S.-C., Kuo, C.-W., Wang, H.-L., Liao, -C.-C. (2007). Nanoparticles-induced vertical alignment in liquid crystal cell. Applied Physics Letters, 91(6), 061112.

Jeong, S.M., Ha, N.Y., Takanishi, Y., Ishikawa, K., Takezoe, H., Nishimura, S., Suzaki, G. (2007). Defect mode lasing from a double-layered dye-doped polymeric cholesteric liquid crystal films with a thin rubbed defect layer. Applied Physics Letters, 90(26), 261108.

Jian, B.-R., Tang, C.-Y., Lee, W. (2011). Temperature-dependent electrical properties of dilute suspensions of carbon nanotubes in nematic liquid crystals. Carbon, 49(3), 910–914.

Jiang, Y., Qin, G., Xu, X., Zhou, L., Lee, S., Yang, D.-K. (2018). Image flickering-free polymer stabilized fringe field switching liquid crystal display. Optics Express, 26(25), 32640–32651.

Jin, O., Fu, D., Wei, J., Yang, H., Guo, J. (2014). Light-induced wide range color switching of liquid crystal blue phase doped with hydrogen-bonded chiral azobenzene switches. RSC Advances, 4(54), 28597–28600.

Jo, J.S., Ozaki, M., Yoshino, K. (2003). Electrooptic effect based on helix deformation in homeotropically aligned ferroelectric liquid crystal. Japanese Journal of Applied Physics, 42(2R), 526.

Jo, Y.-S., Choi, T.-H., Ji, S.-M., Yoon, T.-H. (2018). Control of haze value by dynamic scattering in a liquid crystal mixture without ion dopants. AIP Advances, 8(8), 085004.

John, V.N., Varanakkottu, S.N., Varghese, S. (2018). Flexible, ferroelectric nanoparticle doped polymer dispersed liquid crystal devices for lower switching voltage and nanoenergy generation. Optical Materials, 80, 233–240.

Jones, C. (2012). Bistable liquid crystal displays. In Chen, J., Cranton, W., Fihn, M., Eds., Handbook of Visual Display Technology, Berlin, Heidelberg, Springer Berlin Heidelberg, 1507–1543.

Joubert, C., Angele, J., Boissier, A., Pecout, B., Forget, S., Dozov, I., Stoenescu, D., Lallemand, S., Lagarde, P. (2003). Reflective bistable nematic displays (binem®) fabricated by standard manufacturing equipment. Journal of the Society for Information Display, 11(1), 217–224.

Jung, H.-Y., Kim, H.-J., Yang, S., Kang, Y.-G., Oh, B.-Y., Park, H.-G., Seo, D.-S. (2012). Enhanced electro-optical properties of y2o3 (yttrium trioxide) nanoparticle-doped twisted nematic liquid crystal devices. Liquid Crystals, 39(7), 789–793.

Kang, H., Hong, H., Kim, D.-G., Sohn, E.-H., Shim, J., Kang, D., Lee, J.-C. (2015a). Liquid crystal alignment behaviours on poly (methyl methacrylate) having polyhedral oligomeric silsesquioxane groups. Liquid Crystals, 42(1), 32–40.

Kang, H., Lee, J.-H., Kim, D.-G., Kang, D. (2015b). Control of pretilt angle in liquid crystal and photocurable monomer system. Molecular Crystals and Liquid Crystals, 607(1), 94–103.

Kang, H., Park, J.S., Sohn, E.-H., Kang, D., Rosenblatt, C., Lee, J.-C. (2009). Polyimide blend alignment layers for control of liquid crystal pretilt angle through baking. Polymer, 50(22), 5220–5227.

Kashima, S., Takanishi, Y., Yamamoto, J., Yoshizawa, A. (2014). Flexible taper-shaped liquid crystal trimer exhibiting a modulated smectic phase. Liquid Crystals, 41(12), 1752–1761.

Katariya Jain, A., Deshmukh, R.R. (2019). Electro-optical and dielectric study of multi-walled carbon nanotube doped polymer dispersed liquid crystal films. Liquid Crystals, 46(8), 1191–1202.

Kato, T., Uchida, J., Ichikawa, T., Sakamoto, T. (2018). Functional liquid crystals towards the next generation of materials. Angewandte Chemie International Edition, 57(16), 4355–4371.

Kaur, S. (2016). Elastic properties of bent-core nematic liquid crystals: the role of the bend angle. Liquid Crystals, 43(13–15), 2277–2284.

Kelly, S.M., O'Neill, M. (2001). Chapter 1 – liquid crystals for electro-optic applications. In Singh Nalwa, H., Ed., Handbook of Advanced Electronic and Photonic Materials and Devices, Burlington, Academic Press, 1–66.

Kemiklioglu, E., Chien, L.-C. (2016). Electro-optical properties of carbon nanotube-doped polymer-stabilised blue phase liquid crystal ips cell. Liquid Crystals, 43(8), 1067–1074.

Khan, I.; Saeed, K. & Khan, I. (2019). Nanoparticles: Properties, applications and toxicities. Arabian journal of chemistry, Vol. 12(7), pp. 908–931.

Khan, R.K., Turlapati, S., Rao, N., Pratibha, R., Drzewinski, W., Dabrowski, R., Ghosh, S. (2017a). Novel achiral four-ring bent-shaped nematic liquid crystals with trifluoromethyl and methyl

substituents in the central molecular core: an unusually large Kerr constant in blue phase iii of nematic-chiral dopant mixture. Journal of Materials Chemistry C, 5(27), 6729–6737.

Khan, R.K., Turlapati, S., Rao, N.V., Ghosh, S. (2017b). Elastic and dielectric properties of ferroelectric nanoparticles/bent-core nematic liquid crystal blend. The European Physical Journal E, 40(9), 75.

Khandelwal, H., Debije, M.G., White, T.J., Schenning, A.P. (2016). Electrically tunable infrared reflector with adjustable bandwidth broadening up to 1100 nm. Journal of Materials Chemistry A, 4(16), 6064–6069.

Khoo, I. (2011). Extreme nonlinear optics of nematic liquid crystals. JOSA B, 28(12), A45–A55.

Khoo, I.C. (2009). Nonlinear optics of liquid crystalline materials. Physics Reports, 471(5–6), 221–267.

Kikuchi, H., Yokota, M., Hisakado, Y., Yang, H., Kajiyama, T. (2002). Polymer-stabilized liquid crystal blue phases. Nature Materials, 1(1), 64–68.

Kim, A.-K., Yoon, T.-H. (2016). Bistable chiral nematic liquid crystal device switchable between the transmissive and reflective modes. Journal of Information Display, 17(1), 9–15.

Kim, D.H., Lim, Y.J., Kim, D.E., Ren, H., Ahn, S.H., Lee, S.H. (2014a). Past, present, and future of fringe-field switching-liquid crystal display. Journal of Information Display, 15(2), 99–106.

Kim, H., Lee, J.-H. (2015). Fast falling time of fringe-field-switching negative dielectric anisotropy liquid crystal achieved by inserting vertical walls. Applied Optics, 54(5), 1046–1050.

Kim, H.J., Lim, Y.J., Murali, G., Kim, M.S., Kim, G.H., Kim, Y.H., Lee, G.-D., Lee, S.H. (2017a). Reduction of gamma distortion in oblique viewing directions in polymer-stabilized vertical alignment liquid crystal mode. Current Optics and Photonics, 1(2), 157–162.

Kim, J., Kim, H., Kim, S., Choi, S., Jang, W., Kim, J., Lee, J.-H. (2017c). Broadening the reflection bandwidth of polymer-stabilized cholesteric liquid crystal via a reactive surface coating layer. Applied Optics, 56(20), 5731–5735.

Kim, J.B., Kim, K.C., Ahn, H.J., Hwang, B.H., Hyun, D.C., Baik, H.K. (2007a). Variable liquid crystal pretilt angles on various compositions of alignment layers. Applied Physics Letters, 90(4), 043515.

Kim, J.-H., Huh, J.-W., Oh, S.-W., Ji, S.-M., Jo, Y.-S., Yu, B.-H., Yoon, T.-H. (2017b). Bistable switching between homeotropic and focal-conic states in an ion-doped chiral nematic liquid crystal cell. Optics Express, 25(23), 29180–29188.

Kim, J.-W., Choi, T.-H., Yoon, T.-H., Choi, E.-J., Lee, J.-H. (2014b). Elimination of image flicker in fringe-field switching liquid crystal display driven with low frequency electric field. Optics Express, 22(25), 30586–30591.

Kim, M., Park, K.J., Seok, S., Ok, J.M., Jung, H.-T., Choe, J., Kim, D.H. (2015). Fabrication of microcapsules for dye-doped polymer-dispersed liquid crystal-based smart windows. ACS Applied Materials & Interfaces, 7(32), 17904–17909.

Kim, S.G., Kim, S.M., Kim, Y.S., Lee, H.K., Lee, S.H., Lee, G.-D., Lyu, -J.-J., Kim, K.H. (2007b). Stabilization of the liquid crystal director in the patterned vertical alignment mode through formation of pretilt angle by reactive mesogen. Applied Physics Letters, 90(26), 261910.

Kim, S.-H., Oh, S.-W., Yoon, T.-H. (2018). Enhancement of absorption and haze with hybrid anchoring of dye-doped cholesteric liquid crystals. Optics Express, 26(11), 14259–14266.

Kim, T., Lee, J.H., Yoon, T.-H., Choi, S.-W. (2012). Reflective dual-mode liquid crystal display possessing low power consumption and high contrast ratio under ambient light. Optics Express, 20(14), 15522–15529.

Kim, Y., Tamaoki, N. (2014). A photoresponsive planar chiral azobenzene dopant with high helical twisting power. Journal of Materials Chemistry C, 2(43), 9258–9264.

Kim, Y., Tamaoki, N. (2019). Photoresponsive chiral dopants: light-driven helicity manipulation in cholesteric liquid crystals for optical and mechanical functions. ChemPhotoChem, 3(6), 284–303.

Kizu, Y., Hasegawa, R., Amemiya, I., Uchikoga, S., Wakemoto, H. (2009). Analysis of electro-optical properties of polymer-stabilized ocb and the application to tft-lcds. Journal of the Society for Information Display, 17(8), 647–658.

Ko, Y.-H., Jalalah, M., Lee, S.-J., Park, J.-G. (2018). Super ultra-high resolution liquid-crystal-display using perovskite quantum-dot functional color-filters. Scientific Reports, 8(1), 1–7.

Koden, M., Katsuse, H., Tagawa, A., Tamai, K., Itoh, N., Miyoshi, S., Wada, T. (1992). Four states of surface-stabilized ferroelectric liquid crystal with parallel rubbing. Japanese Journal of Applied Physics, 31(11R), 3632.

Komitov, L., Bryan-Brown, G., Wood, E., Smout, A. (1999). Alignment of cholesteric liquid crystals using periodic anchoring. Journal of Applied Physics, 86(7), 3508–3511.

Konshina, E., Galin, I., Gavrish, E. (2014). Reversible capacitance change of nematic liquid crystal cell doped with semiconductor cdse/zns quantum dots. Universal Journal of Materials Science, 2(1), 1–4.

Kopp, V.I., Fan, B., Vithana, H., Genack, A.Z. (1998). Low-threshold lasing at the edge of a photonic stop band in cholesteric liquid crystals. Optics Letters, 23(21), 1707–1709.

Kuang, Z.-Y., Fan, Y.-J., Tao, L., Li, M.-L., Zhao, N., Wang, P., Chen, E.-Q., Fan, F., Xie, H.-L. (2018). Alignment control of nematic liquid crystal using gold nanoparticles grafted by the liquid crystalline polymer with azobenzene mesogens as the side chains. ACS Applied Materials & Interfaces, 10(32), 27269–27277.

Kumar, J., Manjuladevi, V., Gupta, R.K., Kumar, S. (2016a). Fast response in tn liquid-crystal cells: effect of functionalised carbon nanotubes. Liquid Crystals, 43(4), 488–496.

Kumar, P., Debnath, S., Rao, N.V., Sinha, A. (2018a). Nanodoping: a route for enhancing electro-optic performance of bent core nematic system. Journal of Physics: Condensed Matter, 30(9), 095101.

Kumar, P., Jaggi, C., Sharma, V., Raina, K.K. (2016b). Advancements of vertically aligned liquid crystal displays. Micron, 81, 34–47.

Kumar, P., Kishore, A., Sinha, A. (2016c). Analog switching in the nanocolloids of ferroelectric liquid crystals. Applied Physics Letters, 108(26), 262903.

Kumar, P., Ray, R., Adel, P., Luebkemann, F., Dorfs, D., Pal, S.K. (2018b). Role of zns segment on charge carrier dynamics and photoluminescence property of cdse@ cds/zns quantum rods. The Journal of Physical Chemistry C, 122(11), 6379–6387.

Kumar, R., Raina, K. (2016). Optical and electrical control of circularly polarised fluorescence in cdse quantum dots dispersed polymer stabilised cholesteric liquid crystal shutter. Liquid Crystals, 43(7), 994–1001.

Kuo, C.-W., Jeng, S.-C., Wang, H.-L., Liao, -C.-C. (2007). Application of nanoparticle-induced vertical alignment in hybrid-aligned nematic liquid crystal cell. Applied Physics Letters, 91(14), 141103.

Kurihara, R., Furue, H., Takahashi, T., Yamashita, T.-O., Xu, J., Kobayashi, S. (2001). Fabrication of defect-free ferroelectric liquid crystal displays using photoalignment and their electrooptic performance. Japanese Journal of Applied Physics, 40(7R), 4622.

Kwon, Y.R., Choi, Y.E., Wen, P., Lee, B.H., Kim, J.C., Lee, M.-H., Jeong, K.-U., Lee, S.H. (2016). Polymer stabilized vertical alignment liquid crystal display: effect of monomer structures and their stabilizing characteristics. Journal of Physics D: Applied Physics, 49(16), 165501.

Lagerwall, J.P.F. (2016). An introduction to the physics of liquid crystals. In Fluids, Colloids and Soft Materials: An Introduction to Soft Matter Physics, Hoboken (nj), John Wiley & Sons, inc, 307–340, Wiley Online Library.

Lagerwall, J.P.F., Scalia, G. (2012). A new era for liquid crystal research: applications of liquid crystals in soft matter nano-, bio-and microtechnology. Current Applied Physics, 12(6), 1387–1412.

Lai, Y.-T., Kuo, J.-C., Yang, Y.-J. (2014). A novel gas sensor using polymer-dispersed liquid crystal doped with carbon nanotubes. Sensors and Actuators. A, Physical, 215, 83–88.

Lee, C.-R., Lin, J.-D., Huang, B.-Y., Mo, T.-S., Huang, S.-Y. (2010a). All-optically controllable random laser based on a dye-doped liquid crystal added with a photoisomerizable dye. Optics Express, 18(25), 25896–25905.

Lee, H., Park, H.J., Kwon, O.J., Yun, S.J., Park, J.H., Hong, S., Shin, S.T. (2011). 11.1: Invited paper: The world's first blue phase liquid crystal display. Paper presented at the SID Symposium Digest of Technical Papers, 42(1), 121–124.

Lee, H.M., Chung, H.-K., Park, H.-G., Jeong, H.-C., Han, -J.-J., Cho, M.-J., Lee, J.-W., Seo, D.-S. (2014a). Residual dc voltage-free behaviour of liquid crystal system with nickel nanoparticle dispersion. Liquid Crystals, 41(2), 247–251.

Lee, H.M., Chung, H.-K., Park, H.-G., Jeong, H.-C., Kim, J.-H., Park, T.-K., Seo, D.-S. (2015a). Nickel oxide nanoparticles doped liquid crystal system for superior electro-optical properties. Journal of Nanoscience and Nanotechnology, 15(10), 8139–8143.

Lee, J.H., Kim, T., Shin, H.K., Jhun, C.G., Kwon, S.-B., Kim, D.-G., Kim, W.S., Yoon, T.-H., Kim, J.C. (2010b). Reflective dual-mode liquid crystal display switchable between dynamic and memory modes. Applied Physics Letters, 97(13), 133510.

Lee, J.-H., Yoon, T.-H., Choi, E.-J. (2012). Flexoelectric effect of a rod-like nematic liquid crystal doped with highly-kinked bent-core molecules for energy converting components. Soft Matter, 8(8), 2370–2374.

Lee, J.-H., Yoon, T.-H., Choi, E.-J. (2013). Unusual temperature dependence of the splay elastic constant of a rodlike nematic liquid crystal doped with a highly kinked bent-core molecule. Physical Review E, 88(6), 062511.

Lee, K.-J., Park, H.-G., Jeong, H.-C., Kim, D.-H., Seo, D.-S., Lee, J.-W., Moon, B.-M. (2014b). Enhanced electro-optical behaviour of a liquid crystal system via multi-walled carbon nanotube doping. Liquid Crystals, 41(1), 25–29.

Lee, K.M., Tondiglia, V.P., Godman, N.P., Middleton, C.M., White, T.J. (2017). Blue-shifting tuning of the selective reflection of polymer stabilized cholesteric liquid crystals. Soft Matter, 13(35), 5842–5848.

Lee, K.M., Tondiglia, V.P., Lee, T., Smalyukh, I.I., White, T.J. (2015b). Large range electrically-induced reflection notch tuning in polymer stabilized cholesteric liquid crystals. Journal of Materials Chemistry C, 3(34), 8788–8793.

Lee, K.M., Tondiglia, V.P., McConney, M.E., Natarajan, L.V., Bunning, T.J., White, T.J. (2014c). Color-tunable mirrors based on electrically regulated bandwidth broadening in polymer-stabilized cholesteric liquid crystals. Acs Photonics, 1(10), 1033–1041.

Lee, K.M., Tondiglia, V.P., White, T.J. (2018). Electrically reconfigurable liquid crystalline mirrors. ACS Omega, 3(4), 4453–4457.

Lee, M.-J., Lee, W. (2020). Liquid crystal-based capacitive, electro-optical and dielectric biosensors for protein quantitation. Liquid Crystals, 47(8), 1145–1153.

Lee, S.D., Patel, J., Meyer, R.B. (1990). Effect of flexoelectric coupling on helix distortions in cholesteric liquid crystals. Journal of Applied Physics, 67(3), 1293–1297.

Lee, S.R., Lee, J.H., Jhun, C.G., Kwon, S.-B., Yoon, T.-H., Kim, J.C. (2009). Dual mode operation of bistable chiral splay nematic liquid crystal cell using horizontal switching for dynamic operation. Journal of Applied Physics, 105(7), 074508.

Lee, W., Chen, H.Y., Shih, Y.C. (2008). Reduced dc offset and faster dynamic response in a carbon-nanotube-impregnated liquid-crystal display. Journal of the Society for Information Display, 16(7), 733–741.

Lee, W., Chen, S.-H. (2001). Acousto-optical effect induced by ultrasound pulses in a nematic liquid-crystal film. Applied Optics, 40(10), 1682–1685.

Lee, W., Wang, C.-Y., Shih, Y.-C. (2004). Effects of carbon nanosolids on the electro-optical properties of a twisted nematic liquid-crystal host. Applied Physics Letters, 85(4), 513–515.

Lee, Y.-H., Wang, L., Yang, H., Wu, S.-T. (2015c). Photo-induced handedness inversion with opposite-handed cholesteric liquid crystal. Optics Express, 23(17), 22658–22666.

Li, -C.-C., Tseng, H.-Y., Chen, C.-W., Wang, C.-T., Jau, H.-C., Wu, Y.-C., Hsu, W.-H., Lin, T.-H. (2018a). 43-1: Tri-stable cholesteric liquid crystal smart window. SID Symposium Digest of Technical Papers, 49(1), 543–545.

Li, C.-Y., Wang, X., Liang, X., Sun, J., Li, C.-X., Zhang, S.-F., Zhang, L.-Y., Zhang, H.-Q., Yang, H. (2019). Electro-optical properties of a polymer dispersed and stabilized cholesteric liquid crystals system constructed by a stepwise uv-initiated radical/cationic polymerization. Crystals, 9(6), 282.

Li, G.-P., Dou, H., Chu, F., Song, Y.-L., Wang, Q.-H. (2018b). Low voltage and high transmittance transflective blue-phase liquid crystal display with opposite polar electrodes. Liquid Crystals, 45(3), 410–414.

Li, H., Pan, F., Wu, Y., Zhang, Y., Xie, X. (2017a). Improvement in imaging contrast feature of liquid crystal lens with the dopant of multi-walled carbon nanotubes. Applied Optics, 56(23), 6655–6662.

Li, H., Wang, C., Pan, Y., Yang, Y., Zeng, P. (2017b). Transient holographic grating in azo-dye-doped liquid crystals with off-resonant light. Liquid Crystals, 44(6), 933–938.

Li, L., Salamończyk, M., Shadpour, S., Zhu, C., Jákli, A., Hegmann, T. (2018c). An unusual type of polymorphism in a liquid crystal. Nature Communications, 9(1), 1–8.

Li, P., Sun, Y., Zhao, Y., Wang, Q. (2013a). High transmittance blue-phase liquid crystal displays with slit-shaped electrode. Liquid Crystals, 40(10), 1417–1421.

Li, Y., Luo, D., Chen, R. (2016). Random lasing from cholesteric liquid crystal microspheres dispersed in glycerol. Applied Optics, 55(31), 8864–8867.

Li, Y., Luo, D., Peng, Z.H. (2017c). Full-color reflective display based on narrow bandwidth templated cholesteric liquid crystal film. Optical Materials Express, 7(1), 16–24.

Li, Y., Wang, M., White, T.J., Bunning, T.J., Li, Q. (2013b). Azoarenes with opposite chiral configurations: light-driven reversible handedness inversion in self-organized helical superstructures. Angewandte Chemie International Edition, 52(34), 8925–8929.

Liang, X., Chen, M., Chen, G., Li, C., Han, C., Zhang, J., Zhang, J., Zhang, L., Yang, H. (2018a). Effects of polymer micro-structures on the thermo-optical properties of a flexible soft-mater film based on liquid crystals/polymer composite. Polymer, 146, 161–168.

Liang, X., Chen, M., Guo, S., Wang, X., Zhang, S., Zhang, L., Yang, H. (2018b). Programmable electro-optical performances in a dual-frequency liquid crystals/polymer composite system. Polymer, 149, 164–168.

Liang, X., Chen, M., Wang, Q., Guo, S., Zhang, L., Yang, H. (2018c). Active and passive modulation of solar light transmittance in a hybrid thermochromic soft-matter system for energy-saving smart window applications. Journal of Materials Chemistry C, 6(26), 7054–7062.

Liang, X., Guo, S., Chen, M., Li, C., Wang, Q., Zou, C., Zhang, C., Zhang, L., Guo, S., Yang, H. (2017). A temperature and electric field-responsive flexible smart film with full broadband optical modulation. Materials Horizons, 4(5), 878–884.

Liang, Z.-Y., Tu, C.-Y., Yang, T.-H., Liu, C.-K., Cheng, K.-T. (2018d). Low-threshold-voltage and electrically switchable polarization-selective scattering mode liquid crystal light shutters. Polymers, 10(12), 1354.

Liao, S.-W., Hsieh, C.-T., Kuo, -C.-C., Huang, C.-Y. (2012). Voltage-assisted ion reduction in liquid crystal-silica nanoparticle dispersions. Applied Physics Letters, 101(16), 161906.

Lim, Y.J., Woo, C.W., Oh, S.H., Mukherjee, A., Lee, S.H., Baek, J.H., Kim, K.J., Yang, M.S. (2011). Enhanced contrast ratio of homogeneously aligned liquid crystal displays by controlling the surface-anchoring strength. Journal of Physics D: Applied Physics, 44(32), 325403.

Lin, F.-C., Lee, W. (2011). Color-reflective dual-frequency cholesteric liquid crystal displays and their drive schemes. Applied Physics Express, 4(11), 112201.

Lin, F.-C., Wu, P.-C., Jian, B.-R., Lee, W. (2013a). Dopant effect and cell-configuration-dependent dielectric properties of nematic liquid crystals. Advances in Condensed Matter Physics, 2013.

Lin, J.-D., Lin, H.-L., Lin, H.-Y., Wei, G.-J., Chuang, Y.-C., Chen, L.-J., Huang, S.-Y., Huang, C.-Y., Mo, T.-S., Lee, C.-R. (2017a). Widely tunable photonic bandgap and lasing emission in enantiomorphic cholesteric liquid crystal templates. Journal of Materials Chemistry C, 5(13), 3222–3228.

Lin, J.-D., Lin, Y.-M., Mo, T.-S., Lee, C.-R. (2014). Photosensitive and all-optically fast-controllable photonic bandgap device and laser in a dye-doped blue phase with a low-concentration azobenzene liquid crystal. Optics Express, 22(8), 9171–9181.

Lin, J.-H., Hsiao, Y.-L. (2014). Manipulation of the resonance characteristics of random lasers from dye-doped polymer dispersed liquid crystals in capillary tubes. Optical Materials Express, 4(8), 1555–1563.

Lin, J.-H., Li, Y.-H., Lin, S.-H., Nguyen, B.-H. (2018). Configuration dependent output characteristics with fabry–perot and random lasers from dye-doped liquid crystals within glass cells. Photonics Research, 6(5), 403–408.

Lin, S.-H., Chen, P.-Y., Li, Y.-H., Chen, C.-H., Lin, J.-H., Chen, Y.-H., Tsay, S.-Y., Wu, -J.-J. (2017b). Manipulation of polarized random lasers from dye-doped twisted nematic liquid crystals within wedge cells. IEEE Photonics Journal, 9(2), 1–8.

Lin, T.-H., Jau, H.-C., Chen, C.-H., Chen, Y.-J., Wei, T.-H., Chen, C.-W., Fuh, A.Y.-G. (2006a). Electrically controllable laser based on cholesteric liquid crystal with negative dielectric anisotropy. Applied Physics Letters, 88(6), 061122.

Lin, T.H., Li, Y., Wang, C.T., Jau, H.C., Chen, C.W., Li, C.C., Bisoyi, H.K., Bunning, T.J., Li, Q. (2013b). Red, green and blue reflections enabled in an optically tunable self-organized 3d cubic nanostructured thin film. Advanced Materials, 25(36), 5050–5054.

Lin, Y., Yang, Y., Shan, Y., Gong, L., Chen, J., Li, S., Chen, L. (2017d). Magnetic nanoparticle-assisted tunable optical patterns from spherical cholesteric liquid crystal Bragg reflectors. Nanomaterials, 7(11), 376.

Lin, Y.-H., Ren, H., Gauza, S., Wu, Y.-H., Zhao, Y., Fang, J., Wu, S.-T. (2006b). IPS-LCD using a glass substrate and an anisotropic polymer film. Journal of Display technology, 2(1), 21.

Lin, Y.-H., Wang, Y.-J., Reshetnyak, V. (2017c). Liquid crystal lenses with tunable focal length. Liquid Crystals Reviews, 5(2), 111–143.

Lin, Y.-T., Lin, T.-H. (2011). Cholesteric liquid crystal display with wide viewing angle based on multi-domain phase-separated composite films. Journal of Display technology, 7(7), 373–376.

Liu, B., Ma, Y., Zhao, D., Xu, L., Liu, F., Zhou, W., Guo, L. (2017b). Effects of morphology and concentration of cus nanoparticles on alignment and electro-optic properties of nematic liquid crystal. Nano Research, 10(2), 618–625.

Liu, B.-Y., Chen, L.-J. (2013). Role of surface hydrophobicity in pretilt angle control of polymer-stabilized liquid crystal alignment systems. The Journal of Physical Chemistry C, 117(26), 13474–13478.

Liu, B.-Y., Meng, C.-H., Chen, L.-J. (2017a). Role of monomer alkyl chain length in pretilt angle control of polymer-stabilized liquid crystal alignment system. The Journal of Physical Chemistry C, 121(38), 21037–21044.

Liu, -H.-H., Lee, W. (2010a). Ionic properties of liquid crystals dispersed with carbon nanotubes and montmorillonite nanoplatelets. Applied Physics Letters, 97(17), 173501.

Liu, -H.-H., Lee, W. (2010b). Time-varying ionic properties of a liquid-crystal cell. Applied Physics Letters, 97(2), 023510.

Liu, H.-Y., Wang, C.-T., Hsu, C.-Y., Lin, T.-H., Liu, J.-H. (2010). Optically tuneable blue phase photonic band gaps. Applied Physics Letters, 96(12), 121103.

Liu, J., Ma, H., Sun, Y. (2016a). Blue-phase liquid crystal display with high dielectric material. Liquid Crystals, 43(12), 1748–1752.

Liu, K., Chen, D., Marcozzi, A., Zheng, L., Su, J., Pesce, D., Zajaczkowski, W., Kolbe, A., Pisula, W., Müllen, K. (2014). Thermotropic liquid crystals from biomacromolecules. Proceedings of the National Academy of Sciences, 111(52), 18596–18600.

Liu, M., Liu, Y., Zhang, G., Peng, Z., Li, D., Ma, J., Xuan, L. (2016b). Organic holographic polymer dispersed liquid crystal distributed feedback laser from different diffraction orders. Journal of Physics D: Applied Physics, 49(46), 465102.

Lopatina, L.M., Selinger, J.V. (2009). Theory of ferroelectric nanoparticles in nematic liquid crystals. Physical Review Letters, 102(19), 197802.

Lopatina, L.M., Selinger, J.V. (2011). Maier-saupe-type theory of ferroelectric nanoparticles in nematic liquid crystals. Physical Review E, 84(4), 041703.

Lu, H., Wei, C., Zhang, Q., Xu, M., Ding, Y., Zhang, G., Zhu, J., Xie, K., Zhang, X., Hu, Z. (2019). Wide tunable laser based on electrically regulated bandwidth broadening in polymer-stabilized cholesteric liquid crystal. Photonics Research, 7(2), 137–143.

Lu, H., Xie, X., Xing, J., Xu, C., Wu, Z., Zhang, G., Lv, G., Qiu, L. (2016). Wavelength-tuning and band-broadening of a cholesteric liquid crystal induced by a cyclic chiral azobenzene compound. Optical Materials Express, 6(10), 3145–3158.

Lubensky, T., Radzihovsky, L. (2002). Theory of bent-core liquid-crystal phases and phase transitions. Physical Review E, 66(3), 031704.

Lucchetti, L., Tasseva, J. (2012). Optically recorded tunable microlenses based on dye-doped liquid crystal cells. Applied Physics Letters, 100(18), 181111.

Ma, G., Jia, B., Zhao, D., Yang, Z., Yu, J., Liu, J., Guo, L. (2019). Amorphous mn3o4 nanocages with high-efficiency charge transfer for enhancing electro-optic properties of liquid crystals. Small, 15(19), 1805475.

Ma, J., Huang, W., Xuan, L., Yokoyama, H. (2018). Holographic polymer-dispersed liquid crystals: from materials and morphologies to applications. In Optical Properties of Functional Polymers and Nano Engineering Applications, CRC Press, 160–201.

Ma, J., Li, Y., White, T., Urbas, A., Li, Q. (2010). Light-driven nanoscale chiral molecular switch: reversible dynamic full range color phototuning. Chemical Communications, 46(20), 3463–3465.

Madhuri, P.L., Prasad, S.K., Shinde, P., Prasad, B. (2016). Large reduction in the magnitude and thermal variation of frank elastic constants in a gold nanorod/nematic composite. Journal of Physics D: Applied Physics, 49(42), 425304.

Malik, P., Chaudhary, A., Mehra, R., Raina, K. (2012). Electrooptic and dielectric studies in cadmium sulphide nanorods/ferroelectric liquid crystal mixtures. Advances in Condensed Matter Physics, 2012.

Manda, R., Pagidi, S., Bhattacharyya, S.S., Park, C.H., Lim, Y.J., Gwag, J.S., Lee, S.H. (2017). Fast response and transparent optically isotropic liquid crystal diffraction grating. Optics Express, 25(20), 24033–24043.

Mao, J.-L., Wang, J., Fan, H.-X., Wang, Q.-H. (2016). Low-voltage and high-transmittance blue-phase liquid crystal display with concave electrode. Liquid Crystals, 43(4), 535–539.

Marino, L., Ionescu, A.T., Marino, S., Scaramuzza, N. (2012). Dielectric investigations on a bent-core liquid crystal. Journal of Applied Physics, 112(11), 114113.

Mathews, M., Zola, R.S., Hurley, S., Yang, D.-K., White, T.J., Bunning, T.J., Li, Q. (2010). Light-driven reversible handedness inversion in self-organized helical superstructures. Journal of the American Chemical Society, 132(51), 18361–18366.

Matsushima, T., Seki, K., Kimura, S., Iwakabe, Y., Yata, T., Watanabe, Y., Komura, S. (2018). New fast response in-plane switching liquid crystal mode. Journal of the Society for Information Display, 26(10), 602–609.

Mazur, R., Piecek, W., Raszewski, Z., Morawiak, P., Garbat, K., Chojnowska, O., Mrukiewicz, M., Olifierczuk, M., Kedzierski, J., Dabrowski, R. (2017). Nematic liquid crystal mixtures for 3d active glasses application. Liquid Crystals, 44(2), 417–426.

McConney, M.E., Rumi, M., Godman, N.P., Tohgha, U.N., Bunning, T.J. (2019). Photoresponsive structural color in liquid crystalline materials. Advanced Optical Materials, 7(16), 1900429.

McConney, M.E., Tondiglia, V.P., Natarajan, L.V., Lee, K.M., White, T.J., Bunning, T.J. (2013). Electrically induced color changes in polymer-stabilized cholesteric liquid crystals. Advanced Optical Materials, 1(6), 417–421.

Meng, Q., Cao, H., Kashima, M., Liu, H., Yang, H. (2010). Effects of the structures of epoxy monomers on the electro-optical properties of heat-cured polymer-dispersed liquid crystal films. Liquid Crystals, 37(2), 189–193.

Mertelj, A., Lisjak, D. (2017). Ferromagnetic nematic liquid crystals. Liquid Crystals Reviews, 5(1), 1–33.

Middha, M., Kumar, R., Raina, K. (2016). Improved electro-optical response of induced chiral nematic liquid crystal doped with multi-walled carbon nanotubes. Ferroelectrics, 495(1), 75–86.

Mirzaei, J., Reznikov, M., Hegmann, T. (2012). Quantum dots as liquid crystal dopants. Journal of Materials Chemistry, 22(42), 22350–22365.

Mishra, M., Dabrowski, R.S., Dhar, R. (2016). Thermodynamical, optical, electrical and electro-optical studies of a room temperature nematic liquid crystal 4-pentyl-4'-cyanobiphenyl dispersed with barium titanate nanoparticles. Journal of Molecular Liquids, 213, 247–254.

Mishra, M., Dabrowski, R.S., Vij, J.K., Mishra, A., Dhar, R. (2015). Electrical and electro-optical parameters of 4'-octyl-4-cyanobiphenyl nematic liquid crystal dispersed with gold and silver nanoparticles. Liquid Crystals, 42(11), 1580–1590.

Mizusaki, M., Yoshimura, Y., Yamada, Y., Okamoto, K. (2011). Analysis of ion behavior affecting voltage holding property of liquid crystal displays. Japanese Journal of Applied Physics, 51(1R), 014102.

Moheghi, A., Nemati, H., Li, Y., Li, Q., Yang, D.-K. (2016). Bistable salt doped cholesteric liquid crystals light shutter. Optical Materials, 52, 219–223.

Morris, S., Qasim, M., Cheng, K., Castles, F., Ko, D.-H., Gardiner, D., Nosheen, S., Wilkinson, T., Coles, H., Burgess, C. (2013). Optically activated shutter using a photo-tunable short-pitch chiral nematic liquid crystal. Applied Physics Letters, 103(10), 101105.

Morris, S.M., Clarke, M.J., Blatch, A.E., Coles, H.J. (2007). Structure-flexoelastic properties of bimesogenic liquid crystals. Physical Review E, 75(4), 041701.

Mouhli, A., Ayeb, H., Othman, T., Fresnais, J., Dupuis, V., Nemitz, I.R., Pendery, J.S., Rosenblatt, C., Sandre, O., Lacaze, E. (2017). Influence of a dispersion of magnetic and nonmagnetic nanoparticles on the magnetic fredericksz transition of the liquid crystal 5cb. Physical Review E, 96(1), 012706.

Mucha, M. (2003). Polymer as an important component of blends and composites with liquid crystals. Progress in Polymer Science, 28(5), 837–873.

Mun, H.-Y., Park, H.-G., Jeong, H.-C., Lee, J.H., Oh, B.-Y., Seo, D.-S. (2017). Thermal and electro-optical properties of cerium-oxide-doped liquid-crystal devices. Liquid Crystals, 44(3), 538–543.

Murakami, S., Naito, H. (1997). Charge injection and generation in nematic liquid crystal cells. Japanese Journal of Applied Physics, 36(2R), 773.

Murakami, Y., Furuta, H., Xu, J., Endoh, H., Fukuro, H., Kobayashi, S. (2003). Intrinsic half-v-mode ferroelectric liquid crystal displays fabricated using hybrid alignment exhibiting high contrast ratio and high reliability without dc voltage application to remove layer degeneracy and their electro-optic characteristics. Japanese Journal of Applied Physics, 42(5R), 2759.

Muševič, I. (2016). Liquid-crystal micro-photonics. Liquid Crystals Reviews, 4(1), 1–34.

Mykytiuk, T., Ilchishin, I., Yaroshchuk, O., Kravchuk, R., Li, Y., Li, Q. (2014). Rapid reversible phototuning of lasing frequency in dye-doped cholesteric liquid crystal. Optics Letters, 39(22), 6490–6493.

Naemura, S., Sawada, A. (2003). Ionic conduction in nematic and smectic a liquid crystals. Molecular Crystals and Liquid Crystals, 400(1), 79–96.

Narayan, R., Kim, J.E., Kim, J.Y., Lee, K.E., Kim, S.O. (2016). Graphene oxide liquid crystals: discovery, evolution and applications. Advanced Materials, 28(16), 3045–3068.

Natarajan, L.V., Wofford, J.M., Tondiglia, V.P., Sutherland, R.L., Koerner, H., Vaia, R.A., Bunning, T.J. (2008). Electro-thermal tuning in a negative dielectric cholesteric liquid crystal material. Journal of Applied Physics, 103(9), 093107.

Nayek, P., Li, G. (2015). Superior electro-optic response in multiferroic bismuth ferrite nanoparticle doped nematic liquid crystal device. Scientific Reports, 5, 10845.

Nemati, H., Liu, S., Moheghi, A., Tondiglia, V.P., Lee, K.M., Bunning, T.J., Yang, D.-K. (2018). Enhanced reflection band broadening in polymer stabilized cholesteric liquid crystals with negative dielectric anisotropy. Journal of Molecular Liquids, 267, 120–126.

Nemati, H., Liu, S., Zola, R.S., Tondiglia, V.P., Lee, K.M., White, T., Bunning, T., Yang, D.-K. (2015). Mechanism of electrically induced photonic band gap broadening in polymer stabilized cholesteric liquid crystals with negative dielectric anisotropies. Soft Matter, 11(6), 1208–1213.

Ni, M., Chen, G., Sun, H., Peng, H., Yang, Z., Liao, Y., Ye, Y., Yang, Y., Xie, X. (2017). Well-structured holographic polymer dispersed liquid crystals by employing acrylamide and doping zns nanoparticles. Materials Chemistry Frontiers, 1(2), 294–303.

Nian, Y.-L., Wu, P.-C., Lee, W. (2016). Optimized frequency regime for the electrohydrodynamic induction of a uniformly lying helix structure. Photonics Research, 4(6), 227–232.

Niori, T., Sekine, T., Watanabe, J., Furukawa, T., Takezoe, H. (1996). Distinct ferroelectric smectic liquid crystals consisting of banana shaped achiral molecules. Journal of Materials Chemistry, 6(7), 1231–1233.

Nishikawa, H., Mochizuki, D., Higuchi, H., Okumura, Y., Kikuchi, H. (2017). Reversible broad-spectrum control of selective reflections of chiral nematic phases by closed-/open-type axially chiral azo dopants. ChemistryOpen, 6(6), 710–720.

Nordendorf, G., Hoischen, A., Schmidtke, J., Wilkes, D., Kitzerow, H.S. (2014). Polymer-stabilized blue phases: promising mesophases for a new generation of liquid crystal displays. Polymers for Advanced Technologies, 25(11), 1195–1207.

Ogiwara, A., Watanabe, M., Moriwaki, R. (2013). Formation of temperature dependable holographic memory using holographic polymer-dispersed liquid crystal. Optics Letters, 38(7), 1158–1160.

Oh, S.-W., Baek, J.-M., Heo, J., Yoon, T.-H. (2016). Dye-doped cholesteric liquid crystal light shutter with a polymer-dispersed liquid crystal film. Dyes and Pigments, 134, 36–40.

Oh, S.-W., Baek, J.-M., Kim, S.-H., Yoon, T.-H. (2017). Optical and electrical switching of cholesteric liquid crystals containing azo dye. Rsc Advances, 7(32), 19497–19501.

Oh, S.-W., Kim, S.-H., Baek, J.-M., Yoon, T.-H. (2018a). Optical and thermal switching of liquid crystals for self-shading windows. Advanced Sustainable Systems, 2(5), 1700164.

Oh, S.-W., Kim, S.-H., Yoon, T.-H. (2018b). Self-shading by optical or thermal control of transmittance with liquid crystals doped with push-pull azobenzene. Solar Energy Materials and Solar Cells, 183, 146–150.

Oh, S.-W., Kim, S.-H., Yoon, T.-H. (2018c). Thermal control of transmission property by phase transition in cholesteric liquid crystals. Journal of Materials Chemistry C, 6(24), 6520–6525.

Ong, H.L., Hurd, A.J., Meyer, R.B. (1985). Alignment of nematic liquid crystals by inhomogeneous surfaces. Journal of Applied Physics, 57(2), 186–192.

Ooi, Y.-H., Yeap, G.-Y. (2018). Λ-shaped liquid crystal trimers with dual terminal cholesteryl moieties: synthesis and concomitant of n*, sma and cholesteric glassy phases. Liquid Crystals, 45(2), 204–218.

Oscurato, S.L., Salvatore, M., Maddalena, P., Ambrosio, A. (2018). From nanoscopic to macroscopic photo-driven motion in azobenzene-containing materials. Nanophotonics, 7(8), 1387–1422.

Oseen, C. (1933). The theory of liquid crystals. Transactions of the Faraday Society, 29(140), 883–899.

Osman, F., Yeap, G.-Y., Nagashima, A., Ito, M.M. (2016). Structure property and mesomorphic behaviour of s-shaped liquid crystal oligomers possessing two azobenzene moieties. Liquid Crystals, 43(10), 1283–1292.

Outram, B., Elston, S. (2013a). Alignment of cholesteric liquid crystals using the macroscopic flexoelectric polarization contribution to dielectric properties. Applied Physics Letters, 103(14), 141111.

Outram, B., Elston, S. (2013b). Frequency-dependent dielectric contribution of flexoelectricity allowing control of state switching in helicoidal liquid crystals. Physical Review E, 88(1), 012506.

Outram, B., Elston, S. (2013c). Spontaneous and stable uniform lying helix liquid-crystal alignment. Journal of Applied Physics, 113(4), 043103.

Outram, B., Elston, S., Tuffin, R., Siemianowski, S., Snow, B. (2013). The use of mould-templated surface structures for high-quality uniform-lying-helix liquid-crystal alignment. Journal of Applied Physics, 113(21), 213111.

Ozaki, M., Kasano, M., Ganzke, D., Haase, W., Yoshino, K. (2002). Mirrorless lasing in a dye-doped ferroelectric liquid crystal. Advanced Materials, 14(4), 306–309.

Ozaki, R., Matsui, T., Ozaki, M., Yoshino, K. (2003). Electrically color-tunable defect mode lasing in one-dimensional photonic-band-gap system containing liquid crystal. Applied Physics Letters, 82(21), 3593–3595.

Palffy-Muhoray, P., Cao, W., Moreira, M., Taheri, B., Munoz, A. (2006). Photonics and lasing in liquid crystal materials. Philosophical Transactions of the Royal Society A: Mathematical, Physical and Engineering Sciences, 364(1847), 2747–2761.

Panarin, Y.P., Sreenilayam, S., Vij, J., Lehmann, A., Tschierske, C. (2017). A fast linear electro-optical effect in a non-chiral bent-core liquid crystal. Journal of Materials Chemistry C, 5(47), 12585–12590.

Pandey, D., Singh, U., Dhar, R., Dabrowski, R., Pandey, M. (2019). Dielectric and electro-optic properties of 6chbt nematic liquid crystals and silver nanoparticles composites. Phase Transitions, 92(10), 931–938.

Pandey, S., Vimal, T., Singh, D.P., Gupta, S.K., Pathak, G., Katiyar, R., Manohar, R. (2016). Core/shell quantum dots in ferroelectric liquid crystals matrix: effect of spontaneous polarisation coupling with dopant. Liquid Crystals, 43(7), 980–993.

Pang, X., Lv, J.A., Zhu, C., Qin, L., Yu, Y. (2019). Photodeformable azobenzene-containing liquid crystal polymers and soft actuators. Advanced Materials, 31(52), 1904224.

Park, H.-G., Kim, H.-J., Kim, M.-S., Lee, I.-H., Seo, D.-S. (2012). Electro-optical characteristics of zro2 nanoparticle doped liquid crystal on ion-beam irradiated polyimide layer. Journal of Nanoscience and Nanotechnology, 12(7), 5587–5591.

Park, K.A., Lee, S.M., Lee, S.H., Lee, Y.H. (2007). Anchoring a liquid crystal molecule on a single-walled carbon nanotube. The Journal of Physical Chemistry C, 111(4), 1620–1624.

Park, K.-S., Baek, J.-H., Lee, Y.-J., Kim, J.-H., Yu, C.-J. (2016). Effects of pretilt angle and anchoring energy on alignment of uniformly lying helix mode. Liquid Crystals, 43(9), 1184–1189.

Patel, J., Lee, S.D. (1989). Fast linear electro-optic effect based on cholesteric liquid crystals. Journal of Applied Physics, 66(4), 1879–1881.

Patel, J., Meyer, R.B. (1987). Flexoelectric electro-optics of a cholesteric liquid crystal. Physical Review Letters, 58(15), 1538.

Patel, J.S., Goodby, J.W. (1986). Alignment of liquid crystals which exhibit cholesteric to smectic c*phase transitions. Journal of Applied Physics, 59(7), 2355–2360.

Peng, Z., Liu, Y., Cao, Z., Mu, Q., Yao, L., Hu, L., Yang, C., Wu, R., Xuan, L. (2013). Fast response property of low-viscosity difluorooxymethylene-bridged liquid crystals. Liquid Crystals, 40(1), 91–96.

Pezzi, L., De Sio, L., Veltri, A., Placido, T., Palermo, G., Comparelli, R., Curri, M.L., Agostiano, A., Tabiryan, N., Umeton, C. (2015). Photo-thermal effects in gold nanoparticles dispersed in thermotropic nematic liquid crystals. Physical Chemistry Chemical Physics, 17(31), 20281–20287.

Podgornov, F., Gavrilyak, M., Karaawi, A., Boronin, V., Haase, W. (2018). Mechanism of electrooptic switching time enhancement in ferroelectric liquid crystal/gold nanoparticles dispersion. Liquid Crystals, 45(11), 1594–1602.

Podoliak, N., Buchnev, O., Herrington, M., Mavrona, E., Kaczmarek, M., Kanaras, A.G., Stratakis, E., Blach, J.-F., Henninot, J.-F., Warenghem, M. (2014). Elastic constants, viscosity and response time in nematic liquid crystals doped with ferroelectric nanoparticles. Rsc Advances, 4(86), 46068–46074.

Popov, P., Mann, E.K., Jákli, A. (2017). Thermotropic liquid crystal films for biosensors and beyond. Journal of Materials Chemistry B, 5(26), 5061–5078.

Prodanov, M.F., Buluy, O.G., Popova, E.V., Gamzaeva, S.A., Reznikov, Y.O., Vashchenko, V.V. (2016). Magnetic actuation of a thermodynamically stable colloid of ferromagnetic nanoparticles in a liquid crystal. Soft Matter, 12(31), 6601–6609.

Qi, H., Hegmann, T. (2009). Multiple alignment modes for nematic liquid crystals doped with alkylthiol-capped gold nanoparticles. ACS Applied Materials & Interfaces, 1(8), 1731–1738.

Qi, H., Kinkead, B., Hegmann, T. (2008). Unprecedented dual alignment mode and freedericksz transition in planar nematic liquid crystal cells doped with gold nanoclusters. Advanced Functional Materials, 18(2), 212–221.

Qin, L., Gu, W., Chen, Y., Wei, J., Yu, Y. (2018a). Efficient visible-light full-color tuning of self-organized helical superstructures enabled by fluorinated chiral switches. RSC Advances, 8(68), 38935–38940.

Qin, L., Gu, W., Wei, J., Yu, Y. (2018b). Piecewise phototuning of self-organized helical superstructures. Advanced Materials, 30(8), 1704941.

Qin, L., Wei, J., Yu, Y. (2019). Photostationary rgb selective reflection from self-organized helical superstructures for continuous photopatterning. Advanced Optical Materials, 7(18), 1900430.

Radhika, S., Monika, M., Sadashiva, B.K., Roy, A. (2013). Novel zigzag-shaped compounds exhibiting apolar columnar mesophases with oblique and rectangular lattices. Liquid Crystals, 40(9), 1282–1295.

Rahman, M., Lee, W. (2009). Scientific duo of carbon nanotubes and nematic liquid crystals. Journal of Physics D: Applied Physics, 42(6), 063001.

Rao, L., Ge, Z., Wu, S.-T., Lee, S.H. (2009). Low voltage blue-phase liquid crystal displays. Applied Physics Letters, 95(23), 231101.

Rao, L., Yan, J., Wu, S.-T., Yamamoto, S.-I., Haseba, Y. (2011). A large Kerr constant polymer-stabilized blue phase liquid crystal. Applied Physics Letters, 98(8), 081109.

Rastogi, A., Pathak, G., Srivastava, A., Herman, J., Manohar, R. (2018). Cd1– x znxs/zns core/shell quantum dots in nematic liquid crystals to improve material parameter for better performance of liquid crystal based devices. Journal of Molecular Liquids, 255, 93–101.

Ren, H., Xu, S., Wu, S.-T. (2013). Polymer-stabilized liquid crystal microlens array with large dynamic range and fast response time. Optics Letters, 38(16), 3144–3147.

Reznikov, M., Bos, P.J., O'Callaghan, M.J. (2010). The effect of sio x alignment layer thickness on the switching of smc   bistable liquid crystal devices. Journal of Applied Physics, 107(1), 014103.

Reznikov, Y., Buchnev, O., Tereshchenko, O., Reshetnyak, V., Glushchenko, A., West, J. (2003). Ferroelectric nematic suspension. Applied Physics Letters, 82(12), 1917–1919.

Rokhsar, D.S., Sethna, J.P. (1986). Quasicrystalline textures of cholesteric liquid crystals: blue phase iii?. Physical Review Letters, 56(16), 1727.

Roy, A., Pathak, G., Herman, J., Inamdar, S.R., Srivastava, A., Manohar, R. (2018). Inp/zns quantum-dot-dispersed nematic liquid crystal illustrating characteristic birefringence and enhanced electro-optical parameters. Applied Physics A, 124(3), 273.

Roy, A., Singh, B.P., Yadav, G., Khan, H., Kumar, S., Srivastava, A., Manohar, R. (2019). Effect of gold nanoparticles on intrinsic material parameters and luminescent characteristics of nematic liquid crystals. Journal of Molecular Liquids, 295, 111872.

Rumi, M., Bunning, T.J., White, T.J. (2018). Polymer stabilization of cholesteric liquid crystals in the oblique helicoidal state. Soft Matter, 14(44), 8883–8894.

Ryabchun, A., Bobrovsky, A., Stumpe, J., Shibaev, V. (2015). Rotatable diffraction gratings based on cholesteric liquid crystals with phototunable helix pitch. Advanced Optical Materials, 3(9), 1273–1279.

Salamon, P., Éber, N., Buka, Á., Gleeson, J.T., Sprunt, S., Jákli, A. (2010). Dielectric properties of mixtures of a bent-core and a calamitic liquid crystal. Physical Review E, 81(3), 031711.

Salili, S.M., Xiang, J., Wang, H., Li, Q., Paterson, D.A., Storey, J., Imrie, C., Lavrentovich, O., Sprunt, S., Gleeson, J. (2016). Magnetically tunable selective reflection of light by heliconical cholesterics. Physical Review E, 94(4), 042705.

Salter, P.S., Carbone, G., Jewell, S.A., Elston, S.J., Raynes, P. (2009a). Unwinding of the uniform lying helix structure in cholesteric liquid crystals next to a spatially uniform aligning surface. Physical Review E, 80(4), 041707.

Salter, P.S., Elston, S.J., Raynes, P., Parry-Jones, L.A. (2009b). Alignment of the uniform lying helix structure in cholesteric liquid crystals. Japanese Journal of Applied Physics, 48(10R), 101302.

Sarkar, G., Das, B., Das, M.K., Baumeister, U., Weissflog, W. (2011). Structural investigations of a non calamitic shaped liquid crystalline compound showing unusual phases. Molecular Crystals and Liquid Crystals, 540(1), 188–195.

Sathyanarayana, P., Kumar, T.A., Sastry, V.S.S., Mathews, M., Li, Q., Takezoe, H., Dhara, S. (2010). Rotational viscosity of a bent-core nematic liquid crystal. Applied Physics Express, 3(9), 091702.

Sawada, A., Sato, H., Manabe, A., Naemura, S. (2000). Study of internal electric field of liquid-crystal cell effected by space-charge polarization. Japanese Journal of Applied Physics, 39(6R), 3496.

Schmidtke, J., Stille, W., Finkelmann, H. (2003). Defect mode emission of a dye doped cholesteric polymer network. Physical Review Letters, 90(8), 083902.

Seki, T. (2014). New strategies and implications for the photoalignment of liquid crystalline polymers. Polymer Journal, 46(11), 751–768.

Seo, J.-H., Jang, H.J., Lee, S.R., Yoon, T.-H., Kim, J.C., Kang, I.-B., Oh, C.H. (2007). Wide pretilt angle control of liquid crystal display device by ion beam exposure on the vertical aligning layer. Japanese Journal of Applied Physics, 46(11L), L1074.

Sergan, V.V., Sergan, T.A., Bos, P.J. (2010). Control of the molecular pretilt angle in liquid crystal devices by using a low-density localized polymer network. Chemical Physics Letters, 486(4–6), 123–125.

Shamid, S.M., Dhakal, S., Selinger, J.V. (2013). Statistical mechanics of bend flexoelectricity and the twist-bend phase in bent-core liquid crystals. Physical Review E, 87(5), 052503.

Shankarling, G.S., Jarag, K.J. (2010). Laser dyes. Resonance, 15(9), 804–818.

Sharma, A., Urbanski, M., Mori, T., Kitzerow, H.-S., Hegmann, T. (2017). Metallic and semiconducting nanoparticles in lcs. In Liquid Crystals with Nano and Microparticles, World Scientific, 497–535.

Shcherbinin, D., Konshina, E. (2017). Ionic impurities in nematic liquid crystal doped with quantum dots cdse/zns. Liquid Crystals, 44(4), 648–655.

Shi, L., Srivastava, A.K., Cheung, A., Hsieh, C.T., Hung, C.L., Lin, C.H., Lin, C.H., Sugiura, N., Kuo, C.W., Chigrinov, V.G. (2018). Active matrix field sequential color electrically suppressed helix ferroelectric liquid crystal for high resolution displays. Journal of the Society for Information Display, 26(5), 325–332.

Shi, L., Srivastava, A.K., Tam, A.M.W., Chigrinov, V.G., Kwok, H.S. (2017). 2d–3d switchable display based on a passive polymeric lenticular lens array and electrically suppressed ferroelectric liquid crystal. Optics Letters, 42(17), 3435–3438.

Shibaev, V. (2009). Liquid-crystalline polymers: past, present, and future. Polymer Science Series A, 51(11–12), 1131.

Shibaev, V.P., Bobrovsky, A.Y. (2017). Liquid crystalline polymers: development trends and photocontrollable materials. Russian Chemical Reviews, 86(11), 1024–1072.

Shim, H., Lyu, H.-K., Allabergenov, B., Garbovskiy, Y., Glushchenko, A., Choi, B. (2016a). Enhancement of frequency modulation response time for polymer-dispersed liquid crystal. Liquid Crystals, 43(10), 1390–1396.

Shim, H., Lyu, H.-K., Allabergenov, B., Garbovskiy, Y., Glushchenko, A., Choi, B. (2016b). Switchable response of ferroelectric nanoparticle doped polymer-dispersed liquid crystals. Journal of Nanoscience and Nanotechnology, 16(10), 11125–11129.

Shoarinejad, S., Siahboomi, R.M., Ghazavi, M. (2018). Theoretical studies of the influence of nanoparticle dopants on the ferroelectric properties of a ferroelectric liquid crystal. Journal of Molecular Liquids, 254, 312–321.

Shukla, R., Evans, D., Haase, W. (2016a). Ferroelectric batio3 and linbo3 nanoparticles dispersed in ferroelectric liquid crystal mixtures: electrooptic and dielectric parameters influenced by properties of the host, the dopant and the measuring cell. Ferroelectrics, 500(1), 141–152.

Shukla, R., Feng, X., Umadevi, S., Hegmann, T., Haase, W. (2014a). Influence of different amount of functionalized bulky gold nanorods dopant on the electrooptical, dielectric and optical properties of the flc host. Chemical Physics Letters, 599, 80–85.

Shukla, R., Liebig, C., Evans, D., Haase, W. (2014b). Electro-optical behaviour and dielectric dynamics of harvested ferroelectric linbo 3 nanoparticle-doped ferroelectric liquid crystal nanocolloids. Rsc Advances, 4(36), 18529–18536.

Shukla, R., Mirzaei, J., Sharma, A., Hofmann, D., Hegmann, T., Haase, W. (2015). Electro-optic and dielectric properties of a ferroelectric liquid crystal doped with chemically and thermally stable emissive carbon dots. RSC Advances, 5(43), 34491–34496.

Shukla, R., Sharma, A., Mori, T., Hegmann, T., Haase, W. (2016b). Effect of two different size chiral ligand-capped gold nanoparticle dopants on the electro-optic and dielectric dynamics of a ferroelectric liquid crystal mixture. Liquid Crystals, 43(6), 695–703.

Shukla, R.K., Chaudhary, A., Bubnov, A., Raina, K. (2018). Multi-walled carbon nanotubes-ferroelectric liquid crystal nanocomposites: effect of cell thickness and dopant concentration on electro-optic and dielectric behaviour. Liquid Crystals, 45(11), 1672–1681.

Shukla, R.K., Raina, K.K., Haase, W. (2014c). Fast switching response and dielectric behaviour of fullerene/ferroelectric liquid crystal nanocolloids. Liquid Crystals, 41(12), 1726–1732.

Si, G., Zhao, Y., Leong, E.S.P., Liu, Y.J. (2014). Liquid-crystal-enabled active plasmonics: a review. Materials, 7(2), 1296–1317.

Sims, M.T. (2016). Dyes as guests in ordered systems: current understanding and future directions. Liquid Crystals, 43(13–15), 2363–2374.

Singh, D., Daoudi, A., Gupta, S., Pandey, S., Vimal, T., Manohar, R., Kole, A., Kumbhakar, P., Kumar, A. (2016). Mn2+ doped zns quantum dots in ferroelectric liquid crystal matrix: analysis of new relaxation phenomenon, faster optical response, and concentration dependent quenching in photoluminescence. Journal of Applied Physics, 119(9), 094101.

Singhvi, G., Banerjee, S., Khosa, A. (2018a). Chapter 11 – lyotropic liquid crystal nanoparticles: a novel improved lipidic drug delivery system. In Grumezescu, A.M., Ed., Organic Materials as Smart Nanocarriers for Drug Delivery, William Andrew Publishing, 471–517.

Singhvi, G., Banerjee, S., Khosa, A. (2018b). Lyotropic liquid crystal nanoparticles: a novel improved lipidic drug delivery system. In Organic Materials as Smart Nanocarriers for Drug Delivery, Elsevier, 471–517.

S.J. S., Gupta, R.K., Kumar, S., V, M. (2019). Effect of functionalised silver nanoparticle on the elastic constants and ionic transport of a nematic liquid crystal. Liquid Crystals, 46(12), 1868–1876.

Sluckin, T., Dunmur, D., Stegemeyer, H., Zannoni, C. (2004). Crystals that Flow, London, Taylor & Francis.

Song, M., Seo, J., Kim, H., Kim, Y. (2017). Ultrasensitive multi-functional flexible sensors based on organic field-effect transistors with polymer-dispersed liquid crystal sensing layers. Scientific Reports, 7(1), 1–11.

Song, M.H., Ha, N.Y., Amemiya, K., Park, B., Takanishi, Y., Ishikawa, K., Wu, J.W., Nishimura, S., Toyooka, T., Takezoe, H. (2006). Defect-mode lasing with lowered threshold in a three-layered hetero-cholesteric liquid-crystal structure. Advanced Materials, 18(2), 193–197.

Sreenilayam, S.P., Panarin, Y.P., Vij, J.K., Panov, V.P., Lehmann, A., Poppe, M., Prehm, M., Tschierske, C. (2016). Spontaneous helix formation in non-chiral bent-core liquid crystals with fast linear electro-optic effect. Nature Communications, 7(1), 1–8.

Srivastava, A.K., Chigrinov, V.G., Kwok, H.S. (2015). Electrically suppressed helix ferroelectric liquid crystals for modern displays. Journal of the Society for Information Display, 23(4), 176–181.

Srivastava, A.K., Kim, J., Yeo, S., Jeong, J., Choi, E.-J., Singh, V., Lee, J.-H. (2017). Anomalously high dielectric strength and low frequency dielectric relaxation of a bent-core liquid crystal with a large kink angle. Current Applied Physics, 17(6), 858–863.

Su, C.-W., Liao, -C.-C., Chen, M.-Y. (2015). Color transparent display using polymer-dispersed liquid crystal. Journal of Display Technology, 12(1), 31–34.

Sun, Y., Li, Y., Zhao, Y., Li, P., Ma, H. (2014a). A low voltage and continuous viewing angle controllable blue phase liquid crystal display. Journal of Display Technology, 10(6), 484–487.

Sun, Y., Zhao, Y., Li, Y., Li, P., Ma, H. (2014b). A low operating electric field blue-phase liquid crystal display with wedge protrusion. Journal of Display Technology, 10(9), 797–801.

Sun, Y., Zhao, Y., Li, Y., Li, P., Ma, H. (2014c). Optimisation of in-plane-switching blue-phase liquid crystal display. Liquid Crystals, 41(5), 717–720.

Sznitko, L., Mysliwiec, J., Miniewicz, A. (2015). The role of polymers in random lasing. Journal of Polymer Science. Part B, Polymer Physics, 53(14), 951–974.

Takezoe, H. (2012). Liquid crystal lasers. In Liquid Crystals Beyond Displays, Hoboken (NJ), Wiley, 1–27.

Takezoe, H. (2014). Historical overview of polar liquid crystals. Ferroelectrics, 468(1), 1–17.

Takezoe, H., Takanishi, Y. (2006). Bent-core liquid crystals: their mysterious and attractive world. Japanese Journal of Applied Physics, 45(2R), 597.

Tam-Chang, S.-W., Huang, L. (2008). Chromonic liquid crystals: properties and applications as functional materials. Chemical Communications (17), 1957–1967.

Tan, G., Lee, Y.-H., Gou, F., Chen, H., Huang, Y., Lan, Y.-F., Tsai, C.-Y., Wu, S.-T. (2017). Review on polymer-stabilized short-pitch cholesteric liquid crystal displays. Journal of Physics D: Applied Physics, 50(49), 493001.

Tartan, C.C., Salter, P.S., Booth, M.J., Morris, S.M., Elston, S.J. (2016). Localised polymer networks in chiral nematic liquid crystals for high speed photonic switching. Journal of Applied Physics, 119(18), 183106.

Taushanoff, S., Van Le, K., Williams, J., Twieg, R.J., Sadashiva, B., Takezoe, H., Jákli, A. (2010). Stable amorphous blue phase of bent-core nematic liquid crystals doped with a chiral material. Journal of Materials Chemistry, 20(28), 5893–5898.

Teng, W.-Y., Jeng, S.-C., Kuo, C.-W., Lin, Y.-R., Liao, -C.-C., Chin, W.-K. (2008). Nanoparticles-doped guest-host liquid crystal displays. Optics Letters, 33(15), 1663–1665.

Tian, -L.-L., Chu, F., Dou, H., Li, L., Wang, Q.-H. (2019). Transflective blue-phase liquid crystal display with dielectric protrusion. Liquid Crystals, 1–6.

Tiribocchi, A., Gonnella, G., Marenduzzo, D., Orlandini, E., Salvadore, F. (2011). Bistable defect structures in blue phase devices. Physical Review Letters, 107(23), 237803.

Tomylko, S., Yaroshchuk, O., Kovalchuk, O., Maschke, U., Yamaguchi, R. (2011). Dielectric and electro-optical properties of liquid crystals doped with diamond nanoparticles. Molecular Crystals and Liquid Crystals, 541(1), 35/[273]–243/[281].

Tondiglia, V.P., Natarajan, L.V., Bailey, C.A., McConney, M.E., Lee, K.M., Bunning, T.J., Zola, R., Nemati, H., Yang, D.-K., White, T.J. (2014). Bandwidth broadening induced by ionic interactions in polymer stabilized cholesteric liquid crystals. Optical Materials Express, 4(7), 1465–1472.

Tondiglia, V.P., Rumi, M., Idehenre, I.U., Lee, K.M., Binzer, J.F., Banerjee, P.P., Evans, D.R., McConney, M.E., Bunning, T.J., White, T.J. (2018). Electrical control of unpolarized reflectivity in polymer-stabilized cholesteric liquid crystals at oblique incidence. Advanced Optical Materials, 6(22), 1800957.

Tu, C.-D., Lin, C.-L., Yan, J., Chen, Y., Lai, P.-C., Wu, S.-T. (2012). Driving scheme using bootstrapping method for blue-phase lcds. Journal of Display Technology, 9(1), 3–6.

Turlapati, S., Khan, R.K., Ramesh, P., Shamanna, J., Ghosh, S., Rao, N.V. (2017). Elastic constants, viscosity and dielectric properties of bent-core nematic liquid crystals doped with single-walled carbon nanotubes. Liquid Crystals, 44(5), 784–797.

Tzeng, S.-Y., Chen, C.-N., Tzeng, Y. (2010). Thermal tuning band gap in cholesteric liquid crystals. Liquid Crystals, 37(9), 1221–1224.

Ula, S.W., Traugutt, N.A., Volpe, R.H., Patel, R.R., Yu, K., Yakacki, C.M. (2018). Liquid crystal elastomers: an introduction and review of emerging technologies. Liquid Crystals Reviews, 6(1), 78–107.

Varanytsia, A., Chien, L.-C. (2016). Bimesogen-enhanced flexoelectro-optic behavior of polymer stabilized cholesteric liquid crystal. Journal of Applied Physics, 119(1), 014502.

Varanytsia, A., Chien, L.-C. (2017). Giant flexoelectro-optic effect with liquid crystal dimer cb7cb. Scientific Reports, 7(1), 1–7.

Vardanyan, K.K., Daykin, A., Kilmer, B. (2017). Study on cyanobiphenyl nematic doped by silver nanoparticles. Liquid Crystals, 44(8), 1240–1252.

Vimal, T., Agrahari, K., Sonker, R.K., Manohar, R. (2019). Investigation of thermodynamical, dielectric and electro-optical parameters of nematic liquid crystal doped with polyaniline and silver nanoparticles. Journal of Molecular Liquids, 290, 111241.

Vimal, T., Kumar Gupta, S., Katiyar, R., Srivastava, A., Czerwinski, M., Krup, K., Kumar, S., Manohar, R. (2017). Effect of metallic silver nanoparticles on the alignment and relaxation behaviour of liquid crystalline material in smectic c* phase. Journal of Applied Physics, 122(11), 114102.

Vimal, T., Pandey, S., Gupta, S.K., Singh, D.P., Manohar, R. (2015). Enhanced negative dielectric anisotropy and high electrical conductivity of the swcnt doped nematic liquid crystalline material. Journal of Molecular Liquids, 204, 21–26.

Vinayakumara, D.R., Swamynathan, K., Kumar, S., Adhikari, A.V. (2018). Optoelectronic exploration of novel non-symmetrical star-shaped discotic liquid crystals based on cyanopyridine. New Journal of Chemistry, 42(20), 16999–17008.

Vorflusev, V., Kumar, S. (1999). Phase-separated composite films for liquid crystal displays. Science, 283(5409), 1903–1905.

Wang, C.-T., Liu, H.-Y., Cheng, -H.-H., Lin, T.-H. (2010). Bistable effect in the liquid crystal blue phase. Applied Physics Letters, 96(4), 041106.

Wang, C.-T., Wang, W.-Y., Lin, T.-H. (2011). A stable and switchable uniform lying helix structure in cholesteric liquid crystals. Applied Physics Letters, 99(4), 041108.

Wang, C.-T., Wu, Y.-C., Lin, T.-H. (2014a). Photo-controllable tristable optical switch based on dye-doped liquid crystal. Dyes and Pigments, 103, 21–24.

Wang, H., Bisoyi, H.K., Urbas, A.M., Bunning, T.J., Li, Q. (2019). Reversible circularly polarized reflection in a self-organized helical superstructure enabled by a visible-light-driven axially chiral molecular switch. Journal of the American Chemical Society, 141(20), 8078–8082.

Wang, H., Wang, L., Chen, M., Li, T., Cao, H., Yang, D., Yang, Z., Yang, H., Zhu, S. (2015a). Bistable polymer-dispersed cholesteric liquid crystal thin film enabled by a stepwise polymerization. RSC Advances, 5(73), 58959–58965.

Wang, H.-T., Lin, J.-D., Lee, C.-R., Lee, W. (2014b). Ultralow-threshold single-mode lasing based on a one-dimensional asymmetric photonic bandgap structure with liquid crystal as a defect layer. Optics Letters, 39(12), 3516–3519.

Wang, J., Bergquist, L., Hwang, J.-I., Kim, K.-J., Lee, J.-H., Hegmann, T., Jákli, A. (2018a). Wide temperature-range, multi-component, optically isotropic antiferroelectric bent-core liquid crystal mixtures for display applications. Liquid Crystals, 45(3), 333–340.

Wang, K., Zheng, J., Gao, H., Lu, F., Sun, L., Yin, S., Zhuang, S. (2015b). Tri-color composite volume h-pdlc grating and its application to 3d color autostereoscopic display. Optics Express, 23(24), 31436–31445.

Wang, L., Bisoyi, H.K., Zheng, Z., Gutierrez-Cuevas, K.G., Singh, G., Kumar, S., Bunning, T.J., Li, Q. (2017a). Stimuli-directed self-organized chiral superstructures for adaptive windows enabled by mesogen-functionalized graphene. Materials Today, 20(5), 230–237.

Wang, L., Gutierrez-Cuevas, K.G., Bisoyi, H.K., Xiang, J., Singh, G., Zola, R.S., Kumar, S., Lavrentovich, O.D., Urbas, A., Li, Q. (2015c). Nir light-directing self-organized 3d photonic superstructures loaded with anisotropic plasmonic hybrid nanorods. Chemical Communications, 51(81), 15039–15042.

Wang, L., Gutierrez-Cuevas, K.G., Urbas, A., Li, Q. (2016a). Near-infrared light-directed handedness inversion in plasmonic nanorod-embedded helical superstructure. Advanced Optical Materials, 4(2), 247–251.

Wang, L., He, W., Xiao, X., Wang, M., Wang, M., Yang, P., Zhou, Z., Yang, H., Yu, H., Lu, Y. (2012a). Low voltage and hysteresis-free blue phase liquid crystal dispersed by ferroelectric nanoparticles. Journal of Materials Chemistry, 22(37), 19629–19633.

Wang, L., Huang, D., Lam, L., Cheng, Z. (2017b). Bowlics: history, advances and applications. Liquid Crystals Today, 26(4), 85–111.

Wang, M., Zou, C., Sun, J., Zhang, L., Wang, L., Xiao, J., Li, F., Song, P., Yang, H. (2017c). Asymmetric tunable photonic bandgaps in self-organized 3d nanostructure of polymer-stabilized blue phase i modulated by voltage polarity. Advanced Functional Materials, 27(46), 1702261.

Wang, Q., Kumar, S. (2005). Submillisecond switching of nematic liquid crystal in cells fabricated by anisotropic phase-separation of liquid crystal and polymer mixture. Applied Physics Letters, 86(7), 071119.

Wang, Q., Shang, Y., Yu, L., Zou, C., Yao, W., Zhao, D., Song, P., Yang, H., Guo, L. (2016b). Facet-dependent cu 2 o nanocrystals in manipulating alignment of liquid crystals and photomechanical behaviors. Nano Research, 9(9), 2581–2589.

Wang, W., Gao, F., Yao, Y., Lin, S.-L. (2018b). Directional photo-manipulation of self-assembly patterned microstructures. Chinese Journal of Polymer Science, 36(3), 297–305.

Wang, Y., Li, Q. (2012). Light-driven chiral molecular switches or motors in liquid crystals. Advanced Materials, 24(15), 1926–1945.

Wang, Y., Urbas, A., Li, Q. (2012b). Reversible visible-light tuning of self-organized helical superstructures enabled by unprecedented light-driven axially chiral molecular switches. Journal of the American Chemical Society, 134(7), 3342–3345.

Wang, Y., Zheng, Z.-G., Bisoyi, H.K., Gutierrez-Cuevas, K.G., Wang, L., Zola, R.S., Li, Q. (2016c). Thermally reversible full color selective reflection in a self-organized helical superstructure enabled by a bent-core oligomesogen exhibiting a twist-bend nematic phase. Materials Horizons, 3(5), 442–446.

Wei, Y., Jang, C.-H. (2017). Visualization of cholylglycine hydrolase activities through nickel nanoparticle-assisted liquid crystal cells. Sensors and actuators B, Chemical, 239, 1268–1274.

Wittek, M., Tanaka, N., Wilkes, D., Bremer, M., Pauluth, D., Canisius, J., Yeh, A., Yan, R., Skjonnemand, K., Klasen-Memmer, M. (2012). 4.4: New materials for polymer-stabilized blue phase. Paper presented at the SID Symposium Digest of Technical Papers, 43(1), 25–28.

Woltman, S.J. (2007). Liquid crystal lasers: tunable sources for biology and medicine. In Liquid Crystals: Frontiers in Biomedical Applications, World Scientific, 297–373.

Wu, C.-S., Kuo, L.-Y., Cheng, Y.-H., Lee, K.-L., Chen, T.-J., Wu, -J.-J., Wu, S.-L. (2009). Study of twisted optically compensated bend cell using patterned alignment. Japanese Journal of Applied Physics, 48(8R), 081502.

Wu, C.-Y., Tang, C.-Y., Lee, W. (2010). Electro-optical and capacitive characteristics of stratified polymer/liquid crystal composite devices under dc electric field. Applied Physics Express, 3(11), 111701.

Wu, P.-C., Karn, A., Lee, M.-J., Lee, W., Chen, C.-Y. (2018a). Dye-liquid-crystal-based biosensing for quantitative protein assay. Dyes and Pigments, 150, 73–78.

Wu, P.-C., Lisetski, L.N., Lee, W. (2015). Suppressed ionic effect and low-frequency texture transitions in a cholesteric liquid crystal doped with graphene nanoplatelets. Optics Express, 23(9), 11195–11204.

Wu, P.-C., Wu, G.-W., Timofeev, I.V., Zyryanov, V.Y., Lee, W. (2018b). Electro-thermally tunable reflective colors in a self-organized cholesteric helical superstructure. Photonics Research, 6(12), 1094–1100.

Wu, P.-C., Wu, -J.-J. (2007). The influence of ac electric field on the domain growth and alignment of the ferroelectric liquid crystal cell with n*–sm c* phase transition. Journal of Applied Physics, 101(10), 104513.

Wu, P.-C., Yang, S.-Y., Lee, W. (2016). Recovery of uv-degraded electrical properties of nematic liquid crystals doped with tio2 nanoparticles. Journal of Molecular Liquids, 218, 150–155.

Wu, P.-C., Yeh, E.-R., Zyryanov, V.Y., Lee, W. (2014). Spatial and electrical switching of defect modes in a photonic bandgap device with a polymer-dispersed liquid crystal defect layer. Optics Express, 22(17), 20278–20283.

Wu, S.-T. (1986). Birefringence dispersions of liquid crystals. Physical Review A, 33(2), 1270.

Wu, W.-Y., Wang, -C.-C., Fuh, A.Y.-G. (2008). Controlling pre-tilt angles of liquid crystal using mixed polyimide alignment layer. Optics Express, 16(21), 17131–17137.

Xiang, J., Lavrentovich, O.D. (2013). Blue-phase-polymer-templated nematic with sub-millisecond broad-temperature range electro-optic switching. Applied Physics Letters, 103(5), 051112.

Xiang, J., Li, Y., Li, Q., Paterson, D.A., Storey, J.M., Imrie, C.T., Lavrentovich, O.D. (2015). Electrically tunable selective reflection of light from ultraviolet to visible and infrared by heliconical cholesterics. Advanced Materials, 27(19), 3014–3018.

Xiang, J., Varanytsia, A., Minkowski, F., Paterson, D.A., Storey, J.M., Imrie, C.T., Lavrentovich, O.D., Palffy-Muhoray, P. (2016). Electrically tunable laser based on oblique heliconical cholesteric liquid crystal. Proceedings of the National Academy of Sciences, 113(46), 12925–12928.

Xiang, Y., Jing, H.-Z., Zhang, Z.-D., Ye, W.-J., Xu, M.-Y., Wang, E., Salamon, P., Éber, N., Buka, Á. (2017). Tunable optical grating based on the flexoelectric effect in a bent-core nematic liquid crystal. Physical Review Applied, 7(6), 064032.

Xiang, Y., Liu, Y.-K., Buka, Á., Éber, N., Zhang, Z.-Y., Xu, M.-Y., Wang, E. (2014). Electric-field-induced patterns and their temperature dependence in a bent-core liquid crystal. Physical Review E, 89(1), 012502.

Xie, Z., Meng, Z., Wong, M., Kwok, H. (2002). Permanent grayscales in bistable twisted nematic liquid-crystal displays. Applied Physics Letters, 81(14), 2553–2555.

Xing, Y., Guo, Z., Li, Q. (2018). Reflective blue phase liquid crystal displays with double-side concave-curved electrodes. Liquid Crystals, 45(4), 507–512.

Xu, D., Peng, F., Chen, H., Yuan, J., Wu, S.-T., Li, M.-C., Lee, S.-L., Tsai, W.-C. (2014). Image sticking in liquid crystal displays with lateral electric fields. Journal of Applied Physics, 116(19), 193102.

Xu, X., Zhang, X., Luo, D., Dai, H. (2015). Low voltage polymer-stabilized blue phase liquid crystal reflective display by doping ferroelectric nanoparticles. Optics express, 23(25), 32267–32273.

Xue, C., Xiang, J., Nemati, H., Bisoyi, H.K., Gutierrez-Cuevas, K., Wang, L., Gao, M., Zhou, S., Yang, D.K., Lavrentovich, O.D. (2015). Light-driven reversible alignment switching of liquid crystals enabled by azo thiol grafted gold nanoparticles. ChemPhysChem, 16(9), 1852–1856.

Yadav, S.P., Pande, M., Manohar, R., Singh, S. (2015). Applicability of tio2 nanoparticle towards suppression of screening effect in nematic liquid crystal. Journal of Molecular Liquids, 208, 34–37.

Yadav, S.P., Singh, S. (2016). Carbon nanotube dispersion in nematic liquid crystals: an overview. Progress in Materials Science, 80, 38–76.

Yadav, S.P., Yadav, K., Lahiri, J., Singh Parmar, A. (2018). Ferroelectric liquid crystal nanocomposites: recent development and future perspective. Liquid Crystals Reviews, 6(2), 143–169.

Yan, J., Chen, Y., Xu, D., Wu, S.-T. (2013). Angular dependent reflections of a monodomain blue phase liquid crystal. Journal of Applied Physics, 114(11), 113106.

Yan, J., Rao, L., Jiao, M., Li, Y., Cheng, H.-C., Wu, S.-T. (2011). Polymer-stabilized optically isotropic liquid crystals for next-generation display and photonics applications. Journal of Materials Chemistry, 21(22), 7870–7877.

Yang, D.K. (2008). Review of operating principle and performance of polarizer-free reflective liquid-crystal displays. Journal of the Society for Information Display, 16(1), 117–124.

Yang, D.-K. (2013). Polymer-stabilized liquid crystal displays. In Progress in Liquid Crystal Science and Technology: In Honor of Shunsuke Kobayashi's 80th birthday, World Scientific, 597–628.

Yao, I.-A., Yang, C.-L., Chen, C.-J., Pang, J.-P., Liao, S.-F., Li, J.-H., Wu, -J.-J. (2009). Bistability of splay and π twist states in a chiral-doped dual frequency liquid crystal cell. Applied Physics Letters, 94(7), 071104.

Yaroshchuk, O., Reznikov, Y. (2012). Photoalignment of liquid crystals: basics and current trends. Journal of Materials Chemistry, 22(2), 286–300.

Ye, L., Lv, C., Li, F., Wang, Y., Liu, B., Cui, Y. (2017). Effect of alignment layer on polymer-dispersed liquid crystal random laser. Journal of Modern Optics, 64(14), 1429–1434.

Yeung, F.S., Ho, J.Y., Li, Y., Xie, F., Tsui, O.K., Sheng, P., Kwok, H. (2006). Variable liquid crystal pretilt angles by nanostructured surfaces. Applied Physics Letters, 88(5), 051910.

Yokoyama, S., Mashiko, S., Kikuchi, H., Uchida, K., Nagamura, T. (2006). Laser emission from a polymer-stabilized liquid-crystalline blue phase. Advanced Materials, 18(1), 48–51.

Yoon, J.H., Lee, S.J., Lim, Y.J., Seo, E.J., Shin, H.S., Myoung, J.-M., Lee, S.H. (2018). Fast switching, high contrast and high resolution liquid crystal device for virtual reality display. Optics Express, 26(26), 34142–34149.

Yoshikawa, H., Maeda, K., Shiraishi, Y., Xu, J., Shiraki, H., Toshima, N., Kobayashi, S. (2002). Frequency modulation response of a tunable birefringent mode nematic liquid crystal electrooptic device fabricated by doping nanoparticles of pd covered with liquid-crystal molecules. Japanese journal of applied physics, 41(11B), L1315.

Yu, B.-H., Ji, S.-M., Kim, J.-H., Huh, J.-W., Yoon, T.-H. (2017a). Fabrication of a dye-doped liquid crystal light shutter by thermal curing of polymer. Optical Materials, 69, 164–168.

Yu, B.-H., Ji, S.-M., Kim, J.-H., Huh, J.-W., Yoon, T.-H. (2017b). Light shutter using dye-doped cholesteric liquid crystals with polymer network structure. Journal of Information Display, 18(1), 13–17.

Yu, C.-H., Wu, P.-C., Lee, W. (2017c). Alternative generation of well-aligned uniform lying helix texture in a cholesteric liquid crystal cell. AIP Advances, 7(10), 105107.

Yu, H. (2014). Photoresponsive liquid crystalline block copolymers: from photonics to nanotechnology. Progress in Polymer Science, 39(4), 781–815.

Yu, H., Ikeda, T. (2011). Photocontrollable liquid-crystalline actuators. Advanced Materials, 23(19), 2149–2180.

Yu, Y., Ikeda, T. (2004). Alignment modulation of azobenzene-containing liquid crystal systems by photochemical reactions. Journal of Photochemistry and Photobiology C: Photochemistry Reviews, 5(3), 247–265.

Zakri, C. (2007). Carbon nanotubes and liquid crystalline phases. Liquid Crystals Today, 16(1), 1–11.

Zhang, C., Wang, D., Cao, H., Song, P., Yang, C., Yang, H., Hu, G.H. (2013). Preparation and electro-optical properties of polymer dispersed liquid crystal films with relatively low liquid crystal content. Polymers for Advanced Technologies, 24(5), 453–459.

Zhang, F., Yang, D.-K. (2002). Temperature dependence of pitch and twist elastic constant in a cholesteric to smectic a phase transition. Liquid Crystals, 29(12), 1497–1501.

Zhang, T., Kashima, M., Zhang, M., Liu, F., Song, P., Zhao, X., Zhang, C., Cao, H., Yang, H. (2012). Effects of the functionality of epoxy monomer on the electro-optical properties of thermally-cured polymer dispersed liquid crystal films. RSC Advances, 2(5), 2144–2148.

Zhang, W., Liang, X., Li, C., Li, F., Zhang, L., Yang, H. (2018). Optical and thermal properties of fe3o4 nanoparticle-doped cholesteric liquid crystals. Liquid Crystals, 45(8), 1111–1117.

Zhao, D., Peng, Y., Xu, L., Zhou, W., Wang, Q., Guo, L. (2015). Liquid-crystal biosensor based on nickel-nanosphere-induced homeotropic alignment for the amplified detection of thrombin. ACS Applied Materials & Interfaces, 7(42), 23418–23422.

Zhao, D., Qiu, Y., Cheng, W., Bi, S., Wang, H., Wang, Q., Liao, Y., Peng, H., Xie, X. (2018). Precisely tuning helical twisting power via photoisomerization kinetics of dopants in chiral nematic liquid crystals. Langmuir, 34(2), 700–708.

Zhao, D., Zhou, W., Cui, X., Tian, Y., Guo, L., Yang, H. (2011). Alignment of liquid crystals doped with nickel nanoparticles containing different morphologies. Advanced Materials, 23(48), 5779–5784.

Zhao, Y., Sun, Y., Li, Y., Ma, H. (2014). Optimisation of blue-phase liquid crystal with protrusion. Liquid Crystals, 41(11), 1583–1594.

Zheng, Z., Shen, D., Huang, P. (2010). Wide blue phase range of chiral nematic liquid crystal doped with bent-shaped molecules. New Journal of Physics, 12(11), 113018.

Zheng, Z.-G., Zhang, D., Lin, X.-W., Zhu, G., Hu, W., Shen, D., Lu, Y.-Q. (2012). Bistable state in polymer stabilized blue phase liquid crystal. Optical Materials Express, 2(10), 1353–1358.

Zhou, P., Li, Y., Li, X., Liu, S., Su, Y. (2016). Holographic display and storage based on photo-responsive liquid crystals. Liquid Crystals Reviews, 4(2), 83–100.

Zhou, X., Jiang, Y., Qin, G., Xu, X., Yang, D.-K. (2017). Static and dynamic properties of hybridly aligned flexoelectric in-plane-switching liquid-crystal display. Physical Review Applied, 8(5), 054033.

Zhou, X., Qin, G., Dong, Y., Yang, D.K. (2015). Fast switching and high-contrast polymer-stabilized ips liquid crystal display. Journal of the Society for Information Display, 23(7), 333–338.

Zhu, J.-L., Li, W.-H., Sun, Y., Lu, J.-G., Song, X.-L., Chen, C.-Y., Zhang, Z., Su, Y. (2015). Random laser emission in a sphere-phase liquid crystal. Applied Physics Letters, 106(19), 191903.

Zobov, K., Zharkova, G., Syzrantsev, V. (2016). Effect of dopant nanoparticles on reorientation process in polymer-dispersed liquid crystals. EPL (Europhysics Letters), 113(2), 24001.

A. R. Yuvaraj, Wei Lee, Sandeep Kumar

2 Unconventional liquid crystals: chemical aspects

Abstract: There are a huge number of unconventional liquid crystals (ULCs) reported in the literature and researchers have classified them into several types. Among them, a few interesting compounds and their molecular structures are discussed in this chapter. The ULCs such as dimers, trimers, tetramers, hydrogen-bonded mesogens, dendrimers, polymers, nanocomposites and colloids are explained with their chemical aspects. The molecular structures and liquid crystal properties of linear or nonlinear oligomeric backbones are presented. The mesogenic properties of unconventional molecular structures depend on each mesogenic building block unit as well as, shape and molecular geometry. Apart from this, spacers and terminal alkyl chains play an important role in the mesomorphic properties and transition temperatures of ULCs.

2.1 Introduction

The innovative design and synthesis of liquid crystals (LCs) in the applied LC research are essential because of their diverse physical and chemical properties in various research fields. The production of these precious compounds and design of supramolecular self-organizing molecules are basically a bottom-up approach. Such supramolecular assemblies consist of flexible components and anisometric segments (Goodby et al., 2008). A wide range of both conventional and unconventional LCs are reported in the literature. The conventional LCs are usually designed as per the theoretical aspects of LC namely, calamitic and discotic LCs. For many years, the people believed that molecules must be rod shaped and long in order to exhibit the LC property. Later, discotic liquid crystals (DLCs) concept came into the picture after the evaluation of disk-shaped molecules. Conventional LCs usually consist of a central rigid core connected with long flexible chain(s). Microphase segregation between these incompatible parts leads to various mesophases such as nematic and smectic in calamitic LCs and nematic and columnar in DLCs. LCs which deviate from classical geometries are described as unconventional liquid crystals (ULCs). The molecules with simple to complex ordered fluid alignment and nanosegregation are well-known ULCs (Tschierske, 2001a, 2001b). The ULCs show excellent characteristics in several applications such as sensing, electro-optic switching, gene-transfer vector-mediated drug-delivery therapy, electron/molecule/ion-transporting systems (Goodby et al., 2008; Kato et al., 2006a).

They are classified into two main categories: supermolecular and supramolecular ULCs (Saez and Goodby, 2005; Goodby et al., 2008). Supramolecular assemblies are formed due to the secondary interactions between successive mesogenic molecules such as π–π stacking, van der Waals forces, hydrogen bonding, electrostatic association, solvophobic effects and donor–acceptor interactions (Pal and Kumar, 2017). The supermolecular ULCs are formed by the strong sigma bond connection between the successive mesogens, and they consist of small to giant molecular architectures (Saez and Goodby, 2005; Goodby et al., 2008; Malpezzi et al., 2006). Some important examples of ULCs are liquid crystalline dimers, trimers, tetramers, oligomers, polycatenars, hydrogen-bonded LCs, dendrimers, polymers, colloids/composites, and so on. Often novel phase behavior is observed in these types of ULCs compared to the corresponding monomer analogues. There are some best examples to describe the ULCs, which include, mainly oligomers and dendrimers. Usually, dendrimers are derived from lateral and terminal attachments of promesogenic or mesogenic units, resulting in the formation of branched superstructures whereas, oligomeric LCs are constructed by several mesogenic units connected either laterally, axially, or radially via flexible spacers.

Full coverage of all types of ULCs is beyond the scope of this paper. In this discussion, the molecular structure, design, and chemical aspects of some recent ULCs are explained briefly. Few striking examples are considered in order to explain the importance of ULC designs and their properties.

2.2 Liquid crystal dimers

The architecture of LC dimers is usually composed by two mesogenic units and they are connected to each other via spacers. LC dimers are important category in LC field and in the past few years a plethora of articles have been reported in the literature (Pal and Kumar, 2017). Only a few important examples are discussed in this chapter for the reader's convenience.

Though several LC compounds are reported in the literature, researchers are still working on the synthesis of novel LCs to tune the molecular orientation and peculiar physical properties. In the 1980s, LC dimers attracted the attention of research community. Before, several names were assigned to these compounds such as dimesogens and siamese twins; now, these are collectively known as LC dimers. Among all, rod-shaped dimers are studied extensively in this century; they are also called calamitic dimers. The LC dimers are geometrically constructed by connecting two identical or unidentical counterparts with a flexible or rigid spacer. In the calamitic LCs family, LC dimers are studied in detail on the basis of relative positions of spacer linkage. They are (i) linear, (ii) H-shaped, (iii) T-shaped, (iv) U-shaped, and (v) O-shaped LC dimers. Additionally, discotic and bent-core dimers are also discussed in this chapter.

2.2.1 Linear dimers

The linear dimers are a type of ULC in which the two mesogenic units are connected to each other in an end-to-end manner. The net flexibility and molecular rigidity of LC dimers depend on molecular length, aromaticity, polarity of the flexible spacer, dispersion forces, molecular polarization, and so on. All these factors affect the thermotropic mesomorphic properties. Actually, the types of mesomorphism and degree of mesomorphism are key factors to discuss in the LC chemistry.

Ia

Ib
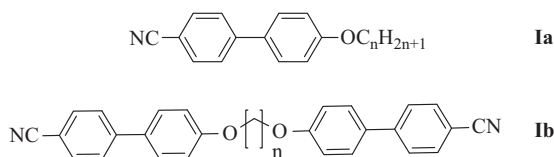
Where, n = 1 to 12

Cyanobiphenyl derivatives, **Ia**, are extensively used LCs in the display industries. The corresponding dimers, **Ib**, are the best studied series of LC dimers (Emsley et al., 2011a; Malpezzi et al., 2006; Pal and Kumar, 2017). These linear LC dimers are the best examples of nematic dimers (Malpezzi et al., 2006). All the compounds in the series of **Ib** are nematic in nature (Emsley et al., 2011a; Malpezzi et al., 2006; Pal and Kumar, 2017). The spacer effect in LC dimer series is very interesting due to the drastic change observed in the physical properties. The linear LC dimers with even number of spacers show higher nematic to isotropic transition temperature than that of the odd number of spacers (Pal and Kumar, 2017). Thus, the flexibility of the spacers impacts a lot in the mesogenic nature of linear LC dimers.

II
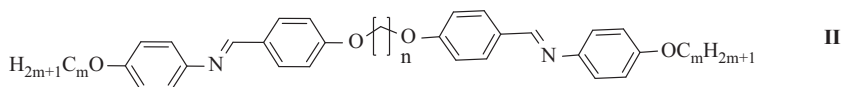
Apart from the flexibility concept of the spacer, Date et al. (2006) designed a series of imine-based linear LC dimer **II** which have flexibility in the aromatic core. This novel molecular design exhibits smectic A, B, C, and F; crystal phase B, E, G, and H; as well as, modular smectic phases. The low-molecular linear dimers **II** showed the transitions of smectic F to A and crystal G to isotropic phase.

IIIa
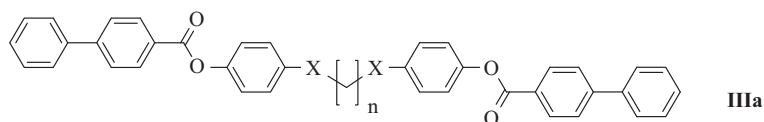
Where, n = 2-10 and X = O, CO_2

IIIb
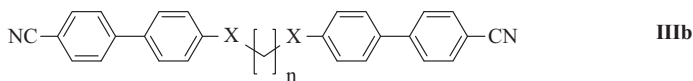
Where, n = 2-10 and X = CH$_2$, O, OCO$_2$

The bridging group between the spacer and aromatic rigid group is also playing a role in the transition properties of linear LC dimers. The mesomorphic properties mainly depend on bridging groups between the spacer and aromatic moieties in the conventional low-molecular mass systems (Gray, 1979). In such systems, the probability of obtaining smectic phases are more in the presence of an ester group than ether group. This is because of the dipole lateral interaction of the carbonyl groups. The similar behavior was observed by Jin et al. (1985) in the case of unconventional linear dimers **IIIa;** introducing the ester in the place of ether facilitated the smectic behavior. The contribution of connecting groups between the spacer and aromatic units can be confirmed by analyzing the series of **IIIb**. The three connecting groups such as methylene (Barnes et al., 2006), ether (Emsley et al., 2011b), and carbonate (Abe et al., 1995; Luckhurst, 1995) are incorporated in these series. Ether-linked linear dimers showed high nematic–isotropic transition temperature than methylene linked dimers (Luckhurst, 1995) and this difference is considerably more in case of odd number of CH$_2$ in the spacers. The transition temperature is decreased with the increase in the spacer length irrespective of odd–even concept (Luckhurst, 1995). By considering these facts, the bridge between the central spacer and aromatic units affects a lot on the mesomorphic behavior of the ULC calamitic dimers. Apart from effect induced by linkage group and odd–even spacers, nature of spacers is also important in the mesomorphic study of calamitic dimers.

Nature of flexible spacers also contributes its own effect on the LC property and other physical properties of calamitic dimers (Yuvaraj et al., 2014). Other than simple methylene units, several LCs with oligoethylene oxide (Creed et al., 2007) and siloxane (Creed et al., 2007; Elhaj et al., 1995) containing spacers have been produced. The siloxane spacer in the place of ordinary methylene spacers induce the smectic behavior over nematic and decreases the glass transition temperature as well as isotropic temperature (Chien et al., 1987; Hoshino et al., 1984; Robinson et al., 1998).

In unconventional linear dimers, the terminal aliphatic chain contributes a lot to the LC phase stabilization. The phase behavior and transition temperature of LC dimers depend on terminal aliphatic chain (Date et al., 2006). This is due to the change in the size of the mesogenic units upon changing the terminal alkyl chain length. The decrease of clearing temperature with elongation of the terminal alkyl chain length has been observed by Imrie and Taylor (1989).

Asymmetrical dimers are also an important category in the ULC dimers family. The center of symmetry is absent in these molecules unlike symmetrical dimers. It means two mesogenic units exist in each molecule of asymmetrical dimers are chemically dissimilar (Imrie and Taylor, 1989). Attard et al. (1994) explained the

mesomorphic nature of unsymmetrical dimer **IV**. The dramatic variation in the iso-
tropization and phase-transition properties are reported in detail (Attard et al.,
1994; Pal and Kumar, 2017).
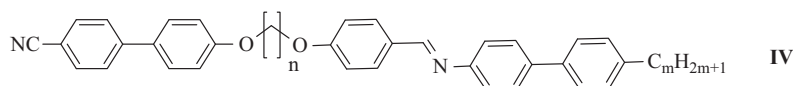
The investigation of chiral LC is much essential in ULC synthesis because of the techno-
logical importance (Goodby, 1991). The chiral LC dimers exhibit enhanced molecular
motion and orientation in the system (Nishiyama et al., 1993). In the case of unconven-
tional linear dimers, chirality occurs from either terminal chains (Ionescu et al., 1997)
or spacer chains (Malpezzi et al., 1991). Blatch et al. (1997) prepared chiral dimer series
V and obtained novel mesophases such as blue phase as well as smectic phases. In the
chiral ULC dimers, twisting power is dependent on nature of chiral group only when
they are doped with nematic solvents. The chiral groups of linear dimers with odd and
even spacer showed similar helical twisting power.
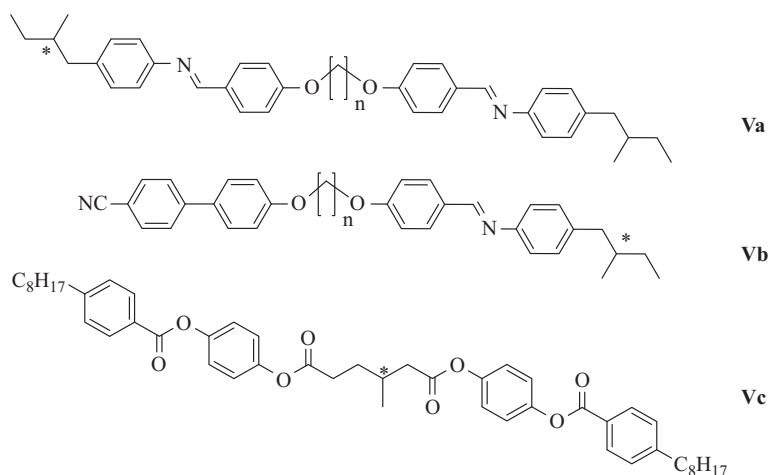
2.2.2 H-shaped dimers

The molecular architecture of the H-shaped dimer consists of two calamitic units
connected in a lateral fashion. The LC behavior of such compounds depends on
the connection between two calamitic rigid cores. Griffin et al. (1981) reported the
H-shaped twin connected through methylene spacers with two different conforma-
tions, **VIa** (parallel) and **VIb** (antiparallel). Two types of conformational isomers
are produced in the synthesis of such twin molecules and they are independent of
each other. The X-ray diffraction confirms the smectic C phases for **VIa** and **VIb**; it

is believed that various smectic C phases form upon melting of conformational iso-
mers in the system. The mesomorphic nature is closely related to the conformation
ratios.

The laterally connected disulfide-bridged dimers were first reported by Pal et al.
(2007). The compounds with the short spacers showed only the nematic phase whereas,
the long spacers exhibited both nematic and smectic phases.

By introducing sulfur, sulfinyl, and sulfonyl spacer **VIc**, Dehne et al. (1989) evalu-
ated the interesting LC properties of the H-shaped dimers. These nematic compounds
are commonly ligated siamese twin type. Above room temperature, **VIc** shows glassy
nematic phase upon quenching. The samples look like viscus nematic phase above the
glassy temperature. Such compounds are employed in the thermotropic electro-optic
displays. The two identical parts of the twin molecules were antiparallel to each other
even in the nematic state, which is proved using X-ray analysis and dielectric measure-
ments.

VIa

VIb

VIc

$R = nC_{10}H_{21}$ x = 0, 1 and 2

z = 1 and 2; m = 1-9; n = 1-4
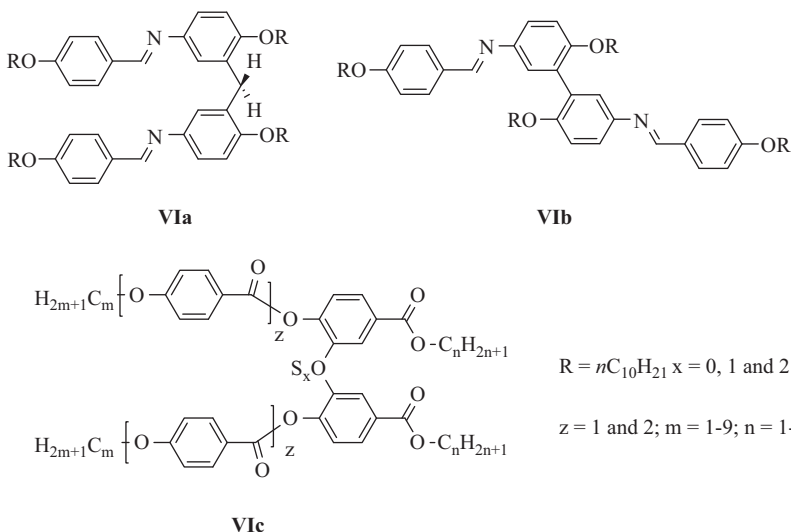
2.2.3 T-shaped dimers

Weissflog et al. (1990) synthesized and studied a variety of laterally substituted LC
dimers **VII**. They are called T-shaped ULC dimers. The compounds of this series
show additional monotropic smectic phase. The increment in the isotropic temper-
ature is observed with increase in benzoyloxy groups. Lee et al. (1999) extended the
study of laterally substituted unconventional dimers with variable spacer lengths
by preparing compound **VIII**. Thermal properties of these compounds are evalu-
ated and, interestingly, multiple isotropization is observed (Lee et al., 1999) and

no crystallization is found even after prolonged cooling. So, spacer effect is really something different here when compared with classical LC molecules.
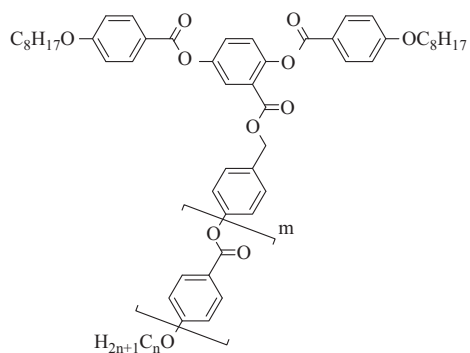
n = 4 - 10 and m = 0,1,2.

VII
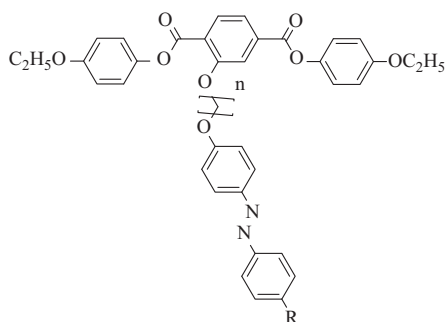
For R = *n*C₄H₉: n = 3-6 and 10

R = phenyl: n = 5-10 and 12

VIII

2.2.4 U-shaped dimers

IXa

IXb

C$_7$H$_{15}$O

IXc

OC$_7$H$_{15}$

H$_{2m+1}$C$_m$O

IXd

OC$_m$H$_{2m+1}$
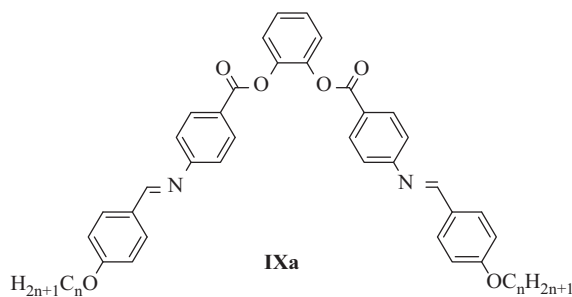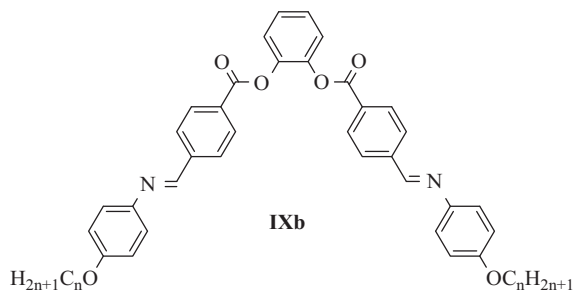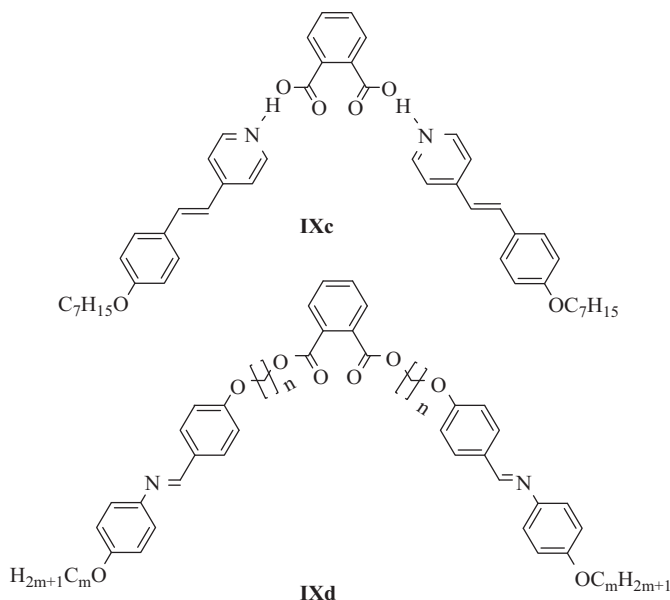
U-shaped ULC compounds consist of two calamitic units connected to a common benzene ring with 1, 2-positions. These U-shaped mesogens, first designed by Vorlander and Apel (1932), showed LC properties. The imine homologous series of **IXa** and **IXb** are composed by 1, 2-disubstituted benzene and they are U-shaped dimers (Kuboshita et al., 1991); many of them showed smectic B phase. Then, Takashi et al. (1992) used stilbazole derivatives to synthesize U-shaped LC dimers **IXc**, which are disubstituted via hydrogen bonding. They are nematic LCs and showed clearing temperatures less than 140 °C. However, 1, 3-substituted and 1, 4-substituted hydrogen-bonded complex structures exhibited smectic phases till their decomposition temperatures nearly 250 °C. Introduction of flexible alkyl spacers in such compounds showed dramatic changes in LC property.

For the determination of relative geometry and intramolecular alkyl chain parities of U-shaped ULC compounds, Attard and Douglass (1997) introduced various spacers in the compound **IXd**. In this case, compounds with the even number of spacers showed smectic phase whereas with the odd number of spacers showed nematic phase. Therefore, spacers play a main role in determining LC polymorphism when terminal alkyl chain length is short (Attard and Douglass, 1997). However, Rahman et al. (2015) synthesized a series of azobenzene-based U-shaped LC dimers and they showed both nematic and smectic A phases irrespective of spacer chain length and parity.

2.2.5 O-shaped dimers

The ULC dimers which do not have the terminals in their individual molecular structure are known as O-shaped or cyclic dimers. The even–odd spacer oscillation in smectic LC behavior is depend on parity and length of flexible spacers.

n = 5 - 10

X
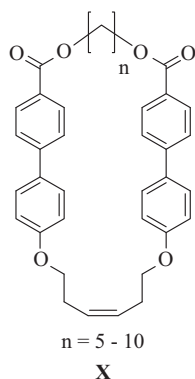
Itoh et al. (2009) synthesized compounds **X** where the spacers connect the calamitic mesogens at both the ends in cyclic manner. The clearing temperature of these compounds was significantly higher than their corresponding linear analogues. If less number of spacer units are present in the cyclic molecules, the smectic temperature is usually higher than linear compounds. Interestingly, macrocyclization forces the folding of spacers between the aromatic rigid cores and favors the rigidity in the molecular conformation.

2.2.6 Discotic dimers

A large variety of disk-shaped molecules has been reported in the literature with peculiar mesomorphic properties. DLC dimers are primarily two types: (i) discotic–discotic dimers and (ii) discotic–calamitic dimers. Most of the aspects of these dimers are available in the book by Pal and Kumar (2017). Here, we have discussed only a few examples of unconventional discotic dimers.

Generally, discotic–discotic dimers are designed by two identical disk-shaped compounds connected via flexible spacers. The properties of these compounds can be altered mostly by using different spacers of various length/nature and nature of connecting groups between spacer and disk-shaped molecular units. In order to enhance the transition temperature range of columnar phase, Krishnan and Balagurusamy (2001) designed **XIa**. As expected, **XIa** showed long-range columnar phase than the corresponding monomer. Praefcke et al. (1990) synthesized **XIb** series;

these dimers exhibit nematic phase and was the first report to describe the nematic mesomorphism of unconventional DLCs.
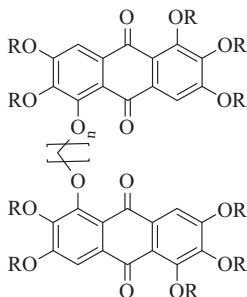
XIa
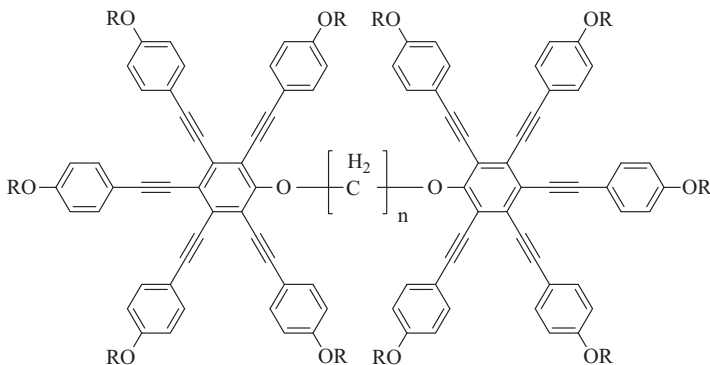
XIb
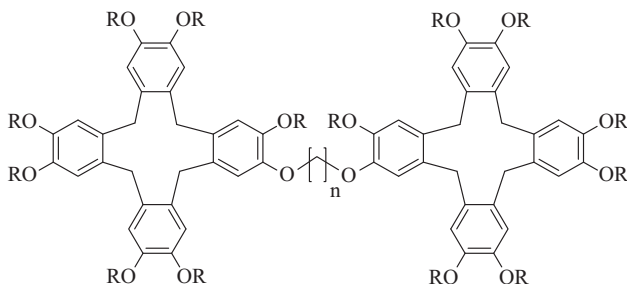
XIc

Percec et al. (1992) observed three different types of columnar phases in **XIc** per heating–cooling cycle. The columnar hexagonal phase appeared at high temperatures near isotropic temperature and the other two mesophases are unidentified columnar phases. These unconventional DLC dimers have lesser clearing temperatures than corresponding monomers. The series of dibenzo[a,c]phenazine unconventional DLC dimers was mainly studied by two groups Tzeng et al. (2011) and Ong (2013). In

the molecular structure, they consist of a bulky alkyl chain at the *alpha* position with respect to the spacer linkage between phenazine cores. The spacer length is taken as constant to design these DLC dimers. The mesomorphic change from hexagonal to lamellar phase is noted while increasing the aliphatic chain length of periphery. The terminal alkyl chains are situated at *alpha* position to spacer linkage; this prohibits the intramolecular intercalation and hence, higher members of **XIIa** series show discotic lamellar phase.

XIIa

XIIb

XIIc
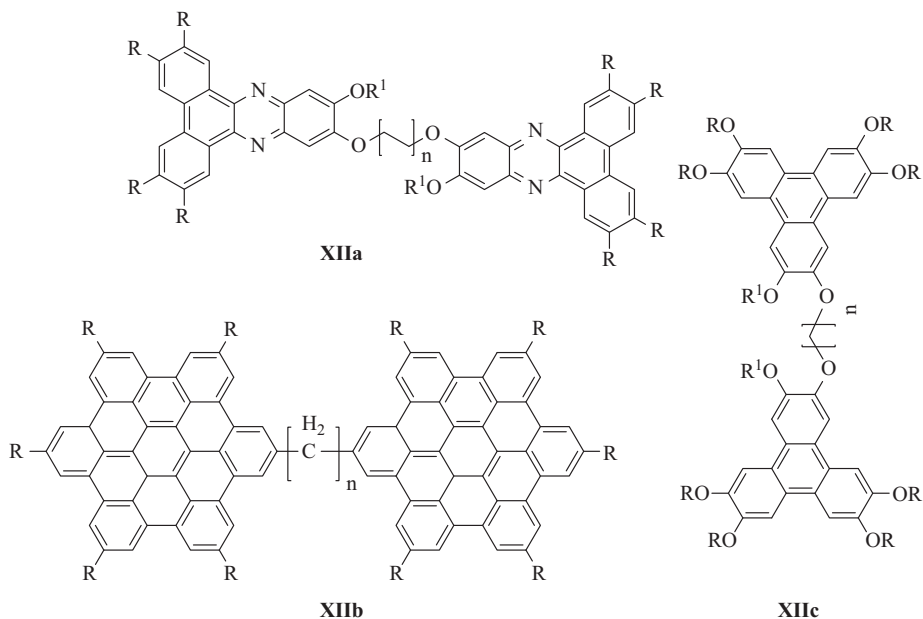
Ito et al. (2000) synthesized the hexa-*peri*-hexabenzocoronene DLC dimer series of **XIIb** to evaluate the mesomorphism of ULCs. The series of **XIIb** showed long-range LC phase from 53 °C to 370 °C. Triphenylene derivatives are one of the extensively studied DCL compounds in the literature. Plenty of reports are available to discuss the mesogenic characteristics of unconventional DLC triphenylene-based dimers **XIIc** (Plesnivy et al., 1995). In **XIIc**, the lower homologous series ($n < 7$) are not mesogenic in nature and glassy state with the columnar order is obtained upon supercooling (Boden et al., 1999). The columnar phase is observed in other higher members in the same series (Boden et al., 1999). Here the stability of glassy state depends on the length of aliphatic spacer chain.

Han et al. (2018) evaluated the mesomorphic properties of room temperature fluorescent unconventional discotic dimers derived from oxadiazole **XIId**. The synthetic route for the preparation of **XIId** is given in Scheme 2.1. This molecule does not consist of disk-shaped aromatic component and it is clear by visualizing the structure. The derivatives of **XIId** showed discotic nematic or columnar hexagonal phase; interestingly, they showed photoluminescence in solution, crystal,

and LC states. The decrease in the fluorescent intensity is noticed in the LC state than crystal state due to the self-quenching aggregates.
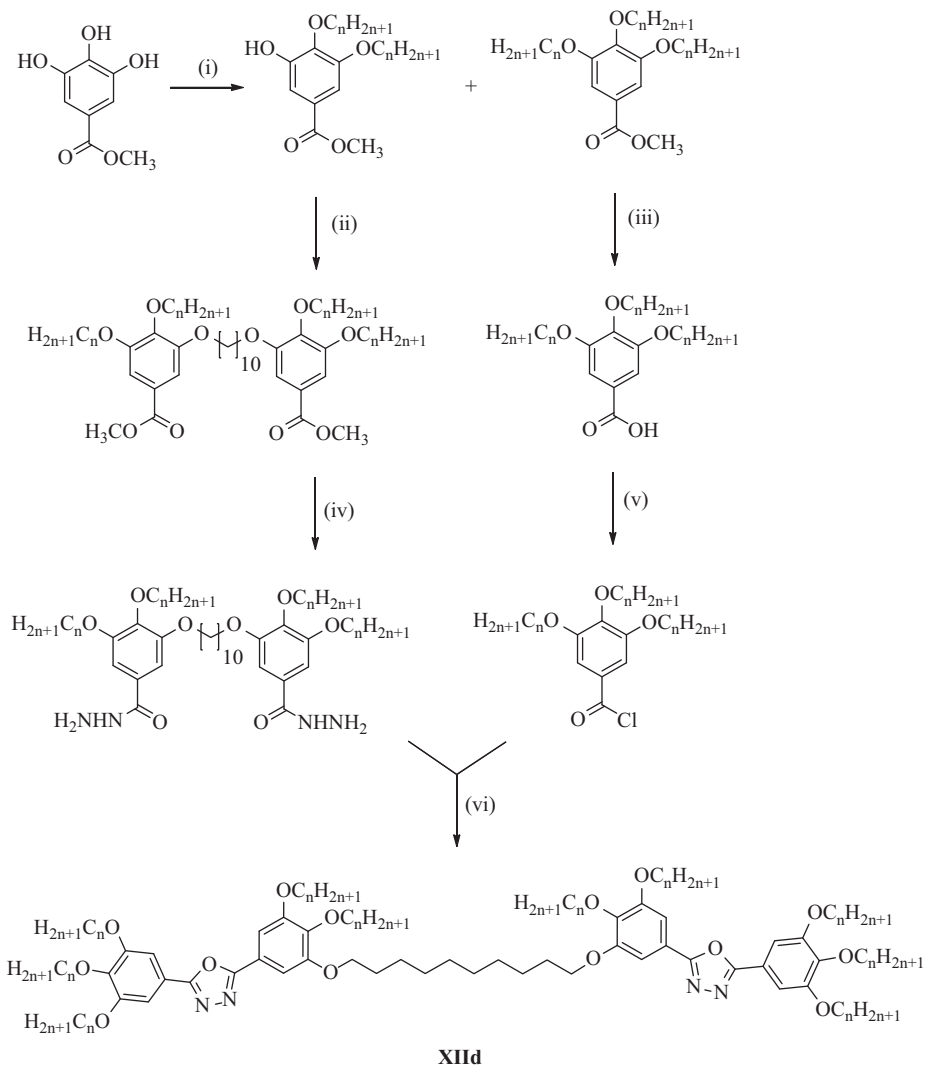
Scheme 2.1: Synthetic rout to unconventional discotic dimers **XIId**. (i) $nC_nH_{2n+1}Br$, K_2CO_3/KI, DMF; (ii) $Br(CH_2)_{10}Br$, K_2CO_3/KI, DMF; (iii) KOH/H_2O, EtOH; (iv) $NH_2NH_2.H_2O$, EtOH, reflex; (v) $SOCl_2$, reflex; and (vi) $POCl_3$, pyridine, reflux.

2.2.7 Bent-core dimers

During the past 20 years, bent-core LCs attracted researchers' attention in the LC community. Especially, the bent-core compounds are showing certain peculiar physical properties which could not be found in calamitic LC compounds, such as chiral phase or polar phase occurrence in achiral systems. In order to use the microsegregation to alter the microstructures of bent-core compounds, bent-core unconventional dimers are designed. In most cases, two mesogenic bent-core units are joined via flexible spacer in a molecular system and is the typical design for unconventional bent-core systems.

In 2002, Dantlgraber et al. (2002) introduced the concept of bent-core unconventional dimers by connecting two bent-core units via a dimethyl siloxane spacer. The motivation for this synthesis is to induce ferroelectricity by suppressing the interlayer fluctuation of the LC system. The X-ray diffraction pattern for **XIIIa** showed a diffuse peak at wide angle, a sharp reflection up to the third order at the small angle region, which is clearly indicating the well-defined layer patterns in the LC media. The tilted mesophase and structure interdigitation is supported by the layer distance, which is greater than the molecular length of each dimeric unit. A chiral superstructure or dark conglomerate phase is found for **XIIIa** under the polarizing optical microscope by rotating the polarizer, and upon fast cooling from the isotropic point, the dark conglomerate phase does not appear (Dantlgraber et al., 2002). To elaborate the concept of unconventional bent-core dimers and dendrimers, Kosata et al. (2006) designed a variety of molecules **XIIIb** with various kind of spacers and terminal chains in bent-core units. The LC properties of such unconventional dimers are entirely different than their corresponding monomers and this is due to the nature of the chemical structure of monomeric unit as well as nature of spacers, which is connecting two mesogenic units in each dimer molecule. In case of **XIIIb**, the unconventional dimers with hydrocarbon CH_2 spacers are nonliquid crystals whereas, dimers with tetraethylene glycol spacers exhibited columnar phases. Moreover, polar smectic phases are obtained from the same dimers **XIIIb** with the siloxane spaces. Other than the spacer effect, there is no major change observed in the phase behavior in the alteration of functional groups. Achten et al. (2007) investigated a series of bent-core unconventional dimers **XIIIc** and observed intercalated smectic phases for the LC compounds consisting of long terminal alkyl chains. In this case, layer spacing is fairly related to the terminal aliphatic chains; interestingly, the mesomorphism is only observed in the compounds consisting of short spacers and long terminal chains.

XXIIIa

XXIIIb

XXIIIc

XXIIId

XXIIIe

XXIIIf
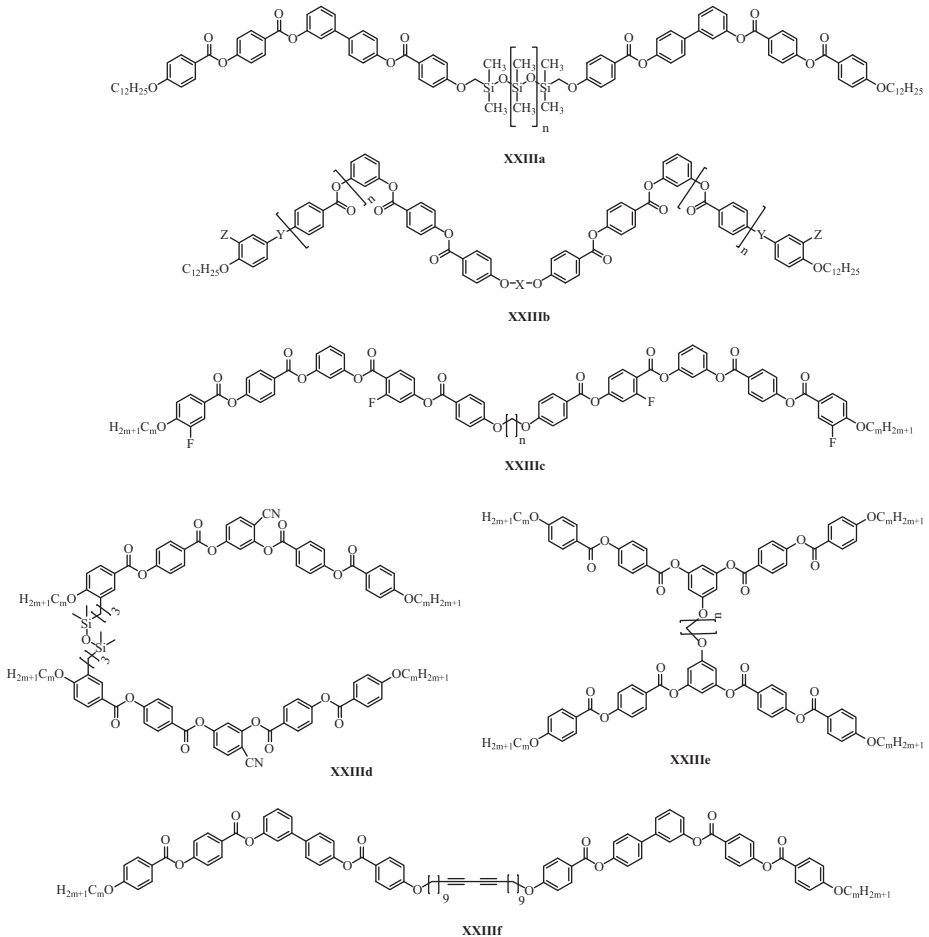
Shanker et al. (2012) evaluated LC properties of laterally connected unconventional dimers **XIIId**. The compounds **XIIId** exhibited broad nematic phase range and low crystallization tendency. However, the stability of laterally connected dimers is less than corresponding monomers. The compound with a short spacer and aliphatic chains are exhibiting nematic phase at ambient temperature. A strong coupling may be achieved in these dimers by reducing the length of spacers and terminal chains. Radhika et al. (2013) synthesized and studied the LC properties of symmetric unconventional dimers **XIIIe**. Mainly, the LC characterization is explained on the basis of the spacer and terminal alkyl chain length. Two orthogonal lamellar phases are observed for **XIIIe** and those obtained phases are literally different with respect to each other. Zhang et al. (2013) studied the synthetic design and LC property of unconventional bent-core dimers **XIIIf** bearing diacetylene spacers along with various terminal spacers. Thermal evaluation studies revealed that the acetylene group is polymerizing under ambient temperature and thermal decomposition is observed

at 260 °C. The monotropic phase with the wide range is also found in the thermal analysis.

2.3 Trimers and tetramers

2.3.1 Liquid crystal trimers

The LCs are composed of three mesogenic units, which are interconnected via spacers and are known as ULC trimers. Imrie and Luckhurst (1998) synthesized two homologous series of LC trimers **XIVa** and **XIVb** with variable number of CH_2 units. All the members of the homologous series showed enantiotropic nematic phase. Additionally, monotropic smectic A phase is observed for 4 to 11 methylene units. The formation of smectic A phase is due to the interaction between unlike mesogenic units such as terminal cyanobiphenyl and central biphenyl or azobenzene moieties. The nematic to isotropic transition temperatures with the entropy change depends on odd–even spacer linkages. The even number of spacer linkages exhibited the high value of transition temperatures. As compared to the order parameter of these unconventional trimers, the corresponding dimers and monomers exhibit high orientational order.

XIVa

XIVb
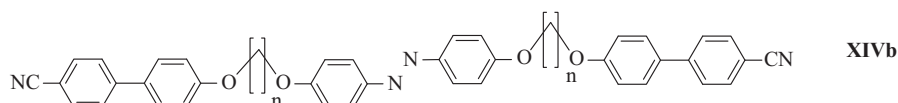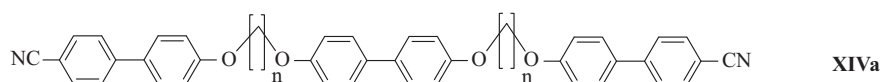
Yelamaggad et al. (2000) designed and analyzed the LC properties of unconventional trimesogens with nonidentical calamitic entities connected between flexible spacers. The compounds **XVa** and **XVb** are multifunctional, photochromic, and thermotropic LCs. These compounds are useful in the preparation of optical storage device. The trimers **XVa** and **XVb**, consisting of azobenzene, cholesteryl, and biphenyls, are connected using odd–even, even–even, and odd–odd spacers linkages. The derivatives which consist of even–even and odd–odd spacers exhibited undulated twist grain boundary phase at the temperatures between 40 °C and 50 °C.

XVa

XVb
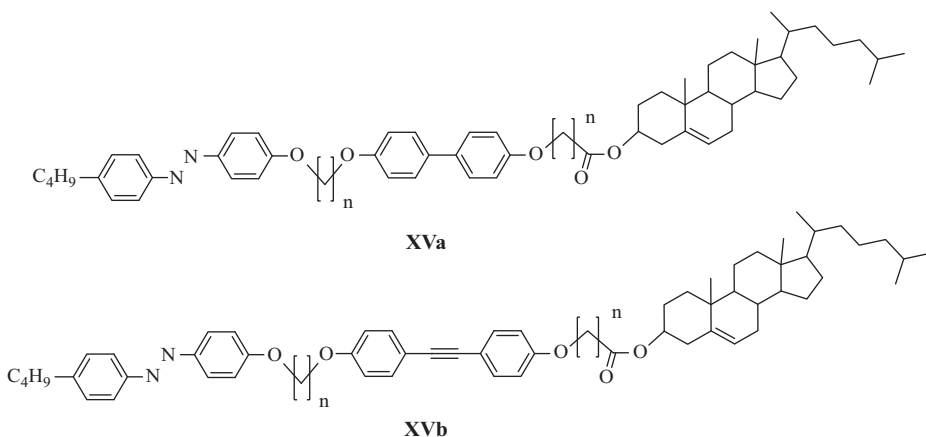
An unconventional charge transfer trimers **XVIa** composed by an electron-rich penta-alkynylbenzene derivative and an electron deficient flat nitrofluorenone is specially designed by Mahlstedt et al. (1999). These two electron donor–acceptor mesogenic units are connected to central calamitic azobenzene via alkyl spacers. The resultant mesophase is frozen glassy state at room temperature for the corresponding trimer molecular design. The X–ray analysis revealed the nematic columnar phase for **XVIa**. The columns are forming due to the intercalated stacking of the flat acceptor–donor intermolecular moieties. The calamitic subunits aligned orthogonal to column's axes rather than parallel alignment. The steric frustration enhances in the molecular system because of the interaction of alkyl substitution to donor penta-alkynylbenzene units.

XVIa

XVIb
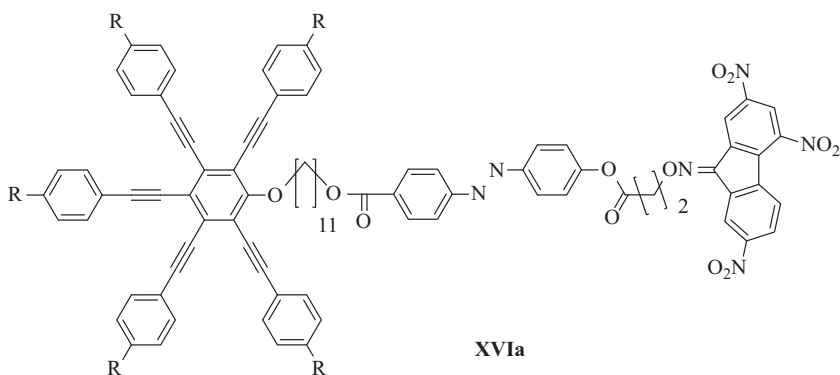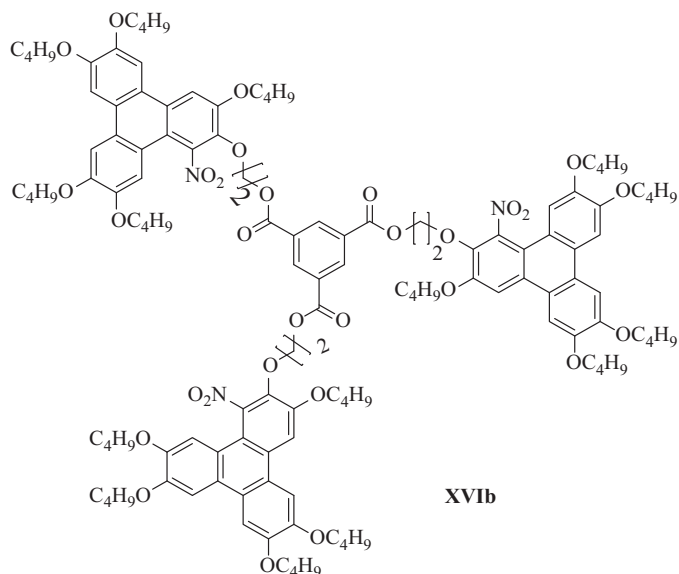
Kumar and Manickam (1999) introduced a new variety of trimer **XVIb** using trisubstituted benzene core and three nitro-functionalized hexa-alkoxy triphenylenes connected through flexible spacers. They showed a monotropic columnar phase at room temperature and no crystallization is observed even at −50 °C. Interestingly, the corresponding compounds without NO_2 functional groups are not LCs in nature.

The twist-bend nematic phase was reported in various bent-core LC trimer molecules. Wang et al. (2015) designed a nanostructured heliconical twist-bend nematic LCs **XVIIa**. This is the first example to describe the properties of achiral hybrid bent-core LC trimers. The compound **XVIIa** consists of two calamitic mesogens connected to the central bent-core unit via hexyloxy spacers. Below 80 °C, a nematic phase and above 80 °C, a twist-bend nematic phase is found for this compound. The twist-bend nematic phase with helical structure appeared for the period of ~19 nm (Wang et al., 2015) at room temperature. Sasaki et al. (2017, 2018) observed the chiral conglomerate phase in trimesogenic LC **XVIIb** composed by three calamitic units. The gyroid-like surface accompanying the periodic distribution of dimples with 100 nm size is evaluated in this compound by various microscopic technics. Usually, the twisted textures are obtained in the bent-core compounds. But, the trimer composed of three calamitic mesogens **XVIIb** interestingly shows dark conglomerate phase.

Yoshizawa and Kato (2018) prepared the achiral flexible LC trimers **XVIIc** consists of octafluorobiphenyl unit as a central core linked with two cyanobiphenyl moieties and these are chiral conglomerate nematic LCs. The trimers with the even number of spacers produced helical state and the chiral nature is not observed in case of the odd number of spacers. The spontaneous mirror symmetry breaking is found and is due to the transient chirality and coupling of the surface anchoring of the octafluorobiphenyl moiety.

Ooi and Yeap (2018) studied two homologous series of λ-shaped ULC trimers **XVIId** which are laterally connected to benzylideneaniline as the central unit and linked with two cholesteryl moieties. These compounds exhibited smectic and chiral nematic phases except the trimers containing long spacers (n = 9 and 10). The elongation of alkyl spacers widens the chiral nematic phase range and destabilizes the smectic A phase. The noncrystalline compounds **XVIId** resemble Grandjean texture under the microscope upon cooling at low temperature.
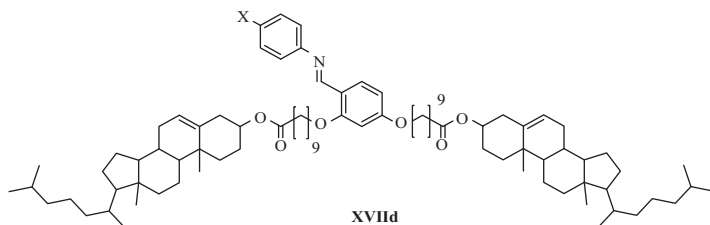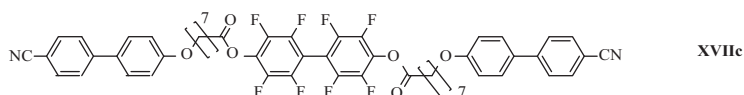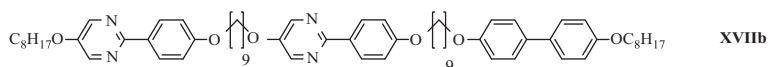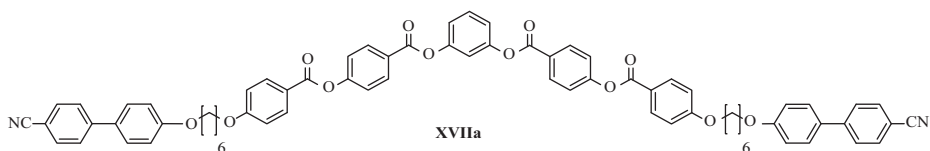
2.3.2 Liquid crystal tetramers

The ULC tetramer homologous series was first reported by Imrie and coworkers (1999). In this series, four calamitic units connected via various spacers **XVIIIa**. They showed the nematic phase except for decyl and dodecyl homologues whereas, the decyl and dodecyl homologues **XVIIIa** exhibited smectic A phase. The transition behavior was interpreted mainly with the discussion of nature and length of spacers in each molecule. Yelamaggad et al. (2002) studied the thermal behavior of ULC tetramers **XVIIIb** designed by four nonidentical mesogens connected through spacers. These compounds are composed of biphenyl, cholesteryl, tolane, and azobenzene moieties. The homologues series **XVIIIb** with even–even–odd and odd–even–odd spacers are showing columnar phase.

Henderson et al. (2001) synthesized ULC tetramers with azobenzene, and imine calamitic mesogens are linked with the specific number of CH_2 units without terminal alkyl chains **XVIIIc**. In this series, the derivatives are differing from one another by the number of spacers as well as the position of substitutions (*meta* and *para*) (Henderson et al., 2001). Some of them showed smectic phase and rest are nematic LCs; nevertheless, disordered crystalline state is observed in this series. Recently, tetramer type of ULC cholesteryl-substituted oligomers are reported by Champagne et al. (2018a). The oligomer consisting of cholesterol mesogenic groups are connected to hybrid of nonpolar hydrophobic chains with polar tetraethylene glycol. The dramatic change in the transition temperature of **XVIIIc** is found as compared to the mesomorphic properties of monomeric units and appreciable thermal stability is recorded.

XVIIId

2.4 Hydrogen-bonded mesogens

XIXa

(alkyl chain)

XIXb

$H_{2n+1}C_nO$

XIXc

H_3CO

XIXd
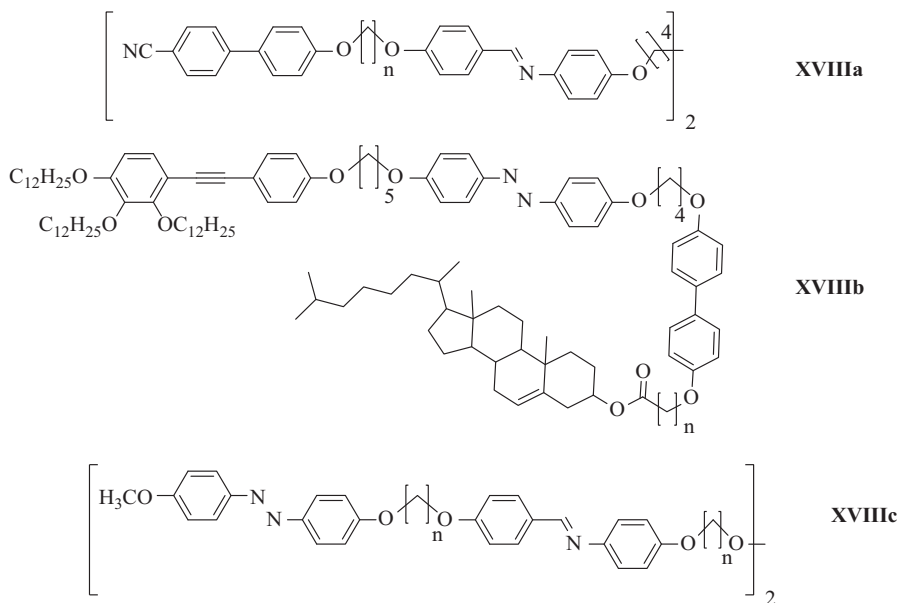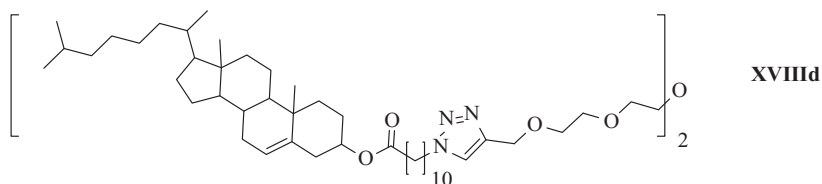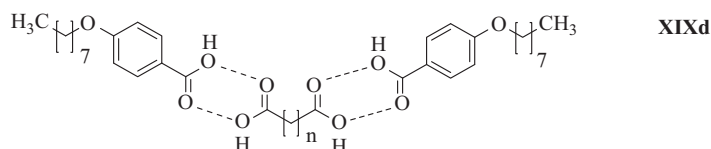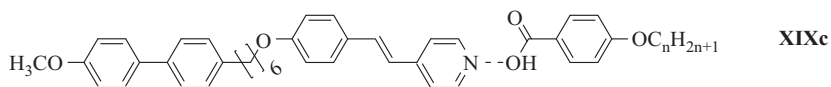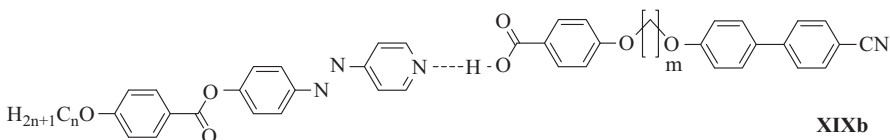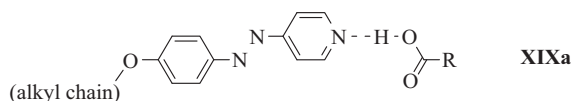
In 2018, a variety of hydrogen-bonded ULCs are reported (Champagne et al., 2018b). Champagne et al. (2018b) synthesized various sets of hydrogen-bonded compounds **XIXa** using a binary mixture of carboxylic acid and pyridylazo derivatives with linear as well as branched terminal chains. The stability of hydrogen bonds is determined by infrared spectroscopy. The hydrogen-bonding connectivity improved the phase-transition behavior and mesomorphic properties. Then, a similar binary series of carboxylic acids and pyridine derivative **XIXb** (Walker et al., 2018) and **XIXc** (Alaasar and Tschierske, 2018) were prepared and studied. Walker et al. (2018) reported the spontaneous formation of chiral phase due to the interaction between acid–base components in the binary system. The ULC compound **XIXb** showed heliconical twist-bend nematic phase. Alaasar and Tschierske (2018) prepared the intermolecular

hydrogen-bond complex of asymmetrical LC dimers **XIXc**. The even–odd effect of spacer, length of terminal aliphatic chains, and polarity of cyano group have significant impact on the LC property of these compounds. They showed enantiotropic nematic mesomorphism over the broad range of temperature. Okumuş (2018) evaluated the LC property of two hydrogen-bonded molecules of 4-octyoxy benzoic acids and central aliphatic long-chain dicarboxylic acid complex. The hydrogen-bond formation is confirmed using infrared spectroscopy. The resultant LC phase formed is nematic and smectic for **XIXd**.

2.5 Oligomers and dendrimers

2.5.1 Liquid crystal oligomers

The LC oligomers are a class of ULC which consist of bulky molecular structures. There are many varieties of LC oligomers reported in the literature and they are usually composed by supermolecular architecture. Among them, star-shaped LC oligomers are extensively studied by LC researchers. There are plenty of star-shaped mesogenic cores with three or more arms (Barber et al., 2006; BarberW et al., 2004; Fan et al., 2001; Gemming et al., 2005; Goldmann et al., 1998; Hatano and Kato, 2006; Katoh et al., 2006; Lehmann et al., 2004a, 2007, 2006; Lin et al., 2002; Meier et al., 2003). Such type of mesogens with internal short aliphatic chain (Meier et al., 2004) as well as without lateral alkyl chains (Goldmann et al., 1998) show a nematic phase. Moreover, mesogens with six or more lateral alkyl chains form columnar textures (Achten et al., 2007; Aquilera and Bernal, 1984; Attard and Douglass, 1997; Barber et al., 2006; BarberW et al., 2004; Blatch et al., 1997; Boden et al., 1999; Champagne et al., 2018a, 2018b; Chien et al., 1987; Creed et al., 2007; Dantlgraber et al., 2002; Dehne et al., 1989; Dia et al., 1994; Elhaj et al., 1995; Goldmann et al., 1998; Goodby, 1991; Griffin et al., 1981; Han et al., 2018; Hatano and Kato, 2006; Henderson et al., 2001; Hogan et al., 1988; Hohmuth et al., 1997; Imrie and Luckhurst, 1998; Imrie and Taylor, 1989; Imrie et al., 1999; Ionescu et al., 1997; Ito et al., 2000; Itoh et al., 2009; Jo et al., 1988; Katoh et al., 2006; Kosata et al., 2006; Krishnan and Balagurusamy, 2001; Kuboshita et al., 1991; Lee et al., 1999; Lehmann et al., 2004a; Lehmann et al., 2006; Lin et al., 2002; Mahlstedt et al., 1999; Malpezzi et al., 1991; Nishiyama et al., 1993; Omenat et al., 1999; Percec et al., 1992; Poths et al., 1995; Praefcke et al., 1990; Radhika et al., 2013; Rahman et al., 2015; Robinson et al., 1998; Shanker et al., 2012; Takashi et al., 1992; Takenaka et al., 1989; Tzeng et al., 2011; Vorländer and Apel, 1932; Wang et al., 2015; Weissflog et al., 1990; Yelamaggad et al., 2000; Yelamaggad et al., 2002; Zhang et al., 2013; Vora et al., 2006). Sometimes, long-range mesophases are observed in case of three-armed star-shaped LCs. The flexibility of the core is an important parameter with respect to the molecular self-assemblies; one such common

example is oligobenzoate compound as shown in Scheme 2.2. Each molecule of oxy-phenylcarboxy groups is shape-persistent and flat. Nevertheless, the ester linkage present in the star-shaped ULCs are responsible for the formation of different shapes such as T-shaped, E-shaped, or star-shaped conformers (Gemming et al., 2005). If the star-shaped compounds **XXa** and **XXb** consist of the planar structure with C_3 symmetry, then there are some unoccupied spaces can be found between their arms.
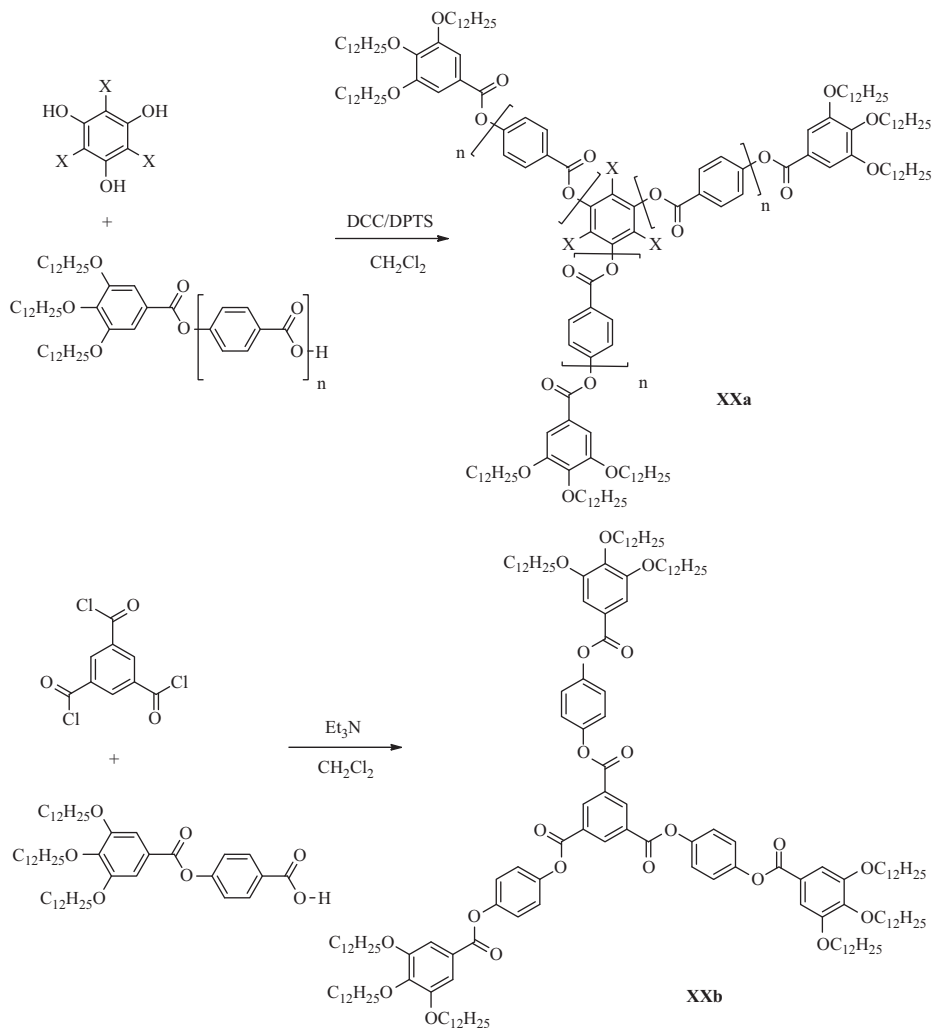
Scheme 2.2: Synthetic design of oligobenzoate derivatives.

Meier et al. (2003) and Lehmann et al. (2007) showed that the intramolecular space or void between the arms can be either filled by the segments of neighboring molecules

or solvents. This is not accepted in the case of neat LC aggregation assuming that co-planar stacking and nanosegregation of these extended molecules are reliable factors (Lehmann et al., 2007) to attain LC nature. Unlikely, the star-shaped molecules easily form the columnar assemblies via discotic arrangements and results in the hexagonal phase formation (Bushby and Lozman, 2002). Gearba et al. (2007) described the hexagonal arrangement of the star-shaped mesogens with C_3 symmetrical arrangement of oligobenzoates. The gap or void between the arms increases, when the size of such oligobenzoate molecules is increased. Smaller columnar diameter is observed for the discotic mesogens than the actual diameter of each star-shaped molecules (Gearba et al., 2007).

Some other derivatives of unconventional LC phases are proposed with *E*-shaped conformation. The ambiguity about the *E* shape of the molecules is confirmed by X−ray analysis. Further, the helical crystal phase is obtained for the *E*-shaped molecules via slow cooling from monotropic hexagonal mesophase at ambient temperature (Percec et al., 2006). The helical mesomorphism is also observed in the derivatives of cyclotriphosphazene (Barber et al., 2005, 2006), stilbenoid derivatives (Holst et al., 2004; Lehmann et al., 2006), and wedge-shaped molecules (Gearba et al., 2007).

XXI
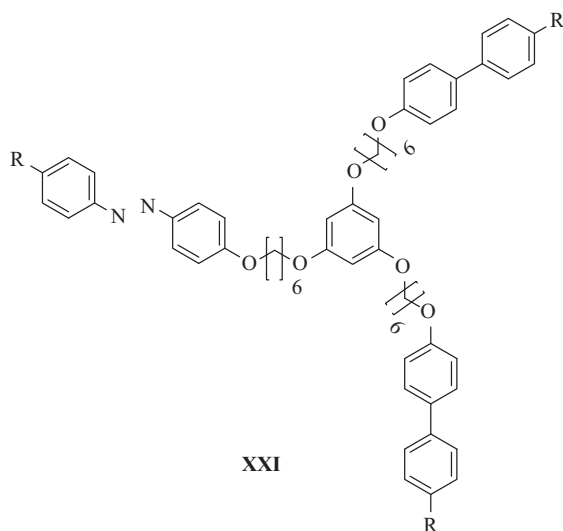
Tomczyk et al. (2013) evaluated the properties of star-shaped low-molecular-weight LC compounds **XXI**. These ULC photochromic azo functionalized compounds are investigated in terms of light-induced anisotropy. The very high value of anisotropy and dichroism was recorded at room temperature upon irradiation of UV light.

The LC chemists are very much interested in nonlinear oligomeric cores which are tethered by aliphatic chains. Saez and Goodby (2003) synthesized Janus LCs **XXIIa** and **XXIIb** with two diversely functionalized mesogenic counterparts. Among them, one substitution is trying to favor chiral nematic and the other one prefers the

formation of smectic phase. These two different characters of the substitutions are tethered symmetrically on either side of the central flexible unit.

Where,

R is

R' is

XXIIa

R is

XXIIb

R' is
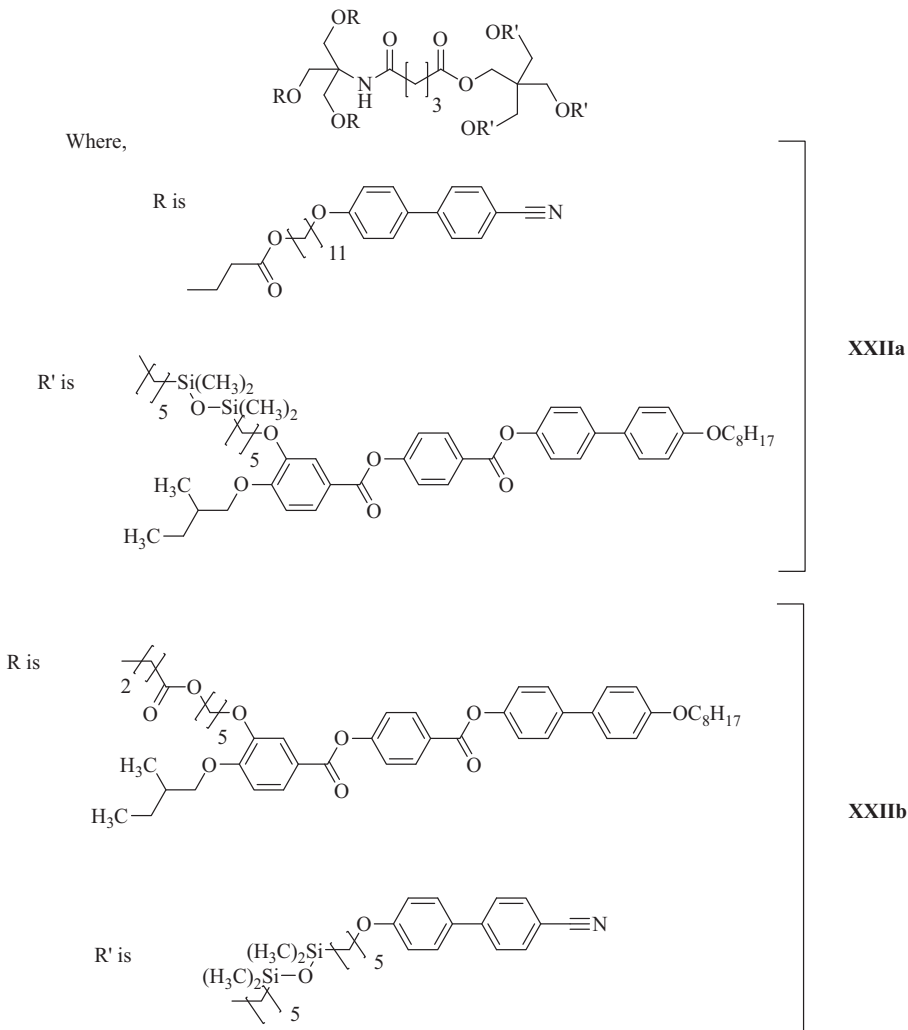
Some unconventional mesogens exhibit excellent photoresponse (Allard et al., 2005); this type of compounds with special molecular architecture is also capable of fast photo-induced charge separation. The inherent mesomorphic properties of unconventional mesogens are the advantage (Nierengarten, 2004) over the conventional LCs for the application point of view. By considering the same analogy, Manickam et al. (2001, 2000) synthesized the series of triphenylene connected to carbazoles through aliphatic spacers **XXIIIa** and **XXIIIb**. These compounds are excellent photorefractive materials when compared to other amorphous polymeric carbazole materials (Manickam et al., 2001, 2000).

XXIIIa

XXIIIb
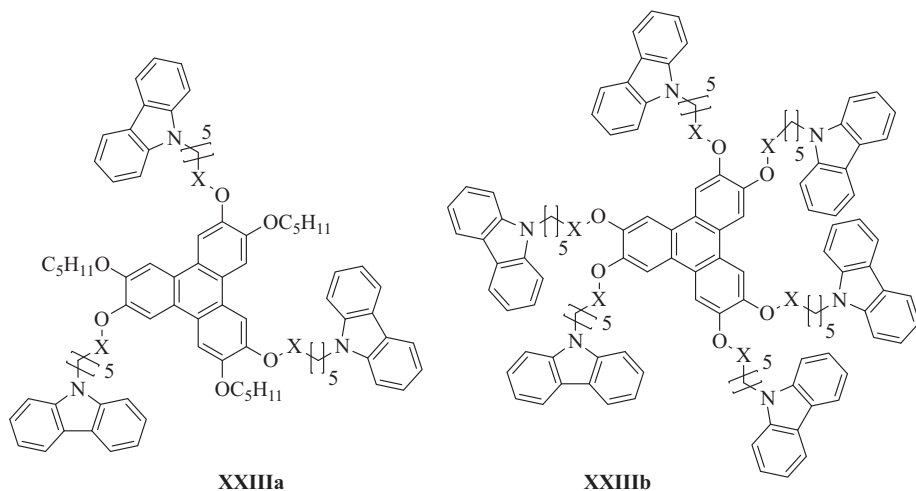
Where, X = CH$_2$ or CO

Triphenylene-based star-shaped oligomer **XXIVa** and azacrown derivative **XXIVb** showed stable hexagonal columnar phase (Plesnivy et al., 1995). The variation in the thermal range of the hexagonal phase and difference in the isotropic temperatures of **XXIVa** is explained in terms of alky spacer length as well as peripheral discotic units (Plesnivy et al., 1995).

XXIVa

Where, -R is

XXIVb

n = 6,9 and 11
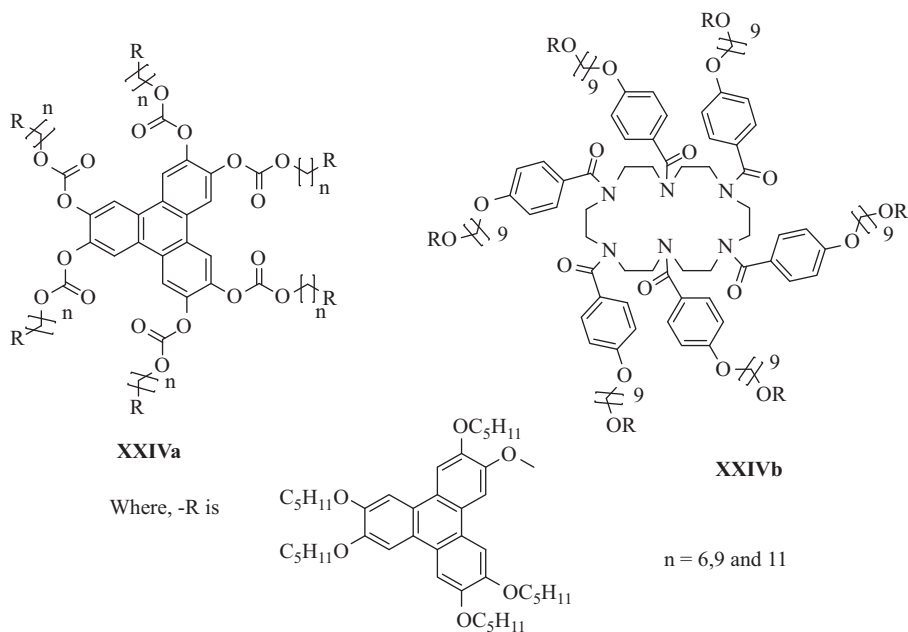
There are some supramolecular oligomers reported with excellent LC properties (Tian et al., 2010). The self-assembly of these molecules can be explained on the basis of hydrogen-bond formation in the system. Parashiv et al. (2006) synthesized 1,3,5-benzenetrisamide core surrounded by covalently linked alkoxy triphenylenes. These compounds show hexagonal columnar plastic phase because the amide linkages present is the compounds are connected to each other via hydrogen-bonding network. Due to this strong core–core interaction, the charge mobility value is high, 0.12 $cm^2 V^{-1} s^{-1}$. This charge mobility is found to be greater than other DLC compounds reported in the literature till date (Tian et al., 2010). Interestingly, ferrocene and tetra-thiafulvalene-based triphenylene compounds exhibited controllable redox potentials; these are good candidates for the study of electrochemical switching (Cooke et al., 2000). Likewise, some other triphenylene-based columnar oligomeric compounds are designed and found versatile in the context of science and technology (Kumar, 2005).

Where, n = 4 to 13

XXV
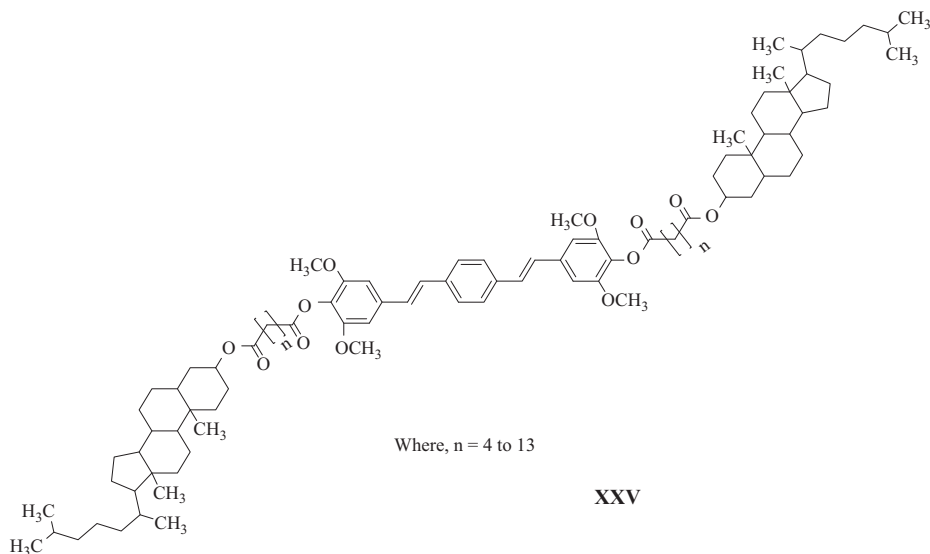
Sentman and Gin (2001) demonstrated a modular approach of oligo(*p*–phenylene vinylene) moiety with dihydrocholesterol units connected via both the sides through various alkyl spacers. In order to design the fluorescent thermotropic LCs, certain homologs of resulting target molecules **XXV** are synthesized. They exhibited smectic phase which is supercooled at ambient temperatures to get the glassy material. The order and alignment of these compounds are good with highly polarized luminescence; to employ such LCs in optical devices.

Lee et al. (2001) designed an interesting oligomeric molecule to obtain a LC; which is a cholesterol connected to two imines through flexible alkyl chains. This LCs compounds showed smectic C phase. Gupta et al. (2009) also made similar molecular design and reported the LC behavior of them.

OC$_{10}$H$_{21}$

R

XXVIa

XXVIb

XXVIc

Where, -R is

—OC$_2$H$_5$

—OC$_{10}$H$_{21}$
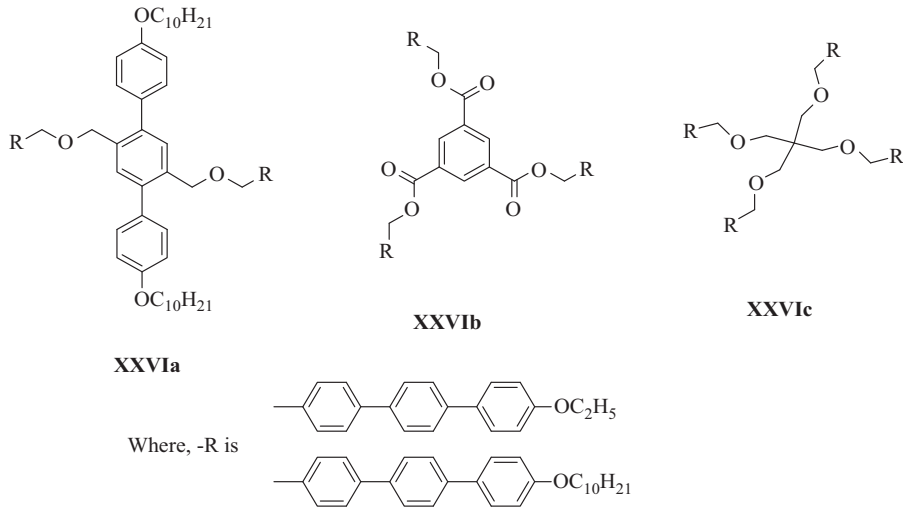
Andersch et al. (1996) prepared three types of nonlinear oligomers. The high isotropic temperature is observed for **XXVIa** and **XXVIb** with short alkyl spacer and mesomorphic behavior is absent in **XXVIc** with short alkyl spacer. Smectic phase is found for **XXVIa−c** with decyloxy chain whereas, the nematic phase is observed with ethyloxy chain.

2.5.2 Liquid crystal dendrimers

Dendrimers and dendrons are the three-dimensional branched supramolecular chemical species, which consist of bridge units as well as terminal functionalities. Usually, they have monomolecular weight and multiple functionalities; such compounds are extensively employed in various applications in the modern research. LC dendrimers are the supramolecular high-molecular-weight compounds. Interestingly, the columnar mesomorphism of star-shaped dendrimer assembly attracted great attention in the thermal analysis (Bertrand and Guillon, 2006; Chang et al., 2005; Grafe and Janietz, 2005). The star-shaped ULC is composed of central rigid core, flexible spacers, and terminal mesogenic units connected to alkyl chains (Grafe and Janietz, 2005); an example is presented here.

Where, -R is
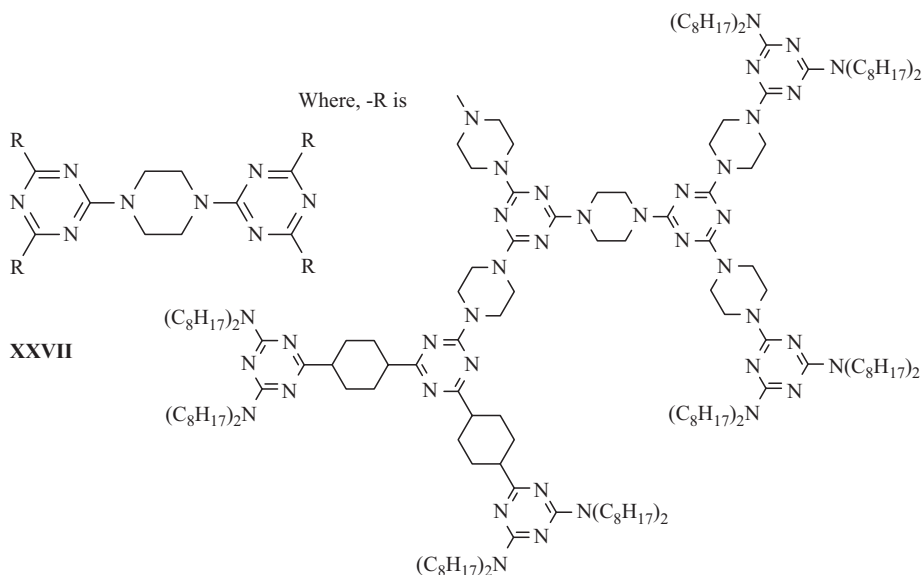
XXVII

Lai et al. (2008) synthesized piperazine and triazine based on the novel dendrimers **XXVII** without protection/deprotection of any functional group with the very good yield. **XXVII** exhibited excellent thermal stability and showed monotropic rectangular as well as hexagonal columnar phase.

2.6 Liquid crystal polymers, composites and colloids

The mesomorphic properties of the conventional LCs are theoretically predetermined in most of the cases whereas, in LC polymers (LCPs), easy theoretical predetermination is not possible. Hence, LCPs comes under ULC category. LCPs are very important materials possessing anisotropic order of LCs and mechanical stability of polymers. LCPs can be classified into different categories like, main chain polymers, side chain polymers, main chain–side chain combined polymers, elastomers, and networks. The vast LCP topic has been well covered in many recent reviews, book chapters, and books (Cammidge and Gopee, 2011; Kumar and Kumar, 2015b; Kumar and Lakshminarayanan, 2004; Singh et al., 2017c) and, therefore, not presented here in detail.

In order to increase the capability of LCs, they are mixed with suitable compounds to make composites or colloids. For example, Yanic et al. (2015) prepared the nanocomposite of 4^1-((S)-3,7-dimethyloctyloxy)phenyl 4-(10-undecen-1-yloxy)benzoate chiral nematic LCs and organomontmorillonite clay to investigate the dispersion

of LC molecules. The increased stability in the mesomorphism is measured using X-ray analysis. Many LCPs are designed and then prepare composites/colloids using various nanostructured materials to enhance the required physical properties. Among them, photoconducting and piezoelectric properties are important in the tailoring of semiconducting, photoconducting nanomaterials, as well as optical materials. In principle, the LC component in the mixture improves the orientation of each nanoparticle only if they are soluble in the LC media (Nagaraju et al., 2010; Topnani et al., 2014). The zinc oxide (ZnO) and titanium dioxide (TiO_2) nanostructure materials have scope in the contemporary research of optics, electronics, and photonics. The nanostructured TiO_2 exhibit good conductivity whereas, ZnO nanoparticles are known to be piezoelectric in nature (Nagaraju et al., 2010). Topnani et al. (2014) analyzed the composite mixture of synthesized nanoparticles ZnO and TiO_2; surface modifying agent polyvinylpyrolidine, 1–decanethiol, trioctylphosphine oxide, and capping agent trioctylphosphine oxide ethylenediamine derivative; which are doped into LC polyurethane and polyacrylate. The highly porous composite is obtained from this mixture after doped with LCs. The mechanism of the formation of the highly porous surface may be because of either expansion of cracks in the pure polymer or pulling out of dopant from the media to the surface (Gojny et al., 2005). The other possible reason for the high porosity is the in situ reaction between the polymer matrix and metal oxides (Liufu et al., 2005). Shukla et al. (2016) harvested the colloid of ferroelectric nanoparticles $LiNbO_3$ and $BaTiO_3$ dispersed in ferroelectric LCs. The nanocolloidal mixture showed excellent electrooptic and dielectric properties. Dutt and Siril (2014) have fabricated zero-dimensional and one-dimensional polyaniline nanostructures by doping with swollen LCs. Domenici et al. (2011) used LC elastomers to obtain the improved alignment of molybdenum oxide nanowires. The composite of nanostructured molybdenum oxide is essentially used in hydrogen sensing, lithium intercalation, and smart windows because of their light-induced characteristics.

We have prepared a number of LC composites by dispersing zero-, one-, and two-dimensional metallic, semiconducting, or carbon nanoparticles in various LCs. These nanocomposites have been studied well for various physical properties. Due to paucity of space, detailed description of these systems is not presented here and interested readers can refer to Cammidge and Gopee (2011), Kumar and Kumar (2015b), Kumar and Lakshminarayanan (2004), and Singh et al. (2017c).

2.7 Summary

The uniqueness in the mesomorphic properties of every LC depends on mobility and order. The order is affected by microsegregation, molecular anisotropy, and intermolecular attractive forces whereas molecular mobility varies with the temperature of the system. Depending on the molecular structure, the thermal behavior and

phase-transition properties of the LC compounds varies. The mesogenic properties of a compound are the intermediate state between the highly ordered crystal and disordered liquid. The rigidity and flexibility of individual molecules are very important parameters in describing the structure–property relationship.

In this chapter, a few examples are discussed in order to explain the chemistry of ULC. Other than the nature of the molecular structure, length and parity of spacers are discussed in the phase-transition behavior. Some examples of the odd–even number of spacer and siloxane spacer effects are discussed with the relative LC characteristics. Along with the spacer, the terminal functional groups and alkyl chains play an important role in the mesomorphic properties of ULCs. The ULCs of various designs, shapes, functional groups, spacers, terminal alkyl chain, and their nanocomposites/colloids are discussed with respect to their phase transition, mesomorphic behavior, as well as required physical properties.

References

Abe, A., Furuya, H., Nam, S.Y., Okamoto, S. (1995). Thermodynamics and molecular ordering of carbonate-type dimer liquid crystals with emphasis on the geometrical characteristics of the linking group. Acta Polymerica, 46, 437–444.

Achten, R., Koudijs, A., Giesbers, M., Marcelis, A.T.M., Sudhölter, E.J.R., Schroeder, M.W., Weissflog, W. (2007). Liquid crystalline dimers with bent-core mesogenic units. Liquid Crystal, 34, 59–64.

Adam, D., Schuhmacher, P., Simmerer, J., Häußling, L., Paulus, W., Siemensmeyer, K., Etzbach, K.-.H., Ringsdorf, H., Haarer, D. (1995). Photoconductivity in the columnar phases of a glassy discotic twin. Advanced Materials, 7, 276–280.

Alaasar, M., Tschierske, C. (2018). Nematic phases driven by hydrogen–bonding in liquid crystalline nonsymmetric dimers. Liquid Crystal. Doi: 10.1080/02678292.2018.1476740.

Allard, E., Oswald, F., Donnio, B., Guillon, D., Delgado, J.U., Langa, F., Deschenaux, R. (2005). Liquid–Crystalline [60] Fullerene–TTF Dyads. Organic Letters, 7, 383–386.

Andersch, J., Diele, S., Lose, D., Tschierske, C. (1996). Synthesis and liquid crystalline properties of novel laterally connected trimesogens and tetramesogens. Liquid Crystal, 21, 103–113.

Aquilera, C., Bernal, L. (1984). Thermotropic liquid crystalline bimesogenic molecules with highly flexible oligosiloxane spacer. Polymer Bulletin, 12, 383–388.

Attard, G.S., Date, R.W., Imrie, C.T., Luckhurst, G.R., Roskilly, S.J., Seddon, J.M., Taylor, L. (1994). Non–symmetric dimeric liquid crystals The preparation and properties of the α–(4–cyanobiphenyl–4′–yloxy)–ω–(4–n–alkylanilinebenzylidene–4′–oxy)alkanes. Liquid Crystal, 16, 529–581.

Attard, G.S., Douglass, A.G. (1997). U–Shaped dimeric liquid crystals derived from phthalic acid. Liquid Crystal, 22(3), 349–358.

Attard, G.S., Garnett, S., Hickman, C.G., Imrie, C.T., Taylor, L. (1990). Asymmetric dimeric liquid crystals with charge transfer groups. Liquid Crystal, 7, 495–508.

Attias, A.–.J., Cavalli, C., Donnio, B., Guillon, D., Hapiot, P., Malthþte, J. (2002). Columnar mesophase from a new disclike mesogen based on a 3,5–dicyano–2,4,6–tristyrylpyridine core. Chemistry of Materials, 14, 375–384.

Avinash, B.S., Krishnamurthy, S., Lakshminarayanan, V., Kumar, S. (2014). Mutually ordered self–assembly of discotic liquid crystal–graphene nanocomposites. Chemical Communications, 50, 710–712.

Avinash, B.S., Kumar, M., Gowda, A., Kumar, S. (2017). Trapping of inorganic nanowires in supramolecular organic nanoribbons. Journal of Molecular Liquids, 244, 1–6.

Avinash, B.S., Kumar, M., Kumar, S. (2018). Lyotropic liquid crystals of CdS nanoribbons. Journal of Molecular Liquids, 264, 352–357.

Avinash, B.S., Kumar, M., Lakshminarayanan, V., Kumar, S. (2015). Self–assembly of thiolated graphene oxide onto gold surface and in the supramolecular order of discotic liquid crystals. RSC advances, 5, 47692–47700.

Avinash, B.S., Lakshminarayanan, V., Kumar, S., Vij, J.K. (2013). Gold nanorods embedded discotic nanoribbons. Chemical Communications, 49, 978–980.

Bacher, A., Bleyl, I., Erdelen, C.H., Haarer, D., Paulus, W., Schmidt, H.-.W. (1997). Low molecular weight and polymeric triphenylenes as hole transport materials in organic two-layer LEDs. Advanced Materials, 9, 1031–1035.

Barber, J., Bardaji, M., Jimenez, J., Laguna, A., Martinez, M.P., Oriol, L., Serrano, J.L., Zaragozano, I. (2005). Columnar mesomorphic organizations in cyclotriphosphazenes. Journal of the American Chemical Society, 127, 8994–9002.

Barber, J., Jimenez, J., Laguna, A., Oriol, L., Perez, S., Serrano, J.L. (2006). Cyclotriphosphazene as a dendritic core for the preparation of columnar supermolecular liquid crystals. Chemistry of Materials, 18, 5437–5445.

BarberW, J., Puig, L., Serrano, J.–.L., Sierra, T. (2004). Structural study on columnar mesophases consisting of h–bonded supramolecules. Chemistry of Materials, 16, 3308–3317.

Barnes, P.J., Douglass, A.G., Heeks, S.K., Luckhurst, G.R. (2006). An enhanced odd–even effect of liquid crystal dimers Orientational order in the α,ω–bis(4′–cyanobiphenyl–4–yl)alkanes. Liquid Crystal, 13, 603–613.

Bertrand, B., Guillon, D. (2006). Liquid crystalline dendrimers and polypedes. Advances in Polymer Science, 201, 45–155.

Bisoyi, H.K., Kumar, S. (2008). Carbon nanotubes in triphenylene and rufigallol–based room temperature monomeric and polymeric discotic liquid crystals. Journal of Materials Chemistry, 18, 3032–3039.

Bisoyi, H.K., Kumar, S. (2011). Liquid crystal nanoscience: an emerging avenue of soft self–assembly. Chemical Society Reviews, 40, 306–319.

Blatch, A.E., Fletcher, I.D., Luckhurst, G.R. (1997). Symmetric and non–symmetric liquid crystal dimers with branched terminal alkyl chains: racemic and chiral. Journal of Materials Chemistry, 7, 9–17.

Boden, N., Bushby, R.J., Cammidge, A.N., El–Mansoury, A., Martin, P.S., Lu, Z. (1999). The creation of long–lasting glassy columnar discotic liquid crystals using 'dimeric' discogens. Journal of Materials Chemistry, 9, 1391–1402.

Boden, N., Bushby, R.J., Cammidge, A.N., Martin, P.S. (1995). Glass–forming discotic liquid–crystalline oligomers. Journal of Materials Chemistry, 5, 1857–1860.

Bushby, R.J., Lozman, O.R. (2002). Discotic liquid crystals 25 years on. Current Opinion in Colloid and Interface Science, 7, 343–354.

Bushey, M.L., Nguyen, T.–.Q., Zhang, W., Horoszewski, D., Nuckolls, C. (2004). Die Steuerung der Selbstorganisation vollständig substituierter Arene durch Wasserstoffbrücken. Angewandte Chemie, 116, 5562–5570.

Cammidge, A.N., Gopee, H. (2011). Chemistry of discotic liquid crystals: from monomers to polymers. Liquid Crystals Today, 20(4), 115.

Champagne, P., Ester, D., Aldosari, S., Williams, V.E., Ling, C.C. (2018b). Synthesis and comparison of mesomorphic behaviour of a cholesterol–based liquid crystal dimer and analogous monomers. Liquid Crystal, 45, 1164–1176.

Champagne, P.–.L., Ester, D., Aldosari, S., Williams, V.E., Ling, C.–.C. (2018a). Synthesis and comparison of mesomorphic behaviour of a cholesterol–based liquid crystal dimer and analogous monomers. Liquid Crystal, 45, 1164–1176.

Chang, J.C., Baik, J.H., Lee, C.B., Han, M.J., Hong, S.–.K. (1997). Liquid crystals obtained from disclike mesogenic diacetylenes and their polymerization. Journal of the American Chemical Society, 119, 3197–3198.

Chang, J.Y. (2000). Synthesis and characterization of mesogenic disklike benzenetricarboxylates containing diacetylenic groups and their polymerization. Chemistry of Materials, 12, 1076–1082.

Chang, T.H., Wu, B.R., Chiang, M.Y., Liao, S.C., Ong, C.W., Hsu, H.F., Lin, S.Y. (2005). Synthesis and mesomorphic behavior of a donor–acceptor–type hexaazatriphenylene. Organic Letters, 7, 4078.

Chien, J.C.W., Zhou, R., Lillya, C.P. (1987). Liquid–crystalline compounds and polymers from promesogens. Macromol, 20, 2340–2344.

Christiano, R., Santos, D.M.P.O., Gallardo, H. (2005). Synthesis and characterization of low molecular mass luminescent liquid crystalline materials with 1,3,4 - oxadiazole units. Liquid Crystal, 32, 7–14.

Cooke, G., Radhi, A., Boden, N., Bushby, R.J., Lu, Z., Brown, S., Heath, S.L. (2000). Synthesis and characterisation of tetrathiafulvalenyl– and ferrocenyl–triphenylenes. Tetrahedron, 56, 3385–3390.

Creed, D., Gross, J.R.D., Sullivan, S.L., Griffin, A.C., Hoyle, C.E. (2007). Effect of molecular structure on mesomorphism. 18.1 twin dimers having methylene, ethylene oxide and siloxane spacers. Molecular Crystals and Liquid Crystals, 149, 185–193.

Dantlgraber, G., Diele, S., Tschierske, C. (2002). The first liquid crystalline dimers consisting of two banana–shaped mesogenic units: a new way for switching between ferroelectricity and antiferroelectricity with bent–core molecules. Chemical Communications, 0, 2768–2769.

Date, R.W., Imrie, C.T., Luckhurst, G.R., Seddon, J.M. (2006). Smectogenic dimeric liquid crystals. The preparation and properties of the α,ω–bis(4–n–alkylanilinebenzylidene–4′–oxy)alkanes. Liquid Crystal, 12, 2006, 203–238.

Dehne, H., Roger, A., Demus, D., Diele, S., Kresse, H., Pelzl, G., Wedler, W., Weissflog, W. (1989). Sulphur ligated siamese twin mesogens. Liquid Crystal, 6, 47–62.

Dhar, R., Pandey, A.S., Pandey, M.B., Kumar, S., Dabrowski, R. (2008). Optimization of the display parameters of a room temperature twisted nematic display material (6CHBT) by doping single–wall carbon nanotubes. Applied Physics Express, 1, 121501.

Dia, F.A., Valdebenito, N.M., Tagle, L.H., Aguilera, C. (1994). Synthesis and characterization of twin mesogens containing siloxane units as central spacers. Liquid Crystal, 16, 105–113.

Domenici, V., Conradi, M., Remsˇkar, M., Virsˇek, M., Zupancˇicˇ, B., Mrzel, A., Chambers, M., Zalar, B. (2011). New composite films based on MoO_{3-x} nanowires aligning a liquid single crystal elastomer matrix. Journal of Materials Science, 46, 3639–3645.

Dutt, S., Siril, P.F. (2014). Morphology controlled synthesis of polyaniline nanostructures using swollen liquid crystal templates. Journal of Applied Polymer Science. Doi: 10.1002/APP.40800.

Elemans, J.A.A.W., Rowan, A.E., Nolte, R.J.M. (2003). Mastering molecular matter. Supramolecular architectures by hierarchical self–assembly. Journal of Materials Chemistry, 13, 2661–2670.

Elhaj, M.I.–., Skoulio S, A., Guillon, D., Newton, J., Hodge, P., Coles, H.J. (1995). Structural characterization of linear dimeric and cyclic tetrameric liquid crystalline siloxane derivatives. Liquid Crystal, 19, 373–378.

Emsley, J.W., Luckhurst, G.R., Shilstone, G.N., Sage, I. (2011a). The preparation and properties of the α,ω−bis(4,4′−Cyanobiphenyloxy)alkanes: nematogenic molecules with a flexible core. Molecular Crystals and Liquid Crystals, 102, 223–233.

Emsley, J.W., Luckhurst, G.R., Shilstone, G.N., Sage, I. (2011b). The preparation and properties of the α,ω−bis(4,4′−Cyanobiphenyloxy)alkanes: nematogenic molecules with a flexible core. Molecular Crystals and Liquid Crystals, 102, 223–233.

Fan, F.Y., Culligan, S.W., Mastrangelo, J.C., Katsis, D., Chen, S.H. (2001). Novel glass−forming liquid crystals. 6. High−temperature glassy nematics. Chemistry of Materials, 13, 4584–4594.

Foster, E.J., Babuin, J., Nguyen, N., Williams, V.E. (2004). Synthesis of unsymmetrical dibenzoquinoxaline discotic mesogens. Chemical Communications, 0, 2052–2053.

Gearba, R.I., Anokhin, D.V., Bondar, A.I., Bras, W., Jahr, M., Lehmann, M., Ivanov, D.A. (2007). Homeotropic alignment of columnar liquid crystals in open films by means of surface nanopatterning. Advanced Materials, 19, 815–820.

Gearba, R.I., Bondar, A., Lehmann, M., Goderis, B., Bras, W., Koch, M.H.J., Ivanov, D.A. (2005). Templating crystal growth at the nanometer−scale with a monotropic columnar mesophase. Advanced Materials, 17, 671–676.

Gemming, S., Lehmann, M., Seifert, G. (2005). Semi−flexible star−shaped molecules: conformational analysis of nano−seggregated mesogens forming columnar liquid−crystal phases. Zeitschrift für Metallkunde, 96, 988–997.

Gojny, F.H., Wichmann, M.H.G., Fiedler, B., Schulte, K. (2005). Influence of different carbon nanotubes on the mechanical properties of epoxy matrix composites – a comparative study. Composites Science and Technology, 65, 2300–2313.

Goldmann, D., Janietz, D., Schmidt, C., Wendorff, J.H. (1998). Liquid crystalline 1,3,5−triazines incorporating rod− like azobenzene sub−units. Liquid Crystal, 25, 711–719.

Goodby, J.W. (1991). Chirality in liquid crystals. Journal of Materials Chemistry, 1, 307–318.

Goodby, J.W., Saez, I.M., Cowling, S.J., Gortz, V., Draper, M., Hall, A.W., Sia, S., Cosquer, G., Lee, S.E., Raynes, E.P. (2008). Transmission and amplification of information and properties in nanostructured liquid crystals. Angewandte Chemie – International Edition, 47, 2754–2787.

Gowda, A., Kumar, S. (2018). recent advances in discotic liquid crystal−assisted nanoparticles. Materials, 11, 382.

Gowda, A.N., Kumar, M., Thomas, A.R., Philip, R., Kumar, S. (2016). Self−assembly of silver and gold nanoparticles in a metal−free phthalocyanine liquid crystalline matrix: structural, thermal, electrical and nonlinear optical characterization. Chemistry Select, 1, 1361–1370.

Grafe, A., Janietz, D. (2005). Star−shaped discotic oligomesogens based on radial pentakisphenylethynylbenzene moieties. Chemistry of Materials, 17, 4979–4984.

Grafe, A., Janietz, D., Frese, T., Wendroff, J.H., Meier, H., Lehmann, M., Kolb, U. (2000). Stilbenoid dendrimers. European Journal of Chemistry, 6, 2462–2469.

Gray, G.W. (1979). The Molecular Physics of Liquid Crystals, Chapter 1, Edited by, Luckhurst, G.R., Gray, G.W., London, Academic press.

Griffin, A.C., Buckley, N.W., Hughes, W.E., Wertz, D.L. (1981). Effect of molecular structure on mesomorphism.11.1 A siamese twin liquid crystal having two independently smectogenic conformations. Molecular Crystals and Liquid Crystals, 64, 139–144.

Gupta, S., Singh, D., Manohar, R., Kumar, S. (2016). tuning phase retardation behaviour of nematic liquid crystal using quantum dots. Current Applied Physics, 16, 79–82.

Gupta, S.K., Singh, D.P., Tripathi, P.K., Manohar, R., Varia, M., Sagar, L.K., Kumar, S. (2013). CdSe quantum dot dispersed DOBAMBC: an electrooptical study. Liquid Crystal, 40, 528–533.

Gupta, V.K., Sharma, R.K., Mathews, M., Yelamaggad, C.V. (2009). Crystal structure of bis (cholesteryl)4,4′−(1,2−phenylenebis(oxy))−dibutanoate: an oligomesogen. Liquid Crystal, 36, 339–343.

Han, J., Wang, Z.–.Z., Wu, J.–.R. (2018). Room–temperature fluorescent liquid crystalline dimers based on discotic 1,3,4–oxadizole. Liquid Crystal, 45, 1047–1054.

Hatano, T., Kato, T. (2006). A columnar liquid crystal based on triphenylphosphine oxide – its structural changes upon interaction with alkaline metal cations. Chemical Communications, 1277–1279.

Heeks, S.K., Luckhurst, G.R. (1993). On the molecular organisation within the nematic phase of liquid crystal dimers. Journal of the Chemical Society Faraday Transactions, 89, 3289–3296.

Henderson, P.A., Inkster, R.T., Seddon, J.M., Imrie, C.T. (2001). Highly non–linear liquid crystal tetramers. Journal of Materials Chemistry, 11, 2722–2731.

Hogan, J.L., Imrie, C.T., Luckhurst, G.R. (1988). Asymmetric dimeric liquid crystals the preparation and properties of the α–(4–cyanobiphenyl–4′–oxy)–ω–(4–n–alkylanilinebenzylidene–4′–oxy) hexanes. Liquid Crystal, 3, 645–650.

Hohmuth, A., Schiewe, B., Heinemann, S., Kresse, H. (1997). Dielectric behaviour of two dimeric liquid crystalline siloxanes. Liquid Crystal, 22, 211–215.

Holst, H.C., Pakula, T., Meier, H. (2004). Liquid crystals in the series of 2,4,6–tristyryl–1,3,5–triazines. Tetrahedron, 60, 6765–6775.

Hoshino, H., Jin, J.-.I., Lenz, R.W. (1984). Liquid crystalline behavior of polymeric glycols terminated with aromatic diester and diacid mesogenic groups. Applied Polymer Science, 29, 547–554.

Imrie, C.T., Luckhurst, G.R. (1998). Liquid crystal trimers. The synthesis and characterisation of the4,4′–bis[ω–(4–cyanobiphenyl–4′–yloxy)alkoxy]biphenyls. Journal of Materials Chemistry, 8, 1339–1343.

Imrie, C.T., Stewart, D., Rémy, C., Christie, D.W., Hamley, I.W., Harding, R. (1999). Liquid crystal tetramers. Journal of Materials Chemistry, 9, 2321–2325.

Imrie, C.T., Taylor, L. (1989). The preparation and properties of low molar mass liquid crystals possessing lateral alkyl chains. Liquid Crystal, 6, 1–10.

Ionescu, D., Luckhurst, G.R., De Silva, D.S. (1997). The elastic behaviour of liquid crystal dimers: an ESR investigation of their induced chiral nematic phases. Liquid Crystal, 23(6), 833–843.

Ito, S., Herwig, P.T., Böhme, T., Rabe, J.P., Rettig, W., Müllen, K. (2000). Bishexa–peri–hexabenzocoronenyl: a "Superbiphenyl". Journal of the American Chemical Society, 122, 7698–7706.

Itoh, M., Tokita, M., Adachi, K., Hayakawa, T., Kang, S., Tezuka, Y., Watanabe, J. (2009). Synthesis of macrocyclised dimetric compounds and their liquid crystal transition behaviours. Liquid Crystal, 36, 1443–1450.

Ivanov, D.A., Gearba, R.I., Anokhin, D., Magonov, S., Lehmann, M. (2006). Two–stage Self–assembly of Star–shaped Mesogens in Double Helices. PMSE Preparation, 94, 655–656.

Jensen, G.V., Bremholm, M., Lock, N., Deen, G.R., Jensen, T.R., Iversen, B.B., Niederberger, M., Pedersen, J.S., Birkedal, H. (2010). Anisotropic crystal growth kinetics of anatase TiO_2 nanoparticles synthesized in a nonaqueous medium. Chemistry of Materials: A Publication of the American Chemical Society, 22, 6044–6055.

Jin, J.–.I., Choi, E.–.J., Ryu, S.–.C., Lenz, R.W. (1986). Thermotropic main chain polyesters with polymethylene spacers and their low molecular weight model compounds – odd–even effect of polymethylene spacers. Polymer Journal, 18, 63–70.

Jin, J.–.I., Seong, C.–.M., Jo, B.–.W. (1985). Synthesis and properties of thermotropic compounds with two terminal mesogenic units and a central spacer (Ⅵ). homologous series of –bis[4–(p–substituted benzoyloxy)benzoyloxy]alkanes. Bulletin of the Korean Chemical Society, 6, 40–45.

Jo, B.W., Choi, J.K., Bang, M.S., Chung, B.Y., Jin, J.I. (1992). Dimesogenic compounds consisting of two aromatic ester or amide type mesogenic units having trifluoromethyl substituents at

terminal phenylene rings and a central dimethylenetetramethyldisiloxyl spacer. Chemistry of Materials, 4, 1403–1409.

Jo, B.–.W., Lim, T.–.K., Jin, J.–.I. (1988). Synthesis and thermotropic properties of dimesogenic homologous series containing disiloxyl spacer, di–4– (p–substituted phenoxycarbonyl) phenoxymethyl tetramethyl disiloxanes. Molecular crystals and liquid crystals incorporating nonlinear optics, 157, 57–67.

Karthik, C., Choudhary, K., Joshi, A., Gupta, A., Manjuladevi, V., Gupta, R.K., Kumar, S. (2014). Studies on thin films of hexa–alkoxy triphenylene(HAT5) and composite of HAT5–TiO_2 nanoparticles. Advanced Science Letters, 20, 1138–1142.

Kato, T., Mizoshita, N., Kishimoto, K. (2006a). Functional liquid–crystalline assemblies: self–organized soft materials. Angewandte Chemie – International Edition, 45, 38–68.

Kato, T., Mizoshita, N., Kishimoto, K. (2006b). Functional liquid–crystalline assemblies: self–organized soft Materials. Angewandte Chemie International Edition, 45, 38–68.

Katoh, M., Uehara, S., Kohmoto, S., Kishikawa, K. (2006). Hexagonal columnar superstructure generated by compact liquid–crystalline molecules possessing disk–shape, C_3–symmetry, and ionic bonding sites. Chemistry letters, 35, 322–323.

Kim, B.G., Kim, S., Park, S.Y. (2001). Star–shaped discotic nematic liquid crystal containing 1,3,5–triethynylbenzene and oxadiazole–based rigid arms. Tetrahedron letters, 42, 2697–2699.

Kosata, B., Tamba, G.–.M., Baumeister, U., Pelz, K., Diele, S., Pelzl, G., Galli, G., Samaritani, S., Agina, E.V., Boiko, N.I., Shibaev, V.P., Weissflog, W. (2006). Liquid–crystalline dimers composed of bent–core mesogenic units. Chemistry of Materials, 18, 691–701.

Krishnan, K., Balagurusamy, V.S.K. (2001). A novel dimeric discotic liquid crystal based on anthraquinone. Liquid Crystal, 28, 321–325.

Kuboshita, M., Matsunaga, Y., Matsuzaki, H. (1991). Mesomorphic behavior of 1,2–Phenylene Bis[4–(4–alkoxybenzylideneamino)benzoates. Molecular Crystals and Liquid Crystals, 199, 319–326.

Kumar, J., Manjuladevi, V., Gupta, R.K., Kumar, S. (2015). Effect of octadecylamine functionalized SWCNTs on the elastic constants and electro–optic response of a liquid crystal. Liquid Crystal, 42, 361–369.

Kumar, J., Manjuladevi, V., Gupta, R.K., Kumar, S. (2016). Fast response in TN liquid–crystal cells: effect of functionalised carbon nanotubes. Liquid Crystal, 43, 488–496.

Kumar, M., Gowda, A., Kumar, S. (2017b). Discotic Liquid crystals with graphene: supramolecular self–assembly to applications. Particle and Particle Systems, 34, 1700003.

Kumar, M., Kumar, S. (2015a). Luminescent CdTe quantum dots incarcerated in supramolecular columnar matrix for optoelectronic applications. RSC advances, 5, 1262–1267.

Kumar, M., Kumar, S. (2015b). Stacking of ultra–thin reduced graphene oxide nanoparticles in supramolecular structures for optoelectronic applications. RSC advances, 5, 14871–14878.

Kumar, M., Varshney, S., Gowda, A., Kumar, S. (2017a). Silver nanodisks in soft discotic matrix: impact on self–assembly, conductivity and molecular packing. Journal of Molecular Liquids, 241, 666–674.

Kumar, P.S., Kumar, S., Lakshminarayanan, V. (2008). Electrical conductivity studies on discotic liquid crystal–ferrocenium donor–acceptor system. The journal of physical chemistry. B, 112, 4865–4869.

Kumar, P.S., Pal, S.K., Kumar, S., Lakshminarayanan, V. (2007a). Dispersion of thiol stablized gold nanoparticles in lyotropic liquid crystalline systems. Langmuir, 23, 3445–3449.

Kumar, S. (2005). Triphenylene-based discotic liquid crystal dimers, oligomers and polymers. Liquid Crystal, 32, 1089–1113.

Kumar, S. (2011). Chemistry of Discotic Liquid Crystals: From Monomers to Polymers, Boca Raton, FL, CRC Press, 20. Doi: doi.org/10.1080/1358314X.2011.610139.

Kumar, S. (2014a). Nanoparticles in the supramolecular order of discotic liquid crystals. Liquid Crystal, 41, 353–367.

Kumar, S. (2014b). Discotic liquid crystal–nanoparticle hybrid systems. NPG Asia Materials, 6, e82.

Kumar, S. (2017). Nanoparticles in discotic liquid crystals. In Liquid Crystals with Nano– and Microparticles, World Scientific, Ch. 13, 461–496.

Kumar, S., Bisoyi, H.K. (2007). Aligned carbon nanotubes in the supramolecular order of discotic liquid crystals. Angewandte Chemie – International Edition, 46, 1501–1503.

Kumar, S., Lakshminarayanan, V. (2004). Inclusion of gold nanoparticles into a discotic liquid crystalline matrix. Chemical Communication, 0, 1600–16601.

Kumar, S., Manickam, M. (1999). Preliminary communication First example of a functionalized triphenylene discotic trimer: molecular engineering of advanced materials. Liquid Crystal, 26, 939–941.

Kumar, S., Pal, S.K., Kumar, P.S., Lakshminarayanan, V. (2007b). Novel conducting nanocomposites: synthesis of triphenylene–covered gold nanoparticles and their insertion into a columnar matrix. Soft Matter, 2, 896–900.

Kumar, S., Pal, S.K., Lakshminarayanan, V. (2005). Discotic–decorated gold nanoparticles. Molecular Crystals and Liquid Crystals, 434, 251–258.

Kumar, S., Sagar, L.K. (2011). CdSe quantum dots in a columnar matrix. Chemical Communications, 47, 12182–12184.

Kumar, S., Schuhmacher, P., Henderson, P., Rego, J., Ringsdorf, H. (1996). Synthesis of new functionalized discotic liquid crystals for photoconducting applications. Molecular Crystals and Liquid Crystals, 288, 211–222.

Lai, L.–.L., Hsu, S.–.J., Hsu, H.–.C., Wang, S.–.W., Cheng, K.–.L., Chen, C.–.J., Wang, T.–.H., Hsu, H.–.F. (2012a). Formation of columnar liquid crystals on the basis of unconventionaltriazine–based dendrimers by the C3–symmetric approach. European Journal of Chemistry, 18, 6542–6547.

Lai, L.–.L., Lee, C.–.H., Wang, L.–.Y., Cheng, K.–.L., Hsu, H.–.F. (2008). Star–shaped mesogens of triazine–based dendrons and dendrimers as unconventional columnar liquid crystals. Journal of Organic Chemistry, 73, 485–490.

Lai, L.–.L., Wang, S.–.W., Cheng, K.–.L., Lee, J.–.J., Wang, T.–.H., Hsu, H.–.F. (2012b). Induction of the columnar phase of unconventional dendrimers by breaking the C_2 symmetry of molecules. European Journal of Chemistry, 18, 15361–15367.

Lattermann, G. (1987). First examples of a new class of discogen. Liquid Crystal, 2, 723–728.

Lee, C.–.H., Yamamoto, T. (2002). Synthesis of liquid–crystalline, highly luminescent π–conjugated 1,3,5–triazine derivatives by palladium–catalyzed cross–coupling reaction. Molecular Crystals and Liquid Crystals, 378, 13–21.

Lee, J.–.W., Piao, X.L., Yun, Y.–.K., Jin, J.–.I., Kang, Y.–.S., Zin, W.–.C. (1999). Synthesis and liquid crystalline properties of T–shaped dimesogenic compounds. Liquid Crystal, 26, 1671–1685.

Lee, K.H., Lee, J.W., Jin, J.–.I. (2001). Liquid crystalline compounds having a tribranched structure: substituted malonic esters consisting of two Schiff's base units and a cholesteryloxyalkyl substituent. Liquid Crystal, 28, 1519–1525.

Lehmann, M., Gearba, R.I., Koch, M.H.J., Ivanov, D. (2004a). Semiflexible star–shaped mesogens as nonconventional columnar liquid crystals. Chemistry of Materials, 16, 374–376.

Lehmann, M., Gearba, R.I., Koch, M.H.J., Ivanov, D. (2004b). New Star–shaped mesogens with three different arms on a 1,3,5–benzene core. Molecular Crystals and Liquid Crystals, 411, 397–406.

Lehmann, M., Gearba, R.I., Koch, M.H.J., Ivanov, D.A. (2004c). Semiflexible star–shaped mesogens as nonconventional columnar liquid crystals. Chemistry of Materials, 16, 374–376.

Lehmann, M., Jahr, M., Sffer, T.R., Lang, H. (2007). Synthesis and solid–state structure of a star–shaped oligobenzoate. Zeitschrift fur Naturforschung. Teil B: Chemie, Biochemie, Biophysik, Biologie, 62, 988–994.

Lehmann, M., Kçhn, C., Meier, H., Renker, S., Oehlhof, A. (2006). Supramolecular order of stilbenoid dendrons: importance of weak interactions. Journal of Materials Chemistry, 16, 441–451.

Lehmann, M., Schartel, B., Hennecke, M., Meier, H. (1999). Dendrimers consisting of stilbene or distyrylbenzene building blocks synthesis and stability. Tetrahedron, 55, 13377–13394.

Levelut, A.M., Morija, K. (1996). Structure of the liquid crystalline state in hexakis (4–(4′–alkyloxy)biphenoxy)cyclotriphosphazenes. Liquid Crystal, 20, 119–124.

Lin, Y.–.C., Lai, C.K., Chang, Y.–.C., Liu, K.–.T. (2002). Liquid Crystal, 29, 237–242.

Liufu, S.C., Xiao, H.N., Li, Y.P. (2005). Thermal analysis and degradation mechanism of polyacrylate/ZnO nanocomposites. Polymer Degradation and Stability, 87, 103–110.

Luckhurst, R.G. (1995). Liquid crystal dimers and oligomers: experiment and theory. Molecular Symposia, 96, 1–26.

Mahlstedt, S., Janietz, D., Schmidt, C., Stracke, A., Wendorff, J.H. (1999). Novel donor–acceptor triple mesogens incorporating disc–like and rod–like molecular sub–units. Liquid Crystal, 26, 1359–1369.

Maliszewskyj, N.C., Heiney, P.A., Josefowicz, J.Y., Plesnivy, T., Ringsdorf, H., Schuhmacher, P. (1995). Structure of Langmuir–Blodgett Films of Star–Shaped Oligomeric Discogens. Langmuir, 11, 1666–1674.

Malpezzi, L., Brückner, S., Galbiati, E., Luckhurst, G.R. (1991). The Structure of α,ω–bis(4–cyanobiphenyl–4′–oxy)heptane. Molecular Crystals and Liquid Crystals, 195, 179–184.

Malpezzi, L., Brückner, S., Galbiati, E., Luckhurst, G.R. (2006). The Structure of α,ω–bis(4–cyanobiphenyl–4′–oxy)heptane. Molecular Crystals and Liquid Crystals, 195, 179–184.

Manickam, M., Belloni, M., Kumar, S., Varshney, S.K., Rao, D.S.S., Ashton, P.R., Preece, J.A., Spencer, N. (2001). The first hexagonal columnar discotic liquid crystalline carbazole derivatives induced by noncovalent π–π interactions. Journal of Materials Chemistry, 11, 2790–2800.

Manickam, M., Kumar, S., Preece, J.A., Spencer, N. (2000). The first hexagonal columnar discotic liquid crystalline carbazole derivative. Liquid Crystal, 27, 703–706.

Manjuladevi, V., Gupta, R.K., Kumar, S. (2012). Effect of functionalized carbon nanotube on electro–optic and dielectric properties of a liquid crystal. Journal of Molecular Liquids, 171, 60–63.

Matsuzaki, H., Matsunaga, Y. (1993). New mesogenic compounds with unconventional molecular structures 1,2–Phenylene and 2,3–naphthylene bis[4–(4–alkoxyphenyliminomethyl) benzoates] and related compounds. Liquid Crystal, 14, 105–120.

McKenna, M.D., Barbera, J., Marcos, M., Serrano, J.L. (2005). Discotic liquid crystalline poly(propylene imine) dendrimers based on triphenylene. Journal of the American Chemical Society, 127, 619–625.

Meier, H. (1992). Die Photochemie stilbenoider Verbindungen und ihre materialwissenschaftlichen Aspekte. Angewandte Chemie, 104, 1425–1576.

Meier, H., Karpouk, E., Lehmann, M., Schollmeyer, D., Enkelmann, V. (2003). Guest–host systems of 1,3,5–tristyrylbenzenes. Zeitschrift fur Naturforschung. Teil B: Chemie, Biochemie, Biophysik, Biologie, 58, 775–781.

Meier, H., Lehmann, M. (1998). Stilbenoide dendrimere. Angewandte Chemie, 110, 666–669.

Meier, H., Lehmann, M., Holst, H.C., Schwçppe, D. (2004). Star–shaped conjugated compounds forming nematic discotic systems. Tetrahedron, 60, 6881–6888.

Meier, H., Lehmann, M., Kolb, U. (2000). Stilbenoid dendrimers. European Journal of Chemistry, 6, 2462–2469.

Mishra, M., Kumar, S., Dhar, R. (2014). Effect of the dispersed colloidal gold nano particles on the electrical properties of a columnar discotic liquid crystal. RSC advances, 4, 62404–62412.

Mishra, M., Kumar, S., Dhar, R. (2017). Effect of high concentration of colloidal gold nanoparticles on the thermodynamic, optical and electrical properties of 2, 3, 6, 7, 10, 11– hexabutyloxytryphenylene discotic liquid crystalline material. Soft mater, 15, 34–44.

Mishraa, M., Kumar, S., Dhar, R. (2016). Gold nanoparticles in plastic columnar discotic liquid crystalline Material. Thermochimica Acta, 631, 59–70.

Moriya, K., Kawanishi, Y., Yano, S., Kajiwara, M. (2000). Mesomorphic phase transition of a cyclotetraphosphazene containing Schiffbase moieties: comparison with the corresponding cyclotriphosphazene. Chemical Communications, 0, 1111–1112.

Nagaraju, G., Ashoka, S., Chithaiah, P., Tharamani, C.N., Chandrappa, G.T. (2010). Surfactant free hydrothermally derived ZnO nanowires, nanorods, microrods andtheir characterization. Materials Science in Semiconductor Processing, 13, 21–28.

Nierengarten, J.–.F. (2004). Chemical modification of C_{60} for materials science applications. New Journal of Chemistry, 28, 1177–1191.

Nishiyama, I., Ishizuka, H., Yoshizawa, A. (1993). Strong helical structures produced by dimeric liquid crystals possessing the chiral centre in the central region of the molecular structure. Ferroelect, 147, 193–204.

Okumuş, M. (2018). Synthesis and characterization of hydrogen–bonded liquid crystal complexes by 4–octyloxy benzoic acid and some dicarboxylic acids. Journal of Molecular Liquids, 266(15), 529–534.

Omenat, A., BarberW, J., Serrano, J.–.L., Houbrechts, S., Persoons, A. (1999). Columnar liquid crystals with highly polar groups: evaluation of the nonlinear optical properties. Advanced Materials, 11, 1292–1295.

Chi Wi Ong, Ya–Chi Chan, Ming–Che Yeh, Hsin–Ying Lin and Hsiu–Fu Hsu. (2013). Lamellar organization of discotic dimer enforced by steric manipulation. RSC advances, 3, 8657–8659.

Ong, C.W., Liao, S.C., Chang, T.H., Hsu, H.F. (2004). In Situ Synthesis of Hexakis(alkoxy) diquinoxalino[2,3–a:2',3'–c]phenazines: Mesogenic Phase Transition of the Electron–Deficient Discotic Compounds. Journal of Organic Chemistry, 69, 3181–3185.

Ooi, Y.–.H., Yeap, G.–.Y. (2018). λ–Shaped liquid crystal trimers with dual terminal cholesteryl moieties: synthesis and concomitant of N*, SmA and cholesteric glassy phases. Liquid Crystal, 45(2), 204–218.

Pal, S.K., Kumar, S.. Publisher: Cambridge University Press, ISBN: 9781316662120, 2017, doi.org/10.1017/9781316662120.

Pal, S.K., Raghunathan, V.A., Kumar, S. (2007). Phase transitions in novel disulphide-bridged alkoxycyanobiphenyl dimers. Liquid Crystal, 34, 135–141.

Pandey, A., Dhar, R., Kumar, S., Dabrawski, R. (2011). Enhancement of the display parameters of 4'–pentyl–4–cyanobiphenyl (5CB) due to the dispersion of functionalized Gold Nano Particles. Liquid Crystal, 38, 115–120.

Pandey, S., Singh, D.P., Agrahari, K., Srivastava, A., Czerwinski, M., Kumar, S., Manohar, R. (2017). CdTe quantum dot dispersed ferroelectric liquid crystal: Transient memory with faster optical response and quenching of photoluminescence. Journal of Molecular Liquids, 237, 71–80.

Parashiv, I., Giesbers, M., Van Lagen, B., Grozema, F.C., Abellon, R.D., Siebbeles, L.D.A., Marcelis, A.T.M., Zuilhof, H., Sudholter, E.J.R. (2006). H–Bond–stabilized triphenylene–based columnar discotic liquid crystals.. Chemistry of Materials, 18, 968–974.

Percec, V., Cho, C.G., Pugh, C., Tomazos, D. (1992). Synthesis and characterization of branched liquid–crystalline polyethers containing cyclotetraveratrylene–based disk–like mesogens. Macromol, 25, 1164–1176.

Percec, V., Glodde, M., Bera, T.K., Miura, Y., Shiyanovskaya, I., Singer, K.D., Balagurusamy, V.S.K., Heiney, P.A., Schnell, I., Rapp, A., Spiess, H.W., Hudson, S.D., Duan, H. (2002). Self–organization of supramolecular helical dendrimers into complex electronic materials. Nature, 417, 384–387.

Percec, V., Glodde, M., Peterca, M., Rapp, A., Schnell, I., Spiess, H.W., Bera, T.K., Miura, Y., Balagurusamy, V.S., Aqad, E., Heiney, P.A. (2006). Self–assembly of semifluorinated dendrons attached to electron–donor groups mediates their p–stacking via a helical pyramidal column. European Journal of Chemistry, 12, 6298–6314.

Pesak, D.J., Moore, J.S. (1997). Designing a solid catalyst for the selective low–temperature oxidation of cyclohexane to cyclohexanone. Angewandte Chemie, 109, 1709–1712.

Plate, N.A. (1993). Chemistry of Liquid Crystal Polymers, New York, Plenum Press, ISBN 978–1–4899–1105–6. Doi: 10.1007/978–1–4899–1103–2.

Plesnivy, T., Ringsdorf, H., Schuhmacher, P., Nuttz, U., Diele, S. (1995). Star–like discotic liquid crystals. Liquid Crystal, 18(2), 185–190.

Poths, H., Wischerhoff, E., Zentel, R., Schönfeld, A., Henn, G., Kremer, F. (1995). From monomeric to polymeric ferroelectric liquid crystals A comparative study of ferroelectric properties. Liquid Crystal, 18, 1995, 811–818.

Praefcke, K., Kohne, B., Singer, D., Demus, D., Pelzl, G., Diele, S. (1990). Thermotropic biaxial nematic phases with negative optical character [1]. Liquid Crystal, 7, 589–594.

Radhika, S., Sadashiva, B.K., Raghunathan, V.A. (2013). A polar novel mesogenic symmetric dimers composed of five-ring bent–core monomeric units. Liquid Crystal, 40, 1209–1222.

Rahman, M.L., Biswas, T.K., Sarkar, S.M., Yusoff, M.M., Maleka, M.N.F.A., Tschierske, C. (2015). New U–shaped liquid crystals azobenzene derived from catechol for photoswitching properties. Journal of Molecular Liquids, 202, 125–133.

Rahman, M.L., Biswas, T.K., Sarkar, S.M., Yusoff, M.M., Yuvaraj, A.R., Kumar, S. (2016). Synthesis of new liquid crystals embedded gold nanoparticles for photoswitching properties. Journal of Colloid and Interface Science, 478, 384–393.

Robinson, W.K., Carboni, C., Kloess, P., Perkins, S.P., Coles, H.J. (1998). Ferroelectric and antiferroelectric low molar mass organosiloxane liquid crystals. Liquid Crystal, 25, 301–307.

Saez, I.M., Goodby, J.W. (2003). Design and properties of "Janus–like" supermolecular liquid crystals. Chemical Communication, 0, 1726–1727.

Saez, I.M., Goodby, J.W. (2005). Supermolecular liquid crystals. Journal of Materials Chemistry, 15, 26–40.

Sasaki, H., Takanishi, Y., Yamamoto, J., Yoshizawa, A. (2017). Achiral flexible liquid crystal trimers exhibiting gyroid–like surfaces in chiral conglomerate phases. Soft Materials, 13, 6521–6528.

Sasaki, H., Takanishi, Y., Yamamoto, J., Yoshizawa, A. (2018). Photo-driven chirality switching in a dark conglomerate phase of an achiral liquid crystal trimer. Chemical Senses, 3, 3278–3283.

Sentman, A.C., Gin, D.L. (2001). Fluorescent trimeric liquid crystals: modular design of emissive mesogens. Advanced Materials, 13, 1398–1401.

Setoguchi, Y., Monobe, H., Wan, W., Terasawa, N., Kiyohara, K., Nakamura, N., Shimizu, Y. (2003). Infrared studies on hydrogen–bond interaction in a homologues series of triphenylene discotic liquid crystals having carboxylic acids at the peripheral chains. Thin Solid Films, 438–439, 407–413.

Shanker, G., Prehm, M., Tschierske, C. (2012). Laterally connected bent–core dimers and bent–core–rod couples with nematic liquid crystalline phases. Journal of Materials Chemistry, 22, 168–174.

Shukla, R.K., Evans, D.R., Haase, W. (2016). Ferroelectric $BaTiO_3$ and $LiNbO_3$ nanoparticles dispersed in ferroelectric liquid crystal mixtures: Electrooptic and dielectric parameters influenced by properties of the host, the dopant and the measuring cell. Ferroelect, 500, 141–152.

Simpson, C.D., Wu, J., Watson, M.D., Mü̈llen, K. (2004). Synthesis and X–ray single crystal structure of a bivalent glycocluster. Chemical Communications, 0, 494–495.

Singh, D.P., Boussoualem, Y., Duponchel, B., Hadj, S.A., Kumar, S., Manohar, R., Daoudi, A. (2017b). Pico–ampere current sensitivity and CdSe quantum dots assembly assisted charge transport in ferroelectric liquid crystal. Journal of Physics D, 50, 325301.

Singh, D.P., Gupta, S.K., Manohar, R., Varia, M.C., Kumar, S., Kumar, A. (2014b). Effect of cadmium selenide quantum dots on the dielectric and physical parameters of ferroelectric liquid crystal. International Journal of Applied Physics, 116, 034106.

Singh, D.P., Gupta, S.K., Pandey, S., Varia, P.T.M., Kumar, S., Manohar, R. (2015). Influence of CdSe quantum dot on molecular/ ionic relaxation phenomena and change in physical parameters of ferroelectric liquid crystal. Liquid Crystal, 42, 1159–1168.

Singh, D.P., Gupta, S.K., Tripathi, P. M.C, Varia, S.K., Manohar, R. (2014c). Reduced ionic contaminations in CdSe quantum dot dispersed ferroelectric liquid crystal and its applications. Liquid Crystal, 41, 1356–1365.

Singh, D.P., Pandey, S., Manohar, R., Kumar, S., Pujar, G.H., Inamdar, S.R. (2017a). Time–resolved fluorescence and absence of förster resonance energy transfer in ferroelectric liquid crystal–quantum dots composites. Journal of Luminescence, 190, 161–170.

Singh, D.P., Visvanathan, R., Duncan, A.E., Duponchel, B., Boussoualem, Y., Kumar, S., Clark, N.A., Blach, J.–.F., Douali, R., Daoudi, A. (2018). CdSe quantum dots in chiral smectic C matrix: experimental evidence of smectic layer distortion by small and wide angle X–ray scattering and subsequent effect on electro–optical parameters. Liquid Crystal, In press.

Singh, U.B., Dhar, R., Pandey, A., Kumar, S., Dąbrowski, R., Pandey, M. (2014a). Electro–optical and dielectric properties of CdSe quantum dots and 6CHBT liquid crystals composites. AIP Advances, 4, Article Number: 117112.

Singh, U.B., Pandey, M.B., Dhar, R., Verma, R., Kumar, S. (2016). Effect of dispersion of CdSe quantum dots on phase transition, electrical and electro–optical properties of 4PP4OB. Liquid Crystal, 43, 1075–1082.

Singh, U.B., Singh, D., Kumar, S., Dhar, R., Pandey, M.B. (2017c). The optical properties of quantum dots in anisotropic media. Journal of Molecular Liquids, 241, 1009–1012.

Supreet, R.P., Kumar, S., Raina, K.K. (2014). Effect of dispersion of gold nanoparticles on the optical and electrical properties of discotic liquid crystal. Liquid Crystal, 41, 933–939.

Supreet, S.K., Raina, K.K., Pratibha, R. (2013). Enhanced stability of the columnar matrix in a discotic liquid crystal by insertion of ZnO nanoparticles. Liquid Crystal, 40, 228–236.

Takashi, K., Hajime, A., Akira, F., Jean, F.M.J. (1992). Self–assembly of liquid crystalline complexes having angular structures through intermolecular hydrogen–bonding. Chemistry letters, 21, 265–268.

Takenaka, S., Masuda, Y., Iwano, M., Morita, H., Kusabayashi, S., Sigiura, H., Ikemoto, T. (1989). Thermal Properties of 4–Alkoxyphenyl 3,4–Di(4–alkoxybenzoyloxy)benzoates. Molecular Crystals and Liquid Crystals, 168, 111–124.

Takenaka, S., Nishimura, K., Kusabayashi, S. (1984). The discotic mesophases of 1,3,5–trisubstituted benzenes. Molecular Crystals and Liquid Crystals, 111, 227–236.

Tian, M., Zhang, B.–.Y., Cong, Y.–.H., He, X.–.Z., Chu, H.–.S., Zhang, X.–.Y. (2010). Bipolar carrier transport in tri–substituted octyloxy–truxene DLC. Liquid Crystal, 545, 1373–1379.

Tomczyk, J., Sobolewska, A., Nagy, Z.T., Guillon, D., Stumpe, B.D.J. (2013). Photo– and thermal–processing of azobenzene–containing star–shaped liquid crystals. Journal of Materials Chemistry C, 1, 924–932.

Topnani, N., Hamplová, V., Kašpar, M., Novotná, V., Gorecka, E. (2014). Synthesis, characterisation and functionalisation of ZnO and TiO_2 nanostructures: used as dopants in liquid crystal polymers. Liquid Crystal, 41, 91–100.

Tripathi, P., Mishra, M., Kumar, S., Dabrowski, R., Dhar, R. (2018). Dependence of physical parameters on the size of silver nano particles forming composites with a nematic liquid crystalline material. Journal of Molecular Liquids, 268, 403–409.

Tripathi, P., Mishra, M., Kumar, S., Dhar., R. (2017). Thermodynamic study of a plastic columnar discotic material 2, 3, 6, 7, 10, 11 hexabutyloxytriphenylene dispersed with gold nanoparticles under elevated pressure. Journal of Thermal Analysis and Calorimetry, 129, 315–322.

Tschierske, C. (2001a). Micro–segregation, molecular shape and molecular topology –partners for the design of liquid crystalline materials with complex mesophase morphologies. Journal of Materials Chemistry, 11, 2647–2671.

Tschierske, C. (2001b). Non–conventional soft matter. Annual Reports on the Progress of Chemistry Section C, 97, 191–267.

Tschierske, C. (2001c). Non–conventional soft matter. Annual Reports on the Progress of Chemistry. Section C: Physical Chemistry, 97, 191–267.

Tschierske, C. (2002). Liquid crystalline materials with complex mesophase morphologies. Current Opinion in Colloid and Interface Science, 7, 69–80.

Tschierske, C. (2007). Liquid crystal engineering – new complex mesophase structures and their relations to polymer morphologies, nanoscale patterning and crystal. Chemical Society Reviews, 36, 1930–1970.

Tzeng, M.–.C., Liao, S.–.C., Chang, T.–.H., Yang, S.–.C., Weng, M.–.W., Yang, H.–.C., Chiang, M.Y., Kai, Z., Wu, J., Ong, C.W. (2011). Enforced liquid crystalline properties of dibenzo[a,c] phenazine dimer and self–assembly. Journal of Materials Chemistry, 21, 1704–1712.

Ungar, G., Liu, Y., Zeng, X., Percec, V., Cho, W.–.D. (2003). Giant Supramolecular Liquid Crystal Lattice. Science, 299, 1208–1211.

Ungar, G., Zeng, X. (2005). Frank–Kasper, quasicrystalline and related phases in liquid crystals. Soft Materials, 1, 95–106.

Van De Craats, A.M., Siebbeles, L.D.A., Bleyl, I., Haarer, D., Berlin, Y.A., Zharikov, A.A., Warman, J.M. (1998). Mechanism of charge transport along columnar stacks of a triphenylene dimer. The journal of physical chemistry. B, 102, 9625–9634.

Van Gorp, J.J., Vekemans, J.A.J.M., Meijer, E.W. (2002). C_3–symmetrical supramolecular architectures: fibers and organic gels from discotic trisamides and trisureas. Journal of the American Chemical Society, 124, 14759–14769.

Van Gorp, J.J., Vekemans, J.A.J.M., Meijer, E.W. (2003). Supramolecular architectures of C_3 – symmetrical and asymmetrical discotics. Molecular Crystals and Liquid Crystals, 397, 191–205.

Varshney, S., Kumar, M., Gowda, A., Kumar, S. (2017). Soft discotic matrix with 0–D silver nanoparticles: impact on molecular ordering and conductivity. Journal of Molecular Liquids, 238, 290–295.

Vijayaraghavan, D., Kumar, S. (2009). Self–assembled superlattices of gold nanoparticles in a discotic liquid crystal. Molecular Crystals and Liquid Crystals, 508, 101–114.

Vimal, T., Gupta, S.K., Katiyar, R., Srivastava, A., Czerwinski, M., Krup, K., Kumar, S., Manohar, R. (2017). Effect of metallic silver nanoparticles on the alignment and relaxation behaviour of liquid crystalline material in smectic C* phase. International Journal of Applied Physics, 122, 114102.

Vora, R.A., Teckchandani, V.R. (2006). Cholesteryl Dicarbonates with Rigid and Flexible Spacers. Molecular Crystals and Liquid Crystals, 209, 285–289.

Vorländer, D., Apel, A. (1932). Die Richtung der Kohlenstoff-Valenzen in Benzolabkömmlingen (II.). Chemische Berichte, 65, 1101–1109.

Walker, R., Pociecha, D., Abberley, J.P., Felipe, A.M.–., Paterson, D.A., Forsyth, E., Lawrence, G.B., Henderson, P.A., Storey, J.M.D., Gorecka, E., Imrie, C.T. (2018). Spontaneous chirality through mixing achiral components: a twist–bend nematic phase driven by hydrogen–bonding between unlike components. Chemical Communication, 54, 3383–3386.

Wan, W., Monobe, H., Sugino, T., Tanaka, Y., Shimizu, Y. (2001). Mesomorphic properties and hydrogen–bonding formation of asymmetrical triphenylene discotic liquid crystals. Molecular Crystals and Liquid Crystals, 364, 597–603.

Wang, Y., Singh, G., Agra–Kooijman, D.M., Gao, M., Bisoyi, H.K., Xue, C., Fisch, M.R., Kumar, S., Li, Q. (2015). Room temperature heliconical twist–bend nematic liquid crystal. CrystEngComm, 17, 2778–2782.

Weissflog, W., Demus, D., Diele, S. (1990). From laterally branched mesogens to novel twin molecules. Part II. Molecular Crystals and Liquid Crystal Incorporating Nonlinear Optics, 191, 9–15.

Yadav, N., Kumar, S., Dhar, R. (2015). Cadmium selenide quantum dots to ameliorate the properties of a room temperature discotic liquid crystalline material. RSC Advances, 5, 78823–78832.

Yaduvanshi, P., Kumar, S., Dhar, R. (2015). Effects of copper nanoparticles on the thermodynamic, electrical and optical properties of a disc–shaped liquid crystalline material showing columnar phase. Phase Transitions, 88, 489–502.

Yaduvanshi, P., Mishra, A., Kumar, S., Dhar, R. (2015a). Enhancement of the thermodynamic, electrical and optical properties of hexabutyloxytriphenylene due to copper nanoparticles. Journal of Molecular Liquids, 208, 160–164.

Yaduvanshi, P., Mishra, A., Kumar, S., Dhar, R. (2015b). Effect of silver nano particles on frequency and temperature dependent electrical parameters of a discotic liquid crystalline material. Liquid Crystal, 42, 1478–1489.

Yanic, S.M., Guzeller, D., Ocak, H., Cakar, F., Erol, I., Cankurtaran, O., Eran, B.B. (2015). Synthesis, preparation, and characterization of liquid crystal/organo–montmorillonite nanocomposites. Molecular Crystals and Liquid Crystals, 607, 23–31.

Yelamaggad, C.V., Hiremath, U.S., Rao, D.S.S., Prasad, S.K. (2000). A novel calamitic liquid crystalline oligomer composed of three non–identical mesogenic entities: synthesis and characterization. Chemical Communication, 0, 57–58.

Yelamaggad, C.V., Nagamani, S.A., Hiremath, U.S., Rao, D.S.S., Prasad, S.K. (2001). Unsymmetrical trimesogens exhibiting the undulated twist grain boundary (UTGBC*) mesophase. Liquid Crystal, 28, 1581–1583.

Yelamaggad, C.V., Nagamani, S.A., Hiremath, U.S., Rao, D.S.S., Prasad, S.K. (2002). The first examples of monodispersive liquid crystalline tetramers possessing four non–identical anisometric segments. Liquid Crystal, 29, 231–236.

Yoshizawa, A., Kato, H. (2018). Coexistence of nematic and chiral nematic phases of an achiral liquid crystal trimer possessing an octafluorobiphenyl unit. Liquid Crystal, 45, 2018, 1443–1450.

Yuvaraj, A.R., Kumar, S. (2018). Writing with light: recent advances in optical storage property of azobenzene derivatives. General Chemistry, 4, 170020.

Yuvaraj, A.R., Mei, G.S., Kulkarni, A.D., Yusoff, M.M., Hegde, G. (2014). Aliphatic/aromatic spacers based azo dye dimers: synthesis and application for optical storage devices. RSC advances, 4, 50811–50818.

Yuvaraj, A.R., Rahman, M.L., Yusoff, M.M., Kumar, S. (2017). Photo–induced characteristics of azobenzene based gold nanoparticles. Micro and Nano Letters, 12, 201–204.

Zamir, S., Poupko, R., Luz, Z., Hueser, B., Boeffel, C., Zimmermann, H. (1994). Molecular ordering and dynamics in the columnar mesophase of a new dimeric discotic liquid crystal as studied by x–ray diffraction and deuterium NMR. Journal of the American Chemical Society, 116, 1973–1980.

Zeng, X., Ungar, G., Liu, Y., Percec, V., Dulcey, A., Hobbs, J.K. (2004). Supramolecular dendritic liquid quasicrystals. Nature, 428, 157–160.

Zerban, G., Meier, H. (1993). Synthesis, liquid crystals and photochemistry of di– and tristyrylbenzeneswith alkoxy side chains. Zeitschrift fur Naturforschung. Teil B: Chemie, Biochemie, Biophysik, Biologie, 48, 171–184.

Zhang, B.–.Y., Yao, D.–.S., Meng, F.–.B., Li., Y.–.H. (2005). Structure and properties of novel three–armed star–shaped liquid crystals. Journal of Molecular Structure, 741, 135–140.

Zhang, L.–.Y., Zhang, Q.–.K., Zhang, Y.–.D. (2013). Design, synthesis, and characterisation of symmetrical bent–core liquid crystalline dimers with diacetylene spacer. Liquid Crystal, 40, 1263–1273.

Abhishek Kumar Srivastava, Valerii V. Vashchenko

3 Ferroelectric liquid crystals and their application in modern displays and photonic devices

3.1 Introduction

Recent trend in the display and photonic industries demands for the high-speed electro-optical modulation of the light in the form of amplitude, phase, or both of the impinging light (Coe-Sullivan, 2016; Colegrove, 2018; Gardiner et al., 2011; Lagerwall, 2004; Lee et al., 2008; Ming and Chen et al., 2017; Okaichi et al., 2018; Wei et al., 2012; Xu et al., 2012). A fast electro-optical amplitude modulation is highly desirable for the efficient field-sequential color displays, augmented reality/virtual reality headset, three-dimensional (3D) cinema, and so on, whereas the fast optical phase modulation is required for the holographic displays, photonics, telecommunications, and optical switches. The fast phase modulation is also important for the field-sequential color displays, where the display power consumption can be reduced by at least 3 times (Gardiner et al., 2011; Lagerwall, 2004; Xu et al., 2012). The response time is the most important requirement for these devices; in addition, the small driving voltage is very important, particularly for high-resolution devices (Srivastava et al., 2012a). In this respect, the ferroelectric liquid crystals (FLCs) can be a great option. The presence of the spontaneous polarization reveals the fast response time even at smaller driving voltages; hence, FLCs have been explored thoroughly (Hegde et al., 2008). There are several ways to realize the electro-optical modulations using FLCs; most of them are summarized in this chapter in terms of chemical and physical peculiarities. The main objective of this chapter is to provide the basic understanding of FLC and to summarize the recent material and device developments.

The appearance and nature of ferroelectricity in liquid crystals (LCs) are bit different from solids. The consideration of the symmetry arguments in solids can depict whether the material will be ferroelectric or not. However, for most of the LCs, the situation is bit more complex because of the allowance of the director sign reversal. The most common LC phases such as nematics (N) and smectics (SmA, SmC, etc.) are not compatible for the existence of the spontaneous polarization vector (p). However, the symmetry plane for the SmC phase composed of the chiral molecule (SmC*) vanishes; therefore, it could show the spontaneous polarization in the pres-

ence of strong boundary conditions (Abdulhalim and Moddel, 1991; Beresnev et al., 1988; Chigrinov, 1999; Clark and Lagerwall, 1980; Hegde et al., 2008; Lagerwall, 2004; Lagerwall and Dahl, 1984; Meyer, 1974; Meyer et al., 1975; Srivastava et al., 2012a). Meyer in 1974 had first realized this fact, and afterward the first FLC, that is, chiral compound p-decyloxybenzylidene-p′-amino-2-methylbutylcinnamate DOBAMBC, was synthesized in 1975 (Meyer, 1974). Later on, Lagerwall and Dahl (1984), based on Neumann's principles, have illustrated how the symmetry consideration of the polarization vector (p) for the chiral smectic C phase leads to ferroelectricity.

In SmC⋆ phase, the symmetry group reduces to C_2; hence, it is possible for a macroscopic polarization to exist along the C_2 axis, that is, along the direction of twofold rotation axis. In other words, the macroscopic polarization vector appears in a direction perpendicular to the director $\hat{n}$. For more details about the discussion, see Lagerwall (2004). The polarization depends linearly on the electric field, that is, $P \sim E$, which means that it changes the sign if we reverse the sign of the field. When E is reduced to zero, the polarization vanishes. For very strong fields, the polarization saturates and eventually the material shows the dielectric breakdown, and the saturated polarization is termed as the spontaneous polarization (P_s) (Abdulhalim and Moddel, 1991; Beresnev et al., 1988; Chigrinov, 1999; Clark and Lagerwall, 1980; Hegde et al., 2008; Lagerwall, 2004; Lagerwall and Dahl, 1984; Meyer, 1974; Meyer et al., 1975; Srivastava et al., 2012a).

Though to make SmC⋆ phase, one can compose it solely from the chiral molecules. But in principle, it is also sufficient if only part of the material is chiral (also known as chiral dopants or chiral guest), while the other part can be non-chiral SmC LCs (non-chiral host). It is worth to mention that these chiral dopants with spontaneous polarization often induce the helix. Although these two properties (Ps and helix) originate from the same phenomena of chirality, they may exist independently. Thus, the customized mixtures show the ferroelectric properties independent of whether there is any observable helix or not. The chiral dopants and their role in various electro-optical modes of the resultant FLCs are discussed later in this chapter.

FLCs show very fast electro-optical modulation because of the presence of the spontaneous polarization. The dynamical equation for FLCs, in the presence of electric field (E), can be given as follows:

$$\Gamma_{\text{Viscous}} = \Gamma_{\text{Dielectric}} + \Gamma_{\text{Elastic}} - \Gamma_{\text{Polarization}} \tag{3.1}$$

This can be reduced to

$$\gamma_\varphi \frac{d\varphi}{dt} = \frac{1}{2}\varepsilon_0\,\Delta\varepsilon E^2\,\sin^2\theta\,\sin 2\varphi + K\nabla^2\varphi - PE\,\sin\varphi \tag{3.2}$$

where y_φ is the rotational viscosity, ε_0 is the permittivity of the vacuum, $\Delta\varepsilon$ is the dielectric anisotropy, θ is the tilt angle, P is the polarization, and φ is the azimuthal angle. The spontaneous polarization torque that exists because of the existence of the spontaneous polarization is considerably larger than the dielectric torque; therefore,

FLCs are characterized by fast electro-optical response (Lagerwall, 2004). In this case, eq. (3.2) transforms into

$$\gamma_\varphi \frac{d\varphi}{dt} = K\nabla^2\varphi - PE\sin\varphi \tag{3.3}$$

Later, the response time (i.e., switching ON and switching OFF time) can be determined for different electro-optical modes depending on the boundary and other conditions, by solving eq. (3.3) (this has been discussed later in the chapter).

3.2 Electro-optical effects in FLCs

The electro-optical operations of FLCs can be classified into two basic types. First, the electro-optical modulations without helix, where the helix is either suppressed, by any external means, or it is extremely large. Second, the electro-optical modulations with helix can be further divided into two subcategories: (a) when the helix always exists during the whole electro-optical operations, and (b) where the helix exists in the absence of electric field and unwinds in the presence of sufficiently large electric field. Several electro-optical modes have been explored for FLCs; in this chapter, we briefly discuss six electro-optical modes, which are most important for display and photonic applications.

a. Clark–Lagerwall effect

The first and most explored electro-optical mode for FLCs, since its discovery in 1975, for different applications is surface-stabilized FLC (SSFLC) (Abdulhalim and Moddel, 1991; Beresnev et al., 1988; Chigrinov, 1999; Clark and Lagerwall, 1980; Elston and Ulrich, 1995; Hegde et al., 2008; Jakli and Saupe, 1991, 1992; Lagerwall, 2004; Lagerwall and Dahl, 1984; Meyer, 1974; Meyer et al., 1975; Rieker et al., 1987; Srivastava et al., 2012a, 2010b; Takanishi et al., 1990; Ulrich et al., 1997; Wang and Bos, 2004). It is also known as the Clark–Lagerwall effect (Clark and Lagerwall, 1980). In this case, the cell gap $d \ll p_o$ (helix pitch of the FLC); as a result, the FLC helix is suppressed by the cell surface, and the smectic layers are arranged perpendicular to the substrates whose axes are normal to the layers and parallel to the cell substrates. In the presence of any alternating electric field (E), the FLC molecule switches in between the two switching positions defined by the FLC cone. The director in both switching positions is parallel to the substrate plane; therefore, the FLC cell behaves like a uniaxial phase plate offering in-plane switching of the director. If the FLC cell is placed between the two crossed polarizers, then the maximum of optical contrast can be achieved when the polarization azimuth of the impinging

light is parallel to one of the FLC switching positions. The total angle of switching equals to the double tilt angle θ (Figure 3.1).
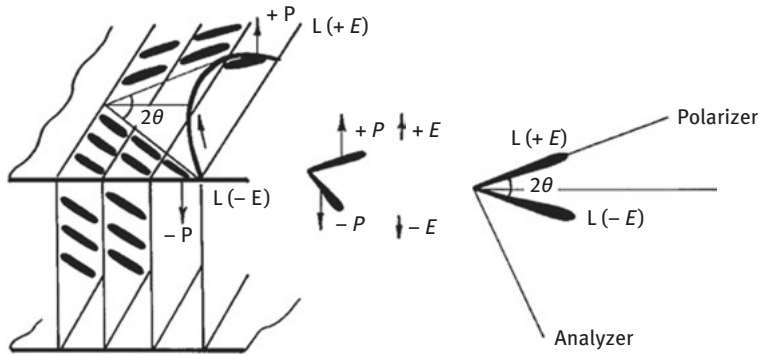
Figure 3.1: Schematic of the FLC cell in the Clark–Lagerwall effect, wherein $d \ll R_o$.

The response times in the Clark–Lagerwall effect are determined by solving the dynamical equation (3.3). The two switching positions are governed only by the polarization torque, which is significantly larger than the elastic torque; therefore, the elastic torque can be neglected. Thus, the switching ON or OFF time can be described as follows:

$$\tau_{ON} \approx \tau_{OFF} \propto \gamma\varphi/P_S E \tag{3.4}$$

The optical transmittance (I) of the FLC cell for the Clark–Lagerwall effect (in the absence of any intrinsic diffraction, and will be discussed later in the chapter), where one of the switching positions of the FLC molecules is parallel to the polarizing axis of the polarizer or analyzer, can be calculated as follows (Coe-Sullivan, 2016; Colegrove, 2018; Okaichi et al., 2018; Wei et al., 2012):

$$I = \sin^2(4\theta)\sin^2(\Delta\pi\Delta nd/\lambda) \tag{3.5}$$

where Δn is the birefringence and λ is the wavelength of the impinging light. As follows from eq. (3.5), the maximum transmittance in the SSFLC mode can be obtained for the half-wave plate condition with optical axis oriented at 45° from the polarization azimuth of the impinging light. Thus, for the maximum transmittance, the tilt angle should be $\theta = 22.5°$.

b. Bistable/multistable switching in FLC cells

The bistable switching in SSFLC geometry takes place above a certain threshold field $E_{th} \propto W_d/K^{1/2}$, where K is an average elastic constant and W_d is a dispersion

anchoring energy, and the polar anchoring energy is taken equal to zero $W_p = 0$ (Chigrinov, 1999). Thus, for the higher increasing anchoring we need higher electric field. The energy of switching electric torque is proportional to the product of $P \times E$; therefore, the bistability threshold is inversely proportional to the value of FLC spontaneous polarization P_s.

The SSFLC mode shows good bistable switching; however, it cannot provide an intrinsic continuous gray scale, unless a time- or space-averaging process is applied (Beresnev et al., 1988; Chigrinov, 1999; Clark and Lagerwall, 1980; Lagerwall and Dahl, 1984). The inherent physical gray scale of passively addressed FLC cells can be obtained only if the FLC possesses multistable electro-optical switching as a consequence of ferroelectric domains, which appear if the spontaneous polarization P_s is high enough (Beresnev et al., 1989; Fukushima et al., 1990; Pozhidaev and Chigrinov, 2006; Pozhidaev et al., 2009a; Rudquist et al., 1999). Ferroelectric domains in a helix-free FLC form a quasi-periodic structure with a variable optical density as it appears between crossed polarizers (Abdulhalim and Moddel, 1991). The bookshelf configuration of smectic layers is preferable for the observation of these domains. If the duration of the electric pulse applied to a helix-free SSFLC layer containing ferroelectric domains is shorter than the total FLC switching time, then the textures shown in Figure 3.2 are memorized after switching off this pulse and they preserve the same gray scale even after the short-circuit of the FLC cell electrodes. The domains appear as a quasi-regular structure of bright and dark stripes parallel to the smectic-layer planes. The bright stripes indicate the spatial regions with a complete switching of the FLC director, while the dark stripes indicate the regions that remain in the initial state. The sharp boundaries between the black and white domain stripes illustrate the fact that only two stable director orientations exist. The variation in the relative area of bright and dark stripes depends on the energy of the applied driving pulses. Both the amplitude and the duration of the driving pulses can be varied by changing the switching energy, which defines the memorized level of FLC cell transmission. Therefore, any level of the FLC cell transmission (intermediate between the maximum and the minimum transmissions) can be memorized after switching off the voltage pulses.

The necessary conditions of multistable switching modes are

(i)   sufficiently high FLC spontaneous polarization $P_s > 50$ nC/cm^2 and

(ii) a relatively low energy of the boundaries between the two FLC states existing in FLC domains (Figure 3.2), which is very common for the antiferrroelectric phase (Chigrinov, 1999; Lagerwall, 2004).

The multistability is responsible for three new electro-optical modes with different shapes of the grayscale curve that can be either S-shaped (double or single depending on the applied voltage pulse sequence and boundary conditions) or V-shaped (depending on the boundary conditions and FLC cell parameters).

The theoretical and experimental investigation of reversible and memorized S- and V-shaped multistable FLC electro-optical modes was proposed by Pozhidaev

(a)

(b)
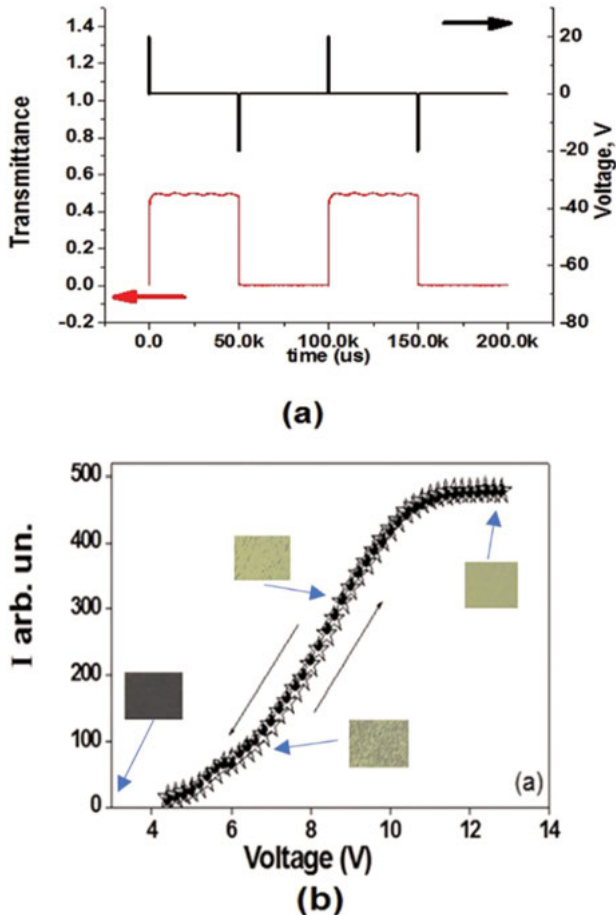
Figure 3.2: (a) Waveform representing the bistable performance. S-shaped (above) and V-shaped (below) FLC multistable switching response of the FLC cell under crossed polarizers. (b) Continuous variation of the width of ferroelectric domains with a change in the applied voltage of the FLC layer between crossed polarizers. Inserts show the optical microscopic images for different gray scales. The picture size is 250 × 250 µm.

et al. (2009a). New electro-optical modes are based on the multistable electro-optical modes in FLC cell (Fukushima et al., 1990; Pozhidaev and Chigrinov, 2006; Pozhidaev et al., 2009a; Ulrich et al., 1997; see Figure 3.2. Several devices based on bistable FLC, that is, spatial light modulators (Pozhidaev and Chigrinov, 2006) and multistable FLC display (Fukushima et al., 1990) have been proposed so far. The electro-optical response for the multistable FLCs is shown in Figure 3.2(a). The gray scale can be controlled by applying the voltage pulse of different magnitudes. The multistable grayscale dependence on the applied voltage pulse magnitude is shown

in Figure 3.2(b). These gray levels are stable after removing the electric field (Pozhidaev and Chigrinov, 2006).

c. Deformed helix ferroelectric effect

The geometry of the FLC cell with a deformed helix ferroelectric (DHF) effect is presented in Figure 3.3 (Beresnev et al., 1989). The polarizer on the first substrate makes an angle with the helix axis and the analyzer is crossed with the polarizer. The FLC layers are perpendicular to the substrates, and the layer thickness d is much higher than the value of the helix pitch p_o ($d \gg p_o$). The DHF liquid crystal (DHFLC) works purely as a birefringent plate for the light beam with the aperture $a \gg p_o$ passing parallel to the smectic layers and $\lambda \gg p_o$. In the presence of an electric field, the FLC helical structure becomes deformed, so that the corresponding dependence of the director distribution $\cos \varphi$, as a function of coordinate $2\pi z/p_o$, oscillates symmetrically in $\pm E$ electric fields (Chigrinov, 1999; Figure 3.3). These oscillations result in a variation of the effective refractive index; therefore, the electrically controlled birefringence appears. The effect takes place up to the electric field of the FLC helix unwinding ($E_u = \pi^2 K_{22} q_0^2/16 P_s$) (Beresnev et al., 1989; Chigrinov, 1999; Chigrinov and Kwok, 2013; Fünfschilling and Schadt, 1989; Hegde et al., 2008; Kiselev et al., 2011; Moddel et al., 1989; Panarin et al., 1991; Pozhidaev, 2001; Pozhidaev and Chigrinov, 2010; Presnyakov et al., 2005; Yoshino and Ozaki, 1984), where K_{22} is the FLC twist elastic constant, $q_0 = 2\pi/p_o$. The characteristic response times τ_c of the effect in small fields $E/E_u \ll 1$ are independent of the spontaneous polarization (P_s) and the field E, and are defined only by the rotational viscosity y_φ, elastic constant, and the helix pitch p_o:

$$\tau_c = \frac{\gamma_\varphi}{K_{22}\ q_0^2\ \sin^2 \theta} \tag{3.6}$$

If $E \leq E_u$, the FLC helix becomes strongly deformed and $\tau_c \propto E^{-\delta}$, where $0 < \delta < 1$ (Panarin et al., 1991). If E is close to the unwinding field E_u, the helix pitch sharply increases ($p \gg p_o$); consequently, the times of the helix relaxation τ_d to the initial state also increases as $\tau_d/\tau_c \propto p^2/p_0^2$. Therefore, for $E \approx E_u$, it is possible to observe the memory state of the FLC structure (Beresnev et al., 1989). The switching time less than 10 μs at the driving voltage of ±20 V can be achieved, which is temperature independent over a broad temperature range (Pozhidaev, 2001). The fast DHF effect with the total response time (i.e., rise and decay time) less than 1 ms in a broad temperature range of 20–80 °C was developed by Srivastava (2015a; Figure 3.3(b)). DHFLCs are characterized by fast electro-optical switching with a broad range of the electrically controlled Δn, and therefore, present very promising candidates for photonic and display applications.
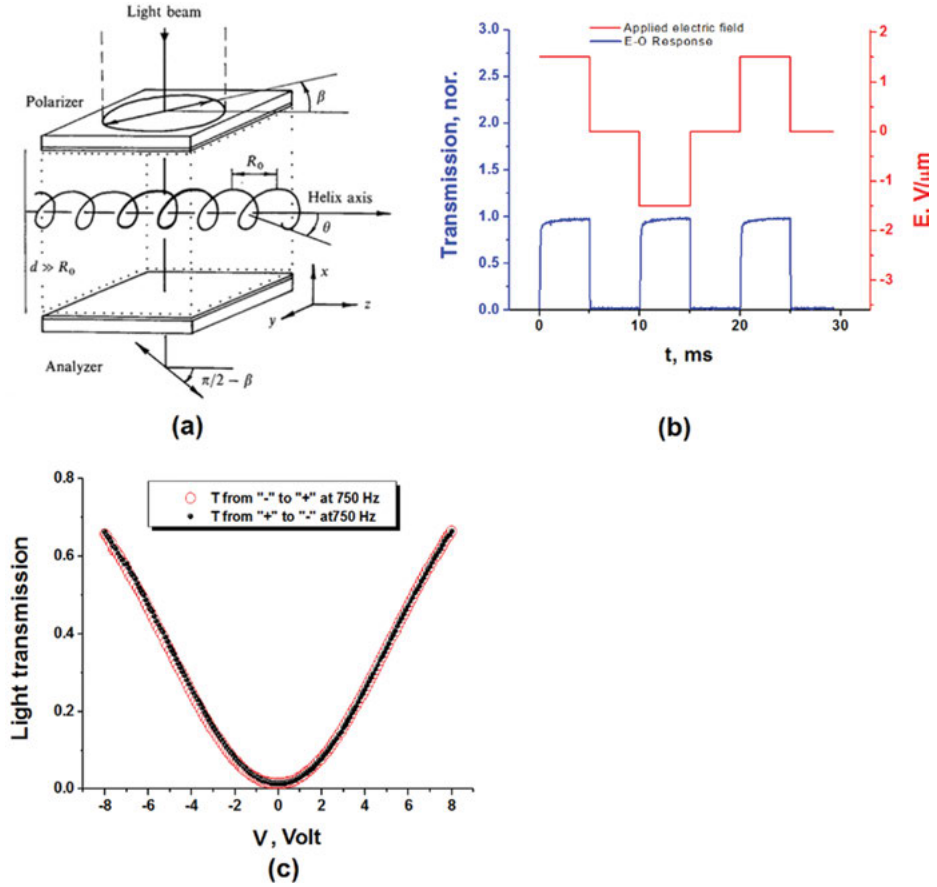
Figure 3.3: Deformed helix ferroelectric (DHF). (a) A schematic of the DHFLC cell effect. (b) Top: the driving voltage waveform applied to the cell; bottom: the electro-optical response of the cell. (c) V-shaped mode in the envelope curve of light transmission saturation states measured at electro-optical response frequency of 750 Hz.

The optical transmission of the DHF cell could be calculated as follows:

$$I = \sin^2(2(\beta - \alpha(z)))\sin^2(\Delta\pi\Delta nd/\lambda) \tag{3.7}$$

where β is the angle between the z-axis and the polarizer (see Figure 3.3(a)); $\alpha(z)$ (where $\alpha(z) = \arctan(\tan\theta\cos\varphi(z))$) is the angle between the projection of the optical axis on y, z-polarizer plane, and the z-axis; and $\Delta n(z) = n_{\text{eff}}(z) - n_\perp$ is the effective birefringence, where

$$n_{\text{eff}} = \frac{n_\| n_\perp}{\left[n_\perp^2 + \left(n_\|^2 - n_\perp^2 \right)\sin^2\theta \, \sin^2\varphi \right]^{1/2}} \tag{3.8}$$

Furthermore, the diffraction in the visible range that appears due to DHFLC pitch can be avoided by keeping $p_o \sim 0.1$–0.2 μm; hence, the selective reflection is below $<\lambda = 0.450$ μm, that is, beyond the diffraction limit of light in the visible region. Using a "natural" gray scale of the DHF mode, many gray levels can be obtained with fast gray to gray response time (Pozhidaev, 2001). New FLC mixtures with the helix pitch $R_0 < 0.3$ μm and tilt angle $\theta > 30°$ have been developed for the DHF effect (Presnyakov et al., 2005). The helix unwinding voltage was about 2–3 V.

A geometry with $\beta = 0$ can be selected to provide nonsensitive to the driving voltage polarity electro-optical response. Maximal light transmission under this condition, as it follows from eq. (3.7), will be only if $\alpha(z) = 45°$ and $\Delta n(z)d = \lambda/2$, and a small deviation in the tilt angle from 45° does not affect the optical quality of the DHFLC cell significantly. A typical V-shaped symmetrical (voltage sign independent) DHF switching is shown in Figure 3.3(c) (Pozhidaev, 2001).

Because of its natural gray scale, fast response time, and good hysteresis-free V-shaped electro-optical response, the DHFLCs were deployed in a field-sequential color displays (Pozhidaev, 2001), shutters, (https://www.crcpress.com/Optical-Applications-of-Liquid-Crystals/Vicari/p/book/9780750308571), and sensors (Brodzeli et al., 2013).

d. Electrically suppressed helix (ESH) mode

A new electro-optic mode proposed recently is called as electrically suppressed helix (ESH) FLC mode (Pozhidaev et al., 2011; Srivastava et al., 2015). The ESHFLC mode is characterized by high contrast ratio and very fast electro-optic response; therefore, it is highly suitable for display and photonic applications. The ESH mode occurs in between the two effects, that is, DHFLC and SSFLC, depending on the boundary conditions. In an example of the ESHFLC material (Pozhidaev et al., 2011; Srivastava et al., 2015), the response time is plotted against the applied voltage in Figure 3.4. The response time for $V \leq 0.4$ V shows voltage dependence like DHFLC mode, where an increase in the voltage results in unwinding of the helix and shows a peak in the response time. The peak in the response time corresponds to the helix unwinding, and the corresponding voltage is called as critical voltage required for the helix unwinding (V_c). After the helix unwinding at $V \geq 1$ V, the dependence is like SSFLC. Thus, in the ESHFLC mode, the helix exists in the cell, without showing any effect of the surface on the helix, and unwinds on the application of the sufficiently high electric field. The electric field dependence on the response time, transmittance, and the optics is very similar to SSFLCs. Despite these similarities with the SSFLC, it should be emphasized that at $V > V_c$, there is no SSFLC mode but an electro-optical mode with ESH mode. There is only formal difference in the initial conditions between SSFLC and ESH modes. The FLC helix for ESHFLC, unlikely in SSFLC, is not affected by the surfaces of the cell; otherwise, the dynamics for both of them is completely identical. The electric field dependence on the response time,

transmittance, and the optics of ESHFLCs is very similar to SSFLCs. However, the presence of helix without the applied voltage is primarily responsible for the unique high alignment quality in ESH mode (see top right insertions in Figure 3.4). The contrast ratio (i.e., the ratio of I_{max}/I_{min}) in ESHFLC mode can be more than 10,000:1 up to 1 kHz at the driving voltage of ±1.5 V and up to 2 kHz at higher driving voltage of ±3 V, the almost maximum light transmission (depending on the total retardation from FLC, see Figure 3.5; Srivastava et al., 2015).
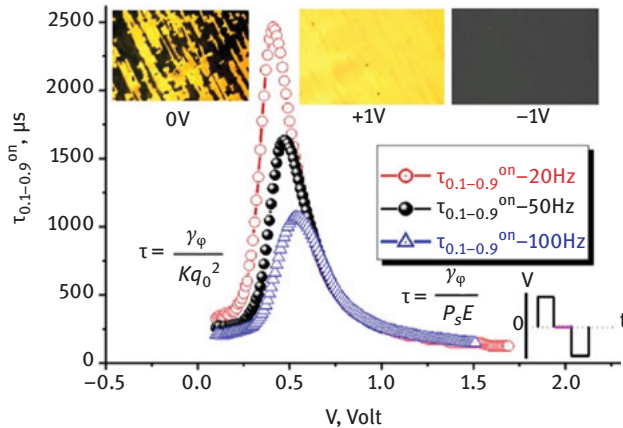
Figure 3.4: Dependence of switching ON time of 1.5-µm-thick cell filled with the FLC-595 (Pozhidaev et al., 2011; Srivastava et al., 2015) for the ESHFLC mode. Inserts: bottom right is the driving voltage waveform; top is the FLC-layer textures between crossed polarizers, and horizontal scale of all images is 200 µm; top left shows that the voltage is not applied and top right shows textures at +1 and −1 V (reproduced from Srivastava et al. (2015) with the permission of Wiley).

Furthermore, the unique high alignment quality, however, is observed only if the helical elastic energy is comparable but obligatory not less than the anchoring energy normalized to d_{FLC}:

$$Kq_0^2 \geq \frac{2W_Q^0}{d_{FLC}} \tag{3.9}$$

where W_Q^0 is a coefficient of the anchoring energy. We have measured $W_Q^0 = 4 \times 10^{-4}$ J/m^2 for the cell, whose properties are illustrated in Figure 3.4, thus confirming the validity of inequality (9), when the outstanding alignment quality (top right insertions in Figure 3.4) is observed.

A very uniform FLC alignment exists just when $V > V_c$ (right top insertion in Figure 3.4), while at $V < V_c$ it is worse because the FLC layer is divided into two domain helical structures with degenerated domains' principal axes positioned at an angle around double FLC tilt angle, that is, 2θ. When observed with a polarizing microscope, these helical domains are perceived as homogeneous dark and bright areas with their
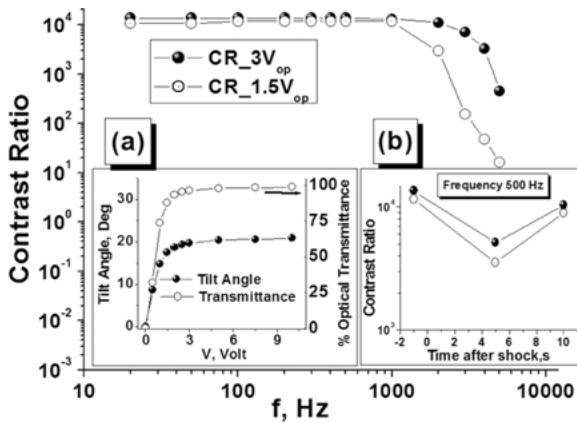
Figure 3.5: Dependencies on the contrast ratio of ESHFLC cell on the driving voltage frequency at V = 1.5 V and V = 3 V. The FLC-595 (Pozhidaev et al., 2011; Srivastava et al., 2015) layer thickness is 1.5 μm, no SiO$_2$ layers, and measurements have been carried out at T = 22 °C and wavelength λ = 0.63 μm. (Left inset) Dependencies on voltage: measured tilt angle and the cell light transmission in comparison with transmission of empty cell placed between crossed polarizers. (Right inset) Contrast ratio dependence on time after the application of mechanical shock (reproduced from Srivastava et al. (2015) with the permission of Wiley).

characteristic sizes of ~10–50 μm (see left top insertion in Figure 3.4). These domains are completely suppressed by applying a weak electric field $E_c < E < 1$ V/μm (right top insertion in Figure 3.4), thus forming perfect defect-free alignment in the ESH mode.

In addition to this, ESHFLC mode possesses good shock stability for the mechanical stress. The mechanical shock stability was studied by applying a mechanical stress that is sufficient to provide 80% of extrusion. Thereafter, the contrast ratio was measured with time after removing the mechanical pressure. The contrast can be restored within 8 s after the removal of the mechanical pressure; however, the contrast ratio is always more than 3,000:1 at any time even in the presence of mechanical pressure. Therefore, unlike nematic liquid crystal displays (LCDs), it is difficult to see any pressure waves on the screen; however, the change in the contrast ratio can be seen experimentally (Figure 3.5). More detail description of the shock stability is given by Pozhidaev et al. (2011) and Srivastava et al. (2015). Because of their extreme optical quality and good shock stability, they have been applied to the micro-displays, active matrix LCD, and other photonic devices, and some of them will be discussed in the chapter later.

e. Kerr effect

The phase-only optical modulation is in high demand for variety of applications like photonic devices, such as tunable lenses, focusers, wave front correctors, co-

relators, and displays, which are the building blocks of optical information processors and other systems (Kotova et al., 2002; Naumov et al., 1999; Ouchi et al., 1988; Ren and Wu, 2003; Xu et al., 2012). The current phase modulators have great limitations either because of the high driving voltages or due to slow response time or both. The LC phase modulators greatly suffer from the slow response time, which can be as long as 100 ms for communication band (i.e., 1,550 nm). Thus, FLC can solve the problem because of the fast response time. However, most of the FLC modes are not suitable for pure phase modulation devices because their optical axes sweep in the plane of the cell substrate that can manipulate the polarization state of the incident light. In order to avoid the optical axis sweeping problem, a device consisting of an FLC half-wave plate sandwiched between two quarter-wave plates was proposed by Freeman et al. (1992). However, for the 2π phase modulation, the FLC tilt angle is required to be equal to 45°, which is a real challenge for the material science (Shen et al., 2015). Some of the anti-FLCs and FLCs that show a tilt angle close to 45° have been developed. However, the response time for these materials increases dramatically when the tilt angle grows up to 45° (Cho, 2012; Hwang et al., 2013; Kim, 2004; Lee et al., 2005; Love and Bhandari, 1994). On the other hand, a Kerr-like nonlinearity has been observed for the vertically aligned DHFLC (VADHFLC) with subwavelength helix pitch (Kim, 2004; Kim et al., 2005; Pozhidaev et al., 2012). Vertical alignment of FLC with interdigital electrodes has been used to orient the helix axis perpendicular to the substrates, while electric field is parallel to smectic layers. In the absence of electric field, the FLC helical structure is optically equivalent to a uniaxial crystal whose principal axis coincides with the axis of the helix. Whereas in the presence of electric field E, the in-plane refractive indices along ($n_{\parallel}$) and perpendicular ($n_{\perp}$) to the field differ from each other, and their difference is proportional to the square of the electric field, that is, $\delta n_{\mathrm{ind}} \propto E^2$.

Figure 3.6(a) reveals the schematic diagram of the VADHFLC cell with the DHFLC principal axis (PA) and its interaction with the applied electric field (Pozhidaev et al., 2012). In the presence of electric field E (i.e., $E < E_c$), PA deviates from its initial position z by an angle $\Delta\alpha$ in a plane perpendicular to the electric field direction; as a consequence, the refractive indices of the helical structure along ($n_{\parallel E}$) and perpendicular ($n_{\perp E}$) to the electric field (Figure 3.6(b)) differ from each other, and their difference corresponds to the biaxiality (δn_{ind}) of the helical structure.

For normally incident light, the electrically controlled birefringence is as follows (Kim, 2004; Pozhidaev et al., 2012):

$$\delta n_{\mathrm{ind}} = n_{\parallel E} - n_{\perp E} = K_{\mathrm{Kerr}} E^2 \tag{3.10}$$

where $n_{\parallel E}$ and $n_{\perp E}$ are the effective DHFLC refractive indexes, induced parallel and perpendicular to the applied electric field, and the "Kerr constant"

$$K_{\mathrm{Kerr}} = 2n_{E=0} \cdot \left(1 - n_{\perp}^2 / n_{E=0}^2 \cdot \chi_E / P_s\right) \tag{3.11}$$
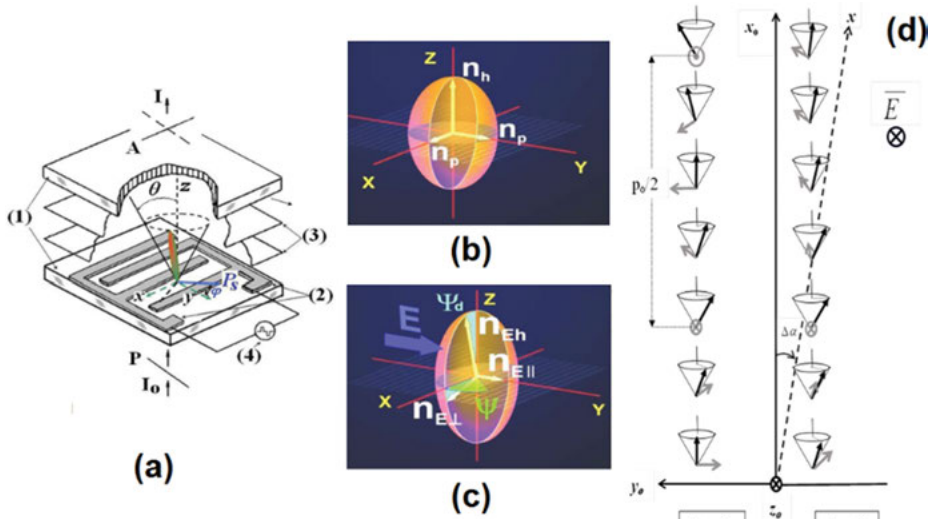
Figure 3.6: (a) Schematic representation of geometry of a vertically aligned DHFLC cell (Ma et al., 2013a): (1) represents glassy plates, (2) represents in-plane electrodes, (3) represents smectic layers parallel to glass substrates, (4) is a voltage generator, P (A) is polarizer (analyzer), θ is the tilt angle of director n in smectic layers, ϕ is the azimuthal angle of the spontaneous polarization vector P_s, I_0 is the intensity of incident light, and I is the intensity of light transmitted through the VADHFLC cell placed between P and A. (b)–(d) Illustration of VADHFLC principal axis deflection in the presence of electric field; (b) schematic representation of the refractive indices ellipsoid in the absence (left) and in the presence (right) of electric field (Pozhidaev et al., 2013) (reproduced from Srivastava et al. (2015) with the permission of Wiley).

is proportional to the "isotropic" refractive index for zero electric field $\alpha_{\text{Kerr}} \sim n_{E=0}$ as follows:

$$n^2{}_{E=0} = \left[n^2{}_\| n^2{}_\perp \big/ \left(n^2{}_\perp + \left(n_\|{}^2 - n_\perp{}^2\right)\cos^2\theta\right)^{1/2} + n^2{}_\perp\right]\big/ 2 \qquad (3.12)$$

$n_\|$ and $n_\perp$ are FLC refractive indexes, θ is the FLC tilt angle, and P_s is the FLC spontaneous polarization; and dielectric susceptibility of the Goldstone mode dielectric susceptibility is defined as $\chi_E = \left(P_s^2 / 2Kq_0^2\right)$, where K is the elastic constant.

The FLC transmittance T as a function of E^2 is shown in Figure 3.7(a). Figure 3.7(b) reveals that the VADHFLC cell shows the 2π phase modulation at the electric field of ~2.1 V/μm. The light transmission of VADHFLC cell between two crossed polarizers can be described by Ma et al. (2013a), Nakatsuhara et al. (2014), and Srivastava et al. (2012a):

$$T = \sin^2 2\Psi \, \sin^2 \frac{\pi \delta n_{\text{ind}} d_{\text{FLC}}}{\lambda} \qquad (3.13)$$

(a)

(b)
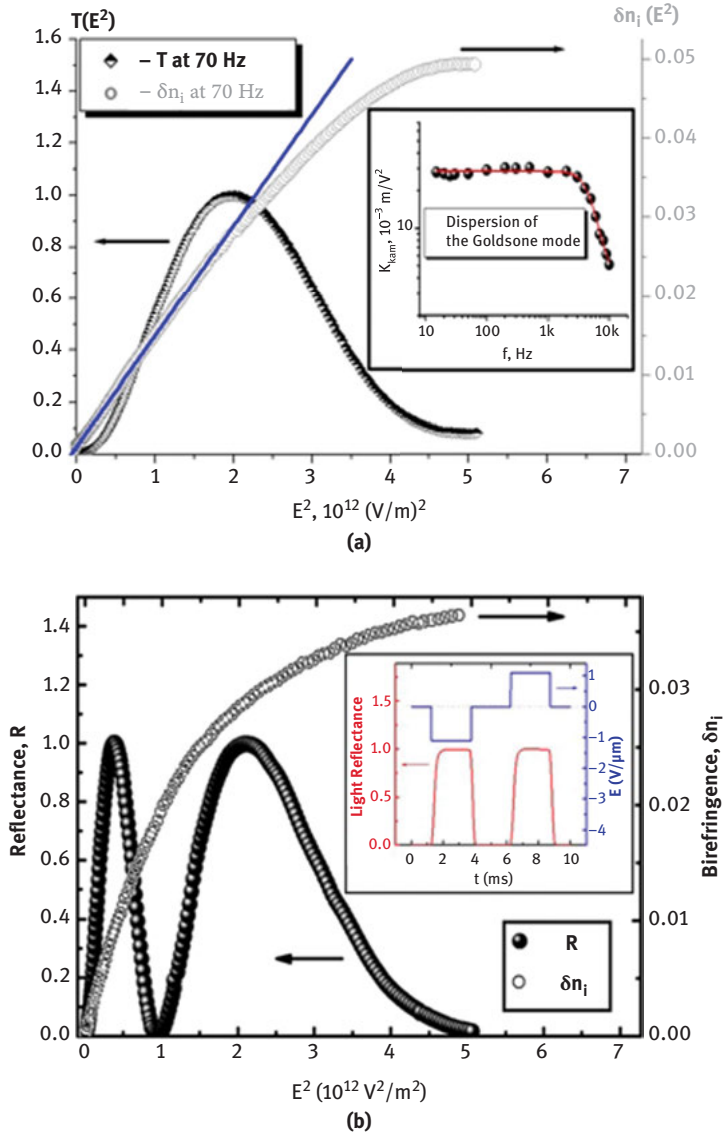
Figure 3.7: The reflectance $R(E^2)$ and $\delta n_i(E^2)$ dependence for VADHFLC cell placed between crossed P and A at 45° at the applied frequency of 70 Hz (Pozhidaev et al., 2013). The solid blue line is the result of theoretical fit of the δn_i according to eq. (3.15). Insert: the electro-optical response of the DHFLCs (reproduced from Srivastava et al. (2015) with the permission of Wiley).

where d_{FLC} corresponds to the FLC layer thickness. Thus, δn_{ind} has been computed from eq. (3.13) and plotted in Figure 3.7(a). The open circular legends represent the experimental data, while the solid blue line represents the theoretical fit of eq. (3.10). The value of δn_{ind} for a short-pitch FLC material (i.e., FLC-587) at saturation is 0.05, which means that 2π modulation can be obtained for FLC thickness-to-wavelength ratio $d_{\text{FLC}}/\lambda = 20$ (Figure 3.7(a)). This is a reasonable thickness of FLC without any destruction in the alignment quality (Ma et al., 2013a; Nakatsuhara et al., 2014; Pozhidaev et al., 2012–2014). $K_{\text{Kerr}} = 27$ nm/V^2 is about two orders of magnitude greater than the Kerr constant of nitrobenzene and is comparable to the Kerr constant of the best-known polymer-stabilized blue phase LC (Rao et al., 2010). K_{Kerr} is constant till the frequency of 2 kHz, and afterward at higher frequencies, it shows clear dispersion. This dispersion can be explained on the basis of eq. (3.11) and the Goldstone mode relaxation frequency. Furthermore, K_{Kerr} depends on the dielectric susceptibility of the Goldstone mode (χ_E); thus, K_{Kerr} in eq. (3.11) can be written as

$$K_{\text{Kerr}} = \frac{n_p}{\lambda} \cdot \frac{\varepsilon_e - \varepsilon_\perp}{\varepsilon_e + \varepsilon_\perp} \cdot \frac{P_s^2 \, p_0^4}{32\pi^2 \, K^2 \, \sin^4\theta} \tag{3.14}$$

Thus, the Kerr constant can be improved with higher P_s and p_0. However, to increase P_s one has to increase either the concentration of the chiral dopant or increase the dipole moment of the FLC molecule. Both of these options result in tremendous increase in the viscosity and so the larger response time that might not be a good alternative for many applications. Furthermore, the increase in p_0 might result in polarization plane rotation and could affect the ellipticity of the modulated light. Hence, a crucial trade-off exists for the fast phase modulation. In an effort, discussed by Pozhidaev et al. (2014), K_{Kerr} of 129 nm/V^2 was achieved by the simple material optimization. The approach for these material optimization has been briefly discussed later in the chapter.

f. Summary of all the electro-optical modes

FLCs have obtained great attention because of the fast switching speed and led to a number of novel electro-optical devices, in particular, display panels. In spite of this fast switching and low driving voltages, the FLC still lags behind the nematic LCs in actual display devices because of some practical difficulties. The most common problem, that is, the disturbance in bookshelf geometry of the smectic layers, appears while FLC is cooled from SmA or SmC to chiral SmC★ phase. At the SmA–SmC★ phase transition, the smectic layers shrink due to the induction of the molecular tilt; therefore, the distance between the smectic layers decreases producing thermal instability (Jakli and Saupe, 1991; Takanishi et al., 1990).Hence, the chevron defects appear, which shows significant light leakage (Jakli and Saupe, 1991). Rieker et al. (1987) have reported the first experimental verification of chevron geometry. Several efforts such as polymer stabilization (Srivastava et al., 2010b), electric field stabilization (Jakli and Saupe, 1992),

and using high pre-tilt angle for the alignment (Wang and Bos, 2004) have been made to avoid such defects. These approaches can only provide momentarily solution of the problem, which is still a big challenge for the academic and industrial world; therefore, we need advanced materials for various applications. In Table 3.1, we list the vital material parameter and electro-optical performance for various electro-optical modes of FLCs. It is clear from the table that a strong control on the helical pitch, tilt angle, spontaneous polarization, and their temperature dependencies are required to design suitable FLC material for various electro-optical modes. The strategies to design advanced FLC materials for different applications are discussed in the next section.

Table 3.1: Comparison of the material and electro-optical performance of various electro-optical modes (reproduced from Srivastava et al. (2015) with the permission of Wiley).

Properties	FLC electro-optical mode				
	SSFLC	Bistable/ multistable	ESHFLC	DHFLC	Kerr-effect
Pitch	>Cell gap	≫Cell gap	≤Cell gap	≪Cell gap (below visible range)	≪Cell gap (below visible range)
Cell gap/pitch (d/p) **ratio**	>1	≫1	In the range of 1−3	≪1	≪1
Ideal tilt angle (°)	22.5	22.5	22.5	45	45
Spontaneous polarization	Low	High	Low	High	High
Alignment	Planar	Planar	Planar	Planar	Vertical
Diffraction	Diffraction due to pitch and ferroelectric domains	Diffraction basically due to ferroelectric domains	No diffraction	Diffraction due to ferroelectric domains	No diffraction
Existence of helix during the operation	No	No	No	Yes	Yes
E-O hysteresis	Yes	Yes	No	No	No
Contrast ratio	1−100:1	~100:1	~10,000:1	~800:1	~1,000:1
Shock stability	Poor	Poor	Excellent	Poor	Good
E-O modulation	Digital	Pseudo-analogue	Digital	Analogue	Analogue
Driving modes	Digital drive	Analogue drive	Digital drive	Analogue drive	Analogue drive

3.3 Chemistry of the modern FLCs

The SSFLC mode is of the most studied EO effects in FLC, and the correlation of required parameters with molecule structure is already given in plenty of sources (Goodby, 1991; Goodby et al., 2014; Hird, 2011, 2014, 2007; Kelly, 2014; Lemieux, 2001; Popova et al., 2006; Walba, 1991); here, we briefly discuss these relations and later expand our discussion to the modern FLC electro-optical modes.

As mentioned above, the FLC materials can be composed of either chiral molecules or as a mixture of non-chiral SmC host and chiral dopants (CD), which may or may not be mesogenic. Though the second approach is a most common approach, few particular cases of all-chiral FLCs are also valuable. In general, the concept "non-chiral guest–chiral host" is much more flexible and offers good control on the FLC material parameters. The non-chiral SmC host mainly defines the phase transition range (working range), in particular (depending on the content of CDs) birefringence, viscosity, and tilt angle. On the other hand, CD is responsible for induction of P_s and p_0. At fairly low content of CD in the FLC mixture, both of P_s and p_0 are proportional to the CD concentration. Whereas for higher CD content, normally above 14–15 mol%, some deviation from linearity may occur, which also affects the other set of FLC properties (i.e., phase transitions, $n\Delta$, etc.).

Non-chiral host, typical chemical structures. Although plenty of chemical structures were proposed as SmC materials (see Vill et al., 2010), the most popular classes of reliable compounds are listed as follows (see also Figure 3.8):
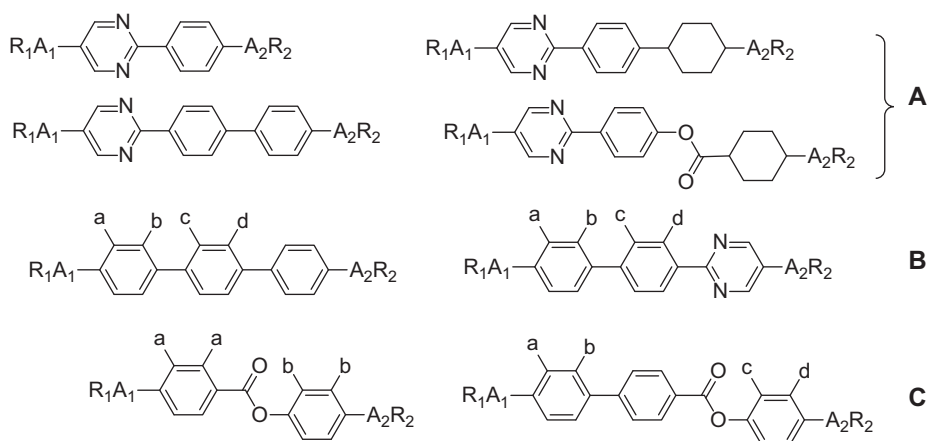
Figure 3.8: Mostly widespread components of non-chiral SmC host in commercial FLC mixtures. A_1, A_2 denote single C–C bond or O atom; R_1, R_2 denote alkyl or alkenyl groups; a, b, c, and d are H or F in different combinations.

- – phenylpyrimidines, two or three rings, rarely four rings (**A**) (Zaschke, 1975; Sakurai et al., 1988; Ohno et al., 1989; Terashima et al., 1988; Illian et al., 1992; Kelly and Fünfschilling, 1994);
- – laterally substituted terphenyls and their heterocyclic analogues (**B**) (Chan et al., 1985; Gray et al., 1989; Reiffenrath et al., 1989a); and
- – seldom – ester derivatives (**C**) (Bradshaw et al., 1987; Brimmell et al., 1989; Chambers et al., 1989; McMillan, 1973; Reiffenrath et al., 1989b; Wulf, 1975).

The mixtures of these components (three and often more number) provide wide enough temperature range of SmC phase, at least within –10 to 60 °C and wider.

Although a big range of CDs suitable for FLCs are known, the best case is achieved for CDs possessing LC phases, particularly having SmC⋆. The chirality in most of these CDs is associated with the branching in terminal tails that seriously affects their LC behavior, in comparison to non-branched (i.e., non-chiral) analogues. It is a big challenge to avoid the adverse effect of chirality on the LC behavior of these CDs, which requires considerably great efforts. Therefore, an alternative strategy involving minor compromise with the temperature range of the non-chiral host, using the non-mesogenic CDs, can be adopted. In some particular cases, non-mesogenic compounds may improve, to some extent, the upper temperature limit of SmC⋆ phase (Kelly, 2014).

Spontaneous polarization. The first property, which is important to all effects, P_s, is dipole moment of the unit volume of the SmC⋆, which is perpendicular to the tilt plane. Therefore, P_s is proportional to the transverse part of the molecular dipole, taking into account the restricted rotation of the molecule around its long axis (Walba, 1991). However, due to rotation, only small part of projection of molecular dipole imparts into P_s. It can be expressed as

$$P_i = \mu_{\perp i} \times \text{ROF}_i \times 1/\varepsilon$$

where P_i is polarization of ith conformer, $\mu_{\perp i}$ is its transverse dipole moment, and ROF_i is a rotational orientational factor from zero to one describing the degree of conformer rotation.

Several approaches were proposed to extract, more or less, an individual impact of CD on P_s induction and analysis of corresponding relationship with the molecular structure of CD. One of the commonly used approaches is introduction of reduced polarization (P_0) and polarization power (δ_P) (Stegemeyer et al., 1991). The coupling between P_s and θ as well as their dependencies on concentration of a chiral dopant (x_G) can be written as

$$P_0(x_G) = P_s(x_G)/\sin\theta(x_G) \tag{3.15}$$

$$\delta_P = (\partial P_0(x_G)/\partial x_G)_{G \to 0} \tag{3.16}$$

For many FLC materials, linear dependence of $P_0(x_G)$ is observed; thus, δ_P can be served as a material constant characterizing CD themselves. It is worth to mention here

that these equations are valid only for high enough values of θ, since for small value $\sin \theta \rightarrow 0$ and $P_0(x_G)$ can adopt unreasonably high values (Stegemeyer et al., 1991).

The dipole group, in general, should be rigidly linked with elements of chirality (in particular, with chiral center) of the CD. According to the Osipov–Stegemeyer classification (Osipov et al., 1996), all CDs of FLC can be classified into two categories: type I CD, when the chirality occurs in a terminal tail, whereas type II CD contains the chirality in the "rigid core." In type I, which is most common, the dipole group should be situated as close as possible to the chiral center, ideally directly attached to it. The most often used polar groups, attached to the chiral center in the order of increasing dipole moment, are:

$$\text{Alkyl} < \, < \text{O (in OAlk)} < \text{Halogens} < \text{CF}_3 < \text{CN}$$
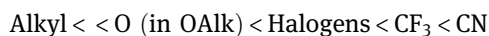
Among halogens, fluorine is the most remarkable polar substituent because of its high dipole moment (~1.41 D), low Van der Waals radius (a bit larger than hydrogen), and low polarizability that favors reducing the dispersion type of intermolecular interaction, thereby not increasing the viscosity significantly. In addition, the fluorine atom mimics the H atom, and therefore, does not affect the LC behavior of these CDs. The bulky groups situated in close vicinity of the chiral center can restrict the free rotation, thereby increasing P_s.

Examples of CD of type II are as follows:

Sakashita et al. (1991)	Mixture in ratio 45:55, Total concentration in SmC host is 20 wt.%) Itoh et al. (1993) and Itoh et al. (1997)
Sakaguchi and Kitamura (1991)	Kutulya et al. (2001a) · Lemieux (2001)
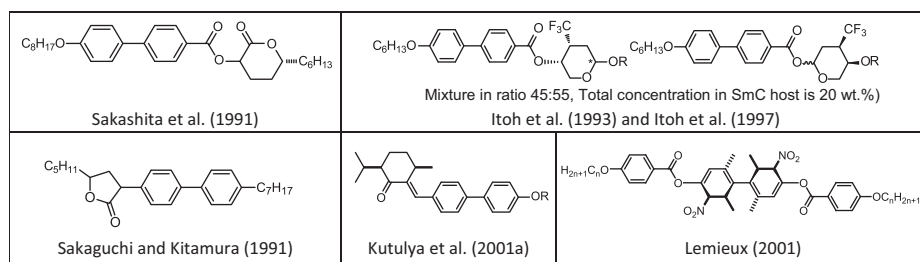
Viscosity is one of the important parameters, defining the response time of FLC. Unlike P_s, there is no well-defined correlations between the molecular parameters and viscosity; however, there are several empirical rules. Generally, viscosity correlates with the energy of intermolecular interaction; thus, all the factors reducing it are favorable to reduce γ_φ. Therefore, the viscosity increases

- with the increasing amount of polar bridge groups (ester, azo-) instead of C–C bonds;
- by changing the C–C bond as a linker of the tail with ether or ester functions;
- with the effective width of the central core, either by imparting the bent shape of the core (hockey stick and banana) or using condensed ring in the rigid core, or by introducing the lateral substituents;
- with the branching of the terminal tails, including introduction of the chirality; and

– with the introduction of any "inhomogeneity" to the terminal tail, for example, polyether chain, dimethylsiloxanes -$(CH_2)_n$-$[Si(Me)_2$-$O]_m$-$SiMe_3$, and fluorinated or even partially fluorinated chains.

Viscosity decreases upon separation of the aromatic units in the "rigid core" with flexible carbon spacers.

Birefringence is another important parameter for all FLC materials, and the high birefringence of the FLC is an issue for long time. Most of the known electro-optical effects in FLCs work on the principle of retardation introduced by the half-wave plate. On the other hand, for DHFLCs, where $p_0 \ll$ than cell gap, the effective birefringence (Δn_{eff}) depends on the smectic tilt angle and can be described by eq. (3.8). Most of the commercially available FLC materials possess Δn in the range of 0.14–0.2 at $\lambda = 0.54$ µm, and therefore, require a cell gap in the range of 1.5–2 µm to meet the half-wave plate conditions. However, in industry, it is extremely difficult to maintain the high manufacturing yield for such a small cell gap. Therefore, it is important to reduce the Δn for the FLC material, preferably in the range of 0.077–0.09 at $\lambda = 0.54$ µm.

The typical value of the tilt angle for DHF effect is in the range of $\theta \sim 32$–37°; therefore, the effective Δn in the cell is relatively smaller and the molecular Δn can be in the range of 0.15–0.18. However, currently available DHFLC materials (Kelly, 2014) are mainly based on three-ring aromatic (or heteroaromatic) compounds that limit $\Delta n > 0.2$.

The total Δn of a multicomponent LC mixtures, which is proportional to the molar impact of each component, can be written as follows (Pelzl, 1998):

$$\Delta n = \sum x_i \Delta n_i \qquad (3.17)$$

where x_i is the molar fraction and Δn_i represents the birefringence of the ith component, provided that Δn_i are related to the same at the reduced temperature. It is worth to mention here that eq. (3.17) is generally correct only for low Δn_i values.

A strategic way to reduce Δn for FLC consists in comprising the mixture of low birefringence compounds. The birefringence of the organic material is strongly related to the molecular polarizability that mainly depends on the lengthening of molecular conjugation of π-electron systems. Thus, the main tools to reduce Δn include exploration of saturated units in the core of LC molecules, exchange of aromatic rings with cyclohexane or cyclohexene, and breaking of the conjugation by means of aliphatic spacers. However, all these tools, especially exchanging the aromatic rings with aliphatic rings, seriously reduce the probability of SmC appearance; here, a vast majority of known SmC liquid crystals possess $\Delta n \sim 0.14$ and higher, which includes at least two aromatic rings in the molecule (Vill et al., 2010).

Thus, the formulation of low Δn FLCs is still a big challenge for the community. Some selected examples of either low Δn SmC compounds or another type of Δn reducers in FLC are as follows:
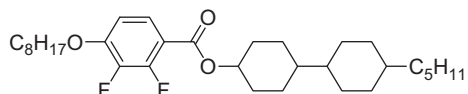
Cr 90 SmC 98N 170 Iso (Reiffenrath et al., 1989a)

The reported value of birefringence is 0.12, and such materials can be used as auxiliary components for reducing the birefringence. Three-ring cyclohexyl- and cyclohexenyl-substituted liquid crystals with low birefringence were proposed in US 6413448:
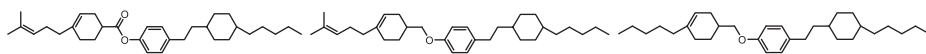
None of these compounds (US 6413448) possess SmC phase. In the given example, its content in the SmC mixtures is limited typically to 10%; when it is higher than 20%, the thermal stability of SmC phase drops down below 50 °C. The Δn of the mixtures is estimated to be ~0.12.

Similar to the above-mentioned compounds (US 6413448), the following cyclohexyl derivative was proposed (JP 2014019647):
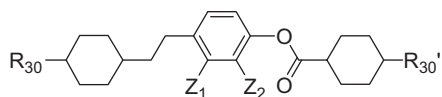
Its effect on SmC phase and Δn is also similar: in the absence of the SmC phase, the total concentration of these compounds is usually limited to 10% w/w, (JP 2014019647); therefore, their role as Δn reducer is not essential.

One of the best solutions for reducing Δn for FLC is given by Sasou et al. (2015):
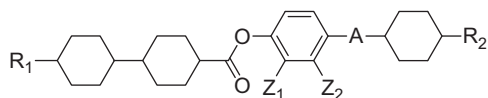
Data on Δn can be extracted from the chromaticity measurements in the FLC mixtures containing the given compounds. The Δn is deduced to be around 0.1; therefore, the cell thickness of 2.7 μm can be used.

Recently, it was shown that phenacyl esters in combination with other auxiliary materials (reducers of Δn, melting point, viscosity, and appropriate CDs) provide

Δn as low as 0.09 for application, in particular, in SSFLC and ESHFLC modes (Vashchenko et al.):

R_1 = C_nH_{2n+1}, n = 4-6
R_2 = C_nH_{2n+1}, n = 6-10

R_1 = C_nH_{2n+1}, n = 6-10
R_2 = C_nH_{2n+1}, n = 3-5   X_1, X_2 = H, F
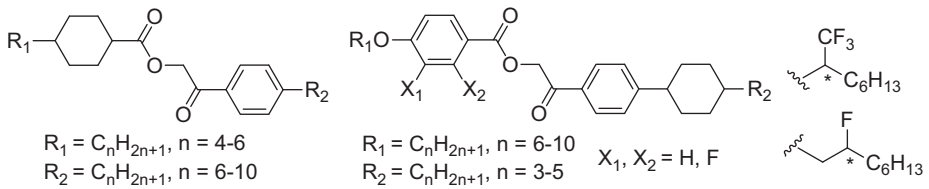
Helix pitch. The ability of a chiral molecule to induce p_0 is quantified with helical twisting power (HTP), and in the first approximation, it depends linearly on the reciprocal pitch:

$$p_0^{-1} = \mathrm{HTP} \cdot c \cdot \mathrm{ee} \tag{3.18}$$

where c is the concentration and ee is enantiomeric excess of CD. However, the square (Itoh et al., 1997) or cubic (Takanishi et al., 1999) type dependencies of p_0^{-1} (c) were also observed. The correlation between molecular structures of CDs with their ability to induce p_0 in SmC is not well established; a summary is given later in the chapter.

According to Table 3.1, the effect can be sorted out in three groups by the ratio of "d/p" and in particular, by pitch values:
  – Low twisted – SSFLC and bistable FLC
  – Moderate twisted – ESHFLC
  – High twisted – DHFLC and Kerr effect

For SSFLC effect, the required pitch is much larger than the cell gap; therefore, most of the CDs proposed to such application do not manifest a high HTP. As mentioned in Table 3.1, SSFLC requires low P_s; thus, the concentration of CD can also be low, within few to 10% w/w. Hence, it is easy to meet their requirements, and most of the CDs can serve the purpose. To optimize the pitch precisely, especially if CD manifests rather than high HTP, the pitch-compensating dopants can be used. These compensating dopants should manifest the opposite sign of HTP and preferably the same sign of P_s or possess its very low magnitude.

Similar to the SSFLC effect, bistable/multistable FLC requires very small d/p ratio; however, it is much more serious in comparison to SSFLC and requires fully compensated pitch in SmC* phase. In most cases, it can be achieved by using pitch-compensating CDs. Additional issue in bistable/multistable FLC mixture design consists in requirements of considerably higher P_s values, ≥100 nC · cm^{-2}. To achieve such polarization, either more polar CD (possessing higher dipole moment or several dipole groups in a CD molecule) or notably increasing CD concentration (to 20 mol% or even higher, up to 30%) is required. It is easy to show that at such CD concentration (dictated by desired P_s), the helix compensation is a challenge, especially at higher HTP values of CDs, taking into account either the error of HTP measurements or helical

pitch temperature dependence. Therefore, for application in bistable/multistable FLC, the chiral compounds with simultaneously high P_s and low HTP values are preferable.

Materials for moderately twisted mode – ESHFLC. General requirements for ESHFLC mixtures ($\theta = 22.5° \pm 2.5$, $P_s = 40–60$ nC/cm^2, $p_0 = 0.7–2$ µm) are quite close to the requirements for SSFLC materials, except the helix pitch values, which have to be relatively shorter. Although the $p_0 = 0.7$ µm in the first reported ESHFLC mixture (Pozhidaev et al., 2011; Srivastava et al., 2015a) was induced with 10 mol% of CD FOTDA-6 (bis-((S)-1,1,1-trifluorooctan-2-yl) [1,1':4',1"-terphenyl]-4,4"-dicarboxylate), which belongs to a "high twisting"-type, (Michailenko et al., 2019; Pozhidaev et al., 2013, 2009b; see also Table 3.3), nevertheless, the wide ranges of suitable P_s and p_0 allow enough room for the application of various less twisting CDs that are capable to provide $\theta \approx 22–23°$.

FOTDA-6
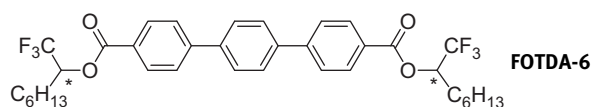
Thus, chiral compounds with considerably less HTP and polarization power than FOTAA-6 show the ESH behavior at their respective concentrations (Vashchenko et al.):
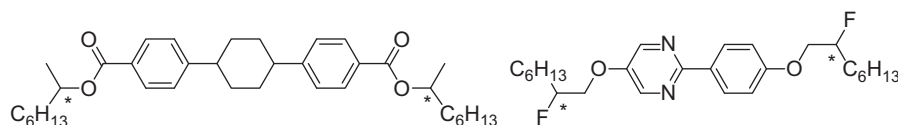
No special requirements to Δn for the ESHFLC materials were imposed (Pozhidaev et al., 2011; Srivastava et al., 2015); however, as this effect also works in the half-wave plate regime, the materials with birefringence reduced to the range 0.09–0.12 are preferable (Vashchenko et al.).

Short-pitch SmC*. The requirements for twisting are mentioned in Table 3.1, where the d/p ratio is significantly large. In addition, the longer pitch can affect the optical quality for devices working in the visible range, if it is in the range of Bragg's diffraction. Thus, it is better to avoid the Bragg diffraction by limiting the SmC* helix for display and visible photonic applications (Haase et al., 1999; Pozhidaev et al., 2009b). The relationship between diffraction wavelength and the helix pitch of SmC* is described with the following equation:

$$2D\langle n\rangle\sin\xi = m\lambda_{max} \tag{3.19}$$

where λ_{max} is the position of maximum reflection spectra, m is the diffraction order, $\langle n\rangle$ is an average refractive index, ξ is the diffraction angle, and D is the periodicity of the structure. Within the SmC* phase, D adopts $p_0/2$ value (half-pitch period) for the single peak in the case of a normal light incidence ($\xi = 90°$). At oblique incidence, two peaks

can be seen: first, $D_1 = p_0/2$ for the shorter wavelength peak, and second, $D_2 = p_0$ (full-pitch period) at the approximately doubled wavelength (Berreman, 1973; Hori, 1982).

In light of the above discussion, one can define the helix limit more precisely and specify a top limit of the helix pitch that is suitable for DHFLC applications. Thus, from eq. (3.6) adopting $\tau_r = 200$ μs, $K_\varphi = 2.4 \times 10^{-11}$ N (Pozhidaev et al., 2010), $y_\varphi = 4$ Poise, the p_0 variation can be estimated from 130 to 180 nm when tilt θ_C changed from 29° to 40°. Independently, as it is follows from eq. (3.18), the condition for full absence of Bragg's diffraction even at oblique light incidence can be satisfied at $p_0 \leq p_{cr} = 130$ nm assuming $\langle n \rangle = 1.6$ (Bahr et al., 1992).

Taking into account that rather tight helical pitch is also assumed be favorable for improving the optical quality of the FLC cells, as low as possible pitches, less than 100 nm, are strongly required for the enhancement of DHFLC performance. The lower limit of the pitch depends on many factors characterizing the host and CD and their relative concentration; however, theoretically the lowest p_0 values can be estimated as follows. Obviously, the twist ($\Delta\varphi$) between two adjacent SmC* layers cannot exceed 180° (actually this structure corresponds to the anticlinic packing). Thus, full pitch in such a case occurs in two layers. Assuming that SmC* interlayer distance is 2–4 nm, then the lowest possible value of p_0 in SmC* will be around 4–8 nm. Even at $\Delta\varphi = 45°$ (full turn is at eight layers that correspond to the pitch ~30 nm), there is still a big room to reduce p_0, further, from currently available values just below 100 nm.

Assuming linear concentration dependence of the reciprocal pitch (p_0^{-1}), the HTP value of chiral compounds should not be lower than 14–15 μm^{-1} to provide $p_{cr} \leq 240$ nm. Furthermore, to avoid the Bragg diffraction at any angle of light incidence (where $p_0 \leq p_{cr} = 130$ nm), HTP has to be higher than 23–25 μm^{-1}.

There are two most popular approaches for designing highly twisted FLC materials. The first, straightforward approach following from eq. (3.19) comprises FLC mixtures solely from chiral mesogens (i.e., the "all-chiral" FLC), some of the important data are collected in Table 3.2 (Bubnov et al., 2018; Fitas et al., 2017; Gough et al., 1999; Hamplova et al., 1999; Kašpar et al., 2004; Kurp et al., 2017; Nakamura and Nohira, 1990; Nguen et al., 2011; Tykarska et al., 2011; Wegłowska et al., 2018; Yasue et al., 2000). The measurement temperature is critically important, while characterizing the CD. From the application viewpoint, one should preferably use a temperature range where parameters show least temperature dependence. Generally, it is adopted by using the "reduced temperature" (T_r):

$$T_r = T_{next} - T_i \qquad (3.20)$$

where T_{next} is the temperature of the phase transition next above SmC* and T_i is current temperature. In nematics (including N*) it was shown that the order parameter (and the pitch, relates to it) becomes independent on any pre-transition effect at $0.95T_{iso}$; hence, often this value is also adopted for SmC*. However, the helix pitch (and some other FLC parameters) often shows significant temperature that is dependent even at

Table 3.2: Helical twisting of individual SmC* mesogens.

Entry	Chiral compound	n/m	p_0 (nm)	$1/p_0$ (μm⁻¹)	d_{cell} (μm)	P_S (nC/cm²)	θ (degree)	f_{GM} (kHz)	τ (μs)	Reference
1.	$H_{2m+1}C_mO$— compound	6/12	High	0.1	–	>100	–	–	~20	Bubnov et al. (2018)
2.	$H_{2m+1}C_mO$— compound	10/6	High	0.1	5	100–110*)	~30*)	–	60–70*)	Gough et al. (1999)
3.	Mixture of CD with various combination of x, y, z, k, n		260	3.8		>180	~40			
4.	C_3F_7—$(H_2C)_n$ compound		150	6.7	2–12	>200	~38	0.1–0.3	– (530–1,600)	Kurp et al. (2017)
5.	C_3F_7—$(H_2C)_n O$— compound	2/6 SmC$_A$*	300	3.3		100	44–45	0.676	>2,500 (235)	
6.		5/6	>2,000	<0.5	–	45		0.260	390 (612)	Fitas et al. (2017)
7.		6/6 SmC$_A$*	290	3.4		45		0.125	125 (1,270)	
8.		7/6 SmC$_A$*	250	4		45		0.600	>2,500 (265)	

(continued)

Table 3.2 (continued)

Entry	Chiral compound	n/m	p_0 (nm)	$1/p_0$ (µm⁻¹)	d_{cell} (µm)	P_S (nC/cm²)	θ (degree)	f_{GM} (kHz)	τ (µs)	Reference
9.		3/4	140	7.1		~150	25	0.08–0.1	(2,000–1,500)	Bubnov et al. (2018)
10.		3/5	317	3.2		~95	23	–	–	
11.		4/4	106	9.4	–	~185	27	0.5–0.8	(320–200)	
12.		4/5	170	5.9		~150	26	–	–	
13.		4/6	270	3.7		~120	22	–	–	
14.		80:20	400	2.5		~160	–			Wegłowska et al. (2018)
15.		60:40	420	2.3	2	~220		–	–	
16.		12/6	–355	2.9	7.5	~90	29	–	–	Nguen et al. (2011)
17.		6/10	600	1.7		195		–		
18.		8/7	>5,000	<0.2		190		–		
19.		8/10	~1,000	1.0	25	205	~40	–	–	Hamplova et al. (1999)
20.		8/12	1,000	1.0		170		–		
21.		6/**	~2,000	0.5		~310		–		
22.		8/**	~2,000	0.5		~330		–		

No.	Structure									Reference
23.	H₂ₘ₊₁CₘO—⟨⟩—N=N—⟨⟩—O—C(O)—⟨⟩—O—CH(CH₃)—C(O)—O—CₙH₂ₙ₊₁	6/6	~450	2.2		~120	38–42	–		Kašpar et al. (2004)
24.		6/8	~1,400	0.7		~110		–		
25.		6/10	~1,800	0.6		~100				
26.	H₂ₘ₊₁CₘO—⟨⟩—N=N—⟨⟩—O—C(O)—⟨⟩—C(O)—O—CH(CH₃)—C(O)—O—CₙH₂ₙ₊₁	7/6			25	60	17	0.5–0.8	(320–200)	
27.		8/6	>5,000	<0.2		65	19			
28.	H₂ₘ₊₁CₘO—⟨⟩—N=N—⟨⟩—O—C(O)—⟨⟩—C(O)—O—CH(CH₃)—CH₂—CH(CH₃)—CₙH₂ₙ₊₁	7/*					27	0.05	(3,200)	
29.		10/*				>120	35			
30.	C₉H₁₉O—⟨⟩—C(O)—O—⟨⟩(F)—O—C(O)—⟨⟩—O—CH₂—CH(C₂H₅)—(CH₂)₂—CF₃ MC815		210	4.8	50–100	230	g41	–	–	Yasue et al. (2000)
31.	C₈H₁₇O—⟨⟩—C(O)—O—⟨⟩—⟨⟩—O—(CH₂)ₙ—CH(CH₃)—C₂H₅	2	–2,200	0.45						Terashima et al. (1986)
		3	<+1,000	>1	200	<0.5	–	–	–	
		4	–2,100	0.48						
		5	+1,200	0.83						
32.	C₃F₇—(H₂C)ₙ—O—⟨⟩—O—C(O)—⟨⟩(F)—⟨⟩—O—C(O)—CH(CH₃)—CₘH₂ₘ₊₁	3/6 SmCₐ*	~230	4.3	–	–	–	–	–	Tykarska et al. (2011)

*Extrapolated to 25 °C.

$0.95T_{next}$ and more or less saturates at considerably low temperatures. Therefore, the data collected in Table 3.2 are mostly at 25–30 °C, whenever it is possible.

As given in Table 3.2, some of the individual chiral SmC⋆ compounds or their mixture indeed demonstrates a high performance (fast electro-optical switching); see examples 1 and 2. However, these compounds do not manifest high HTP and are limited to SSFLC application only. In additional, fluorine brings the chirality in these compounds, which affects the viscosity and switching time in a quite specific manner and differs from other chiral fragments (see above).
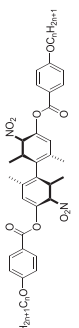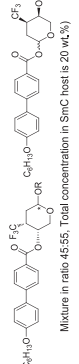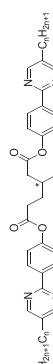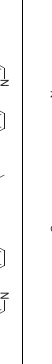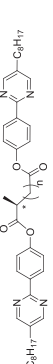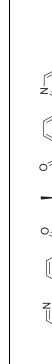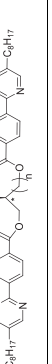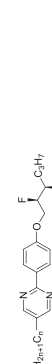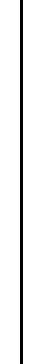
Conversely, in attempts to meet the whole set of DHFLC requirements, the chiral esters were designed and studied; see entries 3–13. However, although all components are individual chiral mesogens, the lowest p_0 reported value overcoming the p_{cr} is 106 nm in sole case; see entry 11. The pitches for another compounds listed in Table 3.2 are not even capable to shift the wavelength of selective reflection out of visible range toward UV ($p > 240$ nm); see entries 3, 10, 13–25, and 31. This approach allows to obtain SmC⋆ DHFLC materials with rather small $p_0 \cong 106$–300 nm (Bubnov et al., 2018; Fitas et al., 2017; Kurp et al., 2017; Terashima et al., 1986; Tykarska et al., 2011; Węgłowska et al., 2018). However, the response time τ_r is reported to be 125–265 μs and 390 μs in SmC$_A$⋆ and SmC⋆, respectively (Węgłowska et al., 2018). The relaxation time can be estimated using the Goldstone mode frequencies (f_{GM}) according to the relation $\tau_r = (2\pi f_{GM})^{-1}$ (Levstik et al., 1990). Based on reported values of $f_{GM} \cong 0.08$–0.8 kHz (Bubnov et al., 2018; Fitas et al., 2017; Tykarska et al., 2011), the τ_r is in the range of $\cong 2$–0.2 ms. The slower electro-optical response can be attributed to increasing y_φ with CD concentration. Furthermore, in the case of LC molecules with branched tail (including CDs with chiral terminal group), obviously higher y_φ (Andreev et al., 1993; Haase et al., 1999) is a dominating factor than a decrease in p_0^2, for slow EO response.

The reciprocal pitch (p^{-1}) given in Table 3.2 formally corresponds to the HTP measured at a CD concentration of $c = 1$; see eq. (3.19). Although in real cases linear dependencies $p^{-1}(c)$ are hardly valid for the whole concentration range, this parameter is convenient to compare the twisting of the "all-chiral" SmC⋆ with "chiral guest–non-chiral host" mixtures.

The alternative and more widely used approach is based on mixing CDs (those can be even non-mesogenic) with non-chiral SmC host. Typically, performance of such type of FLC is not essentially sacrificed until the concentration of CDs exceeds over 30–35 mol% (see, for example, Haase et al., 1999). According to eq. (3.19), the HTP value of CD should not be lower than 14–15 μm^{-1} to provide $p_{cr} \leq 240$ nm. In order to achieve full absence of Bragg's diffraction at any viewing angle ($p_0 \leq p_{cr} = 130$ nm), HTP has to be higher than 23–25 μm^{-1}. Currently, only limited number of CDs can show such high HTP; see the list in Table 3.3.
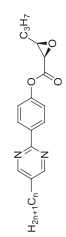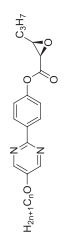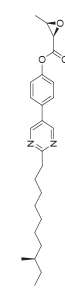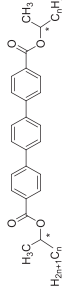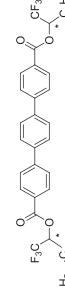
Both types of CD, where chirality is caused by asymmetry either in the "hard core" (type I) or in the terminal tail (type II), manifest high HTP (see Table 3.1, entries 1, 2 and 3–9, respectively). For CDs of type II, the remarkable HTP dependency on the length of alkyl spacer between two "rigid cores" was observed (entries 3–5).

Table 3.3: Chiral compounds possessing high HTP in the SmC* phase, if the phase is induced by mixing of these compounds with the corresponding non-chiral hosts described in subsequent sections (reproduced from Michailenko et al. (2019) with the permission of Elsevier).

Entry	Chiral compound, *n*	Non-chiral host[1]	HTP[2] (μm^{-1})	Reference
1			11–42[3]	Lemieux (2001), Vizitiu et al. (1999), Vizitiu et al. (2001)
2	Mixture in ratio 45:55, Total concentration in SmC host is 20 wt.%	PP + BPP	~30[4]	Itoh et al. (1993), Itoh et al. (1997)
3a	6–8	8PPO6	17	Nishiyama et al. (1993)
3b	9		38	
4a	7		1.4	
4b	6		20	Yoshizawa (1998), Yoshizawa and Nishiyama (1995)
5a	7		~0	
5b	8		0.8	
6a	6	PP	−12.6	
6b	8		−20.3	Wand et al. (1996)
6 c	9		−18.8	
6d	10		−30	

(continued)

Table 3.3 (continued)

Entry	Chiral compound, *n*		Non-chiral host[1]	HTP[2] (μm⁻¹)	Reference
7a		8	PP	7.7	
7b		10		7.2	
7c		12		5.6	
7d		8		4.7	Escher et al. (1993)
7e		8		>0	
7f				13	
8a		2–8	No data[4]	~9–12[4]	Beresnev et al. (1989), Loseva et al. (1991)
8b	LUCh-*n*	6	BPP	22	Michailenko et al. (2019)
9a		4	BPP (PP)	−18 (−11)	
9b		5	BPP (PP)	−32 (−18)	
9c		6	BPP (PP)	−36 (−22)	Pozhidaev et al. (2013), Pozhidaev et al. (2009b), Michailenko et al. (2019)
9d	FOTDA-*n*	7	BPP (PP)	−46 (−25)	
9e		8	BPP (PP)	−47 (−27)	

[1] Mixture of 2,5-disubstituted phenylpyrimidines (PP), or 5,4″-disubstituted 2-(4-biphenylil)pyrimidines (BPP). [2]Recalculation to HTP (mol.%) using data given in corresponding references. [3]At concentration of CDs 2 mol.%. [4]The corresponding references do not contain enough data for host identification, details on pitch measurements, and/or proper calculations of HTP.

It was rationalized considering that at the proper length of the spacer, both "rigid cores" of CD can be situated in two adjacent smectic layers, providing a high twisting torque between the layers (Yoshizawa, 1998, 1998). A similar mechanism can be adopted for the case by increasing the HTP with lengthening of terminal tail (entries 6–9). In all cases, correlation between lengths of CDs and non-chiral host molecules was also observed. Another explanation for the origin of high twisting in SmC⋆, which is based on the flexoelectric interaction, was proposed by Itoh et al. (1997) and Takanishi et al. (1999). It was concluded that "the ultrashort pitch of the present SmC⋆ phase is primarily because of the coupling between the relatively large P_S and large flexoelectric effect determined by the interaction between polar CD molecules" (Itoh et al., 1997). According to the examples in Table 3.3, both mechanisms of twisting in SmC⋆ phase can take place depending on the nature of the CD.

It is worth to mention that the **FOTDA-n** series, where substitution of CH_3 group with CF_3 at chiral centers of well-known CDs of **LUCh** series (Andreev et al., 1993; Chernova et al., 1993; Loseva et al., 1991; Rabinovich et al., 1989; Yoshizawa, 1998), that is, passage from **LUCh-6** to **FOTDA-6**, results in ~1.6 times higher HTP values. Apparently, the effect of dipole–quadrupole interaction plays a key role for the higher HTP for CD of almost equal geometry. In the series of **FOTDA-n** CDs, the HTP values increase with elongation of the terminal tails up to seventh homologue and saturates at the eighth homologue. For all **FOTDA-n** compounds, HTP values in the SmC⋆ phase are essentially higher in the biphenylpyrimidine host (**BPP-65-87**)than in the phenylpyrimidine one, **PP-88-810**. **FOTDA-7** and **FOTDA-8** demonstrate considerably higher HTP in SmC⋆ phase (see entries 9d and 9e).

The dependencies of HTP on the molecular structure of CDs can be summarized as follows. First, HTP depends on the length of the terminal alkyl chain, often being increased with their lengthening (cf. entries 3a and 3b, 4a and 4b, 6a–d and 9a–e, in Table 3.3). However, in some cases, there are an optimal alkyl length for maximum HTP (cf. entries 7a–c). Second, the HTP values correlate with the dipole moment of CD, or actually with induced P_s (cf. entries 8b with 9c).

These regulations match well with empirical rules (Goodby et al., 2014). In general, any factors leading to restriction of molecular rotation for both internal or external (the molecule as a whole) also favor the increase in molecular chirality and thereby increasing HTP.

It is worth also to mention here that two chiral groups on both terminal positions (like in a **LUCh** or **FOTDA**) can almost double the molecular HTP values through a transfer of the chirality in both adjacent smectic interlayer spaces.

For all regulations, it is important that at the proper length of the spacer, each of the "rigid cores" of CD can be placed simultaneously in two adjacent smectic layers providing high twisting torque between them (Nishiyama et al., 1993; Yoshizawa, 1998). Similar mechanism can be adopted for increasing the HTP with lengthening of terminal tail (entries 6–9). In all cases, correlation between lengths of CDs and non-chiral host molecules can also be expected.

Although detailed mechanism of supramolecular helix formation in the SmC⋆ phase is not clear yet, based on the fact that the helix consists of successive layers twisted at a certain fixed angle and the twisting originates mainly as a result of interactions through an interlayer space, the transfer of twisting torque from layer to layer is possible in two ways: either through chiral alkyl–alkyl interlayer interaction as it was suggested in the qualitative model of chirality (Michailenko et al., 2019; Nishiyama et al., 1993; Yoshizawa, 1998) (see Figure 3.9) or through dipole–quadrupole interaction (Itoh et al., 1997; Takanishi et al., 1999). The last hypothesis is based on Pikin–Idenbom consideration showing importance of flexoelectric interaction (Pikin and Idenbom, 1978).
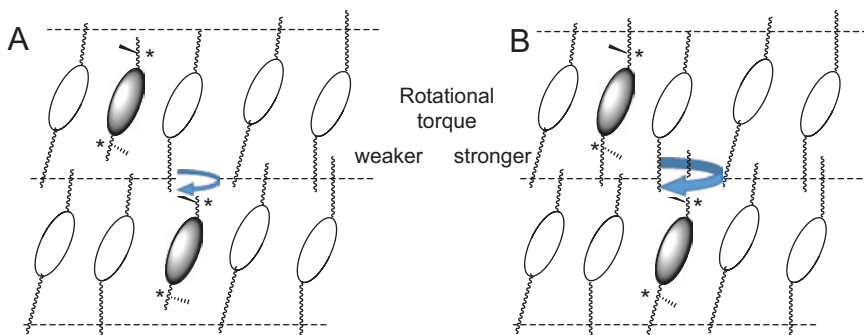
Figure 3.9: Schematic presentation of differences in transfer of rotational torque with chiral molecule of relatively short (a) and long (b) terminal tails (reproduced from Michailenko et al. (2019) with the permission of Elsevier).

Thus, the mechanism of twisting in SmC⋆ considerably differs than that in N⋆ phases, where the core–core chiral interaction is the main origin of high HTP and the twisting ability is almost independent of terminal tail length (Kutulya et al., 2001a, 2001b).

3.4 Effect of alignment-layer anchoring energy

Anchoring energy is a critically important parameter for the FLC alignment. It has been recently disclosed by Guo et al. (2014) that the optical contrast strongly depends on the anchoring energy normalized to the cell gap, which is particularly important for the ESHFLC mode where the anchoring energy is expected to be comparable with the elastic energy of the FLC helix. Figure 3.10 shows the contrast ratio dependence on the anchoring energy for two different FLCs.
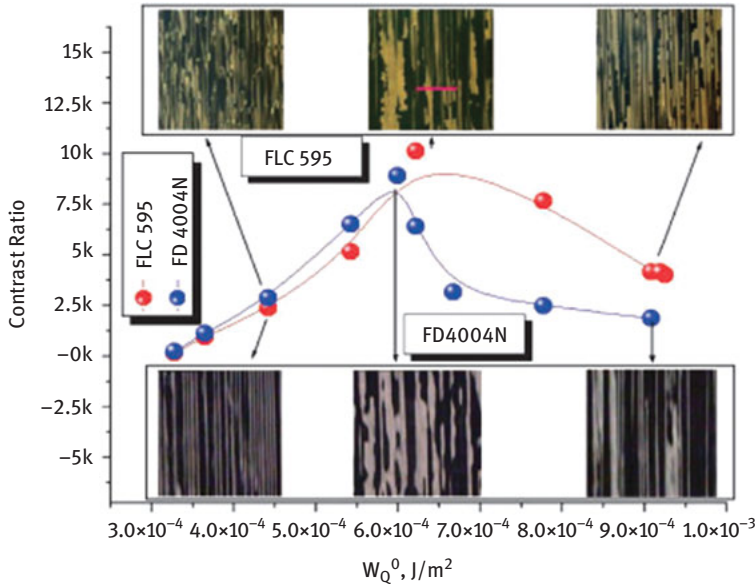
Figure 3.10: The optical contrast of the ESHFLC dependence on the anchoring energy for two different FLCs.

As a conclusion, one can achieve high optical quality for the optimum anchoring energy that will be different for different materials. Furthermore, it is advisable to use the photoalignment process because of two reasons: first, for the smooth alignment surface, and second, for the tunable anchoring energy. The anchoring of the photo-alignment layer can be tuned by the irradiation doses (Guo et al., 2014; Srivastava et al., 2012a, 2010a, 2011).

3.5 Application of FLCs for modern displays

FLCs are mostly being used for the field-sequential color displays type, wherein the color images are generated by illuminating the three (red, green, and blue color frames) subframes sequential in time. The frequency of the subframe rendering should be high enough so that the human eye integrates it in time to perceive a full-color image without color filters (Shi et al., 2018). Micro-display and portable flat panel displays were developed based on different FLC electro-optical modes. SSFLCs were first used by cannon in 1997 to make a ferroelectric LCD (FLCD) prototype (see Figure 3.11(a)), and later Kobayashi et al. showed an FLCD prototype made of polymer-stabilized FLCDs exhibiting V-shaped switching; see Figure 3.11(b)) (Shi et al., 2018). Some of recent efforts to make FLCDs are discussed below.
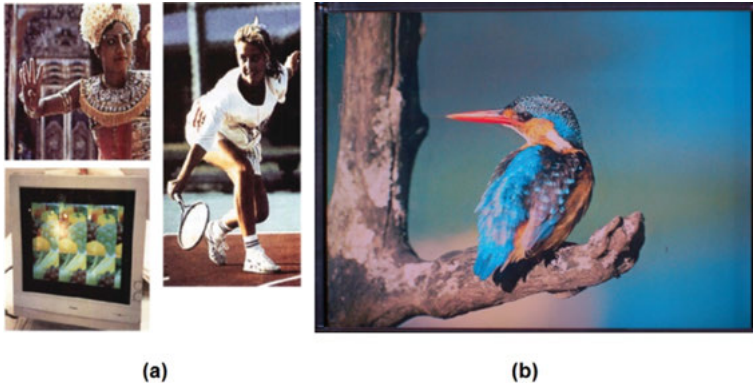
Figure 3.11: (a) SSFLC prototype from cannon and (b) PSVFLC prototype from Kobayashi et al.

a. FLCs for micro-displays

The SSFLC mode was primarily used for micro-displays. The binary electro-optical response of SSFLC combined together with the pulse width modulation were used to show the full-color micro-displays. There are two driving methods to generate the optical gray scale for the LCOS. First is the analogue addressing the modulation of the applied V_{rms}, and second is the pulse width modulation, which is further divided into several types: single pulse width modulation (*S-PWM*), pulse count modulation, binary-weighted pulse width modulation (*B-PWM*), and others. The S-PWM and B-PWM are often used for the binary-mode electro-optical devices such as SSFLCs and ESHFLCs. The B-PWM has the advantage of allowing an all-digital system, but required a higher bit depth than analogue addressing or S-PWM and is subjected to the B-PWM artifacts associated with the eye motion (Armitage et al., 2006; Rankin et al., 1996) and the pulse width modulation (see Figure 3.12). Pulse width modulation is the most common driving scheme for the binary electro-optical mode, such as SSFLC and ESHFLC. Furthermore, in the current solution, people use 0.18-μm node technology for the LCOS; however, for the high-resolution LCOS one has to use the advanced 0.09 μm or even smaller process node, and in this case, the driving voltage will be highly limited (see Figure 3.12(b)). Thus, we can say that FLCs, which show fast response time at the lower driving voltage, have greater potential for high-resolution LCOS. Companies like *Display-tech, Citizen*, and *4DD* have brought many different products based on FLCs on silicon (FLCOS) ranging from view finder, SLMS, and pico-projectors.
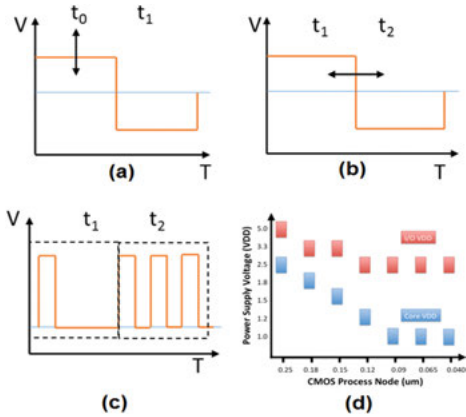
Figure 3.12: Driving scheme for the LCOS: (a) amplitude modulation, (b) pulse width modulation, (c) binary-weighted pulse width modulation, and (d) the maximum power supply voltage dependence on the CMOS process node.

b. Field-sequential color-active matrix displays

The electro-optical response manifests evident saturated bright and dark states of the FLC cell at 500 Hz and ±1.5 V with the response time $\tau_{0.1-0.9} = 130$ μs (Figure 3.4).

Thus, with the outstanding optical quality (with high contrast and no diffraction) and fast electro-optical modulation, the ESHFLCs are characterized by the binary high-quality optical shutter that can be deployed for the display applications. However, because of the binary amplitude modulation, such display demands digital driving unlike analogue driving for the conventional LCDs, where the gray scale is controlled by the amplitude of the driving voltage (Armitage et al., 2006; Rankin et al., 1996). Thus, the gray scale can be generated either by the pulse width modulation or by the multiple pulse modulation of the driving signal, as discussed in the previous section. However, pulse width modulation is more preferable from driving electronics point of view (Ho et al., 2015; Ma et al., 2013a; Shimizu, 2001). Therefore, the ESHFLC has been deployed for the field-sequential color displays with the pulse width modulation. We have been able to demonstrate 8-bit gray scale, that is, 24-bit color by utilizing the pulse width modulation, and several examples have been shown in Figure 3.13.
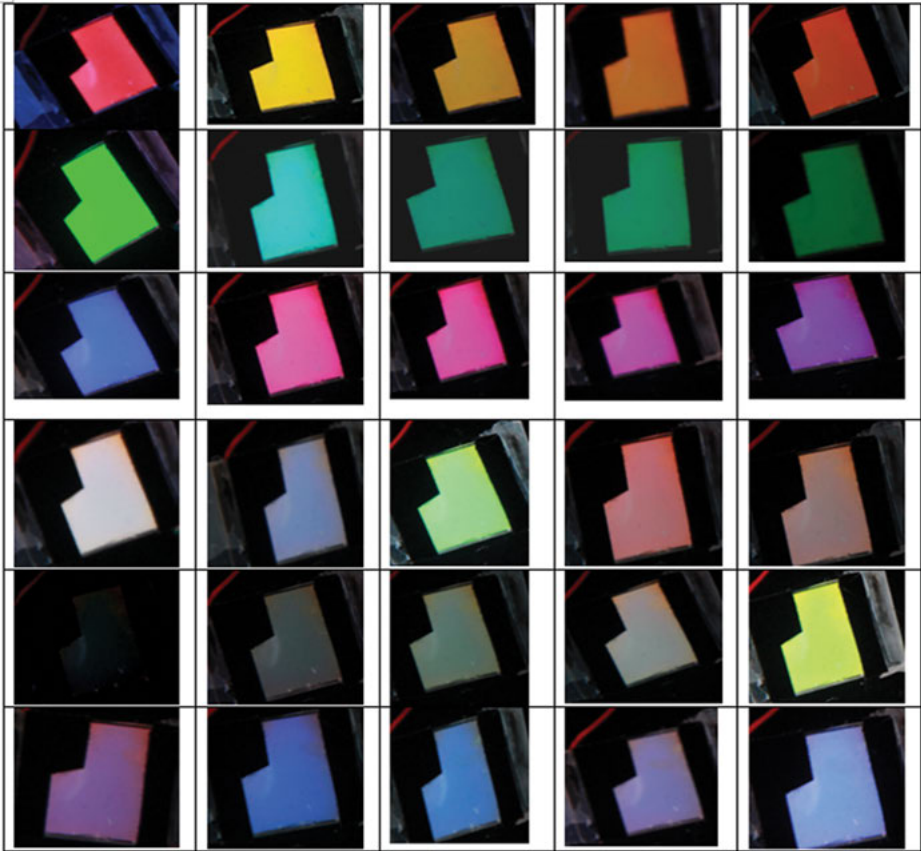
Figure 3.13: Few color samples generated by the ESHFLC-based field-sequential color display, where the gray scale has been generated by means of the pulse width modulation. An 8-bit gray scale has been achieved at the driving voltage of 3 V/µm (reproduced from Srivastava et al. (2015) with the permission of Wiley).

c. DHFLC-based field-sequential color displays

With the approach of generating the analogue gray scale by the amplitude modulation of the driving signal and electric field-independent fast electro-optical response, one can deploy the DHFLC for full-color field-sequential color display, and an attempt has been done by Pozhidaev and Chigrinov (2010). Figure 3.14(b) and (c) shows examples of various grayscale generation, and thus, different colors from the DHFLC cell.
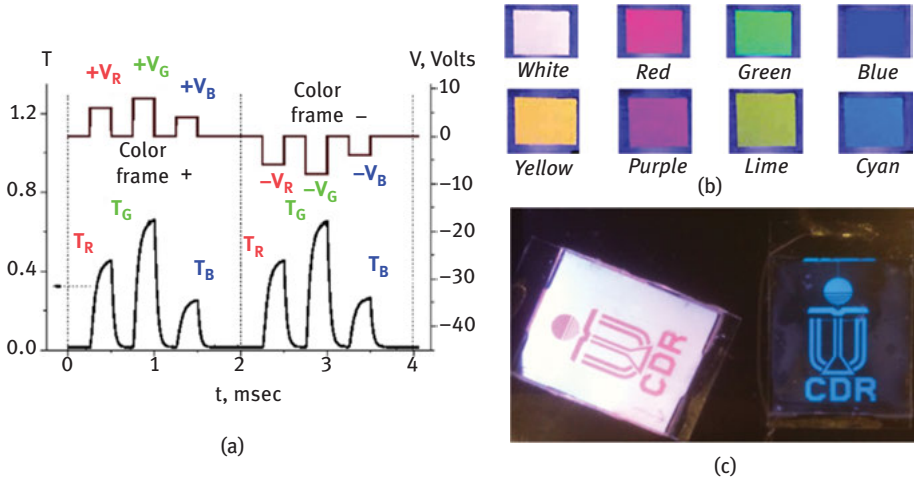
Figure 3.14: Bottom is the electro-optical response of the DHFLC placed between crossed polarizers at $\beta = 0$; T_R, T_G, and T_B are transmissions of the primary red, green, and blue lights. Top is the driving voltage applied to the DHFLC and synchronized sequentially with corresponding red, green, and blue light-emitting diodes; (b) some examples achieved for different colors by the DHFLC FSC cell are shown. (c) DHFLC display cell in normally white and normally black configuration is shown.

3.6 Application of the FLCs for various photonic elements

a. Diffraction in FLC

There are three different approaches that underline the most popular methods used for producing the diffractive profile. These are based on: (1) the intrinsic diffractive properties of LC like cholesteric liquid crystals and FLC (Srivastava et al., 2012a), (2) deploying the patterned electrode (Fan et al., 2012), and (3) defining two or more different alignment regions (Srivastava et al., 2012b). All of these diffractive LC structures have been extensively documented recently (Beresnev et al., 1990; Fan et al., 2012; Ma et al., 2013b; Nakatsuhara et al., 2014; Shteyner et al., 2013; Srivastava et al., 2011, 2012a, 2015, 2012b, 2013, 1643; Wang et al., 2013a). The intrinsic or natural diffraction in the FLCs appears because of the two factors: first, helical pitch; and second, ferroelectric domain structure of the FLC system. Such diffraction lobes become a serious issue for the display application particularly for the dark state. Figure 3.15(a) shows the luminance viewing angle plot for diffraction of the white light LED in the dark state of the FLCs between two crossed polarizers. The intensity profile of the same luminance plot of the diffraction pattern for the bright and dark states has been shown in Figure 3.15(b), whereas the left

(a)

(b)
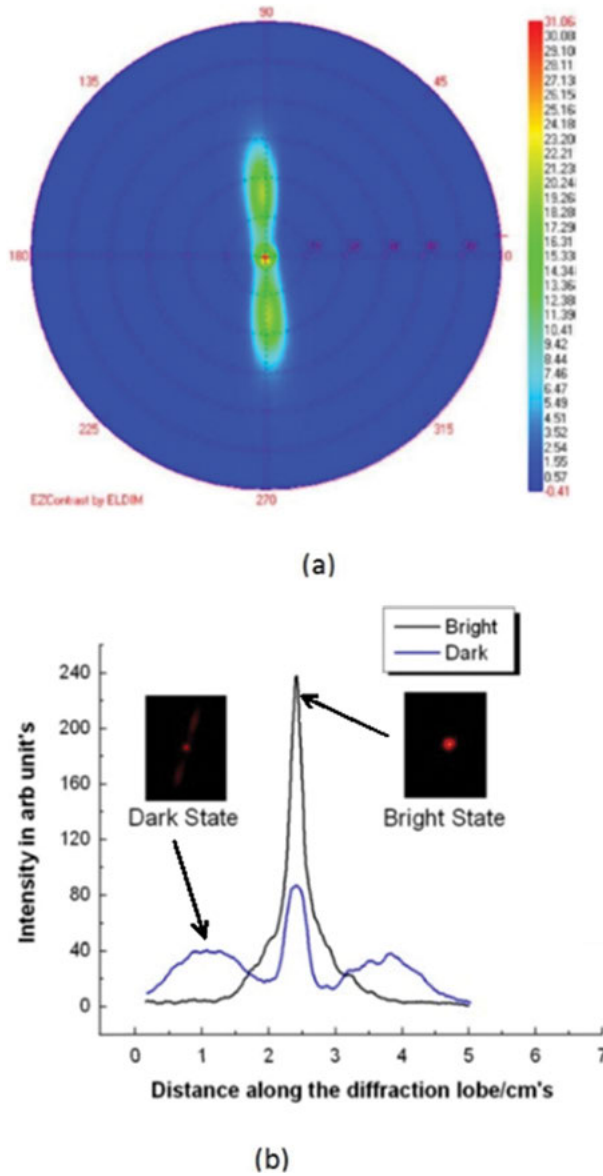
Figure 3.15: (a) The luminance viewing angle plot for the FLC in the dark state. (b) The intensity profile along the diffraction lobe, whereas the left insert shows the photograph of the bright and dark states of the FLC under crossed polarizer and right insert shows the intensity profile of the diffraction lobe at different electric fields (Srivastava et al., 2011, 2010a) (reproduced from Srivastava et al. (2015) with the permission of Wiley).

insertion shows photographs for the bright and dark states. This intrinsic diffraction of FLC and the periodicity of the ferroelectric domain are directly proportional to the spontaneous polarization of the FLC (Beresnev et al., 1990). Moreover, due to the electric field dependence of the polarization, the diffraction efficiency also increases at higher electric field (insert right, Figure 3.15(b)). However, the intrinsic diffraction of FLCs often comes with the scattering due to the chevron defects and it is certainly not good to find any potential application. An effort to improve the diffraction of such natural diffraction of FLCs includes addition of chiral single-wall carbon nanotubes (SWCNTs) in pure FLC matrix (Srivastava et al., 2011). It has been observed that the diffraction properties can be improved but at the same time coagulation of SWCNTs and system instabilities are still an issue.

Second possibility includes the application of the patterned electrodes and controls the diffraction by controlling the inter-digital electric field or restricted periodic vertical electric field. However, for FLCs, in addition to the desired diffraction profile because of the periodic electric field the natural diffraction also appears; therefore, it is very difficult to achieve potential diffraction profile for various applications (Srivastava et al., 2011, 2015).

b. Pattern alignment of FLCs

An approach is based on the periodic distribution of the FLC director to form the periodic index distribution and later on controlling the diffraction profile by the application of electric field (Fan et al., 2012; Ma et al., 2013a, 2013b; Nakatsuhara et al., 2014; Srivastava et al., 2011, 2012a, 2012b). This involves a patterned photoalignment with periodic distribution of the easy axis (Srivastava et al., 2012b). The natural diffraction and hysteresis are issues for this method as well; however, the photoalignment based on the sulfonic azo dye provides, first, the re-writability of the easy axis, and second, the good control on the anchoring energy by means of different irradiation energies (Guo et al., 2014; Srivastava et al., 2012a). Thus, it is possible to achieve a periodic distribution of the FLC director with good optical quality, particularly for ESHFLCs (Srivastava et al., 2012b).

The recent development for ESHFLCs reveals that the ESHFLC shows good optical quality, that is, high contrast, no intrinsic diffraction lobe in either bright or dark state (Guo et al., 2014). Based on this technology, two alignment domains with orthogonal easy axis in the plane of the substrates can be realized by means of two-step exposure (Shteyner et al., 2013). The angle between the two easy axis and periodicity can be varied for different applications, and some of the examples are discussed further.
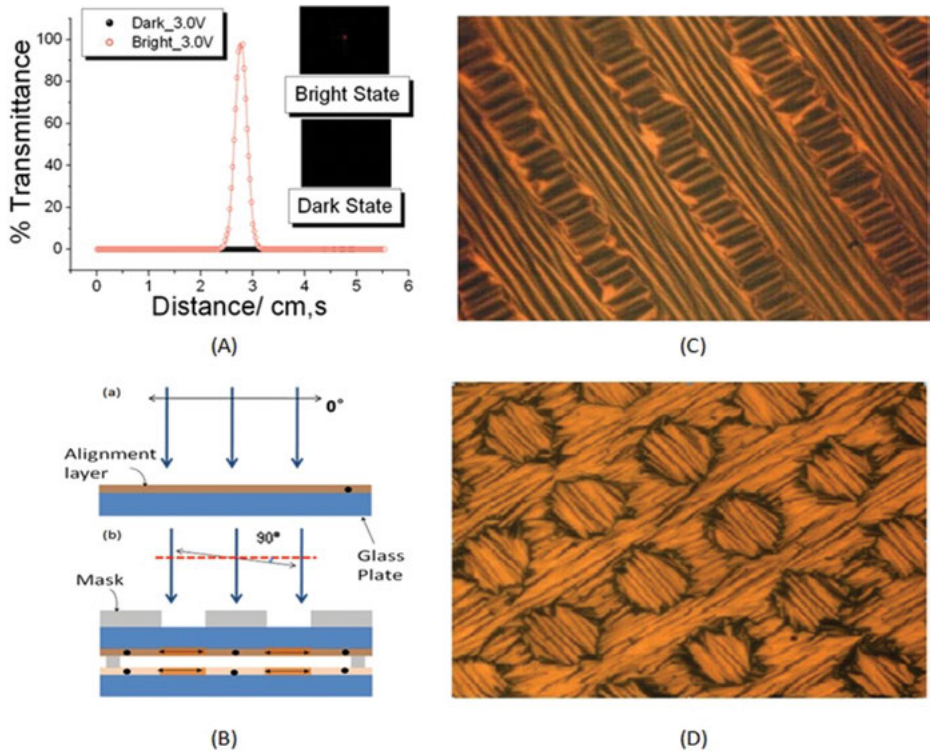
Figure 3.16: (A) The intensity profile of the natural diffraction for ESHFLC cell between crossed polarizers in bright and dark states and insert shows photographs of the respective states. (B) The fabrication procedure of the diffracting element followed by two-step exposure procedures is described in (a) and (b). (C) and (D) show the optical microphotographs of 1D and 2D ESHFLC grating elements (Ma et al., 2013b; Srivastava et al., 2011) (reproduced from Srivastava et al. (2015) with the permission of Wiley).

i. Switchable liquid crystal grating with submillisecond response

One of such efforts has been shown in Figure 3.16, wherein the ESHFLC has been aligned orthogonally in adjacent alignment domains with the periodicity of 50 μm. Figure 3.16(B) shows simple fabrication that include two-step exposures wherein the first exposure step (Figure 3.16(B(a)) provides the uniform monodomain alignment and the dot in the figure shows the direction of the easy axis after the first irradiation. Thereafter, the cell is assembled followed by the second-step exposure with the desired mask; for the shown example it is 1D and 2D mask (Figure 3.16)). The anchoring energy is the key parameter for the ESHFLCs, which should be comparable to the elastic energy of FLCs, and therefore, it is important to have the same anchoring energies in the two adjacent alignment domains (Srivastava et al., 2012b). The 1D and 2D ESHFLC diffraction grating structures are shown in Figure 3.17.
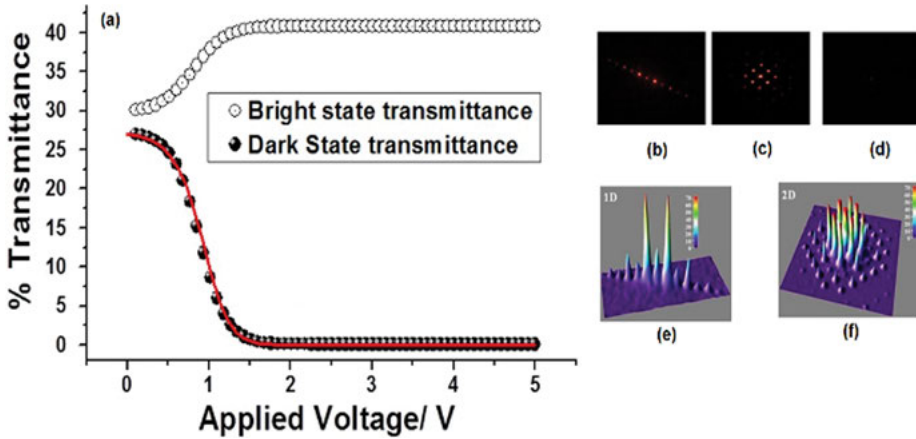
Figure 3.17: The electric field dependence of the transmittance for the first diffraction order in bright and dark states of the ESHFLC diffraction grating element is shown. The solid line represents the curve computed from eq. (3.21). Inserts show diffraction profiles of ESHFLC grating: (a) the diffractive state of 1D grating; (b) the diffractive state of 2D grating; (c) the black state, which is same for both gratings. (d)–(e) show intensity profile measured at the voltage V = 5 V for 1D and 2D gratings, respectively (Srivastava et al., 2012b) (reproduced from Srivastava et al. (2015) with the permission of Wiley).

The diffraction pattern and the intensity profile for 1D and 2D grating are shown in the insert of Figure 3.17(b) and (c), respectively. The inset (d) shows the dark state of the FLC grating, which is the same for both 1D and 2D structures. The transmittance of the first diffraction order is plotted as a function of voltage, in both the bright and dark states, in Figure 3.17. Both the curves reach in the regime of saturation at voltages higher than 2 V (Ma et al., 2013b; Srivastava et al., 2012b); thus, the diffraction efficiency and optical contrast for such gratings are independent of the applied electric field after 2 V.

The theoretical description of the phenomenon can be explained based on a simple electro-optical model describing the FLC grating in the geometry of crossed polarizers. For a plane wave ($\lambda \approx 632$ nm) normally incident on the domain with the helix axis directed along the x-axis (the z-axis is normal to the cell) and the FLC director $(d_x, d_y, d_z) = \cos\theta x + \sin\theta c$, where $c = cos\varphi y + sin\varphi z$ is the c-director and the transmission matrix can be written in the following form:

$$T = R(\psi)\begin{pmatrix} t_e & 0 \\ 0 & t_o \end{pmatrix}R(-\psi), \quad t_{o,e} \approx \exp(in_{o,e}h) \tag{3.21}$$

where $h = 2\pi d/\lambda$; $n_e^2 = [(1-d_z^2)/\varepsilon_{//} + d_z^2/\varepsilon_{\perp}]^{-1}$ and $(n_o^2 = \varepsilon_{\perp})$ are the refractive index of extraordinary and ordinary waves. Whereas $\psi = \arg(d_x + id_y)$ is the azimuthal angle of optical axis and $\mathbf{R}(\psi)$ is the 2×2 rotation matrix. Our grating can be regarded as a

binary FLC grating with the director rotated by $\pi/2$ about the z-axis in the adjacent domains and the transfer matrix

$$T_g = p(y)R(-\pi/2) \cdot T \cdot R(\pi/2) + (1 - p(y))T \tag{3.22}$$

where $p(y)$ is the P_g-periodic diffraction profile function characterized by the Fourier coefficients $c_n = r \exp(i\,\pi n r) \sin c(\pi n r)$ and the first domain fraction ratio $r = P_1/P_g$. in the crossed polarizer geometry, the transmittance coefficients of the diffraction orders are given by

$$T_n = T_{xy} \times \begin{cases} (2r - 1)^2, & n = 0 \\ 4r2[sinc(\pi n r)]^2, & n \neq 0 \end{cases} \tag{3.23}$$

where $T_{xy} \approx sin^2(\delta/2)sin^2[2(\psi + \theta)]$, $\delta = \Delta n h$ is the phase retardation, and $\Delta n = n_e - n_o$ is the birefringence. When the azimuthal angle of FLC director ϕ varies from $\phi = 0$ ($\psi = \theta$) to $\phi = \pi$ ($\psi = -\theta$) the transmittance coefficient T_{xy} decays to zero so that the grating is in the non-diffractive state at $\phi = \pi$.

Another parameter that is equally important is the dynamical response. The electric field dependence on the response time for the first diffraction order is similar to one of the planar aligned FLC cell, which is ~20 μs at the electric field of 6.6 V/μm, the response time is ~20 μs; in some case, depending on the material parameters and mode of operation, it could be even faster. Such a fast response time enables us to drive the device up to very high driving frequency of $f \approx 5$ kHz. The contrast ratio for FLC cell with ESHFLC mode is typically very high, similarly the ESHFLC diffracting elements also show high contrast ratio. The contrast ratio for the first diffraction order (i.e., the ratio of the I_{max}/I_{min} for the first order) is more than 7,000:1.

Using the same theoretical and experimental concepts, it is possible to fabricate various types of photonic elements from ESHFLCs. Some of the recent work has been shown below.

ii. Fresnel lens

Figure 3.18(a) and (b) shows the optical microphotograph of the ESHFLC Fresnel lens under the crossed polarizer. The angle between the easy axes of the two alignment domains is 45°, one can choose different angles depending on the application. The diffraction pattern in the diffractive and non-diffractive states has been shown in Figure 3.18(c) and (d), respectively (Srivastava et al., 2013, 1643; Wang et al., 2013a). Furthermore, the ESHFLC diffraction mode, in association with photoalignment, is capable to provide submicron resolution (Shteyner et al., 2013). Thus, in summary, the ESHFLC diffraction mode offers remarkable opportunity with much better optical and dynamical parameter in the same class diffracting elements.
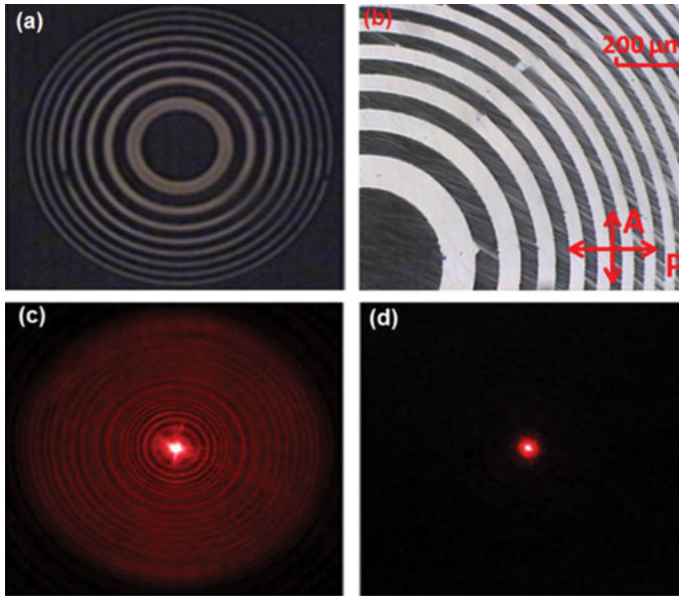
Figure 3.18: (a) and (b) The optical microphotograph of the electrically suppressed helix ferroelectric liquid crystal Fresnel lens under the polarizing microscope. (c) and (d) The photographs of the diffractive and non-diffractive states are shown (reproduced from Srivastava et al. (2015) with the permission of Wiley).

iii. Dammann gratings

The Dammann grating (DG) is a kind of specially designed binary phase (0, π) grating that could create a diffraction pattern, where the intensities of the diffracted spots are equal in some orders (Dammann and Görtler, 1971; Dammann and Klotz, 1977). The idea of these kinds of grating was first proposed by Dammann and Görtler (1971) to obtain multiple images from one input object for optical lithography. Later on, DGs have been proposed for using in lots of interesting application, such as laser beam summation (Veldkamp et al., 1986), optical interconnections (Morrison et al., 1993), 3D optical imaging (Yu et al., 2013), 3D lattice structures generation (Davis et al., 2011), and optical communication (Pozhidaev and Chigrinov, 2006). Moreover, by modifying the grating structure, the optical function of the DG is also extended to be more versatile such as the generation of array of diffractive orders with different vortex phase distribution (Ge et al., 2016; Lei et al., 2015). An ESHFLC-based DG was demonstrated by Fan et al. (2017). The grating can be switched between a diffractive state with 7×7 optical spots array having equal intensities, and a non-diffractive state, electric field polarity (see Figure 3.19).
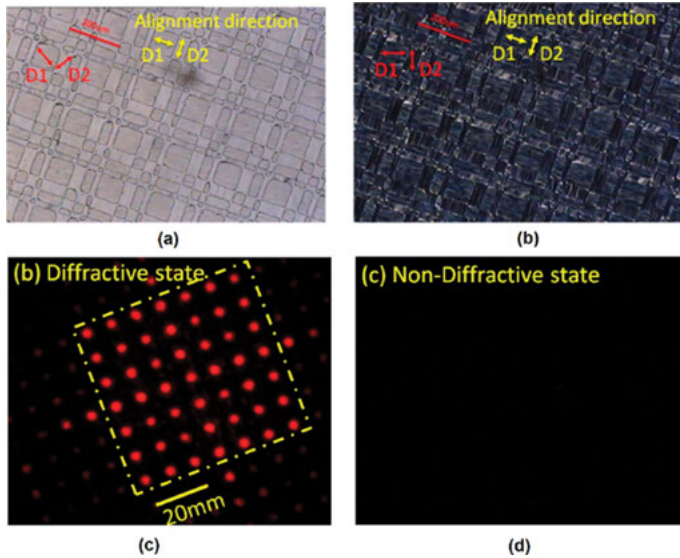
Figure 3.19: The ESHFLC Dammann grating pattern. (a) Microscopic photo of the ESHFLC DG in the diffractive state under crossed polarizer and analyzer, (**b**) microscopic photo of the ESHFLC DG in the non-diffractive state under crossed polarizer and analyzer, (c) diffractive pattern for the diffractive state, and (**d**) diffractive pattern for the non-diffractive state (Fan et al., 2017).

The ESHFLC DG, with switching on time and off time in the range of 80 μs, is significantly faster than DGs based on blue phase LC or dual-frequency LC; therefore, it may be useful for optical communication and beam shaping.

iv. Fork gratings

Optical vortices have attracted great attention and have been extensively studied during the past two decades (Allen et al., 1992; Molina-Terriza et al., 2007; Verbeeck et al., 2013). The optical vortex is a light beam characterized by a helical phase front (Yao and Padgett, 2011). It can be used for optical tweezers, micro-motors, and micro-propellers and have broad applications in the fields of informatics, micromanipulation, and astronomy. So far, several techniques have been explored to generate optical vortex (Carpentier et al., 2008; Ganic et al., 2002; Slussarenko et al., 2011; Uchida and Tonomura, 2010; Vaughan and Willetts, 1979; Yuan et al., 2008). Recently, a very convenient approach for the fabrication of beam vortex is proposed, which is based on fork grating (FG) having a diffraction grating with dislocations centered at the beam axis (Heckenberg et al., 1992). Some of the fields, namely, quantum computing, optical communicating, and micromanipulating demand-tunable use LCs extensively (Li, 2012).

An alternative technique for the generation of fast switchable and reconfigurable optical vortices with high efficiency is based on the fast switchable LCs. The FLCs because of ultra-fast response times and smaller driving voltages claim to be a potential candidate. The unique optical quality of the ESHFLC and in-plane modulation of the FLC optic axis can be used to fabricate two modes of FG, first, DIFF/OFF switchable mode and second, DIFF/TRANS switchable mode by using single-side alignment method (see Figure 3.20). For DIFF/OFF mode grating, it comprises two states, that is, diffraction state (diffractive state forming a diffraction pattern) and OFF state (no light and thus no diffraction pattern). For DIFF/TRANS mode grating, it also involves two states, that is, diffraction state (diffractive state forming a diffraction pattern) and transmission state (light passing through without any diffraction pattern). These gratings can be tuned between these states by applying the alternating electric field. The FLC FG show high diffraction efficiency, fast response time of ~50 μs at 6.67 V/μm, and high contrast ratio >1,550:1 at low driving voltage. Therefore, it offers better possibilities for a variety of modern devices (Ma et al., 2016).

c. FLC lenses

Another important area where FLC has been deployed is lenses. We proposed different types of lenses, that is, Fresnel zone lenses (based on the micropatterning), bistable lenses, ophthalmologic lenses, and so on, and some of them are discussed here.

i. Bistable lenses

Electrically tunable focusing LC lenses have many applications in imaging systems and projection systems, such as portable devices, pico-projections, optical trapping, endoscopy, solar cells, optical zoom systems, and ophthalmic lenses (Asatryan et al., 2010; Chen et al., 2014; Kawamura et al., 2005; Li et al., 2014; Lin and Chen, 2013; Ren and Wu, 2012; Sato, 1979). The concept of the bistable lenses involve the memorization of one functionality on being triggered by the external forces, in this case, electric field. A bistable negative lens with a large aperture size (~10 mm) was proposed in 2014 by integrating a bistable polarization switch made of bistable FLCs with a passively polarization-dependent anisotropic focusing element (Chen et al., 2014; Lin and Chen, 2013). The lens not only exhibits electrically tunable bistability but also fast response time of submilliseconds. The tunable lens power is from 0 to −1.74 Diopters; see Figure 3.21.
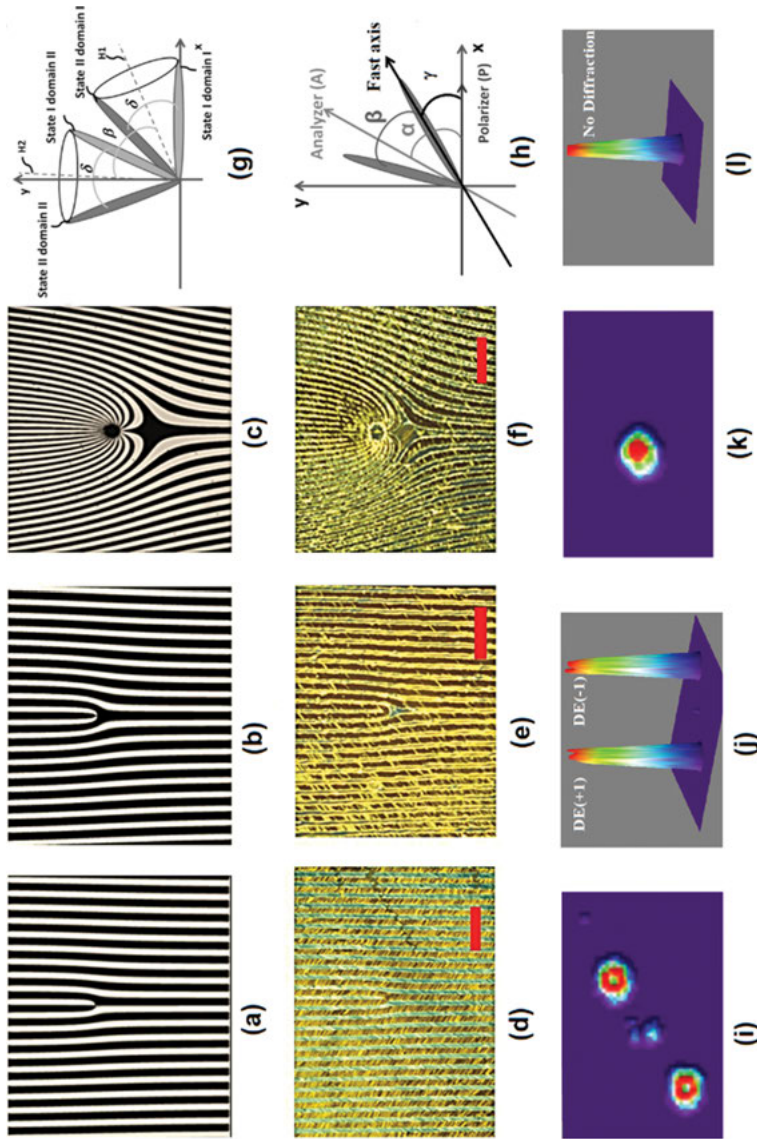
Figure 3.20: Computer-generated holograms for (a) $m = 1$, (b) $m = 2$, and (c) $m = 21$. Microphotographs recorded on FLC cells for (d) $m = 1$, (e) $m = 2$, and (f) $m = 21$. The scale bar is 100 μm. (g) The diagram illustrates FLC molecular orientation in the two states of two domains, in the x–y coordinate. The angle between the easy axes of the two domains is β. (h) The positions of the polarizer, analyzer, and FLC fast axis are illustrated. The angle between the polarizer (P) and the analyzer (A) is α, and γ represents the angle between the FLC fast axis and the polarizer. The CCD camera photographs for FG, with $m = 1$ and the optimization conditions defined above, for top (i) and front views (k) in diffraction state and the transmission state of top (c) and front views (d) (Ma et al., 2016).
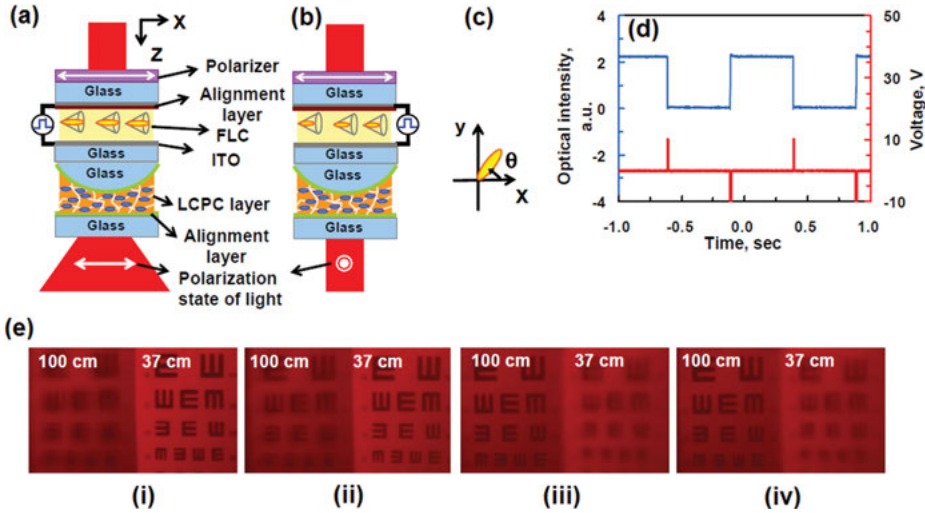
Figure 3.21: Operating principles and the structure of the bistable negative lens at (a) e-state and (b) o-state. The white arrow of the polarizer indicates the transmissive axis. The propagation direction of incident light is along +z direction. (c) The top view of FLC directors of the FLC layer in (a) $\theta = 0$, and $\theta = 46°$ means that the LC lens is at e-state and o-state, respectively. Electro-optical properties of the FLC sample under pulsed voltages of (a) 10 V (image performance of the assembled sample (a) at o-state (−10 V). (b) After the voltage was turned off, the image remains the one at o-state. (c) Image performance at e-state (+10 V). (d) After the voltage was turned off, the image remains the one at e-state (Chen et al., 2014).

The function of FLC layer serves as an electrically bistable polarization switch and thus affects the focusing properties of the passively anisotropic focusing element. The bistable FLC polarization switch can switch the polarization azimuth of the impinging light by the application of the short electric pulse (see Figure 3.21(d)). Thus, the power of the passive focusing element can be tuned by switching the polarization state. Later, the bistable FLC polarization switch memorizes the respective state unless another pulse with other electric polarity is applied. The proposed tunable lens switches power from ~1.74 D to 0 D for the aperture size of 10 mm; see Figure 3.21 (Chen et al., 2014).

ii. A 2D–3D lens array

Three-dimensional displays (both stereoscopic and autostereoscopic) have been heavily explored to accomplish a better viewing experience (Geng, 2013; Son et al., 2005, 2010; Tsai et al., 2009; Tsuboi et al., 2010). Recently, the stereoscopic (with glasses) displays based on the technologies such as an optical shutter and polarization rotation systems were commercialized (Kawai, 2002; Sun et al., 2014). However, these systems

are bulky and limited to the individual audience; therefore, there is a demand for developing auto-stereoscopic displays (Neil, 2005; Wang et al., 2013b). Furthermore, in the shortage of 3D content and representations of text together with 3D content, we need a lens system that can be quickly switched from 3D to 2D or vice versa and that consumes less or no power. An interesting approach utilizing the passive polarization-dependent polymeric lenticular lens array with an active twisted nematic (TN) cell that works as a polarization converter was proposed by Ren et al. In their work, a passive polymeric film was fabricated by LC polymer, in the presence of an in-plane electric field. The TN cell functions as a polarization rotator to switch the focus and defocus states for the lens array. However, the applied voltage to the TN cell is large and comparable to the LCD panel itself, which results in considerably large power consumption (Ren and Wu, 2012). Thus, FLC-based lenses were explored for the same purpose, and a 2D–3D switchable lens unit based on a polarization-sensitive microlens array and a polarization selector unit made of ESHFLC was proposed by Shi et al. (2017). The polarization-dependent passive lens shows the focusing effect only for the P-polarized light; however, the S-polarized light just passes through the lens without showing any focusing effect (see Figure 3.22(a)–(d)). As expected, the ESHFLC-based lenses offer a low electric field (~1.7 V/μm) operations with a small switching time (<50 μs). However, because of the binary electro-optical operations of ESHFLCs, a special driving scheme, to switch between 2D and 3D modes, was used to avoid unwanted issues related to DC accumulation that could affect the optical quality. Surprisingly, the proposed lens, in spite of the fact that it is based on the half-wave plate, shows 3D cross talk <5%. The wavelength dependence of the transmittance and the cross talk (in percent) has been shown in Figure 3.22(e).

d. Fiber sensors based on FLCs

DHFLCs have been exploited for the sensor application because of the linear electro-optical response in a certain range of small electric field. DHFLC with a special selection of angular restriction between angles β and α shows high sensitivity and hysteresis-free fast and linear electro-optical response at the lower electric field which is of great significance for various sensor applications. In a recent report, Brodzelli et al. (2012) have used DHFLC for the development of the voltage sensor and hydrophones. An example of such type of sensor (i.e., pressure sensor) is shown in Figure 3.23. A piezoelectric material converts the pressure into the electrical signal that is amplified by the optically powered amplifier and supplied to the DHFLC cell, wherein the optical signal coupled by the optical fiber shows substantially large modulation after being reflected by the back mirror. The beauty of such sensor is a passive operation regime that does not require any power in the inactive mode, which is crucial for several applications.
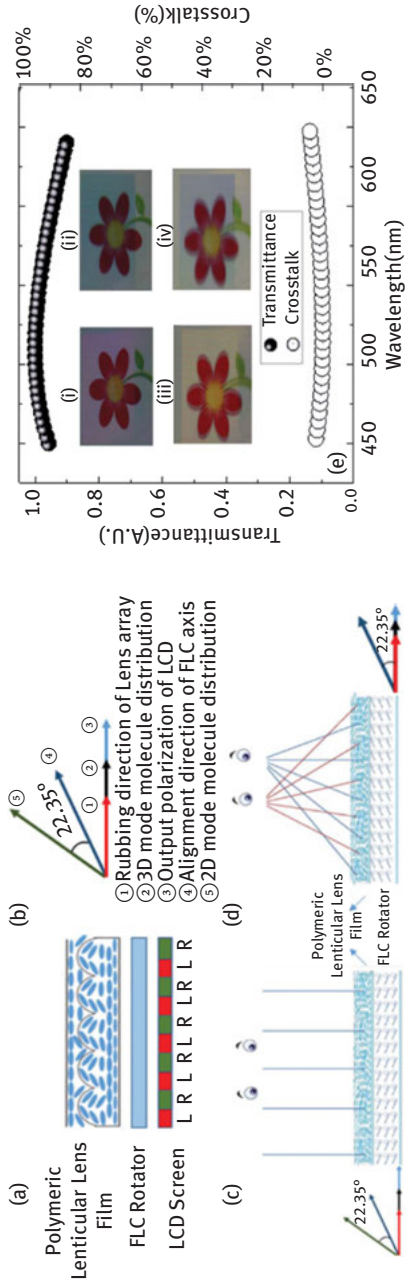
Figure 3.22: Working principle of the 2D–3D switchable display. (a) The auto-stereoscopy system is composed of an LCD screen, ESHFLC polarization selector unit, and polymeric lenticular lens array; (b) illustration of orientational arrangement of lens array, ESHFLC polarization selector unit, and output polarization azimuth of LCD; (c) 2D mode working principle illustration; (d) 3D mode working principle illustration; and (e) solid circles represent the transmittance of ESHFLC, and the open circle represents the cross talk against the optical wavelength, respectively. For insert pictures: (i) 2D content with non-focusing effect (2D mode); (ii) 2D content with focusing effect; (iii) 3D content with non-focusing state; and (iv) 3D content with focusing effect (Shi et al., 2017).
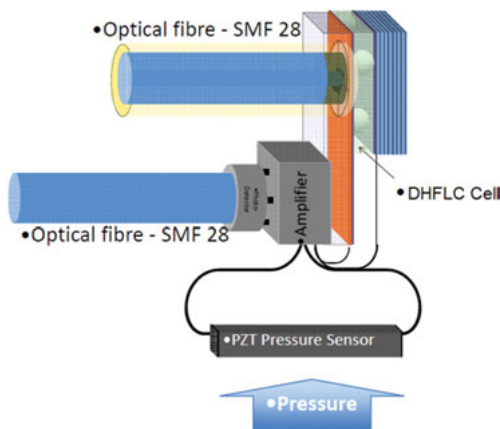
Figure 3.23: The schematic of the DHFLC pressure sensor. The PZT pressure sensor converts the pressure in the electrical signal, which is further amplified by the optically powered amplifier and supplied to the DHFLC cell. Thus, the signal coupled by the optical fiber to the DHFLC cell shows modulated electro-optical response after reflected from the back mirror (Brodzeli et al., 2012).

References

Abdulhalim, I., Moddel, G. (1991). Molecular Crystals and Liquid Crystals, 200(79).

Allen, L., Beijersbergen, M.W., Spreeuw, R.J.C., Woerdman, J.P. (1992). Orbital angular momentum of light and the transformation of Laguerre-Gaussian laser modes. Physical Review A, 45(11), 8185–8189.

Andreev, A.L., Chernova, N.I., Kompanets, I.N., Loseva, M.V., Parfenov, A.F., Pavluchenko, A.I., Pozhidaev, E.P. (1993). SPIE, 2051, 212–219.

Armitage, D., Underwood, I., Wu, S.-T., Introduction to Microdisplays, John Wiley & Sons, 2 Nov 2006, Technology & Engineering.

Asatryan, K., Presnyakov, V., Tork, A., Zohrabyan, A., Bagramyan, A., Galstian, T. (2010). Optical lens with electrically variable focus using an optically hidden dielectric structure. Optics Express, 18(13), 13981–13992.

Bahr, C., Heppke, G., Wuthe, K. (1992). Liquid Crystals, 12, 997.

Beresnev, L.A., Blinov, L.M., Dergachev, D.I. (1988). Ferroelectrics, 85, 561.

Beresnev, L.A., Chigrinov, V.G., Dergachev, D.I., Pozhidaev, E.P., Funfschilling, J., Schadt, M. (1989). Liquid Crystals, 5(1171).

Beresnev, L.A., Loseva, M.V., Chernova, N.I., Kononov, S.G., Adomenas, P.V., Pozhidaev, E.P. (1990). JETP Letters, 51, 516.

Berreman, D.W. (1973). Molecular Crystals and Liquid Crystals, 22, 175–184.

Bradshaw, M.J., Brimmell, V., Raynes, E.P. (1987). Liquid Crystals, 2, 107–110.

Brimmell, V., Constant, J., Pedlingham, H.A., Raynes, E.P., Samra, A.K. (1989). Liquid Crystals, 6, 545–551.

Brodzeli, Z. et.al (2013). Journal of Lightwave Technology, 1(17), 2940.

Brodzeli, Z., Silvestri, L., Michie, A., Chigrinov, V.G., Guo, Q., Pozhidaev, E.P., Kiselev, A.D., Ladouceur, F. (2012). Photonic Sensors, 2(3), 237.

Bubnov, A., Cherviňski, M., Jurkoviĉová, T.V., Piecek, W.A. (2018). Beilstein Journal of Nanotechnology, 9, 333–341.

Carpentier, A.V., Michinel, H., Salgueiro, R.J., David, O. (2008). Making optical vortices with computergenerated holograms. American Journal of Physics, 76(10), 916–921.

Chambers, M., Clemitson, R., Coates, D., Greenfield, S., Jenner, J.A., Sage, I.C. (1989). Liquid Crystals, 5, 153–158.

Chan, L.K.M., Gray, G.W., Lacey, D. (1985). Molecular Crystals and Liquid Crystals, 123, 185–204.

Chen, H.S., Lin, Y.H., Srivastava, A.K., Chigrinov, V.G., Chang, C.M., Wang, Y.J. (2014). A bi-stable negative lens by integrating a polarization switch of ferroelectric liquid crystals with a passively anisotropic focusing element. Optics Express, 22(11), 13138.

Chernova, N.I., Loseva, M.V., Pozhidaev, E.P., Korotkova, N.I. (1993). Ferroelectrics, 138, 95–101.

Chigrinov, V.G. (1999). Liquid Crystal Devices: Physics and Applications, Artech-House, Boston- London.

Chigrinov, V.G., Kwok, H.S., Photoalignment of liquid crystals: applications to fast response ferroelectric liquid crystals and rewritable photonic devices, In a book: "Progress in Liquid Crystal Science and Technology: in Honor of Shunsuke Kobayashi's 80th Birthday", World Scientific, February (2013).

Cho, C., IMID 2012 DIGESTS, P2-60, (2012).

Clark, N.A., Lagerwall, S.T. (1980). Submicrosecond bistable electrooptic switching in liquid crystals. Applied Physics Letters, 36, 899.

Coe-Sullivan, S., SID Symposium Digest of Technical Papers, Wiley Online Library 2016, pp. 239–240.

Colegrove, J., Touch Display Research, SID, Display week, 2018 LA, 2018.

Dammann, H., Görtler, K. (1971). High-efficiency in-line multiple imaging by means of multiple phase holograms. Optics Communications, 3, 312–315.

Dammann, H., Klotz, E. (1977). Coherent optical generation and inspection of two-dimensional periodic structures. Optica Acta, 24, 505–515.

Davis, J.A., Moreno, I., Martínez, J.L., Hernandez, T.J., Cottrell, D.M. (2011). Creating three-dimensional lattice patterns using programmable Dammann gratings. Applied Optics, 50, 3653–3657.

Elston, S.J., Ulrich, D.C. (1995). Journal of Applied Physics, 78, 4331.

Escher, C., Hemmerling, W., Illian, G., Harada, T., Murakami, M., US Pat., 5231528, 1993.

Fan, F. et al. (2012). Applied Physics Letters, 100, 111105.

Fan, F., Yao, L., Wang, X., Shi, L., Srivastava†, A.K., Chigrinov, V.G., Kwok, H.-S., Wen, S. (2017). Ferroelectric liquid crystal dammann grating by patterned photoalignment. Crystals, 7, 79.

Fitas, J., Dłubacz, A., Fryń, P., Marzec, M., Jaworska-Gołąb, T., Deptuch, A., Kurp, K., Tykarska, M., Żurowska, M. (2017). Liquid Crystals, 44, 566–576.

Freeman, M.O., Brown, T.A., Walba, D.M. (1992). Applied Optics, 31, 3917–3929.

Fukushima, S., Kozawaguchi, H., Kurokawa, T., Matsuo, S. (1990). Optics Letter, 15, 285–287.

Fünfschilling, J., Schadt, M. (1989). Journal of Applied Physics, 66(3877).

Ganic, D., Gan, X., Gu, M., Hain, M., Somalingam, S., Stankovic, S., Tschudi, T. (2002). Generation of doughnut laser beams by use of a liquid-crystal cell with a conversion efficiency near 100%. Optics Letter, 27(15), 1351–1353.

Gardiner, D.J., Morris, S.M., Castles, F., Qasim, M.M., Kim, W.S., Choi, S.S., Park, H.J., Chung, I.J., Coles, H.J. (2011). Applied Physics Letters, 98, 263508.

Ge, S., Chen, P., Ma, L., Liu, Z., Zheng, Z., Shen, D., Hu, W., Lu, Y. (2016). Optical array generator based on blue phase liquid crystal Dammann grating. Optical Materials Express, 6, 1087.

Geng, J. (2013). Advances in Optics and Photonics, 5, 456.

Goodby, J.W. (1991). Ferroelectric Liquid Crystals. Principles, Properties and Applications, Gordon and Breach Science Publishers S.A.

Goodby, J.W., Cowling, S.J., Davis, E.J., Jia, X. (2014). Chiral structures in liquid crystals of calamitic systems. In Handbook of Liquid Crystals, 2nd, Wiley-VCH Verlag GmbH & Co. KGaA, Chapter 4.

Gough, N., Parghi, D.D., Lewis, R.A., Hird, M. (1999). Molecular Crystals and Liquid Crystals, 332, 347–354.

Gray, G.W., Hird, M., Lacey, D., Toyne, K.J. (1989). Journal of the Chemical Society, Perkin Transactions 2, 2041–2053.

Guo, Q., Srivastava, A.K., Pozhidaev, E.P., Chigrinov, V.G., Kwok, H.S. (2014). Applied Physics Express, 7, 021701.

Haase, W., Ganzke, D., Pozhidaev, E.P. (1999). Materials Research Society Symposium Proceedings, 599, 15–26.

Hamplova, V., Kaspar, M., Pakhomov, A.B., Bubnov, A.M., Glogarova, M. (1999). Molecular Crystals and Liquid Crystals, 332, 181–188.

Heckenberg, N., McDuff, R., Smith, C.P., White, A.G. (1992). Laser beams with phase singularities. Optical and Quantum, 24(9), S951–S962.

Hegde, G., Xu, P., Pozhidaev, E., Chigrinov, V., Kwok, H.S. (2008). Liquid Crystals, 35, 1137.

Hird, M. (2007). Chemical Society Reviews, 36, 2070–2095.

Hird, M. (2011). Liquid Crystals, 38, 1467–1493.

Hird, M. (2014). Handbook of Liquid Crystals, 2nd, Chapter 8, Wiley-VCH Verlag GmbH & Co. KGaA, 237–261.

Ho, T.K. et.al (2015). SID Symposium Digest of Technical Papers, 73(2).

Hori, K. (1982). Molecular Crystals and Liquid Crystals, 82, 13–17.

Hwang, J.Y., Lee, Y.J., Cho, C., Heo, J.U., Baek, J.H., Kim, Y., Kim, J.H., Yu, C.J. (2013). Journal of Physics D: Applied Physics, 46, 165301.

Illian, G., Müller, I., Wingen, R. (Hoechst) DE 4.116.751 (1992/11/26).

Itoh, K., Takanishi, Y., Yokoyama, J., Ishikawa, K., Takezoe, H., Fukuda, A. (1997). Japanese Journal of Applied Physics, 36, L784.

Itoh, K., Takeda, M., Namekawa, M., Nayuki, S., Murayama, Y., Yamazaki, T., Kitazume, T. (1993). Ferroelectrics, 148, 85–102.

Jakli, A., Saupe, A. (1991). Liquid Crystal, 9, 519.

Jakli, A., Saupe, A. (1992). Physical Review A, 45, 5674.

JP 2014019647 (A) – Compound, ferroelectric liquid crystal composition using the same and liquid crystal display Okimoto Naoko; Wand Michael Dainippon Printing Co Ltd.

Kašpar, M., Bubnov, A., Hamplová, V., Pirkl, S., Glogarová, M. (2004). Liquid Crystals, 31, 821–830.

Kawai, T. (2002). Displays, 23(49).

Kawamura, M., Ye, M., Sato, S. (2005). Optical trapping and manipulation system using liquid-crystal lens with focusing and deflection properties. Japanese Journal of Applied Physics, 44(8), 6098–6100.

Kelly, S.M. (2014). Synthesis of Chiral Smectic Liquid Crystals, in Handbook of Liquid Crystals, 2nd, Wiley-VCH Verlag GmbH & Co. KGaA, Chapter 3.

Kelly, S.M., Fünfschilling, J. (1994). Journal of Materials Chemistry, 4, 1673–1688.

Kim, D., Yu, C., Lim, Y., Na, J.H., Lee, S.D. (2005). Applied Physics Letters, 87, 051917.

Kim, H.R. (2004). Ferroelectrics, 312(1), 57.

Kiselev, A.D., Pozhidaev, E.P., Chigrinov, V.G., Kwok, H.S. (2011). Physical Review E, 83(1–11), 031703.

Kotova, S., Kvashnin, M., Rakhmatulin, M., Zayakin, O., Guralnik, I., Klimov, N., Clark, P., Love, G., Naumov, A., Saunter, C., Loktev, M., Vdovin, G., Toporkova, L. (2002). Optics Express, 10, 1258.

Kurp, K., Czerwiński, M., Tykarska, M., Bubnov, A. (2017). Liquid Crystals, 44,748.

Kutulya, L., Vashchenko, V., Semenkova, G., Shkolnikova, N., Drushlyak, T., Goodby, J.W. (2001a). Molecular Crystals and Liquid Crystals Section A, 361, 125–134.

Kutulya, L.A., Semenkova, G.P., Shkolnikova, N.I., Vashchenko, V.V., Ostis, L.L., Sorokin, V.M., Kozachenko, A.G. (2001b). Molecular Crystals and Liquid Crystals Section A, 357, 43–54.

Lagerwall, S.T. (2004). Ferroelectric and antiferroelectric liquid crystals. Ferroelectrics, 301, 15.

Lagerwall, S.T., Dahl, I. (1984). Molecular Crystals and Liquid Crystals, 114(151).

Lee, J.-H., Kim, D.-W., Wu, Y.-H., Yu, C.-J., Lee, S.-D., Wu, S.-T. (2005). Optics Express, 13, 7732.

Lee, J.H., Liu, D.N., Wu, S.T. (2008). Introduction to Flat Panel Displays, John Wiley & Sons Ltd.

Lei, T., Meng, Z., Li, Y., Ping, J., Liu, G.N., Xu, X., Li, Z., Min, C., Jiao, L., Yu, C. (2015). Massive individual orbital angular momentum channels for multiplexing enabled by Dammann gratings. Light: Science & Applications, 4, e257.

Lemieux, R.P. (2001). Accounts of Chemical Research, 34, 845–853.

Levstik, A., Kutnjak, Z., Filipic, C., Levstik, I., Bregar, Z., Zeks, B., Carlsson, T. (1990). Physical Review A, 42, 2204–2210.

Li, L.W., Bryant, D., Van Heugten, T., Bos, P.J. (2014). Speed, optical power, and off-axis imaging improvement of refractive liquid crystal lenses. Applied Optics, 53(6), 1124–1131.

Li, Q. (2012). Liquid Crystals Beyond Displays: Chemistry, Physics, and Applications, John Wiley & Sons.

Lin, Y.H., Chen, H.S. (2013). Electrically tunable-focusing and polarizer-free liquid crystal lenses for ophthalmic applications. Optics Express, 21(8), 9428–9436.

Loseva, M., Chernova, N., Rabinovich, A., Pozhidaev, E., Narkevich, J., Petrashevich, O., Kazachkov, E., Korotkova, N., Schadt, M., Bucheker, R. (1991). Ferroelectrics, 114, 357–377.

Love, G.D., Bhandari, R. (1994). Optics Communications, 110, 475.

Ma, Y., Srivastava, A.K., Chigrinov, V.G., Kwok, H.S. (2013a). SID Symposium Digest of Technical Papers, 44, 1300.

Ma, Y., Sun, J., Srivastava, A.K., Guo, Q., Chigrinov, V.G., Kwok, H.S. (2013b). Europhysics Letters, 102, 24005.

Ma, Y., Wei, B.Y., Shi, L.Y., Srivastava, A.K., Chigrinov, V.G., Kwok, H.-S., Hu, W., Lu, Y.Q. (2016). Fork gratings based on ferroelectric liquid crystals. Optics Express, 24, 5822.

McMillan, W.L. (1973). Physical Review, 8, 1921.

Meyer, R.B., In abstracts of the 5th International Liquid Crystal Conference: Stockholm, Sweden, 1974, p. 115.

Meyer, R.B., Liebert, L., Strzelecki, L., Keller, P. (1975). Journal of Physical Chemistry Letters, (Orsay, Fr.), 36, L69–L71.

Michailenko, V.V., Krivoshey, A.I., Pozhidaev, E.P., Popova, E.V., Fedoryako, A.P., Gamzaeva, S., Barbashov, V., Srivastava, A.K., Kwok, H.S., Vashchenko, V.V. (2019). Journal of Molecular Liquids, 281, 186–195.

Ming, Y., Chen, P. et al. (2017). Tailoring the photon spin via light–matter interaction in liquid-crystal-based twisting structures. Quantum Materials, 2(1), 6.

Moddel, G., Johnson, K.M., Li, W., Rice, R.A., PaganoStauffer, L.A., Handschy, M.A. (1989). Applied Physics Letters, 55, 537.

Molina-Terriza, G., Torres, J.P., Torner, L. (2007). Twisted photons. Nature Physics, 3(5), 305–310.

Morrison, R.L., Walker, S.L., Cloonan, T.J. (1993). Beam array generation and holographic interconnections in a free-space optical switching network. Applied Optics, 32, 2512–2518.

Nakamura, S., Nohira, H. (1990). Molecular Crystals and Liquid Crystals, 185, 199–207.

Nakatsuhara, K., Kato, A., Hayama, Y. (2014). Optics Express, 22, 9597–9603.

Naumov, A.F., Love, G.D., Yu. Loktev, M., Vladimirov, F.L. (1999). Optics Express, 4, 344.

Neil, A. (2005). Computer, 8(32).

Nguen, H.T., Rouillion, J.C., Cluzeau, P., Sigaud, G., Destrade, C., Isaert, N. (2011). Liquid Crystals, 17, 571–583.

Nishiyama, I., Ishizuka, H., Yoshizawa, A. (1993). Ferroelectrics, 147, 193–204.

Ohno, K., Ushioda, M., Saito, S., Miyazawa, K. (Chisso) EP 313.991 (1989/05/03)

Okaichi, N., Kawakita, M., Sasaki, H., Watanabe, H., Mishina, T. (2018). Journal of the Society for Information Display, 1–12, 2018. Doi: https://doi.org/10.1002/jsid.741.

Optical applications of liquid crystals shutters, L. Vicari. https://www.crcpress.com/Optical-Applications-of-Liquid-Crystals/Vicari/p/book/9780750308571

Osipov, M.A., Stegemeyer, H., Sprick, A. (1996). Physical Review E, 54, 6387–6403.

Ouchi, Y., Takezoe, H., Fukuda, A., Kondo, K., Kitamura, T., Yokokura, H., Mukoh, A. (1988). Japanese Journal of Applied Physics, 27, 5, L733.

Panarin, Y., Pozhidaev, E., Chigrinov, V. (1991). Ferroelectrics, 114(181).

Pelzl, G. (1998). Optical properties of nematic liquid crystals. In Handbook of Liquid Crystals, Vol. 2A, Wiley-VCH Verlag GmbH, Weinheim.

Pikin, P.A., Idenbom, V.L. (1978). Soviet Physics Uspekhi, 22, 487.

Popova, E.V., Fedoryako, A.P., Drushlyak, T.G., Vashchenko, V.V., Kutulya, L.A. (2006). Ferroelectrics, 343, 33–40.

Pozhidaev, E., Chigrinov, V. (2010). SID'10 Digest, 387.

Pozhidaev, E., Chigrinov, V., Hegde, G., Xu, P. (2009a). Joint System Initialization Database, 17/1(53).

Pozhidaev, E., Torgova, S., Minchenko, M., Yednak, C.A.R., Strigazzi, A., Miraldi, E. (2010). Liquid Crystals, 37, 1067–1081.

Pozhidaev, E.P. (2001). SPIE Digest, 4511, 92.

Pozhidaev, E.P., Chigrinov, V.G. (2006). Crystal Representatives, 51, 1030.

Pozhidaev, E.P., Kiselev, A.D., Chigrinov, V.G., Srivastava, A.K., Minchenko, M.V., Kotova, S.P., Orientational Kerr-effect in ferroelectric liquid crystals, Abstracts of 24th Intern. Liq. Cryst. Conf, Mainz, Germany, August (2012).

Pozhidaev, E.P., Kiselev, A.D., Srivastava, A.K., Chigrinov, V.G., Kwok, H.S., Minchenko, M.V. (2013). Physical Review E, 87, 052502.

Pozhidaev, E.P., Minchenko, M., Molkin, V., Torgova, S., Srivastava, A.K., Chigrinov, V., Kwok, H.S., Vashenko, V., Krivoshey, A., High Frequency Low Voltage Shock-Free Ferroelectric Liquid Crystal: A New Electro-Optical Mode with Electrically Suppressed Helix, Oral 1.3, Eurodisplay 2011, Arcachon, France, September, (2011).

Pozhidaev, E.P., Srivastava, A.K., Kiselev, A.D., Chigrinov, V.G., Vashchenko, V.V., Krivoshey, A.I., Minchenko, M.V., Kwok, H.S. (2014). Optics Letters, 39(10), 2900.

Pozhidaev, E.P., Torgova, S.I., Molkin, V.M., Minchenko, M.V., Vashchenko, V.V., Krivoshey, A.I., Strigazzi, A. (2009b). Molecular Crystals and Liquid Crystals, 509, 1042–1050.

Presnyakov, V., Liu, Z., Chigrinov, V.G. (2005). Proceedings of SPIE, 5970, 426.

Rabinovich, A.Z., Loseva, M.V., Chernova, N.I., Pozhidaev, E.P., Petrachevich, O.S., Narkevich, J.S. (1989). Liquid Crystals, 6, 533–543.

Rankin, I.D., Underwood, I., Vass, D.G. et al. (1996). Full color images on a binary spatial light modulator. Ferroelectrics, 181, 139–146.

Rao, L., Yan, J., Wu, S.T., Yamamoto, S., Haseba, Y. (2010). Applied Physics Letters, 98, 081109.

Reiffenrath, V., Krause, J., Plach, H.J., Weber, G. (1989a). New liquid-crystalline compounds with negative dielectric anisotropy. Liquid Crystals, 5(1), 159–170.

Reiffenrath, V., Krause, J., Weber, G., Finkenzeller, U., Waechtler, A., Geelhaar, T., Coates, D., Sage, I.C.; Greenfield, Simon From Ger. Offen. (1989b), DE 3906019 A1 19890921.

Ren, H., Wu, S.T. (2012). Introduction to Adaptive Lenses, John Wiley.

Ren, H., Wu, S.-T. (2003). Applied Physics Letters, 82, 22.

Rieker, T.P., Clark, N.A., Smith, G.S., Parmar, D.S., Sirota, E.B., Safinya, C.R. (1987). Physical Review Letters, 59, 2658.

Rudquist, P., Lagerwall, J.P.F., Buivydas, M., Gouda, F., Lagerwall, S.T., Clark, N.A., Maclennan, J.E., Shao, R., Coleman, D.A., Bardon, S., Bellini, T., Link, D.R., Natale, G., Glaser, M.A., Walba, D. M., Wand, M.D., Chen, X.-H. (1999). Journal of Materials Chemistry, 9(1257).

Sakaguchi, K., Kitamura, T. (1991). Ferroelectrics, 114, 265–272.

Sakashita, K., Shindo, M., Nakauchi, J., Uematsu, M., Kageyama, Y., Hayashi, S., Ikemoto, T. (1991). Molecular Crystals and Liquid Crystals, 199, 119–127.

Sakurai, T., Yokota, T., Komatsu, E., Mikami, N., Higuchi, R., Takeuchi, K. (Ajinomoto) EP 260.077 (1988/03/16)

Sasou, N., Maruyzma, S., Matsushita, T., Wand, M., Birefringence improving agent, ferroelectric liquid crystal composition and liquid crystals, display device using the agent, and compound. WO2015009290 (A1), (2015). Dainippon Printing Co Ltd.

Sato, S. (1979). Liquid-crystal lens-cells with variable focal length. Japanese Journal of Applied Physics, 18(9), 1679–1684.

Shen, Y. et.al (2015). Applied Physics Letters, 106, 191101.

Shi, J., Srivastava, A.K., Cheung, A., Hsieh, C.-T., Hung, C.-L., Lin, C.-H., Sugiura, N., Kuo, C.-W., Chigrinov, V.G., Kwok, H.-S. (2018). Active matrix field sequential color electrically suppressed helix ferroelectric liquid crystal for high-resolution displays. Journal of the Society for Information Display, 26, 325–332.

Shi, L., Srivastava, A.K., Tam, A.M.W., Chigrinov, V.G., Kwok, H.-S. (2017). A 2D-3D switchable display based on passive polymeric lenticular lens array and electrically suppressed ferroelectric liquid crystal. Optics Letters, July, 42(17), 3438.

Shimizu, J.A. (2001). Philips' scrolling color LCOS engine for HDTV rear projection. Information Display, 11, 14–19.

Shteyner, E.A., Srivastava, A.K., Chigrinov, V.G., Kwok, H.S., Afanasyev, A.D. (2013). Soft Material, 9, 5160.

Slussarenko, S., Murauski, A., Du, T., Chigrinov, V., Marrucci, L., Santamato, E., Santamato, E. (2011). Tunable liquid crystal q-plates with arbitrary topological charge. Optics Express, 19(5), 4085–4090.

Son, J.-Y., Javidi, B., Disp, J. (2005). Technol, 1(125).

Son, J.-Y., Javidi, B., Yano, S., Choi, K.-H. (2010). Journal of Display Technology, 6, 394.

Srivastava, A.K. et al. (2011). Applied Physics Letters, 99, 201106.

Srivastava, A.K., Chigrinov, V., Kwok, H.-S. (2015a). Ferroelectric liquid crystals: excilent tool for modern displays and photonics. Journal of the Society for Information Display, 23(6), 253.

Srivastava, A.K., Chigrinov, V.G., Kwok, H.S. "Ferroelectric Liquid crystal Gratings", Invited Talk, Liquid Crystals Photonic Workshop, held at Hong Kong, Dec, (2012a).

Srivastava, A.K., de Bougrenet de la Tocnaye, J.L., Dupont, L. (2010a). Journal of Display Technology IEEE/OSA, 6, 522.

Srivastava, A.K., Hu, W., Chigrinov, V.G., Kiselev, A.D., Lu, Y.Q. (2012b). Applied Physics Letters, 100, 031112.

Srivastava, A.K., Misra, A.K., Shukla, J.P., Manohar, R. (2010b). Polymer Composite, 31(10), 1776.

Srivastava, A.K., Pozhidaev, E.P., Chigrinov, V.G., Manohar, R. (2011). Applied Physics Letters, 99, 201106.

Srivastava, A.K., Wang, X., Chigrinov, V.G., Kwok, H.S., "Liquid Crystal Fresnel Lens" Filled USPTO Application No. US 61/958742 Aug (2013).

Srivastava, A.K., Wang, X., Gong, S.Q., Shen, D., Lu, Y.Q., Chigrinov, V.D.G., Kwok, H.S. (2015b). Micro-patterned photo-aligned ferroelectric liquid crystal fresnel zone lens. Optics Letters, 40(8), 1643.

Stegemeyer, H., Meister, R., Hoffmann, U., Kuczynski, W. (1991). Induced smectic C* phases. Liquid Crystals, 10(3), 295–310.

Sun, J., Srivastava, A.K., Zhang, W., Wang, L., Chigrinov, V., Kwok, H.S. (2014). Optics Letter, 39, 6209.

Takanishi, Y., Ouchi, Y., Takezoe, H., Fukuda, A., Mochizuki, A., Nakatsuka, M. (1990). Japanese Journal of Applied Physics, 29, L984.

Takanishi, Y., Yokoyama, J., Ishikawa, K., Takezoe, H., Fukuda, A., Orihara, H., Osipov, M.A. (1999). Japanese Journal of Applied Physics, 38, L580.

Terashima, K., Ichihashi, M., Kikuchi, M., Furukawa, K., Inukai, T. (1986). Some observations on the sense and magnitude of spontaneous polarization and twisting power of a number of ferroelectric liquid crystal types. Molecular Crystals and Liquid Crystals, 141(3–4), 237–249.

Terashima, K., Ichihashi, M., Takeshita, F., Kikuchi, M., Furukawa, K., Eur. Pat. Appl. (1988), EP 293763 A2 19881207.

Tsai, R.-Y., Tsai, C.-H., Lee, K., Wu, C.-L., Lin, L.-C.D., Huang, K.-C., Hsu, W.-L., Wu, C.-S., Lu, C.-F., Yang, J.-C. (2009). Proceedings of SPIE, 7329, 732903.

Tsuboi, M., Kimura, S., Takaki, Y., Horikoshi, T. (2010). Journal of the Society for Information Display, 18, 698.

Tykarska, M., Czerwinski, M., Zurowska, M. (2011). Liquid Crystals, 38, 561.

Uchida, M., Tonomura, A. (2010). Generation of electron beams carrying orbital angular momentum. Nature, 464(7289), 737–739.

Ulrich, D.C., Cherrill, M.J., Elston, S.J. (1997). Liquid Crystals, 23, 797–802.

US 6, 413,448 B1 Cyclohexyl- and cyclohexenyl-substituted liquid crystals with low birefringence, Michael Wand, William Thurmes, Kundalika M. More, Xin-Hua Chen. Displaytech Inc.

Vashchenko, V.V., Pozhidaev, E.P., Srivastava, A.K., Chigrinov, V.G., Kwok, H.S., "Low birefringence ferroelectric liquid crystal mixture", US2018/0216004 A1, HKUST, Hong Kong.

Vaughan, J., Willetts, D. (1979). Interference properties of a light beam having a helical wave surface. Optics Communications, 30(3), 263–267.

Veldkamp, W.B., Leger, J.R., Swanson, G.J. (1986). Coherent summation of laser beams using binary phase gratings. Optics Letter, 11, 303–305.

Verbeeck, J., Tian, H., Van Tendeloo, G. (2013). How to manipulate nanoparticles with an electron beam?. Advanced Materials, 25(8), 1114–1117.

Vill, V., Peters, G., Thiemann, S., Galewski, Z., LiqCryst Database, Ver. 5.0.28, LCI Publisher GmbH, 2010.

Vizitiu, D., Lazar, C., Halden, B.J., Lemieux, R.P. (1999). Journal of the American Chemical Society, 121, 8229–8236.

Vizitiu, D., Lazar, C., Radke, J.P., Hartley, C.S., Glaser, M.A., Lemieux, R.P. (2001). Chemistry of Materials, 13, 1692–1699.

Walba, D.M. (1991). Advances in the Synthesis and Reactivity of Solids, 1, 173–235.

Wand, M.D., Escher, C., Handschy, M.A., Vohra, R.T., US Patent, 5539555, 1996.

Wang, C., Bos, P.J. (2004). Displays, 25, 187–194.

Wang, X., Srivastava, A.K., Chigrinov, V.G., Kwok, H.S. (2013a). Optics Letters, 38, 1775.

Wang, X., Wang, L., Sun, J., Srivastava, A.K., Chigrinov, V.G., Kwok, H.S. (2013b). Journal of the Society for Information Display, 21, 103.

Wegłowska, D., Perkowski, P., Chrunik, M., Czerwinski, M. (2018). Physical Chemistry Chemical Physics, 20, 9211–9120.

Wei, H., Srivastava, A.K., Xu, F., Sun, J., Lin, X.-W., Cui, H.-Q., Chigrinov, V., Lu, Y.-Q. (2012). Liquid crystal gratings based on alternate TN and PA photo alignment. Optics Express, 20(05), 5384.

Wulf, A. (1975). Physical Review, A11, 365.

Xu, S., Ren, H., Wu, S.T. (2012). Optics Express, 20, 28518.

Yao, A.M., Padgett, M.J. (2011). Orbital angular momentum: origins, behavior and applications. Advances in Optics and Photonics, 3(2), 161–204.

Yasue, Y., Masahiro, J., Tomoyuki, Y., Takahiro, M., EP1039329 (A2), 2000.

Yoshino, K., Ozaki, M. (1984). Japanese Journal of Applied Physics, 23, L385–387.

Yoshizawa, A. (1998). Ferroelectrics, 214, 67–74.

Yoshizawa, A., Nishiyama, I. (1995). Molecular Crystals and Liquid Crystals, 260, 403.

Yu, J., Zhou, C., Jia, W., Ma, J., Hu, A., Wu, J., Wang, S. (2013). Distorted dammann grating. Optics Letter, 38, 474–476.

Yuan, X.-C., Lin, J., Bu, J., Burge, R.E. (2008). Achromatic design for the generation of optical vortices based on radial spiral phase plates. Optics Express, 16(18), 13599–13605.

Zaschke, V.H. (1975). Journal für Praktische Chemie, 317(4), 617–630.

Neelam Yadav, Ravindra Dhar

4 Liquid crystalline materials for efficient solar energy harvesting

4.1 Introduction

In order to overcome the present energy crisis, a lot of work is being done to utilize the most abundant, inexhaustible, and cleanest renewable source of energy, that is, sunlight in the development of photovoltaic (PV) solar cells. Sun provides a lot of energy, and only a fraction of this energy received by the Earth is sufficient to overcome the present energy demand if it can be converted to electrical energy efficiently. Although inorganic solar cells dominate the market with very high efficiencies, they suffer from some drawbacks such as high cost of production because their processing requires high temperatures and vacuum. A promising and new approach is the development of organic solar cells that have captured the attention of researchers since they possess several desirable characteristics such as lightweight, low cost, semitransparency, mechanically flexible, easy fabrication, and large area application. Also, umpteen organic molecules with interesting and different optical and electrical properties are easily available for fabrication of organic solar cells.

Organic semiconducting materials are a potential avenue of intense scientific research, owing to their possible application in light-emitting diodes (LEDs), field-effect transistors, sensors, and PV cells. Organic PV cells are being fabricated with major emphasis being given to circumvent the technological problems so that they can perform better than conventional solar cells. Significant research has been done in increasing their power conversion efficiencies (PCEs) from 0.001% in 1975 (Tang and Albrecht, 1975) to around 12% in 2017 (Green et al., 2017). Such an advancement in efficiency points to the fact that organic PV cells can give competition to inorganic solar cells in the future. Numerous reports on PV cells exist using small molecules, conjugated polymers, liquid crystals (LCs), combinations of polymers and small molecules, or combination of organic and inorganic materials as the active layer (Wu et al., 2013). The layer inside the PV devices that absorb maximum sunlight leading to generation of charges is called the active layer. Many organic materials have been templated with LC mesogens in order to enhance their mobility and conductivity (Fujieda et al., 2016; Ghosh et al., 2018; Kumar and Kumar, 2017). LCs are considered to be the novel generation of organic semiconductors that can self-repair structural defects. They prove to be smart dopants for the advancement of organic PV devices (Fujieda et al., 2016; Ghosh et al., 2018; Kato et al., 2018). LCs are thermally robust, easy processability, and are versatile. Thermal annealing can be used to acquire large single domains (de Cupere et al., 2006; van Breemen et al., 2006). This chapter describes the use of LCs in organic PV cells.

4.2 Working principles

In an organic PV cell, the procedure of converting light energy into electrical energy is achieved by four successive steps: (1) absorption of light energy which leads to the formation of an exciton (bound electron–hole pair), (2) diffusion of exciton to a region, (3) separation of charges (holes and electrons), and (4) finally, transportation of holes to anode and electrons to cathode which leads to flow of current.

The potential energy stored within a pair of separated negative and positive charges corresponds to the difference in their quasi-Fermi levels (Hoppe and Sariciftci, 2004). The photovoltage is directly proportional to the quasi-Fermi-level splitting. The number of positive and negative charges that are collected at the electrodes determines the electric current delivered by a PV solar cell. The overall photocurrent efficiency is the product of the fraction of photons absorbed, the number of excitons dissociated, and the number of separated charges that are transported to the electrodes. The number of absorbed photons depends on the absorption coefficient and the thickness of the active layer. The fraction of excitons dissociated depends on the probability of charge separation in the region where they diffuse (Gregg, 2003).

The driving force behind the transportation of charges to the electrodes is the gradient in the electrochemical potentials of charges. The internal electric fields that lead to drift current and the concentration gradients of charge carriers giving rise to diffusion current are the two forces that contribute to the flow of charges to the respective electrodes. The devices fabricated with thin films (<100 nm) are dominated by the drift current, while thick film devices are dominated by diffusion current since the electric fields inside the bulk are screened.

The metal–insulator–metal (MIM) model is very useful in understanding the rectifying behavior of a pure semiconductor device in the dark. Figure 4.1 depicts a semiconductor crammed between two metal electrodes that differ in work functions. Fermi levels have been depicted for metals, while for semiconductors, the valence band corresponding to lowest unoccupied molecular orbital (LUMO) and the conduction band corresponding to highest occupied molecular orbital (HOMO) are shown in the figure. When no bias is applied (refer Figure 4.1(a)), the current delivered by the cell is called short-circuit current (I_{SC}). Under dark condition, no current flows through the cell, and the built-in potential arising from the difference in the work function of metals is uniformly distributed. Under illumination, the PV device acts as a solar cell with separated charge carriers drifting toward the respective electrodes: electrons moving to the metal with lower work function and holes moving toward the opposite. Transparent indium tin oxide (ITO) with work function of 4.7 eV is often chosen as the electrode with high work function, while aluminum and magnesium with work functions 4.24 and 3.66 eV, respectively, are chosen as low work function counter electrode. Figure 4.1(b) depicts the open-circuit condition, that is, the current flow is zero since charge carriers do not experience any driving
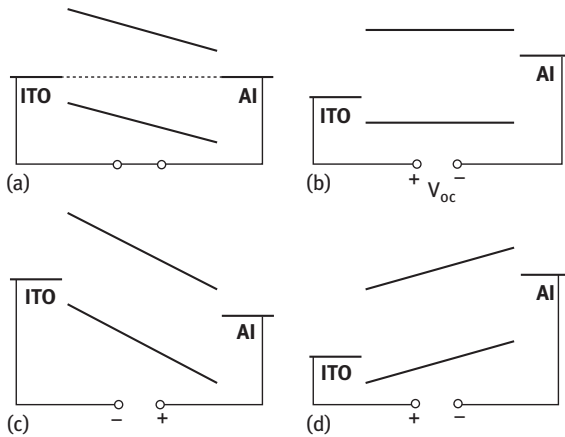
Figure 4.1: Metal–insulator–metal (MIM) model for functioning of organic diode device: (a) no bias applied (closed circuit), (b) open circuit, (c) reversed bias where the diode operates as a photodetector, and (d) applied forward bias is greater than V_{OC}.

force. According to MIM model, this condition is called as flat band condition because the applied voltage (called open-circuit voltage V_{OC} in this case) is equivalent to the difference between the work function of metal electrodes. The built-in field is balanced by V_{OC}. Figure 4.1(c) shows the reverse bias condition in which some negligible dark current flows. Under illumination, the device acts as a photodetector since the generated charge carriers start drifting toward the respective electrodes under the influence of strong electric field. Figure 4.1(d) represents the condition when the forward bias is greater than the open-circuit voltage. Charge carriers are easily injected into the organic layer (semiconductor) from the metal electrodes. The device acts as an LED if the charge carriers recombine radiatively.

Figure 4.2 represents the current–voltage characteristics of a PV solar cell in the dark and under illumination. In the dark, negligible current flows through the cell, except when the applied forward bias is more than the open-circuit voltage, large current flows. Under illumination, the flow of current is in a direction opposite to the injected current. I_{SC} (marked as (a)) in Figure 4.2 is the maximum photocurrent generated. While V_{OC} (marked as (b)) is the voltage when current is zero (flat band condition). The PV cell delivers the maximum power (i.e., product of current (I_P) and voltage (V_P) is maximum) at point (c) which lies in the fourth quadrant. The power generated by a PV cell is compared with the incident light intensity in order to calculate PCE. The ratio of the maximum power delivered by the cell to the product of I_{SC} and V_{OC} is the fill factor (FF). It is determined as FF $= I_P V_P / I_{SC} V_{OC}$. In ideal cases, the value of FF is unity but losses because of recombination of charge carriers and transport restrict its values between 0.2 and 0.5. PCE is the percentage of the
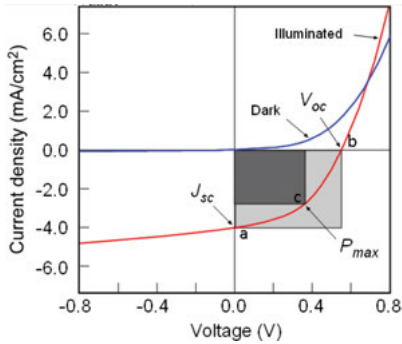
Figure 4.2: Current–voltage characteristics of a PV solar cell.

absorbed solar energy that is converted into electrical efficiency. PCE can be written mathematically as

$$\eta_{PCE} = I_P \times V_P / P_{incident} = FF \times I_{SC} \times V_{OC} / P_{incident} \tag{4.1}$$

The I–V characteristics of a PV solar cell can be defined by the following equation:

$$I = I_D \times \left\{ \exp\left(q/mkT \left(V_{app} - IR_s \right) \right) - 1 \right\} + V_{app} - IR_s / R_{sh} - I_{ph} \tag{4.2}$$

where the dark current is denoted by I_D, q is charge, V_{app} is the applied voltage, m gives the diode ideal factor, R_{sh} is shunt resistance, R_s is series resistance, and the photocurrent is given by I_{ph}. High FF can be achieved by using very high shunt resistance which helps in preventing leakage currents and low series resistance. Low series resistance helps in obtaining a steep rise in the forward current.

Since the mobility is directly related to PCE of a PV solar cell, space-charge-limited current (SCLC) measurements are applied for the evaluation of mobility of charge carriers in the active layer under stable current condition. According to the SCLC model, charge carrier density is defined as

$$J_c = 9/8 \varepsilon_0 \varepsilon_r \mu_h V^2 / l^3 \exp\left(0.89 \sqrt{V/El} \right)$$

where μ_h is the hole mobility under zero field, thickness of film is l, E represents the characteristic field, V is defined as $V = V_{ap} - (V_{sr} + V_{bv})$, with V_{bv} being the built-in voltage, V_{sr} the voltage drop due to series resistance, and V_{ap} is the voltage applied to the device.

4.3 Architecture of PV solar cell

The excitons do not dissociate directly by the built-in fields of the order of 10^6 to 10^7 V/m because the binding energy of exciton in organic semiconductors is usually larger in comparison to silicon (Sariciftci, 1997). So, the architecture of a PV device

is devised in such a way that favors easy dissociation of bound electron–hole pair. The different types of structures of PV devices are (i) single layer, (ii) bilayer, (iii) bulk heterojunction (BHJ), and (iv) dye-sensitized solar cells (DSSCs). The foremost organic solar cells were the single-layered cells. The major variance in these structures lies in the process of dissociation of exciton within the photoactive layer and the subsequent transportation of charges to respective electrodes.

4.4 Discotic liquid crystals in PV cells

Discotics allure researchers because they have an inclination to form one-dimensional columnar structures, which permit for easy migration of charge carriers. Discotic mesogens are made of a core that is flacked by aliphatic chains (Gowda et al., 2017; Piechocki et al., 1982). The fascinating properties (self-healing, easy processability, high charge carrier mobility, and long-range self-assembling) possessed by them makes them viable to be used in PV solar cells (Feng et al., 2008; Kaafarani, 2011; [17]). The efficiency of PV solar cells based on discotic LCs (DLCs) is dependent on the morphology of the active layer (made of donor (D) and acceptor (A) material), where the dissociation of excitons occurs (Julien et al., 2014). In order to get an ideal D–A interface, several parameters have to be controlled: (a) homeotropic alignment of discotic mesogens (Schweicher et al., 2009); (b) using polar side alkyl chains, dewetting has to be circumvented; and (c) the two mesogens should be immiscible and display antagonistic solubility. The above factors have been impediments in the way toward realization of efficient PV solar cells. Although few successful efforts involving active layers made of DLCs and crystalline (Schmidt-Mende et al., 2001a; Schuenemann et al., 2013) or amorphous semiconductors (Jurow et al., 2013) in different types of architectures have been realized, Ide et al. have addressed the relationship between functionality and morphology in a planar-heterojunction PV solar cell with the help of theoretical multiscale modeling approach (Julien et al., 2014). They suggested that for better efficiency, interfaces between A and D mesogens with alike columnar phases should be avoided so that energy losses can be reduced due to fast recombination and the lattice mismatch must be engineered (Julien et al., 2014). This section describes the different types of discotic cores used in solar cells. But before moving to it, a brief overview about the model proposed by Gregg et al. to explain the PV effect observed in cells made of DLCs has been described. Till date, very few models (Garcia et al., 2013) exist on LC-based PV solar cells.

The LC porphyrin (LCP) model: The model proposed by Gregg et al. (1990) for explaining the PV has resemblance with the working principle of photogalvanic cell and sensitization of semiconductor electrodes. They developed two models: the simplified model and the more realistic model.

(1) The simple model: Following assumptions were made: (i) under no bias, upon illumination, the asymmetry formed in these cells based on LCP is due to the injection of electrons (single carriers) into the illuminated electrode and (ii) under dark condition, DLC is not in equilibrium with its electrodes. According to this model (Figure 4.12a), when an exciton reaching the ITO electrode injects a negative charge into it, a radical cation ($P^{\star+}$) or hole in it is left behind in the LCP. The transport of $P^{\star+}$ by hopping to the dark electrode generates the photocurrent, while an electron is injected into the LCP to make it neutral. This model also considers that in the bulk, no charge carriers are generated and the bulk resistance is very small. The authors derived an equation of electron injection current density by using the equation given by Geacintov et al. (1966) as follows:

$$J_{no} = -eI_O P\left(\varphi_{nf}^o/\varphi_{nf}^o + e^{\alpha_n f V_c}\right) + \sigma_n V_c \qquad (4.3)$$

where I_O is the intensity of incident light, e is charge, P is probability that an exciton can reach the surface, σ_n being the rate constant, φ_{nf}^o is the electron injection during short-circuit condition, and V is the voltage.

(2) The modified and detailed model: This model assumes that (i) a faster discharge of charges takes place, which does not limit the flow of current and so it can be neglected; (ii) effect of excitons reaching the back surface can be ignored; and (iii) under dark condition, rate of any injection mechanisms is very small. Under illumination, at the dark electrode, the discharge of $P^{\star+}$ and $P^{\star-}$ and generation of $P^{\star+}$ and $P^{\star-}$ in the bulk happens, including some recombination processes.

4.4.1 Porphyrins in PV solar cells

During photosynthesis, porphyrins are the key molecules that harvest solar energy (Guldi, 2002). They can absorb light over a broad range of solar spectrum with high extinction coefficients. The HOMO and LUMO energy levels of porphyrins match well with that of the electrode materials and electron acceptors. They are known to have high charge carrier mobility and homeotropically aligned structures for efficient harvesting of light. Several derivatives of porphyrin have been effectively utilized in DSSCs, BHJ, and bilayer solar cells (Lee et al., 2011; Li and Diau, 2013; Lia et al., 2008). Gregg et al. (1990) were the first to observe PV effect in solar cells made of porphyrin derivative. Sun et al. (2007) fabricated both bilayer and BHJ solar cells using LCPs (C12Por and C14Por) exhibiting hexagonal LC phase as donors by solution processing. The bilayer solar cells were found to display a low PCE of 0.070% in comparison to that of 0.222% shown by BHJ solar cells because of narrow interfacial area between acceptor and donor, and hole hopping is tough in unaligned LC material due to interstitial spaces, voids, and grain boundaries (Castet et al., 2014; Liu et al., 1993).

4.4.2 Hexabenzocoronene (HBC) in solar cells

Hexabenzocoronenes (HBCs) are p-type semiconductors that promote easy hole transport as they are electron-rich mesogens with a strong inclination toward assembling into columnar structures. HBC is an aromatic mesogen composed of 13 fused 6-membered rings (Wu et al., 2007). Van de Craats et al. (1999) were the first to propose HBCs as an oligomeric version of an infinite graphene sheet. They exhibit very high mobilities (0.5–1 cm^2/V s) along the columns and remain the same up to at least 200 °C (Silvaa et al., 2018). The alkyl chains at the periphery make the mesogens soluble. HBCs have been used in PV cells to achieve better efficiency (Wong et al., 2010a; 2010b).

Schimdt-Mende et al. fabricated PV solar cells using hexaphenyl-substituted HBC (HBC-PhC12). They demonstrated that the external quantum efficiencies (EQEs) action spectrum have peaks above 34% due to efficient transfer of charges (Schmidt-Mende et al., 2001a) and DLCs when combined with perylene derivatives lead to the formation of stable film structures. The high efficiencies can be attributed to the formation of p–n junction by self-assembly. The ball-and-socket-type interaction between the DLC donor and electron acceptor increases the area of the p–n junction, leading to increased efficiencies (Kang et al., 2013). The effect of length of peripheral side chain of HBC donor mesogens on the intermolecular packing was elucidated by Al-Hussein et al. (2011). They averred that the donor–acceptor interaction stabilized the insertion of perylene diimide (PDI) within layers of HBC disks, leading to ordered morphology. HBC derivatives with normal dodecyl peripheral chains were used as hole acceptors in PV diodes fabricated by Schmidtke et al. They reported an EQE of 29.5% at 460 nm. HBC cores with shortest side chains are found to be the best donors with an EQE of 12% (Li et al., 2007).

HBCs can act as amphiphilic interface modifiers (IM) that can induce a change in morphology of the active layer, leading to an enhancement in the efficiency of the devices (Dam et al., 2014). Due to pi–pi interaction, the IMs strongly interact with the fluorenyl-substituted HBC donor mesogens as confirmed by grazing incidence wide-angle X-ray scattering as shown in Figure 4.3. It leads to more well-arranged structures with higher anisotropy.

4.4.3 Phthalocyanine in PV cells

Phthalocyanines are attractive materials to be used in PV solar cells (Levitsky et al., 2004; Walter et al., 2010) due to their eco-friendly characteristics, cost-effectiveness, and sensitivity in the red region of the solar spectrum. LC phthalocyanines retain their columnar architectures in the solid phase after cooling (Markovitsi et al., 1991). Generally, phthalocyanines have donor-like properties, so they can be easily doped with electron acceptors (Claessens et al., 2008) and have high mobility (Chino et al.,
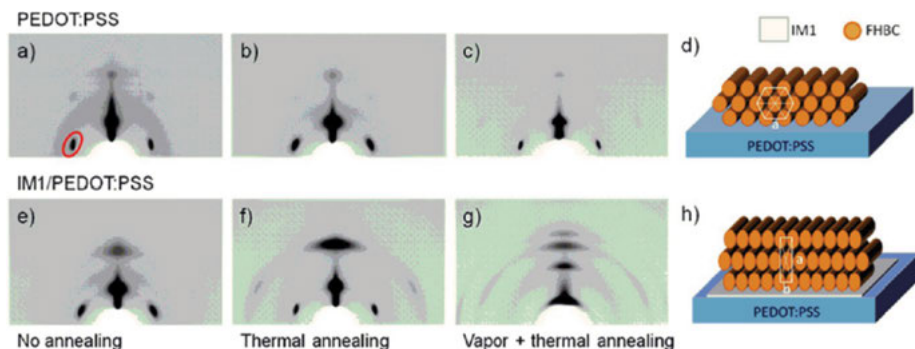
Figure 4.3: Two-dimensional grazing incidence wide-angle X-ray scattering images of FHBC films spin-coated on top of poly(3,4-ethylenedioxythiophene):poly(styrenesulfonate) (PEDOT:PSS) and IM1/PEDOT:PSS substrates. (a, e) Without annealing (010) reflection is indicated by red circle), (b, f) after thermal annealing at 150 °C for 30 s, and (c, g) after annealing for 24 h followed by thermal annealing at 150 °C for 30 s. Panels (d) and (h) are schematic representations of the FHBC molecular packing modes on PEDOT:PSS and IM1/PEDOT:PSS films, respectively (Dam et al., 2014).

2017). Petritsch et al. (1999) developed a double-layer PV device with a discotic phthalocyanine derivative as electron donor and perylene as electron acceptor materials that could convert light from ultraviolet (UV) region to infrared region with a quantum efficiency of nearly 0.5%. They further fabricated blend-type PV cell using chloroform as a solvent and found an enhancement in EQE, reaching 1% at around 500 nm (Petritsch et al., 2000). A phthalocyanine derivative demonstrating high carrier mobility (>1 cm^2/V s) was blended with (3-methoxy-carbonyl)-propyl-1-1-phenyl-(6,6) C61 (PCBM) to obtain an efficiency of 3.1% and a I_{sc} of 9.6 mA/cm^2 by Hori et al. (2010). Further, the efficiency was increased to 3.2% by inserting a hole transporting layer (molybdenum oxide) in the active layer (Hori et al., 2011). The performance of PV cells is affected by the addition of processing additives such as 1,8-diiodooctane (Dao et al., 2012), 1,8-dichlorooctane, 1,8-dibromooctane, and 1,8-octanedithiol during processing. These additives lead to an increment in the values of EQE, PCE, and J_{sc} (refer Figure 4.4) since they control the separation of the donor and acceptor phases. In particular, the quenching of photoluminescence is decreased, the Davydov splitting at the Q-band of the absorbance spectra increases, and the roughness of the surfaces is improved (Dao et al., 2013).

4.4.4 Perylene in solar cells

Perylene tetracarboxylic acid bisimides or perylenebisimides are n-type semiconductors. When peripheral side chains in perylene derivatives are substituted with appropriate molecules, they show columnar phases. A BHJ solar cell was prepared by
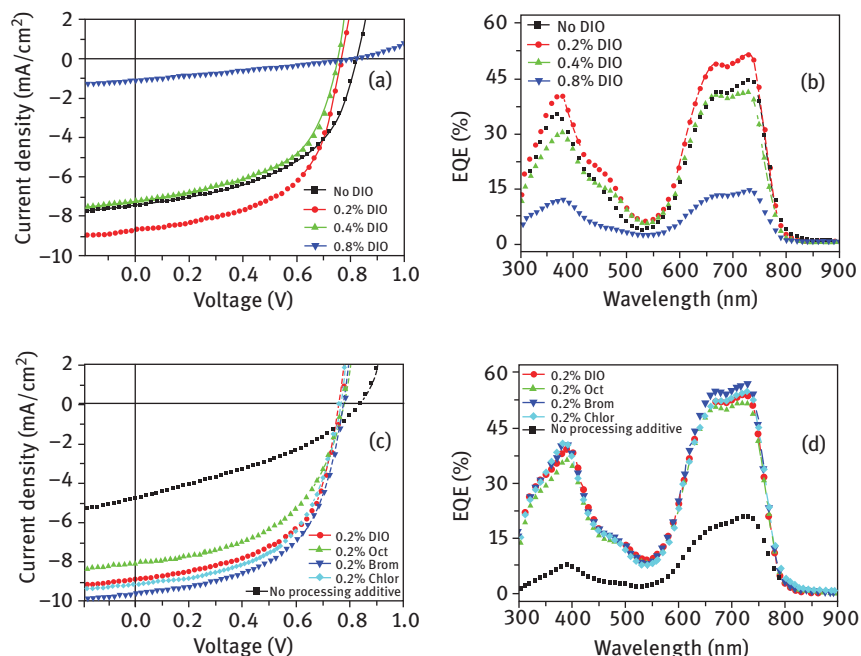
Figure 4.4: *J–V* characteristics of C6PcH2: PCBM BHJ PV solar cells. (a) Different amounts of DIO and (c) with 0.2% v/v of various processing additives. EQE spectra of C6PcH2: PCBM BHJ PV solar cells (b) with different amounts of DIO, and (d) with 0.2% v/v of various processing additives (Dao et al., 2013).

incorporating a PDI, *N, N'*-diheptyl-3,4,9,10-perylenetetracarboxylicdiimide (PTCDI-C7) showing an LC mesophase over 214–403 °C as the electron acceptor and a non-LC material, zinc phthalocyanine as donor (Kim and Bard, 2004). The thickness of the active layer varied (25, 50, and 100 nm) and it was found that the thickness of 25 nm generated the highest I_{sc} of 1.58 mA/cm^2 and FF of 0.40. The better performance of thin cell was attributed to the efficient movement of charge carriers to the respective electrodes and the effective dissociation of excitons. PV devices, in which these derivatives are homeotropically aligned, show an increase in photocurrent by a factor of 16 which can be ascribed to the increase in light absorption and mobility of charge carriers (Cisse et al., 2009).

In another report, derivatives of perylene with shorter side chain showing wide columnar hexagonal phase at room temperature were mixed with another DLC (a pyrene derivative) with a polar alkyl chain to form a bilayer PV cell. The two DLCs were immiscible at elevated temperatures and exhibited antagonist solubility (Thiebaut et al., 2010).

4.4.5 Pyrene in solar cells

LCs with pyrene core have a strong propensity to organize into ordered structures by pi–pi stacking and eliminate defects by self-healing. Pyrene is a completely planar mesogen. Pyrene mesogens with peripheral oligothiophenes were used as an electron donor material in BHJ solar cells and an efficiency of 2.6% was achieved (Takemoto et al., 2012). Pyrene when attached to electroactive molecules leads to aligned crystal packing and promotes intermolecular connectivity. Devices based on pyrene show high values of FF (Lee et al., 2011b).

4.4.6 Triphenylenes in solar cells

DLCs consisting of triphenylene core exhibit columnar mesophases. Slow cooling of these discotic from their isotropic melt leads to homeotropic alignment (i.e., columns made of stacked disks lie perpendicular to the glass substrate). Adam et al. (1994) have reported fast photoconduction (of the order of 0.1 $cm^2/V\ s$) in well-ordered columnar hexagonal phase of triphenylene derivatives, especially 2,3,6,7,10,11-hexahexylthiotriphenylene. Oukachmih et al. (2005) were the first to fabricate bilayer PV cells using triphenylene derivative as a hole transporting material and achieved an EQE of 3%. The authors also investigated the effect of argon plasma and UV–ozone treatment of ITO on the performance of PV cells (Destruel et al., 2006). V_{OC} was found to decrease with UV–ozone treatment while it increased with argon plasma treatment of ITO. Discotics with triphenylene core blended with ruthenium dye and zinc oxide have been used as electron transporting layers (refer Figure 4.5) in polymer solar cells (Shi et al., 2014). Jeong et al. elucidated the effect of adding LCs made of triphenylene core to PV devices with poly(3-hexylthiophene):[6,6]-phenyl-C61-butyric acid methyl ester (P3HT:PC$_{61}$BM) as an active layer. They achieved an efficiency of 4% after annealing the devices (Jeong et al., 2010a). In some reports (Ghosh et al., 2018; Green et al., 2017; Gregg, 2003; Hoppe and Sariciftci, 2004; Kato et al., 2018; Wu et al., 2013), a layer of hexabutoxytriphenylene (HAT4), a DLC showing columnar hexagonal phase, has been inserted to PV devices for better performance (Bajpai et al., 2016a, 2016b; Zheng et al., 2011). Also, additional hole transporting layers such as molybdenum oxide (MoO$_3$) and poly(3,4-ethylenedioxythiophene):poly(styrenesulfonate) were added to these devices to further improve the efficiency.

Triphenylene DLCs have been used as gelators to make gel electrolytes to be utilized in DSSCs. Reduced recombination of electrons at the TiO$_2$ surface and better lifetime due to solvent retention have been achieved by using this type of gel electrolytes (Khan et al., 2017).
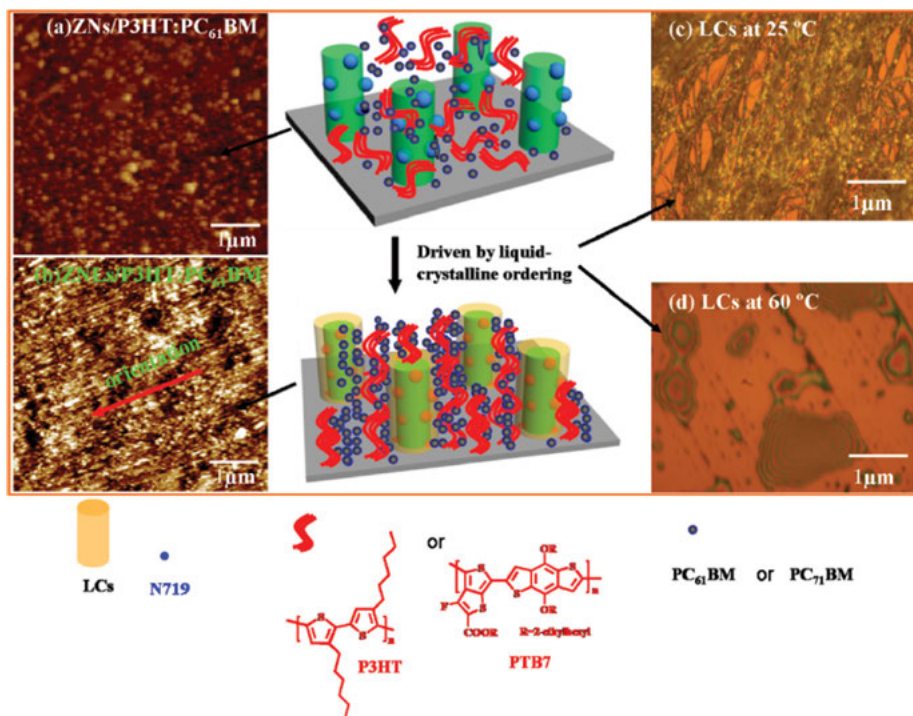
Figure 4.5: Atomic force microscopy images (left) of P3HT:PC$_{61}$BM spin coating onto (a) zinc and (b) zinc + LC surface. Polarizing optical micrography (right) of LC small molecule (c) at 25 °C and (d) 60 °C. Schematic images (middle) show the self-assembly of active layers with the corresponding components below (Shi et al., 2014).

4.4.7 Anthraquinone in solar cells

PV devices utilizing anthraquinone derivatives as electron donors exhibited high V_{OC} which could be ascribed to the low-lying HOMO energy level possessed by these derivatives. These devices displayed an efficiency of 4.8% (He et al., 2014).

4.4.8 Dibenzo[a,c]phenazine in solar cells

When a monomer, 2,3,6,7-tetra-6-hexyloxydibenzo[a,c]phenazine-11-carboxylic, is blended with polyacrylamide, it forms a DLC that can be inserted as a functional template in PV solar cells (Lee and Huang, 2012). Incorporation of this DLC in solar cells leads to enhancement in mobility, and the diffusion length is affected by it (Lee and Huang, 2012).

4.5 Calamitic LCs in PV solar cells

Several reports exist using calamitic LCs in PV solar cells (AlKhalifah et al., 2014; Kamarudin et al., 2018; Liao et al., 2016; Sun et al., 2014). Nematic LCs, when used as additives in PV solar cells, lead to higher absorbance of active layer and changes the acceptor strength (Jeong et al., 2010b). The change in acceptor strength directly affects the open-circuit voltage since it is related to the energy difference between the HOMO and LUMO energy levels. Tsou et al. (2013) demonstrated a concentrating PV device, which gave a steady electrical output using a mixture of E7 with a nematic phase and a liquid crystalline monomer. LCs showing smectic phase such as 5-(10-undecenyloxy)-2-[[[4-hexylphenyl] imino] methyl] phenol improves the crystallinity of the P3HT layer, thus enhancing the performance of the devices based on such LCs (Canli et al., 2014). Iwan et al. (2015) have used photosensitive chiral LC mesogens with azo bond, which possess smectic and cholesteric mesophases as an acceptor in the active layer of PV solar cells. They established that the performance of PV cells depends on the amount of LC material in the active layer and the temperature at which the active layer is annealed. Incorporation of high-temperature nematic LC as a secondary donor in ternary PV devices resulted in an enhancement in PCE from 9.6% to 10.7% and J_{SC} to 19.8 mA/cm^2 (refer Figure 4.6; Geraghty et al., 2016). Measurement of absorption intensity of these devices showed an increased absorption in the 500–600 nm wavelength range. LCs displaying nematic phases such as 40-(pentyloxy)-4-biphenylcarbonitrile, 40-(hexyloxy)-4-biphenylcarbonitrile, and 40-(heptyloxy)-4-biphenylcarbonitrile were embedded in the active layer of P3HT:PCBM-based BHJ solar cells as processing additives. These LCs increased the PCE of PV devices by increasing the short-circuit current density (J_{SC}) via improving the degree of crystallinity and photon absorption property of the BHJ film (Heo et al., 2014).

Sometimes nematic LCs have been used as reflectors in PV solar cells (refer Figure 4.7) to increase the selective absorption of these devices. When LCs such as LC242 and LC756 are used with polymers, they can act as a compensation film (Yang et al., 2014). The number of incident photons increases with the addition of LC reflectors. Due to this, the EQE of the devices is higher. But some nematic LCs have been used as compatibilizers in BHJ to improve the efficiency (Yuan et al., 2014).

Hybrid BHJ solar cells have been fabricated by utilizing nanomaterials such as quantum dots altered with liquid crystalline ligands as electron acceptors and rod–rod diblock polythiophene copolymers consisting of a side-chain liquid crystalline cyanobiphenyl segment and a polyhexylthiophene segment as electron donors (Shi et al., 2013). These devices were found to be efficient because of improved orientation of crystalline domain and closely packed polymer-quantum dot nanocomposites. UV–visible spectra (refer Figure 4.8) showed a red shift, stronger intensity, and broader absorption because the conjugated segments self-assemble and the orientation of the LC mesogens help the block copolymer to organize into well-ordered structures. The performance of BHJ solar cells consisting of benzo[1,2-b:4,5-b′] dithiophene with nematic and smectic phases as a
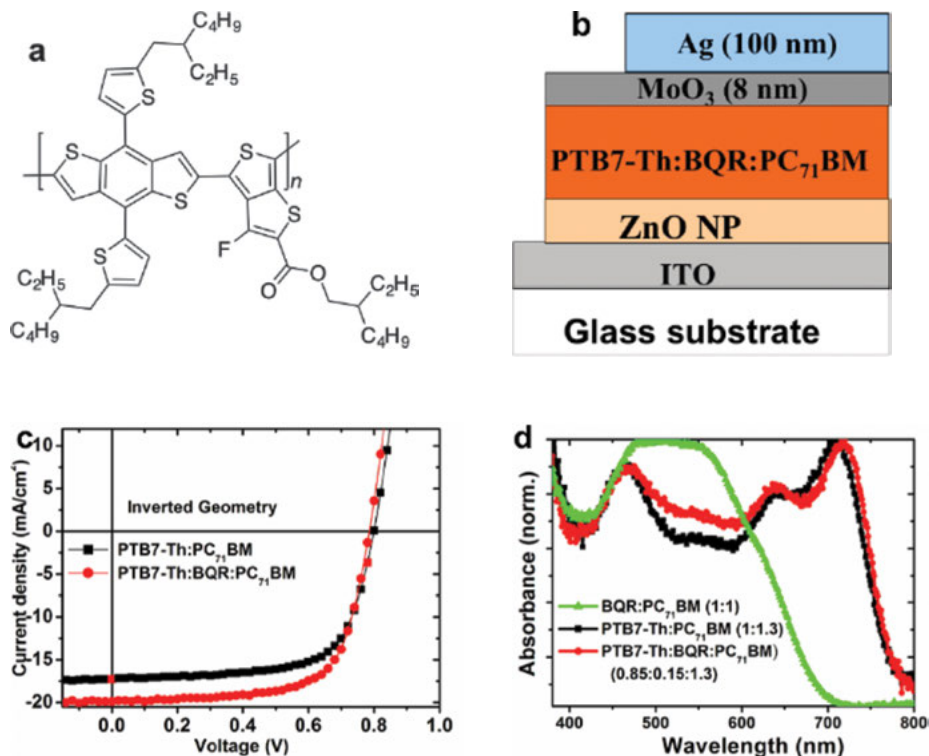
Figure 4.6: *J–V* characteristics of PTB7-Th:BQR:PC$_{71}$BM (fullerene derivative [6,6]-phenyl C71-butyric acid methyl ester) ternary BHJ solar cells. (a) PTB7-Th chemical structure, (b) architecture of device, and (c) *J–V* curve for BQR containing ternary device, and (d) UV–visible absorption spectra of ternary and binary blend active layers BQR:PC$_{71}$BM, PTB7-Th:PC$_{71}$BM, and PTB7-Th:BQR:PC$_{71}$BM (Geraghty et al., 2016).

donor and a fullerene derivative as an acceptor has been investigated. A PCE of 6.9% and internal photon conversion efficiency of 70% within the 500–600 nm range has been achieved without adding any solvents or post deposition techniques (Komiyama et al., 2018).

Li et al. have designed artificial heliotropic devices based on nematic liquid crystalline elastomer doped with single-walled carbon nanotubes displaying full-range heliotropism. Due to this, the output photocurrent from PV devices increases (Li et al., 2012a). Some reports exist where nematic LC gels made from a mixture of non-polymerizable LC and a reactive mesogen have been used in PV solar cells (Carrasco-Orozco et al., 2006; Tsoi et al., 2007).

Calamitic LCs such as 4,7-diphenyl-2,1,3-benzothiadiazole-based LC with a mono-thiol end group and a conjugated LC polymer poly(2,5-bis(3-alkylthiophen-2-yl) thieno [3,2-b] thiophenes) (PBTTT) have been used as templates to grow cadmium sulfide nanocrystals for PV solar cells (Yuan et al., 2014a). The transfer of charges takes place
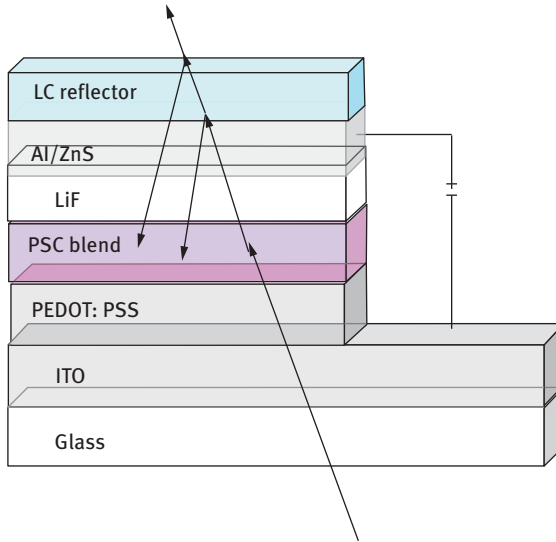
Figure 4.7: Schematic illustration of the semitransparent PV solar cell with an LC reflector (Yang et al., 2014).
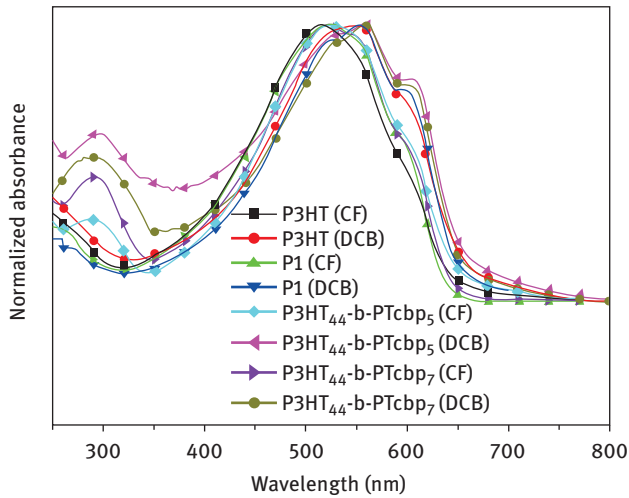
Figure 4.8: UV–visible spectra of pristine P3HT, P1, P3HT44-b-PTcbp5, and P3HT44-b-PTcbp7bfilms prepared by spin coating from CF and DCB solvents (Komiyama et al., 2018).

efficiently making these LC/CdS nanocomposites viable to be used as active layer in PV devices. Diketopyrrolopyrrole (DPP)-based LC mesogens with a bandgap of 1.8 eV, deep HOMO level of −5.5 eV, and showing intense absorption in the visible region have been incorporated in PV solar cells as electron donors. These PV devices generated a high PCE of 4.3% and a V_{OC} of 0.93 V (Shin et al., 2013). In the same year, Han et al. designed a new LC acceptor by inserting cyanobiphenyl mesogens into DPP and realized a PCE of 1.3% (Han et al., 2013).

Nanoparticles (NPs) doped in smectic LCs prove to be beneficial for PV solar cells (Branch et al., 2014; Yuan et al., 2012). The short-circuit current increases due to the crystallinity of nanocomposites because it helps in the dissociation of excitons. Liquid crystalline polythiophene consisting of biphenyl core as a side chain (P3HTbpT) helps in improving the arrangement of polymer chains (Chen et al., 2012). Doping of semiconducting NPs such as ZnO in the entire active layer is promoted by P3HTbpT and it forms continuous pathways for efficient separation of charges. Also, copolymerization of the thiophene units and the electron acceptor benzothiazole forms a new D–A interface, that is, poly[3-(6-(cyanobiphenoxy) thiophene)-alt-4,7-(benzothiadiazole)] which when blended with ZnO NPs forms hybrid PV solar cells (Li et al., 2012b). Yao et al. (2012) copolymerized 2,5-bis(3-bromododecylthiophen-2-yl)thieno[3,2-b]thiophene (BbTTT) monomer with thiophene and thieno[3,2-b]thiophene to synthesize liquid crystalline copolymers PBbTTT-T and PBbTTT-TT. These polymers were blended with a fullerene derivative to form the D–A layer in BHJ solar cells with stable and well-ordered nanostructures, owning to the photocross-linkable bromine functionalized chain. Further, ZnO/P3HT BHJ solar cells were designed by employing LC ligands 4-(5-(1,2-dithiolan-3-yl) pentanoate)-4′-(hexyloxy)-terphenyl (HTph-S) that modify the semiconducting interface between D and A layers (Li et al., 2012c).

The compatibility of NPs with the polymer host is tailored by these LC ligands which ultimately affect the morphologies of the D–A layer (refer Figure 4.9) by creating more surfaces for separation of charges, and annealing of the LC mesogens induces the spontaneous one-dimensional packing of ZnO NPs. It is known that the ordered arrangement of acceptor material enhances the ordering of P3HT molecules (Kennedy et al., 2008). The LUMO of the LC mesogens and semiconducting nature of pie-conjugated structure lead to closer contact and better transport at the NP–polymer and NP–NP interfaces.

Hindson et al. (2010) have fabricated PV solar cells by using a new series of hole transporting materials; triphenylamine-based poly(azomethine) shows liquid crystalline behavior. These mesogens formed stable lyotropic systems, and cyclic voltammetry measurements were performed to calculate the HOMO and LUMO energy levels. The position of HOMO and LUMO levels of materials used in PV solar cells is of paramount importance for achieving better efficiency.

PBTTT-based bilayer solar cells exhibited high J_{sc} because J_{sc} is the product of the charge carrier mobility (μ) and the carrier density (ne): $J_{SC} = ne\mu E$ (Gunes et al.,
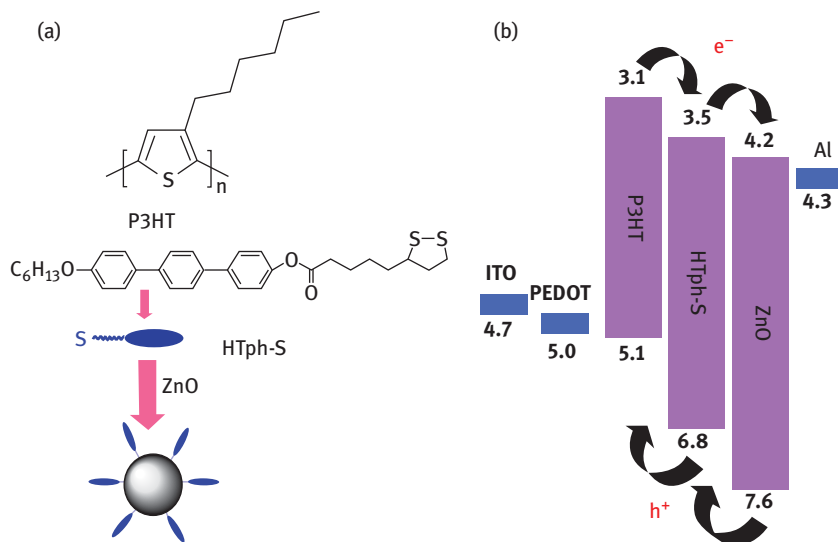
Figure 4.9: Schematic diagram shows (a) the chemical structures of P3HT and HTph-S, and the process of surface modification of ZnO NPs, and (b) the energy-level diagram for P3HT, HTph-S, and ZnO (Li et al., 2012c).

2007). LC mesogens increase n by increasing the absorption capacity of active layer as well as E is increased by additional electrical forces due to the formation of concentration gradient of charges (Sun et al., 2009).

4.6 LCs in DSSCs

DSSCs have gained the attention of researchers since O'Regan and Gratzel (1991) reported a PCE of 12% under an illumination of AM 1.5G. In another report by the same group, E7 and ML-0249 were embedded in a polymeric electrolyte composed of tri-iodide and iodide redox species in polyacrylonitrile (PAN) in order to enhance the performance of DSSCs. Electro-optical measurements prove that LC mesogens contribute significantly to photocurrent density by increasing the order parameter of the polymeric electrolytes and provide a pathway for the transportation of redox species (Kim et al., 2009). The self-assembling property of LCs has been utilized in DDSCs that promotes the iodide/triiodide transport as the local concentration of species is increased by the LC mesogens (Pringle and Armel, 2011). This property of the nematic mesogens reduces the recombination reaction between the electrolyte and the working electrodes (Said et al., 2015). Plastic crystals are a solution to the leakage problems linked with liquid electrolytes used in DSSCs. LCs with room temperature mesophase are better replacement of volatile liquid electrolytes since the

mesophase formed by them possess high conductivity. Side-chain LC polymer showing nematic phase tends to increase the ionic conductivity of the polymer electrolytes used in DSSCs. The electron recombination resistance is also enhanced after these LCs are doped in the electrolytes (Cho et al., 2014).

Ahn et al. (2012) used the technique of electrospinning to construct a DSSC with an LC, E7 embedded in a photochemically stable fluorine polymer, poly(vinylidene fluoride-*co*-hexafluoropropylene). High values of J_{SC} (14.62 mA/cm^2) and PCE (6.8%) were achieved, owing to the high ionic conductivity of E7 embedded polymer electrolyte. Few reports exist which have described the utilization of LCs in DSSCs (Yamanaka et al., 2005). Furthermore, when calamitic mesogens are added to liquid electrolytes of organic molecule-based DSSCs, an enhancement in photovoltage is achieved (Koh et al., 2013). Högberg et al. (2016) have fabricated stable and efficient DSSCs by developing two types of LC electrolytes: one being noncovalent assembly of mixtures composed of iodine dispersed imidazolium ionic liquids and carbonate-terminated LC mesogens and the other being covalent assembly of LC mesogens bonded to an imidazolium moiety doped with iodine. These DSSCs with LCs embedded in them are stable over 1,000 h and can work at higher temperatures.

Costa et al. (2013) used two novel imidazolium ionic LCs to investigate the effect of mesophases on solid-state DSSCs. A good balance was realized between the transport of holes and dye regeneration in the smectic C phase, which led to efficiency of 1.5% and better stability. Embedding LC (ML-0249) in polymer electrolytes of DSSCs upgraded the PV performance (Karim et al., 2010). This LC behaved as a plasticizer and PCEs of 4.7% and 4.8% were achieved for devices based on P1:ML0249 (1:3) and PAN:ML-0249 (1:3), respectively. This was attributed to the lowering of the viscosity of the electrolyte by the addition of LCs, which finally led to the enhanced diffusion of triodide. An ILC showing a smectic A phase was used in DSSC to achieve high short-circuit current density and PCE (Yamanaka et al., 2007). This better performance was due to an increase in conductivity which was possible because a gelator was inserted into the ILC. This gelator led to the organization of conductive pathways between the smectic layers because of increase in order of imidazolium cations which form the LC layers.

Cyanobiphenyl-based benzimidazole can be used to modify the surface of dyed titanium dioxide photoanodes in order to enhance the PV parameters of the fabricated DSSCs which are made of additive free electrolytes (Zhao et al., 2012). Cyanobiphenyl mesogens suppress the recombination rate of charge carriers, optimize the conductivity of the polymer electrolyte, and increase the light harvesting capacity at the anode/electrolyte interface. Addition of cyanobiphenyls to polymer electrolytes increases the stability of DSSCs.

4.7 Effect of thermal annealing

Annealing of the photoactive layers has a significant effect on the performance of PV solar cells (Wang et al., 2017; Yuan et al., 2014a; Yao et al., 2010). On annealing at a temperature within the mesophase range, the photocurrent increases due to reduction in the conformational disorder of the electron donor or acceptor material and it favors the transport of charge carriers. The decrease of lifetime of excitons on annealing the devices within the mesophase range indicates the formation of better morphology. Various techniques such as X-ray diffraction, scanning electron microscopy, and transmission electron microscopy reveal that annealing lead to dramatic variations in the orientation of mesogens, crystallinity, and morphology of devices (Figure 4.10; Yao et al., 2011). Thermal annealing leads to homeotropic alignment of discotic porphyrins, which leads to an increase in Jsc to 5.020 mA/cm^2 and PCE up to 0.775% (Sun et al., 2007). This alignment offers an effective pathway for conduction of charge carriers along the axis of columns and provides large area for better harvesting of light. PV devices made of HBCs exhibited an improvement in V_{OC} and I_{sc} when annealed at 120 °C (Hesse et al., 2010). Atomic force microscopy measurements (refer Figure 4.5, solar) favored these results. The surface morphology improved due to the realignment of discotic mesogens into ordered structures. The devices prepared by Iwan et al. (2015) exhibited an increase in efficiency on annealing within the mesophase range since it could remove defects and optimize the morphology of the active layer.

Lanzi et al. (2016) fabricated PV cells based on a copolymer with a 100–165 °C mesophase range prepared using T6CB and T6H monomers. Scanning electron micrographs (SEM) of the PV cells indicated that when the cells were annealed at 95 °C, some aggregates surrounding the small domains of PCB were visible. While on annealing at 150 °C (temperature within the mesophase range), a smaller and uniform distribution of PCBM domains and an enlarged domains of LC molecules in the side chain were obtained. The phase separation between the electron acceptor and donor materials leads to an increase in transportation of charge carriers and diminished probability of recombination. Transmission electron microscopy images also verified the SEM results. Thus, the performance of cells becomes better because of the ability of LC mesogens to form continuous donor–acceptor regions with a domain size of less than 20 nm on annealing. This is of paramount importance because phase separation of 30 nm or less has been found to be suitable for collection of charge carriers (Vanlaeke et al., 2006). Thermal annealing allows the active layer to get organized into interpenetrating networks (Shi et al., 2014), which are thermodynamically stable at nanoscale. This is beneficial for effective dissociation of excitons in the active layer of solar cells. Water contact gel measurements performed on bilayer solar cells consisting of LC-conjugated polyelectrolytes reveal that the hydrophobicity of the active layers is significantly improved (refer Figure 4.11) on annealing (Liu et al., 2015). The increased
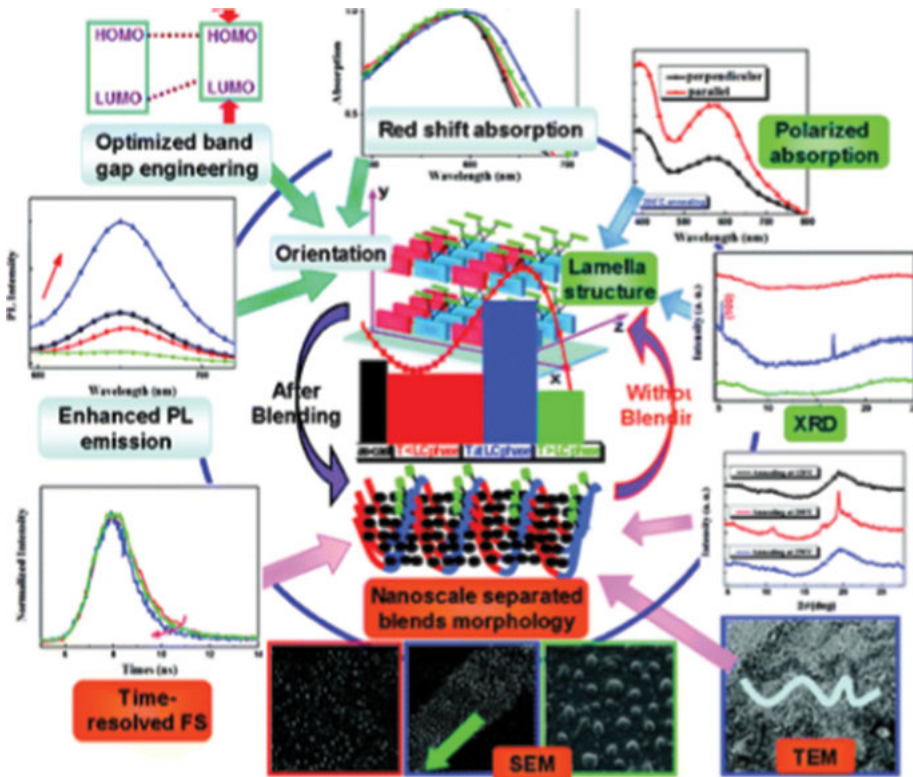
Figure 4.10: X-ray diffraction (XRD), scanning electron microscopy (SEM), and transmission electron microscopy (TEM) of devices (Yao et al., 2011).

hydrophobicity leads to closer interfacial contact with the electrodes favoring easy charge collection and injection.

Sun et al. (2007) found a significant increment in values of FF after annealing devices based on LC mesogens which further contributed to an increase in efficiency. In solar cells, the charge carrier lifetime (τ) multiplied by mobility determines the FF. Therefore, an increased FF points to the fact that annealing leads to better transfer of charge carriers due to formation of large crystalline domains of LC mesogens.

However, in some cases, annealing led to a decrease in efficiency because in the LC phase, the thin film of discotic no longer remains continuous but changes into several thick drop-like regions as confirmed by optical microscopy (Petritsch et al., 1999). Annealing deters the interaction between the donor and acceptor, destroying the heteromolecular assembly and stimulating the columnar assembly (Kang et al., 2013).

We found an increase in efficiency from 4.2% to 5.1% of PV solar cells fabricated by inserting a layer of HAT4 and using blend of poly[*N*-90-heptadecanyl-2,7-carbazole-alt-5,5-(40,70-di-2-thienyl-20,10,30-benzothiadiazole)] and a fullerene derivative [6,6]-
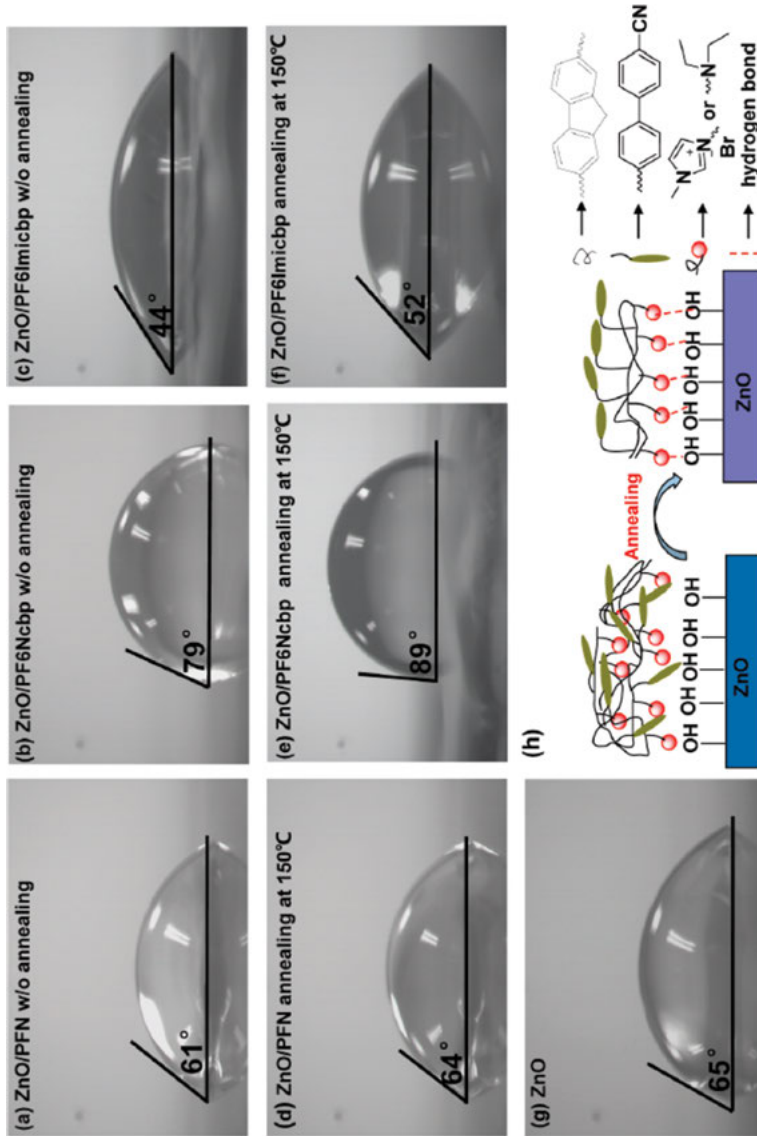
Figure 4.11: Water contact angle images of (a, d) ZnO/PF6Ncbp, (b, e) ZnO/PF6lmicbp, (c, f) ZnO/ PFN, and (g) ZnO films without or with annealing at 150 °C for 10 min. (h) The schematic illustration of the orientation of mesogens after thermal treatment at 150 °C for 10 min (Liu et al., 2015).

phenyl C71-butyric acid methyl ester as the active layer on annealing the device at 125 °C (Bajpai et al., 2016c). From the hole-only devices, mobility was calculated, which showed increased values for devices made of additional HAT4 layer.

4.8 Concluding remarks

Efficient PV solar cells can be developed by exploiting the self-assembling features of various kinds of liquid crystalline mesogens. A lot of progress has been made in this direction, and organic PV solar cells can prove to be competitors to inorganic solar cells in the long run. Although the arena of LC organic solar cells is quite young, high efficiencies have been reported during the past years. Efficiencies close to about 10% have been achieved in PV solar cells with LC mesogens incarcerated in them. Despite possessing fascinating and useful properties, LCs have not been explored enough. More research work and efforts have to be done in order to successfully use them in PV applications.

References

Adam, D., Schuhmacher, P., Simmerer, J., Haussling, L., Siemensmeyer, K., Etzbachi, K.H., Ringsdorf, H., Haarer, D. (1994). Fast photoconduction in the highly ordered columnar phase of a discotic liquid crystal. Nature, 371, 141.

Ahn, S.K., Ban, T., Sakthivel, P., Lee, J.W., Gal, Y.-S., Lee, J.-K., Kim, M.-R., Jin, S.-H. (2012). Development of dye-sensitized solar cells composed of liquid crystal embedded, electrospun poly (vinylidene fluoride-co-hexafluoropropylene) nanofibers as polymer gel electrolytes. ACS Applied Materials & Interfaces, 4, 2096.

Al-Hussein, M., Hesse, H.C., Weickert, J., Dössel, L., Feng, X., Müllen, K., Schmidt-Mende, L. (2011). Structural properties of the active layer of discotic hexabenzocoronene/perylene diimide bulk hetero junction photovoltaic devices: The role of alkyl side chain length. Thin Solid Films, 520, 307.

AlKhalifah, M.S., Lei, C., Myersa, S.A., O'Neill, M., Kitney, S.P., Kelly, S.M. (2014). Solution-processed bilayer photovoltaic devices with nematic liquid crystals. Liquid Crystals, 41, 402.

Bajpai, M., Yadav, N., Kumar, S., Srivastava, R., Dhar, R. (2016a). Bulk heterojunction solar cells based on self assembling disc-shaped liquid crystalline material Liquid Crystals, 43, 305.

Bajpai, M., Yadav, N., Kumar, S., Srivastava, R., Dhar, R. (2016b). Incorporation of liquid crystalline triphenylene derivative in bulk heterojunction solar cell with molybdenum oxide as buffer layer for improved efficiency. Liquid Crystals, 43, 928.

Bajpai, M., Yadav, N., Kumar, S., Srivastava, R., Dhar, R. (2016c). Bulk heterojunction solar cells made from carbazole copolymer and fullerene derivative with an inserted layer of discotic material with improved efficiency Liquid Crystals. Doi: doi:10.1080/02678292.2016.1209793.

Branch, J., Thompson, R., Taylor, J.W., Salamanca-Riba, L., Martınez-Miranda, L.J. (2014). ZnO nanorod-smectic liquid crystal composites: Role of ZnO particle size, shape, and

concentration on liquid crystal order and current–voltage properties. Journal of Applied Physics, 115, 164313.

Canli, N.Y., Safak-Boroglu, M., Bilgin-Eran, B., Günes, S. (2014). Bilayer polymer/fullerene solar cells with a liquid crystal. Thin Solid Films, 560, 71.

Carrasco-Orozco, M., Tsoi, W.C., O'Neill, M., Aldred, M.P., Vlachos, P., Kelly, S.M. (2006). New Photovoltaic Concept: Liquid-Crystal Solar Cells Usinga Nematic Gel Template. Advanced Materials, 18, 1754.

Castet, F., D'Avino, G., Muccioli, L., Cornil, J., Beljonne, D. (2014). Charge separation energetics at organic heterojunctions: on the role of structural and electrostatic disorder. Physical Chemistry Chemical Physics, 16, 20279.

Chen, W., Chen, Y., Li, F., Chen, L., Yuan, K., Yao, K., Wang, P. (2012). Ordered microstructure induced by orientation behavior of liquid-crystal polythiophene for performance improvement of hybrid solar cells. Solar Energy Materials and Solar Cells, 96, 266.

Chino, Y., Ohta, K., Kimur, M., Yasutake, M. (2017). Discotic liquid crystals of transition metal complexes, 53[†]: synthesis and mesomorphism of phthalocyanines substituted by m-alkoxyphenylthio groups. Journal of Porphyrins and Phthalocyanines, 21, 159.

Cho, W., Lee, J.W., Gal, Y.-S., Kim, M.-R., Jin, S.H. (2014). Improved power conversion efficiency of dye-sensitized solar cells using side chain liquid crystal polymer embedded in polymer electrolytes. Materials Chemistry and Physics, 143, 904.

Cisse, L., Destruel, P., Archambeau, S., Seguy, I., Jolinat, P., Bock, H., Grelet, E. (2009). Measurement of the exciton diffusion length in discotic columnar liquid crystals: Comparison between homeotropically oriented and non-oriented samples. Chemical Physics Letters, 476, 89.

Claessens, C.G., Hahn, U., Torres, T. (2008). Phthalocyanines: from outstanding electronic properties to emerging applications. The Chemical Record, 8, 75.

Costa, R.D., Werner, F., Wang, X., Grönninger, P., Feihl, S., Kohler, F.T.U., Wasserscheid, P., Hibler, S., Beranek, R., Meyer, K., Guldi, D.M. (2013). Beneficial effects of liquid crystalline phases in solid-state dye-sensitized solar cells. Advanced Energy Materials, 3, 657.

Dam, H.H., Sun, K., Hanssen, E., White, J.M., Marszalek, T., Pisula, W., Czolk, J., Ludwig, J., Colsmann, A., Pfaff, M., Gerthsen, D., Wong, W.W.H., Jones, D.J. (2014). Morphology change and improved efficiency in organic photovoltaics via hexa-peri-hexabenzocoronene templates. ACS Applied Materials & Interfaces, 6, 8824.

Dao, Q.D., Hori, T., Fukumura, K., Masuda, T., Kamikado, T., Fujii, A., Shimizu, Y., Ozaki, M. (2012). Efficiency enhancement in mesogenic-phthalocyanine-based solar cells with processing additives. Applied Physics Letters, 101, 263301.

Dao, Q.-D., Hori, T., Fukumura, K., Masuda, T., Kamikado, T., Fujii, A., Shimizu, Y., Ozaki, M. (2013). Effects of processing additives on nanoscale phase separation, crystallization and photovoltaic performance of solar cells based on mesogenic phthalocyanine. Organic Electronics, 14, 2628.

de Cupere, V., Tant, J., Viville, P. (2006). Effect of Interfaces on the Alignment of a Discotic Liquid–Crystalline Phthalocyanine. Langmuir, 22, 7798.

Destruel, P., Bock, H., Séguy, I., Jolinat, P., Oukachmih, M., Bedel-Pereira, E. (2006). Influence of indium tin oxide treatment using UV–ozone and argon plasma on the photovoltaic parameters of devices based on organic discotic materials. Polymer International, 55, 601.

Feng, X., Liu, M., Pisula, W., Takase, M., Li, J., Mullen, K. (2008). Supramolecular organization and photovoltaics of triangle-shaped discotic graphenes with swallow-tailed alkyl substituents. Advanced Materials, 20, 2684.

Fujieda, I., Itaya, S., Ohta, M., Ozawa, S., Azmi, N.D.B.M. (2016). Characterization of a liquid crystal/dye cell for a future application in display-integrated photovoltaics. Journal of Photonics for Energy, 6, 028001–1.

Garcia, G., Moral, M., Granadino-Roldan, J., Garzon, A., Navarro, A., Fernandez-Gomez, M. (2013). Theoretical Approach to the Study of Thiophene-Based Discotic Systems As Organic Semiconductors. The Journal of Physical Chemistry C, 117, 15.

Geacintov, N., Pope, M., Kallman, H. (1966). Photogeneration of Charge Carriers in Tetracene. Journal of Chemical Physics, 45, 2639.

Geraghty, P.B., Lee1, C., Subbiah, J., Wong, W.W.H., Banal, J.L., Jameel, M.A., Smith, T.A., Jones, D.J. (2016). High performance p-type molecular electron donors for OPV applications via alkylthiophene catenation chromophore extension. Beilstein Journal of Organic Chemistry, 12, 2298.

Ghosh, S., Ramos, L., Remita, H. (2018). Swollen hexagonal liquid crystals as smart nanoreactors: implementation in materials chemistry for energy applications Nanoscale. Doi: 10.1039/C7NR08457A.

Gowda, A., Kumar, M., Kumar, S. (2017). Discotic liquid crystals derived from polycyclic aromatic cores: from the smallest benzene to the utmost graphene cores. Liquid Crystals, 44, 1990.

Green, M.A., Hishikawa, Y., Warta, W., Dunlop, E.D., Levi, D.H., Hohl-Ebinger, J., Ho-Baillie, A.W.Y. (2017). Solar cell efficiency tables (version 50). Progress in Photovoltaics: Research and Applications, 25, 668.

Gregg, B.A. (2003). Excitonic solar cells The Journal of Physical Chemistry B, 107, 4688.

Gregg, B.A., Fox, M.A., Bard, A.J. (1990). Photovoltaic effect in symmetrical cells of a liquid crystal porphyrin. Journal of Physical Chemistry B, 94, 1586.

Guldi, D.M. (2002). Fullerene–porphyrin architectures; photosynthetic antenna and reaction center models. Chemical Society Reviews, 31, 22.

Gunes, S., Neugebauer, H., Sariciftci, N.S. (2007). Conjugated polymer-based organic solar cells. Chemical Reviews, 107, 1324.

Han, Y., Chen, L., Chen, Y. (2013). Diketopyrrolopyrrole-Based Liquid Crystalline Conjugated Donor–Acceptor Copolymers with Reduced Band Gap for Polymer Solar Cells. Journal of Polymer Science Part A: Polymer Chemistry, 51, 258.

He, B., Pun, A.B., Klivansky, L.M., McGough, A.M., Ye, Y., Zhu, J., Guo, J., Teat, S.J., Liu, Y. (2014). Thiophene fused azacoronenes: regioselectives synthesis, self-organization, charge transport and its incorporation in conjugated polymers. Chemistry of Materials, 26, 3920.

Heo, S.W., Baek, K.H., Song, H.J., Lee, T.H., Moon, D.K. (2014). Improved Performance of P3HT: PCBM-Based Solar Cells Using Nematic Liquid Crystals as a Processing Additive under Low Processing Temperature conditions. Macromolecular Materials and Engineering, 299, 353.

Hesse, H.C., Weickert, J., Al-Hussein, M., Dossel, L., Feng, X., Mullen, K., Schmidt-Mende, L. (2010). Discotic materials for organic solar cells: effects of chemical structure on assembly and performance. Solar Energy Materials & Solar Cells, 94, 560.

Hindson, J.C., Ulgut, B., Friend, R.H., Greenham, N.C., Norder, B., Kotlewskic, A., Dingemans, T.J. (2010). All-aromatic liquid crystal triphenylamine-based poly (azomethine) as hole transport materials for opto-electronic applications. Journal of Materials Chemistry, 20, 937.

Högberg, D., Soberats, B., Yatagai, R., Uchida, S., Yoshio, M., Kloo, L., Segawa, H., Kato, T. (2016). Liquid-crystalline dye-sensitized solar cells: design of two-dimensional molecular assemblies for efficient ion transport and thermal stability. Chemistry of Materials, 28, 6493.

Hoppe, H., Sariciftci, N.S. (2004). Organic solar cells: An overview Journal of Materials Research, 19, 1924.

Hori, T., Fukuoka, N., Masuda, T., Miyake, Y., Yoshida, H., Fujii, A., Shimizu, Y., Ozaki, M. (2011). Bulk heterojunction organic solar cells utilizing 1, 4, 8, 11, 15, 18, 22, 25-octahexylphthalocyanine. Solar Energy Materials and Solar Cells, 95, 3087.

Hori, T., Miyake, Y., Yamasaki, N., Yoshida, H., Fujii, A., Shimizu, Y., Ozaki, M. (2010). Solution processable organic solar cell based on bulk heterojunction utilizing phthalocyanine derivative. Applied Physics Express, 3, 101602.

Iwan, A., Boharewicz, B., Tazbir, I., Hamplová, V., Bubnov, A. (2015). Effect of chiral photosensitive liquid crystalline dopants on the performance of organic solar cells. Solid State Electronics, 104, 53.

Jeong, S., Kwon, Y., Choi, B.-D., Ade, H., Han, Y.S. (2010a). Improved efficiency of bulk heterojunction poly (3-hexylthiophene):[6, 6]-phenyl-C61-butyric acid methyl ester photovoltaic devices using discotic liquid crystal additives. Applied Physics Letters, 96, 183305.

Jeong, S., Kwon, Y., Choi, B.-D., Kwak, G., Han, Y.S. (2010b). Effects of nematic liquid crystal additives on the performance of polymer solar cells. Macromolecular Chemistry and Physics, 211, 2474.

Julien, I., Mereau, R., Ducasse, L., Castet, F., Bock, H., Olivier, Y., Cornil, J., Beljonne, D., D'Avino, G., Roscioni, O.M., Muccioli, L., Zannoni, C. (2014). Charge dissociation at interfaces between discotic liquid crystals: The surprising role of column mismatch. Journal of the American Chemical Society, 136, 2911.

Jurow, M.J., Hageman, B.A., DiMasi, E., Nam, C.-Y., Pabon, C., Black, C.T., Drain, C.M. (2013). Controlling morphology and molecular packing of alkane substituted phthalocyanine blend bulk heterojunction solar cells. Journal of Materials Chemistry A, 1, 1557.

Kaafarani, B.R. (2011). Discotic Liquid Crystals for Opto-Electronic Applications. Chemistry of Material, 23, 378.

Kamarudin, M.A., Khan, A.A., Said, S.M., Qasim, M.M., Wilkinson, T.D. (2018). Composite liquid crystal-polymer electrolytes in dye-sensitised solar cells: effects of mesophase alkyl chain length. Liquid Crystals, 45, 112.

Kang, S.J., Ahn, S., Kim, J.B., Schenck, C., Hiszpanski, A.M., Oh, S., Schiros, T., Loo, Y.-L., Nuckolls, C. (2013). Using self-organization to control morphology in molecular photovoltaics. Journal of the American Chemical Society, 135, 2207.

Karim, M.A., Song, M., Park, J.S., Kim, Y.H., Lee, M.J., Lee, J.W., Lee, C.W., Cho, Y.-R., Gal, Y.-S., Lee, J.H., Jin, S.-H. (2010). Development of liquid crystal embedded in polymer electrolytes composed of click polymers for dye-sensitized solar cell applications. Dyes and Pigments, 86, 259.

Kato, T., Uchida, J., Ichikawa, T., Sakamoto, T. (2018). Functional Liquid Crystals towards the Next Generation of Materials. Angewandte Chemie International Edition, 57, 4355.

Kennedy, R.D., Ayzner, A.L., Wanger, D.D., Day, C.T., Halim, M., Khan, S.I., Tolbert, S.H., Schwartz, B.J., Rubin, Y. (2008). Self-assembling fullerenes for improved bulk-heterojunction photovoltaic devices. Journal of the American Chemical Society, 130, 17290.

Khan, A.A., Kamarudin, M.A., Qasim, M.M., Wilkinson, T.D. (2017). Formation of physical-gel redox electrolytes through self-assembly of discotic liquid crystals: Applications in dye sensitized solar cells. Electrochimica Acta. 244, 162.

Kim, J.Y., Bard, A.J. (2004). Organic donor/acceptor heterojunction photovoltaic devices based on zinc phthalocyanine and a liquid crystalline perylene diimide. Chemical Physics Letters, 383, 11.

Kim, S.C., Song, M., Ryu, T.I., Lee, M.J., Jin, S.H., Gal, Y.S., Kim, H.K., Lee, G.D., Kang, Y.S. (2009). Liquid crystals embedded in polymeric electrolytes for quasi-solid state dye-sensitized solar cell applications. Macromolecular Chemistry and Physics, 210, 1844.

Koh, T.M., Li, H., Nonomura, K., Mathews, N., Hagfeldt, A., Grätzel, M., Mhaisalkar, S.G., Grimsdale, A.C. (2013). Photovoltage enhancement from cyanobiphenyl liquid crystals and 4-*tert*-butylpyridine in Co(ii/iii) mediated dye-sensitized solar cells. Chemical Communications, 49, 9101.

Komiyama, H., To, T., Furukawa, S., Hidaka, Y., Shin, W., Ichikawa, T., Arai, R., Yasuda, T. (2018). Oligothiophene-Indandione-Linked Narrow-Band Gap Molecules: Impact of π-Conjugated Chain Length on Photovoltaic Performance. ACS Applied Materials & Interfaces, 10, 11083.

Kumar, M., Kumar, S. (2017). Liquid crystals in photovoltaics: a new generation of organic photovoltaics. Polymer Journal, 49, 85.

Lanzi, M., Paganin, L., Salatelli, E., Giorgini, L., Benelli, T., Di-Nicola, F.P. (2016). A new thiophene-copolymer with side-chain LC mesogen group for efficient BHJ solar cells. Synthetic Metals, 222, 240.

Lee, -C.-C., Huang, W.-Y. (2012). Insertion of poly(acrylamide) disc-columnar liquid crystals as a functional template in organic photovoltaics. Journal of Applied Polymer Science, 126, E70.

Lee, J.Y., Song, H.J., Lee, S.M., Lee, J.H., Moon, D.K. (2011a). Synthesis and investigation of photovoltaic properties for polymer semiconductors based on porphyrin compounds as light-harvesting units. European Polymer Journal, 47, 1686.

Lee, O.P., Yiu, A.T., Beaujuge, P.M., Woo, C.H., Holcombe, T.W., Millstone, J.E., Douglas, J.D., Chen, M.S., Fréchet, J.M.J. (2011b). Efficient small molecule bulk heterojunction solar cells with high fill factors via pyrene-directed molecular self-assembly. Advanced Materials, 23, 5359.

Levitsky, I.A., Euler, W.B., Tokranova, N., Xu, B. (2004). Hybrid solar cells based on porous Si and copper phthalocyanine derivatives. Journal of Castracane, Applied Physics Letters, 85, 6245

Li, C., Liu, Y., Huang, X., Jiang, H. (2012a). Direct Sun-Driven Artificial Heliotropism for Solar Energy Harvesting Based on a Photo-Thermomechanical Liquid-Crystal Elastomer Nanocomposite. Advanced Functional Materials, 22, 5166.

Li, F., Chen, W., Chen, Y. (2012b). Mesogen induced self-assembly for hybrid bulk heterojunction solar cells based on a liquid crystal D−A copolymer and ZnO nanocrystals. Journal of Materials Chemistry, 22, 6259.

Li, F., Chen, W., Yuan, K., Chen, Y. (2012c). Photovoltaic performance enhancement in P3HT/ZnO hybrid bulk-heterojunction solar cells induced by semiconducting liquid crystal ligands. Organic Electronics, 13, 2757.

Li, J., Kastler, M., Pisula, W., Robertson, J.W.F., Wasserfallen, D., Grimsdale, A.C., Wu, J., Müllen, K. (2007). Organic bulk-heterojunction photovoltaics based on alkyl substituted discotics. Advanced Functional Materials, 17, 2528.

Li, -L.-L., Diau, E.W.-G. (2013). Porphyrin-sensitized solar cells. Chemical Society Reviews, 42, 291.

Li, L., Kang, S.-W., Harden, J., Sun, Q., Zhou, X., Dai, L., Jakli, A., Kumar, S., Li, Q. (2008). Nature-inspired light-harvesting liquid crystalline porphyrins for organic photovoltaics. Liquid Crystals, 35, 233.

Liao, X., Wu, F., Chen, L., Chen, Y. (2016). Crystallization and Optical Compensation by Fluorinated Rod Liquid Crystals for Ternary Organic Solar Cells. The Journal of Physical Chemistry C, 120, 18462.

Liu, C., Tan, Y., Li, C., Wu, F., Chen, L., Chen, Y. (2015). Enhanced power-conversion efficiency in inverted bulk heterojunction solar cells using liquid-crystal conjugated polyelectrolyte interlayer. ACS Applied Materials & Interfaces, 7, 19024.

Liu, C.Y., Pan, H.L., Fox, M.A., Bard, A.J. (1993). High-Density Nanosecond Charge Trapping in Thin Films of the Photoconductor ZnODEP. Science, 261, 897.

Markovitsi, D., Lecuyer, I., Simon, J. (1991). One-dimensional triplet energy migration in columnar liquid crystals of octasubstituted phthalocyanines. Journal of Physical Chemistry B, 95, 3620.

O'Regan, B., Gratzel, M. (1991). A low-cost, high-efficiency solar cell based on dye-sensitized colloidal TiO2 films. Nature, 353, 737.

Oukachmih, M., Destruel, P., Seguy, I., Ablart, G., Jolinat, P., Archambeau, S., Mabiala, M., Fouet, S., Bock, H. (2005). New organic discotic materials for photovoltaic conversion. Solar Energy Materials & Solar Cells, 85, 535.

Petritsch, K., Dittmer, J.J., Marseglia, E.A., Friend, R.H., Lux, A., Rozenberg, G.G., Moratti, S.C., Holmes, A.B. (2000). Dye-based donor/acceptor solar cells. Solar Energy Materials and Solar Cells, 61, 63.

Petritsch, K., Friend, R.H., Lux, A., Rozenberg, G., Moratti, S.C., Holmes, A.B. (1999). Liquid crystalline phthalocyanines in organic solar cells. Synthetic Metals, 102, 1776.

Piechocki, C., Simon, J., Skoulios, A., Guillon, D., Weber, P. (1982). Discotic mesophases obtained from substituted metallophthalocyanines. Toward liquid crystalline one-dimensional conductors. Journal of the American Chemical Society, 104, 19.

Pringle, J.M., Armel, V. (2011). The influence of ionic liquid and plastic crystal electrolytes on the photovoltaic characteristics of dye-sensitised solar cells. International Reviews in Physical Chemistry, 30, 371.

Primary Photo excitations in Conjugated Polymers: Molecular Exciton versus Semiconductor Band Model, edited by, Sariciftci, N.S., World Scientific, Singapore, 1997.

Said, S.M., Zulkifli, A.Z.S.,Kamarudin, M.A., Mainal, A., Subramanian, B., Mohamed, N.S. (2015). Polymer electrolyte liquid crystal system for improved optical and electrical properties. European Polymer Journal, 66, 266.

Schmidt-Mende, L., Fechtenkotter, A., Mullen, K., Moons, E., Friend, R.H., MacKenzie, J.D. (2001a). Self-Organized Discotic Liquid Crystals for High-Efficiency Organic Photovoltaics. Science, 293, 1119.

Schuenemann, C., Petrich, A., Schulze, R., Wynands, D., Meiss, J., Hein, M.P., Jankowski, J., Elschner, C., Alex, J., Hummert, M., Eichhorn, K.-J., Leo, K., Riede, M. (2013). A new route to the Mott-Hubbard metal-insulator transition: Strong correlations effects in $Pr_{0.7}Ca_{0.3}MnO_3$. Organic Electronics, 14, 1704.

Schweicher, G., Gbabode, G., Quist, F., Debever, O., Dumont, N., Sergeyev, S., Geerts, Y.H. (2009). Homeotropic and Planar Alignment of Discotic Liquid Crystals: The Role of the Columnar Mesophase. Chemistry of Materials, 21, 5867.

Shi, Y., Li, F., Tan, L., Chen, Y. (2013). Hybrid Bulk Heterojunction Solar Cells Based on the Cooperative Interaction of Liquid Crystals within Quantum Dots and Diblock Copolymers. ACS Applied Materials & Interfaces, 5, 11692.

Shi, Y., Tan, L., Chen, Y. (2014). Dye-sensitized nanoarrays with discotic liquid crystals as interlayer for high-efficiency inverted polymer solar cells. ACS Applied Materials & Interfaces, 6, 17848.

Shin, W., Yasuda, T., Watanabe, G., Yang, Y.S., Adachi, C. (2013). Self-organizing mesomorphic diketopyrrolopyrrole derivatives for efficient solution-processed organic solar cells. Chemistry of Materials, 25, 2549.

Silva, H.S., Metz, S., Hiorns, R.C., Bégué, D. (2018). Targeting ideal acceptor-donor materials based on hexabenzocoronene. Journal of Molecular Structure. Doi: 10.1016/j.molstruc.2018.02.067.

Sun, K., Xiao, Z., Lu, S., Zajaczkowski, W., Pisula, W., Hanssen, E., White, J.M., Williamson, R.M., Subbiah, J., Ouyang, J., Holmes, A.B., Wong, W.W.H., Jon, D.J. (2014). A molecular nematic liquid crystalline material for high-performance organic photovoltaics. Nature Communications, 6, 6013.

Sun, Q., Dai, L., Zhou, X., Li, L., Li, Q. (2007). Bilayer-and bulk-heterojunction solar cells using liquid crystalline porphyrins as donors by solution processing. Applied Physics Letters, 91, 253505.

Sun, Q., Park, K., Dai, L. (2009). Liquid crystalline polymers for efficient bilayer-bulk heterojunction solar cells. The Journal of Physical Chemistry C, 113, 7892.

Takemoto, K., Karasawa, M., Kimura, M. (2012). Solution-processed bulk-heterojunction solar cells containing self-organized disk-shaped donors. ACS Applied Materials & Interfaces, 4, 6289.

Tang, C.W., Albrecht, A.C. (1975). Photovoltaic effects of metal–chlorophyll-a–metal sandwich cells. Journal of Chemical Physics, 62, 2139.

Thiebaut, O., Bock, H., Grelet, E. (2010). Face-on Oriented Bilayer of Two Discotic Columnar Liquid Crystals for Organic Donor-Acceptor Heterojunction. Journal of the American Chemical Society, 132, 6886.

Tsoi, W.C., O'Neill, M., Aldred, M.P., Kitney, S.P., Vlachos, P., Kelly, S.M. (2007). Distributed bilayer photovoltaics based on nematic liquid crystal polymer networks. Chemistry of Materials, 19, 5475.

Tsou, Y.-S., Chang, K.-H., Lin, Y.-H. (2013). A droplet manipulation on a liquid crystal and polymer composite film as a concentrator and a sun tracker for a concentrating photovoltaic system. Journal of Applied Physics, 113, 244504.

van Breemen, A.J.J.M., Herwig, P.T., Chlon, C.H.T. (2006). Large Area Liquid Crystal Monodomain Field-Effect Transistors Journal of the American Chemical Society, 128, 2336.

Van de Craats, A., Warman, J., Fechtenkötter, A., Brand, J.D., Harbison, M., Müllen, K. (1999). Record charge carrier mobility in a room-temperature discotic liquid crystalline derivative of hexabenzocoronene. Advanced Materials, 11, 1469–72.

Vanlaeke, P., Swinnen, A., Haeldermans, I., Vanhoyland, G., Aernouts, T., Cheyns, D., Deibel, C., D'Haen, J., Heremans, P., Poortmans, J., Manca, J.V. (2006). P3HT/PCBM bulk heterojunction solar cells: Relation between morphology and electro-optical characteristics. Solar Energy Materials & Solar Cells, 90, 2150.

Walter, M.G., Rudine, A.B., Wamser, C.C. (2010). Porphyrins and phthalocyanines in solar photovoltaic cells. Journal of Porphyrins and Phthalocyanines, 14, 759.

Wang, L., Park, S.-Y., Kim, S.-M., Yoon, S., Lee, S.-H., Lee, E., Jeong, K.-U., Lee, M.-H. (2012). Bulk heterojunction photovoltaic cells based on room temperature liquid crystalline tetrathiafulvalene derivatives. Liquid Crystals, 39, 795.

Wong, W.W.H., Ma, C.-Q., Pisula, W., Yan, C., Feng, X., Jones, D.J., Mullen, K., Janssen, R.A.J., Bauerle, P., Holmes, A.B. (2010b). Self-assembling thiophene dendrimers with a hexa-peri-hexabenzocoronene core- synthesis, characterization and performance in bulk heterojunction solar cells. Chemistry of Material, 22, 457.

Wong, W.W.H., Singh, T.B., Vak, D., Pisula, W., Yan, C., Feng, X., Williams, E.L., Chan, K.L., Mao, Q., Jones, D.J., Ma, C.-Q., Mullen, K., Bauerle, P., Holmes, A.B. (2010a). Solution processable fluorenyl hexa-peri-hexabenzocoronenes in organic field-effect transistors and solar cells. Advanced Functional Materials, 20, 927.

Wu, G., Hsieh, L.-H., Chien, H.-W. (2013). Enhanced Solar Cell Conversion Efficiency Using Birefringent Liquid Crystal Polymer Homeotropic Films from Reactive Mesogens. International Journal of Molecular Sciences, 14, 21319.

Wu, J., Pisula, W., Mullen, K. (2007). Graphenes as potential material for electronics. Chemical Reviews, 107, 718.

Yamanaka, N., Kawano, R., Kubo, W., Kitamura, T., Wada, Y., Watanabe, M., Yanagid, S. (2005). Ionic liquid crystal as a hole transport layer of dye-sensitized solar cells. Chemical Communications, 740.

Yamanaka, N., Kawano, R., Kubo, W., Masaki, N., Kitamura, T., Wada, Y., Watanabe, M., Yanagida, S. (2007). Dye-sensitized TiO2 solar cells using imidazolium-type ionic liquid crystal systems as effective electrolytes. The Journal of Physical Chemistry B, 111, 4763.

Yang, S., Wang, T., Zhao, X., Gu, L., Yang, Q., Li, G., Li, X., Fu, G. (2014). Semitransparent Polymer Solar Cells Based on Liquid Crystal Reflectors. International Journal of Photoenergy, 2014, 1689862.

Yao, K., Chen, L., Ting, H., Chen, Y. (2012). Photocrosslinkable liquid–crystalline polymers for stable photovoltaics by adjusting side-chains spacing and fullerene size to control intercalation. Organic Electronics, 13, 1443.

Yao, K., Chen, Y., Chen, L., Li, F., Li, X., Ren, X., Wang, H., Liu, T. (2011). Mesogens Mediated Self-Assembly in Applications of Bulk Heterojunction Solar Cells Based on a Conjugated Polymer with Narrow Band Gap. Macromolecules, 44, 2698.

Yao, K., Chen, Y., Chen, L., Zha, D., Li, F., Pei, J., Liu, Z., Tian, W. (2010). Orientation Behavior of Bulk Heterojunction Solar Cells Based on Liquid-Crystalline Polyfluorene and Fullerene. The Journal of Physical Chemistry C, 114, 18001.

Yuan, K., Chen, L., Chen, Y. (2014a). Direct anisotropic growth of CdS nanocrystals in thermotropic liquid crystal templates for heterojunction optoelectronics. Chemistry European Journal, 20, 11488.

Yuan, K., Chena, L., Chen, Y. (2014). Photovoltaic performance enhancement of P3HT/PCBM solar cells driven by incorporation of conjugated liquid crystalline rod-coil blockcopolymers. Journal of Materials Chemistry C, 2, 3835.

Yuan, K., Li, F., Chen, L., Li, Y., Chen, Y. (2012). Liquid crystal helps ZnO nanoparticles self-assemble for performance improvement of hybrid solar cells. The Journal of Physical Chemistry C, 116, 6332.

Zhao, J., Sun, B., Qiu, L., Caocen, H., Li, Q., Chen, X., Yan, F. (2012). Efficient light-scattering functionalized TiO2 photoanodes modified with cyanobiphenyl-based benzimidazole for dye-sensitized solar cells with additive-free electrolytes. Journal of Materials Chemistry, 22, 18380.

Zheng, Q., Fang, G., Bai, W., Sun, N., Qin, P., Fan, X., Cheng, F., Yuan, L., Zhao, X. (2011). Efficiency improvement in organic solar cells by inserting a discotic liquid crystal. Solar Energy Materials and Solar Cells, 95, 2200.

Mon-Juan Lee, Wei Lee

5 Liquid crystal-based biosensing: exploiting the electrical and optical properties of various liquid crystals in quantitative bioassays

Abstract: Studies of the interaction between biomolecules and liquid crystals (LCs) opened up a promising new field of biosensing technologies. It is established that biomolecules can be detected and analyzed through the disruption of the regular alignment of LCs at an LC–glass or LC–water interface, thus enabling the development of biosensing platforms for DNA, lipids, and proteins, as well as larger biological entities such as pathogens and viruses. Potential clinical application of LC-based bioassays has been demonstrated in the immunodetection of cancer biomarkers, hepatitis-B antibody titering, and early detection of Alzheimer's disease. While conventional LC-based biodetection relies primarily on optical anisotropy in 4-cyano-4′-pentylbiphenyl (5CB), a common and historically significant nematic compound, it has been brought to our attention that a wide variety of novel LC materials, especially those currently investigated in the design of LC display devices, present intriguing electrical and optical properties that are applicable to the detection and quantitation of biomolecules. In this chapter, we focus on the advantages and importance of widening the variety of biosensing mesogens. The biosensing application of LCs other than 5CB, such as nematic LCs of large birefringence, cholesteric LC, blue-phase LC, dye-associated LCs including dye LC and dye-doped LC, and dual-frequency LC at the LC–glass interface, is introduced. Not only do these LCs exhibit birefringent characteristics and biosensing capabilities similar to 5CB when interfaced with biomolecules, but their unique electrical and optical properties contribute to further enhancement in detection sensitivity and, in particular, quantitative analysis. Because one of the technical drawbacks in current LC-based biosensing techniques is the lack of quantitative methods, we elaborate on the innovative approaches of transmission spectrometry, capacitance, electro-optical, and dielectric measurements toward the development of quantitative bioassays. The unique features of LCs as flexible biosensing materials enable the development of unconventional label-free bioassays for cost-effective, fast-screening, and even color-indicating biomedical and biophotonic devices for clinical and point-of-care diagnostics.

5.1 Introduction

5.1.1 Biosensing application of LCs

Biomolecular recognition exploiting liquid crystals (LCs) as the sensing medium is a relatively nascent field in biophotonics and biomedicine, considering that a wide array of LC materials has long been investigated and extensively applied in the liquid crystal display (LCD) industry (Woltman et al., 2007). A typical LC-based biosensing platform usually consists of a LC–glass interface in the form of an LC cell, in which a layer of LC is sandwiched between two glass substrates where the biomolecules are immobilized, or an LC–aqueous interface, including LC films and LC-in-water droplets, at which biomolecules are dispersed in the aqueous phase, or confined within the LC–water interface because of their amphiphilic molecular structure (Carlton et al., 2013; Popov et al., 2017). LCs are usually directed in alignment according to the anchoring force of a self-assembled monolayer of aligning reagent such as octadecyltrichlorosilane (ODTS) or *N,N*-dimethyl-*n*-octadecyl-3-aminopropyltrimethoxysilyl chloride (DMOAP), both of which are homeotropic alignment reagents. The presence of biomolecules weakens the anchoring force of the alignment reagent, causing a disturbance in the regular LC orientation, thus altering the optical appearance of the birefringent LC. Because the interference color and optical texture of LCs sensitively reflect the amount, binding state, or reaction stage of biomolecules at the LC–glass or LC–aqueous interface, label-free detection can be realized by observing under a polarized optical microscope without further labeling with a chromophore or fluorophore, a common practice in conventional bioassays. As shown in Table 5.1, LC-based biosensing platforms have been designed for the detection and signal amplification of glucose (Khan and Park, 2014, 2015a, 2015b, 2017; Kim et al., 2013), proteins (Chiang et al., 2018; Hsiao et al., 2015; Lee et al., 2017; Lin et al., 2016; Nguyen et al., 2015; Tingey et al., 2004; Wu et al., 2018; Zhao et al., 2015), peptides and protein–peptide binding events (Clare and Abbott, 2005; Sadati et al., 2015), enzymatic reactions (Bi et al., 2009; Chuang et al., 2016; Hoogboom et al., 2006; Hussain et al., 2014; Zhang and Jang, 2014), protein–protein interaction and immunoreaction between antigens and antibodies (Chen and Yang, 2012; Hartono et al., 2009; Kim et al., 2000; Luk et al., 2003, 2004b, 2005; Popov et al., 2016; Su et al., 2014, 2015; Sun et al., 2015; Xue et al., 2009; Xue and Yang, 2008), DNA hybridization (Khan et al., 2016; Price and Schwartz, 2008; Shen et al., 2017; Tan et al., 2014, 2010; Yang et al., 2012, 2013), as well as whole cell entities (Helfinstine et al., 2006; Jang et al., 2006; Lockwood et al., 2006).

Table 5.1: Biosensing application of various types of LCs.

Types of application or target of detection	Sensing mesogen	Detection interface	References
Biologically relevant small molecules			
Glucose	5CB	LC droplets	Kim et al. (2013)
Glucose	5CB	LC–aqueous	Khan and Park (2014), (2015a), (2015b), (2017)
Glucose and cholesterol	CLC	LC droplets	Lee et al. (2016a)
Myricetin (DNA-based detection)	5CB	LC–aqueous	Munir and Park (2016)
Phospholipids			
L-DLPC	5CB	LC–aqueous	Brake et al. (2003)
Lipopolysaccharides			
Sepsis-associated endotoxin	5CB	LC–aqueous	McCamley et al. (2007)
Proteins			
BSA	5CB	LC– Au deposited glass	Nguyen et al. (2015)
Biotin-labeled BSA	5CB	LC–glass	Tingey et al. (2004)
BSA	HDN, CLC, BPLC, DLC, DDLC	LC–glass	Chiang et al. (2018), Hsiao et al. (2015), Lee et al. (2017), Lin et al. (2016), Wu et al. (2018)
Thrombin	5CB	LC–glass	Zhao et al. (2015)
Peptides and protein–peptide binding			
Protein–peptide binding	5CB	LC–Au deposited glass	Clare and Abbott (2005)
β-Amyloid peptide (biomarker for Alzheimer's disease)	5CB	LC–aqueous	Sadati et al. (2015)
Protein–protein interaction and immunoreactions			
RNase A and RNase inhibitor	5CB	LC–glass	Luk et al. (2004b)
IgG and anti-IgG	5CB	LC–aqueous	Popov et al. (2016)

Table 5.1 (continued)

Types of application or target of detection	Sensing mesogen	Detection interface	References
IgG and anti-IgG	5CB	LC–glass	Xue and Yang (2008)
IgG and anti-IgG	5CB	LC–glass	Xue et al. (2009)
BSA and anti-BSA antibody	5CB	LC–glass	Kim et al. (2000)
MEK and anti-MEK antibody	5CB	LC–Au deposited glass	Luk et al. (2003)
Ubiquitin and anti-ubiquitin antibody	5CB	LC–aqueous	Hartono et al. (2009)
Hepatitis B antigen and antibody	5CB	LC–glass	Chen and Yang (2012)
IgG and anti-IgG	Lyotropic LCs	LC–glass	Luk et al. (2005)
CA125 and anti-CA125 antibody	HDN	LC–glass	Su et al. (2014), Su et al. (2015), Sun et al. (2015)
Enzymatic activity			
Multiplex protease assay	5CB	LC–glass	Bi et al. (2009)
Lipase	5CB	LC–glass	Hoogboom et al. (2006)
Trypsin	5CB	LC–aqueous	Chuang et al. (2016)
Lipase	5CB	LC–aqueous	Hussain et al. (2014)
Thrombin	5CB	LC–aqueous	Zhang and Jang (2014)
DNA hybridization			
Detection of single-base mismatch in a 22-mer target	5CB	LC–glass	Shen et al. (2017)
Detection of single-base mismatch in a 16-mer target	5CB	LC–aqueous	Price and Schwartz (2008)
Detection of p53 mutation sequence	5CB	LC–aqueous	Tan et al. (2014)
Detection of gold nanoparticle-labeled target DNA	5CB	LC–glass	Yang et al. (2012)
Detection of heavy metal Hg^{2+} based on DNA hybridization	5CB	LC–glass	Yang et al. (2013)

Table 5.1 (continued)

Types of application or target of detection	Sensing mesogen	Detection interface	References
DNA hybridization based on enzymatic metal deposition	5CB	LC–glass	Tan et al. (2010)
Detection of pathogen DNA	E7	LC–aqueous	Khan et al. (2016)
Whole cells			
Human embryonic stem cells	TL205	LC–aqueous with Matrigel	Lockwood et al. (2006)
Microbial immunocomplexes	DSCG	LC–glass	Helfinstine et al. (2006)
Virus envelop structure	5CB	LC–glass	Jang et al. (2006)

5.1.2 Advantages of widening the variety of biosensing mesogens

Although not a practical mesogen for current LCD technologies, the nematic LC 4-cyano-4′-pentylbiphenyl (5CB) is utilized in most LC-based biosensing techniques as the major sensing medium (Table 5.1). LCs other than 5CB, including nematic LC mixtures such as E7, TL205, and a nematic LC of high birefringence (HDN) (Khan et al., 2016; Lin et al., 2016; Lockwood et al., 2006; Su et al., 2014; Su et al., 2015; Sun et al., 2015), chiral nematic LCs such as the cholesteric LC (CLC) and blue-phase LC (BPLC) (Hsiao et al., 2015; Lee et al., 2016a; Lee et al., 2017), dye-associated LCs such as dye LC (DLC) and dye-doped LC (DDLC) (Chiang et al., 2018; Wu et al., 2018), and lyotropic chromonic LCs such as disodium cromoglycate (DSCG) (Helfinstine et al., 2006; Luk et al., 2005) were relatively less reported but their potential in biosensing has been demonstrated as well.

Widening the variety of LCs in biosensing is proven to be advantageous in many aspects, one of which is to improve the design of the biosensor and to accommodate to the conditions necessary for maintaining the structure and activity of the biomolecules. In an LC-based DNA biosensor, E7 was employed to substitute 5CB to facilitate a higher nematic-to-isotropic phase transition temperature (Khan et al., 2016). The birefringence of LCs was found to be a critical factor of sensitivity and detection limit, which were improved when a nematic LC, HDN, with a large birefringence of $\Delta n = 0.333$ at 589.3 nm and 20 °C was substituted for 5CB ($\Delta n = 0.179$ at 589.3 nm and 25 °C) (Su et al., 2014; Su et al., 2015; Sun et al., 2015). For glucose and cholesterol detection, the reflecting color pattern of CLC droplets enables sensitive detection while eliminating the requirement of crossed polarizers necessary for most nematic LC biosensor systems (Lee et al., 2016a). In addition to the color-indicating features, the Bragg reflection of CLC and BPLC along with the dichroic properties

of DLC and DDLC allows protein quantitative methods to be established through transmission spectrometric analysis, which is the center of discussion in Section 5.2.3 (Chiang et al., 2018; Hsiao et al., 2015; Lee et al., 2017; Wu et al., 2018). For the detection of whole cell entities, the growth and differentiation of human embryonic stem cells were monitored on Matrigel at the interface of the cell culture medium and the nematic TL205, which exhibits a relatively low cytotoxicity compared to 5CB and E7 (Lockwood et al., 2006; Luk et al., 2004a). The high birefringence and low viscosity of the lyotropic DSCG provides an amphiphilic environment that is biocompatible with viruses, bacteria, and mammalian cells without damaging the cell membrane or the structure of biomolecules such as immunoglobulin G (IgG) (Helfinstine et al., 2006; Luk et al., 2005). Exploring optimal LC-sensing materials is, as the above results suggest, an important strategy toward the development of mature and practical LC-based biosensor, as there are numerous categories of industrial and commercial LCs that constitute a library of sensing mesogens and eutectic mixtures for direct application or for the preparation of LCs customized to the need of a biosensing system.

5.1.3 Potentials of LC-based biosensing in clinical applications

The clinical potential of LC-based biosensing techniques has been implicated in several disease-related and proof-of-concept models. LC-based glucose detection relying on the catalysis of glucose by glucose oxidase at the LC–aqueous interface in the form of either an LC film or LC droplets offers a promising alternative to conventional blood glucose meters (Khan and Park, 2014, 2015a, 2015b, 2017; Kim et al., 2013; Lee et al., 2016a). The sepsis-associated endotoxin known as lipopolysaccharide, which is released in the bloodstream during bacterial infection, can be detected with an LC-based biosensor at clinically relevant levels (McCamley et al., 2007). The role of LCs as a sensitive and specific reporter for β-amyloid peptide, a marker of neurodegenerative Alzheimer's disease, was demonstrated with a nanomolar detection limit (Sadati et al., 2015). LC-based immunoassays were developed for both hepatitis B antibodies and the cancer biomarker CA125, which provide a label-free and cost-effective option in addition to traditional label-based immunodetection procedures (Chen and Yang, 2012; Chiang et al., 2018; Su et al., 2014; Su et al., 2015; Sun et al., 2015). The observation that the lipid bilayer envelope of viruses induces homeotropic ordering of LCs led to the biodetection method that is capable of discerning between enveloped viruses (i.e., influenza virus, La Crosse virus, and vesicular stomatitis virus) and the nonenveloped adenovirus (Jang et al., 2006). A rapid and sensitive LC-based sensor was designed to detect the release of lipase, or the increase in lipase activity in three cell lines treated with potent chemicals as an indication for cell necrosis, an event that involves the damage of cell membrane and the abnormal release of intracellular enzymes (Hussain et al., 2014). Although still at an early stage of development, current LC-based biosensing technologies provide insights into the extensive scope of

biomedical application of LCs, as well as the potential benefits that can be brought about, including label-free detection, improved sensitivity, simplified procedures, lowered costs, and the possibility of developing LC-based point-of-care devices.

5.1.4 Technical hurdles of current LC-based biosensing techniques

One of the major technical hurdles of LC-based biosensors lies in the unsatisfactory sensitivity or limit of detection to meet the criteria for a clinical assay or medical device. In addition to increasing the LC birefringence in order to achieve a lower detection limit, as mentioned in Section 5.1.2, strengthening the binding affinity between biomolecules and the alignment layer at the LC–glass interface through chemical modification was also proven to be critical (Chen and Yang, 2011; Ong et al., 2014; Su et al., 2015). By shortly exposing the DMOAP monolayer to UV irradiation, the alignment layer becomes slightly more hydrophilic without affecting its anchoring strength (Su et al., 2015). This modification enables more biomolecules to become stably immobilized on the DMOAP-coated glass substrate, thus providing a robust analytical system with improved detection limit and reproducibility. In a DDLC-based quantitative biosensing platform in conjunction with transmission spectrometry, detection sensitivity was improved by adjusting the polarization direction of incident light so that it was parallel to the rubbing direction of the LC cell (Chiang et al., 2018).

Analysis of clinical samples such as blood and urine, which are far more complex systems than those demonstrated with purified analytes in rather ideal or simplified experimental settings in most LC-based biosensor studies, also pose a significant challenge to researchers. Due to the strict bioethics legislation and the required approval from the institutional review board concerning the use of human clinical samples, many studies utilize commercially available human plasma or serum spiked with the target biomolecule as a preliminary substitute to assess the performance of a new technology in a complex environment simulating a clinical sample. Although plasma or serum does affect the diffusion of biomolecules and the response time, or complicate the signal background, the optical response of LCs to the target biomolecules can still be discerned, and detection sensitivity and specificity were consistent with those of the simplified system (Lee et al., 2016b; Su et al., 2015).

Last but not least, current LC-based biosensing techniques lack the signal and data processing components that are essential for a biosensor to produce quantitative outputs. The aim of this chapter is therefore to propose several quantitative approaches by exploring the potential of various types of LCs in biosensing and exploiting the unique electrical and optical properties of LCs in protein quantitation.

5.2 LC-based protein quantitative strategies

A bioassay method without quantitative analysis is insufficient, which is often the case for most LC–based biosensors. Because of the diverse combination of LCs, alignment reagents, detection interfaces, and target biomolecules, strategies to quantitate a target biomolecule are often customized to one sensing platform and may not be applicable to others. Table 5.2 lists several innovative LC-based quantitative approaches proposed for glucose, proteins, and antibodies. Quantitative analysis by backscattering interferometry and measurement of birefringence were reported for glucose detected at the LC–water interface (Khan and Park, 2015a, 2015b, 2017). By determining the anchoring energy, the concentration of anti-phosphotyrosine antibody was determined at an LC–gold-coated interface immobilized with tyrosine-containing peptides (Govindaraju et al., 2007). In this section, we focus on LC-based protein quantitative strategies established for the LC–glass-sensing interface using bovine serum albumin (BSA), a common protein standard, as the major

Table 5.2: LC-based quantitative methods for biomolecules or biologically relevant small molecules.

Target of detection	Sensing mesogen	Detection interface	Parameter or method of quantitation	References
Biologically relevant small molecules				
Glucose	5CB	LC–aqueous	Birefringence Δn	Khan and Park (2015a, 2015b)
Glucose	5CB	LC–aqueous	Backscattering interferometry	Khan and Park (2017)
Proteins				
Anti-phosphotyrosine antibody	5CB	LC–Au deposited glass	Anchoring energy	Govindaraju et al. (2007)
Anti-IgG	5CB	LC–glass	Microfluidic immunoassay	Xue et al. (2009)
BSA	CLC, BPLC, DLC, DDLC	LC–glass	Transmission spectrometry	Chiang et al. (2018), Hsiao et al. (2015), Lee et al. (2017), Wu et al. (2018)
BSA	HDN	LC–glass	Capacitance measurement	Lin et al. (2016)
BSA	HDN, DLC	LC–glass	Electro-optical measurement	Lee et al. (2015), Wu et al. (2018)

study model. We start by familiarizing the reader with conventional protein assays, which are considered here as the gold standard for the development of LC-based quantitative bioassays (Section 5.2.1). We then turn to our initial attempts to establish quantitative methods derived from texture observation (Section 5.2.2), which led us to investigate various electrical and optical properties of LCs that may facilitate protein quantitation (Sections 5.2.3 and 5.2.4).

5.2.1 Conventional protein assays

Protein assays are one of the most essential experimental procedures in biochemical laboratories. It is extensively applied to determine the protein concentration of both purified proteins and protein mixtures such as cell lysates or crude extracts from mammalian, bacteria, or plant cells, as well as biological tissues. Protein assays usually serve as an indispensable first step to estimate the amount of total proteins in a biological sample prior to further quantitative bioassays such as immunoassays or electrophoresis.

Proteins absorb ultraviolet light at a wavelength of 280 nm because of the aromatic amino acids, namely, tyrosine, tryptophan, and phenylalanine, commonly present in their amino acid sequences. However, because absorption at this wavelength is greatly affected by the contents of the aromatic residues and nonprotein impurities with color, considerable error may be incurred, especially for protein mixtures. These shortcomings led to the development of conventional protein assays such as the Bradford or Lowry assay, which are colorimetric protein assays that exploit the binding of dye or the chelation of metal ions to proteins to achieve higher specificity and sensitivity of detection. The dye–protein complex or the metal ion–protein chelate absorbs light within the UV–visible spectrum and its absorbance at a specific wavelength can theoretically be used to calculate protein concentration according to Beer's law:

$$A = \varepsilon bc$$

where A is the absorbance, ε is the molar absorptivity, b is the path length, and c is the molar concentration of the absorbing solution. However, because Beer's law is a limiting law that holds only in dilute solutions, the A versus c correlation often deviates from linearity at high protein concentrations. In addition, the molar absorptivity of protein solutions varies with experimental conditions. Therefore, to utilize the proportionality between A and c, a calibration curve of A versus c is usually constructed with a series of standard solutions, followed by interpolating the A value of the analyte in the calibration curve to obtain the protein concentration c. In a typical protein assay, BSA is often applied as the protein standard. Figure 5.1 is a representative BSA calibration curve obtained with a commercial protein assay kit.

BSA is also frequently used as a model biomolecule in the demonstration of a new bioassay. It is more readily available and cost-effective compared to specific
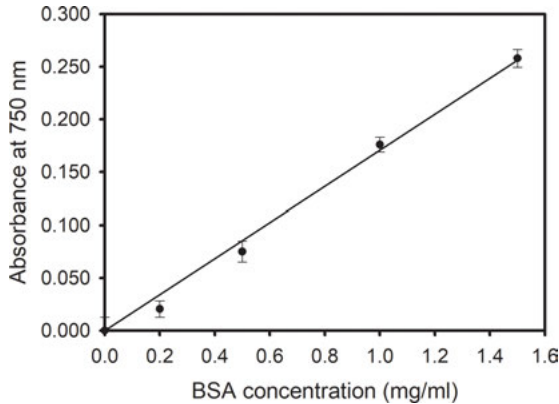
Figure 5.1: BSA calibration curve for protein quantitation. The calibration curve was obtained by reacting five BSA standard solutions of various concentrations (0, 0.2, 0.5, 1.0, 1.5 mg/mL) with reagents of Bio-Rad DC[TM] Protein Assay Kit, a commercial protein assay kit based on Lowry assay, followed by measuring the absorbance at 750 nm.

biomarkers or antibodies. Besides, the molecular weight of BSA (66,463 Da) is close to the average molecular weight of human proteins, which are estimated theoretically from the human genome database to be 40,000–50,000 kDa. It is therefore assumed that if a bioassay works with BSA, it should be reproducible on other proteins.

5.2.2 Quantitative methods derived from texture observation

Because a majority of LC-based biosensing techniques rely on texture observation under a polarized optical microscope, the accuracy of quantitative methods derived from results of such qualitative detection was relatively unsatisfactory. Although the interference color or brightness of LC texture was correlated to the amount of biomolecules, it is also affected by the slight variation in thickness of the LC film confined in an LC cell. In an LC-based microfluidic immunoassay, antibody concentration was quantitated by measuring the length of the bright LC region in the microfluidic channel (Xue et al., 2009). Nevertheless, the cut-off of the bright region may not be definitive enough to serve as a practical quantitative approach, even though a relatively linear correlation was found between the length of the bright region and antibody concentration. Attempts were also made to analyze the brightness of the optical texture of HDN with an image processing software and calculate the relative intensity (RI) as a function of the concentration of biomolecules and immunocomplexes (Sun et al., 2015). However, because RI was calculated by summing up the total RGB value of the optical texture image, the relative error in RI may increase when the interference color of LCs changes significantly at high protein concentrations, or when the protein concentration was extremely low, giving rise to a nearly dark optical response. These results suggest

that quantitation through image analysis of the optical texture of LCs is not an ideal strategy toward the development of quantitative methods for LC-based biosensors. It is therefore necessary to investigate new analytical methods that correlate the amount of biomolecules to properties of LCs other than, or in addition to, optical textures.

5.2.3 Quantitative methods based on transmission spectrometry

The unique Bragg reflection of CLC and BPLC and the dichroic feature of the dye component in DLC and DDLC enable the interaction of these LCs with biomolecules at the LC–glass interface to be analyzed and quantitated by transmission spectrometry (Chiang et al., 2018; Hsiao et al., 2015; Lee et al., 2017; Wu et al., 2018). A typical experimental setup for transmission spectrometric analysis of LCs is shown in Figure 5.2.

5.2.3.1 CLC- and BPLC-based quantitative biosensors

In a label-free and color-indicating biosensor based on CLC, the helical pitch of CLC was sensitive to the amount of BSA immobilized on, in this case, both glass substrates of the LC cell (Figure 5.3), leading to a transition in the reflected color of CLC from orange to purple with increasing BSA concentration (Hsiao et al., 2015). In the absence of or at low concentrations of BSA, the anchoring effect of DMOAP dominated and the CLC molecules were directed to transform in to the focal conic (FC) state at the LC–glass interface, while the rest of the CLC molecules in the LC bulk were in the unobstructed planar (P) state (Figure 5.3). As the amount of BSA increased, thus diminishing the anchoring force of DMOAP, the ratio of CLC molecules in the P state increased and Bragg reflection was in effect. The sophisticated interchange between the FC and P states of the helical CLC in the presence of various amount of biomolecules contributes to the color-indicating feature of the CLC-based biosensor (Figure 5.4(a)). In the transmission spectra of CLC (Figure 5.4(b)), it was observed that the minimum transmittance increased while reflection bandwidth at half maximum of Bragg reflection decreased with increasing BSA concentration (Figure 5.4(c) and (d)). These measurable quantities of spectral parameters determined by transmission spectrometry and their correlation to the amount of biomolecules allow calibration curves to be constructed for protein quantitation.

Similar to CLC, the Bragg reflection of BPLC, a frustrated chiral phase that appears during the LC–isotropic phase transition within a defined temperature range, can also be exploited in the detection and quantitation of biomolecules (Lee et al., 2017). Although BPLC is thermally unstable and requires delicate control of temperature, it is considered a promising material in the design of next-generation fast-response LCD devices (Rahman et al., 2015). The BPLC demonstrated here was prepared
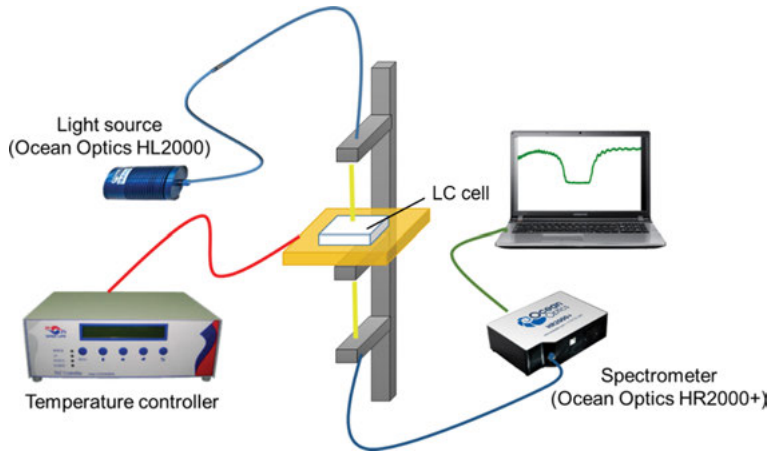
Figure 5.2: Experimental setup of transmission spectrometric measurement for LCs. The temperature controller is included to precisely regulate the temperature of the LC cell so that the transmission spectra of specific phases of LCs that do not exist at room temperature, such as the blue phase, can be recorded.

Major reflection   Major transmission
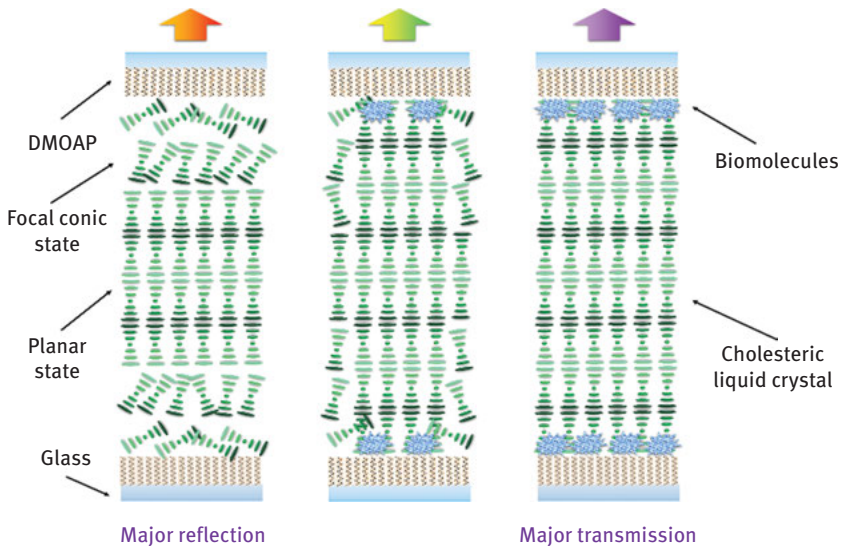
Figure 5.3: CLC-based biosensing platform. In the absence of BSA, the CLC molecules were directed by DMOAP to align homeotropically at the LC–glass interface in the focal conic (FC) state. With the increase in BSA concentration, the orientation of CLC at the LC–glass interface shifted from the FC state to the planar (P) state, resulting in the transition from major reflection to major transmission and thus the change in the reflecting color of CLC (figure adopted from Hsiao et al., 2015).
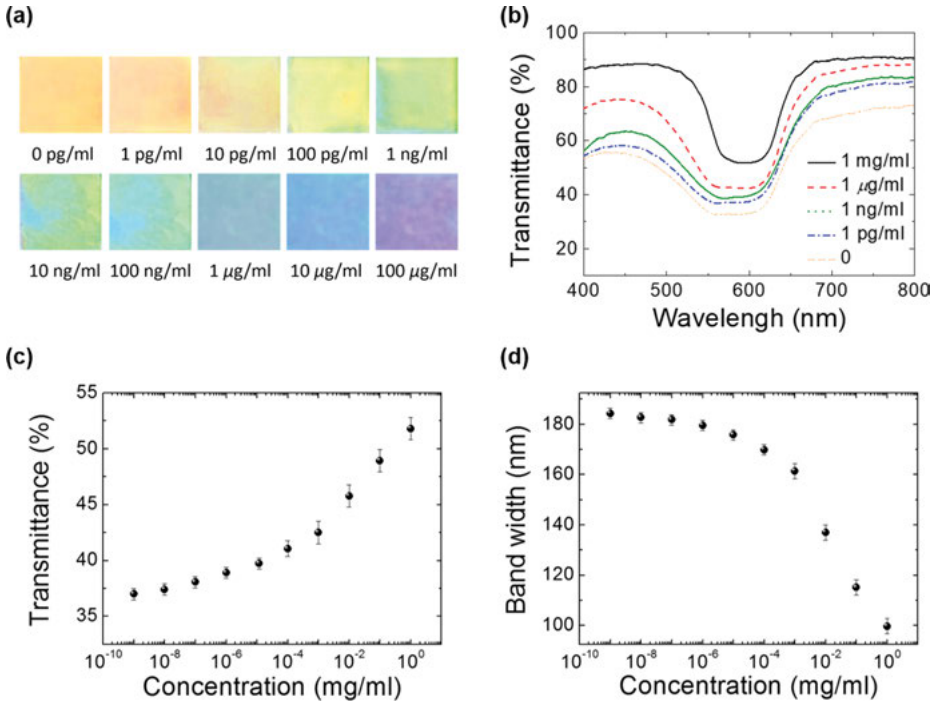
Figure 5.4: Protein quantitation derived from the transmission spectrometric analysis of CLC. (a) The reflected color of CLC in the presence of various concentrations of BSA. (b) Transmission spectra of CLC in the presence of various concentrations of BSA. To facilitate protein quantitation, both the minimum transmittance (c) and the reflection bandwidth at half maximum of Bragg reflection (d) were correlated with BSA concentration (adapted from Hsiao et al., 2015; Lee et al., 2016c).
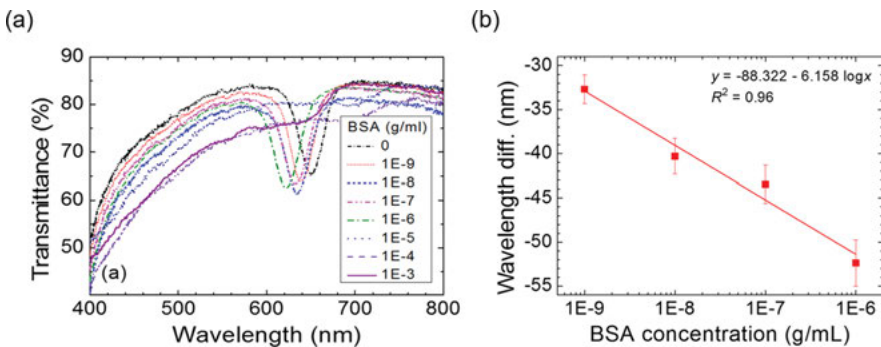
Figure 5.5: Protein quantitation derived from transmission spectrometric analysis of BPLC. (a) Transmission spectra of BPLC in the presence of various concentrations of BSA at 37 °C, which is within the temperature range of BP existence. (b) The correlation between BSA concentration and wavelength difference, calculated by subtracting the peak reflection wavelength from the initial wavelength at which BP first appeared during the cooling process for BP formation (adopted from Lee et al., 2017).

with the nematic host E7 and the chiral dopant S811, which was heated to isotropic phase at 40 °C and then cooled at a constant rate of 0.1 °C/min to reach the blue phase (BP) within the temperature range of 32–38 °C. This chiral nematic LC mixture is selected for biosensing studies because the BP temperature resembles the physiological conditions of most mammalian cells so that the structure and activity of biomolecules are least affected during the heating and cooling process of BP formation. Besides, the BPLC mixture is relatively more thermally stable than traditional BPLCs with a typically narrower temperature range (0.5–1 °C) of BP existence. When analyzed by transmission spectrometry, the disruption in the homeotropic alignment of BPLC by the immobilized BSA at the LC–glass interface led to the disordering of the BPLC lattice and a decrease, or blueshift, in the reflection wavelength (Figure 5.5(a)). By taking advantage of the blueshift of BPLC, it was found that the calculated wavelength difference between the peak reflection wavelength and the initial wavelength where BP first appeared during the cooling process was correlated with BSA concentration within 10^{-9}–10^{-6} g/mL BSA (Figure 5.5(b)). Further cooling of the E7/S811 mixture to 20 °C gave rise to the smectic A phase, in which the transmittance or the transmittance integral calculated from the transmission spectra can also be used in protein quantitation, but for a higher concentration range of 10^{-6}–10^{-3} g/mL BSA (Lee et al., 2017). These results suggest that by manipulating the phase transition of LCs, one can select a suitable LC phase tailored to a specific concentration range of the protein analyte. This may be particularly useful when protein samples of a wide concentration range are being quantitated by the same LC-sensing medium.

5.2.3.2 DLC- and DDLC-based quantitative biosensors

The specific absorption of the dichroic dye component in DLC and DDLC contributes to an intrinsic transmissive color and presents a different biosensing principle from CLC and BPLC. In DLC, the LC mixture includes an azobenzene LC chemically modified with two azo groups that serve as the chromophore, while in DDLC, the LC host is blended with a specific weight percentage of a dichroic dye. When BSA alters the homeotropic alignment of DLC and DDLC, the orientation of (the absorption axis of) the dichroic dye changes with the director of the LC host via the guest–host effect, resulting in an increase in the absorbance of both LCs and the intensity of their reflecting color with increasing BSA concentration (Figure 5.6). Such colorimetric variation in the reflecting color of the LC cell in the presence of various concentrations of BSA can be directly observed with the naked eye and be quantitated through transmission spectrometry.

In the transmission spectra from a DLC-based biosensor, minimum absorption and maximum transmittance at a wavelength of 470 nm were observed in the absence of BSA in that the long axis of DLC molecules was aligned by the anchoring force of DMOAP perpendicularly to the polarization direction of the incident unpolarized white light (Wu et al., 2018). When BSA was immobilized on the LC–glass

interface, optical transmittance decreased and absorption increased with increasing BSA concentration because the component of the LC director parallel to the polarization direction of light was enhanced due to increasing amount of tilted DLC molecules (Figure 5.7(a)). Based on the decreasing trend in the correlation between transmittance and BSA concentration, the standard parameter $S\%$, which represents the difference in transmittance at 470 nm in the presence of BSA (T_{BSA}) relative to that in its absence (T_0) as defined in eq. (5.1), was derived to construct the BSA calibration curve (Figure 5.7(b)). A range of linearity for BSA quantitation was observed between 1 and 7.5 µg/mL BSA for the DLC cell with a cell gap d of 5 µm:

$$S\% = \left(\frac{T_0 - T_{\mathrm{BSA}}}{T_0} \right) \times 100\% \qquad (5.1)$$

Although the dichroic dye in DDLC is not covalently conjugated to the LC host as in DLC, its orientation is consistent with that of LCs since the long axis of the dye and LC molecules tends to align parallel to each other. The orientation and absorption behavior of the dye are therefore representative of that of the LC-sensing medium in contact with biomolecules. The DDLC-based biosensor demonstrated here utilizes the commercial display-grade black dye S428, which has the highest dichroic ratio and order parameter and is characterized by a wide absorption band within the visible spectrum (Chiang et al., 2018). Polarized incident light, instead of unpolarized white light used in DLC-based biosensing described above, was employed and the glass substrates of DDLC cells were rubbed unidirectionally with a rayon-cloth rubbing machine to reduce the background noise as well as to serve as a guide to the polarization direction of the incident light. By comparing the transmission spectra of DDLC obtained with the polarization direction of light either parallel or perpendicular to the rubbing direction, it was observed that the decrease in transmittance with increasing BSA concentration was significantly more pronounced when the polarization direction of light and the rubbing direction were parallel to each other (Figure 5.8(a) and (b)). Due to the different absorption behavior of the dye component in DDLC, a major absorption peak was not observed in the transmission spectra of DDLC as that of DLC. Transmittance at 589 nm was therefore arbitrarily chosen for further quantitative purpose. As shown in Figure 5.8(c), the larger slope of the transmittance-versus-BSA concentration plot at 589 nm indicates higher detection sensitivity when the polarization direction of light was parallel to the rubbing direction. Utilizing the relative difference in transmittance in the parallel and perpendicular settings, reduced transmittance, T_{reduced}, as defined in eq. (5.2) where $T_\perp$ and T_p represent the transmittance at 589 nm with the polarization direction of light perpendicular and parallel to the rubbing direction, respectively, was found to be correlated positively to BSA concentration (Figure 5.8(d)):

$$T_{\mathrm{reduced}} = \frac{T_\perp - T_p}{T_\perp} \qquad (5.2)$$
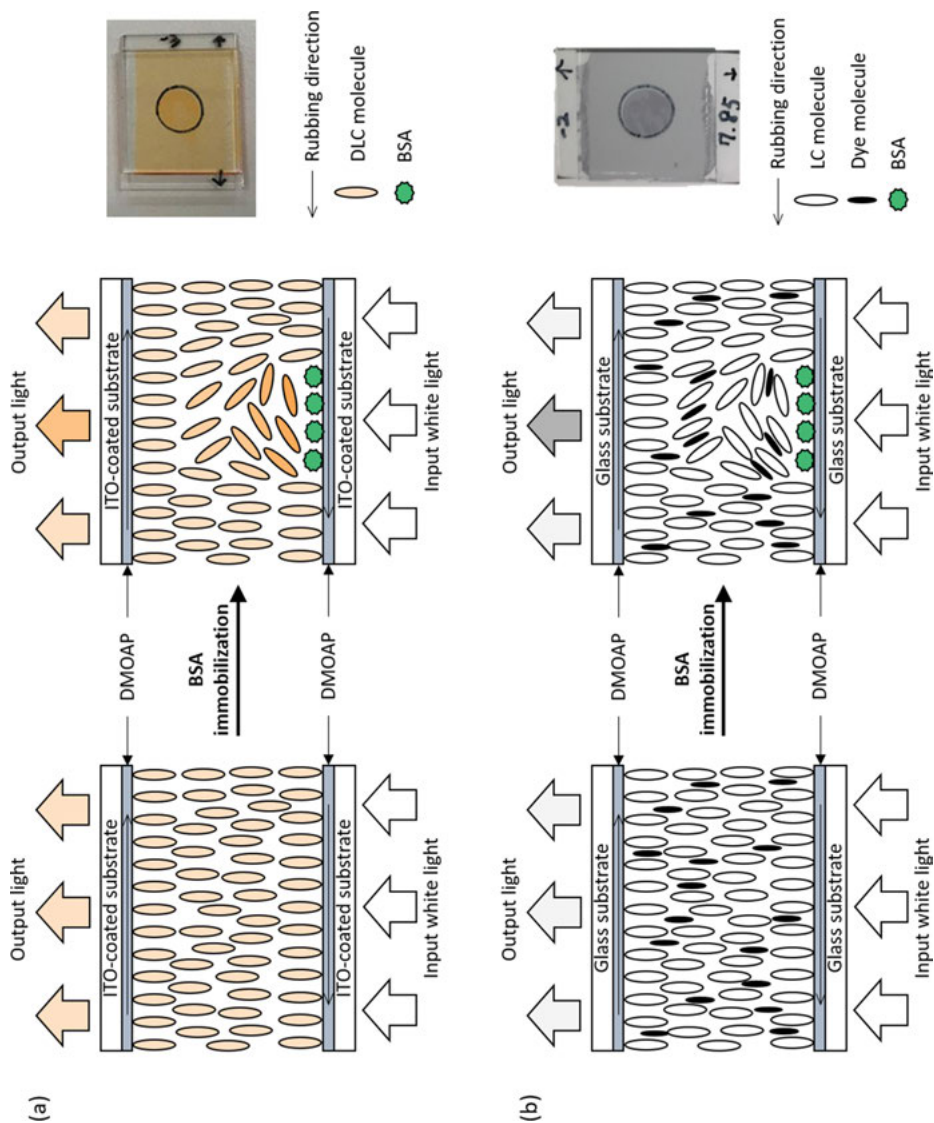
Figure 5.6: DLC- and DDLC-based biosensing platforms. In the absence of BSA, both DLC (a) and DDLC (b) molecules were directed by DMOAP to align homeotropically at the LC–glass interface. With the increase in BSA concentration, the absorbance and the intensity of the reflecting color of the LC cell were enhanced as a result of the increase in the tilted DLC and DDLC molecules disrupted by BSA. Representative photographs of an LC cell of DLC and DDLC with BSA immobilized in the circled area of a diameter of 7 mm were shown in (a) and (b), respectively (Chiang et al., 2018; Wu et al., 2018) (figure adopted from Lee et al., 2018).

(a)

(b)
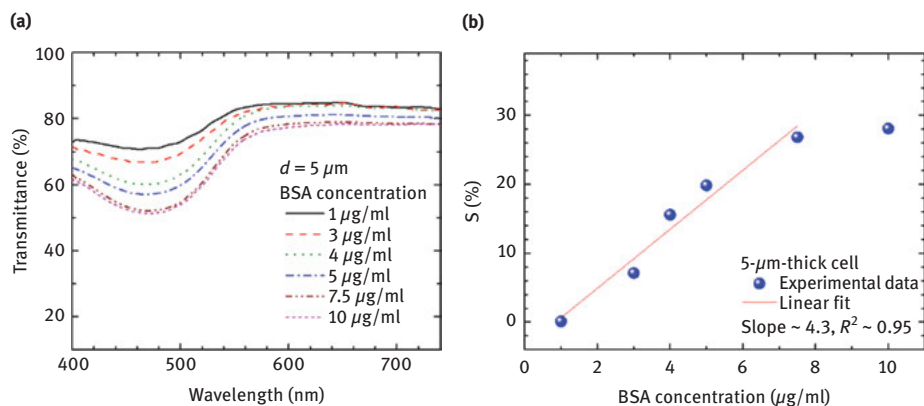
Figure 5.7: Protein quantitation derived from transmission spectrometric analysis of DLC. (a) Transmission spectra of DLC in the presence of various concentrations of BSA. (b) The correlation between the standard parameter S% and BSA concentration was linear within the concentration range of 1–7.5 µg/mL BSA (Wu et al., 2018) (figure adopted from Lee et al., 2018).

5.2.4 Quantitative methods based on the electrical, electro-optical, and dielectric properties of LCs

Most LC-based biosensing techniques utilize the unique optical anisotropy of the birefringent mesogenic material. Although LCs are endowed with many excellent electrical, electro-optical, and dielectric properties, application of their electrical and dielectric characteristics in the development of biosensors was seldom investigated. In this section, we discuss how capacitance and electro-optical measurements as well as dielectric spectroscopy of sandwiched LCs may facilitate protein quantitation.

It is a common practice in biochemical studies to subject proteins or DNA to an electric field in various gel electrophoresis experiments to determine their molecular weight, to separate various proteins and DNA in a mixture, or to study molecular interactions. Unless under the influence of a voltage in the kilovolt-per-meter (kV/m) magnitude or higher, the configuration of most proteins remains unaffected in an externally applied electric field (Bekard and Dunstan, 2014; Freedman et al., 2013; Okumura et al., 2017). For example, in native polyacrylamide gel electrophoresis, the three-dimensional structure of proteins is maintained in an electric field of 100–150 V or 10–20 V/cm depending on the size of the gel and the electrophoretic apparatus, so that the structure of protein complexes or protein–protein interaction can be studied. In the following capacitance, electro-optical, and dielectric measurements of LCs, an electric voltage of not greater than 20 V, which is an order of magnitude lower than conventional protein electrophoresis protocols, was exerted. It is therefore assumed that the native structure and activities of proteins, which are much larger in size than LCs, are maintained in such experimental conditions.

5.2.4.1 Protein quantitation based on capacitance measurement

Figure 5.9 depicts an LC cell in the parallel-plate capacitor structure (Lin et al., 2016). Each glass substrate was coated with a transparent thin film of indium–tin oxide (ITO) to conduct electricity. In the absence of biomolecules, the anchoring strength of the alignment reagent DMOAP directed the long axis of LC molecules to orient homeotropically to the glass substrate. Because the dielectric anisotropy of LCs is positive, and the component of the dielectric permittivity parallel to the applied field direction, $\varepsilon_{\parallel}$, predominates due to the homeotropic alignment, the electric capacitance is at its maximal value, C_{max}, and is independent of the applied voltage. When biomolecules such as BSA was immobilized on the glass substrates and thus
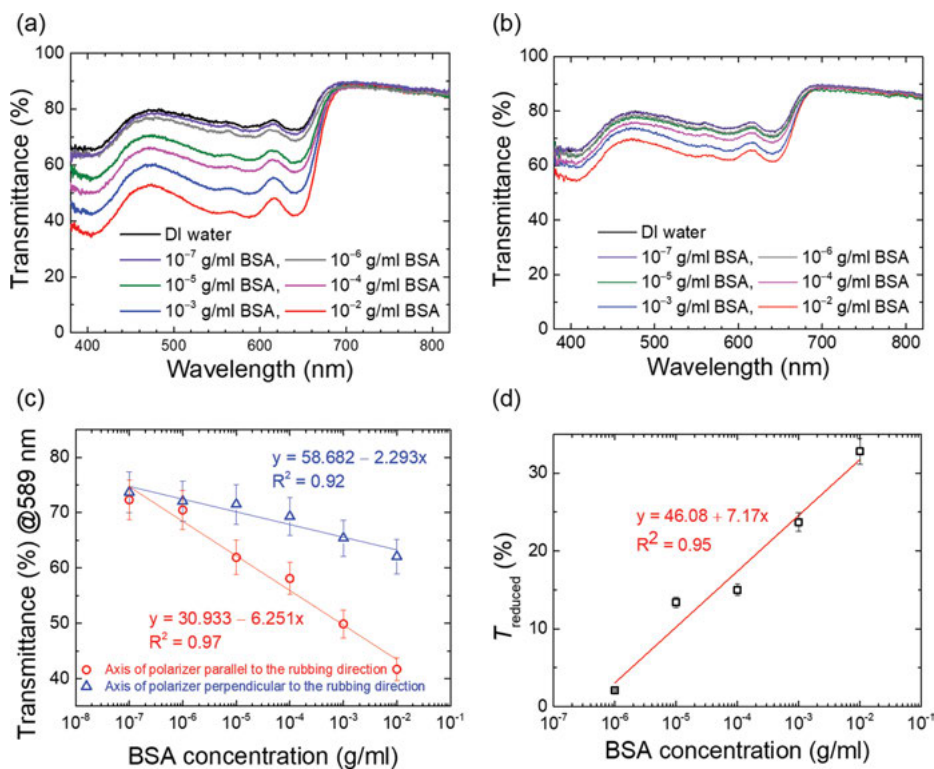
Figure 5.8: Protein quantitation derived from transmission spectrometric analysis of DDLC with polarized incident light. The transmission spectra were determined with the polarization direction of light either (a) parallel or (b) perpendicular to the rubbing direction of the glass substrate coated with DMOAP and immobilized with BSA. (c) The transmittance at 589 nm in (a) and (b) was plotted against BSA concentration to assess detection sensitivity. (d) The reduced transmittance ($T_{reduced}$) calculated with eq. (5.2) was plotted against BSA concentration to serve as the calibration curve for protein quantitation (Chiang et al., 2018) (figure adopted from Lee et al., 2018).
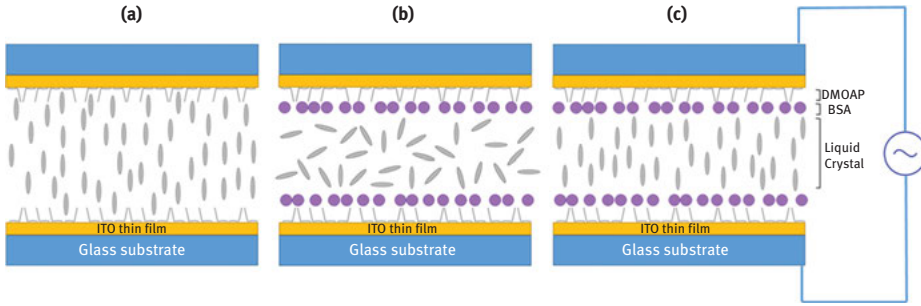
Figure 5.9: HDN-based biosensing platform for capacitance measurement. (a) In the absence of BSA, LCs are aligned homeotropically to the glass substrate due to the anchoring force of the alignment layer DMOAP. The uniform orientation of LCs was disrupted by the immobilized BSA (b) but can be restored by subjecting the LC cell to an external AC field (c). The voltage required to reorient LCs to homeotropic alignment increases with increasing concentration of BSA (Lee et al., 2015; Lin et al., 2016) (figure adopted from Lee et al., 2015).
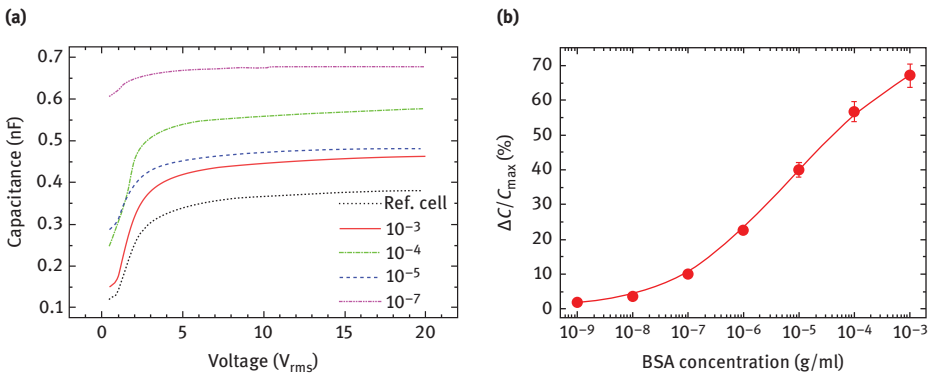
Figure 5.10: Protein quantitation derived from capacitance measurement of HDN. (a) Electric capacitance of HDN as a function of externally applied voltage at various concentrations of BSA. The capacitance versus voltage curve of a reference cell coated with the planar alignment reagent SE-150 instead of DMOAP in the absence of BSA was included to simulate the situation when the anchoring strength of DMOAP was completely blocked by a high concentration of BSA. (b) The positive correlation between the capacitance-derived parameter $\Delta C/C_{max}$ and BSA concentration (figure adopted from Lin et al., 2016).

weakened the anchoring effect of DMOAP, the uniform pattern of LC alignment was disrupted, resulting in a decrease in electric capacitance. Nevertheless, by increasing the voltage of the electric field, the disrupted LC molecules can be electrically induced and reoriented to the homeotropic state. Based on the notion that the level of disturbance in the alignment of LCs grows with increasing amount of BSA at the LC–glass interface, the voltage required to restore the homeotropic alignment increases with

increasing BSA concentration. As shown in Figure 5.10(a), when LC cells coated with various BSA concentrations were subjected to an increasing AC voltage of 0–20 V_{rms}, the electric capacitance of HDN increased until reaching a plateau at C_{max}. The difference between C_{max} and the initial capacitance C_0 at 0.5 V_{rms} in the capacitance versus voltage curve was normalized to C_{max} to eliminate the error caused by cell gap variation. The resulting parameter, $\Delta C/C_{max}$, exhibits a positive correlation to BSA concentration and can be used in protein quantitation (Figure 5.10(b)).

5.2.4.2 Protein quantitation based on electro-optical measurements

Electro-optical or voltage-dependent transmittance measurements were also carried out under an increasing AC voltage externally applied to the LC cell (Figure 5.9), which was installed between two crossed polarizers with a He–Ne laser as the probe to study transmitted light intensity at various BSA concentrations (Lee et al., 2015). Similar to capacitance measurement, the increasing voltage was utilized to reverse the orientation of LCs from a disrupted state caused by the immobilized BSA to homeotropic alignment. By utilizing HDN as the sensing element and subjecting LC cells with BSA spin-coated on both glass substrates modified with DMOAP to electro-optical measurement, plots of optical transmittance versus voltage at each BSA concentration were obtained (Figure 5.11(a)), from which phase retardation δ can be determined for the calculation of the normalized effective birefringence N,

$$N = \frac{\Delta n_{eff}}{\Delta n_{LC}} = \frac{\delta \lambda}{2\pi d \Delta n_{LC}} \tag{5.3}$$

where λ and d represent the wavelength of the incident probe beam and cell gap, respectively, while Δn_{eff} and Δn_{LC} are the effective optical anisotropy and birefringence of HDN, respectively. Similar to the capacitance-derived $\Delta C/C_{max}$, Δn_{eff} was normalized to Δn_{LC} (which is 0.333 at 589.3 nm and 20 °C) to eliminate cell gap variation. The positive correlation between N and BSA concentration therefore facilitates the construction of BSA calibration curve (Figure 5.11(b)).

The feasibility of protein quantitation through electro-optical measurement is also demonstrated in the DLC-based biosensor (Wu et al., 2018). Instead of spin-coating BSA on both glass substrates of the HDN LC cell to form a uniform protein film so that phase retardation can be determined, aqueous solution of BSA was dispensed on and reacted with one of the glass substrates of the LC cell in the DLC-based biosensing platform without spin coating. The latter method, in which the thickness of the BSA coating has negligible effect on the cell gap of the LC cell, allows the results of protein detection to be compared more conveniently with conventional bioassays. The simplified sample preparation procedure takes advantage of the specific absorption of the dichroic DLC, resulting in a different pattern of the transmittance versus voltage curve in which the standard parameter rather than phase retardation was derived for quantitative
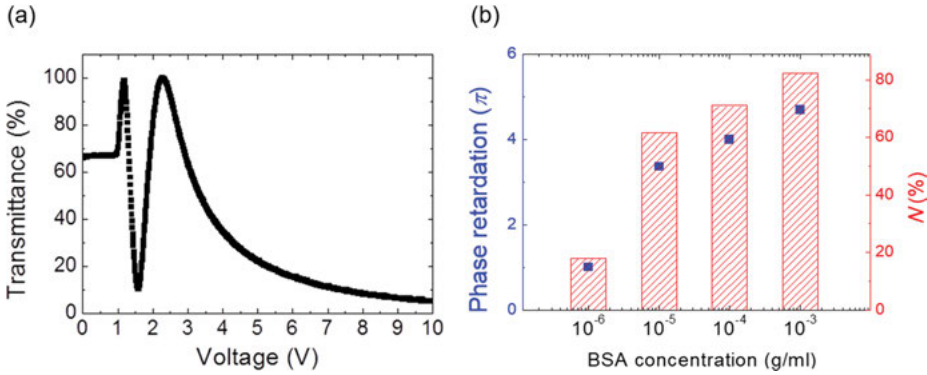
Figure 5.11: Protein quantitation derived from electro-optical measurement of HDN. (a) A representative transmittance versus voltage curve of an LC cell of HDN with 10 μg/mL BSA spin-coated on DMOAP-modified ITO glass substrates and a cell gap d of 5.4 ± 0.1 μm. (b) Correlation of phase retardation δ and normalized effective birefringence N of HDN to BSA concentration. Both parameters were derived from the electro-optical measurement (figure adapted from Lee et al., 2015).
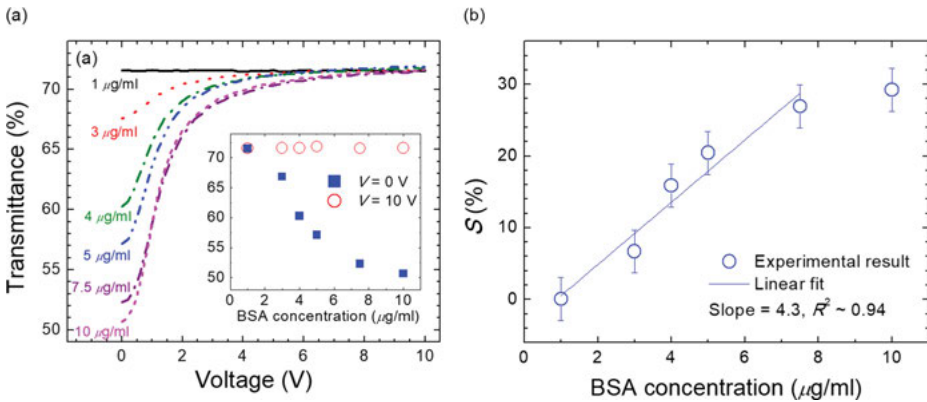
Figure 5.12: Protein quantitation derived from electro-optical measurement of DLC. (a) Voltage-dependent transmittance at 470 nm in the presence of various concentrations of BSA. (b) The linear correlation between the standard parameter S% and BSA concentration. Here S% was calculated by replacing T_0 in eq. (5.1) with the maximum transmittance at $V = 10\ V_{rms}$ (figure adopted from Wu et al., 2018).

purpose (Figure 5.12(a)). The voltage-dependent transmittance of DLC at 470 nm at various BSA concentrations increased with increasing voltage until reaching a plateau at 10 V_{rms}, suggesting that the DLC molecules were gradually reoriented to homeotropic alignment where minimal absorption and maximal transmission of light were observed. Here the standard parameter S% was defined as the relative difference in transmittance at 470 nm at 0 and 10 V in the presence of BSA,

which was found to linearly correlate with BSA concentration within the range of 1–7.5 μg/mL (Figure 5.12(b)).

5.2.4.3 Protein quantitation based on dielectric spectroscopic measurements

By exploiting the unique frequency-dependent dielectric properties of dual-frequency LC (DFLC), which exhibits positive dielectric anisotropy at low frequencies and negative dielectric anisotropy at high frequencies within a reasonable and observable range of frequency in an externally applied electric field, the dielectric spectra obtained in the presence of various concentrations of immobilized BSA may facilitate protein quantitation (Lin et al., 2019). As shown in the real part of the dielectric spectra of DFLC, which was recorded from 100 Hz to 200 kHz in an externally applied electric field of 0.1 V at 10 °C, the dielectric permittivity ε' of DFLC was nearly constant in the low-frequency regime, but decreased with increasing frequency around a crossover frequency f_c of 4.2 kHz, where the dielectric anisotropy ($\Delta\varepsilon$) was zero, until reaching the high-frequency regime (Figure 5.13(a)). When ε' at 200 Hz and 100 kHz was arbitrarily designated as the low-frequency ε', $\varepsilon'(f_L)$, and the high-frequency ε', $\varepsilon'(f_H)$, respectively, it was observed that the relative difference in ε', $\varepsilon'(f_L) - \varepsilon'(f_H)$, decreased with increasing BSA concentration (Figure 5.13(b)). By defining the dielectric parameter ψ,
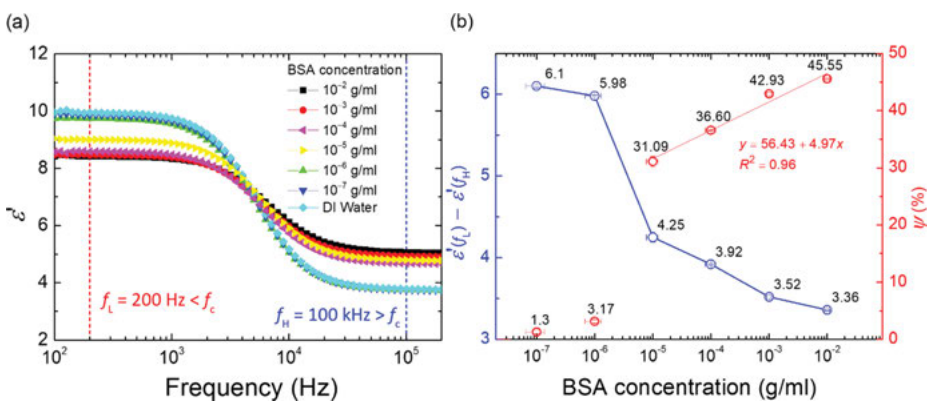
Figure 5.13: Protein quantitation derived from dielectric spectroscopy of DFLC. (a) Dielectric spectra of DFLC when various concentrations of BSA were immobilized on one of the DMOAP-coated glass substrates of the LC cell. The average cell gap d of the LC cells with immobilized BSA was 9.34 ± 0.52 μm. (b) Correlation of BSA concentration to the relative difference in electric permittivity $\varepsilon'(f_L) - \varepsilon'(f_H)$ and the relative electric permittivity parameter ψ, for which linear regression was performed in the BSA concentration range of 10^{-5}–10^{-2} g/mL. The vertical error bars represent the standard deviation of $\varepsilon'(f_L) - \varepsilon'(f_H)$ or ψ, while the horizontal error bars stand for the estimated uncertainty of systematic errors including personal and instrumental errors occurred during the preparation of BSA solutions (adapted from Lin et al., 2019).

$$\psi = \frac{\delta\varepsilon_{\max} - \delta\varepsilon}{\delta\varepsilon_{\max}} \qquad (5.4)$$

where $\delta\varepsilon$ is equivalent to $\varepsilon'(f_L) - \varepsilon'(f_H)$ in the dielectric spectrum of each BSA concentration and $\delta\varepsilon_{\max}$ represents maximum $\delta\varepsilon$ at 0 g/mL BSA, experimental errors associated with cell gap variation can be eliminated, and a positive correlation between ψ and BSA concentration can be derived for the construction of calibration curves (Figure 5.13(b)).

5.3 Conclusions

In this chapter, we emphasize the importance of increasing the variety of biosensing mesogens and LC mesophases as well as exploring the various electrical and optical properties of LCs to optimize and improve the current LC-based biosensing technology. Numerous reports offer strong evidence for the promising sensing capabilities of LCs as an innovative material for biomedical application. However, LC-based biosensors are still at its early stage of development due to the unsatisfying detection sensitivity, the insufficient capability to cope with clinical samples, and the lack of quantitative measurement. The excellent and diverse electrical and optical properties exhibited by various LCs render many new incentives for the improvement of present prototypes or the design of next-generation biosensing platforms. Selecting the optimal-sensing LC may give rise to improved detection limit, or endow the sensing medium with properties such as lower cytotoxicity to accommodate the detection of whole cell entities. In addition, exploiting spectral and electro-optical measurements in quantitative analysis may further assist in the construction of signal and data processing components of the LC-based biosensor. The experimental setting of an LC cell for biodetection at the LC–glass interface is especially advantageous for transmission spectrometry and for the application of an electric field in capacitance, electro-optical, and dielectric measurements. The proposed quantitative approaches may help transform the working theories of existing techniques that rely predominantly on texture observation and provide a new direction for LC-based biosensor design.

References

Bekard, I., Dunstan, D.E. (2014). Electric field induced changes in protein conformation. Soft Matter, 10, 431–37.

Bi, X., Lai, S.L., Yang, K.L. (2009). Liquid crystal multiplexed protease assays reporting enzymatic activities as optical bar charts. Analytical Chemistry, 81, 5503–09.

Brake, J.M., Daschner, M.K., Luk, Y.Y., Abbott, N.L. (2003). Biomolecular interactions at phospholipid-decorated surfaces of liquid crystals. Science, 302, 2094–97.

Carlton, R.J., Hunter, J.T., Miller, D.S., Abbasi, R., Mushenheim, P.C., Tan, L.N., Abbott, N.L. (2013). Chemical and biological sensing using liquid crystals. Liquid Crystal Reviews, 1, 29–51.

Chen, C.H., Yang, K.L. (2012). Liquid crystal-based immunoassays for detecting hepatitis B antibody. Analytical Biochemistry, 421, 321–23.

Chen, C.-H., Yang, K.-L. (2011). Improving protein transfer efficiency and selectivity in affinity contact printing by using UV-modified surfaces. Langmuir, 27, 5427–32.

Chiang, Y.-L., Lee, M.-J., Lee, W. (2018). Enhancing detection sensitivity in quantitative protein detection based on dye-doped liquid crystals. Dyes Pigments, 157, 117–22.

Chuang, C.H., Lin, Y.C., Chen, W.L., Chen, Y.H., Chen, Y.X., Chen, C.M., Shiu, H.W., Chang, L.Y., Chen, C.H., Chen, C.H. (2016). Detecting trypsin at liquid crystal/aqueous interface by using surface-immobilized bovine serum albumin. Biosensors & Bioelectronics, 78, 213–20.

Clare, B.H., Abbott, N.L. (2005). Orientations of nematic liquid crystals on surfaces presenting controlled densities of peptides: amplification of protein-peptide binding events. Langmuir, 21, 6451–61.

Freedman, K.J., Haq, S.R., Edel, J.B., Jemth, P., Kim, M.J. (2013). Single molecule unfolding and stretching of protein domains inside a solid-state nanopore by electric field. Scientific Reports, 3, 1638.

Govindaraju, T., Bertics, P.J., Raines, R.T., Abbott, N.L. (2007). Using measurements of anchoring energies of liquid crystals on surfaces to quantify proteins captured by immobilized ligands. Journal of the American Chemical Society, 129, 11223–31.

Hartono, D., Xue, C.-Y., Yang, K.-L., Yung, L.-Y.L. (2009). Decorating liquid crystal surfaces with proteins for real-time detection of specific protein–protein binding. Advanced Functional Materials, 19, 3574–79.

Helfinstine, S.L., Lavrentovich, O.D., Woolverton, C.J. (2006). Lyotropic liquid crystal as a real-time detector of microbial immune complexes. Letters in Applied Microbiology, 43, 27–32.

Hoogboom, J., Velonia, K., Rasing, T., Rowan, A.E., Nolte, R.J. (2006). LCD-based detection of enzymatic action. Chemical Communication, 434–35.

Hsiao, Y.-C., Sung, Y.-C., Lee, M.-J., Lee, W. (2015). Highly sensitive color-indicating and quantitative biosensor based on cholesteric liquid crystal. Biomedical Optics Express, 6, 5033–38.

Hussain, Z., Zafiu, C., Kupcu, S., Pivetta, L., Hollfelder, N., Masutani, A., Kilickiran, P., Sinner, E.K. (2014). Liquid crystal based sensors monitoring lipase activity: a new rapid and sensitive method for cytotoxicity assays. Biosensors & Bioelectronics, 56, 210–16.

Jang, C.H., Cheng, L.L., Olsen, C.W., Abbott, N.L. (2006). Anchoring of nematic liquid crystals on viruses with different envelope structures. Nano Letters, 6, 1053–58.

Khan, M., Khan, A.R., Shin, J.H., Park, S.Y. (2016). A liquid-crystal-based DNA biosensor for pathogen detection. Scientific Reports, 6, 22676.

Khan, M., Park, S.Y. (2014). Liquid crystal-based proton sensitive glucose biosensor. Analytical Chemistry, 86, 1493–501.

Khan, M., Park, S.Y. (2015a). Glucose biosensor based on GOx/HRP bienzyme at liquid-crystal/aqueous interface. Journal of Colloid and Interface Science, 457, 281–88.

Khan, M., Park, S.Y. (2015b). Liquid crystal-based glucose biosensor functionalized with mixed PAA and QP4VP brushes. Biosensors & Bioelectronics, 68, 404–12.

Khan, M., Park, S.Y. (2017). Liquid crystal-based biosensor with backscattering interferometry: a quantitative approach. Biosensors & Bioelectronics, 87, 976–83.

Kim, J.-Y., Khan, M., Park, S. (2013). Glucose sensor using liquid-crystal droplets made by microfluidics. ACS Applied Materials & Interfaces, 5, 13135–39.

Kim, S.R., Shah, R.R., Abbott, N.L. (2000). Orientations of liquid crystals on mechanically rubbed films of bovine serum albumin: a possible substrate for biomolecular assays based on liquid crystals. Analytical Chemistry, 72, 4646–53.

Lee, H.-G., Munir, S., Park, S.-Y. (2016a). Cholesteric liquid crystal droplets for biosensors. ACS Applied Materials & Interfaces, 8, 26407–17.

Lee, K., Gupta, K.C., Park, S.-Y., Kang, I.-K. (2016b). Anti-IgG-anchored liquid crystal microdroplets for label free detection of IgG. Journal of Materials Chemistry B, 4, 704–15.

Lee, M.-J., Chang, C.-H., Lee, W. (2017). Label-free protein sensing by employing blue phase liquid crystal. Biomedical Optics Express, 8, 1712–20.

Lee, M.-J., Chiang, Y.-L., Karn, A., Wu, P.-C., Lee, W. (2018). Dye- and dye-doped liquid crystals in biosensing. Liquid Crystals XXII, Proc. SPIE 10735, 1073509.

Lee, M.-J., Lin, C.-H., Lee, W. (2015). Liquid-crystal-based biosensing beyond texture observations. Liquid Crystals XIX, Proc. SPIE 9565, 956510.

Lee, M.-J., Sung, Y.-C., Hsiao, Y.-C., Lee, W. (2016c). Chiral liquid crystals as biosensing platforms. Liquid Crystals XX, Proc. SPIE 9940, 99400K.

Lin, C.-H., Lee, M.-J., Lee, W. (2016). Bovine serum albumin detection and quantitation based on capacitance measurements of liquid crystals. Applied Physics Letters, 109, 093703.

Lin, C.-M., Wu, P.-C., Lee, M.-J., Lee, W. (2019). Label-free protein quantitation by dielectric spectroscopy of dual-frequency liquid crystal. Sensors and Actuators B, Chemical, 282, 158–63.

Lockwood, N.A., Mohr, J.C., Ji, L., Murphy, C.J., Palecek, S.P., dePablo, J.J., Abbott, N.L. (2006). Thermotropic liquid crystals as substrates for imaging the reorganization of matrigel by human embryonic stem cells. Advanced Functional Materials, 16, 618–24.

Luk, -Y.-Y., Campbell, S.F., Abbott, N.L., Murphy, C.J. (2004a). Non-toxic thermotropic liquid crystals for use with mammalian cells. Liquid Crystals, 31, 611–21.

Luk, Y.Y., Jang, C.H., Cheng, L.L., Israel, B.A., Abbott, N.L. (2005). Influence of lyotropic liquid crystals on the ability of antibodies to bind to surface-immobilized antigens. Chemistry of Materials: A Publication of the American Chemical Society, 17, 4774–82.

Luk, Y.Y., Tingey, M.L., Dickson, K.A., Raines, R.T., Abbott, N.L. (2004b). Imaging the binding ability of proteins immobilized on surfaces with different orientations by using liquid crystals. Journal of the American Chemical Society, 126, 9024–32.

Luk, -Y.-Y., Tingey, M.L., Hall, D.J., Israel, B.A., Murphy, C.J., Bertics, P.J., Abbott, N.L. (2003). Using liquid crystals to amplify protein–receptor interactions: design of surfaces with nanometer-scale topography that present histidine-tagged protein receptors. Langmuir, 19, 1671–80.

McCamley, M.K., Artenstein, A.W., Opal, S.M., Crawford, G.P. (2007). Optical detection of sepsis markers using liquid crystal based biosensors. Proceedings of SPIE, 6441, 64411Y.

Munir, S., Park, S.-Y. (2016). Liquid crystal-based DNA biosensor for myricetin detection. Sensors and Actuators B, Chemical, 233, 559–65.

Nguyen, T.T., Han, G.R., Jang, C.H., Ju, H. (2015). Optical birefringence of liquid crystals for label-free optical biosensing diagnosis. International Journal of Nanomedicine, 10(Spec Iss), 25–32.

Okumura, T., Yamada, K., Yaegashi, T., Takahashi, K., Syuto, B., Takaki, K. (2017). External AC electric field-induced conformational change in bovine serum albumin. IEEE Transaction on Plasma Science, 45, 489–94.

Ong, L.H., Ding, X., Yang, K.-L. (2014). Mechanistic study for immobilization of cysteine-labeled oligopeptides on UV-activated surfaces. Colloids and Surfaces B, Biointerfaces, 122, 166–74.

Popov, P., Honaker, L.W., Kooijman, E.E., Mann, E.K., Jákli, A.I. (2016). A liquid crystal biosensor for specific detection of antigens. Sensing and Biosensing Research, 8, 31–35.

Popov, P., Mann, E.K., Jákli, A. (2017). Thermotropic liquid crystal films for biosensors and beyond. Journal of Materials Chemistry B, 5, 5061–78.

Price, A.D., Schwartz, D.K. (2008). DNA hybridization-induced reorientation of liquid crystal anchoring at the nematic liquid crystal/aqueous interface. Journal of the American Chemical Society, 130, 8188–94.

Rahman, M.D.A., Suhana Mohd, S., Balamurugan, S. (2015). Blue phase liquid crystal: strategies for phase stabilization and device development. Science and Technology of Advanced Materials, 16, 033501.

Sadati, M., Apik, A.I., Armas-Perez, J.C., Martinez-Gonzalez, J., Hernandez-Ortiz, J.P., Abbott, N.L., de Pablo, J.J. (2015). Liquid crystal enabled early stage detection of beta amyloid formation on lipid monolayers. Advanced Functional Materials, 25, 6050–60.

Shen, J., He, F., Chen, L., Ding, L., Liu, H., Wang, Y., Xiong, X. (2017). Liquid crystal-based detection of DNA hybridization using surface immobilized single-stranded DNA. Microchim Acta, 184, 3137–44.

Su, H.W., Lee, M.J., Lee, W. (2015). Surface modification of alignment layer by ultraviolet irradiation to dramatically improve the detection limit of liquid-crystal-based immunoassay for the cancer biomarker CA125. Journal of Biomedical Optics, 20, 57004.

Su, H.-W., Lee, Y.-H., Lee, M.-J., Hsu, Y.-C., Lee, W. (2014). Label-free immunodetection of the cancer biomarker CA125 using high-Dn liquid crystals. Journal of Biomedical Optics, 19, 077006.

Sun, S.H., Lee, M.J., Lee, Y.H., Lee, W., Song, X., Chen, C.Y. (2015). Immunoassays for the cancer biomarker CA125 based on a large-birefringence nematic liquid-crystal mixture. Biomedical Optics Express, 6, 245–56.

Tan, H., Li, X., Liao, S., Yu, R., Wu, Z. (2014). Highly-sensitive liquid crystal biosensor based on DNA dendrimers-mediated optical reorientation. Biosensors & Bioelectronics, 62, 84–89.

Tan, H., Yang, S., Shen, G., Yu, R., Wu, Z. (2010). Signal-enhanced liquid-crystal DNA biosensors based on enzymatic metal deposition. Angewandte Chemie, 49, 8608–11.

Tingey, M.L., Wilyana, S., Snodgrass, E.J., Abbott, N.L. (2004). Imaging of affinity microcontact printed proteins by using liquid crystals. Langmuir, 20, 6818–26.

Woltman, S.J., Jay, G.D., Crawford, G.P. (2007). Liquid-crystal materials find a new order in biomedical applications. Nature Materials, 6, 929–38.

Wu, P.-C., Karn, A., Lee, M.-J., Lee, W., Chen, C.-Y. (2018). Dye-liquid-crystal-based biosensing for quantitative protein assay. Dyes Pigments, 150, 73–78.

Xue, C.Y., Khan, S.A., Yang, K.L. (2009). Exploring optical properties of liquid crystals for developing label-free and high-throughput microfluidic immunoassays. Advanced Materials (Deerfield Beach, Fla.), 21, 198–202.

Xue, C.Y., Yang, K.L. (2008). Dark-to-bright optical responses of liquid crystals supported on solid surfaces decorated with proteins. Langmuir, 24, 563–67.

Yang, S., Liu, Y., Tan, H., Wu, C., Wu, Z., Shen, G., Yu, R. (2012). Gold nanoparticle based signal enhancement liquid crystal biosensors for DNA hybridization assays. Chemical Communication, 48, 2861–63.

Yang, S., Wu, C., Tan, H., Wu, Y., Liao, S., Wu, Z., Shen, G., Yu, R. (2013). Label-free liquid crystal biosensor based on specific oligonucleotide probes for heavy metal ions. Analytical Chemistry, 85, 14–18.

Zhang, M., Jang, C.H. (2014). Liquid crystal-based detection of thrombin coupled to interactions between a polyelectrolyte and a phospholipid monolayer. Analytical Biochemistry, 455, 13–19.

Zhao, D., Peng, Y., Xu, L., Zhou, W., Wang, Q., Guo, L. (2015). Liquid-crystal biosensor based on nickel-nanosphere-induced homeotropic alignment for the amplified detection of thrombin. ACS Applied Materials & Interfaces, 7, 23418–22.

Chao Ma, Dong Chen, Kai Liu

6 Thermotropic liquids and liquid crystals from DNA and proteins

Abstract: In this chapter, it will be shown that electrostatic complexation of biomacromolecules with surfactants, followed by dehydration, can be a simple generic scheme for the fabrication of highly crowded biomacromolecule thermotropic fluids. Besides the formation of thermotropic liquids, ionic complexation with flexible surfactants also plays an important role for the assembly of anisotropic biomacromolecule architectures, enabling the formation of thermotropic liquid crystals (LCs). These thermotropic LCs exhibit much different mechanical properties than the individual components, that is, surfactant and biomacromolecule. The biomacromolecule LCs are composed of lamellar structures and the characterization of these mesophases will be detailed in this chapter. Furthermore, potential technological applications based on the thermotropic biomacromolecular fluids will be reviewed. In the absence of an electrolyte solution, an electrochromic device based on DNA–surfactant fluids was developed, which exhibited distinctive electrically tunable optical absorption and thermally tunable memory. Thermotropic biological fluids were also used as novel storage and process media and might serve as a scaffold for the delivery of highly concentrated bioactive compounds. Therefore, these new types of liquids represent a class of hybrid biomaterials, which will fuel further studies and applications of biomacromolecules in a much broader context than just the aqueous domain.

6.1 Introduction

Beyond the biological context, biomacromolecular compounds are with mounting interest for amalgamation with technological systems (Kim and Conticello, 2007; Kyle et al., 2009; Gordiichuk et al., 2014; Kwiat et al., 2012; Kwak et al., 2011). However, modularity and processability of the bio-based entities are constrained by approaches developed in aqueous phase due to the insolubility and denaturation of structure in organic media. Thus, for the circumstances that are incompatible with solvent environments such as high-/low-temperature conditions, study on the behavior and function of bio-based thermotropic fluids under solvent-free settings will gain the usefulness of biomolecules beyond the environment dictated by biology. The fabrication of thermotropic liquids containing structurally and functionally intact biomolecules should have a great effect to facilitate the design and assembly of bio-inspired nanostructures. These soft materials might also be developed as

printable and injectable depositories for controlled release of embedded drugs and bioactive compounds, and as barrier dressings for wound healing and artificial skin (Johnston et al., 2012; Ramundo and Gray, 2008). These systems might further enable advanced fabrication of soft bioelectronic entities, where H_2O is detrimental for performance. In brief, the design paradigm of biomacromolecular thermotropic liquid crystals (LCs) and fluids is extremely attractive for both fundamental and applied science.

Thermotropic fluids have been successfully prepared from biomolecules by charge–charge interaction with alkyl surfactants, and subsequently treated with freeze-drying (Leone et al., 2001; Bourlinos et al., 2010a; Liu et al., 2015a; Perriman et al., 2010a). This approach allows fabrication of thermotropic fluids with biological entities ranging from nucleic acids (Leone et al., 2001; Bourlinos et al., 2010a; Liu et al., 2015a) and proteins (Perriman et al., 2010a, 2010b; Liu et al., 2015b) to even whole viruses (Patil et al., 2012; Liu et al., 2014), spanning a size range from only a few nanometers to several microns. Interestingly, biomacromolecular thermotropic LCs were also prepared with fluidity and orientation achieved by electrostatic interaction (Liu et al., 2014; Faul and Antonietti, 2010; Wenzel and Antonietti, 2010; General and Antonietti, 2002). Thus, the flexible assembly of different biological components into anhydrous fluids allows new generation of applications in the field of biocatalysis (Brogan et al., 2014) and bioelectronics (Sharma et al., 2015; Liu et al., 2016).

Here, we review important and latest studies in this emerging topic. The DNA thermotropic fluids working as electronic elements are discussed firstly. A discussion on proteinaceous thermotropic fluids for biocatalysis and electrochemical setup assembly is also reviewed. Virus-derived fluids are introduced in the last section.

6.2 Nucleic acid thermotropic LCs and fluids

To fabricate nucleic acid fluids, an oligonucleotide (<100 bp) and a positively charged surfactant with poly(ethylene glycol) (PEG) chains were complexed with electrostatic interaction, followed by a dehydration treatment (Leone et al., 2001; Bourlinos et al., 2010a). The prepared anhydrous DNA droplets were viscous and optically transparent, and could flow at temperature higher than 60 °C. In addition, an alternative approach toward meltable DNA materials was developed with neutralization of acidized DNA (2,000 bp) by tertiary-PEGylated amines. Thus, a waxy material was obtained and can melt reversibly at around 40 °C (Bourlinos et al., 2010a).

In recent times, it was demonstrated that complexation of DNA and positively charged surfactants is a general protocol to produce a family of DNA liquids, such as smectic LCs and isotropic fluids (Figure 6.1; Liu et al., 2015a, 2014). Thermotropic DNA–surfactant melts were prepared by electrostatic complexation of single-stranded oligonucleotides (6 mer, 14 mer, 22 mer, 50 mer, and 110 mer) with positively charged

lipids with alkyl groups. Dioctyldimethylammonium bromide (DOAB), didecyldimethylammonium bromide (DEAB), and didodecyldimethylammonium bromide (DDAB) were employed to fabricate DNA–lipid LC mesophases and liquid phases. Polarized optical microscopy (POM) results indicated that the DNA LCs show focal-conic patterns, which are characteristic hallmarks of smectic lamellar structures (Figure 6.1(a) and (b)). The ordered smectic layers of hybrids were characterized by small-angle X-ray scattering (SAXS). DNA sublayers and alkyl chain sublayers were repeatedly intercalated (Figure 6.1(a)). Every alternating layer contains a positively charged lipid bilayer that electrostatically interacts with an anionic DNA sublayer. With thermal treatment (heating above the clearing point), the DNA–lipid hybrids underwent a phase transition to amorphous liquid phase (Figure 6.1(c)), and the birefringent behavior vanished correspondingly (Figure 6.1(d)). The X-ray tests also validated the disordered liquid states, presenting no diffraction peaks. RNA LCs and liquids were also prepared with the same approach.

The DNA–lipid liquids could remain persistent over a wide range of temperature until around 200 °C. The phase transition temperatures were tuned over a broad range (Figure 6.2(e); Liu et al., 2015a). Even at –20 °C, DNA liquids can be collected and the temperature window for crystal–LC transitions can be as large as 65 °C. The LC–liquid phase transition can be controlled from 41 to 130 °C. It was also demonstrated that the length of alkyl backbone of surfactants can influence transition temperatures. Specifically, the transition temperatures were lifted when increasing the chain length of lipids.

6.2.1 Electrical studies on nucleic acid thermotropic fluids

DNA thermotropic liquids have demonstrated their usefulness for integration into microelectronic circuits, where DNA can be used for self-assembly and electronic connections (Leone et al., 2001, 2003). When mixed metal surfactants (Co^{2+} and Fe^{2+}) were complexed with DNA for electrochemical investigations, additional oxidation of the guanine base in DNA was observed besides the two electrochemical signals from the oxidation of Co(III/II) and Fe(III/II). This indicated that electrogenerated Fe^{3+} was a sufficiently strong oxidant to oxidize guanine (And and Thorp, 2000). Further investigations demonstrated that in pure Co–DNA melts, DNA could suppress the net electron transfer rate in the reduction process of Co(II/I) due to very low mobility of anionic phosphate groups of the DNA counterion (Leone et al., 2003).

Thermotropic DNA fluids not only perform to be a scaffold for metal redox reactions, but it was found that the nucleobases can be reversibly oxidized in DNA–lipid liquids and a related phase-dependent electrochromism behavior was revealed (Liu et al., 2016). As shown in Figure 6.2(a) and (b), electric field-induced coloration and bleaching had a switching effect for seconds with potential steps of 0 and 4 V, in amorphous phase of DNA hybrids. The magenta color was due to radical cation formation of
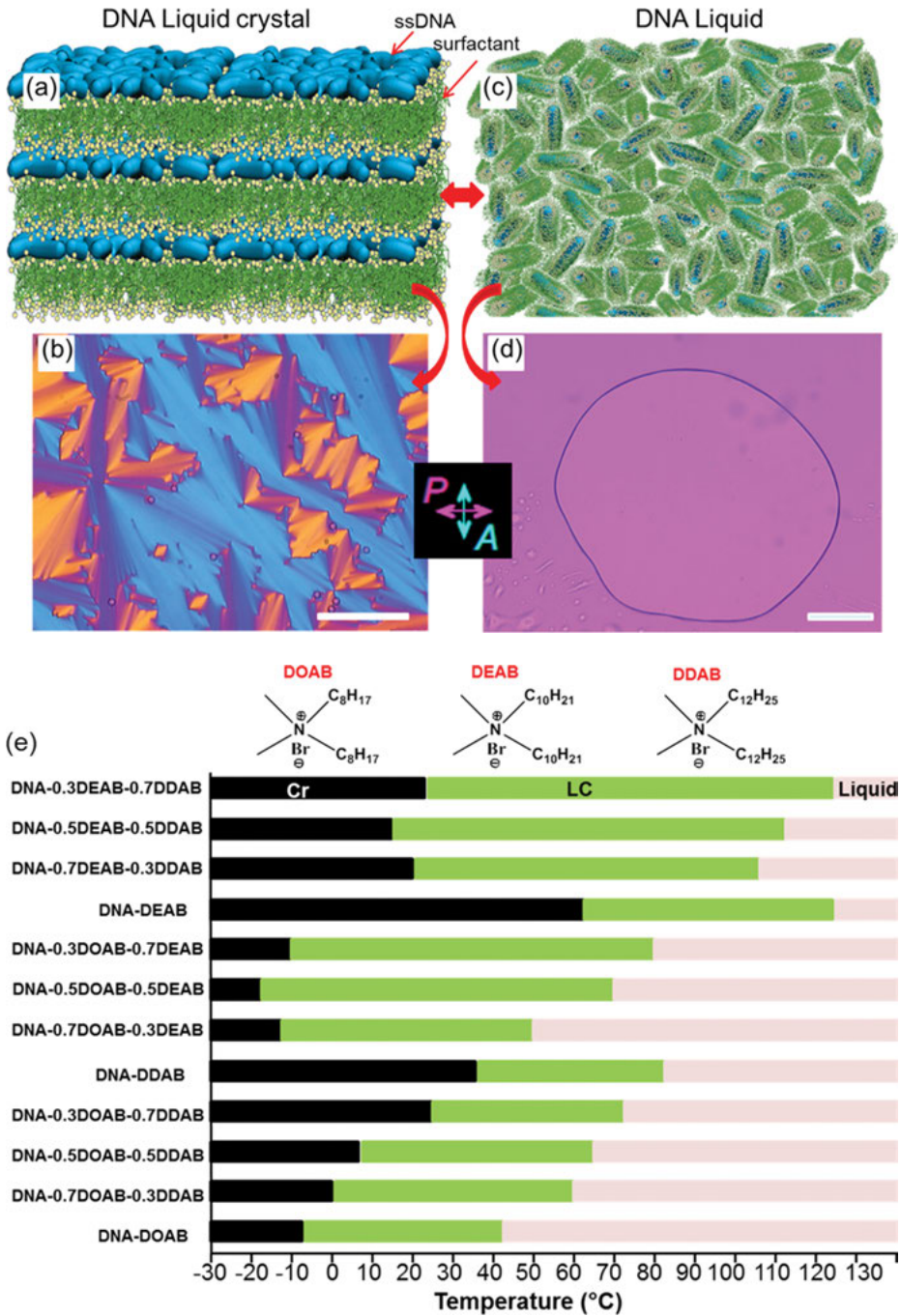
Figure 6.1: Thermotropic liquid crystals and liquids of DNA–surfactant complexes (Liu et al., 2015a, 2014). (a) Proposed lamellar structure in the liquid crystalline phase. (b) Typical polarized

nucleobases (Candeias and Steenken, 1989; Rokhlenko et al., 2014). The time duration of the electrochromic switch correlated with DNA length, indicating that the rate of DNA oxidation was restricted by mass transport to the electrode. When cooled to the smectic LC phase while an applied voltage of 4 V was maintained, a noticeable optical memory of the written state was observed without decaying of color for multiple hours in the absence of applied voltage (Figure 6.2(c)). After returning to 0 V, the color was kept in the mesophase temporally and was fully bleached in 24 h (Figure 6.2(d)). The persistence time of the magenta color prolonged when further cooled to the crystal phase with no applied voltage (Figure 6.2(e) and (f)); hence, the optoelectronic state can be fine-tuned by changing the phase of the DNA–fluid material. It was also observed that reorientation of smectic layers of the oxidized DNA hybrids occurred due to the applied voltage in the transition process from the amorphous to the mesophase. In the parallel aligned oxidized DNA–surfactant complex, the surfactant sublayers may act as an insulating barrier and prevent electron hopping. Therefore, the reduction process of DNA radical cations was slowed down. The electrochromic DNA hybrid material can be developed as a clock device with memory function in the context of ceiling temperature indicator (Figure 6.2(g) and (h)). Thus, this class of DNA liquids holds grand opportunities to achieve smart applications, for example, as indicators for perishable food or medical products that are distributed with cold chains.

6.3 Thermotropic protein LCs and fluids

The Mann group reported the synthesis of thermotropic protein droplets, which was inspired by nanoparticle liquid studies (Perriman et al., 2010a, 2010b; Bourlinos et al., 2010b; Rodriguez et al., 2010; Brogan et al., 2012). The preparation takes three steps: (1) supercharging of ferritin or myoglobin (Mb) proteins via carbodiimide-mediated reaction of the surface-accessible COOH groups with N,N'-dimethyl-1,3-propanediamine; (2) complexation via charge–charge interaction between positively charged proteins and negatively charged surfactants; (3) freeze-drying of the hybrids to collect the protein fluids. The ferritin–surfactant and myoglobin–surfactant liquids showed viscous behavior and melting temperatures at around 25 °C. They were thermally persistent, and degradation temperature was up to 400 °C.

Figure 6.1 (continued)
optical microscopy (POM) image of the DNA–surfactant mesophases, showing well-defined focal-conic textures of smectic layers. (c) Schematic of disordered DNA–surfactant complex in the isotropic liquid phase and (d) corresponding POM image of the isotropic liquid not showing any birefringent textures. Both POM images were acquired with an inserted quarter-wave plate. The scale bar is 100 µm. (e) An overview of phase transition temperatures (melting/clearing points) of binary and ternary DNA–surfactant complexes from crystalline (Cr) to liquid crystalline (LC) and then to isotropic liquid, which depends strongly on the specific length of the aliphatic chains of the surfactants. Copyright 2014 National Academy of Sciences of U.S.A. and 2015 WILEY-VCH.
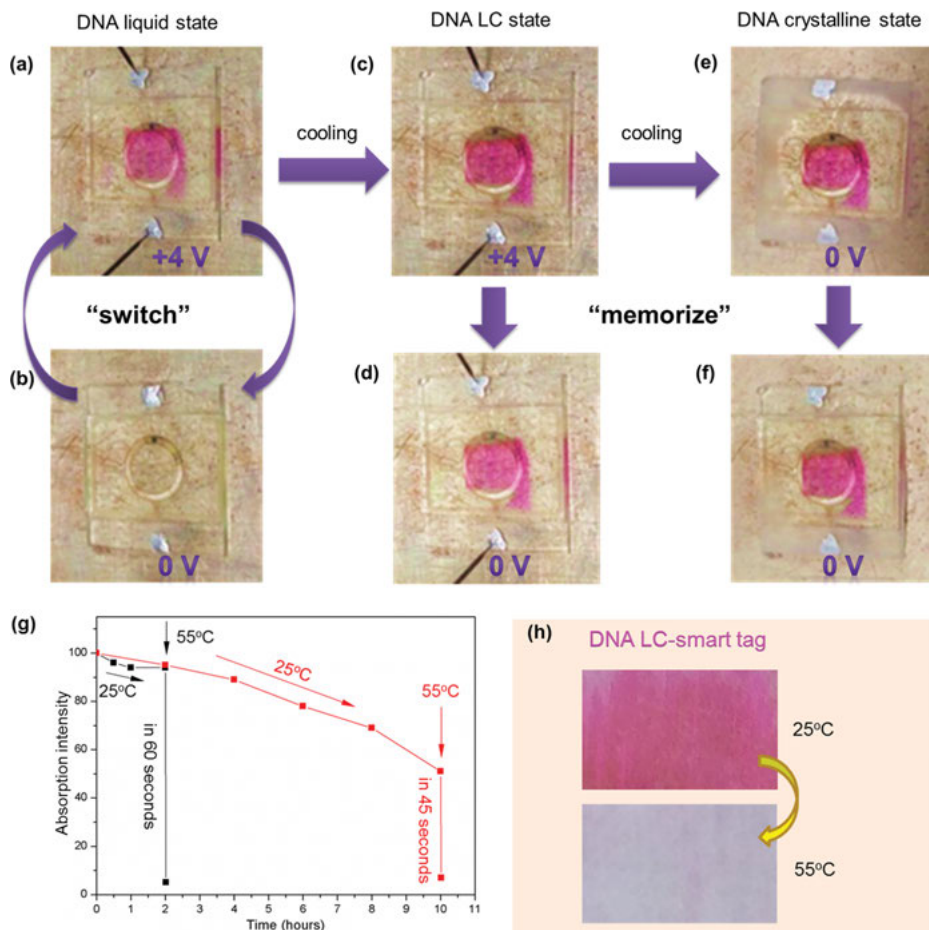
Figure 6.2: Phase-dependent electrochromic device based on thermotropic DNA–surfactant complexes (Liu et al., 2016). (a, b) Switchable electrochromism between the colored (magenta) and colorless states in the isotropic liquid phase. (c, d) Remarkable optical memory of the liquid crystal can be observed as a persistent colored state. (e, f) Cooling the colored DNA liquid crystalline phase to the crystalline phase can further increase the relaxation time of the color impression. (g, h) The activated DNA electrochromic device demonstrated functionality as combined time and temperature indicator. Copyright 2016 Springer Nature.

The ferritin–lipid complexes also showed viscoelastic and smectic LC behavior (Perriman et al., 2010a). Specifically, focal-conic textures were observed using POM in a temperature-dependent manner and the temperature window was at 37 °C. This transition behavior was further validated with differential scanning calorimetry (DSC), where a typical endothermic peak was observed. A lamellar structure with 13 nm layer distance was detected using SAXS, which is approximately the size of a ferritin protein. By heating, SAXS profiles presented no peaks of LC ordering, showing the liquid nature

of the ferritin–lipid hybrids at temperature above the transition point. From the biological point of view, ferritin is a spherical nanoparticle and is not believed to present anisotropic assembly. Yet, the complexation of positively charged ferritin with anionic lipids could make the transition from a globular native protein to an ellipsoidal hybrid (Perriman et al., 2010a). Thus, the new class of ferritin–surfactant complex with shape anisotropy promotes the occurrence of liquid crystalline phase.

Sharma et al. reported an anisotropic enzyme complex consisting of glucose oxidase and oppositely charged lipids. This hybrid showed temperature-dependent phase transition behavior (Sharma et al., 2014). At room temperature condition, this hybrid material was in the crystal phase with a layer distance of 12 nm, which is consistent with alkyl chain and PEG ordering. At 40 °C, a typical birefringent spherulitic texture of LC phase was observed with the preserved enzyme structure. Furthermore, another birefringent pattern with dendritic texture was found below the conformation transition temperature (T_c, 58 °C) of the enzyme and the PEG–PEG ordering was preserved. Thus, one can conclude that the shape anisotropy of the protein–lipid building block played a key role in the generation of structured hybrids.

Apart from the preparation of fluids derived from globular protein, rod-like polypeptides were also used to form thermotropic melts (Wenzel and Antonietti, 2010; General and Antonietti, 2002; Hanski et al., 2008). The assembly of positively charged poly(L-lysine) (PLL) or hexapeptide with lecithin, for example, led to persistent LCs with lamellar structure (Wenzel and Antonietti, 2010; General and Antonietti, 2002). The Ikkala group recently established a novel liquid system, taking advantage of the charge–charge interaction between PLL and dodecylbenzenesulfonate, which complexed with dodecylbenzenesulfonic acid (DBSA) via H-bonding interaction (Hanski et al., 2008). An LC phase can be realized with a ratio of 1.5–2.0 between PLL and DBSA, where PLL adopted an α-helical secondary structure. Increasing the temperature from 120 to 140 °C led to a structural transition of PLL to lamellar β-sheet domains. With a ratio of 3.0 in PLL/DBSA, an increase in temperature resulted in amorphous state with a random coil structure.

Not only structured proteins but unfolded polypeptides were also studied in the contexts of thermotropic LCs and fluids (Figure 6.3; Liu et al., 2015b, 2014). Genetic engineering was employed to construct and fabricate a family of supercharged polypeptides (SUPs). SUPs are derived from elastin-like proteins containing repetitive pentapeptide units (VPGEG)$_n$, where a glutamic acid residue is introduced into the fourth position. After polymerization via recursive directional ligation, multiple SUP molecules having 9, 18, 36, 72, and 144 negative charges are prepared (Figure 6.3(a)). After complexation with positively charged DOAB, DEAB, or DDAB, and subsequent dehydration treatment, the solvent-free SUP–lipid hybrids showed non-Newtonian behavior in smectic LC phase and Newtonian behavior in liquid phase. The complexes were thermally persistent until 200 °C. Two endothermic peaks were recorded using DSC, indicating the phase transitions of crystal state–LC and LC–liquid state.
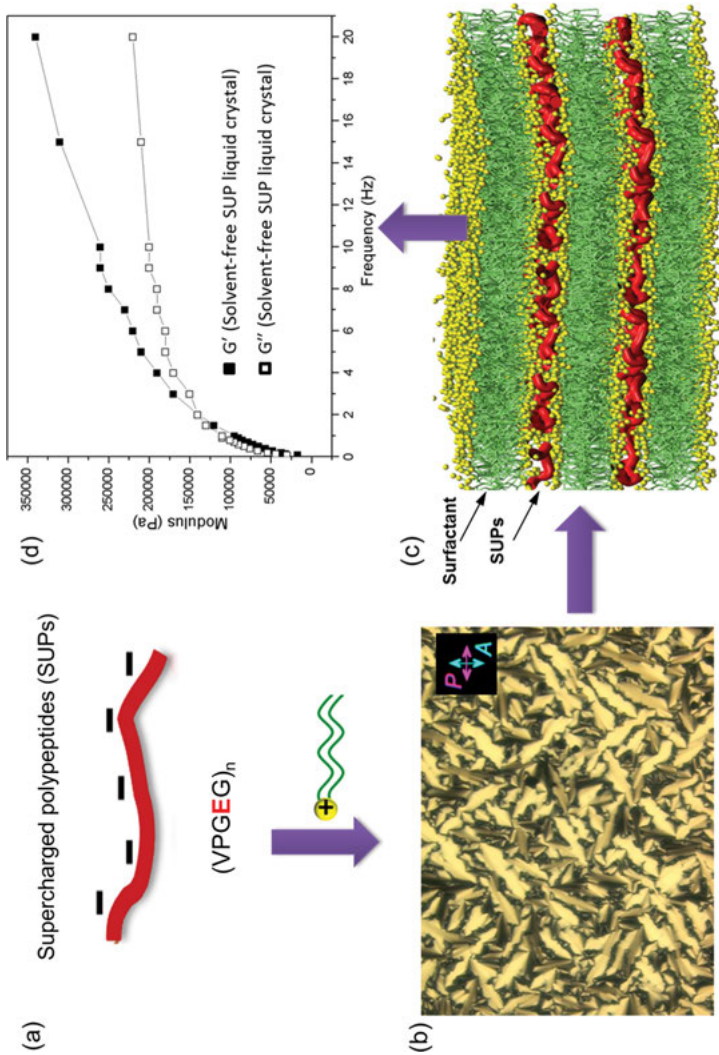
Figure 6.3: Fabrication of thermotropic fluids based on supercharged polypeptides (SUPs) (Liu et al., 2015b). (a) Negatively charged SUPs are produced by genetic engineering and combined with cationic surfactants. (b) POM image of the SUP–surfactant smectic liquid crystal. (c) Proposed lamellar bilayer structure of the liquid crystalline phase. (d) Rheological investigation of the thermotropic SUP–surfactant fluids, indicating high elasticity of the SUP liquid crystals. Copyright 2015 WILEY-VCH.

Characteristic focal-conic textures of smectic layers were observed via POM (Figure 6.3(b)). The SAXS tests confirmed the lamellar ordered structure of SUP–lipid liquids. Each repeating layer contains tail–tail interacting cationic lipids, which are electrostatically complexed with negatively charged SUPs (Figure 6.3(c)). Rheology studies showed that the thermotropic SUP liquids performed a phase transition from LC with viscoelastic properties to Newtonian liquid phase. The elastic moduli magnitude of the SUP hybrid LCs could reach as high as MPa, indicating their striking elasticity. This robust mechanical property resulted from the specific smectic SUP–lipid structures. The mechanical property of the hybrids can also be readily tailored through the backbone length of alkyl chains of lipids and the molecular weight of SUPs. Moreover, it is easy to amalgamate new functionalities using the molecular cloning strategy into the complexes. For example, a protein-based green fluorescent label (GFP) was introduced by fusion to the backbone of SUPs. It was also demonstrated that the typical fluorescence property of GFP can be preserved in the thermotropic liquid systems, which means that the surfactant environment did not influence the function of folded proteins in this complex.

6.4 Thermotropic virus LCs and fluids

Not only nucleic acids and proteins can be prepared into thermotropic fluids, bacteriophages and plant viruses are also good candidates for LCs and fluids preparation because they might perform as new type of storage and transport media, or be used to fabricate the solvent-free system in the context of nanotechnology. In this regard, cowpea mosaic virus (CPMV) was engineered to prepare a thermotropic liquid (Figure 6.4(a); Patil et al., 2012). The melting transition point of the freeze-dried CPMV–lipid hybrids was detected via a DSC setup at 28 °C. It was presented by Fourier-transform infrared tests that the treatment of modification on surface, freeze-drying, and melting did not alter the beta-sheet structure of capsids, and RNA was still preserved inside the core structure. It was also showed that the droplets on leaves of plants could result in robust infection, probably because the bioactivity of viral RNA was largely maintained and the accession to host cells in plants was in good condition even though the viral core entities were embedded within surfactant chains (Figure 6.4(b) and 4(c)). Similarly, a thermotropic liquid derived from tobacco mosaic virus showing a rod-like shape was fabricated with the same approach presenting a melting point of 28 °C. Larger-sized anisotropic virus particles were also successfully fabricated and resulted in thermotropic liquids. Negatively charged M13 bacteriophages, rod-like entities with 1 μm length and ~7 nm width, were complexed with cationic DOAB or DDAB (Liu et al., 2014). The melting point and clearing point of this class of viral hybrids were 14 and 58 °C, respectively. The complexes showed a lamellar structure,

and intact phages were placed along a preferred direction, which were clearly observed by freeze-fracture transmission electron microscopy (Figure 6.4(d) and (e)). POM data exhibited characteristic focal-conic birefringence behavior.
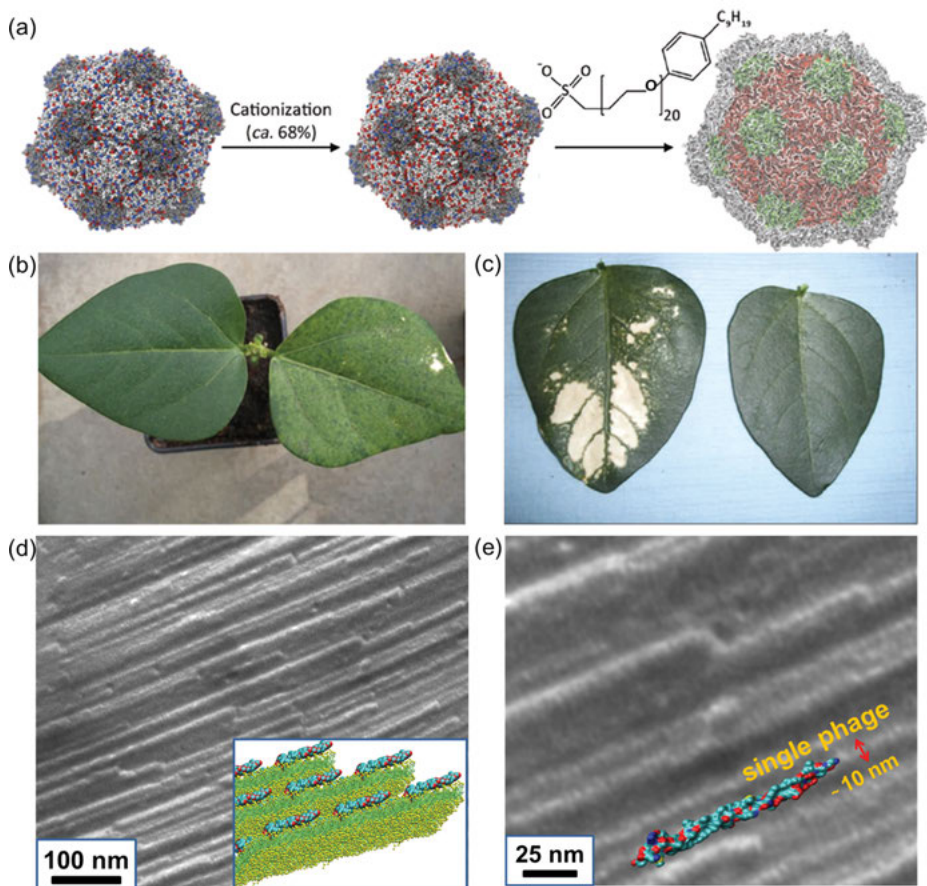
Figure 6.4: Fabrication of thermotropic virus–surfactant fluids. (a) Scheme showing the general route for the preparation of cowpea mosaic virus (CPMV) melt (Patil et al., 2012). Optical images of symptomatic *Vigna unguiculata* plants inspected after infection with aqueous dispersions of wild-type CPMV (b) and thermotropic CPMV–surfactant droplet (c). In each case, pairs of leaves either treated or untreated with the infective agents are shown. (d, e) Anisotropic rod-like viruses (bacteriophage) were also used for fabrication of thermotropic virus liquid crystals and liquids by complexation with surfactant (Liu et al., 2014). The magnifications of freeze-fracture transmission electron microscopy images of the phage–surfactant liquid crystals are shown. Long-range ordered lamellar structure of the phage–surfactant mesophase, where individual phages were identified at the layer edges, indicates the orientational order of phages within the sublayer. The model of phage-based liquid crystals is sketched in the inset (side view). Copyright 2012 WILEY-VCH and 2014 National Academy of Sciences of U.S.A.

6.5 Conclusions and outlook

Novel classes of biomolecular physical phases, that is, thermotropic fluids and LCs, were discussed in this chapter. Embedding DNA, proteins, and virus particles in a confined surfactant shell enables formation of these phases. The protocols are readily feasible through electrostatic complexation of surfactants and biomolecules, regardless of the size of biomolecule entities which can range from a few nanometers to several microns. Complexation of DNA with lipids containing double alkyl chains also enables LC phase formation. The phase transition could be tailored over a wide spectrum of temperatures via optimizing surfactant molecules. Furthermore, new electrochromic devices derived from those novel LC materials were successfully realized. It seems to be a very important aspect to get a stable device by limiting the content of H_2O molecules. Thus, those solvent-free DNA liquids are applicable for diverse investigations, which significantly differ from present studies of DNA devices that work in the aqueous condition.

Electrostatic complexation of lipids with engineered proteins and viruses, subsequent water-free treatment, and thermally induced melting were used as a three-step approach to fabricate polypeptide-based liquids. Importantly, no denaturation of proteins was observed during the processing of freeze-drying and melting. The almost fully preserved structure and function of proteins in the complexes at high temperature allowed the enhancement of catalysis efficiency. Accordingly, solvent-free polypeptide/protein fluids exhibit a grand challenge to current theories on the way of H_2O molecules in maintaining protein structure and function. SUP-derived thermotropic liquids presented robust elasticity. In this regard, amalgamation of other proteins to SUP systems might lead to new biological complex fluids bearing advanced properties.

The examples outlined here would attract more interests and efforts by taking advantage of charge–charge interaction to realize the fabrication of biological thermotropic liquids employing various biomolecules. Thus, this electrostatic complexation paradigm offers novel directions in contexts of biosensing, biocatalysis, biomedicine, and bioelectronics.

References

And, V.A.S., Thorp, H.H. (2000). Electron transfer in tetrads: adjacent guanines are not hole traps in G quartets. Journal of the American Chemical Society, 122(18), 4524–4525.

Bourlinos, A.B. et al. (2010a). Functionalized nanostructures with liquid-like behavior: expanding the gallery of available nanostructures. Advanced Functional Materials, 15(8), 1285–1290.

Bourlinos, A.B. et al. (2010b). Surface-functionalized nanoparticles with liquid-like behavior. Advanced Materials, 17(2), 234–237.

Brogan, A.P.S. et al. (2012). Hyper-thermal stability and unprecedented re-folding of solvent-free liquid myoglobin. Chemical Science, 3(6), 1839–1846.

Brogan, A.P.S. et al. (2014). Enzyme activity in liquid lipase melts as a step towards solvent-free biology at 150 °C. Nature Communications, 5(5), 5058.

Candeias, L.P., Steenken, S. (1989). ChemInform abstract: structure and acid-base properties of one-electron-oxidized deoxyguanosine, guanosine, and 1-methylguanosine. Cheminform, 20(20), 1094–1099.

Faul, C.F.J., Antonietti, M. (2010). Ionic self-assembly: facile synthesis of supramolecular materials. Advanced Materials, 15(9), 673–683.

General, S., Antonietti, M. (2002). Supramolecular organization of oligopeptides, through complexation with surfactants, G. Narr, 2957–2960.

Gordiichuk, P.I. et al. (2014). Solid-state biophotovoltaic cells containing photosystem I. Advanced Materials, 26(28), 4863–4869.

Hanski, S. et al. (2008). Structural and conformational transformations in self-assembled polypeptide–surfactant complexes. Macromolecules, 41(3), 866–872.

Johnston, K.P. et al. (2012). Concentrated dispersions of equilibrium protein nanoclusters that reversibly dissociate into active monomers. ACS Nano, 6(2), 1357–1369.

Kim, W., Conticello, V.P. (2007). Protein engineering methods for investigation of structure-function relationships in protein-based elastomeric materials. Polymer Reviews, 47(1), 93–119.

Kwak, M. et al. (2011). DNA block copolymer doing it all: from selection to self-assembly of semiconducting carbon nanotubes †. Angewandte Chemie, 50(14), 3206–3210.

Kwiat, M. et al. (2012). Non-covalent monolayer-piercing anchoring of lipophilic nucleic acids: preparation, characterization, and sensing applications. Journal of the American Chemical Society, 134(1), 280.

Kyle, S. et al. (2009). Production of self-assembling biomaterials for tissue engineering. Trends in Biotechnology, 27(7), 423–433.

Leone, A.M. et al. (2001). An ionic liquid form of DNA: redox-active molten salts of nucleic acids. Journal of the American Chemical Society, 123(2), 218–222.

Leone, A.M. et al. (2003). Ion atmosphere relaxation and percolative electron transfer in co bipyridine DNA molten salts. Journal of the American Chemical Society, 125(22), 6784–6790.

Liu, K. et al. (2014). Thermotropic liquid crystals from biomacromolecules. Proceedings of the National Academy of Sciences of the United States of America, 111(52), 18596–18600.

Liu, K. et al. (2015a). Frontispiece: solvent-free liquid crystals and liquids from DNA. Chemistry, 21(13), 4898–4903.

Liu, K. et al. (2015b). Polypeptides: solvent-free liquid crystals and liquids based on genetically engineered supercharged polypeptides with high elasticity (adv. Mater. 15/2015). Advanced Materials, 27(15), 2459–2465.

Liu, K. et al. (2016). Controlling the volatility of the written optical state in electrochromic DNA liquid crystals. Nature Communications, 7, 11476.

Patil, A.J. et al. (2012). Liquid viruses by nanoscale engineering of capsid surfaces. Advanced Materials, 24(33), 4557–4563.

Perriman, A.W. et al. (2010a). Solvent-free protein liquids and liquid crystals. Angewandte Chemie, 121(34), 6360–6364.

Perriman, A.W. et al. (2010b). Reversible dioxygen binding in solvent-free liquid myoglobin. Nature Chemistry, 2(8), 622–626.

Ramundo, J., Gray, M. (2008). Enzymatic wound debridement. Journal of Wound, Ostomy, and Continence Nursing : Official Publication of the Wound, Ostomy and Continence Nurses Society / WOCN, 35(3), 273–280.

Rodriguez, R. et al. (2010). Nanoscale ionic materials. Advanced Materials, 20(22), 4353–4358.

Rokhlenko, Y. et al. (2014). Mechanistic aspects of hydration of guanine radical cations in DNA. Journal of the American Chemical Society, 136(16), 5956–5962.

Sharma, K.P. et al. (2014). Self-organization of glucose oxidase-polymer surfactant nanoconstructs in solvent-free soft solids and liquids. Journal of Physical Chemistry B, 118(39), 11573–11580.

Sharma, K.P. et al. (2015). High-temperature electrochemistry of a solvent-free myoglobin melt. Chemelectrochem, 2(7), 976–981.

Wenzel, A., Antonietti, M. (2010). Superstructures of lipid bilayers by complexation with helical biopolymers. Advanced Materials, 9(6), 487–490.

Mikhail Krakhalev, Vitaly Sutormin, Oxana Prishchepa,
Anna Gardymova, Alexander Shabanov, Wei Lee, Victor Zyryanov

7 Liquid crystals doped with ionic surfactants for electrically induced anchoring transitions

Abstract: Two conceptually different approaches can be used to operate liquid crystal (LC) materials. One approach is based on numerous variants of the Frederiks effect, which enables the LC reorientation caused by external stimuli without a change of boundary conditions. All modern optoelectronic LC devices function on the basis of this effect. The other exploits the anchoring transitions through the modification of the surface anchoring strength with a change in the tilt and (or) azimuthal anchoring angle(s) under the external influence (temperature, irradiation, electric field, and so on). This chapter provides an overview of a novel method to control LC materials by electrically induced anchoring transitions. The key element entailed in our method is an ionic surfactant dissolved in LC. The surfactant is adsorbed partially on the LC cell substrate, thus specifying certain boundary conditions. Its concentration at the interface varied under the action of DC electric field resulting in the modification of the surface anchoring. Following this, changing boundary conditions makes the whole bulk of LC reoriented into a different state. The modification of boundary conditions can be realized in both the normal and inverse modes, depending on the content of the ionic surfactant in LC. This ionic-surfactant operation (ISO) method is applicable to both polymer-dispersed LC (PDLC) films and nematic and cholesteric LC layers. Dynamical parameters of the electro-optical response of various LC structures are considered. Response times of the ISO optical cells of twisted -nematic layers are decreased to tens or hundreds of milliseconds at some volts of applied electric voltage. The implementation of the ISO method into operating PDLC devices allows observations of the novel bistability effects in cholesteric droplets. The most impressive feature of the ISO method is the possibility to reorient LC with dielectric anisotropy $\Delta\varepsilon$ of any sign and value, including $\Delta\varepsilon = 0$.

7.1 Introduction

Impetuous development of nanotechnologies renders the study of surface phenomena increasingly topical. The effects occurring at the interface between two media, of which one is liquid crystal (LC), are quite specific (Barbero and Evangelista, 2006; Blinov et al., 1987). The most spectacular feature is that the comparatively weak surface anchoring forces not only can orient the near-surface LC molecules but also can affect the director configuration in a region offset by a few tens of microns from the interface. This property is basic to the functioning of all modern electro-optical LC devices because it allows the desired orientational structure to be organized in an LC layer through the formation of appropriate boundary conditions. An external electric field reorients LC in its bulk but does not markedly change the interface structure. This transformation is typical for the numerous variants of the classical Frederiks effect (Blinov, 1983; Freedericksz and Zolina, 1933). After switching off the field, the forces of surface interaction restore the initial director configuration in the bulk of LC.

A conceptually new approach was developed on the basis of the so-called local Frederiks transitions (Blinov et al., 1987; Dubois-Violette and De Gennes, 1975) or anchoring transitions consisting in the transformations of the director orientation in the bulk as a result of a change in the balance of the orienting actions of the different surface forces. A typical example is the reorientation of a nematic layer screened from a crystal substrate by a thin amorphous film (Blinov et al., 1984; Ryschenkow and Kleman, 1976). The orienting actions of the film and substrate must be different, for example, planar and homeotropic. The variation in the film temperature (Ryschenkow and Kleman, 1976) or the film thickness (Blinov et al., 1984) changes the balance of the orienting forces and, thus, initiates the reorientation of LC layer. In practice, the methods of modifying boundary conditions by an electric field are most essential. For this purpose, for example, the substrates coated with a ferroelectric LC polymer were used by Komitov et al. (2005). After a change in the polarity of the applied voltage, the azimuthal director reorientation in the LC polymer induces the respective orientational transformation in the bulk of the nematic LC (NLC) bordering such a substrate.

There is another opportunity to realize the electrically controlled anchoring transition based on the ionic-surfactant method. In 1972, Proust and his colleagues observed an interesting phenomenon when the concentration of adsorbed cationic surfactant cetyltrimethylammonium bromide (CTAB) influences dramatically the LC surface anchoring (Proust and Ter Minassian Saraga, 1972). They showed that at low content of the surfactant at interface, a planar (tangential) anchoring is formed (Figure 7.1). At high content of CTAB admixture, the surface anchoring becomes homeotropic (perpendicular). This result underlay the technique offered by Petrov and Durand (1994) to implement an electrically controlled change of boundary conditions in the planar nematic layer with an ionic surfactant preliminarily deposited on

substrates of the LC cell. However, an anchoring transition was not realized in the pure form because electrohydrodynamic instability was the dominant effect.
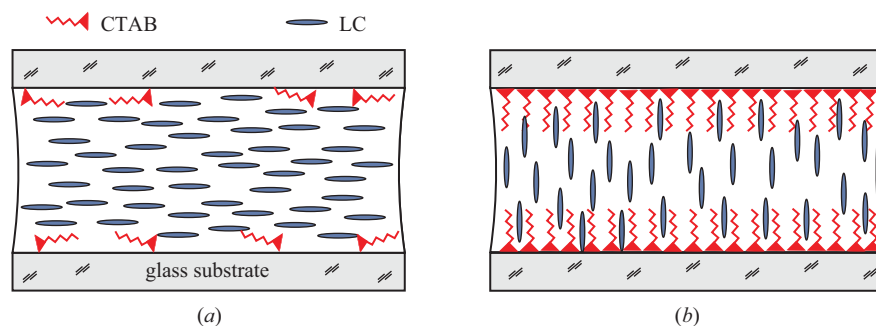
Figure 7.1: A planar anchoring of LCs is formed at low content of CTAB molecules at interface (a). An increase in CTAB concentration leads to the formation of a homeotropic surface anchoring (b).

In our experiments, the ability of CTAB to dissolve slightly in LC and dissociate into ions was used. A method of controlling the LC structure which is based on the modification of surface anchoring by electric-field-driven ionic surfactant was implemented for the first time for nematic droplets (Zyryanov et al., 2007b). We believe that the development of this approach can lead to the creation of principally new LC materials capable of significantly expanding the functional possibilities of optoelectronic devices.

This chapter reviews the previous works of authors primarily done on the development of LC materials with electro-optical characteristics controlled using ionic-surfactant method.

7.2 Polymer-dispersed liquid crystal films controlled by ionic-surfactant method

7.2.1 Composition and sample preparation

We used the following material components for the preparation of polymer-dispersed LC (PDLC) films (Figure 7.2): well-known nematics 4-*n*-pentyl-4′-cyanobiphenyl (5CB) with dielectric anisotropy $\Delta\varepsilon = +13.3$ at 25 °C (Bradshaw et al., 1985) and 4-methoxybenzylidene-4′-*n*-butylaniline (MBBA) $\Delta\varepsilon = -0.54$ at 25 °C (Klingbiel et al., 1974), polymers polyvinyl butyral (PVB) and polyvinyl alcohol (PVA) specifying the tangential (planar) boundary conditions, glycerin as a plasticizer for PVA, cationic surfactant CTAB, and a chiral additive cholesteryl acetate (ChA) to prepare cholesteric LCs (ChLCs).

The samples of PDLC films based on PVB were prepared by the solvent-induced phase separation (SIPS) method (Crawford and Zumer, 1996; Zharkova and Sonin, 1994). A mixture of LC 5CB and polymer PVB taken in a weight ratio of 1:1 with the surfactant CTAB of varied concentration was dissolved in ethanol. The solution was poured on the substrates with indium–tin -oxide (ITO) electrodes and dried. After ethanol evaporation, the polymer film was formed with LC droplets dispersed in it. The film thickness and LC droplet's size were specified by the conditions of the SIPS process (the ratio of the material components and rate of evaporation).

The emulsification method was used to prepare the samples of PDLC films based on polymer PVA (Drzaic, 1995). At that, a nematic LC doped with the cationic surfactant CTAB was emulsified into an aqueous solution of the film-forming PVA polymer plasticized with glycerin. The ratio of used components varied according to each case under consideration.
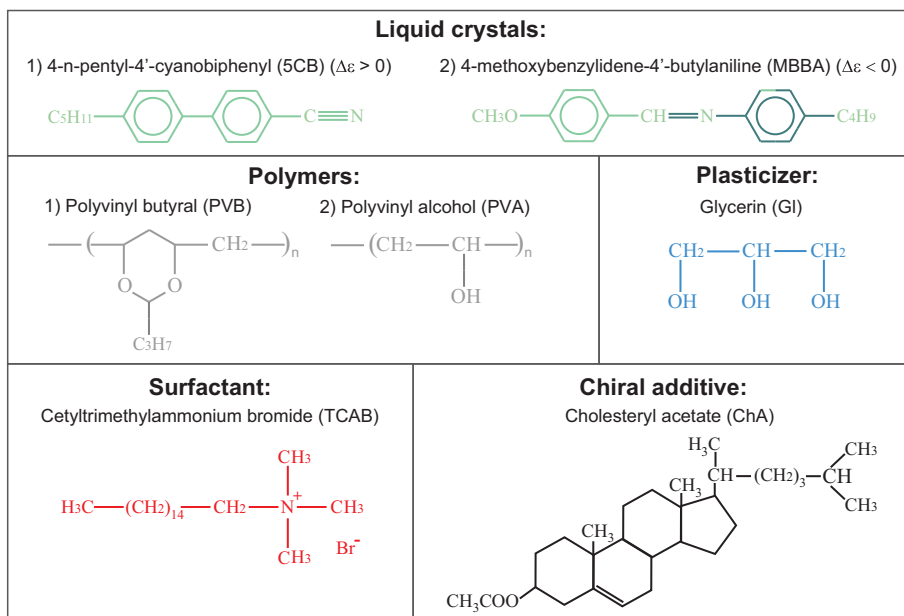
Figure 7.2: Material components to prepare liquid crystal/surfactant/polymer composite structures.

7.2.2 Normal mode of the electrically induced anchoring transition in nematic droplets

CTAB was used as an ion-forming surfactant providing normal (homeotropic) boundary conditions (Cognard, 1982; Proust and Ter Minassian Saraga, 1972) at a certain concentration. When dissolved in LC, this compound dissociates into a negatively

charged Br^- ion and a positive CTA^+ ion. The surface-active properties of CTAB are only due to the cations, which when adsorbed at the interface can form molecular layers in which the long alkyl chains $C_{16}H_{33}$ are aligned perpendicular to the surface.

To study the textural changes and orientational structures (director configurations) in nematic droplets, a PDLC cell with in-plane applied electric field was prepared (Figure 7.3). The gap between the electrode strips at the substrate was 100 μm. Experiments were performed with composite films that are uniaxially stretched. Monopolar rectangular electrical pulses of 1-s duration with an amplitude varying from 0 to 1,000 V were applied to the electrodes. The texture patterns of the LC droplets were observed using a polarizing optical microscope (POM) in the geometry of crossed polarizers and with the analyzer turned off.

(a)   (b)
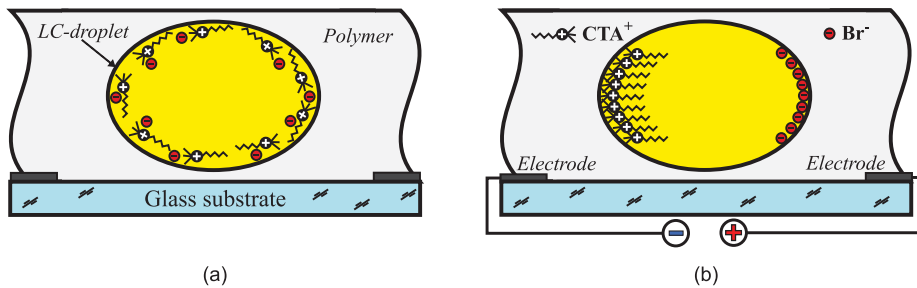
Figure 7.3: Scheme of PDLC cell with a CTAB dissolved in the nematic droplets. The content of CTA^+ ions adsorbed at the droplet surface is not enough to block the orienting forces of polymer walls and specify homeotropic anchoring; therefore, the tangential (planar) boundary conditions are realized in the initial state (a). When DC electric field is switched on, the CTA^+ ions are localized in the part of droplet near the cathode and modify an anchoring at the interface from tangential to homeotropic (b).

The droplets of 5CB nematic dispersed into a pure PVB matrix with the tangential anchoring are characterized by a bipolar director configuration (Prishchepa et al., 2005). The texture patterns of the nematic droplet and the corresponding director configurations typical for the studied composite film are demonstrated in Figure 7.4. One can see that the orientational structure of the droplets is bipolar with two surface point defects – boojums – in initial state (Figure 7.4(a)), evidencing the tangential anchoring for the chosen concentration of the CTAB surfactant.

In the geometry of crossed polarizers (Figure 7.4(a), top row), two extinction bands originate from the defects located at the ends of the droplet's major axis and expand gradually shading the central part of the droplet. The bipolar director configuration in the central section of the nematic droplet is schematically shown by the dashed lines at the bottom row of Figure 7.4(a).

In the geometry with the turned-off analyzer (Figure 7.4(a), middle row), two boojum defects (Volovik and Lavrentovich, 1983) are seen as dark spots at the ends

of the major axis of a prolate droplet. This became possible because of the large gradient of the refractive index near the defects and, hence, intense local light scattering. For the same reason, the parts of the droplet boundary are also clearly seen, where the light polarization coincides with the local director orientation. The gradient of the extraordinary refractive index of nematic droplet, $n_{\parallel}$, and the refractive index of polymer, n_p, $\Delta n = n_{\parallel} - n_p$, is maximal at these points. The boundary sections with the orthogonal arrangement of the director and light polarization are defined less sharply because the gradient $\Delta n = n_{\perp} - n_p$ is minimal in this region, where $n_{\perp}$ is an ordinary refractive index of nematic droplet.

The droplet's pictures corresponding to the end of the pulse when the electric vector is directed rightward are shown in Figure 7.4(b). Analysis of the corresponding textures shows that the right boojum decomposes in this case, and the director lines are almost uniformly aligned with the applied field at right half of the droplet. At the left half, the texture is unchanged suggesting that the initial director configuration is retained. The orientational structure corresponding to the new state of the droplet is shown at the bottom row of Figure 7.4(b). Of the previously described structures, the field-free monopolar structure (Prishchepa et al., 2005) of the lecithin-doped nematic droplets is a closest analogue to this configuration. The reversal of the field direction (Figure 7.4(c)) induces symmetric changes in textures: the left defect decomposes, while the initial director distribution in the right half of the droplet is retained.

In this situation, the orienting action of the external field on the LC bulk is not crucial. The concentration of the ionic impurity in the samples was so high that the applied field was almost fully screened inside the droplet by the field of spatially separated ionic charges (Barannik et al., 2005).

The observed transformation of the orientational structure in the LC droplet can convincingly be explained by the ion rearrangement (Figure 7.3). Under the action of the external field, the surface-active cations are concentrated near the droplet boundary close to the cathode forming here the close-packed CTA^+ layers with alkyl chains aligned perpendicular to the interface (Figure 7.3(b)). In the LC droplets studied, the fraction of CTAB was ~0.5 wt% or ~2.6×10^{-12} g for a spherical droplet with a radius of 5 μm. Regarding the molecular weight $M_{CTAB} = 6.04 \times 10^{-22}$ g, such a droplet contains ~4.3×10^9 CTAB molecules. The projection of a homeotropically arranged CTA^+ cation onto the interface is about 0.15×10^{-18} m^2 for the straightened *trans*-conformation of the alkyl chain. With these parameters, four close-packed monolayers of the CTA^+ cations can form at the half of droplet surface close to the cathode. Clearly, the number of monolayers is maximal at the point closest to the cathode and it decreases gradually with distance from this point. For comparison, the critical number of polar monolayers of stearic acid (whose molecules are similar in size and shape to the CTA^+ ions) in 5CB LC is two, while the number of nonpolar bilayers is ten (Blinov et al., 1984). In our case, the cationic monolayers screen also the orienting action of the PVB matrix and change the surface anchoring from tangential to homeotropic.
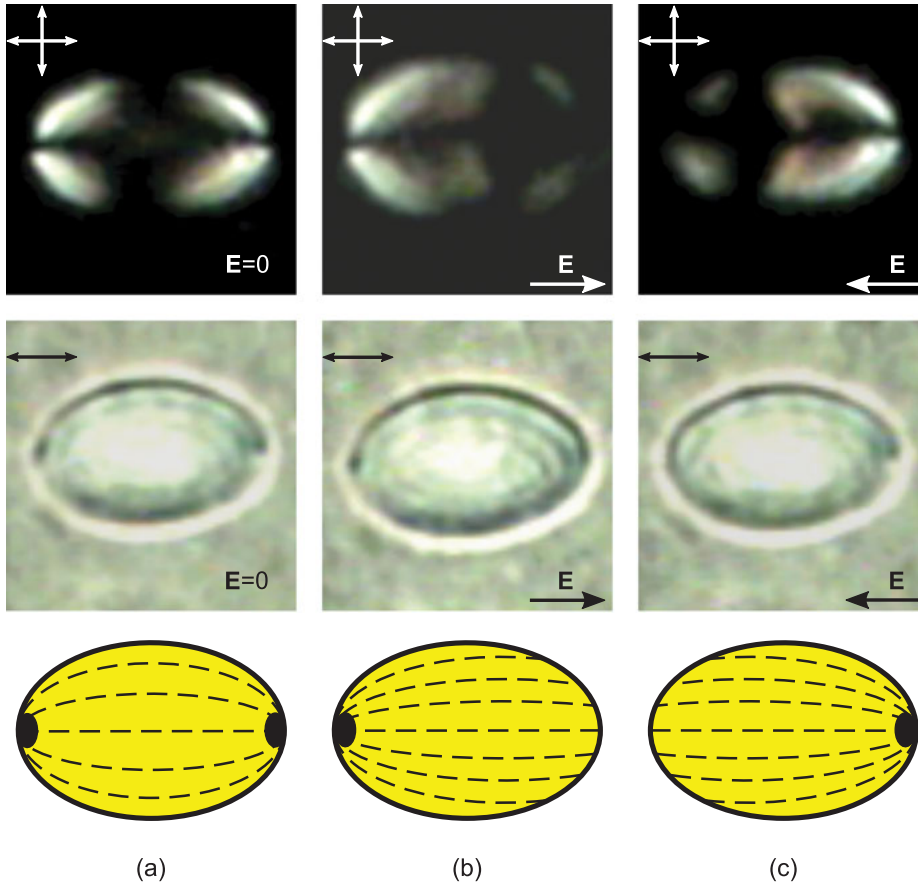
Figure 7.4: POM images of a nematic droplet between crossed polarizers (top row), with the turned-off analyzer (middle row), and the corresponding director configurations (bottom row). The electric field is switched off (a). The electric field $U = 280$ V is directed along the droplet's major axis to the right (b) and to the left (c). A gap between the electrodes is 100 μm, and a size of droplet's major axis is 13 μm. The polarizer orientations here and in the following figures are shown by the duplex arrows.

The modification occurs locally at the boundary area closest to the negative electrode. At a distance from it, the concentration of the cationic surfactant decreases and the anchoring angle θ (between the LC director and the normal to the surface) can change gradually from 0 (in the point of the destroyed defect) to 90° at the boundary area adjacent to the minor axis of the ellipsoidal droplet. After the field reversal, the CTA^+ ions transfer to the left half of the droplet and form there homeotropic anchoring. After a cation departure, the tangential boundary conditions and the surface boojum are restored at the right half of the droplet. As shown, the local increase in concentration of the Br^- anions does not cause the surface anchoring transition.

The orientational structure transformations occurring in LC droplet under electric field applied perpendicular or nearly perpendicular to the bipolar axis (Figure 7.5) are explained in a similar manner. In this case, the curved monopolar structure is formed (Figure 7.5(b) and (c)). One of the boojums is retained in the right half of the droplet in Figure 7.5(b) and in the left half in Figure 7.5(c). The other boojum decomposes, and the director lines deflect either upward (Figure 7.5(b)) or downward (Figure 7.5(c)) and crop out at the surface area saturated with the cations, where the boundary conditions become homeotropic and nearly homeotropic. At the opposite side of the droplet, where the Br anions are localized, the tangential anchoring is retained, as in the case shown in Figure 7.4(b) and (c).
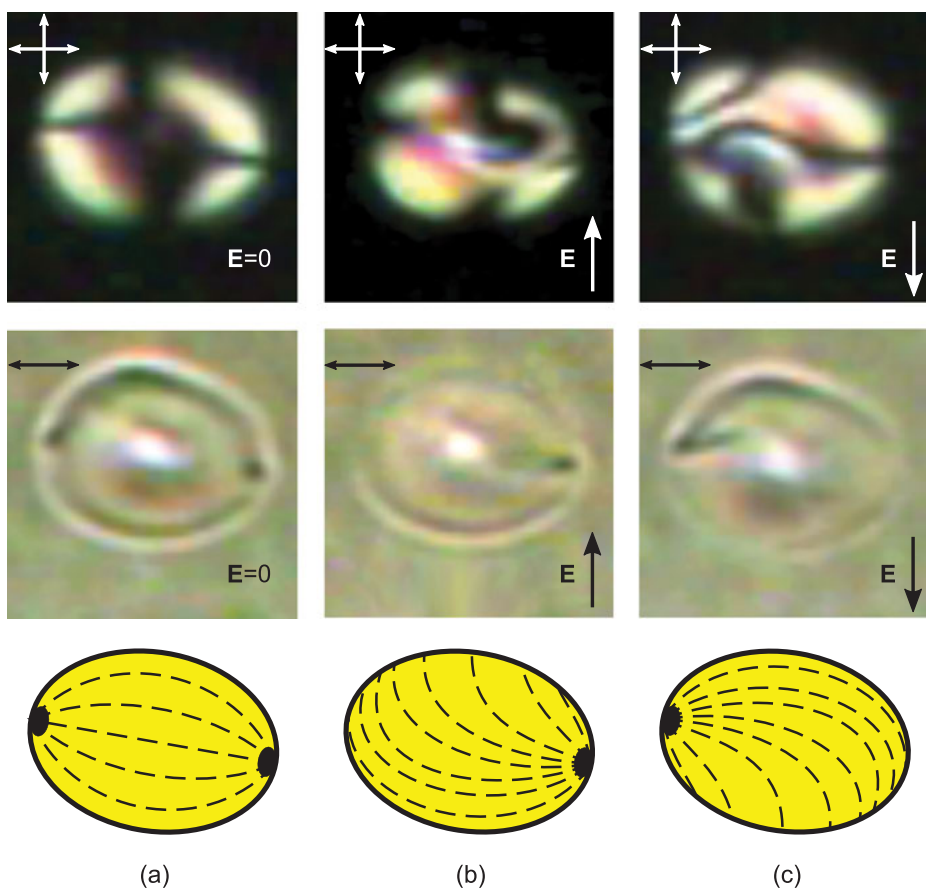
Figure 7.5: The arrangement of pictures and notations are as in Figure 7.4. The electric field $U = 950$ V is directed at an angle of 81° to the droplet's major axis. The field is switched off (a); the electric vector **E** is directed upward (b) and downward (c) in the figure plane. The major axis of the droplet is 15 μm.

Noteworthy is the fact that almost half of the visible droplet boundary is blurred when the field is perpendicular to the bipolar axis (top border in Figure 7.5(b) and bottom one in Figure 7.5(c), middle row). This occurs because the refractive indices of LC and polymer are matched; as a result, the light scattering for this polarization becomes markedly smaller for such LC structure than for the bipolar configuration. This inference is consistent with the results of our measurements of light transmission of PDLC film under direct current (DC) electric field applied perpendicular to the film, which show that the transmittance increased approximately doubles evidencing the promise to use this effect in electro-optical devices.

The possibility that the monopolar structure can appear was analyzed theoretically by the computer simulation of director distribution in a nematic droplet. The LC free energy was minimized in a single-constant approximation (Zumer and Doane, 1986):

$$F = \frac{1}{2} \int K \left[(\nabla \cdot \mathbf{n})^2 + (\nabla \times \mathbf{n})^2 \right] dV \qquad (7.1)$$

where a unit vector $\mathbf{n}$ is the nematic director, and K is the averaged value of the basic NLC elastic constants $K = (K_{11} + K_{22} + K_{33})/3$, where K_{ii} ($i = 1,2,3$) were taken from Bunning et al. (1981). This method was adapted earlier for the calculation of orientational structures in the spherical nematic droplets with inhomogeneous boundary conditions (Prishchepa et al., 2005). We extended this approach for the simulation of nematic droplets shaped as ellipsoid (Prishchepa et al., 2006). As discussed above, the field of spatially separated ions in the droplets compensates the action of the external electric field. For this reason, the terms accounting for the LC energy in the electric field were omitted in eq. (7.1). The boundary conditions were chosen according to the experiment demonstrated in Figure 7.4. Using the data obtained for the director configuration (Figure 7.6, bottom row), the corresponding texture patterns for the crossed polarizers were calculated by the well-known theoretical method (Ondris-Crawford et al., 1991) (Figure 7.6, top row).

One can see that these calculations properly describe the bipolar director configuration and the texture for the prolate nematic droplets (Figure 7.6(a)). To simulate the monopolar structure shown in Figure 7.4(b) and (c), tangential anchoring was assumed for the most part of the droplet surface (~0.7 of the visible boundary; see Figure 7.6(b)). The homeotropic boundary conditions are introduced in a small portion (~0.1 of the boundary on the right). The boundary conditions were assigned to be free between these two areas. The resulting director configuration and the texture pattern (Figure 7.6(b)) agree basically with the experiment (Figure 7.4(b) and (c)), confirming that the above analysis of the experimental data is correct.

The distinctions between the observed effect and other phenomena initiated by ionic impurities in nematic LCs should be discussed. Among these phenomena, various types of electrohydrodynamic instability of nematics in an alternating electric field are well known (Blinov et al., 1984; Fréedericksz and Tsvetkov, 1935). In such
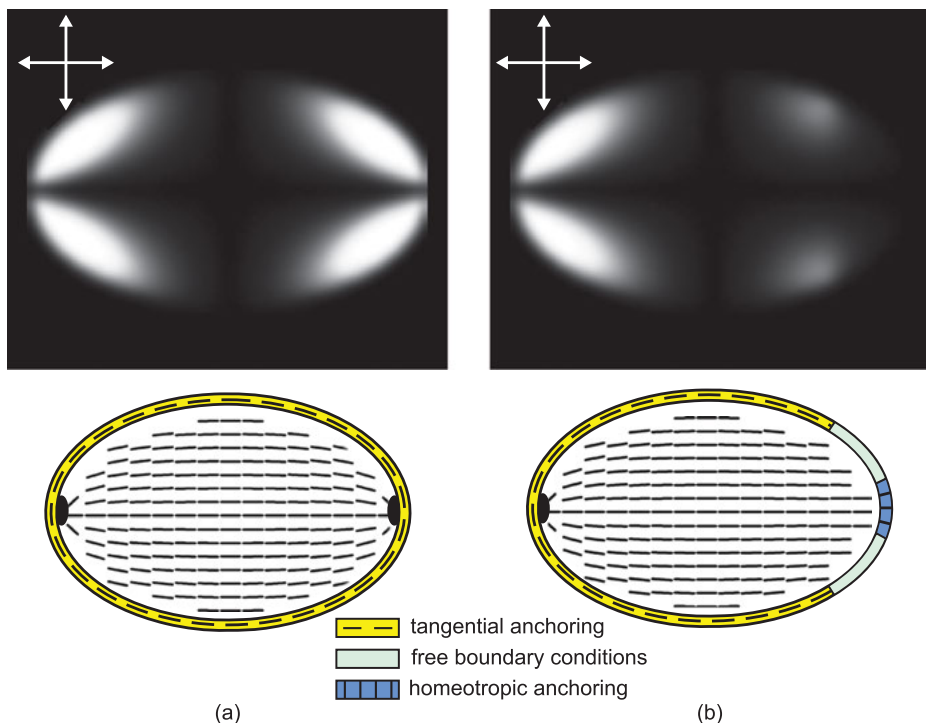
Figure 7.6: Numerical calculation of the director configurations (bottom row) and the corresponding textures (top row) in crossed polarizers for a nematic droplet with the size parameters and boundary conditions close to the experiment (see Figure 7.4). The boundary conditions (tangential, free, and homeotropic) are indicated in the droplet shells (bottom row in the figure). Bipolar orientational structure with the homogeneous tangential anchoring (a). Monopolar structure with the inhomogeneous boundary conditions (b).

systems, the ionic vortex motion initiates corresponding flows in the LC. The initially homogeneous director orientation becomes destroyed and the LC bulk breaks down into a lot of light-scattering vortices.

Another type of phenomena is described in detail by Barbero and Evangelista (2006) and is associated with the selective absorption of ions by the interface in the absence of an external field, as a result of which an electrical double layer forms near the surface. The electric field of the double layer can dominate other orientational actions of the substrate and can govern the director orientation at the LC cell surface.

The electrically induced anchoring transition in LC doped with CTAB is based on the combined action of two properties of the used dopant. The ion-forming ability of the additive makes possible the electrically controlled transport of certain ions to the required area of the LC cell. The surface-active property of the CTA^+ layers formed in this area allows the tangential orientational influence of the PVB matrix

to be screened and the surface anchoring to be changed from tangential to homeotropic. A similar screening effect is described by Blinov et al. (1984) for Langmuir layers formed by molecules of stearic acid. However, the use of electrically neutral molecules does not permit electrically controlled modification of the surface anchoring.

7.2.3 Inverse mode of the electrically induced anchoring transition in nematic droplets

In this section, the possibility of an inverse regime for the ionic modification of surface anchoring is considered and it is shown that this effect can be observed at a higher surfactant concentration than for the above-described case. PDLC films prepared by emulsification of LC in a polymer solution followed by solvent evaporation were studied (Drzaic, 1995). For this purpose, the weight ratio 5CB:PVA:Gl:CTAB of the components was 1:19:6:0.1. Note that the surfactant concentration was 10 times higher than for the normal mode (Zyryanov et al., 2007). It is known that the nematic 5CB is aligned tangentially at the surface of PVA even in the presence of glycerin additions (Drzaic, 1995). The CTA^+ ions, being adsorbed on the interface, can form nanosized layers that specify the homeotropic alignment of the LC molecules at a certain concentration (Cognard, 1982).

The samples of the composite films of 30 μm thickness were placed on a glass substrate with electrodes allowing a DC electric field to be applied along the film plane (Figure 7.7). The size of LC droplets was in the 7–11 μm range. Some of the studied samples were subjected to the uniaxial stretching for the purpose of studying specific features of the structural transformations in prolate droplets. For the material components used, the ordinary refractive index $n_\perp$ of LC is approximately equal to the polymer refractive index n_p. This is convenient for analyzing the director orientation at
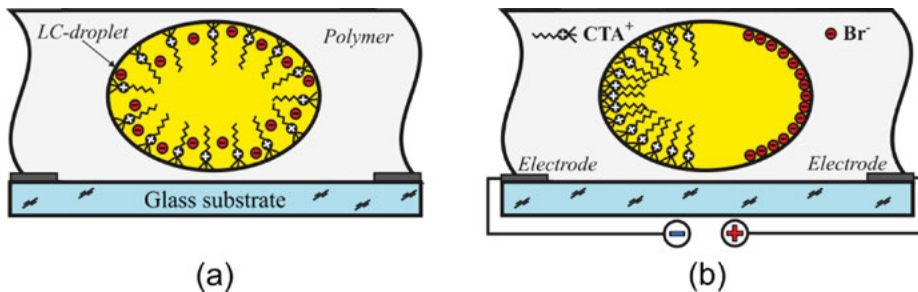
Figure 7.7: Schemes of electrically controlled ionic arrangement at LC droplet boundary for inverse mode. When the electric field is switched off, CTA^+ ions adsorb homogeneously at the interface and specify the homeotropic LC orientation at whole droplet surface (a). Under the action of DC electric field, CTA^+ ions leave a part of the surface close to the anode (b) where the tangential boundary conditions are formed.

the interface between the nematic and polymer. In the case of a switched-off analyzer, the droplet boundary is virtually unseen in the areas where light is polarized perpendicular to LC director. And vice versa, due to the strong light scattering, the interface is clearly seen as a dark line in the areas where the director coincides with the light polarization.

The experiments were accompanied by the numerical calculations of the director configurations in LC droplets and the corresponding textural patterns. The orientational structures were calculated by the well-known method of minimizing the energy of elastic distortions of the director field in the bulk of LC, as discussed above. The droplet shape and the boundary conditions were taken in accordance with the experimental data. The textural patterns of LC droplets in the crossed polarizers were calculated using the theoretical model (Ondris-Crawford et al., 1991).

In all studied samples of the composite films, the radial structure (Figures 7.8–7.10, top row) with the bulk hedgehog defect (Volovik and Lavrentovich, 1983) in the droplet center was initially formed. The typical textural pattern of the droplets in crossed polarizers has a form of Maltese cross. This implies that the used concentration of homeotropic surfactant suffices to form a CTA^+ layer over the entire surface blocking the tangential orienting action of the polymer matrix.

The corresponding schemes of the director distribution in the bulk of the droplets (Figures 7.8(d)–7.10(d), top row, where the central section of the droplet parallel to the film plane is shown) and their textural patterns (Figures 7.8(c)–7.10(c), top row) can be calculated using the condition of the homogeneous homeotropic director alignment over the entire droplet surface. In some droplets, the extinction bands are bent (Figure 7.10(b), top row), indicating that the director lines are twisted. In this case, a small chirality of the nematic structure should be considered in the analysis.

The textural patterns change drastically under the action of an electric field (Figures 7.8–7.10, bottom rows). In this case, the observed transformations can proceed following three various scenarios that ultimately result in the formation of three novel structures, whose specifics are determined by director distribution near the surface in the region with tangential anchoring.

Transition of the radial configuration into the structure containing surface point defect (boojum) and linear ring-shaped surface defect (Figure 7.8). At the beginning of the transformation, a small area with tangential anchoring surrounded by a region with a gradual change of the director orientation from tangential to homeotropic appears on the right side of the droplet surface. A point surface defect (hyperbolic boojum (Meyer, 1972)) is formed at the center of the region with tangential anchoring. Unlike a radial boojum (Volovik and Lavrentovich, 1983), the director lines in this case do not enter this defect and deflect from it along the trajectories close to the hyperbola. Then the region with the tangential director alignment expands, while the hedgehog moves from the droplet center to the hyperbolic boojum and merges with it forming a radial boojum. At the end of the process, the tangential anchoring occupies more than half of the droplet surface. The edges of this region are situated where a
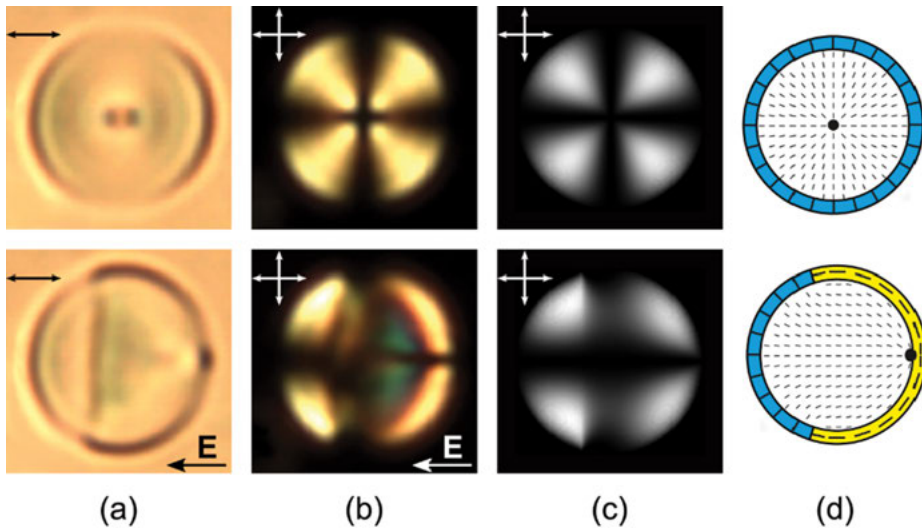
Figure 7.8: Transformation of the radial director configuration (top row) into the structure containing boojum and ring-shaped surface defect (bottom row) under the action of the in-plane applied DC electric field **E**. Photographs of nematic droplets with a switched-off analyzer (a) and in crossed polarizers (b). Calculated director configurations in cross section of the droplet (d) and the corresponding droplet textures in crossed polarizers (c). The boundary conditions (tangential or homeotropic) are indicated in the droplet shells (d). The droplet size is 10 μm.
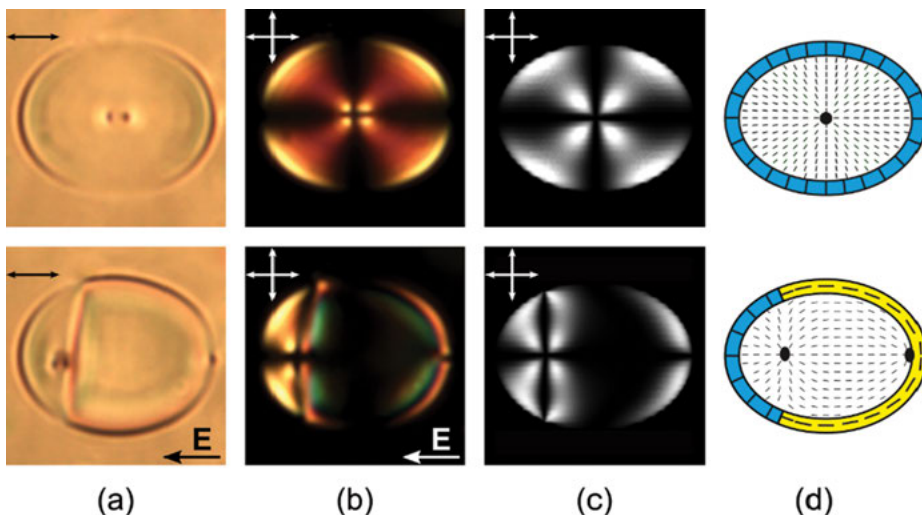
Figure 7.9: Electrically induced transformation of the radial configuration (top row) into the structure containing a hedgehog, boojum, and ring-shaped surface defect (bottom row). Photo positions, simulation data, and notations as in Figure 7.8. The major axis of the droplet is 19 μm.
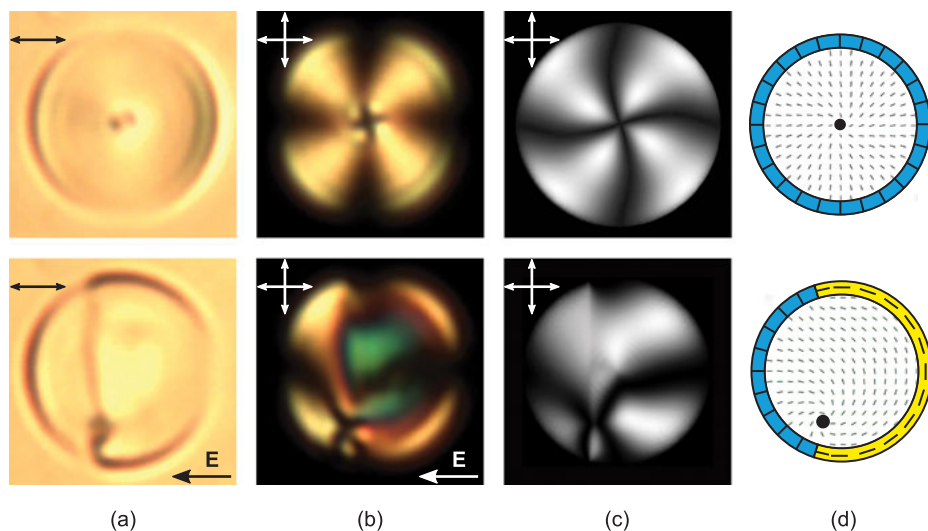
Figure 7.10: Electrically induced transformation of the radial configuration (top row) into the structure containing a hedgehog and ring-shaped surface defect (bottom row). Photo positions, simulation data, and notations as in Figure 7.8. The droplet size is 10 μm.

dark line corresponding to the strong light scattering terminates abruptly at the droplet boundary (Figure 7.8(a), bottom row). Two regions with different director orientations on the polymer wall are separated by a surface defect in the form of a ring perpendicular to the film plane. It is seen in the bottom row of Figure 7.8(a) as a dark vertical line to the left of the droplet center. The structure described in this figure can form in the spherical droplets, although its occurrence is possible in the prolate droplets if the electric field is directed along their minor axis. The resulting director distribution can be modeled using the appropriate boundary conditions (Figure 7.8(d), bottom row). It should be emphasized that, in this case, the director field lines must emerge from the boojum radially in all directions in LC bulk. The droplet texture (Figure 7.8(c), bottom row) obtained using the calculated configuration coincides basically with the experimental pattern (Figure 7.8(b), bottom row), confirming correctness of the analysis.

Transition of the radial configuration into the structure containing a hedgehog, boojum, and surface ring-shaped defect (Figure 7.9). This transformation occurs most frequently in the prolate droplets if the electric field is directed along their major axis. At the beginning of the process, boojum arises on the right side of the surface. Near the boojum, a ring-shaped surface defect forms at the interface between the areas with the tangential and homeotropic anchoring, whereupon it gradually moves to the left half of the droplet. The hedgehog shifts to the plane of the ring-shaped defect. This completes the structural transformation. As shown, the simulation data also describe the experiment well.

Transition of the radial configuration into the structure containing a hedgehog and ring-shaped surface defect (Figure 7.10). This process is observed most frequently in the radial droplets with the originally twisted director lines and proceeds in a qualitatively different way. In this structure, a ring-shaped surface defect also appears at the interface between the tangential and homeotropic anchoring. The hedgehog moves from the droplet center to the plane of the ring-shaped defect and shifts to the surface stopping short of reaching it. Analysis of the photos shows that the defect-free, nearly homogeneous director distribution is formed in the tangential surface zone. In our calculations, we tried to take this fact into account by specifying the director lines at the tangential surface area to be parallel to the line shown in droplet shell (bottom row of Figure 7.10(d)). Although the resulting texture (Figure 7.10(c), bottom row) does not fully coincide with the experimental pattern (Figure 7.10(b), bottom row), the main features (hedgehog position, direction of extinction bands emerging from hedgehog) agree with each other.

All processes described above are reversible. It should be noted that all three variants of the structural transition can occur in the same spherical droplet under the same experimental conditions. The reasons for which one or another transformation scenario is realized call for further investigations. It is likely that the decisive role in these systems is played by the thermal fluctuations producing certain distortions of the radial structure at the instant the electric field is switched on. However, it is shown above that the balance between the probabilities of these processes can be strongly shifted by varying the material parameters or experimental conditions.

A characteristic distinction between the two modes of the electrically controlled ionic modification of the interface is as follows. In the normal regime of the effect (Zyryanov et al., 2007), the initial alignment of the LC is determined by the polymer matrix, while the electric field induces the formation of a layer of surface-active ions in the respective region of the droplet surface, thereby blocking here the orienting effect of the polymer. Zyryanov et al. (2007) mention that the initial tangential LC alignment was changed in a local region of the interface to the homeotropic alignment inherent in the used surfactant. However, the reverse reconstruction of the boundary conditions in a normal mode is also possible, for example, for a composite of homeotropically orienting polymer and ionic surfactant providing the tangential anchoring.

In the inverse regime considered in this section, the initial structure of the LC droplets is governed by the nanosized layer of the surface-active ions, which covers the entire interface because of a high surfactant concentration. Under the action of electric field, ions leave the corresponding surface region, where the boundary conditions characterizing a polymer matrix are formed. By choosing various combinations of the orienting abilities of the polymer and surfactant, one can implement other variants in the reconstruction of the boundary conditions and, respectively, various scenarios of the structural transformations. Moreover, our study has shown that

the resulting director configurations and, hence, the optical properties of the PDLC films are quite sensitive to the material and structural parameters of the medium, such as the surfactant concentration, LC chirality, and droplet anisometry.

7.2.4 Optical response dynamics of polymer-dispersed nematic liquid crystal films

In this section, the electro-optical characteristics of a composite film based on a polymer containing dispersed NLC doped with an ionic surfactant are considered. The polymer matrix of PDLC films was PVA plasticized by glycerin (Gl). The nematic 5CB doped with a cationic surfactant CTAB was encapsulated in the PVA matrix using emulsification technique (Drzaic, 1995b). The ratio of components in the obtained PVA–Gl–5CB–CTAB composition was 9.3:3.7:1:0.02 by weight. The indicated CTAB content was enough to assign normal boundary conditions at LC–polymer interface, so that a radial director configuration was formed inside the NLC droplets in the initial state. These conditions are characteristic of the inverse regime of ion modification of the interface (Zyryanov et al., 2008). The LC droplets had an average diameter of 2–3 μm in plane of the film which had a thickness of about 16 μm. The sample film was formed on a glass substrate with two stripe electrodes spaced by 1 mm. Thus, the field between the electrodes was oriented mainly parallel to the PDLC film. The voltage applied to the electrodes had the shape of rectangular monopolar pulses of variable duration and amplitude.

The electro-optical characteristics of PDLC film were studied using radiation of a Mitsubishi ML101J21-01 semiconductor laser operating at $\lambda = 658$ nm. The laser radiation was sequentially transmitted through the linear polarizer, sample, and diaphragm and then measured by a photodetector. The diameter of the beam cross section was about 0.8 mm. Scattered radiation was blocked by the diaphragm, so that only the straight passing light was detected. The cell with PDLC film was arranged so that the electric field was perpendicular to the laser beam and the light polarization.

NLC droplets in the initial state observed in the geometry of crossed polarizers exhibit structures of the Maltese cross type, which are characteristic of a radial director configuration with a point defect in the droplet center. The structure remains almost unchanged under the action of an applied electric field with a strength of up to 0.03 V/μm. As the field strength is increased further, part of the interface closest to the anode becomes free of CTA^+ surfactant ions and, as a result, tangential boundary conditions (characteristic of the given polymer) are restored in this surface region. For this reason, the configuration of the LC director is transformed so that the fraction of the droplet surface that produces strong scattering of the incident radiation sharply increases (see, for example, Figure 7.8(a), bottom row). These changes in the orientational structure of NLC droplets are clearly manifested in the macroscopic optical response.

Figure 7.11 shows the typical time-evolved waveforms of the optical response of a PDLC film to electric field pulses of various amplitudes. The light transmission T of the film for a normally incident light was 0.77 at small electric field strength up to $E = 0.03$ V/μm. The application of a field with $E = 0.04$ V/μm leads to a decrease in the optical transmission, which can be plainly explained for the employed scheme of measurements by the enhanced light scattering by the NLC droplets with a modified orientational structure. After switching off the field, the transmission is restored to the initial level within a time of approximately 11 s. The dependence of the transmittance change, $\Delta T \propto E$, exhibits saturation at $E = 0.05$ V/μm (Figure 7.11(a)), for which it reaches a level of $\Delta T \propto 0.23$ (Figure 7.12). This value of ΔT is retained as the field strength is increased up to $E = 0.07$ V/μm (Figure 7.11(b)) and decreases with further growth in the field strength.
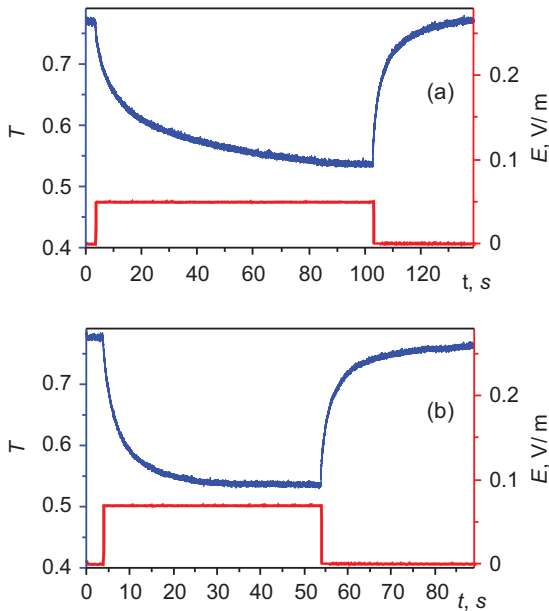
Figure 7.11: Oscillograms of the optical response of a PDLC film to electric field pulses of various amplitudes: $E = 0.05$ V/μm (a) and $E = 0.07$ V/μm (b). T is a light transmission of the PDLC cell.

Analogous variations can be traced for the field dependences of the dynamic parameters of the optical response (Figure 7.12). The response switch-on time τ_{on} decreases to 10 s at $E = 0.07$ V/μm, which is explained by a diffusion character of the ion motion. Indeed, the higher the field strength, the shorter time is sufficient to destroy the screening layer of ionic surfactant at the surface of NLC droplet. However, this tendency is only retained until $E = 0.07$ V/μm. As the field strength increases further, the τ_{on} value begins to increase, exhibits a local maximum at $E = 0.08$ V/μm, and then drops again.
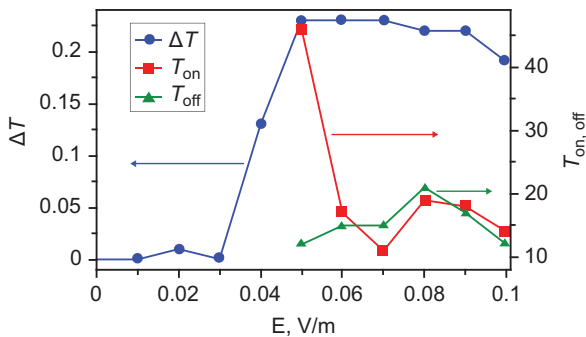
Figure 7.12: Plots of the transmittance modulation ΔT, optical response time (τ_{on}) and relaxation time (τ_{off}) versus applied electric field strength E for the PDLC film.

In contrast, the relaxation process exhibits no such a strong dependence on the applied field amplitude. The relaxation time varies within $\tau_{off} = 10$–20 s. In the range of field amplitudes up to $E = 0.08$ V/μm, this value first somewhat increases and then begins to decrease.

Thus, using the ionic-surfactant method to modify the surface anchoring of NLC droplets in PDLCs, it is possible to transform the orientational structure of LCs and, hence, to control the macroscopic optical characteristics of these composite films. A specific feature of this method is the use of a DC electric field, whose switch-off leads to recovery of the initial LC state. The optical response exhibits a threshold character of its dependence on the applied field strength. In a sample used in this study, the reorientation proceeds rather slowly, with a minimum response and relaxation times of about 10 s. However, as it will be shown later, the response speed may be increased by optimizing the composition, structure of LC material, and experimental conditions. An evident advantage of ionic-surfactant operation (ISO) method is the small strength of the control field, which is three times less compared with that for conventional PDLC films with analogous morphology parameters (Doane, 1991) that operate based on the Frederiks effect.

7.2.5 Bistability in polymer-dispersed cholesteric liquid crystals operated by ionic-surfactant method

In this section, a memory effect is considered which is caused by the ionic modification of the surface anchoring under the action of electric field in the polymer-dispersed ChLC (PDChLC) films.

Lately, technologies aimed at reducing the energy consumed by LC devices have been developing extensively. One of the effective solutions to this problem can be based on the use of a bistability phenomenon that allows a preset optical state to be

retained in the absence of an electric field. In this respect, much attention is devoted to ChLCs in which the bistable optical states of various types can be realized (Berreman and Heffner, 1981; Crawford and Zumer, 1996; Grawford, 2005; Greubel, 1974; Hsu et al., 2004; Yang, 2006; Yang et al., 1997). A most widely used effect that is already employed in display devices consists in switching a ChLC between stable states with a planar structure and a focal conic domain structure (Crawford and Zumer, 1996; Yang, 2006; Yang et al., 1997). The cholesteric helix pitch P must be much smaller than the size D of a cavity filled with the LC. The planar structure of a ChLC selectively reflects the circularly polarized light component, while the domain structure intensively scatters all radiation. If a ChLC is put onto a light absorbing substrate, the cell would reflect the light at a certain wavelength in one state and appear black in the other state. This effect is operative in both planar ChLC layers and ChLC droplets dispersed in a polymer film (Crawford and Zumer, 1996; Yang et al., 1997). The latter case is of special interest, since it enables the development of flexible bistable reflective displays (Yang, 2006), although the small pitch of the cholesteric helix makes necessary large control voltages. The memory effect is also characteristic of PDChLC films with a helicoid pitch comparable to the diameter of ChLC droplets ($P \cong D$) (Zyryanov et al., 1994), but the retention of recorded information in this case requires a supporting voltage (Barannik et al., 2005).

The aim of this study was to assess the alternative possibility of using PDChLC films in bistable optoelectronic devices and displays with nonvolatile data storage. The samples of PDChLC films were prepared by the emulsification of a ChLC in an aqueous solution of PVA plasticized by glycerin (Gl), followed by the evaporation of solvent (Drzaic, 1995; Klingbiel et al., 1974). The ChLC was a mixture of nematic LC 5CB with 1.5 wt% of ChA. The cationic surfactant CTAB was dissolved in the ChLC mixture before the preparation of emulsion. The ratio of components in the obtained ChLC–PVA–Gl–CTAB composition was 1:19:6:0.1 (w/w). At this concentration, CTA^+ ions adsorbed on a polymer surface form a layer that changes the surface anchoring from tangential to homeotropic (Zyryanov et al., 2008b).

The photographs in Figures 7.13–7.15 show the fragments of PDChLC films in various states as observed in crossed polarizers. PDChLC film was confined between two glass plates with transparent ITO electrodes. This sandwich structure was arranged between crossed polarizers, and an AC electric signal of rectangular or sinusoidal shape was applied to the electrodes. The radiation of a semiconductor laser operating at $\lambda = 658$ nm was transmitted through the optical cell and detected by photodiode, and the output signal of which was analyzed using a digital oscilloscope.
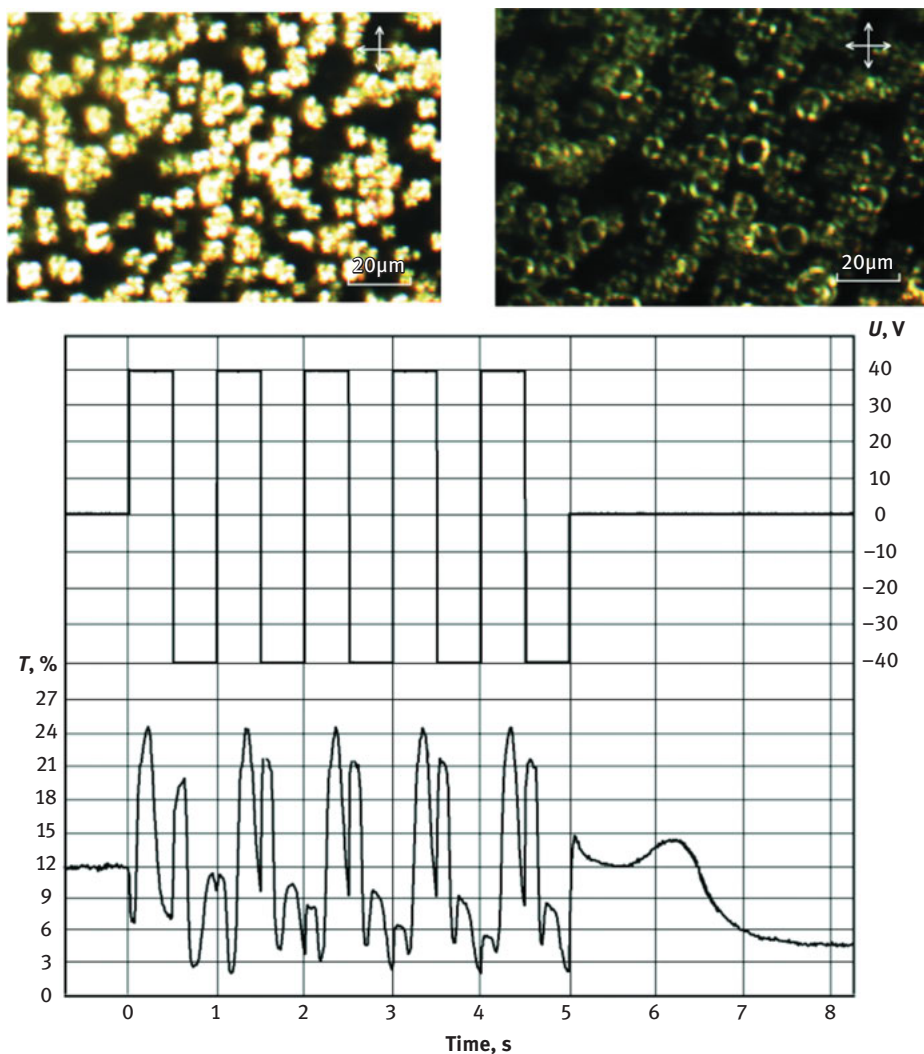
Figure 7.13: Waveforms of applied electric voltage U (top) and optical transmittance of a PDChLC film switched from the initial state with a twisted radial structure into a stable intermediate state (bottom). Photographs of film fragment in equilibrium states before (top row, left) and after (top row, right) electric field application. Here and below, the photographs are taken in crossed polarizers oriented parallel to picture sides.

The PDChLC film thickness was 75 µm. The ChLC droplets in the film plane had round shapes with an average diameter of 9 µm. These droplets were arranged in the film without overlap, which allowed the orientational structure of ChLC to be identified. In ChLC droplets without a surfactant, a twisted bipolar configuration of the LC director was formed, which correspond to a tangential anchoring. ChLC droplets

containing about 10% CTAB exhibited a twisted radial structure corresponding to a homeotropic orientation of LC molecules on the surface of the polymer matrix. The optical textures of these droplets in crossed polarizers resemble a bent Maltese cross (Figure 7.13, top row, left). Since the droplet transmits only a fraction of the incident light, while the optically isotropic polymer matrix does not transmit light in crossed polarizers, the total optical transmittance of a PDChLC film in the initial state amounts to only about 12% (Figure 7.13).

Under the action of an applied electric field, the ChLC droplets can transform into either the stable state with a homogeneous orientation of the director perpendicular to the film plane or into some intermediate stable structures. In the former case, the birefringence of the ChLC does not manifest and the light is not transmitted through these droplets (Figure 7.14, top row, right). Note that a small fraction of droplets (not exceeding 2% for the sample studied) does not transform into a homogeneous state, which accounts for a weak residual transmittance (Figure 7.14, top row, right). In the intermediate states, the LC director in the central part is close to the normal to the film surface and is tilted in the equatorial region. For this reason, the light only passes through the side regions (adjacent to the visible boundaries) of droplets (Figure 7.13, top row, right).

Thus, the optical transmittance of the PDChLC film in stable states can vary within 1.5–12%. From the initial state with $T = 12\%$, the PDChLC film can be switched to stable intermediate states by applying rectangular electrical signal at a frequency of 1 Hz (Figure 7.13). Under the action of this AC field, ChLC droplets exhibit a complicated process of transformation of the orientational structure, which involves the contributions of various physical phenomena including the Frederiks effect, modification of boundary conditions, and electrohydrodynamic instability related to the ion transport. The reorientation of the droplets manifests in the form of optical response, which varies during the electric signal within $T = 2.0–24.5\%$. After switching off, the droplets relax within about 3 s to an equilibrium intermediate state. The resulting transmittance can be controlled by varying the number, amplitude, and duration of pulses.

The minimum optical transmittance in a stable intermediate state achieved for the given samples controlled by rectangular pulses was about 4.5–5%. This value can be further reduced to 1.5%, but this requires applying a 1.3 kHz sinusoidal signal for 2 s after the rectangular pulses (Figure 7.14). This additional action leads to a homogeneous orientation of the LC director in droplets and the resulting almost complete darkening of the optical picture (Figure 7.14, top row, right). After this transition to a homogeneous orientation, only a small fraction of droplets (about 1%) can relax over time (for the first 100 h) to an intermediate structure, after which the system is completely stabilized.

Both intermediate and homogeneous structures of ChLC droplets can be returned to the initial state by applying rectangular voltage pulses with a frequency of 2 Hz, for example, to return droplets into the initial state with a twisted radial configuration of the director and the corresponding optical transmittance, it is possible
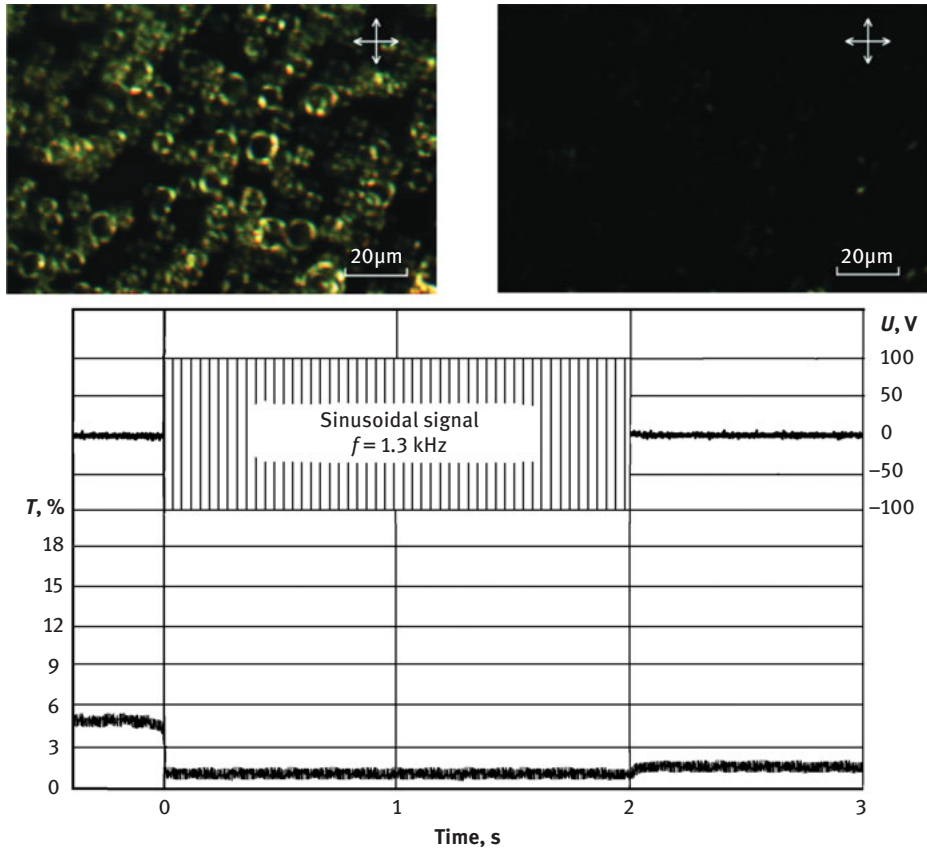
Figure 7.14: Waveforms of the control sinusoidal electric voltage *U* (top) and optical response of a PDChLC film switched from an intermediate state into a stable state with homogeneous LC director orientation in the droplets (bottom). Photographs of the film fragment in an intermediate state (top row, left) and in a stable state with homogeneous director orientation perpendicular to the film plane (top row, right).

to use the sequence of signals shown in Figure 7.15, with a gradually decreased (from 40 to 25 V) amplitude.

Thus, using ionic surfactants that modify the boundary conditions under the action of an applied electric field, it is possible to obtain many stable structural and optical states of a PDChLC film containing weakly twisted ChLC (i.e., with helicoid pitch comparable to the droplet size). This film material has good prospects for the development of electro-optical devices that do not require a fast response (electronic books, optical shutters, smart windows, etc.), but ensuring nonvolatile conservation of recorded information or a preset level of optical transmittance. Additional advantages of the proposed material are related to its flexibility, mechanical strength, and simple manufacturing technology.
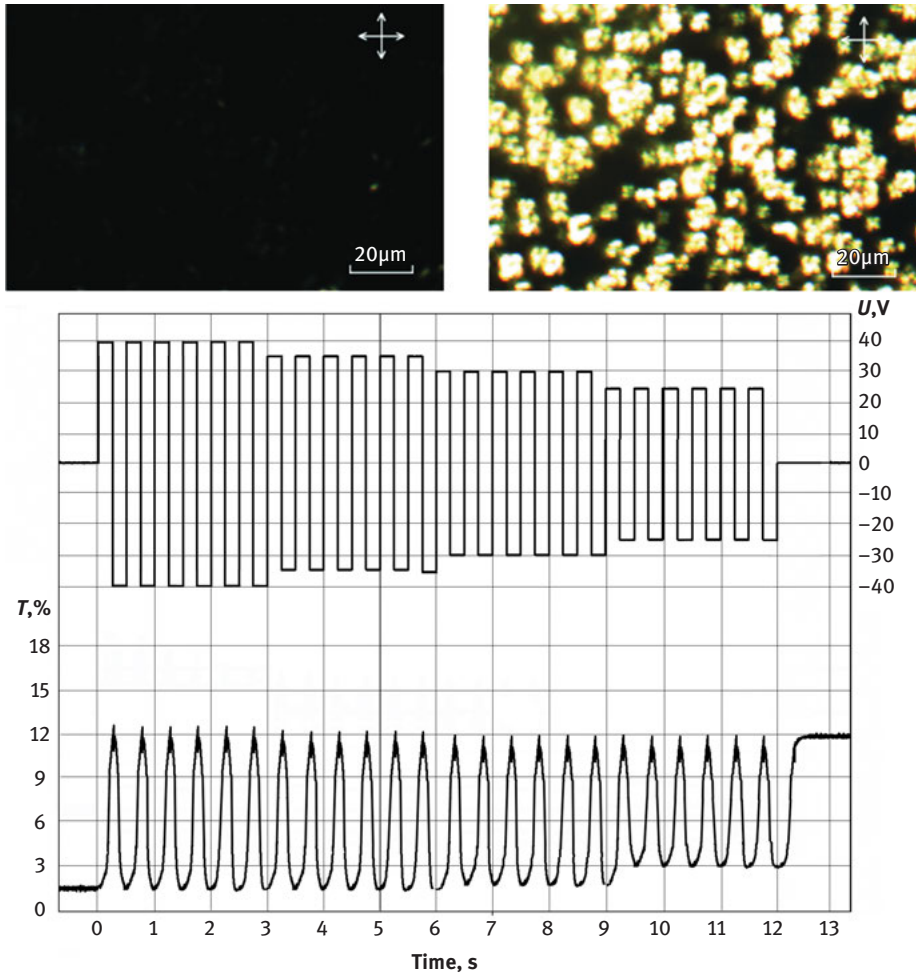
Figure 7.15: Waveforms of control electric voltage *U* (top) and optical response of a PDChLC film switched from a state with homogeneous LC director orientation into the initial state with a twist radial structure in the droplets (bottom). Photographs of the film fragment in a state with homogeneous director orientation perpendicular to the film plane (top row, left) and in a state with a twist radial structure in the droplets (top row, right).

The list of LC structures to which the ISO method can be applied is not restricted by the PDLC materials. These can be various LC structures in which the role of the substrate or matrix is performed by solid media, polymers, liquids, and others.

7.3 Liquid crystal layers controlled by ionic-surfactant method

7.3.1 Ionic-surfactant-doped nematic layer with homeotropic– homeoplanar configuration transition

LC cells consisting of two glass substrates with transparent ITO electrodes on the inner sides and a nematic layer between them can also be controlled by the ISO method. The nematic LC 5CB doped with CTAB was used in the experiments. Polymer films with a thickness of about 1.5 μm were preliminarily deposited on the electrodes. These films serve simultaneously as an orienting coating and a protective layer preventing the contact of surfactant ions with the electrodes. Polymer films based on PVA and glycerin solved in water were formed by the method of spin coating of the solution with subsequent drying. It is known that such films specify planar boundary conditions for the nematic 5CB (Cognard, J. 1982). The easy orientation axis was formed by the mechanical rubbing of the polymer surface in a required direction. The cells were filled with the LC by the capillary method in the isotropic phase. The thickness of the LC layer in the samples under study was about 6 μm.

The optical textures of nematic layer were studied by POM Axio Imager A1 (Carl Zeiss), which allows taking the photo and video recording of proceeding processes. The observations and measurements were carried out in the crossed polarizer geometry. Rectangular monopolar pulses of the electric field from an AHP 3122 (AKTA-KOM) generator were applied to the ITO electrodes. To study the dynamics of the macroscopic optical response of LC cell, we used a He–Ne laser (Linos) with a wavelength of $\lambda = 633$ nm. The laser radiation passed successively through the polarizer, an LC cell, and an analyzer and arrived at a photoreceiver. The diameter of the cross section of the laser beam was 1 mm. The angle between the direction of the rubbing of the substrates and the direction of polarizers was 45°.

Figure 7.16 shows the scheme for implementing the effect of the electrically controlled modification of the surface anchoring. It is necessary to choose the concentration of CTAB in 5CB such that the nanolayer of CTA^+ cations adsorbed at the interface can screen the planar orienting action of the polymer film and specify the homeotropic surface anchoring (inverse ISO mode). In this case, the homogeneous ordering of the director oriented perpendicularly to the substrates appears in the entire nematic layer in the initial state (see Figure 7.16(a)). When a static electric field is applied, surfactant ions move toward the corresponding electrode and one of the substrates becomes free of the layer of CTA^+ surface-active cations. As a result, planar anchoring conditions characteristic of a polymer coating are formed on this substrate (Figure 7.16(b)). Finally, the orientational transition from the homeotropic structure to the hybrid homeoplanar configuration of the director occurs in the LC cell.
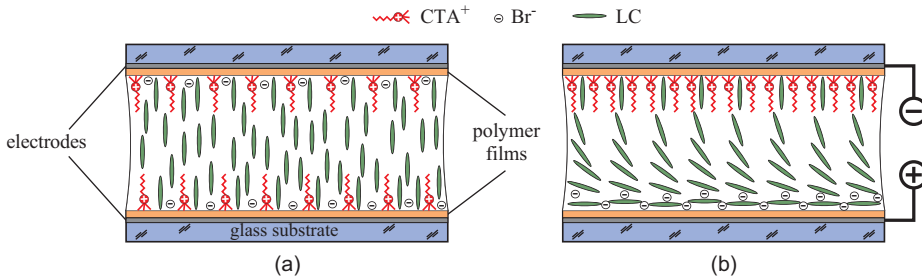
Figure 7.16: Scheme for implementing the effect of the ionic modification of the surface anchoring in the nematic layer. Electric field is switched off; the number of CTA$^+$ ions adsorbed at the interface is sufficient for the formation of homeotropic anchoring on the top and bottom substrates (a). Bottom substrate under DC electric field becomes free of CTA$^+$ ions; the orienting polymer film on this substrate specifies the planar ordering of the liquid crystal (b).

The experimental conditions necessary for implementing the schemes described above can be ensured with the use of polymer coatings with the weight ratio of components PVA:Gl = 1:0.243 and nematic 5CB doped with the ionic surfactant in the ratio of 5CB:CTAB = 1:0.01. The photographs of the optical textures of the LC cell are shown in Figure 7.17, where the electrically controlled switching of surface anchoring is demonstrated. One of the substrates (bottom) was preliminarily rubbed, whereas the other substrate (top) was used without rubbing. In the initial state, light does not pass through the optical system irrespective of its azimuthal rotation in crossed polarizers (see Figure 7.17(a)). This indicates the homeotropic orientation of the director throughout the entire nematic layer. When a DC electric field directed from bottom to top is applied (Figure 7.17(b)), the homogeneous bright pattern of LC layer is observed in the steady-state regime. This means that the homogeneous planar ordering of the director oriented along the rubbing direction **R** over the entire area is formed on the bottom substrate. When the polarity of the electric signal is changed, the transmittance
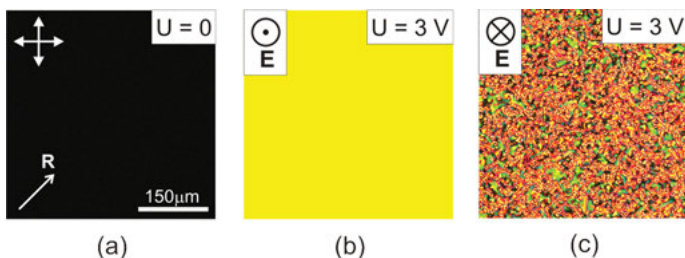
Figure 7.17: POM images of the optical textures of the liquid crystal layer in the initial state (a) and under the DC electric field **E** (b, c) directed from the bottom substrate to the top one (b) and from the top substrate to the bottom one (c). The value of applied DC voltage is $U = 3$ V. The bottom substrate was rubbed in the direction **R** at an angle 45° to the polarizers. The top substrate was not rubbed.

is high, but the optical pattern becomes sharply inhomogeneous (Figure 7.17(c)). This is explained by the absence of an azimuthally preferable direction (easy orientation axis) on the unrubbed substrate with planar anchoring.

These changes of the transmittance of LC cell cannot be attributed to the classical Frederiks effect (Freedericksz and Zolina, 1933) because the nematic 5CB with $\Delta\varepsilon > 0$ was used in the experiment. In the case of this effect, the application of the external electric field perpendicular to the plane of the LC layer would lead to the stabilization of the initial homeotropic orientation of the director. Thus, these observations convincingly demonstrate the anchoring transition in the planar nematic layer, which is due to the switching of surface anchoring from homeotropic to planar on the substrate with the anode electrode.

Figure 7.18 shows photographs demonstrating the optical textures of the LC layer for various control field strengths. In this case, both substrates were rubbed and put so that their rubbing directions were antiparallel. The reorientation process caused by the ionic-surfactant modification of surface anchoring is of a threshold character. The reorientation process begins with the field strength $U = 2.8$ V. The threshold character is due to the existence of the critical density of the layer of adsorbed CTA^+ ions below which the orienting action of the polymer coating is no longer screened. When the critical surface density is reached at certain electric field strength, the modification of surface anchoring begins. The anchoring transition is observed in the pure form in the range 2.8 V < U < 3.5 V (Figure 7.18(b) and (c)). At $U = 3.6$ V, the formation of the texture pattern of domains mainly elongated perpendicular to the rubbing directions begins in the LC layer. These domains are clearly seen at $U = 4.0$ V (Figure 7.18(d)). The formation of domains can be attributed to various surface phenomena (Proust and Ter Minassian Saraga, 1972), and the analysis of which is beyond the scope of this work.
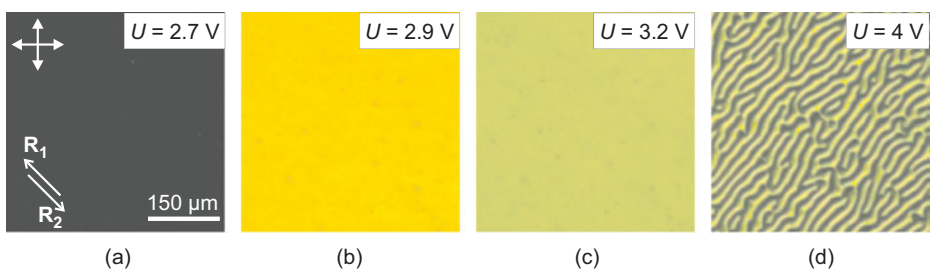
Figure 7.18: POM images of the optical textures of the 5CB layer doped with the ionic surfactant taken under DC voltages $U = 2.7$ V (a), 2.9 V (b), 3.2 V (c), and 4.0 V (d). The notation is the same as in Figure 7.17; R_1 and R_2 are the rubbing directions of the top and bottom substrates, respectively.

The texture patterns considered above correspond to the equilibrium state of modified boundary conditions under DC voltage. However, the most interesting features

of the effect under study are manifested in the response dynamics of LC layer near of the leading and trailing edges of the rectangular electric pulse (Figure 7.19). The pulse duration was 10 s. The transmittance of the cell in the crossed polarizer for the homeotropic LC orientation in initial state (Figure 7.18(a)) is close to zero. Any deviation of the director from the normal always leads to an increase in transmittance.
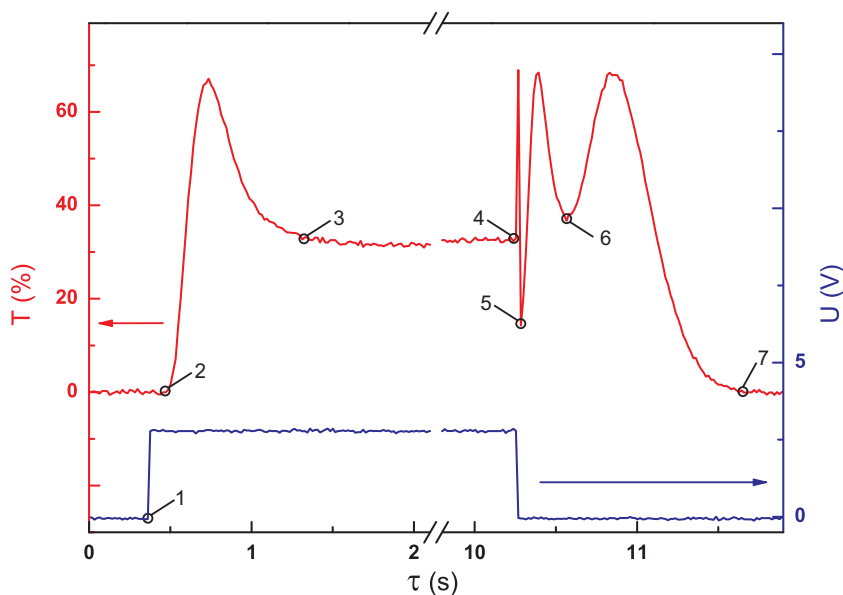
Figure 7.19: Optical response of an LC cell to the pulse of an electric field of 2.8 V. Numbers at transmittance *T* and voltage *U* curves mark the limits of the characteristic time intervals.

The complicated curve of the optical response can be divided into a sequence of time intervals in each of which a certain physical effect dominates. First, a noticeable delay of the optical response with respect to the forward edge of the electric pulse is noteworthy ($\tau_{12} = 0.14$ s, where the subscript "12" indicates two points in Figure 7.19 and the interval between which is considered). This delay appears because ions cannot instantly block the action of switched-on external electric field $\mathbf{E}_0$ in the bulk of the LC. Therefore, in this interval, the classical Frederiks effect occurs stabilizing homeotropic orientation of the nematic with $\Delta\varepsilon > 0$, and the transmittance remains zero. The time of separation of the ion cloud can be approximately taken as the time of the ions passage through the LC layer (Blinov and Chigrinov, 1993):

$$\tau_T = \frac{d^2}{U_{LC} \cdot \mu} \tag{7.2}$$

where d is the thickness of the LC layer, U_{LC} is the voltage applied to the layer, and µ is the mobility of ions. Using the values $µ = 10^{-6}$ cm$^2 \cdot$ s$^{-1} \cdot$ V^{-1} (Blinov and Chigrinov, 1993b), $U_{LC} = 1.4$ V (obtained taking into account the presence of polymer coatings), and $d = 6$ µm, we obtain the estimate $\tau_T = 0.26$ s, which is an upper limit for the possible action of the classical Frederiks effect. In reality, it is switched off faster when the effective field $\mathbf{E}_{eff} = \mathbf{E}_0 + \mathbf{E}_i$ (where $\mathbf{E}_i$ is the electric field of the separated ions) decreases below the threshold value of the Frederiks transition. Indeed, the delay time τ_{12} is noticeably shorter than the transit time τ_T.

At time instant 2, the external electric field $\mathbf{E}_0$ is mainly compensated by the field of ions $\mathbf{E}_i$. The planar orienting coating free of CTA$^+$ cations on one of the substrates begins to turn the director of the LC leading to an increase in transmittance. The T curve reaches a maximum of about 68%, then decreases to 33%, and is finally saturated. This behavior of transmittance can be predicted using the known relation (Born and Wolf, 1999) for an anisotropic plate in crossed polarizers. With the parameters of our experiment, it can be written in the simplified form as follows:

$$T = \sin^2 \left(\frac{\pi \int_0^d \Delta n(z) \mathrm{d}z}{\lambda} \right) \qquad (7.3)$$

The numerator is the integral optical path difference for the ordinary and extraordinary beams on the thickness of the LC layer and λ is the wavelength of laser radiation. For the homeotropic nematic layer, the integral is in eq. (7.3) and, hence, the transmittance is zero. For the homeoplanar layer of LC 5CB ($n_{\parallel} = 1.7057$, $n_{\perp} = 1.5281$ at $t = 25$ °C and $\lambda = 0.633$ µm (Bunning et al., 1986)) with a thickness $d = 6$ µm, this integral gives 0.511 µm in the approximation of a linear change of director slope over the thickness of the layer. This means that, when the orientational structure of LC varies smoothly from the homeotropic structure into the homeoplanar one, the transmittance increases to a maximum at an integral value of 0.317 µm and then decreases to $T = 32\%$, corresponding to an integral value of 0.511 µm. This behavior of transmittance is in good agreement with the experiment. It confirms the formation of the homeoplanar structure in the electric field.

The time of reaching the steady-state regime $\tau_{23} = 0.75$ s is in essence the time of the switching of surface anchoring plus the relaxation time of the homeotropic configuration in LC bulk into the homeoplanar structure (Figure 7.20(a)). The relaxation processes in LC are described by the formula (Blinov and Chigrinov, 1993)

$$\tau_{rel} = \frac{\gamma \cdot d^2}{\pi^2 \cdot K} \qquad (7.4)$$

where γ is the rotational viscosity of LC and K is the corresponding elasticity modulus. Taking the average value $K = 6.3$ pN (Cui and Kelly, 1999b) and $\gamma = 0.09$ Pa·s (Skarp et al., 1980b) for the 5CB LC, we obtain $\tau_{rel} = 0.05$ s. The τ_{23} value is larger

than τ_{rel} by a factor of 15 apparently because of the total effect of two orientational processes indicated above.

The transmittance curve behavior after the switching off electric pulse is even more complicated. In this case, LC layer at the beginning is subjected to the field of separated ions $E_i = E_0$. The classical Frederiks effect again occurs and is manifested in the reorientation of most of LC bulk along the field except for a thin layer near the lower substrate (Figure 7.20(b)). In the time interval $\tau_{45} = 0.02$ s, the transmittance undergoes the inverse evolution, first increasing to the same value of 68% and, then, decreasing to 14%. The complete quenching is impossible because of the presence of the above-mentioned surface region, where a certain phase mismatching of the beams is collected. The switch-on time of the classical Frederiks effect is given by the formula (Blinov and Chigrinov, 1993)

$$\tau_{on} = \frac{\gamma \cdot d^2}{\varepsilon_0 \cdot \Delta\varepsilon \cdot E^2 \cdot d^2 - \pi^2 \cdot K} \tag{7.5}$$

where $\Delta\varepsilon$ is the dielectric anisotropy of the nematic and E is the electric field strength acting on LC. Taking the above γ, d, and K values, as well as $\Delta\varepsilon = 11.2$ (Chandrasekhar, 1977b) and $E = 0.23 \times 10^6$ V/m, which were calculated considering the polymer coatings, we obtain $\tau_{on} = 0.03$ s. This estimate exceeds τ_{45} because the reorientation of LC by the field of ions in experiment remains incomplete. After the external field is switched off, two clouds of separated ions move toward each other. This leads both to a decrease in the LC layer between them, which is subjected to the field E_i, and to a gradual decrease in the field to zero. At the same time, the nematic layer adjacent to the electrode from which bromide anions leave grows rapidly. The recovery of the homeoplanar structure begins here. This process becomes dominant at time instant 5 and lasts at $\tau_{56} = 0.3$ s. This reorientation is in essence like a local transition in interval τ_{23}.

The process begins to complete at time instant 6; when surface-active CTA$^+$ ions approach, owing to diffusion, the substrate with the planar orienting coatings (Figure 7.20(c)). They are adsorbed on this substrate and begin to form the homeotropically orienting layer, returning the orientational structure of LC to the initial state (Figure 7.20(d)). In this case, the character of a transmittance change becomes opposite. For this reason, the shape of the curve section in the interval τ_{67} is an almost specular reflection of the interval τ_{56} at point 6, but is extended in time to the value $\tau_{67} = 0.95$ s.

Hence, compared with the classical Frederiks effect, where oscillations of the optical response to the leading and trailing edges of the rectangular electric pulse coincide in the number of extrema (Blinov and Chigrinov, 1993b), anchoring transition leads to a more complicated behavior of transmittance (Sutormin et al., 2012).

In addition, we considered the applied voltage dependences of the optical response dynamics of LC cell under study. Figure 7.21 shows the control electric pulses and optical response for several field values. Without an electric field, the transmittance of the cell is close to zero, and transmittance remains invariable as the control
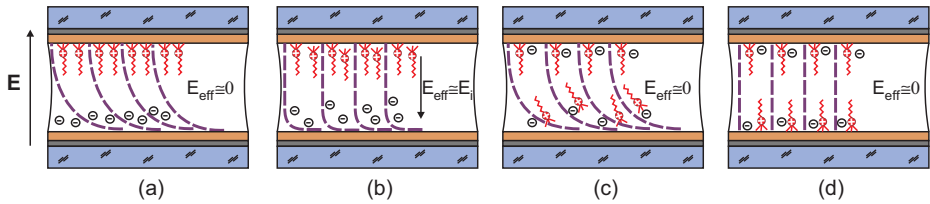
Figure 7.20: Distributions of the director and surfactant ions in the liquid crystal layer at time instants marked by the following numbers in Figure 7.19: (a) 4, (b) 5, (c) 6, and (d) 7.

voltage increases up to $U = 2.5$ V. When $U = 2.6$ V is attained, the variation in the transmittance of LC cell is observed: it reaches the maximum of 67% and then decreases to 29% by the time of the end of the electric pulse (Figure 7.21(a)). This variation is explained by the transition of the director from the homeotropic orientation into the hybrid (homeoplanar) one due to the ionic modification of the surface anchoring. An increase in the control field leads to gradual growth of the transmittance at the electric pulse finish to 64% at $U = 3.1$ V (Figure 7.21(b) and (c)). However, with further increase in the voltage, T gradually drops to 50% (Figure 7.21(d)). The physical mechanisms underlying the specific behavior of the curve $T(\tau)$ during the action of an electric pulse and after its switching off were described in detail above.

Figure 7.22 presents voltage dependences of the dynamic parameters of the optical response. Let us consider the first delay time τ_{del} determined as the time interval between the electric pulse switching on and the start of the transmittance variation (Figure 7.21(a)). As the pulse amplitude grows from 2.6 to 3.3 V, delay time τ_{del} drops from 1.6 to 0.1 s (Figure 7.22(a)). In contrast to the voltage dependence of τ_{del}, the dependence of the on-time τ_{on} determined as the interval between the electric pulse start and transmittance saturation (Figure 7.21(d)) is non-monotonic (Figure 7.22(b)). The value of τ_{on} rapidly decreases from 4.8 to 0.8 s in the voltage range 2.6–2.8 V. This drop in τ_{on} is caused by the acceleration of the modification of the surface anchoring on the substrate with the anode. However, at $U = 2.9$ V, τ_{on} jumps from 0.8 to 3.4 s, and then the on-time smoothly decreases again to 2.1 s at $U = 3.3$ V. It should be noted that an analogous anomaly was observed above in PDLC film controlled by the ionic-surfactant method (Krakhalev et al., 2011). In the range 2.6–2.8 V, τ_{off} grows from 0.3 to 1.1 s and then remains almost invariable up to 3.3 V (Figure 7.22(a)). Such a behavior is typical of many relaxation processes occurring, in particular, in LC cells with the classical Frederiks transition (Blinov, 2011).

The anchoring transitions in LC layers are very sensitive to the concentration and composition of the components. A key role of the protective layer should be noted, which prevents the direct arrival of surfactant ions at the ITO electrodes. In the absence of this layer in our experiments, as well as in Petrov and Durand (1994), electrohydrodynamic instability dominated in the transformation of the LC structure and prevented the observation of the modification of boundary conditions.
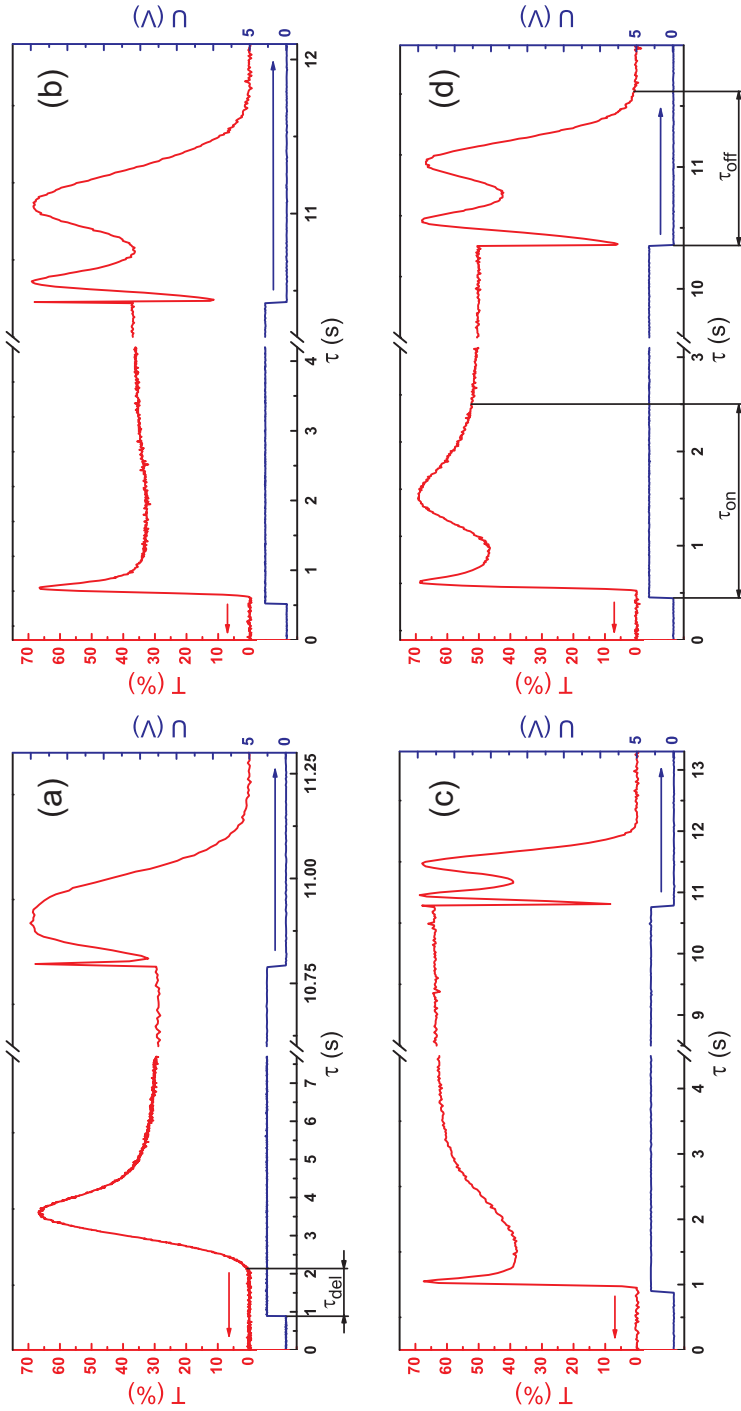
Figure 7.21: Dynamics of the optical response of LC cell controlled by ionic-surfactant method. The amplitude of applied voltage $U = 2.6$ V (a), 2.9 V (b), 3.1 V (c), and 3.3 V (d). The LC layer thickness is 6 µm.
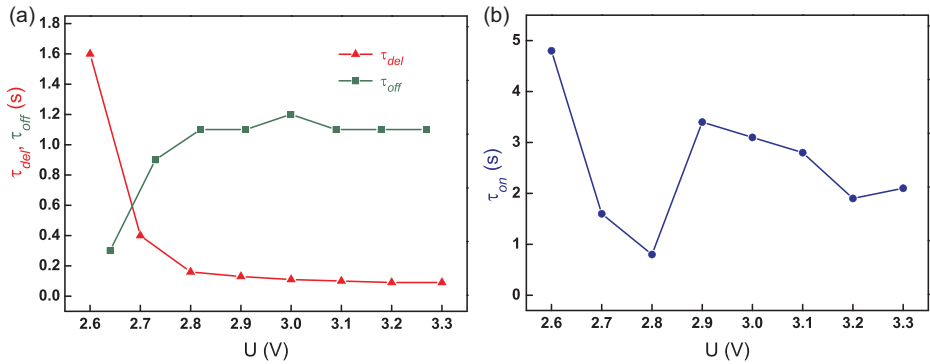
Figure 7.22: Control voltage dependences of delay time τ_{del} (a), relaxation time τ_{off} (a) and on-time τ_{on} (b) of LC cell.

7.3.2 Electrically induced anchoring transition in nematics with small or zero dielectric anisotropy

These experiments were carried out with sandwich-like cells (Figure 7.16). The rubbed polymer films based on the PVA doped with Gl in the weight ratio PVA:Gl = 1:0.29 were used as orienting coatings. The utilized LC materials were the nematic LC MBBA with $\Delta\varepsilon = -0.54$ at 25 °C and the MBBA−5CB mixture in the weight ratio 1:0.02, respectively. The MBBA−5CB mixture had the zero dielectric anisotropy. The nematics were preliminarily doped with ionic-surfactant CTAB in the weight ratio LC:CTAB = 1:0.008.

Since the main factor influencing the anchoring transition is the displacement of the surface-active ions, the same variant of the director reorientation can be realized for the different LCs independently of the sign and value of their dielectric anisotropy (Figure 7.16). For instance, the transition from the homeotropic director configuration to the homeoplanar one caused by the ionic modification of surface anchoring begins at $U = 2.7$ V for the cell based on MBBA ($\Delta\varepsilon < 0$) doped with CTAB. This value is close to the threshold voltage ($U_{th} = 2.8$ V) of 5CB cell operated by the ionic-surfactant method. The reorientation of MBBA cannot be explained by the Frederiks effect since the threshold field would be about 4 V for our cell. The reorientation of LC director is not accompanied by the electrohydrodynamic instability in the range of the control voltage 2.7 V ≤ U ≤ 4 V. The domain structure was formed only at the voltage $U ≥ 4.1$ V. The on/off time of the MBBA cell under the action of rectangular electric pulse is tens of seconds and exceeds the same parameters for the 5CB cell ($\propto 1$ s).

It should be emphasized that the analogous transformation of the orientational structure (Figure 7.16) occurs for the nematic with zero dielectric anisotropy. In the inserts of Figure 7.23, we demonstrate the change in the optical texture of the LC

cell based on the MBBA–5CB mixture ($\Delta\varepsilon = 0$) doped with CTAB and placed between the crossed polarizers under the action of DC electric field. In the initial state, the optical texture of the LC layer is a uniform dark area (left insert of Figure 7.23). The DC electric field induces the modification of the surface anchoring which results in the formation of the hybrid LC structure. This transition leads to the increase of the light transmission of the system (right insert of Figure 7.23). As for other LCs, the reorientation in the cell filled with MBBA–5CB mixture ($\Delta\varepsilon = 0$) exhibits a threshold character starting from 3 V which is approximately equal to the threshold voltages of 5CB cell and MBBA cell operated by the ionic-surfactant method. At the control voltage 3.0 V ≤ U ≤ 4.1 V, the optical texture of LC layer is a uniform light area without a domain structure which begins to form at U > 4.1 V. Thus, the ionic-surfactant method provides an opportunity of the electrically controlled director reorientation of LC with zero dielectric anisotropy.
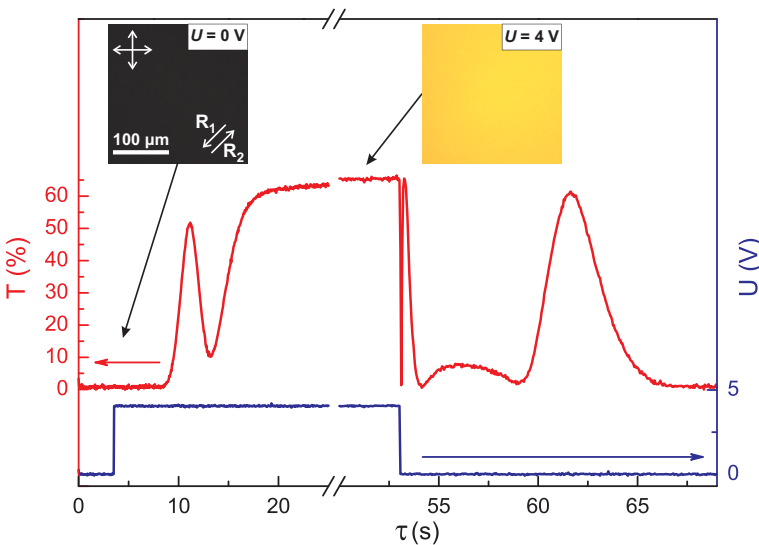
Figure 7.23: Optical response of LC cell based on the MBBA–5CB mixture ($\Delta\varepsilon = 0$) doped with CTAB (the top curve) and electric 4 V pulse (the bottom curve). The inserts show optical textures of LC cell in the initial state (left insert) and under the DC electric field 4 V (right insert). R_1 and R_2 are rubbing directions of the top and bottom substrates, respectively.

7.3.3 Ionic-surfactant-doped nematic layer with homeoplanar– twisted configuration transition

In this section, the transition from the homeoplanar orientational structure to the twisted one induced by the ionic modification of surface anchoring is considered. Such orientational transition leads to a decrease in switching times of LC cell with

ISO. LC cell under study was comprised of two glass substrates with ITO electrodes covered by different polymer films and nematic layer between them (Figure 7.24). The bottom substrate was coated with PVA, while the film of PVA doped with glycerin compound (Gl) in the weight ratio 1:0.432 was deposited at the top substrate. The polymer films were formed using a spin coating technique and then were rubbed. The rubbing directions of polymer films at both substrates were mutually perpendicular. The cell gap was filled with LC 5CB containing CTAB in the weight ratio 1:0.008. The LC layer thickness was 6 μm.

Figure 7.24 demonstrates the scheme of transition from the homeoplanar orientational structure to the twisted configuration. The homeoplanar director configuration was realized, owing to the different polymer films at the substrates of the LC cell. The homeotropic surface anchoring was formed at the top substrate covered with PVA–Gl film (Figure 7.24(a)). The PVA and glycerin assign the planar boundary conditions for nematic (Cognard, 1982; Volovik and Lavrentovich, 1983), but the surface-active CTA^+ cations adsorbed at the top substrate screen the orienting action of the PVA–Gl film and specify normal boundary conditions. The film of pure PVA deposited at the bottom substrate specified the planar surface anchoring for considered concentrations of CTAB in 5CB. Probably, the pure PVA exhibits a stronger planar action than the PVA containing Gl.
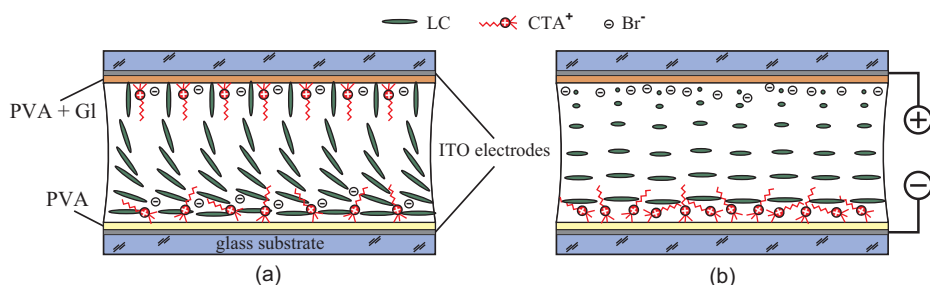
Figure 7.24: Scheme of transition of nematic layer from the homeoplanar orientational structure (a) into the twisted one (b) induced by the ionic modification of surface anchoring. (a) In the absence of electric field, the planar boundary conditions are formed at the bottom substrate while the surface anchoring at the top substrate is homeotropic. (b) The application of DC voltage with indicated polarity initiates the modification from homeotropic boundary conditions to planar one at the top substrate. At the same time, the surface anchoring at the bottom substrate is unchanged. The rubbing directions of the polymer orienting coatings are mutually orthogonal.

The applied DC electric field of suitable polarity leads to the decrease of the surface density of the CTA^+ cations at the top substrate and the planar surface anchoring is formed at this substrate (Figure 7.24(b)). The planar boundary conditions at the bottom substrate remain unchanged. As a result, the 90° twisted director configuration is realized in the LC cell due to the mutually orthogonal rubbing directions at the

substrates. The described orientational transition corresponds to the inverse regime of electrically controlled ionic modification of surface anchoring which was observed previously inside the nematic droplets (Zyryanov et al., 2008).

The changes of the optical texture of the LC layer caused by the transition from homeoplanar orientational structure to the twisted one are demonstrated in Figure 7.25. In the initial state, the LC cell placed between crossed polarizers was observed as uniform dark area when α angle between rubbing direction of the bottom substrate ($\mathbf{R}_1$) and polarizer was 0° or 90° (Figure 7.25(a) and (c), first row). The brightest optical texture appeared at $\alpha = 45°$ (Figure 7.25(b), first row). Such changes of optical texture are the evidence that the homeoplanar orientational structure was formed in the LC cell. It should be noted that the LC cell with uniform planar director configuration shows similar changes of optical textures when the sample is rotated between crossed polarizers. However, in LC cell under study the rubbing directions of orienting layers at both substrates were mutually orthogonal and, consequently, the untwisted planar configuration was unrealizable.

The optical textures of LC cell placed between crossed polarizers are not dark at any α angle when the DC voltage of 3.3 V was applied to the sample (Figure 7.25, second row). At the same time, the dark optical texture was observed in the scheme of parallel polarizers when α angle was equal to 0° or 90° (Figure 7.25(a) and (c), third row). It shows that the LC layer rotated a light polarization by 90°. Thus, the twisted director configuration was formed in the sample under the applied voltage.

It should be emphasized that the changes of LC patterns cannot be attributed to the Frederiks effect (Chandrasekhar, 1977), since the nematic 5CB has the positive dielectric anisotropy, and the electric field applied perpendicularly to the LC layer would lead to the formation of homeotropic director configuration. LC cell with such director configuration placed between crossed polarizers exhibits the dark optical pattern for any α angle. However, this disagrees with experimental observations (Figure 7.25, second row). Consequently, the observed changes of optical texture initiated by the ionic modification of boundary conditions at one of the substrates confirm the transition of nematic layer from the homeoplanar orientational structure into the twisted configuration.

Figure 7.26 shows the electro-optical response of the LC cell placed between crossed polarizers. An LC cell is controlled by square-wave monopolar (Figure 7.26(a) and (b)) and bipolar (Figure 7.26(c)) electric pulses. The positive-polarity pulse amplitude is 3.3 V and its duration is 9.8 s. For negative-polarity pulse, the amplitude is 2.2 V and its duration is 0.16 s.

The change of light transmittance of the LC cell with $\alpha = 45°$ is presented in Figure 7.25(b), and first and second rows are shown in Figure 7.26(a). The reorientation of LC induced by the ionic modification of surface anchoring leads to the change of phase retardation between two linearly polarized components of light passed through the nematic layer. For this case, the values of both on-time τ_{on} and
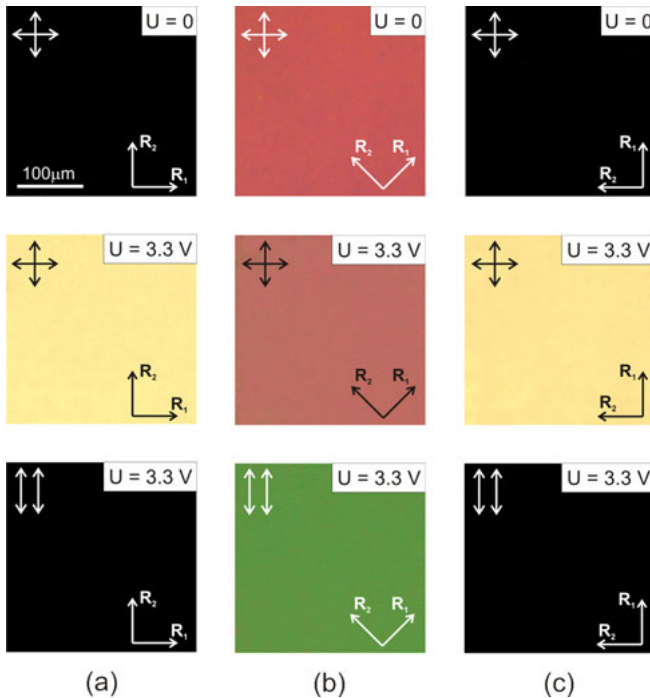
Figure 7.25: Photos of LC cell filled with 5CB containing CTAB taken in crossed polarizers scheme (first and second rows) and in parallel polarizers (third row). The α angle between the rubbing direction of the bottom substrate (R_1) and the polarizer is 0° (a), 45° (b), and 90° (c). R_2 is the rubbing direction of the top substrate. The first row presents the switched-off state. The second and third rows are the optical patterns under DC voltage $U = 3.3$ V.

off-time τ_{off} were close to the response times of the LC cell with transition from homeotropic director configuration to homeoplanar one (Sutormin et al., 2012, 2013).

The optical responses of the LC cell for $\alpha = 0°$ or 90° (see Figure 7.25(a) and (c), first and second rows) are presented in Figure 7.26(b) and (c). In this case, the single linearly polarized light component passes through the nematic layer. When the electric field is switched off, the light transmission of LC cell with homeoplanar orientational structure is close to zero. The positive-polarity pulse of the applied electric field leads to the formation of the twisted director configuration and the transmittance grows to 60%.

When the monopolar electric pulse is applied (Figure 7.26(b)), the values of τ_{on} and τ_{off} for LC cell with $\alpha = 0°$ or 90° are equal to 190 and 240 ms, respectively. These values are much less than the switching times both of the LC cell for $\alpha = 45°$ (Figure 7.26(a)) and the LC cell with homeotropic–homeoplanar configuration transition (Sutormin et al., 2012, 2013).

The switching-off time of the LC cell with ISO can be considerably decreased by varying the waveform of the electric pulse. For instance, the application of the bipolar electric pulse allowed decreasing τ_{off} to 11 ms (Figure 7.26(c)). When the negative-polarity electric pulse was applied to the LC cell, the CTA$^+$ cations returned to the top substrate faster and, consequently, the homeoplanar orientational structure was restored more rapidly.
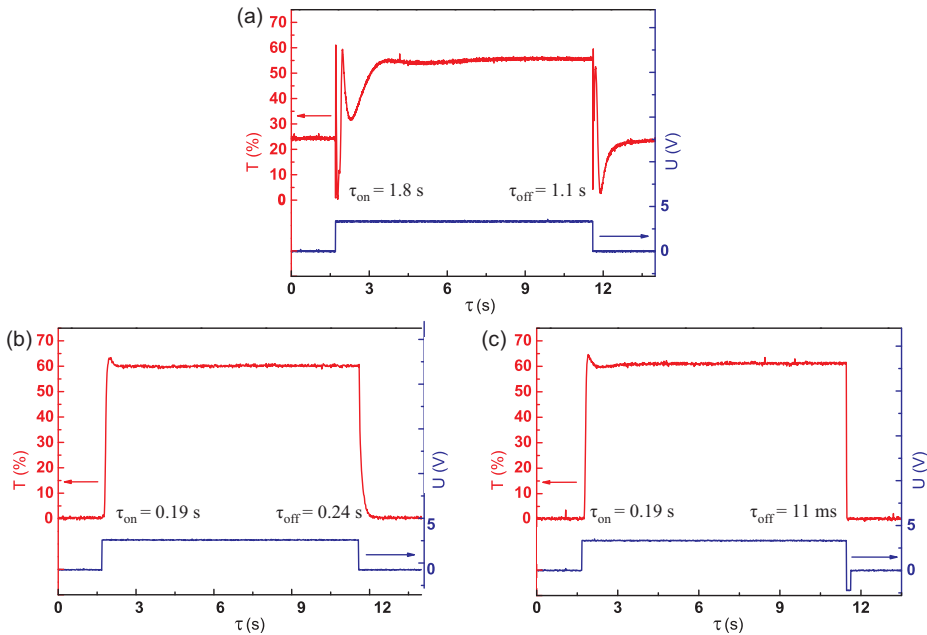
Figure 7.26: Optical responses of LC cell filled with nematic 5CB containing CTAB in crossed polarizers. The LC cell with $\alpha = 45°$ was controlled by a monopolar electric pulse (a), with $\alpha = 0°$ or 90° controlled by a monopolar electric pulse (b), and with $\alpha = 0°$ or 90° controlled by a bipolar electric pulse (c). τ_{on} and τ_{off} represent the on-time and off-time, respectively.

It should be emphasized that other methods to decrease the switching times of LC cells with ISO can be implemented; for instance, the utilization of LCs with lower viscosity and the decreasing of LC layer thickness.

7.3.4 Electrically induced anchoring transition in the ionic-surfactant-doped cholesteric layers with different confinement ratios

Electrically induced anchoring transition in the ionic-surfactant-doped cholesteric layers with confinement ratio $\rho < 1$. In this section, a reorientation of ChLC with a large helix pitch induced by the electrically controlled ionic modification of the surface anchoring

is considered (Sutormin et al., 2017). LC cells under study comprises two glass substrates with ITO electrodes coated with polymer films and the cholesteric layer between them. The polymer films based on PVA doped with glycerin compound in the weight ratio PVA:Gl = 1:0.383 were used as orienting coatings. The polymer films were deposited by spin coating and rubbed. The cell gap thickness d was set using teflon spacers and measured by means of the interference method (Huibers and Shah, 1997) with the spectrometer. Cholesteric mixtures were prepared using the nematic 5CB with the chiral additive ChA in the weight ratio of 5CB:ChA from 1:0.0030 to 1:0.0155, respectively. The nematic was preliminary doped with CTAB in the weight ratio of 5CB: CTAB = 1:0.002. The helical twisting power HTP = 6.5 μm^{-1} of the additive ChA in the nematic 5CB was determined with the droplet method (Candau et al., 1973). The used mixtures had pitch $10 \leq p \leq 51$ μm as calculated from $p = 1/(HTP \times c_w)$, where c_w is weight concentration of the chiral agent. The confinement ratio $\rho = d/p$ in LC cells was $0.16 \leq \rho \leq 0.85$.

Figure 7.27 demonstrates the change of optical texture of the cholesteric layer doped with the ionic surfactant under DC voltage. In the given LC cell, the confinement ratio $\rho = 0.4$. When the electric field is switched off, the optical texture of LC layer in crossed polarizers is a uniform dark area (Figure 7.27(a)) independently of the sample rotation on the microscopic stage. Such an optical texture remains invariable until $U = 2.3$ V. The latter was accompanied with the increase in light transmission. In the range of control voltages 2.6 V ≤ U ≤ 3.4 V, the optical texture of the cell is a uniform bright area (Figure 7.27(b)). At that, the sample rotation relative to the crossed polarizers does not lead to the dark texture. The optical textures shown in Figure 7.27(b) and (c) prove this. Here, the angle α between the rubbing direction and polarizer is 45° and 0°, respectively. Besides, at $\alpha = 0°$ (Figure 7.27(c)), the dark texture is not obtained either under the analyzer rotation. At the control voltage $U = 3.5$ V, the domains began to form in the LC cell and they appear clearly at $U = 3.7$ V (Figure 7.27(d)).
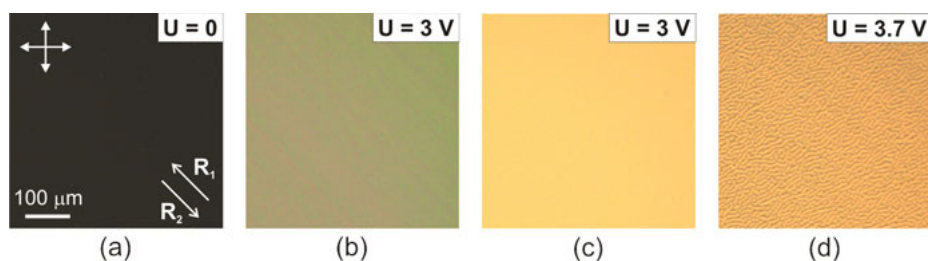
Figure 7.27: POM images of the optical textures of the cholesteric layer doped with ionic surfactant taken under variable control voltage U and α-angles between the rubbing direction of the bottom substrate (**R₁**) and the polarizer: (a) $U = 0$ V, $\alpha = 45°$; (b) $U = 3$ V, $\alpha = 45°$; (c) $U = 3$ V, $\alpha = 0°$; (d) $U = 3.7$ V, $\alpha = 45°$. The cell gap thickness $d = 8.1$ μm. Confinement ratio is $\rho = 0.4$. **R₂** is the rubbing direction of the top substrate.

The similar changes of optical texture were observed in LC cells with $\rho = 0.16$ and 0.85 approximately under the same control voltage. The only difference of the initial texture of cholesteric layer with $\rho = 0.85$ is the presence of a small number of cholesteric bubbles (Kleman and Friedel, 1969). However, after the application of AC voltage, the cholesteric bubbles disappear, and the optical texture of LC layer is the uniform dark area.

The dark texture of LC layer in the absence of electric field (Figure 7.27(a)) and its invariability at the sample rotation relative to the crossed polarizers indicate a complete untwisting of the cholesteric helix and the formation of the homeotropic director orientation due to the ionic-surfactant CTAB added (Figure 7.28(a)). The cholesteric helix untwisting occurs as an effect of the normal anchoring of LC molecules with the substrates (Harvey, 1977). The formation of homeotropic or twisted structures within the cholesteric layer with rigid normal anchoring depends on the confinement ratio ρ. The transition threshold ρ_{th} value is defined by the following equation (Zel'dovich and Tabiryan, 1981):

$$\rho_{th} = K_{33}/(2K_{22}) \tag{7.6}$$

where K_{33} and K_{22} are elastic constants of the bend and twist deformations in LC, respectively. When $\rho < \rho_{th}$, the helix pitch is completely untwisted inside the LC cell with rigid normal anchoring. The twist structure is formed at $\rho > \rho_{th}$. The typical materials have the threshold value ρ_{th} of about 1 (Oswald et al., 2000). The samples under study have $\rho < 1$, which makes the helix pitch completely untwisted in the initial state.

When the DC electric field is applied, the surface anchoring on the electrode–anode substrate is modified, and the planar anchoring proper to the polymer orienting coating is restored at this substrate. The modification of the boundary conditions results in the reorientation of the LC structure and, consequently, in the change of the optical texture of the LC cell in the crossed polarizers (Figure 7.27(b)). Since the considered optical texture does not get dark completely during the sample rotation on the microscope stage relative to the crossed polarizers (Figure 7.27(b) and (c)), it means that the twisted orientational structure is formed within the LC layer. Thus, the optical textures of the LC layer presented in Figure 7.27(b) and (c) correspond to the hybrid-aligned cholesteric (HAC) structure (Belyaev et al., 1988; Dozov and Penchev, 1986; Hsiao et al., 2015; Lewis and Wiltshire, 1987; Ryabchun et al., 2015). Its orientational structure is schematically shown in Figure 7.28(b). It should be emphasized that the observable changes of optical texture cannot be induced by the Frederiks effect because the LC used in our experiment has positive dielectric anisotropy. In this case, the Frederiks effect could result only in the stabilization of the initial homeotropic director configuration.

As mentioned above, the optical texture (Figure 7.27(c)) does not become dark completely under the analyzer rotation when the polarization direction of incident
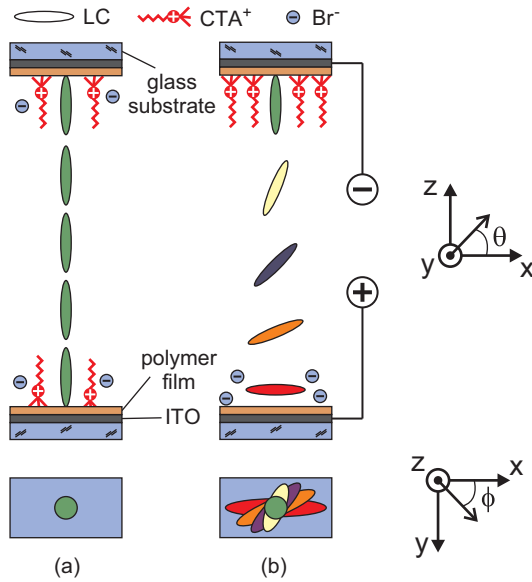
Figure 7.28: Scheme of the orientational transition induced by the DC electric field inside the cell filled with the ChLC doped by the ionic surfactant. The homeotropically aligned LC layer in initial state (a). The cholesteric layer with a hybrid structure is formed, owing to the homeotropic–planar change of surface anchoring on the electrode–anode substrate (b). θ is a tilt angle and ϕ is a twist angle. The bottom row is a top view.
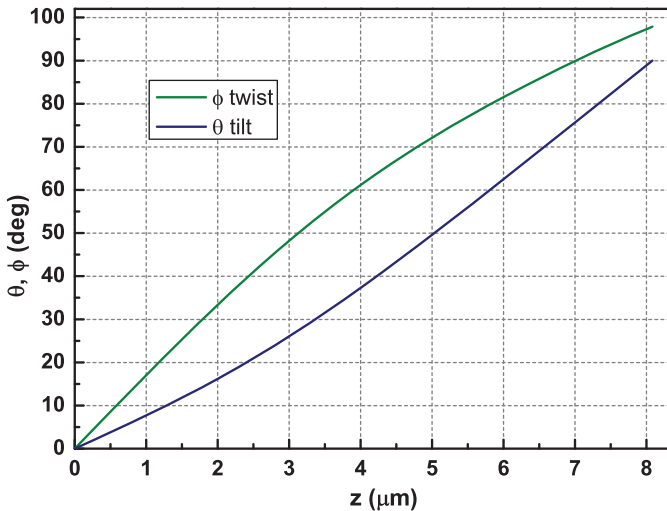
Figure 7.29: Calculation data of tilt angle θ and twist angle ϕ of the director versus the z-coordinate perpendicular to the cell substrates for the hybrid-aligned cholesteric structure. $z = 0$ and $z = 8.1\ \mu m$ correspond to the substrates with planar and homeotropic surface anchoring, respectively. Thickness of the LC layer is $d = 8.1\ \mu m$. The helix pitch is $p = 21\ \mu m$.

light coincides with the substrate rubbing direction. It indicates that the light after passing through the layer of hybrid-aligned ChLC is no longer linearly polarized. The light polarization change for such a system has been simulated. First, the cholesteric orientational structure within the cell was calculated by means of the energy minimization of elastic deformations of the director field (Timofeev et al., 2012) under asymmetric boundary conditions. The LC surface anchoring on one of the substrates was planar and another one was homeotropic. Then applying the Berreman 4×4-matrix method (Berreman, 1972), the light polarization after the LC-layer transmission was simulated. The following parameters of 5CB were used for the calculations: the elastic constants of the splay deformation $K_{11} = 5.7$ pN, the twist deformation $K_{22} = 3.5$ pN, and the bend deformation $K_{33} = 7.7$ pN (Cui and Kelly, 1999b); the extraordinary and ordinary refractive indices $n_e = 1.7002$, $n_o = 1.5294$ ($\lambda = 632.8$ nm), respectively (Bunning et al., 1986); the thickness of LC layer $d = 8.1$ μm, the helix pitch $p = 21$ μm, and the confinement ratio $\rho = 0.4$.

Figure 7.29 shows the calculation data for the hybrid-aligned cholesteric structure. The simultaneous tilt and twist of the director are shown to occur inside the LC layer. The total twist angle of director is 98°. The Berreman method simulation has revealed that the linearly polarized light beam ($\lambda = 632.8$ nm) passing through such an LC orientational structure gets elliptically polarized. The ratio of major axis to minor axis of the polarization ellipse is 3.8. At that, the β angle between the polarization direction of incident light and the major axis of elliptically polarized light is 68° when leaving the LC layer.

We measured β angle depending on the control voltage value. The cell was placed between the crossed polarizers so that the rubbing direction of input substrate coincided with the polarization direction of incident He–Ne laser beam. After that, the DC voltage was applied to the LC cell. When the light transmission reached the saturation, which corresponds to the formation of the hybrid-aligned ChLC, the minimal light transmission of the system was found by means of the analyzer rotation. In this case, the direction of major axis of the elliptically polarized light was perpendicular to the analyzer direction. In the range 2.6–3.2 V of control voltages, β angle changed from 62° to 64°, respectively. These data are in good accordance with the calculated results.

Figure 7.30 shows the oscillograms of the square-wave response of the LC cell placed between crossed polarizers. The pulse amplitude is 2.6 V and its duration is 10 s. The oscillogram in Figure 7.30(a) corresponds to the situation when the polarization of incident light coincides with the rubbing direction ($\alpha = 0°$), and $\alpha = 45°$ in Figure 7.30 (b). In the initial state, the light transmission of the system is close to zero because of the homeotropic director orientation. The applied electric pulse increases the light transmission caused by the formation of the HAC structure. If the polarization of incident light coincides with the rubbing direction (Figure 7.30(a)), the light transmission saturation reaches 58%. The on-time τ_{on} was 0.31 s, and the off-time τ_{off} was 0.51 s. For $\alpha = 45°$, the transmittance saturation reached 51% (Figure 7.30(b)),

τ_{on} = 0.13 s, τ_{off} = 0.59 s. Under the control voltages $2.6 \leq U \leq 3.2$ V, the on-time τ_{on} did not practically change. The off-time τ_{off} in the same range of voltages increased up to 1.75 s. It should be noted that the change in the control pulse form is able to lead to a significant improvement of the dynamic characteristics of an LC cell with electrically controlled ionic modification of the surface anchoring (Sutormin et al., 2014).

Electrically induced anchoring transition in the ionic-surfactant-doped cholesteric layers with confinement ratio $\rho > 1$. We considered also a change of ChLC orientation initiated by the ionic modification of boundary conditions in the layers with confinement ratio $\rho > 1$ (Sutormin et al., 2018b). The investigations were performed with the same LC cells as in the previous section. The substrates of the cells were covered by the polymer films using spin coating technique and then these layers were unidirectionally rubbed. The polymer films were PVA containing glycerin compound (Gl) in the weight ratio PVA:Gl = 1:0.479. The cholesteric under study was a mixture of nematic 5CB and ChA in the weight ratio ranging between 1:0.0233 and 1:0.0658. In addition, ChLC contained ionic-surfactant CTAB in a weight ratio 5CB:CTAB = 1:0.0041. In the utilized mixtures, the intrinsic cholesteric pitch varied from 2.6 to 7.1 μm, and the confinement ratio was $1.2 \leq \rho \leq 8$. Filling of cells was performed with ChLC in the isotropic phase. The diffraction patterns were observed utilizing He–Ne laser with wavelength λ = 632.8 nm.

At first, the reorientation of the director in LC cells under application of the 1 kHz AC voltage was studied. The optical patterns of the ChLC layer with the confinement ratio ρ = 1.2 observed for several values of the applied AC voltage are presented in Figure 7.31. The intrinsic pitch p was 7.1 μm and the ChLC thickness d = 8.2 μm. In the absence of electric field the fingerprint pattern is observed (Figure 7.31(a)). When AC voltage is applied to the sample, the initial optical texture changes gradually into a dark area (Figure 7.31(b)–(d)). It should be noted that the rotation of the sample between two crossed polarizers does not lead to the changing of dark optical pattern.
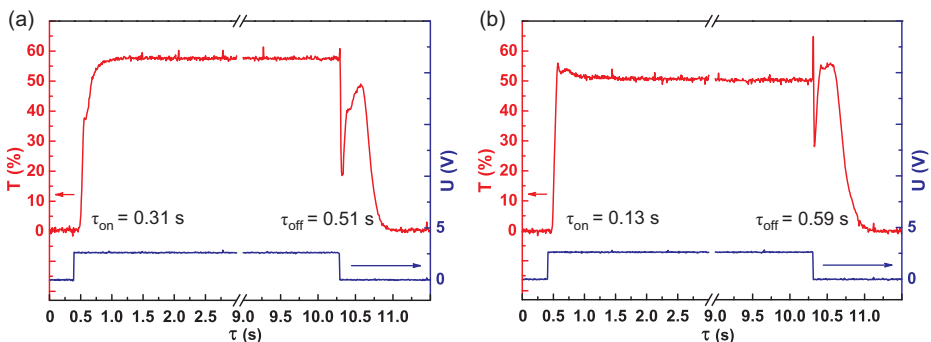
Figure 7.30: Optical response of the LC cell filled with the ionic-surfactant-doped cholesteric layers in crossed polarizers at different α-angles between the polarizer and the rubbing direction: (a) α = 0°; (b) α = 45°. Applied voltage amplitude is 2.6 V. Confinement ratio is ρ = 0.4.
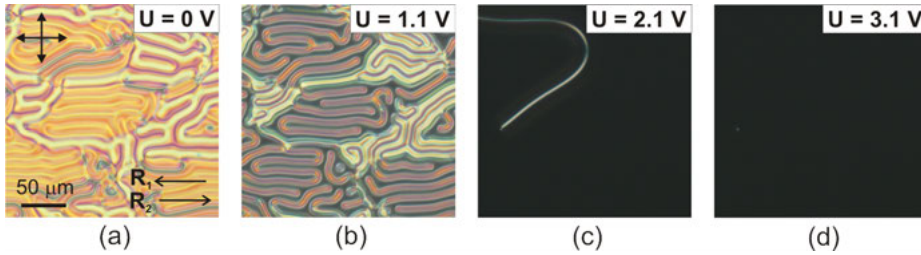
Figure 7.31: Photos taken in crossed polarizers of the cholesteric layer with the ionic surfactant additive for AC voltages $U = 0$ V (a), 1.1 V (b), 2.1 V (c), and 3.1 V (d). The intrinsic cholesteric pitch $p = 7.1$ μm. Confinement ratio $\rho = 1.2$. The rubbing directions of the bottom and top substrates are marked by $\mathbf{R}_1$ and $\mathbf{R}_2$, hereinafter.

As stated above, depending on the ratio d/p the untwisted or twisted ChLC orientational structures in the cell with rigid homeotropic boundary conditions can be realized. The transition between these configurations occurs at the critical value of d/p, which is assigned by the ratio of elastic constants for bend and twist deformations (Zel'dovich and Tabiryan, 1981). In typical LC substances, the critical value of d/p is about 1 (Oswald et al., 2000) and for this reason, the fingerprint pattern corresponding to the twisted director configuration was realized in the sample with $\rho = 1.2$ (Figure 7.31(a)).

Applied AC voltage initiates the reorientation of LC director along the electric field owing to the positive dielectric anisotropy of the cholesteric. This process leads to the transition of twisted ChLC alignment into the homeotropic orientational structure whose optical pattern is demonstrated in Figure 7.31(d). The similar change of director configuration occurred in other samples with ρ ranging between 1.2 and 8. The higher AC voltage was necessary to produce the homeotropic orientational structure in samples with larger values of confinement ratio. Furthermore, in some samples, the AC voltage initiated the hydrodynamic flows, which led to the formation of particular optical textures (Figure 7.32) like the ones demonstrated by Ribiére et al. (1994).
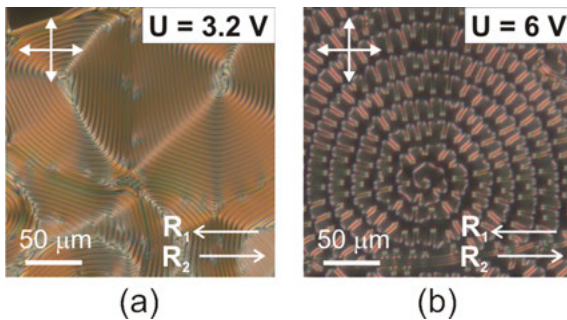
Figure 7.32: Photos taken in crossed polarizers of the cholesteric layers with the ionic-surfactant additive under application of an AC voltage. (a) $\rho = 1.9$ and $U = 3.2$ V; (b) $\rho = 3.2$ and $U = 6$ V.

Completely different changes of the ChLC optical pattern were observed under the action of a DC electric field (Figure 7.33). In the initial state, the fingerprint texture is realized (Figure 7.33(a)). When the value of applied DC voltage is smaller than 2.7 V, the fingerprint texture does not change. The striped domain structure with defects is formed in the range of DC voltage from 2.7 to 3.3 V (Figure 7.33(b)–(d)). A higher value of DC voltage leads to the appearance of domains that are due to electro-hydrodynamic instability in cholesteric layers. A number of defects in the striped domain structure can be decreased considerably using the preliminary action of AC voltage pulse.
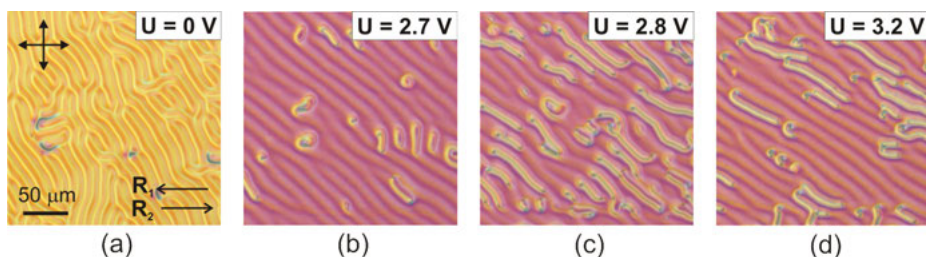
Figure 7.33: Photos taken in crossed polarizers of the cholesteric layer with the ionic-surfactant additive for DC voltages $U = 0$ V (a), 2.7 V (b), 2.8 V (c), and 3.2 V (d). The intrinsic cholesteric pitch $p = 7.1$ μm. Confinement ratio $\rho = 1.2$.

As an example, Figure 7.34 demonstrates the striped domain structures realized under DC voltage $U = 3.0$ V with and without preliminary action of 1 kHz AC voltage of 10.3 V value. Obviously, in the case of preliminary action of AC voltage, the number of defects in the striped domain structure decreased considerably. The transformations of ChLC optical texture presented in Figure 7.33 are initiated by the modification of boundary conditions at the anode−substrate. Initially, the normal surface anchoring of cholesteric layer is realized on both substrates due to the adsorbed CTA^+ cations. Applied DC electric field causes decreasing the surface density of CTA^+ cations at the anode−substrate. As a result, the tangential surface anchoring specifying the polymer layer is formed at this substrate and the director configuration inherent in HAC layer is realized in the bulk. Depending on the ratio between ChLC thickness and cholesteric pitch, the director configuration of uniform HAC (UHAC) or modulated HAC (MHAC) structure can be appeared in the layer with asymmetric boundary conditions (Dozov and Penchev, 1986b). The simultaneous twist and tilt of director takes place along the normal to the substrates in the orientational structure of HAC. LC orientation in the plane of the layer is uniform in the case of UHAC director configuration. But in the MHAC structure, the surface layer with periodically distorted cholesteric helix axis is formed near the substrate with normal surface anchoring (Baudry et al., 1996; Dozov and Penchev, 1986).

For this reason, the cholesteric layers with UHAC and MHAC director configurations exhibit the different optical textures. The cholesteric with UHAC director configuration appears as a uniform bright area, whereas the optical texture of ChLC with MHAC director configuration is a stripe domain pattern and orientation of domains is specified by the confinement ratio (Baudry et al., 1996; Belyaev et al., 1988; Dozov and Penchev, 1986; Lin et al., 2012; Nose et al., 2010; Ryabchun et al., 2015). It was shown by Belyaev et al. (1988) that the change between UHAC and MHAC director configuration occurs at the confinement ratio of about 1 and this agrees with our experimental data.
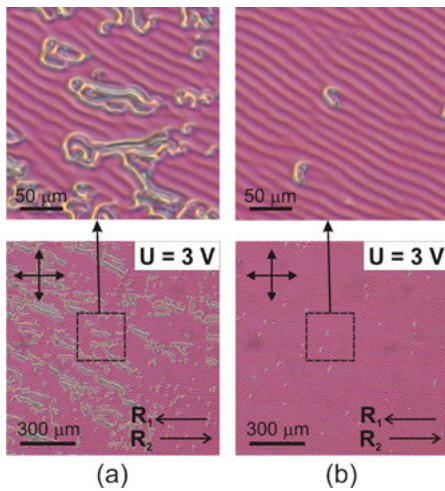
Figure 7.34: Photos taken in crossed polarizers of the cholesteric layer containing the ionic-surfactant additive for DC voltage $U = 3.0$ V without the preliminary action of AC electrical field (a) and with the preliminary effect of 1 kHz AC electrical field of 10.3 V value (b). The scaled-up parts of LC textures are shown in the top row. The intrinsic cholesteric pitch $p = 7.1$ µm and confinement ratio $\rho = 1.2$.

The electrically controlled ionic modification of boundary conditions induced the appearance of UHAC director configuration in the samples with $\rho < 1$ and the optical pattern of ChLC layer looked like a uniform bright area (Sutormin et al., 2017b). In LC layer with $\rho = 1.2$, the application of DC voltage (Figures 7.33 and 7.34) initiated the formation of MHAC director configuration, and the stripe domain pattern was observed.

Figure 7.35 demonstrates the change of optical pattern of ChLC layer under the action of DC electric field in the sample with a confinement ratio $\rho = 1.9$. It is seen that the transformation of the pattern is similar to the observed changes in the sample with $\rho = 1.2$. The initial optical pattern does not change when the value of applied DC voltage is smaller than 2.6 V. The striped domain texture with defects is formed in the range of DC voltages from 2.7 to 3.4 V. But a number of defects were
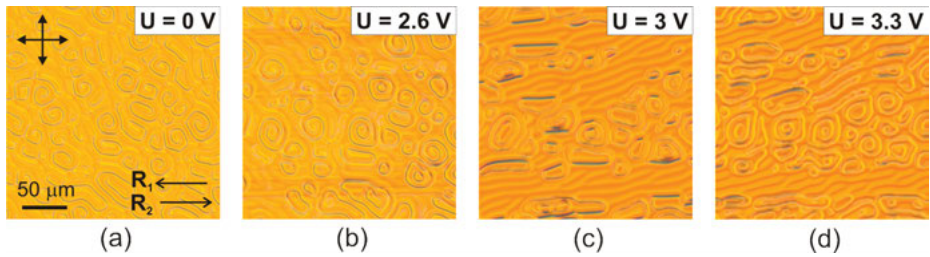
Figure 7.35: Photos taken in crossed polarizers of the cholesteric layer with the ionic-surfactant additive for DC voltages $U = 0$ V (a), 2.6 V (b), 3.0 V (c), and 3.3 V (d). The intrinsic cholesteric pitch $p = 4.2$ μm, and confinement ratio $\rho = 1.9$.

greater than the sample with confinement ratio $\rho = 1.2$, and a high-quality stripe domain pattern could not be formed utilizing the preliminary influence of AC voltage.

In the sample with confinement ratio $\rho = 3.2$ (Figure 7.36), the director reorientation process initiated by the ionic modification of boundary conditions starts from the DC voltage $U = 2.7$ V, whose value is close to the threshold voltages in samples with $\rho = 1.2$ and 1.9. One can see that the layer areas with a periodic stripe domain texture are very small (Figure 7.36(c)). In the sample with confinement ratio $\rho = 8$, the action of DC electric field did not initiate the visible transformations of optical pattern at all.

Lin et al. (2012) experimentally showed that the MHAC director configuration appears as high-quality stripe domain pattern only in a narrow range of the confinement ratios. When the confinement ratio exceeded the upper range limit, a large number of defects were observed in the stripe domain pattern. It was proposed that the strength of tangential surface anchoring became insufficient to produce a defect-free structure (Lin et al., 2012). This is probably the reason for the formation of the striped domain pattern with a different number of defects in our investigated samples. Besides, the observed striped domain pattern had more defects in the samples with higher values of confinement ratio.

The dynamic characteristics of the LC cell driven by ionic-surfactant method are specified by a number of processes such as the motion of CTA^+ cations, the modification of boundary conditions, and the change of LC orientation in the layer (Sutormin et al., 2012). The on-time and off-time of investigated cholesteric cells were of the order of 1 s. These dynamic characteristics agreed with the response times of nematic cells driven by the ionic-surfactant method (Sutormin et al., 2012, 2013).

It is known that the MHAC structure is suitable to produce the diffraction grating, which can be controlled by the electric field, light radiation, or temperature (Lin et al., 2012; Nose et al., 2010; Ryabchun et al., 2015). The external actions change the cholesteric pitch and initiate the rotation of the stripe domains. For this reason, it is interesting to investigate the diffraction patterns obtained after passing the laser beam through the cholesteric cell with ISO. The sample with confinement ratio $\rho = 1.2$ was examined. To obtain the high-quality stripe domain pattern (Figure 7.34(b)), the preliminary
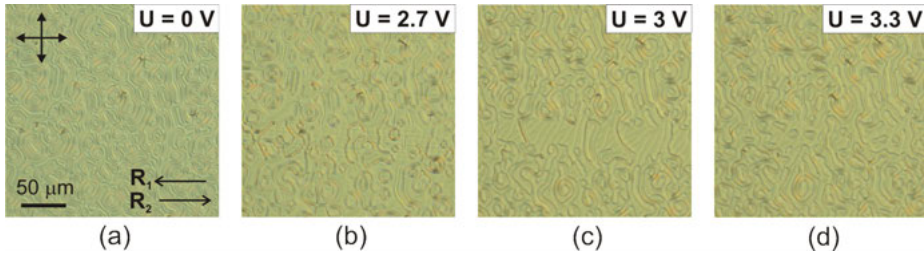
Figure 7.36: Photos taken in crossed polarizers of the cholesteric layer with the ionic-surfactant additive for DC voltages $U = 0$ V (a), 2.7 V (b), 3.0 V (c), and 3.3 V (d). The intrinsic cholesteric pitch $p = 2.6$ μm, and confinement ratio $\rho = 3.2$.

action of 1 kHz AC voltage of 10.3 V was used. Figure 7.37 presents the change in diffraction pattern initiated by the applied DC voltage $U = 3.0$ V. In the initial state, the diffraction pattern was concentric rings (Figure 7.37(a)) owing to the fingerprint texture without preferred domain orientation was formed in the sample (Figure 7.33 (a)). Applied DC voltage initiated the formation of optical texture containing the stripe domains (Figure 7.34(b)), and the diffraction pattern changed to a set of three light reflexes (Figure 7.37(b)). The diffraction pattern remained almost unchanged in the range of applied voltages from 2.7 to 3.2 V, and it was the evidence that the rotation of stripe domains did not occur. Consequently, a switching between only two diffraction patterns can be obtained by using the ionic modification of boundary conditions.
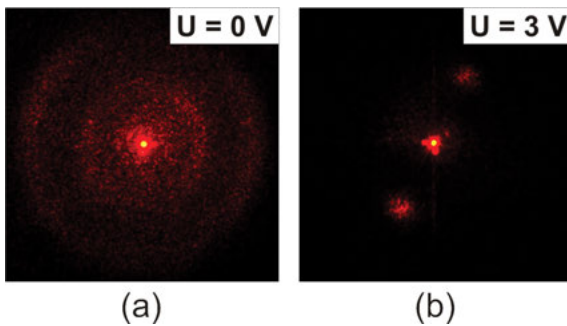
Figure 7.37: Change of diffraction pattern behind the ChLC layer under the application of DC voltage. (a) $U = 0$ V and (b) $U = 3.0$ V. The intrinsic cholesteric pitch $p = 7.1$ μm, and confinement ratio $\rho = 1.2$.

7.4 Conclusions

In this chapter, we have demonstrated that the ISO method can be successfully applied to the state switching of NLCs and ChLCs irrespective of both the value and sign of their dielectric anisotropy $\Delta\varepsilon$, and it is even applicable to LCs with $\Delta\varepsilon = 0$. It is well known that zero-$\Delta\varepsilon$ LCs cannot in principle be controlled by the classical Frederiks effect. Apart from the LC systems, the ISO method has been proved to be suitable for the operation of polymer/LC composite systems such as PDLC films, where a modification of boundary conditions can be realized in both the normal and inverse modes depending on the content of ionic surfactant in LC.

The values of the response times for the ISO method take several seconds or tens of seconds. But these parameters can be improved by several ways. For example, one may choose LC with low viscosity because the well-known LCs 5CB and MBBA exemplarily discussed in this chapter are not optimal materials regarding this aspect. Ion transport velocity under the action of electric field in low-viscosity LCs will increase and hence the response times will drop. Another approach is to use the orientational transition between the homeoplanar configuration and the twisted structure in a nematic layer. As shown above, the response times decrease in this case to some hundreds of milliseconds. If to apply additionally the opposite pulse before the field is turned off, the relaxation time decreases to 11 µs.

In cholesteric layers with a confinement ratio in the range of 0.16–0.85, the DC electric field induced the transition from the homeotropic director configuration to the UHAC structure. The on-time for such LC cells was tenth parts of a second and off-time was about a second. Initially, the fingerprint texture was realized in the LC cells with confinement ratios exceeding 1. The DC electric field induced the formation of MHAC structure whose optical texture appeared as periodic stripes.

Obviously, the ISO method for switching LC states has its pros and cons. A few drawbacks can be listed, including the slower electro-optical response in comparison with that of the similar orientational transitions induced by the Frederiks effect, and the probable electrochemical degradation of the substrates and LC structures. Among the advantages, the method allows operating various surface phenomena in plasmonics, light reflection, and others; the method practically depends neither on the value nor the sign of LC dielectric anisotropy; this method requires a small value of control voltage; it enables low power consumption of LC structures with novel types of bistability effects; the special production technologies are not required because the manufacturing lines for conventional LC displays can be used to produce the LC devices controlled by the ionic-surfactant method. All these allow believing that the development of this approach can lead to the creation of principally new LC materials capable of significantly expanding the functional possibilities of optoelectronic LC devices.

References

Barannik, A., Shabanov, V., Zyryanov, V., Lapanik, V., Bezborodov, V. (2005). Interference and ion effects in the electro-optical response of PDNLC films. Journal of the Society for Information Display, 13, 273–279.

Barbero, G., Evangelista, L.R. (2006). Adsorption Phenomena and Anchoring Energy in Nematic Liquid Crystals, Taylor and Francis, Boca Raton, 352.

Baudry, J., Brazovskaia, M., Lejcek, L., Oswald, P., Pirkl, S. (1996). Arch-texture in cholesteric liquid crystals. Liquid Crystals, 21(6), 893–901.

Belyaev, S.V., Barnik, M.I., Beresnev, G.A., Malimonenko, N.V. (1988). Optical and electrooptical properties of homeoplanar layers of cholesteric liquid crystals. Liquid Crystals, 3, 1279–1282.

Berreman, D.W. (1972). Optics in stratified and anisotropic media: 4×4-matrix formulation. Journal of the Optical Society of America, 62(4), 502–510.

Berreman, D.W., Heffner, W.R. (1981). New bistable liquid-crystal twist cell. Journal of Applied Physics, 52, 3032–3039.

Blinov, L.M. (1983). Electro-Optical and Magneto-Optical Properties of Liquid Crystals, Wiley, New York, 384.

Blinov, L.M. (2011). Structure and Properties of Liquid Crystals, Springer, Dordrecht, Heidelberg, London, New York.

Blinov, L.M., Chigrinov, V.G. (1993). Electrooptic Effects in Liquid Crystal Materials, Springer, New York.

Blinov, L.M., Davydova, N.N., Sonin, A.A., Yudin, S.G. (1984). The local frederiks transition in nematic liquid crystals. Kristallografiya, 29(3), 537–541.

Blinov, L.M., Kats, E.I., Sonin, A.A. (1987). Surface physics of thermotropic liquid crystals. Soviet Physics-Uspekhi, 30(7), 604–619.

Born, M., Wolf, E. (1999). The Principles of Optics. Nauka, Moscow, Vol. 1973, 6th ed., Cambridge Univ. Press, Cambridge.

Bradshaw, M.J., Raynes, E.P., Bunning, J.D., Bunning, J.D., Faber, T.E. (1958). The Frank constants of some nematic liquid crystals. Journal de Physique, 46(9), 1513–1520.

Bunning, J.D., Crellin, D.A., Faber, T.E. (1986). The effect of molecular biaxiality on the bulk properties of some nematic liquid-crystals. Liquid Crystals, 1(1), 37–51.

Bunning, J.D., Faber, T.E., Sherrell, P.L. (1981). The Frank constants of nematic 5CB at atmospheric pressure. Journal de Physique, 42(8), 1175–1182.

Candau, S., Le Roy, P., Debeauvais, F. (1973). Magnetic field effects in nematic and cholesteric droplets suspended in a isotropic liquid. Molecular Crystals and Liquid Crystals, 23, 283–297.

Chandrasekhar, S. (1977). Liquid Crystals, Raman Research Institute, Cambridge Univ. Press, Cambridge, 1977; Mir, Moscow, 1980.

Cognard, J. (1982). Alignment of Nematic Liquid Crystals and Their Mixtures, Gordon and Breach, Paris, 104.

Crawford, G.P., Zumer, S. (1996). Liquid Crystals in Complex Geometries, Taylor and Francis, London, 584.

Cui, M., Kelly, J.R. (1999). Temperature dependence of visco-elastic properties of 5CB. Molecular Crystals and Liquid Crystals, 331, 1909–1917.

Doane, J.W. (1991). Polymer-dispersed liquid-crystals-boojums at work. MRS Bulletin, 16, 22–28.

Dozov, I., Penchev, I. (1986). Structure of a hybrid aligned cholesteric liquid crystal cell. Journal de Physique France, 47, 373–377.

Drzaic, P.S. (1995). Liquid Crystal Dispersions, World Scientific, Singapore, 429.

Dubois-Violette, E., De Gennes, P.G. (1975). Local Frederiks transitions near a solid/nematic interface. Journal de Physique Letters, 36(10), L255–L258.

Fréedericksz, V., Tsvetkov, V. (1935). Concerning the orienting action of an electric field on molecules of anisotropic liquids. Doklady Akademii Nauk SSSR, 2, 528–531.

Freedericksz, V.K., Zolina, V. (1933). Forces causing the orientation of an anisotropic liquid. Transactions of the Faraday Society, 29, 919–930.

Gardymova, A.P., Zyryanov, V.Y., Loiko, V.A. (2011). Multistability in polymer-dispersed cholesteric liquid crystal film doped with ionic surfactant. Technical Physics Letters, 37(9), 805–808.

Grawford, G.P. (2005). Flexible Flat Panel Displays, John Wiley & Sons, Hoboken.

Greubel, W. (1974). Bistability behavior of texture in cholesteric liquid crystals in an electric field. Applied Physics Letters, 25, 5–7.

Harvey, T.B. (1977). A boundary induced cholesteric-nematic phase transition. Molecular Crystals and Liquid Crystals, 34, 225–229.

Hsiao, Y.-C., Timofeev, I.V., Zyryanov, V.Y., Lee, W. (2015). Hybrid anchoring for a color-reflective dual-frequency cholesteric liquid crystal device switched by low voltages. Optical Materials Express, 5(11), 2715–2720.

Hsu, J.S., Liang, B.J., Chen, S.H. (2004). Bistable chiral tilted-homeotropic nematic liquid crystal cells. Applied Physics Letters, 85, 5511–5513.

Huibers, P.D.T., Shah, D.O. (1997). Multispectral determination of soap film thickness. Langmuir, 13, 5995–5998.

Kleman, M., Friedel, J. (1969). Lignes de Dislocation Dans les Cholestériques. Journal de Physique. Colloques 30 (Suppl. C4), 43, C4-43–C4-53.

Klingbiel, R.T., Genova, D.J., Bucher, H.K. (1974). The temperature dependence of the dielectric and conductivity anisotropies of several liquid crystalline materials. Molecular Crystals and Liquid Crystals, 27, 1–21.

Komitov, L., Helgee, B., Felix, J., Matharu, A. (2005). Electrically commanded surfaces for nematic liquid crystal displays. Applied Physics Letters, 86(2), 023502.

Krakhalev, M.N., Loiko, V.A., Zyryanov, V.Y. (2011). Electro-optical characteristics of polymer-dispersed liquid crystal film controlled by ionic-surfactant method. Technical Physics Letters, 37, 34–36.

Krakhalev, M.N., Prishchepa, O.O., Zyryanov, V.Y. (2009). Inverse mode of ion-surfactant method of director reorientation inside nematic droplets. Molecular Crystals and Liquid Crystals, 512, 1998–2003.

Lewis, M.R., Wiltshire, C.K. (1987). Hybrid aligned cholesteric: a novel liquid-crystal alignment. Applied Physics Letters, 51, 1197–1199.

Lin, C.-H., Chiang, R.-H., Liu, S.-H., Kuo, C.-T., Huang, C.-Y. (2012). Rotatable diffractive gratings based on hybrid-aligned cholesteric liquid crystals. Optics Express, 20(20), 26837–26844.

Meyer, R.B. (1972). Point disclinations at a nematic-isotropic liquid interface. Molecular Crystals and Liquid Crystals, 16, 355–369.

Nose, T., Miyanishi, T., Aizawa, Y., Ito, R., Honma, M. (2010). Rotational behavior of stripe domains appearing in hybrid aligned chiral nematic liquid crystal cells. Japanese Journal of Applied Physics, 49, 051701.

Ondris-Crawford, R., Boyko, E.P., Wagner, B.G., Erdmann, J.H., Zumer, S., Doane, J.W. (1991). Microscope textures of nematic droplets in polymer dispersed liquid crystals. Journal of Applied Physics, 69(9), 6380–6386.

Oswald, P., Baudry, J., Pirkl, S. (2000). Static and dynamic properties of cholesteric fingers in electric field. Physics Reports, 337, 67–96.

Petrov, A.G., Durand, G. (1994). Electric field transport of biphilic ions and anchoring transitions in nematic liquid crystals. Liquid Crystals, 17(4), 543–554.

Prishchepa, O.O., Shabanov, A.V., Zyryanov, V.Y. (2005). Director configurations in nematic droplets with inhomogeneous boundary conditions. Physical Review E, 72, 031712.

Prishchepa, O.O., Shabanov, A.V., Zyryanov, V.Y., Parshin, A.M., Nazarov, V.G. (2006). Friedericksz threshold field in bipolar nematic droplets with strong surface anchoring. Journal of Experimental and Theoretical Physics Letters, 84(11), 607–612.

Proust, J.E., Ter Minassian Saraga, L. (1972). Orientation of a nematic liquid crystal by suitable boundary surfaces. Solid State Communications, 11(9), 1227–1230.

Ribiére, P., Oswald, P., Pirkl, S. (1994). Crawling and spiraling of cholesteric fingers in electric field. Journal de Physique II, 4(1), 127–143.

Ryabchun, A., Bobrovsky, A., Stumpe, J., Shibaev, V. (2015). Rotatable diffraction gratings based on cholesteric liquid crystals with phototunable helix pitch. Advanced Optical Materials, 3(9), 1273–1279.

Ryschenkow, G., Kleman, M. (1976). Surface defects and structural transitions in very low anchoring energy nematic thin films. The Journal of Chemical Physics, 64, 404–412.

Skarp, K., Lagerwall, S.T., Stebler, B. (1980). Measurements of hydrodynamic parameters for nematic 5CB. Molecular Crystals and Liquid Crystals, 60(3), 215–236.

Sutormin, V.S., Krakhalev, M.N., Prishchepa, O.O., Lee, W., Zyryanov, V.Y. (2014). Electro-optical response of an ionic-surfactant-doped nematic cell with homeoplanar–twisted configuration transition. Optical Materials Express, 4(4), 810–815.

Sutormin, V.S., Krakhalev, M.N., Prishchepa, O.O., Zyryanov, V.Y. (2012). Electrically controlled local fredericksz transition in a layer of a nematic liquid crystal. Journal of Experimental and Theoretical Physics Letters, 96, 511–516.

Sutormin, V.S., Krakhalev, M.N., Zyryanov, V.Y. (2013). The dynamics of the response of an electro-optic cell based on a nematic layer with controlled surface anchoring. Technical Physics Letters, 39(7), 583–586.

Sutormin, V.S., Timofeev, I.V., Krakhalev, M.N., Prishchepa, O.O., Zyryanov, V.Y. (2017). Orientational transition in the cholesteric layer induced by electrically controlled ionic modification of the surface anchoring. Liquid Crystals, 44(3), 484–489.

Sutormin, V.S., Timofeev, I.V., Krakhalev, M.N., Prishchepa, O.O., Zyryanov, V.Y. (2018). Electrically induced anchoring transition in cholesteric liquid crystal cells with different confinement ratios. Liquid Crystals, 45(8), 1129–1136.

Timofeev, I.V., Lin, Y.-T., Gunyakov, V.A., Myslivets, S.A., Arkhipkin, V.G., Vetrov, S.Y., Lee, W., Zyryanov, V.Y. (2012). Voltage-induced defect mode coupling in a one-dimensional photonic crystal with a twisted-nematic defect layer. Physical Review E, 85(1), 011705.

Volovik, G.E., Lavrentovich, O.D. (1983). Topological dynamics of defects: boojums in nematic drops. Journal of Experimental and Theoretical Physics, 58(6), 1159–1166.

Yang, D.K. (2006). Flexible bistable cholesteric reflective displays. Journal of Display Technology, 2, 32–37.

Yang, D.K., Huang, X.Y., Zhu, Y.M. (1997). Bistable cholesteric reflective displays: materials and drive schemes. Annual Review Materials Science, 27, 117–146.

Zel'dovich, B.Y., Tabiryan, N.V. (1981). Freedericksz transition in cholesteric liquid crystals without external fields. Journal Experimental and Theoretical Physics Letters, 34, 428–430.

Zharkova, G.M., Sonin, A.S. (1994). Mesomorphic composites. Nauka, Novosibirsk, 214.

Zumer, S., Doane, J.W. (1986). Light scattering from a small nematic droplet. Physical Review A, 34(4), 3373–3386.

Zyryanov, V.Y., Krakhalev, M.N., Prishchepa, O.O., Shabanov, A.V. (2007). Orientational structure transformations caused by the electric-field-induced ionic modification of the interface in nematic droplets. Journal of Experimental and Theoretical Physics Letters, 86(6), 383–388.

Zyryanov, V.Y., Krakhalev, M.N., Prishchepa, O.O., Shabanov, A.V. (2008). Inverse regime of ionic modification of surface anchoring in nematic droplets. Journal of Experimental and Theoretical Physics Letters, 88(9), 597–601.

Zyryanov, V.Y., Smorgon, S.L., Zhuikov, V.A., Shabanov, V.F. (1994). Memory effects in polymer-encapsulated cholesteric liquid-crystals. Journal of Experimental and Theoretical Physics Letters, 59, 547–550.

Zyryanov, V.Y., Zhuikov, V.A., Smorgon, S.L., Shabanov, V.F. (1996). Thermooptical recording of information in polymer-capsulated cholesteric liquid crystals. Technical Physics, 41(8), 799–802.

Kenji Katayama, Woon Yong Sohn

8 Time-resolved dynamics of dye-doped liquid crystals and the origin of their optical nonlinearity

Abstract: Liquid crystals (LCs) are promising materials not only for the display purpose but also for active matters, such as a biological membrane. They are soft and flexible, caused by the long molecular interaction. However, the dynamic change of LCs has been difficult to clarify because of their nonlinear responses, collective behavior, and orientation dependence, even though various time-resolved techniques have been utilized to study the dynamics by monitoring the change of LCs after a photoinduced trigger. Here, the history of such studies is reviewed, and it is described that the recent development of new techniques gradually has clarified the complicated processes. Especially the heterodyne transient grating method is a powerful tool to study the photoinduced dynamics of LCs, by applying a simple optical setup and large-area excitation. The studies on the host–guest interaction, photochemical phase transition, propagation of molecular orientation change, and the emergence of optical nonlinearity are introduced.

8.1 Introduction

8.1.1 Photo-response of dye-doped liquid crystals

Liquid crystals (LCs) have been industrially utilized as a display material, by arranging the molecules in a large area and by controlling the collective orientation electrically. The liquid crystalline state can also be found in the biological membranes and condensed solutions of proteins and DNA. The key feature of LCs is the collective ordering, but also the softness and flexibility, while maintaining the collective ordering, is another feature. This is possible because of the long-range molecular interaction on a millimeter scale, and there are no other materials with similar properties like LCs.

Thanks to this long-range molecular interaction, the objects made of LCs can move or change their shape. In the last 15 years, photomechanical objects made of

LCs have been developed starting from the pioneering work by Yu et al. (2003). Even in recent years, motion due to the photomechanically induced force has been demonstrated for wavy motion (Gelebart et al., 2017), and flow control by a photo-mechanical tube (Lv et al., 2016). This photomechanical motion is based on the photochemical phase transition reported by Haas et al. (1974). In the photochemical phase transition, guest molecules are subjected to photoexcitation, causing the phase transition of host LCs under the isotropic condition. Azobenzene and its derivatives have been used as guest molecules, and the effect of the molecular structure was intensively studied in the 1990s (Ikeda et al., 1990a, 1990b). The host LC could be controlled by the guest dyes attached on a substrate, too, which is called the "command surface" (Ichimura et al., 1988).

Other energy sources have been utilized for the motion, which has been noticed in the field of active matter; this indicates the spontaneous motion of small objects using the gradient of chemical concentration and surface tension using biological energy (Sánchez et al., 2015). A macroscopic flow inside an LC was induced by putting bacteria due to the restriction of the motion direction (Zhou et al., 2014), and the flow direction can be controlled by patterning the substrates (Peng et al., 2016). The motion of a capsule made of LC was controlled by several numbers of topological defects (Keber et al., 2014a).

The combination of host LCs and guest dyes has attracted researchers in the field of nonlinear optics as well. LCs themselves have been well known to possess huge optical nonlinear coefficients ($n^2 \sim 10^{-5}$ cm^2/W) (Durbin et al., 1981; Zel'dovich et al., 1980; Zolot'ko et al., 1980). This study has been further accelerated by the finding of the enhancement of the optical nonlinearity ($n_2 \sim 10^{-3}$ cm^2/W) in dye-doped LC systems. Various nonlinear optical processes have been demonstrated (Beeckman and Neyts, 2011), including supercontinuum generation due to self-phase modulation (Dudley et al., 2006), soliton wave formation due to self-focusing (Peccianti and Assanto, 2012), and the photorefractive effect (Khoo, 1996). The working principle was first explained by the dye-induced torque (Jánossy, 1994; Manzo et al., 2006), and several other explanations have since been given, such as the anchoring condition change (Lucchetti et al., 2002) and photorefractive-like effect (Khoo, 1996). In the 2000s, another huge enhancement of optical nonlinearity was found under the condition that the nematic phase was very close to the isotropic phase ($n_2 \sim 10^{0}$–10^{3} cm^2/W), which was referred to as "colossal optical nonlinearity" (Lucchetti et al., 2005; Ramos-Garcia et al., 2006; Simoni et al., 2001). The huge optical nonlinearity was utilized for the control of soliton waves (Peccianti et al., 2004; Piccardi et al., 2008), optical switching (Lucchetta et al., 2010), and various photonic applications (Beeckman et al., 2011; Lucchetti and Tasseva, 2012). In recent years, not only dyes but also inorganic materials such as carbon nanotubes and quantum dots dispersed in LCs could exhibit an enhancement of nonlinear refractive index (Anczykowska et al., 2012; Lee et al., 2004), and further new materials are expected.

The stable structure or physical properties under steady state have been well investigated. However, there have not been many studies on the properties such as long-range molecular interactions, which is important to understand the dynamic behavior like macroscopic motion or shape change and nonlinear process. We need to establish the method to define the unsteady states of LCs, and especially how fast and how long the molecular interaction occurs and propagates (Sato and Katayama, 2017).

To study the property of the unsteady state of LCs, the photoinduced dynamics has been measured with time-resolved measurement techniques for dye-doped LCs where the dye is added for light absorption. The transient absorption, birefringence, and grating methods have been utilized for the dynamic measurements (Kurihara et al., 1990, 1991; Sasaki et al., 1992; Shishido et al., 1997; Terazima et al., 1996). Photoinduced disordering/reorientation, phase transition/phase recovery, and the interaction between the host LC and the guest dyes have been studied. In this chapter, the recent progress of the studies on the photoinduced dynamic measurements is described.

8.1.2 Overview of the dynamics study of dye-doped LCs

To study the photoinduced unsteady-state dynamics of the dye-doped LCs, various time-resolved techniques have been utilized, where the material response is measured after a pulse light irradiation. For LCs, polarization-dependent transient absorption or birefringence has been measured (Ikeda et al., 1991; Kurihara et al., 1990, 1991). However, the response time of LCs varied for orders depending on the methods and the experimental conditions, and the dynamics have not been well understood, although several explanations have been made such that the phase transition occurred locally or the phase transition behavior was different near the alignment layer (Shishido et al., 1997). When the photoinduced dynamics was observed by the reflection measurement for an LC on a glass substrate under a total reflection configuration, the response of the LC was six orders faster than that obtained for conventional transmission measurement. This result indicates that the phase transition near the glass interface is much faster than the phase transition in the whole region of the LC. Furthermore, the analysis of the ratio of the phase transition region suggested that not all the region was phase -transitioned, and partial phase transition was proposed. It is always controversial on the photochemical phase transition because it is difficult to estimate how much thermal effect affects the phenomena, which cannot be avoided in any photoinduced process. Also, this study reminds us of the difference between the partial phase transition and the total phase transition.

On the other hand, the photoinduced dynamics has been measured via the change in the refractive index because LCs usually show a large refractive index

change. Transient grating (TG) is one of the most frequently utilized methods. As shown in Figure 8.1, two pump pulses are crossed at a sample, and as a result, a stripe pattern of light is irradiated to a sample, inducing a photoinduced change like the same pattern, causing the refractive index change (TG), and TG is monitored by a diffraction of another probe light. The photoinduced dynamics was measured, and the molecular reorientation, rotation, and diffusion were discussed (Khoo, 1996; Ohta et al., 1995; Yoon et al., 1998). However, this method has not been utilized for the study of the phase transition dynamics of LC due to the complicated optical setup, because it is difficult to adjust the actual light intensity at the sample position, which affects the LC response drastically. However, it was difficult to assign each photoinduced process correctly. There are two main difficulties: firstly, different from the dynamics on the molecular level, the photoinduced dynamics of LCs are caused by the collective behavior of molecules, and the reorientation and the rotational motion depend on the size of the assembly; secondly, nonlinear processes happen easily for LCs as mentioned in the previous section, and the nonlinear response depends on the guest molecules. Typically, the laser pulse is focused down to less than 100 μm in diameter in conventional time-resolved techniques; LCs easily show a nonlinear response; and, to make things worse, the inhomogeneous nonlinear response occurs within the beam due to the Gaussian intensity distribution.
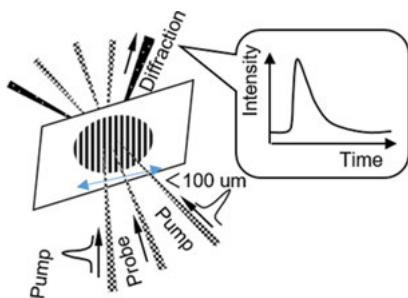
Figure 8.1: Schematic drawing of the optical setup for the transient grating method.

We have developed a new TG technique called the heterodyne TG (HD-TG) technique (Katayama et al., 2003; Okuda and Katayama, 2007), featuring a simple optical setup and highly sensitive detection using the amplification by the HD technique, and there are several features of this method which is favorable for the photoinduced dynamics of LCs. As shown in Figure 8.2, in this technique, a transmission diffraction grating is placed in front of a sample, and the near-field light pattern is illuminated to excite the sample. The probe light takes the same optical path as the pump light, and it is diffracted by the TG (signal), and also it is diffracted by the transmission grating (reference), and they are mixed and detected with a photodiode. (It is mentioned that this measurement is called the HD detection in spite of the fact that the signal and the reference have the same frequency because the detection of only the signal is
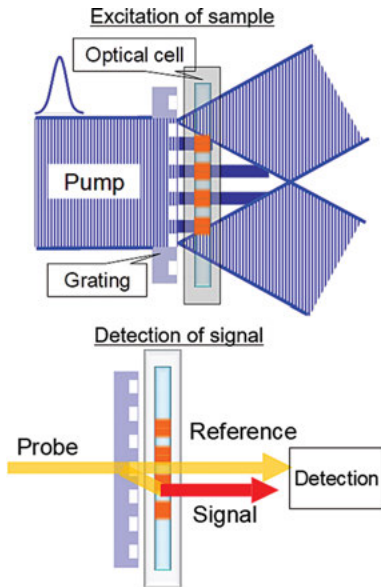
Figure 8.2: Schematic drawing of the heterodyne transient grating (HD-TG) method.

termed the homodyne detection in this field.) The phase difference between the signal and the reference can be controlled by the distance between the sample and the transmission grating, which provides the optimization of the signal intensity. Compared with the conventional TG method, the HD-TG method has some advantages for measurements of LCs. Firstly, the nonlinear effect can be controlled because the pump laser beam has the diameter around ~10 mm since the lens optics is not used in the HD-TG method. Secondly, it is superior in the distinction of the sign of the refractive index change, which allows easier assignment of the signal component especially for the LC sample, and also in the distinction between the ordinary and extraordinary refractive index changes by the dependence on the probe polarization. These improvements have made it possible for the study on the photoinduced LC dynamics. We studied the disorder/orientation dynamics of 4-methoxybenzylidene-4'-n-butylaniline (MBBA) after photoexcitation (Chiba et al., 2013), and molecular dynamics of a liquid crystalline polymer including azobenzene (Fujii et al., 2014), and phase transition/recovery dynamics (Sato et al., 2017).

Typically, the obtained index change for the photoinduced LCs is divided into three components depending on the physical origins as follows:

$$\Delta n(t) = \Delta n_T(t) + \Delta n_\rho(t) + \Delta n_S(t) \tag{8.1}$$

where the terms on the right-hand side correspond to the index change due to the temperature T, density ρ, and order parameter S respectively. The term $\Delta n_T(t)$ is known to be small usually. The term $\Delta n_\rho(t)$ is expanded to

$$\Delta n_\rho(t) = \left(\frac{\partial n}{\partial \rho}\right)_T \left(\frac{\partial \rho}{\partial T}\right) \Delta T(t) \tag{8.2}$$

Then the temporal response of this signal corresponds to the thermal grating of LC. For most of LCs, $(\partial n/\partial \rho)_T > 0$ and $(\partial \rho/\partial T) < 0$; then the index change is negative, and also the sign is not dependent on the polarization of the probe. The term $\Delta n_S(t)$ is the main cause of the disordering and reorientation dynamics of LC, and it can be expanded into

$$\Delta n_S(t) = \left(\frac{\partial n}{\partial S}\right)_\rho \Delta S(t) \tag{8.3}$$

It is mentioned that the change in the order parameter and temperature behaved differently in the temporal response. For an oval molecule aligned in the direction of y-axis, the index change for the x- and y-polarized light is,

$$\frac{\Delta n_{S,y}}{\Delta n_{S,x}} = \frac{\alpha_y}{\alpha_x} = -2 \tag{8.4}$$

where α_x and α_y are the polarizabilities in x and y directions. This is the reason why the sign of the signal for a different polarization of the probe beam is reversed for LCs. The order parameter is defined as

$$S(\theta) = \frac{1}{2}\left(3\langle\cos^2\theta\rangle - 1\right) \tag{8.5}$$

where θ is defined as the angle between the director and the molecular axis, and $\langle\cos^2\theta\rangle$ indicates the average of $\cos^2\theta$. Looking into eq. (8.5), the change in the order parameter is caused by two factors: the θ change and the ordering change because disordering reduces $\langle\cos^2\theta\rangle$ even for the same θ.

8.2 Dynamics of photo-responsive LCs

8.2.1 Photoinduced disordering and its recovery dynamics

As a photo-responsive LC, MBBA was utilized, and it is in the nematic state at room temperature. MBBA has a C = N double bond, which is subject to the photo-isomerization by UV light. The phase transition temperature from the nematic to isotropic phase is 46.9 °C. The sample was put into an LC cell with a thickness of ~3 μm, where the director axis is maintained by the alignment polyimide layer on the inside surface. As shown in Figure 8.3, the directions of the director axis, the polarization of the pump light, and the probe light were assigned. By matching the probe polarization and the LC director, we could obtain the response of the change in the extraordinary refractive
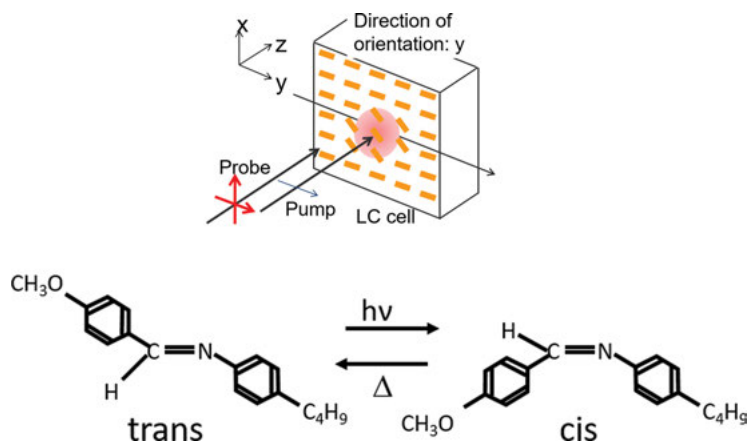
Figure 8.3: (Top) Schematic drawing of the optical configuration of a sample, a director, and polarizations of the pump and probe for the HD-TG measurement of liquid crystals. The photo-isomerization reaction of MBBA is shown at the bottom.

index (Δn_e), and by making them vertical, the change in the ordinary refractive index (Δn_o) can be measured.

The processes were measured by the HD-TG method after the cell was irradiated with a UV pump pulse. The pump light was Nd:YAG pulse laser (pulse width: 4 ns, wavelength: 355 nm, irradiation intensity: 0.14 mJ/pulse) and the probe light was Nd:YVO$_4$ laser (wavelength: 532 nm, irradiation intensity: 5 mW). The dependence of the photo-responses of Δn_e and Δn_o on the pump intensity is shown in Figure 8.4.
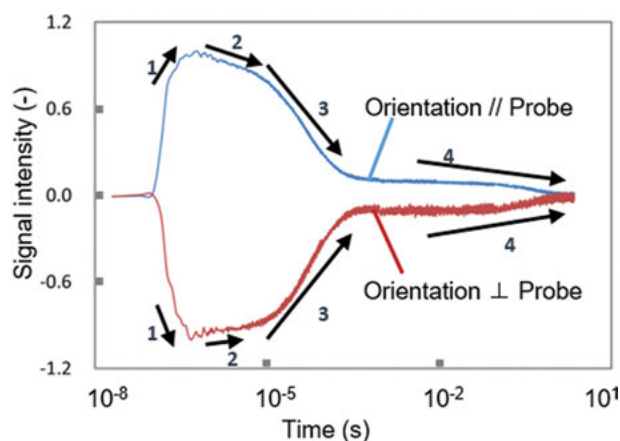
Figure 8.4: The dependence of the HD-TG responses of MBBA on the probe polarization direction. The numbers in figures express each component of the exponential function obtained in the multi-exponential fitting. The time axis is shown in a logarithmic timescale and, the pump intensity was 0.14 mJ/pulse.

The Δn_e showed a negative change, while Δn_o showed a positive one. It was confirmed that the sign of the refractive changes corresponded with the prediction under the assumption of the molecular structure with one-dimensional cylinder.

The refractive index changes for the probe polarization are represented as $\Delta n_x(t)$ and $\Delta n_y(t)$. As explained in the theory, the signal sign is dependent on the probe polarization if the refractive index change is due to the change in the order parameter, while the signal for the thermal response does not. The HD-TG signal $I(t)$ was fitted with a sum of four exponential functions as follows:

$$I(t) = \sum_{i=1}^{4} A_i \exp(-t/\tau_i) \tag{8.6}$$

where τ_i is a time constant and A_i is the amplitude for the ith component.

Figure 8.5 shows the pump intensity dependence of the responses. The behavior of the responses was different depending on the pump intensity around 1 mJ/pulse. Under the weak pump intensities, the number of exponential components were less (two components corresponding to the rise and the decay), but there were four components included for the higher pump intensities. For the lowest intensities studied
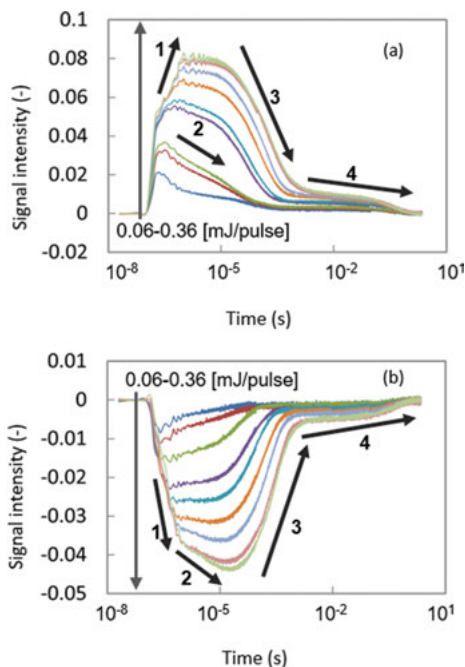
Figure 8.5: The dependence of the HD-TG responses on the pump light intensity for (a) extraordinary and (b) ordinary refractive index changes. The numbers in figures express each component of the exponential function obtained by the multi-exponential fitting.

here, the response time depended on the pump intensity for MBBA. The method as to how to assign each component is described in detail elsewhere (Chiba et al., 2013), and the components were assigned as follows: 1 for disordering; 2 and 3 for two types of reorientation processes due to molecular ordering and rotation; 4 for the back transformation from *cis* to *trans* isomer.

By investigating the time constants and the amplitudes for each component (Figure 8.6), the time constants for the first to the third processes suddenly increased for the pump intensity greater than a threshold intensity, and also the first and second processes had a polarization dependence of the probe light. From these dependencies, not only the molecular level change but also an assembly change, namely, the domain formation, can be predicted, and the disordering and the reorientation processes depended on the pump intensity due to different-sized domains.
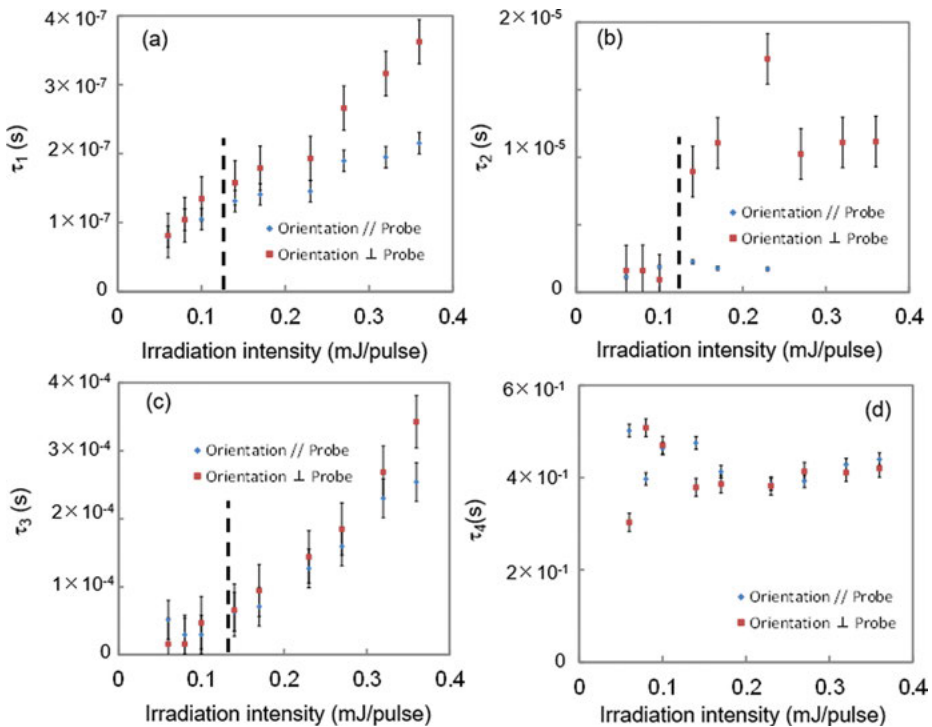
Figure 8.6: Dependence of τ_1–τ_4 on the pump intensity for components 1–4.

8.2.2 Photochemical phase transition and its recovery dynamics

To study the dynamics of the photochemical phase transition, the photo-response dependence on the guest molecules was studied. As a host LC material, 7-heptyloxy-4-cyanobiphenyl (7OCB)（$T_{NI} = 74$ °C）was employed, and azobenzene (Azo) and solvent red 111 (SR) were utilized as guest dyes. Azo is one of the most well-known dyes causing the photochemical phase transition, and SR is well known as a thermal dye. The pump light was Nd:YAG pulse laser (pulse width: 4 ns, wavelength: 355 or 532 nm) and the probe light was a He–Ne laser (wavelength: 633 nm, irradiation power: 5 mW). The irradiation intensity changed in the range of 0.2–1 mJ/pulse.

In the previous section, the result of the disordering/reorientation response was shown, and in this section, the response for the phase transition/recovery response was investigated. To examine the difference between the disordering/reorientation response and the phase transition/recovery response, the temperature dependence of the photoinduced responses is shown in Figure 8.7. One of the responses was for the
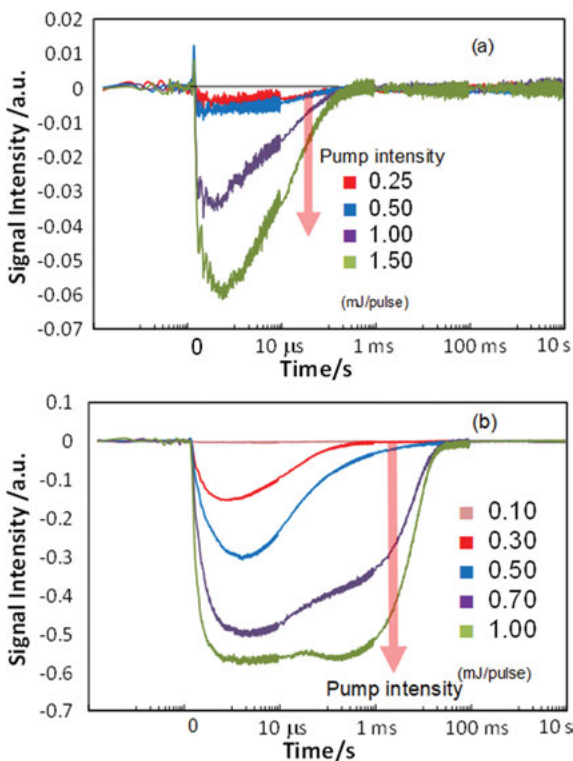
Figure 8.7: The HD-TG responses of the LC doped with azobenzene for different pump intensities were shown. The initial temperature was (a) 56 and (b) 70 °C, respectively. The responses show the extraordinary refractive index change.

temperature much lower than T_{NI}, while the other was for the temperature close to T_{NI}. When the setting temperature (sample temperature) was 56 °C, much lower than T_{NI}, the nematic phase remained, and the observed response corresponds to the disordering/reorientation. On the other hand, the TG signal intensity for 70 °C was one order larger than the response for the lower pump intensity; we can understand that the phase transition from the nematic to the isotropic phase was induced by the photochemical change of the guest molecules. The response in Figure 8.7(b) indicates the phase transition from the nematic phase to the isotropic phase, and the phase recovery from the isotropic phase to the nematic phase was observed.

The comparison between Azo and SR as guest dyes is shown in Figure 8.8 for different setting temperatures. In the case of SR, the photoinduced refractive index change was small until the setting temperature was close to T_{NI}, and the change jumped up around T_{NI}. On the other hand, about 20% of the maximum refractive index change was observed for the much lower temperature than T_{NI}, and the photoinduced refractive index change gradually increased as the temperature approached T_{NI}. This indicates that the photochemical phase transition was induced due to the photochemical phase transition for the temperature lower than T_{NI}. Since the refractive index change gradually increased, phase transition was induced partially, suggesting domain formation of isotropic regions.
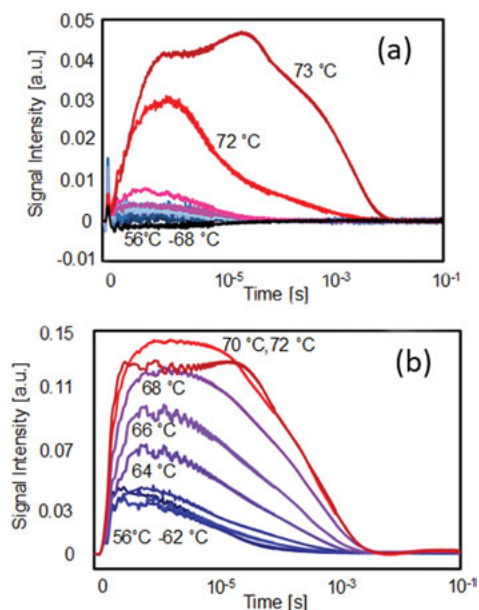
Figure 8.8: The HD-TG responses for different initial temperatures of the probe polarization parallel to the director axis. Phase transition was induced by guest dyes (a) solvent red and (b) azobenzene, respectively.

Furthermore, we found the difference in the responses of Δn_e and Δn_o in the phase transition/recovery processes for the photo-response of the LC, including Azo as a guest dye, as shown in Figure 8.9, and the difference was enhanced as the temperature increased. Looking at the recovery process on the timescale of milliseconds, Δn_e responses decayed within a millisecond, while Δn_e responses extended to 10 ms. This indicates that the observed refractive index was caused by the anisotropic domains and that the recovery time became longer because the domain extended to the director axis and difficult to recover in the director axis. This anisotropic dependence of the assembly is one of the characteristic properties of LCs.
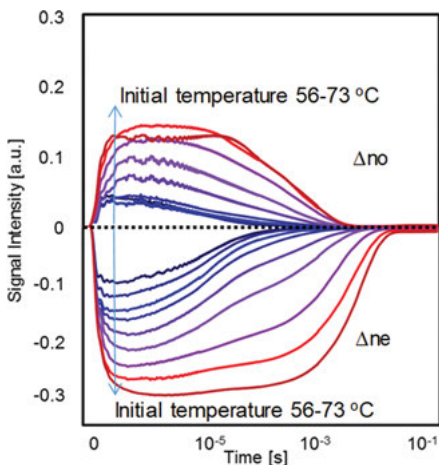
Figure 8.9: The HD-TG responses for different initial temperatures of probe polarizations parallel (Δn_e) and perpendicular (Δn_o) to the director axis.

8.2.3 Disordering propagation dynamics in the phase transition

LCs are subject to the macroscopic structural change induced by a change on a molecular scale because of the collective molecular interactions, and sometimes reaching distances on the order of millimeters. Long-range molecular interaction can be found in the field of photoinduced phase transition for spin-crossover complexes (Ogawa et al., 2000), conjugated polymers (Hosaka et al., 1999), and strongly correlated electron systems interleaved by donor and acceptor layers (Koshihara et al., 1999). They are caused by the macroscopically correlated interaction between electrons, spins, and phonons. Different from crystalline materials, LCs are soft and can have curved structures, which enables to comprise a cell membrane. An orientational or structural change of molecules could trigger the whole structural change by an increase in the domain region.

Owing to this softness, LCs have been regarded as a good platform of active matter, which has been a recent area of interest for research. An active capsule composed of LCs was demonstrated, and it was clarified that the active motion was controlled by a couple of topological defects. The topological defect indicates the position where the molecular orientation cannot be defined (Keber et al., 2014). A macroscopic flow was induced in the LC direction by injecting a small fraction of bacteria (Peng et al., 2016). In any active matter using LCs, a small trigger induced a macroscopic structural change, owing to the long-range molecular interaction of the LCs. For the long-range molecular interaction, it is important to know how fast and for how long this molecular interaction extends. In the previous sections, the photo-response of LCs involves the dynamics of molecular assembly such as domains, and this caused the nonlinear response. Furthermore, the essence of the long-range molecular interaction of LCs would be the response of the molecular assembly, and it is necessary to clarify both the temporal and the spatial responses.

In the TG technique, we could obtain the information on the propagation phenomena if the physical response causes the propagation in the direction perpendicular to the grating stripes (refer to Figure 8.1). The information can be obtained experimentally by changing the interval of the stripes. The response time depends on the grating interval when the propagation phenomena are included in the response.

Using the same optical configuration as Figure 8.3, Δn_e and Δn_o responses were measured for different grating spacings (Figure 8.10). An LC sample doped with a small fraction of dye (2.7 mol%) was enclosed in a thermally controlled LC cell with an alignment layer. The polarization–absorption spectrum for each guest dyes with 7OCB and 7CB was measured to confirm the absorbance at the pump wavelength.

We measured the grating interval dependence of the phase transition response from the nematic to the isotropic phase (the initial part of Figure 8.5). The results showed the clear dependence on the grating spacing only for Δn_e responses, and not for Δn_o responses. These responses correspond to the change of the nematic phase to the isotropic phase, and the grating spacing dependence indicates the spatial expansion of the nematic region, namely, the result means the molecular disordering spatially expanded. Interestingly, the spatial expansion was observed only for the Δn_e responses, even though the molecular disordering was induced in any direction. This can be understood that the Δn_o responses entail the local disordering, while Δn_e responses include the local disordering and also the expansion of the isotropic phase.

Next, the mechanism of the disordering was investigated. Generally, the propagation process is categorized into diffusion and ballistic processes. In the former process, the propagation time is proportional to the square of the propagation distance, while it is proportional to the propagation distance in the latter process. In the TG measurement, the propagation distance (grating spacing) and the propagation time (rise time) can be correlated. For the analysis of TG responses, the square roots of the normalized TG responses were fitted with an exponential rise function:
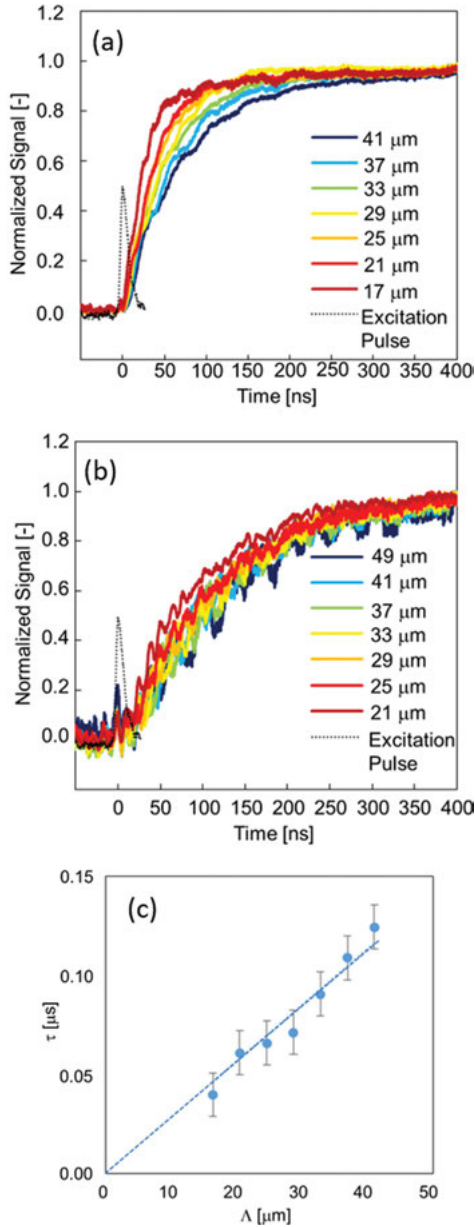
Figure 8.10: The TG responses for different fringe spacing in the initial rising part of the responses. The setup configuration corresponds to Figure 8.4. The sample was 7CB including azobenzene as a guest molecule. (a) Δn_e and (b) Δn_o. The measurement temperature was set at 25 °C. The timing of the pump pulse irradiation was shown. The time constants for the rise component of (a) were shown for the different fringe spacing (c).

$1 - \exp(-t/\tau)$ (τ is the time constant). The dependence of the phase transition time on the fringe spacing indicates that the phase transition region expands, which means that the isotropic region (stripe pattern) becomes larger. The time constant is expressed when the propagation is diffusive:

$$\tau_{\text{propagation}} = \frac{1}{D} \left(\frac{\Lambda}{2\pi} \right)^2 \tag{8.7}$$

where D is the diffusion coefficient and Λ is the fringe spacing. When the propagation is ballistic,

$$\tau_{\text{propagation}} = \frac{1}{v} \left(\frac{\Lambda}{\pi} \right) \tag{8.8}$$

where v is the velocity of phase transition propagation. In Figure 8.10, the relation is plotted, and clearly, it shows that the process was ballistic. The velocity was ~100 m/s, obtained from the slope of the plot. The ballistic propagation indicates that there was no scattering event for the propagation, and clearly, it shows no hindrance of the disordering propagation on the order of tens of micron. This would be consistent that the molecular interaction of LCs is smooth and extends for a long distance.

8.2.4 Phase transition dynamics and its anchoring effect

Since the molecular interaction extends for a long distance for LCs, the surface/interface plays a dominant role to control the overall structure of LCs. It was demonstrated that the photo-responsive molecule on the surface can change the LC structure. Ichimura et al. (1988) developed "command surfaces," where azobenzene moiety was on an LC cell, and the LC orientation was controlled by the UV-induced molecular change. It is expected that the surface anchoring will affect the phase transition/recovery processes. The effect was studied by comparison of the phase transition/recovery dynamics for different LC thicknesses.

Thioindigo (TI) and SR were used as photochemical and photo-thermal guest dyes, respectively, and 7OCB was used as a host LC ($T_{\text{NI}} = 74$ °C). The sample cell had thicknesses of ca. 3, 5, and 15 μm, with an alignment layer for the planar alignment. The temperature was controlled by an aluminum frame covering the cell, which was temperature controlled.

In this study, a new analysis method was introduced. As shown in Section 8.2.1, the photo-responses of LCs typically consist of multiple exponential components and can be fitted with a sum of multiple exponential functions. Since the fitting with a sum of multiple exponentials cannot be trusted as an increase in the number of exponentials, we introduced the maximum entropy (ME) method combined with the nonlinear least square (NLS) minimization of error. The mathematical formula is given as

$$
\begin{pmatrix} S(t_0) \\ S(t_1) \\ . \\ . \\ S(t_n) \end{pmatrix} = \begin{pmatrix} \exp(-t_0/\tau_1) & \exp(-t_0/\tau_2) & \ldots & \exp(-t_0/\tau_M) \\ \exp(-t_1/\tau_1) & \exp(-t_1/\tau_2) & \ldots & \exp(-t_1/\tau_M) \\ . & . & & . \\ \exp(-t_N/\tau_1) & \exp(-t_N/\tau_2) & \ldots & \exp(-t_N/\tau_M) \end{pmatrix} \begin{pmatrix} A_0 \\ A_1 \\ . \\ . \\ . \\ A_M \end{pmatrix} \tag{8.9}
$$

where $S(t_i)$ is the signal intensity for different times t_i ($i = 1$–N), the time constants are discretized by M, and Aj ($j = 1$–M) is the amplitude corresponding to the exponential with the time constant, τ_j. When eq. (8.9) is written as $S = A\,a$, this was solved in the typical NLS method as

$$
\widehat{a} = \arg \min_{a} \left\{ \|S - Aa\|_2^2 \right\} \tag{8.10}
$$

and the coefficient vector a is obtained. However, many possible combinations of A_j can be obtained for the answer. Thus, instead of solving eq. (8.10),

$$
\widehat{a} = \arg \min_{a} \left\{ \|S - Aa\|_2^2 + \lambda(-E) \right\} \tag{8.11}
$$

was solved, where E is the entropy of data error, and λ is the adjustment parameter between the mean square error and the entropy term. $(-E)$ is minimized by changing the sign of entropy instead of maximizing entropy. E is expressed as

$$
E = \sum_{i=1}^{N} [S(t_i) - M(t_i) - S(t_i)\log(S(t_i)/M(t_i))] \tag{8.12}
$$

where $M(t_i)$ is the assumed model function. This calculation was made by MemExp (Steinbach, 2002; Steinbach et al., 2002).

Figure 8.11 shows the responses for SR as guest molecules for different cell thicknesses. In both guest molecules and for the different cell thicknesses, the responses showed a plateau region on the microsecond order and decayed on the millisecond order, as the temperature increased (Sato et al., 2017). It indicates that the phase transition was induced by the thermal release or structural change of guest molecules. The signal intensity was proportional to the refractive index change, which is determined by the ratio of the region phase transitioned. The photoinduced phase transition from the nematic phase to the isotropic phase was of the order of 100 ns, and the transition from the isotropic to nematic phase was of the order of 100 μs to 100 ms.
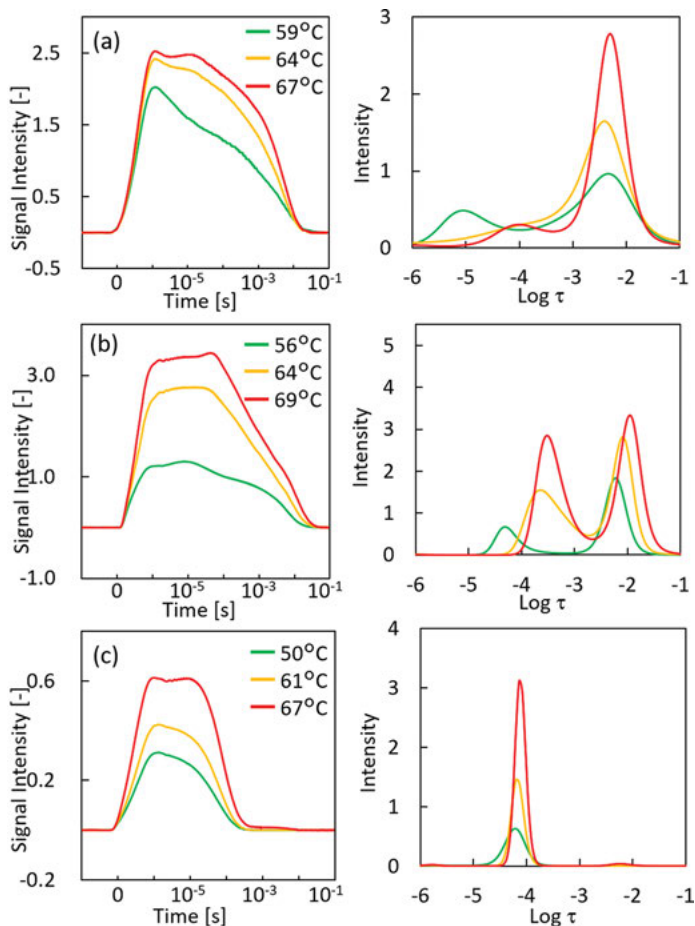
Figure 8.11: Transient grating responses for different cell thicknesses (3, 5, 15 μm) for different guest molecules; (a)–(c) solvent red. The host liquid crystal was 7-heptyloxy-4-cyanobiphenyl (7OCB). The initial temperature varied as indicated in the figure. Lifetime distribution for the responses is shown on the right side, obtained by the max entropy nonlinear least square analysis.

The phase recovery time became shorter as the cell thickness became thicker for both the dyes. Although there were slight differences for the guest molecules, the general trend of the recovery processes did not depend on the guest dye investigated as long as the cell thickness was maintained. For the cell thickness of 3 μm, the phase recovery showed a slower decay. As the cell thickness increased, the recovery time became shorter for the cell thickness of 15 μm.

The ME-NLS analyses for the phase recovery region were performed, and they are shown in the right column of Figure 8.11. It is obvious that there were two time constants for the phase recovery process depending on the cell thickness (~10^{-2} and ~10^{-4} s).

For the thinner cells, the slower component is dominant, while only the slower process could be observed for the thicker cell. Based on these results, two types of mechanisms for the phase recovery were proposed: surface-dominant process and bulk-dominant process. In the surface-dominant process, the phase recovery is induced by the interaction between the LC molecules and the alignment layer, and this is dominant for the thinner samples. In the bulk-dominant process, the intrinsic property of molecules dominates the recovery, namely, the host LC itself. It is assumed that the molecules at the interface were affected by the inhomogeneity of the alignment polymer layer (Katayama et al., 2014) and that the decay time extended for wide temporal order.

8.2.5 Dynamics of pre-transitional state

Another issue for the dye-doped LCs is the optical nonlinearity. Almost 20 years ago, "colossal optical nonlinearity" was discovered for the dye-doped LCs (Simoni et al., 2001) when they are just below the nematic–isotropic phase transition temperature (Li et al., 2016; Lucchetti et al., 2005; Ramos-Garcia et al., 2006). The nonlinear effect in the pre-phase transitional state was initially explained by the dye-induced torque (Jánossy, 1994; Manzo et al., 2006), and several other explanations were given such as photorefractive effect (Khoo, 1996) or surface adsorption effect (Simoni et al., 2001), and the working mechanism is still not sufficiently clear.

We measured the HD-TG responses under the pre-phase transitional state. By approaching the temperature to the phase transition temperature or increasing the pump intensity, the LC condition was set to the pre-phase transitional states. From the HD-TG responses, very large refractive index change was observed in the millisecond time region only when the condition was set to the pre-phase transitional state. This observation was general for various combinations of the dyes (guest) and the LCs (host), and also for pure LC like MBBA.

The pump light was Nd:YAG pulse laser (pulse width: 4 ns, wavelength: 355 or 532 nm), and the probe light was a Nd:YAG laser or a He–Ne or laser (wavelength: 532 or 633 nm, irradiation power: 5 mW). The diameter of the irradiated area by the pump pulse was 5 mm. The pump intensity was changed in the range of 0.2–1 mJ/pulse. For a dye-doped LC sample, disperse red (DR) and 4-cyano-4′-pentylbiphenyl (5CB) were used as a guest dye and a host LC (T_{NI} = 34.5 °C), respectively, and MBBA was used as photo-responsive LC.

The enhancement of the refractive index was monitored for MBBA from the observation of the diffraction light pattern under the same optical configuration as in the TG study (Figure 8.12). For the lower pump intensities, a spot of the first-order light was visible, which is typical for a Raman–Nath diffraction. However, for the intensities >0.30 mJ/cm^2, the diffraction drastically became stronger and changed into the pattern including many high diffraction orders.
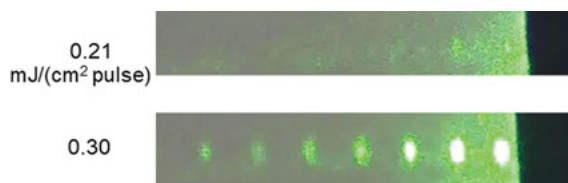
Figure 8.12: Diffraction light patterns of the probe light induced by the photoinduced nonlinear refractive index, which was observed on the screen. The sample was MBBA.

The dye-doped LCs were measured by the TG method. The intensity dependence at 34.9 °C is shown in Figure 8.13 At the pump intensities 0.03–0.07 mJ/cm^2, it was confirmed that a typical phase transition/phase recovery response was observed, as described previously. By irradiation of the pump pulse, heat released from DR induced the phase transition from the nematic state to the isotropic state (<1 μs), and it returned to the nematic state again on the order of 100 μs to 10 ms. However, a strange response was observed by further increasing the pump intensity; after a fast response was observed, another response was identified around 1–100 ms. (No response was observed at a higher temperature beyond T_{NI}.) The threshold pump intensity was close to the intensity when the higher-order diffraction patterns were observed. Consider that the response was in the logarithmic timescale and that the integrated light intensity was much higher for the longer time response, even if the signal amplitude was small. This peak must originate from the nonlinear refractive index change observed for the pre-transitional state. This happened after the photoinduced molecular responses (such as the molecular rotation) had finished.
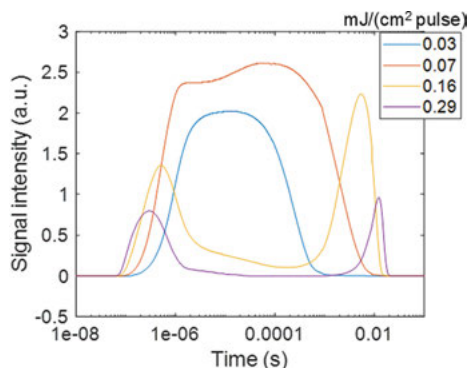
Figure 8.13: Pump intensity dependence of the TG responses for the dye-doped LC at 34.9 °C. The guest and host molecules are DR and 5CB.

To verify our assumption, the temperature dependence was studied because this could always happen under the condition close to the phase transition. For the constant pump intensity (0.12 mJ/cm^2), the temperature was gradually increased. The observed TG responses are shown in Figure 8.14. As we expected, typical phase transition/phase recovery responses were observed for the lower initial temperatures. At a threshold temperature of 35 °C, the response drastically changed just by increasing 0.1 °C. The responses showed a fast decay (<100 μs) and revived the response around 1–100 ms. At 36.0 °C, higher than T_{NI}, almost no responses were observed. This is the same tendency as the pump intensity dependence. From this result it was confirmed that this nonlinear refractive index change appeared when the LC condition was close to the isotropic state, whichever the pump intensity or the temperature was used to accomplish the condition.
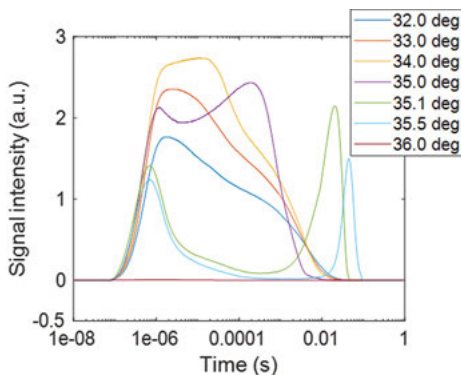
Figure 8.14: Temperature dependence of the TG responses for the dye-doped LC at the pump intensity of 0.12 mJ/cm^2. The guest and host molecules are DR and 5CB, respectively.

The pre-phase transitional state of MBBA was also studied. The pump intensity dependence was shown in Figure 8.15. The similar signal responses were observed. For the lower pump intensities, the response exhibited a typical phase transition/phase recovery response. Similar to the dye-doped LCs, we could observe the slower response in milliseconds for the higher pump intensities as the sample condition was close to the isotropic state.

8.3 Conclusions

LCs can be functionalized by dye doping, which has been utilized for photomechanical applications. Furthermore, dye doping in LCs gives optical nonlinearity with a huge enhancement. However, dye doping provided a complicated issue on the
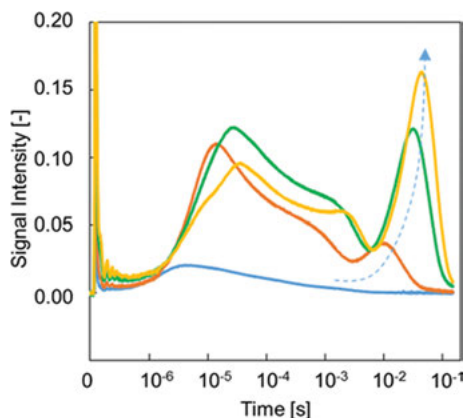
Figure 8.15: Pump intensity dependence of the TG responses for the pure LC at 30 °C. The LC is MBBA. The pump intensities were 0.30, 0.51, 0.80, 1.2 mJ/cm^2.

mechanism of how the functionality is established. In this chapter, the origin of the photo-functionality of the dye-doped LCs was investigated by using the TG technique, which offers the photoinduced response of LCs from nanosecond to second timescale. Depending on the light intensity and temperature, various nonlinear responses were observed. LCs showed complicated responses when compared with the photo-response of "molecules" because their responses include not only the molecular motion but also the formation of domains and their responses. In the phase transition/ recovery, disordering/reorientation, and nonlinear response, the dynamics of the molecular assembly (domain) must be considered.

References

Anczykowska, A., Bartkiewicz, M., Nyk, M., Mysliwiec, J. (2012). Study of semiconductor quantum dots influence on photorefractivity of liquid crystals. Applied Physics Letters, 101, 101107.

Beeckman, J., Neyts, K., Vanbrabant, P.J.M. (2011). Liquid-crystal photonic applications. Optical Engineering, 50(8). 081202. Doi: https://doi.org/10.1117/1.3565046.

Chiba, T., Inoue, H., Kuwahara, S., Katayama, K. (2013). Disorder/reorientation dynamics of 4-methoxybenzylidene-4-n-butylaniline observed by heterodyne transient grating method. Journal of Photochemistry and Photobiology A-Chemistry, 266(August). 1–5. Doi: https://doi.org/10.1016/j.jphotochem.2013.05.016.

Dudley, J.M., Genty, G., Coen, S. (2006). Supercontinuum generation in photonic crystal fiber. Reviews of Modern Physics, 78(4), 1135–1184.

Durbin, S.D., Arakelian, S.M., Shen, Y.R. (1981). Optical-field-induced birefringence and freedericksz transition in a nematic liquid crystal. Physical Review Letters, 47(19), 1411–1414.

Fujii, T., Kuwahara, S., Katayama, K., Takado, K., Ube, T., Ikeda, T. (2014). Molecular dynamics in azobenzene liquid crystal polymer films measured by time-resolved techniques. Physical Chemistry Chemical Physics, 16(22). 10485–10490. Doi: https://doi.org/10.1039/c4cp00457d.

Gelebart, A.H., Mulder, D.J., Varga, M., Konya, A., Vantomme, G., Meijer, E.W., Selinger, R.L.B., Broer, D.J. (2017). Making waves in a photoactive polymer film. Nature, 546(7660), 632–636.

Haas, W.E., Nelson, K.F., Adams, J.E., Dir, G.A. (1974). U.V. Imaging with nematic chlorostilbenes. J. Electrochem. Soc., 121, 1667.

Hosaka, N., Tachibana, H., Shiga, N., Matsumoto, M., Tokura, Y. (1999). Photoinduced phase transformation in polythiophene. Physical Review Letters, 82(8). 1672–1675. Doi: https://doi.org/10.1103/PhysRevLett.82.1672.

Ichimura, K., Suzuki, Y., Seki, T., Hosoki, A., Aoki, K. (1988). Reversible change in alignment mode of nematic liquid crystals regulated photochemically by command surfaces modified with an azobenzene monolayer. Langmuir, 4(5). 1214–1216. Doi: https://doi.org/10.1021/la00083a030.

Ikeda, T., Miyamoto, T., Kurihara, S., Tazuke, S. (1990a). Effect of structure of photoresponsive molecules on photochemical phase-transition of liquid-crystals: 3. photochemical phase-transition behaviors of photochromic azobenzene guest ester host mixtures. Molecular Crystals and Liquid Crystals, 188, 207–222.

Ikeda, T., Miyamoto, T., Kurihara, S., Tazuke, S. (1990b). Effect of structure of photoresponsive molecules on photochemical phase-transition of liquid-crystals: 4. photochemical phase-transition behaviors of photochromic azobenzene guest polymer liquid-crystal host mixtures. Molecular Crystals and Liquid Crystals, 188, 223–233.

Ikeda, T., Miyamoto, T., Kurihara, S., Tsukada, M., Tazuke, S. (1990a). Effect of structure of photoresponsive molecules on photochemical phase-transition of liquid-crystals: 1. synthesis and thermotropic properties of photochromic azobenzene derivatives. Molecular Crystals and Liquid Crystals, 182, 357–371.

Ikeda, T., Miyamoto, T., Kurihara, S., Tsukada, M., Tazuke, S. (1990b). Effect of structure of photoresponsive molecules on photochemical phase-transition of liquid-crystals: 2. photochemical phase-transition behaviors of photochromic guest host mixtures. Molecular Crystals and Liquid Crystals, 182, 373–385.

Ikeda, T., Sasaki, T., Kim, H.B. (1991). Intrinsic response of polymer liquid-crystals in photochemical phase-transition. Journal of Physical Chemistry, 95(2), 509–511.

Jánossy, I. (1994). Molecular Interpretation of the Absorption-Induced Optical Reorientation of Nematic Liquid Crystals. Physical Review E, 49(4), 2957–2963.

Katayama, K., Choi, Y., Kang, J.W., Yaqoob, Z., So, P.T.C., Fujii, T., Kuwahara, S., Takado, K., Ikeda, T. (2014). Depth-selective microscopic observation of a photomobile liquid crystal polymer under UV illumination. Physical Chemistry Chemical Physics, 16(48). 27074–27077. Doi: https://doi.org/10.1039/c4cp04602a.

Katayama, K., Yamaguchi, M., Sawada, T. (2003). Lens-free heterodyne detection for transient grating experiments. Applied Physics Letters, 82(17). 2775–2777. Doi: https://doi.org/10.1063/1.1569051.

Keber, F.C., Loiseau, E., Sanchez, T., DeCamp, S.J., Giomi, L., Bowick, M.J., Marchetti, M.C., Dogic, Z., Bausch, A.R. (2014). Topology and dynamics of active nematic vesicles. Science, 345(6201), 1135–1139.

Khoo, I.C. (1996). Orientational photorefractive effects in nematic liquid crystal films. IEEE Journal of Quantum Electronics, 32(3), 524–534.

Koshihara, S.-Y., Takahashi, Y., Sakai, H., Tokura, Y., Luty, T. (1999). Photoinduced cooperative charge transfer in low-dimensional organic crystals. The Journal of Physical Chemistry B, 103 (14). 2592–2600. Doi: https://doi.org/10.1021/jp984172i.

Kurihara, S., Ikeda, T., Sasaki, T., Kim, H.B., Tazuke, S. (1990). Time-resolved observation of isothermal phase-transition of liquid-crystals triggered by photochemical-reaction of dopant. Journal of the Chemical Society-Chemical Communications, 24(December), 1751–1752.

Kurihara, S., Ikeda, T., Sasaki, T., Kim, H.B., Tazuke, S. (1991). Time-resolved observation of isothermal phase-transition of liquid-crystals induced by photoisomerization of azobenzene dopant. Molecular Crystals and Liquid Crystals, 195, 251–263.

Lee, W., Wang, C.-Y., Shih, Y.-C. (2004). Effects of carbon nanosolids on the electro-optical properties of a twisted nematic liquid-crystal host. Applied Physics Letters, 85(4). 513–515. Doi: https://doi.org/10.1063/1.1771799.

Li, H., Wang, J., Wang, C., Zeng, P., Pan, Y., Yang, Y. (2016). Enhanced diffraction properties of photoinduced gratings in nematic liquid crystals doped with disperse Red 1. Proceedings of the Japan Academy, Series B, 92(8). 330–335. Doi: https://doi.org/10.2183/pjab.92.330.

Lucchetta, D.E., Vita, F., Simoni, F. (2010). All-optical switching of diffraction gratings infiltrated with dye-doped liquid crystals. Applied Physics Letters, 97(23). 231112. Doi: https://doi.org/10.1063/1.3525174.

Lucchetti, L., Gentili, M., Simoni, F. (2005). Pretransitional enhancement of the optical nonlinearity of thin dye-doped liquid crystals in the nematic phase. Applied Physics Letters, 86(15). 151117. Doi: https://doi.org/10.1063/1.1905796.

Lucchetti, L., Lucchetta, D.E., Francescangeli, O., Simoni, F. (2002). Sine: Surface induced nonlinear effects. Molecular Crystals and Liquid Crystals, 375(1). 641–650. Doi: https://doi.org/10.1080/10587250210594.

Lucchetti, L., Tasseva, J. (2012). Optically recorded tunable microlenses based on dye-doped liquid crystal cells. Applied Physics Letters, 100(18). 181111. Doi: https://doi.org/10.1063/1.4711203.

Lv, J.-A., Yuyun, L., Wei, J., Chen, E., Qin, L., Yu, Y. (2016). Photocontrol of fluid slugs in liquid crystal polymer microactuators. Nature, 537(7619), 179–184.

Ogawa, Y., Koshihara, S., Koshino, K., Ogawa, T., Urano, C., Takagi, H. (2000). Dynamical aspects of the photoinduced phase transition in spin-crossover complexes. Physical Review Letters, 84(14). 3181–3184. Doi: https://doi.org/10.1103/PhysRevLett.84.3181.

Ohta, K., Terazima, M., Hirota, N. (1995). Diffusion process of a liquid crystal probed by the transient grating method. Bulletin of the Chemical Society of Japan, 68(10), 2809–2815.

Okuda, M., Katayama, K. (2007). Selective Detection of Real and Imaginary Parts of Refractive Index Change in Solutions Induced by Photoexcitation Using Near-Field Heterodyne Transient Grating Method. Chemical Physics Letters, 443(1–3). 158–162. Doi: https://doi.org/10.1016/j.cplett.2007.06.056.

Peccianti, M., Assanto, G. (2012). Nematicons. Nematicons, 516(4). 147–208. Doi: https://doi.org/10.1016/j.physrep.2012.02.004.

Peccianti, M., Conti, C., Assanto, G., De Luca, A., Umeton, C. (2004). Routing of anisotropic spatial solitons and modulational instability in liquid crystals. Nature, 432(7018). 733–737. Doi: https://doi.org/10.1038/nature03101.

Peng, C., Turiv, T., Guo, Y., Wei, Q.-H., Lavrentovich, O.D. (2016). Command of active matter by topological defects and patterns. Science, 354(6314). 882. Doi: https://doi.org/10.1126/science.aah6936.

Piccardi, A., Assanto, G., Lucchetti, L., Simoni, F. (2008). All-optical steering of soliton waveguides in dye-doped liquid crystals. Applied Physics Letters, 93(17). 171104. Doi: https://doi.org/10.1063/1.3009658.

Ramos-Garcia, R., Lazo-Martínez, I., Guizar-Iturbide, I., Sanchez-Castillo, A., Boffety, M., Rück, P. (2006). Colossal nonlinear optical effect in dye-doped liquid crystals. Molecular Crystals and Liquid Crystals, 454(1). 179–[581]-185-[587]. Doi: https://doi.org/10.1080/15421400600654082.

Sánchez, S., Soler, L., Katuri, J. (2015). Chemically powered micro- and nanomotors. Angewandte Chemie International Edition, 54(5). 1414–1444. Doi: https://doi.org/10.1002/anie.201406096.

Sasaki, T., Ikeda, T., Ichimura, K. (1992). Time-resolved observation of photochemical phase-transition in polymer liquid-crystals. Macromolecules, 25(14), 3807–3811.

Sato, T., Katayama, K. (2017). Direct Measurement of the Propagation of the Phase-Transition Region of Liquid Crystals. Scientific Reports, 7(March), 44801.

Sato, T., Kuwahara, S., Katayama, K. (2017). Host-guest molecular interactions in the phase transition of liquid crystals. Molecular Crystals and Liquid Crystals, 644(1). 44–51. Doi: https://doi.org/10.1080/15421406.2016.1277327.

Shishido, A., Tsutsumi, O., Kanazawa, A., Shiono, T., Ikeda, T., Tamai, N. (1997). Rapid optical switching by means of photoinduced change in refractive index of azobenzene liquid crystals detected by reflection-mode analysis. J Am Chem Soc, 119(33), 7791–7796.

Simoni, F., Lucchetti, L., Lucchetta, D.E., Francescangeli, O. (2001). On the origin of the huge nonlinear response of dye-doped liquid crystals. Optics Express, 9(2). 85–90. Doi: https://doi.org/10.1364/OE.9.000085.

Steinbach, P.J. (2002). Inferring lifetime distributions from kinetics by maximizing entropy using a bootstrapped model. Journal of Chemical Information and Computer Sciences, 42(6). 1476–1478. Doi: https://doi.org/10.1021/ci025551i.

Steinbach, P.J., Ionescu, R., Robert Matthews, C. (2002). Analysis of kinetics using a hybrid maximum-entropy/nonlinear-least-squares method: application to protein folding. Biophysical Journal, 82(4). 2244–2255. Doi: https://doi.org/10.1016/S0006-3495(02)75570-7.

Terazima, M., Kojima, Y., Hirota, N. (1996). Dynamics of a liquid crystal molecule at a solid-liquid interface detected by the time-resolved transient grating method. Chemical Physics Letters, 259(3). 451–458. Doi: https://doi.org/10.1016/0009-2614(96)00785-3.

Yoon, B., Kim, S.H., Lee, I., Kim, S.K., Cho, M., Kim, H. (1998). Dynamics of nematic MBBA film induced by transient grating under a strong absorption condition. The Journal of Physical Chemistry B, 102(40). 7705–7713. Doi: https://doi.org/10.1021/jp981276k.

Yu, Y.L., Nakano, M., Ikeda, T. (2003). Directed bending of a polymer film by light – miniaturizing a simple photomechanical system could expand its range of applications. Nature, 425(6954), 145–145.

Zel'dovich, B.Y., Pilipetsukii, N.F., Tabiryan, N.V. (1980). Finding optical nonlinearity. JETP Letter, 31, 263.

Zhou, S., Sokolov, A., Lavrentovich, O.D., Aranson, I.S. (2014). Living liquid crystals. Proceedings of the National Academy of Sciences, 111(4), 1265–1270.

Zolot'ko, A.S., Kitaeva, V.F., Kroo, N., Sobolev, N.N., Chilag, L. (1980). Finding of optical nonlinearity. JETP Letter, 32, 158.

Wenbin Huang, Zhi-gang Zheng, Dong Shen, Yan-qing Lu, Quan Li

9 Light reconfigurable chiral liquid crystal superstructure for dynamic diffraction manipulations

Abstract: Liquid crystal has attracted sufficient attentions in the sciences and industries due to the booming development of liquid crystal display in the recent 20 years. The specific anisotropy and stimuli-responsiveness of liquid crystal enables a wide range applications not only in display but diverse potentials in optics and photonics.

Recently, the chiral liquid crystals, having a twisted helical self-organized superstructure with a pitch which is comparable to the scale of light wavelength, exhibit a fantastic effect as a soft photonic crystal, and thus inspire a broader and respective application in integrated optical system and photonics on a chip.

The diffraction device is ubiquitous in various optical systems. On the other aspect, the light controllable diffraction device plays an irreplaceable role in the all-optical system which is one of the vital part in photonics on a chip. Chiral liquid crystal with a self-organized superstructure as well as stimuli-responsiveness under light irradiation is an appropriate and preferable material for realizing the attribute of light manipulation. However, a comprehensive review on the relevant topic is insufficient and even rarely, therefore the proposed chapter herein is necessary and will provide a new concept and insight as a kind of nonconventional liquid crystals.

Keywords: cholesteric liquid crystals, blue phase liquid crystals, photoresponsive, diffraction, manipulation

9.1 Introduction

Supramolecular chiral structures are omnipresent in natural environment. They have been the foundation of biological structures and are very critical in determining the resultant biological functions. The double helix of DNA that carries genetic information for all livings represents a dynamic helical superstructure for genetic editing and copying, whereas beetle surface cells represent examples of static chiral helical assembling,

exhibiting marvelous and brilliant colors in appearance. These chiral superstructures have inspired scientists to develop artificial materials not only to reveal the molecule–superstructure interactions but also to explore and demonstrate the potential in many technological applications. Liquid crystal (LC) molecules (mesogens) also show supramolecular helical structures, when they are made chiral (Dierking, 2014). Chirality means an ideally symmetry image realized in a plane mirror is unable to be brought to overlap with itself. Chiral properties of different handedness, which is a subtle difference from the molecular structures, could result in profound functional performance change. Principally, there have been two methods to obtain chiral LCs: (1) introducing the chirality into the LC molecules, which can be done by substituting asymmetrically one or more of the carbon atoms with different ligands; (2) adding chiral dopants to the host liquid crystal molecules to introduce chirality into the material system.

Chiral LC phases, including the cholesteric LC (CLC) phase, the smectic C* phase, the blue phase (BP), and the twist grain boundary (TGB) phase, have shown to display quite attractive electro-optical properties when compared with nonchiral ones. Cholesteric LCs, with the introduction of chirality into the nematic LC phases, exhibit helical organization of mesogenic molecules (slightly twisted molecules with respect to their neighbors as shown in Figure 9.1(a)) with dynamic response capabilities to various external stimuli. The handedness—describing the direction in which the molecular orientation rotates along the helical axis—and the pitch—indicating the distance over which the director rotates by a full 360°—are the major parameters to characterize the CLC. Due to the periodic and helical superstructure, CLC has a very important property of the selective reflection of circularly polarized light. The common pitch in a CLC is on the scale of hundred nanometers, resulting in a visible reflection band as a 1D photonic crystal. The 1D photonic crystal structure is of particular interest for applications such as displays, lasers, and sensors. The chiral smectic C* phase shown in Figure 9.1(d) exhibits a helix superstructure, giving rise to the formation of a spontaneous polarization and its ferroelectric properties. The spontaneous polarization exhibits bistable response to external electric fields, resulting in an ultra-fast switching process on the microsecond scale for fast modulation applications. Apart from the chiral nematic and smectic structures, novel frustrated phases such as the BP and the TGB phase have been observed in chiral LCs. Blue phases are only present in materials with a high chirality, and they are commonly stable only in a temperature range of 1 to 2 K. There are three types of blue phases: BPI is shown schematically in Figure 9.1(b) and BPII is shown in Figure 9.1(c). BPI and BPII are composed of double twist LC cylinders arranged in body-centered cubic and simple cubic lattice structures, respectively. Blue phase commonly has a lattice parameter of several hundred nanometers and appears in blue color under white light illumination, due to the selective reflection. As the temperature increases, BPIII can be observed, which is an amorphous phase with a local cubic defect structure. Due to the subwavelegth periodic structures, blue phase LCs can be regarded as soft self-assembled 3D

photonic crystal materials which are of importance in realizing integrated optical devices. As for the TGB phase, it is present between the fluid smectic phase and the cholesteric phase, occurring through the competition between the high chirality and not allowed twist distortions in layered architecture. As shown in Figure 9.1(e), the TGB phase comprises smectic layers broken up into slab widths of ~100 nm, with the helical axis orienting perpendicular to the adjacent LC molecular. The TGB phase also occurs only in highly chiral mesogens with a very narrow temperature range, having a pitch of a few nanometers mediated by the grain and the regular lattice of screw dislocations. The introduction of chirality in LC system induces new LC phases with supramolecular helical structures, exhibiting numerous interesting electro-optical properties.

double twist
cylinders

double twist
cylinders

(a)　　　　　(b)　　　　　(c)

(d)　　　　　grain boundaries
　　　　　　　(e)
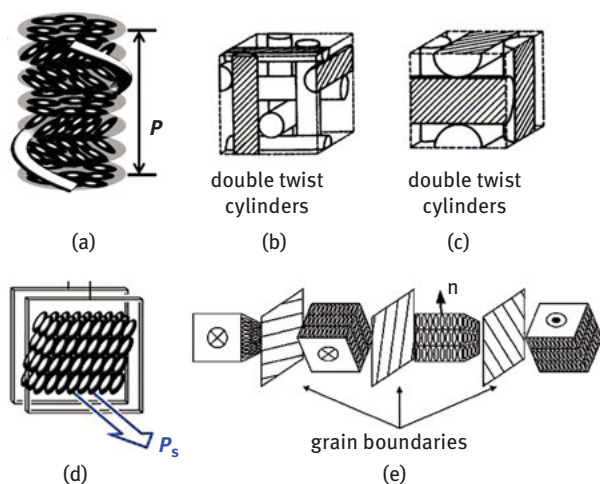
Figure 9.1: Schematic representation of chiral LC phases: (a) the cholesteric LC phase, (b) the BP I phase, (c) the BP II phase, (d) the smectic C* phase and (e) the twist grain boundary phase.

An extremely attracting property of the chiral LCs is the ability to respond to external stimuli for a dynamical and on-demand modulation of particular functionalities in constructing molecular devices. Despite the great efforts in utilizing heat and the electric field as the driving force to control the orientation of chiral LCs, light is adopted as the most simple and convenient means to bring directed changes in chiral LC alignment with the inherent benefits of remote, temporal, and spatial control, providing a rapid and reversible control over the functional properties (Bisoyi and Li, 2014, 2016). Light responsive chiral LCs capable of self-organizing into helical supermolecular structures represent such an elegant system. It has been demonstrated that doping chiral LCs with photo-charge generating and transporting agents endows the material with photorefractive capabilities. Under light illumination, the doped dye molecules would separate onto the cell surface and alter the alignment of LCs. Moreover, the inner space-charge field could be set up which induces a refractive-index change in

accordance with the light intensity distribution. These nonlinear effects are of importance for optically written and erasable diffractive devices. It has been further observed that chiral LCs containing photo-isomerizable molecular switches can undergo phase transition directed by light irradiation, either order-decreasing or order-increasing phase transitions is possible, depending on the molecular compatibility between the doped photo-isomer with the LC molecules. In addition, chiral switch photo-isomerization could result in changes in the helical-twisted power and molecular conformation, which could influence the pitch or handedness of chiral LCs, rendering huge flexibility in designing photo-responsive properties. To date, light controlled chiral LC systems have been applied in many applications such as tunable color filters, all-optical displays, tunable lasers, dynamic rearview mirrors, smart textiles, biosensors, electronic paper, smart buildings, and so on.

In this chapter, we cover the recent progress in light-driven chiral LC materials for dynamical diffraction modulations. We intend to deliver various topics through a unified approach and have tried to highlight how the basic concepts are applied to modulate the properties of light-driven chiral CLCs and enable their applications in practical devices. We will introduce the photo-responsive chiral liquid crystal systems enabled by the photorefractive effect caused by photorefractive dyes and photoconductive materials, the photo-isomerization effect caused by common azobenzene moieties, and the photothermal-effect caused by light-induced surface plasmon polaritons in metal-nanoparticle-loaded system, or nonradiative process in dye molecules. In addition, the novel liquid crystal Torons generated in chiral system caused by the interaction balance between the twisted elastic torque and mechanical torque under light irradiation will be reviewed in this chapter. Furthermore, diffraction grating formations and the corresponding light-modulated properties will be discussed herein.

9.2 Photorefractive chiral liquid crystal for dynamic diffraction manipulations

Photorefractivity (PR) defines the material's capability to exhibit nonlocal reversible refractive index change controlled by light. Photorefraction takes place in photoresponsive and photoconductive materials where an inhomogeneous light intensity irradiated onto such a sample would result in a refractive-index modulation in space. The procedure is as follows: The positive and negative charges with different motilities are photogenerated with the low-mobility charge staying in bright areas while the high-mobility charge moving to dark areas, forming the charge-separated state. As a result, there would be an internal electric field in the areas between the bright and the dark regions, giving rise to the refractive-index modulation through the electro- photorefractive effects in the materials with regard to the light intensity distribution (Figure 9.2). In addition, the refractive index and the optical patterns are

phase-shifted for the energy exchange among different light beams, which is beneficial for small optical signal amplification demonstration. Photorefractive LCs have been widely studied due to their structural and chemical flexibility, high optical gain, large refractive-index modulation, and low cost of processing which are extremely attractive for dynamic holography and optical data processing. However, LC materials are usually not intrinsically photoconductive. It thus requires either doping LC materials with agents capable of photo-charge generation and transportation (bulk PR) or confining them between photoconducting materials (surface PR) to set up the space charge field (Figure 9.2). Regarding the domination of the bulk or the surface mechanism during the PR process, this chapter summarizes the photorefractive chiral liquid crystal into three subsections: Methyl red (MR)-based photorefractive systems featuring combined bulk and surface photorefractivity, chiral liquid crystal with bulk photorefractivity, and chiral liquid crystal with photoconductive substrates.
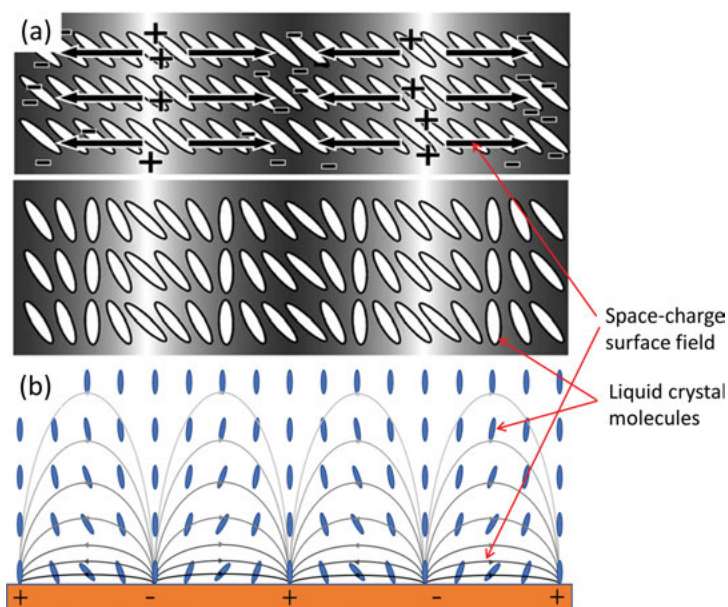
Figure 9.2: Schematic illustration of the (a) bulk photorefractivity (Sasaki et al., 2011). Copyright 2011 *The Royal Society of Chemistry* and (b) surface photorefractivity process.

9.2.1 Methyl-red-based photorefractive systems

The material mixture formed by doping the azo dye MR into the LC pentycyanobiphenyl (5CB) has been widely investigated as an amazing light-responsive system showing excellent photoalignment effects and large nonlinear optical response (Khoo et al., 1998; Lucchetti et al., 1999; Simoni et al., 1997). Under proper blue-green light

irradiation, MR molecules adsorbed onto the substrate surface with the alignment determined by the incident light polarization, reorienting the LC molecules through the intermolecular interactions. The competition at the irradiated surface between desorption and adsorption processes plays an important role in determining the light-induced surface effects. It has been observed that in such a MR-doped LC system the LC molecule photoalignment depends strongly on the pump-beam intensity (Ouskova et al., 2001b). Two mechanisms including adsorption and desorption, which dominate in strong and weak intensity regimes, respectively, are utilized to explain the photoalignment effects. It is claimed that the adsorption effect tends to reorient LC molecules parallel to the polarization direction of the pump beam while the desorption effect acts the opposite (Ouskova et al., 2001a). C.-R. Lee et al. further utilized SEM and AFM measurements to directly investigate the effect of morphology of the surface adsorbed with MR molecules on the photo-controlled alignment of LCs (Lee et al., 2004). Three morphologies are observed and clarified a homogeneous layer of adsorbed dye molecules, an adsorbed MR layer patterned in microgrooves, and a rough adsorbed layer with ribbons. The former uniform and microgroove morphologies dominate in the weak-intensity regime depending on the irradiation time, and they are shown to tend to reorient the LC molecules perpendicular and parallel to the pump beam polarization. As for the last MR layer with rough morphology, it dominates in the strong-intensity regime and would possibly disturb the orientation of LC molecules, resulting in a random configuration.

Lin et al. demonstrated 1D and 2D reflective diffraction devices by photorefractive MR-doped cholesteric liquid crystals in the weak-intensity alignment regime (Lin et al., 2006). Without surface treatment, the cholesteric liquid crystal initially exhibited focal conic texture with randomly aligned reflection zones as shown in Figure 9.3(a). Under the weak-linearly polarized laser irradiation, the MR dye adsorbed onto the surface and induced LC alignment perpendicular to the polarization direction, resulting aligned CLC domains as shown in Figure 9.3(b). With the aid of the photomask, 1D and 2D reflective diffraction elements could be realized as shown in Figure 9.3(c). Cheng et al. further demonstrated a reflective Fresnel zone plate based on MR-doped CLCs in the strong-intensity alignment regime with electrically switchable and optically rewritable capabilities (Cheng et al., 2007). The CLC was surface-treated to initially exhibit the uniform planar texture. A high-intensity linearly polarized laser beam was incident onto the sample through a photomask with the Fresnel zone pattern, randomizing the cholesteric liquid crystal domains in exposed areas. The amplitude difference between the planar and focal conic textures gives rise to the diffraction component. Wang et al. also demonstrated a polarization-independent grating by photorefractive MR-doped cholesteric liquid crystals in the strong-intensity alignment regime (Wang et al., 2006). The initial planar CLC was irradiated using the interference pattern of an unpolarized light source. In bright regions, the rough adsorbed dye surface induced homeotropic LC alignment while the planar texture remained in dark regions. Optical efficiencies as high as 90% for polarization-independent beams were demonstrated and they decrease
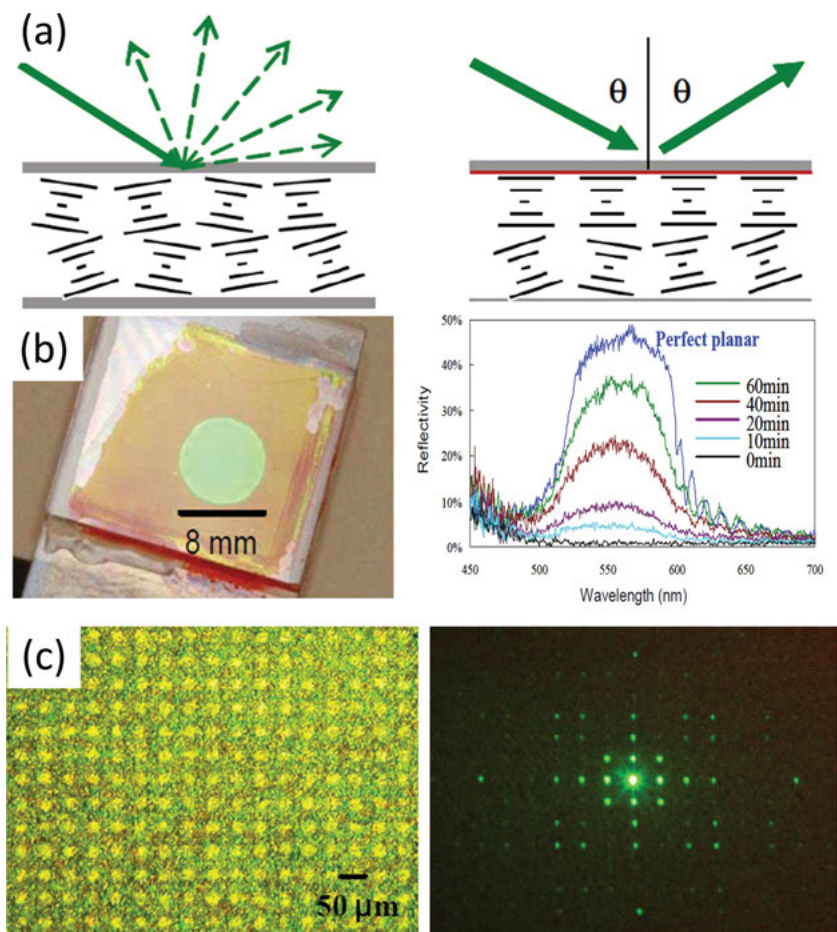
Figure 9.3: (a) Schematic illustration of the cholesteric LCs before and after light irradiation, (b) image of the irradiation region with green reflection and reflection spectra with the pump time and (c) image of the 2D patterned reflection grating and the diffraction pattern (Lin et al., 2006). Copyright 2006 *Optical Society of America*.

as the grating period narrows down. Li et al. figured out a approach to modulating the fingerprint-textured CLCs doped with MR molecules through asymmetric photoalignment (Li et al., 2017). It is shown that dashed-curve-and dashed-line-shaped fingerprint textures could be generated by one-step polarization holography utilizing two orthogonal beams with circular polarizations and linear polarizations, respectively. Apart from the different alignment effects of different MR adsorbed surfaces on cholesteric liquid crystals, it is also shown that the cholesteric liquid crystal director configuration could, in return, align the adsorbed dye molecules (Voloschenko and Lavrentovich, 1999). A single polarized laser beam irradiated onto the fingerprint-textured cholesteric

liquid crystal. Methyl red molecules would phase separate and assemble onto the cell surface into micro scales from the LC host. The density of adsorbed dye molecules is dictated by the LC director modulation with respect to the light polarization. The AFM investigation after LC removal on the cell surface clearly shows a helical distribution of dye molecules with a pitch in agreement with that of the fingerprint texture.

Kim et al. further demonstrated an all-optically switchable grating based on ferro-electric liquid crystals (FLC) doped with MR molecules (Kim et al., 2015). The periodic polymer structure was first constructed through the selective photo-polymerization of mesogens as controlled by the photomask. The subsequent infiltration of the FLC molecules into such polymer networks would result in a uniform alignment in the surface-stabilized geometry. The MR-doped LC in the polymer network regions is photonically insensitive due to the cross-linkage of polymers while that between the polymer walls is photosensitive. Under the pump beam, the photorefractive FLC alters its alignment and the resultant optically controllable diffraction properties arise. The rising and falling times during the optical-switching process were estimated to be 296 ms and 744 ms, respectively. The photorefractive performance of the MR-doped blue phase liquid crystal could be more complex. Chen et al. conducted a real-time monitoring of the photoinduced grating formation in blue phase LCs doped with MR molecules where two pump beams were used to construct the interference pattern (Chen et al., 2015). Both transient and persistent gratings come into forming with the former attributed to thermal indexing and lattice distortion while the latter attributed to lattice distortion/expansion. These effects are all caused by MR molecule isomerization under optical irradiation. In addition to the BP LC diffraction gratings, it is found that a prolonged exposure would red-shift the reflection band peak to 625 nm by a wavelength spacing of 40 nm. These nonlinear effects have made MR-doped BP LCs candidates for all-optical photonic applications.

9.2.2 Photorefractive systems enabled by photoconductive materials

In bulk photorefractivity, charge carriers are generated and redistributed directly in the LC volume. As a result, the photoinduced self-generated electric fields in the material bulk is responsible for the refractive-index adjustment. In this case, the surface electrical properties or surface morphology of the substrates plays an insignificant role. Photorefractive chiral smectic liquid crystals doped with photo-charge generating and transporting agents are frequently utilized to investigate the bulk photorefractive effects for their possible bistability and ultra-fast reorientation times. It was soon realized that the birefringence induced by the high electric fields used to pole the chromophores is also responsible for the high index modulations (Moerner et al., 1994). In the case of ferroelectric phases, the electric field alters the spontaneous polarization direction in the areas between bright and dark fringes, inducing the

orientation of the FLC molecules depending on light intensity. This is different from the processes that occur in other photorefractive LC materials in that the molecular dipole directly responds to the electric field rather than the bulk polarization. The refractive-index amplitude modulation in photorefractive chiral smectic phases could be calculated by considering parameters including LC birefringence, the spontaneous tilt angle, the electroclinic coefficient, the amplitudes of the effective fields, and light polarization (Termine and Golemme, 2002). Calculation results show a possible, large refractive-index modulation with optimized sample orientation and light polarization and they agree well with experimental results.

Talarico et al. demonstrated stable, easily erasable and rewritable refractive-index patterns utilizing the fullerenes doped FLC (Talarico and Golemme, 2006). C70 was chosen as the photosensitizer due to the good solubility and was doped into the FLC at a concentration of 0.2 wt%. Two interfering laser beams irradiate on the sample with a simultaneous electric field application for a time duration. The applied electric field not only erased previous refractive-index modulations but also speeded up charge photogeneration and provided a drift mobility to improve the photo-responsibility of the doped FLC. Due to fast reorientation dynamics and orientational bistability, the nonlocal refractive-index patterns can be erased in 10 μs by the electric field and rewritten in 100 μs. Phase-shift measurements were performed to confirm the existence of the phase grating with a phase shift being $\Theta = 40° \pm 10°$. The intensity exchange between the incident beams and the diffractive beams in the phase-shifted refractive index grating led to the amplification of one of the beams. The authors further demonstrated the use of the photorefractive system in optical thresholding, where spontaneous polarization switching can be obtained only when the electric field is above a certain value (Talarico et al., 2007).

Although the fullerenes could work as the doped photosensitizer into the FLC for bulk photorefractive demonstrations, the poor solubility and lack of chirality limit the photorefractive performance in terms of the response time and gain coefficient. Sasaki et al. synthetized four terthiophene compounds with chirality and they were mixed with common smectic LCs to enable a photo-responsive system (Sasaki et al., 2011). The magnitude of the photocurrent under optical actuation was affected by the miscibility of the novel chiral compounds in the LC host. Two-beam coupling experiments on the photoconductive mixtures reveal that it exhibits a fast response time (5 ms) and a large gain coefficient (110 cm^{-1}). The authors further optimized the compositions of the material mixture and demonstrated its application to optical signal amplification (Sasaki et al., 2014). Figure 9.4(a) depicts the experimental setup which consists of two beam interference and normal electric field. As shown in Figure 9.4(b) and (c), the gain increases linearly with the applied voltage up to 2 V/μm while the response time decreases. The performance of the gain and response time becomes better when the doping concentration of the chiral compound increases. The optimized FLC compound exhibits a high gain coefficient (1,200 cm^{-1}) and a very fast response time (1 ms). Real-time image amplification was also demonstrated due to the large gain and fast response
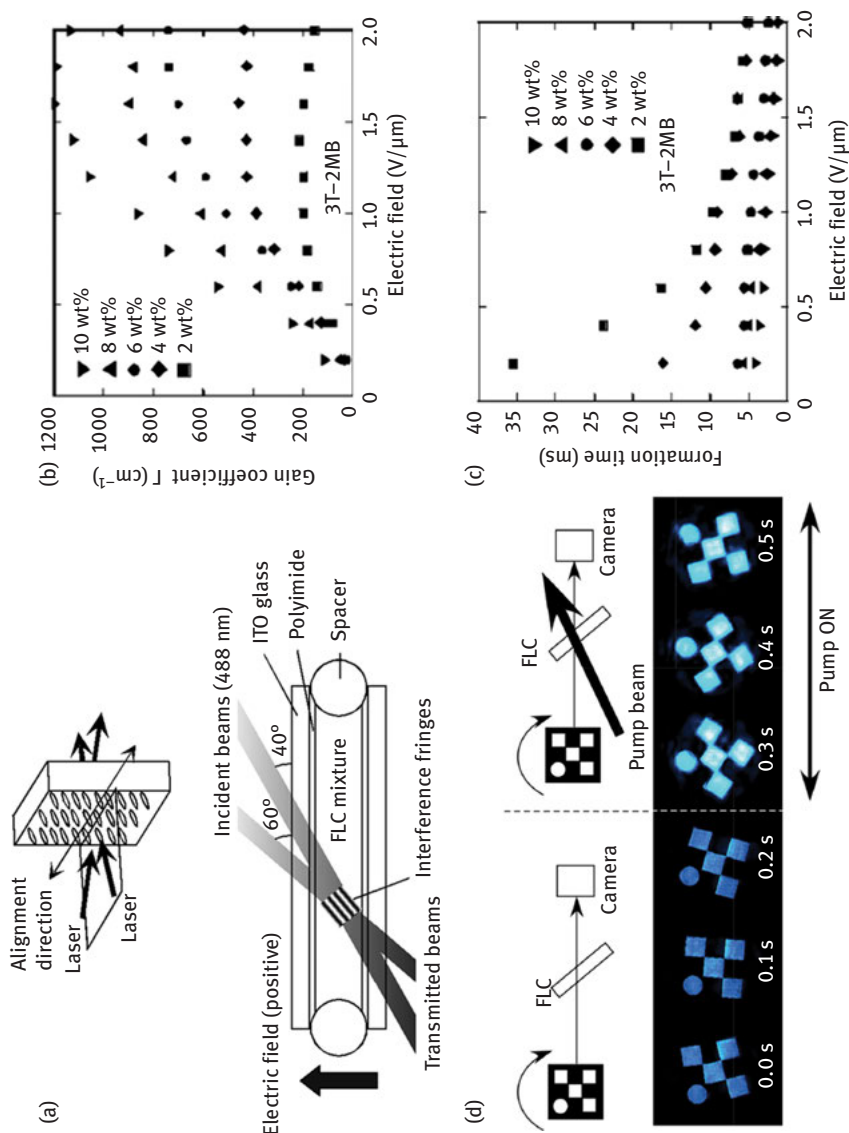
Figure 9.4: (a) Experimental setup with two writing beams and an applied electric field. (b) Gain coefficient as a function of the dopant concentration and applied electric field. (c) Grating formation time as a function of the dopant concentration and applied electric field. (d) image amplification (Sasaki et al., 2014). Copyright 2014 *The Royal Society of Chemistry*.

as shown in Figure 9.4(d). Furthermore, realistic application of 3D display was demonstrated by the formation of a dynamic hologram (Sasaki et al., 2013).

9.2.3 Chiral liquid crystal with specific photorefractive materials

Surface photorefractivity, in which the LC layer is confined between photoconducting or photorefractive materials could expand the photo-generated gratings to the Bragg diffraction regime with large gain coefficients. The evanescent field from the photoconductive window, which could penetrate a distance approximately 1.5 times the cell gap (Jones and Cook, 2004), exerts a torque on the nearby LC molecules, reorienting them to obtain a modulated refractive index. The large unidirectional gain is a result from a combination of the locally pre-tilted liquid crystal molecules together with splay-induced flexopolarization (Reshetnyak et al., 2012). The energy transfer efficiency increases as the ratio of grating constant or periodicity to cell thickness reduces and a gain coefficient up to 3,700 cm^{-1} was demonstrated, which is two orders of magnitude higher than those found in common inorganic crystals (Evans and Cook, 2007; Reshetnyak et al., 2010).

Cook et al. investigated the gain properties of CLC with inorganic photorefractive Ce:SBN as windows (Cook et al., 2007). As for the single-window hybrid cell, the gain coefficient increases when the grating pitch decreases, while for the dual-window hybrid cell, the gain characteristics exhibit an inversion dependence. The highest gain coefficient was measured in the Bragg regime with the single-window hybrid cell. In addition, the gain performance in CLC cells was barely affected by the rubbing direction. The authors further theoretically investigated two-beam energy exchange process in the hybrid photorefractive inorganic–cholesteric cell with a single-window geometry (Reshetnyak et al., 2014). As a result, the authors stated that altering the initial flexopolarization may increase the sensitivity on the space charge field which could be achieved via an inhomogeneous cholesteric with a pitch gradient.

Termine et al. further investigated photorefractive properties of SmA* phases sandwiched between photoconducting layers (Termine et al., 2001). Due to the chiral molecular components in SmA* phases, the phase symmetry is reduced which induces the electroclinic effect. As the same with the bulk photorefractivity, the electroclinic effect is responsible for the refractive-index modulation in this surface photorefractive geometry. An organic photoconductive layer which consists of polyvinyl carbazole and (2, 4, 7-trinitro-9-fluorenylidene malononitrile) was spin-coated onto the ITO glass with a thickness of 5 μm. An additional rubbed PVA layer was further coated onto the photoconductive layer to induce surface alignment. An electric field was also applied to provide a charge drift mechanism for improved photogeneration efficiency. A net optical coupling gain of 600 cm^{-1} was achieved where the grating period is 30 μm. However, there appears no optical gain when the grating period is smaller than 7 μm, possibly

due to the increased elastic energy on shorter-length scales. The authors further studied the photorefractive performance of photoconductive films containing droplets of smectic SmA* LC (Termine and Golemme, 2001). After evaporation of the chloroform, the elastic film containing the polymer, liquid crystal, and photorefractive material was heated while being mechanically stretched, resulting in a 50 μm-thick film dispersed with SmA* LC droplets in a cylindrical shape. A low gain coefficient of 30 cm^{-1} at 43 V/μm was measured through the two-beam coupling technique, due to the small volume fraction of the phase-separated LCs in droplets. The time for the buildup of the grating was measured to be around 25 ms which is mainly restricted by the buildup time of space-charge field instead of the LC director reorientation rate.
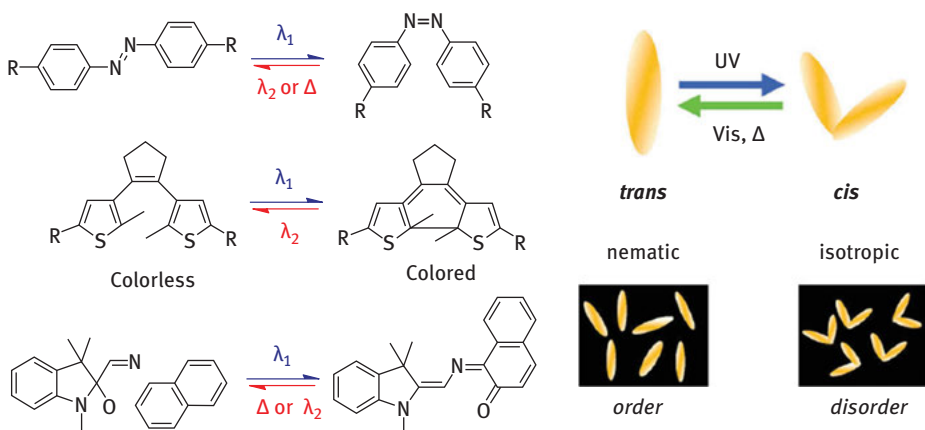
Figure 9.5: Left: Some photo-isomerizable molecules as chiral switches, Right: Schematic illustration for the trans and cis isomer structures (Bisoyi and Li, 2014). Copyright 2014 American Chemical Society.

In principle, the photorefractive effect in chiral LCs could respond to the irradiated light patterns via the locally adjusted refractive-index modulation. The refractive index modulation was induced by the LC reorientation in terms of the adsorbed dye surface morphology or inner space-charge field directed by the light pattern. The induced refractive-index modulation may be permanent or transient and could be optically or electrically rewritten depending on the material and the recording conditions. The light pattern could be provided by a photomask or the interference pattern constructed by several coherent beams. The recording of the periodic or quasi-periodic pattern in the photorefractive chiral LCs gives rise to the formation of the diffraction grating which could be optically switchable or tunable. However, the intrinsic superstructure exhibited by the chiral LCs in the helical geometry was not fully exploited. We would show in the next section the recent developments on the introduction of photo-isomerization into the self-assembled superstructure of chiral LCs. A wide range of electro-optical

properties of the self-assembled superstructures—including the LC phase type, the alignment ordering, the handedness and the pitch—could be optically controlled, enabling more versatile and flexible photonic-modulated devices.

9.3 Photo-isomerized chiral liquid crystal for dynamic diffraction manipulations

Photo-isomerization defines the material property of reversible *trans–cis* isomerization upon light irradiation. For example, a photo-isomerized material may undergo isomerization from *trans* to *cis* under ultraviolet (UV) light irradiation and the reverse process from *cis* to *trans* can occur thermally or photochemically with visible light. Figure 9.5 shows some photo-isomerizable molecules as chiral switches. The *trans* and *cis* molecules schematically shown in Figure 9.5 have different geometrical properties and such geometrical changes could produce concomitant changes in physical and chemical properties, not only in the photo-isomerized material itself but also in the surrounding matrices. The combination of self-assembled superstructures with photo-isomerization capabilities opens a novel approach for efficient optical modulation, resulting in a number of applications such as light-addressable displays, optically tunable laser and optically modulated beam-steering gratings. Due to the anisotropic properties of LC molecules, the intermolecular interactions among these molecules could be transferred over a macroscopic range. This peculiar LC property provides a mechanism for the amplification of the photo-isomerization effect, leading to efficient light modulation with low intensities. We would show in detail in this chapter that the dramatic difference in molecular geometry of the *trans* and *cis* forms endows chiral LCs with various optically modulated properties. The diffraction grating with chiral LCs could be switched on and off or be efficiency-tunable when suitable light induces the *trans* and *cis* isomerization. The chiral LC may be optically switched among different phases due to the reversible photo-isomerization effect. The handedness and the helical pitch in chiral nematic LCs could be adjusted on purpose by light illumination with different wavelengths, opening up new possibilities for tunable photonic crystals. In addition, the phase transition and bandgap tunability were also demonstrated using photo-isomerization in blue phase LCs.

Chiral LCs could be made photo-isomerizable, and this could be done by doping photo-isomerizable molecules into inert LCs. Depending on the molecular structure of the photo-isomerizable compound and its interaction with the host LC, the photoreactive compounds embedded in the liquid crystals could be achiral or chiral. In the former case, the photoreactive molecules could be further classified into mesogenic or non-mesogenic compounds. Due to the compatibility of the mesogenic dopants with the host LCs, a higher concentration of the photoreactive compounds could be doped into the system, when compared with the non-mesogenic one. However, the host liquid

crystal should be chiral or added with additional nonphotoreactive chiral dopant to exhibit a chiral LC phase. The isomerization of the photoreactive compound changes its molecular geometry, which in turn modulates the LC alignment, resulting in interesting, optically controlled phenomena. The latter is the case in which photoreactive compounds dispersed in liquid crystals are chiral. The twisting power or the handedness of the photoreactive compound alters after the photoreaction, which changes the helical pitch or handedness of the chiral liquid crystal on demand.

9.3.1 Azobenzene-based photoresponsive chiral liquid crystal

Some of the first work in the area of photochirals focused on azobenzene molecules which shows good thermal stability and photo-reversibility (Ichimura, 2000; Ichimura et al., 2000; Sackmann, 1971). Upon suitable light irradiation, azobenzene molecules undergo reversible *trans–cis* transformations, and a dramatic difference in molecular geometry of the azobenzene molecules arises. Such photoinduced geometrical change of the light-responsive molecules can transfer to LCs by molecular cooperative interactions, driving the whole mesognes into ordered states with a small amount of photo-responsive chiral switches. This is very useful in photo-driven actuators with a large system change at the cost of a low energy input. Depending on the photo-isomerization-induced characteristics in chiral LCs, the performance of azobenzene-based photoresponsive chiral liquid crystal discussed in this section was further divided into three subsections: optically controllable diffractive performance in chiral LC gratings, optically modulated self-assembled superstructures in chiral LC, and light-induced phase transition in chiral LCs.

9.3.1.1 Optically controllable diffractive performance in chiral LC gratings

This subsection summarizes the recent results in azobenzene-based photoresponsive chiral liquid crystal with controllable diffractive performance. These investigations did not directly utilize the self-organized superstructure in the chiral LCs for diffractive demonstrations. Instead, periodic or quasi-periodic light patterns introduced additional routes such as the interference pattern or the photomask to demonstrate the diffractive properties. In this case, azobenzene-based chiral LCs serve as the photoreactive system for optical control. Noga et al. presented the holographic grating recording in chiral azobenzene LCs (Noga et al., 2016). The formation of the diffraction grating is a result of the isotropic-to-nematic phase transition, that is, in bright regions of the interference pattern constructed by two green laser beams, the isomerization happens and the azobenzene LC changes from the rodlike LC form into the bent-shaped isotropic form, resulting in a refractive-index modulation between dark and bright regions in the sample. The grating formation

process has two stages with the first being connected with the pre-domain grating and the second one being attributed to the light-induced phase transition. Sasaki et al. established the holographic recording of phase gratings working in dual reflection and transmission modes by doping the azo dye DR1 into the chiral LCs (Sasaki et al., 2009). The LC mixtures were sandwiched between planar-alignment cells with antiparallel rubbing. The interference pattern formed by two pump beams (532 nm, linearly polarized perpendicular to the rubbing direction) was used for illumination. In bright fringes, the helical pitch blue-shifted, generating transmission or reflection intensity to differ under suitable operating wavelengths. The intensity modulation corresponding to the periodic interference pattern gives rise to a transmission or refection grating. The pitch variation under optical pumping was around 4 nm. The hybrid grating showed polarization dependence as a result of the polarization-sensitive CLC. Hsiao et al. demonstrated a polarization independent grating in azo-doped polymer-dispersed chiral liquid crystals (Hsiao and Chang, 2010). The interference pattern was used to irradiate the sample mixture containing monomers, chiral liquid crystal, and azo-LC. In bright regions, the monomers undergo photoinduced polymerization which leads to the phase separation of chiral LCs into dark regions. Under optical pumping, the phase-separated chiral LCs transformed from the CLC phase to the isotropic phase as a result of the photo-isomerization of the azo-LC. The refractive index of the polymer/LC grating is thus modulated, leading to a diffraction efficiency adjustment from 81% to 77%.

Apart from the formation of optically modulated gratings by the single interference field, there are further investigations of the utilization of biphotonic illumination at different wavelengths. The experimental setup is shown in Figure 9.6(a), in which an interference pattern at a wavelength and a homogeneous illumination at a different wavelength are used to irradiate the sample. Yeh et al. demonstrated such an optically modulated biphotonic grating in azo dye-doped chiral liquid crystal (Yeh et al., 2007a). The compound mixture was injected into the planar cells with parallel rubbing and was illuminated with a homogeneous green beam and an interference pattern of red beams simultaneously. The helical pitch in the original form was estimated to 1.5 μm to avoid reflections in visible wavelengths. The green beam induced *trans–cis* isomerization while red beam suppressed this by *cis–trans* isomerization. The balance of the forth and back isomerization processes resulted in homeotropic-like and planar-like chiral LC phases in dark and bright regions of the interference pattern, respectively, giving rise to a refractive-index modulation. The grating diffraction efficiency could be modulated by adjusting the intensities of different beams. The authors further demonstrated another biphotonic grating in a different azo dye-doped chiral LC mixture (Yeh, 2011). As the same, the homogeneous green beam illumination leads to *cis–trans* isomerization of the azo dye while the interferencing red beams induces *trans–cis* isomerization in bright fringes. However, the effect of isomerization on the chiral LC alignment was different, that is, the *cis–trans* isomerization tends to elongate the helical pitch while the reverse isomerization

suppresses the elongation. As a result, the grating showed a strong dependence on the handedness of incident circularly polarized light. Kuo et al. demonstrated a transflective Fresnel biphotonic lens using the azo dye-doped chiral LCs (Kuo and Yeh, 2012). The Fresnel interference pattern by two green beams and the homogeneous UV beam were simultaneously illuminated onto the sample. In dark regions, the UV light induced the *trans–cis* isomerization and the planar CLC structure was destroyed, leading to irregular multidomains with low transmittance. The decreased reflection efficiency as a function of UV illumination time is shown in Figure 9.6(b). In bright regions, the green light suppressed the conformational transformations. As a result, the reflection and transmission of the CLCs in bright regions result in a focusing lens working in the transflective mode. The focusing patterns are shown in the above and below sub-pictures for the transmissive and reflection modes, respectively. The focusing efficiencies as a function of the green beam intensity for both working modes are shown in Figure 9.6(d). A maximum efficiency of 20% is observed for the transmissive mode when the green beam intensity is around 15 mW/cm^2.
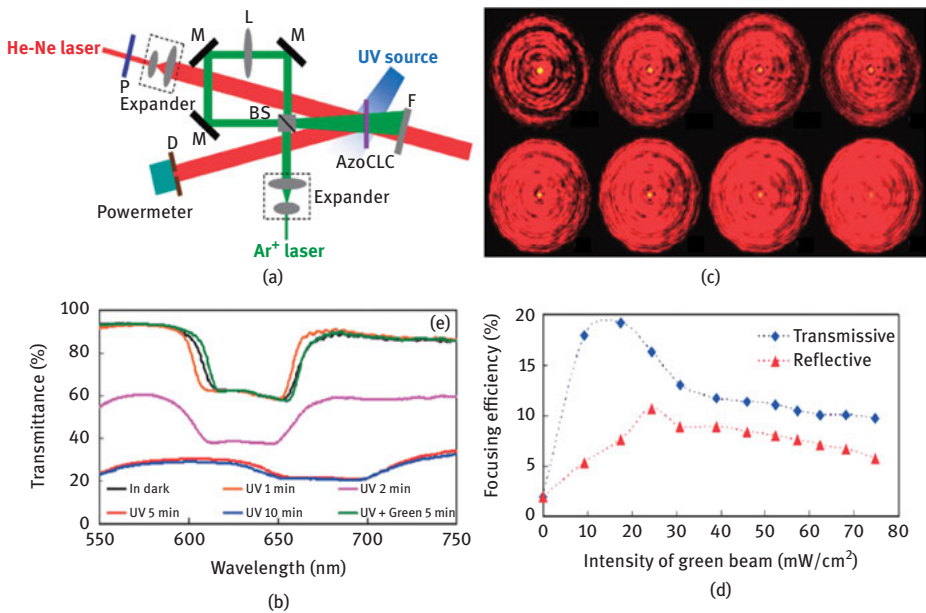
Figure 9.6: (a) Experimental setup for biphotonic recording of the Fresnel pattern. (b) Decreased reflection efficiency with UV irradiation. (c) Above: Focusing pattern for the transmission mode; Below: Focusing pattern for the reflection mode. (d) Focusing efficiencies as a function of the green beam intensity for both the transmissive and reflective modes (Kuo and Yeh, 2012). Copyright 2012 *The Japan Society of Applied Physics*.

9.3.1.2 Optically modulated self-assembled superstructures in chiral LC

In the last subsection, researchers have employed the interference light field to write diffractive gratings in azo-doped chiral LCs. The photo-isomerizable azobenzene compound functions as the photo-sensitive material for refractive index recording or modulation which leads to optically switchable or tunable diffractive optical devices. This approach is direct and efficient; however, it requires the setup of the holographic recording apparatus. It is known that chirality endows liquid crystal soft materials with the capability to self-assemble into helical superstructures. These superstructures may be periodic or quasi-periodic and exhibit fascinating diffractive properties for versatile light manipulation, such as the diffraction of reflective phase grating, known as the Bragg reflection, the utilization of the self-organized superstructures formed in chiral LCs as novel and advanced micro-nano optical devices is straight and removes the requirement of additional nanofabrication techniques. The addition of the azobenzene compound into the chiral LCs offers an efficient route to optically tune the parameters of the self-assemble superstructures such as the helical pitch and the handedness. This subsection would thus summarize the recent results on optically modulated self-assembled superstructures in chiral LC.

The ability of a chiral dopant to induce a twist in a nematic host is represented by the helical twisting power (HTP). HTP is equal to $\text{HTP} = (p \times c)^{-1}$ where c is the concentration of the chiral dopant and p is the helical pitch. HTP has a complex dependence on the dopant structure, the chirality nature and the dopant's interaction with the host. Depending on the azobenzene dopant structure, the photoreactive compounds may be chiral or achiral. In the former case, HTP or handedness of the chiral azobenzene switch would change when photo-isomerization takes place, which results in the adjustment of the helical pitch or handedness. In the latter case, it is considered that *trans–cis* isomerization causes changes in the helical pitch according to the thermal pitch coefficient brought by the photoinduced order/disorder process (Ruslim and Ichimura, 2000). However, achiral photo-responsive molecules generally provide a limited helical pitch tuning range (<100 nm). The former approach is free from the addition of the chiral dopants into the mixture and the geometrical change induced by the photo-isomerization of the chiral switch could bring about a large difference in HTP, and thus the former approach is more efficient in optically tuning the helical superstructures in chiral LCs.

In this chapter, we would introduce two kinds of azobenzene chiral switches depending on their effects on the helical superstructures during the photo-isomerization process. One is described as the HTP-changing photo-chiral switch and the other is the handedness-inverting photo-chiral switch (Eelkema and Feringa, 2006). The HTP-changing photo-chiral switch yields tunable optical responses governed by a direct reversible change in the helical pitch, resulting in the Bragg reflection adjustment which is of potential for tunable optical devices. In common cases, the HTP decreases along with the *trans–cis* photo-isomerization and, accordingly, the pitch is elongated

and the reflection band red-shifts. As for handedness-inverting photo-chiral switch, the photo-isomerization could induce not only a change in the helical pitch but also a change in the sign of HTP. The inverted HTP sign means an inverttion of handedness of the helical superstructure. It is also interesting that the helical pitch elongates as the pitch unwinds in one handedness and compresses as the pitch contracts in the other handedness during the photo-isomerization of chiral switches (Slaney et al., 1992). Apart from the tuning range in the helical pitch and the handedness-inverting capability of the azobezene chiral switches, other characteristics including the isomerization wavelength, reversibility, thermal relaxation times, cycling life-time and stability, should also be taken into consideration when designing and optimizing the molecular structures of the photo-sensitive chiral switch.

Generally speaking, photo-isomerizable chiral switches with properties of high HTP and a large reversible HTP change among their isomeric forms are preferred. The high initial HTP reduces the required chiral switch concentration for the desired super-molecular helical structure. This is beneficial for the stability of the liquid crystal-line phase and other electro-optical properties. Meanwhile, a large reversible HTP change during the photo-isomerization ensures a wide tunability of the helical pitch and related optical responses. Experimental and theoretical results show that high structural rigidity and low conformational freedom of both the chiral switch and the host LC are beneficial for high HTP values, whereas a large conformation change in *trans* and *cis* chiral switch isomers is desirable for a wide tunability of the helical pitch (Bossi et al., 2006; Delden et al., 2002; Earl and Wilson, 2003; Kawamoto et al., 2007; Ruslim and Ichimura, 2001). The early investigations primarily focused on azobenzene switches with only one chiral center (Kurihara et al., 2001, 2000; Li et al., 2005). Math-ews et al. designed planar chiral bicyclic azobenzene derivatives as efficient chiral switches (Mathews and Tamaoki, 2008). The structural rigidity was beneficial for the generation of a large HTP value at the initial state. In addition, the azobenzene moiety was in the rigid chiral core unit, thus a great geometrical and chiral conformational change is expected to take place when the photochromic unit undergoes isomeriza-tion. The planar azobenzene chiral switch showed a HTP of 43 (wt.%)μm^{-1}. The reflec-tion band was tuned from 450 nm to 630 nm with a UV illumination duration of 120 s. The thermal relaxation from the cis isomer to the trans isomer is ten times faster (Li et al., 2007). On the other hand, azobenzenes with axial chirality have attracted a lot of interest. They commonly exhibit large initial HTP values and large tuning ranges, probably due to the advantage of molecular asymmetry in bringing chirality. Li et al. designed and synthesized azobenzene switches incorporating axially chiral binaphthyl units (Li et al., 2007). Two flexible long alkyloxy chains were introduced into the molec-ular structure to increase the solubility in the nematic LC host. It was found that these axially chiral photo-switches possessed a high HTP of 57 (wt.%)μm^{-1} when doped in the nematic LC E7. Due to the two azo linkages in these axially chiral switches, revers-ible *trans–cis* isomerization of azo configurations took place in turn, producing isomers containing one or two *cis* configurations. The ratio of *trans/cis* configurations could be

photochemically controlled, allowing a fine tuning of the reflection color from the helical periodic structures. In their work, by doping 5.0% of the axially chiral dopant into the LC host, the cell reflection changed from dark blue (approximately corresponds to a wavelength range of 200 nm) to red under UV irradiation. The reverse isomerization process could happen via visible light irradiation or thermal relaxation in dark for 24 h. Wang et al. synthesized two axially chiral azobenzene switches with extended conjugation that undergo *trans–cis* transformation under visible lights (Wang et al., 2012). When they are doped in achiral nematic LCs at a large concentration (20 wt.%), a dynamical helical superstructure without using UV light was demonstrated. In addition, the HTP value was increased from the switch *trans* isomer to the *cis* isomer under 440 nm irradiation, while it was decreased from the *cis* isomer to the *trans* isomer under 550 nm irradiation, exhibiting a reverse HTP change compared with common chiral switches. The initial HTP value was 52 (mol%)μm^{-1}, and after a illumination duration of about 30 s with 440 nm light, it increased to 89 (mol%)μm^{-1}, providing a tuning range of the reflection band of around 200 nm. Ma et al. reported an azobenzene axially chiral switch which enabled reversible tuning of the reflection peak over the whole visible band (Ma et al., 2010). The molecular structure and its molecular conformation change under UV and visible light illumination were shown in Figure 9.7(a). The photoreactive axially chiral switch contained two azo linkages, and a mesogenic building block was introduced when designing the molecular structure. The molecular structure ensured better *cis*-to-*trans* conversion and could induce a dramatic geometrical change upon photo-isomerization. Experiments showed that the chiral switch HTP changed from 90 (wt.%)μm^{-1} to 26 (wt.%)μm^{-1} upon a low power UV light irradiation for 50 s. The large reversible HTP change of the chiral switch under photo-isomerization led to a wide tuning range of the reflection band between 460 nm and 820 nm. The reflection color images and corresponding reflection spectra under UV and visible were shown in Figure 9.7(b) and (c). Light-induced bistable display was also demonstrated by using the stable focal conic textures after light irradiation and the stable planar textures without light irradiation. White et al. further demonstrated an ultra-wide tuning range of the superstructure reflection band by utilizing axially chiral azo switches containing two azo-linkages (White et al., 2009). The azo chiral switch was doped into the nematic LC MDA-00-1444 at a concentration between 2 wt.% and 10 wt.%. The initial Bragg reflection shifted from the IR to the UV spectrum, as the concentration of the azo chiral switch was increased. Photopumping the sample with a switch concentration of 6 wt.% by UV light red-shifted the reflection peak from 600 nm to over 2,400 nm, covering the visible, near-IR, and shortwave IR spectra. As for the photo-tuning rate, it increased with the increase in pump light intensity, while it was reduced with the increase in the cell gap.

The CLCs reflect light as a 1D photonic cystal and the bandwidth is dictated by the refractive-index modulation and the pitch. Another remarkable characteristic associated with CLCs is the handedness selection, and right- or left-handed CLCs could be selectively prepared by modulating the intrinsic chirality of the dopants. For example,
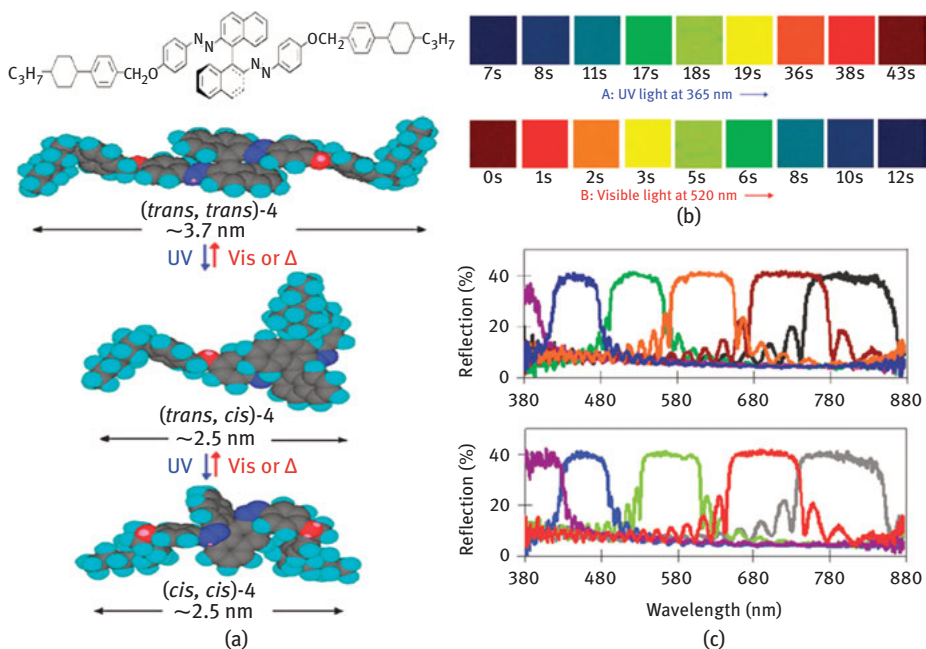
Figure 9.7: (a) Molecular structure of the axially chiral azobenzene switch and its schematic molecular conformation change under UV and visible light illumination. (b) Reflection color images of the planar CLC sample with UV and visible light illumination with different durations. (c) Reflection spectra of the planar CLC sample. Top: under UV illumination with different times; Bottom: under visible illumination with different times (Ma et al., 2010). Copyright 2010 *The Royal Society of Chemistry*.

enantiomers of a chiral mesogen can be used to obtain an equal HTP with the opposite signs (Mathews and Tamaoki, 2008). In addition to the above-mentioned investigations into the tunability of the cholesteric pitch to obtain a large tuning of the reflection band, a reversible switching of the helical superstructure handedness via photo-isomerization also attracts significant interest. van Delden et al. prepared a binaphthyl derivative containing two azobenzene chromophores as the chiral switch (Delden et al., 2004). The chirality arose from the two dihedral naphthalene moieties and the chiral bi-naphthyl moiety is unbridged with the methylene tether to enable considerable conformational flexibility. Accordingly, the molecular photo-isomerization would have a pronounced effect on the overall molecule geometry and, as a consequence, on the chirality. Due to the presence of two azo-linkages, there are three isomers corresponding to the all-*trans* isomer tt-(S), *cis* 1 isomer ct-(S) and *cis* 2 isomer cc-(S). The HTP values of the three isomers were calculated to be +10.9 (wt.%)μm^{-1}, −8.4 (wt.%)μm^{-1} and −39.3 (wt.%)μm^{-1}, respectively. This chiral switch exhibited inversed handedness with a considerable tuning range. However, the initial HTP value of the *trans* isomer was low and thermal isomerization to the initial state was slow. Mathews et al. synthesized planar chiral bicyclic azobenzenophane as the photo-responsible switch

(Mathewsa and Tamaoki, 2009). The *trans and cis* isomers exhibited different HTP values with opposite signs, generating a handedness inversion when they are doped into LCs for helix induction. The initial HTP of the *trans* isomer is still very low. The group further demonstrated a fast light-controlled reversible handedness inversion of the helix using cyclic azobenzenophanes with axial chirality (Mathews et al., 2010). The switch consisted of an axially chiral binaphthyl moiety bonded to the meta positions with three methylene linking groups, providing the compound with a high conformation flexibility. The chiral switch in the LC K15 exhibited an initial HTP value of 50 (wt.%)μm^{-1} in the *trans* isomer. After *trans–cis* photo-isomerization of the compound under UV irradiation, the HTP value changed to -10 (wt.%)μm^{-1}, showing a high initial HTP value and a large HTP change upon irradiation. The reflection band would be tuned between 450 nm and 800 nm with a combination of handedness inversion reversibly in a few seconds. Recently, Wang et al. demonstrated monodispersed chiral microspheres with optically controlled dynamic chirality (Wang et al., 2017b). The handedness reversible transformations of these chiral LC microspheres were vividly observed. They have synthesized axially chiral azobenzene switch and they were doped into the LC SLC1717 at a concentration of 7 wt.% as shown in Figure 9.8(a). The reflection colors and spectra are shown in Figure 9.8(b), a reversible photo-tuning of the uniform and brilliant reflection colors across the whole visible band were observed. The photo-responsive chiral LCs were shaped into microsized droplets with the aid of a capillary-based microfluidic device. Real-time adjustment of the helical pitch and the handedness inversion in these droplets under photo-pumping were directly observed by the polarization optical microscope as shown in Figure 9.8(c).

Apart from the 1D helical superstructures in CLCs, the blue phase LC that self-organizes into a 3D periodic cubic lattice could also be made photo-responsible by loading with the azobenzene chiral switch, opening the scope for optically tunable 3D photonic crystals. Lin et al. synthesized a new axially chiral azobenzene switch with two azo-linkages (Lin et al., 2013). The azobenzene chiral switch was co-doped into an achiral LC host with two chiral dopants S811 and R811 to enable the self-assembly into the BP phase. Under 408 nm light irradiation, reversible *trans–cis* isomerization of the two azo-configurations took place, producing two *cis* isomers containing one or two *cis* configurations, respectively. As mentioned, the photoinduced geometrical configuration change from (*trans*, *trans*) to (*cis*, *cis*) isomers would decrease the chirality and thus affect the periodicity or phase behavior as shown in Figure 9.9(a). The photonic bandgap of the BPs was tunable over the whole visible region (~420 nm–~720 nm) as controlled merely by visible light as shown in Figure 9.9(b). A different optical tuning characteristic in the BP blue was observed when compared with the common CLCs. The optically tunable reflection band shifted with a phase transition from the BP II to BP I phase during the yellow-green reflection transition as shown in Figure 9.9(c).
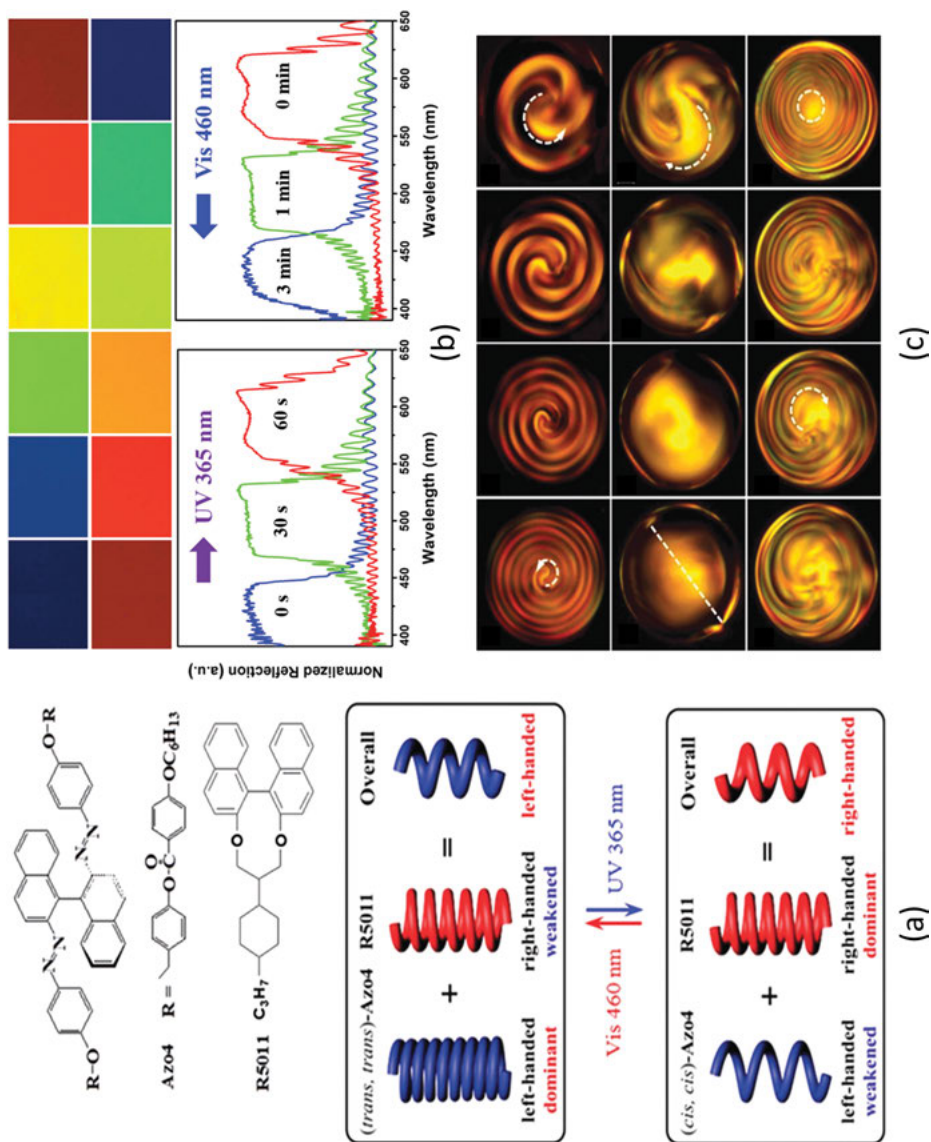
Figure 9.8: (a) Chemical structures of the axially chiral molecular switch and a photo-insensitive chiral dopant R5011. Illustrations for light-driven handedness inversion using Azo4 and R5011. (b) Reflection colors and spectra of planar cholesteric LCs upon UV irradiation and visible irradiation for different times. (c) Real-time changes in cholesteric microdroplets, indicating handedness inversion (Wang et al., 2017b). Copyright 2017 *The Royal Society of Chemistry*.

A

UV Light

408 nm / 532 nm

BP II (100)   BP II (100)   BP II (100)   BP I (110)   BP I (110)

B

100 µm

BP II (100) | BP II (100) | BP II (100) | BP I (110) | BP I (100)

0 s   2 s   8 s   10 s   27 s

C

0 s   2 s   8 s   10 s   27 s
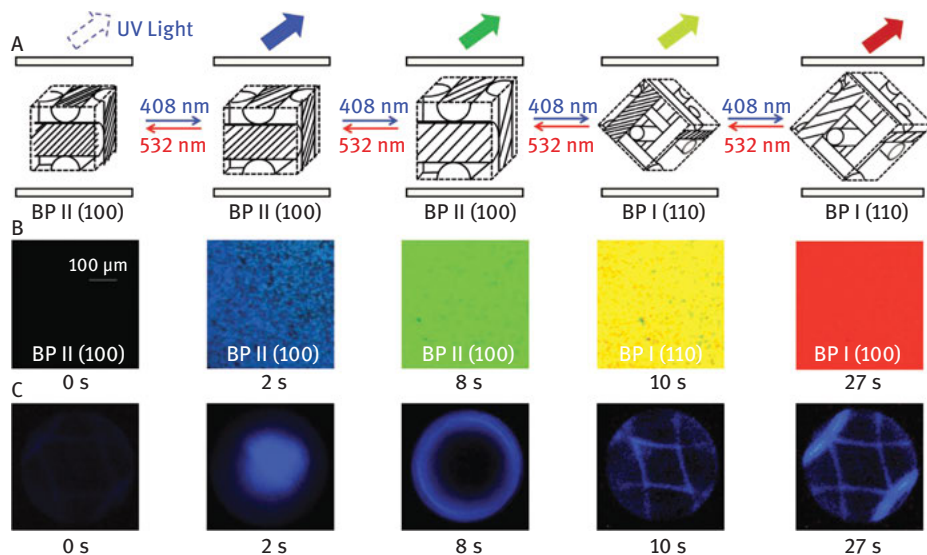
Figure 9.9: (a) The phototuning of the BPLC configuration. (b) Reflection images of the phototunable BP LC at different irradiation time. (c) The corresponding Kossel diagrams (Lin et al., 2013). Copyright 2013 WILEY-VCH.

9.3.1.3 Light-induced phase transition in chiral LCs

Due to the HTP or chirality difference of different isomers induced by photo-isomerization of the azobenzene chiral switches, the transition between different superstructures or chiral LC phases is possible. The last subsection mainly deals with the optically tunable diffractive LCs with the capability in the photo-isomerization-induced modulation of the refractive index contrast or the lattice periodicity. The transition between different self-assembled superstructures or LC phases was merely mentioned. We would give a brief summary of recent results on this topic in this subsection. As the classification of LCs into different phases is mainly dependent on the alignment of LC directors or the self-organization of LC molecules, the effect of photo-isomerization on the superstructure transition or phase transition is referred to as the phase transition. There are observations that light could induce self-organized periodic or quasiperiodic superstructures in azo-doped chiral LC mixtures. These superstructures are a result of the equilibrium among surface interactions, molecule toques, and elastic strains. Hrozhyk et al. reported a macroscopic scale transformation of CLC into 2D complex patterns (Hrozhyk et al., 2007). A low power light radiation was used to stimulate the self-organization process in the azo-LC doped chiral LCs. After an illumination period of 15 s, square LC domains of tens of micrometers stretching with different orientations were observed, and these domains formed complex 2D patterns. It is anticipated that the strain in the CLC layers caused by *trans–cis* photo-isomerization of azo-LC

molecules, accumulation of *cis*-isomers, and change in CLC equilibrium pitch value was responsible for self-assembled superstructures. The pattern depended on some parameters such as the azo-LC concentration and cell gap. The self-assembling process happens before the photo-isomerization-induced helical pitch change and this super-structure was unstable. Yeh et al. also observed the 2D grating formation in azo dye-doped chiral LCs (Yeh et al., 2007b). Green beam irradiation induced the *trans–cis* isomerization, elongating the helical pitch. When the green beam was turned off, meta-stable 2D gratings appeared as the CLCs was relaxing back. The normal strain caused by a drop in the CLC helical pitch was thought to be the attributing reason. The meta-stable 2D grating lifetime was found to be strongly dependent on the green beam in-tensity. Varanytsia et al. demonstrated photoswitchable bubble domain textures in negative (dielectric anisotropy) LC doped with azobenzene chiral switches (Varanysia and Chien, 2015). The chiral switch in *cis* conformation under UV irradiation induced more LC disorder and thus had a smaller HTP in comparison with the *trans* con-formation. As a result, the confinement ratio of the CLC could be tuned by photo-isomerization. Once the confinement ratio was tuned, the sample can be switched with an applied electric field between fingerprint and bubble domain textures, or ho-meotropic and bubble domain textures. The packing density of bubbles could further be optically controlled. Apart from these metastable superstructures formed in chi-ral LCs induced by photo-isomerization, there are also demonstrations showing the in-triguing stable superstructures. Zheng et al. presented zigzag-shaped patterns in liquid crystals doped with azo-chiral switches by a combination of the electric field and light irradiation (Zheng et al., 2017). The zigzag-shaped pattern was realized in a photores-ponsive CLC fluid with an initial lying helix geometry as shown in Figure 9.10(a)–(d). The initial lying helix geometry CLC was formed by the application of a low electric field of 1 V/µm. Irradiation of the photoreactive compound mixture with UV light in-duced a change in the helical pitch, breaking the equilibrium d/P ratio to a value where the uniform lying helix structure was deformed as shown in Figure 9.10(e)–(k). The resulting self-assembled patterns can be controlled by varying the environmental parameters such as the electric field, light intensity, and irradiation time.

Wang et al. demonstrated a photo-controllable phase transition among finger-print, focal conic, and homeotropic textures in liquid crystal doped with an azo-chiral switch (Wang et al., 2014). The thickness/pitch ratio was adjusted by the photo-responsive azo-chiral switch which enabled the transform among the three textures in a homeotropically aligned LC cell. In addition, these states can stably exist for several hours. The addition of the dichroic dye into the mixture enabled the realization of an optically controlled switch. The device showed attenuation, scattering, and transparent states in the fingerprint, focal conic, and homeotropic textures, respec-tively. Hsiao further demonstrated a photo-switchable transition among three stable states, for example, the tilted-homeotropic state, the tilted-twist state and the finger-print state, in nematic host E7 doped with an left-handed azo-chiral compound (Hsiao et al., 2017). The cell surfaces were coated with a mixture of planar and vertical
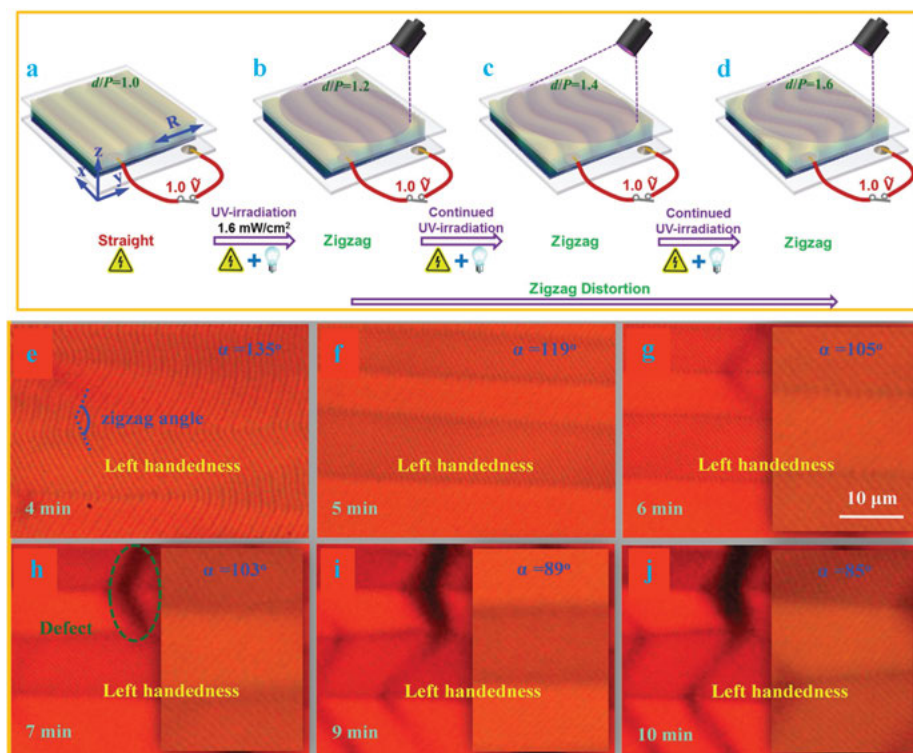
Figure 9.10: (a)–(d) Schematic generation of the zigzag-shaped pattern. (e)–(f) The evolution of the zigzag-shaped pattern upon light irradiation (Zheng et al., 2017). Copyright 2017 WILEY-VCH.

alignment agents which induced a pretilt angle of 78° from the substrate plane. The photo-isomerization of the azo-chiral compound caused a reversible elongation of the helix pitch, which leads to a transition among the three phases. The dye was doped and the sample exhibited different transmittance with regard to phase transition, opening possible applications in polarizer-free display and light modulators. Wu et al. showed photoinduced BPLC in chiral nematic liquid crystal doped with azobenzene (Wu et al., 2013). UV light initiated the *trans–cis* photo-isomerization and it remained open until the azobenzene groups fully isomerized. Then, the UV light was turned off and a visible light source was turned on. The *cis* isomer then turned back to the *trans* isomer, giving rise to cubic BP. The photoinduced BP existed when the *cis–trans* isomerization degree was between 79% and 18%. The large geometric bent angle of the *cis* isomer is supposed to contribute to the BP transition (Chanishvili et al., 2005).

9.3.2 Chiral liquid crystal polymer with azobenzene mesogens

The loading of the photoreactive compounds into the common LCs sandwiched between two glass substrates to enable optically tunable capabilities is straightforward. Common LC devices are fabricated in this way due to the fluidic state of the mesogenic materials and the requirement for the electrodes to apply the electric field. However, recent significant advancement in optically tunable chiral LC devices has shown that the light field could be both efficient and flexible to dynamically modulate the device properties. In this regard, the glass substrates with transparent electrodes are no longer a necessity in fabricating optically controllable chiral LC devices. Chiral LC polymers or elastomers with azobenzene mesogens attract much interest due to the free-standing possibility, mechanical flexibility, and novel optical responsibility. The chiral or achiral azobenzene compounds could be loaded into the LC polymer directly or the LC polymer side groups could be replaced with azobenzene-based groups. The azobenzene chiral LC polymer films were often fabricated by simply spin-coating or over-coating the liquid crystalline polymer solution onto the substrates. After solvent evaporation, high-quality LC polymer films with photo-responsibility could be obtained. It has been observed that the photo-responsibility of the chiral LC polymer magnifies itself in two physical mechanisms: (1) a refractive index modulation caused by the reorientation of LC directors or the change in the helical pitch and (2) a surface relief and a bulk density modulation by mass transport initiated by the photo-isomerization of the azo-groups. The latter mechanism was induced by mass transport in the polymer and expressed as the surface corrugation. Blinov et al. developed a two-step image recording method by a chiral LC side chain polymer grafted with azobenzene chromophores (Blinov et al., 2000). Photomask was used to selectively illuminate the LC polymer film with UV light. The *cis* isomer was very stable and resided in the exposed regions with spatial information. The film was isotropic and no images could be observed. After that, the illumination of the film with polarized visible light reveal the recorded pattern due to the refractive index modulation caused by photo-isomerization. Ryabchun et al. demonstrated a dual photo-recording by means of helix pitch tuning and LC director reorientation in azobenzene-containing LC polymer films using different pump wavelengths (Ryabchun et al., 2012). The selective reflection pattern was obtained by illuminating the LC polymer film with UV light through the photomask, elongating the helical pitch in exposed regions. After that, a polarization interference pattern constituted by two green laser beams was used to irradiate the LC polymer film. The azobenzene groups would stabilize in the rod-like *trans* state, inducing a realignment of adjacent LC directors perpendicular to the light polarization. The final LC polymer film exhibited both selective reflection and polarization grating diffraction with deformed helical structures. Surface relief gratings were also observed in this dual photo-recording system, however, the grating depth inscribed in the cholesteric films was lower (~20 nm) than that in the nematic films (~60 nm) (Ryabchun et al., 2014). Liu demonstrated the

formation of 3D fingerprint structures in polymerized chiral LCs with a copolymerized azobenzene compound (Liu and Broer, 2014). Initially, the helix direction is brought in parallel with the substrate by surface modifying the substrate surface with strong perpendicular treatment. Under UV light illumination, the azobenzene compounds in the film undergo *trans−cis* isomerization, decreasing the LC polymer order parameter. The film surface formed protrusions at the homeotropic positions while it formed wells at the planar anchoring regions, a generating 3D fingerprint structure. Thermal relaxation by the reverse isomerization to the flat surface occurred within 1 min. The elevated structures during the photo-isomerization process were further used to tune the friction force, demonstrating the possibility in optically controlled actuators.

9.3.3 Photoresponsive chiral liquid crystal containing specific isomerized materials

Aside from azobenzenes, other photo-isomerizable chromophores such as overcrowded alkene, dithienylcyclopentene, spirooxazine derivatives, cinnamates, and coumarins have also been used as functional groups in preparation of photo-responsive chiral LCs. In this section, we would briefly introduce some of them. Overcrowded alkenes are also frequently studied for applications as molecular switches to photo-generate dynamic optical effects in chiral LCs. An overcrowded alkene photo-isomerizable chiral switch is shown in Figure 9.11(a), which is composed of a lower functional group linked with an asymmetric upper functional group via an alkene. These molecules can be designed to have a few stable conformations and commonly have fast helix inversion among these isomers. Van Delden et al. demonstrated a chiral LC helix modulation and inversion by the unidirectional rotary motion of overcrowded alkene switches (Delden et al., 2002). The complete rotation process involved four steps of two light-induced *trans−cis* steps combined with two thermal helix inversion (*cis−trans*) steps. The reflection wavelength of the chiral LCs can be tuned throughout the entire visible range due to the initial high HTP and large HTP change during the photo-isomerization process. White et al. reported a wide photo-tunable reflection range of CLCs doped with an overcrowded alkene chiral switch (White et al., 2011). The reflection tuning range over 1,000 nm was accompanied by a handedness reversal and could thermally relax back to initial refection wavelength in a very short time (~1 min) when compared with the azobenzene chiral switch. The relaxation rate of photo-tunable CLCs doped with overcrowded alkene was fully determined by the helix inversion of the molecular dopants and can be accelerated by programming the switch's molecular structure (Aßhoff et al., 2013).

Diarylethenes are another class of photo-chirals with high thermal stability and excellent photo-fatigue resistance. These molecules undergo a reversible photo-isomerization from the colorless open form to the colored closed form upon UV exposure. The reverse isomerization from the closed form to the open one could not happen
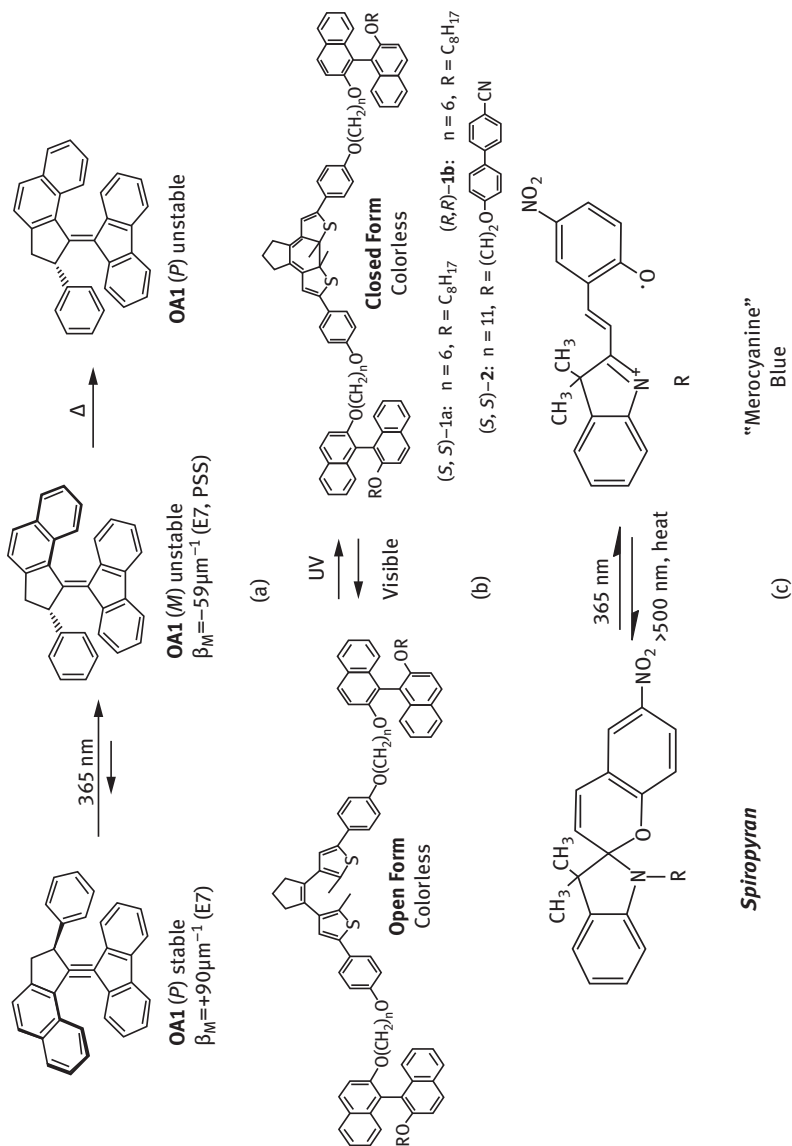
Figure 9.11: Molecular structures of photo-isomerization of chiral switches for (a) Overcrowded alkene (White et al., 2011), Copyright 2011 WILEY-VCH (b) Diarylethenes (Li et al., 2011b) Copyright 2011 *American Chemical Society* and (c) Spirooxazines (Natarajan et al., 1991). Copyright 1991 *American Chemical Society*.

by thermal relaxation but only via visible light irradiation, exhibiting thermal stability in both isomeric states. A diarylethenes photo-isomerizable chiral switch is shown in Figure 9.11(b). However, only a few diarylethenes are capable of inducing photo-responsive CLCs with low HTP values. Rameshbabu et al. reported thermally irreversible photochromic CLCs using a diarylethene as the chiral switch with a decent HTP value. The diarylethene contained one dithienylcyclopentene moiety linked to two mesogenic cholesteryl groups via flexible carbonyldioxyalkoxy spacers (Rameshbabu et al., 2011). Li et al. further synthesized axially chiral dithienylcyclopentenes for the preparation of photoreactive chiral LCs (Li et al., 2011b). The initial HTP of (S,S) isomer in E7 exhibited a high value of 84 (wt.%)μm^{-1} and was adjusted to 71 (wt.%)μm^{-1} upon 290 nm light irradiation for 10 min and was shown to be switched back to 82 (wt.%)μm^{-1} with 520 nm light illumination. The optically tunable reflection wavelength change was below 100 nm due to the small HTP variation. The authors further synthesized a new series of dithienylcyclopentene motors by replacing the two bridged binaphthyl units with dithienylcyclopentene groups (Li et al., 2013). When chiral switches were doped into nematic LCs, they exhibited high HTPs over 150 (molar)μm^{-1} in both isomer states. Reversible phototuning of the reflection wavelength from 480 nm to 620 nm was demonstrated by using the new dithienylcyclopentene switch with a modulation of the handedness.

Spirooxazines are another interesting family of photo-responsive materials with properties of strong photo-coloration, photo-fatigue resistance, and fast thermal relaxation. Upon UV irradiation, a spirooxazine undergoes the transition from the ring-closed spiro form to the ring-opened merocyanine form, whereas the reverse process occurs via thermal relaxation or visible-light irradiation. A Spirooxazines photo-isomerizable chiral switch is shown in Figure 9.11(c). A unique feature of spirooxazines is its significantly increased dipole moment from the spiro form to the merocyanine form, leading to a pronounced conformational molecular change. However, their HTP values in inducing chiral LC phases are moderate and not much research has been carried out in utilizing them for realizing photoreactive chiral LCs. The initial attempts on this topic were conducted with CLC spirooxazine compounds (Natarajan et al., 1991) or liquid crystalline polymers containing spiropyran groups (Hattori and Toshiyuki, 2001). Interesting photochromic behaviors such as colored LC films, metastable isomers, and selective isomerization under photonic and thermal effects were reported. In order to tailor the functionalities of chiral spirooxazines, novel axially chiral spirooxazines with bridged chiral spirooxazines possessing high HTPs were fabricated (Jin et al., 2010). These chiral switches were found efficient in eliciting self-organized helical superstructures in LCs with fast UV light-induced ring-opening processes and thermally reversible ring-closing processes.

9.3.4 Applications of photo-isomerized chiral liquid crystals

In the above sections, we have summarized the performance of optically controlled chiral LC systems doped with different photo-isomerizable materials. The molecular conformation differences between isomers during the reversible photo-isomerization processes change the chirality, director orientation, HTP or handedness of the chiral switches, which leads to LC superstructures with optically tunable characteristics such as the refractive-index modulation, the helical pitch, the photonic band gap, the handedness of the helix, a superstructure, or phase transition, and so on. The versatile optical control on parameters of the superstructure formed in chiral LCs opens possibility for tunable photonic devices based on subwavelength periodic structures. Due to the photonic band gaps in photonic crystals, they have been widely utilized to obtain light manipulation and a number of applications, including bend waveguides, color filters and lasers have be demonstrated. However, as for operation in the visible range, the linewidth of these subwavelength structures should fall in the hundred-nanometer regime, exhibiting difficulties in fabrication techniques. As a result, the fabrication process mainly relies on sophisticated techniques such as the electron beam lithography and the focused ion beam lithography. Etching or deposition processes are often required in transferring the nanopattern to desired substrates. In addition, these optical structures are commonly inert and lack the capability for dynamic tuning which further limit the application in diverse fields. As mentioned, the chiral LCs exhibit 1D or 3D periodic structures from the self-assembly of the soft rod-like molecules for efficient light manipulation. Furthermore, the addition of photo-reactive compounds such as the photo-isomerizable chiral switches endows the chiral LCs with dynamic tuning capability in various working parameters. As a result, the photo-isomerizable chiral liquid crystal systems are extremely appealing in providing practical photonic devices with optically tunable capabilities. This section reviews the recent results on the utilization of the photo-isomerized chiral liquid crystals in light-addressable displays, optically tunable lasers and optically controlled beam steering gratings.

9.3.4.1 Light-addressable displays with photo-isomerized chiral liquid crystals

As mentioned in Section 9.3.1.2, the photo-isomerization of the azobenzene chiral switch changes its HTP due to the difference in molecular conformation between the *trans* and *cis* isomers, which leads to an adjustment of the cholesteric liquid crystal reflection band in the whole visible range. This characteristic has been exploited to fabricate light-addressable displays. Yoshioka et al. demonstrated light-addressable red, green, blue (RGB) pixels in the nematic LC host E44 doped with chiral azobenzene switches (Yoshioka et al., 2005). A grey-scale photomask in accordance with the pixel distribution was utilized to control light intensity and

distribution illuminated onto the sample. Vivid RGB reflection pixels were realized with the pixel size down to 70 μm holding the potential for high-resolution display. Li et al. demonstrated colored red and green images with the blue color as the background using achiral LC host doped with the dithienylethene photoreactive compound (Li et al., 2012). The photomask bearing the image was utilized to selectively irradiate the sample region. By controlling the illumination duration, green- and red-colored images corresponding to the photomask can be realized. The sample was optically erasable and rewritable due to the reversible photo-isomerization induced by light of different wavelengths. Venkataraman et al. demonstrated a photo-writable and electric-switchable photochiral displays by utilizing the bistability of the CLCs (Montbach et al., 2008; Venkataraman et al., 2009). Only simple planar electrodes were required for driving the display and the display film could be made flexible and large area. Azo binaphthyl chiral compounds were used as the photonic switch and doped into the nematic LC host. With the aid of the photomask, the helical pitch in the exposed regions shrank, which led a blue-shift of the reflection color from red to green. The threshold voltage is inversely proportional to the pitch length. This relationship provided a voltage range at which a planar texture was obtainable in the unexposed region and a focal-conic texture was obtainable in the exposed region. These two texture are stable and a single pulse voltage is required for electrical switching of the image which is quite power-efficient. The exposed planar structure showed green reflections while the focal conic structure exhibited the underneath black background. Diffusion of the photochiral dopant would cause a deterioration of the resolution and this problem could be overcome by encapsulating the display film in the polymers. The applied voltage had to fall in the narrow range in order to switch the exposed and unexposed regions into different textures. In order to address this limitation, Li et al. demonstrated a photo-addressable and multi-switchable CLC display using axially chiral azobenzene switches (Li et al., 2011a; Ma et al., 2010). The mixture was injected into cells with homeotropic alignment-treated glass substrates. The working mechanism and sample images of this multi-switchable display were shown in Figure 9.12. The weak anchoring force by the alignment layer yielded a poly-domain CLC structure with the helical axis loosely orientating along the surface normal. The image was recorded by illumination through the photomask by a difference in the reflection band induced by photo-isomerization. With a pulsed voltage, the loosely bounded planar texture converted to the focal conic texture and the image was erased. The planar texture reappeared with the application of a mechanical force or with the application a high pulsed voltage, restoring the original image. The investigation into light-addressable display with the photo-isomerizable chiral LC systems is of interest for low power consumption and flexible displays. However, more efficient frame refreshing approaches have to be developed and the refreshing rate limited by the response of the photoreactive compounds should be improved for practical applications.
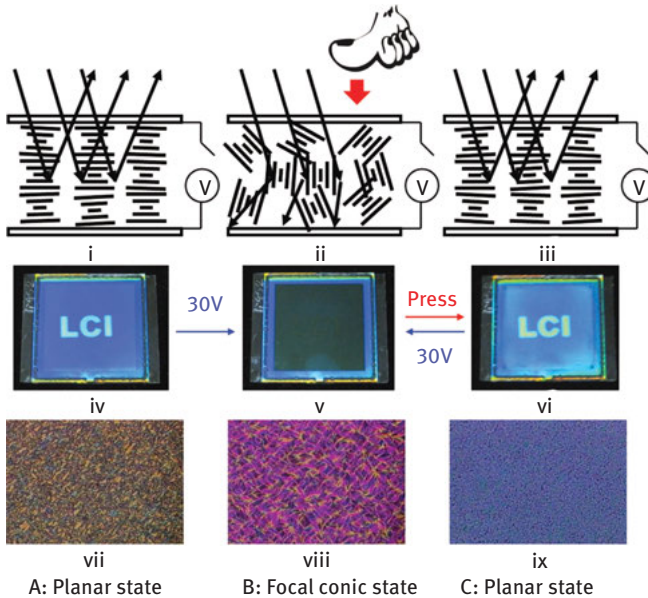
Figure 9.12: A photoaddressed and multi-switchable CLC display (Li et al., 2011a). Copyright 2011 WILEY-VCH.

9.3.4.2 Optically tunable lasers

The helical periodic superstructure in chiral LCs works as the photonic crystal featuring a photonic band gap in which photons are prohibited. As a result, the group velocities are reduced, leading to a prolonged interaction time of the photon with the superstructure. If the gain media are introduced into the superstructure, photons in the photonic band gap would be amplified through the stimulated emission process and when the optical gain exceeds the loss, lasing occurs. Chiral LCs have long been exploited as mirrorless laser resonators. Dye molecules have been frequently doped into the LC host as the gain media. Electrically tunable LC lasers have also been intensively investigated due to the helical pitch sensitivity to the electric field and the ease to apply the electric field. The advancement of all-optical circuits calls for optically tunable lasers as photon sources. One difficulty in realizing optically tunable chiral LC lasers lies in the fact that the dye molecules rely on high intensity optical pumping energy to stimulate the laser action. Thus a fine optimization of the pump beam used to induce isomerization for the helical pitch tuning and the pump beam for excitation of dye molecules have to be adopted. In addition, the thermal effect during the pumping of the laser dye on the helical pitch variation should also be taken into consideration. Chilaya et al. reported tunable lasing performance in chiral LCs containing photosensitive nematic azo-components and

photo-insensitive chiral dopants (Chilaya et al., 2007). The sample was illuminated with an LED source of 405 nm for the *cis* isomerization and an LED source of 466 nm for reverse (i.e., *trans*) isomerization, respectively. DCM dye was doped into the azo-chiral LC mixture and pumped with a pulsed laser at 532 nm. The conformational difference between linear *trans*-isomers and bent *cis*-isomers led to an adjustment to the helical pitch and thus the lasing wavelength was tuned between 579 nm and 647 nm. Chen et al. replaced the common laser dye with quantum dots as gain media to improve the device lifetime (Chen et al., 2014b). The azobenzene chiral switch was transformed using 365 nm UV light and reversibly using the visible light at 442 nm. The quantum dots were pumped using a 532 nm laser. The laser device showed a tunable range between 598 nm and 638 nm due to the narrow gain spectrum. The laser performance was quite stable with a high damage threshold over 85 µJ/Pulse. Zheng et al. demonstrated a wide tuning range of the azo-chiral LC laser by suspending the LC droplets in a polyvinyl alcohol matrix (Zheng et al., 2015). The conformation transition of the chiral switch led to changes in not only the molecular geometry, but also the molecular interactions with other materials, thus rendering the variation in helical pitch for a wide tuning range of 112 nm. Chen et al. demonstrated optically tunable laser action from monodisperse CLC microshells (Chen et al., 2014a). An axially chiral molecular motor was doped into the LC E7 and the mixture was overcoated onto the polyvinyl alcohol droplets as outside shells by a microfluidic device as shown in Figure 9.13(a) and (b). The radial orientation of the CLC helices within the shells act as an axial photonic band edge laser cavity and the lasing wavelength shifts from ~590 nm to ~640 nm during the pumping process due to the motor photo-isomerization as shown in Figure 9.13(c). The emitted lasing wavelength recovered to its initial state, after 12 h storage in darkness. Apart from the CLC that works as the 1D distributed feedback resonator, blue phase LC has also been exploited as 3D organic cavity. Lin et al. demonstrated an optically switchable laser device based on BP LCs (Lin et al., 2014). UV irradiation transformed the rod-like azo-LC *trans* isomers into bend-shaped *cis* isomers, which disturbed LCs. BPI was unstable and quickly became a random BPIII-like texture, erasing the laser action due to the lack of coherent feedback.

9.3.4.3 Optically controlled beam steering gratings

The CLC is commonly in the planar texture with a normal helical axis perpendicular to the substrate. The configuration yields selective reflection depending on the grating pitch and the incident angle. The light-addressable display and optically tunable lasers with chiral LCs are mainly in this setup and we could see colored images or obtain laser emission from the film normal. However, there also exists a fingerprint texture for chiral LCs in which the helical axis lies in the surface plane. If the planar texture can be regarded as a reflection grating or mirror, then the fingerprint texture could be regarded as a transmission grating, upon which, light diffraction into different
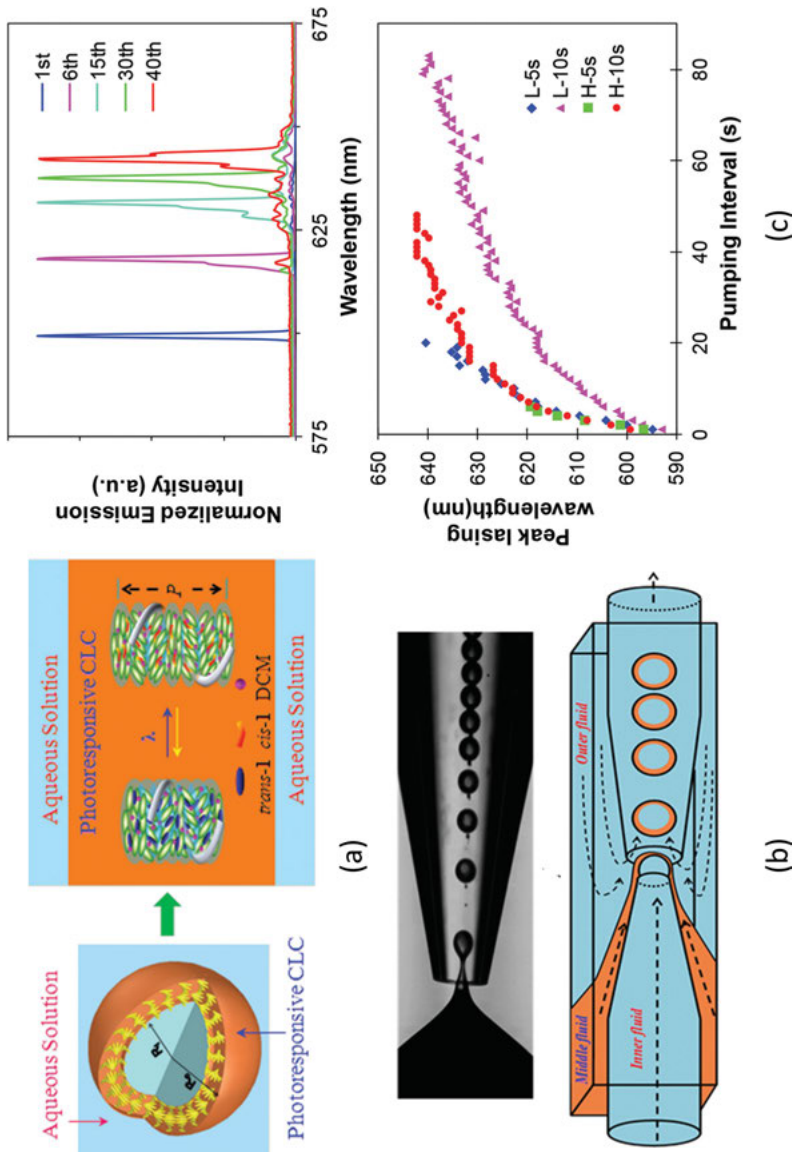
Figure 9.13: (a) Schematic structure of the monodisperse CLC microshell with light-tunability. (b) Generation of monodisperse CLC microshells using a microfluidic device. (c) Variation of laser emission under visible pumping (Chen et al., 2014a). Copyright 2014 WILEY-VCH.

directions corresponding to different Bragg orders takes place. The diffraction direction and angle are dependent on the helical pitch and direction. Thus, if the helix parameters could be dynamically controlled, the fingerprint texture of chiral LCs could be exploited as beam-steering devices. The fingerprint texture often results from a balance between the surface alignment force and the LC inner elastic torque, and the electric torque can be obtained by application of a suitable voltage across the planar CLC. Jau et al. reported an optically tunable beam steering grating by doping achiral azobenzene molecules into chiral LCs (Jau et al., 2010). Under light irradiation, the azobenzene underwent reversible *trans*-and-*cis* isomerization. The *trans* isomer favored the stabilization of the cholesteric phase, but the *cis* isomer tended to disorganize the molecular orientations, thereby reducing the pitch length. Due to the limited conformation difference of the achiral azobenzene isomers, the diffracted laser spot could be only tuned in a range of 6°. Jau et al. further reported a light-driven beam steering grating with a wide range by using an axially chiral azobenzene switch (Ryabchun et al., 2015a). The chiral switch had a large initial HTP and a big HTP change upon photo-isomerization. The diffraction angle of the first-order beam could be tuned reversibly between 33° and 54° by low-power violet and green LED irradiation within 40 s. The widely tunable grating was further demonstrated as a dispersive element for a scanning spectrometer. The wavelength for scanning can be adjusted from 472 nm to 713 nm with *cis*–*trans* isomerization, and can be tuned back with green light which prompted the reverse *cis*–*trans* isomerization. In addition to the 1D optically controlled beam steering gratings, fingerprint textures could also function as 2D beam steering diffractive component that enable the diffraction beams to dynamically scan across the whole plane. Ryabchun et al. demonstrated such a beam steering grating with optically controlled rotatable diffraction (Ryabchun et al., 2015b). In order to maximize the photoinduced HTP difference of the azobenzene switch and realize a handedness inversion, an inert chiral dopant with the opposite handedness (low HTP) was co-doped into the LC host. The hybrid alignment approach was utilized to obtain the fingerprint texture, because the CLC molecules had to exhibit a sinusoidal periodic tilt to minimize their free energy. The CLC gratings rotated clockwise with UV irradiation and counterclockwise with visible light irradiation. An unprecedented rotation angle as high as 692° was manifested with a dynamic scanning of laser spots in the plane. Recently, a light-driven 3D control of the CLC helical axis orientation was demonstrated using an axial chiral molecular switch as the chiral dopant (Zheng et al., 2016). The 3D optical control over the direction of the helical axis was illustrated in Figure 9.14(a). Upon UV irradiation, the standing helix transformed to a lying helix and it further rotated in the plane until the system reached the photo-stationary state. The system can be driven back under visible light irradiation. The whole scanning process could be completed in around 1 min and the response time is dependent on light intensity. Researchers further showed the utilization of the photo-sensitive system for optically controlled reversible 2D beam steering as shown in Figure 9.14(b). Non-mechanical beam steering in the 2D plane with a wide scanning range of about 52° × 8° was further performed.
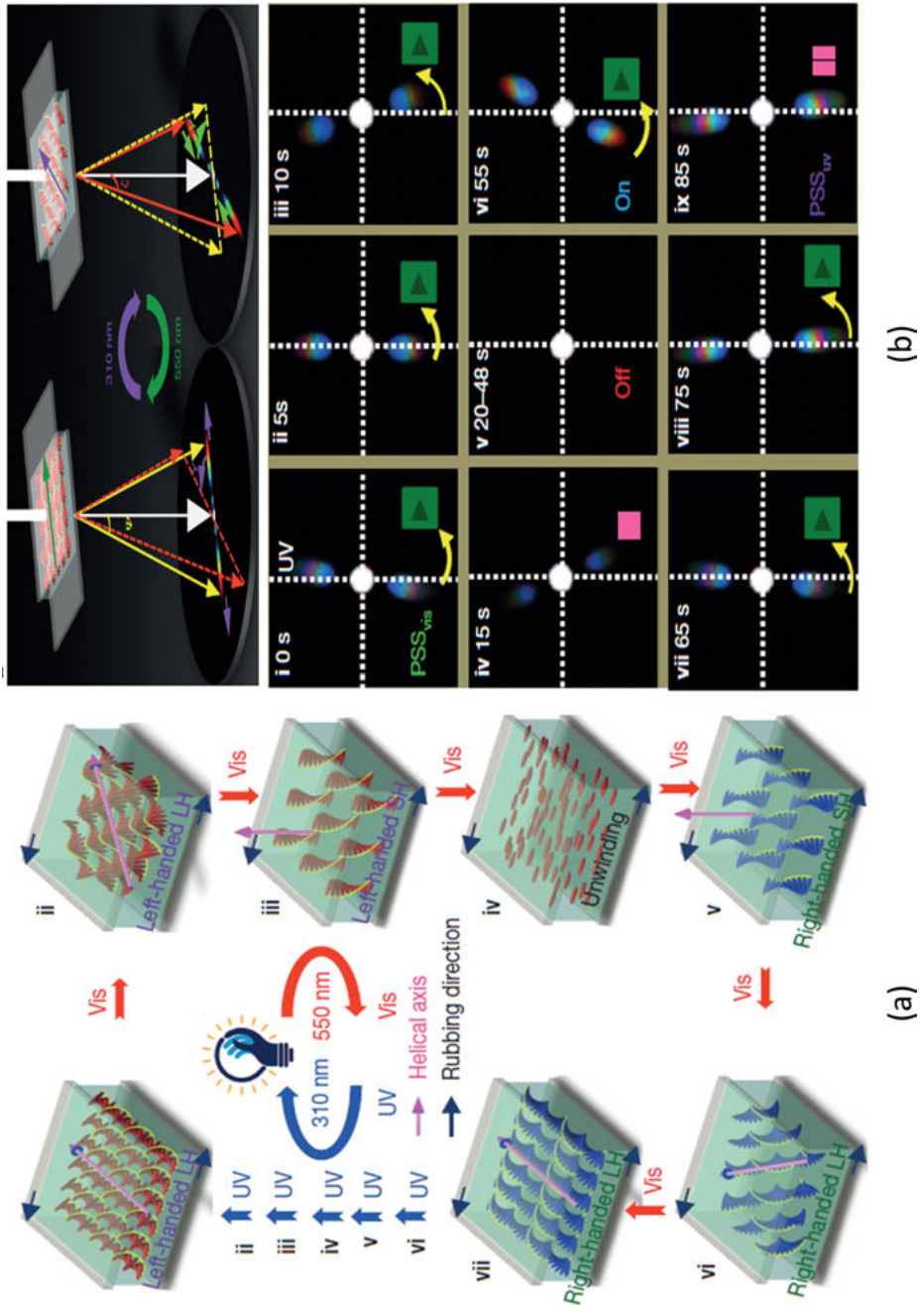
Figure 9.14: (a) Illustration of 3D control over helical axis. (b) Light-controllable 2D beam steering (Zheng et al., 2016). Copyright 2016, Macmillan Publishers Limited.

9.4 Light-induced liquid crystal Torons for dynamic diffraction manipulations

Light is electromagnetic waves with oscillating electric and magnetic fields perpendicular to its propagation direction. LCs are birefringent materials with electric and magnetic response capabilities. In this sense, LCs are in nature photo-responsive even without the addition of photorefractive or photo-isomerizable materials. In most cases, the interaction of LCs with light is very weak, as a result, photoreactive dopants are often necessary to make the LC properties optically controllable. However, there are exceptions that light could directly interact with LCs and induce LC realignment, leading to light-induced distorted or twisted LC director distribution in uniformly aligned LC background. These defects caused by located LC director redistributions are quasiparticles and were referred to as Torons. Cholesteric LCs are interesting from this standing point. For the generation of light-induced Torons, two requirements are needed. One is that the cell thickness should be smaller than the cholesteric helical pitch and the other is that the cell inner surfaces should be homeotropically treated. When it is irradiated using laser beams with optical phase singularities, the director would reorient to transform to a twisted configuration with point or line singularities, generating Torons as shown in Figure 9.15(a). The Torons formation characteristics are significantly influenced by laser beam intensity. First, there exists a threshold power value P_{th} = (30–50) mW above which LC director n(r) begins to be rotated by the in-plane electric field of the incident laser beam to the cell normal, inducing a distortion for Torons generation in an initial unwounded LC state. However, this initial distortion would disappear within 5–10 ms to minimize the elastic energy as long as the laser beam is turned off. Second, when the laser power reaches the second threshold P_{th2}~(1.2–2.2)P_{th}, the LC director distortion transforms into permanent Torons. The generated Torons with twisted director distribution are embedded in uniformly aligned LC molecules and have a characteristic size comparable to the helical pitch in all directions. For a direct characterization of the quasi-particles, cross-sections of Torons perpendicular can be visualized utilizing the three-photon fluorescence polarized microscopy as shown in Figure 9.15(b). It relies on fluorescence signals excited through the three-photon absorption process in the LCs, free from doping samples with dyes. The Torons can be further controlled by electric fields and arranged into periodic arrays.

Smalyukh et al. have embedded the localized 3D LC molecule director twist into the uniform background by illuminating the CLCs with vortex laser beams, generating triple-twist Torons (Smalyukh et al., 2010). The ring-shaped intensity distribution of the Laguerre Gaussion vortex beams were utilized to control the initial director title of LC molecules, resulting in triple-twist Torons with high symmetry. Versatile generation of Torons offers the possibility for applications ranging from all-optical devices to new multi-stable information displays. Ackerman et al. demonstrated arrayed quasiparticle
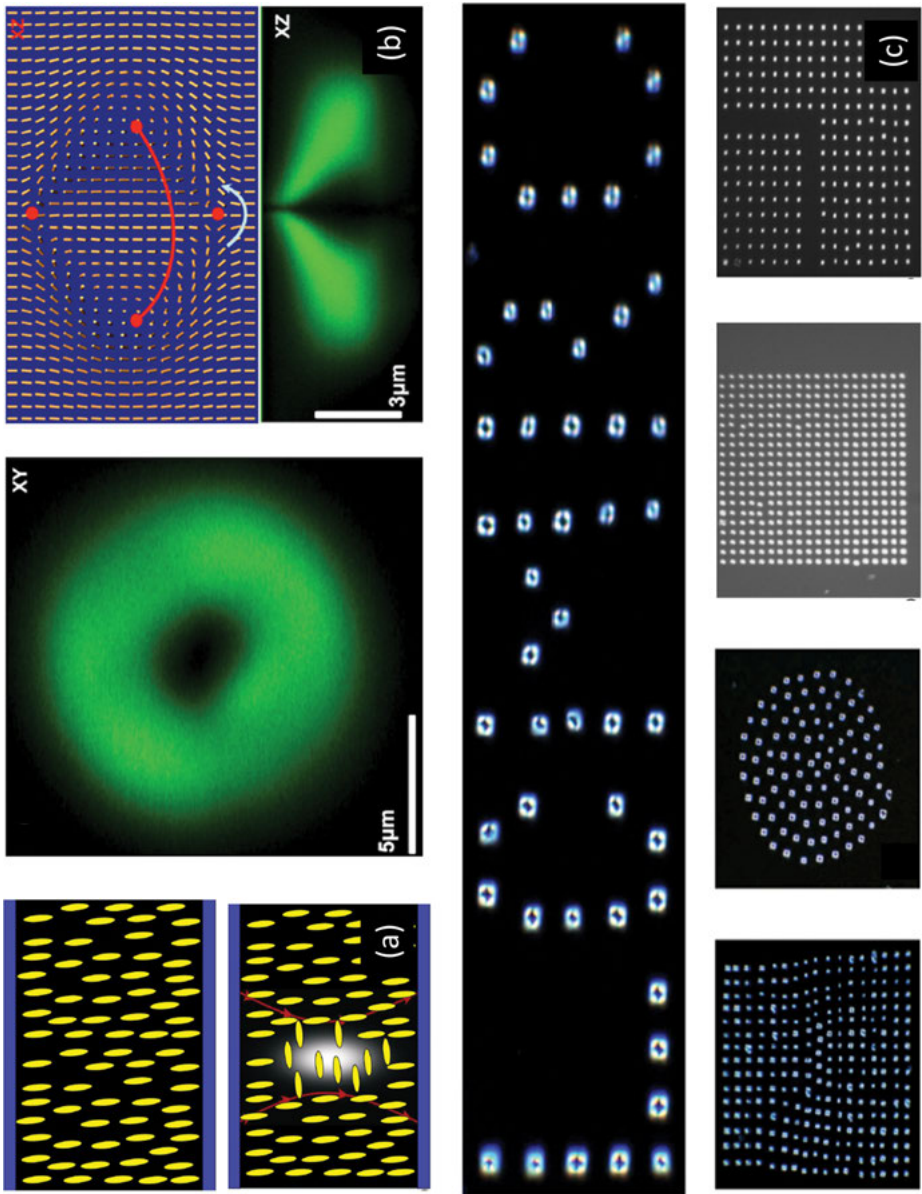
Figure 9.15: (a) Schematic illustration for the generation of Torons in homeotropic CLCs. (b) Images of director structures of Torons by three-photon excitation fluorescence polarized microscopy. (c) Polarized optical micrographs of Torons in various patterns (Smalyukh et al., 2012). Copyright 2012 *Optical Society of America*.

Torons in 2D crystalline, quasi-crystalline, and even arbitrary patterns with vortex beam scanning as shown in Figure 9.15(c). (Ackerman et al., 2012a, 2012b). They were generated by a fast sequential scanning of the focused beam with the tweezers system. The Torons lattice constant of these structures was dependent on the equilibrium pitch of the CLCs and can be tuned through a wide range by varying the helical pitch and optimizing the generation scheme. Diffraction gratings composed of arrayed Torons are potential candidates for powerless or low-power multimodal light manipulation. Smalyukh demonstrated the generation of Torons in periodic crystal lattice structures using the single beam steering and holographic patterning approaches (Smalyukh et al., 2012). The Torons lattice structures were tailored by tuning their periodicity, introducing defects and reorienting their crystallographic axes. Trushkevych et al. enhanced the optical response of CLCs into Torons by doping a small amount of fullerene (Trushkevych et al., 2010). It is shown that Torons could be generated by different laser wavelengths under the bulk or surface physical origins. When the laser spot with a wavelength of 488 nm was utilized, the fullerene strongly absorbed the light and they were deposited onto illuminated surface areas. These deposited areas lead to the formation of long-term stable Torons that could be electrically switched. When the laser spot with a typical wavelength of 1,064 nm was utilized, stable Torons similar to previous investigations could also be formed with a significantly reduced intensity threshold, although the wavelength was out of the fullerene absorption band. Three-dimensional formation of Torons array was further demonstrated by a layer-by-layer stacking of CLC films (Evans et al., 2013). Liquid crystal films with 2D arrayed Torons were stabilized through photo-polymerization. This opens a route to fabricated 3D periodic structures for light manipulation.

Triple-twist Torons could be generated in CLCs under specific helical pitch, cell thickness, and boundary conditions. The Toron pattern could be conveniently controlled by the focused laser spot type in terms of the focused beam intensity distribution, the wavelength, and vortex symmetry. Single, lined, periodic, quasi-periodic Torons patterns with desired defects could be generated by the tweezers system. Their multistable characteristics and facile electro-optical controllability made them suitable for many applications.

9.5 Photo-thermal chiral liquid crystal for dynamic diffraction manipulations

Liquid crystal phases undergo phase transitions or superstructure parameter modulations in response to temperature change, which is a direct result of the adjustment of interaction forces among LC molecules. Compared with other stimulation forces, such as the electric, the magnetic and the lightfield, thermal modulation in LC phases or superstructures is straightforward; however, the precise control of the

temperature requires bulky equipment which complicates the dynamic modulation capability (Bisoyi et al., 2018). In this section, we would cover the recent investigations on photo-thermal chiral liquid crystals for dynamic diffraction manipulations. We would show the photo-thermal effect as a simple and noncontact approach to localized thermal manipulation with nanometer precision. In order to achieve chiral LCs with photo-thermal capabilities, it is necessary to bring a material into the system which could efficiently absorb light to generate heat, thereby modifying the phase or physical properties of LC phases in localized manner. A variety of photo-thermal agents including metal nanoparticles, carbon nanomaterials, organic dyes, and conjugated polymers have been attempted for remote driving of chiral LCs using light. As for metal nanoparticles, light in the plasmonic absorption band is absorbed by metal nanoparticles to excite the plasmonic waves. These hybrid electron-photon waves attenuate and relax by colliding with the metal lattice, resulting in an increase in local temperature. Similarly, organic compounds such as dyes or conjugated polymers exhibit strong light absorption which lead to the generation of a number of electron excitations. These excitations could relax back to the ground state through the radiative or nonradiative process. The possibility of the relaxation process depends on the electron configuration and molecular structure of the organic compounds and could be engineered chemically. In the case of the nonradiative process, heat is generated, leading to a temperature increase in the localized region. The absorption band of either the metal nanoparticles or the organic compounds could be tailored from the UV to the near infrared (NIR) via the particle geometrical control or the HOMO−LUMO energy level manipulation, respectively.

Fuh et al. demonstrated an optically controlled fingerprint texture diffraction grating by doping CLCs with a dichroic guest-host photo-thermal dye (Fuh et al., 2001). When the fingerprint diffraction grating was irradiated by green light, the diffraction efficiency of the first order decreased while that of the second order increased. In addition, the diffractive angle decreased with light irradiation, indicating the helical pitch elongation due to the thermal effect. It required 4 min for the sample to reach the stable state where the heat generated by light was balanced with sample cooling. The change in the diffraction efficiencies of different orders was attributed to the broadened cell interior region as a result of the weakened surface anchoring force during heating. In previous sections on light controlled chiral LCs, for example, the photorefractive or the photo-isomerization effect, UV or visible light is frequently utilized for remote driving. However, the use of high-energy UV light in such systems might result in material damage and NIR light would be much preferred in the areas of life sciences and aerospace applications. In this regard, NIR absorbing photo-thermal agents have earned special attention. Sio et al. reported NIR-controlled reflection from the planar CLCs with gold nanorods as the photo-thermal agent (Sio et al., 2013). The gold nanorods were surface-functionalized with specific groups to obtain a high compatibility with the chiral LC host. Under NIR light irradiation, the reflection band of the CLC red-shifted linearly from 520 nm to 650 nm due to the thermal-induced
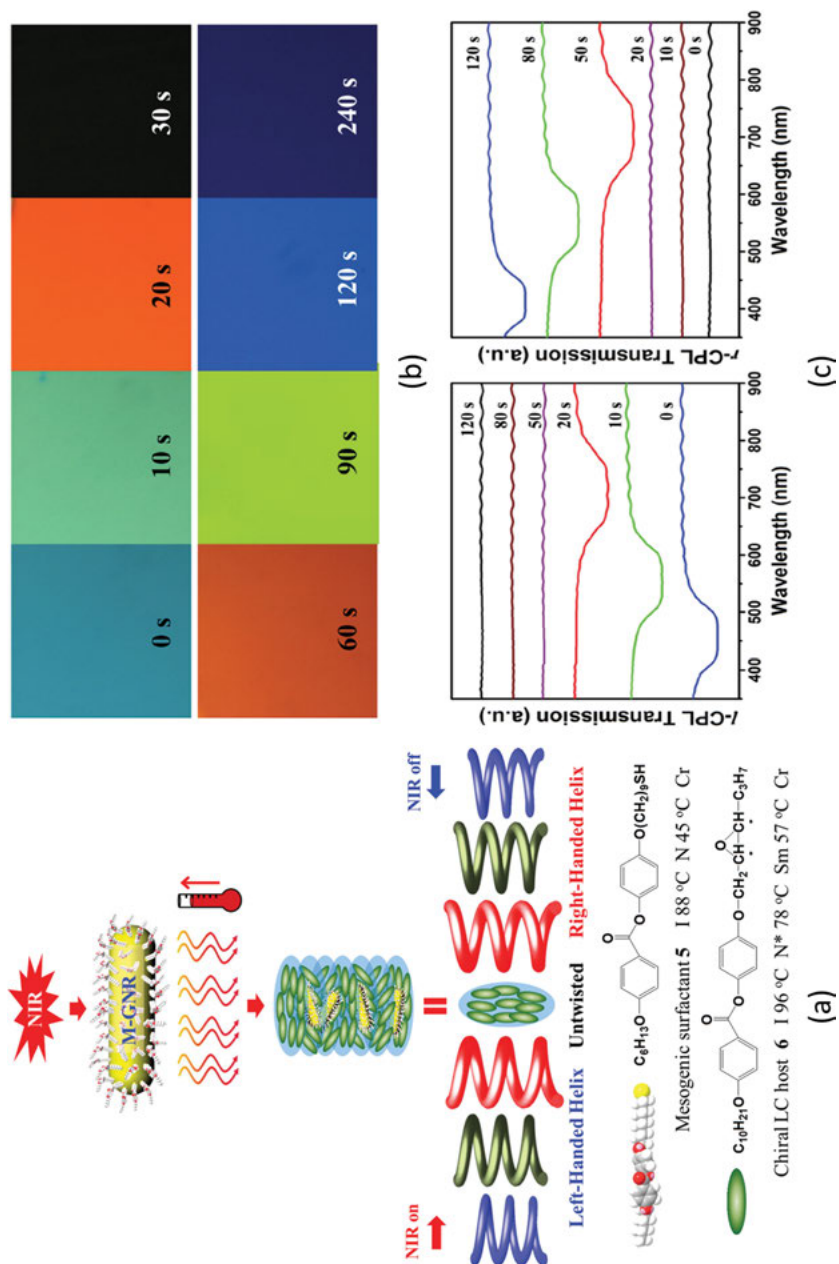
Figure 9.16: (a) Schematic illustration of handedness inversion by the photo-thermal effect. (b) Dynamic photonic reflection color images and (c) Spectra from the CLCs under NIR illumination with different durations (Wang et al., 2016). Copyright 2016 WILEY-VCH.

helical pitch elongation. It took 70 s to reach the final stable reflection peak. The absorption band of the gold nanorods was also found to red-shift from 680 nm to 730 nm. The light-driven behaviors were strongly dependent on the light polarization as a result of the anisotropic extinction cross sections of the nanorods. The authors further demonstrated that a careful choice of the cell thickness could decouple the reflection peak shift from the reflection efficiency adjustment, showing the pure reflection amplitude modulation controlled by light (Sio et al., 2016). Characteristics of the CLCs such as the helical pitch and the reflection efficiency could be controlled photo-thermally by the NIR light. Apart from these, Wang et al. demonstrated a handedness inversion and subsequent reversible reflection band shift controlled by the photo-thermal effect as shown in Figure 9.16(a). (Wang et al., 2016). The gold nanorods were functionalized with mesogenic groups and the aspect ratio was tailored for NIR absorption. When the NIR light was turned on, the left-handedness reflection red-shifted from 450 nm to 700 nm in 20 s. With further NIR irradiation, the texture was transformed to an untwisted transient dark state. After that, right-handed circularly polarized light reflection appeared around 700 nm and blue-shifted to 420 nm in 70 s. The reverse process from right-handedness to untwisted transient state to left-handedness occurred immediately upon light irradiation removal. The reflection color images and spectra were shown in Figure 9.16(b) and (c), respectively. The response time could be in part improved by an increasing amount of the gold nanorods. The achiral untwisted transient state was important to the handedness inversion by the photo-thermal effect. Wang et al. further demonstrated a phase transition between the transparent SmA* phase and the opaque focal conic texture utilizing the photo-thermal effect (Wang et al., 2017a). The transmittance difference between the two states was exploited to fabricate adaptive windows. The transparent homeotropic SmA* phase was polymer-stabilized in a cell with homeotropic anchoring. The mesogen-functionalized graphene was doped into the chiral LCs as the photo-thermal agent. Upon NIR irradiation for 60 s or direct heating, a focal conic texture was formed to replace the initial homeotropic texture. Correspondingly, the transmittance of the sample at 700 nm decreased significantly from 90% to 1%. It could relax back to the transparent homeotropic texture quickly upon removing the NIR light (30 s) or upon application of a low electric field of 18 V. Apart from the chiral nematic phase and the SmA* phase, the blue phase LCs with 3D self-organized superstructures could also be controlled by the photo-thermal effect. Wang et al. showed a photo-thermal controlled transition between BP I and BP II LCs with different helical pitches (Wang et al., 2015). The mesogen-functionalized gold nanorods were doped at a low concentration between 0.03 wt.% to 0.07 wt.% into the blue phase mixture and the BP phase temperature was found slightly broadened. Upon NIR irradiation, the LC stayed in the BP I in the first 10 s with a blue-shift (from 610 nm to 560 nm) of the reflection band. Upon further irradiation, the reflection band experienced an abrupt blue-shift to 480 nm which was attributed to the BP II transition. The LCs would become isotropic if the NIR continue to heat the sample.

9.6 Conclusions

The integration of chiral liquid crystal with photo-sensitive functional materials has become a common practice to realize advanced and tunable materials with enhanced properties for high-tech applications. In this chapter, we have reviewed the recent effects on various approaches including the photo-refractive effect, the photo-isomerization effect, the photo-induced Torons, and the photo-thermal effect to achieve photo-responsive chiral liquid crystals for dynamical diffraction modulations. The photorefractive effect is enabled by doping the chiral LCs with MR or photoconductive agents. The adsorbed dye molecules on the cell surface or the generated inner electric field led to a re-alignment of LC molecules with regard to the light field distribution, recording the light information through an adjustment in the refractive index. As for the photo-isomerization effect, the chiral LC was doped with photo-isomerizable molecules with the capability to undergo reversible *trans*-and-*cis* isomerization under UV and visible light irradiation. The isomerization led to a significant change in molecular conformation and subsequent interaction with the host LC material. It is manifested in terms of the HTP or the handedness, leading to a direct modulation in the helical pitch or the helical handedness of the self-organized superstructure in chiral LCs for a dynamical diffraction modulation. Torons could be generated by the focused laser spots directly in the chiral LCs with homeotropic surface treatment without addition of dopants. Localized LC alignment could be transiently or permanently altered by the electric field of the laser spot, resulting in Torons in arbitrary patterns controlled by the spot scanning. The photo-thermal effect was realized by doping chiral LCs with metal nanoparticles or organic dyes to generate heat upon suitable light illumination, resulting in a phase transition or a parameter change of the superstructure. Due to the flexibility in designing the chiral or achiral photo-isomerizable switches, the photo-isomerization approach was proved to be robust to ensure light-controlled chiral LCs with wide tunability and phase transition capability among various novel superstructures. The applications in light-addressable displays, optically tunable lasers and optically controlled beam steering gratings were also presented, indicating a firm step toward all-optical, on-chip devices for practical applications.

References

Ackerman, P.J., Qi, Z., Lin, Y., Twombly, C.W., Laviada, M.J., Lansac, Y., Smalyukh, I.I. (2012a). Laser-directed hierarchical assembly of liquid crystal defects and control of optical phase singularities. Scientific Reports, 2, 414.

Ackerman, P.J., Qi, Z., Smalyukh, I.I. (2012b). Optical generation of crystalline, quasicrystalline, and arbitrary arrays of torons in confined cholesteric liquid crystals for patterning of optical vortices in laser beams. Physical Review E, 86, 021703.

Aßhoff, S.J., Iamsaard, S., Bosco, A., Cornelissen, J.J.L.M., Feringa, B.L., Katsonis, N. (2013). Time-programmed helix inversion in phototunable liquid crystals. Chemical Communications, 49, 4256–4258.

Bisoyi, H.K., Li, Q. (2014). Light-directing chiral liquid crystal nanostructures: from 1D to 3D. Accounts of Chemical Research, 47, 3184–3195.

Bisoyi, H.K., Li, Q. (2016). Light-driven liquid crystalline materials: from photo-induced phase transitions and property modulations to applications. Chemical Reviews, 116, 15089–15166.

Bisoyi, H.K., Urbas, A.M., Li, Q. (2018). Soft materials driven by photothermal effect and their applications. Advanced Optical Materials, 6, 1800458.

Blinov, L.M., Cipparrone, G., Kozlovsky, M.V., Lazarev, V.V., Scaramuzza, N. (2000). Holographic 'development' of a hidden UV image recorded on a liquid crystalline polymer. Optics Communications, 173, 137–144.

Bossi, M.L., Murgida, D.H., Aramendía, P.F. (2006). Photoisomerization of azobenzenes and spirocompounds in nematic and in twisted nematic liquid crystals. The Journal of Physical Chemistry B, 110, 13804–13811.

Chanishvili, A., Chilaya, G., Petriashvili, G., Collings, P.J. (2005). Trans-cis isomerization and the blue phases. Physical Review E, 71, 051705.

Chen, C.-W., Lin, T.-H., Khoo, I.C. (2015). Dynamical studies of the mechanisms for optical nonlinearities of methyl-red dye doped blue phase liquid crystals. Optics Express, 23, 21650–21656.

Chen, L., Li, Y., Fan, J., Bisoyi, H.K., Weitz, D.A., Li, Q. (2014a). Photoresponsive monodisperse cholesteric liquid crystalline microshells for tunable omnidirectional lasing enabled by a visible light-driven chiral molecular switch. Advanced Optical Materials, 2, 845–848.

Chen, L.-J., Lin, J.-D., Lee, C.-R. (2014b). An optically stable and tunable quantum dot nanocrystal-embedded cholesteric liquid crystal composite laser. Journal of Materials Chemistry C, 2, 4388–4394.

Cheng, K.-T., Liu, C.-K., Ting, C.-L., Fuh, A.Y.-G. (2007). Optics Express, 15, 14078–14085.

Chilaya, G., Chanishvili, A., Petriashvili, G., Barberi, R., Bartolino, R., Cipparrone, G., Mazzulla, A., Shibaev, P.V. (2007). Reversible tuning of lasing in cholesteric liquid crystals controlled by light-emitting diodes. Advanced Materials, 19, 565–568.

Cook, G., Beckel, E., Reshetnyak, V., Saleh, M.A., Evans, D.R. (2007). Cholesteric-inorganic hybrid photorefractives Photorefractive effects, photosensitivity, fiber gratings, photonic materials and more. Optical Society of America, SuC4.

Delden, R.A.V., Koumura, N., Harada, N., Feringa, B.L. (2002). Unidirectional rotary motion in a liquid crystalline environment: color tuning by a molecular motor PNAS, 99, 4945–4949.

Delden, R.A.V., Mecca, T., Rosini, C., Feringa, B.L. (2004). A chiroptical molecular switch with distinct chiral and photochromic entities and its application in optical switching of a cholesteric liquid crystal. Chemistry—A European Journal, 10, 61–70.

Dierking, I. (2014). Chiral liquid crystals: structures, phases, effects Symmetry, 6, 444–472.

Earl, D.J., Wilson, M.R. (2003). Predictions of molecular chirality and helical twisting powers: a theoretical study. The Journal of Chemical Physics, 119, 10280.

Eelkema, R., Feringa, B.L. (2006). Amplification of chirality in liquid crystals. Organic and Biomolecular Chemistry, 4, 3729–3745.

Evans, D.R., Cook, G. (2007). Bragg-matched photorefractive two-beam coupling in organic-inorganic hybrids. Journal of Nonlinear Optical Physics & Materials, 16, 271–280.

Evans, J.S., Ackerman, P.J., Broer, D.J., Lagemaat, J.V.D., Smalyukh, I.I. (2013). Optical generation, templating, and polymerization of three-dimensional arrays of liquid-crystal defects decorated by plasmonic nanoparticles. Physical Review E, 87, 032503.

Fuh, A.Y.-G., Lin, C.-H., Hsieh, M.-F., Huang, C.-Y. (2001). Cholesteric gratings doped with a dichroic dye. Japanese Journal of Applied Physics, 40, 1334–1338.

Hattori, H., Toshiyuki, U. (2001). Photochromic chiral liquid crystalline systems containing spiro-oxazine with a chiral substituent I. Synthesis and characterization of compounds. Liquid Crystals, 28, 25–34.

Hrozhyk, U.A., Serak, S.V., Tabiryan, N.V., Bunning, T.J. (2007). Periodic structures generated by light in chiral liquid crystals. Optics Express, 15, 9273–9280.

Hsiao, V.K.S., Chang, W.-T. (2010). Optically switchable, polarization-independent holographic polymer dispersed liquid crystal (H-PDLC) gratings. Applied Physics B, 100, 539–546.

Hsiao, Y.-C., Huang, K.-C., Lee, W. (2017). Photo-switchable chiral liquid crystal with optical tristability enabled by a photoresponsive azo-chiral dopant. Optics Express, 25, 2687–2693.

Ichimura, K. (2000). Photoalignment of liquid-crystal systems Chemical Reviews, 100, 1847–1874.

Ichimura, K., Oh, S.-K., Nakagawa, M. (2000). Light-driven motion of liquids on a photoresponsive surface Science, 288, 1624–1626.

Jau, H.-C., Lin, T.-H., Fung, R.-X., Huang, S.-Y., Liu, J.-H., Fuh, A.Y.-G. (2010). Optically-tunable beam steering grating based on azobenzene doped cholesteric liquid crystal. Optics Express, 18, 17498–17503.

Jin, L.-M., Li, Y., Ma, J., Li, Q. (2010). Synthesis of novel thermally reversible photochromic axially chiral spirooxazines. Organic Letters, 12, 3552–3555.

Jones, D.C., Cook, G. (2004). Theory of beam coupling in a hybrid photorefractive-liquid crystal cell. Optics Communications, 232, 399–409.

Kawamoto, M., Aokia, T., Wada, T. (2007). Light-driven twisting behaviour of chiral cyclic compounds. Chemical Communications, 0, 930–932.

Khoo, I.C., Slussarenko, S., Guenther, B.D., Shih, M.-Y., Chen, P., Wood, W.V. (1998). Optically induced space-charge fields, dc voltage, and extraordinarily large nonlinearity in dye-doped nematic liquid crystals. Optics Letters, 23, 253–255.

Kim, J., Suh, J.-H., Lee, B.-Y., Kim, S.-U., Lee, S.-D. (2015). Optically switchable grating based on dye-doped ferroelectric liquid crystal with high efficiency. Optics Express, 23, 12619–12627.

Kuo, Y.-C., Yeh, H.-C. (2012). Optically controllable transflective Fresnel lens in azobenzene-doped cholesteric liquid crystals using a Sagnac interferometer. Applied Physics Express, 5, 021701.

Kurihara, S., Nomiyama, S., Nonaka, T. (2000). Photochemical switching between a compensated nematic phase and a twisted nematic phase by photoisomerization of chiral azobenzene molecules. Chemistry of Materials, 12, 9–12.

Kurihara, S., Nomiyama, S., Nonaka, T. (2001). Photochemical control of the macrostructure of cholesteric liquid crystals by means of photoisomerization of chiral azobenzene molecules. Chemistry of Materials, 13, 1992–1997.

Lee, C.-R., Fu, T.-L., Cheng, K.-T., Mo, T.-S., Fuh, A.Y.-G. (2004). Surface-assisted photoalignment in dye-doped liquid-crystal films. Physical Review E, 69, 031704.

Li, Q., Green, L., Venkataraman, N., Shiyanovskaya, I., Khan, A., Urbas, A., Doane, J.W. (2007). Reversible photoswitchable axially chiral dopants with high helical twisting power. Journal of the American Chemical Society, 129, 12908–12909.

Li, Q., Li, L., Kim, J., Park, H.-S., Williams, J. (2005). Reversible photoresponsive chiral liquid crystals containing a cholesteryl moiety and azobenzene linker. Chemistry of Materials, 17, 6018–6021.

Li, Q., Li, Y., Ma, J., Yang, D.-K., White, T.J., Bunning, T.J. (2011a). Directing dynamic control of red, green, and blue reflection enabled by a light-driven self-organized helical superstructure. Advanced Materials, 23, 5069–5073.

Li, -S.-S., Shen, Y., Chang, Z.-N., Li, W.-S., Xu, Y.-C., Fan, X.-Y., Chen, L.-J. (2017). Dynamic cholesteric liquid crystal superstructures photoaligned by one-step polarization holography. Applied Physics Letters, 111, 231109.

Li, Y., Urbas, A., Li, Q. (2011b). Synthesis and characterization of light-driven dithienylcyclopentene switches with axial chirality. The Journal of Organic Chemistry, 76, 7148–7156.

Li, Y., Urbas, A., Li, Q. (2012). Reversible light-directed red, green, and blue reflection with thermal stability enabled by a self-organized helical superstructure. Journal of the American Chemical Society, 134, 9573–9576.

Li, Y., Xue, C., Wang, M., Urbas, A., Li, Q. (2013). Photodynamic chiral molecular switches with thermal stability: From reflection wavelength tuning to handedness inversion of self-organized helical superstructures. Angewandte Chemie International Edition, 52, 13703–13707.

Lin, J.-D., Lin, Y.-M., Mo, T.-S., Lee, C.-R. (2014). Photosensitive and all-optically fast-controllable photonic bandgap device and laser in a dyedoped blue phase with a low-concentration azobenzene liquid crystal. Optics Express, 22, 9171–9181.

Lin, T.-H., Huang, Y., Zhou, Y., Fuh, A.Y.G., Wu, S.-T. (2006). Photo-patterning micro-mirror devices using azo dye-doped cholesteric liquid crystals. Optics Express, 14, 4479–4485.

Lin, T.-H., Li, Y., Wang, C.-T., Jau, H.-C., Chen, C.-W., Li, -C.-C., Bisoyi, H.K., Bunning, T.J., Li, Q. (2013). Red, green and blue reflections enabled in an optically tunable self-organized 3D cubic nanostructured thin film. Advanced Materials, 25, 5050–5054.

Liu, D., Broer, D.J. (2014). Self-assembled dynamic 3D fingerprints in liquid-crystal coatings towards controllable friction and adhesion. Angewandte Chemie International Edition, 53, 4542–4546.

Lucchetti, L., Simoni, F., Reznikov, Y. (1999). Fast optical recording in dye-doped liquid crystals. Optics Letters, 24, 1062–1064.

Ma, J., Li, Y., White, T., Urbas, A., Li, Q. (2010). Light-driven nanoscale chiral molecular switch: reversible dynamic full range color phototuningw. Chemical Communications, 46, 3463–3465.

Mathews, M., Tamaoki, N. (2008). Planar chiral azobenzenophanes as chiroptic switches for photon mode reversible reflection color control in induced chiral nematic liquid crystals. Journal of the American Chemical Society, 130, 11409–11416.

Mathews, M., Zola, R.S., Hurley, S., Yang, D.-K., White, T.J., Bunning, T.J., Li, Q., Am, J. (2010). Light-driven reversible handedness inversion in self-organized helical superstructures. Chemical Society, 132, 18361–18366.

Mathewsa, M., Tamaoki, N. (2009). Reversibly tunable helicity induction and inversion in liquid crystal self-assembly by a planar chiroptic trigger molecule. Chemical Communications, 24, 3609–3611.

Moerner, W.E., Silence, S.M., Hache, F., Bjorklund, G.C. (1994). Orientationally enhanced photorefractive effect in polymers. Journal of the Optical Society of America B, 11, 320–330.

Montbach, E., Venkataraman, N., Khan, A., Shiyanovskaya, I., Schneider, T., Doane, J.W., Green, L., Li, Q. (2008). Novel optically addressable photochiral displays. SID 08 DIGEST, 39, 919–922.

Natarajan, L.V., Bunning, T.J., Klei, H.E., Crane, R.L., Adams, W.W. (1991). Novel photochromic cholesteric liquid crystal siloxane. Macromolecules, 24, 6554–6556.

Noga, J., Sobolewska, A., Bartkiewicz, S., Galewski, Z. (2016). Holographic recording in chiral and linear isomers of single-component phototropic liquid crystals: an experiment and theoretical approach. Liquid Crystals, 43, 758–769.

Ouskova, E., Fedorenko, D., Reznikov, Y., Shiyanovskii, S.V., Su, L., West, J.L., Kuksenok, O.V., Francescangeli, O., Simoni, F. (2001a). Hidden photoalignment of liquid crystals in the isotropic phase. Physical Review E, 63, 021701.

Ouskova, E., Reznikov, Y., Shiyanovskii, S.V., Su, L., West, J.L., Kuksenok, O.V., Francescangeli, O., Simoni, F. (2001b). Photo-orientation of liquid crystals due to light-induced desorption and adsorption of dye molecules on an aligning surface. Physical Review E, 64, 051709.

Rameshbabu, K., Urbas, A., Li, Q. (2011). Synthesis and characterization of thermally irreversible photochromic cholesteric liquid crystals. The Journal of Physical Chemistry B, 115, 3409–3415.

Reshetnyak, V.Y., Pinkevych, I.P., Cook, G., Evans, D.R., Sluckin, T.J. (2010). Two-beam energy exchange in a hybrid photorefractive-flexoelectric liquid-crystal cell. Physical Review E, 81, 031705.

Reshetnyak, V.Y., Pinkevych, I.P., Cook, G., Evans, D.R., Sluckin, T.J. (2012). Two-beam energy exchange in a hybrid photorefractive inorganic-cholesteric cell. Molecular Crystals and Liquid Crystals, 560, 8–22.

Reshetnyak, V.Y., Pinkevych, I.P., Sluckin, T.J., Cook, G., Evans, D.R. (2014). Beam coupling in hybrid photorefractive inorganic-cholesteric liquid crystal cells: Impact of optical rotation. Journal of Applied Physics, 115, 103103.

Ruslim, C., Ichimura, K. (2000). Conformational effect on macroscopic chirality modification of cholesteric mesophases by photochromic azobenzene dopants. The Journal of Physical Chemistry B, 104, 6529–6535.

Ruslim, C., Ichimura, K. (2001). Conformatio-assisted amplification of chirality transfer of chiral Z–azobenzenes. Advanced Materials, 13, 37–40.

Ryabchun, A., Bobrovsky, A., Sobolewska, A., Shibaev, V., Stumpe, J. (2012). Dual photorecording on cholesteric azobenzene-containing LC polymer films using helix pitch phototuning and holographic grating recording. Journal of Material Chemistry, 22, 6245–6250.

Ryabchun, A., Bobrovsky, A., Stumpe, J., Shibaev, V. (2015a). Rotatable diffraction gratings based on cholesteric liquid crystals with phototunable helix pitch. Advanced Optical Materials, 3, 1273–1279.

Ryabchun, A., Bobrovsky, A., Stumpe, J., Shibaev, V. (2015b). Rotatable diffraction gratings based on cholesteric liquid crystals with phototunable helix pitch. Advanced Optical Materials, 3, 1273–1279.

Ryabchun, A., Sobolewska, A., Bobrovsky, A., Shibaev, V., Stumpe, J. (2014). Polarization holographic grating recording in the cholesteric azobenzene-containing films with the phototunable helix pitch. Journal of Polymer Science, Part B: Polymer Physics, 52, 773–781.

Sackmann, E. (1971). Photochemically induced reversible color changes in cholesteric liquid crystals. Journal of the American Chemical Society, 93.

Sasaki, T., Emoto, A., Shioda, T., Ono, H. (2009). Transmission and reflection phase gratings formed in azo-dye-doped chiral nematic liquid crystals. Applied Physics Letters, 94, 023303.

Sasaki, T., Ikegami, M., Abe, T., Miyazaki, D., Kajikawa, S., Naka, Y. (2013). Real-time dynamic hologram in photorefractive ferroelectric liquid crystal with two-beam coupling gain coefficient of over $800 cm^{-1}$ and response time of 8 ms. Applied Physics Letters, 102, 063306.

Sasaki, T., Kajikawa, S., Naka, Y. (2014). Dynamic amplification of light signals in photorefractive ferroelectric liquid crystalline mixtures. Faraday Discuss, 174, 203–218.

Sasaki, T., Miyazaki, D., Akaike, K., Ikegami, M., Naka, Y., Mater, J. (2011). Photorefractive effect of photoconductive ferroelectric liquid crystalline mixtures composed of photoconductive chiral compounds and liquid crystal. Chem, 21, 8678–8686.

Simoni, F., Francescangeli, O., Reznikov, Y., Slussarenko, S. (1997). Dye-doped liquid crystals as high-resolution recording media. Optics Letters, 22, 549–551.

Sio, L.D., Placido, T., Comparelli, R., Curri, M.L., Tabiryan, N., Bunning, T.J. (2016). Plasmonic photoheating of gold nanorods in thermo-responsive chiral liquid crystals. Journal of Optics, 18, 125005.

Sio, L.D., Placido, T., Serak, S., Comparelli, R., Tamborra, M., Tabiryan, N., Curri, M.L., Bartolino, R., Umeton, C., Bunning, T. (2013). Nano-localized heating source for photonics and plasmonics. Advanced Optical Materials, 1, 899–904.

Slaney, A.J., Nishiyama, I., Styring, P., Goodby, J.W. (1992). Twist inversion in a cholesteric material containing a single chiral centre. Journal of Material Chemistry, 2, 805–810.

Smalyukh, I.I., Kaputa, D., Kachynski, A.V., Kuzmin, A.N., Ackerman, P.J., Twombly, C.W., Lee, T., Trivedi, R.P., Prasad, P.N. (2012). Optically generated reconfigurable photonic structures of elastic quasiparticles in frustrated cholesteric liquid crystals. Optics Express, 7, 6870–6880.

Smalyukh, I.I., Lansac, Y., Clark, N.A., Trivedi, R.P. (2010). Three-dimensional structure and multistable optical switching of triple-twisted particle-like excitations in anisotropic fluids. Nature Materials, 9, 139–145.

Talarico, M., Golemme, A. (2006). Optical control of orientational bistability in photorefractive liquid crystals. Nature Materials, 5, 185–188.

Talarico, M., Termine, R., Golemme, A. (2007). Photorefractive organic material for optical thresholding. Applied Physics Letters, 91, 081110.

Termine, R., Golemme, A. (2001). Polymer-dispersed chiral smectic A with photorefractive properties. Optics Letters, 26, 1001–1003.

Termine, R., Golemme, A. (2002). Photorefractive index modulation in chiral smectic phases. The Journal of Physical Chemistry B, 106, 4105–4111.

Termine, R., Simone, B.C.D., Golemme, A. (2001). Photorefractive chiral smectic A phases. Applied Physics Letters, 78, 688–690.

Trushkevych, O., Ackerman, P., Crossland, W.A., Smalyukh, I.I. (2010). Optically generated adaptive localized structures in confined chiral liquid crystals doped with fullerene. Applied Physics Letters, 97, 201906.

Varanysia, A., Chien, L.-C. (2015). Photoswitchable and dye-doped bubble domain texture of cholesteric liquid crystals. Optics Letters, 40, 4392–4395.

Venkataraman, N., Magyar, G., Lightfoot, M., Montbach, E., Khan, A., Schneider, T., Doane, J.W., Green, L., Li, Q. (2009). Thin flexible photosensitive cholesteric displays. Journal of the Society for Information Display, 17, 869–873.

Voloschenko, D., Lavrentovich, O.D. (1999). Light-induced director-controlled microassembly of dye molecules from a liquid crystal matrix. Journal of Applied Physics, 86, 4843–4846.

Wang, C.-T., Wu, Y.-C., Lin, T.-H. (2014). Photo-controllable tristable optical switch based on dye-doped liquid crystal. Dyes and Pigments, 103, 21–24.

Wang, L., Bisoyi, H.K., Zheng, Z., Gutierrez-Cuevas, K.G., Singh, G., Kumar, S., Bunning, T.J., Li, Q. (2017a). Stimuli-directed self-organized chiral superstructures for adaptive windows enabled by mesogen-functionalized graphene. Materials Today, 20, 230–237.

Wang, L., Chen, D., Gutierrez-Cuevas, K.G., Bisoyi, H.K., Fan, J., Zola, R.S., Li, G., Urbas, A.M., Bunning, T.J., Weitz, D.A., Li, Q. (2017b). Optically reconfigurable chiral microspheres of self-organized helical superstructures with handedness inversion. Materials Horizons, 4, 1190.

Wang, L., Gutierrez-Cuevas, K.G., Bisoyi, H.K., Xiang, J., Singh, G., Zola, R.S., Kumar, S., Lavrentovich, O.D., Urbasd, A., Li, Q. (2015). NIR light-directing self-organized 3D photonic superstructures loaded with anisotropic plasmonic hybrid nanorods. Chemical Communications 51, 15039–15042.

Wang, L., Gutierrez-Cuevas, K.G., Urbas, A., Li, Q. (2016). Near-infrared light-directed handedness inversion in plasmonic nanorod-embedded helical superstructure. Advanced Optical Materials, 4, 247–251.

Wang, Y., Urbas, A., Li, Q. (2012). Reversible visible-light tuning of self-organized helical superstructures enabled by unprecedented light-driven axially chiral molecular switches. Journal of the American Chemical Society, 134, 3342–3345.

Wang, Y.-J., Pei, M., Peng, P., Carlisle, G.O. (2006). All-optical polarization-independent diffraction in dye-doped cholesteric liquid crystal. Journal of Materials Science: Materials in Electronics, 17, 385–394.

White, T.J., Bricker, R.L., Natarajan, L.V., Tabiryan, N.V., Green, L., Li, Q., Bunning, T.J. (2009). Phototunable azobenzene cholesteric liquid crystals with 2000 nm range. Advanced Functional Materials, 19, 3484–3488.

White, T.J., Cazzell, S.A., Freer, A.S., Yang, D.-K., Sukhomlinova, L., Su, L., Kosa, T., Taheri, B., Bunning, T.J. (2011). Widely tunable, photoinvertible cholesteric liquid crystals. Advanced Materials, 23, 1389–1392.

Wu, Y., Zhou, Y., Yin, L., Zou, G., Zhang, Q. (2013). Photoinduced liquid crystal blue phase by bent-shaped cis isomer of the azobenzene doped in chiral nematic liquid crystal. Liquid Crystals, 40, 726–733.

Yeh, H.-C. (2011). Time-domain analysis of optically controllable biphotonic gratings in azo-dye-doped cholesteric liquid crystals. Optics Express, 19, 5500–5510.

Yeh, H.-C., Chen, G.-H., Lee, C.-R., Mo, T.-S. (2007a). Optically switchable biphotonic gratings based on dye-doped cholesteric liquid crystal films. Applied Physics Letters, 90, 261103.

Yeh, H.-C., Chen, G.-H., Lee, C.-R., Mo, T.-S. (2007b). Photoinduced two-dimensional gratings based on dye-doped cholesteric liquid crystal films. The Journal of Chemical Physics, 127, 141105.

Yoshioka, T., Ogata, T., Nonaka, T., Moritsugu, M., Kim, S.N., Kurihara, S. (2005). Reversible-photon-mode full-color display by means of photochemical modulation of a helically cholesteric structure. Advanced Materials, 17, 1226–1229.

Zheng, Z.-G., Li, Y., Bisoyi, H.K., Wang, L., Bunning, T.J., Li, Q. (2016). Three-dimensional control of the helical axis of a chiral nematic liquid crystal by light Nature, 531, 352–356.

Zheng, Z.-G., Liu, B.-W., Zhou, L., Wang, W., Hu, W., Shen, D. (2015). Wide tunable lasing in photoresponsive chiral liquid crystal emulsion. Journal of Materials Chemistry C, 3, 2462–2470.

Zheng, Z.-G., Zola, R.S., Bisoyi, H.K., Wang, L., Li, Y., Bunning, T.J., Li, Q. (2017). Controllable dynamic zigzag pattern formation in a soft helical superstructure. Advanced Materials, 29, 1701903.

Takahiro Seki, Nobuhiro Kawatsuki

10 Photoalignment of liquid crystalline polymers attained from the free surface

Abstract: Recently, the fabrication of liquid crystal (LC) displays in industry largely relies on the photoalignment technologies. The photoalignment is based on the anisotropic photochemical reaction taking place on substrate surfaces. Until recently, the photoalignment layers have been placed on solid substrates, however, recent efforts have revealed that the photoalignment layer can be positioned also on the free surface instead of solid surface in cases of LC polymer films. This chapter reviews recent unconventional approaches for the photoalignment achieved from the free surface. As mentioned here, the free surface is very influential for the alignment of mesogens, and various strategies can be applied. Expectedly, these new types of alignment procedures will provide new possibilities for the LC film technologies.

10.1 Introduction

The alignment procedures of liquid crystalline (LC) molecules are of essence for practical application in display panels, optical elements, and recording media. LC orientations are strongly affected by the nature of substrate surface, which is the key to fabricate the LC display panels. In the last decade, the photoalignmnet techniques have been applied to the LC cell fabrication (Kunimatsu et al., 2014; Miyachi et al., 2010). The photoalignment technology is based on the orientation effect of LC molecules on the photoreactive layers on the solid substrate. Various types of photoreactive units and LC materials have been used in the photoalignment processes (Ichimura, 2000; O'Neill et al., 2000; Yaroshchuk et al., 2012; Seki et al., 2013; Seki, 2014a, 2014b, 2016; Nagano, 2016; Priimagi et al., 2014,). It has been demonstrated that photoalignment processes, non-contact and high resolution means, have great advantages over conventional rubbing processes. In these cases, the photoreactions at the interface of solid substrate and LC phase are essential for the LC alignment (Figure 10.1(a)).

Recent efforts on the LC photoalignment control revealed that the alignment process can be further achieved from the free surface (air-side) instead of solid substrate surface for side-chain LC polymers (SCLCPs) (Fukuhara et al., 2013, 2014, 2017; Kawatsuki et al., 2014; Miyake et al., 2016; Nakai et al., 2016; Seki, 2014a) (Figure 10.1(b)). The density difference between a condensed matter and a gas is large (approximately 1,000 times difference), and thus the motions of the condensed matter freely take place, and are virtually unaffected by the gas phase. Thus, the interface between a condensed phase and gas phase is called a free surface or free interface. It is anticipated that the development of LC alignment using this unconventional approach will greatly extend further opportunities in the LC technologies. This chapter introduces various examples of the photoalignment of mesogens of SCLCP films and related phenomena achieved from the free surface. Attempts have been made using azobenzene (Az), cinnamate (CA), and *n*-benzylideneaniline (NBA). Some related free surface-mediated processes of SCLCP films will be also introduced.
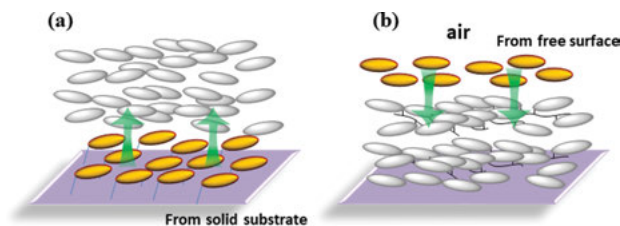
Figure 10.1: Schematic of conventional command layers: (a) at the solid surface and (b) at the free surface.

10.2 Initial motivation of photoalignment from the free surface

The orientation induction of LC molecules affected at interfaces has been an issue of fundamental scientific interest. The long axis of rod-like LC crystal molecules tends to be oriented homeotropically with respect to the free surface plane to reduce the free energy (excluded volume effect). This orentation behavior has been confirmed both experimentally (Ocko et al., 1986; Pershan, 1990) and theoretically (Canabarro et al., 2008; Chen et al., 1991; Kimura et al., 1985; Scaramuzza et al., 2004).

In the course of studies on the photoalignment of microphase separation structures in Az-containing LC block copolymer films (Nagano, 2016; Nagano et al. 2012; Sano et al., 2015a, 2014), it was revealed that, when the amorphous block part consists of a flexible polymer such as poly(butyl methacrylate) (PBMA-*b*-PAz; Figure 10.2), the mesogens were always aligned planarly. It was confirmed that this flexible and
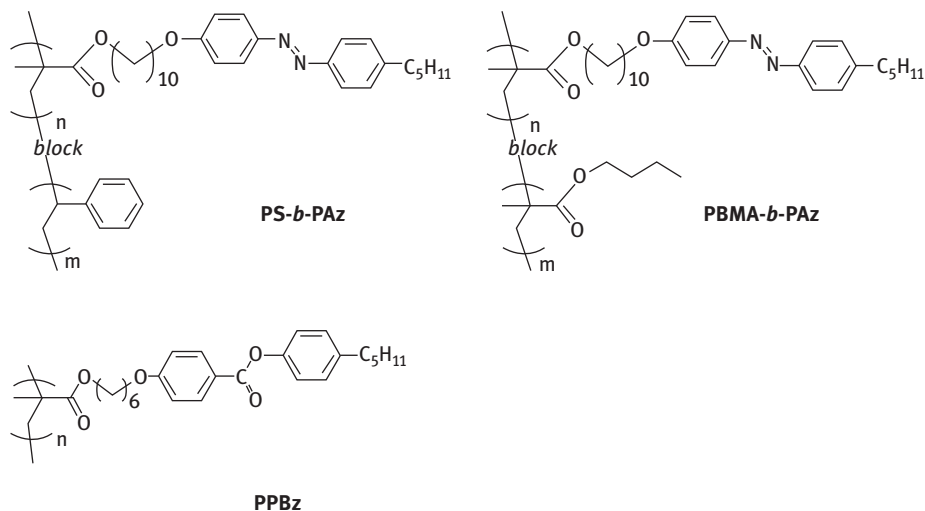
Figure 10.2: Chemical structures of PS-*b*-PAz, PBMA-*b*-PAz, and PPBz.

lower energy polymer block segregates to the free surface (Fukuhara et al., 2013). A film of polystyrene (PS)-containing block copolymer (PS-*b*-PAz; Figure 10.2) providing the vertical orientation of PS cylinders was converted to the planar one when a trace of PBMA-*b*-PAz was mixed and successively annealed at 130 ℃ (corresponding to above the glass transition temperature (T_g) of PS, and above the clearing point (iso-tropization temperature) of PAz). The same annealing procedure for a pure PS-*b*-PAz film at 130 ℃ provided the mesoscopic cylinders of PS in the homeotropic mode. By blending few wt% of PBMA-*b*-PAz in the spincast film, the successive annealing led to an entirely different mesogen orientation. A transmission electron microscopy (TEM) image indicated the formation of a skin layer of segregated PBMA-*b*-PAz (thickness: ca. 20 nm) at the free surface (Fukuhara et al., 2013).

In the above investigation, all mesogens were composed of Az units. A more challenging and fascinating endeavor would be to control orientations of non-photoreactive LC polymer films. For this purpose, a trace of PBMA-*b*-PAz was min-gled in a phenyl benzoate side chain polymer (PPBz). After appropriate annealing, the photoresponsive top layer of PBMA-*b*-PAz was formed on the air side, and this layer essentially functioned as a free-surface command layer for the PPBz film. The mesogens of PPBz was aligned according to the photoaligning action of the photoresponsive skin layer on the top (Fukuhara et al., 2014).

Based on these data, it was anticipated that local surface modifications by a print-ing technique such as inkjet printing will further validate this new method (Figure 10.3 (a)). The superfine-inkjet printing was achieved on a PPBz film, and the film was suc-cessively annealed. Only the printed areas showed the planar alignment, and un-printed parts gave the homeotropic one. After irradiation with linearly polarized light
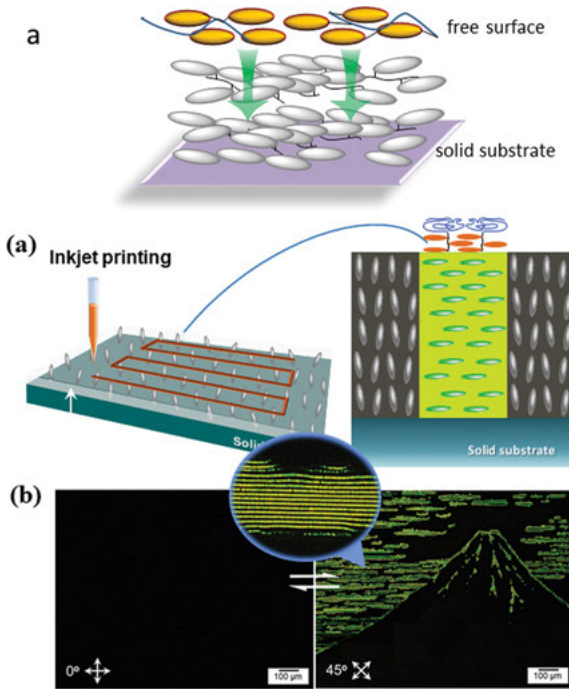
Figure 10.3: (a) Schematic of inkjet printing of the photoresponsive polymer of PBMA-*b*-PAz on a light-inert LC film of PPBz, followed by the local photoalignment by LPL at the printed areas. (b) An example of birefringent picture drawn in this process. Adapted from Fukuhara et al. (2014). Copyright 2014, *The Nature Publishing*.

(LPL) at 436 nm, the planar areas were homogeneously aligned. In this free-surface mediated system, a resolution with 1 m was obtained as revealed by a birefringence observation through crossed polarizers. Figure 10.3(b) shows an example (Seki, 2014a; Fukuhara et al., 2014). Only the printed areas alternately became bright and dark at every 45° when the polarizers were rotated. Here, PBMA-*b*-PAz can be considered as a "command ink," namely, the ink itself does not have intrinsic functions such as color, emission, conductivity and so on but has the ability to induce the structure and molecular orientation changes of the underlying base polymer film.

10.3 Mesogen orientation in cyanobiphenyl SCLCPs

The chemical structure of poly(alkyl acrylate)s and poly(alkyl methacrylate)s are similar, but the substituent of hydrogen or methyl group at the *α*-position in the backbone polymer chain leads to a great difference in the chain rigidity. Many

characteristics such as thermal properties (typically reflected to T_g) (Rogers et al., 1957; Wiley et al., 1948), the packing states in a 2D monolayer (Arriaga et al., 2011) and in the LC state (Boeffel et al., 1986; Percec et al., 1990; Zentel et al., 1987), and photoinduced mass transfer efficiency (Ando et al., 2009) are changed by the main chain rigidity. It was demonstrated that this parameter further alters the mesogen orientation of the cyanobipheny (CB)-containing SCLCPs in the thin film state (Tanaka et al., 2015).
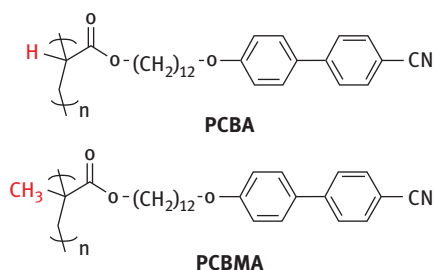
Figure 10.4: Chemical structures of PCBA and PCBMA.

Spincast films of two homologous CB-containing SCLCPs ((poly[12-((4′-cyano-[1,1′-biphenyl]-4-yl)oxy)dodecyl acrylate] (PCBA) and poly[12-((4′-cyano-[1,1′-biphenyl]-4-yl)oxy)dodecyl methacrylate] (PCBMA), Figure 10.4) were prepared on a quartz plate. Both UV-visible absorption spectroscopic and grazing incidence angle x-ray scattering (GI-SAXS) measurements revealed that the CB mesogoens of PCBA and PCBMA were oriented in the homeotropic and planar orientation, respectively, in the film state (Tanaka et al., 2015). Most of SCLCP films adopt the homeotropic orientation owing to the excluded volume effect, as mentioned in the previous section. Therefore, the CB mesogens of PCBMA are exceptionally oriented in the planar mode. Clear explanations for this behavior has not been given, but it is obvious that difference in the main chain structure (rigidity) seems to be the only factor to cause this effect. The rigid polymer backbone may restrict the direction of side chains and impede a vertically aligned side chain at the free surface. Having these contrasting results, a line by inkjet printing was achieved to confirm the role of the free surface. A line of PCBMA (50 nm thickness) was printed on a PCBA film (typically 150–200 nm thickness), and inversely a line of PCBA on a PCBMA film. After appropriate annealing, polarizing optical microscopic (POM) observations were made. As shown in Figure 10.5(a), a planar alignment was observed locally in the line-printed region with PCBMA for PCBA film. On the other hand, a homeotropic alignment was obtained selectively in the line-printed region with PCBA for the PCBMA film (Figure 10.5(b)). These results clearly show that the mesogen orientation was controlled from the free surface side. In this way, the essential role of the free surface is further indicated in the CB-containing SCLCP film systems. It is to be noted that Komura

et al. successfully took a TEM image where the alignment of side chain mesogens and mirophase separation structure is initated from the free surface (Komura et al., 2015).
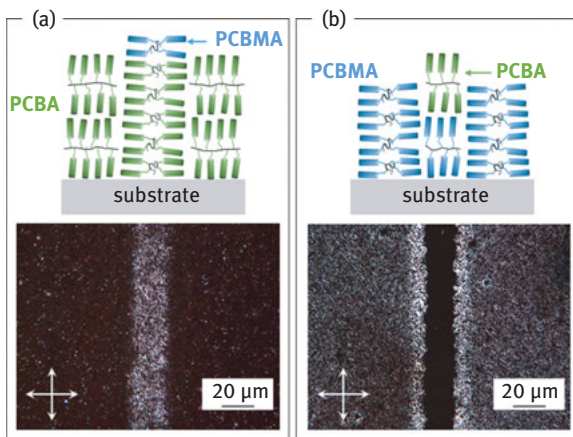
Figure 10.5: POM images of LC films possessing inkjet-printed line (20 μm width) after annealing. (a) PCBMA line is printed on a PCBA film. (b) PCBA line is printed on a PCBMA film. Schematics of the mesogen orientation are indicated in the upper part of each image. Adapted from Tanaka et al. (2015). Copyright 2015, *American Chemical Society*.

Most of the mesogens in the PCBA film adopt the homeotropic orientation, however, a careful observation of GI-SAXS showed that some mesogens were planarly oriented. UV-visible spectroscopic measurements using a series of PCBA films with varied thickness, and GI-SAXS measurements using a tender (low energy) synchrotron X-ray beam showed that planarly oriented mesogens exist in the vicinity of substrate surface region of ca. 10 nm thickness. In the regions away from this critical thickness, the CB mesogens were oriented homeotropically (Tanaka et al., 2016).

10.4 Switchable homeotropic-planar command effect from the free surface

Additional attempts were made for the optical switching of mesogen orientation from the free surface. PCBMA was mixed with PAz (typically 10% by weight) and a spincast film was prepared with 200 nm thickness. Upon annealing, PAz was segregated on the surface of PCBMA. In this initial state, the overall film shows a homeotropic alignment despite the fact that a pure PCBMA gave a planar alignment (Nakai et al., 2016). Also in this case, the orientation of overall mesogens were controlled by the orientation of PAz existing at the free surface. UV light (365 nm) irradiation

onto this hybrid film on heating above the isotropization temperature for the both LC polymers and successive cooling led to the planar orientation. The same procedure with visible light (436 nm) turned back to the homeotropic alignment again (Figure 10.6(a)) (Nakai et al., 2016). The mesogen orientations were confirmed by both UV-visible spectroscopic and GI-SAXS measurements. These cycles could be repeated at least several times (Figure 10.6(b)). Therefore, the mesogen orientation between the homeotropic and planar modes can be switched photochemically. This repeatable process can be compared with the first demonstration of the photochemical command surface using an Az layer on the substrate surface (Ichimura et al., 1988; Seki et al., 1993).
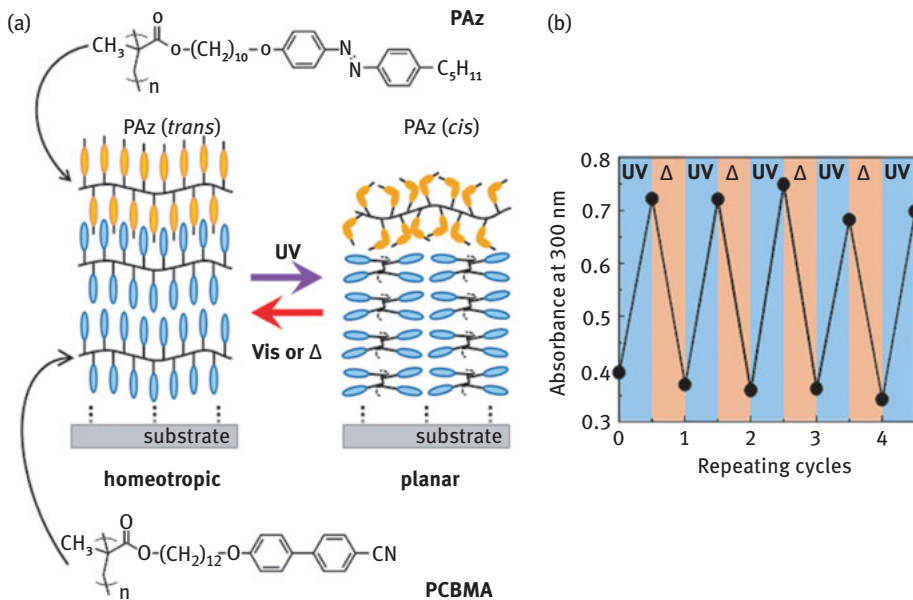
Figure 10.6: Schematic illustration of photoswitching between the homeotropic and planar orientations of PCMA driven by a photorersponsive PAz on the top. Adapted from Nakai et al. (2016). Copyright 2016, *American Chemical Society*.

The film thickness of PCBMA was changed from 150 nm to 700 nm while the surface skin layer of PAz was kept constant (20 nm) (Figure 10.7(a)). Within these conditions, the out-of-plane switching from the free surface was observed in the same manner. The photopatterning was also achieved by using a photomask. The birefringent image where dark and bright regions corresponds to the homeotropically and planary oriented areas, respectively, appeared and disappeared by the alternating irradiation with UV and visible light irradiation (Figure 10.7(b)). The patterned image formation was again erasable and rewritable.
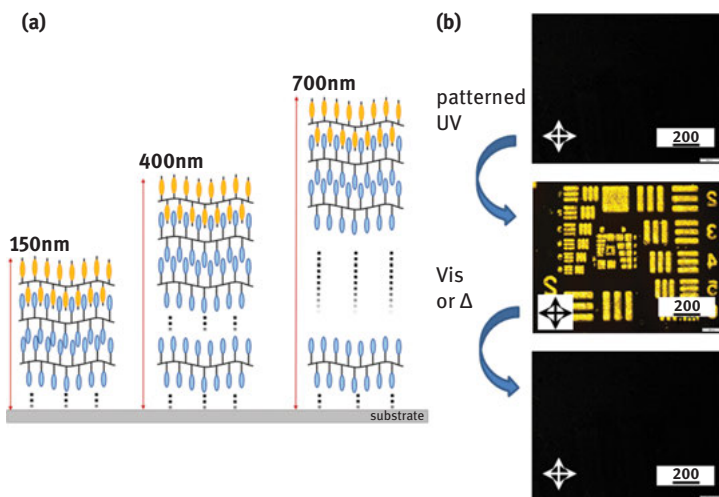
Figure 10.7: (a) Schematic illustration of PAz-segregated PCBMA films with various film thickness (b: 150 nm, c: 400 nm, d: 700 nm). (b) An example of photopatterned image using a photomask. Adapted from Nakai et al. (2016). Copyright 2016, *American Chemical Society*.

10.5 Formation of photoalignable *n*-benzylideneaniline moieties at the free surface

N-benzylideneaniline derivatives are well known to be mesogenic cores for liquid crystals (LCs), and they are easily synthesized from phenylaldehyde (PA) and phenylamine derivatives by the condensation (Figure 10.8(a)) (Kosaska et al., 1994). Axis-selective *trans–cis–trans* photoisomerization of NBA using linearly polarized ultraviolet (LPUV) light exposure to NBA-containing polymeric films undergoes photoinduced reorientation perpendicular to polarization (**E**) of LPUV light similar to the Az derivatives (Figure 10.8(b)) (Kawatsuki et al., 2013, 2014). Copolymerization of NBA-containing polymers with a comonomer composed of photoinactive mesogenic side groups has attained cooperative thermally stimulated molecular reorientation (Kawatsuki et al., 2015a, b). Due to its facile synthesis of NBA, phenylamine monomeric derivatives (AN, Figure 10.2) doped in a polymethacrylate composed of phenylaldehyde (PA) side groups (PPA100, Figure 10.9) lead in situ formation of NBA moieties, where the similar photoinduced reorientation is observed to that of NBA-containing polymeric films (Kawatsuki et al., 2015).

Based on the in situ formation of NBA, sublimation-coating of AN on the free-surface of PPA100 film attains the formation of NBA moieties at the desired region, which introduces the similar photoinduced reorientation behavior to the NBA-containing polymeric films. Adjusting the sublimation time controls the amount of

(a)

(b)

E

Axis-selective photoisomerization

Reorientation perpendicular to *E*
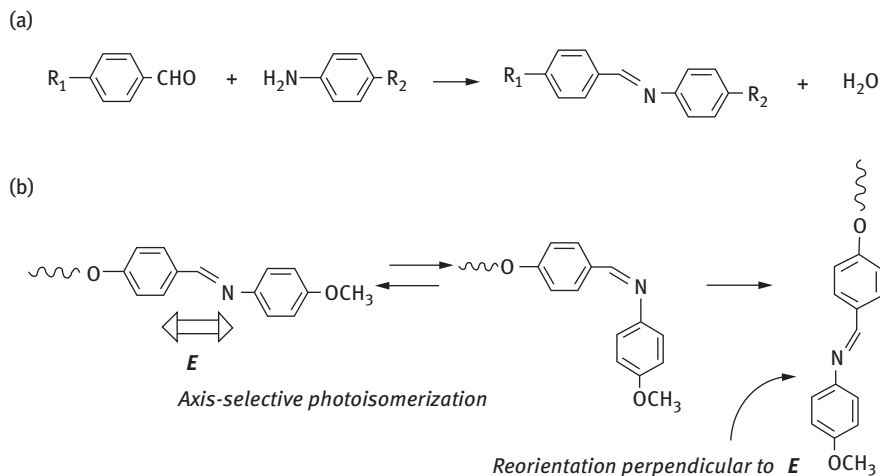
Figure 10.8: (a) Synthesis of NBA by condensation from phenylaldehyde and phenylamine derivatives. (b) Mechanism of photoinduced reorientation of NBA derivatives based on axis-selective photo-isomerization.

NBA formation at the free-surface, showing different photoinduced orientation performance with different photoinduced birefringence (Δn) (Figure 10.10(a)). Additionally, calligraphy and AN-crystal coating on the PPA100 film achieve selective formation of NBA, where the precise birefringent pattern is easily attained (Figures 10(b), 10(c)) (Kawatsuki et al., 2015).

In many cases for the photoinduced reorientation of the photoalignable materials, photosensitive groups remain after the reorientation processes, resulting in their poor photo-durability. Photo-durable birefringent pattern can be realized by using PA-containing polymer copolymerized with a comonomer with benzoic acid (BA) side groups (Figure 10.11(a)) (Kawatsuki et al., 2018). Because the BA side groups show the LC characteristics, cooperative reorientation of the NBA and BA side groups is generated when the PA side groups transform to NBA. The decomposition of the NBA moieties after the cooperative molecular reorientation gives the film photodurable. Figures 10.11(b) and 11(c) plot change in the polarized UV-vis spectra of a PPA20/AN (1/2 mol/mol) film after exposure to LP 365 nm light for 20 J/cm^2 and subsequent annealing at 130 °C (LC temperature range of PPA20) for 10 min, and that post-annealed at 125 °C for 80 min, respectively. The significant cooperative reorientation of NBA and BA side groups at the initial stage of the thermal stimulation (Figure 10.11(b)), but the absorption band of the NBA side groups at 335 nm is diminished after the post-annealing procedure (Figure 10.11(c)). Because the optical anisotropy of the BA side groups barely changed, no-NBA absorption band suggests the occurrence of thermal hydrolysis of NBA, which reforms PA side groups without changing the reorientation characteristics of the BA side groups. In this case, the
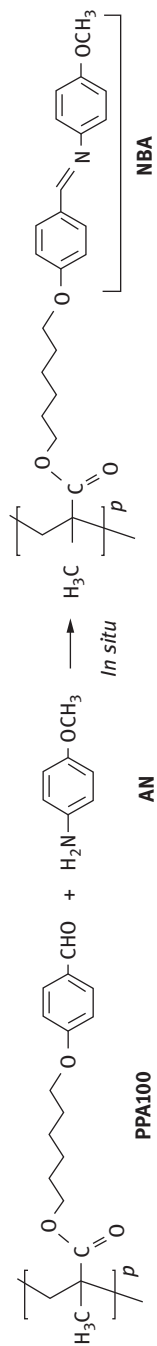
Figure 10.9: NBA side groups in polymer is in situ formed in polymer with phenyl aldehyde (PA) side groups and phenylamine (AN).
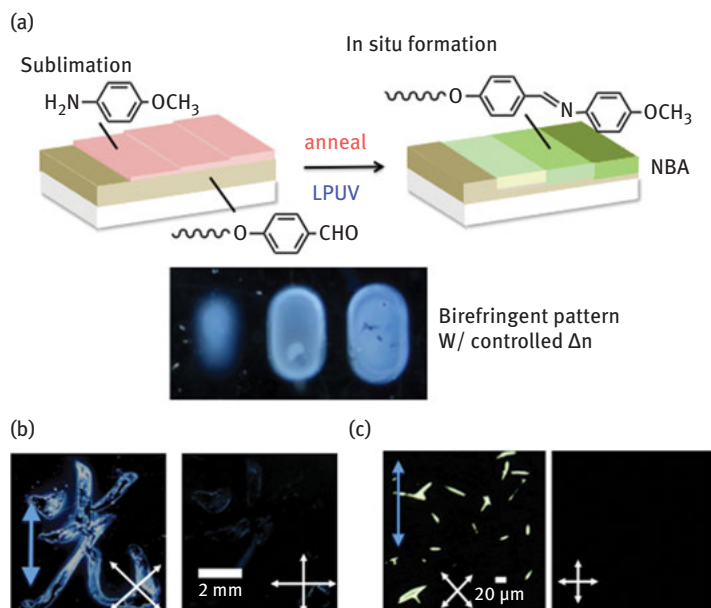
Figure 10.10: (a) Image of NBA side groups formation on PPA100 coated with AN, and photoinduced birefringent pattern of the films coated with AN with different sublimation times. (b) Photoaligned Chinese character painted from AN solution onto PPA100. (c) Thermally stimulated photoinduced birefringent pattern of a PPA100 film with AN crystals. Blue arrows indicate the polarization of LP 365 nm light, while white arrows are the polarizer and analyzer directions. Adapted from Kawatsuki et al. (2015b). Copyright 2015, *American Chemical Society*.

estimated thermal hydrolysis rate was 10 times slower than that the thermally stimulated self-organization rate of mesogenic side groups (Kawatsuki et al., 2018).

Due to the reformation of PA side groups in the reoriented photodurable film after the post-annealing, recoating AN molecules by the inkjet coating in a different area achieved new birefringent patterns. Then we fabricated multiple birefringent patterns with different orientation directions, corresponding to the first and second inkjet coatings with exposure of different LPUV light polarization (**E**) (Figure 10.12(a)). Additionally, annealing in the isotropic temperature range of the copolymer erased the oriented structure and subsequent recoating of AN molecules rewrote the birefringence pattern (Figure 10.12(b)). This inscription of the birefringent pattern can be repeated.

(a)

PPA100: x/y=100/0, **PPA20**: x/y=20/80

(b)

(c)
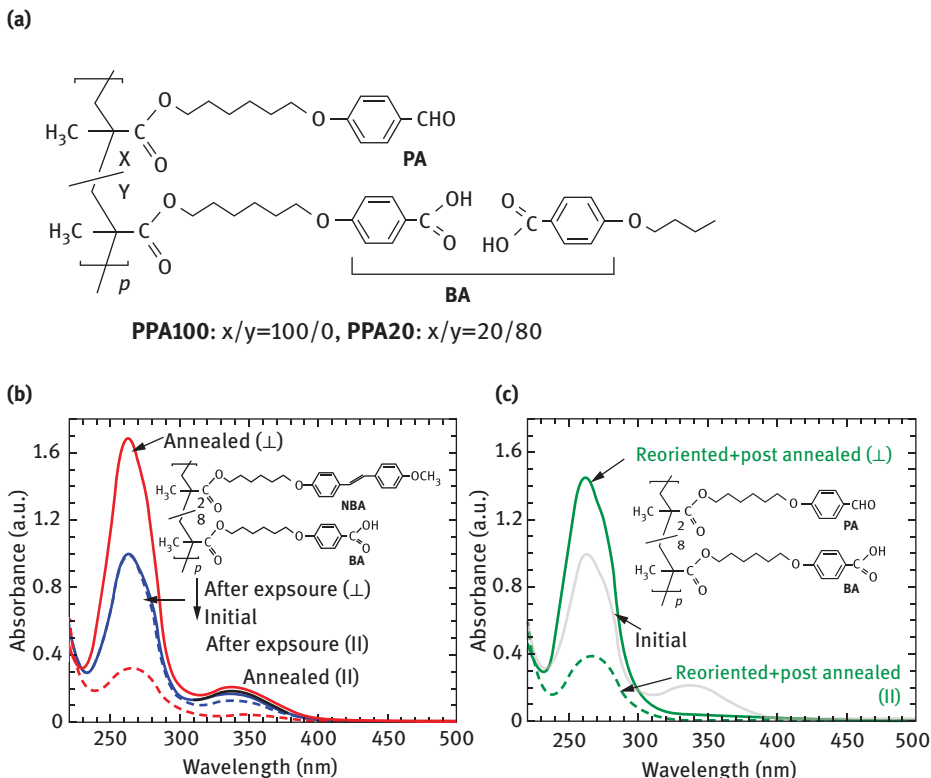
Figure 10.11: (a) Chemical structure of a copolymer with PA side groups and BA side groups. (b) Change in the polarized UV-vis spectra of a PPA20/AN (1/2 mol/mol) film after exposure to LP 365 nm light for 20 J/cm², followed by annealing at 130 °C for 10 min, and (c) after subsequent post-annealing at 125 °C for 80 min under RH = 35%. The insets show the chemical structure of the reoriented film.

10.6 Photoalignment with photosensitive low-molecular material via H-bonds at the free surface

Functional low-molecular-weight species can form H-bonds with appropriate side groups in polymers (Kato et al., 1989, 2006). A route toward patterned, photoalignable LCP films will be provided by the selective introduction of these mobile, photosensitive moieties into photoinactive LC polymeric (LCP) films. Effective photoinduced orientation and patterned alignment of a photoinactive LC polymeric film containing benzoic acid (BA) side groups (P6BAM) film by applying a top-coating of 4-methoxy cinnamic acid (MCA) (Figure 10.13(a)) (Kawatsuki et al., 2017; Minami et al., 2016).
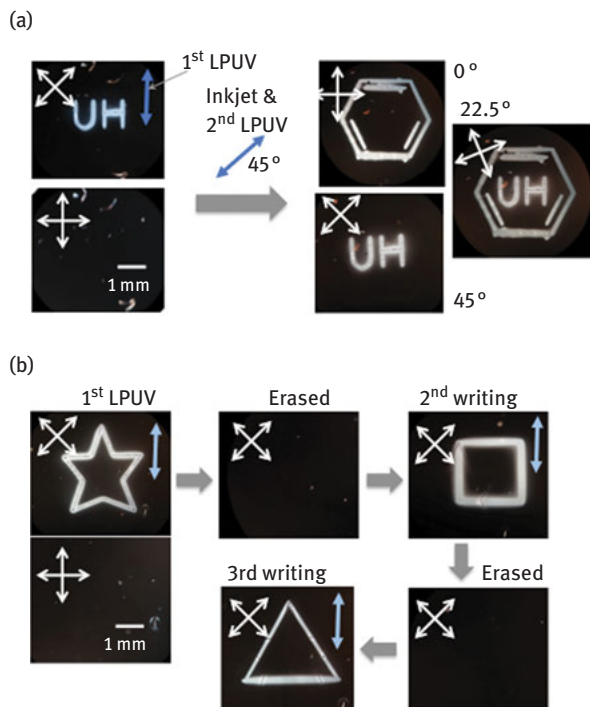
Figure 10.12: POM observation of the patterned and oriented PPA20 films irradiated with LP 365 nm light for 20 J/cm^2 followed by annealing. White arrows indicate the polarizer and analyzer directions, while the blue arrows indicate polarization (**E**) of LP 365 nm light. (a) 1st birefringent pattern (UH) formation with post-annealing at 125 °C for 80 min, and 2nd inkjet coating of AN (Benzene pattern) with a change in the polarization angle to 45° exposure, and subsequent annealing with post-annealing at 125 °C for 80 min. (b) 1st birefringent pattern (star pattern) and post-annealing at 140 °C for 10 min, 2nd inkjet coating of AN (square pattern) and irradiation for the reorientation and post-annealing at 140 °C, and 3rd inkjet coating of AN (triangle pattern) followed by irradiating for the reorientation.

As shown in Figure 10.13(b), a P6BAM film coated with MCA (sublimation coating) irradiated with LP 313 nm light shows axis-selective photoreaction, even though the P6BAM film itself is photoinactive. The subsequent annealing stage significantly increased the absorbance of the BA absorption band perpendicular to **E**, while the parallel absorbance decreased, showing the molecular reorientation of P6BAM. The MCA molecules simultaneously sublimed upon annealing, resulting in the reoriented film photoinactive (reoriented P6BAM), based on the similar strategy as described in above section (Kawatsuki et al., 2017).

Inkjet coating the MCA layer onto the polymer film provides the multiple patterned orientations of P6BAM films (Figure 10.14(a)). Although MCA molecules penetrate into the P6BAM film, birefringence was not observed after inkjet coating. When the film was exposed to LP 313 nm followed by annealing at LC temperature range of P6BAM, the

(a)

(b)
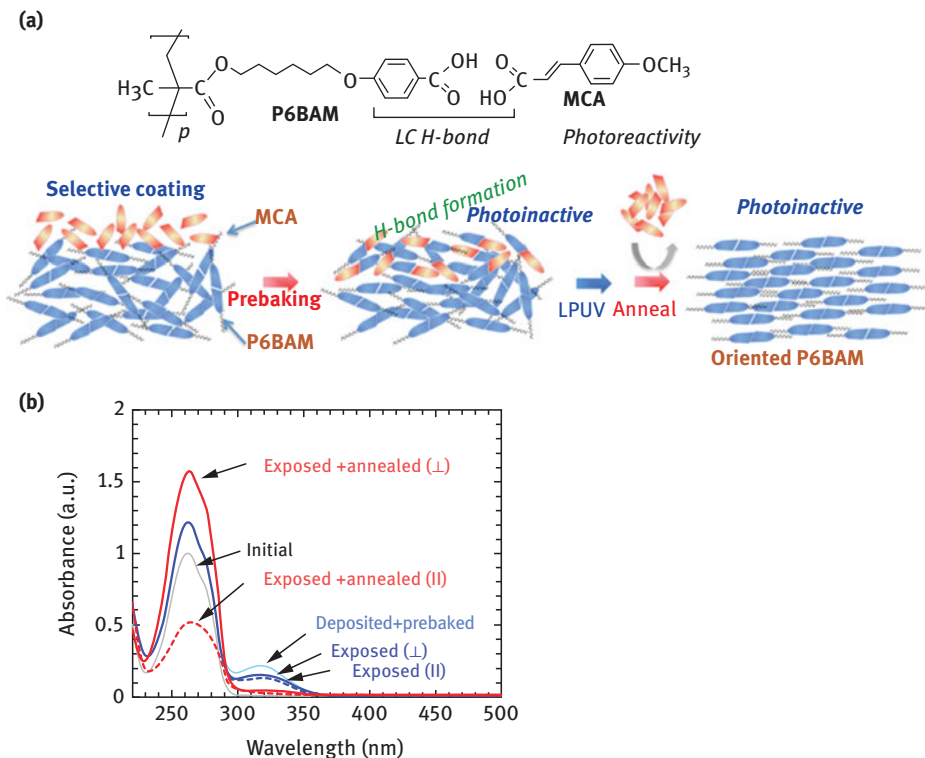
Figure 10.13: (a) Photoalignable H-bonded LC composed by P6BAM and MCA, and schematic image of photoalignment of photoinactive LCP coated with photoresponsive materials via H-bond. (b) Change in the polarized UV-vis spectra of a P6BAM film coated with MCA after exposure to LP 313 nm light for 0.5 J/cm^2 and subsequent annealing at 170 °C for 10 min.

formation of a birefringent pattern was appeared in the MCA-coated region due to thermally stimulated molecular reorientation and the recorded birefringent pattern exhibited durability to 313 nm UV light. Additionally, the second MCA pattern was applied to the film in a non-patterned area, introducing the fabrication of birefringent patterns corresponding to the first and second inkjet coatings with different orientation directions. The second exposure did not affect the first alignment pattern because the BA side groups do not absorb 313 nm light, resulting in the multiple alignment directions of the BA side groups. Furthermore, annealing the film at the isotropic temperature of P6BAM can erase the reoriented structure, and MCA recoating the erased film by the same procedure led to the patterned and reoriented molecular structure reformation (Figure 10.14(b)) (Kawatsuki et al., 2017).
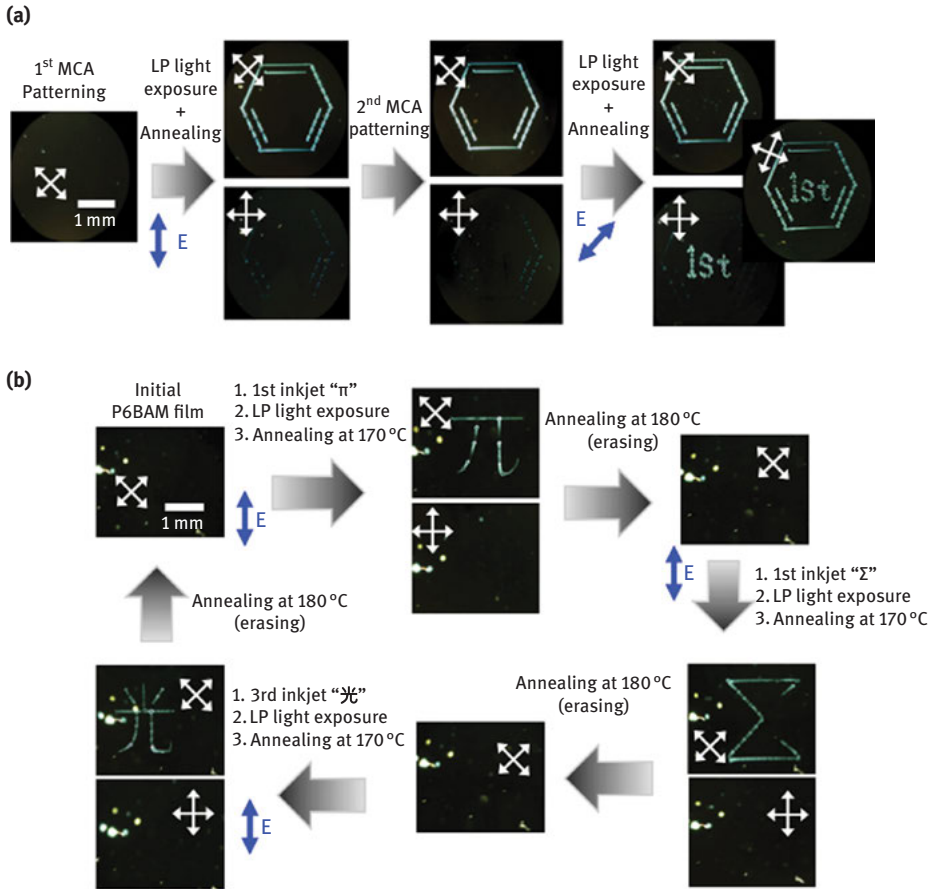
Figure 10.14: The patterned and oriented P6BAM film photographs between crossed polarizers of POM (white arrows indicate the polarizer and analyzer directions, while the blue arrows indicate polarization (**E**) of LP 313 nm light). The birefringent pattern was formed by LP 313 nm light exposure for 0.5 J/cm^2 followed by annealing at 170 °C with simultaneous sublimation of MCA. (a) 1st inkjet coating of MCA (aromatic ring shape), after irradiation with LP 313 nm light for 0.5 J/cm^2 and subsequent annealing at 170 °C for 10 min; 2nd inkjet coating of MCA ("1st" shape) and after irradiation with LP 313 nm light for 0.5 J/cm^2 with a changed polarization angle of 45° followed by subsequent annealing at 170 °C for 10 min. (b) Initial P6BAM film, first pattern (π) formation, pattern erasure by annealing at 180 °C, second pattern (Σ) formation, second erasure by annealing at 180 °C, and third pattern (光) formation. Adapted from Kawatsuki et al. (2017), Copyright 2017, *American Chemical Society*.

10.7 Orientation direction control by adjusting the free-surface condition

The in-plane and out-of-plane orientations in LCP films are facilely controlled by adjusting the free-surface condition. Several types LCP films exhibit thermally generated in-plane or out-of-plane motion of the mesogenic side groups (Tanaka et al., 2016). The top coating with aromatic molecules onto LC polymethacrylate films with NBA or 4-methoxybiphenyl (MB) side groups (PNBAM or PMBM) and subsequent annealing generate a random planar orientation with simultaneous removal of the coated aromatic molecules. In contrasts, annealing non-coated films induces a homeotropic orientation of the mesogenic side groups (Miyake et al., 2016).

Figures 10.15(a) and 15(b) demonstrate the birefringent pattern formation of a PNBAM film with top-coating of AN at the free surface, where the AN molecules are coated on the PNBAM film by calligraphy from a methanol solution and inkjet printing from an ethylene glycol solution, respectively. After removal of AN molecules from the AN-coated films by annealing, the AN-coated area shows slightly bright

(a)

(b)

(c)
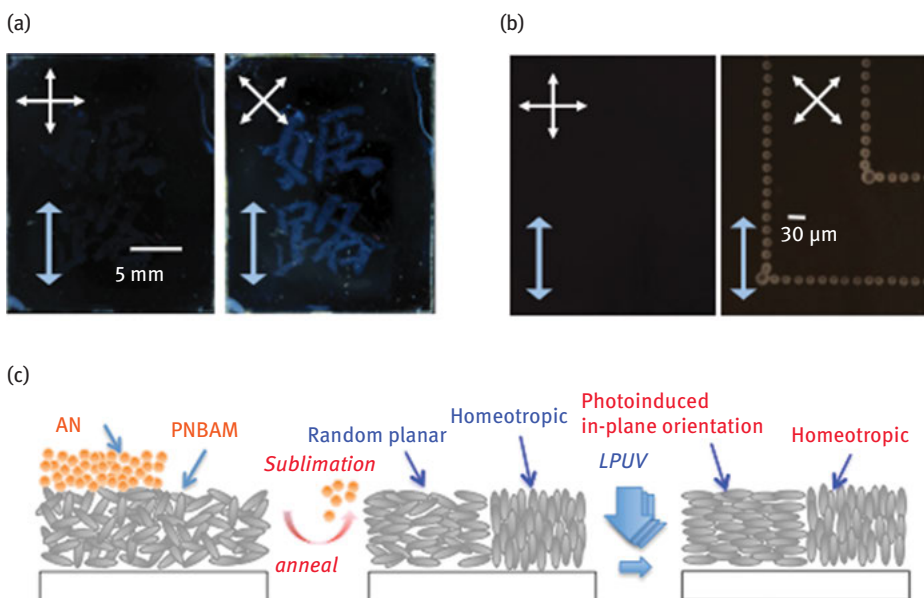
Figure 10.15: (a and b) Photographs of patterned PNBAM films under POM (white arrows indicate the polarizer and analyzer directions, and blue arrows are the in-plane orientation direction). (a) Calligraphy coating of AN from a methanol solution and (b) inkjet printing from an ethylene glycol solution, and the films are subsequently annealed at 100 °C followed by irradiating with LP 365-nm light for 10 J/cm^2. (c) Schematic of the orientation-pattern formation of the PNBAM film. Adapted from Miyake et al. (2016). Copyright 2016, *American Chemical Society*.

regardless of the polarizer's direction, suggesting the random-planar oriented structure of the NBA side groups. In contrast, the non-coated area is dark due to the thermally stimulated homeotropic orientation. These results indicate that the top coating restricts the out-of-plane motion of the mesogenic NBA side groups upon annealing. The subsequent exposure to LP 365 nm light generates the axis-selective photoisomerization of NBA side groups at the in-plane region and the thermal stimulation of the in-plane molecular reorientation at the AN-coated region was occurred after the annealing procedure. However, the non-coated region exhibited no-photoreaction due to the out-of-plane structure of the NBA moieties as schematically illustrated in Figure 10.15(c). Similarly, the patterned random-in-plane and out-of-plane orientation structure of the PMBM film is available although that the photoinduced in-plane orientation due to no-photoreactivity (Miyake et al., 2016). Thus precise out-of-plane and in-plane orientation control can be achieved based on the top coating of the aromatic molecules which can be sublimely removed in the LC temperature range of the LCPs, using inkjet technology combined with LP light exposure.

10.8 Conclusion

This chapter briefly summarized the current efforts and advances on the photoalignment process for SCLCP films achieved from the free surface. Low molecular mass LCs with a high fluidity need to be sealed between solid substrates, and therefore, the orientation regulation can be performed only from the solid substrate. However, LC polymer films, in many cases, one side or both sides, are exposed to the air having free surfaces(s). As indicated in these studies, the orientation regulation from the free surface for SCLCP cases is found to be highly efficient. One characteristic advantage to use the free surface is that the various types of substrates can be used including both inorganic and organic substrates. Polymer sheets are fascinating as the substrate, which provide flexible LC devices. It is expected that the new approaches from the free surface will provide new opportunities for the fabrication of LC devices and contribute a great deal to the LC imaging technologies.

References

Ando, H., Tanino, T., Nakano, H., Shirota, Y. (2009). Photoinduced surface relief grating formation using new polymers containing the same azobenzene chromophore as a photochoromic amorphous molecular material. Materials Chemistry and Phyics, 113(1), 376–381.

Arriaga, L.R., Monroy, F., Langevin, D. (2011). Influence of backbone rigidity on the surface rheology of acrylic Langmuir polymer films. Soft Matter, 7(17), 7754–7760.

Boeffel, C., Spiess, H.W., Hisgen, B., Ringsdorf, H., Ohm, H., Kirste, R.G. (1986). Molecular order of spacer and main chain in polymeric side-group liquid crystals. Die Makromolekulare Chemie, Rapid Communications, 7(12), 777–783.

Canabarro, A.A., de Oliveira, I.N., Lyra, M.L. (2008). Homeotropic surface anchoring and the layer-thinning transition in free-standing films. Physical Review E, 77(1), 011704.

Chen, S.-M., Hsieh, T.-C., Pan, R.-P. (1991). Magnetic-field-induced Fréedericksz transition and the dynamic response of nematic liquid-crystal films with a free surface. Physical Review A, 43(6), 2848–2857.

Fukuhara, K., Fujii, Y., Nagashima, Y., Hara, M., Nagano, S., Seki, T. (2013). Liquid-crystalline polymer and block copolymer domain alignment controlled by free-surface segregation. Angewandte Chemie International Edition, 52(23), 5988–5991.

Fukuhara, K., Nagano, S., Hara, M., Seki, T. (2014). Free-surface molecular command systems for photoalignment of liquid crystalline materials. Nature Communications, 5(1–8), 3320.

Ichimura, K. (2000). Photoalignment of liquid-crystal systems. Chemical Reviews, 100(5), 1847–1873.

Ichimura, K., Suzuki, Y., Seki, T., Hosoki, A., Aoki, K. (1988). Reversible change in alignment mode of nematic liquid crystals regulated photochemically by command surfaces modified with an azobenzene monolayer. Langmuir, 4(5), 1214–1216.

Kato, T., Fréchet, J.M. (1989). A new approach to mesophase stabilization through hydrogen bonding molecular interactions in binary mixtures. Journal of the American Chemical Society, 111, 8533–8534.

Kato, T., Mizoshita, N., Kishimoto, K. (2006). Functional liquid-crystalline assemblies: self-organized soft materials. Angewandte Chemie International Edition, 45, 38–68.

Kawatsuki, N., Fujii, R., Fujioka, Y., Minami, S., Kondo, M. (2017). Birefringent pattern formation in photo-inactive liquid crystalline polymer films based on a photoalignment technique with top-coating of cinnamic acid derivatives via H-bonds. Langmuir, 33, 2427–2432.

Kawatsuki, N., Inada, S., Fujii, R., Kondo, M. (2018). Photoinduced birefringent pattern and photoinactivation of liquid crystalline copolymer films with benzoic acid and phenylaldehyde side groups. Langmuir, 34, 2089–2094.

Kawatsuki, N., Matsushita, H., Kondo, M., Sasaki, T., Ono, H. (2013). Photoinduced reorientation and polarization holography in a new photopolymer with 4-Methoxy-N-benzylideneaniline side groups. APL Materials, 1, 022103.

Kawatsuki, N., Matsushita, H., Washio, T., Kozuki, J., Kondo, M., Sasaki, T., Ono, H. (2014). Photoinduced orientation of photoresponsive polymers with N-benzylideneaniline derivative side groups. Macromolecules, 47, 324–332.

Kawatsuki, N., Miyake, K., Kondo, M. (2015a). Thermal amplification of photoinduced cooperative reorientation of liquid crystalline copolymer films comprised of N-benzylideneaniline and benzoic acid side groups. Molecular Crystals and Liquid Crystals, 617, 14–20.

Kawatsuki, N., Miyake, K., Kondo, M. (2015b). Facile fabrication, photoinduced orientation, and birefringent pattern control of photoalignable films comprised of N-benzylideneaniline side groups. ACS Macro Letters, 4, 764–768.

Kimura, H., Nakano, H. (1985). Statistical theory of surface tension and molecular orientations at the free surface in nematic liquid crystals. Journal of the Physical Society of Japan, 54(5), 1730–1736.

Komura, M., Yoshitake, A., Komiyama, H., Iyoda, T. (2015). Control of air-interface-induced perpendicular nanocylinder orientation in liquid crystal block copolymer films by a surface-covering method. Macromolecules, 48(3), 672–628.

Kosaka, Y., Kato, T., Uryu, T. (1994). Synthesis and the smectic mesophase of copolymers containing a mesogenic (carbazolylmethylene)aniline group as the electron donor and a (4′-Nitrobenzylidene)aniline group as the electron acceptor. Macromolecules, 27, 2658–2663.

Kunimatsu, N., Sonoda, H., Hyodo, Y., Tomioka, Y. (2014). Photoalignment technology for high performance IPS-LCDs: IPS-NEO technology. SID Symposium Digest of Technical Papers, 45(1), 1406–1409.

Minami, S., Kondo, M., Kawatsuki, N. (2016). Fabrication of UV-inactive photoaligned films by photoinduced orientation of H-bonded composites of non-photoreactive polymer and cinnamate derivative. Polymer Journal, 48, 267–271.

Miyachi, K., Kobayashi, K., Yamada, Y., Mizushima, S. (2010). The world's first photo alignment LCD technology applied to generation ten factory. SID Symposium Digest of Technical Papers, 41(1), 579–582.

Miyake, K., Ikoma, H., Okada, M., Matsui, S., Kondo, M., Kawatsuki, N. (2016). Orientation direction control in liquid crystalline photoalignable polymeric films by adjusting the free-surface condition. ACS Macro Letters, 5, 761–765.

Nagano, S. (2016). Inducing planar orientation in side-chain liquid-crystalline polymer systems via interfacial control. The Chemical Record, 16(1), 378–392.

Nagano, S., Koizuka, Y., Murase, T., Sano, M., Shinohara, Y., Amemiya, Y., Seki, T. (2012). Synergy effect on morphology switching: real-time observation of photo-orientation of microphase separation in a block copolymer. Angewandte Chemie International Edition, 51(24), 5884–5888.

Nakai, T., Tanaka, D., Hara, M., Nagano, S., Seki, T. (2016). Free surface command layer for photoswitchable out-of-plane alignment control in liquid crystalline polymer films. Langmuir, 32(3), 909–914.

O'Neill, M., Kelly, S.M. (2000). Photoinduced surface alignment for liquid crystal displays. Journal of Physics D: Applied Physics, 33(10), R67–R84.

Ocko, B.M., Braslau, A., Pershan, P.S., Als-Nielsen, J., Deutsch, M. (1986). Quantized layer growth at liquid-crystal surfaces. Physical Review Letters, 57(1), 94–97.

Percec, V., Tomazos, D. (1990). Can the rigidity of a side-chain liquid-crystalline polymer backbone influence the mechanism of distortion of its random-coil conformation?. Polymer, 31(9), 1658–1662.

Pershan, P.S. (1990). Structure of surfaces and interfaces as studied using synchrotron radiation. Liquid surfaces. Faraday Discussions of the Chemical Society, 89, 231–245.

Priimagi, A., Barrett, C.J., Shishido, A. (2014). Recent twists in photoactuation and photoalignment control. Journal of Materials Chemistry C, 2(35), 7155–7162.

Rogers, S., Mandelkern, L. (1957). Glass transitions of the poly-(n-Alkyl methacrylates). The Journal of Physical Chemistry, 61(7), 985–991.

Sano, M., Hara, M., Nagano, S., Shinohara, Y., Amemiya, Y., Seki, T. (2015a). New aspects for the hierarchical cooperative motions in photoalignment process of liquid crystalline block copolymer films. Macromolecules, 48(7), 2217–2223.

Sano, M., Nakamura, S., Hara, M., Nagano, S., Shinohara, Y., Amemiya, Y., Seki, T. (2014). Pathways toward photoinduced alignment switching in liquid crystalline block copolymer films. Macromolecules, 47(20), 7178–7186.

Sano, M., Shan, F., Hara, M., Nagano, S., Shinohara, Y., Amemiya, Y., Seki, T. (2015b). Dynamic photoinduced realignment processes in photoresponsive block copolymer films: effects of the chain length and block copolymer architecture. Soft Matter, 11(29), 5918–5925.

Scaramuzza, N., Berlic, C., Barna, E.S., Strangi, G., Barna, V., Ionescu, A.T. (2004). Molecular simulation of the free surface order in NLC samples. The Journal of Physical Chemistry B, 108(10), 3207–3210.

Seki, T. (2014a). New strategies and implications for the photoalignment of liquid crystalline polymers. Polymer Journal, 46(11), 751–768.

Seki, T. (2014b). Meso- and microscopic motions in photoresponsive liquid crystalline polymer films. Macromolecular Rapid Communications, 35(3), 271–290.

Seki, T. (2016). Light-directed alignment, surface morphing and related processes: recent trends. Journal of Materials Chemistry C, 4(34), 7895–7910.

Seki, T., Nagano, S., Hara, M. (2013). Versatility of photoalignment techniques: from nematics to a wide range of functional materials. Polymer, 54(22), 6053–6072.

Seki, T., Sakuragi, M., Kawanishi, Y., Suzuki, Y., Tamaki, T., Fukuda, R., Seki, T. (1993). "Command surfaces" of Langmuir-Blodgett films. Photoregulations of liquid crystal alignment by molecularly tailored surface azobenzene layers. Langmuir, 9(1), 211–218.

Tanaka, D., Mizuno, T., Hara, M., Nagano, S., Saito, I., Yamamoto, K., Seki, T. (2016). Evaluations of mesogen orientation in thin films of polyacrylate with cyanobiphenyl side chain. Langmuir, 32(15), 3737–3745.

Tanaka, D., Nagashima, Y., Hara, M., Nagano, S., Seki, T. (2015). Alternation of side-chain mesogen orientation caused by the backbone structure in liquid-crystalline polymer thin films. Langmuir, 31(42), 11379–11383.

Wiley, R.H., Brauer, G.M. (1948). Refractometric determination of second-order transition temperatures in polymers. III. Acrylates and methacrylates. Journal of Polymer Science, 3(5), 647–651.

Yaroshchuk, O., Reznikov, Y. (2012). Photoalignment of liquid crystals: basics and current trends. Journal of Materials Chemistry, 22(2), 286–300.

Zentel, R., Benalia, M. (1987). Stress-induced orientation in lightly crosslinked liquid-crystalline side-group polymers. Die Makromolekulare Chemie, 188(3), 665–674.

Shuai Huang, Haifeng Yu

11 Photoresponsive liquid-crystalline block copolymers with hierarchical structures

Abstract: Block copolymers (BCs) usually self-assemble into nanoscale multistructures upon microphase separation (MPS) in bulk films. However, it is difficult for these nanostructures to be regulated into macroscopic ordering. The introduction of mesogenic ordering combines the responsive feature of liquid crystals under an external stimulus with the MPS characteristics of BCs, providing an elegant method to fabricate highly ordered nanostructures upon hierarchical self-assembly. Because of the excellent capabilities of being adjusted in a noncontact way, photoresponsive liquid-crystalline block copolymers (PLCBCs) especially containing azobenzene chromophores have attracted lots of research interests. The photoresponsive mesogens of azobenzene moieties can help manipulate the ordered MPS nanostructures. Here, we overview the fabrication and photomanipulation of a series of PLCBCs with hierarchical structures. Both polarized and unpolarized light can be utilized to adjust the MPS process. In addition, PLCBCs exhibit various responsiveness under irradiation with a certain wavelength, including photoinduced phase transition, photo-controlled supramolecular cooperative motion, and photo-triggered mass transfer. Based on these light-responsive properties, PLCBCs have been applied in many fields involving photonic materials, information storage, holographic grating, nanotemplates for nanofabrication, and so on.

11.1 Introduction

11.1.1 Hierarchical structures in liquid-crystalline block copolymers

Block copolymers (BCs) are usually made up of two or more polymer modules named "blocks" linked by chemical bonding (Fasolka and Mayes, 2001). Driven by the competition between the incompatible but strongly bonded blocks, microphase separation (MPS) often occurs in nanoscale. Thus, various nanostructures such as spheres, cylinders, gyroids, and lamella ranging from 10 to 100 nm usually appear in BC films, as shown in Figure 11.1 (Bates and Fredrickson, 1999). Generally, the thermodynamic equilibrium effect determines the MPS structures in self-consistent field theory (Fasolka and Mayes, 2001). Besides, the volume content, the film thickness, thermal treatment condition, and other processing ways influence the MPS structures of BCs.
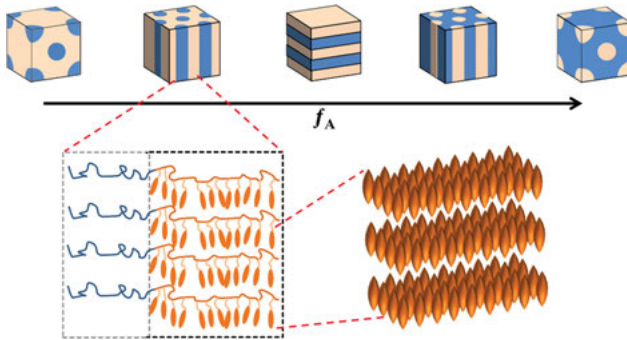
Figure 11.1: MPS structures of LCBCs with different volume content of the mesogenic block.

The introduction of liquid crystal (LC) ordering into BCs may contribute to obtaining liquid-crystalline block copolymers (LCBCs). Therefore, LCBCs can combine the inherent MPS properties of BCs with the self-assembly feature of anisotropic mesogens, which often brings about novel and interesting properties. More importantly, the responsive feature of LCs under an external stimulus enables one to manipulate MPS nanostructures into macroscopic ordering, which should broaden the potential applications of LCBCs. As shown in Figure 11.1, the combination of BCs and LCs in one LCBC system could introduce the following advantages. First, we can acquire different MPS nanostructures by adjusting the volume ratio of either the mesogenic blocks or the nonmesogenic ones. Second, the orientation of mesogens in the continuous phase significantly influences the MPS nanostructures in the separated phase due to the supramolecular cooperative motion (SMCM) effect. Third, the responsive feature of mesogens makes it possible to realize the regulation of the ordered nanostructures by using various methods generally used for LC alignment. Finally, the relatively high value of Flory–Huggins–Staverman parameter (χ) in LCBCs, along with the self-assembly of one-dimensional (1D) or two-dimensional (2D) ordered LCs, helps fabrication of ordered nanostructures in macroscopic scale, which makes sure the reliability of their potential applications.

The interference function between the self-assembly of mesogens and MPS of the immiscible polymer segments results in hierarchically self-assembled nanostructures of LCBCs. On the one hand, the immiscible blocks in the minority phase disperse in the continuous phase of the polymer matrix, forming various MPS nanostructures. On the other hand, both thermal history and mechanical treatment significantly affect the MPS morphology as well, indicating that the MPS structures can be manipulated by controlling the processing technology. More importantly, the multiresponsive property of LCs makes it possible for manipulation of the MPS via all kinds of external stimuli such as electric field, magnetic field, mechanical force, and light, which are generally applied in mesogenic regulation.

11.1.2 Photoresponsive liquid-crystalline block copolymers

LCBCs can acquire light-responsive features by judiciously designing with photoresponsive mesogens, and the obtained photoresponsive liquid-crystalline block copolymers (PLCBCs) often show photocontrollable multiscale structures. Photochemical process often brings about great changes in material properties, including refractive index, density, solubility, modulus of elasticity, and dielectric parameters. These light-triggered performances are of particular importance in fabricating various kinds of intelligent light-driving materials. Photoresponsive groups are usually divided into three classes according to the photoreaction mechanism: photoisomerization, photo-crosslinking, and photodegradation.
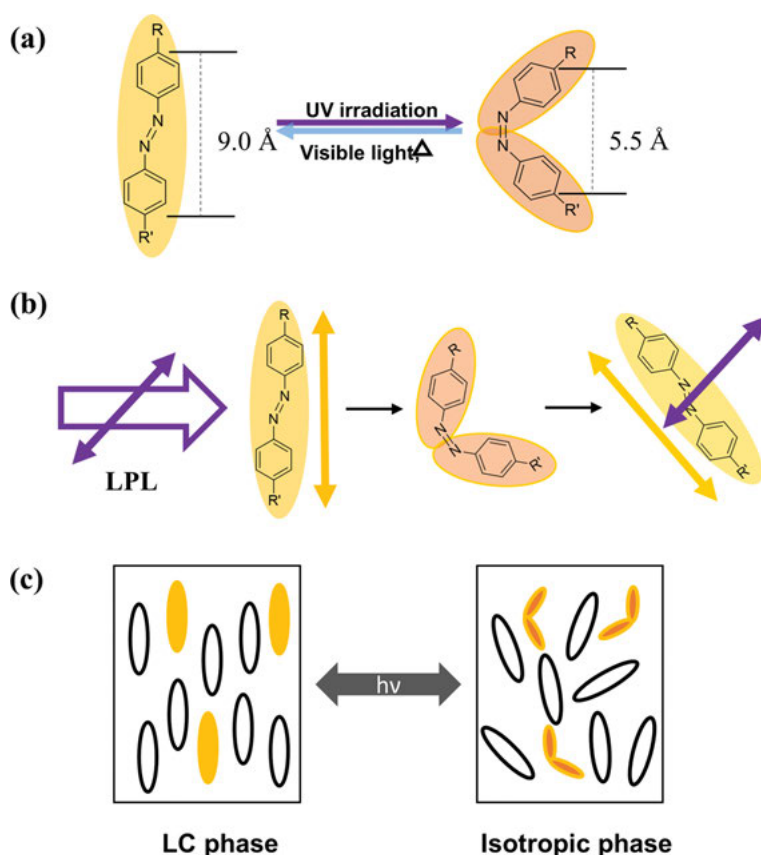
Figure 11.2: Interesting properties of azobenzene-containing materials. (a) Typical photoisomerization; (b) photoalignment under irradiation of linearly polarized light (LPL); and (c) photoinduced phase transition from an LC phase containing azobenzene chromophores to isotropic phase.

An azobenzene moiety is a typical photoactive functional group which can undergo isomerization upon irradiation of actinic light. Its rigid rod-like shape of the thermally stable *trans*-configuration has been widely utilized as photoactive mesogens in synthesizing photoresponsive liquid-crystalline polymers (LCPs). On exposure of light with a certain wavelength, an azobenzene often transforms from its *trans*-configuration to *cis*-isomer, and will thermally return back to the stable *trans*-isomer (Figure 11.2(a)). It is well-known that the substituent groups on the aromatic rings strongly influence the lifetime of the *cis*-isomer. Based on the Weigert effect, the employment of linearly polarized light (LPL) can be an effective method to control the orientation of the azobenzenes or azobenzene-containing mesogens (Figure 11.2(b)). The alignment direction is usually perpendicular to the polarization direction of LPL.

Natansohn and Kumar have summarized the correlation between the photoresponsive properties and the substituent groups on the aromatic rings of azobenzene according to the lifetime of *cis*-isomers (Natansohn and Rochon, 2002; Rau, 2002; Kumar and Neckers, 1989). They classified the types of azobenzenes into three categories as the following: (1) Ordinary azobenzenes that exhibit a relatively lower photoresponsive rate. This kind of azobenzenes does not show any electronic cloud migration. Nearly no overlap of the absorption peaks of their n–π* and π–π* transitions can be observed in their UV–vis absorption spectra. Thus, the lifetime of the *cis*-isomers is relatively long; (2) amino-azobenzenes that exhibit a faster photoresponsive rate possess an electron-donating group at one end of the azobenzene. Significant overlap of their n–π* and π–π* absorption peaks can be observed in the UV–vis absorption spectra. Thus, the lifetime of the *cis*-isomers is shorter than ordinary azobenzenes; (3) pseudo-stilbenes that exhibit a quite rapid photoresponsive rate have an electron-donating group at one end and an electron-withdrawing group at the other end. Hence, very high-degree overlap of their n–π* and π–π* absorption can be observed in the UV–vis absorption spectra, and the lifetime of the *cis*-isomers is very short (Natansohn and Rochon, 2002).

Some rod-like *trans*-azobenzene molecules with substituents of soft spacers (like a long alkyl chain) often exhibit LC phases in a certain temperature range. However, their *cis*-isomers seldom show LC properties because of the bent shape, which destabilizes the LC ordering. Therefore, photoinduced order–disorder transition (ODT) (from LC phase to isotropic phase) often takes place as the *trans*-isomers transform into their *cis*-isomers. Such a photoinduced phase transition often induces significant changes in physical and chemical properties of materials containing azobenzene mesogens. In addition, introduction of a small amount of azobenzenes as the dopants can cause the light-triggered phase transition and the photoalignment of light-inert LCs via the effect of molecular cooperative motion (MCM) as shown in Figure 11.2(c). This has been applied to modulate the ordering and the alignment of various kinds of LCs.

Since azobenzene moieties can act as both a photoresponsive group and a mesogenic unit, LCP that contains azobenzene chromophores has been considered as a promising functional material for various advanced applications. In such polymer

materials, the mechanical, optical, and thermodynamic properties can be modulated based on their photocontrollable features through various efficient strategies such as photochemical phase transition, photoinduced molecular alignment and photo-triggered MCM. Therefore, PLCBCs containing azobenzenes have received much attention in recent years. The hierarchical nanostructures in PLCBCs exhibit robust responsiveness upon photoirradiation, including photoinduced phase transition, photo-controlled SMCM, and photo-triggered mass transfer, which inherit photoresponsive LCPs (Natansohn and Rochon, 2002). These enable PLCBCs to find applications in photonic materials (Yu 2014a), information storage (Hirai et al., 2000; Ikeda and Tsutsumi, 1995), holographic grating (Hasegawa et al., 1999a, b and c; Yamamoto et al., 2000; Yamamoto et al., 2001), drug delivery materials (Addison et al., 2010; Chang and Dong, 2013), and so on.

11.2 Synthesis of well-defined PLCBCs

Benefiting from recent progresses in polymer and materials chemistry, a lot of PLCBCs have been successfully designed and synthesized. To fabricate ordered MPS nanostructures in a PLCBC film, well-defined molecular structures, which means a sufficiently high molecular weight and a narrow polydispersity, are usually required. As far as we can see, there are several polymerization methods such as anionic, cationic, coordination, ring-opening, and controllable free radical polymerization that meet these requirements. However, the existence of a long conjugation of common π-electrons in mesogenic monomers restricts the utilization of living polymerization techniques in synthesizing well-defined PLCBCs. Therefore, controllable living radical polymerization, including atom transfer radical polymerization (ATRP), reversible addition-fragmentation chain transfer polymerization (RAFT), and nitroxide-mediated polymerization (NMP), is considered as the popular universal method to synthesize PLCBCs with a suitable molecular weight and a narrow polydispersity.

11.2.1 Direct polymerization

For living radical polymerization, the polymerization is often initiated from a living active point (small molecule or macroinitiator), and the azobenzene mesogenic monomers and other monomers participate in the reaction in sequence as shown in Figure 11.3. The polymer product also keeps the reactivity and can be further used as one macroinitiator for the following polymerization. Accordingly, copolymers with more constitute blocks such as AB-type, ABC-type triblock copolymers and even multiblock copolymers can be synthesized by this way. The first azobenzene-containing AB-type PLCBC was synthesized by anionic polymerization (Bohnert and Finkelmann, 1994). Based on this

method, a series of well-defined polystyrene (PS) and poly(methacrylate) (PMMA)-based PLCBCs were synthesized (Lehmann et al., 2000). However, there are still some disadvantages: (1) The purity of monomers and reagents is rigorous, (2) harsh dying condition is necessary, (3) difficult purification and treatment process for the reagents, and (4) sometimes an extreme condition is required, for example, a very low temperature. Generally, living radical processes, including ATRP, RAFT, and NMP, have been the most adopted approach in synthesis of PLCBCs containing an azobenzene moiety in a side chain as the photoresponsive mesogens (Yoshida et al., 2005; Yu, et al. 2006a; Zhang et al., 2007).
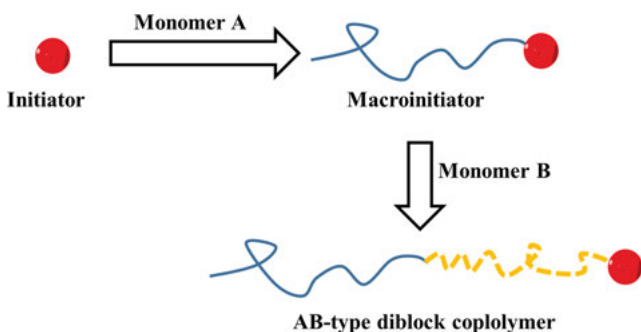
Figure 11.3: Preparation of well-defined PLCBCs by direct polymerization of photoresponsive monomers.

11.2.2 Postfunctionalization

In addition, postfunctionalization has been also applied in synthesizing PLCBC containing azobenzenes. Such method usually starts from a well-defined BC with a high content of pendent functional groups. Generally, it is difficult to directly polymerize the monomers containing amino-azobenzene or their push–pull derivatives to synthesize PLCBCs by a living radical process due to their inhibition effect toward free radicals. As a result, postfunctionalization reactions such as esterification (Frenz et al., 2004; Hayakawa et al., 2002; Mao et al., 1997), azo-coupling reaction (Wang et al., 2007; Wang et al., 2009), Sonogashira cross-coupling reaction (Yu et al., 2009), and other coupling reactions have been introduced as the convenient way (Figure 11.4).

11.2.3 Supramolecular self-assembly

BCs containing pendent functional groups can be modified by supramolecular interactions such as hydrogen bonds, ionic bonds, halogen bonds, and coordination bonds, as shown in Figure 11.4. BCs containing a poly(4-vinylpyridine) (P4VP) block (Ikkala and Brinke 2002; Zhao et al., 2009) or a poly(acrylic acid) block (Chao et al., 2004) are
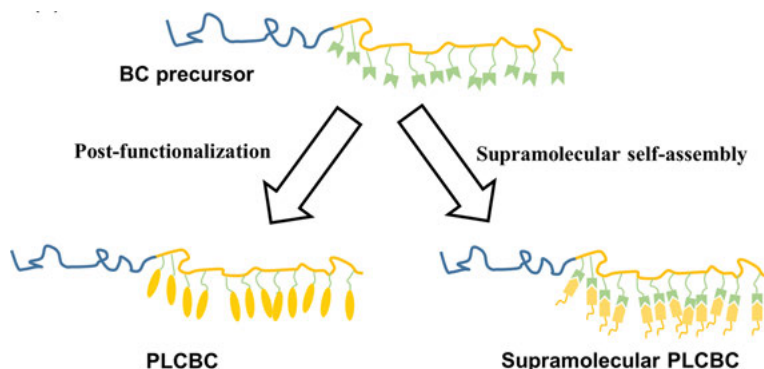
Figure 11.4: Preparation of well-defined PLCBCs by postfunctionalization and supramolecular functionalization.

the most common macromolecules modified with low-molecular-weight molecules to form supramolecular complexes. In addition, LC properties have also been introduced via supramolecular interactions, which makes an important effect on the MPS structures. Several advantages of this method have been summarized as followings: (1) The directionality of selective hydrogen bonding between one of the blocks and the additive, (2) obvious nanoscale MPS rather than macroscopic phase separation in bulk films, (3) the additive can be easily removed by selective solvents, and (4) formation of hierarchical nanostructures (Yu, 2014b).

11.2.4 Other methods

Other unique processes have also been applied in synthesizing PLCBCs. For instance, two polymer chains can be connected via chemically coupling reaction when the active points at the end of the chains crash together; thus, one new chain forms by this way. Such method helps broaden the variety of synthesized PLCBCs. However, only diblock copolymers are prepared up until now because of the dynamic hindrance of the macromolecular chains and the low content of active points in the long polymer main chains.

11.3 Manipulation of hierarchical structures in PLCBCs

11.3.1 Phase diagram of MPS

If the chemical structure of one BC is well defined, then the immiscibility of different blocks will give rise to MPS behaviors. Figure 11.5 shows the universal phase diagram of symmetric AB-type diblock copolymers proposed by theoretical calculation
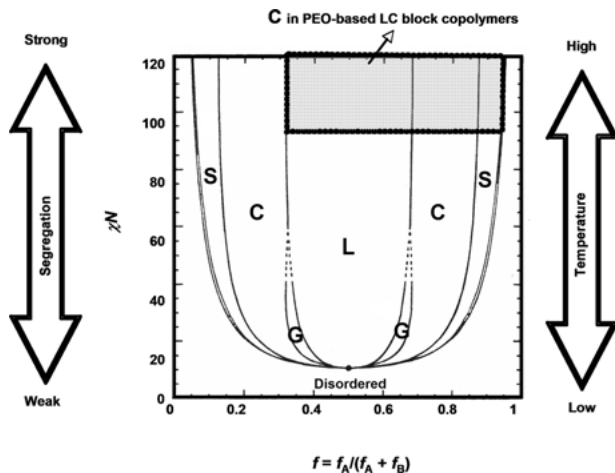
Figure 11.5: Phase diagram of AB-type diblock copolymers calculated using self-consistent mean-field theory. One PEO-based LCBCs showed nanocylinder phase in the gray area. G, gyroid; S, sphere; C, cylinder; L, lamellar. (Adapted from Matsen and Bates, 1996. Copyright 1996 American Chemical Society.)
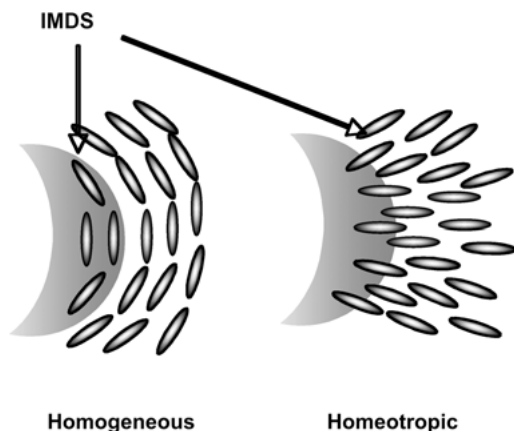
Figure 11.6: Illustration of the possible LC anchoring on IMDS in LCBCs. LC molecules are in homogeneous or homeotropic alignment at the interface.

according to self-consistent mean-field theory (Matsen and Bates, 1996). Here, χ is the Flory–Huggins–Staverman interaction parameter, N is the degree of polymerization, and f represents the volume fraction of each block. The additional LC properties could bring in several factors including conformational asymmetry and structural asymmetry, which greatly influence the MPS behaviors. As a result, the phase diagram of LCBCs is a little different from Figure 11.5. Another factor that affect the

phase-segregated behaviors is the anchoring of the LC ordering to the intermaterial dividing surface (IMDS) (Figure 11.6; Osuji et al., 1999). Therefore, to obtain well-ordered MPS structures in LCBCs, the driving force must be carefully considered, which should include the following points:

(1) The interfacial energy should be minimized.
(2) The conformational entropy of polymers should be optimized.
(3) The additional elastic deformation of the LC phases should be minimized.
(4) The competition between the self-organization of LC and MPS should be optimized.

As reported by Anthamatten et al. (1999) the preferential orientation of mesogens strongly depends on the IMDS because of surface stabilization effects. As shown in Figure 11.6, the LC molecules are likely to align perpendicular or parallel to the interface, thus showing two possible mesogenic orientations at an interface which are usually termed as homeotropic or homogeneous, respectively. Osuji et al. have described the phenomena from the geometric point of view. If the pendant mesogens are decoupled from the polymer backbone by relatively short spacers, homogenous anchoring is preferred, while homeotropic anchoring is often accepted if the mesogens are hanged with a long spacer in LCBCs (Osuji et al., 1999, 2000). According to the volume extent of the block segregation in BCs, three regimes of MPS are defined; they are: weak (the segregation strength $\chi N \approx 10$), intermediate ($\chi N \approx 10-100$), and strong segregation ($\chi N \geq 100$) regimes. It can be expected that the Flory–Huggins parameter χ in LCBCs is much greater than that in conventional amorphous BCs because of the formation of mesophase. As a result, the ODT temperature becomes higher due to such a large χ. The high ODT temperature is sometimes difficult to be measured, because the LCBCs might get decomposed thermally before reaching their ODT. However, one of the most important advantages of the large χ and high ODT is that the MPS structures of LCBCs can be preserved even in their isotropic phase. These factors result in the special phase diagram of LCBCs, which is a little different from that of amorphous BCs with a lower upper critical eutectic temperature.

In addition, the structural asymmetricity of LCBCs also results in an asymmetric phase diagram. For instance, a poly(ethylene oxide) (PEO)-based diblock copolymer composed of a hydrophilic PEO block and a hydrophobic polymethacrylate containing a pendant azobenzene moiety exhibits a large range of nanocylinder phase region when PEO serves as the dispersed phase in LC matrix. Its nanocylinder phase range is given in the gray area of Figure 11.5 (Yoon et al., 2008). However, the complexity of LCBCs increases the difficulty of theoretical calculation so that it is still difficult to draw a universal phase diagram like the amorphous AB-like diblock copolymer. If the mesogenic block serves as the major phase, it would play the major role in the self-assembly. However, the condition is totally different as the mesogenic block serves as the minor phase, where the low content of mesogens restricts their impact on the physical and chemical properties of the LCBCs. For

example, a PEO-based LCBC exhibits good hydrophilicity, ionic conductivity, and crystallinity (Yu and Ikeda, 2011). One PS-based LCBC improves the glass transition temperature (T_g) and restricts the realignment of azobenzene mesogens (Morikawa et al., 2007).
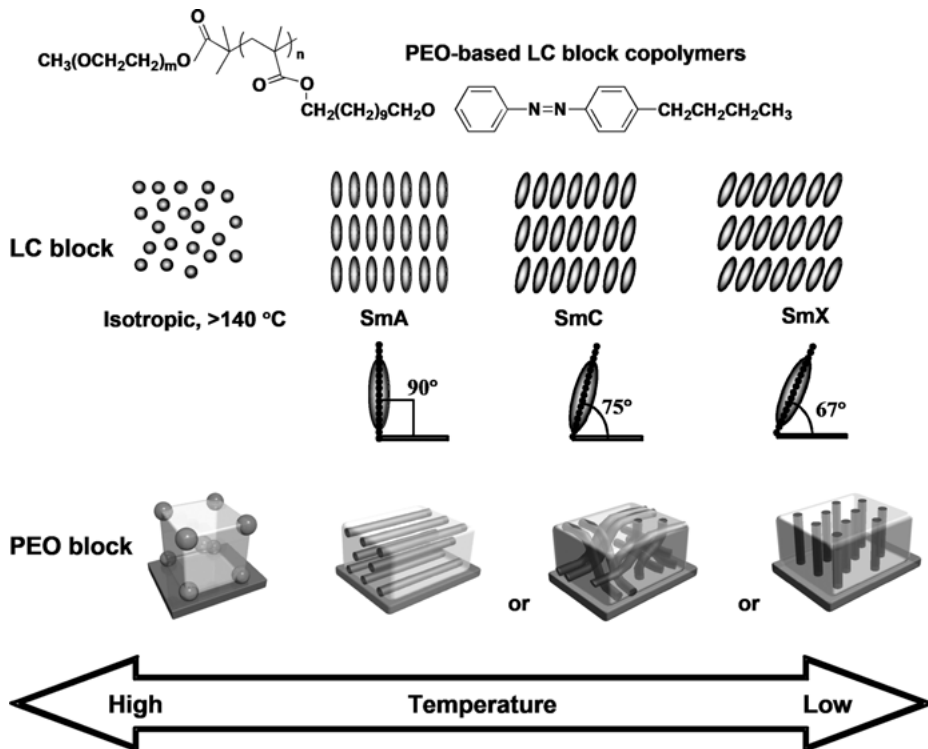
Figure 11.7: MPS of PEO-based PLCBCs. (Adapted from Yu et al., 2011. Copyright 2011, John Wiley & Sons.)

The MPS nanostructures of LCBCs often changed when passing over the ODT point of the mesogenic block. For instance, the PS-based smectic LCBCs (with 50–58% volume fraction of LC samples) changed from cylindrical or mixed-layered morphology to a lamellar morphology when heated from the LC temperature to the isotropic phase, as reported by Hammond et al. (1999). Another example is one PEO-based PLCBC (Figure 11.7) which shows nanosphere phase of the PEO block dispersed in the isotropic phase (>140 °C) of the azobenzene mesogenic block. If the PLCBC is cooled below its clearing point, smectic A (SmA), smectic C (SmC), and smectic X (SmX) or semicrystalline phase would form in sequence, accompanied by the transformation from nanospheres to nanocylinders (Tian et al., 2002). The orientation of PEO nanocylinders is random if no special treatment is employed onto the PLCBCs. Because thermal history and mechanical treatment significantly affects the MPS,

thus the MPS structures can be controlled by adjusting the processing technology. Therefore, the introduction of photoresponsive azobenzene mesogens make it possible to manipulate the MPS via all kinds of external stimuli such as electric field, magnetic field, mechanical force, and light. A universal method to prepare well-organized MPS structures is annealing, including thermal annealing and solvent annealing. Thermal annealing accelerates the dynamic process of MPS and promotes the system to reach its thermal equilibrium state rapidly by adjusting the temperature. Solvent annealing provides free mobility for the segments to reorganize by immersing the PLCBCs in proper solvent atmosphere. The self-assembly of mesogens also gets influenced during the thermal or solvent annealing process. If the mesogenic block makes up for the major phase, the organization and alignment of mesogens will markedly impact on the MPS structures.
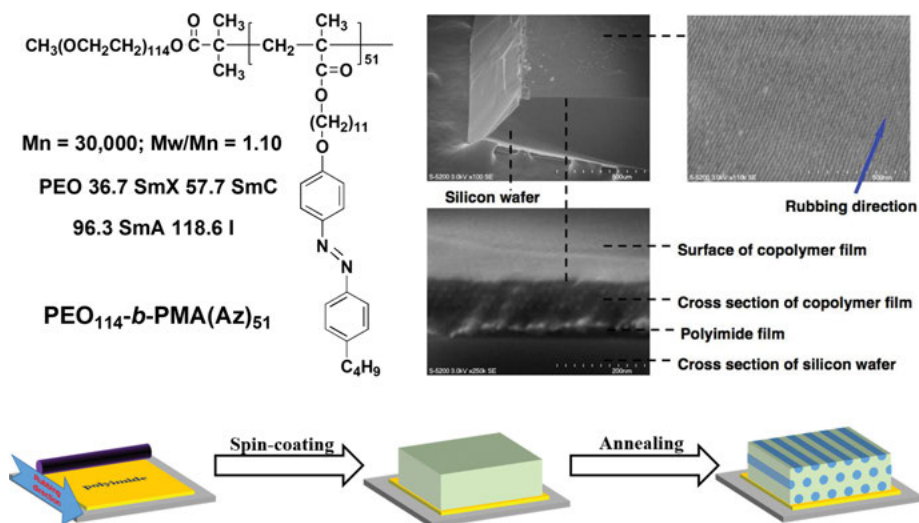
Figure 11.8: Rubbing induces the orientation of MPS nanocylinders in PLCBCs by SMCM. (Adapted from Yu et al., 2006a. Copyright 2006, John Wiley & Sons.)

11.3.2 Rubbing-induced alignment method

As one of the popular methods to orient small-molecule LCs for commercial production of LC displays, the mechanically rubbing-induced alignment method has been introduced in LCBCs containing azobenzene mesogens in 2006. Yu et al. prepared a series of PEO-based PLCBCs, which form PEO nanocylinders in film upon phase segregation. With the assistance of rubbed polyimide (PI) films, the orientation of the nanocylinder structures was elegantly realized in a large area (in a centimeter scale) (Yu et al., 2006a). As shown in Figure 11.8, an alignment layer has been prepared by

coating a polyvinyl alcohol or a PI film on the glass slide or silicon wafer. After being mechanically treated with a rubbing machine, the surface of the alignment layer was coated with the PLCBC film. Well-ordered cylinder nanostructures were successfully acquired after the film underwent a thermal annealing process. The alignment direction is always parallel to the orientation direction of the azobenzene mesogens, along with the rubbing direction. However, the stability of these ordered and oriented nanostructures is usually poor. Far recently, Yu et al. reported a confined self-assembly strategy for stabilizing and patterning nanostructures by a top-coating layer accompanied with the traditional rubbing method. The supramolecular interactions between the top-coating layer and selected block in the LCBC restricted the reorganization of the segments though the alignment of mesogens was still under control of the rubbing direction. Hence, the top coating layer helps stabilization of the MPS structures and their orientation. Thus, patterned structures could be easily obtained by a selected-area confined self-assembly method (Chen et al., 2019).
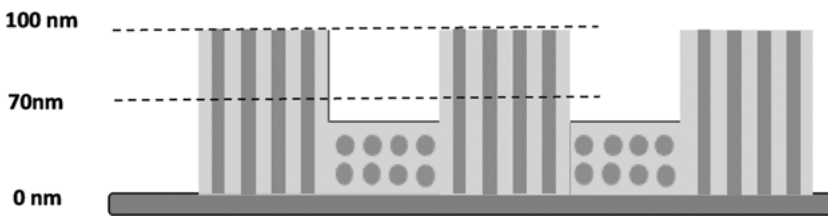
Figure 11.9: Orientation of MPS by periodical film thickness obtained upon holographic recording of PLCBC thin films.

11.3.3 Photoalignment method

Photoalignment of azobenzene mesogens offers a convenient method for control over the LC alignment and the MPS morphologies in noncontact way. The mesogenic orientation can be manipulated by adjusting the polarization direction of LPL, which also has a significant impact on the orientation of MPS structures in PLCBCs via SMCM, where the mesogenic block serves as the continuous major phase. Seki et al. studied the photoalignment of nanocylinders in PLCBC films. They revealed that whether the mesogens along with the nanocylinders orient in-plane or out-of-plane depended on the thickness of LCBC films, as shown in Figure 11.9 (Morikawa et al., 2006). Yu et al. proposed an optical method to control a homogeneous in-plane alignment of PEO nanocylinders in PEO-based amphiphilic PLCBCs (Yu et al., 2006b). First, PEO nanocylinder perpendicular to the substrate was fabricated by thermal annealing; then, this alignment was easily converted into homogeneously

in-plane orientation with the control of LPL polarization direction. This method is clean, simple, and convenient, affording a novel approach toward getting regular surface patterns even on a curved surface, as shown in Figure 11.10.
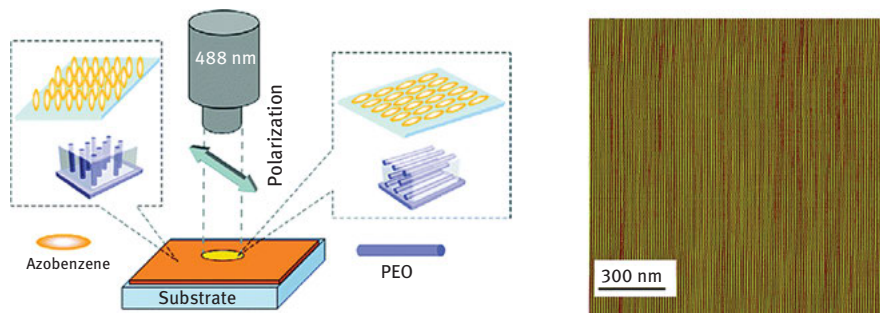
Figure 11.10: Photocontrollable ordered MPS in large scale prepared by a PEO-based photoresponsive LCBC containing a smectic azobenzene mesogen. (Adapted from Yu et al., 2006b. Copyright 2006, American Chemical Society.)

Recently, Nagano and Seki et al. studied in detail the mechanism of the realignment process of MPS nanocylinders in a poly(butyl methacrylate) (PBMA)-based PLCBC, which consists of three stages as shown in Figure 11.11: (1) an induction period where the prealigned smectic layer becomes fluctuated forming subdomains; (2) drastic overall synchronized realignment events involving azobenzene mesogens, smectic layers, and the MPS cylindrical meso-structures with retention of the smectic layer structure; and finally (3) fusion and growth of the nanodomains directing to the realigned direction (Nagano et al., 2012; Sano et al., 2014).
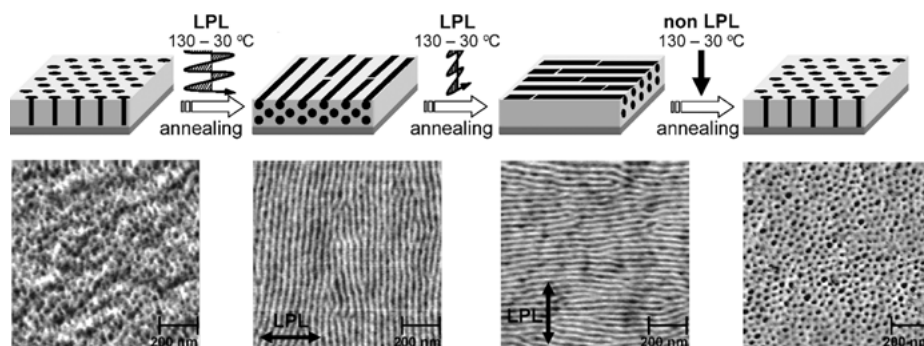
Figure 11.11: Rewritable information storage by photocontrol of the orientation of nanocylinders in a PS-based photoresponsive LCBC. (Adapted from Morikawa et al., 2007. Copyright 2007, American Chemical Society.)

Photoalignment of nanocylinder phase is also significantly affected by the glass transition temperature (T_g) and crystallization temperature (T_c) of the minor phase in PLCBCs. Seki et al. studied the photoresponsive properties of one PS-based PLCBC containing smectic azobenzene mesogens as the major phase (Morikawa et al., 2007). As shown in Figure 11.11, nanocylinders oriented perpendicular to the substrate after directly thermal annealing without any other treatments, which should be induced by the self-organization of the smectic azobenzene block. Employment of LPL irradiation along with the suitable thermal treatment could induce an in-plane orientation of both mesogens and the nanocylinders. Besides, the orientation direction of the nanocylinders would be changed corresponding to the polarization direction of LPL, keeping the direction perpendicular to the polarization direction. Highly ordered MPS nanostructures were also observed in a 1D ordered nematic PEO-based PLCBC, indicating that the thermal properties (mainly T_g and T_c) of the soft blocks which form the minor phase are the critical factors that determine the degree of ordering (Yu et al., 2011). Thus, a series of PBMA-based PLCBCs were synthesized for fabricating ordered light-controllable MPS structures, because PBMA has a softer molecular chain and a much lower T_g than the PEO block. Whereas, PBMA segments aggregated at the air–polymer interface due to the interface effect, inducing a disordered in-plane distribution after the thermal annealing (Nagano et al., 2012). However, as it was much easier for the soft PBMA segments to move and assemble, a nearly real-time photocontrolled reorientation phenomenon was observed with an elegant method, and the ordered alignment state was acquired in several minutes, which was induced by photo-triggered SMCM in PLCBCs.
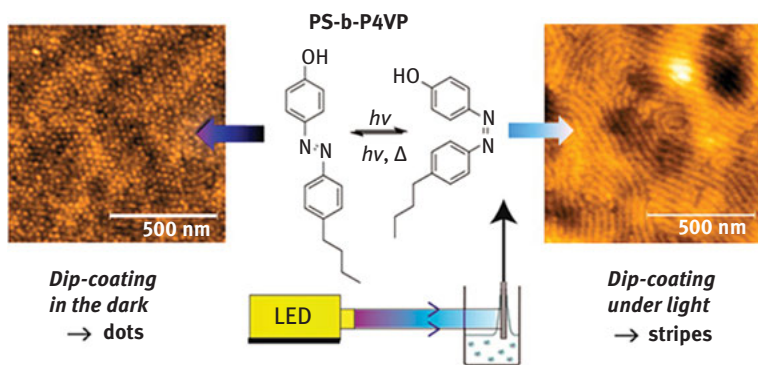
Figure 11.12: In situ photocontrol of a P4VP-*b*-PS/BHAB film by dip-coating under irradiation of unpolarized light. (Adapted from Vapaavuori et al., 2015. Copyright 2015, American Chemical Society.)

More recently, unpolarized light was also applied in manipulating the cylindrical MPS nanostructures. Vapaavuori et al. fabricated a composite film of P4VP-*b*-PS/4-butyl-4′-hydroxyazobenzene (BHAB) by a dip-coating method (Vapaavuori et al., 2015). Here, the spherical morphology in the thin films could be fabricated by dip-coating in a tetrahydrofuran solution at slow withdrawal rates in dark. However, cylindrical morphology would form if the dip-coating process was performed under illumination. This was attributed to volume expansion of the P4VP/BHAB phase due to *trans–cis* photoisomerization combined with a photoinduced increase in BHAB uptake in the supramolecular hydrogen-bonded film (Figure 11.12). Furthermore, planar orientation of the cylindrical structures in PEO-based PLCBCs containing azobenzenes could be rapidly transformed to vertical alignment upon photoirradiation of unpolarized UV light (Wang et al., 2017). It was considered that the *trans–cis* isomerization of azobenzene mesogens changed the steady state of the cylindrical alignment, and in the meanwhile provided sufficient free volume for the PEO segments to reorganize into another ordered orientation state (Figure 11.13). In addition, hierarchical structures in PLCBCs had been considered to be difficult for manipulation if the photoresponsive azobenzene mesogenic block serves as the minor phase, before a series of photoresponsive hybrid oligo(dimethylsiloxane) LCPs that form periodic cylindrical nanostructures with periodicities between 3.8 and 5.1 nm was fabricated by Nickmans et al. (2017). The azobenzene mesogens here can be oriented in-plane by exposure to LPL and out-of-plane by exposure to unpolarized light.

Hierarchical internal phase nanostructures have also been fabricated in LCBCs by introduction of hydrogen bonds without any dopants. As shown in Figure 11.14, both out-of-plane and in-plane orientations of nanocylinders were successfully obtained in the PEO-based PLCBCs (PEO-*b*-PM11UAZ) depending on the film thickness mentioned previously. However, the newly introduced urethane groups in the side chain of the hydrophobic block of PLCBCs also interfered with the ether groups of the hydrophilic PEO block due to the hydrogen bonding formation, which should greatly influence the crystallization process of the PEO blocks. Thus, a sub-10 nm inner-phase nanostructure was successfully induced in the PLCBC film (Huang et al., 2018a).

There have been few reports on photocontrollable lamellar phase in PLCBCs containing azobenzenes up until now, except one work carried out by Seki's group (Beppu et al., 2017). They investigated the MPS nanostructures and photoalignment behavior of a diblock copolymer consisting of two kinds of side-chain LCPs (the mesogens of photoresponsive azobenzene and nonphotoresponsive cyanobiphenyl, respectively). The nearly defect-free morphology of this LC-LC diblock copolymer after the photoalignment treatment was a distinct feature when compared with those of coil (amorphous)-LC diblock copolymer films possessing the same azobenzene side chain, because mesogens exist in both the minor phase and the major phase, and the effect of SMCM should be much stronger here.

Generally, there are five kinds of mesogenic orientation states including nonalignment or random (Figure 11.15(a)), homeotropic (Figure 11.15(b)), homogeneous
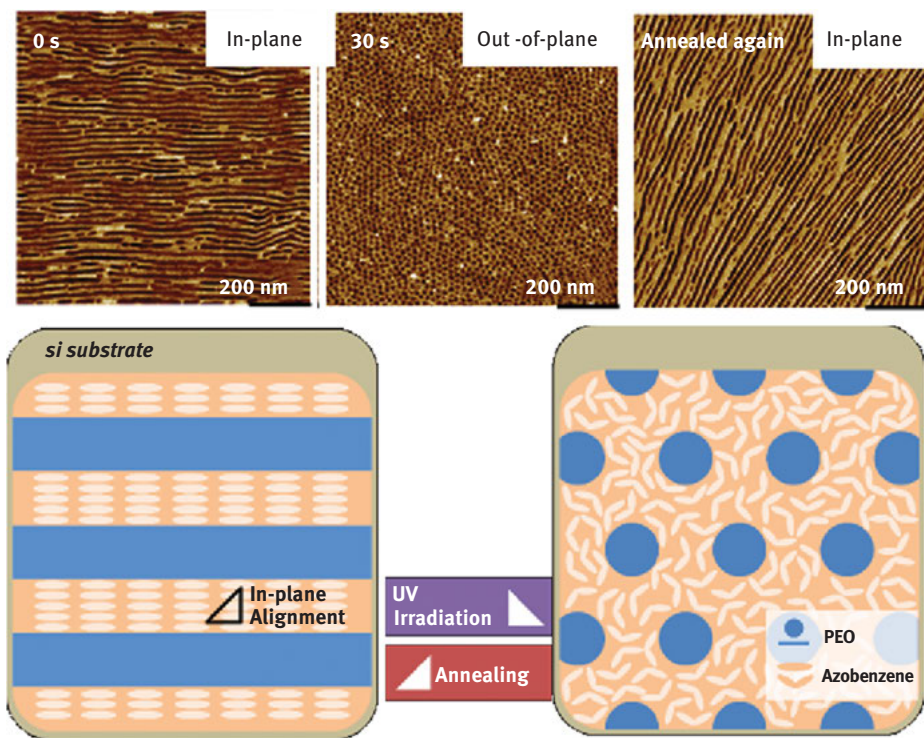
Figure 11.13: Photoinduced orientation transition by unpolarized light and thermal recovery of a PEO-based PLCBC. (Adapted from Wang et al., 2017. Copyright 2017, American Chemical Society.)

(Figure 11.15(c), (d)), isotropic amorphousness (Figure 11.15(e)), and thermally isotopic liquid (Figure 11.15(f)) that can be conveniently achieved by light treatment and thermal treatment (Yu et al., 2011), based on the photoresponsive and manipulatable properties of mesogenic orientation of the LCPs. SMCM effect enables to easily obtain a designed orientation of MPS nanostructures upon supramolecular self-assembly in PLCBCs. As shown in Figure 11.15, both in-plane nanocylinders which were parallel to the substrate and out-of-plane nanocylinders which were perpendicular to the substrate in PEO-based PLCBCs can be accordingly achieved by photomanipulation and thermal treatment; otherwise, when heated above the clearing point, the PLCBC films with nanocylinder structures in the dispersed phase changed into nanospheres after reaching the isotropic phase of the mesogenic block (Figure 11.15(f)). All the above methods make it possible to reversibly modulate the patterning and ordering of the MPS nanostructures by manipulating the phase transition and photoalignment behaviors of mesogens in the LCP blocks. In general, the 1D- or 2D-ordered LC phases are capable of controlling the nanostructures upon MPS of PLCBCs in a 3D fashion (Figure 11.15).
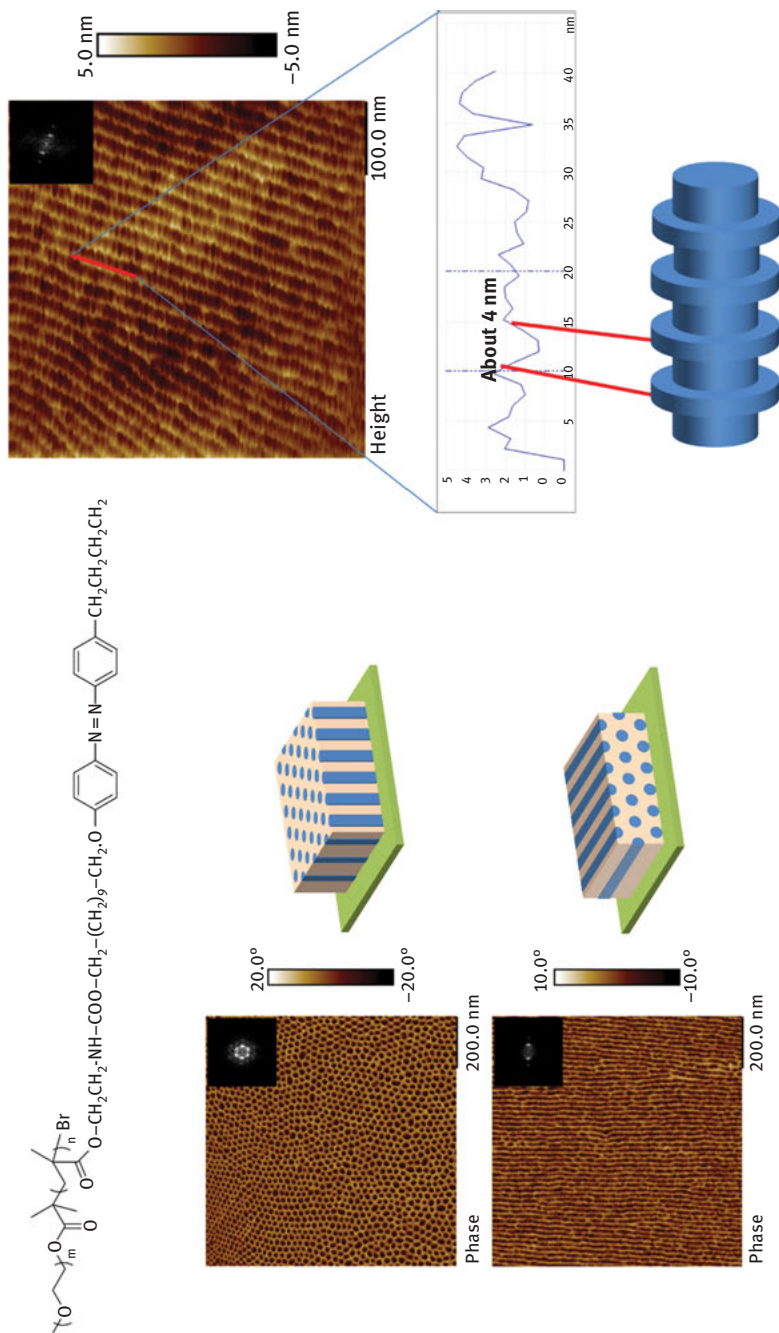
Figure 11.14: Morphologies of the out-of-plane alignment, in-plane alignment and the internal phase structure in the hydrogen-bond-containing LCBC. (Adapted from Huang et al., 2018a. Copyright 2018, John Wiley & Sons.)
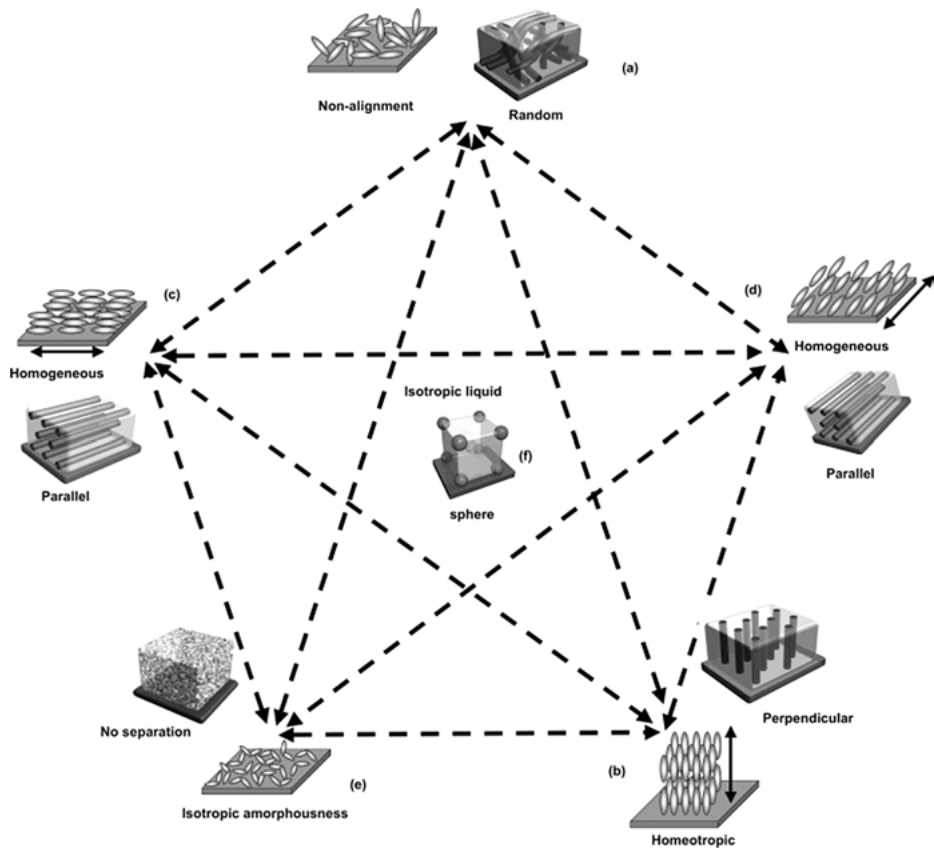
Figure 11.15: The supramolecular cooperative motion in PEO-based PLCBCs, enabling the LC ordering to help supramolecular self-assembly in bulk films. The arrows are directions of LC alignment. (a) Without any treatment, LCs are random and the nanocylinders are in nonalignment states. (b) Upon thermal annealing or function of external fields (electric and magnetic), LCs are in homeotropic alignment and nanocylinders are perpendicular to the substrate. (c) and (d) are homogeneously aligned LCs by rubbing treated substrate or photoalignment, and all the nanocylinders are parallel patterning. (e) Photoinduced LC-to-isotropic phase transition occurs when the azobenzene-containing PLCBCs are irradiated with UV light, which causes disappearance of the nanocylinder phase at room temperature. (f) Heating the PLCBCs above the clearing point, nanocylinders are changed into nanospheres dispersed in isotropic liquid-like PLCBCs. (Adapted from Yu et al., 2011. Copyright 2011, John Wiley & Sons.)

11.4 Applications

The photoresponsive properties and the controllable ordered hierarchical nanostructures promise various applications of PLCBCs in photonics, nanotemplates, and nanolithography. One of the most investigated applications of PLCBCs is holographic

storage. Due to the phase transition or phase changes induced by irradiation with actinic light, the surface and volume of the materials in local area that are irradiated might change accordingly, which helps recording the illumination history. The optical information storage can be realized by this way. PLCBCs are better materials than homopolymers with azobenzene mesogens for recording holographic gratings, owing to the following reasons: (1) introduction of another block improves transmittance of film; (2) MPS in nanoscale prohibits light scattering; and (3) macroscopic mass migration and surface undulation can be greatly restricted. For example, Yu et al. have fabricated holographic gratings with a PMMA-based PLCBC where the azobenzene mesogenic block played as the major phase (Figure 11.16) (Yu et al., 2008). Schmit et al. injected a PS-based PLCBC containing azobenzene mesogens into a mold, and obtained a transparent film with the thickness of 1.1 mm, where the spherical mesogenic phase was dispersed in the PS-based major phase (Hackel et al., 2005). The photoresponsive properties of the PLCBC enable steadily written and read of optical information in the rewritable films.

PLCBCs with hierarchical structures exhibit good potentials to be applied in nanoengineering for various nanofabrication. PLCBC films possessing well-ordered nanostructures can serve as nanotemplates in fabricating metallic and inorganic materials with special nanostructures. For instance, a PEO-based PLCBC film has been used as nanotemplate to fabricate templated patterning of $CaCO_3$ nanoparticles by immersing the PLCBC film in 0.5 mol/L $CaCl_2$ solution, which was then treated with O_2 plasma for 5 min, and placed in the air (Figure 11.17(a)). Because of the selective coordination between PEO and Ca^{2+}, $CaCO_3$ nanoparticles would be formed and manipulated in accordance with the alignment of the PEO nanocylinders. With and without light regulation, different morphologies were observed due to the light-regulated MPS nanostructures, as shown in Figure 11.17(b). Similarly, various metal nanostructures such as Ag and Ag/Co alloy nanoparticles have been fabricated by using the photocontrollable hierarchical nanostructures as nanotemplates (Figure 11.17(c)). This provides an elegant strategy for precise and rapid control of functional nanostructures at room temperature, which can be further utilized in fast control of ordered nanostructures for nanofabrication and nanoengineering (Wang et al., 2017). Besides, silver ion (Ag^+) was introduced into the PEO-based PLCBC and selectively combined with PEO segments through coordination interactions (Li et al., 2007a). After these processes, both the photoreduction of Ag^+ and a concomitant etching of the copolymer template were achieved by applying a 172-nm photon source. Furthermore, various nanodots and nanorods have been synthesized based on the selectively interactions of different phases of PLCBCs (Watanabe et al., 2007; Chen et al., 2008). These studies indicate the feasibility of applying MPS in nanolithography and nanotemplates. MPS and SMCM have been utilized to manipulate some unique functions introduced by the certain blocks. For example, PEO nanocylinders doped with Ag^+ could also serve as an anisotropic channel for ion transport due to the electroconductivity of PEO (Li et al., 2007b).
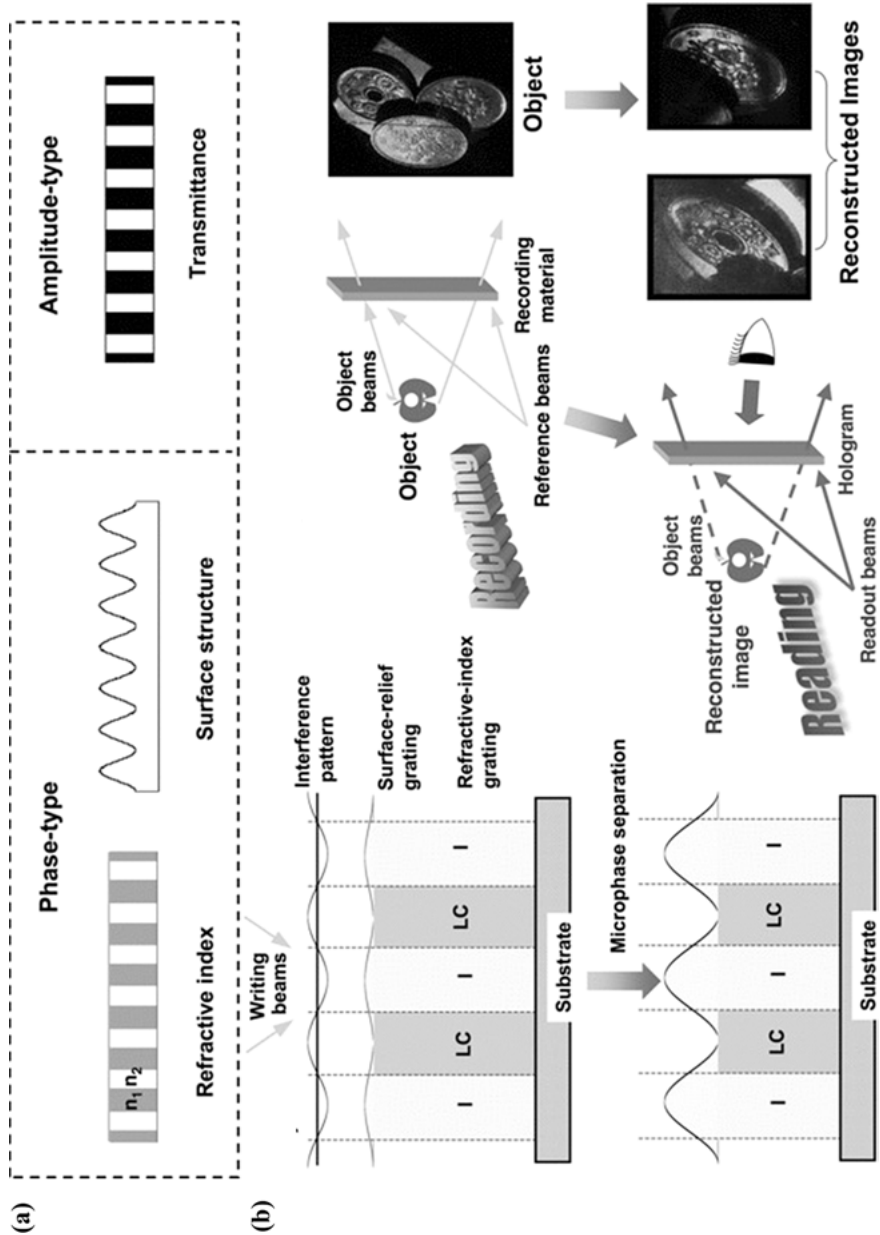
Figure 11.16: (a) Schematic illustration of the two categories of holographic gratings; (b) fabrication and enhancement of surface-relief grating based on the MPS of photoresponsive LCBC, and the reading–writing process of 3D images. (Adapted from Yu and Ikeda et al., 2011. Copyright 2011, John Wiley & Sons.)
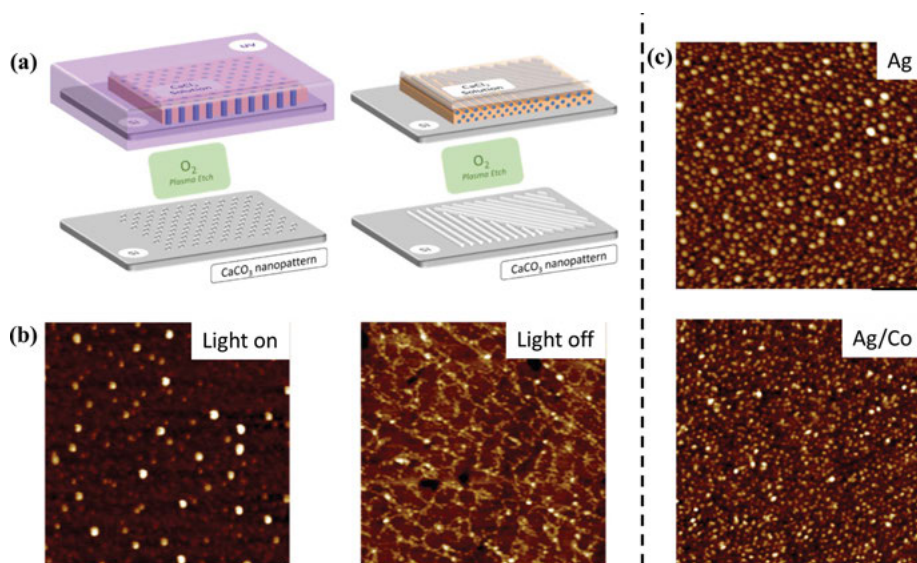
Figure 11.17: (a) Schematic illustration for fabrication of patterned CaCO₃ using nanotemplates of PLCBC MPS nanostructures with and without photoregulation; (b) AFM height images of CaCO₃ nanoparticles fabricated on the nanotemplates with and without photoregulation; (c) AFM height images of Ag and Ag/Co alloy nanoparticles fabricated based on the PLCBC nanotemplates. (Adapted from Wang et al., 2017. Copyright 2017, American Chemical Society.)

The introduction of chirality into PLCBCs could induce unique helical nanostructures which have potential applications as nanotemplates for fabricating complicated nanostructures. As shown in Figure 11.18, the controllable MPS of a PLCBC consisting of hydrophilic PEO and hydrophobic azobenzene-containing poly(methylacrylate) and chirality transfer effect was combined together, to fabricate helical nanostructures by doping with chiral additives (enantiopure tartaric acid). Through hydrogen-bonding interactions, chirality was transferred from the dopant to the aggregation, which directed the hierarchical self-assembly in the composite system. Upon optimization of the annealing condition and the chiral dopant amount, helical structures in film were successfully fabricated by the induced aggregation chirality. Accordingly, the photoresponsive azobenzene mesogens in the PLCBC helped photoregulation of the self-assembled helical morphologies. This provides a simple but elegant method for construction and noncontact manipulation of complicated nanostructures (Huang et al., 2018b).

In addition, self-assembly and applications of PLCBCs in solution is another hot topic. Typically, amphiphilic PLCBCs usually form vesicles or micelles in solutions, before the sol–gel transition takes place triggered by photoisomerization as the polarity of the mesogenic block changes (Su et al., 2010; Tong et al., 2005; Wang et al., 2004; Yang et al., 2005; Yang et al., 2006). These photoresponsive
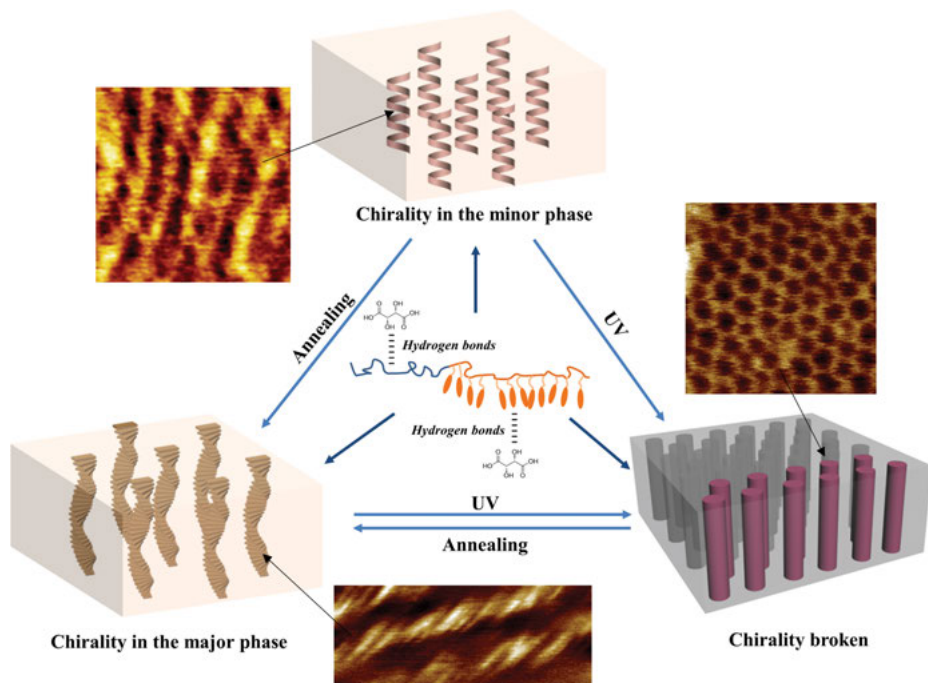
Figure 11.18: Illustration for the transfer, photoinduced breaking, and regeneration of the aggregation chirality in film of an amphiphilic LCBC doped with chiral tartaric acid. Here, aggregation chirality was obtained by chiral transfer from the minor phase to the major phase through hydrogen bonds by optimizing the annealing condition along with the dopant amount. Reversible photomanipulation of the aggregation chirality was observed by light-induced phase transition of the photoresponsive azobenzene mesogens and the supramolecular cooperative motion.
(Adapted from Huang et al., 2018b. Copyright 2018, John Wiley & Sons.)

vesicles and micelles have the potentials in medicine targeting delivery and controlled release (Mabrouk et al., 2009). Self-assembly of PLCBCs in solution could also induce manipulatable fluorescence. For example, one amphiphilic diblock copolymer poly(NIPAm-b-M6AzCOONa) in which one block was the thermal responsive poly(N-isopropylacrylamide) (PNIPAM) and the other block contained the pH-, UV-responsive, and fluorescent sodium azocarboxylate units, was nonfluorescent in good solvent, but showed fluorescence emission when it formed micelle-like structures in water. The acquired fluorescence can be adjusted by UV or pH, which was strongly related to the aggregation tightness and size of the micelles. The BC also showed reversible fluorescent enhancement in a large range of pH value (pH = 3 ~ 11) driven by thermally induced coil-to-globule transition due to the existence of the PNIPAM block, which leads to a more closely tightened aggregation of azobenzene moieties. These multiple-responsive fluorescence behaviors enable the PLCBC to find its applications for wide-pH-range fluorescence thermometer and

fluorescence probe (Ren et al., 2016). Besides, introduction of charged end-groups in such a PLCBC would lead to unusual responsive behaviors. By changing the ionic environment of the solution, a quick micelle-to-vesicle transition could be realized attributed to the joint effect of the charged end-group stabilization and the changed hydrophilic–hydrophobic balance of PNIPAM, providing a new way for design of stimuli-responsive polymer (Ren et al., 2018).

11.5 Conclusions

In this chapter, we provide an overview of the hierarchical self-assembly and manipulation of a series of LCBCs containing photoresponsive azobenzene chromophores. The introduction of LCs into BCs could combine the self-assembly of BCs and the anisotropy of mesogens together, bringing about the hierarchical nanostructures along with some excellent properties. The trigger-responsive property of photoresponsive LCs can help manipulate the ordered MPS nanostructures. With the development of information technology, new waves are surging, driving the manipulation of such hierarchical nanostructures as the future engineering plastics for optoelectronics and nanotechnology. Although researches of PLCBCs are still at a premature stage, understanding in this novel field is in progress, and it is being pushed ahead to realize their diverse potential applications in optoelectronics, information storage, nanotechnology, as well as biotechnology.

References

Addison, T., Cayre, O.J., Biggs, S., Armes, S.P., York, D. (2010). Polymeric microcapsules assembled from a cationic/zwitterionic pair of responsive block copolymer micelles. Langmuir, 26(9), 6281–6286.

Anthamatten, M., Zheng, W., Hammond, P. (1999). A morphological study of well-defined smectic side-chain LC block copolymers. Macromolecules, 32(15), 4838–4848.

Bates, F.S., Fredrickson, G.H. (1999). Block copolymers – designer soft materials. Physics Today, 52(2), 32–38.

Beppu, K., Nagashima, Y., Hara, M., Nagano, S., Seki, T. (2017). Photoalignment of vertically oriented microphase separated lamellae in LC-LC diblock copolymer thin film. Macromolecular Rapid Communications, 38, 13.

Bohnert, R., Finkelmann, H. (1994). Liquid-crystalline side-chain AB block copolymers by direct anionic polymerization of a mesogenic methacrylate. Macromolecular Chemistry and Physics, 195(2), 689–700.

Chang, X., Dong, C.-M. (2013). Synthesis of hyperbranched polypeptide and PEO block copolymer by consecutive thiol-Yne chemistry. Biomacromolecules, 14(9), 3329–3337.

Chao, C.-Y., Li, X.-F., Ober, C.K., Osuji, C., Thomas, E.L. (2004). Orientational switching of mesogens and microdomains in hydrogen-bonded side-chain liquid-crystalline block copolymers using AC electric fields. Advanced Functional Materials, 14(4), 364–370.

Chen, A., Komura, M., Kamata, K., Iyoda, T. (2008). Highly ordered arrays of mesoporous silica nanorods with tunable aspect ratios from block copolymer thin films. Advanced Materials, 20(4), 763–767.

Chen, Y.-X., Huang, S., Wang, T.-J., Dong, Z.-J., Yu, H.-F. (2019). Confined self-assembly enables stabilization and patterning of nanostructures in liquid-crystalline block copolymers. Macromolecules, 52(4), 1892–1898.

Fasolka, M.J., Mayes, A.M. (2001). Block copolymer thin films: physics and applications. Annual Review of Materials Research, 31(1), 323–355.

Frenz, C., Fuchs, A., Schmidt, H.W., Theissen, U., Haarer, D. (2004). Diblock copolymers with azobenzene side-groups and polystyrene matrix: synthesis, characterization and photoaddressing. Macromolecular Chemistry and Physics, 205(9), 1246–1258.

Hackel, M., Kador, L., Kropp, D., Frenz, C., Schmidt, H.W. (2005). Holographic gratings in diblock copolymers with azobenzene and mesogenic side groups in the photoaddressable dispersed phase. Advanced Functional Materials, 15(10), 1722–1727.

Hasegawa, M., Yamamoto, T., Kanazawa, A., Shiono, T., Ikeda, T. (1999a). A dynamic grating using a photochemical phase transition of polymer liquid crystals containing azobenzene derivatives. Advanced Materials, 11(11), 675–677.

Hasegawa, M., Yamamoto, T., Kanazawa, A., Shiono, T., Ikeda, T. (1999c). Photochemically induced dynamic grating by means of side chain polymer liquid crystals. Chemistry of Materials, 11(10), 2764–2769.

Hasegawa, M., Yamamoto, T., Kanazawa, A., Shiono, T., Ikeda, T., Yu, N., Akiyama, E., Takamura, Y. (1999b). Real-time holographic grating by means of photoresponsive polymer liquid crystals with a flexible siloxane spacer in the side chain. Journal of Material Chemistry, 9(11), 2765–2769.

Hayakawa, T., Horiuchi, S., Shimizu, H., Kawazoe, T., Ohtsu, M. (2002). Synthesis and characterization of polystyrene-b-poly(1,2-isopreneran-3,4-isoprene) block copolymers with azobenzene side groups. Journal of Polymer Science. Part A, Polymer Chemistry, 40(14), 2406–2414.

Hirai, T., Hirano, T., Komasawa, I. (2000). Preparation of Y_2O_3: Eu^{3+} phosphor fine particles using an emulsion liquid membrane system. Journal of Material Chemistry, 10(10), 2306–2310.

Huang, S., Chen, Y.-X., Ma, S.-D., Yu, H.-F. (2018b). hierarchical self-assembly in liquid-crystalline block copolymers enabled by chirality transfer. Angewandte Chemie International Edition. Doi: 10.1002/anie.201807379.

Huang, S., Pang, -L.-L., Chen, Y.-X., Zhou, L.-M., Fang, S.-M., Yu, H.-F. (2018a). Hydrogen bond induces hierarchical self-assembly in liquid-crystalline block copolymers. Macromolecular Rapid Communications, 1700783. Doi: (DOI: 10.1002/marc.201700783).

Ikeda, T., Tsutsumi, O. (1995). Optical switching and image storage by means of azobenzene liquid-crystal films. Science, 268(5219), 1873–1875.

Ikkala, O., Brinke, G. (2002). Functional materials based on self-assembly of polymeric supramolecules. Science, 295(5564), 2407–2409.

Kumar, G.S., Neckers, D. (1989). Photochemistry of azobenzene-containing polymers. Chemical Reviews, 89(8), 1915–1925.

Lehmann, O., Förster, S., Springer, J. (2000). Synthesis of new side-group liquid crystalline block copolymers by living anionic polymerization. Macromolecular Rapid Communications, 21(3), 133–135.

Li, J.-Z., Blake, J., Delaney, C. (2007a). Template-and vacuum-ultraviolet-assisted fabrication of a Ag-nanoparticle array on flexible and rigid substrates. Advanced Materials, 19(9), 1267–1271.

Li, J.-Z., Kamata, K., Komura, M., Yamada, T., Yoshida, H., Iyoda, T. (2007b). Anisotropic ion conductivity in liquid crystalline diblock copolymer membranes with perpendicularly oriented PEO cylindrical domains. Macromolecules, 40(23), 8125–8128.

Mabrouk, E., Cuvelier, D., Brochardwyart, F., Nassoy, P., Li, M.-H. (2009). Bursting of sensitive polymersomes induced by curling. Proceedings of the National Academy of Sciences of the United States of America, 106(18), 7294–7298.

Mao, G., Wang, J., Clingman, S.R., Ober, C.K., Chen, J.T., Thomas, E.L. (1997). Molecular design, synthesis, and characterization of liquid crystal–coil diblock copolymers with azobenzene side groups. Macromolecules, 30(9), 2556–2567.

Matsen, M.W., Bates, F.S. (1996). Unifying weak- and strong-segregation block copolymer theories. Macromolecules, 29(4), 1091–1098.

Morikawa, Y., Kondo, T., Shusaku Nagano, A., Seki, T. (2007). Photoinduced 3D ordering and patterning of microphase-separated nanostructure in polystyrene-based block copolymer. Chemistry of Materials, 19(7), 1540–1542.

Morikawa, Y., Nagano, S., Watanabe, K., Kamata, K., Iyoda, T., Seki, T. (2006). Optical alignment and patterning of nanoscale microdomains in a block copolymer thin film. Advanced Materials, 18(7), 883–886.

Nagano, S., Koizuka, Y., Murase, T., Sano, M., Shinohara, Y., Amemiya, Y., Seki, T. (2012). Synergy effect on morphology switching: real-time observation of photo-orientation of microphase separation in a block copolymer. Angewandte Chemie-International Edition, 51(24), 5884–5888.

Natansohn, A., Rochon, P. (2002). Photoinduced motions in azo-containing polymers. Chemical Reviews, 102(11), 4139–4176.

Nickmans, K., Bogels, G.M., Sanchez-Somolinos, C., Murphy, J.N., Leclere, P., Voets, I.K., Schenning, A.P.H.J. (2017). 3D orientational control in self-assembled thin films with sub-5 nm features by light. Small, 13, 33.

Osuji, C., Chen, J.-T., Mao, G., Ober, C., Thomas, E. (2000). Understanding and controlling the morphology of styrene–isoprene side–group liquid crystalline diblock copolymers. Polymer, 41(25), 8897–8907.

Osuji, C., Zhang, Y., Mao, G., Ober, C., Thomas, E. (1999). Transverse cylindrical microdomain orientation in an LC diblock copolymer under oscillatory shear. Macromolecules, 32(22), 7703–7706.

Rau, H. (2002). Photoisomerization of Azobenzenes, The Netherlands, Elsevier Science: Dordrecht.

Ren, H., Chen, D., Shi, Y., Yu, H.-F., Fu, Z.-F. (2016). Multi-responsive fluorescence of amphiphilic diblock copolymer containing carboxylate azobenzene and N-Isopropylacrylamide. Polymer, 97, 533–542.

Ren, H., Chen, D., Shi, Y., Yu, H.-F., Fu, Z.-F., Yang, W. (2018). Charged end-group terminated poly (N-isopropylacrylamide)-b-poly (carboxylic azo) with unusual thermoresponsive behaviors. Macromolecules, 51(9), 3290–3298.

Sano, M., Nakamura, S., Hara, M., Nagano, S., Shinohara, Y., Amemiya, Y., Seki, T. (2014). Pathways toward photoinduced alignment switching in liquid crystalline block copolymer films. Macromolecules, 47(20), 7178–7186.

Su, W., Han, K., Luo, Y.-H., Wang, Z., Li, Y.-M., Zhang, Q.-J. (2010). Formation and photoresponsive properties of giant microvesicles assembled from azobenzene-containing amphiphilic diblock copolymers. Macromolecular Chemistry and Physics, 208(9), 955–963.

Tian, Y.-Q., Watanabe, K., Kong, X., Abe, J., Iyoda, T. (2002). Synthesis, nanostructures, and functionality of amphiphilic liquid crystalline block copolymers with azobenzene moieties. Macromolecules, 35(9), 3739–3747.

Tong, X., Wang, G., Soldera, A., Zhao, Y. (2005). How can azobenzene block copolymer vesicles be dissociated and reformed by light? Journal of Physical Chemistry B, 109(43), 20281–20287.

Vapaavuori, J., Grosrenaud, J., Pellerin, C., Bazuin, C.G. (2015). in situ photocontrol of block copolymer morphology during dip-coating of thin films. ACS Macro Letters, 4(10), 1158–1162.

Wang, D.-R., Ye, G., Wang, X.-G. (2007). Synthesis of aminoazobenzene-containing diblock copolymer and photoinduced deformation behavior of its micelle-like aggregates. Macromolecular Rapid Communications, 28(23), 2237–2243.

Wang, D.-R., Ye, G., Zhu, Y., Wang, X.-G. (2009). Photoinduced mass-migration behavior of two amphiphilic side-chain azo diblock copolymers with different length flexible spacers. Macromolecules, 42(7), 2651–2657.

Wang, G., Tong, X., Zhao, Y. (2004). Preparation of azobenzene-containing amphiphilic diblock copolymers for light-responsive micellar aggregates. Macromolecules, 37(24), 8911–8917.

Wang, T.-J., Li, X., Dong, Z.-J., Huang, S., Yu, H.-F. (2017). Vertical orientation of nanocylinders in liquid-crystalline block copolymers directed by light. ACS Applied Material & Interfaces, 9(29), 24864–24872.

Watanabe, S., Fujiwara, R., Hada, M., Okazaki, Y., Iyoda, T. (2007). Site-specific recognition of nanophase-separated surfaces of amphiphilic block copolymers by hydrophilic and hydrophobic gold nanoparticles. Angewandte Chemie-International Edition, 46(7), 1120–1123.

Yamamoto, T., Ohashi, A., Yoneyama, S., Hasegawa, M., Tsutsumi, O., Kanazawa, A., Takeshi Shiono, A., Ikeda, T. (2001). Phase-type gratings formed by photochemical phase transition of polymer azobenzene liquid crystal. 2. rapid switching of diffraction beams in thin films. Journal of Physical Chemistry B, 105(12), 2308–2313.

Yamamoto, T., Yoneyama, S., Tsutsumi, O., Kanazawa, A., Shiono, T., Ikeda, T. (2000). Holographic gratings in the optically isotropic state of polymer azobenzene liquid-crystal films. Journal of Applied Physics, 88(5), 2215–2220.

Yang, J., Levy, D., Deng, W., Keller, P., Li, M.-H. (2005). Polymer vesicles formed by amphiphilic diblock copolymers containing a thermotropic liquid crystalline polymer block. Chemical Communications, 34(34), 4345–4347.

Yang, J., Pinol, R., Gubellini, F., Levy, D., Albouy, P.A., Keller, P., Li, M.-H. (2006). Formation of polymer vesicles by liquid crystal amphiphilic block copolymers. Langmuir, 22(18), 7907–7911.

Yoon, J., Jung, S., Ahn, B., Heo, K., Jin, S., Iyoda, T., Yoshida, H., Ree, M. (2008). Order–order and order–disorder transitions in thin films of an amphiphilic liquid crystalline diblock copolymer. The Journal of Physical Chemistry B, 112, 8486–8495.

Yoshida, E., Ohta, M. (2005). Preparation of micelles with azobenzene at their coronas or cores from 'nonamphiphilic' diblock copolymers. Colloid and Polymer Science, 283(5), 521–531.

Yu, H.-F. (2014a). Recent advances in photoresponsive liquid-crystalline polymers containing azobenzene chromophores. Journal of Material Chemistry C, 2(17), 3047–3054.

Yu, H.-F. (2014b). Photoresponsive liquid crystalline block copolymers: from photonics to nanotechnology. Progress in Polymer Science, 39(4), 781–815.

Yu, H.-F., Ikeda, T. (2011). Photocontrollable liquid-crystalline actuators. Advanced Materials, 23(19), 2149–2180.

Yu, H.-F., Iyoda, T., Ikeda, T. (2006b). Photoinduced alignment of nanocylinders by supramolecular cooperative motions. Journal of the American Chemical Societiy, 128(34), 11010–11011.

Yu, H.-F., Naka, Y., Shishido, A., Ikeda, T. (2008). Well-defined liquid-crystalline diblock copolymers with an azobenzene moiety: Synthesis, photoinduced alignment and their holographic properties. Macromolecules, 41(21), 7959–7956.

Yu, H.-F., Kobayashi, T., Ge, Z.-Y. (2009). Precise control of photoinduced birefringence in azobenzene-containing liquid-crystalline polymers by post functionalization. Macromolecular Rapid Communications, 30(20), 1725–1730.

Yu, H.-F., Kobayashi, T., Yang, H. (2011). Liquid-crystalline ordering helps blockcopolymer self-assembly. Advanced Materials, 23(29), 3337–3344.

Yu, H.-F., Li, J.-Z., Ikeda, T., Iyoda, T. (2006a). Macroscopic parallel nanocylinder array fabrication using a simple rubbing technique. Advanced Materials, 18(17), 2213–2215.

Zhang, -Y.-Y., Cheng, Z.-P., Chen, X.-R., Zhang, W., Wu, J.-H., Zhu, J., Zhu, X.-L. (2007). Synthesis and photoresponsive behaviors of well-defined azobenzene-containing polymers via RAFT polymerization. Macromolecules, 40(14), 4809–4817.

Zhao, Y., Thorkelsson, K., Mastroianni, A.J., Schilling, T., Luther, J.M., Rancatore, B.J., Matsunaga, K., Jinnai, H., Wu, Y., Poulsen, D., Frechet, J.M.J., Alivisatos, A.P., Xu, T. (2009). Small-molecule-directed nanoparticle assembly towards stimuli-responsive nanocomposites. Nature Materials, 8(12), 979–985.

Gregor Skačej, Claudio Zannoni

12 Molecular modeling of liquid crystal elastomers

Abstract: Liquid crystal elastomers are fascinating functional materials combining the properties of rubbers and liquid crystals. Understanding their properties at molecular level is extremely difficult in view of the complex chemical structure of the mesogens and the fact that many of their features depend on the fabrication procedure. Molecular modeling can offer considerable help in this respect, and here we propose to demonstrate this procedure by reviewing the strategy and the main applications of coarse-grained computer simulation techniques to reproduce the main features of liquid crystal elastomers and interpret their properties.

12.1 Introduction

Liquid crystal elastomers (LCE) (Broer et al., 2011; Warner and Terentjev, 2003) are made of sparsely cross-linked polymeric networks with embedded mesogenic (i.e., liquid crystal-forming) units possessing an inherent coupling between polymer network deformations and the mesogenic orientational order. This coupling may result in pronounced elastic deformations if the material is actuated by an appropriate external stimulus, with important possibilities of applications ranging from artificial muscles (Buguin et al., 2006; de Gennes, 1975; Li and Keller, 2006; Madden et al., 2004; Marshall et al., 2014; Mirfakhrai et al., 2007; Ohm et al., 2010; Spillmann et al., 2007), tissue engineering (Prevot et al., 2018), haptic displays (Torras et al., 2014, 2013), micro pumps (Fleischmann et al., 2012), morphing shapes and surfaces (Visschers et al., 2018; White, 2017) to photonics (Castles et al., 2014; Finkelmann et al., 2001) and materials with spatially localized mechanical responses (Babakhanova et al., 2018; Ware et al., 2016). A classical case is that of a temperature variation sufficient to switch the molecular organization of the LCE liquid crystal units between isotropic and anisotropic, with the attendant shape change of the sample. Other stimuli include electric fields (Fukunaga et al., 2009; Shahinpoor, 2000) or, if the LCE contains suitable photoresponsive moieties such as azobenzenes, irradiation with light of suitable wavelength (Camacho-Lopez et al., 2004; Mamiya et al., 2015; White, 2017). The opposite phenomenon also occurs with soft deformation modes involving mesogenic re-alignment and orientational order induced when an appropriate external stress is applied (Bladon et al., 1994; Warner and Terentjev, 2003).

Modeling of LCE behavior has been mainly performed at continuum theory level (Biggins et al., 2009; Warner and Terentjev, 2003) rather than with bottom up, molecular, computer simulations. This is not surprising given, on one hand, the complexity of these systems from the chemical point of view and, on the other, the rather large scale of the mechanical deformations involved. Indeed the first generation of computer simulations has been based on relatively simple lattice models lacking molecular translational degrees of freedom, with the strain-alignment coupling of LCEs typically introduced in an ad hoc manner requiring additional assumptions regarding the coupling nature and strength (Pasini et al., 2005; Selinger and Ratna, 2004; Skačej and Zannoni, 2006, 2008) to study thermomechanical and electromechanical actuation in uniaxial or biaxial systems. No such assumptions are necessary in the more elaborate off-lattice molecular modeling (mostly coarse grained (Darinskii et al., 2007, 2006; Ilnytskyi et al., 2009, 2006, 2012; Lyulin et al., 1998; Skačej and Zannoni, 2011, 2012, 2014; Whitmer et al., 2013) but also atomistic (Chung et al., 2016)), which have become feasible more recently, also thanks to the significant increase of available computer resources. In this chapter, we would like to focus mainly on the research performed on coarse-grained off-lattice systems (Darinskii et al., 2007, 2006; Ilnytskyi et al., 2009, 2006, 2012; Lyulin et al., 1998; Skačej and Zannoni, 2011, 2012, 2014; Whitmer et al., 2013). These models have the great advantage of being suitable for introducing the basic, but essential, features in LCEs, in particular, taking into account the shape and interaction anisotropy of the monomers, allowing the study of smectic as well as nematic LCE, introducing the topology of the polymer chains, e.g. modeling main chain or side chain LCE, varying the details of cross-linking and, importantly, including protocols for the fabrication. This last aspect, often neglected, allows to start understanding the difference in properties between LCE produced by polymerization in the isotropic phase and then cooled down (the so-called *isotropic genesis*) from those where polymerization takes place in an oriented liquid crystal state to start with. Experimentally these aspects are known to be important and constitute the basis, e.g. for the famous two-stage polymerization and cross-linking introduced by Finkelmann and collaborators (Brömmel et al., 2012; Küpfer and Finkelmann, 1991).

Here, we shall consider particularly systems based on the Gay–Berne (GB) intermolecular potential (Berardi et al., 2004; Gay and Berne, 1981; Micheletti et al., 2005; Zannoni, 2001), modified to increase its softness (Berardi et al., 2011, 2009), covering topics such as the nematic–isotropic transition and the electromechanic effect in monodomain LCEs, the poly-to-monodomain transition, the role of swelling and LCE sample architecture, and so on. We also plan to review the predictions obtained from computer simulations for selected experimental observables, including deuterium nuclear magnetic resonance spectra, X-ray diffraction patterns, specific heat, and elastic moduli.

12.2 Molecular model

We start introducing our molecular model, where each monomer is represented by an anisotropic bead, a polymer by a connected chain of these, and an elastomer by a network where these chains are to some extent cross-linked. We discuss applications and results for the so-called main-chain LCE where the mesogenic molecules also act as building blocks of the polymer backbone (Brommel et al., 2012; Donnio et al., 2000; Zentel, 1986), even if the model can be applied also to the study of side-chain systems, where the mesogens are appended laterally to the polymer backbone. In general, the main-chain materials feature a more pronounced strain-alignment coupling in comparison with the side-chains ones. Our simulated samples are typically swollen, that is, they contain, apart from polymer network molecules, also a significant percentage of non-bonded GB excess monomers to enhance the mobility of the network during simulation (while still conveying nematicity) (Skačej and Zannoni, 2011), as well as to mimic real experimental samples (Urayama et al., 2005; Zentel, 1986).

The main-chain LCE networks were obtained by assembling (i.e., somehow mimicking real polymerization, connecting monomeric units according to a well-defined protocol) elongated liquid-crystalline monomers – uniaxial ellipsoids σ_s wide and $\sigma_e = 3\sigma_s$ long –, interacting via a soft-core (SC) GB potential (Berardi et al., 2009). The original GB potential (Gay and Berne, 1981) is an anisotropic version of the well-known Lennard-Jones 6–12 potential that promotes parallel side-to-side molecular alignment necessary for the formation of various liquid-crystalline phases (Berardi et al., 1993). Its SC modification makes the repulsive part of the potential less harsh and thus introduces, in an effective way, a certain degree of chain-chain interpenetration functional to achieving a denser packing somewhat similar to what is obtained, through chain conformational mobility, in real polymer chains. Even more importantly, softness facilitates the equilibration of relatively dense polymeric networks in simulation (Skačej and Zannoni, 2011, 2012, 2014). To mimic the onset of polymerization by linking GB ellipsoids with semiaxes σ_e and σ_s into a polymeric network, bonding sites were assumed (Berardi et al., 2004) at all particle heads and tails, as well as on their equator wherever needed so as to model cross-link locations (Skačej and Zannoni, 2011). The bonds themselves have been represented by springs through the Finitely Extendable Nonlinear Elastic (FENE) potential often used in modeling polymer chains (Bird et al., 1971), applied to both bond stretching and bending. The key feature of the FENE potential is to penalize larger distortions more severely than an usual harmonic one while imposing, at the same time, a maximum deformation and bending range.

For a pair of mesogens (bonded or non-bonded), with their long axes given by unit vectors u_i and u_j, whose centers of mass are separated by $\mathbf{r}_{ij}$ ($r_{ij} = |\mathbf{r}_{ij}|$, $\hat{\mathbf{r}}_{ij} = \mathbf{r}_{ij}/r_{ij}$), the interaction energy (following the original GB potential (Gay and Berne, 1981)) is written as

$$U_{ij}^{GB} = 4 \in_{ij} \left\{ \left[\frac{\sigma_s}{r_{ij} - \sigma_{ij} + \sigma_s} \right]^{12} - \left[\frac{\sigma_s}{r_{ij} - \sigma_{ij} + \sigma_s} \right]^{6} \right\}. \tag{12.1}$$

Here $\sigma_{ij} = \sigma_s \Omega\left(\chi, \mathbf{u}_i, \mathbf{u}_j, \hat{\mathbf{r}}_{ij}\right)^{-1/2}$ is the core-range parameter, where

$$\Omega(\chi, \mathbf{u}_i, \mathbf{u}_j, \hat{\mathbf{r}}_{ij}) = 1 - \frac{\chi}{2} \left[\frac{(\mathbf{u}_i \cdot \hat{\mathbf{r}}_{ij} + \mathbf{u}_j \cdot \hat{\mathbf{r}}_{ij})^2}{1 + \chi(\mathbf{u}_i \cdot \mathbf{u}_j)} + \frac{(\mathbf{u}_i \cdot \hat{\mathbf{r}}_{ij} - \mathbf{u}_j \cdot \hat{\mathbf{r}}_{ij})^2}{1 - \chi(\mathbf{u}_i \cdot \mathbf{u}_j)} \right], \tag{12.2}$$

with $\chi = (\kappa^2 - 1)/(\kappa^2 + 1)$, and $\kappa = \sigma_e/\sigma_s$. Moreover, the strength parameter $\in_{ij} = \in (\in_{ij}')^{\mu}(\in_{ij}'')^{\nu}$ introduces an anisotropy in attractive interaction forces, $\in$ being a characteristic interaction energy, while the exponents μ and ν are dimensionless quantities that modify the shape of the potential well; $\in_{ij}' = \Omega(\chi', \mathbf{u}_i, \mathbf{u}_j, \hat{\mathbf{r}}_{ij})$ and $\in_{ij}'' = [1 - \chi^2(\mathbf{u}_i \cdot \mathbf{u}_j)^2]^{-1/2}$ according to the original empirical proposal of Gay and Berne (Gay and Berne, 1981). Here, $\chi' = (\kappa'^{1/\mu} - 1)/(\kappa'^{1/\mu} + 1)$ and $\kappa' = \in_s/\in_e$, where $\in_s = \in$ and $\in_e$ denote the depths of the attractive potential well for the side-by-side and end-to-end particle configurations, respectively. We use the SC modification of the original GB potential that replaces the strong repulsion at close distances by a softer linear potential $U_{ij}^{SC} = m(r_{ij} - \sigma_{ij})$ (Berardi et al., 2009) with a slope parameter m. Then the GB and SC potentials are continuously blended for given $\mathbf{u}_i$, $\mathbf{u}_j$, and $\hat{\mathbf{r}}_{ij}$, which results in

$$U_{ij}^{GBS} = (1 - f_{ij}) U_{ij}^{GB} + f_{ij} U_{ij}^{SC}; \tag{12.3}$$

here $f_{ij} = 1 / \left\{ 1 + \exp\left[n(\sigma_{ij} - r_{ij}) \right] \right\}$. In our work, we have used $\mu = 1$, $\nu = 3$, $\sigma_e/\sigma_s = 3$, $\in_s/\in_e = 5$ (known to provide a broad enough region of stable nematic in the phase diagram), $m = -70 \in/\sigma_s$, and $n = -100/\sigma_s$ (Berardi et al., 2009; Skačej and Zannoni, 2011). For elongated, prolate mesogens, typical values used are $\sigma_s \approx 5 \times 10^{-10}$ m and $\in = \in_s \approx 1.38 \times 10^{-21}$ J (Skačej and Zannoni, 2011). A reduced temperature scale, $T^* = k_B T / \in$, can be conveniently introduced.

We also write the bond energies for stretching and bending as (Berardi et al., 2004; Micheletti et al., 2005)

$$U_{ij}^{FENE} = -k_s \delta s_m^2 \log\left[1 - \frac{\delta s_{ij}^2}{\delta s_m^2} \right] - k_\theta \delta\theta_m^2 \log\left[1 - \frac{\delta\theta_{ij}^2}{\delta\theta_m^2} \right], \tag{12.4}$$

where, given a bond that connects two adjacent ellipsoids i and j in the polymer chain, δs_{ij} represents the deviation of the bond length s_{ij} from its equilibrium value s_e, limited to a maximum value δs_m, so that $\delta s_{ij} < \delta s_m$. Similarly, a bending angle θ_{ij} between the axes of two bonded ellipsoids (Berardi et al., 2004) can be introduced, together with its deviation $\delta\theta_{ij}$ from its equilibrium value limited to a plausible range: $\delta\theta_{ij} < \delta\theta_m$. The preferred bond directions were taken parallel to the long and short ellipsoid axes for all bonding sites at the ellipsoid ends and on the equator, respectively. In practice, we have assumed $s_e = 0.15\sigma_s$, $\delta s_m = 0.25\sigma_s$, and

$k_s = 500 \in /\sigma_s^2 \approx 2.76 \, \mathrm{Nm}^{-1}$ for stretching; $\theta_e = 0°$, $\delta\theta_m = 150°$, and $k_\theta = 3.8 \times 10^{-4}$ $\in \mathrm{deg}^{-2} \approx 1.72 \times 10^{-21} \, \mathrm{Jrad}^{-2}$ for bending (Berardi et al., 2004; Micheletti et al., 2005; Skačej and Zannoni, 2011).

As we have mentioned in the Introduction, one of the main reasons of interest for LCE is their ability to respond to an external field. This type of experimental conditions can be relatively easily implemented in our modeling. In particular, to simulate such electromechanical actuation, a Hamiltonian representing the coupling of each particle to the field can be added to the internal energy. More explicitly, the external field coupling energy of a GB particle with a long axis $\boldsymbol{u}_i$ can be modeled by $U_i^F = - \in \eta(\boldsymbol{u}_i \cdot \boldsymbol{f})^2$ (de Gennes and Prost, 1993), where $\boldsymbol{f} = \boldsymbol{E}/E$ and $\boldsymbol{E}$ stands for the electric field vector, with $E = |\boldsymbol{E}|$, and $\eta = \in_0 \in_a E^2 V_0/(2\in)$ is a field-alignment coupling parameter. Here $\in_0$ denotes the dielectric permittivity of vacuum, $\in_a = \in_{||} - \in_\perp$ is the microscopic (molecular) dielectric constant anisotropy, the symbols $||$ and $\perp$ referring to the direction of the molecular long axis, and V_0 is the volume effectively occupied by one mesogenic unit. For $\eta > 0$, $\boldsymbol{u}_i$ tend to be aligned along $\boldsymbol{E}$. Typically, our simulations were performed considering N GB ellipsoids in a volume V at a reduced number density $\rho^* = N\sigma_s^3/V \approx 0.29$; therefore, $V_0 = V/N \approx 4.3 \times 10^{-28} \, \mathrm{m}^3$. Then, taking $\in_a \langle P_2 \rangle \approx 11$ with $\langle P_2 \rangle \approx 0.54$ (values for 5CB at $T \approx 300$ K), $\eta = 0.1$ roughly corresponds to a field strength of 60 V/μm. (Here $\langle P_2 \rangle$ is the standard orientational nematic order parameter (de Gennes and Prost, 1993).) For simplicity, the electric field was assumed to be homogeneous throughout the sample; herewith, repeated solving of Maxwell equations in the course of the simulation was avoided.

12.3 Monte Carlo simulations

Having defined the model and the intramolecular and intermolecular potentials, the next step is choosing a simulation method to connect the microscopic and macroscopic levels. The alternatives are essentially the molecular dynamics and Monte Carlo (MC) techniques (Allen and Tildesley, 2017). The first is a deterministic approach, that solves time step after time step Newton's equations of motion for all the molecules. It is the method of choice for realistic atomistic simulations with full chemical details (Roscioni et al., 2017; Roscioni and Zannoni, 2016; Tiberio et al., 2009). However, realism has its disadvantages, in particular since the time span of the trajectories studied, typically of the order of 100 ns, while sufficient for the equilibration of low molecular mass, low viscosity systems, is inadequate for the LCE samples we wish to study here. When resorting to lower resolution, coarse grained, models a second method, Metropolis MC (Allen and Tildesley, 2017; Frenkel and Smit, 2002) can also be conveniently used. Monte Carlo allows sampling of the system phase space following a stochastic Markov process rather than a sequential

deterministic dynamics. Even if this means losing the possibility of studying dynamic properties, at least along a true timeline, we believe that for a system like the current one, it has advantages in properly exploring the configurations available to the system and thus we have adopted it in all our LCE work. In particular, in simulated experiments performed on our LCE samples, we have used isostress MC simulations, following a modified Metropolis algorithm (Frenkel and Smit, 2002; Skačej and Zannoni, 2011). To implement this, the total interaction energy U of N particles was obtained by considering all pair interactions, together with the external field contribution,

$$U = \sum_{i=1}^{N} \left[\sum_{j=i+1}^{N} (U_{ij}^{GBS} + w_{ij} U_{ij}^{FENE}) + U_i^F \right], \tag{12.5}$$

where $w_{ij} = 1$ if the particles i and j are bonded, and $w_{ij} = 0$ otherwise. The overall computational effort was reduced using Verlet neighbor lists, as well as cell linked-lists during the list updates (Allen and Tildesley, 2017), with the interaction and neighbor list cutoffs set at $4\sigma_s$ and $5\sigma_s$, respectively. Parallelization of the code was also employed to provide additional speedup when running on a computer cluster.

To ensure a phase space sampling that is sufficiently efficient, different trial move types were carried out: (i) *Translational moves.* Random displacement of a GB ellipsoid, maintaining its orientation. (ii) *Rotational moves.* Random ellipsoid rotation with respect to a Cartesian axis selected randomly (Barker and Watts, 1969), maintaining its position. (iii) *Bonded pair rotations.* Such moves affected only bonded bifunctional GB particles, excluding cross-links; each of the selected molecular pairs was rotated by a random angle about an axis connecting the far-away ends of the bonded pair. (iv) *Resize moves.* Collective trial moves that involved all ellipsoids: two sides of the cuboidal simulation box were picked at random, each of them to undergo a different random change, while the remaining box side was determined from the sample incompressibility constraint since LCE deformations are normally assumed to take place at constant volume. In this move, the GB particle orientations were maintained but their positions were rescaled affinely with the simulation box change.

One MC cycle consisted of attempting translational and rotational moves for each GB particle, and bonded pair rotations for all eligible pairs. In addition, at every five cycles a collective resize move was attempted. Any proposed move, resulting in an energy change ΔU and a simulation box deformation $\Delta\lambda_z$ along the z-axis (box side normalized with respect to the "reference" sample side; see below), was accepted with a probability given by $\min\{1, \exp[-(\Delta U - \Sigma_{zz} V \Delta\lambda_z)/k_B T]\}$ (Frenkel and Smit, 2002; Skačej and Zannoni, 2011), where V is the sample volume, T the temperature, and Σ_{zz} the external engineering stress applied along the z axis. Reduced engineering stress was defined as $\sigma^* = \Sigma_{zz}\sigma_s^3/\in$.

All trial move amplitudes were adjusted dynamically to achieve move acceptance ratios within $(50 \pm 5)\%$. The Verlet neighbor lists were rebuilt after every cycle

(or every five cycles deep in the aligned nematic phase), while the cell-linked lists were updated every 5,000 cycles. Typical equilibration run lengths ranged from several 10^6 to several 10^7 MC cycles, depending on the simulated experiment, while typical production runs were $\sim 10^6$ cycles long. Usually, MC runs at given conditions were launched directly from the so-called "reference" samples (see below for an explanation). Alternatively, this was done from configurations pre-equilibrated at a near value of temperature or stress (if available), for example, to speed up the slow relaxation of layered smectic phases. Stress-strain experiments in polydomain samples required a particularly long equilibration.

12.4 Selected observables

After successful equilibration, different averages of interest can be calculated and analyzed, starting with the standard thermodynamics quantities, like the reduced energy U^* whose fluctuations can be related to the sample heat capacity, C_V. The resulting reduced specific heat (per particle) is defined as $c_V^* = C_V/Nk_B = N(\langle U^{*2}\rangle - \langle U^*\rangle^2)/(T^*)^2$ and can be used, as in real differential scanning calorimetry experiments, to detect structural phase transitions.

Other observables, essential to study LCEs and their deformations, that can be extracted from simulations, are the average sample dimensions and aspect ratio. In several of the plots that we shall show later on the average reduced box sides λ_x, λ_y, and λ_z are displayed; here the normalization was done with respect to the cubic reference sample. The $\lambda_{x,y,z}$ data (as a function of external stress σ^*) can be also used to calculate the relevant elastic moduli and their temperature dependence.

In LCE, like in any liquid-crystalline system, it is natural to measure (or calculate) orientational order parameters based on the second-rank ordering matrix (de Gennes and Prost, 1993). It is also useful, differently from low molar mass systems at equilibrium, to distinguish between global and local scalar order parameters and also to introduce order parameters with respect to a certain laboratory direction, for example, with respect to the direction of pulling in a stress-strain experiment or to the direction of an applied electric field. It is thus convenient to review briefly these various quantities. For the jth particle with orientation $\mathbf{u}_j$ in a certain configuration (here at a certain MC sample sweep), the 3×3 ordering matrix reads as follows:

$$Q_j = \frac{1}{2}(3\mathbf{u}_j \otimes \mathbf{u}_j - I),\tag{12.6}$$

I being the 3×3 identity matrix. The degree of global orientational order, P_2, can be obtained by calculating the largest eigenvalue of the sample-averaged ordering matrix $(1/N)\sum_{j=1}^{N} Q_j$ in each MC cycle, and then subsequently averaging these eigenvalues over MC cycles. At the same time, it may make sense to explore local ordering,

which can be done by separately diagonalizing each of the local (i.e., molecular) ordering matrices $\langle Q_j \rangle$, obtained as an average of Q_j over MC cycles, providing the corresponding largest eigenvalues P_2^j for each molecule, and calculating a sample-averaged local order parameter $P_2^L = (1/N) \sum_{j=1}^N P_2^j$. In monodomain systems, any notable deviation of P_2^L from P_2 reveals a difference between ensemble and time averages, and can represent a signature of glassy ordering in the system considered. To introduce an order parameter monitoring molecular alignment with respect to a fixed axis (say, z), we can write $P_2^z = [3\langle (\boldsymbol{u}_i \cdot \boldsymbol{z})^2 \rangle_i - 1]/2$, where $\boldsymbol{z}$ stands for a unit vector along z and the average $\langle \cdots \rangle_i$ is taken over GB particles.

Local orientational order is often probed experimentally by deuterium magnetic resonance (^{2}H NMR) (Cordoyiannis et al., 2009, 2007; Disch et al., 1994; Lebar. et al., 2005). Quadrupolar interactions in suitably deuterated mesogens yield an orientation-dependent frequency splitting (Dong, 1994) that, for the jth deuteron-containing unit, reads $\omega_Q^j = \pm \delta\omega_Q[3(\boldsymbol{u}_j \cdot \boldsymbol{b})^2 - 1]/2$, where $\boldsymbol{u}_j$ gives the orientation of the molecular long axis, $\boldsymbol{b}$ denotes a unit vector parallel to the magnetic field of the NMR spectrometer, and $\delta\omega_Q$ is a coupling constant (Dong, 1994). In our simulations, we used a sequence of molecular configurations to obtain the corresponding predicted ^{2}H NMR spectra. Like in an actual pulsed-NMR experiment, the spectra were calculated by first generating the free induction decay (FID) signal $G(t) = \langle \exp[i \int_0^t \omega_Q^j(t') \, dt'] \rangle_j$, where t stands for time and $\langle \cdots \rangle_j$ denotes averaging over particles, and then Fourier-transforming it (Chiccoli et al., 1999). The length of the thus generated FID signal was 2^{20} MC cycles, while the duration of one NMR cycle ($2\pi/\delta\omega_Q$) was 1,024 MC cycles.

The scattering of X-rays is another important experimental technique employed in LCE studies, capable of probing both positional and orientational order (Zubarev et al., 1999). To calculate the scattered X-ray patterns, we adopted the procedure presented in Ref. (Bates and Luckhurst, 2003; Guinier, 1994), assuming that the scattering factor for a uniaxial ellipsoidal particle can be written as $F_j(\boldsymbol{q}, \boldsymbol{u}_j) = 3(\sin \gamma_j - \gamma_j \cos \gamma_j)/\gamma_j^3$. Here $\boldsymbol{q}$ is the scattering vector, while γ_j carries the information on particle orientation $\boldsymbol{u}_j$ and shape (Guinier and Fournet, 1995); $\gamma_j = (q\sigma_s/2)$ $(\kappa^2 \cos^2 \phi_j + \sin^2 \phi_j)^{1/2}$, $q = |\boldsymbol{q}|$, and $\cos \phi_j = (\boldsymbol{q} \cdot \boldsymbol{u}_j)/q$. ($\kappa$ and σ_s have the same meaning as in Section 12.2.) Now the total scattering amplitude for N particles is given by $F_T(\boldsymbol{q}) = \sum_{j=1}^N F_j(\boldsymbol{q}, \boldsymbol{u}_j) \exp(i\boldsymbol{q} \cdot \boldsymbol{r}_j)$, where $\boldsymbol{r}_j$ is the position of the jth particle. Finally, the total scattering intensity was calculated as $I(\boldsymbol{q}) = F_T(\boldsymbol{q}) F_T^*(\boldsymbol{q})$. The X-ray patterns were calculated every 200 MC cycles and averaged over a production period of $\sim 3 \times 10^5$ cycles. Here, as large as possible (64,000- and 216,000-particle) samples had to be studied in order to minimize the finite-size cross-like artifacts close to the center of the calculated pattern corresponding to the long-wavelength features of our finite system.
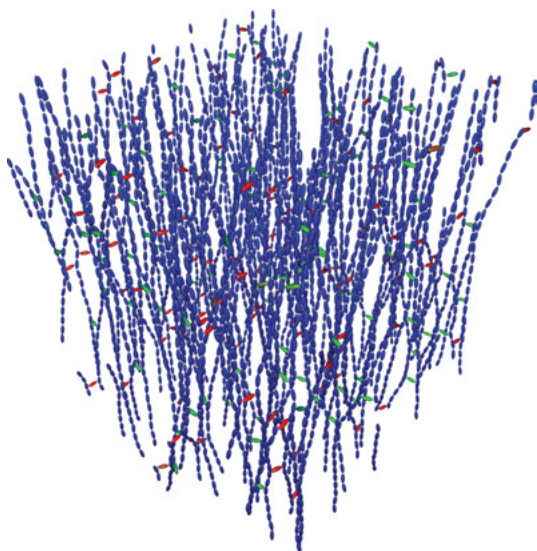
Figure 12.1: Monodomain LCE sample network architecture as revealed after a large negative pressure is applied. The colors red, green, and blue code the molecular alignment along *x*, *y*, and *z*, respectively; the swelling monomer molecules are not shown. The imprinted orientational anisotropy axis is parallel to *z*. [Reprinted figure with permission from Ref. (Skačej and Zannoni, 2011). Copyright 2011 by Royal Society of Chemistry.].

12.5 Monodomain LCE

12.5.1 Sample preparation

Before any simulated experiments can be performed, a responsive enough LCE sample has to be prepared. A particularly high macroscopic responsivity to external stimuli (temperature variation, application of electrical field) can be expected in aligned monodomain samples. Experimentally, a two-stage cross-linking procedure is required to obtain such samples (Küpfer and Finkelmann, 1991). In the first stage of the procedure, polymer chains are grown and weakly cross-linked. Then, chains are aligned by a suitable external field (mechanical, electric), which is followed by a second polymerization step resulting in reticulation with a cross-link density below ∼10%. This procedure provides an imprinted directional anisotropy throughout the sample and thus results in a pronounced strain-alignment coupling.

Trying to imitate these experimental steps, we built our monodomain sample within an initially cubic simulation box as a regular square array of vertical parallel polymer strands (Figure 12.1), thereby imprinting an orientational anisotropy along the *z*-axis. (For simplicity, the sample was constructed exclusively from identical GB particles.) Then, each of the strands was linked via a single GB particle to its nearest

neighbors along x and y, at a random position. Finally, the remaining empty space was uniformly filled with non-bonded GB monomers, and the so swollen sample was isotropically compressed to approach close-packing, that is, to a reduced density $\rho^* \approx 0.29$, yielding a cubic so-called "reference" sample. The smallest sample considered contains a total of 8,000 GB ellipsoids, out of which 3,872 GB particles belong to the elastomeric network and the rest are swelling monomers. Larger samples containing 64,000 or 216,000 particles, with the same swelling monomer percentage, are also considered. In all cases, periodic boundary conditions (PBC) were applied at the outer simulation box boundaries to mimic a bulk sample.
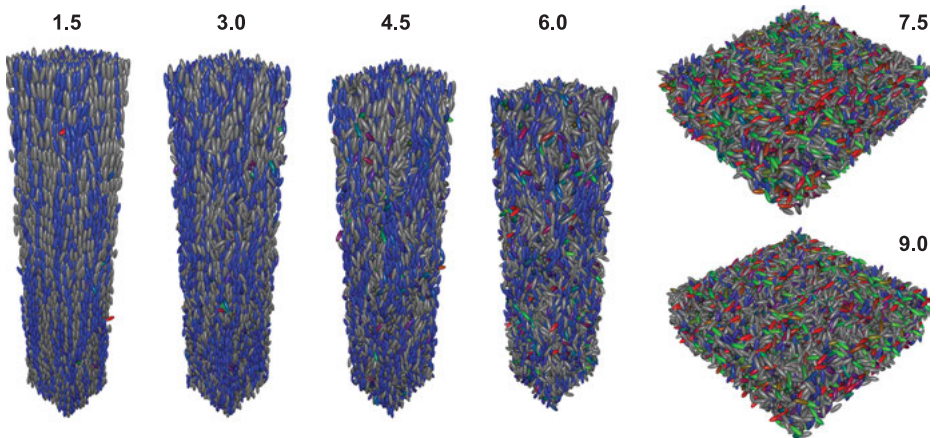
Figure 12.2: Monodomain sample snapshots at different temperatures, with corresponding reduced temperature values indicated next to each image. The orientational color coding for the network particles is the same as in Figure 12.1, while all swelling monomers are shown in grey. Isotropic, nematic, and smectic phases can be observed. [Reprinted figure with permission from Ref. (Skačej and Zannoni, 2011). Copyright 2011 by Royal Society of Chemistry.].

12.5.2 Thermomechanical actuation

We started by performing a series of simulations at different temperatures and zero stress: typical molecular organization snapshots are reported in Figure 12.2, while the corresponding temperature dependences of the specific heat, sample dimensions, and nematic order parameters are displayed in Figure 12.3 In the temperature scan, two specific heat anomalies hint at the existence of two phase transitions. The nematic-isotropic (NI) transition at $T_{NI}^* \approx 6.25 \pm 0.25$ results in a major change not only in the molecular organization itself, but also in sample shape. Below T_{NI}^* the mesogenic units are nematically ordered and the sample is visibly elongated along the z-axis – the direction of the orientational anisotropy (and of the aligning "mechanical field") imprinted upon sample preparation. On the other hand, the sample becomes
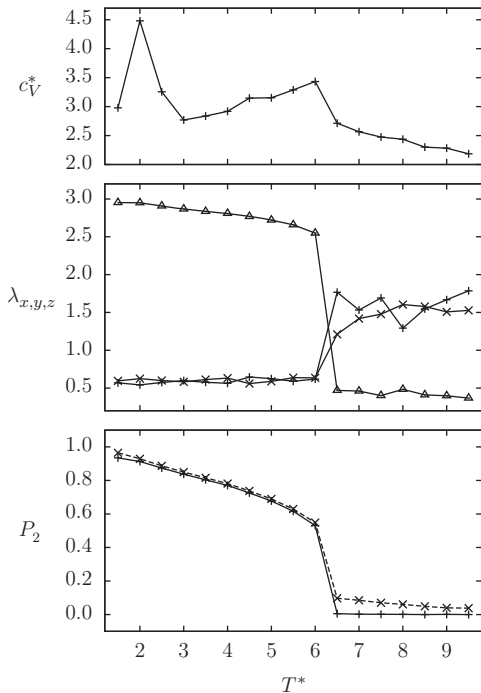
Figure 12.3: Monodomain LCE: temperature scan at zero external stress. *Top.* Specific heat. *Center.* Simulation box sides: λ_x (+), λ_y (×), and λ_z (△). *Bottom.* Nematic order parameters: global P_2 (+) and local P_2^L (×). [Reprinted figure with permission from Ref. (Skačej and Zannoni, 2011). Copyright 2011 by Royal Society of Chemistry.].

orientationally isotropic above T_{NI}^*, and is, consequently, flattened along the z-axis. In both cases the overall deformation (measured from the cubic reference sample) is quite uniaxial. Note also that at temperatures below $T_{SN}^* \approx 2.0 \pm 0.5$ smectic layering occurs. The smectic-nematic (SN) transition temperature is almost unchanged in comparison with the original monomeric GB system (Berardi et al., 1993), but the NI transition in a monomeric system is observed at $T_{NI}^* \approx 4.9$ (Berardi et al., 2009), which is quite different. Indeed, in a partially bonded system the ordered phase is stabilized by the imprinted mechanical field and the NI transition is hence found at a higher temperature. On the other hand, the SN transition mainly concerns translational degrees of freedom, and is less affected by the presence of the elastomer network.

Looking at the P_2 and $\lambda_{x,y,z}$ dependences in Figure 12.3 one can conclude that the NI transition is rather sharp and discontinuous, which is also supported by the existence of persistent metastable states at $T^* = 6.25$. Experimentally, a much smoother NI transition is usually observed (Lebar. et al., 2005; Selinger et al., 2002) and its smoothness can be controlled, e.g. by changing the cross-link concentration and
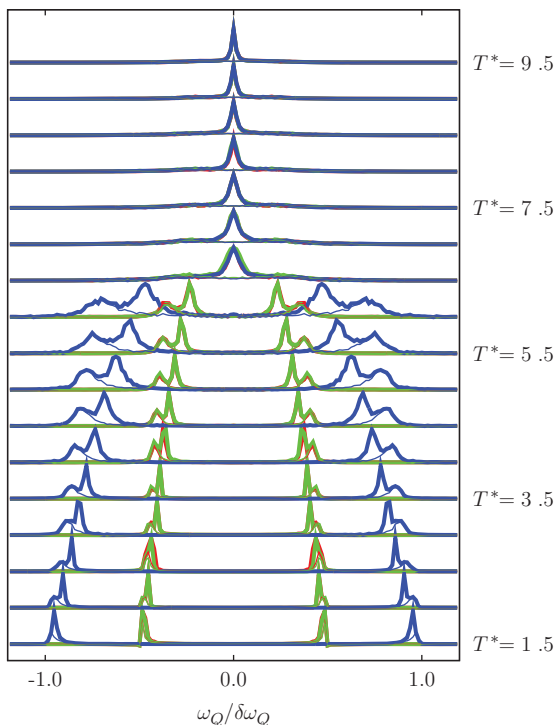
Figure 12.4: Monodomain LCE, ^{2}H NMR spectra: A temperature scan with the spectrometer field **b** directed along *x*, *y*, and *z*-axis shown in red, green, and blue, respectively. The elastomer network contribution (light lines) is shown separately from the total NMR response (heavy lines) comprising also the swelling monomers. The overlap of the spectral sets shown in red and in green confirms uniaxial molecular ordering with the respect to the *z*-axis. [Reprinted figure with permission from Ref. (Skačej and Zannoni, 2011). Copyright 2011 by Royal Society of Chemistry.].

the swelling monomer content (Cordoyiannis et al., 2009, 2007; Lebar. et al., 2005). The NI transition sharpness in the simulated sample can be attributed to its rather regular architecture. Subsequent simulated experiments involving more irregular (but still monodomain) samples have indeed demonstrated a smoother NI behavior (Skačej, 2018a). Note also that a single NI transition is observed in our swollen system; apparently, there is no major phase separation of the bonded and non-bonded (monomeric) mesogens in the temperature range studied. However, a significant phase separation featuring separate NI transitions in each subsystem can indeed be observed when increasing the swelling monomer content from the current ∼50% to ∼80% (Skačej, 2018a).

More information can be deduced from the deuterium NMR spectra plotted in Figure 12.4. For clarity, in the Figure the signal originating from the elastomeric network is separated from the total response that also includes the free swelling monomers. Above T_{NI}^*, the molecular motions average out the nuclear quadrupolar

interactions, which gives a single spectral peak at zero splitting. Below T_{NI}^* in the nematic (and also smectic) phase, however, a pronounced splitting is observed; the splitting for field $\boldsymbol{b}$ parallel to the z-axis being approximately twice the value obtained for $\boldsymbol{b}$ perpendicular to it. Moreover, the contribution from the bonded network is seen at a somewhat larger splitting than that of the monomers, which can be attributed to a lower degree of order for the non-bonded monomer molecules when compared with the bonded ones. (Note that for $\boldsymbol{b}$ parallel to the nematic director, z-axis, the reduced quadrupolar splitting $\omega_Q/\delta\omega_Q$ is simply equal to the local nematic degree of ordering, P_2^L. Similarly, for $\boldsymbol{b}$ perpendicular to z, it is equal to $P_2^L/2$ (Dong, 1994).) Assuming that there are no spatial variations of the local nematic director across the sample, from the spectra at $T^* = 3.0$ the P_2^L estimates for the network and monomer GB particles are ~ 0.88 and ~ 0.82, respectively. Moreover, there appears to be a single NI phase transition, as mentioned above. The spectra also reveal weak residual paranematic order above T_{NI}^* (mostly due to the bonded network), which reflects in nonzero values of the local order parameter P_2^L (Figure 12.3, *bottom*).

12.5.3 Stress-strain experiments

In LCE materials it is possible to induce orientational ordering not only by cooling, but also by subjecting the sample to a mechanical field, i.e., to external stress. Here stress was applied to samples equilibrated at $T^* = 3.0$ and $T^* = 5.0$ in the nematic phase, as well as to samples at $T^* = 7.0$ and $T^* = 9.0$ in the isotropic phase, in all cases along the direction of imprinted mechanical anisotropy, z-axis. (In the interesting case where the stress is applied perpendicular to the director, "soft" elastic deformations should be invoked; this will be addressed later.)

The simulated stress-strain isotherms are shown in Figure 12.5. Pulling along the z-axis when inside the nematic phase, the orientational order is enhanced and the sample only slightly elongated. The corresponding elastic moduli estimates are 770 MPa and 310 MPa for $T^* = 3.0$ and $T^* = 5.0$, respectively, exceeding experimental values by more than one order of magnitude (Beyer et al., 2007; Nishikawa et al., 1997). However, in both cases polymer strands are quite ordered already before applying stress and the additional elongation is mainly due to an extension of FENE bonds. This and the observed decrease of the elastic modulus with increasing temperature suggest that in this case the origin of elasticity is energetic rather than entropic. (Hairpins that might give rise to entropic elasticity in aligned samples (Adams and Warner, 2005; Tokita et al., 2006) appear to be absent in the current system due to the relatively short distance between cross-links.)

In the isotropic phase, the pulling experiment starts from an orientationally disordered sample. At $T^* = 7.0$ one observes a discontinuous stress-induced isotropic-to-nematic transition at $\sigma^* \approx 0.05$, while for $T^* = 9.0$ the stress-strain curve is rather smooth, which implies that there should be a critical point in between the two
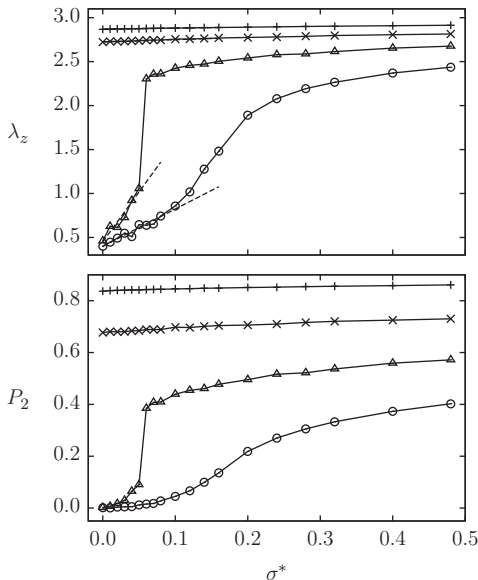
Figure 12.5: Monodomain LCE, stress-strain isotherms: Sample dimension along the *z*-axis (*top*) and the global nematic order parameter (*bottom*); $T^* = 3.0$ (+), $T^* = 5.0$ (×), $T^* = 7.0$ (Δ), and $T^* = 9.0$ (○). Here $\sigma^* = 0.1$ approximately corresponds to 1.1 MPa engineering stress. The dotted lines are the linear fits used to estimate the elastic moduli. [Reprinted figure with permission from Ref. (Skačej and Zannoni, 2011). Copyright 2011 by Royal Society of Chemistry.].

isotherms. Such critical behavior is consistent with phenomenological predictions (de Gennes, 1975), as well as with the findings of an early lattice model (Pasini et al., 2005). Again, the elastic moduli can be estimated for small deformations and low σ^*. The estimates for $T^* = 7.0$ and $T^* = 9.0$ are 210 kPa and 410 kPa, respectively, and compare well with experiment (Beyer et al., 2007). The simulated LCE material is hence substantially softer in the isotropic phase, with an elastic modulus that increases with increasing temperature – a signature of entropic elasticity. This phenomenon occurs only if the polymer chains can sample different pathways between the crosslinks, and in our samples this indeed appears to be the case in the disordered isotropic phase, as also suggested by the calculated ^{2}H NMR spectra where motional averaging results in a quadrupolar splitting that is essentially equal to zero.

12.5.4 Electromechanical actuation

Among the possible actuation stimuli in monodomain LCE, an external electric field seems to be particularly appealing, even though not easy to implement, since rather high field strengths are required to induce deformations and this can, amongst

other practical problems, lead to dielectric breakdown. This difficulty can be partly overcome by exploiting the soft or semisoft deformation modes – nematic director rotation accompanied by shear – where notable strain can be achieved at a rather low effort and free energy cost (Golubović and Lubensky, 1989; Olmsted, 1994; Petelin and Čopič, 2009; Terentjev et al., 1994, 1999). Experimentally, electromechanical actuation has been implemented in unconstrained and swollen samples, by Urayama and collaborators, applying an external electric field normal to the nematic director, using infrared and optical spectroscopy to detect changes in orientational ordering (Fukunaga et al., 2009; Urayama et al., 2005, 2006). These experiments were accompanied by various analyses using continuum theory (Corbett and Warner, 2009; Fukunaga et al., 2008), but not much had been done to obtain molecular-level insight into the actuation phenomena in LCE. Attempting to simulate the switching experiments presented in Refs. (Fukunaga et al., 2009; Urayama et al., 2006), we started (Skačej and Zannoni, 2012) by considering an equilibrated and aligned monodomain LCE sample at $T^* = 3.0$, with its director along the z-axis. Then, a transversal external electric field was applied along the x-axis, perpendicular to the director. (The mechanical analogue of such an experiment would be sample stretching perpendicular to the director.) Figure 12.6 shows selected snapshots of equilibrated configurations for different values of electric field strength, E. The latter is conveniently expressed through η, the dimensionless field coupling parameter proportional to E^2. In the snapshots, director rotation (accompanied by macroscopic sample deformation) becomes obvious above a switching threshold (Figure 12.6, *center* and *right*) at approximately $\eta \approx 0.35 \pm 0.05$ (or $\sim$110 MV/m). To meet the PBC assumed in simulation, domains of opposite director rotation and shear appear in the sample, which, however, is not the case for the unconstrained finite samples studied in experiments. These domains are similar to the "stripe domains" observed after external stress is applied perpendicular to the nematic director (Conti et al., 2002; Finkelmann et al., 1997; Mbanga et al., 2010; Verwey et al., 1996; Zubarev et al., 1999). In a carefully equilibrated sample, a simulation box accomodates only two domains of opposite rotation to minimize the number of energetically unfavorable domain walls. This tendency is supported also by considering different sample sizes, ranging from $N = 8000$ to 64,000 GB particles.

The results for the average reduced simulation box sides λ_x, λ_y, and λ_z as a function of $\sqrt{\eta} \propto E$ are plotted in Figure 12.7, showing the data for two samples consisting of the same polymer network, but with different swelling monomer contents. The corresponding degrees of monomer swelling Q (swollen/dry volume ratios) are equal to 2.1 and 4.5. The switching threshold appears to remain essentially the same for both Q values, but the process itself occurs over a narrower field strength range for the more swollen (and thus internally mobile) sample. In both samples, the reorientation of the non-bonded monomers turns out to be closely correlated with the switching of the polymer network.
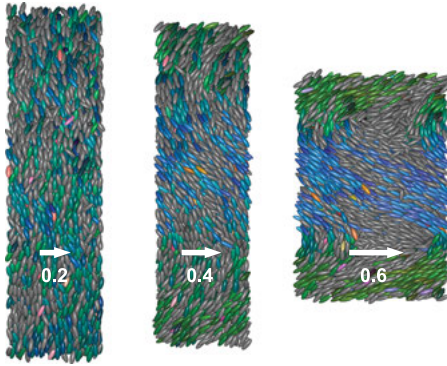
Figure 12.6: Monodomain LCE – sample snapshots in transversal electric field (arrows), together with the corresponding η values; weakly swollen sample with N = 8000 particles and a swelling degree Q ≈ 2:1. Ellipsoid orientation and type are color-coded: the predominantly green and blue areas correspond to the domains of clockwise and counterclockwise director rotation of the polymer network, respectively, while all swelling monomers are shown in grey regardless of their orientation. [Reprinted figure with permission from Ref. [37]. Copyright 2012 by National Academy of Sciences.]
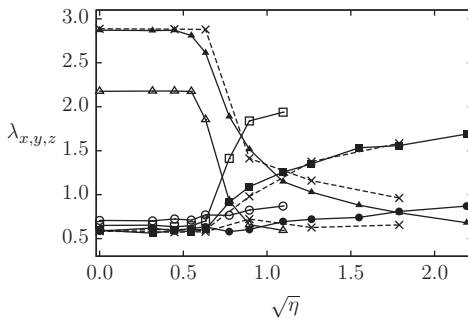
Figure 12.7: Monodomain LCE in transversal electric field (initial director along *z*-axis, field along *x*-axis): average simulation box sides λ_x (□), λ_y (○), and λ_z (△). Nematic phase at $T^* = 3.0$; closed and open symbols correspond to weakly (Q ≈ 2.1, N = 8000) and strongly (Q ≈ 4.5, N = 17576) swollen samples, respectively. The dashed lines connect the data obtained for the weakly swollen large sample (Q ≈ 2.1, N = 64000) (×). [Reprinted figure with permission from Ref. (Skačej and Zannoni, 2012). Copyright 2012 by National Academy of Sciences.].

It is instructive to analyze the observed bimodal director rotation also via simulated X-ray patterns, Figure 12.8 Below the switching threshold ($\eta = 0.2$ and 0.4) one can observe a nematic-like scattered pattern, with diffuse lateral arcs and two marked reflections along the vertical axis that corresponds to the nematic director. The first-order peaks along the director are observed at $q_{||} \approx 0.33 \times 2\pi/\sigma_s$ from the centre, but the lateral arcs peak at $q_\perp \approx 0.99 \times 2\pi/\sigma_s$. Both results are compatible with nearly closely
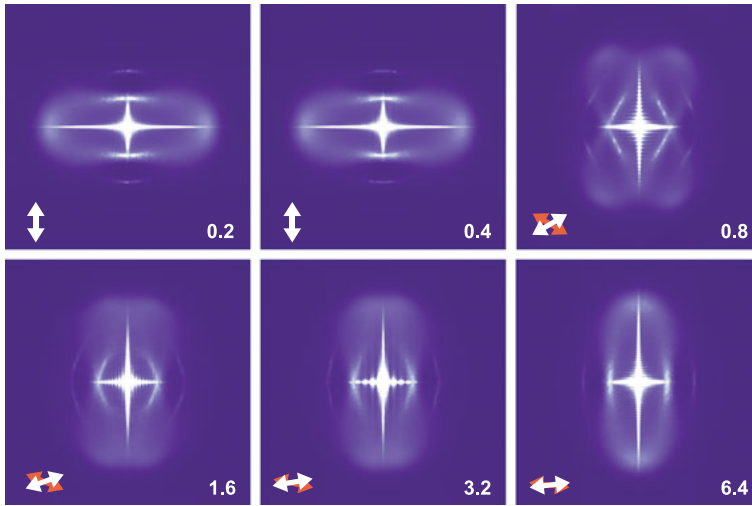
Figure 12.8: Monodomain LCE – scattered X-ray patterns ($N = 64000$ and $Q \approx 2.1$) for different values of the η parameter: from weak to strong field (*top left* to *bottom right*, respectively). Initially, the nematic director is vertical, and the electric field is applied horizontally. The contribution of the two oppositely rotated orientational domains is particularly visible at intermediate field strengths, the double-headed arrows indicating the corresponding nematic directors. [Reprinted figure with permission from Ref. (Skačej and Zannoni, 2012). Copyright 2012 by National Academy of Sciences.].

packed and well aligned ellipsoids $3\sigma_s$ long and σ_s wide. (A cross-like artifact visible close to the center of all patterns is a finite-size effect that should be ignored (Bates and Luckhurst, 2003).) Above the switching threshold, two nematic patterns, signatures of the two oppositely rotated domains, are superimposed. From the patterns it can moreover be deduced that an almost full (90°) rotation of the director is obtained in a strong field. Note also that while the nematic director rotation takes place in the *xz*-plane, the sample dimension along the *y*-axis is almost unchanged (Figure 12.7), as also seen in experiments (Fukunaga et al., 2009; Urayama et al., 2006).

Experimentally (Fukunaga et al., 2009; Urayama et al., 2006) it has been found that orientational switching in LCE is characterized by a critical field strength rather than by a critical voltage. To investigate this aspect, we considered another sample with $Q \approx 2.1$, however, with its all sides doubled, thereby maintaining the architecture of the smaller sample. The resulting $\lambda_{x,y,z}$ versus η dependences, also plotted in Figure 12.7, largely agree with those obtained for the smaller sample, including the switching threshold. Such behavior agrees with experiments, but also with the theoretical model of an external field that competes with a bulk (rather than surface) mechanical aligning field. The very existence of a switching threshold suggests that the simulated LCE in our current setup are semisoft rather than perfectly soft. Note also that the estimated value for the switching threshold, ~110 V/μm, is indeed rather high.

12.6 Polydomain LCE

In the absence of an aligning field (mechanical stress or electric) before cross-linking during LCE sample synthesis, an inhomogeneous sample consisting of micron-sized orientational domains is obtained (Warner and Terentjev, 2003). Such polydomain LCE are less understood than their monodomain counterparts; their ground state has been attributed to quenched orientational disorder originating from anisotropic cross-links (Fridrikh and Terentjev, 1997–1999). On stretching, a polydomain LCE sample, with an opaque appearance because of scattering, is transformed into a transparent well-aligned monodomain sample (Fridrikh and Terentjev, 1999). The corresponding stress-strain response strongly depends on sample preparation history. For example, nematic polydomain elastomers cross-linked in the isotropic state feature a stress-strain curve with a characteristic plateau corresponding to so-called "supersoft" elastic deformations requiring almost no effort for stretching, while samples cross-linked in the ordered nematic state exhibit a rather standard plateau-less response (Biggins et al., 2009, 2012; Uchida, 2000; Urayama et al., 2009). There are examples of reversible (Higaki et al., 2012; Urayama et al., 2009) and irreversible (Giamberini et al., 2005; Tokita et al., 2006) stress-strain behavior. Experimental stress-strain studies have been carried out also in smectic polydomain LCE (Giamberini et al., 2005; Ishige et al., 2008; Ortiz et al., 1998; Sánchez-Ferrer and Finkelmann, 2011), showing behavior that was qualitatively similar.

Computer simulations again seem to be a natural methodological choice when investigating polydomain LCE and elucidating the miscroscopic origin of supersoft elasticity. Here, however, one is presented with several difficulties: First, rather large samples need to be prepared to mimic a truly representative polydomain sample. Further, the isotropic genesis procedure, apparently essential in experimental observations of the phenomenon, has to be appropriately reproduced in simulations.

12.6.1 Sample preparation via isotropic genesis procedure

Again, main-chain LCE networks were built by polymerizing uniaxial elongated ellipsoids with a 3:1 aspect ratio (our monomers), considering the same non-bonding (soft GB) and bonding (FENE) interactions as in the previously studied monodomain systems, and preparing the "reference" sample in a cubic simulation box with PBC (Skačej and Zannoni, 2014). In our simulated polymerization protocol, the polymer chains were first generated at low density, each starting from a random position to grow along a randomly directed and straight line. In each growth step, chains were terminated with a probability of 0.125, which resulted in a polydisperse collection of strands $\sim 8 \pm 7.5$ monomers long. After completing this first stage of polymerization, cross-linking was simulated by transversally connecting the head (or tail) site of each terminal ellipsoid to the nearest unoccupied equatorial site belonging to another chain

[Figure 12.9(a), 12.9(b)]. This resulted in a heavily interconnected and, in large enough samples, an almost isotropic elastomeric network. Like in monodomain systems, the sample was soaked with swelling monomers (51.5% particle number fraction) and isotropically compressed in an isobaric MC run at a nematic temperature. This increased the sample density approximately 25 times to $\rho^* \approx 0.29$, almost reaching close-packing.
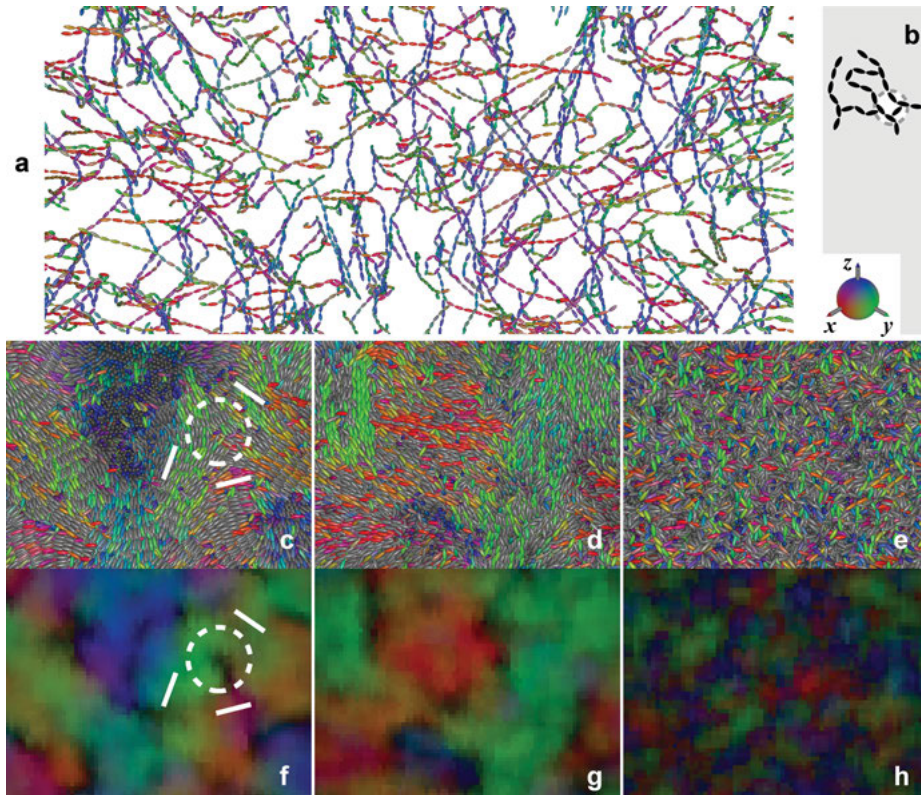
Figure 12.9: Simulated polydomain LCE network: (a) snapshot of a thin sample slice after an exposure to negative pressure and (b) a detail where the dashed circle highlights a highly cross-linked group of molecules that might represent a source of quenched orientational disorder. Sample snapshots at zero stress (c-e), together with the corresponding coarse-grained visualizations (f-h): smectic at $T^* = 1.0$ (c,f), nematic at $T^* = 3.0$ (d,g), and isotropic phase at $T^* = 7.0$ (e,h). The same color coding for molecular orientations and type as in Figure 12.2 is used. Bright and dark regions in the coarse-grained snapshots represent areas with strong and weak orientational order, respectively. The dashed white circles in the left column (c,f) expose one of the $-1/2$ strength disclinations, while the three white lines represent the local nematic directors within the nearby domains. [Reprinted figure with permission from Ref. (Skačej and Zannoni, 2014). Copyright 2014 by *American Chemical Society*.].

Such a preparation protocol should not imprint any preferred chain orientation prior to cross-linking and yield a nematic phase only after reticulation. The resulting polymer network is quite irregular and fairly entangled (see Figure 12.9(a)). The cross-link fraction (~12%) is somewhat higher than in the simulated monodomain samples. Note that the generated polymer chains are polydisperse, several of them being only one unit long. Together with their adjacent cross-linkers, these short chains represent small molecular clusters (e.g. highlighted by a dashed circle in Figure 12.9(b)) that may be difficult to reorient and might hence act as potential anisotropic sources of quenched disorder (Fridrikh and Terentjev, 1997, 1999). Finally, to examine issues related to possible finite-size effects we considered different sample sizes: $N = 8000$, 64,000, and 216,000 GB particles.

12.6.2 Coarse-grained sample visualization and domain characterization

Apart from traditional snapshots, Figure 12.9 also presents coarse-grained sample snapshots that are particularly convenient for the visualization of large polydomain samples. In the coarse-graining, samples were first virtually split into a mesh with spacing $\sim\sigma_s$, yielding cuboidal voxels. Then, for each of the voxels the neighboring bonded and swelling particles within a 216-voxel cuboid were identified, and the corresponding ordering matrix was calculated. Its diagonalization (de Gennes and Prost, 1993) gave the largest eigenvalue, that is, the voxel degree of order s_k, and the corresponding eigenvector, the local director n_k. The voxel was then colored using the same color-coding scheme as for the traditional snapshots. Its brightness was scaled quadratically between the smallest possible s_k value and the largest s_k value detected in the snapshot. Hence, the dark areas can be used to determine the locus of disclinations (i.e., topological defect lines), here identified by setting $s_k < 0.3$.

This post hoc coarse-graining is also convenient in identifying the size and other properties of orientational domains whose shape can be rather complex. Hence, from each voxel a recursive walk on the cubic mesh was performed to search for all neighboring voxels that are nearly mutually parallel but still well-ordered (i.e., with directors satisfying $(n_k \cdot n_j)^2 > 0.9$ and $s_k > 0.3$). The approximate number of domain molecules (n) was calculated by dividing the domain volume by $\sigma_s^3/\rho^* \approx 3.48\,\sigma_s^3$ representing the volume occupied (on average) by a single molecule. Note that, using this algorithm, the domains pertaining to neighboring voxels strongly overlap. In addition, for molecules within each domain, a second-rank orientational order parameter was calculated, to give (after a further average over all voxels) the so-called domain order parameter P_2^d.

12.6.3 Polydomain ground state

We first explored our LCE samples at different temperatures and zero stress. Again, MC runs were launched from the reference sample, releasing the cubic simulation box constraint. The latter was essential to observe only orientational domains occurring due to the irregular nature of the polymer network, avoiding those created as a finite-size effect. It turned out that the sample containing 216,000 monomers was the smallest that could qualify as an isotropic polydomain because in smaller samples the parallel aligning tendency of the mesogens, assisted by the polymer strand bending rigidity, managed to overcome the polymer network-induced disorder. Such samples then adopted an elongated shape with an anisotropic domain distribution. This must not be surprising: In real polydomain LCE, the micrometric domain size significantly exceeds the nanometric average distance between cross-links.

A collection of molecular snapshots obtained at different temperatures T^* is shown in Figure 12.9(c)–12.9(e) for the $N = 216000$ sample. At $T^* = 3.0$ the elastomer turns out to be in the nematic phase consisting of several domains with different director orientations. Locally, the system is ordered, with a nonzero value of the local order parameter, P_2^L. On the other hand, a global order parameter calculated for the sample as a whole, in a large enough sample should approach zero. (In a ^{2}H-NMR experiment, one would expect to see the characteristic Pake-type powder pattern (Dong, 1994).) After cooling the system down to $T^* = 1.0$, pronounced smectic layering occurs in the system. On the other hand, heating the sample, the degree of orientational ordering is at first just reduced, but at $T^* = 7.0$ all ordering seems to disappear and the sample becomes isotropic. All these observations are in agreement with the coarse-grained snapshots, Figure 12.9(f)–12.9(h). Further, in the orientationally ordered low-temperature phases one can notice the dark spots corresponding to regions where the nematic director cannot be unambiguously defined, that is, the topological defects, an example of which is highlighted by the dashed white circles in Figure 12.9(c), 12.9(f)). More quantitatively, the nematic–isotropic and smectic–nematic transition temperatures (identified from specific heat anomalies and order parameter values) are $T^*_{NI} \approx 5.5 \pm 0.5$ and $T^*_{SN} \approx 1.5 \pm 0.5$, respectively. Comparing with the corresponding transition temperatures previously seen in simulated regular monodomain samples (Skačej and Zannoni, 2011), in a polydomain system both transitions have moved toward a lower T^*.

Examining the average simulation box sides $\lambda_{x,y,z}$, in the isotropic phase their values are close to ~1, as expected, but in the locally aligned nematic phase a weak spontaneous elongation along the y-axis (~18% at $T^* = 3.0$) is observed. It also turns out that the global orientational order at $T^* = 3.0$ does not vanish completely; instead, a residual global order parameter of ≈ 0.15 can be detected. In phenomenological terms, a weak aligning mechanical field has been established along the y-axis. Nevertheless, the effects of such residual order turn out to decrease with increasing sample size and, as already mentioned, the 216,000-particle system is the smallest that appears as a sufficiently isotropic polydomain (see Figure 12.10(a)). The domain shapes
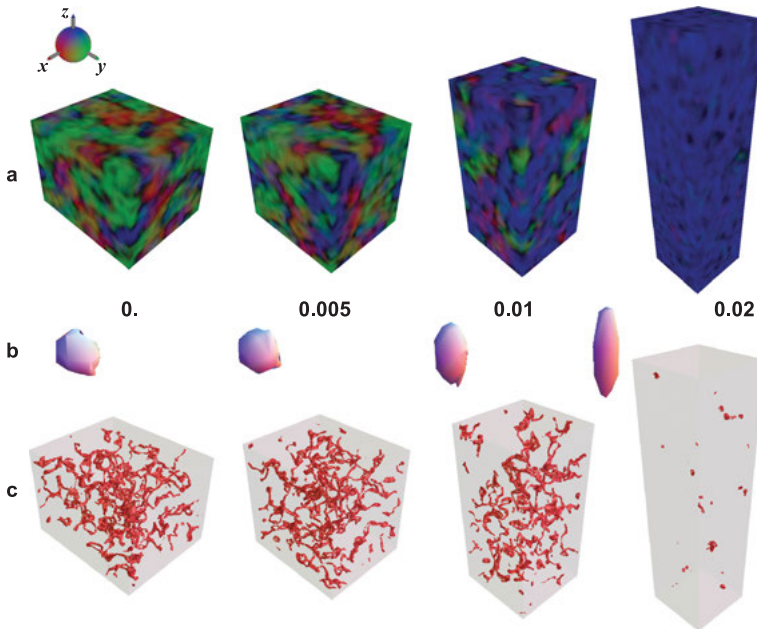
Figure 12.10: Polydomain LCE, stress-strain experiment in the nematic phase ($T^* = 3.0$). (a) Coarse-grained snapshots for different σ^* stress values displayed next to each plot. (b) Polymer chain end-to-end probability distribution isosurfaces. (c) Evolution of disclinations when σ^* is increased. [Adapted figure with permission from Ref. (Skačej and Zannoni, 2014). Copyright 2014 by *American Chemical Society*.].

are quite irregular and some of the domains turn out to be also percolating. An average domain consists of $\langle n \rangle \sim 10^4$ GB particles, while the largest domain sizes approach even $n \approx 2.3 \times 10^4$. The essentially isotropic character of the sample is additionally confirmed by the quite isotropic shape of the calculated polymer strand end-to-end vector probability distribution at zero stress (see Figure 12.10(b)). We also observe that the inter-domain boundaries, although rather diffuse, are often accompanied by disclinations visualized separately in Figure 12.10(c). The non-trivial defect structure largely consists of $\pm 1/2$-strength defect lines, Figure 12.10(c), 12.10(f), the least costly in free energy (Lubensky and Chaikin, 1997).

12.6.4 Stress-strain experiments

In order to observe the presence of (super)soft elastic deformations and trying to elucidate its origin in polydomain LCE, simulated stress-strain experiments were performed with the $N = 216,000$ sample at a nematic temperature $T^* = 3.0$. External stress was applied by pulling along the z-axis, that is, perpendicular to the residual

self-established mechanical field and the nematic director, y-axis. The corresponding coarse-grained snapshots are displayed in Figure 12.10, and the engineering stress versus strain curve in Figure 12.11, *top*. The curve looks similar to the experimental ones in nematic isotropic-genesis LCE (Giamberini et al., 2005; Higaki et al., 2012; Tokita et al., 2006; Urayama et al., 2009): it exhibits an initial region of small elongation in a narrow low-stress range, followed by a rather soft region where a significant elongation of more than 200% is achieved with only a small increase of stress, and by a third region with Hooke-like behavior, where the sample becomes stiffer and requires more effort for further elongation. Only a slight elongation of $\sim$20% is observed in the low-stress region, with a Young elastic modulus (estimated from the slope of the stress-strain curve) close to $E\sim$200 kPa. Then, after overcoming the weak transversal mechanical field at around $\sigma^*\sim$0.005 (i.e., $\sim$55 kPa), the slope decreases significantly and the curve exhibits a somewhat tilted plateau with $E\sim$100 kPa going up to $\sim$200% deformation. Then, the sample becomes much stiffer, and the Young elastic modulus increases to several MPa toward the end of the plotted curve. The total work density necessary to reach the end of the stress-strain plateau and thus take the sample across the polydomain-monodomain (PM) transition is estimated from the area under the stress-strain curve as $<300\,\mathrm{kJm}^{-3}$. Larger samples turn out to enter the plateau at lower stress than the smaller ones because of their less pronounced global order leading to a weaker transversal mechanical field to be overcome. Moreover, as shown in Ref. (Fridrikh and Terentjev, 1999), the existence of orientational domain walls also contributes to this mechanical field and to a nonzero plateau stress.

Now we can discuss some of the possible microscopic mechanisms involved in the PM transition. (i) *Domain rotation*. Within this scenario each of the isotropically distributed domains would rotate independently when the sample is stretched (Fridrikh and Terentjev, 1999; Warner and Terentjev, 2003). The global order parameter P_2 would then increase from an initial small value and approach the original local P_2^L at the end of the process, while the average domain size $\langle n \rangle$ would remain largely unchanged. (ii) *Domain growth*. Alternatively, the domains already favorably aligned along the stretching direction could grow at the expense of others. In this case, the global order parameter would grow together with the domain size $\langle n \rangle$. Evidence exists that (i) and (ii) can be combined (Ortiz et al., 1998; Whitmer et al., 2013). (iii) *Order destruction and reconstruction*. Since domains of differing shapes are not easy to rotate, another mechanism could act through a destruction of the existing local orientational order, followed by its reconstruction along the new (global) mechanical field-imposed direction, like in Ref. (Berardi et al., 2008). Here, the initial and final degree of local (P_2^L) and domain (P_2^d) order would be comparable, but the nature of the intermediate state would result in a notable drop of their values. (iv) *Quake-like release of local tension*. Yet another mechanism [possibly accompanying (i) and (ii)] could exploit the presence of excess elastic free energy stored in the topological defect lines throughout the sample. Above a certain stretching force
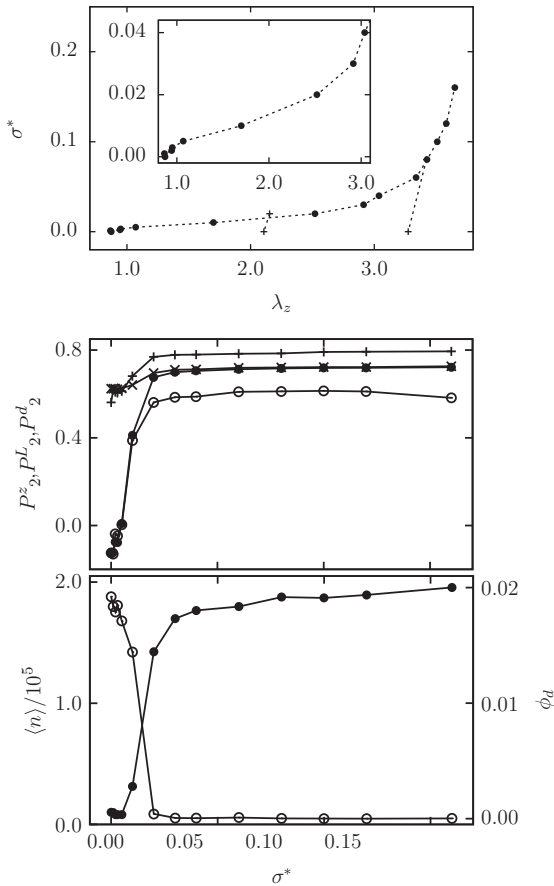
Figure 12.11: Polydomain LCE. *Top:* Stress-strain curves (●) at $T^* = 3.0$, with low-stress behavior shown as inset, and two examples of an irreversible stress-release run (+). *Center:* Stress dependence of orientational order parameters: P_2^z calculated for all particles (●) and for the cross-linking length-one strands (○); local P_2^L (+) and domain P_2^d (×). *Bottom:* Average domain size $\langle n \rangle$ (●) and disclination volume fraction ϕ_d (○) versus stress. $\sigma^* = 0.01$ corresponds to ~110 kPa engineering stress. [Adapted figure with permission from Ref. (Skačej and Zannoni, 2014). Copyright 2014 by *American Chemical Society*].

threshold, this free energy excess could be suddenly released when domains rotate and/or grow, thereby reducing the overall defect volume fraction, in some kind of irreversible quake.

Figure 12.11, *bottom*, shows the average domain size $\langle n \rangle$ against stress dependence. At first, below the stress-strain plateau, $\langle n \rangle$ slightly decreases, while the shape of the domain size distribution remains essentially unaffected by the stretching. The accompanying modest elongation of the sample seems to originate mostly in the reorientation of molecules, as suggested by an increase of the order parameter P_2^z

that monitors the orientational order with respect to the fixed stretching direction (Figure 12.11, *center*). In the plot, $P_2^z < 0$ demonstrates that the pulling direction is perpendicular to the initial (residual) director, *y*-axis. Once the stress-strain plateau is reached, both $\langle n \rangle$ and P_2^z swiftly increase, suggesting simultaneous substantial reorientation and merging of domains. Above the plateau ($\lambda_z > 3$, $\sigma^* > 0.04$) both quantities saturate, and the sample here becomes a single elongated and quite well-aligned domain with $\langle n \rangle \rightarrow N$ and $P_2^z > 0$. This is suggested by the coarse-grained snapshots, but also by the isosurfaces of the polymer chain end-to-end spatial distribution, Figure 12.10(b): the initially rather isotropic polydomain distribution slowly transforms into a prolate monodomain one when stress is applied.

In Figure 12.11, central plate, we also plot the P_2^z versus σ^* dependence (empty circles) separately for the short cross-linker strands [see Figure 12.9(b)]. This dependence is similar to that obtained for all mesogens; therefore, the cross-linkers appear to reorient more or less together with other surrounding mesogens upon stretching, instead of maintaining their initial quenched orientations. At the same time, across the PM transition, local nematic ordering is preserved, which can be deduced from Figure 12.11, *center*, where the stress dependence of the local order parameter P_2^L is plotted. It starts from $P_2^L \sim 0.56$ in the absence of stress and is monotonically enhanced to ~ 0.79 when σ^* increases. In the same plot, the domain order parameter P_2^d is shown as well, behaving similarly as P_2^L. – The reorientation and growth of the domains are accompanied by a decrease of the disclination line length/volume (see Figure 12.10(c)). This trend can be confirmed by looking at the volume fraction occupied by the disclinations, ϕ_d, and its dependence on stress σ^*. It is plotted in Figure 12.11, *bottom*, and is closely related to the $\langle n \rangle$ dependence.

Within and above the observed stress-strain plateau, our samples seem to present considerable memory effects. When stress is removed, they typically do not return to their initial shape and merely a slight elongation decrease can be detected (see Figure 12.11, *top*). Such behavior agrees with the findings in some experimental main-chain systems (Giamberini et al., 2005; Tokita et al., 2006).

According to our simulations, the stress-strain behavior across the PM transition is phenomenologically similar to the theoretical predictions made for non-ideal supersoft LCE: The supersoft plateau is reached only above a stress threshold attributed to an intrinsic mechanical field that breaks the symmetry but tends to diminish when sample size is increased. The behavior reproduced in our simulations may not be completely soft in the sense of the neoclassical rubber elastic theory (Bladon et al., 1993; Warner et al., 1994; Warner and Terentjev, 2003) that suggests pure domain rotation, whereby the distribution of polymer chain end-to-end vectors is rotated but remains otherwise unaltered. Instead, on the stress-strain plateau combined domain growth and rotation appear to take place in our simulated system. At the same time, any destruction of local orientational order can be safely excluded (Berardi et al., 2008). By the end of the stress-strain plateau, the aligning process seems to have been thorough enough to reorient even the hypothetical sources of

quenched disorder. As a consequence, the simulated stress-strain behavior is irreversible, featuring pronounced memory effects. Such irreversibility and the disclination removal under applied stress are both compatible with the creation of microquakes although in our simulations none of them has been directly observed.

Note that the plateau stress, Young elastic moduli, and the mechanical work density all scale as $\in/\sigma_s^3$ and therefore sensitively depend on particle size σ_s, as well as on the characteristic GB energy scale $\in$. For an alternative (and realistic) dataset with $\sigma_s = 1$ nm and $\in = 9.3 \times 10^{-22}$ J (Skačej and Zannoni, 2014), the plateau threshold stress is reduced to $\sim$5 kPa. This compares well with the value measured for a nematic main-chain elastomer in Ref. (Tokita et al., 2006).

The simulated stress-strain curve is also similar to the experimental ones reported for reversible nematic side-chain systems (Higaki et al., 2012; Urayama et al., 2009). Moreover, although the occurrence of supersoft elasticity has been theoretically predicted for nematic elastomers, many properties of our simulated LCE material also qualitatively agree with those observed experimentally in smectic main-chain systems (Giamberini et al., 2005; Ishige et al., 2008; Ortiz et al., 1998; Sánchez-Ferrer and Finkelmann, 2011).

In the only other molecular-level investigation of the supersoft elasticity phenomenon in LCE systems we are aware of, de Pablo and collaborators (Whitmer et al., 2013) employed coarse-grained molecular dynamics simulations to study a system of side-chain LCE also based on GB monomers, although of the standard type (Gay and Berne, 1981), using tetra-functional cross-links and a perfect tetrahedral network. Even if their procedure is quite different and without a two-stage isotropic genesis strategy, they also observed a stress-strain plateau, but in a smectic side-chain system and only in a dynamical experiment, while the equilibrium stress-strain behavior appeared to be similar to Hookean, that is, plateau-less.

12.7 Conclusions and outlook

Coarse-grained off-lattice molecular simulations (like the ones presented in this Chapter) belong to a second generation of microscopic LCE modeling research. The first-generation studies, lattice modeling (Broer et al., 2011), faced a serious problem when trying to adequately treat the key feature of LCE, the strain-alignment coupling. In the second-generation approaches allowing for explicitly engineered polymer networks with appropriately embedded mesogenic units, this issue has been largely resolved. To date, several phenomena of experimental and applicative interest have already been reproduced in nematic systems: thermo- and electromechanical actuation (Skačej and Zannoni, 2011, 2012), stress-induced isotropic-to-nematic phase transition (Skačej and Zannoni, 2011), as well as the poly-to-monodomain transition featuring supersoft elasticity (Skačej and Zannoni, 2014). Moreover, coarse-

grained molecular simulation has been used to study the impact of polymer network architecture and sample swelling on the nematic–isotropic transition (Skačej, 2018a), as well as to explore the possibility of using LCE materials in elastocaloric heating/cooling devices (Skačej, 2018b). Many phenomena in smectic systems have been explored too: memory effects and stress-induced transitions (Ilnytskyi et al., 2012), including a poly-to-monodomain transition (Whitmer et al., 2013). Of course at this coarse-grained level of modeling various intramolecular details are neglected, allowing to treat phenomena involving, for example, ultra-violet light-induced isomerization of azobenzene-based LCE, only in an approximate manner (Ilnytskyi et al., 2016). In such cases, third-generation, atomistic, simulations could be successful in supplying the necessary missing information (Chung et al., 2016), provided the key issue of at least an order of magnitude increase in computer resources will be resolved.

References

Adams, J.M., Warner, M. (2005). Hairpin rubber elasticity. European Physical Journal E, 16, 97–107.

Allen, M.P., Tildesley, D.J. (2017). Computer Simulation of Liquids, Oxford University Press, Oxford.

Babakhanova, G., Turiv, T., Guo, Y.B., Hendrikx, M., Wei, Q.H., Schenning, A.P.H.J., Broer, D.J., Lavrentovich, O.D. (2018). Liquid crystal elastomer coatings with programmed response of surface profile. Nature Communications, 9, 456.

Barker, J.A., Watts, R.O. (1969). Structure of water; a Monte Carlo calculation. Chemical Physics Letters, 3, 144–145.

Bates, M.A., Luckhurst, G.R. (2003). X-ray scattering patterns of model liquid crystals from computer simulation: calculation and analysis. The Journal of Chemical Physics, 118, 6605–6614.

Berardi, R., Emerson, A.P.J., Zannoni, C. (1993). Monte-Carlo investigations of a Gay-Berne liquid-crystal. Journal of the Chemical Society-Faraday Transactions, 89, 4069–4078.

Berardi, R., Lintuvuori, J.S., Wilson, M.R., Zannoni, C. (2011). Phase diagram of the uniaxial and biaxial soft-core Gay-Berne model. The Journal of Chemical Physics, 135, 134119.

Berardi, R., Micheletti, D., Muccioli, L., Ricci, M., Zannoni, C. (2004). A computer simulation study of the influence of a liquid crystal medium on polymerization. The Journal of Chemical Physics, 121, 9123–9130.

Berardi, R., Muccioli, L., Zannoni, C. (2008). Field response and switching times in biaxial nematics. The Journal of Chemical Physics, 128, 024905.

Berardi, R., Zannoni, C., Lintuvuori, J.S., Wilson, M.R. (2009). A soft-core Gay-Berne model for the simulation of liquid crystals by hamiltonian replica exchange. The Journal of Chemical Physics, 131, 174107.

Beyer, P., Terentjev, E.M., Zentel, R. (2007). Monodomain liquid crystal main chain elastomers by photocrosslinking. Macromolecular Rapid Communications, 28, 1485–1490.

Biggins, J.S., Warner, M., Bhattacharya, K. (2009). Supersoft elasticity in polydomain nematic elastomers. Physical Review Letters, 103, 037802.

Biggins, J.S., Warner, M., Bhattacharya, K. (2012). Elasticity of polydomain liquid crystal elastomers. Journal of the Mechanics and Physics of Solids, 60, 573–590.

Bird, R.B., Armstrong, R.C., Hassager, D. (1971). Dynamics of Polymeric Liquids, Wiley, New York.

Bladon, P., Terentjev, E.M., Warner, M. (1993). Transitions and instabilities in liquid-crystal elastomers. Physical Review E, 47, R3838–R3840.

Bladon, P., Terentjev, E.M., Warner, M. (1994). Deformation-induced orientational transitions in liquid-crystals elastomer. Journal de Physique Ii, 4, 75–91.

Broer, D.J., Crawford, G.P., Žumer, S. editors (2011). Cross-Linked Liquid Crystalline System. From Rigid Polymer Networks to Elastomers, CRC Press, London.

Brömmel, F., Kramer, D., Finkelmann, H. (2012). Preparation of liquid crystalline elastomers. Liquid Crystal Elastomers: Materials and Applications, 250, 1–48.

Buguin, A., Li, M.H., Silberzan, P., Ladoux, B., Keller, P. (2006). Micro-actuators: when artificial muscles made of nematic liquid crystal elastomers meet soft lithography. Journal of the American Chemical Society, 128, 1088–1089.

Camacho-Lopez, M., Finkelmann, H., Palffy-Muhoray, P., Shelley, M. (2004). Fast liquid crystal elastomer swims into the dark. Nature Material, 3, 307–310.

Castles, F., Morris, S.M., Hung, J.M.C., Qasim, M.M., Wright, A.D., Nosheen, S., Choi, S.S., Outram, B.I., Elston, S.J., Burgess, C., Hill, L., Wilkinson, T.D. (2014). H. J.) Coles. Stretchable liquid-crystal blue-phase gels. Nature Materials, 13, 817–821.

Chiccoli, C., Pasini, P., Skačej, G., Žumer, S., Zannoni, C. (1999). NMR spectra from Monte Carlo simulations of polymer dispersed liquid crystals. Physical Review E, 60, 4219–4225.

Chung, H., Choi, J., Yun, J.-H., Cho, M. (2016). Nonlinear photomechanics of nematic networks: upscaling microscopic behaviour to macroscopic deformation. Scientific Reports 6, 20026.

Conti, S., DeSimone, A., Dolzmann, G. (2002). Semisoft elasticity and director reorientation in stretched sheets of nematic elastomer. Physical Review E, 66, 061710.

Corbett, D., Warner, M. (2009). Deformation and rotations of free nematic elastomers in response to electric fields. Soft Matter, 5, 1433–1439.

Cordoyiannis, G., Lebar, A., Rožič, B., Zalar, B., Kutnjak, Z., Žumer, S., Brömmel, F., Krause, S., Finkelmann, H. (2009). Controlling the critical behavior of paranematic to nematic transition in main-chain liquid single-crystal elastomers. Macromolecules, 42, 2069–2073.

Cordoyiannis, G., Lebar, A., Zalar, B., Žumer, S., Finkelmann, H., Kutnjak, Z. (2007). Criticality controlled by cross-linking density in liquid single-crystal elastomers. Physical Review Letters, 99, 197801.

Darinskii, A.A., Zarembo, A., Balabaev, N.K. (2007). Molecular dynamic simulation of side-chain liquid crystalline elastomer under load. Macromolecular Symposia, 252, 101–109.

Darinskii, A.A., Zarembo, A., Balabaev, N.K., Neelov, I.M., Sundholm, F. (2006). Molecular dynamic simulation of side-chain liquid crystalline elastomer. Macromolecular Symposia, 237, 119–127.

de Gennes, P.G. (1975). Réflexions sur un type de polymères nématiques (some reflections about a type of nematic liquid crystal polymers). Comptes Rendus de l' Académie des Sciences, 281, 101–103.

de Gennes, P.G., Prost, J. (1993). The Physics of Liquid Crystals, Oxford University Press, Oxford.

Disch, S., Schmidt, C., Finkelmann, H. (1994). Nematic elastomers beyond the critical point. Macromolecular Rapid Communications, 15, 303–310.

Dong, R.Y. (1994). Nuclear Magnetic Resonance of Liquid Crystals, Springer Verlag, New York.

Donnio, B., Wermter, H., Finkelmann, H. (2000). A simple and versatile synthetic route for the preparation of main-chain liquid-crystalline elastomers. Macromolecules, 33, 7724–7729.

Finkelmann, H., Kim, S.T., Muñoz, A., Palffy-Muhoray, P., Taheri, B. (2001). Tunable mirrorless lasing in cholesteric liquid crystalline elastomers. Advanced Materials, 13, 1069.

Finkelmann, H., Kundler, I., Terentjev, E.M., Warner, M. (1997). Critical stripe-domain instability of nematic elastomers. Journal De Physique II France, 7, 1059–1069.

Fleischmann, E.K., Liang, H.L., Kapernaum, N., Giesselmann, F., Lagerwall, J., Zentel, R. (2012). One-piece micropumps from liquid crystalline core-shell particles. Nature Communication, 3, 1178.

Frenkel, D., Smit, B. (2002). Understanding Molecular Simulation: From Algorithms to Applications, Academic Press, San Diego.

Fridrikh, S.V., Terentjev, E.M. (1997). Order-disorder transition in an external field in random ferromagnets and nematic elastomers. Physical Review Letters, 79, 4661–4664.

Fridrikh, S.V., Terentjev, E.M. (1998). Exponential decay of correlations in a model for strongly disordered 2D nematic elastomers. Physical Review Letters, 81, 128–131.

Fridrikh, S.V., Terentjev, E.M. (1999). Polydomain-monodomain transition in nematic elastomers. Physical Review E, 60, 1847–1857.

Fukunaga, A., Urayama, K., Koelsch, P., Takigawa, T. (2009). Electrically driven director-rotation of swollen nematic elastomers as revealed by polarized Fourier transform infrared spectroscopy. Physical Review E, 79, 051702.

Fukunaga, A., Urayama, K., Takigawa, T., DeSimone, A., Teresi, L. (2008). Dynamics of electro-opto-mechanical effects in swollen nematic elastomers. Macromolecules, 41, 9389–9396.

Gay, J.G., Berne, B.J. (1981). Modification of the overlap potential to mimic a linear site-site potential. The Journal of Chemical Physics, 74, 3316–3319.

Giamberini, M., Cerruti, P., Ambrogi, V., Vestito, C., Covino, F., Carfagna, C. (2005). Liquid crystalline elastomers based on diglycidyl terminated rigid monomers and aliphatic acids. Part 2. Mechanical characterization. Polymer, 46, 9113–9125.

Golubović, L., Lubensky, T.C. (1989). Nonlinear elasticity of amorphous solids. Physical Review Letters, 63, 1082–1085.

Guinier, A. (1994). X-Ray Diffraction in Crystals, Imperfect Crystals and Amorphous Bodies, Dover, New York.

Guinier, A., Fournet, G. (1995). Small Angle Scattering of X-Rays, Wiley, New York.

Higaki, H., Urayama, K., Takigawa, T. (2012). Memory and development of textures of polydomain nematic elastomers. Macromolecular Chemistry and Physics, 213, 1907–1912.

Ilnytskyi, J., Saphiannikova, M., Neher, D. (2006). Photo-induced deformations in azobenzene-containing side-chain polymers: molecular dynamics study. Condensed Matter Physics, 9, 87–94.

Ilnytskyi, J.M., Neher, D., Saphiannikova, M. (2009). Molecular dynamics simulations of photo-induced deformations in azobenzene-containing polymers. In Garrido, P.L., Hurtado, P.I., Marro, J., editors, Modeling and Simulation of New Materials, volume 1091 of AIP Conference Proceedings, 253–255.

Ilnytskyi, J.M., Saphiannikova, M., Neher, D., Allen, M.P. (2012). Modelling elasticity and memory effects in liquid crystalline elastomers by molecular dynamics simulations. Soft Matter, 8, 11123–11134.

Ilnytskyi, J.M., Saphiannikova, M., Neher, D., Allen, M.P. (2016).Computer simulation of side-chain liquid crystal polymer melts and elastomers. In Thakur, V.K., Kessler, M.R., editors, Liquid Crystalline Polymers, Springer International Publishing Switzerland, Basel, 93–129.

Ishige, R., Osada, K., Tagawa, H., Niwano, H., Tokita, M., Watanabe, J. (2008). Elongation behavior of a main-chain smectic liquid crystalline elastomer. Macromolecules, 41, 7566–7570.

Küpfer, J., Finkelmann, H. (1991). Nematic liquid single crystal elastomers. Macromolecular Rapid Communications, 12, 717–726.

Lebar., A., Kutnjak, Z., Žumer, S., Finkelmann, H., Sánchez-Ferrer, A., Zalar, B. (2005). Evidence of supercritical behavior in liquid single crystal elastomers. Physical Review Letters, 94, 197801.

Li, M.H., Keller, P. (2006). Artificial muscles based on liquid crystal elastomers. Philosophical Transactions of the Royal Society A, 364, 2763–2777.

Lubensky, T.C., Chaikin, P.M. (1997). Principles of Condensed Matter Physics, Cambridge University Press, Cambridge.

Lyulin, A.V., Al-Barwani, M.S., Allen, M.P., Wilson, M.R., Neelov, I., Allsopp, N.K. (1998). Molecular dynamics simulation of main chain liquid crystalline polymers. Macromolecules, 31, 4626–4634.

Madden, J.D.W., Vandesteeg, N.A., Anquetil, P.A., Madden, A., Takshi, P.G.A., Pytel, R.Z., Lafontaine, S.R., Wieringa, P.A., Hunter, I.W. (2004). Artificial muscle technology: physical principles and naval prospects. IEEE Journal of Oceanic Engineering, 29, 706–728.

Mamiya, J., Kuriyama, A., Yokota, N., Yamada, M., Ikeda, T. (2015). Photomobile polymer materials: photoresponsive behavior of cross-linked liquid-crystalline polymers with mesomorphic diarylethenes. Chemistry-A European Journal, 21, 3174–3177.

Marshall, J.E., Gallagher, S., Terentjev, E.M., Smoukov, S.K. (2014). Anisotropic colloidal micromuscles from liquid crystal elastomers. Journal of the American Chemical Society, 136, 474–479.

Mbanga, B.L., Ye, F.F., Selinger, J.V., Selinger, R.L.B. (2010). Modeling elastic instabilities in nematic elastomers. Physical Review E, 82, 051701.

Micheletti, D., Muccioli, L., Berardi, R., Ricci, M., Zannoni, C. (2005). Effect of nanoconfinement on liquid-crystal polymer chains. The Journal of Chemical Physics, 123, 224705.

Mirfakhrai, T., Madden, J.D.W., Baughman, R.-H. (2007). Polymer artificial muscles. Materials Today, 10, 30–38.

Nishikawa, E., Finkelmann, H., Brand, H.R. (1997). Smectic A liquid single crystal elastomers showing macroscopic in-plane fluidity. Macromolecular Rapid Communications, 18, 65–71.

Ohm, C., Brehmer, M., Zentel, R. (2010). Liquid crystalline elastomers as actuators and sensors. Advanced Materials, 22, 3366–3387.

Olmsted, P.D. (1994). Rotational invariance and Goldstone modes in nematic elastomers and gels. Journal De Physique II France, 4, 2215–2230.

Ortiz, C., Wagner, M., Bhargava, N., Ober, C.K., Kramer, E.J. (1998). Deformation of a polydomain, smectic liquid crystalline elastomer. Macromolecules, 31, 8531–8539.

Pasini, P., Skačej, G., Zannoni, C. (2005). A microscopic lattice model for liquid crystal elastomers. Chemical Physics Letters, 413, 463–467.

Petelin, A., Čopič, M. (2009). Observation of a soft mode of elastic instability in liquid crystal elastomers. Physical Review Letters, 103, 077801.

Prevot, M.E., Ustunel, S., Hegmann, E. (2018). Liquid crystal elastomers-a path to biocompatible and biodegradable 3D-LCE scaffolds for tissue regeneration. Materials, 11, 377.

Roscioni, O.M., Muccioli, L., Zannoni, C. (2017). Predicting the conditions for homeotropic anchoring of liquid crystals at a soft surface. 4- n-pentyl-4-cyanobiphenyl on alkylsilane self-assembled monolayers. ACS Applied Materials & Interfaces, 9, 11993–12002.

Roscioni, O.M., Zannoni, C. (2016).Molecular dynamics simulation and its applications to thin-film devices. In Da Como, E., De Angelis, F., Snaith, H., Walker, A.B., editors, Unconventional Thin Film Photovoltaics, Royal Society of Chemistry, London, 391–419.

Sánchez-Ferrer, A., Finkelmann, H. (2011). Polydomain-monodomain orientational process in smectic-C main-chain liquid-crystalline elastomers. Macromolecular Rapid Communications, 32, 309–315.

Selinger, J.V., Jeon, H.G., Ratna, B.R. (2002). Isotropic-nematic transition in liquid-crystalline elastomers. Physical Review Letters, 89, 225701.

Selinger, J.V., Ratna, B.R. (2004). Isotropic-nematic transition in liquid-crystalline elastomers: lattice model with quenched disorder. Physical Review E, 70, 041707.

Shahinpoor, M. (2000). Electrically activated artificial muscles made with liquid crystal elastomers. In Smart Structures and Materials 2000: Electroactive Polymer Actuators and Devices (EAPAD), Vol. 3987, International Society for Optics and Photonics, 187–193.

Skačej, G. (2018a). Sample preparation affects the nematic-isotropic transition in liquid crystal elastomers: insights from molecular simulation. Soft Matter, 14, 1408–1416.

Skačej, G. (2018b). Elastocaloric effect in liquid crystal elastomers from molecular simulations. Liquid Crystals, 45, 1964–1969.

Skačej, G., Zannoni, C. (2006). External field-induced switching in nematic elastomers: a Monte Carlo study. European Physical Journal E, 20, 289–298.

Skačej, G., Zannoni, C. (2008). Biaxial liquid-crystal elastomers: a lattice model. European Physical Journal E, 25, 181–186.

Skačej, G., Zannoni, C. (2011). Main-chain swollen liquid crystal elastomers: a molecular simulation study. Soft Matter, 7, 9983–9991.

Skačej, G., Zannoni, C. (2012). Molecular simulations elucidate electric field actuation in swollen liquid crystal elastomers. Proceedings of the National Academy of Sciences of the United States of America, 109, 10193–10198.

Skačej, G., Zannoni, C. (2014). Molecular simulations shed light on supersoft elasticity in polydomain liquid crystal elastomers. Macromolecules, 47, 8824–8832.

Spillmann, C.A., Naciri, J., Martin, B.D., Farahat, W., Herr, H., Ratna, B.R. (2007). Stacking nematic elastomers for artificial muscle applications. Sensors and Actuators A, 133, 500–505.

Terentjev, E.M., Warner, M., Bladon, P. (1994). Orientation of nematic elastomers and gels by electric fields. Journal De Physique II France, 4, 667–676.

Terentjev, E.M., Warner, M., Meyer, R.B., Yamamoto, J. (1999). Electromechanical Fredericks effects in nematic gels. Physical Review E, 60, 1872–1879.

Tiberio, G., Muccioli, L., Berardi, R., Zannoni, C. (2009). Towards in silico liquid crystals. Realistic transition temperatures and physical properties for n-cyanobiphenyls via Molecular Dynamics simulations. ChemPhysChem, 10, 125–136.

Tokita, M., Tagawa, H., Niwano, H., Sada, K., Watanabe, J. (2006). Temperature-induced reversible distortion along director axis observed for monodomain nematic elastomer of cross-linked main-chain polyester. Japanese Journal of Applied Physics, 45, 1729–1733.

Torras, N., Zinoviev, K.E., Camargo, C.J., Campo, E.M., Campanella, H., Esteve, J., Marshall, J.E., Terentjev, E.M., Omastova, M., Krupa, I., Teplicky, P., Mamojka, B., Bruns, P., Roeder, B., Vallribera, M., Malet, R., Zuffanelli, S., Soler, V., Roig, J., Walker, N., Wenn, D., Vossen, F., Crompvoets, F.M.H. (2014). Tactile device based on opto-mechanical actuation of liquid crystal elastomers. Sensors and Actuators A, 208, 104–112.

Torras, N., Zinoviev, K.E., Esteve, J., Sánchez-Ferrer, A. (2013). Liquid-crystalline elastomer micropillar array for haptic actuation. Journal of Materials Chemistry C, 1, 5183.

Uchida, N. (2000). Soft and nonsoft structural transitions in disordered nematic networks. Physical Review E, 62, 5119–5136.

Urayama, K., Honda, S., Takigawa, T. (2005). Electrooptical effects with anisotropic deformation in nematic gels. Macromolecules, 38, 3574–3576.

Urayama, K., Honda, S., Takigawa, T. (2006). Deformation coupled to director rotation in swollen nematic elastomers under electric fields. Macromolecules, 39, 1943–1949.

Urayama, K., Kohmon, E., Kojima, M., Takigawa, T. (2009). Polydomain-monodomain transition of randomly disordered nematic elastomers with different cross-linking histories. Macromolecules, 42, 4084–4089.

Verwey, G.C., Warner, M., Terentjev, E.M. (1996). Elastic instability and stripe domains in liquid crystalline elastomers. Journal De Physique II France, 6, 1273–1290.

Visschers, F.L.L., Hendrikx, M., Zhan, Y.Y., Liu, D.Q. (2018). Liquid crystal polymers with motile surfaces. Soft Matter, 14, 4898–4912.

Ware, T.H., Biggins, J.S., Shick, A.F., Warner, M., White, T.J. (2016). Localized soft elasticity in liquid crystal elastomers. Nature Communications, 7, 10781.

Warner, M., Bladon, P., Terentjev, E.M. (1994). Soft elasticity – deformation without resistance in liquid-crystal elastomers. Journal de Physique II, 4, 93–102.

Warner, M., Terentjev, E.M. (2003). Liquid Crystal Elastomers, Oxford University Press, Oxford.

White, T.J. editor (2017). Photomechanical Materials, Composites, and Systems: Wireless Transduction of Light into Work, Wiley.

Whitmer, J.K., Roberts, T.F., Shekhar, R., Abbott, N.L., de Pablo, J.J. (2013). Modeling the polydomain-monodomain transition of liquid crystal elastomers. Physical Review E, 87, 020502.

Zannoni, C. (2001). Molecular design and computer simulations of novel mesophases. Journal of Materials Chemistry, 11, 2637–2646.

Zentel, R. (1986). Shape variation of cross-linked liquid-crystalline polymers by electric fields. Liquid Crystal, 1, 589–592.

Zubarev, E.R., Kuptsov, S.A., Yuranova, T.I., Talroze, R.V., Finkelmann, H. (1999). Monodomain liquid crystalline networks: reorientation mechanism from uniform to stripe domains. Liquid Crystals, 26, 1531–1540.

Dan Luo, Yue Shi

13 Liquid crystal polymer films with high reflectivity

Abstract: The growing demand for flexible low-power reflective photonics and display devices has fueled research for high-quality flexible materials with hyper-reflectivity and high stability resistant to environmental influences such that they are of broad working temperature range and excellent mechanical stress insensitivity. Despite the tremendous efforts that have been dedicated to developing cholesteric film materials with hyper-reflectivity or high stability, challenges still remain in achieving both due to the existence of liquid crystal that is susceptible and sensitive to external stimuli, such as temperature or mechanical stress. Herein, we demonstrate a novel flexible film possessing hyper-reflectivity, broad working temperature range, and excellent mechanical stress insensitivity via "washout-refill-assemble" approach by refilling polymer (optical adhesive) into cholesteric film assembled by two cholesteric templates with opposite handedness based on liquid crystal/reactive mesogens, where no liquid crystals exist in the final fabricated multilayer film. These materials show great application potentials in such as low-power flexible reflective displays, and other photonic flexible devices including laser, smart window, color pixels in digital photographs, and colored cladding of variety of objects. In addition, we experimentally demonstrate hyper-reflective, electrically switchable, fast responsive, and colorful reflective displays based on multilayer blue phase liquid crystal (BPLC) films consisting of two single-layer BPLC templates with opposite handedness. Our study on hyper-reflective BPLC film provides an attractive platform for future development including sequential colorful reflective displays and switchable optoelectronic devices.

13.1 Introduction

13.1.1 Overview of the development of cholesteric liquid crystal films

Cholesteric liquid crystals (CLCs), which belong to one-dimensional chiral photonic crystal, have attracted great research interest for many applications during past decades, including displays (Hsiao et al., 2017; Hu et al., 2010), lasers (Uchimura et al., 2010; Wardosanidze et al., 2014), smart windows (Lu et al., 2014), mirrors (Petriashvili et al., 2013), and biosensors (Lee et al., 2016). Due to the Bragg reflection (Arkhipkin et al., 2008, 2007; Kitzerow, 2002; Wu et al., 2012, 2011), the circularly polarized light with the same handedness will be reflected by the CLC. It is known that the total reflectance of a single CLC film cannot exceed 50% for the incident unpolarized light beam (Mitov, 2012). Cholesteric liquid crystal film (CLCF), which is usually fabricated based on CLCs and polymer, has also attracted a plenty of interests in recent years due to its additional flexibility from polymer network compared to CLC (Bae et al., 2011; Choi et al., 2010; Lin et al., 2015; Matranga et al., 2013; McConney et al., 2011). The CLCF is featured by flexibility, full color, single substrate, simplicity, and ease of use, which is a good candidate for flexible reflective displays (Lin and Lin, 2011) and optical sensors such as pH sensor (Shibaev et al., 2002), amino acid sensor (Shibaev et al., 2004), alcohol sensor (Chang et al., 2012), metal ion sensor (Stroganov et al., 2012), humidity sensor (Herzer et al., 2012), amine sensor (Stumpel et al., 2014), and strain sensor (Picot et al., 2013).

Hyper-reflectivity is extremely desirable in a lot of optical and photonic devices. Earlier efforts in obtaining high-reflective CLCs include combining two individual CLC cells with opposite handedness (Makow, 1980), or sandwiching a half-wave plate between two CLCs with the same handedness (Caveney, 1971; Wang et al., 2005), both of which suffer from disadvantages of high weight, insertion attenuation induced by interfaces, and complicated configuration. Recently, a single film that reflects both left- and right-handed (LH and RH) circularly polarized lights was proposed for overcoming aforementioned disadvantages (Mitov and Dessaud, 2006). Then, the same group reported CLCs that were polymerized by a monomer doped with a thermal inverter. The mixture initially led to a RH helical structure when the temperature was high (120 °C) and then changed to a LH helical structure when the temperature was low (60 °C) (Mitov and Dessaud, 2007). Guo et al. (2008, 2011, 2010, 2009) reported a polymer with helical structure through a "wash-out" and "refill" multistep procedure, which was achieved by refilling CLC with RH helical structure into the polymer network with a LH helical structure, where the CLC in polymer network was washed-out first to form the network structure. Next, a photoinduced super-reflective CLC with spatially segregated reflection with the thickness of the cell was successfully realized by constructing two separated homogeneous regions (polymer and CLC) with opposite handedness. The major advantage of these approaches,

which are usually fabricated by polymer network and CLC, is the tunability under external stimuli including temperature, mechanical stress, optical radiation, electric filed, or magnetic field (McConney et al., 2011; Michael et al., 2010). However, for a super-reflective film composed of CLC, the susceptibility to temperature or mechanical stress turns out to be a drawback in specific applications such as static colorful advertisement and laser safety glass, where the premier requirement is stability not the tunability (Görl et al., 2016; Mur et al., 2017; Wood et al., 2016; Zheng et al., 2016).

13.1.2 Overview of the development of blue phase liquid crystal films

Blue phase, which exists between isotropic and chiral nematic phase, is a phase of liquid crystal with self-assembled three-dimensional (3D) nanostructure (Dierking, 2000; Kitzerow et al., 1990). There are three blue phases including BPIII, which is amorphous phase, BPII and BPI, which possess double-twisted cylinders arranging in a simple cubic crystalline structure and body-centered cubic symmetry, respectively. All three blue phases are expected to appear in between the chiral nematic and isotropic phase (Coles and Pivnenko, 2005; Kikuchi et al., 2002). Due to advantages of sub-millisecond response time, optically isotropic dark state, and periodic helical structure on the order of the visible wavelength, blue phase liquid crystal (BPLC) demonstrates a broad application range from field sequential displays (Chen et al., 2010; Kim et al., 2010), full-color reflective displays (Xu et al., 2015; Yan et al., 2013), electrically switching devices (Chen and Wu, 2013; Chen et al., 2013; Cheng et al., 2011; Xu et al., 2014), tunable photonic crystals (Coles and Morris, 2010; Yokoyama et al., 2006), phase modulator optical devices (Lu and Chien, 2010; Yan et al., 2011; Zhu et al., 2012), to soft template for 3D colloidal crystals (Ravnik et al., 2011).

For unpolarized or linearly polarized incident light, the total reflectance of BPLC is limited to 50% because only the circularly polarized incident light with the same handedness of BPLC will be reflected, while the circularly polarized light with opposite handedness will not be reflected. However, the hyper-reflectance of BPLC is desirable and useful for applications such as reflective displays, color filters, lasers, and mirrors. It has been reported that the reflectance can be increased by assembling one BPLC template with another reflective layer with opposite handedness, for example, BPLC or CLC. Castles et al. reported the fabrication of flexible and stretchable BPLC films by refilling liquid crystals into BPLC templates made from reactive mesogens and liquid crystals (Castles et al., 2012, 2014). Jau et al. (2013) studied the electro-optical characteristics of templated BPLC as well as the effects of the helical twisting power of the filling mesogen. Simulations were applied to numerically model the resulting surface anchoring generated from the transfer of blue phase orientational order to polymer matrix surface (Ravnik and Fukuda, 2015). Based on the BPLC template, Guo et al. reported that a double-layer BPLC film reflects both left- and

right-circularly polarized light, where two kinds of double-layer structures had been demonstrated: one was fabricated by R-BPLC template and L-BPLC filling, with reflectance of 25% (Guo et al., 2014); another was fabricated by R-BPLC template and pure L-CLC, with reflectance of 36% (Guo et al., 2008). Both low reflectance from the BPLC film and strong scattering from refractive index mismatch between the BPLC film and BPLC/CLC led to low total reflectance. Therefore, the reflectance of BPLC is still far from satisfaction and hyper-reflectivity in visible light range is highly desirable in practical applications.

13.1.3 Scope of this chapter

In this chapter, both cholesteric and BPLC films with hyper-reflection have been investigated. In the first part, flexible CLC films with high reflectivity and stability are studied, where the films are processed by "wash-out" and "refill" methods to assemble two CLC films with opposite handedness by refilling optical adhesive. Total reflectivity of more than 80% for all of red, green, and blue colors has been obtained. The effects of temperature and mechanical stress on the films have also been investigated, and the demonstration of static flexible displays with vivid colors is shown. For the second part, we demonstrate multilayer BPLC film consisting of two BPLC templates with opposite handedness formed in BPII. The proposed BPLC film is hyper-reflective, electrically switchable, and fast responsive, which can largely improve the performance of sequential colorful reflective displays. It can be also applied in other photonic applications such as switchable optoelectronic components, lasers, and mirrors.

13.2 Hyper-reflection cholesteric liquid crystals polymer films

13.2.1 Fabrication process

In the CLC polymer film fabrication, a mixture of a nematic liquid crystal (NLC, E7, $n_e = 1.74$, and $n_o = 15.2$, from HCCH), chiral dopant (R5011, from HCCH), reactive mesogens (RMs, from HCCH), and photoinitiator (Darocur1173, Sigma-Aldrich) was used. The mixture was sandwiched in a 30-μm-thick cell, fabricated by a pair of indium –tin- oxide glass coated with antiparallelly rubbed polyimide. Figure 13.1 depicts the procedure of the proposed film fabrication. (i) LH and RH chiral templates were fabricated from LC/RM mixtures doped with LH and RH chiral dopants, respectively. (ii) The films were exposed under 15 mW/cm^2 UV light for 15 min for polymerization. (iii) The glass cells were opened and immersed in toluene for 2 min to soak out CLC and unpolymerized monomers, and the left films were then refilled with the
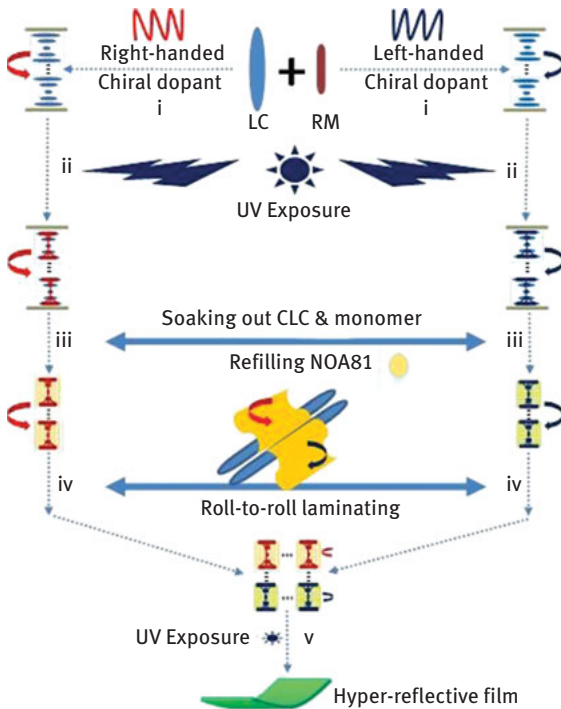
Figure 13.1: Fabrication process of the hyper-reflectivity flexible films based on CLCs. (i) LC/RM mixtures were doped with LH and RH chiral dopants, respectively; (ii) the mixtures were photopolymerized under UV exposure; (iii) the samples were immersed in toluene to soak out CLC and unpolymerized monomers, and then refilled with NOA81; (iv) a roll-to-roll laminating was used to assemble films with opposite handedness; (v) UV exposure for NOA81 polymerization (Li et al., 2017).

optical adhesive NOA 81. (iv) A roll-to-roll laminating process was used to assemble two films with opposite handedness together. (v) The assembled films were exposed to UV light for adhesive polymerization to achieve hyper-reflectivity flexible films.

13.2.2 Hyper-reflection multilayer cholesteric liquid crystals polymer films

The multilayer CLC film consists of two stacked individual CLC films with opposite handedness (layers 1 and 3) and a lamination layer of the isotropic adhesive NOA 81 (layer 2) as shown in the cross-sectional image by scanning electron microscopy (SEM) in Figure 13.2(a). It can be seen that the LH and RH CLC films are firmly combined together through adhesive polymerization. The thicknesses of the CLC films are both fixed at 25 µm which consist of more than 50 periods to provide enough reflection of each color. The thickness of layer 2 is not optimized here. If this
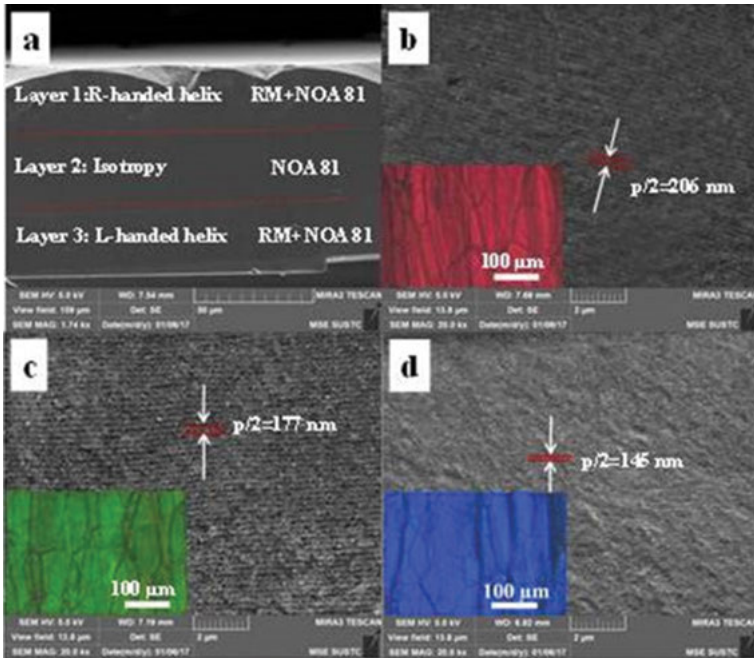
Figure 13.2: SEM images of the composite multilayer CLC films. (a) Cross-sectional SEM image of a multilayer film. SEM image of multilayer CLC film designed for (b) red, (c) green, and (d) blue color, respectively. The insets show the corresponding films observed under a reflective POM (Li et al., 2017).

thickness can be reduced, a reduction in scattering and an increase in reflection are expected. The multilayer CLC films have been designed for red, green, and blue colors, named as sample C1, C2, and C3, respectively, obtained by carefully adjusting the concentrations of the chiral dopants. The pitches (p) of the three-color films are measured to be 412 nm ($p/2 = 206$ nm), 354 nm ($p/2 = 177$ nm), and 290 nm ($p/2 = 145$ nm), respectively, as shown in the SEM images in Figure 13.2(b)–2(d). The insets show the multilayer CLC films with red, green, and blue colors observed under the reflective polarizing optical microscope (POM, Nikon Ti). The typical planar textures of CLC are observed in the fabricated composite films, indicating that the helical structures are preserved in the all-solid films.

In order to obtain the multilayer CLC films with hyper-reflectivity of different colors, the concentrations of LH and RH chiral dopants were carefully adjusted to ensure the reflective central wavelength of two films with opposite handedness were completely superposed. Figure 13.3 demonstrates the optical setup (Figure 13.3(a)) and reflection spectrum measurements of the multilayer CLC films with red, green, and blue colors (C1, C2, and C3), where the reflective wavelength is centered at 645 nm, 554 nm, and 453 nm, respectively (Figure 13.3(b)–3(d)). All the reflection spectra were measured with unpolarized light using a spectrometer (Ocean Optics). For CLCs, the central wavelength of reflection band can be calculated by $\bar{\lambda} = n.p$, where n is the
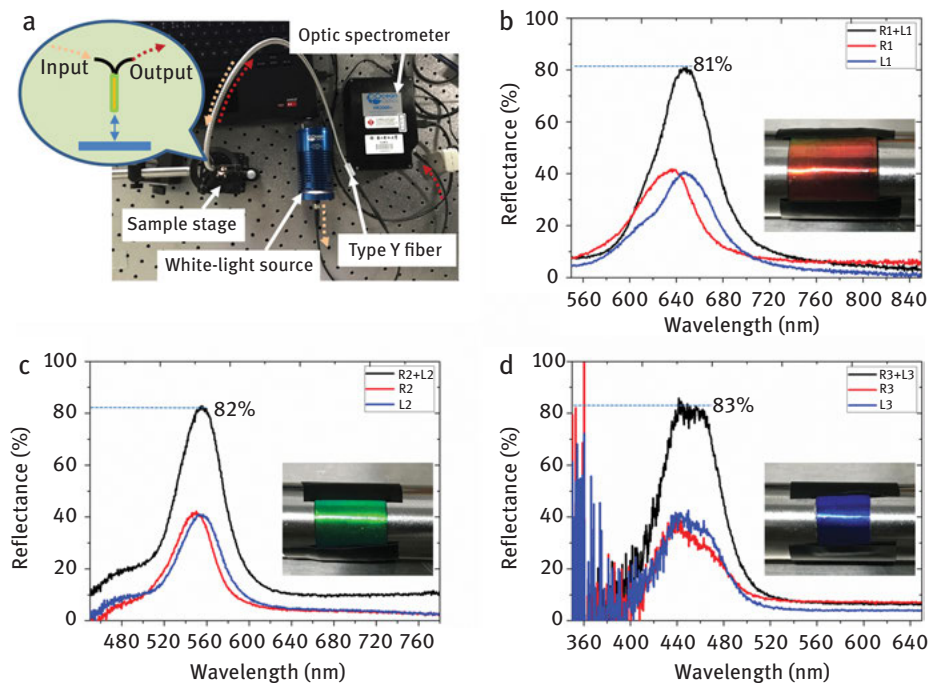
Figure 13.3: Reflectance measurement system and the measured spectra of the multilayer CLC films. (a) Optical setup for reflectance measurement that consists of a white-light source, a type Y fiber, an optical spectrometer and a sample stage. Reflection spectrum measurement of multilayer CLC film refilled by adhesive NOA 81 showing reflective (b) red, (c) green, and (d) blue color, respectively. The blue and red curves represent the reflection spectra of LH and RH CLC films, and the black curves are the reflection spectra of the composite multilayer CLC films. The insets show photo images of CLC films taken under a fluorescent lamp, corresponding to red, green and blue colors, respectively (Li et al., 2017).

average refractive index, and p is the pitch. Herein, the calculated central wavelengths locate at 643 nm, 552 nm, and 452 nm with estimated average refractive index of 1.56 based on SEM measurements (Figures 13.2(b)–13.4(d)), which are highly consistent with the measured spectral results. The maximal central reflectance of each film with one handedness R1~R3 (L1~L3) is 37% (38%), 42% (44%) and 34% (43%), respectively. After laminating the two films with opposite handedness, the maximal reflectance is enhanced to 81%, 82% and 83% at the central wavelength, respectively. Therefore, the fabricated multilayer CLC films possess hyper-reflectivity that is higher than 80% for all three colors. The insets of Figure 13.3(b)–(d) show photos of the multilayer CLC films taken under a fluorescent lamp, illustrating the full color, hyper-reflectivity, and flexible films fabricated based on this method. Compared with the previously reported hyper-reflectivity films fabricated with at least one layer of CLC (Guo et al., 2008, 2011, 2010, 2009; Makow, 1980), the proposed all-solid multilayer CLC films

not only have hyper-reflectivity, but also possess the intrinsic advantages of substrate-free, compatibility, and flexibility. Here, a proposed application of the hyper-reflective color films is demonstrated for static display with vivid colors as shown in Figure 13.4. The patterned films with our university logo are demonstrated showing vivid reflective colors under white light on both a hard glass substrate (Figure 13.4 (a)) and a flexible polyethylene terephthalate substrate (Figure 13.4(b)). Therefore, the proposed all-solid multilayer CLC films with hyper-reflectivity provide potential applications in the fields of advertisements, displays, and wearable devices with low energy consumption.
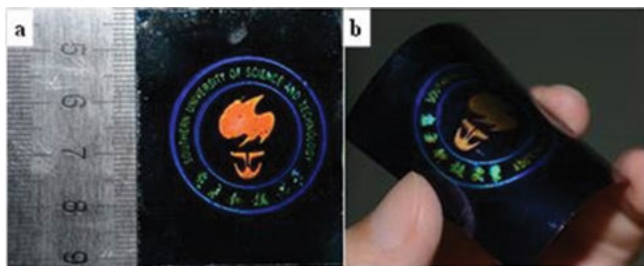
Figure 13.4: The colorful logos fabricated by hyper-reflective CLC films. The university logo was printed on (a) a hard glass substrate and (b) a flexible PET substrate, respectively (Li et al., 2017).

13.3 Blue phase liquid crystal films

13.3.1 Fabrication process

The fabrication process of BPLC polymer film is similar to CLCF. Figure 13.5(a) shows the schematic lattice structures of LH and RH BPII LCs in form of double-twisted cylinders and disclination lines, which are constructed by LH and RH chiral dopant- doped LCs. The LH and RH BPLCs selectively reflect the LH and RH circularly polarized light, respectively. The reflection wavelength is determined by the equation of $\lambda = 2na/\sqrt{(h^2 + k^2 + l^2)}$, where n and a represent the respective average refractive index and lattice constant of BP, and h, k, and l are the Miller indices of a crystal plane (Yan et al., 2013). In our experiment, a left-handed blue phase liquid crystal (L-BPLC) layer and a right-handed blue phase liquid crystal (R-BPLC) layer were fabricated separately, where the Bragg reflection bands were adjusted by the concentrations of the LH and RH chiral dopants. Then, the L-BPLC and R-BPLC templates were obtained after washing out LC and unpolymerized RMs (step I), leaving only the porous polymer networks which retained the lattice structure of BPLC as shown in Figure 13.5(b). The multilayer BPLC film was then achieved by assembling two BPLC templates with opposite handedness together (step II) and refilling with achiral NLC of HTG135200-100
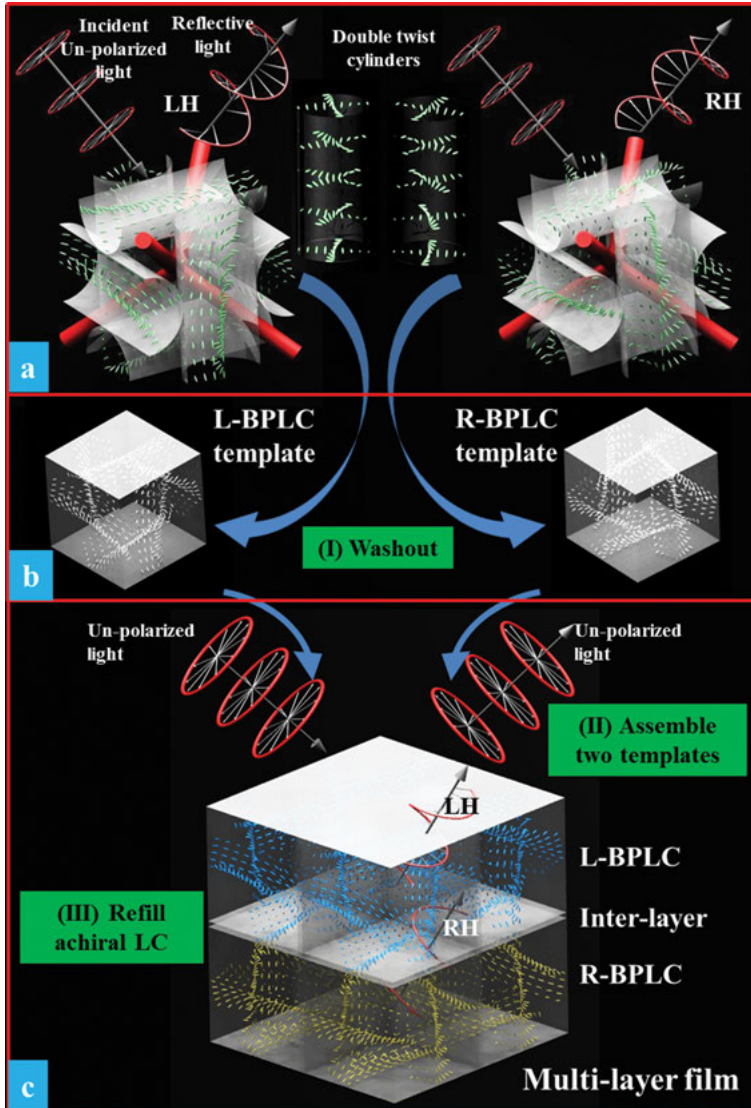
Figure 13.5: (a) Schematic illustration of LH and RH BPII LCs with simple cubic lattice structure. The LC molecules are self-assembled as double-twisted cylinders in BP. The LH- and RH-BPLC could selectively reflect LH and RH circularly polarized light, respectively. (b) (step I) L-BPLC and R-BPLC templates are obtained through immersing BPLC sample in toluene, where the LC molecules and unpolymerized RMs will be washed out. (c) The proposed multilayer film consists of three layers including L-BPLC, R-BPLC, and interlayer in-between. The multilayer BPLC film is achieved by (step II) assembling two BPLC films with opposite handedness together and (step III) then refilling achiral NLC of HTG135200-100 (Hecheng Display, China) (Xu et al., 2018).

(from HCCH) (step III). After LC refilling, BPII could be reformed in both L-BPLC and R-BPLC layers. Figure 13.5(c) shows the proposed three-layer structure of multilayer BPLC films consisting of L-BPLC, R-BPLC and interlayer in-between. Under unpolarized light illumination, the fabricated multilayer BPLC film can reflect LH and RH circularly polarized light simultaneously at the same band if the reflection spectra of L-BPLC and R-BPLC are overlapped, which can therefore increase the reflectance compared with a single-layer BPLC with only one handedness.

Figure 13.6(a) depicts the surface morphology of the single-layer L-BPLC template observed by SEM, and the template cross section is also demonstrated in the inset, indicating a collapsed porous polymer network. Figure 13.6(b) shows the cross-sectional SEM image of the multilayer BPLC film assembled in step II. Two polymer layers, including a 8.7-μm-thick R-BPLC layer and a 7.7-μm-thick L-BPLC layer, are observed. The thicknesses of the L-BPLC and R-BPLC layers are designed to be identical and the difference is due to the washout process and fabrication errors. In addition to the R-BPLC and L-BPLC layers, a 1-μm-gap is found in-between due to the surface roughness of the two BPLC films. After a chiral NLC refilling, the collapsed polymer
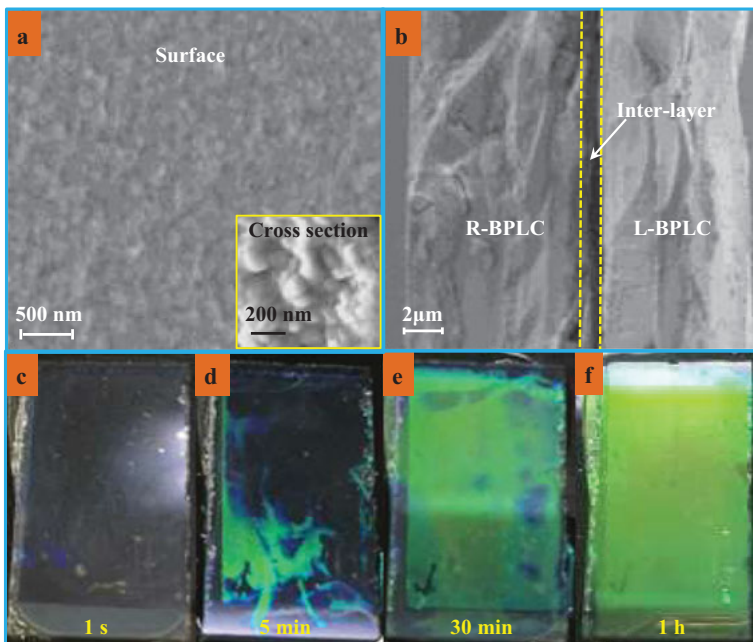
Figure 13.6: (a) The surface morphology of the single-layer L-BPLC template observed by SEM. The cross section is shown in the inset. (b) The cross-sectional SEM image of multilayer BPLC film, where no LCs have been refilled yet. The thickness of R-BPLC, L-BPLC, and interlayer is 8.7 μm, 7.7 μm, and 1 μm, respectively. The photo images captured during refilling process of multilayer BPLC film with central reflective wavelength of 545 nm at time of (c) 1 s, (d) 5 min, (e) 30 min, and (f) 1 h, respectively (Xu et al., 2018).

network becomes BPII again gradually by LC occupation, and the in-between gap is also filled with LC. Figure 13.6(c)–(f) demonstrate the refilling process of multilayer BPLC film with 545 nm central reflective wavelength at 1 s, 5 min, 30 min, and 1 h of refilling time, respectively. It can be seen that the multilayer BPLC template is transparent at the beginning, and shows reflective green color gradually during the refilling process and finally reveals a uniform bright reflective green color.

13.3.2 Hyper-reflection multilayer blue phase liquid crystals polymer films

Figure 13.7(a)–(c) demonstrates the reflection spectra of multilayer BPLC films refilled with achiral NLC corresponding to red, green, and blue reflective colors, respectively. All reflection spectra were measured under unpolarized light using the optical setup of Figure 13.3(a). In order to obtain multilayer BPLC films with hyper-reflectivity of different colors, the chiral dopant concentrations in L-BPLC and R-BPLC were carefully adjusted to ensure the reflective central wavelengths of the two films were superposed. The maximal reflectance of each film LR, LG, LB, (RR, RG, RB) with one handedness is 45% (48%), 43% (47%), and 38% (36%), respectively, at the central reflective wavelength. After assembling the two films together and refilling the achiral NLC, the reflection spectrum of multilayer BPLC film is centered at 650 nm, 550 nm, and 440 nm, with maximal reflectance of 89%, 82%, and 68%, respectively. The insets of Figure 13.7(a)–(c) show photos of multilayer BPLC films taken under a fluorescent lamp, evidencing full color, hyper-reflective films fabricated by this method. Compared with previously reported BPLC films consisting of a BPLC template or BPLC with single handedness achieved in BPI (Ravnik and Fukuda, 2015; Yan et al., 2013) and the BPLC films fabricated by R-BPLC template with L-BPLC filling
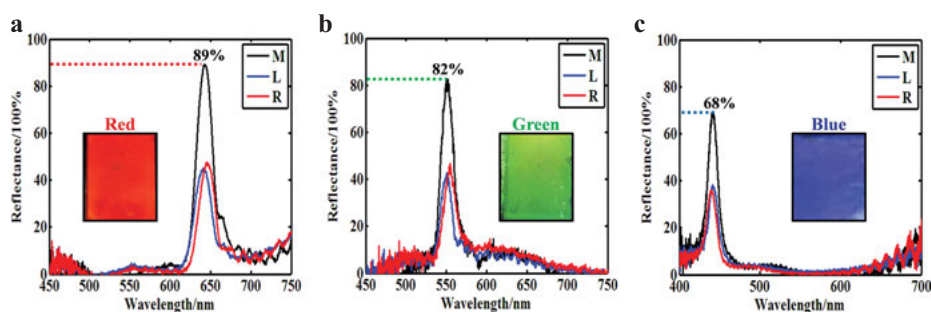
Figure 13.7: Reflection spectra of multilayer BPLC films refilled by NLC to reflective (a) red, (b) green, and (c) blue colors, respectively. The blue and red curves represent the reflection spectra of LH and RH single-layer BPLC films, and the black curves shows the reflection spectra of multilayer BPLC films. The insets show photo images of BPLC films taken under a fluorescent lamp correspondingly (Xu et al., 2018).

(Guo et al., 2014), the proposed multilayer BPLC film consisting of two BPLC templates with opposite handedness in BPII demonstrates distinguished advantage of hyper-reflectivity (2–4 times) over previously reports. As a proof of concept, we successfully demonstrate that the multilayer BPLC films with opposite handedness can dramatically improve the reflectance in red, green, and blue colors.

The optoelectric properties of the multilayer such a BPLC films were explored with external AC electric field. The configuration of such a BPLC film under electric field is depicted in Figure 13.8(a). The optical performance can be discussed in three cases: (i) The L-BPLC and R-BPLC are in the bright state without electric field. However, the achiral NLCs in the interlayer are randomly oriented which will partially reduce the total reflectance of BPLC due to light scattering by disordered NLCs. Therefore, the reflectance is high (68%, 82%, and 89% at 450 nm, 545 nm, and 654 nm, respectively) but not the highest without electric field as shown in Figure 13.8(b). (ii) When the electric field is higher than the threshold of NLC in the interlayer but lower than the threshold of LC in BPLC, the NLC molecules in the interlayer will be uniformly aligned along the electric field, resulting in a small increase in reflectance due to the absence of light scattering. The threshold voltage of NLC in interlayer is lower than that of LC in BPLC because the polymer network of BPLC imposes significant confinement to LC molecules. Herein, the highest reflectances of 72%, 86%, and 94% at 450 nm, 545 nm, and 654 nm are obtained at 1 V/μm (Figure 13.8(b)). (iii) When the applied electric field becomes higher than the threshold of LC in BPLC network, the LC molecules are aligned while the lattice structures of blue phase can be hardly deformed by the electric field. The reduced refractive index difference between aligned LCs and polymers in BPLC thus decreases the reflectance under electric field (Lee et al., 2016). The POM images of the multilayer BPLC films in blue, green, and red reflection colors are demonstrated in various electric field conditions as shown in Figure 13.8(b). When the electric field increases from 1 V/μm to 15 V/μm, the reflectance gradually decreases from 72%, 86%, 94% to 5%, 5%, 4% for blue, green, and red colors, respectively, as illustrated in Figure 13.8(c)–(d) and summarized in Figure 13.8(f). It is worth mentioning that, if the interlayer thickness can be further reduced, the highest reflectance should appear at lower or even zero electric field. The rising and decay times of the multilayer BPLC film in green color are measured to be 0.36 ms, and 0.53 ms, respectively, which are defined as the time required for reflectance to change from 10% to 90% and 90% to 10% with AC electric field on and off (15 V/μm, 1 kHz). The Bragg reflection of multilayer BPLC films also shows hysteresis effect under electric field cycling, similar to that of traditional BPLC (Lin et al., 2015). Therefore, the multilayer BPLC films still retain the intrinsic quality of BPLC that is electrically switchable and of fast response. By stacking two BPII templates with opposite handedness together, the multilayer BPLC films will bring significant enhancement in reflectivity, and therefore improve the performance of fast switchable colorful reflective displays and photonic devices based on BPLCs.
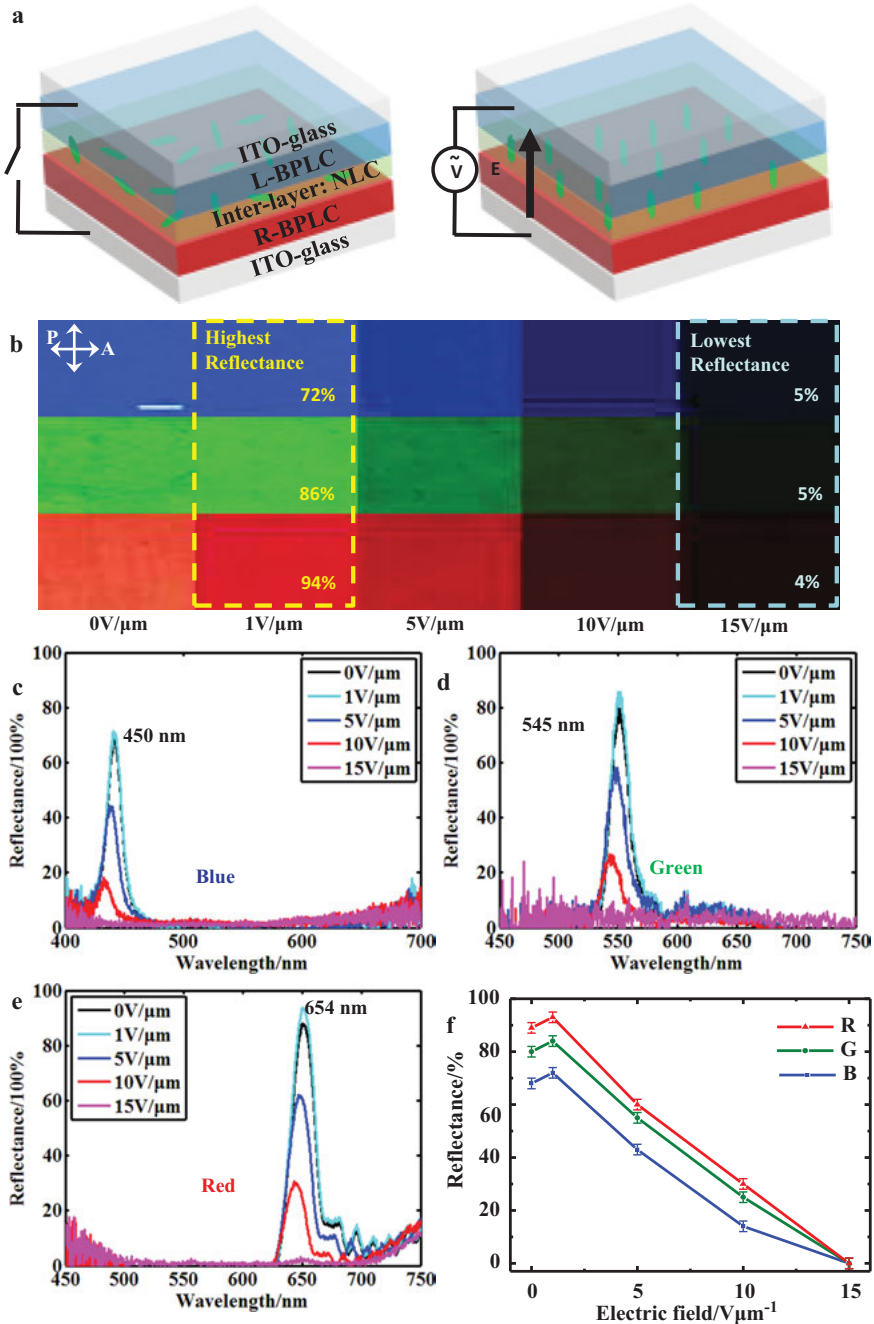
Figure 13.8: (a) The configurations of BPLC film with and without electric field. The BPLC films consist of L-BPLC, interlayer of achiral NLC, and R-BPLC. (b) Reflective POM images of multilayer BPLC films with blue, green, and red colors under increasing electric field. The scale bar is 100 μm. Reflection

13.4 Conclusions

In this chapter, two types of hyper-reflection films, CLC polymer film and BPLC polymer film, have been demonstrated. For he CLC polymer type, hyper-reflectivity and high stability flexible films by refilling the optical adhesive NOA81 into two CLC films with opposite handedness have been fabricated through a "wash-out" and "refill" process. Hyper-reflectivity over 80% for all red, green, and blue colors has been successfully achieved. Compared to non-solid films that are refilled by NLC, the fabricated films discussed in this chapter can maintain the hyper-reflectivity in a broad temperature range (–70–70 °C), and a stress (up to 7.88×10^5 Pa), indicating excellent stability. Colorful flexible static displays with vivid colors on glass/flexible substrates have been demonstrated based on the all-solid multilayer CLC polymer films. These flexible films with hyper-reflectivity, high stability, broad working temperature range, and excellent mechanical stress insensitivity enable potential applications in the fields of flexible reflective displays, advertisements, wearable devices, lasers, smart windows, and colored cladding for a variety of objects. For the BPLC polymer type, hyper-reflective, electrically switchable, multilayer BPLC films have been fabricated based on two BPII templates with opposite handedness refilled with NLC. Hyper-reflectivity of 89%, 82%, and 68% in red, green, and blue reflection colors, respectively, has been achieved. The proposed multilayer BPLC films substantially improve the overall reflection efficiency by 2–4 times higher (in red, green, and blue color, respectively), comparing to previously reported BPLC films. The highest reflectance of 94%, 86%, and 72% in red, green, and blue color has been achieved under 1 V/μm electric field, due to the field-aligned interlayer NLC. The reflectance switching can be achieved by unwinding the refilled NLCs in blue phase templates with electric field. The fast responsive and colorful reflective displays based on the proposed BPLC films have been demonstrated experimentally. This kind of electrically switchable and hyper-reflective BPLC films with submillisecond response time brings significant improvement in performance of colorful reflective displays with high reflectivity. This technology can also be used in switchable optoelectronic devices, lasers, mirrors, and so on.

Figure 13.8 (continued)
spectra of multilayer BPLC films with (c) blue, (d) green, and (e) red colors, respectively. The applied electric fields are 0 V/μm, 1 V/μm, 5 V/μm, 10 V/μm, and 15 V/μm. (f) Relationship of reflectance versus electric field at 450 nm, 545 nm, and 654 nm, respectively, for the BPLC films with blue, green, and red colors (Xu et al., 2018).

References

Arkhipkin, V.G., Gunyakov, V.A., Myslivets, S.A., Gerasimov, V.P., Zyryanov, V.Y., Vetrov, S.Y., Shabanov, V.F. (2008). One-dimensional photonic crystals with a planar oriented nematic layer: temperature and angular dependence of the spectra of defect modes. Journal of Experimental and Theoretical Physics, 106(2), 388–398.

Arkhipkin, V.G., Gunyakov, V.A., Myslivets, S.A., Zyryanov, V.Y., Shabanov, V.F. (2007). Angular tuning of defect modes spectrum in the one-dimensional photonic crystal with liquid-crystal layer. The European Physical Journal E, 24(3), 297–302.

Bae, K.S., Cha, U., Lee, Y.J., Moon, Y.K., Choi, H.C., Kim, J.H., Yu, C.J. (2011). Single pixel transmissive and reflective liquid crystal display using broadband cholesteric liquid crystal film. Optics Express, 19(9), 8291–8296.

Castles, F., Day, F.V., Morris, S.M., Ko, D.H., Gardiner, D.J., Qasim, M.M., Nosheen, S., Hands, P.J.W., Choi, S.S., Friend, R.H. (2012). Blue-phase templated fabrication of three-dimensional nanostructures for photonic applications. Nature Materials, 11(7), 599–603.

Castles, F., Morris, S.M., Hung, J.M.C., Qasim, M.M., Wright, A.D., Nosheen, S., Choi, S.S., Outram, B.I., Elston, S.J., Burgess, C., Hill, L., Wilkinson, T.D., Coles, H.J. (2014). Stretchable liquid-crystal blue-phase gels. Nature Materials, 13, 817–821.

Caveney, S. (1971). Cuticle reflectivity and optical activity in scarab beetles: the role of uric acid. Proceedings of the Royal Society of London. Series B, 178, 205–225.

Chang, C.K., Bastiaansen, C.M.W., Broer, D.J., Kuo, H.L. (2012). Alcohol-responsive, hydrogen-bonded, cholesteric liquid-crystal networks. Advanced Functional Materials, 22(13), 2855–2859.

Chen, K.M., Gauza, S., Xianyu, H.Q., Wu, S.T. (2010). Hysteresis effects in blue-phase liquid crystals. Journal of Display Technology, 6(8), 318–322.

Chen, Y., Wu, S.T. (2013). Electric field-induced monodomain blue phase liquid crystals. Applied Physics Letters, 102(17), 171110.

Chen, Y., Xu, D., Wu, S.T., Yamamoto, S., Haseba, Y. (2013). A low voltage and submillisecond-response polymer-stabilized blue phase liquid crystal. Applied Physics Letters, 102(4), 141116.

Cheng, H.C., Yan, J., Ishinabe, T., Wu, S.T. (2011). Vertical field switching for blue-phase liquid crystal devices. Applied Physics Letters, 98(26), 261102.

Choi, S.S., Morris, S.M., Huck, W.T., Coles, H.J. (2010). Simultaneous red-green-blue reflection and wavelength tuning from an achiral liquid crystal and a polymer template. Advanced Materials, 22(1), 53–56.

Coles, H., Morris, S. (2010). Liquid-crystal lasers. Nature Photonics, 4(10), 676–685.

Coles, H.J., Pivnenko, M.N. (2005). Liquid crystal 'blue phases' with a wide temperature range. Nature, 436(7053), 997–1000.

Dierking, I. (2000). Polymer network–stabilized liquid crystals. Advanced Materials, 12(3), 167–181.

Görl, D., Soberats, B., Herbst, S., Stepanenko, V., Würthner, F. (2016). Perylene bisimide hydrogels and lyotropic liquid crystals with temperature-responsive color change. Chemical Science, 7, 6786–6790.

Guo, J., Wu, H., Chen, F., Zhang, L., He, W., Yang, H., Wei, J. (2010). Fabrication of multi-pitched photonic structure in cholesteric liquid crystals based on a polymer template with helical structure. Journal of Materials Chemistry, 20(20), 4094–4102.

Guo, J.B., Cao, H., Wei, J., Zhang, D., Liu, F., Pan, G.H., Zhao, D.Y., He, W.L., Yang, H. (2008). Polymer stabilized liquid crystal films reflecting both right- and left-circularly polarized light. Applied Physics Letters, 93(20), 201901.

Guo, J.B., Chen, F.J., Qu, Z.J., Yang, H., Wei, J. (2011). Electrothermal switching characteristics from a hydrogen-bonded polymer network structure in cholesteric liquid crystals with a

double-handed circularly polarized light reflection band. The Journal of Physical Chemistry B, 115(5), 861–868.

Guo, J.B., Wang, J., Zhang, J.Y., Shi, Y., Wang, X.W., Wei, J. (2014). Photo- and thermal switching of blue phase films reflecting both right- and left-circularly polarized light. Journal of Materials Chemistry C, 2(43), 9159–9166.

Guo, J.B., Yang, H., Li, R., Ji, N., Dong, X.M., Wu, H., Wei, J. (2009). Effect of network concentration on the performance of polymer-stabilized cholesteric liquid crystals with a double-handed circularly polarized light reflection band. The Journal of Physical Chemistry C, 113(37), 16538–16543.

Herzer, N., Guneysu, H., Davies, D.J.D., Yildirim, D., Vaccaro, A.R., Broer, D.J., Bastiaansen, C.W.M., Schenning, A.P.H.J. (2012). Printable optical sensors based on h-bonded supramolecular cholesteric liquid crystal networks. Journal of the American Chemical Society, 134(18), 7608–7611.

Hsiao, Y.C., Yeh, E.R., Lee, W. (2017). Advanced color-reflective dual-frequency cholesteric liquid crystal displays and the driving matrix. Molecular Crystals and Liquid Crystals, 644(1), 12–18.

Hu, W., Zhao, H.Y., Song, L., Yang, Z., Cao, H., Cheng, Z.H., Liu, Q., Yang, H. (2010). Electrically controllable selective reflection of chiral nematic liquid crystal/chiral ionic liquid composites. Advanced Materials, 22(4), 468–472.

Jau, H.C., Lai, W.M., Chen, C.W., Lin, Y.T., Hsu, H.K., Chen, C.H., Wang, C.C., Lin, T.H. (2013). Study of electro-optical properties of templated blue phase liquid crystals. Optical Materials Express, 3(9), 1516–1522.

Kikuchi, H., Yolota, M., Hisakado, Y. (2002). Polymer-stabilized liquid crystal blue phases. Nature Materials, 1(1), 64–68.

Kim, M., Kang, B.G., Kim, M.S., Kim, M.K., Kumar, P., Lee, M.H., Kang, S.W., Lee, S.H. (2010). Measurement of local retardation in optically isotropic liquid crystal devices driven by in-plane electric field. Current Applied.

Kitzerow, H. (2002). Tunable photonic crystals. Liquid Crystals Today, 11(4), 3–7.

Kitzerow, H.S., Crooker, P.P., Kwok, S.L., Xu, J., Heppke, G. (1990). Dynamics of blue-phase selective reflections in an electric field. Physical Review A, 42(6), 3442–3448.

Lee, H.G., Munir, S., Park, S.Y. (2016). Cholesteric liquid crystal droplets for biosensors. ACS Applied Materials & Interfaces, 8(39), 26407–26417.

Li, Y., Liu, Y.J., Dai, H.T., Zhang, X.H., Luo, D., Sun, X.W. (2017). Flexible cholesteric film with super-reflectivity and high stability based on multi-layer helical structure. Journal of Materials Chemistry C, 5(41), 10828–10833.

Lin, J.D., Chu, C.L., Lin, H.Y., You, B., Horng, C.T., Huang, S.Y., Mo, T.S., Huang, C.Y., Lee, C.R. (2015). Wide-band tunable photonic bandgaps based on nematic-refilling cholesteric liquid crystal polymer template samples. Optical Materials Express, 5(6), 1419–1430.

Lin, Y.T., Lin, T.H. (2011). Cholesteric liquid crystal display with wide viewing angle based on multi-domain phase-separated composite films. Journal of Display Technology, 7(7), 373–376.

Lu, H., Xu, W., Song, Z., Zhang, S., Qiu, L., Wang, X., Zhang, G., Hu, J., Lv, G. (2014). Electrically switchable multi-stable cholesteric liquid crystal based on chiral ionic liquid. Optics Letters, 39(24), 6795–6798.

Lu, S.Y., Chien, L.C. (2010). Electrically switched color with polymer-stabilized blue-phase liquid crystals. Optics Letters, 35(4), 562–564.

Makow, D.M. (1980). Peak reflectance and color gamut of superimposed left-and right-handed cholesteric liquid crystals. Applied Optics, 19(8), 1274–1277.

Matranga, A., Baig, S., Bolan, J., Newton, C., Taphouse, T., Wells, G., Kitson, S. (2013). Biomimetic reflectors fabricated using self-organising, self-aligning liquid crystal polymers. Advanced Materials, 25(4), 520–523.

McConney, M.E., Tondiglia, V.P., Hurtubise, J.M., Natarajan, L.V., White, T.J., Bunning, T.J. (2011). Thermally induced, multicolored hyper-reflective cholesteric liquid crystals. Advanced Materials, 23(12), 1453–1457.

Michael, E., Tondiglia, V.P., Hurtubise, J.M., White, T.J., Bunning, T.J. (2010). Photoinduced hyper-reflective cholesteric liquid crystals enabled via surface initiated photopolymerization Mcconney. Chemical Communications, 47(1), 505–507.

Mitov, M. (2012). Cholesteric liquid crystals with a broad light reflection band. Advanced Materials, 24(47), 6260–6276.

Mitov, M., Dessaud, N. (2006). Going beyond the reflectance limit of cholesteric liquid crystals. Nature Materials, 5(5), 361–364.

Mitov, M., Dessaud, N. (2007). Cholesteric liquid crystalline materials reflecting more than 50% of unpolarized incident light intensity. Liquid Crystals, 34(2), 183–193.

Mur, M., Sofi, J.A., Kvasić, I., Mertelj, A., Lisjak, D., Niranjan, V., Muševič, I., Dhara, S. (2017). Magnetic-field tuning of whispering gallery mode lasing from ferromagnetic nematic liquid crystal microdroplets. Optics Express, 25(2), 1073–1083.

Petriashvili, G., Japaridze, K., Devadze, L., Zurabishvili, C., Sepashvili, N., Ponjavidze, N., Santo, M.P.D., Matranga, M.A., Hamdi, R., Ciuchi, F., Barberi, R. (2013). Paper like cholesteric interferential mirror. Optics Express, 21(18), 20821–20830.

Picot, O.T., Dai, M., Billoti, E., Broer, D.J., Peijs, T., Bastiaansen, C.W.M. (2013). A real time optical strain sensor based on a cholesteric liquid crystal network. RSC Advances, 3(41), 18794–18798.

Ravnik, M., Alexander, G.P., Yeomans, J.M., Žumer, S. (2011). Three-dimensional colloidal crystals in liquid crystalline blue phases. Proceedings of the National Academy of Sciences of the United States of America, 108(13), 5188–5192.

Ravnik, M., Fukuda, J. (2015). Templated blue phases. Soft Matter, 11(43), 8417–8425.

Shibaev, P.V., Madsen, J., Genack, A.Z. (2004). Lasing and narrowing of spontaneous emission from responsive cholesteric films. Chemistry of Materials, 16(8), 1397–1399.

Shibaev, P.V., Schaumburg, K., Plaksin, V. (2002). Responsive chiral hydrogen-bonded polymer composites. Chemistry of Materials, 14(3), 959–961.

Stroganov, V., Ryabchun, A., Bobrovsky, A., Shibaev, V. (2012). A novel type of crown ether-containing metal ions optical sensors based on polymer-stabilized cholesteric liquid crystalline films. Macromolecular Rapid Communications, 33(21), 1875–1881.

Stumpel, J.E., Wouters, C., Herzer, N., Ziegler, J., Broer, D.J., Bastiaansen, C.W.M., Schenning, A.P.H.J. (2014). An optical sensor for volatile amines based on an inkjet-printed, hydrogen-bonded, cholesteric liquid crystalline film. Advanced Optical Materials, 25(9), 459–464.

Uchimura, M., Watanabe, Y., Araoka, F., Watanabe, J., Takezoe, H., Konishi, G.I. (2010). Development of laser dyes to realize low threshold in dye-doped cholesteric liquid crystal lasers. Advanced Materials, 22(40), 4473–4478.

Wang, J.H., Song, M.H., Park, B., Nishimura, S., Toyooka, T., Wu, J.W., Takanishi, Y., Ishikawa, K., Takezoe, H. (2005). Electro-tunable optical diode based on photonic bandgap liquid-crystal heterojunctions. Nature Materials, 4(5), 383–387.

Wardosanidze, Z.V., Chanishvili, A., Petriashvili, G., Chilaya, G. (2014). Cholesteric liquid crystal holographic laser. Optics Letters, 39(4), 1008–1010.

Wood, S.M., Castles, F., Elston, S.J., Morris, S.M. (2016). Wavelength-tuneable laser emission from stretchable chiral nematic liquid crystal gels via in situ photopolymerization. RSC Advances, 6(38), 31919–31924.

Wu, X., Yu, L., Cao, H., Guo, R., Li, K., Cheng, Z., Wang, F., Yang, Z., Yang, H. (2011). Wide-band reflective films produced by side-chain cholesteric liquid-crystalline elastomers derived from a binaphthalene crosslinking agent. Polymer, 52(25), 5836–5845.

Wu, X.J., Cao, H., Guo, R.W., Li, K.X., Wang, F.F., Gao, Y.Z., Yao, W.H., Zhang, L.Y., Chen, X.F., Yang, H. (2012). Influence of interim alkyl chain length on phase transitions and wide-band reflective behaviors of side-chain liquid crystalline elastomers with binaphthalene crosslinkings. Macromolecules, 45(13), 5556–5566.

Xu, D., Yan, J., Yuan, J., Peng, F., Chen, Y., Wu, S.T. (2014). Electro-optic response of polymer-stabilized blue phase liquid crystals. Applied Physics Letters, 105(1), 011119.

Xu, X.W., Liu, Z., Liu, Y.J., Zhang, X.H., Zheng, Z.G., Luo, D., Sun, X.W. (2018). Electrically switchable, hyper-reflective blue phase liquid crystals films. Advanced Optical Materials, 6(3), 1700891.

Xu, X.W., Zhang, X.W., Luo, D., Dai, H.T. (2015). Low voltage polymer-stabilized blue phase liquid crystal reflective display by doping ferroelectric nanoparticles. Optics Express, 23(25), 32267–32273.

Yan, J., Li, Y., Wu, S.T. (2011). High-efficiency and fast-response tunable phase grating using a blue phase liquid crystal. Optics Letters, 36(8), 1404–1406.

Yan, J., Wu, S.T., Cheng, K.L., Shiu, J.W. (2013). A full-color reflective display using polymer-stabilized blue phase liquid crystal. Applied Physics Letters, 102(8), 081102.

Yokoyama, S., Mashiko, S., Kikuchi, H., Uchida, K., Nagamura, T. (2006). Laser emission from a polymer-stabilized liquid-crystalline blue phase. Advanced Materials, 18(1), 48–51.

Zheng, Z.G., Li, Y., Bisoyi, H.K., Wang, L., Bunning, T.J., Li, Q. (2016). Three-dimensional control of the helical axis of a chiral nematic liquid crystal by light. Nature, 531(7594), 352–356.

Zhu, G., Li, J.N., Lin, X.W., Wang, H.F., Hu, W., Zheng, Z.G., Cui, H.Q., Shen, D., Lu, Y.Q. (2012). Polarization-independent blue-phase liquid-crystal gratings driven by vertical electric field. Journal of the Society for Information Display, 20(6), 341–346.

V. Manjuladevi, Raj Kumar Gupta

14 Ultrathin films of nanomaterials: a lyotropic liquid crystalline system and its sensing application

Abstract: The ultrathin films of nanomaterials provide remarkable features that can be potentially employed for efficient device fabrication. In this chapter, an overview of ultrathin films of nanomaterials at different interfaces, along with their sensing capabilities, is discussed. From the symmetry point of view, the ultrathin films and sensing applications of the nanoparticles with spherical geometry (e.g. amphiphilic gold and TiO_2 nanoparticle), one-dimensional system (single-walled carbon nanotube) and two-dimensional systems (functionalized graphene) are highlighted.

14.1 Introduction

Liquid crystals can be considered as a new state of matter that can exhibit intermediate phases (mesophases) between highly ordered crystalline and a disordered liquid phases. These mesophases can be classified by ordering of the molecules or symmetry of the medium. The mesophases appear due to change in temperature, concentration, pH, and ion contents. In general, thermotropic liquid crystals exhibit mesophases that are dependent on temperature, whereas the mesophases of lyotropic liquid crystals appear due to a change in concentration. There are several examples of lyotropic liquid crystals available in nature, namely, biomembranes, protein aggregates, vesicles, soap, detergent, and cosmetics. A simple lyotropic system can be developed in laboratory by dissolving surfactant molecules in water. The surfactant in aqueous medium shows different structure of the aggregates as a function of concentration of the molecules (Pershan, 1982). These surfactants are usually amphiphilic in nature with a very strong polar group. Such molecules dissolve in the water medium and form various stable three-dimensional (3D) structures as a function of concentration of the surfactant molecules. The 3D structures regulate the physicochemical properties of the medium that can be considered as mesophases. A suitable class of amphiphilic molecules anchor to the water surface to form a stable monolayer. These monolayer exhibit a variety of surface phases as a function of surface density of the molecules. The phase transitions in such monolayer system can be either weakly first order

or second order in nature (Pershan, 1982). The stable monolayer system at the air–water (A/W) interface can be considered as a lyotropic system (Hiltrop, 1994).

The molecules in a single layer are constrained to the two-dimensional smooth surface of aqueous medium is popularly known as Langmuir monolayer. Generally, amphiphilic molecules with a proper balance in hydrophilicity and hydrophobicity can adsorb at the A/W interface to yield a stable layer of molecules. The surface density of the molecules can be increased and surface pressure is recorded as a function of surface density. The surface pressure (π) is defined as change in surface tension due to presence of amphiphilic molecules on the water surface (y) with reference to pure water subphase without the molecules (y_o) i.e., $\pi = y_o - y$. A variation of π as a function of area occupied by each molecules in the monolayer (A) at a given temperature is known as isotherm (Gupta, 2015; Manjuladevi, 2015). The isotherm reveals the surface phases and the phase transitions during the occurrence of such phases. There are numerous materials that can form stable Langmuir monolayer and exhibit a variety of surface phases. These surface phases are largely dependent on nature of intermolecular and molecule-water interactions. Therefore, by altering the chemistry of the molecules, different surface phases may occur. Table 14.1 shows the list of molecules that can form Langmuir monolayer and exhibit interesting surface phases.

Table 14.1: List of materials forming stable Langmuir monolayer.

Sl no	Materials	References
1	Fatty acids	(Finer and Phillips, 1973; Overbeck and Moebius, 1993; Schwartz and Knobler, 1993; Bibo and Peterson, 1990; Durbin et al., 1994)
2	Phospholipids	(Gopal and Lee, 2001; Dufrêne et al., 1997; Moraille and Badia, 2002)
3	Liquid crystals	(de Mul and Mann, 1994; Gupta and Manjuladevi, 2012; Giner et al., 2009; Gupta et al., 2012; Karthik et al., 2014)
4	Cholesterol and derivatives	(Takano et al., 1997; Berring et al., 2005; Lafont et al., 1998; Gupta and Suresh, 2004)
5	Polymers	(Gaines, 1991; Kim and Swager, 2001; Bjørnholm et al., 1998)
6	Nanomaterials	(Gupta et al., 2008a; Santhanam et al., 2003; Feng et al., 2003b; Jehoulet et al., 1992)

The most commonly studied molecules in this field are fatty acids. The monolayer of fatty acids behaves classically on the two-dimensional surface. The thermodynamics of the system have been studied and phase diagrams have been constructed.

The phases were identified based on positional and orientational ordering of the head-group and tail-group of the molecules. There are 17 different surface phases of Langmuir monolayer of fatty acid reported in literature (Kaganer et al., 1999). The Langmuir monolayer can also serve as a model membrane in the biological system. A large number of biological molecules ranging from normal fatty acids to complicated protein molecules were studied by forming their Langmuir monolayer. The study on Langmuir monolayer of technologically important polymers, liquid crystal molecules, and nano-materials can provide useful insight regarding their properties when employed as thin films for device fabrication. The Langmuir monolayer can be transferred onto solid substrates by a vertical dipping mechanism known as Langmuir–Blodgett (LB) technique. The LB technique ensures not only the surface phase of the monolayer but also the number of layers to be deposited onto the solid substrates. The technique is simple and can be extended to mass scale production at the industry level. However, there are certain challenges in LB technique. Due to weak physical interaction between the molecules and substrate, often LB deposition technique supports only one layer of film deposition. Due to a difference in thermodynamical condition from water to substrate, the molecules rearrange onto the substrate to minimize the overall surface energy (Mitsuya, 1991). These challenges can be resolved by addressing the intermolecular and molecule-substrate interactions. The molecules of technological importance can be dispersed in an organic matrix that can yield a stable Langmuir monolayer and uniform LB films at different interfaces.

Ultrathin films have shown tremendous potential for industrial applications. The reduction in the dimension of bulk material and approaching to a limit of two-dimensional (2D) system by fabricating ultrathin films of the material provides a remarkable increase in surface-to-volume (SV) ratio as compared to the bulk material. Such huge increase in SV ratio increases the activities of the material enormously and thereby the material properties, e.g. catalysis, reactivity, and adhesion, will be significantly different compared to the bulk. The most important aspect of ultrathin film is that the molecular state can be controlled during the deposition process. This leads to the development of material engineering wherein electrical and optical properties can be controlled by altering the molecular state in the ultrathin films. Among different thin film deposition techniques, the ultrathin film deposition through Langmuir–Blodgett (LB) technique is quite popular. LB technique provides opportunity to deposit ultrathin film on any non-hygroscopic solid substrate with a control over the surface density and the number of layers to be deposited. However, in order to deposit LB film of any material, a stable Langmuir monolayer of the material should be obtained at the air–water (A/W) interface (Gaines, 1966; Schwartz, 1997; Zasadzinski et al., 1994).

The stability of Langmuir monolayer is largely dependent on the amphiphilic characteristic of the molecules. However, there are several studies which indicate that even purely hydrophobic materials, e.g. polymers, nanoparticles, and carbon nanotubes, can form a stable Langmuir monolayer. Such systems may attain stability

due to a balance between attractive van der Waals interaction and steric repulsion between the moiety (Broniatowski et al., 2004; Langevin and Monroy, 2010; Paso et al., 2008; Tabe et al., 2002). The LB films of such hydrophobic materials can be deposited on solid substrate and their application can be explored.

14.2 Langmuir monolayer of amphiphilic gold nanoparticles at A/W interface

The field of nanoscience and nanotechnology is growing rapidly due to fascinating basic science research and their potential for technological applications. In this chapter, we will discuss briefly about the Langmuir film (LF) and LB films of nanoparticles, nanotubes, and graphene. There are few studies on Langmuir monolayer and LB film of nanomaterials. These are listed in Table 14.1. In 1993 Giersig and Mulvaney reported the formation of ordered monolayer of gold nanoparticles fabricated onto carbon-coated copper grid of electron microscope through electrophoretic deposition technique (Giersig and Mulvaney, 1993). They found monolayer domains for a large length scale (~of few hundred of μm). The nanoparticles of mean size 14.1 nm were found to arrange on a hexagonal lattice in the monolayer domains. In order to form large monodomains of single layer of gold nanoparticles with a control over the interparticle separation, efforts have been invested by altering the organic ligands of the nanoparticles and studying its Langmuir and LB films at different interfaces. In 1994, Dabbousi et al. (Dabbousi et al., 1994) have deposited LB films of CdSe nanoparticles on various substrates by forming the traditional LF of the material at A/W interface. They found that the absorption and luminescence properties of the LB films of CdSe remain same as that of nanoparticles in free state. This indicated that though the particles were assembled in a closed pack hexagonal form in the LB film, there was no influence of interparticle separation on their physical properties. The group of Heath and Collier (Collier et al., 1997; Markovich et al., 1998) have reported the formation of LF of purely hydrophobic silver nanoparticles at the A/W interface and observed a quantum interference between the particles on changing interparticle separation during compression of the LF. As a consequence, metal-insulator (MI) transition in the LF of hydrophobic silver nanoparticles at the A/W interface was observed. As the separation between the surface of the metal core is reduced from 1.2 nm to 0.5 nm, the linear as well as non-linear optical properties revealed the evidence of both classical and quantum coupling phenomena. Whenever the separation was reduced below 0.5 nm, a sharp insulator-metal transition was observed. The MI transition was reversible on increasing/decreasing the interparticle separation (Collier et al., 1997). These studies have laid the foundation for controlling the physical properties of ultrathin films of nanoparticles through classical and quantum coupling by altering the interparticle separation. Interparticle separation became one of the important criteria for

altering the physicochemical properties. Other parameters could be charging energy of the particles, strength of interaction between the particle and symmetry of lattice formed by the particles. All these parameters can be precisely maneuvered in Langmuir monolayer at the A/W interface. The interparticle separation can be controlled by altering the area available for the monolayer between the compressing barriers in a Langmuir trough. The interparticle interaction can be manipulated by attaching suitable ligands encapsulating the nanoparticles and altering the ambient for the LF. The lattice parameter can be changed by altering shape and size of the nanoparticles and forming the LF at the A/W interface. Among all the above parameters, it is essential that the nanoparticles should disperse on water surface and form stable LF at A/W interface. Traditionally, amphiphilic molecules with a proper balance between the hydrophobic and hydrophilic parts can spread and form a stable LF. There were few attempts for obtaining the stability of LF of nanoparticles at the A/W interface. In 2003, Swami et al. formed a mixed monolayer of hydrophobic gold nanoparticle and octadecanol. The reported isotherms show the signature of instability that may be due to non-mixing nature of octadecanol and the hydrophobic gold nanoparticles (Swami et al., 2003). The LF of hydrophobic PbS nanoparticles at the A/W interface was reported to be compressible only till 4.5 mN/m (Greene et al., 2003). Similarly, there were few other reports on LF of purely hydrophobic nanoparticles. In 2004, Fukuto et al. reported the formation of LF of amphiphilic gold nanoparticles at the A/W interface. The monolayer was compressible only till 5 mN/m and thereafter it undergoes a transition to bilayer (Fukuto et al., 2004). In 2008, Gupta et al. chemically synthesized amphiphilic gold nanoparticles (AGNs) with a core diameter of 5.5 ± 1 nm. The particles were given amphiphilic nature by chemically functionalizing the gold surface using mercapto-1-undecanol. ^{1}H-NMR analysis of AGNs indicated the presence of mercapto-1-undecanol and hexanethiol moieties in 2:1 ratio. This composition of the organic ligands was found to be optimum for providing suitable amphiphilicity to the AGNs for forming a stable Langmuir monolayer at the A/W interface (Gupta et al., 2008b). The chemical structure of the AGN along with TEM image is shown in Figure 14.1. The Langmuir monolayer of AGNs at the A/W interface was formed and the surface pressure (π) – area per particle (A_p) was recorded at different temperature.

The isotherms corresponding to low temperature clearly indicate a first-order phase transition from a low-ordered liquid (L_1) phase to high-ordered liquid (L_2) phase on increasing the surface density. The plateau corresponding to the coexistence of the two phases can be observed from the isotherm (I + II). The surface pressure rises monotonically and sharply on further compression of the film till it collapses at around 35 nm^2. The system behaved classically and, therefore, the thermodynamical analysis was possible. The transition temperature for L_1-L_2 phase transition rises on increasing the temperature of the isotherms. The coexistence region corresponding to L_1-L_2 phase transition shrinks and finally vanishes above 28.4 °C. This temperature can be considered as critical temperature for L_1-L_2 phase transition. Surprisingly, in the temperature range 29.4 °C ≤ T ≤ 36.3 °C, the L1 phase undergoes a transition to bilayer of L2 phase
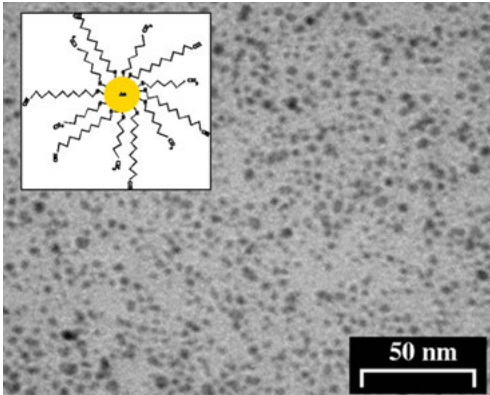
Figure 14.1: Transmission electron microscope image of AGNs spread over carbon evaporated copper grid. The inset shows structure of a AGN.
[Reprinted with permission (Gupta et al., 2008b).]
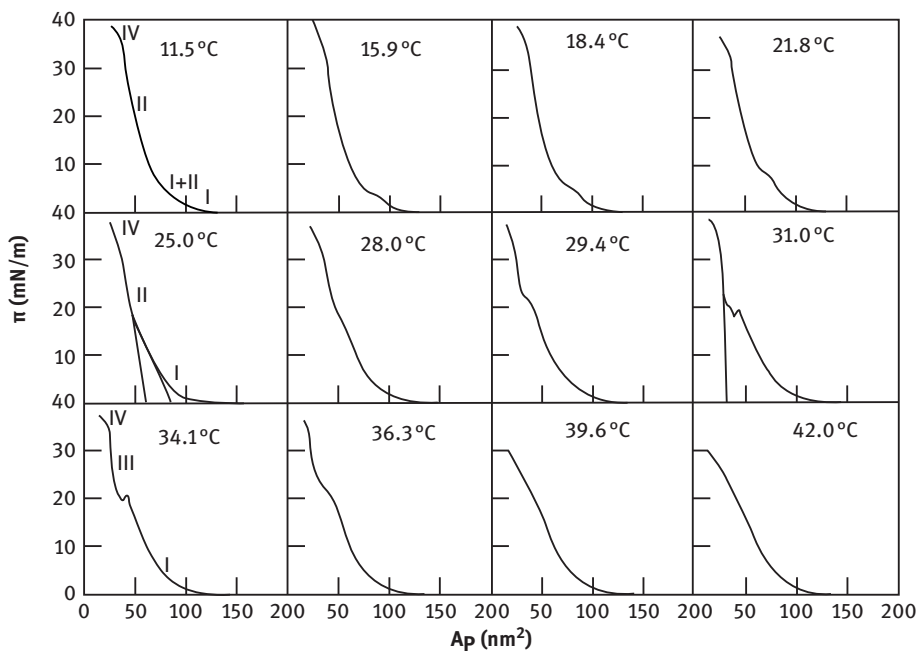
Figure 14.2: Surface pressure (π) – area per particle (A_p) isotherms of the AGNs at different temperature. The symbols I, II, III and IV are used to represent low-ordered liquid (L_1), high-ordered liquid (L_2), bilayer (Bi) phases and collapsed state, respectively. The extrapolated lines in the isotherms corresponding to 25 °C and 31 °C are shown to indicate the area occupied by each particles in those phases.
[Reprinted with permission (Gupta et al., 2008b).]

before approaching toward the usual collapsed state. These phases were characterized by Brewster angle microscopy and Fourier transformed infrared spectroscopy. Based on the results, a phase diagram showing the important phases was proposed. The phase diagram is shown in Figure 14.3.
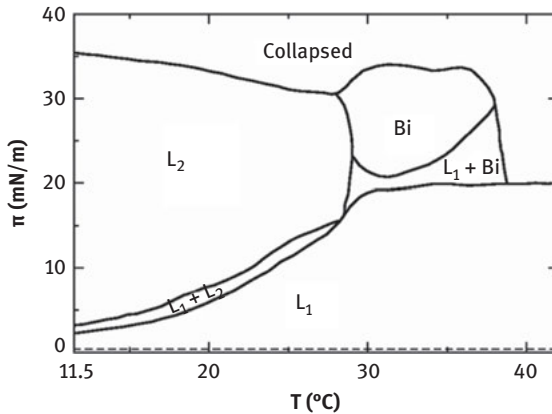
Figure 14.3: Phase diagram showing the phases of Langmuir monolayer of AGNs at A/W interface. The L_1, L_2, and Bi are low-ordered, high-ordered, and bilayer of L_2 phases, respectively. The coexistence of L_1-gas phase was observed even at very large area per particle and zero surface pressure. This is shown by the horizontal dashed line. The coexistence of the phases is shown by " +" symbol. [Reprinted with permission (Gupta et al., 2008b).]

This study indicated that the Langmuir monolayer of nanoparticles can exhibit a variety of phases as it was observed in the case of fatty acid. Such phases of the Langmuir monolayer of nanoparticle appear due to an interplay of interparticle interactions that is essentially governed by the nature of the core, functional group of the ligands encapsulating the particles, interparticle separation and the 2D aggregation and nucleation. These phases can be transferred onto substrates by the highly controlled LB deposition technique. The LB films of gold nanoparticles can find application in plasmonic-based devices and biosensors.

14.3 Langmuir and LB films of TiO$_2$ nanoparticles at different interfaces

The nanoparticles of titanium dioxide (TiO$_2$) are one of the widely studied materials due to their interesting physicochemical properties. They can be employed as the functional material for sensors, solar cells, and photocatalytic devices (Sang et al., 2014).

Because of the efficient catalytic behavior, stability, and a good tolerance at high temperature, TiO_2 nanoparticles can be used as the functional material for gas/chemical sensors. The mixed phase of TiO_2 nanoparticles (consists of anatase and rutile phases) is considered to be more efficient for sensing application as there is a large possibility of separating electron and holes at the interface between these two phases. The mixed phase of TiO_2 nanoparticles can create catalytic hotspot at the rutile-anatase interface. An ultrathin film of mixed phase of TiO_2 nanoparticles can exhibit a very high surface density of such catalytic hotspots. The sensing performance of ultrathin film of TiO_2 nanoparticles is expected to be larger than a thick film. In 2015, Choudhary et al. (Choudhary et al., 2015) reported their studies on Langmuir and LB films of mixed phase of TiO_2 nanoparticles having a composition of anatase:rutile as 80:20. The nanoparticles do not possess any organic ligands so as to have amphiphilic characteristics. The TiO_2 nanoparticles were spread on A/W interface and the surface manometry was conducted. The surface pressure (π) – area (A) isotherm of the LF of TiO_2 nanoparticles at A/W interface was recorded (Figure 14.4). The trend of the isotherm appears classically similar to any standard amphiphilic molecules. The surface pressure remains zero at very large area resembling the gas phase. The surface pressure rises very slowly till the film is compressed at around 450 cm^2. This is loose-packing (LP) phase of LF of TiO_2 nanoparticles. On further compression, the surface pressure rises rapidly till the film is compressed completely in the trough. This is the closed-packing (CP) phase of the LF of TiO_2 nanoparticles. There is no evidence of collapse of the LF from the isotherm. The maximum surface pressure was found to be 24 mN/m. The variation of in-plane isothermal elastic modulus (E) as a function of area shows a sharp rise at the onset of the CP phase. The maximum value of E was found to be 22 mN/m at around 300 cm^2. The trend of E reversed on further compression indicating an initiation of collapse state. The stability of the LF of TiO_2 nanoparticles was probed by isocycle measurements and it was reported that the LF was stable and reversible. Though the TiO_2 nanoparticles do not exhibit any amphiphilic nature, the stability was attained due to attractive van der Waals interaction and steric repulsion between the particles. Several reports in literature also indicate that the stability of LF of non-amphiphilic nanoparticles can be achieved by the above-mentioned reason (Collier et al., 1997; Heath et al., 1997; Lin et al., 2007; Markovich et al., 1998; Poonia et al., 2014).

The LB films of TiO_2 nanoparticles were deposited onto atomically smooth Si/SiO$_2$ substrates at different target surface pressures and surface morphology was obtained using field emission scanning electron microscope (FESEM). The LB films of TiO_2 nanoparticles deposited in LP and CP phases are shown in Figure 14.5(a) and (b), respectively.
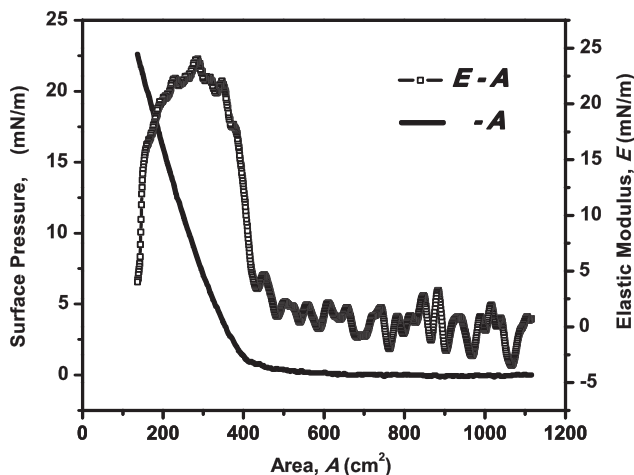
Figure 14.4: Surface pressure (π) – area (A) isotherm and in-plane elastic modulus (E) as a function of A of LF of mixed phase of TiO_2 nanoparticles.
[Reprinted with permission, (Choudhary et al., 2015).]

14.3.1 Ethanol gas sensing using LB film of TiO_2 nanoparticle

The FESEM images of the LB films show ultrathin films of the TiO_2 nanoparticles. The film deposited in LP phase (Figure 14.5(a)) shows two-dimensional percolated domains of TiO_2 nanoparticles. The LB deposited in CP phase shows closed packing with lesser defects (Figure 14.5(b)). The density of catalytic hotspots is expected to be large in the LB film deposited in CP phase than compared to that deposited in LP phase. The ultrathin nature of the film may ensure high sensitivity toward any analytes during sensing. A resistance-based sensor setup was developed (Banerjee et al., 2013) and the LB film of TiO_2 nanoparticles deposited in CP phase was employed for sensing ethanol gas. The ethanol sensing mechanism by the LB film of TiO_2 nanoparticles follows the classical gas sensing theory wherein the surface adsorbed ionized oxygen species (O^-, O^{-2}, etc.) react readily with the ethanol vapor yielding either acetaldehyde or carbon dioxide and water as the by-product. During such chemical reaction, the free electrons will be released onto the oxide surface, which effectively reduces the sensor resistance. The sensing performance of LB films (~70 nm) was compared to that of spin-coated thick film (~4,000 nm). The ethanol gas sensing response from spin-coated and LB films of TiO_2 nanoparticles as a function of time is shown in Figure 14.6. The response from spin-coated film of TiO_2 was not stable and does not reveal the usual rise and decay in the response due to switching on and off of ethanol gas flow. At the same time, the response from the LB film of TiO_2 nanoparticles was very stable and displayed the characteristic rise and fall of

(a)

(b)
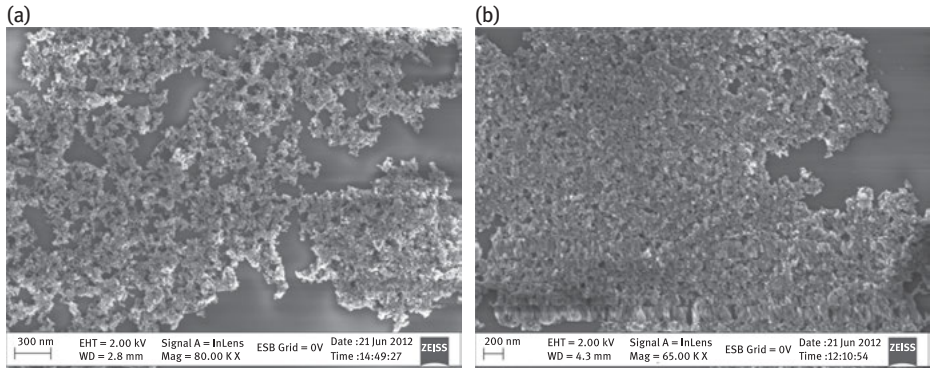
Figure 14.5: Field emission scanning electron microscope (FESEM) images of LB films of TiO_2 nanoparticles deposited at target surface pressure of (a) 1 mN/m and (b) 10 mN/m corresponding to LP and CP phases of the LF. The films were deposited on Si/SiO$_2$ substrates.
[Reprinted with permission (Choudhary et al., 2015).]

(a)

(b)
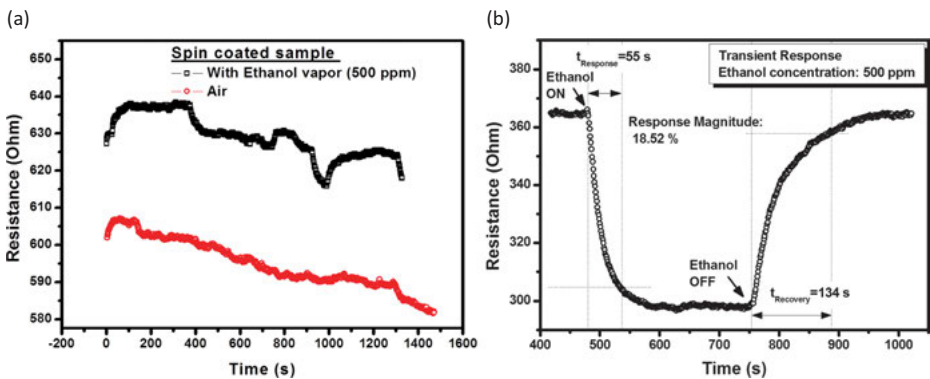
Figure 14.6: Response curve from the TiO_2 based nanoparticle sensor fabricated using (a) spin coating and (b) LB deposition technique. The LB film was deposited at 10 mN/m corresponding to CP phase of the LF of TiO_2 nanoparticles. The temperature was 300 °C.
[Reprinted with permission. (Choudhary et al., 2015).]

the response due to switching off and on of the ethanol vapor, respectively. The response and recovery time was found to be 55 and 134 s, respectively.

The repeated response cycles for sensing ethanol by the LB film of TiO_2 is shown in Figure 14.7. The variation indicates excellent sensing performance by the LB films with respect to its recovery, stable baseline, and repeatability.
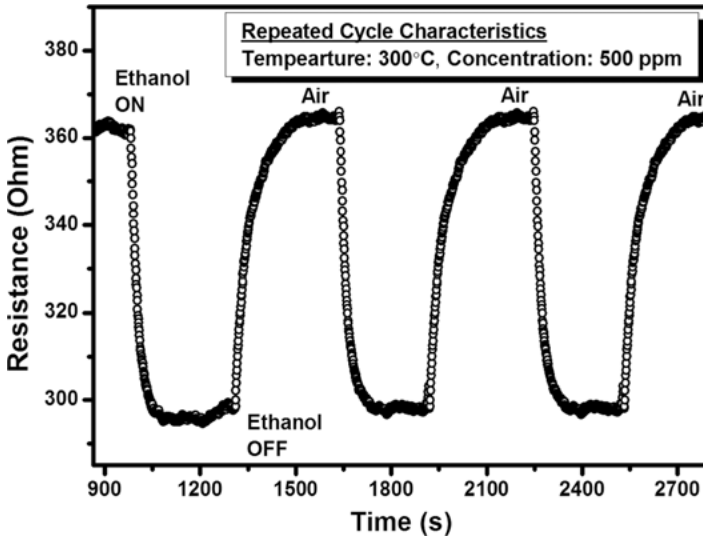
Figure 14.7: The repeated cycles of sensing from LB film of TiO_2 nanoparticles deposited in CP phase of the LF from A/W interface.
[Reprinted with permission. (Choudhary et al., 2015).]

The density of catalytic hotspot is expected to be very large in the case of LB films of TiO_2 nanoparticles. These hotspots react with the ethanol and yield the desired response. The large number of these hotspots in the spin-coated film of TiO_2 nanoparticles might be embedded into depth and not available for reaction with ethanol molecules and, therefore, the response curve was unstable and not repeatable.

These results show that LB film of nanoparticles can be employed as a functional material for sensing. It displays enhanced sensing performance as compared to that of thick film.

14.4 Langmuir and LB films of pristine single-walled carbon nanotubes at different interfaces

Single-walled carbon nanotubes (SWCNTs) are one of the most successful nanomaterials owing to their remarkable physicochemical properties. SWCNTs are highly shape-anisotropic materials exhibiting a large anisotropy in electrical and optical properties. The research and development in the field of SWCNTs promises a large number of devices with much superior features. SWCNTs can be metallic or semiconducting in nature. The semiconducting behavior of SWCNTs depends on the geometry of the nanotubes (Dresselhaus, 2005; Dresselhaus et al., 2001; Heller et al.,

2008; Iijima, 1991; Kong et al., 2000; Wang et al., 1998; Wei et al., 2006). Practically, the geometry of the SWCNTs is difficult to control. However, a control over the assembly of SWCNTs can regulate the properties on an average scale. There are few attempts for regulating the intertubular spacing of the SWCNTs so as to achieve the material with unique properties. The SWCNTs can be aligned onto surface by the application of external field (Yamamoto et al., 1998), nano-template (Hwang et al., 2005), self-assembly (Shimoda et al., 2002), electrospinning (Gao et al., 2004) and LB techniques (Feng et al., 2003a; Guo et al., 2002; Jia et al., 2008). As the SWCNTs are aligned, the coherent behavior of the tubes enhances the device performance. Field emission–based devices employing the SWCNTs need a preferential alignment of the nanotubes.

SWCNTs can be aligned in ultrathin film by LB film deposition technique. However, in order to achieve uniform and defectless LB films, it is essential to form a stable LF at the A/W interface. There are several attempts for forming stable LF of SWCNTs. Most of the reports indicate the stabilization of LF of SWCNTs can be achieved by mixing it with some stabilizers (Feng et al., 2003a; Guo et al., 2002; Jia et al., 2008; Kim et al., 2003; Li et al., 2007). There are few attempts to form LF of pristine SWCNTs at the A/W interface; however, the stability of the film was not addressed (Massey et al., 2011; Venet et al., 2010). In 2014, Poonia et al., reported the formation of stable LF of pristine SWCNTs at the A/W interface (Poonia et al., 2014). The dispersion of the SWCNTs in organic solvent was reported to be very crucial. The FESEM images show that the SWCNTs exist in bundle form where each tubule binds very strongly with each other via van der Waals interaction. The pristine SWCNTs can be dispersed in dimethylformamide (DMF) solvent. A homogeneous
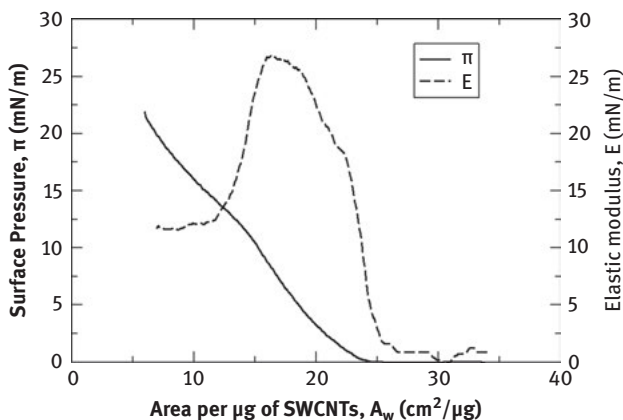
Figure 14.8: Surface pressure (π) – area per microgram (A_w) isotherm of pristine SWCNTs at the A/W interface. The dashed curve represents the variation of elastic modulus (E) as a function of A_w. [Reprinted with permission (Poonia et al., 2014).]

solution of SWCNTs in DMF was obtained by ultrasonicating the solution for about 1 hour. The LF was formed at the A/W interface by the traditional methodology and surface pressure (π) – area per microgram (A_w) isotherm was recorded (Figure 14.8).

The trend of the isotherm reveals that the LF of SWCNTs also behaves like a classical system. On compressing the film, the sequence appears successively as the gas phase at very large A_w, a sharp transition at around 25 cm^2/µg indicating the onset of liquid-like phase, a monotonic increase in surface pressure till it collapses at ~ 15 mN/m, indicating the collapsed state. The variation in elastic-modulus indicates the presence of liquid-like phase with a maximum value of E to be around 27 mN/m. The stability and the reversibility of the liquid-like phase were studied by measuring isocycles through repeated compression and expansion of the film and recording the surface pressure simultaneously as a function of A_w. The LF of SWCNTs at the A/W interface was found to be very stable and the liquid-like phase was completely reversible. The LB films of SWCNTs were deposited onto different substrates at different target surface pressures. The surface morphology of SWCNTs in the LB films was reported to be very interesting. The LB films deposited at very low surface pressure reveal aligned bundles of SWCNTs where the long axis of the tubes was found be parallel to the dipping direction during the LB film deposition process (Figure 14.9(a)). The LB film deposited at higher surface pressure shows the donut-like structure formed by the coiled SWCNTs (Figure 14.9(b)). The coiling of SWCNTs leading to ring structure was reported in another study by Martel et al. in 1999 (Martel et al., 1999). Such coiling may arise due to strong van der Waals interaction between the tubes.

(a) (b)
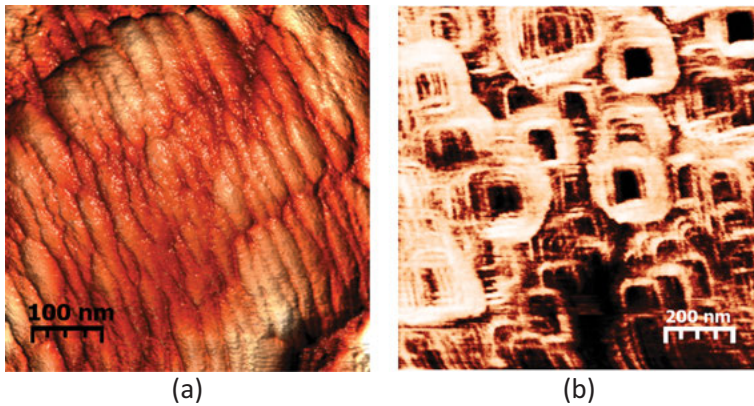
Figure 14.9: Conducting atomic force microscope images displaying the tunneling map of LB films of SWCNTs deposited at the target surface pressure of (a) 0.5 mN/m and (b) 6 mN/m. [Reprinted with permission (Poonia et al., 2014).]

This study clearly indicates the possibility of obtaining interesting supramolecular assemblies of the nanotubes. In an another report, it was demonstrated that the bundles of SWCNTs can be aligned in preferential direction depending on the experimental conditions of the LB film fabrication process. The electric field applied in the orthogonal directions to the LB film of SWNCTs deposited at lower target surface pressure clearly indicated the ohmic and insulating behaviors (Poonia et al., 2015). Similarly, the surface plasmon resonance study on the LB films suggested a large optical anisotropy in the thin film in the orthogonal directions (Devanarayanan et al., 2016b).

14.4.1 Methane gas sensing using LB films of SWCNTs

The assembly of bundles of SWCNTs in the ultrathin LB film can be employed for numerous applications. The donut-like structure of the bundles of SWCNTs can be used for molecular trapping in biosensors. The oriented bundles of SWCNTs in the ultrathin film offer a large anisotropy in electrical and optical properties that can be potentially employed for sensing applications. In an interesting study, LB films of pristine SWCNTs was used for sensing methane gas (Poonia et al., 2015). The pristine SWCNTs can be considered as p-type semiconducting material where holes are the major charge carrier. Methane is considered to be weak acid and, therefore, its adsorption on the SWCNTs can result in depletion of electrons due to donation of holes by the molecule. As the major charge density increases due to adsorption of methane, the Kelvin probe (KP) response enhances. This enhancement in the KP response from the LB film of SWCNTs due to adsorption of methane gas was found to be very rapid or step-like due to a change in the concentration of the methane gas. The sensing performance of the LB film of SWCNTs was compared with that of drop-casted film of SWCNTs. Though the KP response from the drop-casted film was reported to be a monotonic rise, there is no indication of change in concentration in methane gas from the response curve. Even for a given concentration, the response shows increasing trend. The FESEM image of drop-casted film was found to be a random network-like structure of the bundles of SWCNTs. The degree of anisotropy in drop-casted film is much less as compared to that of LB film. Therefore, the charge transport in the LB film is more coherent and unidirectional than compared to that of randomly oriented network of SWCNTs in drop-casted film. It was also reported that the methane gas sensing performance is found to be better in the presence of relative humidity (Poonia et al., 2015). This study presented the role of alignment of SWCNTs in the LB film in sensing performance. These alignments indeed can be obtained by the simple and economically viable LB technique.

14.5 Langmuir and LB films of carboxylated graphene (G-COOH) at different interfaces and urea sensing application of LB film of G-COOH from the aqueous medium

The nanomaterials with two-dimensional (2D) planar geometry are drawing large attention of academia and industries. This is due to the fact that they exhibit extraordinary physicochemical properties. The 2D nanomaterials are easily processable and can be fabricated at a large scale. For the past few years, various 2D nanomaterials are proposed with their amazing properties. Some of the commonly reported 2D nanomaterials are transition metal dichalcogenides (TMDs). The electronic properties of the TMDs can be manipulated by transforming from bulk to single layer. It was found that indirect band gap of bulk TMDs can be transformed to direct band gap in the single layer. The interesting properties of TMDs promises applications in developing transistors, spintroncs, optoelectronics and energy harvesting devices (Chia et al., 2015; Manzeli et al., 2017; Wang et al., 2012). There are other interesting 2D materials like MoO_3, h-BN, Bi_2T_3, and Sb_2Se_3 whose electronic properties are such that they can span the entire range of electronic structure, i.e., from metal to insulator (Xu et al., 2013). Among the various 2D materials, graphene has received the enormous scientific attention due to its unique electrical and optical properties. Graphene can be chemically modified easily and, therefore, provides an avenue for altering its physicochemical properties (Geim and Novoselov, 2007; Li et al., 2008; Zhu et al., 2008). The thin films of such materials can offer a large gain in surface-to-volume ratio, which in turn enhances the device performance remarkably (Yan et al., 2012; Lee et al., 2012).

There are a number of reports on Langmuir and LB films of graphene and its nanocomposites. In 2013, Kim et al. (H. Kim et al., 2013) reported the formation of LB film of pristine graphene mixed with methyl pyrrolidone. They reported that the optoelectronic properties of the LB film of graphene is largely dependent on flake size and film thickness. With optimization using these parameters, the LB film of graphene can be employed for optoelectronic devices. The LB film of graphene or graphene oxide can be potentially used to replace the existing commercial transparent conducting film (Zheng et al., 2011). The LB film of graphene can be used for sensing application.

The fabrication of thin film from a solution medium is practically tedious as solvent-assisted dispersion of pristine graphene is difficult to achieve. In order to improve the processability, the graphene can be chemically modified. Such chemical modification not only enhances the solubility of the material in solvent but also prevents van der Waals–mediated stacking of graphene layers (Kuila et al., 2012). The dispersed solution can be employed to obtain a stable LF and thus LB film of the functionalized graphene can be deposited and employed for device fabrication. In 2018, Poonia et al. (Poonia et al., 2018) reported their study on Langmuir and LB film of

carboxylated graphene (G-COOH). The LFof G-COOH was reported to be very stable at the A/W interface. The LB films were deposited and its urea sensing capability was assessed and compared to that of spin-coated thick film. The presence of hydrophilic carboxylic group (-COOH) renders sufficient amphiphilicity to the G-COOH, which consequently stabilizes the LF at the A/W interface. As observed in the case of Langmuir monolayer of fatty acid, the isotherms are very sensitive to the presence of ions in the aqueous subphase; G-COOH is expected to behave similarly at the A/W interface due to the presence of ions in the water medium. The surface pressure (π) – area (A) isotherms of the LF of G-COOH from aqueous subphase containing urea as analyte at different pH is shown in Figure 14.10. The interaction of urea with LF of G-COOH was studied only at a basic pH. This is due to the fact that –COOH tends to dissociate at basic pH which can attract the –NH2 groups of urea through electrostatic interaction. The isotherm of LF of G-COOH on ion-free water behaves like a classical system. On compression, the surface pressure of the film was found to be negligible at very large
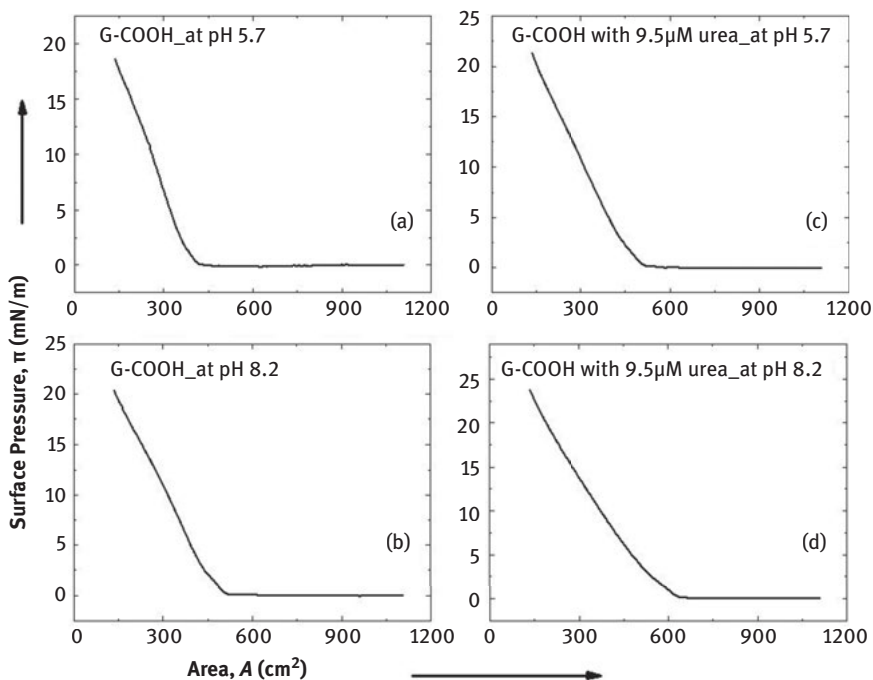
Figure 14.10: Surface pressure (π) – Area (A) isotherm of LF of G-COOH obtained from an aqueous subphase containing (a) ultrapure ion-free water, (b) basic pH = 8.2, (c) 9.5 µM urea in ultrapure water and (d) 9.5 µM urea in basic pH in water. The pH of ultrapure water was 5.7 due to absorption of CO_2 from ambient and consequently formation of weak carbonic acid. The basic pH was obtained by adding ammonia solution in ultrapure water.
[Reprinted with permission (Poonia et al., 2018).]

area. The isotherm indicated a sharp rise in surface pressure with A ≤ 400 cm^2. Thereafter, the surface pressure of the film rises monotonically and sharply till the film is completely compressed in the trough. The signature of collapse of the film was not evident from the isotherm. The stability of the LF of G-COOH at the A/W interface was found to be stable and reversible. The film at higher pH indicates a swelling phenomenon that arises due to electrostatic repulsion of the ionized carboxyl group of G-COOH. Therefore, the lift-off area obtained from the LF of G-COOH at pH 8.2 was 500 cm^2. Similarly, due to adsorption of urea on the LF of G-COOH through the aqueous medium, the lift-off area is expected to increase. The lift-off area of the LF of G-COOH from the aqueous subphase containing 9.5 mM of urea in normal pH and basic pH is found to be 520 and 630 cm^2, respectively. This indicates that though urea interacts with LF of G-COOH in normal ion-free water, it reacts significantly in the basic pH. Such a study reveals the potential of LB film of G-COOH to be employed for urea sensing.

The surface morphology of the LB film of G-COOH was studied using FESEM and AFM. The AFM image (Figure 14.11) shows domains of graphene sheets (~20–30 nm in size). The domains are found to be distributed uniformly all over the surface. On exposure to the urea, the thickness of the domains increases.
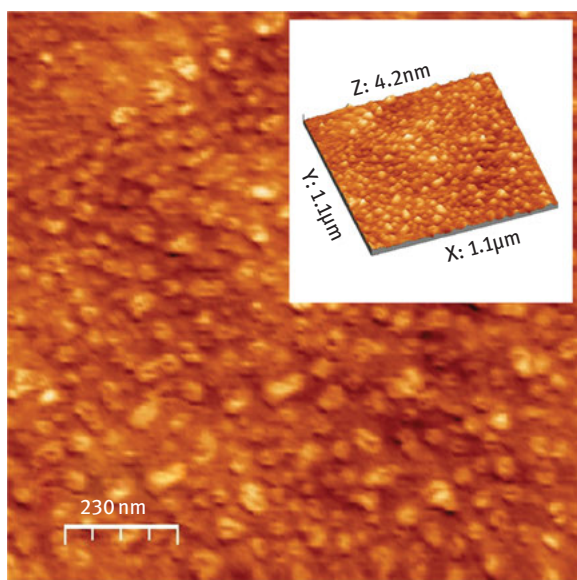
Figure 14.11: Atomic force image of LB film of G-COOH deposited onto Si/SiO$_2$ substrate at a target surface pressure of 5 mN/m.
[Reprinted with permission (Poonia et al., 2018).]

The urea sensing performance of LB film of G-COOH was evaluated and compared to that of spin-coated film of G-COOH. The sensing curve is shown in Figure 14.12.

(a)

(b)
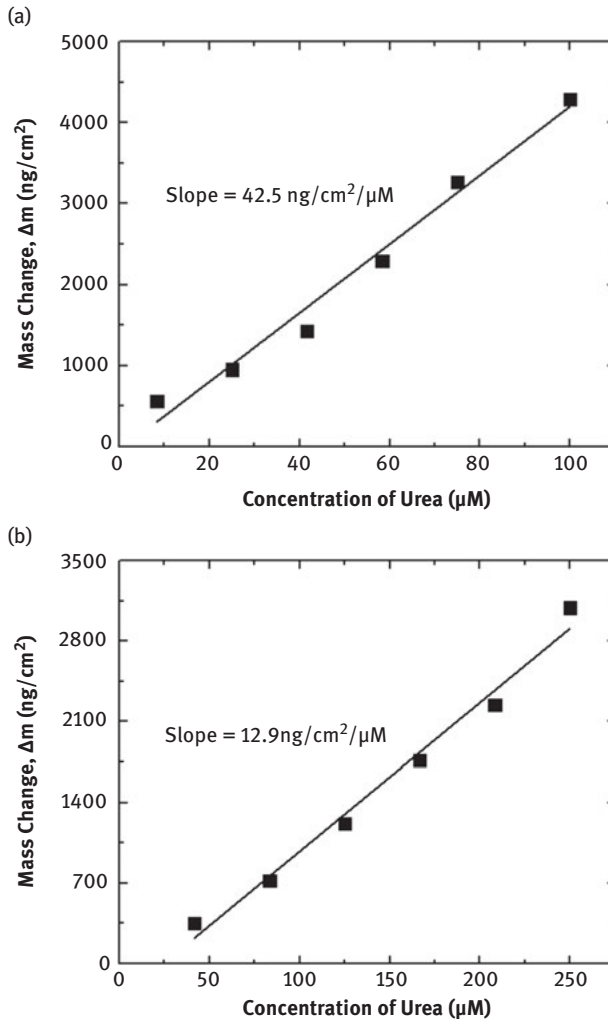
Figure 14.12: Adsorption of urea onto functional layer of (a) LB film of G-COOH and (b) spin-coated film of G-COOH fabricated onto quartz wafers. The LB film was deposited at a target surface pressure of 5 mN/m. The sensing curve was obtained using a quartz crystal microbalance. [Reprinted with permission (Poonia et al., 2018).]

The adsorption curve during urea sensing obtained using a quartz crystal micro-balance (QCM) employing the LB and spin-coated films of G-COOH as functional layer shows a linear trend due to change in the concentration of urea in the aqueous medium. The slope of the curve can be related to the sensitivity of the analyte using the functional layer in a sensing device (Devanarayanan et al., 2016a). The slope of the adsorption curves obtained from LB and spin-coated films was reported to be 42.5 and 12.9 ng/cm^2/µM, respectively. This indicates that sensitivity of LB film is
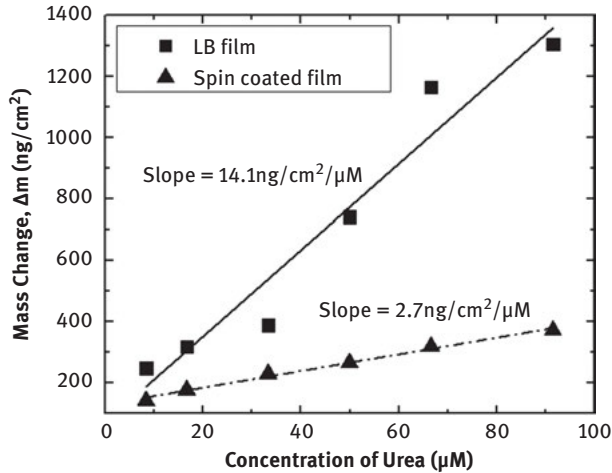
Figure 14.13: Adsorption of urea from the adulterated milk sample onto functional layer of (a) LB film of G-COOH and (b) spin-coated film of G-COOH fabricated onto quartz wafers. The LB film was deposited at a target surface pressure of 5 mN/m. The sensing curve was obtained using a quartz crystal microbalance.
[Reprinted with permission (Poonia et al., 2018).]

about 3 times better than that of spin-coated film. The sensitivity of LB film enhances due to enormous gain in surface-to-volume ratio and some ordering in the film. The functional layer of LB and spin-coated films of G-COOH was employed for sensing urea in milk. The adulterated sample was prepared in the laboratory and the sensing performance was measured using the QCM (Figure 14.13). The variation indicates a linear trend in the given concentration range of urea. In such measurement, the sensitivity of urea sensor employing the LB films of G-COOH is found to be superior to that of spin-coated film.

14.6 Conclusion

The nature of aggregation and nucleation of nanomaterials in ultrathin films governs their physicochemical properties. The LB film deposition technique provides a precise control over the surface density, alignment of nanomaterials in the film and its thickness. These parameters have proved to be essential for harnessing the interesting properties of the thin film for any device application. In this chapter, we reviewed briefly three different types of nanomaterials forming Langmuir and LB films at different interfaces. These nanomaterials are different from their shape anisotropy. The spherical gold nanoparticles can be functionalized chemically by suitable ligands so as to achieve amphiphilic

gold nanoparticles. The Langmuir monolayer of mixed phase of TiO2 nanoparticles was reported to be stable. The performance toward ethanol sensing by LB films of TiO_2 was found to be very stable and repeatable. The study on the LF of AGNs reveals interesting surface phases. The rod-shaped pristine single-walled carbon nanotubes can yield a stable LF. The surface morphology of LB films of SWCNTs shows supramolecular assembly. The LB film of SWCNTs shows the aligned bundles of the nanotubes which can be employed for sensing methane gas. The sensing response from the LB film of SWCNTs was found to be step-like function that can be utilized for the development of methane gas ON-OFF state sensor. The study on Langmuir and LB film of G-COOH indicated promising results on urea sensing from the aqueous medium by the LB films. The interesting field of ultrathin films should be explored for nanomaterials and their potential for device fabrication should be highlighted.

References

Banerjee, N., Roy, S., Sarkar, C.K., Bhattacharyya, P. (2013). High dynamic range methanol sensor based on aligned ZnO nanorods. IEEE Sensors Journal, 13(5), 1669–1676. Doi: https://doi.org/10.1109/JSEN.2013.2237822.

Berring, E.E., Borrenpohl, K., Fliesler, S.J., Serfis, A.B. (2005). A comparison of the behavior of cholesterol and selected derivatives in mixed sterol–phospholipid Langmuir monolayers: a fluorescence microscopy study. Chemistry and Physics of Lipids, 136(1), 1–12. Doi: https://doi.org/10.1016/j.chemphyslip.2005.03.004.

Bibo, A.M., Peterson, I.R. (1990). Phase diagrams of monolayers of the long chain fatty acids. Advanced Materials, 2(6–7), 309–311. Doi: https://doi.org/10.1002/adma.19900020608.

Bjørnholm, T., Greve, D.R., Reitzel, N., Hassenkam, T., Kjaer, K., Howes, P.B., . . . McCullough, R.D. (1998). Self-assembly of regioregular, amphiphilic polythiophenes into highly ordered π-stacked conjugated polymer thin films and nanocircuits. Journal of the American Chemical Society, 120(30), 7643–7644. Doi: https://doi.org/10.1021/ja981077e.

Broniatowski, M., Sandez Macho, I., Miñones, J., Dynarowicz-Łątka, P. (2004). Langmuir monolayers characteristic of (perfluorodecyl)-alkanes. The Journal of Physical Chemistry B, 108(35), 13403–13411. Doi: https://doi.org/10.1021/jp0402481.

Chia, X., Eng, A.Y.S., Ambrosi, A., Tan, S.M., Pumera, M. (2015). Electrochemistry of nanostructured layered transition-metal dichalcogenides. Chemical Reviews. Doi: https://doi.org/10.1021/acs.chemrev.5b00287.

Choudhary, K., Manjuladevi, V., Gupta, R.K., Bhattacharyya, P., Hazra, A., Kumar, S. (2015). Ultrathin films of TiO $_2$ nanoparticles at interfaces. Langmuir, 31(4), 1385–1392. Doi: https://doi.org/10.1021/la503514p.

Collier, C.P., Saykally, R.J., Shiang, J.J., Henrichs, S.E., Heath, J.R. (1997). Reversible tuning of silver quantum dot monolayers through the metal-insulator transition. Science, 277(5334), 1978–1981. Doi: https://doi.org/10.1126/science.277.5334.1978.

Dabbousi, B.O., Murray, C.B., Rubner, M.F., Bawendi, M.G. (1994). Langmuir-Blodgett manipulation of size-selected CdSe nanocrystallites. Chemistry of Materials, 6, 216–219. Doi: https://doi.org/10.1021/cm00038a020.

de Mul, M.N.G., Mann, J.A. (1994). Multilayer formation in thin films of thermotropic liquid crystals at the air-water interface. Langmuir, 10(7), 2311–2316. Doi: https://doi.org/10.1021/la00019a048.

Devanarayanan, V.P., Manjuladevi, V., Gupta, R.K. (2016a). Surface plasmon resonance sensor based on a new opto-mechanical scanning mechanism. Sensors and Actuators. B, Chemical, 227, 643–648. Doi: https://doi.org/10.1016/j.snb.2016.01.027.

Devanarayanan, V.P., Manjuladevi, V., Poonia, M., Gupta, R.K., Gupta, S.K., Akhtar, J. (2016b). Measurement of optical anisotropy in ultrathin films using surface plasmon resonance. Journal of Molecular Structure, 1103. Doi: https://doi.org/10.1016/j.molstruc.2015.09.018.

Dresselhaus, M.S. (2005). Physical properties of carbon nanotubes. Carbon Nanotubes. https://doi.org/10.1142/p080

Dresselhaus, M.S., Dresselhaus, G., Avouris, P. (2001). Carbon nanotubes synthesis, structure, properties, and applications. Carbon Nanotubes Synthesis, Structure, Properties, and Applications. https://doi.org/10.1080/20014091104189

Dufrêne, Y.F., Barger, W.R., Green, J.-B.D., Lee, G.U. (1997). Nanometer-scale surface properties of mixed phospholipid monolayers and bilayers. Langmuir, 13(18), 4779–4784. Doi: https://doi.org/10.1021/la970221r.

Durbin, M.K., Malik, A., Ghaskadvi, R., Shih, M.C., Zschack, P., Dutta, P. (1994). X-ray diffraction study of a recently identified phase transition in fatty acid langmuir monolayers. The Journal of Physical Chemistry, 98(7), 1753–1755. Doi: https://doi.org/10.1021/j100058a005.

Feng, L., Li, H., Li, F., Shi, Z., Gu, Z. (2003a). Functionalization of carbon nanotubes with amphiphilic molecules and their Langmuir-Blodgett films. Carbon, 41, 2385–2391. Doi: https://doi.org/10.1016/S0008-6223(03)00293-8.

Feng, L., Li, H., Li, F., Shi, Z., Gu, Z. (2003b). Functionalization of carbon nanotubes with amphiphilic molecules and their Langmuir–Blodgett films. Carbon, 41(12), 2385–2391. Doi: https://doi.org/10.1016/S0008-6223(03)00293-8.

Finer, E.G., Phillips, M.C. (1973). Factors affecting molecular packing in mixed lipid monolayers and bilayers. Chemistry and Physics of Lipids, 10(3), 237–252. Doi: https://doi.org/10.1016/0009-3084(73)90004-2.

Fukuto, M., Heilmann, R.K., Pershan, P.S., Badia, A., Lennox, R.B. (2004). Monolayer/bilayer transition in Langmuir films of derivatized gold nanoparticles at the gas/water interface: an x-ray scattering study. Journal of Chemical Physics, 120(7), 3446–3459. Doi: https://doi.org/10.1063/1.1640334.

Gaines, G.L. (1966). Insoluble Monolayers at Liquid-Gas Interfaces, New York, Interscience.

Gaines, G.L. (1991). Monolayers of polymers. Langmuir, 7(5), 834–839. Doi: https://doi.org/10.1021/la00053a005.

Gao, J., Yu, A., Itkis, M.E., Bekyarova, E., Zhao, B., Niyogi, S., Haddon, R.C. (2004). Large-scale fabrication of aligned single-walled carbon nanotube array and hierarchical single-walled carbon nanotube assembly. Journal of the American Chemical Society, 126, 16698–16699. Doi: https://doi.org/10.1021/ja044499z.

Geim, A.K., Novoselov, K.S. (2007). The rise of graphene. Nature Materials, 6(3), 183–191. Doi: https://doi.org/10.1038/nmat1849.

Giersig, M., Mulvaney, P. (1993). Preparation of ordered colloid monolayers by electrophoretic deposition. Langmuir, 97, 6334–6336. Doi: https://doi.org/10.1021/la00036a014.

Giner, I., Gascón, I., Vergara, J., López, M.C., Ros, M.B., Royo, F.M. (2009). Molecular arrangement in Langmuir and Langmuir–Blodgett films of a mesogenic bent-core carboxylic acid. Langmuir, 25(20), 12332–12339. Doi: https://doi.org/10.1021/la901614p.

Gopal, A., Lee, K.Y.C. (2001). Morphology and collapse transitions in binary phospholipid monolayers. The Journal of Physical Chemistry B, 105(42), 10348–10354. Doi: https://doi.org/10.1021/jp012532n.

Greene, I.A., Wu, F., Zhang, J.Z., Chen, S. (2003). Electronic conductivity of semiconductor nanoparticle monolayers at the air|water interface. The Journal of Physical Chemistry B, 107(24), 5733–5739. Doi: https://doi.org/10.1021/jp027692t.

Guo, Y., Wu, J., Zhang, Y. (2002). Manipulation of single-wall carbon nanotubes into aligned molecular layers. Chemical Physics Letters, 362, 314–318. Doi: https://doi.org/10.1016/S0009-2614(02)01085-0.

Gupta, R.K., Manjuladevi, V. (2012). Liquid crystals at interfaces. Israel Journal of Chemistry, 52(10), 809–819. Doi: https://doi.org/10.1002/ijch.201200030.

Gupta, R.K., Manjuladevi, V. (2015). Ultrathin Films. (M. Aliofkhazraei, Ed.). Nova Publishers, USA. Retrieved from https://www.novapublishers.com/catalog/product_info.php?cPath=185_232_247&products_id=54292&osCsid=882e0126f4c213ea2ef8f38fdfe92397

Gupta, R.K., Manjuladevi, V., Karthik, C., Kumar, S., Suresh, K.A. (2012). Studies on Langmuir monolayer of tricycloquinazoline based disk-shaped liquid crystal molecules. Colloids and Surfaces. A, Physicochemical and Engineering Aspects, 410, 91–97. Doi: https://doi.org/10.1016/j.colsurfa.2012.06.023.

Gupta, R.K., Suresh, K.A. (2004). AFM studies on Langmuir-Blodgett films of cholesterol. The European Physical Journal E, 14(1), 35–42. Doi: https://doi.org/10.1140/epje/i2003-10088-4.

Gupta, R.K., Suresh, K.A., Kumar, S. (2008a). Monolayer of amphiphilic functionalized gold nanoparticles at an air-water interface. Physical Review E, 78(3), 032601. Doi: https://doi.org/10.1103/PhysRevE.78.032601.

Gupta, R.K., Suresh, K.A., Kumar, S. (2008b). Monolayer of amphiphilic functionalized gold nanoparticles at an air-water interface. Physical Review E – Statistical, Nonlinear, and Soft Matter Physics, 78(3), 032601. Doi: https://doi.org/10.1103/PhysRevE.78.032601.

Heath, J.R., Knobler, C.M., Leff, D.V. (1997). Pressure/temperature phase diagrams and superlattices of organically functionalized metal nanocrystal monolayers: the influence of particle size, size distribution, and surface passivant. The Journal of Physical Chemistry B, 101, 189–197. Doi: https://doi.org/10.1021/jp9611582.

Heller, I., Janssens, A.M., M??nnik, J., Minot, E.D., Lemay, S.G., Dekker, C. (2008). Identifying the mechanism of biosensing with carbon nanotube transistors. Nano Letters, 8, 591–595. Doi: https://doi.org/10.1021/nl072996i.

Hiltrop, K. (1994). Lyotropic liquid crystals. In Liquid Crystals, Heidelberg, Steinkopff, 143–171. Doi: https://doi.org/10.1007/978-3-662-08393-2_4.

Hwang, S.K., Lee, J., Jeong, S.H., Lee, P.S., Lee, K.H. (2005). Fabrication of carbon nanotube emitters in an anodic aluminium oxide nanotemplate on a Si wafer by multi-step anodization. Nanotechnology, 16, 850–858. Doi: https://doi.org/10.1088/0957-4484/16/6/040.

Iijima, S. (1991). Helical microtubules of graphitic carbon. Nature, 354, 56–58. Doi: https://doi.org/10.1038/354056a0.

Jehoulet, C., Obeng, Y.S., Kim, Y.T., Zhou, F., Bard, A.J. (1992). Electrochemistry and Langmuir trough studies of fullerene C60 and C70 films. Journal of the American Chemical Society, 114(11), 4237–4247. Doi: https://doi.org/10.1021/ja00037a030.

Jia, L., Zhang, Y., Li, J., You, C., Xie, E. (2008). Aligned single-walled carbon nanotubes by Langmuir-Blodgett technique. Journal of Applied Physics, 104, 074318. Doi: https://doi.org/10.1063/1.2996033.

Kaganer, V., Möhwald, H., Dutta, P. (1999). Structure and phase transitions in Langmuir monolayers. Reviews of Modern Physics, 71(3), 779–819. Doi: https://doi.org/10.1103/RevModPhys.71.779.

Karthik, C., Manjuladevi, V., Gupta, R.K., Kumar, S. (2014). Pattern formation in Langmuir–Blodgett films of tricycloquinazoline based discotic liquid crystal molecules. Journal of Molecular Structure, 1070, 52–57. Doi: https://doi.org/10.1016/j.molstruc.2014.04.036.

Kim, H., Mattevi, C., Kim, H.J., Mittal, A., Mkhoyan, K.A., Riman, R.E., Chhowalla, M. (2013). Optoelectronic properties of graphene thin films deposited by a Langmuir–Blodgett assembly. Nanoscale, 5(24), 12365. Doi: https://doi.org/10.1039/c3nr02907g.

Kim, J., Swager, T.M. (2001). Control of conformational and interpolymer effects in conjugated polymers. Nature, 411(6841), 1030–1034. Doi: https://doi.org/10.1038/35082528.

Kim, Y., Minami, N., Zhu, W., Kazaoui, S., Azumi, R., Matsumoto, M. (2003). Langmuir-Blodgett films of single-wall carbon nanotubes: layer-by-layer deposition and in-plane orientation of tubes. Japanese Journal of Applied Physics, Part 1: Regular Papers and Short Notes and Review Papers, 42, 7629–7634. Doi: https://doi.org/10.1143/JJAP.42.7629.

Kong, J., Franklin, N.R., Zhou, C., Chapline, M.G., Peng, S., Cho, K., Dai, H. (2000). Nanotube molecular wires as chemical sensors. Science, 287, 622–625. Doi: https://doi.org/10.1126/science.287.5453.622.

Kuila, T., Bose, S., Mishra, A.K., Khanra, P., Kim, N.H., Lee, J.H. (2012). Chemical functionalization of graphene and its applications. Progress in Materials Science, 57(7), 1061–1105. Doi: https://doi.org/10.1016/j.pmatsci.2012.03.002.

Lafont, S., Rapaport, H., Sömjen, G.J., Renault, A., Howes, P.B., Kjaer, K., . . . Lahav, M. (1998). Monitoring the nucleation of crystalline films of cholesterol on water and in the presence of phospholipid. The Journal of Physical Chemistry B, 102(5), 761–765. Doi: https://doi.org/10.1021/jp973074e.

Langevin, D., Monroy, F. (2010). Interfacial rheology of polyelectrolytes and polymer monolayers at the air–water interface. Current Opinion in Colloid & Interface Science, 15(4), 283–293. Doi: https://doi.org/10.1016/j.cocis.2010.02.002.

Lee, S.K., Jang, H.Y., Jang, S., Choi, E., Hong, B.H., Lee, J., . . . Ahn, J.H. (2012). All graphene-based thin film transistors on flexible plastic substrates. Nano Letters. Doi: https://doi.org/10.1021/nl300948c.

Li, D., Müller, M.B., Gilje, S., Kaner, R.B., Wallace, G.G. (2008). Processable aqueous dispersions of graphene nanosheets. Nature Nanotechnology, 3(2), 101–105. Doi: https://doi.org/10.1038/nnano.2007.451.

Li, X., Zhang, L., Wang, X., Shimoyama, I., Sun, X., Seo, W.K., Dai, H. (2007). Langmuir-Blodgett assembly of densely aligned single-walled carbon nanotubes from bulk materials. Journal of the American Chemical Society, 129, 4890–4891. Doi: https://doi.org/10.1021/ja071114e.

Lin, B., Schultz, D.G., Lin, X.-M., Li, D., Gebhardt, J., Meron, M., Viccaro, P.J. (2007). Langmuir monolayers of gold nanoparticles. Thin Solid Films, 515(14), 5669–5673. Doi: https://doi.org/10.1016/j.tsf.2006.12.023.

Manzeli, S., Ovchinnikov, D., Pasquier, D., Yazyev, O.V., Kis, A. (2017). 2D transition metal dichalcogenides. Nature Reviews Materials, 2(8), 17033. Doi: https://doi.org/10.1038/natrevmats.2017.33.

Markovich, G., Collier, C.P., Heath, J.R. (1998). Reversible metal-insulator transition in ordered metal nanocrystal monolayers observed by impedance spectroscopy. Physical Review Letters, 80(17), 3807–3810. Doi: https://doi.org/10.1103/PhysRevLett.80.3807.

Martel, R., Shea, H.R., Avouris, P. (1999). Rings of single-walled carbon nanotubes. Nature, 398 (6725), 299–299. Doi: https://doi.org/10.1038/18589.

Massey, M.K., Pearson, C., Zeze, D.A., Mendis, B.G., Petty, M.C. (2011). The electrical and optical properties of oriented Langmuir-Blodgett films of single-walled carbon nanotubes. Carbon, 49, 2424–2430. Doi: https://doi.org/10.1016/j.carbon.2011.02.009.

Mitsuya, M. (1991). Effect of the surface free energy of the substrate on the morphology of vacuum-deposited organic films. Langmuir, 7(4), 814–816. Doi: https://doi.org/10.1021/la00052a034.

Moraille, P., Badia, A. (2002). Highly parallel, nanoscale stripe morphology in mixed phospholipid monolayers formed by Langmuir–Blodgett transfer. Langmuir, 18(11), 4414–4419. Doi: https://doi.org/10.1021/la020129h.

Overbeck, G.A., Moebius, D. (1993). A new phase in the generalized phase diagram of monolayer films of long-chain fatty acids. The Journal of Physical Chemistry, 97(30), 7999–8004. Doi: https://doi.org/10.1021/j100132a032.

Paso, K., Helberg, R.M.L., Raaen, S., Sjöblom, J. (2008). Hydrophobic monolayer preparation by Langmuir–Blodgett and chemical adsorption techniques. Journal of Colloid and Interface Science, 325(1), 228–235. Doi: https://doi.org/10.1016/j.jcis.2008.05.015.

Pershan, P.S. (1982). Lyotropic liquid crystals. Physics Today. Doi: https://doi.org/10.1063/1.2915092.

Poonia, M., Gupta, R.K., Manjuladevi, V., Gupta, S.K., Akhtar, J. (2014). Supramolecular assembly of single-walled carbon nanotubes at air-solid interface. Journal of Nanoparticle Research, 16(8), 2572. Doi: https://doi.org/10.1007/s11051-014-2572-2.

Poonia, M., Manjuladevi, V., Gupta, R.K. (2018). Ultrathin film of carboxylated graphene at air-water and air-solid interfaces. Surfaces and Interfaces, 13, 37–45. Doi: https://doi.org/10.1016/j.surfin.2018.07.007.

Poonia, M., Manjuladevi, V., Gupta, R.K., Gupta, S.K., Singh, J., Agarwal, P.B., Akhtar, J. (2015). Ultrathin films of single-walled carbon nanotubes: a potential methane gas sensor. Science of Advanced Materials, 7(3), 455–462. Doi: https://doi.org/10.1166/sam.2015.1989.

Sang, L., Zhao, Y., Burda, C. (2014). TiO_2 nanoparticles as functional building blocks. Chemical Reviews, 114(19), 9283–9318. Doi: https://doi.org/10.1021/cr400629p.

Santhanam, V., Liu, J., Agarwal, R., Andres, R.P. (2003). Self-assembly of uniform monolayer arrays of nanoparticles. Langmuir, 19(19), 7881–7887. Doi: https://doi.org/10.1021/la0341761.

Schwartz, D.K. (1997). Langmuir-Blodgett film structure. Surface Science Reports, 27(7–8), 245–334. Doi: https://doi.org/10.1016/S0167-5729(97)00003-4.

Schwartz, D.K., Knobler, C.M. (1993). Direct observations of transitions between condensed Langmuir monolayer phases by polarized fluorescence microscopy. The Journal of Physical Chemistry, 97(35), 8849–8851. Doi: https://doi.org/10.1021/j100137a005.

Shimoda, H., Oh, S.J., Geng, H.Z., Walker, R.J., Zhang, X.B., McNeil, L.E., Zhou, O. (2002). Self-assembly of carbon nanotubes. Advanced Materials, 14, 899–901. Doi: https://doi.org/10.1002/1521-4095(20020618)14:12<899::aid-adma899>3.0.CO;2-2.

Swami, A., Kumar, A., Selvakannan, P.R., Mandal, S., Sastry, M. (2003). Langmuir-Blodgett films of laurylamine-modified hydrophobic gold nanoparticles organized at the air-water interface. Journal of Colloid and Interface Science, 260(2), 367–373. Doi: https://doi.org/10.1016/S0021-9797(03)00047-X.

Tabe, Y., Yamamoto, T., Nishiyama, I., Aoki, K.M., Yoneya, M., Yokoyama, H. (2002). Can hydrophobic oils spread on water as condensed Langmuir monolayers?. Journal of Physical Chemistry B, 106, 12089–12092. Doi: https://doi.org/10.1021/jp026724+.

Takano, E., Ishida, Y., Iwahashi, M., Araki, T., Iriyama, K. (1997). Surface chemical and morphological study on monolayers of cholesterol, cholestanol, and their derivatives conjugated with amino acid. Langmuir, 13(21), 5782–5786. Doi: https://doi.org/10.1021/la9705423.

Venet, C., Pearson, C., Jombert, A.S., Mabrook, M.F., Zeze, D.A., Petty, M.C. (2010). The morphology and electrical conductivity of single-wall carbon nanotube thin films prepared by the Langmuir-Blodgett technique. Colloids and Surfaces. A, Physicochemical and Engineering Aspects, 354, 113–117. Doi: https://doi.org/10.1016/j.colsurfa.2009.07.037.

Wang, Q.H., Kalantar-Zadeh, K., Kis, A., Coleman, J.N., Strano, M.S. (2012). Electronics and optoelectronics of two-dimensional transition metal dichalcogenides. Nature Nanotechnology, 7(11), 699–712. Doi: https://doi.org/10.1038/nnano.2012.193.

Wang, Q.H., Setlur, A.A., Lauerhaas, J.M., Dai, J.Y., Seelig, E.W., Chang, R.P.H. (1998). A nanotube-based field-emission flat panel display. Applied Physics Letters, 72, 2912–2913. Doi: https://doi.org/10.1063/1.121493.

Wei, Y., Weng, D., Yang, Y., Zhang, X., Jiang, K., Liu, L., Fan, S. (2006). Efficient fabrication of field electron emitters from the multiwalled carbon nanotube yarns. Applied Physics Letters, 89, 063101. Doi: https://doi.org/10.1063/1.2236465.

Xu, M., Liang, T., Shi, M., Chen, H. (2013). Graphene-like two-dimensional materials. Chemical Reviews. Doi: https://doi.org/10.1021/cr300263a.

Yamamoto, K., Akita, S., Nakayama, Y. (1998). Orientation and purification of carbon nanotubes using ac electrophoresis. Journal of Physics D: Applied Physics, 31, L34–L36. Doi: https://doi.org/10.1088/0022-3727/31/8/002.

Yan, C., Cho, J.H., Ahn, J.H. (2012). Graphene-based flexible and stretchable thin film transistors. Nanoscale. Doi: https://doi.org/10.1039/c2nr30994g.

Zasadzinski, J.A., Viswanathan, R., Madsen, L., Garnaes, J., Schwartz, D.K. (1994). Langmuir-Blodgett films. Science. Doi: https://doi.org/10.1126/science.8134836.

Zheng, Q., Ip, W.H., Lin, X., Yousefi, N., Yeung, K.K., Li, Z., Kim, J.-K. (2011). Transparent conductive films consisting of ultralarge graphene sheets produced by Langmuir–Blodgett assembly. ACS Nano, 5(7), 6039–6051. Doi: https://doi.org/10.1021/nn2018683.

Zhu, Y., Murali, S., Cai, W., Li, X., Suk, J.W., Potts, J.R., Ruoff, R.S. (2010). Graphene and graphene oxide: synthesis, properties, and applications. Advanced Materials. Doi: https://doi.org/10.1002/adma.201001068.

Rajiv Manohar

15 Quantum-dot-dispersed liquid crystals: mesogenic science to smart applications

Abstract: This chapter enumerates the significance of dispersion of guest entities to liquid crystal (LC) mesophase. The opening preface has been entailed upon LCs and quantum dots (QDs), signifying the amalgamation of both the spheres of material science. Introduction to basic parameters of LC such as dielectric polarizability, photomicrographs, response time, photoluminescence (PL), birefringence, and viscoelectric parameters has been provided with appropriate figure and diagrams to achieve better understanding in a comprehensive manner. Step by step, the effect of the combination of LC and QD nanoscience on these material parameters of LC has been meticulously analyzed. This chapter reviews the major research conducted in dissemination of QDs in the LC mesogenic matrix along with citations and graphs from the research articles. Fabrication of optimized applications with smart functionality and efficient responsiveness such as photonic waveguides and optical data-processing devices also been elaborated. This chapter aims to offers a better interface to the readers about the delicacy of this flowing crystal, its properties, and utility in the architecture of nanodevices when dispersed with QDs.

15.1 Introduction

15.1.1 Liquid crystal

Liquid crystal (LC) is a delicate phase of matter sharing its properties with isotropic liquid and crystalline solid phase. Since its discovery in 1888 by Austrian botanist Friedrich Reinitzer, LC opened a gateway to vast technological opportunities (Reinitzer, 1888, 1989). LCs possess some characteristic properties of liquids such as fluidity, absence of support shear, and formation of microdroplets, along with some preached properties of solids namely, electrical, optical and magnetic anisotropy, and arrangement of molecules in a periodic fashion. LC molecules consist of aromatic ring attached to aliphatic tail, where the aromatic ring offers the rigidity like solids and the aliphatic tail supplies the fluidity to the LC molecules (Andrienko, 2006). LC has since been known in various industrial applications of photonics, rheology, biology,

optical, and electro-optical elements such as LC displays, attenuators, tunable polarizers, spatial light modulators (SLM), and photonic sensors (Ge et al., 2008; Mirzaei et al., 2011b; Roy et al., 2018).

LC is a unique material displaying an agglomeration of different phases with change in temperature. With decrease in temperature from isotropic liquids, nematic phases emerge following various smectic phases as shown in Figure 15.1.
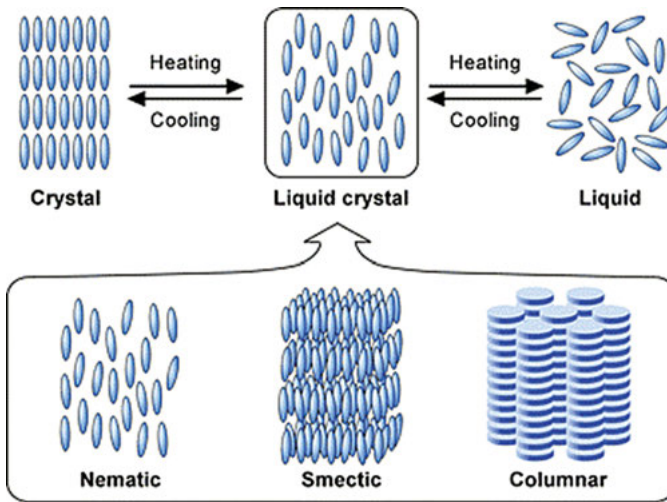
Figure 15.1: Schematic illustration of phase transition behavior and the molecular order of liquid crystal (Kato et al., 2007).

Nematic phase is the simplest type of mesomorphic phase found just below the isotropic phase during the cooling cycle. The transition from nematic to isotropic phase is the first-order phase transition. In nematic LC phase, the molecules possess no positional order and point in the same average direction called director (Friedel et al., 1922; Pershan, 1988). The electro-optical response time of the nematic LC-based display devices is basically governed by the coupling between the applied electric field and the dielectric anisotropy of the LC material itself (Komorowska et al., 2001; Pathak et al. 2018). The performance of nematic LC-based devices depends mainly on physical parameters such as threshold voltage, voltage holding ratio, birefringence, and dielectric anisotropy. In cholesteric LC, a chiral molecule is incorporated into a nematic LC causing a twist in the nematic structure. The direction of the long molecular axes forms an angle with the direction of the axis of molecules in each layer (Kumar, 2001).

The next class of thermotropic LC is constituted by smectic phases, chiefly smectic A and smectic C. The smectic phases represent a higher ordering state in comparison to nematic state. This higher order is instated in smectic phase as the

molecules maintain the orientational order along with tending to align themselves in layers or planes. Hence, the molecules experiences constrained motion within these planes and these individual planes flow past each other. This geometrical configuration of the molecules in smectic phase cultivates various fascinating parameters which have been rigorously employed in device designing. The popular smectic phase is chiral smectic C phase (SmC*), also known as ferroelectric liquid crystals (FLCs).
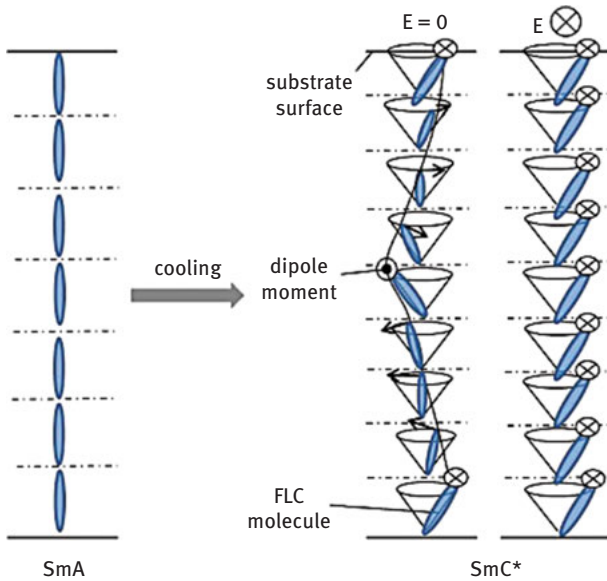
Figure 15.2: *S*chematic model of molecular alignment structure in vertically aligned FLC cell (Furue, 2014).

In chiral smectic C phase (SmC*) phase, the director (average orientation of molecules) of SmC* is tilted at an angle with respect to layer normal. The director rotates from one layer to the next around the layer normal and projects a helical structure as shown in Figure 15.2. The helical axis of SmC* phase is perpendicular to smectic layers. When the molecules in SmC* phases possess a permanent dipole moment perpendicular to their long axes, then this phase exhibits ferroelectric properties and it is generally classified as FLCs (Meyer et al., 1975). FLCs strongly depend on their inherent properties such as spontaneous polarization, rotational viscosity, and tilt angle anchoring fields, and the modification of these characteristics via molecular structure engineering is limited and needs much efforts. To meet such improvements in the electro-optical properties of the FLC materials, insertion of nanomaterials has long been appreciated by the researchers worldwide.

LCs are fascinating soft materials harboring spectacular properties. A weak field or stress or any minute change in temperature can generate huge response in their dielectric, magnetic, and optical properties (Coles et al., 2010). This ability of LCs makes them an ideal candidate for device applications. Major scientific group and research association has been attracted to this flowing beauty emanating such qualitative features (Čopič et al., 2002; Kumar et al., 2009). Early decades in LC research has only witnessed the display applications; however, LC is now playing a major role in fields of other technological advancements (Calucci et al., 2010; Podgornov et al., 2009). With the revolution introduced by nanomaterials, LC has developed a symbiotic affiliation with the nanofield. The LC–nanoparticle science has opened another portal of enthralling research befitting both the worlds of LC and nanoparticles.

15.1.2 Quantum dots

Quantum dots (QDs) have attracted the scientific and industrial sector with their captivating optical properties originating from discrete energy levels. QDs are semiconductor nanoparticles, with diameter of 2–10 nm, combining the elements from groups II and VI, such as CdSe and ZnO, elements from groups III and V, for example, InP, and also elements from groups IV and VI, for example, PbS. When a semiconductor is irradiated with photon energy, group of electrons gains passage to conduction band from valence band, leaving behind bunch of "holes" is in valence band. This bound state of electron–hole pair is referred to as "exciton." The exciton radius of QD is less than the exciton Bohr radius of the material promoting a strong confinement of electron–hole pair, known as quantum confinement effect (Alivisatos, 1996; Mandal et al., 2007). The band gap energy of QDs is correlated to its size as the smallest QD can emit light of longest wavelength and vice versa. Thus, the luminescence intensity can actually be controlled with the size of the QD (Dey et al., 2013).

QDs possess high surface to volume ratio leading to development of surface traps or imperfections. These surface defects carry electronic energy and interferes with the emission wavelength of the QDs. Quantum yield of QDs greatly depend on the radiative efficiency of the QDs. These surface traps capture electron or hole thereby reducing quantum yield of QDs (Mansur, 2010). This negative impact of surface effects can be reduced by combining two or more semiconductor QDs forming a hetero-junction called core–shell QDs. The schematic representation of the band structure in solids has been given in Figure 15.3.

The quantization of energy and size-dependent optical properties of LC have led to various applications in the field of biology (Jamieson et al., 2007), biolabeling (Bruchez Jr. et al., 1998), cancer therapy (Shao et al., 2011), light-emitting diode (Caruge et al., 2008), photovoltaic devices (Semonin et al.), and advance device designing (Guo et al.). Another intriguing attribute of QD is observed in the field of
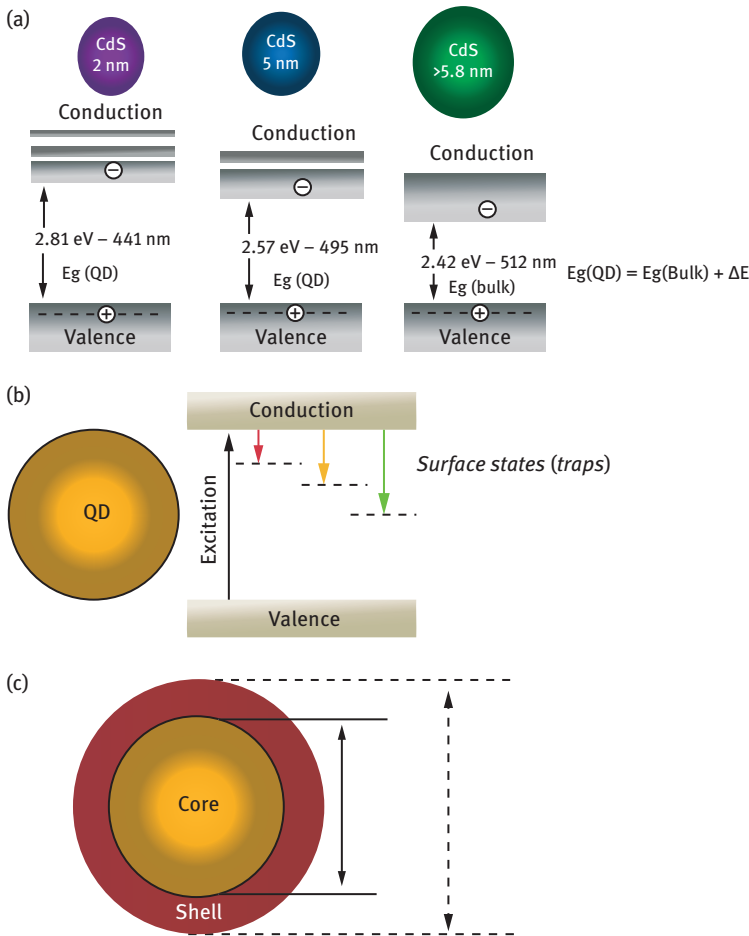
Figure 15.3: A schematic representation of the band structure in solids: (a) quantum confinement effect on changing QD size; (b) surface trap sites with their electronic energy states localized within the QDs bandgap; (c) the electronic structure of a core–shell QD made of two semiconductors forming a heterojunction (core surrounded by the shell of a wider bandgap) (Mansur, 2010).

alternate energy source employing the role of quantized energy (Kongkanand et al., 2008). Recent advances in QD have also leaded to discovery of "QD memory" (Darma et al., 2014). QDs hold efficient optical yield and stable luminescent properties. QD has enveloped the world with its captivating optical properties and paved a way to quantum development of science and technology.

15.2 Guest–host effect: dispersion of quantum dot in liquid crystal

Introduction of any guest entity (particularly for here, QDs) to LC mesogens, the composite system is termed as "Guest–host system" and the interaction between the guest molecule and LC molecules is known as guest–host effect. This dispersion method ensures the eradication of ionic impurities, eradication of unwanted entities, and modifies the host LC with better prospective. Dispersion of QD to LC mesogens induces chemical and photochemical stability, provides wide temperature range platform and optimized optical, and electro-optical parameters required for device fabrication. A slight change in size, type, and concentration of dispersed QD can manipulate the properties of LC at a huge scale. The interaction of LC with QD has attracted the attention of scientists and industries and flamed the architecture of efficient modern nanodevices.

QD contains dense core with loose bonds dangling at the surface. These dangling bonds act as surface traps as well as facilitate interaction with ligand molecules of LC mesogens. The LC molecules surrounding the QD are supported with enticing alignment and optical properties which spread in the presence of external electric field. Hence, researchers investigate the properties of LC host molecules dispersed with QD in presence of external bias voltage, magnetic field, or photonic irradiation. The transfer of energy between QD and LC molecules paves the way for further experimental explorations.

QD-LC composite are most often formulated by adding the predispersed QDs to pristine LC. QDs are predispersed in appropriate solvent such as toluene, carbon tetra chloride, and chloroform (Hirst et al., 2010; Basu and Iannacchione, 2009). This solvent capping ensures the protection of QDs from surface corrosion and decaying in size. The solution is further ultrasonicated and magnetic stirred for approximately 1–4 h above the clearing temperature of the LC in order to gain a uniform dispersion. The QD-dispersed solvent is then evaporated by preheating at solvent sublimation temperature. Now highly dense dispersed mixture at varied concentration is filled into cells through capillary action for principle characterization.

Kamanina et al. have successfully demonstrated the introduction of CdSe/ZnS QD, which has accelerated the temporal response of nematic LC. This efficiency in response time denotes here that the presence of QD has reduced the time required by the molecules to switch from planar to homeotropic orientation under the influences of a bias voltage (Shurpo et al., 2010). Size dependence of QDs highly facilitates PL emission in LC mesogens. Biradar et al. did a commendable analysis highlighting the effect of ZnS QDs on PL characteristics of dispersed FLC (Kumar et al., 2012). Another study of ZnS QD by our group has formented the effect generated on spontaneous polarization of FLC (Vimal et al., 2017). Another hugely explored QD in LC mesogens is CdTe and CdSe QD. Cadmium possessing highly dense nucleus

influences greater density of LC molecules. Many results have been popularized with doping of cadmium-based QD in LC mesogens such as sharp drop in threshold voltage, pronounceable memory effect, enhanced electro-optical response, and size dependent PL emission (Kumar et al., 2010, 2011; Mirzaei et al., 2011a and 2011b; Pandey et al., 2017).
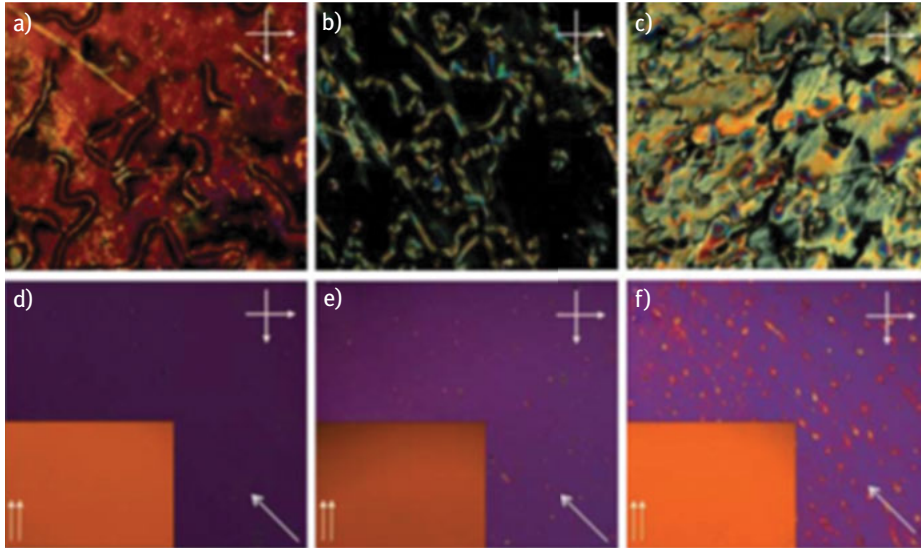
Figure 15.4: POM photomicrographs (crossed polarizers) of LC doped with CdSe QD at (top, (a)–(c): plain glass; bottom, (d)–(f): 4.0 mm anti-parallel planar cell): (a and d) wt%, (b and e) 2.5 wt%, (c and f) 5 wt%. White arrows in the bottom right corner in (d–f) show the rubbing direction of the cell, and the insets in (d)–(f) show the same area with parallel polarizers (Mirzaei et al., 2011).

Polarized optical microscope (POM) photomicrographs for LC dispersed with QDs have been shown in Figure 15.4. The addition of nonmesogenic materials in LC matrix is one of the most successful methodology with a great potential to harness the true energy of host molecule. Presence of QD modifies the electrical, optical, and electro-optical properties of LC host. Pronounceable amount of response can be collected from LC with minute change in shape, size, and interactions ability of QDs. LC nanoscience is befitting to both industrial sector and research community. Commercialization of many devices has solidified the utility of LC in various technological transformations other than only display applications. This transformation greatly signifies to the guest–host effect generated by dispersion of QD in LC substrate indicating toward effective solutions to many miscellaneous problems.

15.3 Effect of dispersion of QDs on properties of liquid crystals

15.3.1 Dielectric polarizability

An insulating material that can be polarized when subjected to externally applied field is known as dielectrics. LCs are pronounced dielectric materials whose property displays modification in presence of even weakly polarizing field. LC materials are further characterized in two prominent categories:

– Polar LC dielectrics: differences in electro-negativity give rise to shift in the charges on the atoms of the molecules resulting in permanent dipole moment
– Nonpolar LC dielectrics: generation of an induced dipole moment in atoms of molecules arising due to the distortion in electronic distributions and nuclear positions of molecules under the influence of external electro field.

A variable electric field induces polarization caps on atoms of the LC molecules resulting in transitory delay in the dielectric parameters of the LC material. This phenomenon governing largely the dielectric properties of LC materials is known as Dielectric Relaxation. Schematic diagram of pristine and QD-dispersed nematics has been shown in Figure 15.5.
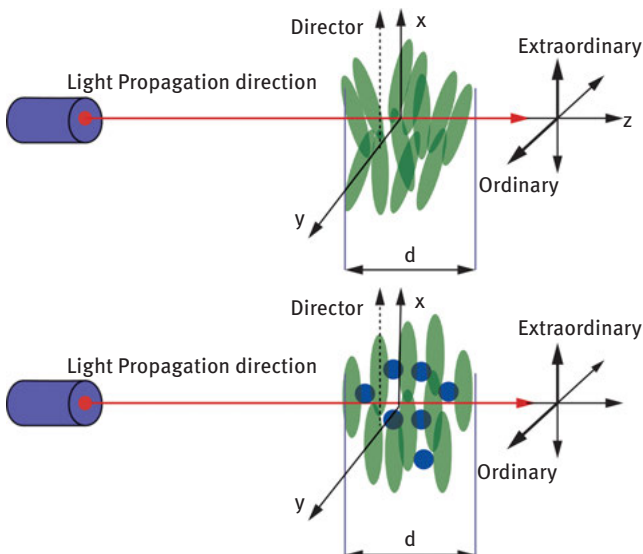
Figure 15.5: Schematic diagram of pristine and QDs dispersed nematics (Tripathi et al., 2017).

15.3.1.1 Effect of dispersion of QDs on dielectric properties of LC

Kumar et al. investigated the induced homeotropic alignment on dispersing CdTe in FLC. The alignment was noticed in ITO portion of sample holders indicating the role played by ITO in mediating an interaction between QD and FLC. The application of bias has also reversed the anisotropy of the host system. This result portrays another important effect generated by QD as the change in anisotropy from homeotropic to planar arrangement is seldom accompanied by sign reversal (Kumar et al., 2011). Dispersion of QD also affects the nematic ordering of the LC host due to the formation of clusters. QD acts as the nucleation site of these clusters surrounded by LC ligands creating a separate ordering other than the normal nematic ordering; this greatly influences the polarizing ability of host molecules (Singh et al., 2014). Tripathi et al. have meticulously demonstrated the influence of core/shell QD on nematic LC through dielectric loss. The study focuses on QD–QD and QD–LC interaction exhibited through shifting in relaxation frequency of the dispersed nematic system. With increase in concentration of QD dopants, the QD–QD interaction dominates the system with suppression of ionic effects resulting in shifting of relaxation frequency to higher frequency spectrum (Tripathi et al., 2017). In another study made by our group, CdSe QD has been dispersed in the FLC. Result drawn from this investigation produces a fascinating feature created by QD in FLC. The nonmesogenic entity perturbs the helical structure of FLC and also brings change in smectic ordering affecting the molecular relaxation (Singh et al., 2015). Behavior of dielectric anisotropy has been shown in Figure 15.6.
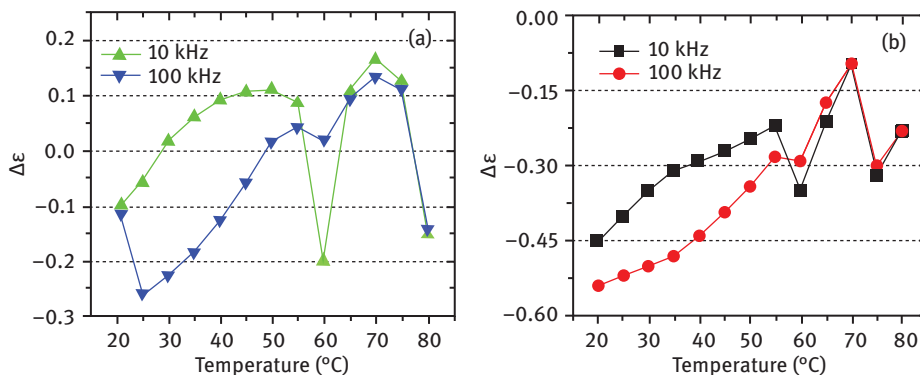
Figure 15.6: (Color online) Behavior of dielectric anisotropy (De) of (a) 1 and (b) 3 wt% CdTe QDs doped CS1026 material with temperature at different (10 and 100 kHz) frequencies. (Mirzaei et al., 2011b).

15.3.2 Electro-optical properties

15.3.2.1 Response time

On application of external electric field, LC molecules experience perturbation in their local domains and try to align themselves in the direction of the field. The switching ability of the LC molecules on presence and absence of electric field is characterized by response time measurement. This transition time experienced by LC molecules in hyperspace on rotating with respect to an electric field applied or removed is classified as rise time and fall time. Rise time is the time required for switching the molecule in the direction of the applied electric field, whereas fall time is the time required by the molecule to attain its initial position on removal of the applied field. Schematic diagram displaying the essential components of electro-optical measurements has been shown in Figure 15.7.
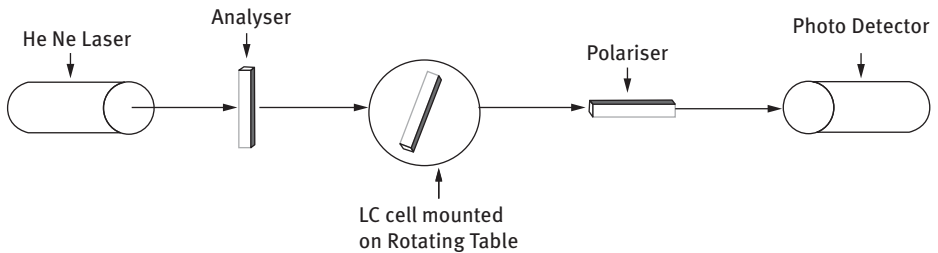
Figure 15.7: Schematic diagram displaying the essential components of electro-optical measurements.

Figure 15.7 shows a typical arrangement of the technical components required for the measurement of the response time of LC molecules. Here, a square wave is applied to the LC cell. The cell is set at angle 45° crossed polarizer and analyzer. Rise time (τ_{on}) and fall time (τ_{off}) is further calculated by the output waveform. Response time measurement mechanism has been shown in Figure 15.8.

In mathematical form, rise time is the time required for the transmittance to rise from 10% to 90% and fall time is the time required for the transmittance to fall from 90% to 10%. The total response time is given by $\tau_{total} = \tau_{rise} + \tau_{fall}$ (Blinov and Chigernov, 1996):

$$\tau_{rise} = \tau_{90} - \tau_{10}$$

$$\tau_{fall} = \tau_{90} - \tau_{10}$$
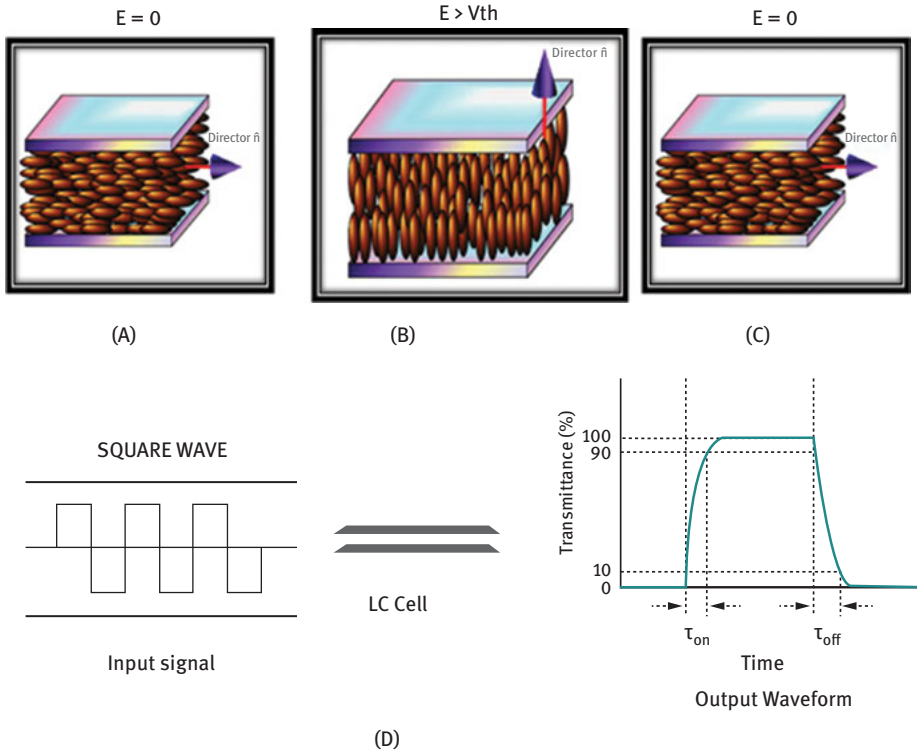
Figure 15.8: Response time measurement mechanism (Blinov et al., 1996).

15.3.2.2 Tilt angle

Smectic phases of LC are defined by primary order parameter known as tilt angle (θ). Chiefly observed in FLCs, tilt angle is the angle made by the director with respect to z-axis in the main geometrical configuration of SmC★ phase. Figure 15.8, describing the electro-optical setup, can be used for the measurement of tilt angle.

The director in FLCs is inclined by an angle θ to either side of the layer normal. A very low frequency (0.2–1 Hz) square wave is applied to the SmC★ phase in order to measure tilt angle. The switching of the molecules can directly be observed in the microscope under the influence of applied field. The director fluctuates between two polar positions with respect to layer normal in presence of external electric field making an angle of 2θ. The perturbation in orientational director is analyzed through the light transmitted through the cell. In brevity, FLCs behave like a uniaxial optical plate with two possible directions of their optical axis corresponding to two different polarities of external electric field separated by an angle of 2θ. The half of the angle between two polar positions gives the value of tilt angle.

15.3.2.3 Spontaneous polarization

As tilt angle is the primary order parameter for SmC⋆ phase, spontaneous polarization garners the position of secondary order parameter for FLCs. FLCs exhibit spontaneous electric polarization due to the property of ferroelectricity that reverses with the polarity of external electric field. The synchronous configuration of chiral molecular symmetry and monoclinic symmetry defines ferroelectricity of the tilted smectic phase. For measuring spontaneous polarization of FLC phase, a triangular input wave is applied on the planar aligned LC cell resulting in whole FLC sample to attain either of the two polarization states, parallel but opposite to the field. A depolarizing field is generated through residual charges accumulating on the opposite polarity electrode. This depolarizing field opposes the applied electric field. A polarization reversal current, generated due to the switching between two polarization states, appears in form of a hump in the output waveform. The area under the polarization reversal hump of the output waveform data gives the value of spontaneous polarization (P_S).

15.3.2.4 Birefringence

Experimental setup for the measurement of birefringence is shown in Figure 15.9. Birefringence is one of the most celebrated optical properties of an anisotropic material. Birefringence varies with temperature in LCs and decreases with increase in temperature and vanishes at isotropic temperature.

The intensity of the transmitted laser light can be given as (Yusuf et al., 2003; West et al., 2005):

$$I_t = \frac{\sin^2 2\theta}{2}(1 - \cos \Delta\varphi)$$

where $\Delta\varphi$ is the phase difference and θ is the angle between the polarizer and optical axis. The birefringence is calculated from the measured intensity:

$$\Delta\varphi = \frac{2\pi}{\lambda}\Delta n d$$

where Δn is the difference of two indices of refraction, d is the thickness of the LC sample cell, and λ is the wavelength of light through the sample. The angle θ is set at 45° to optimize the intensity (Pandey et al., 2014):

$$I = I_0 \sin^2\left(\frac{\Delta\varphi}{2}\right)$$
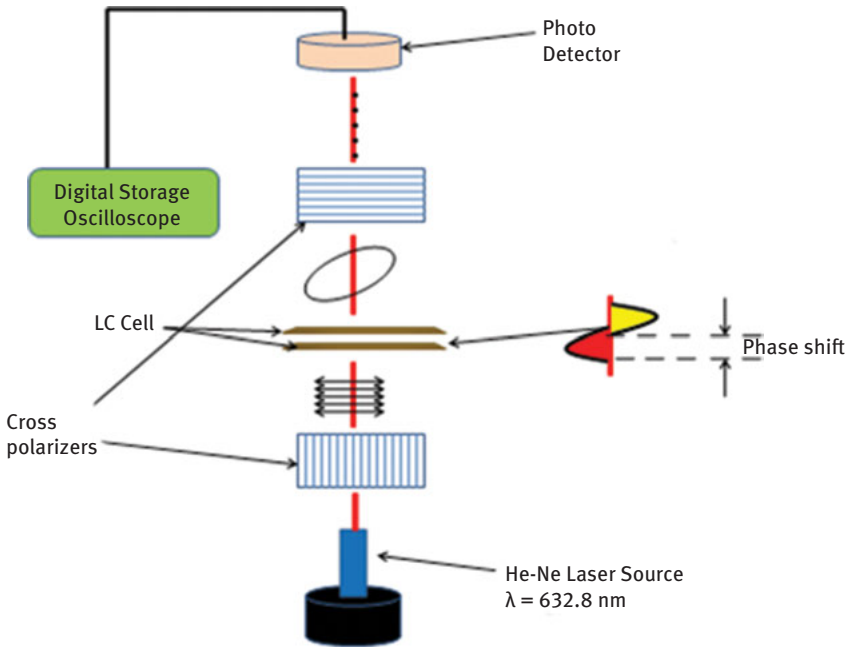
Figure 15.9: Experimental setup for the measurement of birefringence of pure nematic LC and NPs dispersed systems (Wu et al., 1984, appl. Opt., Pathak et al., 2018, *Optoelectronic review*).

$$\Delta\varphi = m\pi + 2\,\sin^{-1}\sqrt{\frac{I - I_{\min}}{I_{\max} - I_{\min}}}\ \text{for}\ m\ =\ 0, 2, 4, \ldots$$

$$\Delta\varphi = (m+1)\pi - 2\,\sin^{-1}\sqrt{\frac{I - I_{\min}}{I_{\max} - I_{\min}}}\ \text{for}\ m\ =\ 1, 3, 5, \ldots$$

where m is number of peaks in voltage–transmittance (VT) curve, I is transmitted light intensity, and $I_{\max}$ and $I_{\min}$ are the maximum and minimum intensities of LCs sample cell, respectively, for pure LC and LC–QD system.

15.3.2.5 Effect of dispersion of QDs on electro-optical properties of LC

With the dispersion of QD to LC phase, a pronounced enhancement has been achieved in electro-optical properties of host molecules. Joshi et al. investigated the dipolar interaction between ZnO and FLC molecules which has resulted in improved optical contrast and low operating voltage of the composite systems. The large dipole moment of ZnO originated from internal bonding geometry, asymmetrical shape, and the surface localized charges. The strain anchoring of

FLC molecules around the dispersed QDs have been attributed for improved electro-optical characteristics (Joshi et al., 2010). The variation of spontaneous polarization is shown in Figure 15.10 and variation in the value of tilt angle is shown in Figure 15.11.
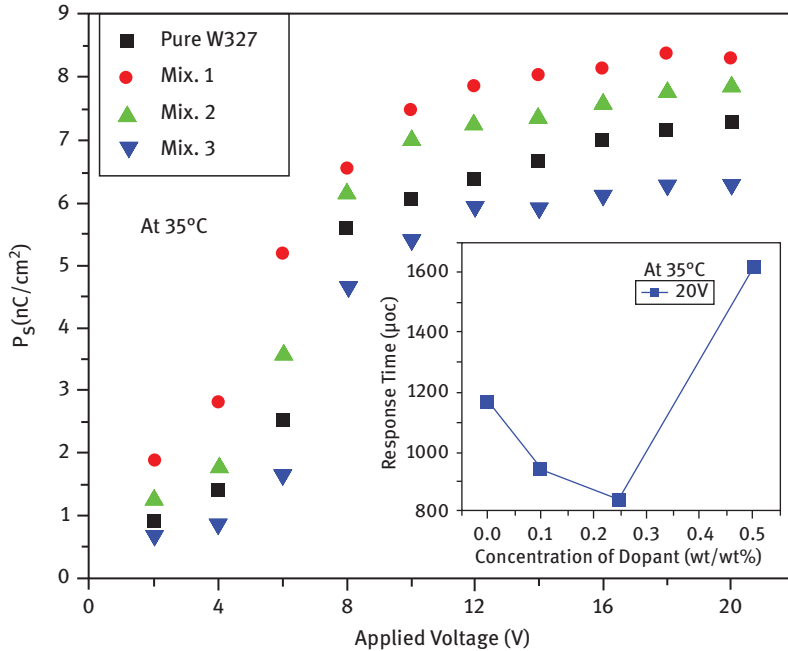
Figure 15.10: The variation of spontaneous polarization with applied voltage for pure and FLC/QD mixtures at 35 °C. The inset shows the variation of response time with concentration of dopant at 20 V and 35 °C. (Kumar et al., 2011).

Addition of CdSe/ZnS has increased the switching time of nematic molecules and the enhancement has been elaborated through a donor–acceptor mechanism (Shurpo et al., 2010). A faster response time achieved on dispersion of ZnO–graphene QDs to LC meta material. The surface-trapping ability that has been discussed here is for capturing the impurity ions on surface of resulting in enhanced response time (Choa et al., 2014). The fluorescent properties of CdSe QDs have been explored with its union in cholesteric matrix. QD manipulates the circularly polarized fluorescence intensity thereby improving the electro-optic switching behavior of cholesteric molecules (Kumar et al., 2016). The investigations conducted by the group discussed the aftermath of CdTe and CdSe QDs in LC mesophases, respectively. The dipole moment plays an important aspect in determination of response time, spontaneous polarization and tilt angle. The intermolecular dipolar interaction between guest and host molecules brings about the variation in the value of electro-optical parameters (Gupta et al., 2013; Kumar et al., 2011).
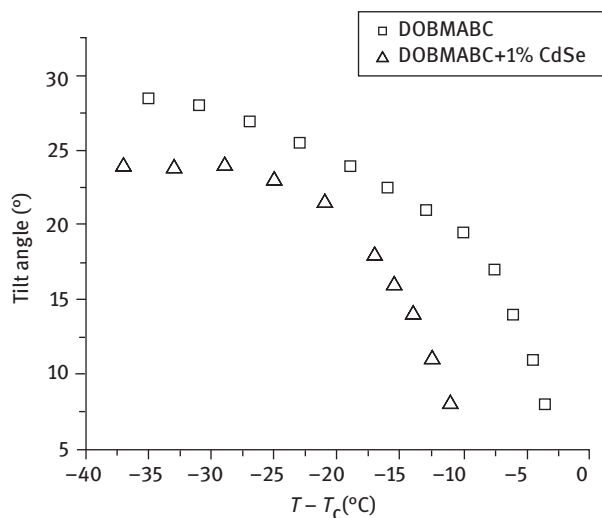
Figure 15.11: Variation in the value of tilt angle (θ) as a function of reduced temperature for pure and 1% CdSe QD-doped DOBAMBC. A square wave of 20 Vpp has been applied at 0.2 Hz. Reduced temperature has been taken relative to SmA–SmC∗ transition temperature of pure DOBAMBC (Gupta et al., 2013).

15.3.3 Optical properties

15.3.3.1 Photoluminescence

When light of sufficient energy is incident on a LC material, energy photons are absorbed followed by creation of electronic excitations states. Within a certain interval of time, when these excitations relax, the electrons return to the ground state. The radiative relaxation experienced by the electron emitting in the form of light is called PL. This light is collected through viable measurement techniques. The collected light imparts information about the photoexcited material, the quality of surface, and interfaces. The PL spectrum can be used to determine electronic energy levels through transition energy schemes. The relative rates of radiative and nonradiative recombination can also be analyzed by PL intensity. Principle characterization includes variation of the PL intensity with external parameters like temperature and applied voltage and its influence on the underlying electronic states of LC molecules.

15.3.3.2 Texture

The flowing crystal obtained its title through the oldest experimental technique, observation of texture through polarizing optical microscope. In order to identify

different phases of LC, polarizing optical microscopy proves to be a vital tool. When sample holder containing LC is placed between crossed polarizer, optical texture is generated due to its birefringent nature and interaction with incident white light. With variation in temperature, the optical texture associated with thermotropic LCs displays visible change. This change is a significant evidence of transition of one LC phase to the other owing to the variation in an intermolecular interaction field in different phases. Effect created by QDs can be witnessed first hand through polarizing micrographs. The texture plays an essential role in detection of alignment of LC sample in cell holders. Complete setup for optical micrograph having polarizing optical microscope and optical texture on computer through interfacing software has been shown in Figure 15.12.

Figure 15.12: Complete setup for optical micrograph having polarizing optical microscope and optical texture on computer through interfacing software.

15.3.3.3 Effect of dispersion of QDs on optical properties of LC

One of the foremost features of QD is size-dependent optical and photoluminescent activity. Optical activity measures the spatial distribution of QD on LC bedspread. CdSe/ZnSe core/shell QDs provide effective alignment and an enhancement is observed in FLC luminescence. In core/shell QDs, the electron and hole are confined together in the core region of doped QDs. This ensures minimal possibility of charge leakage and effective luminescence (Doke et al., 2018). In another investigation, the emission wave function of ZnS QDs constructively overlaps with that of FLC resulting in enhanced PL

intensity. The smectic layering of FLC scatters the electromagnetic light with change in refractive index. Hence, the intensity of the composite system is also obtained to be redshifted (Basu and Iannacchione, 2009). Biradar et al. demonstrated the time-dependent evolution of photoluminescence intensity in FLC material doped with ZnS QDs. A remarkable shift in the emission band is observed in the composite samples with time-depending characteristics. This study has intrigued many possible outcomes and had also laid way for futuristic device applications (Kumar et al., 2013). PL spectra are shown in Figures 15.13 and 15.14.
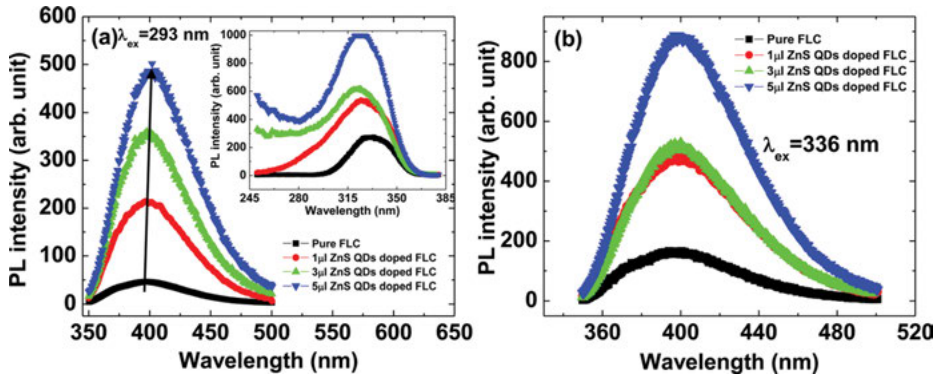
Figure 15.13: (a) Comparison of excitation (inset) and emission spectra (recorded at 293 nm) of FLC material KCFLC 7S doped with different (1, 3, and 5 ll) concentrations of ZnS QDs and (b) emission spectra of FLC material KCFLC 7S doped with different (1, 3, and 5 ll) concentrations of ZnS QDs by exciting with 336 nm. (Basu and Iannacchione, 2009).
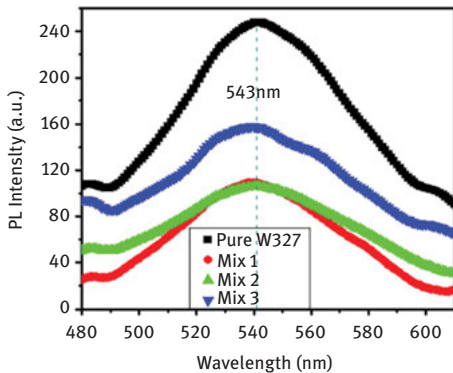
Figure 15.14: The PL spectrum of pure and FLC/QD mixtures at room temperature for the wavelength interval of 480–610 nm (Kumar et al., 2011).

Quenching of PL is another aspect observed by the researchers in LC meso-phases. A strong LC luminescence quenching was observed on dispersing CdSe/ZnS QDs to nematic LC. This significant change in the spectral luminescence properties of an NLC has been referred to indicate an efficient interaction between QDs and LC molecules in the excited state (Kurochkina et al., 2015). CdTe dispersed FLC also de-picts quenching in PL intensity. The reason has been conferred upon the action of the surface properties and the alignment ability imparted by QDs to FLC smectic layering. The disruption in helical conformation of FLC due to the presence of QD has decreased the PL intensity (Kumar et al., 2011). Textures also reveal significant amount of contribution of QD dispersed in LC mesogens. Given below are some micrographs of various LC mesophase dispersed with QDs. POM images are shown in Figures 15.15 and 15.16.
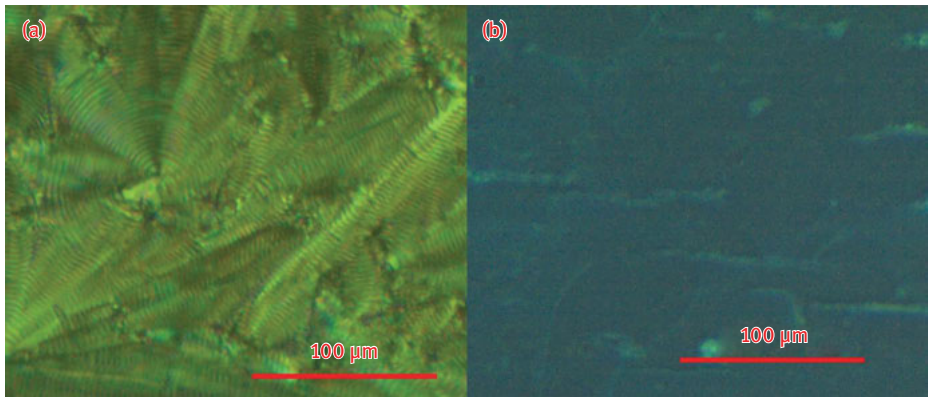
Figure 15.15: POM images of (a) DOBAMBC and (b) CdSe QD-doped DOBAMBC in unaligned plain glass slides under crossed polarizer condition at 75 °C. (Gupta et al., 2013).

15.3.4 Viscoelastic parameters

15.3.4.1 Elastic constants

LC materials exert an elastic restoring torque when a perturbation is inflicted on the mesophases tending to restore to the free energy state or undistorted state of the molecules. Thus, three types of deformations exist in LC, named as splay, twist, and bend linked with elastic constants K_1, K_2, and K_3, respectively. The external pertur-bation or variation in temperature generates fluctuations in director. Hence, each of these elastic constants is temperature and stress dependent. The elastic constant is obtained to be very weak in FLC, hence can be easily modified by dispersion of non-mesogenic dopants (Collings et al., 1990; Singh et al., 2013). Basic types of LC defor-mations are shown in Figure 15.17.
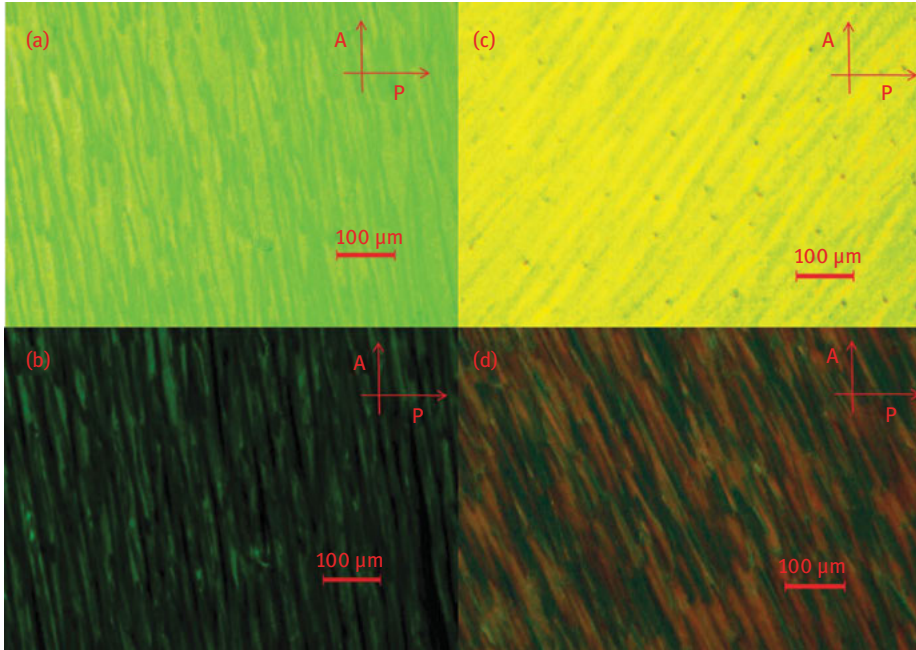
Figure 15.16: POM images of DOBAMBC material doped with 0% and 1% wt/wt CdSe QDs (a), (c) bright states and (b), (d) dark state at 75 °C, respectively. The bright and dark state has been taken by rotating the sample cell under polarizing microscope under crossed polarizer condition. (Gupta et al., 2013).
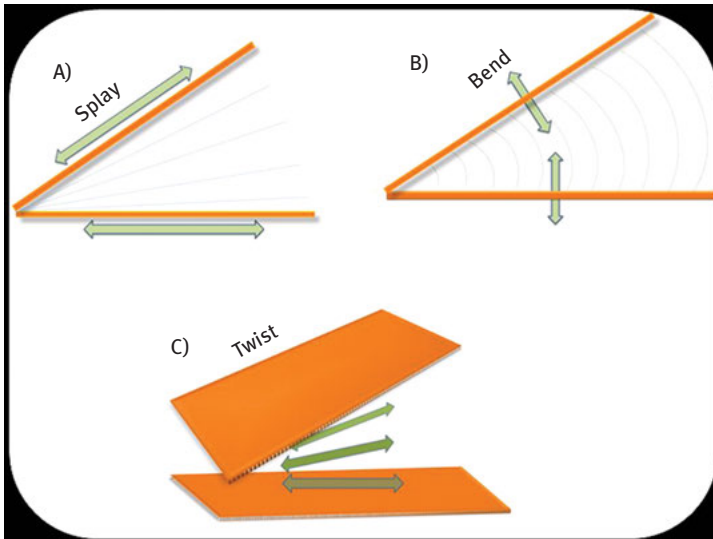
Figure 15.17: Basic types of liquid crystal deformations: (a) splay, (b) bend, and (c) twist. The figure has been borrowed from the Internet.

15.3.4.2 Rotational viscosity

LC materials are anisotropic fluids exhibiting flow and viscous characteristics. The flow ability of the LC is governed by three viscosity coefficients (γ_θ, γ_ϕ, γ_l). y_θ is the tilt fluctuation, y_ϕ denotes phase fluctuation, and y_l refers to the molecular reorientation around the long molecular axis respectively. The temporal response of the LC materials also depends upon the value of rotational viscosity under the influence of external field.

Elastic constants and rotational viscosity together constitute the molecular dynamics of the systems widely elaborating the geometrical configurational and hyperspace constraints imposed upon the mesogenic phases. Influence of QD is vividly studied on these viscoelastic parameters as they signify the sustenance of the materials alginates the external environment.

15.3.4.3 Effect of dispersion of QDs on viscoelastic properties of LC

An increase in rotational viscosity has been observed on doping CdSe QDs to FLC. The increment has been subjected to the variation in relaxation strength of the FLC with dispersion of QDs. The perturbation of helical conformations arises from such variation in which the molecules do not reach their de-excited state even on removal of field (Shukla et al., 2014). The dispersion of $Cd_{1-x}Zn_xS/ZnS$ core/shell QDs in FLC displays decrease in the rotational viscosity with the variation of applied voltage at 80°C temperature is shown in Figure 15.18.

The decrease in the value rotational viscosity of the composite system is accounted by the molecular dynamics between QD and FLC molecules. The rotation viscosity governed by phase fluctuation is rigorously investigated here as the *Z*th component of rotational viscosity governing the molecular dynamics depends upon the surface geometry of FLC and concentrations of QDs (Agrahari et al., 2017; Lagerwall et al., 1999).

15.4 Device applications

15.4.1 Voltage-modulated optical waveguide

Optical fibers filled with LCs give interesting controllable behavior to the optical fibers. LC can be easily modulated by external stress and can call huge response with a tint of disturbance in local environment. Piegdon et al. have developed microdisks made from GaAs with embedded InAs QDs. The designed disks are immersed in the nematic LC. The embedded QDs serve as emitters feeding the optical modes of the
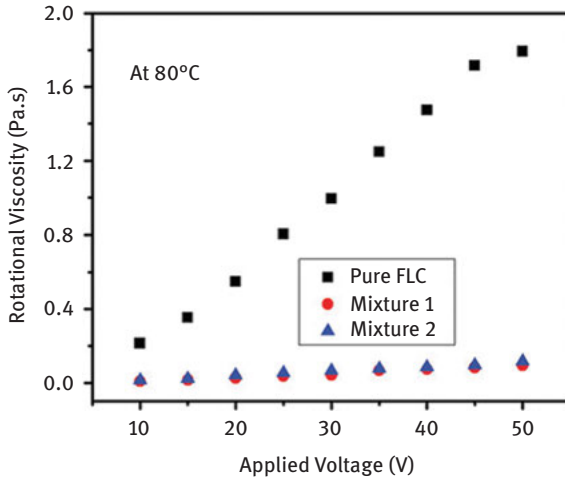
Figure 15.18: The variation of rotational viscosity with change in applied voltage for pure FLC and QDs dispersed FLC system (Agrahari et al., 2017).

LC filled photonic cavity. As the temperature changes, the LC experiences phase transition from the isotropic to the nematic state. This transition energy is used as an effective tuning mechanism of the photonic modes of the cavity (Piegdon et al., 2010). Application of LC waveguide structure includes low-power photonic devices (Asquini et al., 2018). LC based photonic devices have engrossed attention of researchers in the past few years due to effective electro-optic effect that employs application of small voltages to control light in optical channels. LC can be used as either core or an over layer that are electrically modulated by external voltage. The application of LC in voltage modulated optical waveguides permits the manufacturing of various kinds of photonic devices such as integrated optical switches, and tunable optical filters (Davis et al.). Low-driving power levels and manufacturing cost are benefited to the consolidated and reliable flat panel display technology. The nonlinear optical effect in LC discloses promising scenario for low-power optical devices (Davis et al.).

Waveguides have found profound application in the switching devices (Bryan-brown et al., 1993; Rahlves et al., 2016). One of the classified waveguides involves grating waveguide structure that is attractive as a switching element. LC grating waveguide structure suffers from disorderness in the surface regions due to surface defects. These defects will be overcome through the insertion of QDs. The incorporation of QDs in LCs provides improved order as well as alignment in LC which effectively enhances the optical properties of LC. Such LC-QD grating waveguide will be applicable in fast optical switches in reflection or transmission.

15.4.2 Optical telecommunication

Padilla et al. observed that the incorporation of LC in novel metamaterial can be developed into electronically tunable metamaterial absorbers. The wavelength spectrum covered experimentally is of terahertz regime. Insertion of active LC into confined locations within the metamaterial unit cell can modify the absorption by 30% at 2.62 THz bandwidth (Chen et al., 2013). Electro-optic laser scanner providesa wide field of view, high speed of operation, simple and compact design with low cost etc. The promising application for electro-optic scanner is new free space optical FSO components that enable new multi access FSO networks. EO scanner provides high optical power capability, rapid scanning, extremely wide angular coverage, high resolution, and low cost. The novel architecture design of LC-QD waveguide architecture overcomes the shortcomings of EO beam steering as in the waveguide plane, prism-shaped patterned electrode is made. This enables the tuning of index inside the prism with respect to surrounding areas. The tuning at the nonnormal interface follows the Snell's law of refraction. The addition of prism in series helps in building deflection.

The increased attention of researchers in optical communication, data/signal/ image processing, nonlinear optics, optical sensing has diverted the route to non-display application of LCs. The exclusive crystalline phase characterized by partial ordering and large anisotropy of LC allows the realization of external modulation of optical properties of LC-based devices that make LCs suited for both optical communication and optical sensing system.

15.4.3 Signal processing and scanning systems

Scanning systems have been investigated in cholesteric LC dispersed with QDs. Hirst et al. have shown that the clustered QD in the cholesteric helix can emanate strong coupling of signals when the system is bombarded with electromagnetic photons (Rodarte et al., 2015). The hybrid LC functionalized semiconductor nanoparticles or QDs encase strong attachment. The study conducted by Anczykowska et al. have initiated the innovation of possibly faster and more efficient holographic materials. Such material can be efficiently harnessed for dynamic data-processing systems (Anczykowska et al., 2012).

The advancement in LC and VLSI technology have enabled multiphase SLM. The attention grasping features of SLM is utilized potentially in optical telecommunication applications based on LC/SLMs (Ahderom et al.). The combination of LC and VLSI technologies can produce high-performance LC spatial light modulators (LC-SLMs) that facilitate the insight of key dynamic optical components for next generation reconfigurable optical telecommunication systems. The ability of LC-SLMs to comprehend optical beam positioning as well as temporal and spatial beam shaping and topologies of LC-SLM-based dynamic optical components, such as

optical switch, dynamic spectral equalizer, and tunable optical filter. Fiber-coupled electro-optical light modulator uses Mach–Zehnder interferometer principle (Hsiao and Yu) in waveguides that enables to transmit signals with high modulation frequencies up to GHz range, that is, VIS and IR spectral range. LC-based SLM modulate light output based on specific fixed spatial pattern (pixel) and projecting light controlled in either amplitude only, phase only or both. This finds application in liquid crystal display (LCD) projectors.

15.4.4 Storage devices

QD-dispersed LC has largely been exploited for development of memory devices. QD perturbs the helical pitch of the FLC. This perturbation is accelerated in presence of external electric field. However, on removal of the field, the molecule does not reach to its ground state immediately, persisting the excited energy state. This unceasing reminiscence of the molecular energy state is deciphered as memory-retaining ability of the mesogenic phase. This ability is highly accelerated in presence of QD dispersion as reported by various research groups (Vimal et al., 2017). The addition of QDs into LC causes faster response time and has been effectively employed in data storage devices and security code system (Pandey et al., 2017). The trapping of impurity ions on the surface of QDs are responsible for development of ionic impurity-free memory devices. QDs have large data-storage capacity due to its persistent hole-burning effect and low dark current infrared photo detection and imaging.

The attempt to use LCs QDs for electronic data storage have had restricted success. In reliable recording and rewriting data, researchers have figured the way to control the orientation of LC molecules by chemical manipulation through rubbing in one direction in order to align molecules in preferred direction. This alignment has been further improved by the inclusion of QDs into LCs. The application of electric field can align LC molecules in a polymer and store data on QDs which can be erased and used again.

15.5 Conclusion

Dispersion of QDs in liquid crystalline materials is attracting most of researchers nowadays because of its vast applications. Size constrained and surface traps supported QDs augments the development of LC-driven novel photonic devices. The chapter focuses in the basic aspects of LC and QD and the effect generated by their union. A detail discussion has been entailed upon each primary property such as dielectric polarization, rotational viscosity, elastic constant, optical micrographs, and

luminescence study followed by the present scenario of the research in that particular property. Several electro-optical, optical, and dielectric parameters can be enhanced by dispersing the QDs into LCs. Now, if talk about electro-optical parameters, then we can say that response time, spontaneous polarization, tilt angle, and several properties of the LC can be enhanced by doping of QDs. Birefringence is also very important parameter to measure and we can tune it by doping of QDs into nematic LCs. Optical features are also important in LC-based devices, therefore, we can also perform optical studies for QDs–LCs composite systems. PL can be enhanced which has very much applicability in luminescent devices. UV absorbance and Fourier-transform infrared spectroscopy studies may also help to understand the optical nature of these materials. Dielectric parameters are also very much significant for this system. Relative permittivity, tan delta, conductivity, and several other parameters can be measured to understand these systems. These QDs–LCs composite systems have many applications in voltage-modulated optical waveguide, optical telecommunication, signal processing and scanning systems, and storage devices. The QDs-dispersed FLC plays a major role to enhance memory effects by trapping the impurity ions under the application of bias voltage. These studies would be helpful to provide an idea for ionic impurity free memory devices (storage devices) having microsecond optical response and in security coded transmission. Fast optical response can be achieved by the dispersion of QDs into LCs. Generally all LCDs requires fast response time, therefore this system may play an very important role to enhance the LCDs features. Enhanced birefringence can also be achieved by QD–NLC system and this enhanced birefringence has many applications in flat panel displays. Therefore, due to all these important applications, the study of QD-dispersed LCs is growing very fast all over the world. The application of QDs as dopants for enhancing the LC properties is gaining more attention due to the nova quantum confinement effect of the former. LC–QD composite systems can be a breakthrough for innovation of new LC devices with faster switching time and less energy consumption for the next generation of futuristic technology. This can change the future of upcoming displays based on LCs.

References

Agrahari, K., Pathak, G., Katiyar, R., Yadav, G., Vimal, T., Pandey, S., Singh, D.P., Gupta, S.K., Manohar, R. (2017). Effect of $Cd_{1-x}Zn_xS/ZnS$ core/shell quantum dot on the optical response and relaxation behaviour of ferroelectric liquid crystal. Molecular Crystals and Liquid Crystals, 652.

Ahderom, S., Raisi, M., Lo, K., Alameh, K.E., Mavaddat, R., Applications of liquid crystal spatial light modulators in optical communications, Opto-VLSI Group – Centre for Very High Speed Microelectronic Systems.

Alivisatos, A.P. (1996). Semiconductor clusters, nanocrystals and quantum dots. Science, 271.

Anczykowska, A., Bartkiewicz, S., Nyk, M., Mysliwiec, J. (2012). Study of semiconductor quantum dots influence on photorefractivity of liquid crystals. Applied Physics Letters, 101, 101107.

Andrienko, D. (2006), Introduction to Liquid Crystals, International Max Planck Research School, Bad Marienberg.

Asquini, R., Chiccoli, C., Pasini, P., Civita, L., d'Alessandro, A. (2018). Low power photonic devices based on electrically controlled nematic liquid crystals embedded in poly(dimethylsiloxane). Liquid Crystals, 45.

Basu, R., Iannacchione, G.S. (2009). Evidence for directed self assembly of quantum dots in a nematic liquid crystal. Physical Review E, 80, 010701–4(R).

Blinov, L.M., Chigernov, V.G. (1996). Electro-Optic Effects in Liquid Crystal Materials, Springer-Verlag, New York.

Bruchez Jr., M., Moronne, M., Gin, P., Weiss, S., Paul Alivisatos, A. (1998). Semiconductor nanocrystals as fluorescent biological labels. Science, 281.

Bryan-brown, G.P., Sambles, J.R. (1993). Grating coupled liquid crystal waveguide. Liquid Crystal, 13(5), 615–621.

Calucci, L., Ciofani, G., Marchi, D.D., Forte, C., Menciassi, A., Menichetti, L., Positano, V. (2010). Boron Nitride Nanotubes as T2 Weighted MRI Contrast Agents. The Journal of Physical Chemistry Letters, 1, 2561.

Caruge, J.M., Halpert, J.E., Wood, V., Bulovic, V., Bawendi, M.G. (2008). Colloidal quantum-dot light-emitting diodes with metal-oxide charge transport layers. Nature Photonics, 2.

Chen, W.-C., Padilla, W.J. (2013). Liquid crystal tunable metamaterial absorber David Shrekenhamer. PRL, 110, 177403.

Choa, M.J., Gyu Parka, H., Chang Jeonga, H., -Won Leea, J., Junga, Y.H., Kima, D.-H., Kima, J.-H., Leeb, J.-W., ShikSeoa, D. (2014). Superior fast switching of liquid crystal devices using graphene quantum dots. Liquid Crystals, 41, 761–767.

Coles, H., Morris, S. (2010). Liquid-crystal lasers. Nature Photonics, 4, 676.

Collings, P. (1990). Liquid Crystals: Nature's Delicate Phase of Matter, Princeton University Press, Princeton, NJ.

Čopič, M., Maclennan, J.E., Clark, N.A. (2002). Structure and dynamics of ferroelectric liquid crystal cells exhibiting thresholdless switching. Physical Review E, 65, 021708.

Darma, Y., Rusydi, A. (2014). Quantum dot based memory devices: current status and future prospect by simulation perspective. AIP Conference Proceedings, 1586, 20.

Davis, S.R., Farca, G., Rommel, S.D., Johnson, S., Anderson Vescent, M.H. Photonics Inc., 4865 E. 41st Ave., Denver CO 80216; Liquid Crystal Waveguides: New Devices Enabled by >1000 Waves of Optical Phase Control.

Dey, S.C., Nath, S.S. (2013). Size-dependent photoluminescence and electroluminescence of colloidal CdSe quantum dots. International Journal of Nanoscience, 12(2), 1350013.

Doke, S., Sonawane, K., Raghavendra Reddy, V., Ganguly, P., Mahamuni, S. (2018). Low power operated highly luminescent ferroelectric liquid crystal doped with CdSe/ZnSe core/shell quantum dots. Liquid Crystals.

Friedel, G. (1922). Annales de Physique, 18, 273.

Furue, H., Horiguchi, T., Yamamichi, M., Oka, S., Komura, S., Kobayashi, S. (2014). Fabrication of vertical alignment in ferroelectric liquid crystals for display application. Japanese Journal of Applied Physics, 53(09), PC03.

Ge, Z., Wu, S.T. (2008). Nanowire grid polarizer for energy efficient and wide-view liquid crystal displays. Applied Physics Letters, 93, 121104. doi:10.1063/1.2988267..

Guo, F.M., You, H., Gu, W.Q., Han, D.D., Zhu, Z.Q. (8194). Weak-light automatic readout collection and display on the resonant-cavity-enhanced quantum dot photoelectric sensor. Proceedings of SPIE.

Gupta, S.K., Singh, D.P., Tripathi, P.K., Manohar, R., Varia, M., Sagar, L.K., Kumar, S. (2013). CdSe quantum dot-dispersed DOBAMBC: an electro-optical study. Liquid Crystals, 40(4), 528–533.

Hirst, L.S., Kirchhoff, J., Inman, R., Ghosh, S., Chien, L.-C. (2010). Quantum dot self-assembly in liquid crystal media. Proceedings of SPIE, 7618, 76180F.

Hsiao, L.-T., Yu, C.-P. (2012). Mach-Zehnder Fiber Interferometers Based on Liquid-filled Photonic Crystal Fibers.

Jamieson, T., Bakhshi, R., Petrova, D., Pocock, R., Imani, M., Seifalian, A.M. (2007). Biological applications of quantum dots. Biomaterials, 28, 4717–4732.

Joshi, T., Kumar, A., Prakash, J., Biradar, A.M. (2010). Low power operation of ferroelectric liquid crystal system dispersed with zinc oxide nanoparticles. Applied Physics Letters, 96, 253109.

Kato, T., Hirai, Y., Nakaso, S., Moriyama, M. (2007). Liquid-Crystalline Physical Gels, 36(12), 1845–2128.

Komorowska, K., Pawlik, G., Mitus, A.C., Miniewicz, A. (2001). Electro-optic phenomena in nematic liquid crystals studied experimentally and by Monte-Carlo simulations. Journal of Applied Physics, 90, 1836.

Kongkanand, A., Tvrdy, K., Takechi, K., Kuno, M., Kamat, P.V. (2008). Quantum dot solar cells, tuning photoresponse through size and shape control of CdSe-TiO$_2$ architecture. Journal of the American Chemical Society, 130, 4007–4015.

Kumar, A., Biradar, A.M.. (2011). Effect of cadmium telluride quantum dots on the dielectric and electro-optical properties of ferroelectric liquid crystals, 041708.

Kumar, A., Prakash, J., Deshmukh, A.D., Haranath, D., Silotia, P., Biradar, A.M. (2012). Applied Physics Letters, 100, 134101.

Kumar, A., Prakash, J., Khan, M.T., Dhawan, S.K., Biradar, A.M. (2010). Memory effect in cadmium telluride quantum dots doped ferroelectric liquid crystals. Applied Physics Letters, 97, 163113.

Kumar, A., Prakash, J., Mehta, D.S., Biradar, A.M., Haase, W. (2009). Applied Physics Letters, 95, 023117.

Kumar, A., Silotia, P., Biradar, A.M. (2011). Sign reversal of dielectric anisotropy of ferroelectric liquid crystals doped with cadmium telluride quantum dots. Applied Physics Letters, 99, 072902.

Kumar, A., Tripathi, S., Deshmukh, A.D., Haranath, D., Singh, P., Biradar, A.M. (2013). Time evolution photoluminescence studies of quantum dot doped ferroelectric liquid crystals. Journal of Physics D: Applied Physics, 7 46 195302.

Kumar, R., Raina, K.K. (2016). Optical and electrical control of circularly polarised fluorescence in CdSe quantum dots dispersed polymer stabilised cholesteric liquid crystal shutter. Liquid Crystals, 43(7), 994–1001.

Kumar, S. (2001). "Liquid Crystals: Experimental Study of Physical Properties and Phase Transitions", Cambridge University Press, UK.

Kumar, S., Sagar, L.K. (2011). CdSe quantum dots in a columnar matrix. Chemical Communications, 47, 12182–12184.

Kurochkina, M.A., Konshina, E.A. (2015). Luminescence quenching of nematic liquid crystal upon doping with CdSe/ZnS quantum dots. Optics and Spectroscopy, 118(1).

Lagerwall, S.T. (1999), Ferroelectric and antiferroelectric liquid crystals, Wiley-VCH, New York, NY.

Mandal, A., Nakayama, J., Tamai, N., Biju, V.P., Isikawa, M. (2007). Optical and dynamic properties of water-soluble highly luminescent CdTe quantum dots. The Journal of Physical Chemistry B, 111, 12765–12771.

Mansur, H.S. (2010). Quantum dots and Nanocomposites, Vol. 2, John Wiley & Sons, Inc.

Meyer, R.B., Liebert, L., Strzelecki, L., Keller, P. (1975). Journal De Physique Letters, 36, L69.

Mirzaei, J., Urbanski, M., Yu, K., Kitzerow, H.-S., Hegmann, T. (2011a). Nanocomposites of a nematic liquid crystal doped with magic-sized CdSe quantum dots. Journal of Materials Chemistry, 21, 12710.

Mirzaei, J., Urbanski, M., Yu, K., Kitzerowb, H.-S., Hegmann, T. (2011b). Nanocomposites of a nematic liquid crystal doped with magic-sized CdSe quantum dots. Chem, 21, 12710–12716.

Pandey, S., Singh, D.P., Agrahari, K., Srivastava, A., Czerwinski, M., Kumar, S., Manohar, R. (2017). CdTe quantum dot dispersed ferroelectric liquid crystal: transient memory with faster optical response and quenching of photoluminescence. Journal of Molecular Liquids, 237, 71–80. http://dx.doi.org/10.1016/j.molliq.2017.04.035.

Pandey, S., Vimal, T., Singha, D.P., Gupta, S.K., Pathak, G., Katiyar, R., Manohar, R. (2016). Core/shell quantum dots in ferroelectric liquid crystals matrix: effect of spontaneous polarisation coupling with dopant. Liquid Crystals, 43, 980–993.

Pathak, G., Katiyar, R., Agrahari, K., Srivastava, A., Dabrowski, R., Garbat, K., Manohar, R. (2018). Analysis of birefringence property of three different nematic liquid crystals dispersed with TiO2 nanoparticles. Opto-Electronics Review, 26, 11–18.

Pathak, G., Agrahari, K., Yadav, G., Srivastava, A., Strzezysz, O., Manohar, R. (2018). Tuning of birefringence, response time, and dielectric anisotropy by the dispersion of fluorescent dye into the nematic liquid Crystal. Applied Physics A, 124(7), 463–471.

Pershan, P.S. (1988). "Structure of Liquid Crystal Phases", World Scientific, New Jersey.

Piegdon, K.A., Declair, S., Förstner, J., Meier, T., Matthias, H., Urbanski, M., Kitzerow, H.-S., Reuter, D., Wieck, A.D., Lorke, A., Meier, C. (2010). Tuning quantum-dot based photonic devices with liquid crystals. Optics Express, 18(8), 7946.

Podgornov, F.V., Suvorova, A.M., Lapanik, A.V., Haase, W. (2009). Chemical Physics Letters, 479, 206.

Rahlves, M. (2016). Flexible and low-cost production of waveguide based integrated photonic devices. Procedia Technology, 26, 309–315.

Reinitzer, F. (1989). Liquid Crystals, 5(7).

Reinitzer, F. (1888). Wiener MonatscherChemie, 9, 421.

Rodarte, A.L., Cisneros, F., Hein, J.E., Ghosh, S., Hirst, L.S. (2015). Quantum dot/liquid crystal nanocomposites in photonic devices. Photonics, 2, 855–864.

Roy, A., Agrahari,K., Srivastava, A., Manohar, R. (2018). Plasmonic resonance instigated enhanced photoluminescence in quantum dot dispersed nematic liquid crystal. Liquid Crystals, 46(8), 1224–1230.

Semonin, O.E., Luther, J.M., Beard, M.C. (2012). Quantum dots for next generation photovoltaic's. Materials Today, 15(11), 508–515.

Shao, L., Gao, Y.F., Yan, F. (2011). Semiconductor quantum dots for biomedicial applications. Sensors, 11, 11736–11751.

Shukla, R.K., Galyametdinov, Y.G., Shamilov, R.R., Haase, W. (2014). Effect of CdSe quantum dots doping on the switching time, localised electric field and dielectric parameters of ferroelectric liquid crystal. Liquid Crystals, 41(12), 1889–1896.

Shurpo, N.A., Vakshtein, M.S., Kamanina, N.V. (2010). Effect of CdSe/ZnS semiconductor quantum dots on the dynamic properties of nematic liquid-crystalline medium. Technical Physics Letters, 36(4), 319–321.

Singh, D.P., Gupta, S.K., Pandey, K.K., Yadav, S.P., Varia, M.C., Manohar, R. (2013). Journal of Non-Crystalline Solids, 363, 178.

Singh, U.B., Dhar, R., Pandey, A.S., Kumar, S., Dabrowski, R., Pandey, M.B. (2014). Electro-optical and dielectric properties of CdSe quantum dots and 6CHBT liquid crystals composites. AIP Advances, 4, 117112.

Singha, D.P., Gupta, S.K., Pandey, S., Vimal, T., Tripathi, P., Varia, M.C., Kumar, S., Manoharand, S., Manohar, R. (2015). Influence of CdSe quantum dot on molecular/ionic relaxation phenomenon and change in physical parameters of ferroelectric liquid crystal. Liquid Crystals.

Tripathi, P.K., Joshi, B., Singh, S. (2017). Pristine and quantum dots dispersed nematic liquid crystal: impact of dispersion and applied voltage on dielectric and electro-optical properties. Optical Materials, 69.

Vimal, T., Pandey, S., Singh, D.P., Gupta, S.K., Agrahari, K., Kumbhakar, P., Kole, A.K., Manohar, R. (2017). ZnS quantum dot induced phase transitional changes and enhanced ferroelectric mesophase in QDs/ FLC composites. Physical Review E, 100, 134–142. 83.

West, J.L., Zhang, G., Glushchenko, A. (2005). "Fast birefringent mode stressed liquid crystal". Applied Physics Letters, 86, 031111–3.

Wu, S.T., Efron, U., Hess, L.D. (1984). Birefringence measurements of liquid crystals. Applied Optics, 23, 3911–3915.

Yusuf, Y., Sumisakiand, Y., Kai, S. (2003). Birefringence measurement of liquid single crystal elastomer swollen with low molecular weight liquid crystal. Chemical Physics Letters, 382, 198–202.

Index

https://doi.org/10.1515/9783110584370-016